

FHWA/IN/JTRP-2007/5

Final Report

**SAW-CUTTING GUIDELIENS FOR CONCRETE
PAVEMENTS: EXAMINING THE
REQUIREMENTS FOR TIME AND DEPTH OF
SAW-CUTTING**

**Kambiz Raoufi
Tony Their
W. Jason Weiss
Jan Olek
Tommy Nantung**

January 2009

Final Report
FHWA/IN/JTRP-2007/5

Saw-Cutting Guidelines for Concrete Pavements:
Examining the Requirements for Time and Depth of Saw-Cutting

By

Kambiz Raoufi
Graduate Research Assistant

Tony Thier
Graduate Research Assistant

W. Jason Weiss
Principal Investigator
Professor of Civil Engineering

Jan Olek
Co-Principal Investigator
Professor of Civil Engineering

Tommy E. Nantung
Co-Principal Investigator
Section Manager of INDOT Office of Research and Development

Joint Transportation Research Program
Project No. 656-1284-0289
File No. 5-8-39
SPR-2863

Conducted in Cooperation with the
Indiana Department of Transportation and
the Federal Highway Administration

The contents of this report reflect the views of the authors who are responsible for the facts and accuracy of the data presented herein. The contents do not necessarily reflect the official views or policies of the Indiana Department of Transportation and Federal Highway Administration. This report does not constitute a standard, specification, or regulation.

Purdue University
West Lafayette, Indiana
January 2009

1. Report No. FHWA/IN/JTRP-2007/5	2. Government Accession No.	3. Recipient's Catalog No.	
4. Title and Subtitle Saw-Cutting Guidelines for Concrete Pavements: Examining the Requirements for Time and Depth of Saw-Cutting		5. Report Date January 2009	
7. Author(s) Kambiz Raoufi, Tony Their, Jason Weiss, Jan Olek, Tommy Nantung		6. Performing Organization Code 8. Performing Organization Report No. FHWA/IN/JTRP-2007/5	
9. Performing Organization Name and Address Joint Transportation Research Program 1284 Civil Engineering Building Purdue University West Lafayette, IN 47907-1284		10. Work Unit No. 11. Contract or Grant No. SPR-2863	
12. Sponsoring Agency Name and Address Indiana Department of Transportation State Office Building 100 North Senate Avenue Indianapolis, IN 46204		13. Type of Report and Period Covered Final Report	
15. Supplementary Notes Prepared in cooperation with the Indiana Department of Transportation and Federal Highway Administration.		14. Sponsoring Agency Code	
16. Abstract Joints are placed in portland cement concrete pavements (PCCP) to control random cracking. These joints provide a weakened plane that enables a crack to form in a controlled manner, relieving residual stresses that develop when thermal, hygral, or hydration movements are resisted by subgrade and adjoining pavement. While the concept of creating a weakened plane through saw-cutting is straightforward, determining the time and depth of the saw-cut has proven to be complicated. The goal of this project was to reduce the risk for joint raveling and random cracking. Specifically, this project has focused on: developing a procedure for determining the appropriate saw-cutting time window for typical pavements constructed in the state of Indiana, determining the depth of the saw-cut that minimizes the risk of micro-cracking and random crack development, and developing tools and training materials for paving contractors and state inspectors that aid in implementing the findings of this study in concrete pavements. Toward this end the project was divided into three phases. The first phase of the project consisted of shadowing five pavement projects in Indiana. From these field investigations practical information was gained which was useful in developing the laboratory testing program. The second phase of this work involved in the development of the laboratory testing program. This phase in large part was involved in the development and commissioning of a new tensile wedge testing approach to determine the early age properties of concrete. Finally, finite element simulations were performed to simulate the early-age behavior of pavements constructed under a variety of saw-cutting sequences, environmental conditions. A strength reduction factor was computed based on the depth of the saw-cut. It was shown that the time of the saw-cut introduction needs to occur before the residual stress divided by the product of the strength reduction factor and tensile strength was equal to unity. It was also shown that shallower saw-cut depths were more prone to construction and material property variability. Recommendations are made to assist contractors in determining when saw-cuts are placed that can greatly improve field operations.			
17. Key Words concrete, early-age, pavement, sawcutting, cracking		18. Distribution Statement No restrictions. This document is available to the public through the National Technical Information Service, Springfield, VA 22161	
19. Security Classif. (of this report) Unclassified	20. Security Classif. (of this page) Unclassified	21. No. of Pages 809	22. Price

TABLE OF CONTENTS

	Page
LIST OF TABLES	viii
LIST OF FIGURES	x
CHAPTER 1.INTRODUCTION	1
1.1 Background	1
1.2 Research Objectives	4
1.3 Organization of the Report.....	5
CHAPTER 2: LITERATURE REVIEW	6
2.1 Introduction.....	6
2.2 Maturity of concrete.....	7
2.2.1 Background	7
2.2.2 Maturity functions.....	8
2.2.3 Strength-maturity relationships.....	14
2.2.4 Choice of maturity method	15
2.2.5 Choice of strength testing	16
2.2.6 Aggregate influence on maturity method predictions.....	16
2.3 Saw-cut depth and timing considerations	17
2.4 Spalling and Raveling.....	19
2.4.1 Definition and classification	19
2.4.2 Material and equipment parameters	21
2.5 Saw-cutting equipment	24
2.5.1 Span saws.....	24
2.5.2 Conventional saws	25
2.5.3 Early-entry saws.....	26
2.5.4 Blades.....	28
2.6 Hiperpav software	32
2.6.1 Background	32
2.6.2 Hiperpav analysis.....	32
2.6.3 Hiperpav models	34
2.6.4 Hiperpav and the maturity method	34
2.6.5 Hiperpav and saw-cutting	36
2.7 Literature review conclusions	39

CHAPTER 3: FIELD ASSESSMENT OF THE MATURITY METHOD AS A TOOL FOR SAW-CUTTING GUIDELINES	41
3.1 Introduction.....	41
3.2 Site visit #1 (9/11/03).....	42
3.2.1 Site visit #1 overview.....	42
3.2.2 Site visit #1 mixture design.....	43
3.2.3 Site visit #1 placement of the thermocouples	44
3.2.4 Site visit #1 weather.....	45
3.2.5 Site visit #1 equipment.....	46
3.2.6 Site visit #1 synopsis.....	47
3.3 Site visit #2 (10/30/03).....	50
3.3.1 Site visit #2 project overview	50
3.3.2 Site visit #2 mixture design.....	51
3.3.3 Site visit #2 placement of the sensor.....	52
3.3.4 Site visit #2 weather.....	54
3.3.5 Site visit #2 equipment.....	55
3.3.6 Site visit #2 synopsis.....	56
3.4 Site visit #3 (11/20/03-11/21/03).....	59
3.4.1 Site visit #3 project overview	59
3.4.2 Site visit #3 placement of the sensor.....	60
3.4.3 Site visit #3 weather.....	62
3.4.4 Site visit #3 synopsis.....	62
3.5 Site visit #4 (12/16/03-12/17/03).....	65
3.5.1 Site visit #4 project overview	65
3.5.2 Site visit #4 mixture design.....	66
3.5.3 Site visit #4 placement of the sensor.....	66
3.5.4 Site visit #4 weather.....	67
3.5.5 Site visit #4 synopsis.....	67
3.6 Site visit #5 (5/3/04-5/4/04).....	70
3.6.1 Site visit #5 project overview	70
3.6.2 Site visit #5 placement of the meters	71
3.6.3 Site visit #5 weather.....	72
3.6.4.1 Site visit #5 synopsis of joint A	73
3.6.4.2 Site visit #5 synopsis of joint B	76
3.7 Comparison and summary of site visits	79
3.7.1 Overview sections summary	79
3.7.2 Mixture design sections summary	82
3.7.3 Placement of the sensor sections summary.....	83
3.7.4 Weather sections summary	86
3.7.5 Equipment sections summary	87
3.7.6 Synopsis sections summary	88

	Page
CHAPTER 4: EXPERIMENTAL PROGRAM.....	93
4.1 Introduction.....	93
4.2 Experimental approach	93
4.3 Mixture materials, proportions, and procedures	94
4.3.1 Constituent materials	94
4.3.2 Mixture proportions	96
4.3.3 Mixing procedure.....	97
4.4 Test's performed to evaluate mechanical properties	98
4.4.1 Tensile wedge test.....	98
4.4.1.1 Design considerations	98
4.4.1.2 Basic testing geometry and loading considerations	99
4.4.1.3 Specimen dimensions.....	100
4.4.1.4 Analysis of the wedge specimen.....	104
4.4.1.5 Bond.....	105
4.4.1.6 Notch.....	107
4.4.1.7 Friction elimination – Teflon sheets	108
4.4.1.8 Casting and Curing	109
4.4.1.9 Testing equipment and procedures	111
4.4.2 Flexural beam testing.....	112
4.4.3 Shrinkage test.....	113
4.4.5 Compression testing.....	114
4.4.6 Splitting tensile test.....	115
4.5 Tests to examine raveling	116
4.5.1 Mortar set times	116
4.5.2 Early-entry saw-cut.....	117
CHAPTER 5: EXPERIMENTAL RESULTS AND ANALYSIS.....	119
5.1 Introduction.....	119
5.2 Tensile wedge test.....	120
5.2.1 An overview of the tensile wedge test	120
5.2.1.1 Specimen displacement calculations.....	122
5.2.1.2 Local specimen deformations – LVDT data.....	128
5.2.2 Pre-peak stable crack growth.....	130
5.2.3 Early age plasticity.....	141
5.2.4 Notch depth propagation probability	145
5.3 Flexural beam test results.....	148
5.4 Early age shrinkage test results.....	151
5.5 Compressive cylinder test results.....	152
5.6 Split cylinder test results.....	156
5.7 Mortar set time.....	157
5.8 Early entry saw test.....	158
5.9 Summary.....	158

CHAPTER 6: LITERATURE REVIEW FOR COMPUTER MODELING: A DISCUSSION OF MATERIAL PROPERTY INPUT AS WELL AS BOUNDARY CONDITIONS	161
6.1 Introduction.....	161
6.2 Thermal Behavior of Concrete.....	162
6.2.1 Measurement of Temperature	164
6.2.2 FEMMASSE Heat Models	166
6.2.2.1 Core Model	167
6.2.2.2 Danish Model.....	169
6.2.3 Thermal Conductivity	172
6.2.4 Thermal Capacity.....	173
6.3 Maturity Model	174
6.4 Hygral Behavior of Concrete	176
6.5 Time Dependent Deformation of Concrete.....	178
6.5.1 Thermal Expansion	178
6.5.2 Autogenous Shrinkage.....	178
6.5.3 Creep and Relaxation.....	179
6.6 Stress Behavior of Concrete	182
6.6.1 Elastic Modulus	182
6.6.2 Tensile Strength	183
6.6.3 Compressive Strength	184
6.6.4 Softening Behavior	184
6.7 Boundary Conditions	187
6.7.1 Hygral Boundary Condition.....	187
6.7.2 Thermal Convection Boundary Condition.....	188
6.7.3 Subbase and Subgrade	189
6.8 Summary	190
CHAPTER 7: SIMULATION OF SAW-CUTTING IN CONCRETE PAVEMENTS USING FINITE ELEMENT ANALYSIS: AN OVERVIEW OF TYPICAL MODEL DEVELOPMENT INPUTS AND OUTPUTS	191
7.1 Introduction.....	191
7.2 General Modeling Approach.....	191
7.2.1 Description of the FEMMASSE Software Used in Computer Simulations	191
7.2.2 The Development of a Pavement Model Inputs	192
7.2.2.1 The Pavement Geometry.....	192
7.2.2.2 The Subbase and Subgrade	193
7.2.2.3 The Saw-cut Geometry	193
7.2.2.4 The Mechanical Boundary Conditions	193
7.2.2.5 The Environmental Boundary Conditions	194
7.3 The Data Inputting for Computer Simulation.....	195
7.3.1 Drawing the Slab, Reinforcement, Subbase and Subgrade.....	198

	Page
7.3.2 Defining the Thermal Boundary Conditions.....	201
7.3.3 Defining the Hygral Boundary Conditions	202
7.3.4 Defining the Mechanical Boundary Conditions	203
7.3.5 Defining the Finite Element Mesh.....	204
7.3.6 Determining Computational Time Steps and Storage Frequency.....	207
7.4 Viewing the Computed Results	207
7.4.1 Viewing Contour Plots of the Simulation Results	207
7.4.2 Line Cuts in Contour Plots.....	223
7.4.3 Data History of Quantities at Selected Points.....	225
7.5 Processing the Simulation Results	225
7.5.1 Pavement End Reactions and Stresses	225
7.5.2 Average Tensile Strength.....	226
7.5.3 Crack Width Opening Displacement	227
7.5.4 Cracking Potential.....	228
7.6 Conclusion	228
CHAPTER 8: FINITE ELEMENT SIMULATIONS OF CONCRETE	
PAVEMENTS.....	232
8.1 Introduction.....	232
8.2 Saw-cut Depth.....	232
8.2.1 Computer Simulations to Investigate the Effect of Saw-cut Depth.....	233
8.2.2 Analysis of the Simulation Results	233
8.2.2.1 Crack Tip Opening Displacement and Stresses at the Saw-cut Tip ..	233
8.2.2.2 The Influence of Saw-cut Depth on Pavement Cracking	249
8.2.3 Computer Simulations to Investigate the Effect of the Pavement	
Depth on the Pavements Cracking behavior	259
8.2.3.1 Stress and Crack Opening at the Tip of a Saw-cut	259
8.2.3.2 The Influence of the Depth of Pavements on the Cracking	
Behavior of Pavements	264
8.3 Factors Influencing the Time of Saw-cut Introduction.....	271
8.3.1 The Effect of Ambient Temperature on Cracking Behavior of	
Pavements	272
8.3.1.1 The Effect of Constant Ambient Temperature on Cracking	
Behavior	273
8.3.1.1.1 The General Modeling Approach	273
8.3.1.1.2 The Results and Analysis.....	273
8.3.1.2 The Effect of Periodical Ambient Temperature on Cracking	
Behavior	278
8.3.1.2.1 The General Modeling Approach	279
8.3.1.2.2 The Results and Analysis.....	280
8.3.1.3 Paving at Different Times of Day.....	285
8.3.1.3.1 The General Modeling Approach	285
8.3.1.3.2 Results and Analysis	286
8.3.1.4 Determination of the Saw-cutting Time Window.....	287

	Page
8.3.1.4.1 The Influence of the Time of Saw-cut Introduction on the Cracking Behavior of Pavements.....	288
8.3.1.4.2 The Influence of the Ambient Temperature on the Cracking Behavior of Pavements.....	312
8.3.1.4.3 The Influence of the Saw-cut Depth on the Saw-cutting Time Window	324
8.3.2 The Influence of Rate of Reaction on the Time of Saw-cut Introduction ..	324
8.3.2.1 The General Modeling Approach	325
8.3.2.2 The Behavior of the Pavement Built with Rapid Setting Concrete ...	325
8.3.2.3 The Behavior of Pavement Built with Slow Setting Concrete	327
8.3.2.4 The Comparison and Discussion	328
8.4 Summary	329
CHAPTER 9: A PROPOSED SIMPLIFIED METHODOLOGY TO DETERMINE THE TIME OF SAW-CUTTING CONSIDERING SAW-CUT DEPTH	331
9.1 Introduction.....	331
9.2 Fracture Mechanics Analysis of Pavements Containing a Saw-Cut.....	332
9.3 A Recommendation for a Procedure to Minimize Random Cracking.....	338
9.4 The Probability of Cracking.....	346
9.4 Summary	351
CHAPTER 10: SUMMARY AND RECOMMENDATIONS	353
10.1 Introduction.....	353
10.2 A Summary of Important Findings	354
REFERENCES	360
APPENDICES	
Appendix A.....	367
Appendix B.....	730
Appendix C.....	746
Appendix D.....	762

LIST OF TABLES

Table	Page
2.1. Mohs scale	29
2.2. Aggregate hardness classification (Norland, 2004).....	30
3.1. Site visit #1 mixture proportions.....	43
3.2. Site visit #2 mixture proportions.....	52
3.3. Site visit #4 mixture proportions.....	66
3.4. Comparison of overview sections	80
3.5. Mixture design comparison.....	83
3.6. Sensor placement comparison.....	84
3.7. Weather comparison	86
3.8. Equipment comparison	87
3.9. Synopsis comparison	88
4.1. Chemical properties of Lonestar Type I cement.....	94
4.2. Coarse aggregate gradation.....	95
4.3. Fine aggregate gradation.....	95
4.4. Constituent weights for 1.65 ft ³ batch.....	96
4.5. Chemical admixture dosage rate.....	97
4.6. Mixing procedure.....	97
5.1. Tensile wedge test schedule.....	122
5.2. Thermal induced stresses	139

Table	Page
5.3. Sigmoidal trend line constants	154
5.4. Early-entry saw test.....	158
6.1. Hansen's function coefficients for curves shown in Figure 6.7.....	170
6.2. Autogenous shrinkage used in computer modeling.....	179
6.3. Maxwell chain model used in modeling the viscoelasticity of concrete	181
6.4. The measured UPV elastic modulus Barde (2004).....	183
6.5. Tensile strength values used in computer modeling	183
6.6. Compression strength values used in finite element analysis	184
6.7. Softening parameters used in computer simulations	186
6.8. The subbase and subgrade properties	189
8.1. List of simulations that consider saw-cut depth and time.....	233
8.2. Calculation of thermal stresses	313
10.1. $\Phi_{saw-cut}$ for selected values of saw-cut to depth ratios	359

LIST OF FIGURES

Figure	Page
2.1. Age conversion factors versus temperature ($T_o = -10^{\circ}\text{C}$, $E = 50,000$ Joule/Mole) ...	11
2.2. Age conversion Factor versus temperature at various activation energies (Carino, 1991, p. 122).....	12
2.3. Strength development at high versus low early-age temperatures (Carino, 1991, p. 122).....	13
2.4. Severity classification of raveling (ACPA, 2002 a).....	20
2.5. Saw-cut rating versus compressive strength.....	22
2.6. Saw-Cut direction (Norland, 2004).....	25
2.7. Conventional wet-cut saw.....	26
2.8. Detached Soff-Cut ® anti-ravel skid plate and diamond blade.....	27
2.9. Attached Soff-Cut ® anti-ravel skid plate and diamond blade.....	27
2.10. Soff-Cut early-entry saw.....	28
2.11. Hiperpav analysis showing the elapsed time since construction (x-axis) versus the tensile strength or stress development in the slab (y-axis).....	33
2.12. Hiperpav evaporation rate analysis showing the elapsed time since construction (x-axis versus the evaporation rate at various wind speeds).....	33
2.13. Mixture proportion parameters window of the Hiperpav software.....	35
2.14. Hiperpav option to input laboratory maturity in Nurse-Saul format.....	35
2.15. “User Defined” saw-cutting parameter.....	36
2.16. “Optimum (Early Entry)” saw-cutting parameter.....	37
2.17. “No Saw-Cutting” parameter.....	37
2.18. Indirect determination of the end of the saw-cutting window.....	38
3.1. Site visit #1 9/11/03 timeline.....	43
3.2. Site visit #1 placement of thermocouples.....	44

Figure	Page
3.3. 9/11/03 Weather – ambient temperature, dew point, and wind speed from ASOS station.....	46
3.4. Conventional 65 horsepower wet-cut saw with 18 1/8” diamond blade	47
3.5. 9/11/03 Pavement temperature 7.0”, ambient temperature, and cumulative maturity 7.0”	48
3.6. Cumulative maturity at 3.5”, 7.0”, 10.5”, and ambient temperature	48
3.7. Picture of examined joint.....	49
3.8. Master curve calculated flexural strength.....	50
3.9. Site visit #2 10/30/03 timeline	51
3.10. Placement of I-button maturity sensor.....	53
3.11. Placement of maturity sensor connecting cord	53
3.12. Covering of maturity sensor.....	54
3.13. 10/30/03 Weather – temperature, dew point, and wind speed.....	55
3.14. Conventional wet cut 65 horsepower saw with 20” diamond blade.....	56
3.15. 10/30/03 Pavement temperature, ambient temperature, and cumulative maturity at 20°C	57
3.16. Depth of examined joint.....	57
3.17. No raveling at joint	58
3.18. Master curve calculated flexural strength.....	59
3.19. 11/20/03-11/21/03 timeline.....	60
3.20. Placement of I-button maturity sensor.....	61
3.21. Covering of maturity sensor.....	61
3.22. 11/20-11/21/03 Weather – temperature, dew point, and wind speed	62
3.23. 11/20-11/21/03 Pavement temperature, ambient temperature, and cumulative maturity at 20°C	63
3.24. Picture of examined joint.....	64
3.25. Master curve calculated flexural strength.....	64
3.26. 12/16/-12/17/03 timeline.....	65
3.27. 12/16/03-12/17/03 Weather – temperature, dew point, and wind speed	67
3.28. 12/16- 12/17/03 Pavement temperature, ambient temperature, and cumulative maturity at 20°C	68

Figure	Page
3.29. Picture of examined joint	69
3.30. Master curve calculated flexural strength	69
3.31. 5/3-5/4/04 timeline	71
3.32. Vertical placement of I button maturity meters	71
3.33. I-button sensors and connecting cord	72
3.34. 5/03/04-5/04/04 Weather – temperature, dew point, and wind speed	73
3.35. Pavement temperature, ambient temperature, and cumulative maturity at 20°C for 2.5” sensor at joint A	74
3.36. Pavement temperature, ambient temperature, and cumulative maturity at 20°C for 5.0” sensor at joint A	74
3.37. Comparison of pavement temperature and corresponding Arrhenius maturity for the 2.5” and 5.0” sensors at joint A	75
3.38. Examination of joint A	75
3.39. Depth of joint at location A	76
3.40. Pavement temperature, ambient temperature, and cumulative maturity at 20°C for 5.0” sensor at joint B	77
3.41. Comparison of 5” sensors at locations A and B	77
3.42. Examination of joint B	78
3.43. Depth of joint at location B	78
3.44. Master curve calculated flexural strength	79
3.45. Pavement temperature versus Arrhenius maturity for site visits # 3, 4, and 5	90
3.46. Master curve comparison	91
4.1. General picture of tensile wedge apparatus setup	100
4.2. General schematic of tensile wedge apparatus movements	100
4.3. Original tensile wedge apparatus dimensions - top view without wedge	101
4.4. Original tensile wedge apparatus dimensions - front view without wedge	101
4.5. Tensile wedge apparatus – top viewpoint without wedge	102
4.6. Tensile wedge apparatus – front view without wedge	102
4.7. Tensile wedge apparatus – front view with wedge	103
4.8. Tensile wedge apparatus – side view with wedge	103

Figure	Page
4.9. Wedge schematic	104
4.10. Side teflon sheets attached to the mold before casting	106
4.11. Side and bottom teflon sheets after specimen failure	106
4.12. Front view of the polycarbonate notch (all dimensions in inches)	107
4.13. Notch forming assembly placed in specimen	108
4.14. Teflon sheet placed on the base plate	109
4.15. Location of internal vibration points.....	109
4.16. Thermocouples location.....	110
4.17. LVDT's glued in place.....	111
4.18. Preparation of shrinkage specimens.....	114
4.19. 6"x12" cylinder tested in compression at an age of 1 day.....	115
4.20. Splitting tensile test.....	116
4.21. Early entry specimen before saw-cut.....	117
4.22. Early entry specimen after it was saw-cut	118
5.1. Typical temperature development data for a tensile wedge specimen (specimen #31).....	121
5.2. An illustration of the vertical to horizontal displacement ratio (1:0.1486).....	123
5.3. Components of specimen displacement.....	124
5.4. Displacement controlled model	124
5.5. (a) $F-\Delta$ for bulk material, and (b) $F-\Delta$ in cracking region.....	125
5.6. Load versus displacement for specimen number 20	127
5.7. Seating correction for displacement normalization (specimen number 16)	127
5.8. Typical experimental measurements for test #11 illustrating the relationship between load, horizontal wedge displacement and the measured LVDT displacement at the notch for a specimen with a 2.83" (D/3) notch at maturity of 18 eq. age hours	129
5.9. Typical experimental measurements for test #11 illustrating the relationship between load and the average measured LVDT displacement at the notch for a specimen with a 2.83" (D/3) notch at maturity of 18 equivalent age hours	130

Figure	Page
5.10. Experimental results for specimen 20: load versus specimen displacement and LVDT versus specimen displacement (2.83" (D/3) @ 30 eq. age hours).....	131
5.11. Experimental results for specimen 22: load versus specimen displacement and LVDT displacement versus specimen displacement (4.25" (D/2) @ 29 eq. age hours).....	132
5.12. Experimental results for test 22: load versus LVDT displacement (4.25" (D/2) @ 29 eq. age hours).....	133
5.13. Experimental results for specimen 33: load versus specimen displacement and LVDT displacement versus specimen displacement (2.00" (D/4.25) @ 38 eq. age hours)	134
5.14. Hypothetical fracture process zone.....	135
5.15. A conceptual illustration of the size of fracture process zone and its relation to the size of the initial flaw (notch).....	136
5.16. Corrected specimen displacement versus maturity for all tests	137
5.17. Ultimate tensile load versus maturity for all specimens (including load at 1 st peak displayed in load versus specimen displacement curve for shallow notches).....	138
5.18. Assumed specimen temperature gradient (temperature shown as difference from mid-depth).....	140
5.19. The stress distribution for (a) plastic and (b) brittle failure	141
5.20. Development of characteristic length with age (from Peterson (1981)).....	143
5.21. Various notch – early age data normalized for 10 equivalent age hours	144
5.22. Average LVDT displacement versus maturity for the 2.83" (D/3) specimens.....	144
5.23. Crack propagation for specimen #23 which was cast with a 1.00" (D/8.5") notch and tested at 9 equivalent age hours.....	146
5.24. Crack propagation for specimen #24 which was cast with a 1.00" (D/8.5") notch and tested at 9 equivalent age hours.....	146
5.25. Introduction of the saw-cut notch using the early-entry saw	147
5.26. Flexural strength versus maturity fitted with sigmoidal trend line	148
5.27. Comparison of tensile wedge strength and flexural strength.....	149
5.28. Actual and assumed stress distribution in concrete specimen tested in flexure	150
5.29. Micro-strain versus time for sealed and two sided drying shrinkage specimens....	151
5.30. Early age 6"x12" compressive strength versus maturity	152

Figure	Page
5.31. Compressive and flexural strength plots.....	153
5.32. Flexural strength conversion from raveling guidelines based on compressive strength.....	154
5.33. Equation 5.7 used to convert flexural to compressive strength for 0-60 equivalent age hours	155
5.34. Equation 5.7 used to convert flexural to compressive strength for 0-20 equivalent age hours	156
5.35. Normal probability density for splitting tensile tests.....	157
6.1. Layout of MDV and MPE windows in MLS-Database program	162
6.2. Heat evolution rate of tricalcium silicate during hydration (Mindess, 2002)	163
6.3. Adiabatic temperature curves as a function of mixture temperature (Springenschmid, 1999).....	164
6.4. Adiabatic temperature curve for a concrete with w/c of 0.35 (Bentz, 1998).....	165
6.5. An overview of Material Database Viewer of FEMMASSE.....	166
6.6. A window illustrating the Core Model (i.e., Equation 2.4)	169
6.7. Heat of hydration curves using Hansen’s function	171
6.8. Layout of the Danish Model (available under the “Source” sub-tab).....	172
6.9. Layout of the MLS Database thermal conductivity window	173
6.10. Layout of MPE and MPV windows in MLS Database after the maturity function is activated	176
6.11. Desorption isotherm layout of MPE and MPV windows	178
6.12. Maxwell chain model composed of spring and dashpot units (FEMMASSE manual).....	180
6.13. Maxwell model layout of MPE and MPV windows in MLS Database.....	182
6.14. Pre-peak and post-peak behavior of concrete in a deformation control experiment	185
6.15. Stress-crack opening graph obtained from the wedge splitting test Østergaard (2003)	186
6.16. MPE and MPV layouts of the softening model window in MLS Database	187
6.17. Layout of the hygral boundary property window	188

Figure	Page
7.1. A schematic illustration of the finite element model used in analysis consisting of pavement, subbase, and subgrade.....	194
7.2. Baseline Case Ambient Temperature Function	195
7.3. Series of actions to be performed in FEMMASSE software (FEMMASSE manual).....	197
7.4. Main window of FEMMASSE	198
7.5. Design panel tools of FEMMASSE.....	199
7.6. General macro properties window	200
7.7. Pavement model with magnified saw-cut macro	201
7.8. Window used to assign thermal boundary properties window	202
7.9. Hygral boundary conditions window.....	203
7.10. Model Support Conditions.....	204
7.11. Applying the Finite Element Mesh to the Model.....	205
7.12. The Finite Element Mesh of Model.....	206
7.13. Elements of the model close to the saw-cut.....	206
7.14. Contour plot of principal stresses at 23.3 hours.....	207
7.15. Temperature distribution contour plot at 6 hours	209
7.16. Temperature distribution contour plot at 12 hours	209
7.17. Temperature distribution contour plot at 18 hours	210
7.18. Temperature distribution contour plot at 23.3 hours	210
7.19. Maturity distribution contour plot at 6 hours.....	211
7.20. Maturity distribution contour plot at 12 hours.....	211
7.21. Maturity distribution contour plot at 18 hours.....	212
7.22. Maturity distribution contour plot at 23.3 hours.....	212
7.23. Tensile strength distribution contour plot at 6 hours	213
7.24. Tensile strength distribution contour plot at 12 hours	213
7.25. Tensile strength distribution contour plot at 18 hours	214
7.26. Tensile strength distribution contour plot at 23.3 hours	214
7.27. Principal stress distribution contour plot at 6 hours.....	215
7.28. Principal stress distribution contour plot at 12 hours.....	216

Figure	Page
7.29. Principal stress distribution contour plot at 13 hours.....	216
7.30. Principal stress distribution contour plot at 18 hours.....	217
7.31. Principal stress distribution contour plot at 23.3 hours.....	217
7.32. End reaction plot at 12 hours	218
7.33. End reaction plot at 18 hours	218
7.34. End reaction plot at 23.3 hours	219
7.35. The graphs of end reactions of pavement at various hours. The distance on “y” axis is measured from the bottom of pavement.....	220
7.36. Damage distribution contour plot at 21 hours.....	221
7.37. Damage distribution contour plot at 23.3 hours.....	221
7.38. X-direction distribution contour plot at 12 hours	222
7.39. X-direction distribution contour plot at 18 hours	222
7.40. X-direction distribution contour plot at 21 hours	223
7.41. X-direction distribution contour plot at 23.3 hours	223
7.42. Contour plot of principal stresses at 23.3 hours with a defined line cut passing through the joint.....	224
7.43. Left end finite elements of pavement.....	226
7.44. X-direction displacement contour plot.....	227
7.45. Measured CTOD versus time at the tip of saw-cut.....	228
7.46. History graphs of selected quantities calculated at the tip of the saw-cut	230
8.1. Fracture process zone crack growth of concrete.....	234
8.2. Cracking behavior of concrete under different stages of load (Shah et al., 1995)	236
8.3. Stress response of concrete at different crack positions (Shah et al., 1995).....	237
8.4. Average end reactions of pavement at various hours. Distance is..... measured from the bottom of the pavement.	238
8.5. Post-peak stress crack width curves of concrete.....	239
8.6. Tensile strength and stress at the tip of D/2 saw-cuts	240
8.7. CTOD for pavements with D/2 depth of saw-cut applied at 0 and 12 hours.....	241
8.8. CTOD for pavements with D/2 saw-cuts.....	242

Figure	Page
8.9. Tensile strength and stresses at the tip of D/3 saw-cuts.....	242
8.10. Contour plots of stresses at different times for a pavement with D/3 saw-cut introduced at 12 hours	243
8.11. Crack tip opening displacements for pavements with a D/3 depth of saw-cut	244
8.12. Strength and local stresses of pavements with a saw-cut depth of D/4	245
8.13. CTOD of pavements with a saw-cut depth of D/4 applied at different times.....	245
8.14. Tensile strength and stresses of pavements with D/6 saw-cuts	246
8.15. CTOD of pavements with a saw-cut depth of D/6 applied at different times.....	246
8.16. Tensile strength and stresses of pavements with D/8 saw-cuts	247
8.17. CTOD of pavements with a saw-cut depth of D/8 applied at different times.....	247
8.18. Tensile strength and stresses of pavements with D/100 saw-cuts	248
8.19. CTOD of pavements with a saw-cut depth of D/100 applied at different times.....	249
8.20. Notch sensitivity strength behavior of brittle and ductile materials (Shah et al., 1995)	250
8.21. The average end stress and average tensile strength for a pavement with a D/2 saw-cut depth	251
8.22. Average end stress to average tensile strength ratios for pavements with a D/2 saw-cut	254
8.23. Average end stress to average tensile strength and phi ratio for a saw-cut depth of D/2	257
8.24. Tensile stresses at the tip of D/3 saw-cuts of 10-inch thick pavements.....	260
8.25. CTOD graphs of 10-inch thick pavements with saw-cut depth of D/3.....	260
8.26. Tensile strength and stresses in x-direction of 10 inch thick pavements with D/8 saw-cuts	261
8.27. CTOD of 10-inch thick pavements with D/8 saw-cuts introduced at 12 hours	262
8.28. Tensile strength and stresses in the x-direction for 10-inch thick pavements	263
8.29. CTOD graphs of 10-inch thick pavement with different saw-cut depths	263
8.30. Tensile strength and stresses in x-direction of 10-inch thick pavements with different saw-cut depths.....	264
8.31. CTOD behaviors of 10-inch thick pavements with different saw-cut depths.....	264
8.32. Average tensile strength and average end stresses of 10-inch thick pavements with D/3 saw-cuts	266

Figure	Page
8.33. Average end stress to average tensile strength ratios of 10-inch thick pavements with D/3 saw-cuts	268
8.34. Average end stress over average tensile strength and phi of 10-inch thick pavements with D/3 saw-cut depth	270
8.35. Principal stresses at the tip of D/3 saw-cuts introduced at 12 hours.....	274
8.36. CTOD of pavements with D/3 saw-cut depth.....	275
8.37. Principal stresses at the tip of D/8 saw-cut depth	276
8.38. CTOD of pavements with D/8 saw-cut depth.....	276
8.39. Principal stresses at the tip of D/8 and D/3 saw-cuts introduced at 12 hours for pavements exposed to 23°C ambient temperature.....	277
8.40. Principal stresses at the tip of D/8 and D/3 saw-cuts introduced at 12 hours for pavements exposed to 36°C ambient temperature.....	278
8.41. The C sinusoidal ambient temperature function	279
8.42. The M sinusoidal ambient temperature function	280
8.43. Tensile strength and principal stresses of pavements exposed to “H” temperature function.....	281
8.44. CTOD of pavements exposed to “H” temperature function	281
8.45. Tensile strength and principal stresses of pavements exposed to “M” temperature function	282
8.46. CTOD at the tip of D/3 saw-cuts of pavements exposed to “M” temperature function	283
8.47. Tensile strength and principal stresses of pavements exposed to “C” temperature function.....	284
8.48. CTOD at the tip of D/3 saw-cuts of pavements exposed to “C” temperature function	284
8.49. Sinusoidal ambient temperature function “H”	285
8.50. Stresses of pavements cast at different times of day.....	286
8.51. CTOD of pavements cast at different times of day.....	287
8.52. End and local stresses and crack width of pavements at 36°C with D/3 saw-cut depths.....	289
8.53. The cracking behavior of pavements with D/3 saw-cut depths cured at 36°C	292
8.54. End and local stresses and crack width of pavements at 23°C with D/3 saw-cut depths.....	295

Figure	Page
8.55. The cracking behavior of pavements with D/3 saw-cut depths cured at 23°C	297
8.56. End and local stresses and crack width of pavements at 23°C with D/2 saw-cut depths.....	299
8.57. The cracking behavior of pavements with D/2 saw-cut depths cured at 23°C	301
8.58. End and local stresses and crack width of pavements at 10°C with D/3 saw-cut depths.....	303
8.59. The cracking behavior of pavements with D/3 saw-cut depths cured at 10°C	305
8.60. End and local stresses and crack width of pavements at 23°C with D/8 saw-cut depths.....	307
8.61. The cracking behavior of pavements with D/8 saw-cut depths cured at 23°C	309
8.62. Crack initiation maturities of pavements with different saw-cut sizes and at different ambient temperatures	311
8.63. Unstable cracking maturities of pavements with different saw-cut sizes and at different ambient temperatures	312
8.64. End and local stresses and crack width of pavements with D/2 saw-cut depths cured at different ambient temperature	314
8.65. The cracking and stress behavior of pavements with D/2 saw-cut depths cured at different ambient temperatures	315
8.66. End and local stresses and crack width of pavements with D/3 saw-cut depths cured at different ambient temperatures.....	317
8.67. The cracking and stress behavior of pavements with D/3 saw-cut depths cured at different ambient temperatures	319
8.68. End and local stresses and crack width of pavements with D/8 saw-cut depths cured at different ambient temperatures.....	321
8.69. The cracking and stress behavior of pavements with D/8 saw-cut depths cured at different ambient temperatures.....	322
8.70. The cracking behavior of pavements at 23°C	324
8.71. Three adiabatic temperature rise curves used in computer simulations	325
8.72. Stresses at the tip of saw-cuts for pavements built with rapid-set concrete.....	326
8.73. CTOD of pavements built with rapid-set concrete	326
8.74. Stresses of pavements built with slow-set concrete.....	327
8.75. CTOD of pavements built with slow-set concrete	328
8.76. Stresses of pavements built with different types of concrete.....	329

Figure	Page
8.77. CTOD of pavements built with different types of concrete.....	329
9.1. The stress-elongation behavior for different types of material: (a) brittle material, (b) ductile material, and (c) quasi-brittle material	332
9.2. The stress distribution of different materials: (a) brittle materials, (b) ductile materials, and (c) quasi-brittle materials	334
9.3. The failure stress of an infinitely large plate with a single edge notch (crack)	336
9.4. A plate with a single edge notch under uniaxial tensile.....	337
9.5. The effect of a saw-cut on the cracking behavior of concrete pavements: (a) residual stress prediction when cracking is not considered, (b) stress behavior with the introduction of saw-cut, (c) damage distribution or crack propagation of the sawed pavement	340
9.6. Predicted and calculated stress to strength ratios.....	341
9.7. Average failure stress to tensile strength ratio for different 380 mm (15 in.) and 254 mm (10 in.) thick pavements.....	343
9.8. (a) The development of failure envelopes for different depths of the saw-cut, and (b) the time of cracking for different depths of saw-cut.....	345
9.9. Probability of cracking for different $\Phi_{saw-cut}$, assuming 10% variability of tensile strength and residual stress.....	347
9.10. The risks of uncontrolled cracking of a given slab for different saw-cutting depths, assuming 10% variability of tensile strength and residual stress	347
9.11. Probability of cracking for pavements, assuming 1%, 10%, and 20% variability of tensile strength and residual stress: (a) no saw-cut, (b) D/8 saw-cut, and (c) D/6 saw-cut.....	349
9.12. A 5% risk of random cracking considering different levels of variability of tensile strength and residual stress.....	351
A.1. Pavement with a D/2 saw-cut depth introduced at 0 hour	368
A.2. Pavement with a D/2 saw-cut depth introduced at 6 hours.....	370
A.3. Pavement with a D/2 saw-cut depth introduced at 9 hours.....	372
A.4. Pavement with a D/2 saw-cut depth introduced at 12 hours.....	374
A.5. Pavement with a D/2 saw-cut depth introduced at 15 hours.....	376

Figure	Page
A.6. Pavement with a D/2 saw-cut depth introduced at 18 hours.....	378
A.7. Pavement with a D/2 saw-cut depth introduced at 24 hours.....	380
A.8. Pavement with a D/2 saw-cut depth introduced at 30 hours.....	382
A.9. Pavement with a D/3 saw-cut depth introduced at 0 hour	384
A.10. Pavement with a D/3 saw-cut depth introduced at 6 hours.....	386
A.11. Pavement with a D/3 saw-cut depth introduced at 9 hours.....	388
A.12. Pavement with a D/3 saw-cut depth introduced at 12 hours.....	390
A.13. Pavement with a D/3 saw-cut depth introduced at 15 hours.....	392
A.14. Pavement with a D/3 saw-cut depth introduced at 18 hours.....	394
A.15. Pavement with a D/3 saw-cut depth introduced at 21 hours.....	396
A.16. Pavement with a D/3 saw-cut depth introduced at 22 hours.....	398
A.17. Pavement with a D/3 saw-cut depth introduced at 23 hours.....	400
A.18. Pavement with a D/3 saw-cut depth introduced at 24 hours.....	402
A.19. Pavement with a D/3 saw-cut depth introduced at 30 hours.....	404
A.20. Pavement with a D/4 saw-cut depth introduced at 0 hour	406
A.21. Pavement with a D/4 saw-cut depth introduced at 6 hours.....	408
A.22. Pavement with a D/4 saw-cut depth introduced at 9 hours.....	410
A.23. Pavement with a D/4 saw-cut depth introduced at 12 hours.....	412
A.24. Pavement with a D/4 saw-cut depth introduced at 15 hours.....	414
A.25. Pavement with a D/4 saw-cut depth introduced at 18 hours.....	416
A.26. Pavement with a D/4 saw-cut depth introduced at 21 hours.....	418
A.27. Pavement with a D/4 saw-cut depth introduced at 24 hours.....	420
A.28. Pavement with a D/4 saw-cut depth introduced at 30 hours.....	422
A.29. Pavement with a D/6 saw-cut depth introduced at 0 hour	424
A.30. Pavement with a D/6 saw-cut depth introduced at 6 hours.....	426
A.31. Pavement with a D/6 saw-cut depth introduced at 9 hours.....	428
A.32. Pavement with a D/6 saw-cut depth introduced at 12 hours.....	430
A.33. Pavement with a D/6 saw-cut depth introduced at 15 hours.....	432
A.34. Pavement with a D/6 saw-cut depth introduced at 18 hours.....	434

Figure	Page
A.35. Pavement with a D/6 saw-cut depth introduced at 21 hours.....	436
A.36. Pavement with a D/6 saw-cut depth introduced at 24 hours.....	438
A.37. Pavement with a D/6 saw-cut depth introduced at 30 hours.....	440
A.38. Pavement with a D/8 saw-cut depth introduced at 0 hour	442
A.39. Pavement with a D/8 saw-cut depth introduced at 6 hours.....	444
A.40. Pavement with a D/8 saw-cut depth introduced at 9 hours.....	446
A.41. Pavement with a D/8 saw-cut depth introduced at 12 hours.....	448
A.42. Pavement with a D/8 saw-cut depth introduced at 15 hours.....	450
A.43. Pavement with a D/8 saw-cut depth introduced at 18 hours.....	452
A.44. Pavement with a D/8 saw-cut depth introduced at 21 hours.....	454
A.45. Pavement with a D/8 saw-cut depth introduced at 24 hours.....	456
A.46. Pavement with a D/8 saw-cut depth introduced at 30 hours.....	458
A.47. Pavement with a D/8 saw-cut depth introduced at 36 hours.....	460
A.48. Pavement with a D/100 saw-cut depth introduced at 0 hour	462
A.49. Pavement with a D/100 saw-cut depth introduced at 12 hours.....	464
A.50. Pavement with a D/100 saw-cut depth introduced at 24 hours.....	466
A.51. Pavement with a D/100 saw-cut depth introduced at 36 hours.....	468
A.52. Pavement with a D/100 saw-cut depth introduced at 48 hours.....	470
A.53. 10-inch thick pavement with a D/3 saw-cut depth introduced at 0 hour	472
A.54. 10-inch thick pavement with a D/3 saw-cut depth introduced at 6 hours.....	474
A.55. 10-inch thick pavement with a D/3 saw-cut depth introduced at 9 hours.....	476
A.56. 10-inch thick pavement with a D/3 saw-cut depth introduced at 12 hours.....	478
A.57. 10-inch thick pavement with a D/3 saw-cut depth introduced at 15 hours.....	480
A.58. 10-inch thick pavement with a D/3 saw-cut depth introduced at 18 hours.....	482
A.59. 10-inch thick pavement with a D/3 saw-cut depth introduced at 24 hours.....	484
A.60. 10-inch thick pavement with a D/8 saw-cut depth introduced at 0 hour	486
A.61. 10-inch thick pavement with a D/8 saw-cut depth introduced at 6 hours.....	488
A.62. 10-inch thick pavement with a D/8 saw-cut depth introduced at 12 hours.....	490

Figure	Page
A.63. 10-inch thick pavement with a D/8 saw-cut depth introduced at 18 hours.....	492
A.64. 10-inch thick pavement with a D/8 saw-cut depth introduced at 21 hours.....	494
A.65. 10-inch thick pavement with a D/8 saw-cut depth introduced at 24 hours.....	496
A.66. 10-inch thick pavement with a D/8 saw-cut depth introduced at 30 hours.....	498
A.67. 10-inch thick pavement with a D/8 saw-cut depth introduced at 36 hours.....	500
A.68. 10-inch thick pavement with a D/8 saw-cut depth introduced at 42 hours.....	502
A.69. 10-inch thick pavement with a D/2 saw-cut depth introduced at 12 hours.....	504
A.70. 10-inch thick pavement with a D/4 saw-cut depth introduced at 12 hours.....	506
A.71. 10-inch thick pavement with a D/6 saw-cut depth introduced at 12 hours.....	508
A.72. 12-inch thick pavement with a D/3 saw-cut depth introduced at 12 hours.....	510
A.73. 17-inch thick pavement with a D/3 saw-cut depth introduced at 12 hours.....	512
A.74. Pavement cured at “M” ambient temperature with a D/3 saw-cut depth introduced at 0 hour	514
A.75. Pavement cured at “M” ambient temperature with a D/3 saw-cut depth introduced at 6 hours.....	516
A.76. Pavement cured at “M” ambient temperature with a D/3 saw-cut depth introduced at 9 hours.....	518
A.77. Pavement cured at “M” ambient temperature with a D/3 saw-cut depth introduced at 12 hours.....	520
A.78. Pavement cured at “M” ambient temperature with a D/3 saw-cut depth introduced at 15 hours.....	522
A.79. Pavement cured at “M” ambient temperature with a D/3 saw-cut depth introduced at 18 hours.....	524

Figure	Page
A.80. Pavement cured at “M” ambient temperature with a D/3 saw-cut depth introduced at 30 hours.....	526
A.81. Pavement cured at “C” ambient temperature with a D/3 saw-cut depth introduced at 0 hour	528
A.82. Pavement cured at “C” ambient temperature with a D/3 saw-cut depth introduced at 24 hours.....	530
A.83. Pavement cured at “C” ambient temperature with a D/3 saw-cut depth introduced at 36 hours.....	532
A.84. Pavement cured at “C” ambient temperature with a D/3 saw-cut depth introduced at 48 hours.....	534
A.85. Pavement cured at “C” ambient temperature with a D/3 saw-cut depth introduced at 60 hours.....	536
A.86. Pavement cured at “C” ambient temperature with a D/3 saw-cut depth introduced at 72 hours.....	538
A.87. Pavement cured at “C” ambient temperature with a D/3 saw-cut depth introduced at 84 hours.....	540
A.88. Pavement cured at “C” ambient temperature with a D/3 saw-cut depth introduced at 96 hours.....	542
A.89. Pavement cured at “C” ambient temperature with a D/3 saw-cut depth introduced at 108 hours.....	544
A.90. Pavement cured at 10°C ambient temperature with a D/3 saw-cut depth introduced at 0 hour	546
A.91. Pavement cured at 10°C ambient temperature with a D/3 saw-cut depth introduced at 12 hours.....	548
A.92. Pavement cured at 10°C ambient temperature with a D/3 saw-cut depth introduced at 18 hours.....	550
A.93. Pavement cured at 10°C ambient temperature with a D/3 saw-cut depth introduced at 24 hours.....	552
A.94. Pavement cured at 10°C ambient temperature with a D/3 saw-cut depth introduced at 36 hours.....	554
A.95. Pavement cured at 10°C ambient temperature with a D/3 saw-cut depth introduced at 48 hours.....	556
A.96. Pavement cured at 10°C ambient temperature with a D/3 saw-cut depth introduced at 60 hours.....	558

Figure	Page
A.97. Pavement cured at 10°C ambient temperature with a D/3 saw-cut depth introduced at 72 hours.....	560
A.98. Pavement cured at 10°C ambient temperature with a D/3 saw-cut depth introduced at 84 hours.....	562
A.99. Pavement cured at 10°C ambient temperature with a D/3 saw-cut depth introduced at 96 hours.....	564
A.100. Pavement cured at 23°C ambient temperature with a D/2 saw-cut depth introduced at 0 hour	566
A.101. Pavement cured at 23°C ambient temperature with a D/2 saw-cut depth introduced at 6 hours.....	568
A.102. Pavement cured at 23°C ambient temperature with a D/2 saw-cut depth introduced at 12 hours.....	570
A.103. Pavement cured at 23°C ambient temperature with a D/2 saw-cut depth introduced at 18 hours.....	572
A.104. Pavement cured at 23°C ambient temperature with a D/2 saw-cut depth introduced at 21 hours.....	574
A.105. Pavement cured at 23°C ambient temperature with a D/2 saw-cut depth introduced at 24 hours.....	576
A.106. Pavement cured at 23°C ambient temperature with a D/2 saw-cut depth introduced at 30 hours.....	578
A.107. Pavement cured at 23°C ambient temperature with a D/2 saw-cut depth introduced at 36 hours.....	580
A.108. Pavement cured at 23°C ambient temperature with a D/3 saw-cut depth introduced at 0 hour	582
A.109. Pavement cured at 23°C ambient temperature with a D/3 saw-cut depth introduced at 3 hours.....	584
A.110. Pavement cured at 23°C ambient temperature with a D/3 saw-cut depth introduced at 6 hours.....	586
A.111. Pavement cured at 23°C ambient temperature with a D/3 saw-cut depth introduced at 9 hours.....	588
A.112. Pavement cured at 23°C ambient temperature with a D/3 saw-cut depth introduced at 12 hours.....	590
A.113. Pavement cured at 23°C ambient temperature with a D/3 saw-cut depth introduced at 15 hours.....	592

Figure	Page
A.114. Pavement cured at 23°C ambient temperature with a D/3 saw-cut depth introduced at 18 hours.....	594
A.115. Pavement cured at 23°C ambient temperature with a D/3 saw-cut depth introduced at 20 hours.....	596
A.116. Pavement cured at 23°C ambient temperature with a D/3 saw-cut depth introduced at 21 hour	598
A.117. Pavement cured at 23°C ambient temperature with a D/3 saw-cut depth introduced at 22 hours.....	600
A.118. Pavement cured at 23°C ambient temperature with a D/3 saw-cut depth introduced at 24 hours.....	602
A.119. Pavement cured at 23°C ambient temperature with a D/3 saw-cut depth introduced at 30 hours.....	604
A.120. Pavement cured at 23°C ambient temperature with a D/3 saw-cut depth introduced at 36 hours.....	606
A.121. Pavement cured at 23°C ambient temperature with a D/8 saw-cut depth introduced at 0 hour	608
A.122. Pavement cured at 23°C ambient temperature with a D/8 saw-cut depth introduced at 6 hours.....	610
A.123. Pavement cured at 23°C ambient temperature with a D/8 saw-cut depth introduced at 12 hours.....	612
A.124. Pavement cured at 23°C ambient temperature with a D/8 saw-cut depth introduced at 18 hours.....	614
A.125. Pavement cured at 23°C ambient temperature with a D/8 saw-cut depth introduced at 24 hours.....	616
A.126. Pavement cured at 23°C ambient temperature with a D/8 saw-cut depth introduced at 30 hours.....	618
A.127. Pavement cured at 23°C ambient temperature with a D/8 saw-cut depth introduced at 36 hours.....	620
A.128. Pavement cured at 23°C ambient temperature with a D/8 saw-cut depth introduced at 48 hours.....	622
A.129. Pavement cured at 36°C ambient temperature with a D/8 saw-cut depth introduced at 0 hour	624
A.130. Pavement cured at 36°C ambient temperature with a D/8 saw-cut depth introduced at 3 hours.....	626

Figure	Page
A.131. Pavement cured at 36°C ambient temperature with a D/8 saw-cut depth introduced at 6 hours.....	628
A.132. Pavement cured at 36°C ambient temperature with a D/8 saw-cut depth introduced at 9 hours.....	630
A.133. Pavement cured at 36°C ambient temperature with a D/8 saw-cut depth introduced at 12 hours.....	632
A.134. Pavement cured at 36°C ambient temperature with a D/8 saw-cut depth introduced at 15 hours.....	634
A.135. Pavement cured at 36°C ambient temperature with a D/8 saw-cut depth introduced at 18 hours.....	636
A.136. Pavement cured at 36°C ambient temperature with a D/8 saw-cut depth introduced at 24 hours.....	638
A.137. Pavement cured at 36°C ambient temperature with a D/100 saw-cut depth introduced at 0 hours.....	640
A.138. Pavement cured at 4°C ambient temperature with a D/2 saw-cut depth introduced at 0 hour	642
A.139. Pavement cured at 10°C ambient temperature with a D/2 saw-cut depth introduced at 0 hour	644
A.140. Pavement cured at 18°C ambient temperature with a D/2 saw-cut depth introduced at 0 hour	646
A.141. Pavement cured at 30°C ambient temperature with a D/2 saw-cut depth introduced at 0 hour	648
A.142. Pavement cured at 36°C ambient temperature with a D/2 saw-cut depth introduced at 0 hour	650
A.143. Pavement cured at 4°C ambient temperature with a D/3 saw-cut depth introduced at 0 hour	652
A.144. Pavement cured at 8°C ambient temperature with a D/3 saw-cut depth introduced at 0 hour	654
A.145. Pavement cured at 10°C ambient temperature with a D/3 saw-cut depth introduced at 0 hour	656
A.146. Pavement cured at 12°C ambient temperature with a D/3 saw-cut depth introduced at 0 hour	658
A.147. Pavement cured at 18°C ambient temperature with a D/3 saw-cut depth introduced at 0 hour	660

Figure	Page
A.148. Pavement cured at 23°C ambient temperature with a D/3 saw-cut depth introduced at 0 hour	662
A.149. Pavement cured at 30°C ambient temperature with a D/3 saw-cut depth introduced at 0 hour	664
A.150. Pavement cured at 36°C ambient temperature with a D/3 saw-cut depth introduced at 0 hour	666
A.151. Pavement cured at 4°C ambient temperature with a D/8 saw-cut depth introduced at 0 hour	668
A.152. Pavement cured at 10°C ambient temperature with a D/8 saw-cut depth introduced at 0 hour	670
A.153. Pavement cured at 18°C ambient temperature with a D/8 saw-cut depth introduced at 0 hour	672
A.154. Pavement cured at 23°C ambient temperature with a D/8 saw-cut depth introduced at 0 hour	674
A.155. Pavement cured at 36°C ambient temperature with a D/8 saw-cut depth introduced at 0 hour	676
A.156. Pavement casted at “H” ambient temperature at 1:00 p.m. and sawed with a D/3 saw-cut depth after 12 hours	678
A.157. Pavement casted at “H” ambient temperature at 7:00 p.m. and sawed with a D/3 saw-cut depth after 12 hours	680
A.158. Pavement casted at “H” ambient temperature at 1:00 a.m. and sawed with a D/3 saw-cut depth after 12 hours	682
A.159. Pavement casted at “M” ambient temperature at 1:00 p.m. and sawed with a D/3 saw-cut depth after 12 hours	684
A.160. Pavement casted at “M” ambient temperature at 7:00 p.m. and sawed with a D/3 saw-cut depth after 12 hours	686
A.161. Pavement casted at “M” ambient temperature at 1:00 a.m. and sawed with a D/3 saw-cut depth after 12 hours	688
A.162. Pavement casted at “C” ambient temperature at 1:00 p.m. and sawed with a D/3 saw-cut depth after 12 hours	690
A.163. Pavement casted at “C” ambient temperature at 7:00 p.m. and sawed with a D/3 saw-cut depth after 12 hours	692
A.164. Pavement casted at “C” ambient temperature at 1:00 a.m. and sawed with a D/3 saw-cut depth after 12 hours	694

Figure	Page
A.165. Pavement built with rapid setting materials and a D/3 saw-cut depth introduced at 0 hour	696
A.166. Pavement built with rapid setting materials and a D/3 saw-cut depth introduced at 6 hours	698
A.167: Pavement built with rapid setting materials and a D/3 saw-cut depth introduced at 12 hours	700
A.168. Pavement built with rapid setting materials and a D/3 saw-cut depth introduced at 18 hours	702
A.169. Pavement built with rapid setting materials and a D/3 saw-cut depth introduced at 24 hours	704
A.170. Pavement built with rapid setting materials and a D/2 saw-cut depth introduced at 6 hour	706
A.171. Pavement built with rapid setting materials and a D/6 saw-cut depth introduced at 6 hour	708
A.172. Pavement built with rapid setting materials and a D/8 saw-cut depth introduced at 6 hours	710
A.173. Pavement built with slow setting materials and a D/3 saw-cut depth introduced at 0 hour	712
A.174. Pavement built with slow setting materials and a D/3 saw-cut depth introduced at 12 hours	714
A.175. Pavement built with slow setting materials and a D/3 saw-cut depth introduced at 24 hours	716
A.176. Pavement built with slow setting materials and a D/3 saw-cut depth introduced at 30 hours	718
A.177. Pavement built with slow setting materials and a D/3 saw-cut depth introduced at 36 hours	720
A.178. Pavement built with slow setting materials and a D/3 saw-cut depth introduced at 42 hours	722
A.179. Pavement built with slow setting materials and a D/2 saw-cut depth introduced at 6 hours	724
A.180. Pavement built with slow setting materials and a D/6 saw-cut depth introduced at 6 hours	726
A.181. Pavement built with slow setting materials and a D/8 saw-cut depth introduced at 6 hours	728

Figure	Page
B. 1. The average end stress and average tensile strength for a pavement with a D/2 saw-cut depth	731
B. 2. The average end stress and average tensile strength for a pavement with a D/3 saw-cut depth	733
B. 3. The average end stress and average tensile strength for a pavement with a D/4 saw-cut depth	735
B. 4. The average end stress and average tensile strength for a pavement with a D/6 saw-cut depth	737
B. 5. The average end stress and average tensile strength for a pavement with a D/8 saw-cut depth	739
B. 6. The average end stress and average tensile strength for a pavement with a D/100 saw-cut depth	741
B. 7. The average end stress and average tensile strength for a 10-inch thick pavement with a D/3 saw-cut depth.....	742
B. 8. The average end stress and average tensile strength for a 10-inch thick pavement with a D/8 saw-cut depth.....	744
C. 1. Average end stress to average tensile strength ratios for 15-inch thick pavements with a D/2 saw-cut depth	747
C. 2. Average end stress to average tensile strength ratios for 15-inch thick pavements with a D/3 saw-cut depth	749
C. 3. Average end stress to average tensile strength ratios for 15-inch thick pavements with a D/4 saw-cut depth	751
C. 4. Average end stress to average tensile strength ratios for 15-inch thick pavements with a D/6 saw-cut depth	753
C. 5. Average end stress to average tensile strength ratios for 15-inch thick pavements with a D/8 saw-cut depth	755
C. 6. Average end stress to average tensile strength ratios for 15-inch thick pavements with a D/100 saw-cut depth	757
C. 7. Average end stress to average tensile strength ratios for 10-inch thick pavements with a D/3 saw-cut depth	758
C. 8. Average end stress to average tensile strength ratios for 10-inch thick pavements with a D/8 saw-cut depth	760

Figure	Page
D. 1. Average end stress to average tensile strength and phi ratios for 15-inch thick pavements with a saw-cut depth of $D/2$	763
D. 2. Average end stress to average tensile strength and phi ratios for 15-inch thick pavements with a saw-cut depth of $D/3$	765
D. 3. Average end stress to average tensile strength and phi ratios for 15-inch thick pavements with a saw-cut depth of $D/4$	767
D. 4. Average end stress to average tensile strength and phi ratios for 15-inch thick pavements with a saw-cut depth of $D/6$	769
D. 5. Average end stress to average tensile strength and phi ratios for 15-inch thick pavements with a saw-cut depth of $D/8$	771
D. 6. Average end stress to average tensile strength and phi ratios for 15-inch thick pavements with a saw-cut depth of $D/100$	773
D. 7. Average end stress to average tensile strength and phi ratios for 10-inch thick pavements with a saw-cut depth of $D/3$	774
D. 8. Average end stress to average tensile strength and phi ratios for 10-inch thick pavements with a saw-cut depth of $D/8$	776

CHAPTER 1: INTRODUCTION

1.1 Background

Joints are placed in portland cement concrete pavements (PCCP) as a method to control random cracking. These joints serve to provide a weakened plane, thereby enabling cracking to occur in a controlled manner at a specific location. These cracks act to relieve the residual stresses that develop when thermal, hygral, or hydration (chemical shrinkage) movements are resisted by the subgrade and adjoining pavement.

Joints can be induced in early age concrete using several methods which include the use of hand-tools, preformed strips, and saw-cutting. While these three approaches are all valid, practical considerations for slip-form paving operations result in the nearly exclusive use of saw-cutting as the method of choice for inducing joints. Generally it is thought that three main methods of saw-cutting joints exist including conventional wet-cut (water-injection) saws, conventional dry-cut saws, and the more recently developed early-entry dry-cut saws.

While the concept of creating a weakened plane by saw-cutting may appear straightforward, determining the time and depth of the saw-cut has proven to be much more complicated (Okamoto, 1994). To be effective, the saw-cut must be placed within a specific window of time during the construction operation. The window of time for saw-cutting starts when the concrete has gained enough strength to prevent raveling when it is sawed and the window ends when residual stress buildup can lead to cracking at random locations. Generally, the random cracks do not occur where load transfer occurs, which can lead to severe deterioration and potentially be expensive to replace. The saw-cutting

window greatly depends on the constituent materials that are used, the fresh mixture properties, available restraint from sub-grade or adjacent pavement (i.e., tied sections), and ambient weather conditions. Determining the time for saw-cutting in the field is based on the saw operator's experience and a simple and subjective test which involves scratching the surface of the pavement.

Guidance from national agencies regarding time the saw-cut should be placed is limited. For example, the American Concrete Institute (ACI Committee 224.3, 1995) recommends that "the joints should be sawed as soon as practical wherein the concrete should have hardened enough". This recommendation exists since sawing too early can result in raveling and spalling at the edges of the cut, while sawing too late can result in random cracking and ineffectual contraction joints that do not open or function properly.

INDOT standard specification 503.03 specifies 2 to 12 hours as the window of opportunity to saw-cut for transverse joints and "sufficiently hardened" pavement for longitudinal joints. It has also been shown that late sawed pavement which exhibit no visible random cracking can reach stress levels (40-50% of the tensile strength) that are sufficient to cause micro-cracking around the aggregates (Yang et al. 2004). This micro-cracking has the potential to reduce long-term durability (Mindess and Young, 2003, Yang et al., 2004). Micro-cracking due to late saw-cutting is related to increased water absorption and may be associated with initial damage that ultimately results in the development of 'random' or 'mid-panel' visible cracks.

Not only is the saw-cutting timing difficult to determine, but the appropriate depth of the saw-cut is largely debated. A shallow cut is faster and less demanding on the saw-cutting equipment, especially the saw-blade. However, shallow cuts still need to achieve a sufficient depth to weaken the section sufficiently (with reasonable confidence) so that it will be able to define where the crack occurs. Questions regarding the adequate depth of the saw-cut have been magnified due to new light-weight early-entry saws that may enable joints to be cut at an earlier age which may require a shallower depth of the cut.

A recent American Concrete Paving Association (ACPA) report (Voigt, 2000) approximated that 96% of the state agencies required a minimum cut depth (a) of at least

one-quarter of the pavement thickness (D) (i.e., $a/D = 1/4$) for jointed plain concrete pavement. The ACPA recommends different saw-cut depths depending on the degree of restraint in the pavement (ACPA, 2002a). The ACPA recommends that the saw-cut should be $1/3$ the pavement depth (i.e., $a/D = 1/3$) for all longitudinal contraction joints, and transverse contraction joints in pavement placed on stabilized and open-graded subbases, while a joint depth of $a/D = 1/4$ is recommended for transverse contraction joints in pavements placed on dense granular subbases. The $a/D = 1/3$ recommendation is consistent with Indiana Department of Transportation (INDOT) specified type D-1 contraction joints. The specification is clearly illustrated in current INDOT standard drawing E 503-CCPJ-01.

One testing technique which may be able to assist contractors in determining the time of the saw-cutting window is the maturity method. The maturity method has proven to be an effective, economical, and non-invasive way to predict the rate of strength gain and stiffness development in concrete. Because the maturity method has already been implemented in Indiana, contractors are familiar with the maturity method and many have the equipment necessary for maturity measurement and prediction. Past research (Okamoto, 1994) has begun to examine the saw-cutting window using non-destructive techniques which included the maturity method. The guidelines developed were based on cement content and the type and shape of coarse aggregate.

Small, but significant, steps have been taken to remove the guesswork from the saw-cutting of concrete pavements. Several computer programs such as HIPERPAV have been developed to predict early-age stress development. These models consider material property development, environmental inputs, and contractor operations. Although these programs estimate concrete strength and stresses during the early ages of the pavement's development, they do not consider the effect of saw-cutting.

This study examines the saw-cutting window using the maturity method as a predictor of tensile strength and fracture properties. It is the hypothesis of this work that the residual stresses can be computed based on simple rules and that these stresses can be compared to the permissible stress (i.e., either strength or critical stress from fracture

mechanics) predicted from maturity concepts to define a saw-cutting depth and time window that considers the risk associated with raveling or random cracking.

1.2 Research Objectives

The seven primary objectives of this research are as follows:

- *The first objective of this work is to perform field experiments which will determine the approximate saw-cutting time window in the State of Indiana given the range of environmental and material parameters. In addition, the field experiments will assess the potential implementation of the maturity method as a tool to assist contractors with saw-cutting.*
- *The second objective of this work was to examine the relationship between compressive, flexural, and direct tensile strength during the saw-cutting time window.*
- *The third objective of this work was to compare early-entry saws to conventional saws in regard to timing, depth, and possible influences on the durability of the pavement.*
- *The fourth objective of this work was to assess the influence of saw-cut depth taking into consideration the potential for extensive residual stress development which can lead to random cracking.*
- *The fifth objective of this work was to investigate the effect of the time of saw-cut introduction on residual stress development and cracking behavior of concrete pavements.*
- *The sixth objective of this work was to determine the influence of ambient weather conditions and constituent materials on the saw-cutting time window.*
- *The seventh objective of this work was to develop a methodology to explain when a saw-cut should be placed considering the depth of saw-cut.*

1.3 Organization of the Report

This study is divided into three major components. The first component includes field investigations to assess the current saw-cutting practices by state contractors. The second component of this work involves using the data obtained from the field investigations in developing the laboratory testing program and for testing predictive models. The third component of this work includes computer simulation. The commercial finite element software, FEMMASSE, is used to investigate the stress and cracking behavior of pavements. This, in large part, is involved in development of a model and investigating the effect of different timing and depth of saw-cutting under different environmental conditions.

CHAPTER 2: LITERATURE REVIEW

2.1 Introduction

This chapter provides a review of literature related to determining the saw-cutting window. In addition, this chapter provides a review of the Hiperpav software that can be used to determine early age property development in concrete pavement.

It should be noted that in order to determine the appropriate time for saw-cutting, a wide range of factors and properties must be taken into consideration. This chapter investigates these factors so they can be considered in the development of the research plan. It is the intent of this chapter to provide the necessary information in order to develop an accurate and efficient testing and analysis program.

The literature review will discuss factors associated with the saw-cutting window and the maturity method in four separate sections. The literature review begins by comparing the two most commonly used maturity functions and maturity-strength relationships. This section explains why the Arrhenius maturity function was chosen instead of the Nurse-Saul function for this project.

The literature review then includes a discussion of raveling, which is a common problem associated with sawing at too early of age. Raveling is a condition when the edges of the slab break, chip, or fray. This section also includes a description of the classification, problems, and associated parameters of raveling in pavements.

The fourth section will review saw-cutting tools and equipment. This will include an in-depth assessment of early-entry saws. Early-entry saws are fundamentally different from conventional saws and are designed to perform at an earlier age.

The fifth section will review the HIPERPAV software program and analyze its implications on this research project. The HIPERPAV software has applications that can be implemented into this research project.

2.2 Maturity of Concrete

2.2.1 Background

In the late 1940's a method was developed to consider the effects of temperature and time on the rate of strength gain in concrete. Concepts related to maturity first started with ideas original to McIntosh (1949) and Nurse (1949). McIntosh experimented with accelerated curing methods and Nurse suggested that the product of time and temperature could be used to analyze the effects of different steam curing cycles. In 1951, Saul (Saul, 1951) elaborated on the idea of combining time and temperature into a single number, which he called "maturity". The "maturity" could also be used to estimate the strength gain of concrete samples using their temperature and time history. Saul also introduced the concept of a datum temperature which was the lowest temperature at which the chemical reaction and corresponding strength gain could occur. Saul's proposal was based on the concept that the exothermic reaction between cement and water can be used to determine strength gain in concrete. Therefore, Saul was trying to quantify the influences of temperature on the rate of strength gain through the term "maturity".

Since Saul's initial proposal of the maturity method, significant research has been conducted to challenge the validity of this method and to provide modifications to improve its accuracy. McIntosh among others (McIntosh, 1956) demonstrated that specimens of the same maturity, exposed to lower early-age temperatures were weaker at early maturities and stronger at later maturities than those exposed to higher early-age temperatures. This later became known as the "cross-over" effect and is further explained in section 2.2.2.

Technological advancements have made the method more practical by simplifying the process of obtaining data and calculating the corresponding maturity. Maturity systems now have the ability to record temperature every minute and send the data to the user via wireless connections. The concrete industry, as a whole, has made vast technological and organizational advancements since the 1950's. These advancements have provided a significant improvement in quality control, most notably the consistency, placement, and consolidation of mixes. With the advancement of the industry and maturity system components, the method is now considered a practical and simple way to predict strength gain using the temperature and time history. As the accuracy and practicality of the maturity method continue to improve, there will be significant benefits. These benefits include savings in time, material, and labor. In addition, the maturity method can provide valuable information for construction scheduling and estimating.

2.2.2 Maturity Functions

A maturity function is a mathematic formula that translates temperature and time history into a number (or factor) that represents the maturity (strength gain) of the concrete. Saul (1951) added to Nurse's concept and proposed that time and temperature calculations should be determined with respect to a "datum temperature". The datum temperature should be the lowest temperature that strength gain is most commonly observed. Nurse proposed Equation 2.1 (commonly known as the Nurse-Saul maturity function) to calculate maturity. In Equation 2.1 the datum temperature (T_0) is subtracted

$$M = \sum_{t=0}^t (T - T_0) \Delta t \quad (2.1)$$

from the average temperature (T) during the relevant time interval (Δt). In the Nurse-Saul maturity function, the maturity (M) is given as a time temperature factor (TTF). Two observations should be noted from the Nurse-Saul maturity function: 1) only

temperatures above the datum temperature are included in the calculations, and 2) the cumulative TTF is simply equal to the area under the time-temperature curve.

In 1962 (Copeland et al., 1962) proposed that the Arrhenius equation could better represent the effect of changes in temperature which influence the rate of chemical reaction of cement hydration. The Arrhenius equation is based on fundamental thermodynamic concepts. Overall the Arrhenius equation was used to quantify how an increase in temperature will increase the probability that two gas molecules will collide with one another. This method has been extended to chemical reactions over the years to quantify the amount of activation energy required for the reaction to occur. In 1977 an expression was derived to represent the maturity of concrete based on the Arrhenius equation (Freiesleben et al., 1977) and is shown in Equation 2.2. The

$$t_e = \sum_{t=0}^t e^{\frac{-E}{R} \left(\frac{1}{273+T} - \frac{1}{273+T_r} \right)} \Delta t \quad (2.2)$$

equivalent age (t_e) is calculated based on the reference temperature (T_r) and average temperature (T) during the time interval (Δt) while also considering the activation energy (E) in Joule / mol and universal gas constant (R) as 8.3114 J/ (mol-K).

The Nurse-Saul equation can be revised to express the maturity value in equivalent age units. The equivalent age maturity is the duration of time that a specimen would need to be cured at a specified reference temperature (usually 20°C) to equal the maturity of the specimen stored at various temperatures. The equivalent age is a simple way to express the maturity in terms of time. The equivalent age concept can be applied to most maturity functions and provides an ample means of comparison between the Nurse-Saul and Arrhenius maturity function. The Nurse-Saul equivalent age maturity is defined by

$$t_e = \frac{\sum (T - T_0)}{(T_r - T_0)} * \Delta t \quad (2.3)$$

the average temperature (T) during the time interval (Δt), and the datum (T_0) and reference temperature (T_r). In order to compare the two equations in equivalent age form we look at the “age conversion factor” can be called α . The age conversion factor simply converts the curing interval (Δt) to the equivalent age (t_e) duration at the standard reference temperature (T_r). The age conversion factor (α) can be substituted into both equivalent age equations which is shown in Equation 2.4. The age conversion factor (α) is shown in Equations 2.5 and 2.6 for the Nurse-Saul and Arrhenius equations respectively:

$$t_e = \sum_{t=0}^t \alpha \Delta t \quad (2.4)$$

$$\alpha = \frac{(T - T_0)}{(T_r - T_0)} \quad (2.5)$$

$$\alpha = e^{\frac{-E}{R} \left(\frac{1}{273+T} - \frac{1}{273+T_r} \right)} \quad (2.6)$$

Figure 2.1 illustrates the fundamental difference between the age conversion factor equations by plotting the age conversion factors (α) versus the temperature (T) at the same reference temperature (T_r) while using standard values of the activation energy (E) and the gas constant (R). From the figure we find that the Nurse-Saul age conversion factor is a linear function of the curing temperature based on the datum temperature whereas the Arrhenius age conversion factor is an exponential function of curing temperature varied with the activation energy.

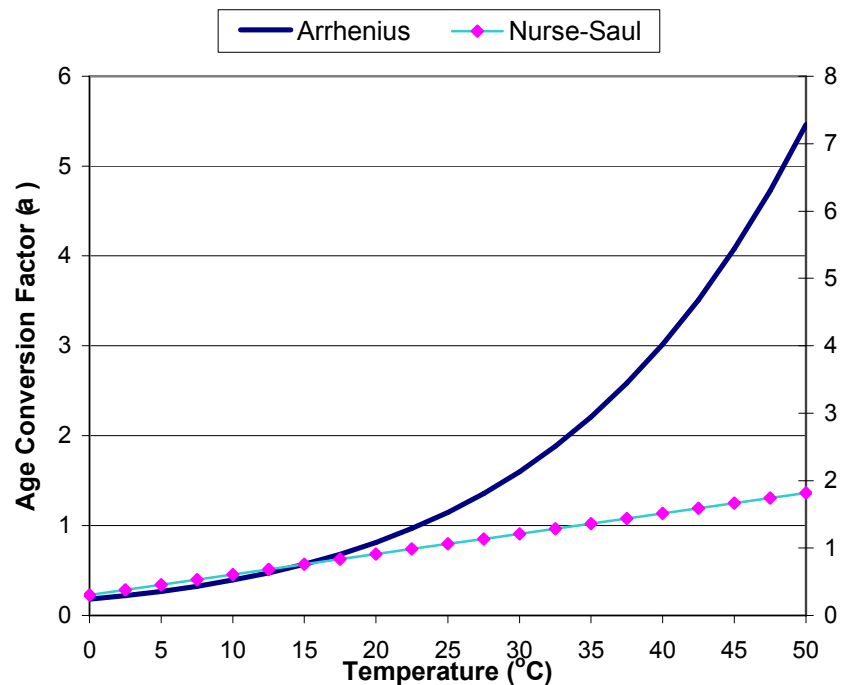


Figure 2.1: Age conversion factors versus temperature ($T_o = -10^\circ\text{C}$, $E = 50,000$ Joule/Mole)

Figure 2.2 shows how activation energy changes the shape of the age conversion factor vs. temperature curve. Activation energy values can be determined on mortar tests which are outlined in ASTM C 1074-04. For this research project an activation energy

value of 40 kJ/mol will be used as this value has proven valid by INDOT and accurate for ASTM Type I cements (Carino, 1991).

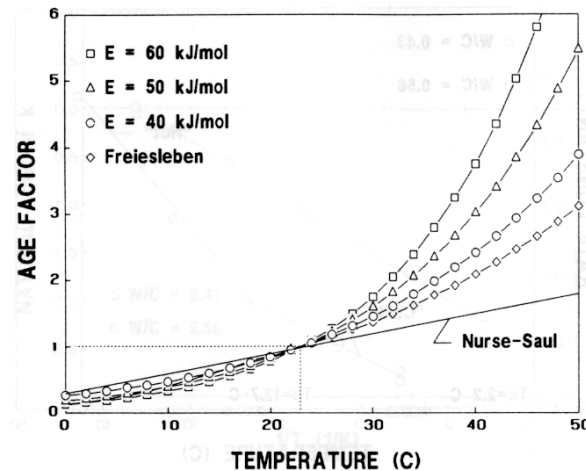


Figure 2.2: Age conversion Factor versus temperature at various activation energies
(Carino, 1991, p. 122)

Early use of the Nurse-Saul maturity function revealed deficiencies in the maturity method. One of the deficiencies is known as the “cross-over effect”. The cross-over effect is exhibited in specimens exposed to low early-age temperatures which appear weaker at early maturities and stronger at later maturities than specimens exposed to a higher early-age temperature. This is demonstrated in Figure 2.3. If the Nurse-Saul maturity equation held true there would be a

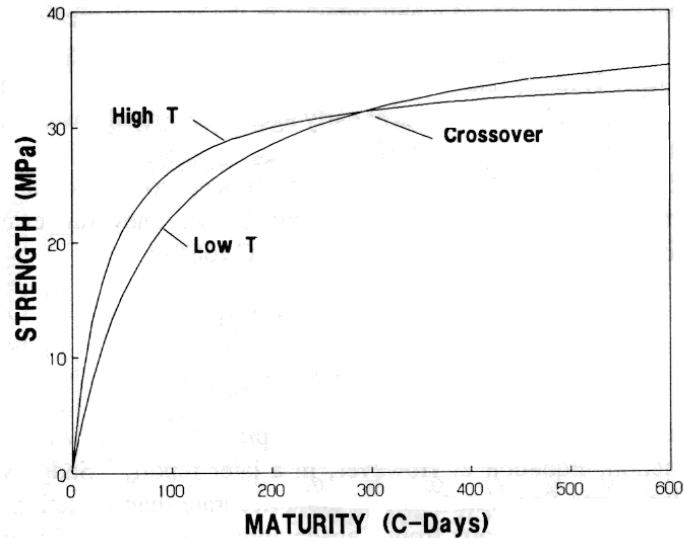


Figure 2.3: Strength development at high versus low early-age temperatures (Carino, 1991, p. 122)

single strength versus maturity curve. Verbeck and Helmuth (Verbeck, 1968) provide an explanation for the “cross-over” effect. They suggest that higher early-age temperatures result in a higher proportional increase in the initial rate of hydration than is captured in the Nurse-Saul equation. Therefore, concrete cured at higher temperatures is stronger than that cured at lower temperatures at early ages and opposite at late ages despite having the same Nurse-Saul maturity. The difference in long-term strength comes from the non-uniform distribution of hydration products within the pores during early-age rapid hydration. The non-uniform distribution leads to more large pores which decrease later-age strength and impedes the continued hydration of cement particles. Taking this into consideration, the Arrhenius equation has proven to better reflect the influences of a wider range of temperatures on the rate of hydration. Both maturity equations will provide an interpretable value that represents the time and temperature history of the concrete but in order to use this value to predict strength a Strength-Maturity Relationship must be established.

2.2.3 Strength-Maturity Relationship

Maturity functions are used to relate temperature to the maturity of concrete. This section will discuss the relationship between maturity and strength development for concrete. ASTM C 1074 establishes a strength-maturity relationship by drawing a best-fit curve through data, and also notes that a relationship can be established by using regression analysis from Equation 2.7 which was originally proposed by Plowman (Plowman, 1956). Plowman showed that when strength was plotted as a function of the logarithm of maturity the data correlated with a straight line significantly. The constants (a) and (b) are determined from experiments using the corresponding mixture design

$$S = a + b \log(M) \quad (2.7)$$

while the maturity (M) is calculated using the Nurse-Saul equation. This strength-maturity relationship has two limitations. First, the relationship predicts infinite strength gain with increasing maturity and secondly, the linear relationship between the strength and logarithm of maturity is only valid at intermediate values of maturity (Carino et al., 1991). This is the relationship currently used by Indiana Test Method 402-99T, which is used to predict in-place flexural strength for the opening of traffic to pavement. The opening of traffic to pavement, which occurs at a predicted 550 psi flexural strength, is considered to be an intermediate to later value of maturity.

As discussed in section 2.2.2, the Nurse-Saul maturity function and corresponding Plowman strength-maturity relationship may not accurately represent strength gain over a wide range of temperatures. During early-ages, concrete often undergoes a wide range of temperature fluctuations due the heat of hydration; therefore Arrhenius maturity function and hyperbolic strength-maturity provide a more accurate representation of strength gain.

Equation 2.8 shows the hyperbolic strength-maturity relationship proposed by Bernhardt (1956). For this hyperbolic equation the maturity (M) is defined by

$$S = \frac{M}{\frac{1}{A} + \frac{M}{S_{\infty}}} \quad (2.8)$$

the ultimate strength (S_{∞}), and the initial slope of the strength versus maturity response (A). The hyperbolic equation fits data well at later ages but does not correlate well with strength at early ages. The limitation can be traced to the fact that the hyperbolic equation assumed that the strength development began at a maturity of 0 ($M = 0$). To improve on the prediction capabilities of the hyperbolic equation an offset maturity value (M_o) was introduced which led to the derivation of Equation 2.9. The offset maturity

$$S = \frac{(M - M_o)}{\frac{1}{A} + \frac{(M - M_o)}{S_{\infty}}} \quad (2.9)$$

value takes into consideration that strength development does not begin until a certain maturity value (i.e. the offset maturity, M_o) has been reached. If the hyperbolic relationship holds true, the data should lie on a straight line when the inverse of strength versus the inverse of maturity is plotted. From this plot, we can find the ultimate strength and the initial slope of the hyperbolic curve by taking the inverse of the intercept and slope respectively. Theoretically the hyperbolic strength-maturity relationship has proven to be superior to the strength versus log (maturity) relationship. This is demonstrated in greater detail in CRC Handbook on Nondestructive Testing of Concrete Chapter 5.

2.2.4 Choice of Maturity Method

The Nurse-Saul maturity function is often used due to its relatively simple calculations which ease implementation. With the current state of technology in construction and maturity equipment, both maturity functions and strength-maturity relationships are equally capable of being implemented. The linear relationship between

the rate constant from Nurse-Saul equation and the temperature of the concrete does not provide an accurate maturity prediction over a wide range of temperatures which occur at early ages. The Arrhenius maturity function however provides a more precise representation of the hydration reaction. This research will analyze data using both the Nurse-Saul and Arrhenius equations but will develop models and further research based on the Arrhenius equation and hyperbolic strength-maturity relationship.

2.2.5 Choice of Strength Testing

To provide reference data regarding the strength development of the mixture, flexural tests procedures will be followed according to AASHTO T 97. Flexural strength has shown to correlate better than compressive strength tests in relation to saw-cutting factors (Okamoto, 1994). These saw-cutting factors include the strength required to prevent raveling of the saw-joint. In addition, Indiana Test Method 402 currently uses flexural testing for the maturity method calculations. Use of flexural testing in this research will allow accurate comparison of results and promote the implementation of any procedures developed from this research.

2.2.6 Aggregate Influence on Maturity Method Predictions

A recent study at Purdue University has examined the influence of aggregates on early-age maturity predictions (Barde et al., 2004). Results have shown that at early ages (less than 2.5 days) flexural failure is controlled by the paste while at later ages strength is controlled by aggregate failure. In these studies, maturity was correlated to non-evaporable water content and plotted versus flexural strength for paste, mortar, and concrete. The mortar and concrete reveal a bi-linear relationship at which the change in slope is called the knee point.

The hypothesis affirms that at low ages (i.e. prior to reaching knee point), failure is dependent on the paste strength which is governed by the hydration reaction and is not significantly affected by the inclusion of aggregates. This implies that the maturity

method predictions are more accurate up to the knee point. After the knee point is reached, the rate of flexural strength development is lower in the mortar and concrete than in the paste. Preliminary visual analysis appears to indicate that the knee point correlates well with the beginning of fractures in aggregates. An increasing number of aggregate fractures occurred on specimens that were tested after the knee point. To determine the influence of the strength of aggregates, similar mixtures were prepared using aggregates of varying hardness and strength. The results showed that as the strength of the aggregate increases the knee point occurs at a higher maturity and strength. This supports the conclusion that the knee point will not occur until the aggregates begin to fracture.

Preliminary analysis shows that the knee point will occur after the end of the saw-cutting window for most mixture designs used in Indiana. While this will need to be verified with experimental examination, there are various reasons for understanding this knee point and its relevance to maturity predictions. One of these reasons is that strength to maturity relationship may show high variance at or around the knee point. If the saw-cutting window does occur before the knee point, as expected, the current maturity method will work provided there is accurate early age information. If the knee point occurs during the window, the method will need to be altered. Some possible mathematical alterations are suggested to incorporate the behavior of the aggregates (Barde et al., 2004).

2.3 Saw-cut Depth and Timing Considerations

A significant portion of this research project will focus on saw-cut depth related issues which have proven to be a complicated issue with many confounding factors (Okamoto, 1994). Currently there are a wide range of specifications within the industry regarding the depth of the saw-cut. An ACPA report (Voigt, 2000) approximated that 96% of the state agencies required a minimum cut depth (a) of at least one-quarter of the pavement thickness (d) (i.e., $a/d = 1/4$) for jointed plain concrete pavement. The ACPA also recommends different saw-cut depths for different degrees of restraint on the

pavement (ACPA, 2002a). INDOT currently recommends a joint depth of $a/d = 1/3$ for type D-1 contraction joints (INDOT, 2004). The issue of proper saw-cut depth has been magnified due to new light-weight early-entry saws which are discussed in section 2.5 of this report. Early-entry saw-cuts are usually placed at a significantly earlier age and at shallower depths. Soares proposed that the appropriate depth, in regards to crack initiation, is largely influenced by the time the joint is placed (Soares, 1997). Therefore, greater potential for crack control exists with early-entry systems due to lower fracture toughness of the concrete at early ages. In addition, it also has been suggested that shallower saw-cuts ($< D/4$) may take advantage of higher stress gradients near the surface as opposed to those at $D/3 - D/4$ depths. These higher gradients may lead to superior crack initiation. Field experiments have found that early-entry shallower saw-cuts can be just as effective as traditional $D/4$ to $D/3$ depths in controlling cracking (Missouri Department of Transportation (MODOT), 2001) (Zollinger, 1993). In one field study (MODOT, 2001) it was concluded that cracking often occurs more rapidly with deeper saw-cut's but early-entry shallow saw-cut's provided equally adequate control of random cracking (Soares, 1997). In another field study (Zollinger, 1993) saw-cuts were placed in a pavement on November 8, 1991 to depths of 1" ($D/12$) and 3" ($D/4$) for a 12" pavement. No visible cracks were found in the pavement until November 26, 1991 and many joints did not visually show any cracking. It was noted that a significant number of cracks developed after the pavement was subject to greater temperature fluctuations in the summer months of June and July. Since the pavement had gained significant strength before the increase in visible cracking it was suggested that cracking likely initiated at an early age but was not visible until later and larger temperature fluctuations caused the crack to propagate throughout the slab and become visible. Joints that do not propagate through the pavement and joints that are sawed too late can absorb larger quantities of stress which can increase the risk of random cracking and influence durability through microcracking (Yang et al., 2004)

Overall, there are three inter-related factors that need to be considered in determining the optimal depth of the saw-cut. The first and most important is the timing of the saw-cut. In general, the earlier the saw-cut is placed the greater chance it will have

to initiate a crack at the earliest time to relieve stress. The second factor to consider is the stresses that will be encountered at the depth of the saw-cut. It may be possible for shallower notches to reach higher stress concentrations at their tips due to thermal and hygral gradients, therefore a shallower notch may be more inclined to initiate a crack. The third factor to consider is whether or not the crack will propagate through the slab when initiated. As the concrete continues to gain strength and fracture toughness, the crack may be less likely to propagate through the slab when initiated.

2.4 Spalling and Raveling

The start of the saw-cutting window is defined as the time when the saw-cut can be performed without causing excessive spalling and raveling. Excessive spalling and raveling can compromise the durability of the joint. The beginning of the saw-cutting window is typically defined as the time at which there is the smallest probability of random cracking.

2.4.1 Definition and Classification

Spalling is defined by the ACPA as the cracking, breaking, chipping, or fraying of slab edges within 0.6 meter of a transverse joint. If spalling is severe, it will affect both the appearance and durability of the joint. Raveling is defined by the ACPA as the displacement of aggregate or paste near the slab surface from sawing. Raveling is an indication that the concrete strength may be too low for sawing. Thus, when the joint edges are severely raveling, the sawing must be delayed until the concrete gains adequate strength. Classifying raveling and spalling is subjective and no accurate specification exists in describing their severity. The severity of raveling has previously been quantified in square millimeter of raveling per lineal foot of sawing (Okamoto, 1994). This calculation proves tedious and difficult in determining square millimeters and does not account for the depth of raveling, but is a logical quantification of raveling. In South Carolina (SCDOT, 2000) it is believed that a small amount of raveling can signal the correct time to perform the sawing. There specification reads, “Some raveling of the

green concrete must be expected in order for the sawing process to prevent uncontrolled shrinkage cracking. If sharp edged joints are being obtained, the sawing processes shall be speeded up to the point where some raveling is observed”. Stereomicroscope examination of cores has shown that there is no relationship between external damage from early-age saw-cutting and internal damage to the concrete (Lofsjogard, 2001). These examinations show that small amounts of erosion should not affect the integrity or durability of concrete adjacent to the saw-cuts. It should also be noted that some raveling is acceptable when a second saw cut will be made for a joint sealant. The Indiana specification (INDOT, 1999) recommends the “initial saw cut commences as soon as the concrete has hardened sufficiently to permit sawing without raveling, usually 2 to 12 hour after placement. All joints shall be saw-cut before uncontrolled shrinkage cracking takes place. The second saw cut shall be made after the concrete has sufficiently cured”. Figure 2.4 shows different levels of severity in raveling. Determining the severity is very subjective and an adequate specification is needed within the industry.

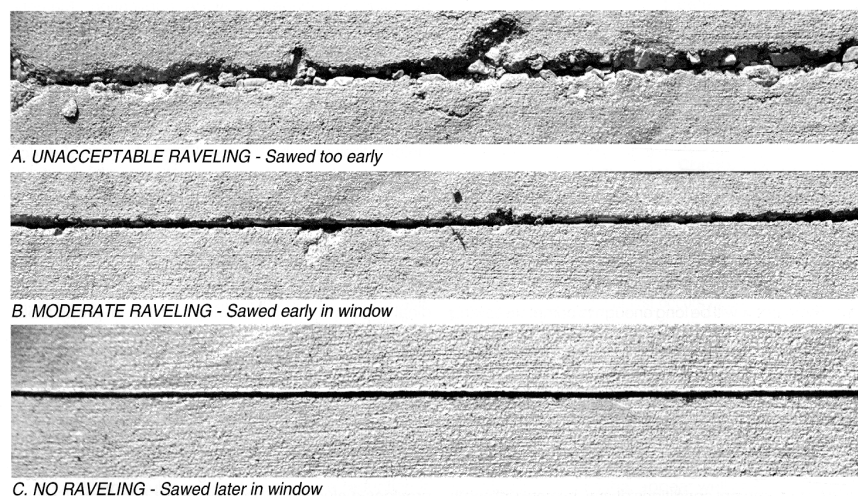


Figure 2.4: Severity classification of raveling (ACPA, 2002 a)

2.4.2 Material and Equipment Parameters

Raveling occurs when the exit force of the blade causes surface aggregates and attached paste to be dislodged from the pavement. Numerous material and equipment parameters are considered when examining raveling. The material parameters include: strength of paste, coarse aggregate shape, coarse aggregate size, coarse aggregate strength, coarse aggregate hardness, aggregate bond, bleed water around aggregates, fine aggregate abrasiveness, and heat transfer of saw-blade. The strength of paste is a vital component to determining when raveling will occur. When raveling occurs, the paste can not “hold” the aggregate in the pavement when struck by the blade. The maturity method, which is based on the hydration of the cement, has shown significant correlation in predicting the strength gain in paste therefore it should provide ample means of determining the strength of the paste.

Previous work has determined beginning of the saw-cutting window guidelines based on compressive strength and its correlation to raveling (Okamoto, 1994). Raveling was classified into five degrees of severity from its measured surface distress. The five categories ranged from “1-Badly Spalled” through “5-Excellent”. Equation 2.10 is an equation from Okamoto’s work which based the required compressive strength on four factors. These four factors included the saw-cut rating (R), coarse aggregate hardness (H, soft=0, hard=1), coarse aggregate geometry (G, round = 0, crushed = 1) and cement content per cubic yard (C). Using this equation Figure 2.5 shows a plot of common mixture designs used in the State of Indiana based on cement per cubic yard (C), soft limestone aggregate (H=0), and crushed aggregate geometry (G = 1).

$$\sqrt{f'c} = 13.9432 + 5.1931 * R + 8.7086 * H + 5.4198 * G - .0263 * C \quad (2.10)$$

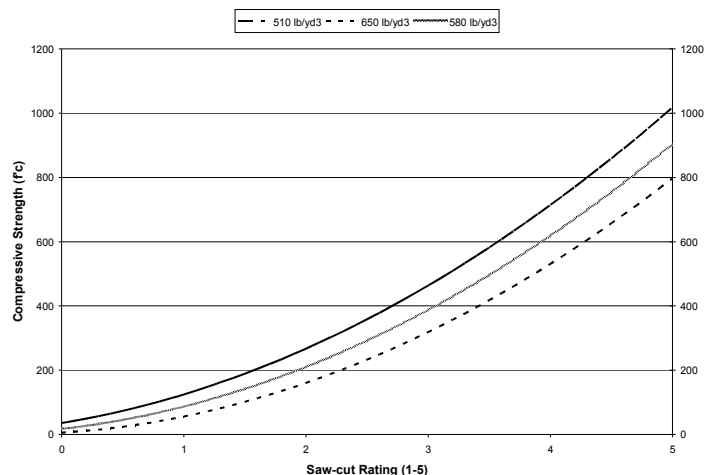


Figure 2.5: Saw-cut rating versus compressive strength

In considering coarse aggregate factors it should be noted that the majority of surface aggregates that are dislodged in moderate to severe raveling are 1/2" and smaller. From Equation 2.10 we find that a crushed aggregate requires more strength than a given rounded aggregate to achieve the same raveling. The exact influence of the shape of the aggregate on raveling was not stated, however, it does seem likely that a crushed aggregate would provide more tearing and surface distress when dislodged which would lead to an increase in visually measured raveling. In this study (Okamoto, 1994) it should be noted that two different hard crushed aggregates (quartzite and river gravel) were used whereas one rounded hard river gravel was used. It seems possible that the specification of "hard" and "soft" is not specific enough and the variation in hardness of the crushed aggregates may provide the variance in the results. Coarse aggregate strength and hardness which are highly correlated material properties have shown to have an influence on raveling. Aggregates which are strong and hard require more force from the saw-blade, which in return create stronger exit forces on aggregates. Equation 2.10 considers aggregate hardness as one of its parameters and shows an increase in required strength, for a given level of raveling, with an increasing hardness of aggregate. It is also worth mentioning that in general softer limestone aggregates form better bonds with the matrix than harder siliceous aggregates. Therefore the hardness of the aggregate may

also be indirectly correlated to the bond between the aggregate and the paste which would keep the aggregate from dislodging when struck with the blade.

A large coarse aggregate size is believed to make diamond blades cut at a slower pace but no direct effect of coarse aggregate size have been verified through research. Usually there is little variation of surface aggregates which are commonly of diameter smaller than $\frac{1}{2}$ ". Therefore any size larger than the $\frac{1}{2}$ " may prove insignificant to raveling but the percent of aggregates that fall between $\frac{1}{2}$ " and fines may prove significant. The influence of the quantity of aggregates between $\frac{1}{2}$ " and fines on raveling has not been determined through research.

The bond that occurs between paste and aggregates is what prevents the aggregate from dislodging when struck by the saw blade. The bond of the aggregate and paste often forms an area of high porosity which is further increased when excessive bleed water is trapped under aggregates. Bleed water has not been considered as a component of raveling but warrants examination when determining the strength of the bond. Typical slip-form pavement mixtures are of relatively low w/c ratio (<0.43), therefore bleed water should have a minimal effect on the bond. The texture of the aggregate will directly influence the bond of the aggregate and paste. A smooth aggregate will not form as strong of a bond as an aggregate with a coarse texture.

The abrasiveness of a mixture determines the wear on the segment and core of a diamond blade. The two factors which determine the abrasive wear are the type of fine aggregate and amount of free fine aggregate. Fine aggregate is either sharp, which is abrasive, or rounded, which is non-abrasive. The abrasiveness of sand is usually determined by its source. Crushed sand and bank sand are usually abrasive whereas river sand is usually non-abrasive. More free fine aggregate occurs at earlier ages when paste is not strong enough to hold the sand in place. More free sand that works past the blade causes more wear. The effects of abrasive concrete can be compensated for with a harder bonded blade therefore the only direct effects of the abrasiveness of the mix come from the selection of a different blade. The specifics of blade selection will be discussed in 2.4.4.

Theoretically it is possible for aggregates to expand when heated considering their coefficient of thermal expansion. This expansion could cause the aggregates to create forces that would cause them to break their bond with the paste and cause them to dislodge easier which would result in raveling. The frictional heat transfer from saw-blade to aggregate has been examined by Rick Norland (2004) using thermal imaging. From personal communication with Norland it was found that the heat transfer is insignificant from cutting friction because the heat is transferred to the dust or slurry and insignificant residual heat is conducted to the surface of the aggregate being cut.

Raveling is usually caused by a lack of material property development but it can also be caused by the saw equipment. Some mechanical problems which can lead to spalling include the misalignment and vertical beating of the saw blade. These mechanical problems amplify the blade exit forces and dislodgment of surface aggregates. A blade must be compatible with the power output of the saw, the concrete mixture, and the application. If an improper saw blade is used it will quickly dull and potentially dislodge aggregates during the cut. In some cases raveling can be corrected by switching to a different saw blade.

2.5 Saw-cutting Equipment

Within the concrete saw-cutting industry there are numerous sawing techniques and various types of equipment available. Saw-cutting the primary joint can be divided into three general categories: 1) Span, 2) Conventional, and 3) Early-Entry.

2.5.1 Span Saws

Span saws are mechanical saw devices that “span” the width of the pavement for which the saw traverses without a walk behind manual operator. They are the least common because they are expensive relative to conventional and early-entry walk-behind saws. Contractors often choose to use span saws for transverse joints on wide pavement where the saw can complete the joint in one pass, thus increasing productivity. Spans

saws are heavier than walk-behind saws and apply larger loads onto the pavement at early ages. No span saws were encountered during the site visits that occurred during the fall of 2003 and in a brief phone survey of contractors around the State of Indiana it was found that they were not prevalently used.

2.5.2 Conventional Saws

The conventional method of saw-cutting uses a walk-behind saw and performs a wet cut. A wet cut uses water to cool the blade which produces a slurry of material. The equipment is usually powered by a self-contained engine, although some are electrically or pneumatically driven. Horsepower range from 35-65 in walk behind saws. The higher horsepower saws are capable of performing the cut in a shorter time. Conventional saws should be operated at approximately 8-10 feet per minute which has been determined the most economical cutting speed based on labor costs, blade costs, and operations costs. Wet cutting can extend blade life but it has numerous drawbacks. Most conventional wet-cut saws turn their blades in the down cut direction. The term “down-cut” denotes that the front of the blade goes down into the joint first whereas an “up-cut” would represent the rear of the blade going first into the pavement. Figure 2.6 illustrates the direction of

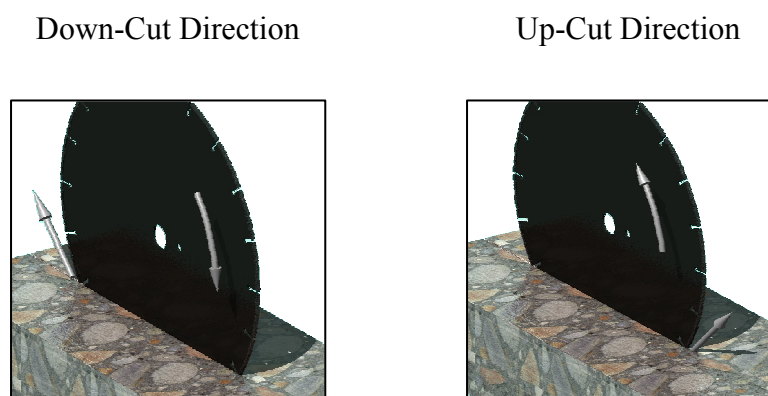


Figure 2.6: Saw-Cut direction (Norland, 2004)

blade rotation for the “down-cut” and “up-cut” directions. The down cut thrusts slurry into the joint and behind the saw whereas the up cut thrusts slurry out of the joint and in front of the saw. Performing a wet cut requires water hoses, water pumps, water trucks, and line saver paint so the chalk line won’t be erased by the water slurry. Dry cuts using conventional methods eliminate the attachments and saver paint, but can lead to significant blade cost compared to the wet cut methods. Figure 2.7 shows a picture of a conventional 65hp wet-cut saw being used to saw a longitudinal joint in the Indianapolis metropolitan area.



Figure 2.7: Conventional wet-cut saw

2.5.3 Early-entry Saws

The early-entry sawing method and saw was first introduced in 1988 by Chiuminatta of Chiuminatta Concrete Concepts. The early-entry technology developed from various needs in the saw-cutting industry. The ability to perform the saw-cut at an earlier maturity has numerous benefits. When pavement is sawed at an earlier maturity internal stresses are relieved before they generate cracking. Also, due to the earlier sawing of the joint, it is has been suggested that the cracking at the joint will propagate with a shallower depth of saw-cut. Early-entry technology uses an upwards cut, which reduces slurry in the joint, and a spring loaded skid plate to apply pressure to the concrete

while it is being cut. The skid plates keep surface aggregates from flying free when jolted by the blade. Figures 2.8 and 2.9 show pictures of the anti-ravel skid plate and diamond blade on a Soff-Cut[®] early-entry saw.

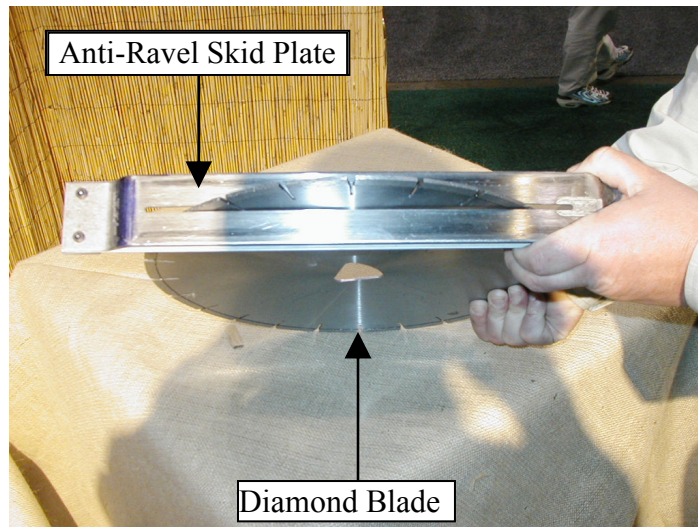


Figure 2.8: Detached Soff-Cut[®] anti-ravel skid plate and diamond blade

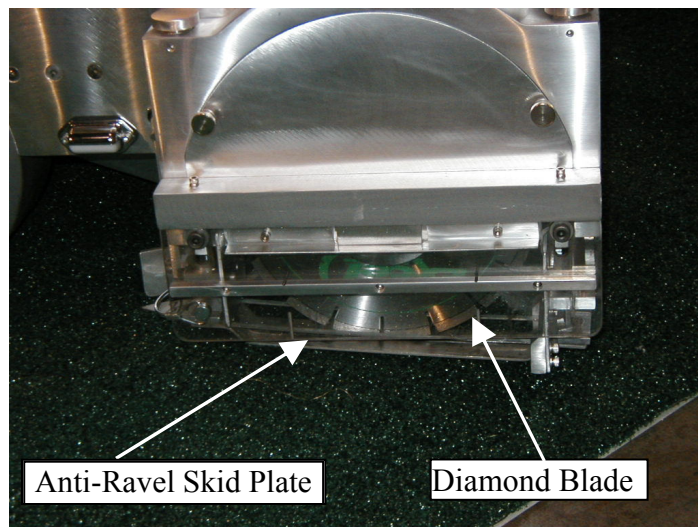


Figure 2.9: Attached Soff-Cut[®] anti-ravel skid plate and diamond blade

Early-entry saws can improve efficiency because they do not require source of water. However, due to the lack of supplied water the friction is increased between the blades and the concrete which causes them to wear down faster. Therefore, the cost is higher per inch blade per foot of cutting basis. In addition, airborne dust is minimized due to the early-age properties of the concrete. Overall productivity in lineal feet per hour per saw has been shown to be comparable and sometimes improved with early-entry saws as opposed to conventional saws (MODOT, 1991). Figure 2.10 is a picture of a standard early-entry saw (Soff-Cut, 2004) used for full depth pavements.



Figure 2.10: Soff-Cut early-entry saw

2.5.4 Blades

The two major types of blades used for saw-cutting concrete are consumable abrasive and diamond impregnated. When abrasive blades are used it is important to monitor the wear and to set a limit at which the blade needs to be replaced. If not properly monitored, the depth of the cut may vary and prove to be insufficient in weakening the plane cracking. Abrasive blades have been replaced for almost all practical full-depth pavement purposes by the more durable and consistent diamond blade. Diamond blades are significantly more expensive initially but can prove to be cost-effective when the labor expense of changing blades is considered on larger jobs.

Diamond blades can cut all concrete materials whereas abrasive blades are only economically sufficient to cut softer aggregates, and are rarely used on hard aggregates. The use of diamond blades has become conventional practice for sawing pavement in the state of Indiana. Different diamond blades are available depending on the hardness of the coarse aggregate and abrasiveness of concrete. Table 2.1 shows Mohs scale and Table 2.2 shows a general classification of aggregates by hardness based on Mohs scale.

Table 2.1: Mohs scale

<u>Mohs Scale</u>	
1 - Talc	6 – Feldspar
2 - Gypsum	7 – Quartz
3 - Calcite	8 – Topaz
4 - Fluorite	9 – Corundum
5 - Apatite	10 – Diamond

Table 2.2: Aggregate hardness classification (Norland, 2004)

<u>Mohs Range</u>	<u>Description</u>	<u>Aggregates</u>
8-9	Critically Hard	Flint, Chert, Trap Rock, Basalt
6-7	Hard	Some River Rock, Some Granites, Basalt, Quartz, Trap Rock
4-5	Medium Hard	Some Granites, Some River Rock
3-4	Medium	Dense Limestone, Sandstone
2-3	Medium Soft	Soft Limestone

Harder aggregates dull diamonds more quickly therefore the segment bonds (matrix) of the blade need to be softer when cutting hard aggregate. This allows the matrix to wear normally and allow the diamond grit to reach the surface more rapidly. Softer aggregate does not dull the diamond grit as rapidly, therefore a harder blade matrix is necessary to keep diamonds in place to utilize their full potential before they are replaced. Abrasive concrete causes the segment to wear faster, therefore abrasive sand and early-age concrete must be included when considering the hardness of the blade matrix and the rate at which it should wear for optimal performance.

Diamonds are manufactured in a wide range of sizes for saw blades. The size of the diamond used in saws determines the amount of diamond that is exposed above the cutting surface (Norland, 2004). The exposure of the diamond protrusion determines the material removal rate by influencing the depth of the cut. Therefore, larger crystals are generally used for softer aggregates and are potentially capable of removing material faster. The mesh size of a diamond is the number of crystals per carat. Larger diamonds will have smaller mesh numbers. The mesh size influences the equipment's life and power requirements and must be balanced with the concentration of diamond in the

cutting segment for optimal performance. The concentration is a measure of the number of diamonds particles in a cubic inch of segment. A common unit of measurement is 100 con which equals 75 carats/cubic inch. No single measurement standard has been agreed upon in the saw-cutting industry (Norland, 2004).

There is a distinct relationship between the shape of diamonds and their performance. A large proportion of irregularly and angular shaped crystals work best for less severe diamond load applications whereas “blockier” crystal work better for severe diamond loads. Block shaped crystals provide the greatest resistance to fracturing due to the large number of edges and minimum surface contact. The ideal diamond shape for sawing concrete is a shape called a “cubo-octahedron” (Norland, 2004) which is a combination of a cube and octahedron where the octahedral faces meet at the middle of the cubic edges.

The impact strength of a diamond product is a measure of the ability of the crystals to withstand the impact of the loads during sawing. The impact strength is influenced by the crystal shape, size, inclusions, and there distribution. Tougher materials require greater impact strength up to the limiting impact strength required. As the severity of the diamond load increases, the minimum impact strength required increases. The measure of impact strength of diamond is known as the Toughness Index (TI). More information regarding toughness index can be found from manufactures of diamond blades for concrete pavements. The impact strength of blades should be an indication of the striking force that is applied to the aggregates when being sawed. Keeping all other variables constant, a blade with high impact strength will distribute a higher force to the concrete and aggregates than a blade with lower impact strength. The operating speed of blades is another component of the striking force that blades apply. Operating speeds are blade specific and based on the blade size and the type of material being cut. The actual operating speed is usually adjusted for the specific type of aggregate being cut.

2.6 Hiperpav Software (V.2.5.1)

2.6.1 Background

It has been established in the concrete pavement industry that controlling stress and strength behavior during early ages (first 72 hours) can lead to superior durability (Hiperpav, 2004). Inadequate control can prove costly due to delays, replacement of pavement, and reduced service life. Hiperpav, an acronym for High Performance Paving, is the name given to a software program developed to predict and analyze pavement performance in the first 72 hours. Hiperpav's development and innovation resulted from FHWA's Special Project 201, entitled "Fast-track Concrete Pavements". Special project 201 evaluated accelerated strength gain of concrete pavements due to changes in cement type and quantity. These changes resulted in accelerated strength but also resulted in excessive temperatures and temperature gradients. FHWA issued a contract with The Transtec Group to provide guidelines on the temperature issues of these pavements. The Transtec Group, in recognition of the complexity of the issues, implemented computer models which developed into the Hiperpav program. The software program was developed using data collected from the field and validated with field experiments.

2.6.2 Hiperpav Analysis

The analysis of this section will be predicated on Hiperpav version 2.5.1 which models jointed concrete pavement. Hiperpav is designed to predict the stress and strength performance of pavement during the first 72 hours. Users of the software input information into four major categories: pavement design, mixture proportions, environmental parameters, and construction parameters. Two different analyses can be run once the user has input the necessary information. The first, Hiperpav analysis, gives a detailed prediction of the pavement strength and corresponding stress during the first 72 hours. The second is the evaporation rate analysis; this provides the evaporation rate at various wind speeds during the first 8 hours. Figures 2.11 and 2.12 show the Hiperpav and evaporation rate analysis for the default mix design.

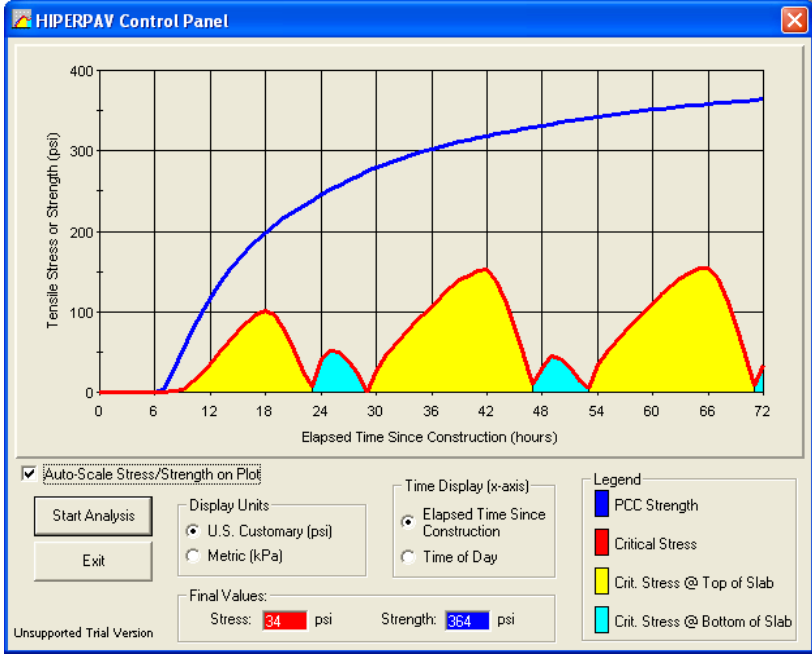


Figure 2.11: Hiperpav analysis showing the elapsed time since construction (x-axis) versus the tensile strength or stress development in the slab (y-axis)

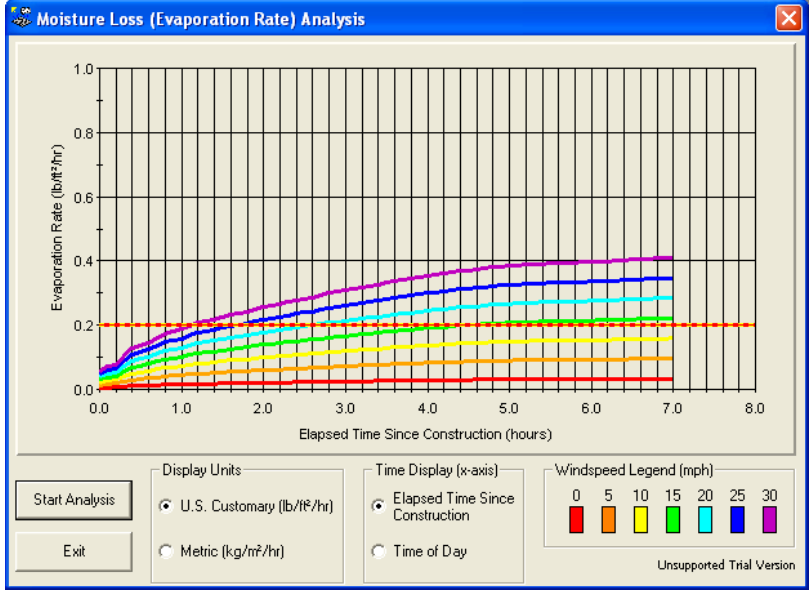


Figure 2.12: Hiperpav evaporation rate analysis showing the elapsed time since construction (x-axis versus the evaporation rate at various wind speeds

2.6.3 Hiperpav Models

Hiperpav incorporates and integrates 20 different models based on temperature development, mechanical properties, and restraint to free movement. Some of these models include: Pavement Temperature Prediction Model, Thermal Coefficient of Expansion Model, Pavement Curling Model, Drying Shrinkage Model, Axial Restraint Model, and Modulus of Elasticity Model. Although no detailed explanations will be given in this report regarding the models that Hiperpav implements, more information can be found on the official Hiperpav website (www.hiperpav.com).

2.6.4 Hiperpav and the Maturity Method

Maturity calculations are incorporated into Hiperpav predictions through several components. The Arrhenius equation itself is used indirectly in the concrete Pavement Temperature Prediction Model and is also used to predict the elastic modulus of in the modulus of elasticity model. In the pavement temperature prediction model the Arrhenius equation is used to determine the amount of heat that is exothermically released. In the modulus of elasticity model the Arrhenius equation is used to predict the degree of hydration which is then used to estimate the strength gain and modulus of elasticity.

Maturity data can be directly input when the “Enter Maturity Data” tab, which is shown in Figure 2.13, is chosen in the “JCP Mix Design Parameters” window. When this option is selected, Figure 2.14 is opened and allows the user to input maturity data using the Nurse-Saul equation. When this data is input it will supersede the default strength gain determined by the models. It is also noted that the 28-day strength value comes from the input on the “Design” table and not from the maturity data. The next version of Hiperpav is planned to allow maturity data to be input using the Arrhenius equation in equivalent age form.

JCP Mix Design Parameters

Cement Type:

Use Default Strength Gain? Yes No, Use Laboratory Maturity Data:

Use Default Heat of Hydration? Yes No, Use Cement Chemical Composition Data:

Coarse Aggregate Type:

Concrete Coefficient of Thermal Expansion: $\mu/\text{°F}$

PCC Mix Volumetrics

Coarse Aggregate Content: lb/yd³ Water/Cement (w/c) Ratio:

Fine Aggregate Content: lb/yd³ Water/Cementitious Materials (w/cm) Ratio:

Water Content: lb/yd³

Cement Content: lb/yd³

Silica Fume Content: lb/yd³

Class C Fly Ash Content: lb/yd³

Class F Fly Ash Content: lb/yd³

Ground Slag Content: lb/yd³

PCC Volumetrics

Chemical Admixtures

Water Reducer Retarder

Super Water Reducer Accelerator

Figure 2.13: Mixture proportion parameters window of the Hiperpav software

Laboratory Maturity Data

Number of Maturity Data Points:

Datum Temperature:

Point 1 Age:

Point	Age (hours)	Maturity (°F-hours)	Strength (psi)
1	25	703	293
2	25	703	293
3	25	703	319
4	49	1327	483
5	49	1327	457
6	49	1327	496
7	73	1887	616
8	73	1887	608
9	73	1887	579
10	97	2441	621
11	97	2441	561
12	97	2441	657

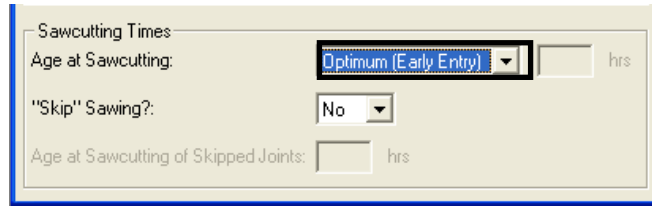
Figure 2.14: Hiperpav option to input laboratory maturity in Nurse-Saul format

2.6.5 Hiperpav and Saw-cutting

Hiperpav allows the user several indirect options in analyzing the timing of the saw cutting window. The user can select one of three options for the age at saw-cutting to be used in the analysis. When the “User Defined” age is entered, Hiperpav simulates stress development for a semi-infinite slab until the defined time at which the joints are saw-cut. After the user defined time has passed, the stress development is simulated as a function of the transverse joint spacing entered. When “Optimum (Early Entry)” option is selected, Hiperpav performs a similar analysis as the “User Defined” option only the time at which the joints are sawed is the time of the “set”. The time of “set” is calculated using various models which take into consideration numerous assumptions. The “set” is considered the ideal time to saw if early-entry saw methods are used and there is no distinct raveling. At the time of this report no data was reported on the accuracy of the time of set calculation. When the “No Sawcutting”, option is chosen, the analysis is performed on a continuous slab throughout the 72 hour period. The three saw-cutting options in the JCP Construction Parameters window are represented with boxes in Figures 2.15, 2.16, and 2.17.

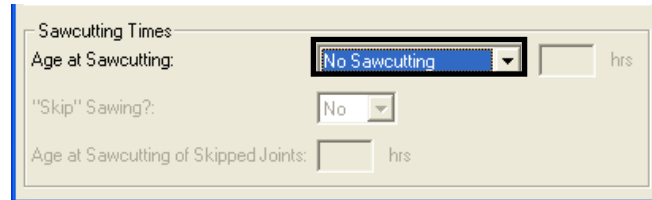
The image shows a software dialog box titled "JCP Construction Parameters". It contains several input fields and dropdown menus. The "Sawcutting Times" section is highlighted with a red rectangular box. In this section, the "Age at Sawcutting" dropdown menu is set to "User Defined" and the "Skip Sawing?" dropdown menu is set to "No". Other visible fields include "Time of Day of Construction" (12:00 Noon), "Initial PCC Mix Temperature" (65 °F), "Initial Subbase Temperature" (65 °F), "Curing Method" (Single Coat Liquid Curing Compound), "Age at Application of Curing" (0 hrs), and "Age at Removal of Curing" (72 hrs). There are "OK" and "Cancel" buttons in the top right corner.

Figure 2.15: “User Defined” saw-cutting parameter



The screenshot shows a software window titled "Sawcutting Times". It contains four input fields: "Age at Sawcutting:" with a dropdown menu set to "Optimum (Early Entry)" and an empty text box followed by "hrs"; "'Skip' Sawing?:" with a dropdown menu set to "No"; "Age at Sawcutting of Skipped Joints:" with an empty text box followed by "hrs"; and a "Sawcutting Times" label at the top left.

Figure 2.16: “Optimum (Early Entry)” saw-cutting parameter



The screenshot shows the same software window as Figure 2.16, but with the "Age at Sawcutting:" dropdown menu set to "No Sawcutting". The other fields remain the same: "'Skip' Sawing?:" set to "No", and "Age at Sawcutting of Skipped Joints:" empty.

Figure 2.17: “No Saw-Cutting” parameter

The “No Sawcutting” option can indirectly determine the “end” of the saw-cutting window by recording the time that the stress first surpasses the strength of the slab. At this point random cracking would be expected to occur in the pavement. This is shown with an arrow in Figure 2.18.

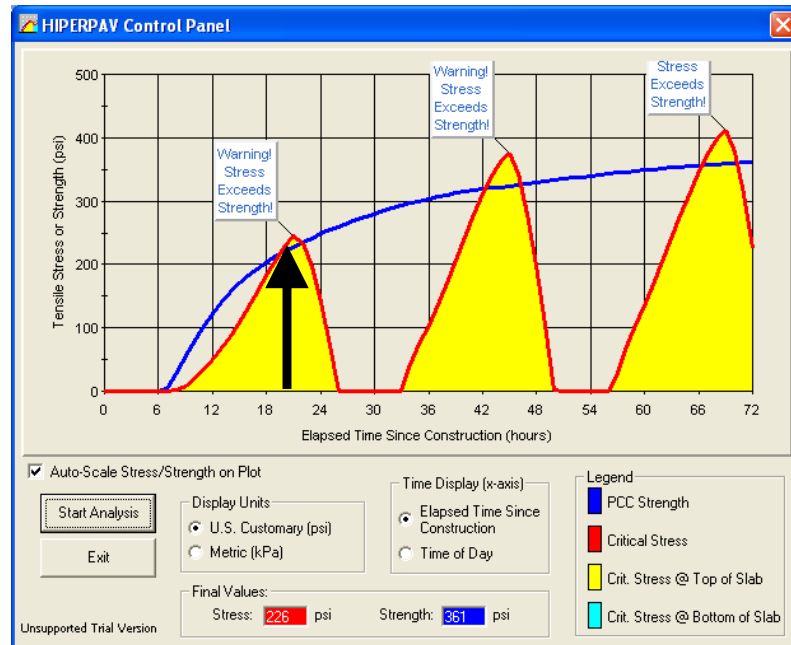


Figure 2.18: Indirect determination of the end of the saw-cutting window

It should be noted that Hiperpav is only a planning tool and does not consider numerous factors that may influence the saw-cutting window. Specifically, the software does not provide a method to analyze when the concrete has gained sufficient strength to begin saw-cutting without significant raveling which determines the start of the window. Specifically, no provisions are made to consider the influence of the hardness and shape of the aggregates which can influence raveling. Further, saw-cut depth is not considered as a parameter that may change how and when the cracks propagate and there corresponding stress relief. Numerous models in the software (HIPERPAV, 2004) are based on the temperature prediction model which has not shown significant correlation with actual pavement temperature at early-ages (McCullough, 1999). In addition it would prove to be beneficial for the purposes of this research if the software would display the temperatures that were predicted for the pavement. In summary, the software provides an indirect determination of the end of the saw-cutting window but does not provide a method of analyzing the start of the saw-cutting window and a large part of the software is based on the temperature prediction model which needs further calibration.

2.7 Literature Review Conclusions

The following paragraph provides a summary of subjects discussed in this chapter. First, an examination of the two commonly used maturity functions and strength-maturity relationships was performed. It was determined that the Arrhenius equation would prove to be more accurate during the relevant saw-cutting time periods because during this time period a wide range of temperatures are encountered for which the Arrhenius equation better reflects the material property development. In regards to strength testing, flexural strength will be used as a parameter instead of compressive strength due to the fact that it is consistent with current Indiana methods and shows better correlation to saw-cutting factors. The influence of aggregates was considered in flexural strength predictions based on the maturity method but this parameter is not expected to have a significant influence due to the early age of the saw-cutting window.

Previous research has shown that the relationship between saw-cut depth and timing is extremely complex. Three interrelated factors prove to be the timing of the cut, the stress concentration at the depth of the saw-cut, and the ability of the crack to propagate unstably through the pavement.

Raveling is relatively subjective parameter that defines when the saw-cutting can begin. Studies on cores have shown that moderate distress from surface raveling does not lead to internal damage to the joint. Previous work has determined guidelines based on compressive strength and its correlation to raveling. Aggregate shape and hardness have shown to influence raveling whereas heat transfer from the blade to aggregate has been found to be insignificant.

In regards to saw-cutting equipment, three types of saws exist for saw-cutting concrete. Of these three types of saws, the conventional saws are the most common in Indiana and the early-entry saw is a new technology that incorporates an anti-ravel skid plate which allows it to enter pavements at earlier ages without significant raveling. Diamond blades for the saws are chosen based upon the hardness of the coarse aggregates and the abrasiveness of the sand. If improper blades are used unnecessary raveling can occur. The measure of the impact strength of a diamond is known as the toughness index

(TI). The toughness index multiplied by the recommended operating speed of the blade could be considered as a parameter that influences the strength of the pavement to prevent raveling. The Hiperpav software can provide an indirect determination of the end of the saw-cutting window but does not provide a method or means of analyzing the start of the window. The software largely relies on its temperature prediction model which needs further calibration.

CHAPTER 3: FIELD ASSESSMENT OF THE MATURITY METHOD AS A TOOL FOR SAW-CUTTING GUIDELINES

3.1 Introduction

The current practice of determining the saw-cutting window is based on operators experience and a simple-scratch test. The scratch test simply involves scratching the surface of the pavement with an abrasive object and subjectively determining its age and strength. This chapter provides information obtained regarding the possible implementation of the maturity method as a means of determining the saw-cutting window. In order to properly assess the use of the maturity method as a tool for saw-cutting joints, five site visits were performed to gather relevant information about the current state of practice in Indiana. Information was obtained regarding the maturity of the pavement and the weather conditions from time of placement to cutting. In addition, information about the mixture design and associated equipment was collected. Information was also obtained from workers who were directly and indirectly involved with the saw-cutting and performance of the pavement. Most notably, saw-cutting crew members provided insight regarding the most feasible and practical way to utilize results from research so it can be implemented into the field. The intent of the field assessment was to provide the following information: 1) define the range of maturity and strength of Indiana pavements at the time of saw-cut, 2) determine the significant factors regarding the implementation of the method, and 3) examine the sensitivity of the data to construction and environmental variables. The collection of the data and information obtained from the field assessment provided the basis for laboratory work. This chapter is organized as follows. Sections 3.2 to 3.6 give a detailed summary of each of the five site visits and section 3.7 compares the data from the site visits.

In order to determine the range of the saw-cutting window in Indiana site visits had to be performed over a wide range of temperatures. Therefore site visits were chosen based on providing a wide range of ambient temperatures and conditions. In addition, one site visit was chosen because it was a night pave which provided the environmental conditions in opposite order to the prevailing practice of paving during the day.

3.2 Site Visit #1 (9/11/03)

3.2.1 Site Visit #1 Overview

On September 11, 2003 Berns Construction slip formed approximately 1500 cubic yards of 14" inch deep pavement. The pavement was placed over an unbound crushed aggregate base that conformed to INDOT standards and specification (section 300, 1999). It should be noted that the pavements at all the site visits conformed to the same standards. The job was located at 56th Street on the east side of Indianapolis. The paving operation began at 7 a.m. and the thermocouples were embedded into the pavement at 9:10 a.m. The examined joint was sufficiently sawed at 3:10 p.m. Figure 3.1 shows a timeline of the significant events throughout the testing period which includes the following:

- Paving Started @ 7:00 a.m.
- Tested Load Batched @ 7:57 a.m.
- Tested Load Placed @ 8:15 a.m.
- Thermocouples Placed @ 9:10 a.m.
- Tined at Joint @ 9:45 a.m.
- Cure Agent at Joint @ 10:20 a.m.
- Started Sawing @ 2:45 p.m.
- Sawed Joint at Thermocouple @ 3:10 p.m
- Paving Finished @ 5:00 p.m.

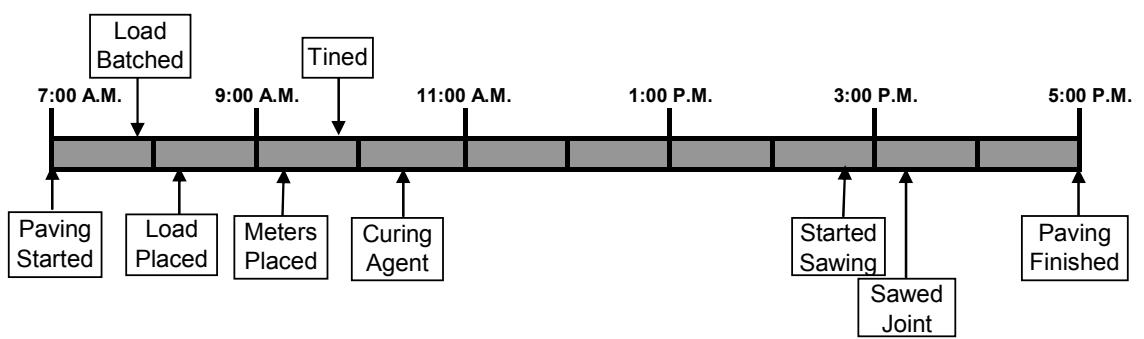


Figure 3.1: Site visit #1 9/11/03 timeline

3.2.2 Site Visit #1 Mixture Design

The proportions for the mixture design of one cubic yard of are shown in Table 3.1. The central mix plant produced concrete in 10 cubic yard batches.

Table 3.1: Site visit #1 mixture proportions

<u>Constituent</u>	<u>Unit</u>	<u># / yd³</u>
Cement	lb.	445
Fly Ash (Type C)	lb.	70
Mix Water	lb.	187
Fine Aggregate (INDOT #23 - Natural)	lb.	1525
Coarse Aggregate (INDOT #8 - Crushed Limestone)	lb.	1720
Air Entrainment	oz.	5.8
Water Reducer	oz.	15.3

3.2.3 Site Visit #1 Placement of the Thermocouples

Six type T thermocouples were placed into the pavement; in addition one type T thermocouple was placed 3" into the sub-grade. Figure 3.2 shows the placement of the thermocouples in the pavement. The thermocouples were placed at depths of 3.5", 7", and 10.5" on both sides of the joint. The thermocouples innermost to the joint were 3.5" and the outermost 10.5" with approximately two inches in-between. The thermocouples were placed approximately 3 feet from the edge of the pavement and 1 ½ feet to the sides of the joint. The 3 feet length from the edge of the pavement is consistent with Indiana Test Method 402 (ITM 402).

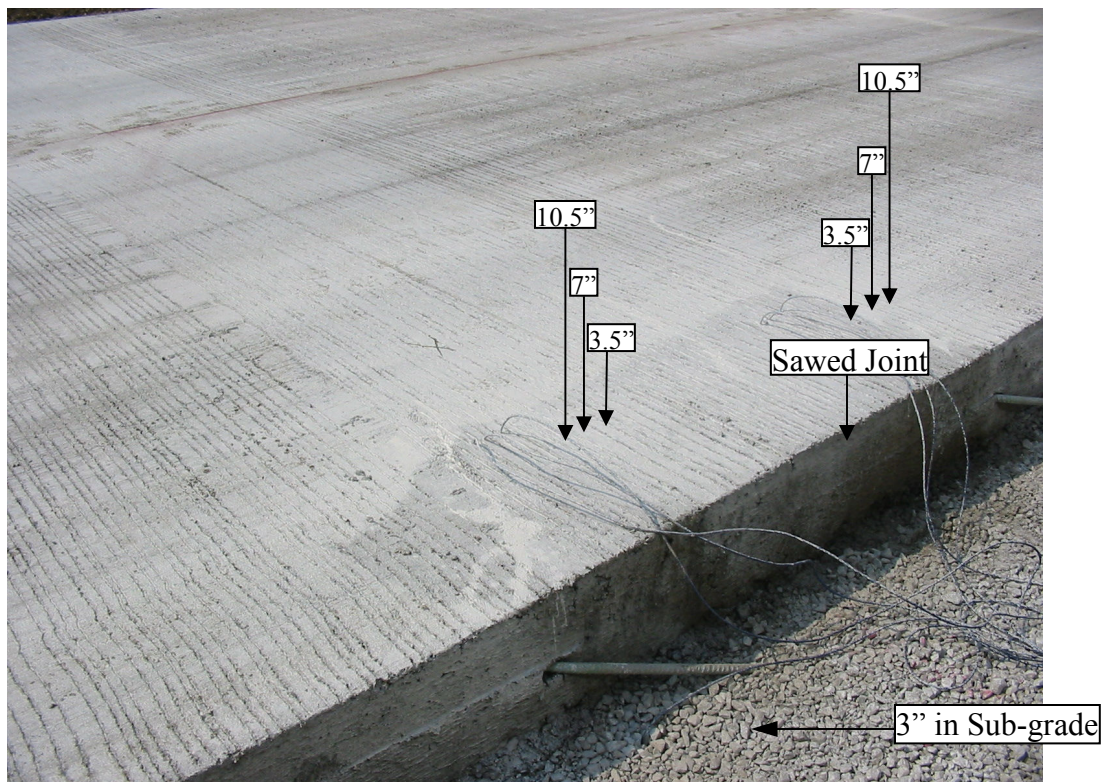


Figure 3.2: Site visit #1 placement of thermocouples

3.2.4 Site Visit #1 Weather

The average ambient temperature for the day was 72 °F with a maximum temperature of 81 °F and a minimum of 63 °F. There was no precipitation recorded, and the average humidity was 69 % with a high of 90 % and minimum of 52 %. The average wind speed was 8 mph with a maximum gust of 12 mph. Figure 3.3 shows weather information from the Weather Underground's Indianapolis weather station. The Weather Underground station records information from Automated Surface Observation Systems (ASOS) at the Indianapolis International Airport which was approximately 15 miles from the job site. The ASOS system is maintained by the Federal Aviation Administration and further information can be obtained regarding the ASOS stations at <http://www.nws.noaa.gov/asos/>. The weather conditions are updated once per hour or more frequently when adverse aviation weather occurs. It should be noted that the wind speeds are usually recorded at a distance 10 feet above the ground.

A Davis Weather Monitor II portable weather station was set up along side of the pavement to record weather information. The weather information was manually recorded approximately every hour. This data included the current ambient temperature, humidity, and wind speeds. This data was compared with the information obtained from the ASOS system. The weather information between the two systems correlated by ± 1.5 °F for the temperature data and ± 1 % for the humidity data. There was believed to be a mechanical defect with the portable weather station's anemometer which was corrected at approximately 1:00 P.M. The wind speed data after this point also correlated within ± 2 miles per hour with the information from the ASOS. The ASOS weather information was used in the analysis because it proved to correlate with local data and provided more frequent and reliable data. Figure 3.3 shows the data from the ASOS station regarding the temperature, dew point, and wind speed on September 11, 2003.

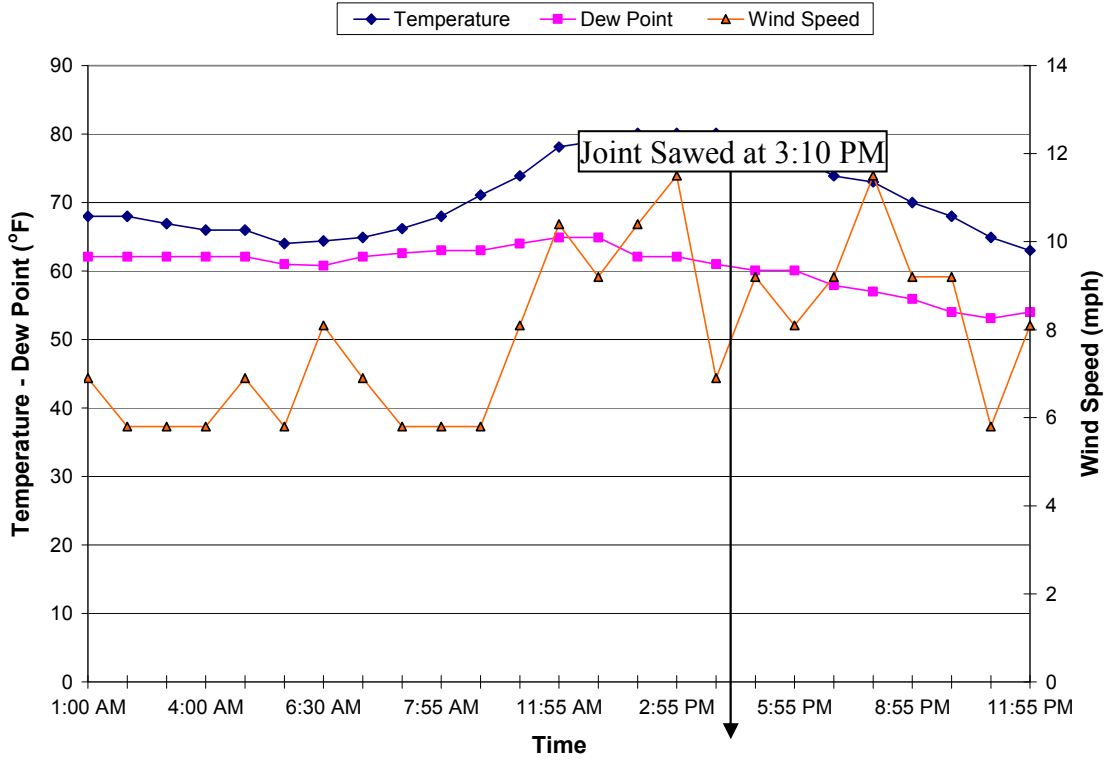


Figure 3.3: 9/11/03 Weather – ambient temperature, dew point, and wind speed from ASOS station

3.2.5 Site Visit #1 Equipment

The saw-cutting crew used a conventional wet cut 65 horsepower saw with 18” diameter x 1/8” width diamond blade. The saw-cutting operator reported that there were no problems or difficulties associated with the equipment while sawing the joint. Figure 3.4 shows saw used to cut the examined joint.



Figure 3.4: Conventional 65 horsepower wet-cut saw with 18 1/8" diamond blade

3.2.6 Site Visit #1 Synopsis

The saw-cut was performed at 3:10 p.m. to a depth of 4 2/3" (D/3) with small but insignificant raveling. No random cracking was noticed throughout the length of the pavement at the time of the saw-cut. An average of the two sensors at each depth was used to calculate the three maturity values. The temperature history of the pavement before the maturity thermocouple began recording was estimated using the first recorded temperature at 9:05 A.M. The Arrhenius maturity at 20 °C reference temperature was 11.8 hours at mid-depth when the saw-cut was performed. It should also be noted that the tested portion of the pavement was in the shade (due to a retaining wall) until approximately 11:00 A.M. whereas the recorded ambient temperature was in direct sunlight throughout the day. Figure 3.5 shows a graph of the ambient temperature, pavement temperature at mid-depth (7"), and the cumulative Arrhenius maturity (mid-depth) throughout the testing period. Figure 3.6 shows the calculated values of cumulative maturity at the three depths and ambient temperature over the testing period. Figure 3.7 shows a picture of the examined joint which reveals slight raveling and a saw-cut to the appropriate depth of 4 2/3" (D/3).

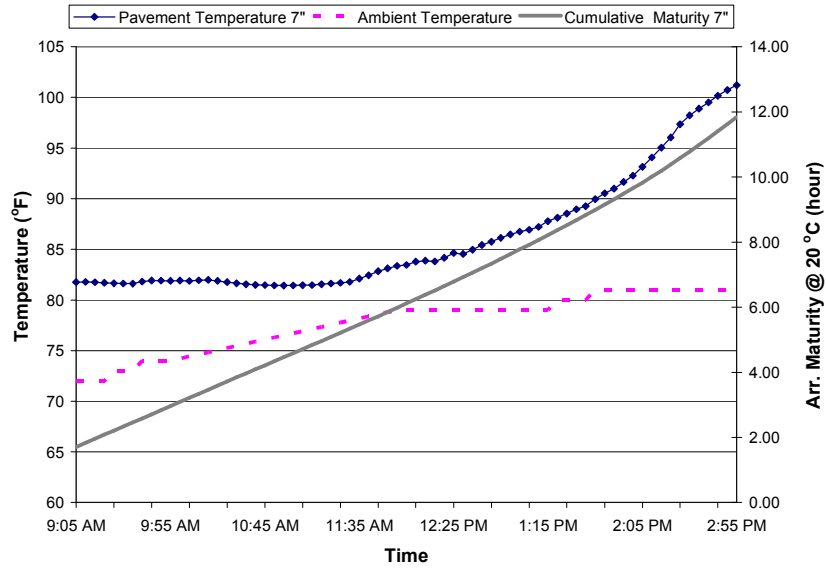


Figure 3.5: 9/11/03 Pavement temperature 7.0", ambient temperature, and cumulative maturity 7.0"

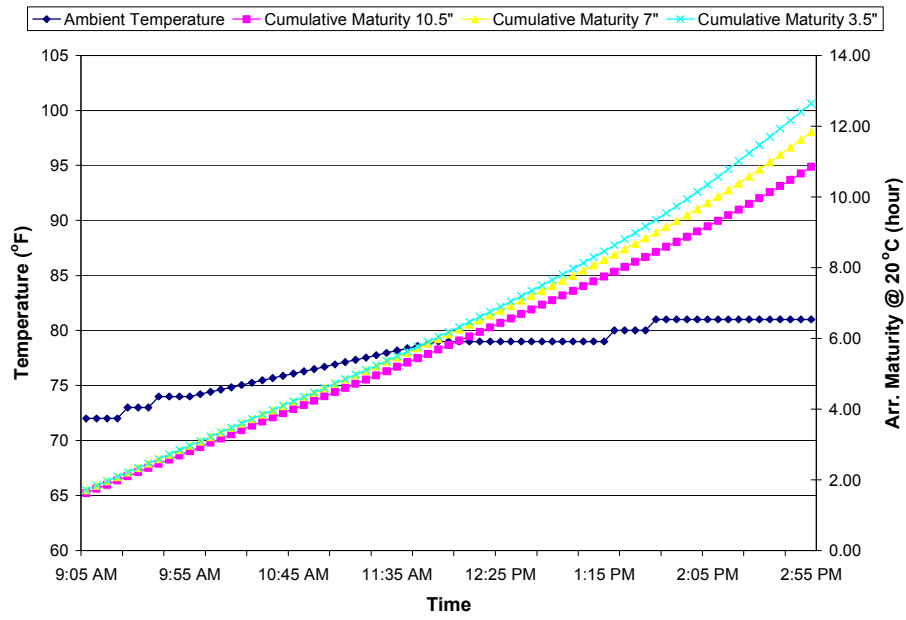


Figure 3.6: Cumulative maturity at 3.5", 7.0", 10.5", and ambient temperature

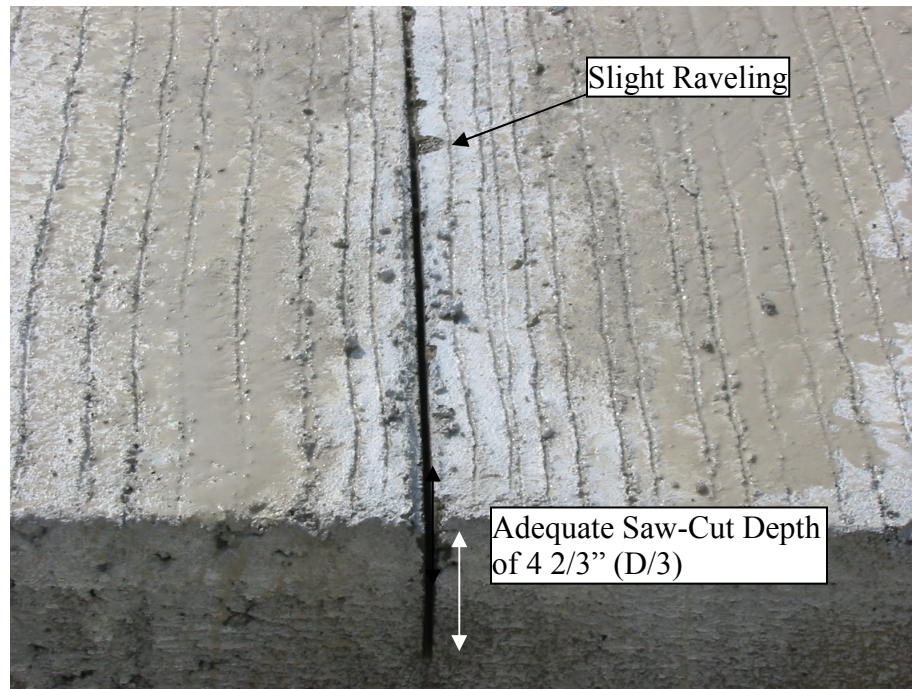


Figure 3.7: Picture of examined joint

Figure 3.8 is the master curve plot that was developed by the contractor for use with Indiana Test Method 402. The master curve is derived using the Nurse-Saul equation (TTF) and the breaking of 3 beams each at approximate ages of 24, 36, 48, and 60 hours. The logarithm of TTF maturity is plotted versus flexural strength and fit using a linear trend line. The calculated TTF maturity at mid-depth (7" deep) for the time of the saw-cut was 2.44 °C-hr which predicts a strength of 236 psi. The accuracy of this prediction is further discussed in section 3.7 of this chapter.

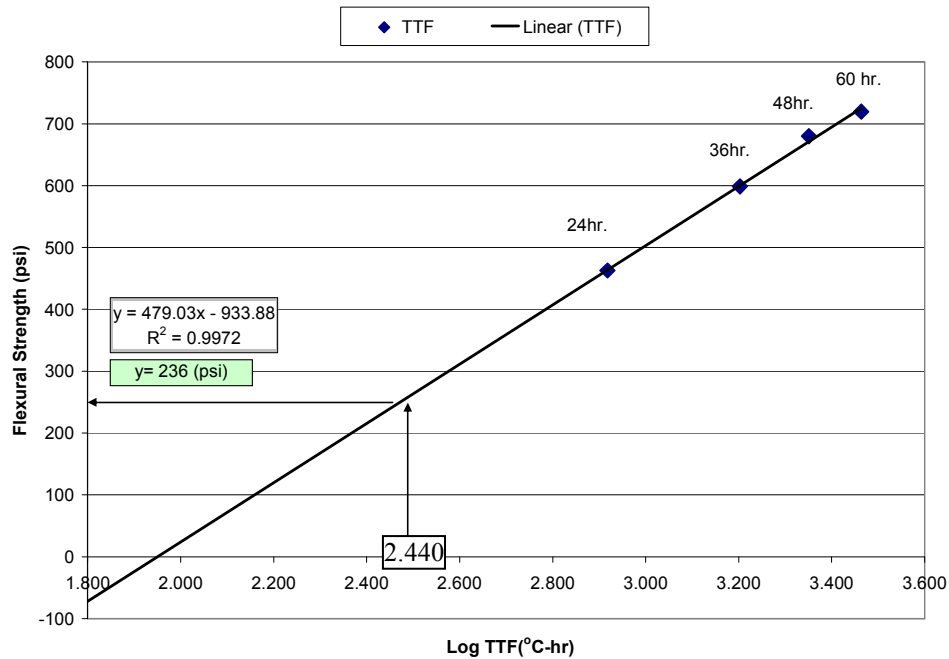


Figure 3.8: Master curve calculated flexural strength

3.3 Site Visit #2 (10/30/03)

3.3.1 Site Visit #2 Project Overview

Walsh Construction slip formed approximately 2000 cubic yards of 15" pavement over an unbound crushed aggregate base. The project was located on the I-70 interchange on the West Side of Indianapolis. The paving operation began approximately at 7:00 a.m. and finished at approximately 5:30 p.m. The I-button maturity sensor was paved over at approximately 10:15 a.m. and the joint at the sensor was sawed at 7:00 p.m. Figure 3.9 shows a timeline of the significant events throughout the testing period which includes the following:

- Paving Started @ 7:00 a.m.
- Sensor Placed @ 9:45 a.m.
- Load at the Sensor Batched @ 10:10 a.m.

- Sensor Covered with Concrete @ 10:15 a.m.
- Cure Agent at the Joint Nearest the Sensor @ 12:00 p.m.
- Started Sawing @ 5:10 p.m.
- Paving Finished @ 5:30 p.m.
- Sawed Joint at Sensor @ 7:00 p.m.

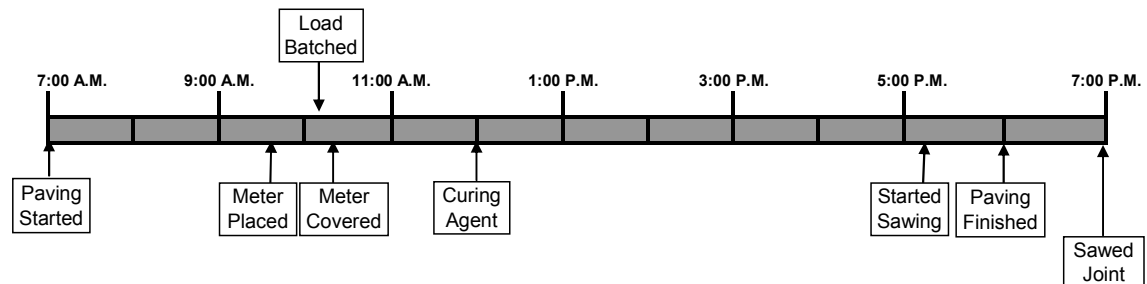


Figure 3.9: Site visit #2 10/30/03 timeline

3.3.2 Site Visit #2 Mixture Design

The proportions for the mixture design of one cubic yard are shown in Table 3.2. A central mix plant at the project was used to produce concrete in 12 cubic yard batches. It should be noted that this mixture design in Table 3.2 in comparison to that shown in Table 3.1 does not contain any fly ash.

Table 3.2: Site visit #2 mixture proportions

<u>Constituent</u>	<u>Unit</u>	<u># / yd³</u>
Cement	lb.	575
Mix Water	lb.	250
Fine Aggregate (INDOT #23 – Natural)	lb.	1300
Coarse Aggregate (INDOT #8 – Crushed)	lb.	1738
Air Entrainment	oz.	4.8
Water Reducer	oz.	17.3

3.3.3 Site visit #2 placement of the sensor

One modified ThermoChron I-button maturity sensor was placed approximately one inch below mid-depth (6.5” from sub-grade). The sensor was intended to be placed at mid-depth but upon measurement it was observed to be 1” below mid-depth. The I-button maturity sensors connecting wires were coated with silicon to provide protection and rigidity when the sensor was covered with concrete from the paving machine. The connecting cord was buried approximately 3” in the sub-grade to protect it from the passing paving machinery. Figure’s 3.10, 3.11, and 3.12 show the placement of the sensor.

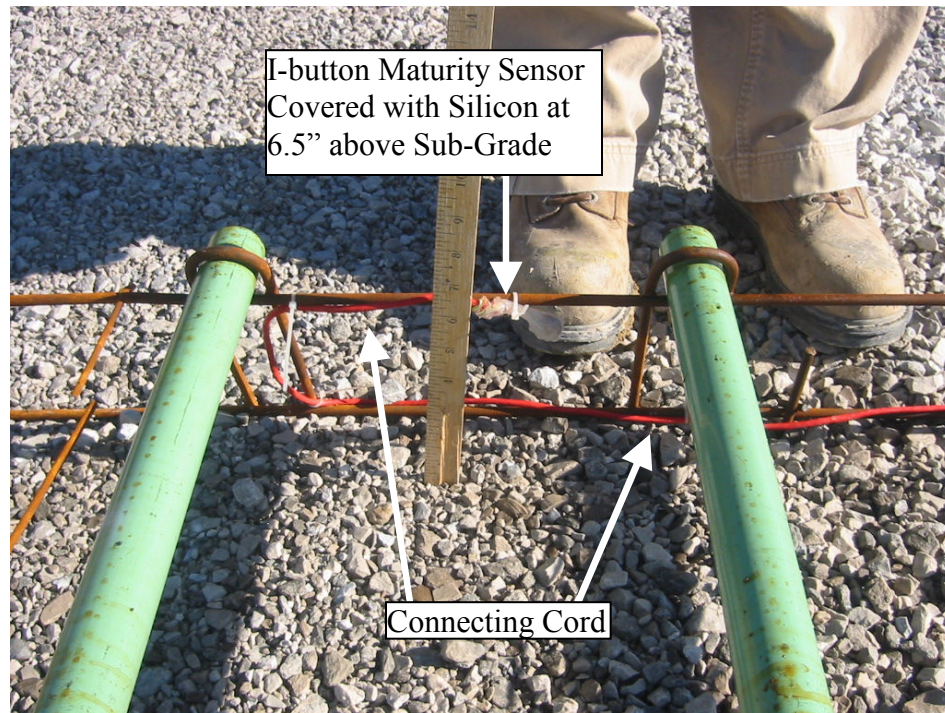


Figure 3.10: Placement of I-button maturity sensor

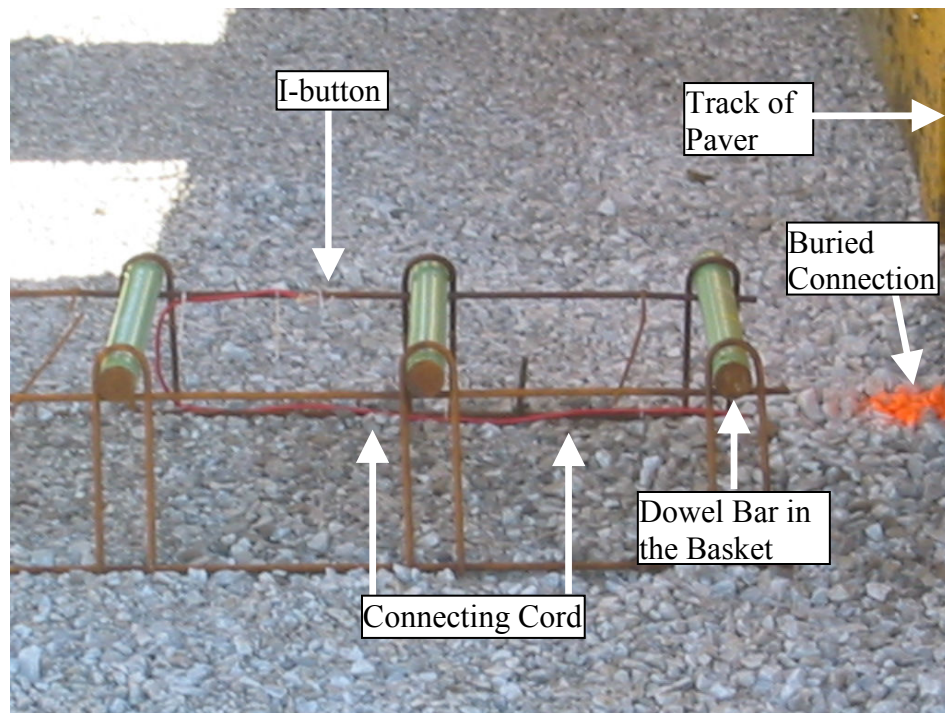


Figure 3.11: Placement of maturity sensor connecting cord



Figure 3.12: Covering of maturity sensor

From Figures 3.10, 3.11, and 3.12 we can see that the sensor was attached to the dowel basket approximately 2 feet from the edge of the pavement. It should also be noted that in comparison to the temperature sensors that included the thermocouple wires, the I-button device was placed prior to the passing of the paver and does not require a data logger or reader due to its self contained logging capability.

3.3.4 Site Visit #2 Weather

The average temperature for the day was 57 °F with a maximum temperature of 73 °F and minimum of 41 °F. There was no precipitation recorded and the average humidity was 62% with a high of 82 % and minimum of 37 %. The average wind speed was 13 mph with a max gust of 32 mph. Figure 3.13 is from the Weather Undergrounds recordings from the ASOS system at the Indianapolis International Airport which is located approximately 5 miles from the location of the pavement.

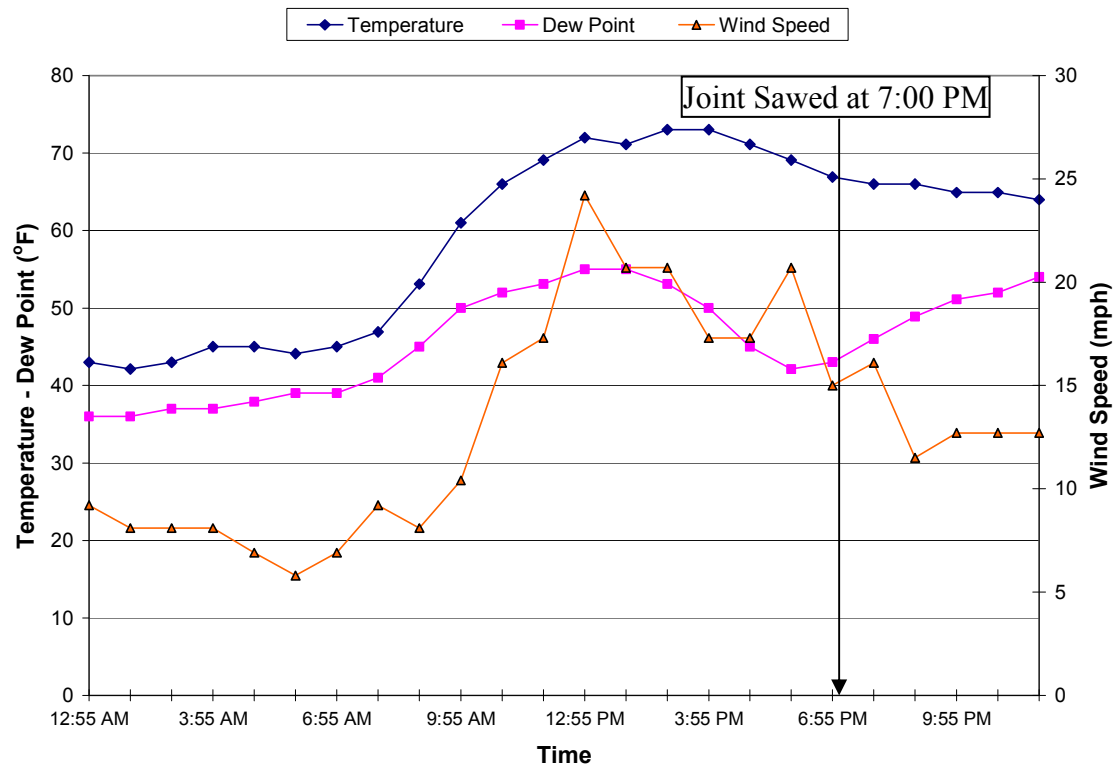


Figure 3.13: 10/30/03 Weather – temperature, dew point, and wind speed

3.3.5 Site Visit #2 Equipment

The saw-cutting crew used a wet cut 65 horsepower saw with 20”x 1/8” diamond impregnated blade. The saw-cutting crew reported no equipment problems while performing the cut on the examined joint. Figure 3.14 shows a picture of the saw that was used to cut the examined joint.



Figure 3.14: Conventional wet cut 65 horsepower saw with 20” diamond blade

3.3.6 Site Visit #2 Synopsis

The saw-cut was performed at 7:00 p.m. to a 5” depth (D/3) with no raveling. No random cracking was noticed throughout the length of the pavement at the time of the saw-cutting. The Arrhenius maturity using 20 °C as the reference temperature was 9.7 hours at the 8.5” (1” below mid-depth) sensor. Figure 3.15 shows a dual-axis graph of the ambient temperature, pavement temperature, and the cumulative Arrhenius maturity at the 8.5” deep sensor throughout the testing period. Figures 3.16 and 3.17 show pictures of the examined joint after it was cut. In Figure 3.16 the depth of the saw-cut is shown and in Figure 3.17 a closer look at the joint reveals no raveling and shows the discharged wet-cut slurry from the saw.

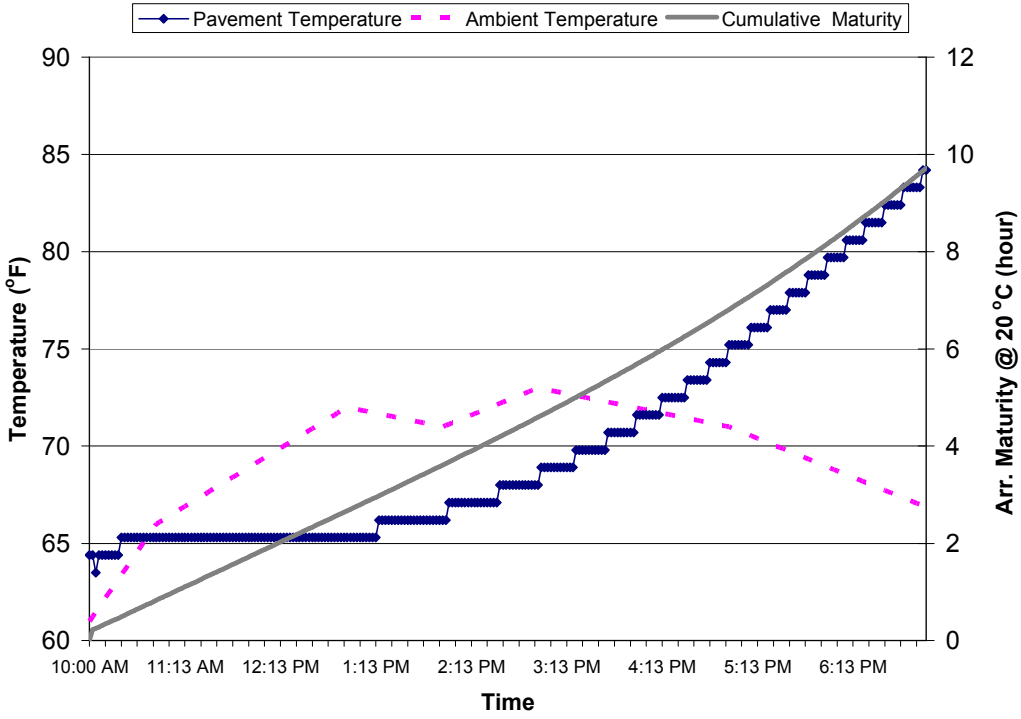


Figure 3.15: 10/30/03 Pavement temperature, ambient temperature, and cumulative maturity at 20°C

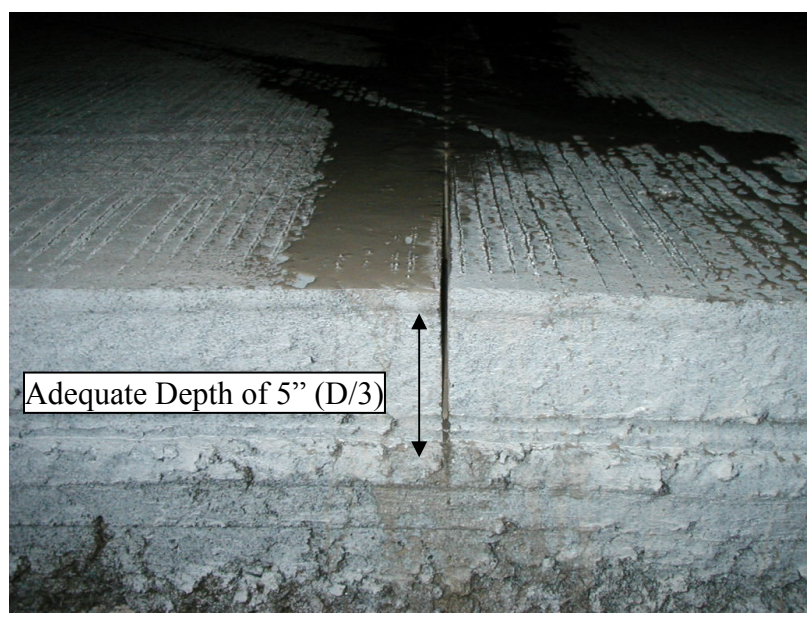


Figure 3.16 Depth of examined joint

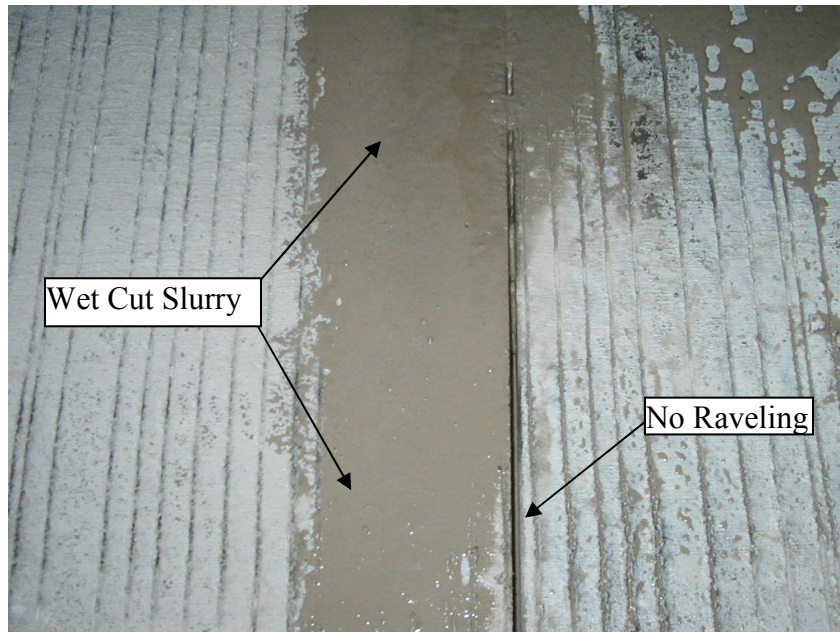


Figure 3.17: No raveling at joint

Figure 3.18 is the master curve plot that was developed by the contractor for which the casting, curing, and testing procedures followed that of ITM 402. The master curve derived cumulative maturity using the Nurse-Saul equation (TTF) and the breaking of 3 beams each at approximate ages of 12, 24, and 36 hours. The logarithm of TTF maturity is plotted versus flexural strength and fitted linearly. The calculated TTF maturity at the 8.5" deep sensor at the time of the saw-cut was 2.44 °C-hr. which predicts a flexural strength of 272 psi.

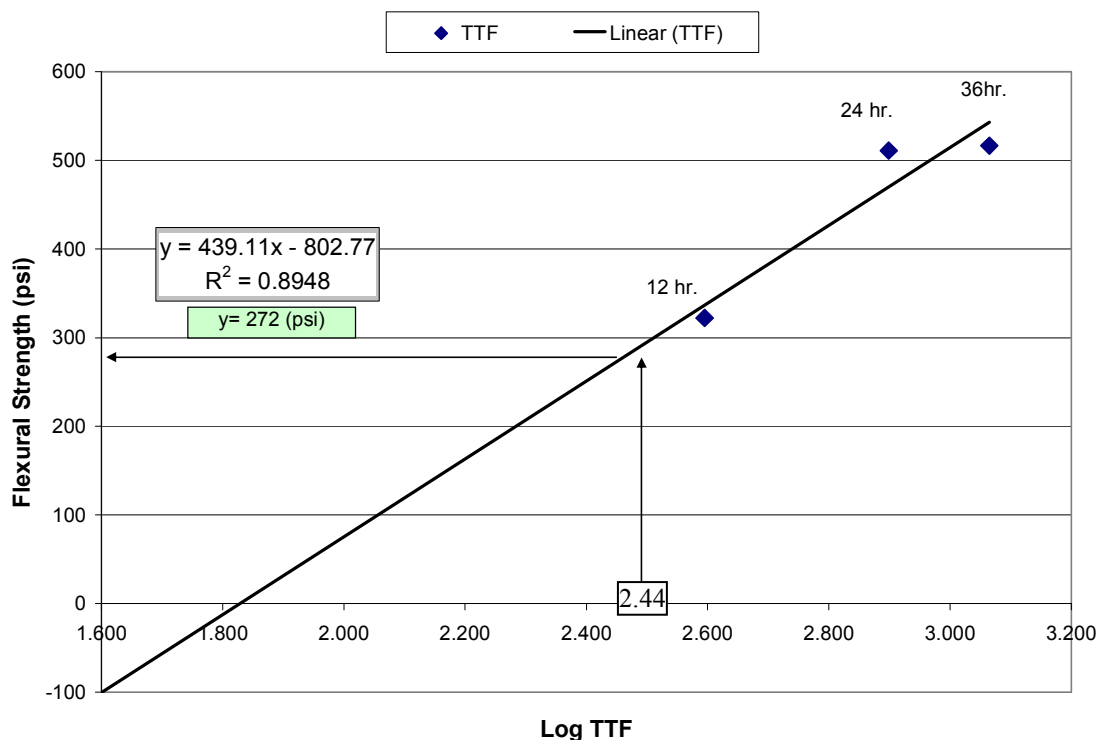


Figure 3.18: Master curve calculated flexural strength

3.4 Site Visit #3 (11/20/03-11/21/03)

3.4.1 Site Visit #3 Project Overview

Walsh Construction slip formed approximately 2000 cubic yards of 15" pavement over an unbound crushed aggregate base. The project was located on the I-70 interchange on the West Side of Indianapolis which was the same project as site visit #2 took place. The paving operation began approximately at 7:00 a.m. and finished at approximately 5:00 p.m. The mixture proportions and saw-cutting equipment were the same as that of site visit #2 (Table 3.2 and Figure 3.14). The maturity sensor was covered by the paver at approximately 10:45 a.m. and the joint was sawed at 2:00 a.m. the following morning. Figure 3.19 shows a timeline of the significant events throughout the testing period which included the following:

- Paving Started @ 7:00 a.m.
- Sensor Placed @ 9:50 a.m.
- Load Batched @ 10:40 a.m.
- Sensor Covered with Concrete @ 10:45 a.m.
- Cure Agent at Joint @ 12:30 p.m.
- Paving Finished @ 5:00 p.m.
- Started Sawing @ 1:00 a.m.
- Sawed Joint at Sensor @ 2:00 a.m.

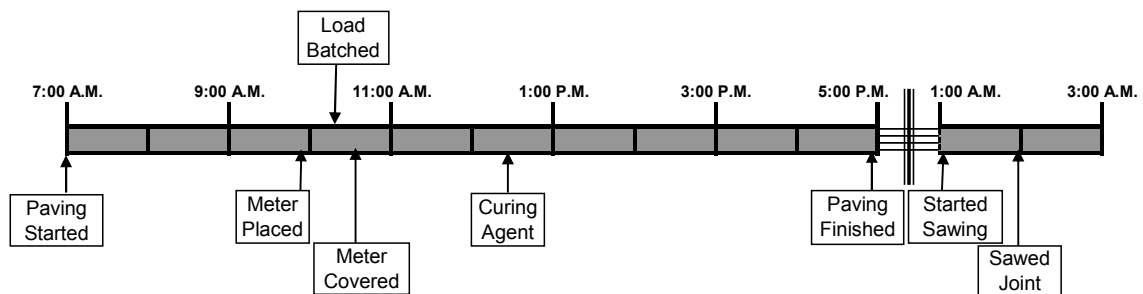


Figure 3.19: 11/20/03-11/21/03 timeline

3.4.2 Site Visit #3 Placement of the Sensor

One modified Thermochron I-button maturity sensor was placed at mid-depth in the 15” pavement. The I-button maturity sensor’s wires were coated with silicon to provide protection and rigidity when the sensor was covered with concrete from the paving machine. The connecting cord was connected to the dowel bar basket and then buried approximately 3.5” in the sub-grade to protect it from the passing paving machinery. Figures 3.20 and 3.21 show the placement of the maturity sensor before paving operations began. In Figure 3.20 the depth of the sensor (7.5”) is shown and Figure 3.21 illustrates that the sensor was attached to the third dowel bar which is approximately 2.5’ from the edge of the pavement.



Figure 3.20: Placement of I-button maturity sensor

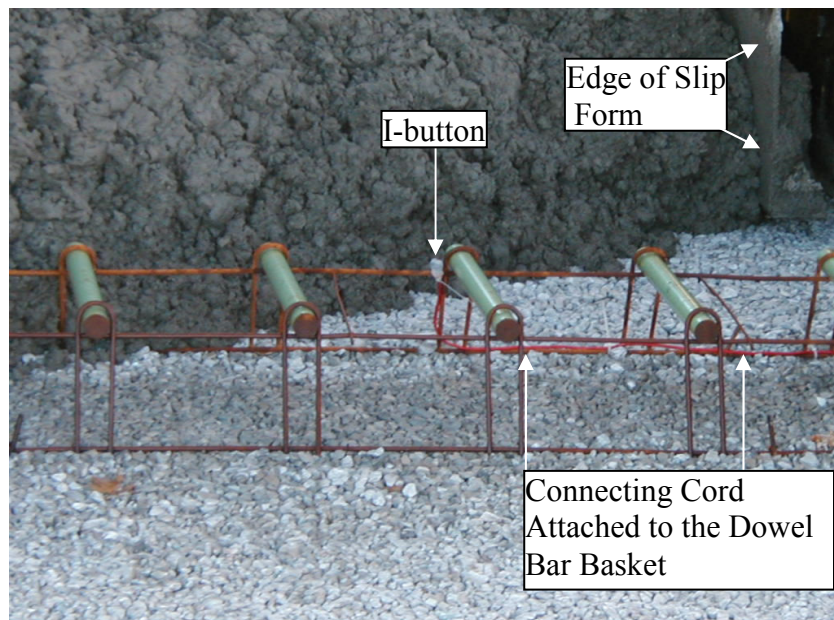


Figure 3.21: Covering of maturity sensor

3.4.3 Site Visit #3 Weather

The average ambient temperature during the saw-cutting period was 51 °F with a maximum temperature of 65 °F and minimum of 37 °F. There was no precipitation recorded and the average humidity was 65 % with a high of 89 % and minimum of 41 %. The average wind speed was 10 mph with a maximum gust of 21 mph. Figure 3.22 is from the Weather Undergrounds recordings from the ASOS system at the Indianapolis International Airport which is located approximately 5 miles from the location of the pavement.

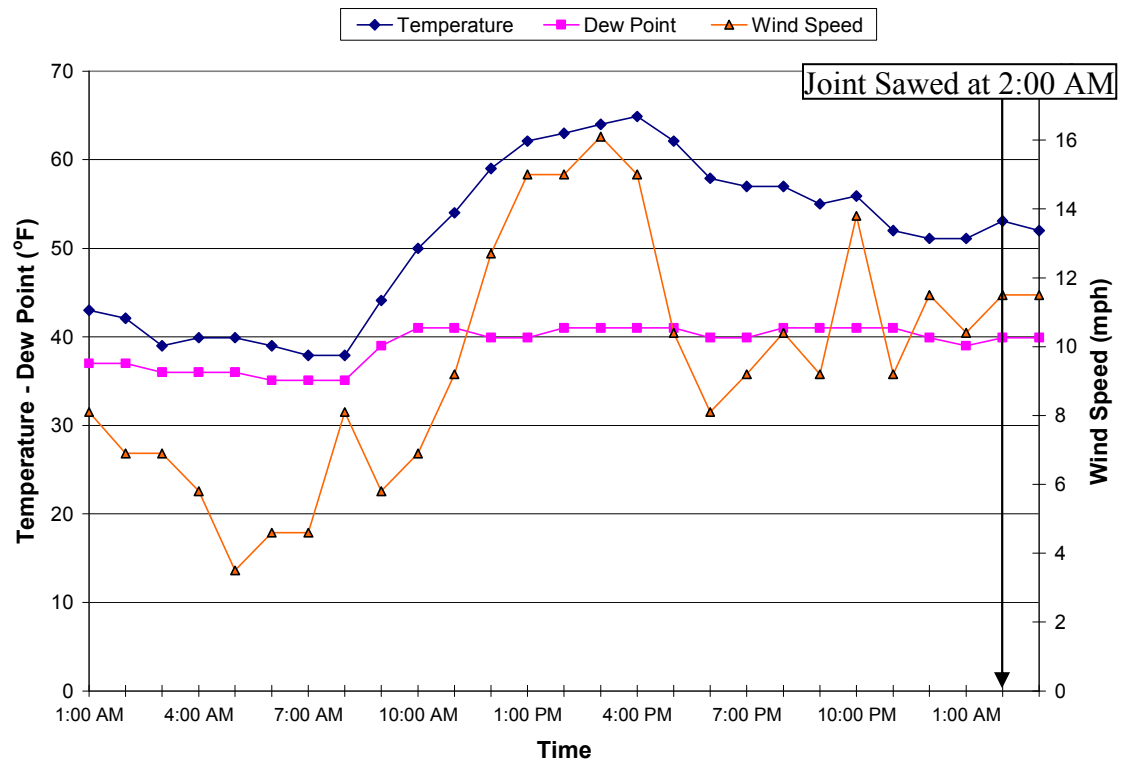


Figure 3.22: 11/20-11/21/03 Weather – temperature, dew point, and wind speed

3.4.4 Site Visit #3 Synopsis

The saw-cut was performed at 2:00 a.m. to a 4” depth which is 1” less than the specified 5” (D/3). No random cracking or raveling was noticed throughout the length of

the pavement at the time of the saw-cut. The saw-cutting crew verbally communicated to the author that the sawing occurred at a later age than they preferred based on their experience. The Arrhenius maturity using 20 °C as the reference temperature was approximately 21 hours at the mid-depth sensor. Figure 3.23 shows the ambient temperature, pavement temperature (at mid-depth), and the cumulative Arrhenius maturity throughout the testing period. Figure 3.24 shows a picture of the tested joint 26 days after it was cut. Notice that the joint crack has propagated to the bottom of the slab and that a second joint widening cut has been performed to ¼”.

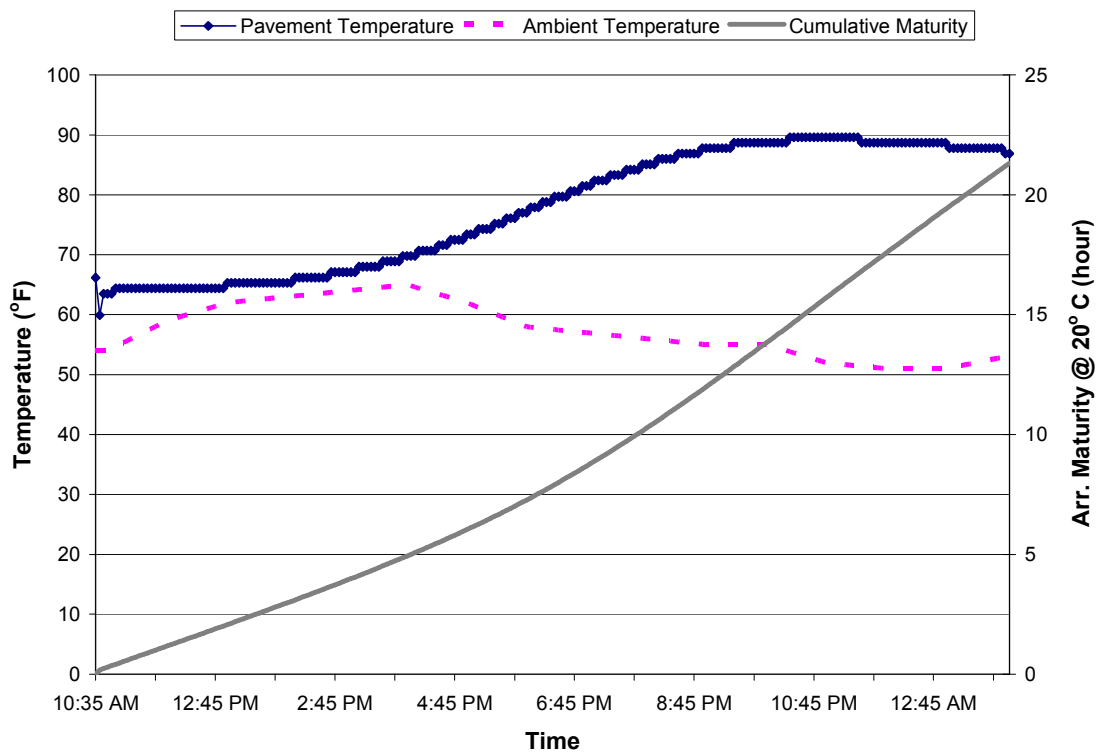


Figure 3.23: 11/20-11/21/03 Pavement temperature, ambient temperature, and cumulative maturity at 20°C

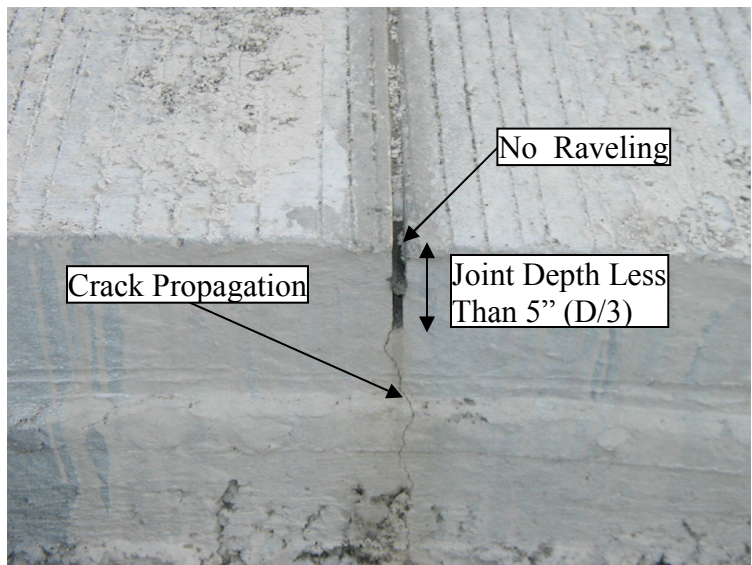


Figure 3.24: Picture of examined joint

Figure 3.25 is the master curve plot that is the same as at that used for site visit #2. The calculated TTF maturity for the mid-depth sensor (7.5" deep) at the time of the saw-cut was 2.74 °C-hr which corresponds to a flexural strength of 399 psi.

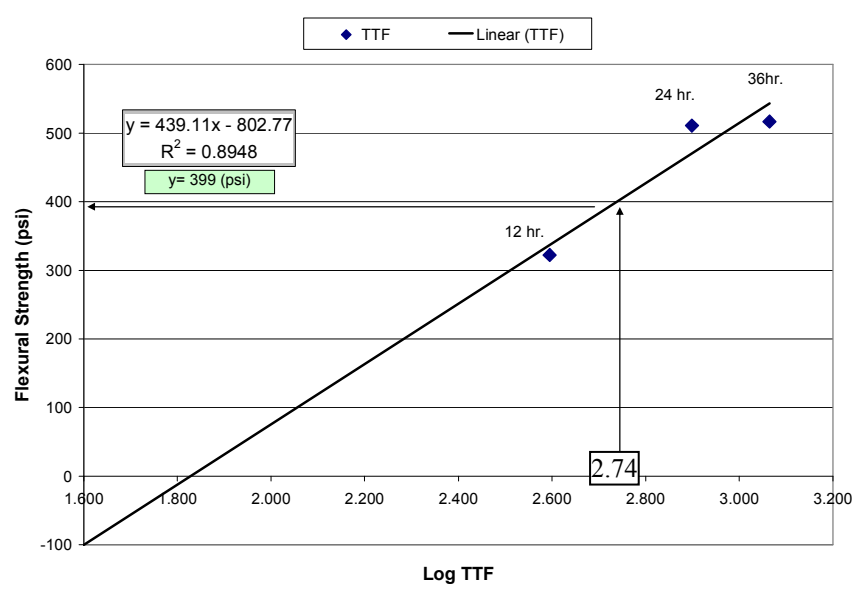


Figure 3.25: Master curve calculated flexural strength

3.5 Site Visit #4 (12/16/03-12/17/03)

3.5.1 Site Visit #4 Project Overview

Berns Construction slip formed approximately 500 cubic yards of 12" pavement onto an unbound crushed aggregate subbase. The job site was located at US-40 on the West Side of Indianapolis. The paving operation began approximately at 8:45 a.m. on December 16th and finished at approximately 2:00 p.m. on December 16th. The maturity sensor was placed at approximately 10:30 a.m. and the joint was sawed at 10:10 a.m. on December 17th. The saw-cutting equipment was the same as that used in site visit #1 and is shown in Figure 3.4. Figure 3.26 shows a timeline of the significant events throughout the testing period which included the following:

- Paving Started @ 8:45 a.m.
- Sensor Placed @ 10:30 a.m.
- Load Batched @ 10:50 a.m.
- Sensor Covered with Concrete @ 11:00 a.m.
- Cure Agent @ 12:00 p.m.
- Covered With Blanket @ 1:00 p.m.
- Paving Finished @ 2:00 p.m.
- Started Sawing @ 9:30 a.m.
- Sawed Joint at Sensor @ 10:10 a.m.

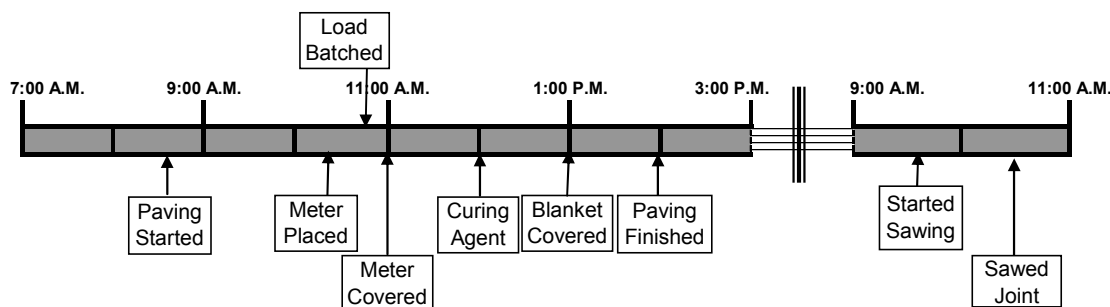


Figure 3.26: 12/16/-12/17/03 timeline

3.5.2 Site Visit #4 Mixture Design

The mixture proportions for one cubic yard are shown in Table 3.3. The central mix plant produced concrete in 8 cubic yard batches. It should be noted that although the mix did not utilize fly ash the cement content was equal to the sum of the cement and fly ash that was used in site visit #1 shown in Table 3.1.

Table 3.3: Site visit #4 mixture proportions

<u>Constituent</u>	<u>Unit</u>	<u># / yd³</u>
Cement	lb.	515
Mix Water	lb.	211
Fine Aggregate (INDOT #23 – Natural)	lb.	1511
Coarse Aggregate (INDOT #8 – Crushed Limestone)	lb.	1674
Air Entrainment	oz.	5.2
Water Reducer	oz.	13.3

3.5.3 Site Visit #4 Placement of the Sensor

One modified Thermochron I-button maturity sensor was attached to the second dowel bar from the edge of the pavement. The sensor was placed at mid-depth of the 12” pavement. The I-button maturity sensor’s connecting wires were coated with silicon to provide protection and rigidity when covered with concrete from the paving machine. The connecting cord was not buried but the end was protected with a plastic shell. No pictures were taken of the placement of the sensor.

3.5.4. Site Visit #4 Weather

The average ambient temperature for the testing period was 34 °F with a maximum temperature of 46 °F and minimum of 24 °F. There was 0.22 inches of precipitation recorded in the form of rain. The average humidity was 80 % with a high of 98 % and minimum of 61 %. The average wind speed was 17 mph with a max gust of 31 mph. Figure 3.23 is from the Weather Undergrounds recordings from the ASOS station at the Indianapolis International Airport which is located approximately 8 miles from the construction site.

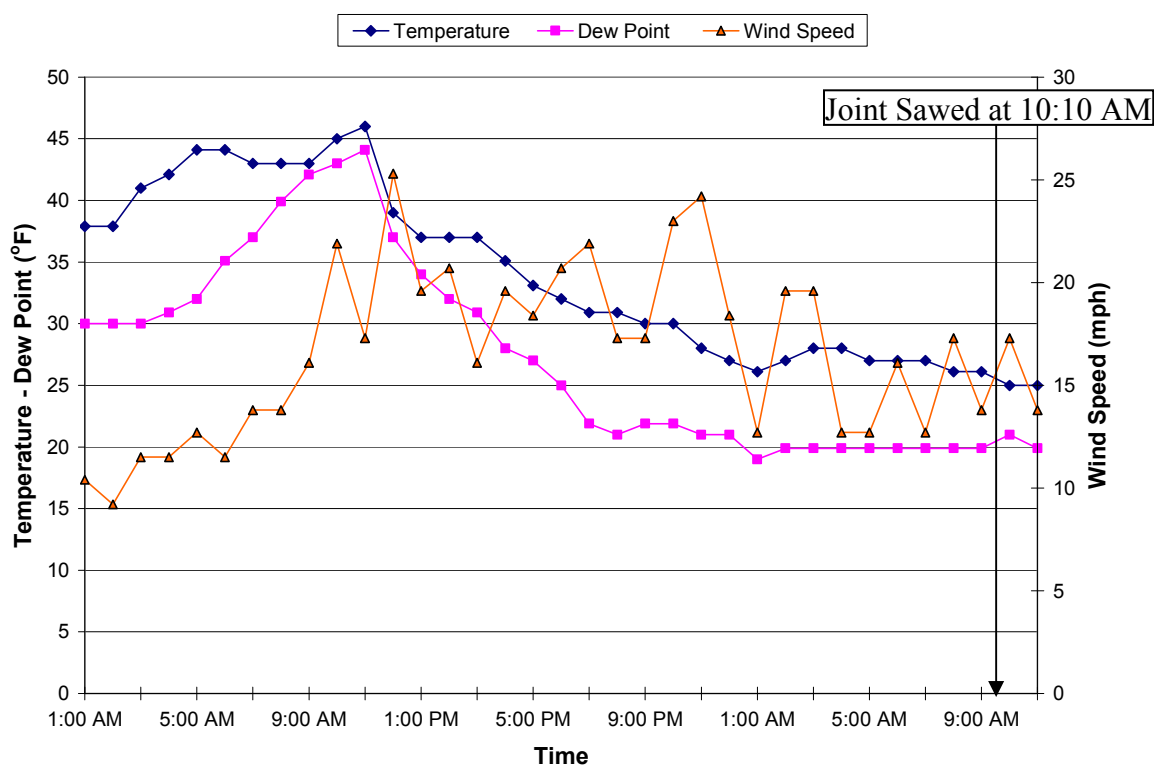


Figure 3.27: 12/16/03-12/17/03 Weather – temperature, dew point, and wind speed

3.5.5. Site Visit #4 Synopsis

The saw-cut was performed at 10:10 A.M. on December 17, 2003 to a 4” depth (D/3). The author did not observe the saw-cutting but it was reported by the saw-cutting superintendent that there were no unusual problems with the equipment during the saw-

cut. No random cracking or other significant problems were noticed throughout the length of the pavement at the time of saw-cut. The Arrhenius maturity at the mid-depth sensor, using 20 °C, as the reference temperature was 15.6 hours. Figure 3.28 shows a dual-axis graph of the ambient temperature, pavement temperature, and the cumulative Arrhenius maturity throughout the testing period. Figure 3.29 shows the examined joint three hours after it was cut which revealed little or no raveling.

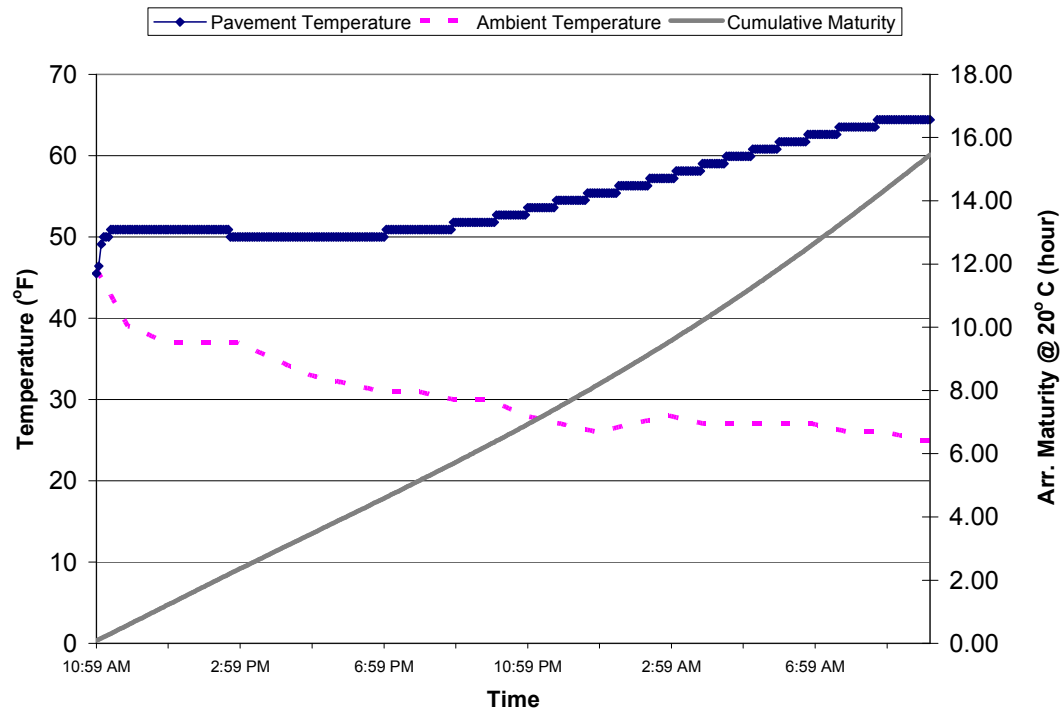


Figure 3.28: 12/16- 12/17/03 Pavement temperature, ambient temperature, and cumulative maturity at 20°C

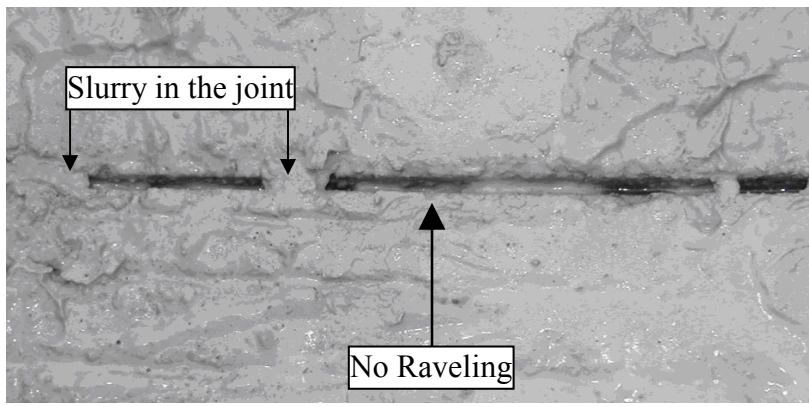


Figure 3.29: Picture of examined joint

Figure 3.30 is the master curve plot that was developed by the contractor for use with Indiana Test Method 402. The master curve is derived by cumulative maturity using the Nurse-Saul equation (TTF) and the breaking of 3 beams each at approximate ages of 24, 36, 48, and 60 hours. The logarithm of TTF maturity is plotted versus flexural strength and fitted linearly. The calculated TTF maturity using the mid-depth sensor (6" deep) at the time of the saw-cut was 2.72 which correlates to a strength of 443 psi.

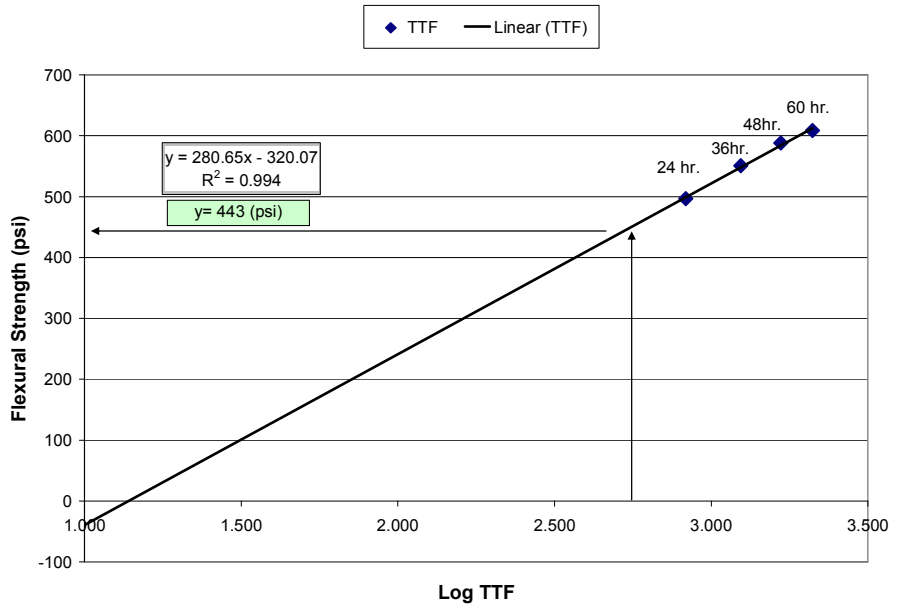


Figure 3.30: Master curve calculated flexural strength

3.6 Site Visit #5 (5/3/04-5/4/04)

3.6.1 Site Visit #5 Project Overview

Berns Construction slip formed approximately 1000 cubic yards of 10” pavement onto an unbound crushed aggregate subbase. The job site was located at 116th Street on the East side of Indianapolis. The paving operation began at 8:00 p.m. on 5/3/04 and concluded on 5/4/04 at approximately 3:00 a.m. The mixture design used was the same as that used in site visit #1 which is shown in Table 3.1. The concrete was produced by Builders Concrete whereas the concrete used in site visit #1 was produced by Berns. Two I-button maturity sensors were placed at two separate locations which were named A and B. There were 10 joints between joint A and B. Joint A was covered by the paver at 11:20 p.m. while joint B was covered at 11:50 p.m. Joints A and B were sawed at 5:30 p.m. and 6:10 p.m. on 5/4/04. The saw-cutting equipment was the same as site visit’s #1 and #4 which is shown in Figure 3.4. Figure 3.31 shows a timeline of the significant events throughout the testing period of which the following are included:

- Paving Started @ 9:00 p.m.
- Sensors Placed @ 10:00 p.m.
- Load A Batched @ 11:05 p.m.
- Sensor A Covered with Concrete @ 11:20 p.m.
- Load B Batched @ 11:30 p.m.
- Sensor B Covered with Concrete @ 11:50 p.m.
- Curing Agent at Joint A @ 12:45 a.m.
- Curing Agent at Joint B @ 1:15 a.m.
- Paving Finished @ 3:00 a.m.
- Started Sawing @ 4:10 p.m.
- Sawed Joint at Sensor A @ 5:30 p.m.
- Sawed Joint at Sensor B @ 6:10 p.m.

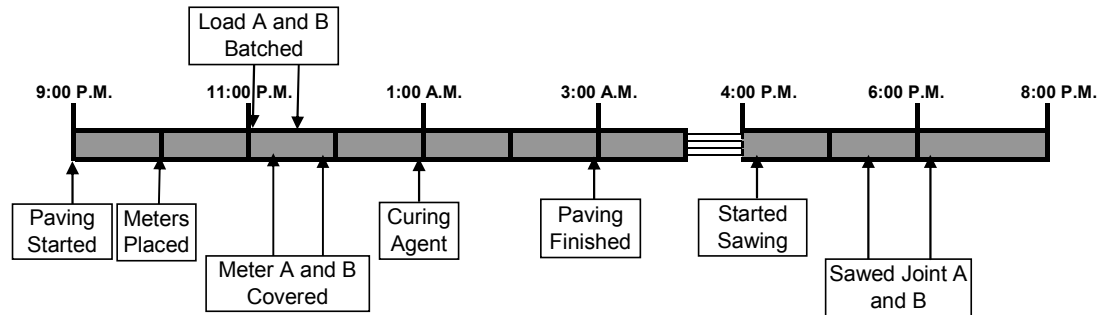


Figure 3.31: 5/3-5/4/04 timeline

3.6.2 Site Visit #5 Placement of the Meters

Two meters were placed at both location A and B. The meters were set to depths of 2.5" and 5" at both locations using a connecting steel rod. There was approximately 10 joints between location A and B. Figure 3.32 shows the vertical depth of the meters while Figure 3.33 shows the distance from the edge of the pavement.

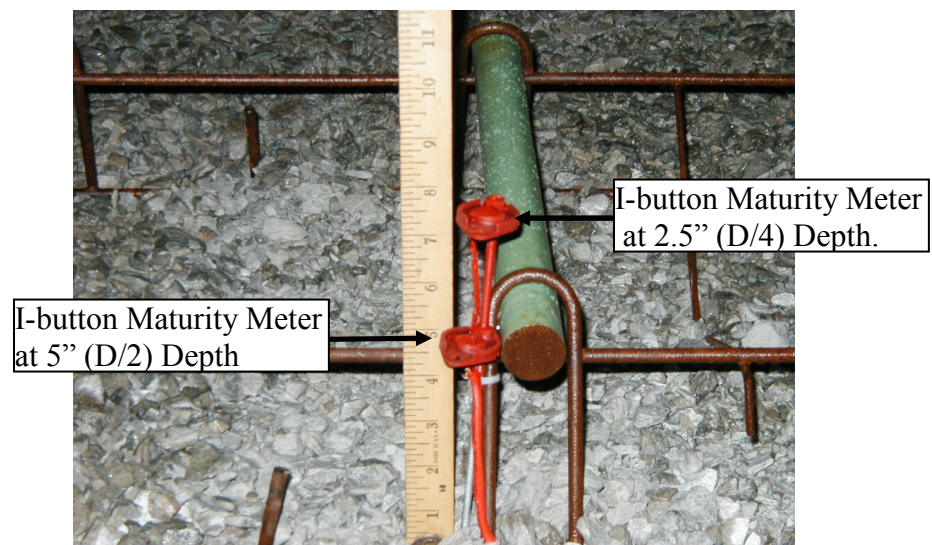


Figure 3.32: Vertical placement of I button maturity meters

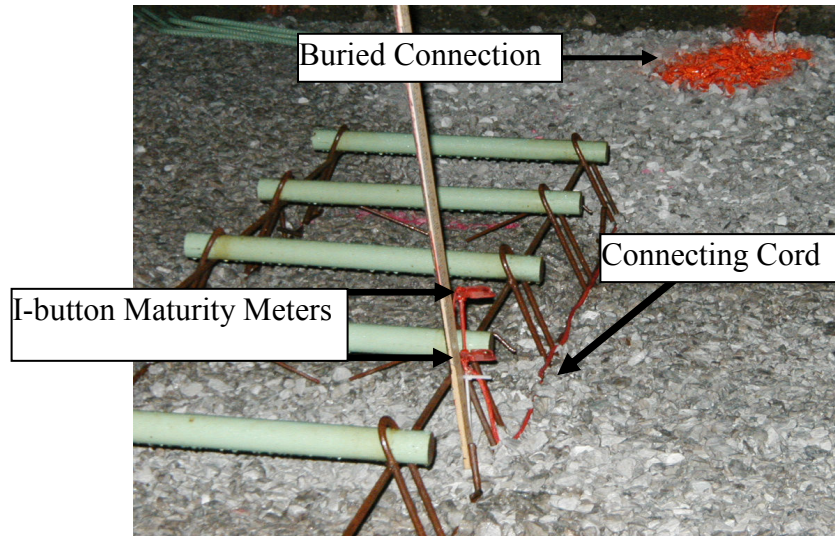


Figure 3.33: I-button sensors and connecting cord

3.6.3 Site Visit # 5 Weather

The average ambient temperature for the testing period was 49 °F with a maximum temperature of 62 °F and minimum of 38 °F. There was no precipitation recorded and the average humidity was 74 % with a high of 93 % and minimum of 53 %. The average wind speed was 9 mph with a max gust of 24 mph. Figure 3.34 is from the Weather Undergrounds recordings from the ASOS system at the Indianapolis International Airport which was approximately 10 miles from the job site.

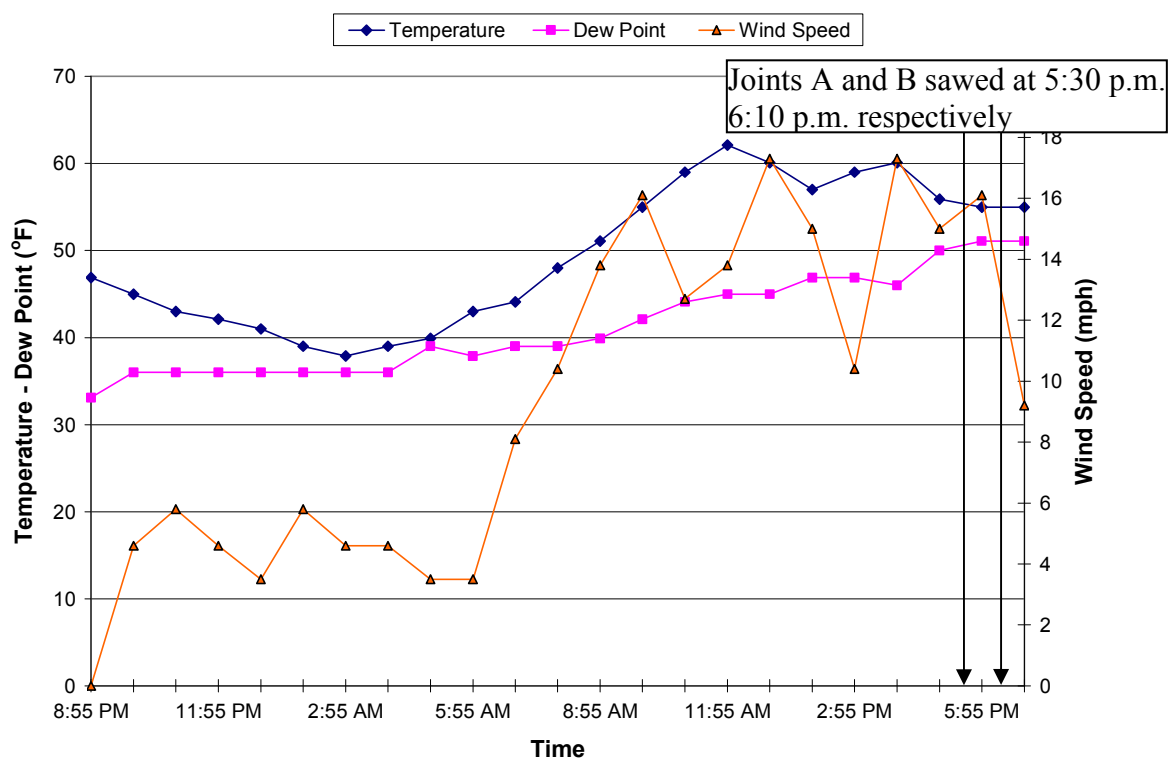


Figure 3.34: 5/03/04-5/04/04 Weather – temperature, dew point, and wind speed

3.6.4.1 Site Visit # 5 Synopsis of Joint A

The saw-cut was placed on joint A at 5:30 p.m. on 5/4/04. No random cracking was noticed throughout the length of the pavement at the time of saw-cut as well as any raveling or other significant problems. The maturity value calculated using the Arrhenius method at both 2.5” and 5.0” sensor depths was 16.9 equivalent age hours. Figure 3.35 and 3.36 show dual-axis graphs of the ambient temperature, pavement temperature, and the cumulative Arrhenius maturity throughout the testing period for the 2.5” and 5.0” sensors respectively. Figure 3.37 shows the comparison of the data from the 2.5” sensor and the 5.0” sensor. Figures 3.38 and 3.39 show pictures of the examined joint.

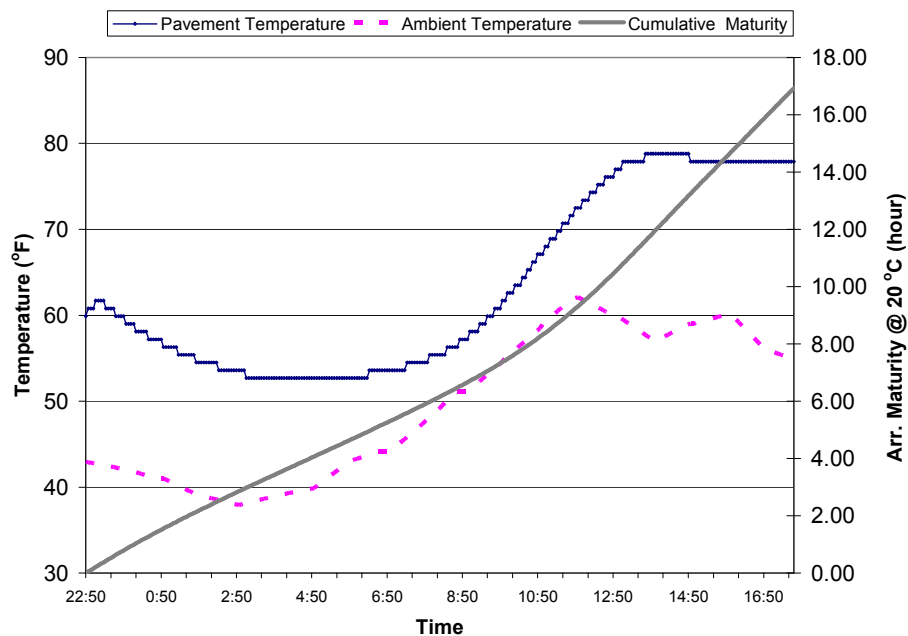


Figure 3.35: Pavement temperature, ambient temperature, and cumulative maturity at 20°C for 2.5" sensor at joint A

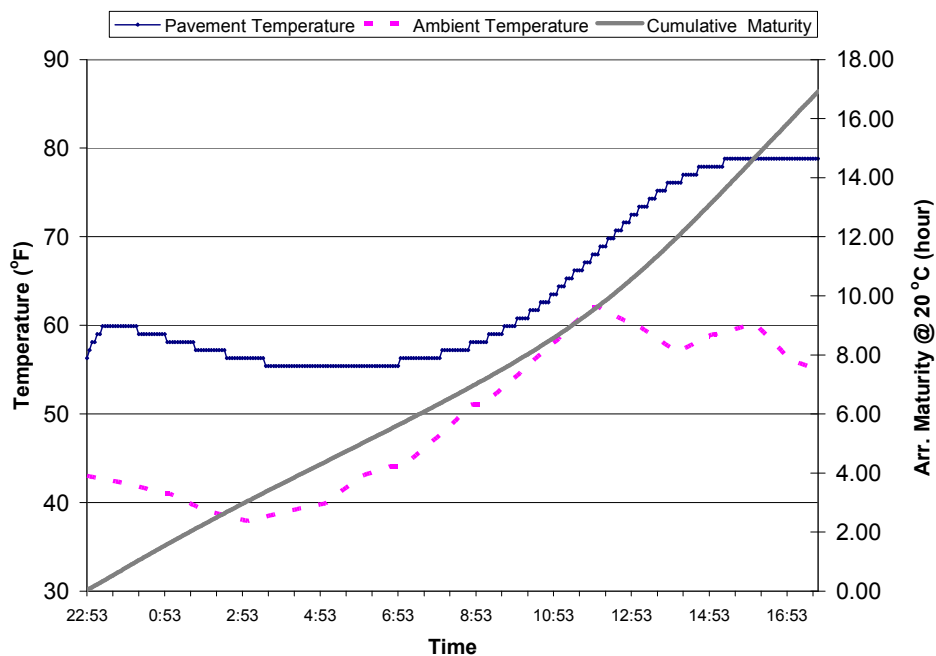


Figure 3.36: Pavement temperature, ambient temperature, and cumulative maturity at 20°C for 5.0" sensor at joint A

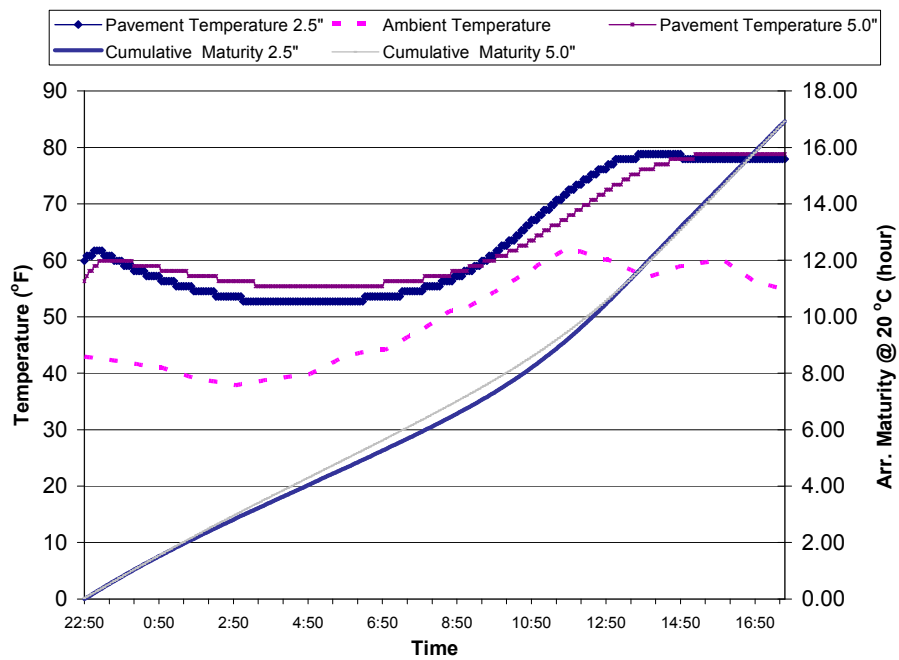


Figure 3.37: Comparison of pavement temperature and corresponding Arrhenius maturity for the 2.5" and 5.0" sensors at joint A

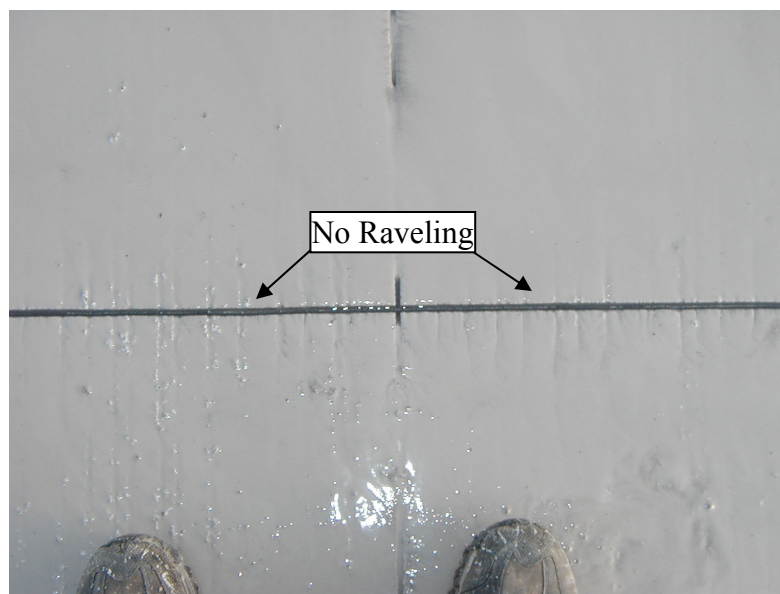


Figure 3.38: Examination of joint A

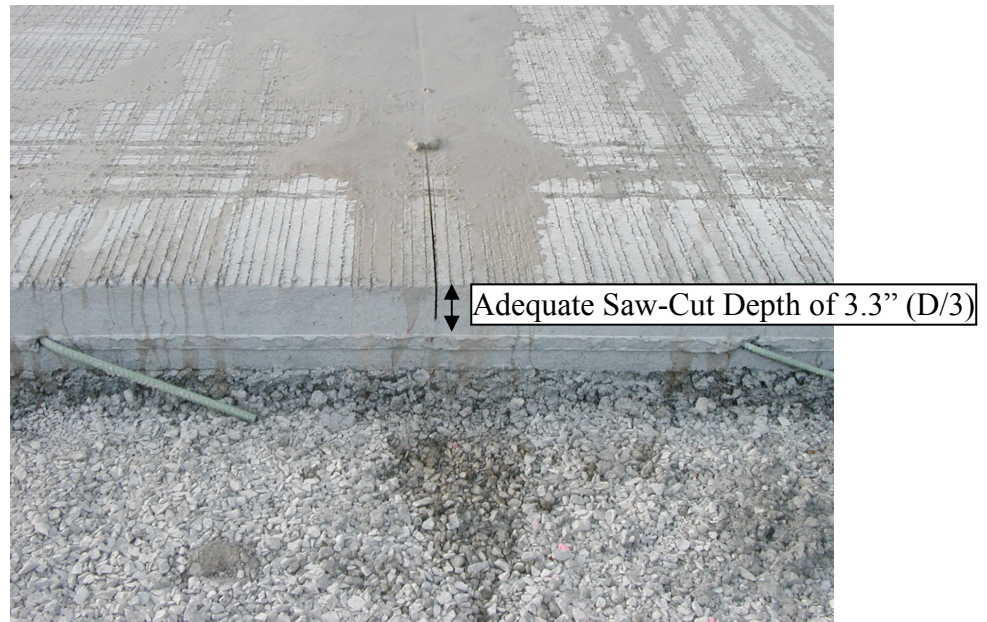


Figure 3.39: Depth of joint at location A

3.6.4.2. Site Visit #5 Synopsis of Joint B

The saw-cut was performed on joint B at 6:10 p.m. on 5/4/04. No random cracking was noticed throughout the length of the pavement at the time of saw-cut as well as any raveling or other significant problems. The 2.5" sensor at location B did not proceed to log data whereas the 5" sensor returned an equivalent age value of 17.7 hours at the time of the saw-cut. Figure 3.40 show dual-axis graphs of the ambient temperature, pavement temperature, and the cumulative Arrhenius maturity throughout the testing period for the 5" sensor. Figure 3.41 shows a comparison of the temperature development of the pavement at joint locations A and B for the 5" deep sensor. Figures 3.42 and 3.43 show pictures of the examined joint.

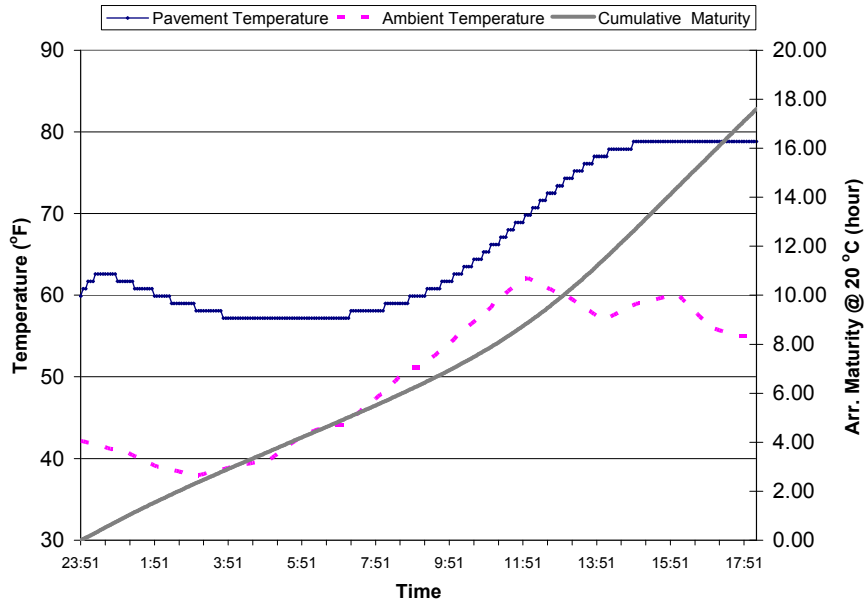


Figure 3.40: Pavement temperature, ambient temperature, and cumulative maturity at 20°C for 5.0” sensor at joint B

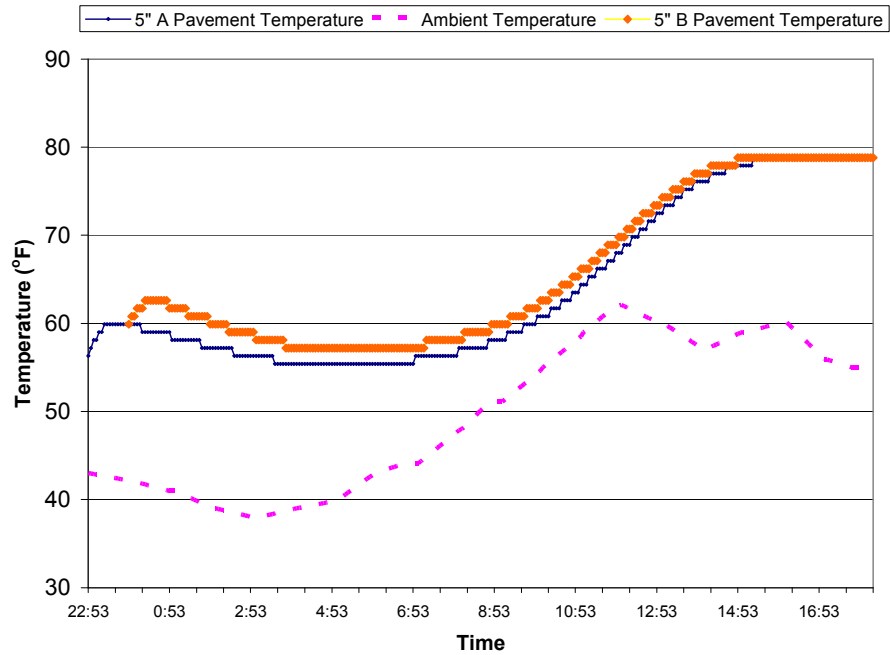


Figure 3.41: Comparison of 5” sensors at locations A and B

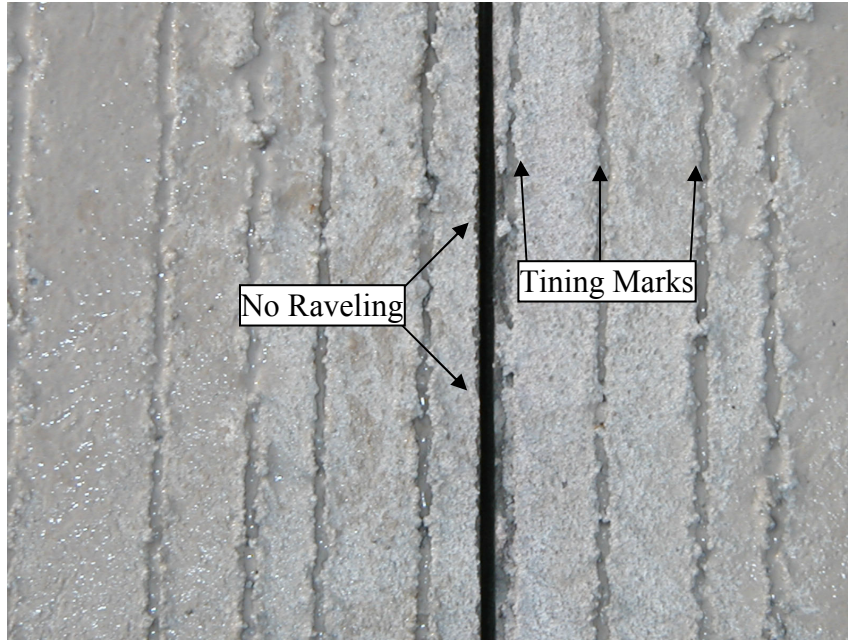


Figure 3.42: Examination of joint B

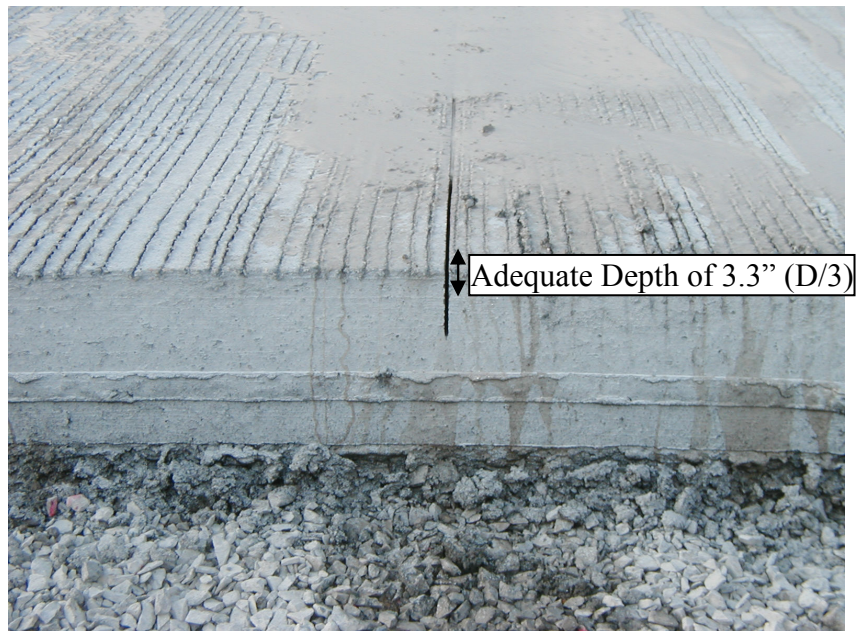


Figure 3.43: Depth of joint at location B

Because the same mixture design was used in site visit #5 as site visit #1, the same master curve (Figure 3.44) was use for predicted strengths. At mid-depth (5”) the TTF values for joint location A and B were both 2.72. Thus using the equation from the linear relationship the predicted strengths were 367 and 371 respectively.

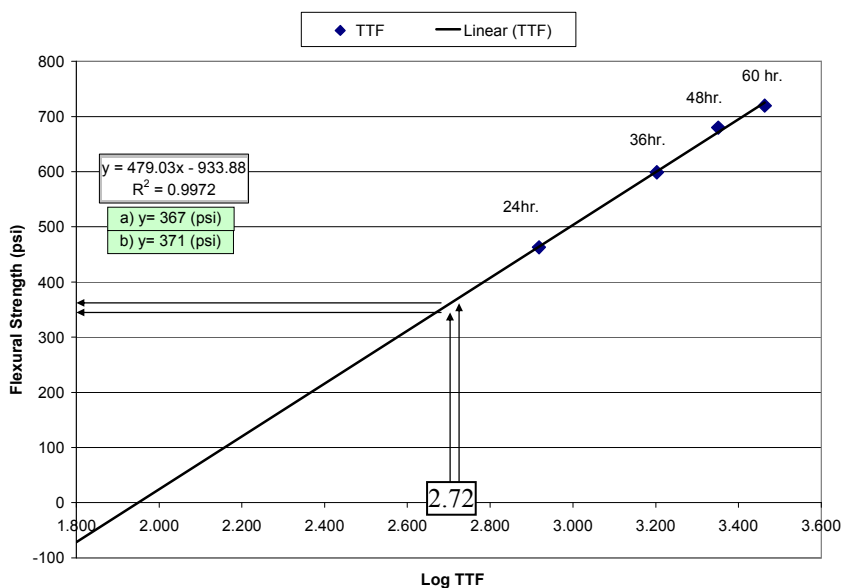


Figure 3.44: Master curve calculated flexural strength

3.7. Comparison and Summary of Site Visits

In this section of the chapter the information and data from the five site visits is compiled and analyzed. The section is organized in order that the information was presented for each site visit: Overview, Mixture Design, Placement of Meters, Weather, Equipment, and Synopsis. Each section begins with a table of the data relevant to the section and follows with short discussion on the notable and relevant observations.

Section 3.7.1 Overview Sections Summary

Table 3.4 summarized the information that was discussed in the overview sections of this chapter.

Table 3.4: Comparison of overview sections

Criteria	Unit	Site Visit # 1 (9/11/03)	Site Visit #2 (10/30/03)	Site Visit #3 (11/20-21/03)	Site Visit #4 (12/16-17/03)	Sight Visit #5 (5/3-4/04)	
						A	B
Depth of Pavement	(in.)	14	15	15	12	10	
Time Paving Began	(time)	7:00 AM	7:00 AM	7:00 AM	8:45 AM	9:00 PM	
Time Meters Covered	(time)	9:10 AM	10:15 AM	9:50 AM	10:30 AM	10:50 PM	11:50 PM
Time Sawed	(time)	3:10 PM	7:00 PM	2:00 AM	10:10 AM	5:30	6:10
Lag Time Between Batch and Maturity Recording	(min.)	78	5	5	5	10	10
Time from Concrete Placement to Application of Curing Agent	(h:mm)	2:05	1:45	1:45	1:00	2:00	2:00
Subbase	-	Unbound INDOT #8 Crushed	Unbound INDOT #8 Crushed	Unbound INDOT #8 Crushed	Unbound INDOT #8 Crushed	Unbound INDOT #8 Crushed	

The overview comparison revealed several noteworthy items. An interesting point of examination is the time of placement of the meters and time of the paving itself. The time of pavement and associated environmental factors can be compared between site visit # 5 and site visit #1 since they incorporated the same mixture design and were at similar ambient temperatures (See Table 3.7). Site visit #5 was a night pave where the maturity was started recording at 10:50 p.m. and site visit #1 was a typical day pave where the maturity began recording at 9:10 a.m. Therefore the site visits had opposite sequences of environmental events during their saw-cutting windows. The environmental events include solar radiation, ambient temperature, wind speeds, and relative humidity. The joints at site visit #5 were successfully sawed at a mid-depth maturity's of approximately 17 equivalent age hours without any raveling. This number can be compared to that of site visit #1's 11.8 equivalent age hours which revealed slight raveling. It can be concluded that the site visit #1 was at the beginning of the saw-cutting window at 11.8 equivalent age hours and the concrete tested in site visit #5 was stronger at an approximate maturity of 17 hours. Therefore the night pave which applied the environmental stimuli in reverse order produced no fallacies in the maturity prediction.

The variation in the lag time between when the concrete was batched and when the maturity was first recorded has a significant influence on the maturity prediction at

early-ages. In order to calculate the maturity during the lag time the first temperature recorded was assumed to be the temperature of the mixture during the lag time. Therefore as the lag time is increased, the precision of the maturity calculation is decreased. The lag time proves to be influenced by the choice of maturity sensors as well as the haul time. All the haul times for the site visits were between 5-15 minutes; therefore, haul time had an insignificant influence on varying the lag time. In regards to the maturity sensors, the first site visit utilized thermocouples which were connected to a data logger. Due to the requirement of connecting to the data logger, it was not feasible to embed the thermocouples until the pavement had been finished. This added approximately an additional 35-45 minutes to the lag time. It was also necessary to move the data logger next to the side of the pavement in order for the tinning machinery to pass. The thermocouples were embedded through the surface of the pavement which lead to further difficulties for the tinning machine operator. These inconveniences could be avoided by placing the thermocouples after the tining machinery had passed but this would also increase the lag time. In order to decrease the lag time and not slow the productivity of the paving crew a maturity sensor should have the following characteristics: 1) Capable of recording intervals of 15 minutes or shorter, 2) Capable of being embedded at or before the concrete is placed, 3) Not disrupt the construction with logging necessities or attachments, and 4) Not compromise the quality of the pavement.

The time at which the curing agent is applied challenges one of the basic assumptions made in the maturity method. The maturity method assumes that the in-place concrete is cured the same as the tested specimens which were used to develop the master curve. The tested specimens are cured where there is proper moisture to ensure the strength development. Mixture designs and environmental factors have the largest influence on the amount of moisture that is sustained in the pavement. A worst case scenario for inadequate hydration would include a mixture design that would provide very little bleeding upon consolidation and environmental factors of high temperature, high wind speed, and low relative humidity. These factors can contribute to inadequate hydration at the surface and edges where the saw-cut is to be performed. The maturity method does not compensate for lack of hydration due to moisture content and will

record strength gain relative to the temperature. If the curing agent is applied late and the conditions promote rapid evaporation with little bleed water there is the possibility that the maturity prediction of strength development will be inaccurate at the surface due to ceased hydration. The ceased hydration at the surface could lead to an increase in the amount and severity of raveling at the joint. It is usually the responsibility of the contractor to provide ample means for proper hydration which include curing methods and their timing. In order for the maturity method to be used effectively for saw-cutting timing, the curing of the pavement will need to be closely monitored and taken into consideration when assessing raveling. One possible method to take this into consideration would be to incorporate an evaporation rate calculation which can be found in ACI 305 Hot weather concreting (ACI 305, 1999).

3.7.2 Mixture Design Sections Summary

Table 3.5 is a summary of the information presented in the mixture design sections of this chapter.

Table 3.5: Mixture design comparison

<u>Constituent</u>	<u>Unit</u>	<u>Site Visit # 1</u> <u>(9/11/2003)</u>	<u>Site Visit #2</u> <u>(10/30/2003)</u>	<u>Site Visit #3</u> <u>(11/20-21/03)</u>	<u>Site Visit #4</u> <u>(12/16-17/03)</u>	<u>Sight Visit #5</u> <u>(5/3-4/04)</u>
Cement	(lb./yd ³)	445	575	575	515	445
Fly Ash	(lb./yd ³)	70	0	0	0	69
Mix Water	(lb./yd ³)	187	250	250	211	187
Fine Aggregate	(lb./yd ³)	1525	1300	1300	1511	1525
Coarse Aggregate	(lb./yd ³)	1720	1738	1738	1674	1720
Air Entrainment	(oz./yd ³)	5.8	4.8	4.8	5.2	5.8
Water Reducer	(oz./yd ³)	15.25	17.3	17.3	13.3	15.25
W/CM	-	0.420	0.435	0.435	0.410	0.420

Three different mixture designs were used. In addition, three different concrete producers manufactured the concrete described herein. The concrete for site visit's #2 and #3 was produced out of the same batch plant and incorporated the same mixture design. Site visit's #1 and #5 both incorporated the same mixture design but for site visit #1 the concrete was produced by another supplier. For site visit #4 the mixture design was different and the concrete was from a different batch plant than that which was used for site visit #1. The fly ash and cement constituents varied due to the fact fly ash is not allowed to be used after October, 15 according to INDOT specification 501.05. Feedback from various paving contractors has confirmed that these mixture designs are representative of the majority of paving performed in Indiana. Therefore, the mixture used for the laboratory testing was designed to be similar to these mixtures with regard to the volume of fine and coarse aggregates, dosages of admixtures, and quantity of cementitious material.

3.7.3 Placement of the Sensor Sections Summary

The following table provides a summary of the information that was presented in the sensor placement sections of this chapter.

Table 3.6: Sensor placement comparison

<u>Criteria</u>	<u>Unit</u>	<u>Site Visit # 1</u>	<u>Site Visit #2</u>	<u>Site Visit #3</u>	<u>Site Visit #4</u>	<u>Sight Visit #5</u>	
		<u>(9/11/2003)</u>	<u>(10/30/2003)</u>	<u>(11/20-21/03)</u>	<u>(12/16-17/03)</u>	<u>(5/3-4/04)</u>	
						<u>A</u>	<u>B</u>
Maturity Equipment	-	Thermo. (T)	I-button	I-button	I-button	I-button	
Location From Edge of Pavement	(feet)	2	2	2.5	2.5	3	3
Location From the Saw Joint	(feet)	1.5	0.5	0.5	0.5	0.5	0.5
Depth of Maturity Meter(s)	(in.)	7	8.5	7.5	6	2.5/5.0	2.5/5.0
Total Number of Meters Placed	(#)	6	1	1	1	2	2

Sensor depth was varied to examine the influence on maturity predictions and determine the proper depth for saw-cutting window predictions. Various factors must be taken into consideration when specifying the appropriate depth of the maturity sensor. A sensor at mid-depth will provide the best indication of the overall pavement temperature development whereas a sensor closer to the saw-cut would be more representative of the relative concrete. It seems logical that the maturity sensor should be placed at mid-depth of the saw-cut depth in order to get the best index of the concrete that is going to be cut. For example, if a pavement was 15” thick and the saw-cutting requirement was D/3, a 5” saw-cut would be necessary. This would require that the sensor be placed at 2.5” from the surface. At this depth, depending on the type of maturity sensor and system, it will likely become receptive to causing durability and other associated problems in the pavement. Placing a sensor at mid-depth of the pavement, before the placement of concrete, is easily done without any mechanical support because the sensor can be attached to the dowel bars at mid-depth.

In the first and fifth site visit the temperature sensor depths were varied between $\frac{1}{4}$ depth and mid-depth, whereas in site visits #2, #3, and #4 a single sensor was placed at mid-depth. The equivalent age maturities for the first site visit at depths of 3.5”, 7”, and 10.5” were 12.57, 11.79, and 10.83 equivalent hours respectively. If we examine the strength predictions based on the TTF maturity and master curve shown in Figure 3.8 we find strength predictions of 241 psi for the 3.5” ($\frac{1}{4}$ depth) sensor and 235 psi for the 7.0” (mid-depth) sensor. The difference in 6 psi can be compared to a standard deviation

of 46 psi which was obtained from splitting tensile tests at an age of one day and is shown in section 5.2.5 of this report. From comparison we can conclude that the difference of 6 psi between the 3.5” and 7.0” predictions is relatively insignificant. The equivalent age maturities from the sensors placed at 2.5” (1/4 depth) and 5” (mid-depth) at joint location A in site visit five (night pave) were 17.07 and 17.04. Considering the small difference (0.03 eq. age hour) in maturity, the depth of sensor location does not lead to significant differences in strength predictions.

The discrepancy between maturities at various depths depends on the temperature gradient throughout the pavement. The temperature gradient is influenced by numerous factors. These include: ambient temperature, wind speed, relative humidity (precipitation), solar radiation, sub-grade temperature, and sub-grade type. Often the temperature gradient is assumed to be linear from top to bottom for which the mid-depth temperature provides the average. It should also be taken into consideration that the maturity method can also be used for determining the modulus of elasticity and shrinkage of pavement (Hiperpav, 2004) for which the average (mid-depth) temperature value is a necessary component. In addition, Indiana Test Method 402-04T, which utilizes the maturity method to determine pavement strength for opening to traffic, specifies the sensors be placed at mid-depth. If contractors can utilize a single maturity sensor for multiple results they are more inclined to implement the maturity method and purchase the appropriate components.

In summary, placing a sensor at mid-depth proves to be a better than 1/4 depth because there is little variation between maturity predictions and a sensor at mid-depth has the following advantages. First, a sensor at mid-depth is easier to place because of the dowel bars and there are no durability concerns with regard to the surface of the pavement. In addition, contractors would prefer to use one sensor, for practical reasons, and a sensor at mid-depth is more efficient because it can be used to determine the modulus of elasticity and shrinkage along with ITM-402 predictions.

In site visit #5 two joint locations with ten joints in between locations were placed with meters. The purpose of the two sensor locations was two fold. The first purpose

was to compare how the pavement temperature developed at different locations. This was in effect determined by placing the sensors at separate locations that were undergoing the similar environmental stimuli. As expected, both locations followed very similar temperature developments. This is illustrated in Figure 3.41. The second purpose was to determine how sensitive the maturity calculations were to the speed of the saw-cutting crew as they progress the length of the pavement. For example, if the saw-cutting crew operated significantly slower or faster than the concrete was placed in the paving operation there would be a large variance between the maturities at the joints which may require sensors to be placed at more than one location. For the two locations tested the maturities for the 5” sensors at the time of the saw-cut were 17.07 and 17.72 equivalent age hours for joint A and B respectively. This shows that the saw-cutting crew progressed at a similar pace to that of the paving operation. Since the progression of the saw-cutting crew was similar to the progression of the paving it can be concluded from this site visit that one sensor towards the beginning (100’) of pavement is enough to predict when the saw-cutting crew should begin sawing.

3.7.4 Weather Sections Summary

Table 3.7 provides a summary of the data that was presented in the weather sections of this chapter.

Table 3.7: Weather comparison

Criteria	Unit	Site Visit # 1 (9/11/2003)	Site Visit #2 (10/30/2003)	Site Visit #3 (11/20-21/03)	Site Visit #4 (12/16-17/03)	Sight Visit #5 (5/3-4/04)
Average Temperature	(°F)	72	57	51	34	49
Max Temperature	(°F)	81	73	65	46	62
Low Temperature	(°F)	63	41	37	24	38
Average Humidity	(%)	69	62	65	80	74
Max Humidity	(%)	90	82	89	98	93
Low Humidity	(%)	52	37	41	61	53
Precipitation Recorded	(in.)	0	0	0	0.22	0
Average Wind Speed	(mph)	8	13	10	17	9
Maximum Gust	(mph)	16	32	21	31	24

The influence that weather has on pavement temperature development and also on the stress development of pavement is a broad and intricate topic which is outside the scope of this section. The environmental factors include the air temperature, wind speed, relative humidity, and solar radiation. The purpose of the maturity monitoring is to encapsulate the effects that the environment and surrounding structures have on the strength development of the in-situ concrete. Therefore, it should be noted from this subsection that a wide range of weather conditions were encountered during the site visits. The maximum and minimum ambient temperatures were 81°F and 24 °F respectively. The minimum temperature of 24 °F is believed to be at or near the limit that paving operations will encounter whereas the maximum of 81 °F will often be exceeded in the summer months when temperatures commonly climb to 100 °F. In addition, the humidity ranged from a low of 37% to a high of 98%.

3.7.5 Equipment Sections Summary

Table 3.8 provides a summary of the information provided in the equipment sections of this Chapter.

Table 3.8: Equipment comparison

Criteria	Unit	Site Visit # 1 (9/11/2003)	Site Visit #2 (10/30/2003)	Site Visit #3 (11/20-21/03)	Site Visit #4 (12/16-17/03)	Sight Visit #5 (5/3-4/04)
Type of Saw	-	Target 65hp	CoreCut 65hp	CoreCut 65hp	Target 65hp	Target 65hp
Blade Type	-	Diamond	Diamond	Diamond	Diamond	Diamond
Blade Size - Diameter	(in.)	18 1/8	20	20	18 1/8	18 1/8

The equipment used on all five of the site visits were conventional wet-cut 65 horsepower saws with diamond blades. The only difference between the equipment was the diameter of the blades which varied slightly with the depth of the pavement. In examining raveling the analysis of the equipment is an important consideration because malfunctioning equipment can cause increased or avoidable raveling. The specific

influence of components of blades and saws were discussed in Section 2.4 of this research report. No early-entry dry cut saws were encountered on the site-visits. Early-entry saws are not currently specified for use on INDOT projects.

3.7.6 Synopsis Sections Summary

Table 3.9 provides a summary of the information that was discussed in the synopsis sections of this chapter.

Table 3.9: Synopsis comparison

Criteria	Unit	Site Visit # 1	Site Visit #2	Site Visit #3	Site Visit #4	Sight Visit #5	
		(9/11/2003)	(10/30/2003)	(11/20-21/03)	(12/16-17/03)	(5/3-4/04) A	B
Raveling (little-none, slight, significant)	-	slight	little -none	little - none	little - none	little - none	
Maturity at Time of Saw (mid-depth)	(eq. hr.)	11.8	9.7	21.3	15.6	16.9	17.7
Maturity at Time of Saw (mid-depth) TTF	(°C-hr)	2.442	2.447	2.736	2.719	2.716	2.723
TTF Predicted Strength	(PSI)	236	272	399	443	367	371
Actual Time from Placement of Meter to Sawing	(hr.)	6	9	16	24	18	18
Joint Sawed to Specified Depth	-	Yes	Yes	No	Yes	Yes	Yes
Temp of Pavement When Sawed	(°F)	101	84	87	64	79	79
Peak Temperature	(°F)	Undetermined	86*	90	64	79	79
Sawed Pre-Peak, Peak, Post-Peak	-	Undetermined	Pre	Post	Peak	Peak	Peak
Maturity at Middle of Peak Temperature	(eq.hr.)	Undetermined	Undetermined	15.6	15.3	15.9	15.3

Raveling was classified by the author into three general categories. These include little-none, slight, and significant. “Significant” raveling is classified as raveling that will lead to deterioration of the joint and cause durability problems. “Little-None” raveling is that which has no significant raveling apparent to the human eye. Slight raveling is any raveling that is not “Significant” or “Little-None”. Classifying raveling has been attempted to be quantified (Okamoto, 1994) but the process proves to be extremely time

consuming. Thus a more detailed and consistent classification process of raveling is necessary. The research results will facilitate the development of classifying raveling.

The monitoring of a general “rule of thumb” during the site visits provided a point a reference for determining the approximate saw-cutting window. A “rule of thumb” followed by many in the industry is that the saw-cut should be performed when the pavement temperature peaks after placement. For the sake of this paper the highest temperature that the pavement reaches at mid-depth after placement will be considered the peak temperature. The “rule of thumb” is based on the stages of the heat of hydration curve for which the onset of the rate of heat evolution curve is the beginning of the set time and the peak of the curve is the conclusion of the set time. The heat released in the exothermic hydration reaction will either cause the temperature of the concrete to increase or release to the surroundings. Therefore the pavement temperature is a function of the rate at which heat is released to its surroundings and the peak pavement temperature at mid-depth is representative of the “final set”. It should be noted that the depth of the pavement and maturity sensor play an important role in the peak temperature determination. A thinner pavement and or a sensor closer to the surface will be more sensitive to environmental effects for which the relationship to set time may not hold true.

All of the maturities and temperatures referred to in this section are those that were recorded at mid-depth. For site visit #1 the thermocouples had to be taken out in order for the saw-cutting crew to perform the cut; therefore, no data was recorded past the temperature at which the saw-cut was performed. The saw-cut was performed pre-peak during site visit #2 at a maturity of 9.7 hours. The time-temperature history was recorded for an hour after the saw-cut was performed and the temperature was still climbing. The maturity when the data recording stopped, 1.5 hours after sawing, was 12.0 hours. It is undetermined what the maturity value would have been at the exact peak temperature.

During sight visit #3 the saw-cut was performed post-peak at a maturity of 21 hours. If the saw-cut were to be performed at the peak temperature of 90 °F the equivalent age maturity would have been 15.0 hours. In site visit #4 the saw-cut was

performed at the peak temperature for which the equivalent age maturity was 15.6 hours. During site visit #5 the saw-cuts were performed post-peak at maturities of 16.9 and 17.7 for joints A and B respectively. The maturities at peak temperatures for joints A and B were 15.9 and 15.3 respectively. Therefore, maturity at the peak temperature for site visits #3, #4, and #5 were approximately 15 equivalent age hours. Figure 3.45 shows the temperature development for the three site visits at the corresponding Arrhenius maturity. In Figure 3.45 there are separate plots for joint locations A and B regarding site visit #5.

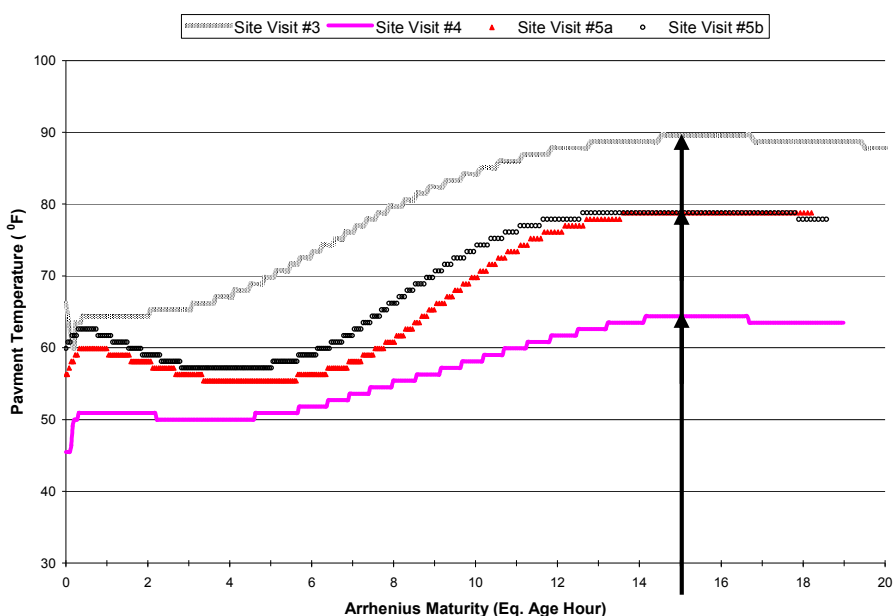


Figure 3.45: Pavement temperature versus Arrhenius maturity for site visit's # 3, 4, and 5

It is interesting to note that visits #3, #4, and #5 were all different mixture designs and the range of temperature varied from a high of 65 °F and a low of 24 °F. In addition, site visit # 5 was a night pave which provided the opposite environmental stimuli as that of site visits #3 and #4. From the analysis of the maturity values at peak temperature it can be concluded that a maturity of 15 equivalent age hours is a reference point for the height of the pavement temperature curve at mid-depth in concrete pavement.

The strength predictions based on TTF at the time of sawing are shown in Table 3.9. It can be seen that a relatively wide range of strengths were observed (236-443 psi), which may be explained by the following observations. All values calculated were based on the Nurse-Saul (TTF) maturity at mid-depth. The master curves were derived by fitting a linear plot to the logarithm of the Nurse-Saul maturity (TTF). Various drawbacks regarding the Nurse-Saul maturity function and logarithmic strength-maturity relationship were discussed in Chapter 2 of this report. Also discussed in Chapter 2 was previous work done by (Barde et al., 2004) which has suggested a fundamental transition in flexural strength versus maturity plots at approximately 36 hours (real time) of curing. The master curves that were used for site visit #1, #4, and #5 were all developed for use in Indiana Test Method 402. The beams for ITM 402 are tested at hours of 24, 36, 48, and 60 hours. The beams that were used to develop the master curve for site visit #3 and #4 were tested at 12, 24, and 36 hours. Figure 3.46 shows a plot of all three master curves

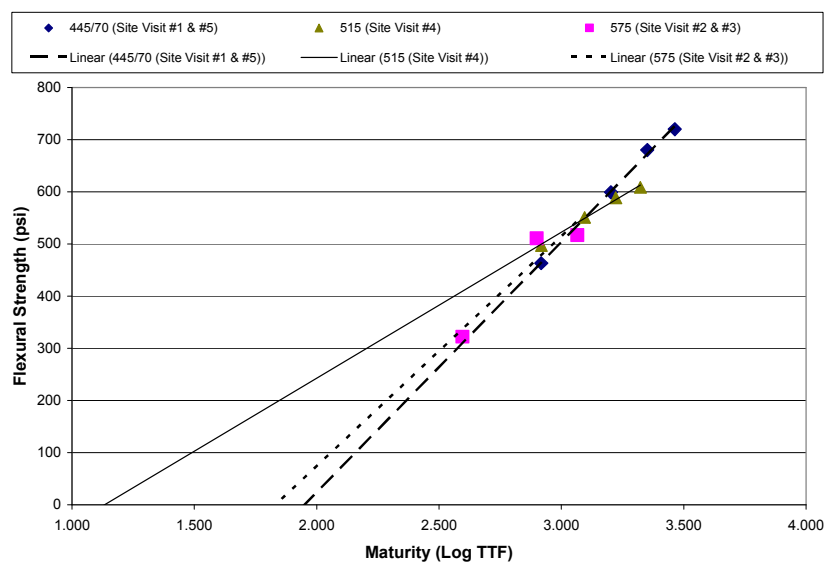


Figure 3.46: Master curve comparison

for their respective mixture designs. As mentioned in section 3.6.2 (Table 3.5) of this chapter the 445/70 represents the mixture design for site visits #1 and #5 which had 440

pounds of cement and 70 pounds of fly ash per cubic yard of concrete. The 575 reflects the cement content per cubic yard for site visits #2 and #3 as well as the 515 label is representing the same for the mixture of site visit #4. The master curve from site visit #4 is clearly an overestimating curve as it predicts strength gain to occur at approximately time zero. It is evident that different master curves which are more accurate at earlier ages are required in order to analyze the saw-cutting window. The purpose of the plots was to provide a reference for further testing and predict an approximate strength at the times at which saw-cuts occurred. It should be noted that site visit #1 had slight raveling and was sawed at the lowest predicted strength value of 236 psi and in site visit #3 the saw-cutting crew verbally communicated that they believed they were sawing later than they would have preferred based on their experience. The predicted flexural strength for site visit #3 was a flexural strength of 399 psi.

CHAPTER 4: EXPERIMENTAL PROGRAM

4.1 Introduction

The intent of this chapter is to provide information about the experimental portion of this research project. The chapter is divided into four sections. In section 4.2 the experimental approach is described which includes an explanation of the types of testing that were performed. Section 4.3 provides details about the constituent materials, mixture proportions, and mixing procedures. Section 4.4 focuses on the tests that were performed to assess the mechanical properties of the concrete. Research was conducted to assess how mechanical properties change as a function of early-age maturity. Specifically focusing on early-age properties, section 4.5, describes experiments that were performed to assess the potential for early age raveling of concrete.

4.2 Experimental Approach

The objective of the experimental program was to provide data that can be incorporated into a model that can be used for determining the saw-cutting window based on the maturity concept. It is anticipated that the model will utilize a probabilistic assessment to calculate the risk of cracking. Specifically, the experimental phase of the project included five tests to assess mechanical property development and two tests to assess the potential for raveling. The five tests for assessing mechanical property development included the 1) Tensile Wedge Test, 2) Flexural Beam Test, 3) Early Age Shrinkage Test, 4) Compressive Cylinder Test, and 5) Split Cylinder Test. The two tests that were performed to assess the potential for raveling included the 1) Mortar Set Time and 2) Early-Entry Saw Test.

4.3. Mixture Materials, Proportions and Procedures

In this section details are provided regarding the materials, proportions, and procedures used for making the specimens. It should be noted that all of the specimens tested in the laboratory have the same materials and proportions which will be described herein.

4.3.1 Constituent Materials

Lonestar Type I portland cement was used in all of the laboratory specimens. The cement was produced at the Lonestar plant in Greencastle, Indiana. In Table 4.1 the cement's chemical properties are shown.

Table 4.1: Chemical properties of Lonestar Type I cement

	C₃S	C₂S	C₃A	MgO	SO₃	LOI	Insoluble Residual	Total Alkali
Content (%)	52.00	21	10.00	1.45	3.31	1.78	0.47	0.70

The coarse aggregate used for all the mixtures was supplied by Vulcan Materials from their Monon, Indiana quarry. The coarse aggregate had a gradation that met INDOT #8 specifications. In order to ensure proper gradation the coarse aggregate was sieved separately for each mixture and recombined to meet target values within the #8 guidelines. The target values, which are shown in Table 4.2, are those used by an area contractor in a paving mixture with cement content of 515 lb/yd³ and w/c ratio of 0.42.

Table 4.2: Coarse aggregate gradation

Sieve Size	INDOT #8 %Passing (max.)	INDOT #8 %Passing (min.)	Target % Passing	Target % Retained
1" (25mm)	100	100	100	0
3/4" (19mm)	95	75	90	10
1/2" (12.5mm)	70	40	49	41
3/8" (9.5mm)	50	20	29	20
#4 (4.75)	15	0	7	22
#8 (2.36)	10	0	2	6
Decant (PCC)	1.5	0	0	2
			Total	100

The fine aggregate used in all of the mixtures was a local natural sand with a relative density (SSD), absorption, and fineness modulus of 2.63, 1.85%, and 2.88 respectively. The fine aggregate was taken directly from the aggregate storage unit and was not sieved specifically for each mixture, however the gradations were periodically confirmed throughout the duration of this investigation. The gradation of the fine aggregate is shown in Table 4.3. As you can see from Table 4.3 the gradation meets Indot classification #23 requirements.

Table 4.3: Fine aggregate gradation

Sieve Size	Sieve Size (mm)	INDOT #23 Max. % Passing	INDOT #23 Min. % Passing	Sample % Passing
3/8	9.5	100	100	100
4	4.75	95	100	99
8	2.36	80	100	92
16	1.18	50	85	65
30	0.6	25	60	39
50	0.3	5	30	13
100	0	0	10	3
Pan	0	0	0	0

The admixtures used in these mixtures included a water reducer admixture (WRDA-82) and an air entraining admixture (Daravair) that were manufactured by Grace Construction Products. The relative density of the water reducer and air entrainment were 1.15 and 1.05 respectively.

4.3.2 Mixture Proportions

The following section explains the mixture proportions used for the laboratory specimens. The mixture was proportioned to resemble paving mixtures used in the State of Indiana and that used in previous research (Yang et al., 2004, Graven et al., 2003). The batch weights used for the mixtures are shown in Table 4.4 by weight for a volume of 1.65 ft³. All specimens were cast, with the exception of shrinkage specimens, using a 1.65 ft³ batch.

Table 4.4: Constituent weights for 1.65 ft³ batch

Material	Batch Weight for Specimen Volume (lbs.)	Batch Weight for 1 yd³ (lbs)
Coarse Aggregate	102.3	1674
Fine Aggregate	83.8	1371
Cement	35.4	579
Water	17.4	285
Water Reducer	0.09	1.47
Air Entrainment	0.01	0.16
Total Weight	239	3911

In order to compensate for mortar retained by the mixing pan, an additional 0.07 ft³ of mortar was added to each 1.65 ft³ batch of concrete. The mortar was of the same proportions as the mixture design shown in Table 4.4 and was added to the batch weight for final proportioning. This follows the “Over-Mortaring” procedure recommended by ASTM C 192. The chemical admixtures were weighed in grams for which Table 4.5 shows the conversion to pounds and the corresponding dosage rates.

Table 4.5: Chemical admixture dosage rate

Admixture	Weight	Weight	Dosage Rate
	(lbs.)	(grams.)	(fl. Oz. / 100 lb cement)
Water Reducer	0.09	38.9	3.37
Air Entrainment	0.01	4.5	0.43

4.3.3 Mixing Procedure

The following mixing procedure steps were used for all of the specimens that were cast. The coarse aggregate was the first material loaded into the pan mixer followed by the fine aggregate. Once all of the aggregate was placed into the pan, the mixer was started and 40% of the total water was added into the mixer. The mixer was allowed to run for 30 seconds before the cement was added. After the cement was completely loaded, the air entrainment, which was mixed with 40% of the water, was added. These materials mixed for 20 additional seconds before the final 20% of water, which was mixed with the water reducer, was added. After all of the materials were loaded, mixing continued for 3 minutes, was turned off for 3 minutes, and restarted for a final 2 minutes. The “3 minutes on - 3 minutes off - 2 minutes on” procedure is recommended by ASTM C 192. However, it should be noted that this differs from field practices.

Table 4.6: Mixing Procedure

Procedure		
<i>Prior to mixing</i>		
Step#	Material	% of Total
1	Coarse Agg	100%
2	Fine Aggregate	100%
<i>Start mixer</i>		
3	Water	40%
<i>Mix for additional 30 seconds before cement</i>		
4	Cement	100%
5	Water w/ A.E	40%
<i>Mix for additional 20 seconds before water reducer</i>		
6	Water w/ W.R.	20%
<i>Mix for 3 min. / OFF for 3 min. / Mix for 2 min.</i>		

4.4. Test's Performed to Evaluate Mechanical Properties

This section of the chapter will discuss the tests that were performed to evaluate the mechanical properties of the concrete at early-ages. This section is further divided into sub-sections for each of the specific tests.

4.4.1. Tensile Wedge Test

The tensile wedge test was specifically designed for this research project to analyze the influence of a notch on the early-age properties of concrete when it is loaded in tension. In this sub-section, design considerations, specifications, test procedures, and analysis of the tensile wedge test will be discussed.

4.4.1.1 Design Considerations

The broad consideration for the design of the testing apparatus was that it could apply a direct tensile load to a representative cross section in a practical manner to a specimen of sufficient size. A common hindrance in early age tensile testing is the ability to “grip” the ends of the specimen. The geometry of the tensile wedge apparatus allowed the ends to be “gripped” using compression. This geometry is illustrated in Figure 4.7. More specifically the Tensile Wedge Test (TWT) was designed to incorporate the following criteria:

- 1) apply a direct tensile load under stable conditions,
- 2) apply a load at ages immediately after set time,
- 3) assess the influence of a notch of various depths,
- 4) match pavement temperature development,
- 5) capable of casting the specimen on the testing machine to prevent movement before loading.

In addition, St Venants principle and a “rule of thumb” regarding direction of crack propagation in concrete were taken into consideration. St. Venants principle defines how far away the load should be applied in order to have a normal stress distribution across the tested cross section. The load should be applied at a distance no smaller than the smallest dimension of the tested cross section. In the case of the tensile wedge, the load was applied 11” from the tested cross section which had a largest dimension (depth) of 8.5”. This is illustrated in section 4.4.1.2 of this report. The “rule of thumb” (ACI 446, 1991) states that the direction of crack propagation should be at least three times (preferably five times) the maximum aggregate size. The direction of crack propagation depends on the size of the notch for tensile wedge setup. The largest notch used was 4.25” (D/2) notch which is 4.25 times larger than the maximum aggregate size of 1”. Therefore the design of the tensile wedge substantially meets the design guidelines of St. Venants principle and the “rule of thumb” by ACI 446..

4.4.1.2 Basic Testing Geometry and Loading Considerations

The basic design of the tensile wedge apparatus was to convert the compressive load from the MTS machine to a tensile load on the specimen. The load is converted using an 8.5° wedge that transfers the compressive load to the radial ball bearings attached to the specimen form. Two radial ball bearings were attached per bolt for a total of eight radial ball bearings. The bearings had an outer diameter of $1\frac{3}{4}$ ” and the bearing width surface was $\frac{1}{2}$ ”. The bearings transferred the load to the steel forms which compressed on the ends and pushed the specimen apart. As the ends of the specimen are pushed apart they induce a tensile load along the length of the specimen. Figure 4.1 shows a picture of the tensile wedge apparatus setup on the universal testing machine whereas Figure 4.2 shows a schematic of the basic mechanics for the tensile wedge apparatus with the arrows representing the movement of the machine and formwork.

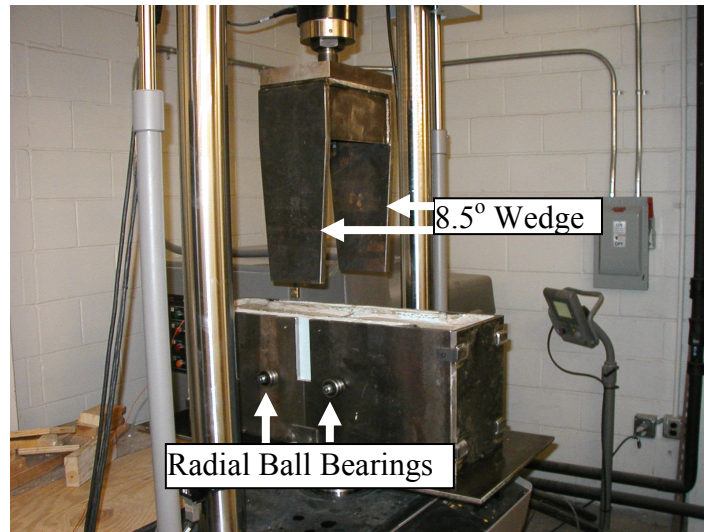


Figure 4.1: General picture of tensile wedge apparatus setup

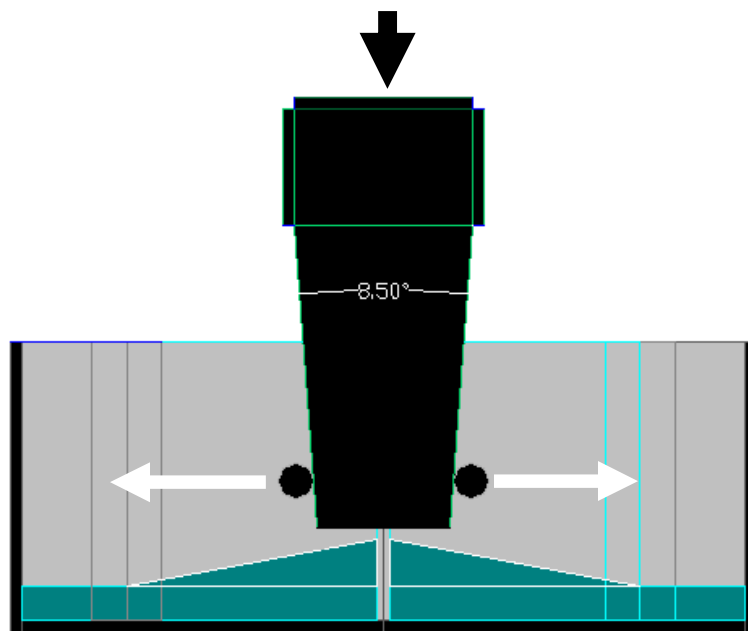


Figure 4.2: General schematic of tensile wedge apparatus movements

4.4.1.3 Specimen Dimensions

This section details the dimensions of the tensile wedge specimen. Preliminary testing of the original tensile wedge apparatus lead to alterations of the specimen

geometry which included tapering depth and width of the neck. Figures 4.3 and 4.4 show the dimensions of the apparatus before it was altered and illustrate the location of the cracking.

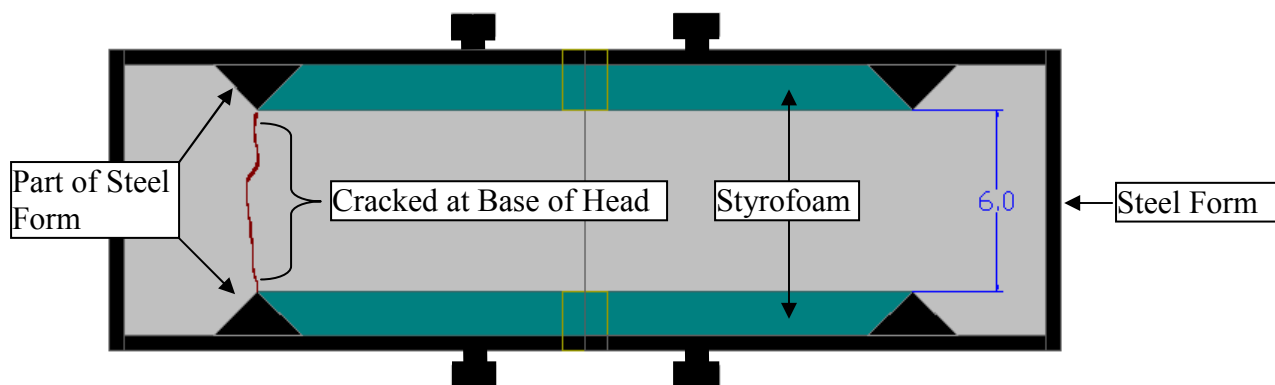


Figure 4.3: Original tensile wedge apparatus dimensions - top view without wedge

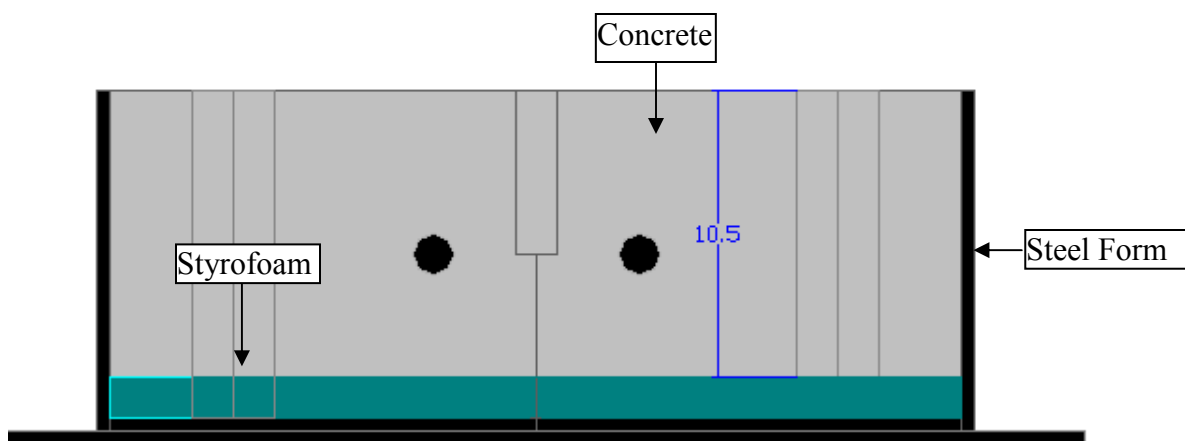


Figure 4.4: Original tensile wedge apparatus dimensions - front view without wedge

In order to correct for the cracking at the head of the specimen alterations were made to the geometry of the test. The depth and width of the section were tapered 2" and 1.5" respectively. After the section was tapered, the cross section in the middle of the

specimen was decreased from 10.5" x 6" to 8.5" x 4.5". The Figure 4.5, Figure 4.6, Figure 4.7 and Figure 4.8 display the dimensions after the alterations from the top, front, and left viewpoints. All of the dimensions are in inches.

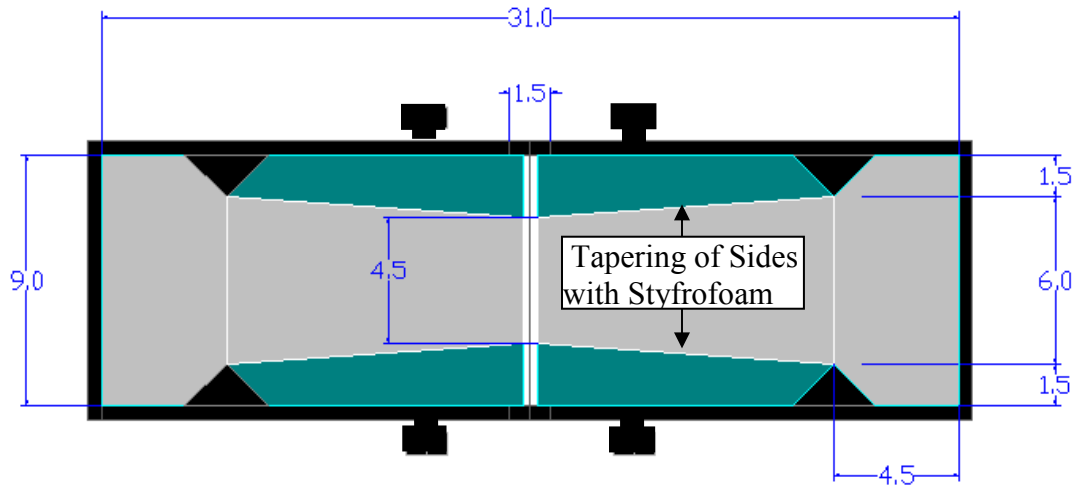


Figure 4.5: Tensile wedge apparatus – top viewpoint without wedge

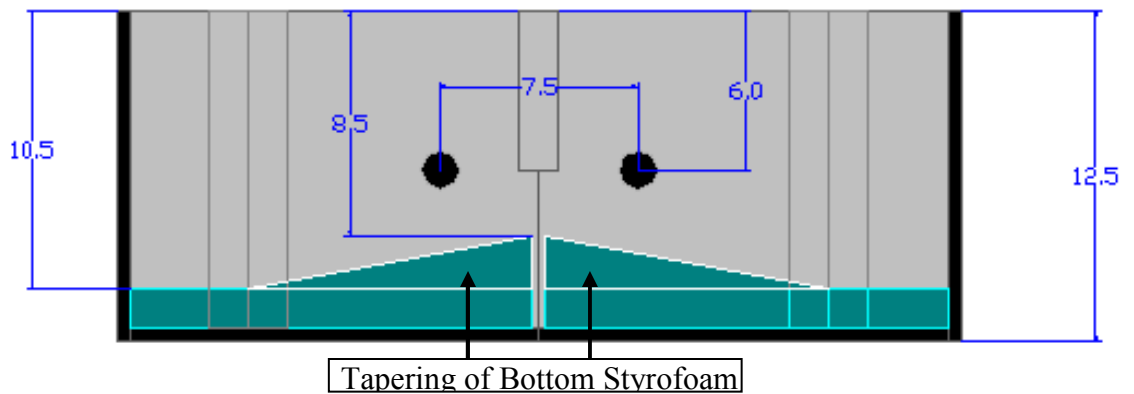


Figure 4.6: Tensile wedge apparatus – front view without wedge

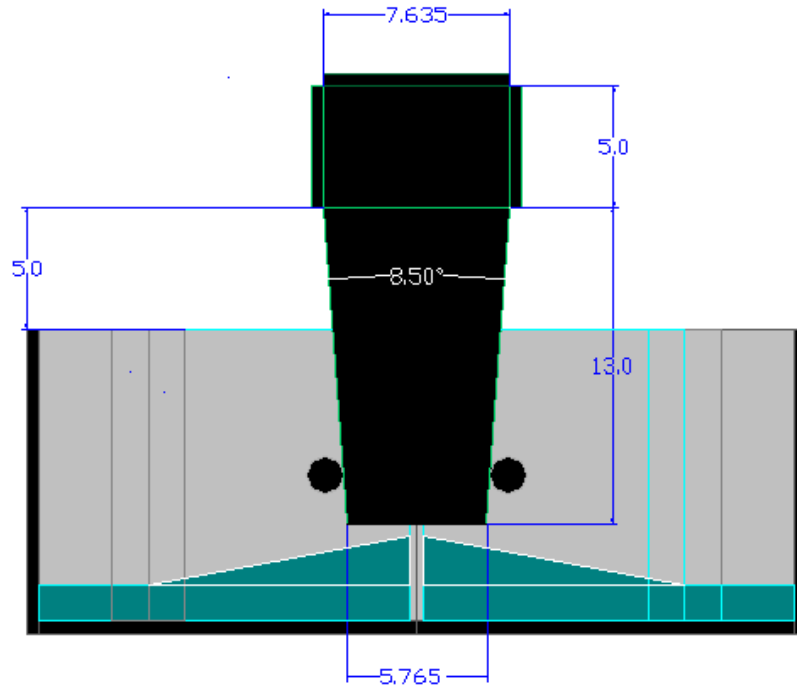


Figure 4.7: Tensile wedge apparatus – front view with wedge

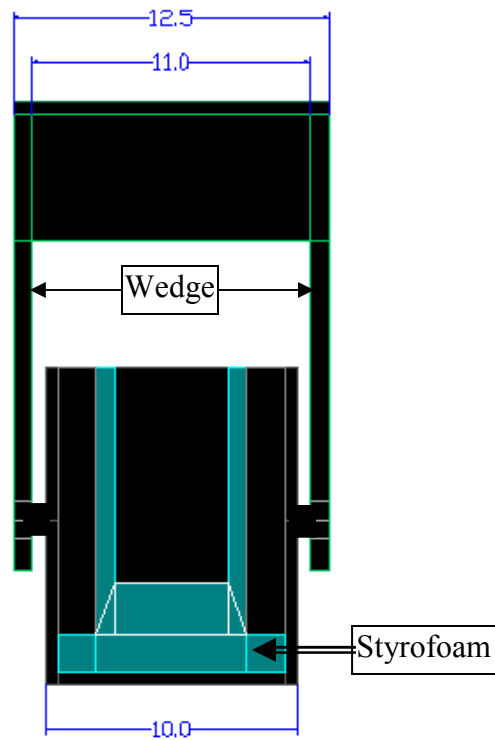


Figure 4.8: Tensile wedge apparatus – side view with wedge

4.4.1.4 Analysis of the Wedge Specimen

In order to calculate the tensile load that is applied to the specimen, the compressive force measured by the testing machine needs to be converted to the force that is applied to the specimen through the wedge. This requires the mechanical advantage of the wedge (mechanical advantage is defined as the force exerted by a machine to the force applied to it) to be computed by summing the forces in the vertical and horizontal directions. From the summation of forces, Equation 4.1 was obtained. Equation 4.1 shows the conversion of the vertical force (F_v) to the horizontal force (F_h). As shown in Figure 4.9, the vertical force (F_v) can be considered the force that is applied

$$F_h = \frac{F_v}{2 * \tan(\beta)} \quad (4.1)$$

by the machine, which is measured by the load cell, and the horizontal force (F_h) can be considered the force that is transferred to the specimen using the wedge. The angle of the incline plane (β) is equal to one-half of the wedge. It should be noted, that for all of the

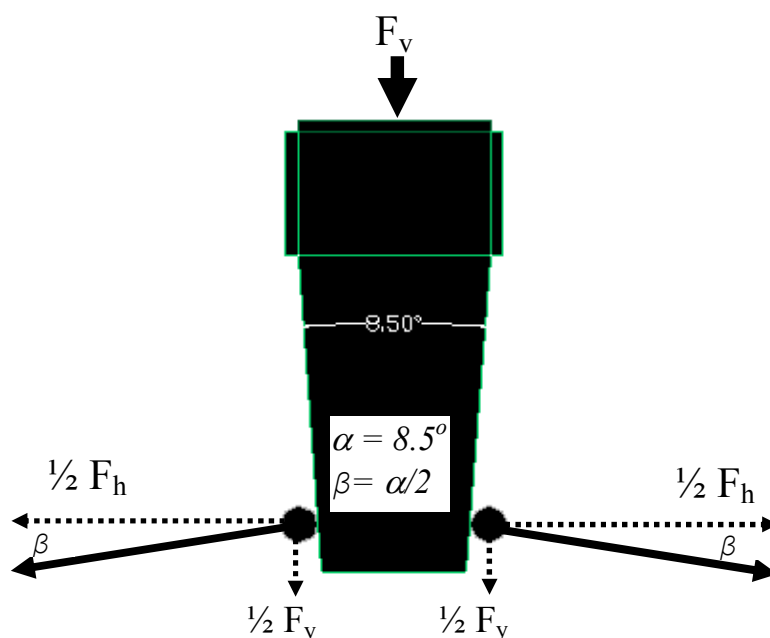


Figure 4.9: Wedge schematic

tests described in this research report the wedge had an $\alpha=8.5$ degrees which creates a mechanical advantage equal to 6.728. This equates to 6.728 pounds of horizontal force for every 1 pound of vertical force applied by the machine, assuming friction was neglected. Two factors were considered when choosing the angle of the wedge. The advantage of a decreasing wedge angle is that it increases the compliance of the testing machine and creates an increasingly stable test. The compromise of a decreasing wedge angle is that it increases the frictional losses of energy to the bearings. The wedge angle of $\alpha=8.5^\circ$ was recommended by Reider, who has done research on a similar testing apparatus (Reider, 2001), as the optimal angle to use considering the previously mentioned factors. For the wedge angle of $\alpha=8.5^\circ$ a mechanical advantage of 6.728 was used in calculating the loads transferred to specimens and frictional losses were considered negligible.

4.4.1.5 Bond

Teflon was placed along the sides and bottom of the joint to eliminate any bonding across the joint. The side pieces of the teflon were 5" x 8.5" and the bottom piece was 4.5" x 5". Figure 4.9 shows a picture of the two side pieces of teflon that were kept in place with tape before casting. Figure 4.10 shows a picture of the bottom and side pieces of teflon after the specimen was tested. In addition, the sides and bottom of the mold in the specimen's neck area were coated with form oil to eliminate any bonding.

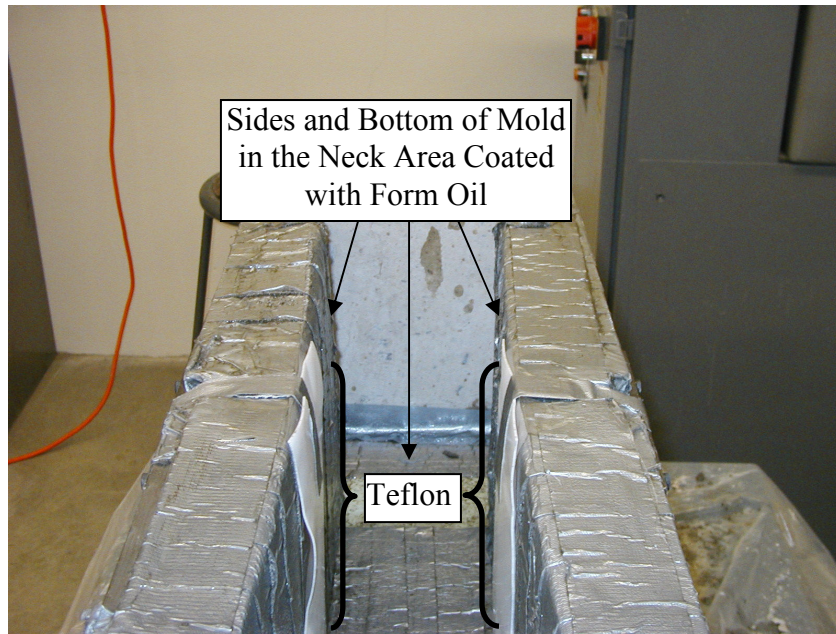


Figure 4.10: Side teflon sheets attached to the mold before casting

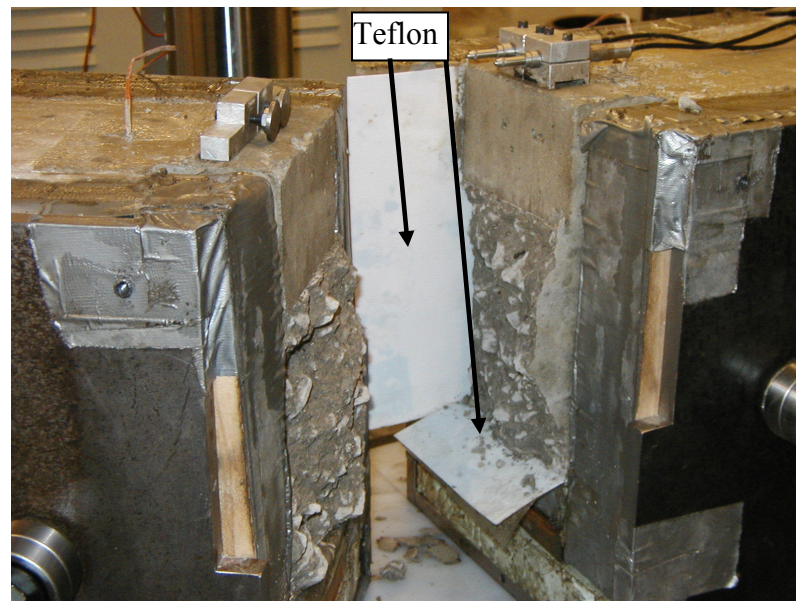


Figure 4.11: Side and bottom teflon sheets after specimen failure

4.4.1.6 Notch

In order to induce a notch into the specimen, a 1/8" thick piece of polycarbonate was manually placed during casting and removed approximately 15 minutes before testing. Figure 4.12 shows the dimensions of the polycarbonate piece that was used to create a 2 7/8" (Depth/3) notch in the specimen.

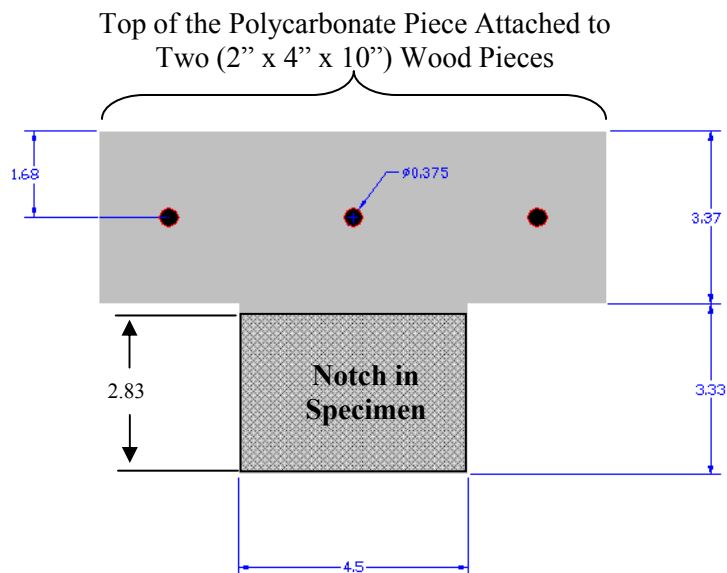


Figure 4.12: Front view of the polycarbonate notch (all dimensions in inches)

To ensure proper alignment and depth of the notch, the polycarbonate notch was bolted between two 2" x 4" x 10" pieces of wood. It should be noted that when the notch shown in Figure 4.11 was bolted between the two 2" x 4" pieces of wood the effective notch depth was 2 7/8". Figure 4.13 shows a notch forming assembly after it has been placed in a specimen.

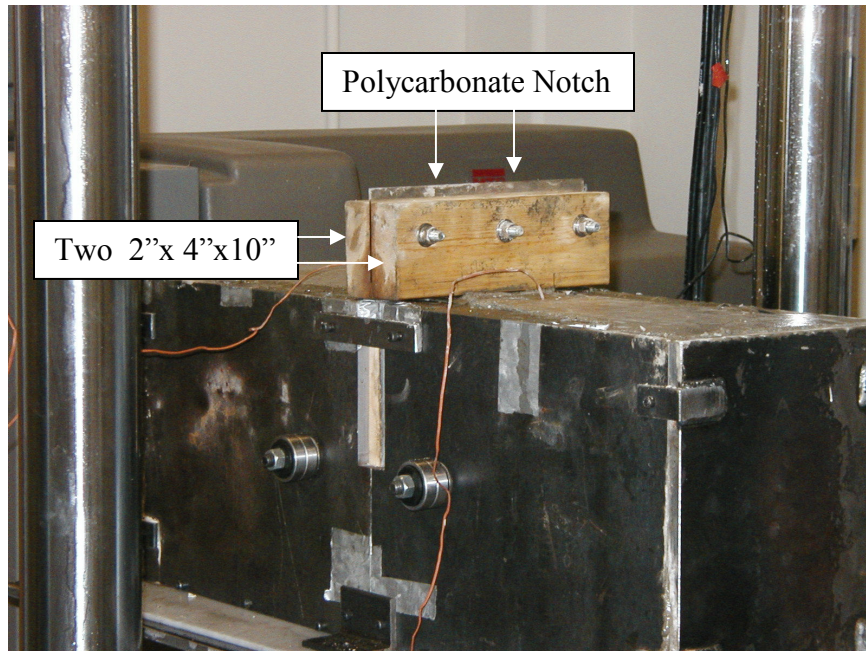


Figure 4.13: Notch forming assembly placed in specimen

4.4.1.7 Friction Elimination - Teflon Sheets

In order to minimize friction between the bottom of the tensile wedge forms and the base plate, a sheet of teflon was placed between the bottom of the mold and the base plate. In addition, the surface of the teflon was coated with standard form oil and special attention was paid to keeping the surface free of debris. Figure 4.14 shows the placement of the teflon layer in relation to the base plate, which is attached to the universal testing machine.

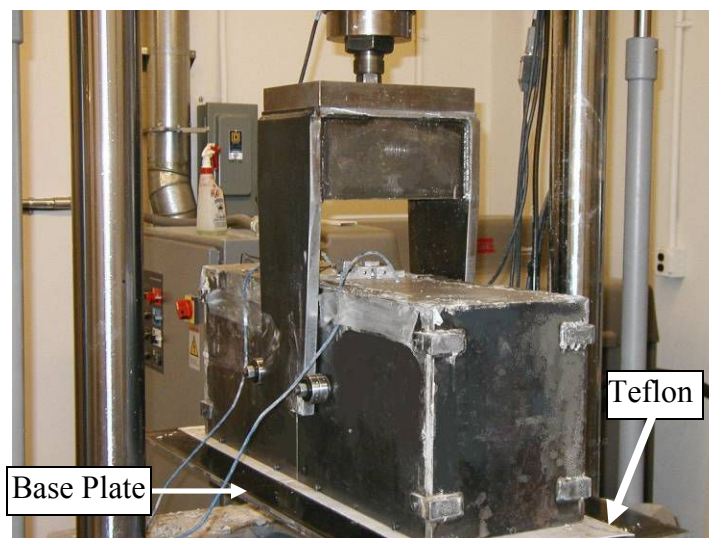


Figure 4.14: Teflon sheet placed on the base plate

4.4.1.8 Casting and Curing

After the mixing was completed, the concrete was transported using a cart to the tensile wedge form which was pre-positioned on the testing machine. The specimens were cast in two layers and consolidated using an internal vibrator. The location of the vibration sites per each layer is indicated by a dot and shown in Figure 4.15. The location closest to the notch was vibrated first, followed by the location at the base of the

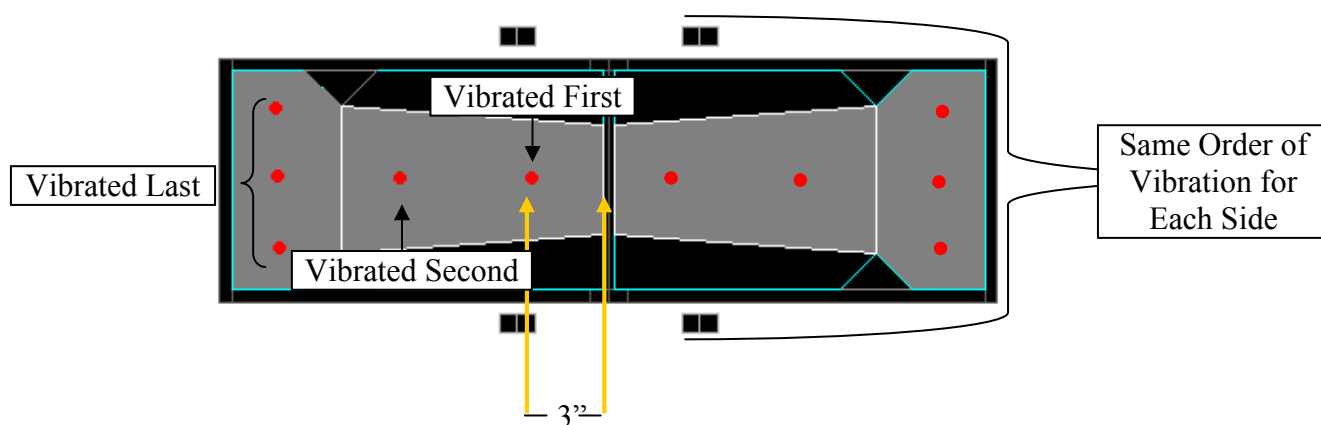


Figure 4.15: Location of internal vibration points

head and completed with the vibration at the head of the specimen. The duration of vibration at each point was approximately 12 seconds or until a consistent level of consolidation was achieved. During the vibration of the top layer, two type T thermocouples were placed close to the location of the first vibration points which were approximately 3" away from the notch location. Figure 4.16 shows a picture of the thermocouples embedded into the specimen. One thermocouple was placed at a depth of 4.25" ($D/2$) and another was placed at a depth of 2.83" ($D/3$). Next, the notch forming piece was coated lightly with form oil and placed in the top layer of concrete before it was consolidated.

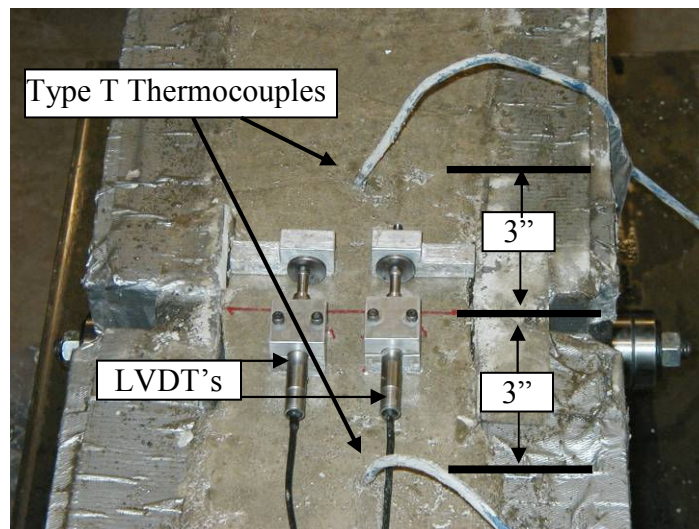


Figure 4.16: Thermocouples location

After the surface of the concrete was finished using a hand trowel, the thermocouples were plugged into a CR-10X data logger which logged the average temperature every minute. The concrete was allowed to cure for 30 minutes before the specimen was covered with 3 layers of wet burlap. The burlap was rewet as necessary to provide a moist environment for the curing of the concrete.

4.4.1.9 Testing Equipment and Procedures

A series of tasks were performed in order to prepare the specimen for loading. It should be noted that test preparation did not require the specimen to be moved since the specimens were cast on the testing machine.

First, the notch was removed manually at approximately 15 minutes before testing. Next, two linear variable differential transformers (LVDT's) were placed across the notch. The LVDT's were connected to the surface of the concrete using super glue. Figure 4.17 shows a picture of the LVDT's after being glued in place. After the LVDT's were in place, the four small steel pieces that were attached to the sides of the formwork were removed. These steel pieces kept the opposite sides of the formwork together while the specimen was cast and cured.

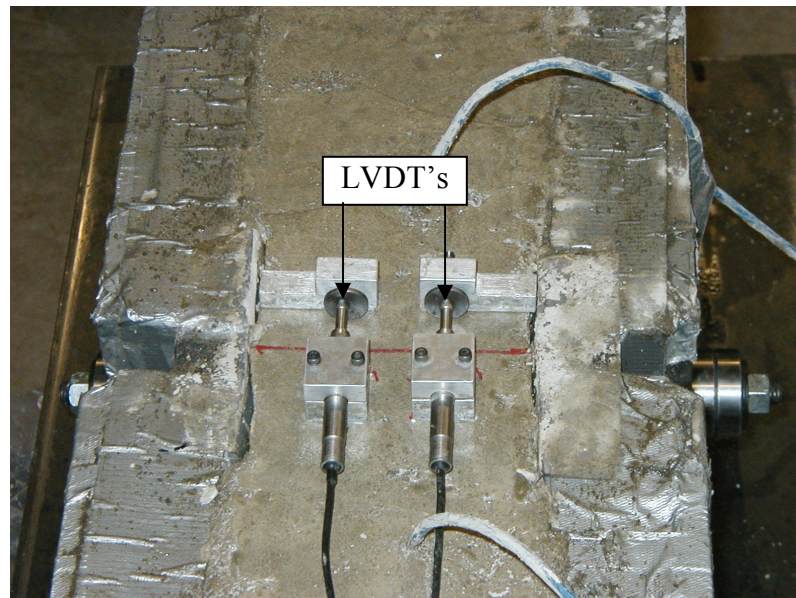


Figure 4.17: LVDT's glued in place

After the steel attachments were removed, the specimen was ready to be tested on the universal testing machine (MTS ®). The first step in testing the specimens was to lower the head on the MTS machine (with the wedge attached) to the point where the

bottom of the wedge was aligned with the top of the radial bearings but not in contact with them. After the head was lowered and locked into place the machine was placed into force control mode. Force control was used to apply an initial load to the specimen. The initial load varied between 15-25 lbs depending on the age of the specimen. After the machine applied the input force it remained at this load level. After the initial load was applied the specimen was programmed to apply a cross head displacement in a controlled manner. The displacement control was programmed to apply a movement in the vertical direction at a rate of 0.1189 in/min (0.3019 cm/min). This vertical direction can be converted to horizontal displacement using the wedge factor which is 6.728. While the machine was running in displacement mode it recorded axial force and LVDT values every second. The test was manually stopped after the axial force values reached a constant value for 1 minute.

4.4.2 Flexural Beam Testing

Flexural strength is closely correlated to tensile strength and is currently used for determining the time at which pavement can be opened to traffic (Indiana Test Method 402). Flexural companion beams were cast from the same batches that were used for the tensile wedge specimens for two reasons. The first purpose was to correlate the tensile wedge test results with flexural strength. The tensile wedge test had never been performed, and due to its nature, it demanded a significant quantity of time to produce a single test. Therefore if unexpected results were obtained from the tensile wedge test they could be compared with the results of the flexural beam tests. The second reason was to develop an early age flexural strength versus maturity curve. Therefore, a single companion beam was cast from the 1.65 ft³ batches used for the tensile wedge specimens. The 6" x 6" x 22" beams were cast immediately after mixing was completed and were consolidated using a vibrating table according to AASHTO T 97-03. In each flexural beam, a type T thermocouple was inserted at mid-depth and connected to a Campbell Scientific CR-10x data logger which recorded the average temperature at 1 minute intervals. After curing for 30 minutes, the beams were covered with wet burlap which was rewetted as

necessary. The flexural beams were cured next to the tensile wedge specimen until they were ready to be tested. The beams were tested in third point loading on a 60 kip Satec Universal Testing Machine following AASHTO T 97-03 with a loading rate of 1500 lb/min.

4.4.3 Shrinkage Test

Shrinkage is one of the driving forces behind residual stress development which can lead to random cracking in pavements. In order to define the early age drying and autogenous shrinkage, seven 3" x 3" x 12" specimens were cast. The specimens were cast with doweled tips, in accordance with ASTM C 157 procedures for measurement with a comparator. After the specimens were cast, they were covered with burlap until set time as determined by their maturity. The maturity was calculated using two type T thermocouples which were embedded to mid-depth of two of the specimens. After the specimens reached final set (four real time hours) they were de-molded and covered with aluminum foil tape on either two sides or all four sides. The foil tape was placed on all four sides of four specimens to simulate autogenous shrinkage and was placed on two sides of three specimens to simulate drying shrinkage. After the specimens were covered with tape, they were weighed and measured, using a comparator. The comparator measured the length of the specimens to within 0.0001 inches and the scale was accurate to within 0.1 grams. After the specimens were weighed and measured, they were placed in a 50% relative humidity room until being taken out for further measurements. The mass and length was recorded every 4-6 hours for the first day and every 2-3 days for the following 4 weeks. Figure 4.18 shows a picture of the shrinkage specimens being prepared with foil tape after the concrete has set.

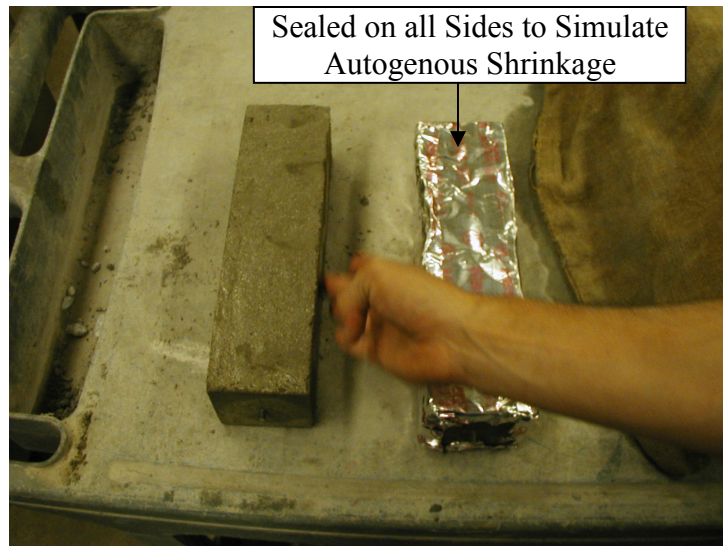


Figure 4.18: Preparation of shrinkage specimens

4.4.5 Compression Testing

Previous research (Okamoto, 1994) has used compressive strength to define the start of the saw-cutting window taking into consideration the severity of raveling. To enable this work to be compared with Okamoto's, compressive tests were performed following ASTM C 39. Cylinders were consolidated in two equal layers using a vibrating table and finished with a hand trowel. After the cylinders were finished, they were covered with wet burlap and polyurethane sheeting. A total of thirteen 6" x 12" cylinders were tested between set time and a real time of 30 hours. A Thermochron I-button sensor was placed at mid-depth in one of the cylinders to record the temperature every third minute which was used to calculate maturity. In addition to the thirteen 6" x 12" cylinders, twelve 4" x 8" cylinders were cast to determine the strength of the mixture at 3, 7, and 28 days. These specimens were de-molded at 1 day and placed in a moist curing room until testing. All of the cylinders were tested on a 100 kip Satec Universal Testing Machine. The loading was applied at a rate of 120 psi/min for the test's that occurred at an age of less than 10 equivalent age hours to ensure an accurate reading due to the low strength of the cylinder. For the cylinders between 10 equivalent age hours and 1 day the loading rate was raised to 1000 psi/min and for the testing that occurred at

3, 7, and 28 days the loading rate was 1680 psi/min which is the minimum rate per ASTM C 39 specifications. Figure 4.19 shows a picture of one of the 6" x 12" cylinders being tested in compression at an age of 1 day.



Figure 4.19: 6"x12" cylinder tested in compression at an age of 1 day

4.4.6 Splitting Tensile Test

Splitting tensile tests were performed in order to determine the variability that could be expected from early age tensile tests. The splitting tensile test variability could then be compared to the variability of the tensile wedge results. Eight 6"x12" cylinders were consolidated in two equal layers using the vibrating table. After completing the consolidation, the specimens were finished with a hand trowel and covered with polyurethane sheeting and wet burlap which was rewetted as necessary. The cylinders were tested according to ASTM C 496 at 27 hours real time (45 equivalent age hours). The tests were performed on a 100 kip Satec Universal Testing with a loading rate of 100 psi/min. Figure 4.20 shows a picture of one of the cylinders being tested for splitting tensile strength.



Figure 4.20: Splitting tensile test

4.5. Tests to Examine Raveling

Early-entry saws, which were discussed in Chapter 2 of this report, are reported to be capable of cutting concrete at earlier ages with significantly less raveling (Soff-cut, 2004). A mortar set time test and an early-entry saw-cut test were performed to more clearly define the age and strength that these saw-cuts can be performed at. These tests are discussed in sections 4.5.1 and 4.5.2 respectively.

4.5.1 Mortar Set Times Tests

Mortar set time tests were performed following the procedure of ASTM C 403. The mortar was wet sieved out from the concrete using a #4 sieve and placed in 6" x 6" cylindrical molds. Three 6"x 6" cylindrical molds were insulated using styrofoam in order to create a temperature development similar to that of the tensile wedge apparatus. All three specimens included a Type T thermocouple inserted into the middle of the specimens from the side of the molds. The thermocouples were connected to a CR-10X

data logger which recorded the average temperature every minute. All three 6"x 6" cylindrical specimens were tested at 4 different maturities to determine set time.

4.5.2 Early Entry Saw-Cut Test

Early-entry saws, which were discussed in Chapter 2 of this report, utilize an anti-ravel skid plate and up-cut saw-cut direction. For this experiment, a handheld Soff-Cut X-50 early entry saw was used to assess raveling at early-ages. A 43.5"x12"x5.5" specimen was cast with 1.5" styrofoam insulation on all four sides and the bottom. The specimen was consolidated in two equal layers using a vibrating table and embedded with Type T thermocouples to mid-depth at various locations. The thermocouples were connected to a CR-10x data logger which recorded the average temperature at 1 minute intervals. The surface of the specimen was finished with a hand held steel trowel and then covered with wet burlap. The early-entry saw was traversed across the specimen at four different maturities and the associated raveling was monitored visually. Figures 4.21 and 4.22 respectively show pictures of the specimen before and after it was saw-cut.

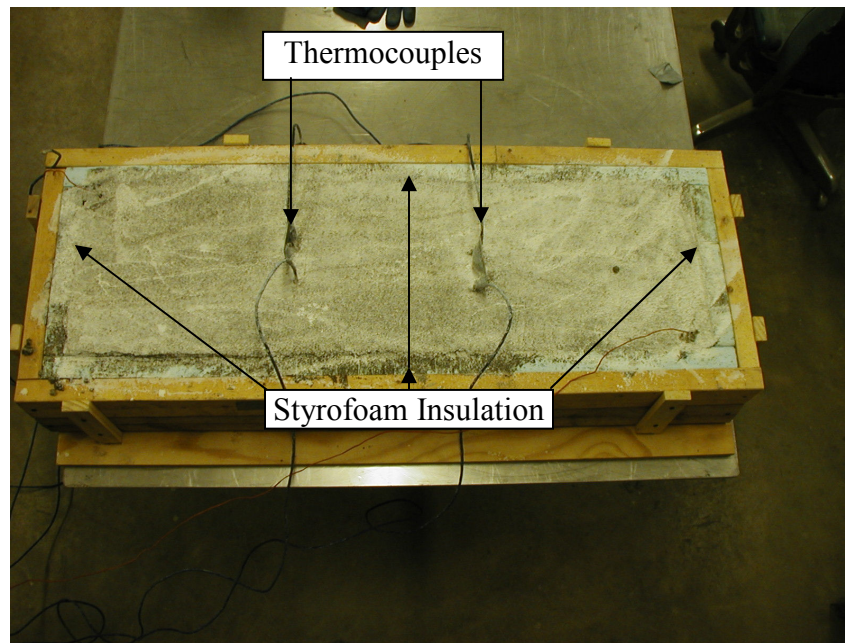


Figure 4.21: Early entry specimen before saw-cut

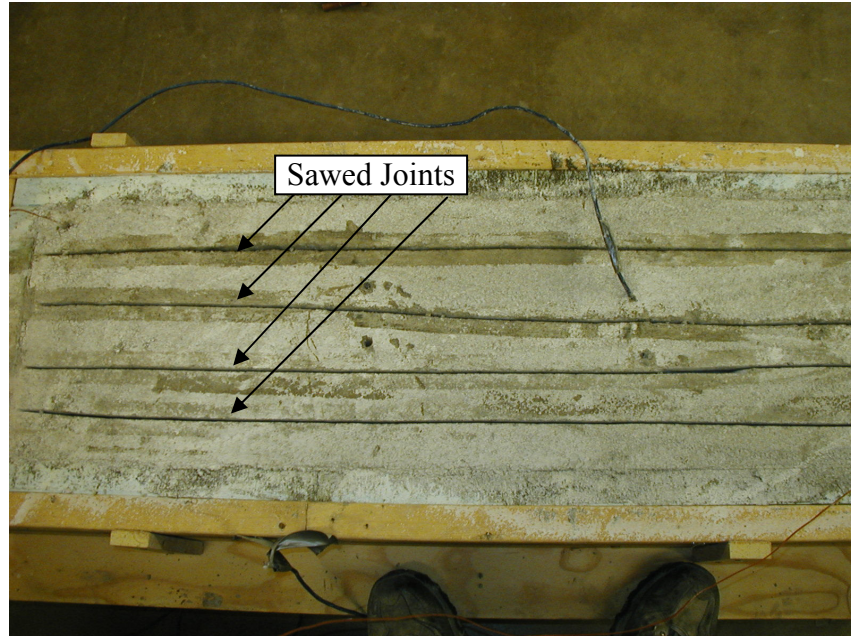


Figure 4.22: Early entry specimen after it was saw-cut

CHAPTER 5: EXPERIMENTAL RESULTS AND ANALYSIS

5.1 Introduction

This chapter provides an analysis of the results from the experimental work described in Chapter 4. This chapter provides data for the development of a modeling framework that will use the maturity method to describe the time for saw-cutting. Data from the tensile wedge test will be used in this model to provide an indication of the time for saw-cutting and the depth of the cut. The results of the compressive, flexural, and tensile experiments were compared to establish an early-age correlation between these properties to enable field implementation of the model.

The experimental data reported in this chapter is defined using the maturity method that considers ‘time-zero’ as the time when the cement and water come in contact in the mixer. Although no temperature was recorded in the time between mixing and placement, the temperature for this time period was assumed to be the first temperature recorded by the sensors when placed in the specimens. In addition, all of the maturities were computed in ‘equivalent age’ form using the Arrhenius equation with a reference temperature of 20° C.

All of the material properties (such as strength) were fit using a sigmoidal relationship. The sigmoidal relationship is shown in Equation 5.1 and is used to define the strength (or any material property) at a given time (S_t) by the maturity (M_t) and three parameters S_∞ , τ , and α .

$$S_t = \frac{S_\infty}{e^{\left(\frac{\tau}{M_t}\right)^\alpha}} \quad (5.1)$$

5.2 Tensile Wedge Test

In this section, the results of the tensile wedge experiments are presented. The first section (5.2.1) presents a general overview of the experimental results. The remaining three sections discuss three trends that were observed in the tensile wedge test data. These include section 5.2.2 which discusses the observation of pre-peak stable crack growth in light of its influence on ‘semi-stable’ crack propagation in specimens with different size notches, section 5.2.3 which examines the possibility of early-age plastic behavior, and section 5.2.4 which describes probability that the crack will propagate from the notch.

5.2.1 An Overview of the Tensile Wedge Test

Before deciding on a “final” tensile wedge configuration, ten preliminary tests were performed. The preliminary tests were performed to assist in refining the geometry and experimental setup for the tensile wedge test. These refinements included tapering the cross section (as described in Chapter 4) and the addition of Teflon® sheet at the base plate to reduce friction. Once the final configuration of the experimental setup was determined, a total of 24 tensile wedge tests were performed using specimens with various notch depths. The various notch depths included a maximum depth of 4.25” (D/2), 2.83” (D/3) (coincidentally this is the typical depth used by the Indiana Department of Transportation), 2.00” (D/4.25), 1.00” (D/8.5), and no notch. In addition, one notch was placed with an early-entry saw and is labeled notch 1.00” - saw. Details regarding the specimens that were tested are provided in Table 5.1.

The maturity was calculated using the average temperature from two thermocouples. The two thermocouples were placed in each specimen at a distance that was half the depth from the surface (4.25” or mid-depth) and at a distance that was one-third of the depth from the surface (2.83”). These depths were chosen to represent the depths that are commonly used in pavement measurements (i.e., these were the same depths that were used in the site visits described in chapter 3). The average temperature of the two thermocouples was used to provide a maturity index, which can be used as an indication of the concrete strength development.

Figure 5.1 shows a typical example of the temperature development at both thermocouples from a typical specimen (specimen #31). From Figure 5.1 it can be seen that the specimen reached a maximum temperature of 107 °F after approximately 9 hours. It should be noted that eleven specimens were tested at a late enough age that they reached their maximum temperature at mid-depth (4.25"). The average maximum temperature at mid-depth was 108 °F with a range from 112 °F to 105 °F and a standard deviation of 2.4 °F. Table 5.1 provides a column in which the temperature drop is computed for the specimens that were tested after the peak temperature was reached. The temperature drop is simply the temperature of the specimen at the time of testing subtracted from the maximum temperature the specimen reached. It is currently believed that this temperature decrease may result in the development of some residual stresses and the importance of these residual stresses will be discussed in section 5.2. The maximum load shown in Table 5.1 was used for the data analysis. This maximum value is simply the maximum load measured by the load cell multiplied by the wedge factor of 6.728 (as explained in Chapter 4).

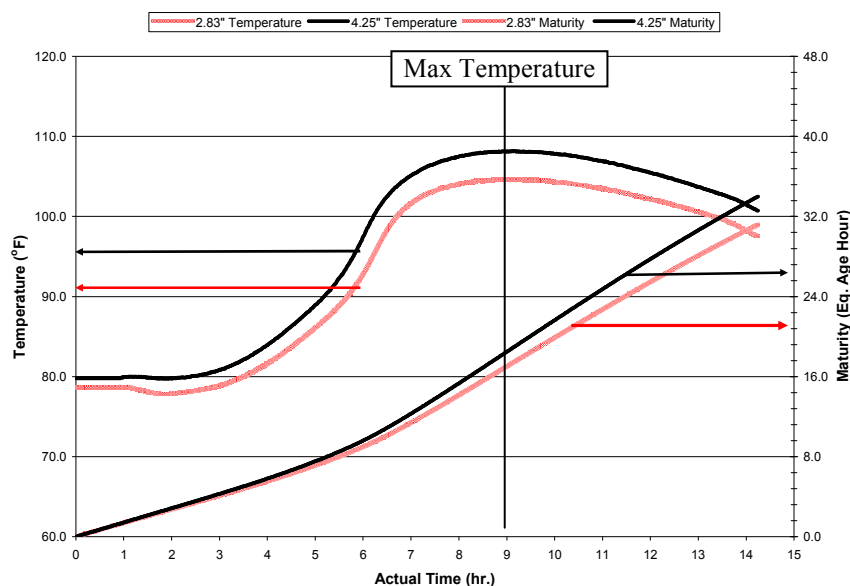


Figure 5.1: Typical temperature development data for a tensile wedge specimen (specimen #31)

Table 5.1: Tensile wedge test schedule

Test Number	Notch	Relative Depth	Maturity	Actual Age	Max. Load	Specimen Displacement at Max. Load (Uncorrected)	Specimen Displacement at Max. Load (Corrected)	Temp. Drop (Max - Final)
(#)	(in.)	(D/#)	(eq. age hr.)	(hh:mm)	(lb.)	(in.)	(in.)	(°F)
30	0.00	N/A	7.59	5:34	1504	0.0181	0.0171	0.0
34		N/A	38.39	14:55	6284	0.0396	0.0421	10.8
23	1.00-Cast	(D/8.5)	9.14	5:43	2263	0.0263	0.0203	0.0
24			29.10	13:50	6223	0.0439	0.0369	6.3
28	1.00-Saw	(D/8.5)	9.64	6:55	2422	0.0272	0.0247	0.0
26	2.00	(D/4.25)	28.15	13:12	5294	0.0340	0.0330	7.9
27			8.73	6:05	1690	0.0281	0.0221	0.0
29			32.21	13:45	5865	0.0395	0.0385	5.7
33			38.83	15:29	6617	0.0442	0.0442	13.1
11	2.83	(D/3)	18.33	9:30	6395	0.0258	0.0243	0.0
12			16.28	10:15	4675	0.0211	0.0191	0.0
13			21.10	10:45	6258	0.0296	0.0256	0.0
14			26.12	5:20	7798	0.0313	0.0323	4.1
15			22.88	11:21	7980	0.0363	0.0363	0.0
16			15.76	11:04	5617	0.0442	0.0342	0.0
17			5.00	8:10	81	0.0000	0.0000	0.0
18			8.19	4:10	1463	0.0147	0.0137	0.0
19			12.33	5:28	3157	0.0258	0.0238	0.0
20			29.93	6:59	6393	0.0307	0.0257	6.6
31			32.55	14:15	9201	0.0415	0.0375	7.3
21	4.25	(D/2)	20.52	9:46	2595	0.0243	0.0208	0.0
22			29.42	13:21	4593	0.0275	0.0205	5.0
25			10.42	6:25	2628	0.0307	0.0287	0.0
32			33.72	14:10	4441	0.0240	0.0215	7.5

5.2.1.1 Specimen Displacement Calculations

As discussed in Chapter 4, the testing machine was programmed to apply a stroke displacement at a constant rate. The vertical deformation of the machine was programmed to displace at a rate of 0.1189 in/min (0.3019 cm/min) which can be converted to a horizontal displacement at the radial bearings of 0.0176 in/min (0.04487 cm/min) considering the geometry of the wedge (see Figure 4.9). The ratio of horizontal displacement to vertical displacement created by the geometry of the wedge is illustrated in Figure 5.2.

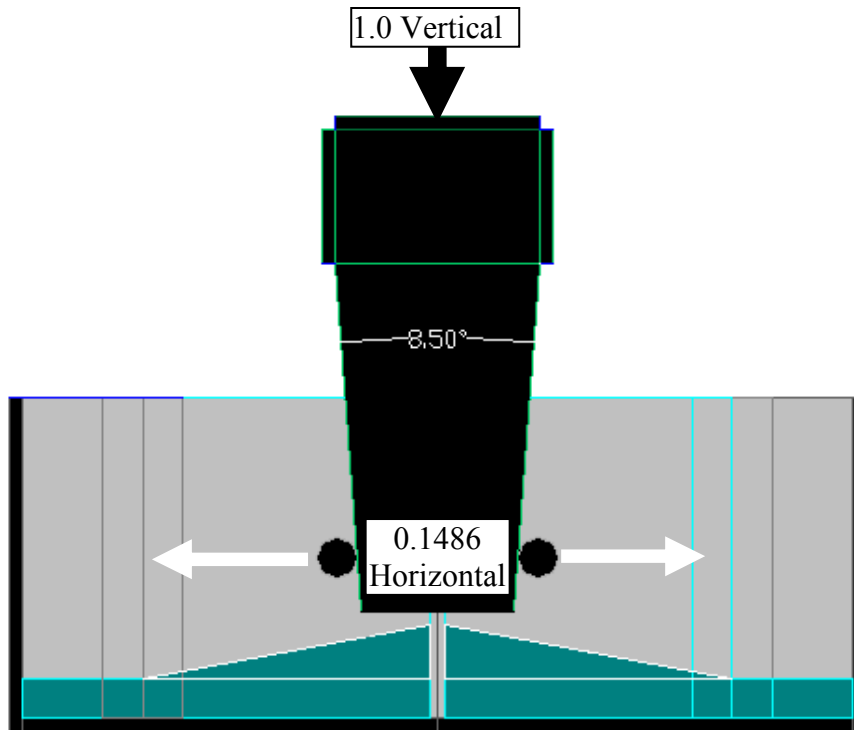


Figure 5.2: An illustration of the vertical to horizontal displacement ratio (1:0.1486)

The horizontal displacement applied by the wedge is transferred from the wedge to the bearings that are attached to the formwork and the formwork then applies a tensile load to the specimen. The bearings and formwork were assumed to be perfectly stiff (although it is known that some flexibility exists in reality and some slip likely occurs between the walls of the forms (at the angle grips) and the specimen), and it is therefore assumed the displacement from the wedge is a measure of the displacement in the specimen. For the sake of this discussion the horizontal component of the displacement will be used synonymously with the specimen displacement. Figure 5.3 illustrates the components of specimen displacement, which include the displacement of the concrete material and the displacement at the crack.

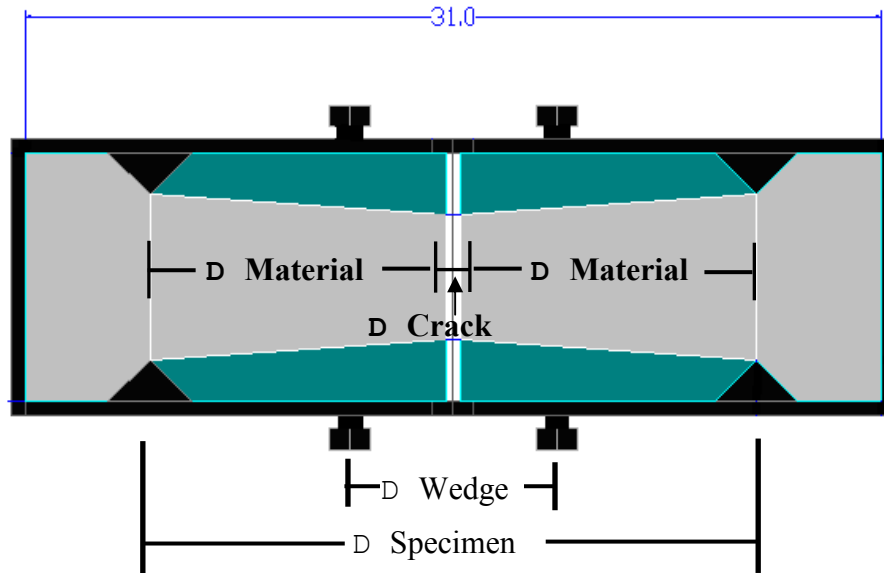


Figure 5.3: Components of specimen displacement

The specimen displacement (i.e., DS) can be thought of as consisting of two components as shown in the displacement controlled model in Figure 5.4 and in Equation 5.2. These displacements are the displacement of the bulk material (i.e. DM) and the displacement of the crack region (i.e., the region below the LVDT's in the fracture process zone (DC)).

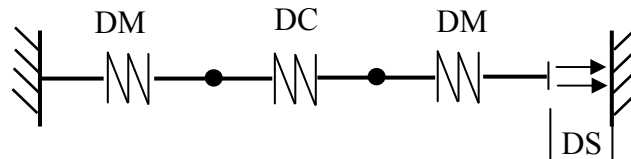


Figure 5.4: Displacement controlled model

$$\Delta_{Specimen} = 2\Delta M + \Delta C \quad (5.2)$$

Equation 5.2 can be further examined by considering the relationship between force (F) and displacement (D) for the two different regions (bulk material and cracking) of the specimen (Figure 5.5). In investigating the relationships shown in Figure 5.5, it can be seen that force equilibrium requires that the force in both regions are the same. This force causes displacements to develop in the bulk and crack regions because they are both assumed to behave as a linear elastic material. As load is applied to the specimen (i.e., consider application of a load that produces displacement at point A on the graph) both regions begin to displace by an amount that is proportional to the load, geometry of the section, and the modulus of elasticity. If a displacement is applied that is greater than the displacement that corresponds to the peak strength it can be assumed the crack will extend and the stiffness of the cracked element will be reduced. The development of the crack is accompanied by a reduction in load; as such the load in the elastic region also reduces to maintain force equilibrium. This can be seen as the point C denoted in Figure 5.5.

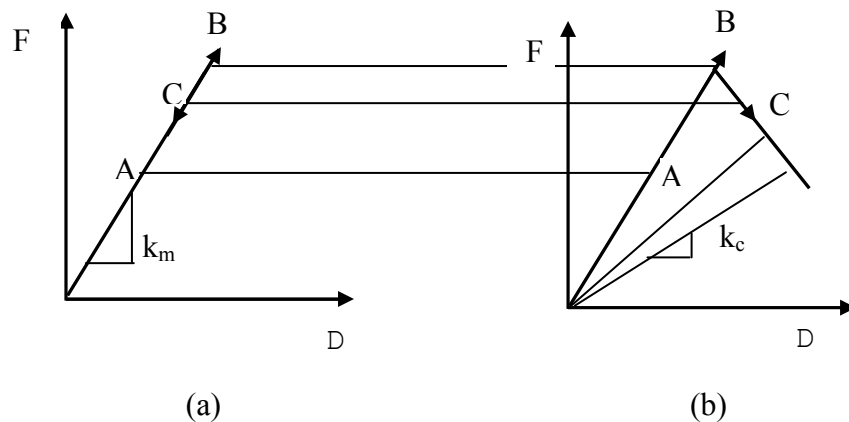


Figure 5.5: (a) F-D for bulk material, and (b) F-D in cracking region

Furthermore, the displacement in each region (i.e., the bulk material and cracking region) can be calculated using Equation 5.3. As the crack develops, the stiffness of the specimen (k) decreases. While the total stiffness decreases, it is frequently useful to separate the stiffness (k) into values for the bulk material region (k_m) and the cracking

region (k_c). This is frequently done since the stiffness of the bulk region is assumed to not change throughout the duration of the test, thereby greatly simplifying calculation procedures. The value of total displacement of the specimen, as a function of the two stiffnesses, is given by Equation 5.4. The important characteristic of Equation 5.4 is that it can be used to consider a decreasing stiffness while the displacement remains constant. As the value of k_c decreases, which corresponds to the extension of a crack, the force (F) has to decrease correspondingly to maintain the displacement. Therefore in a displacement controlled test (like those described in this chapter) the development of cracking corresponds to a decrease in force (F).

$$\Delta = \frac{F}{k} \quad (5.3)$$

$$\Delta_{specimen} = F \left(\frac{1}{k_m} + \frac{1}{k_c} \right) \quad (5.4)$$

While the previous section describes some of the basic concepts that will be used in the analysis of the experimental data, Figure 5.6 shows a typical result from the wedge tests. In this figure, the load is plotted on the vertical axis and the horizontal specimen displacement on the horizontal axis.

Further examination of the curve shown in Figure 5.6 illustrates that the horizontal specimen displacement was very large for low levels of loads which corresponds to specimen seating which resulted in a significant amount of displacement before the load was completely transferred to the specimen. In order to correct for the seating issues, the stiffness was determined from a chord line drawn between 30% and 70% of the maximum load. A “corrected” load versus specimen displacement is shown in Figure 5.7. In Figure 5.7 we find a correction value of -0.01” for specimen 16. This procedure was followed for all the specimens in order to normalize the specimen displacement

values. These values are shown in Table 5.1 as specimen displacement at maximum load after being corrected.

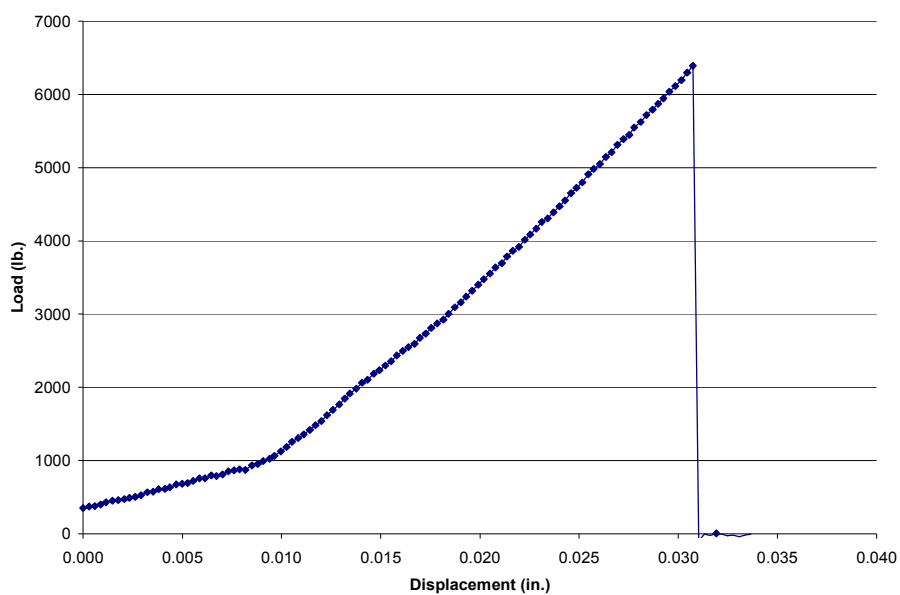


Figure 5.6: Load versus displacement for specimen number 20

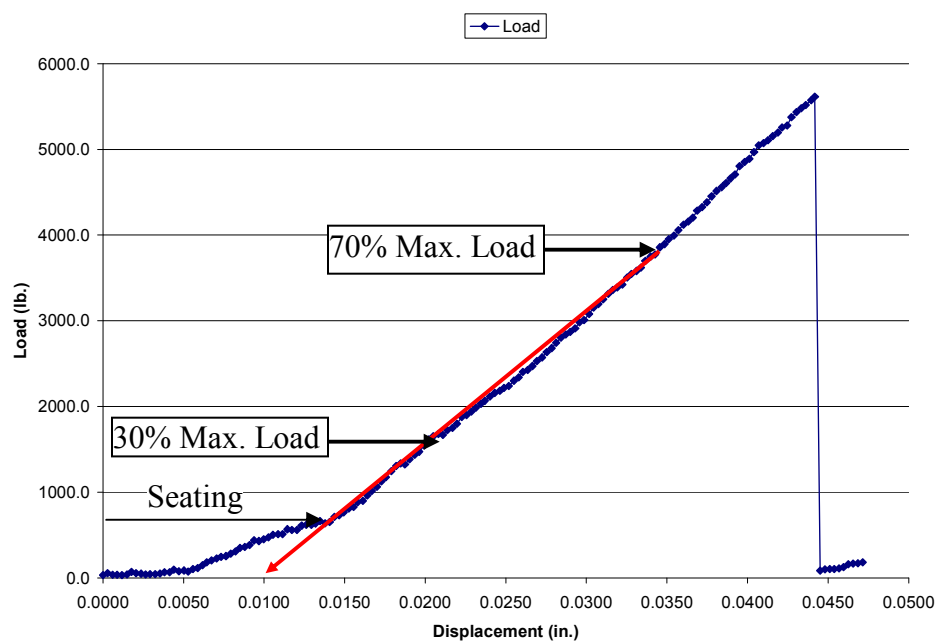


Figure 5.7: Seating correction for displacement normalization (specimen number 16)

5.2.1.2 Local Specimen Deformations - LVDT Data

While the previous section described data obtained from the horizontal displacement of the wedge and its relationship to the overall displacement of the specimen, this section describes the deformations that were measured directly above the saw-cut (notch) using data from the linear variable differential transformers (LVDT's) displacement transducers. It should be noted that generally speaking the LVDT measurements were more consistent in specimens with deeper notches (i.e., 2.83" (D/3) and 4.25" (D/2)) which may be due in large part to the greater deformations exhibited by these specimens. When the shallow notches were used (i.e., notches less than 2.83" (D/3)) the data from the LVDT's was less consistent, however the LVDT's still provided useful information in many cases. Some of the inconsistencies may occur due to the fact that the crack may originate from one side of the specimen before the crack works across the entire specimens cross section. It should be noted that in a few tests LVDT #2 was observed to 'stick'. As a result the measured values for LVDT #2 were not always recording an actual specimen displacement but rather when the LVDT was sticking it was recording a constant reading. In experiments when this 'sticking' was noticed the data from LVDT #2 was not included in the analysis.

Figure 5.8 provides an example of the load versus displacement (horizontal displacement at the bearings and the LVDT measurements) for a specimen with a 2.83" (D/3) notch that was tested at a maturity of 18 equivalent age hours (i.e., test #11). Figure 5.9 provides a plot of the load versus the average value of measured LVDT displacement for the same specimen. It should be noted that for the LVDT measurements the gage length over which the LVDT operated was 1.5 inches. It can be seen that the horizontal specimen displacement is much larger than the displacement that is measured directly over the crack. This is attributed to the fact that the horizontal measurement corresponds to a longer section of material that includes the bulk regions described in Equation 5.2 and these measurements include displacements that may occur in the machine, grips, or forms. It should be noted that the LVDT deformation is relatively proportional to the horizontal deformation up to the point when the stress reaches 90% of the peak load at which time the LVDT begins to increase at a faster rate. This is

consistent with fact that localized damage (i.e., cracking) will occur in the region of the specimen under the LVDT which would result in a reduced stiffness and greater deformation for the same applied force as described in section 5.2.1.2

Figure 5.9 provides the best indication of the material response in the cracking region. It can be seen that the slope of the LVDT displacement versus load curve is relatively linear up to approximately 85% (5300 lb.) of the peak load. This implies that the crack was not growing extensively until the load reached 85% of the peak load. It should be noted that the slope of the load versus LVDT displacement can provide a measure of the stiffness in the cracking region (k_c) which can be used as an indicator of the size of the crack as described in greater detail in the following section.

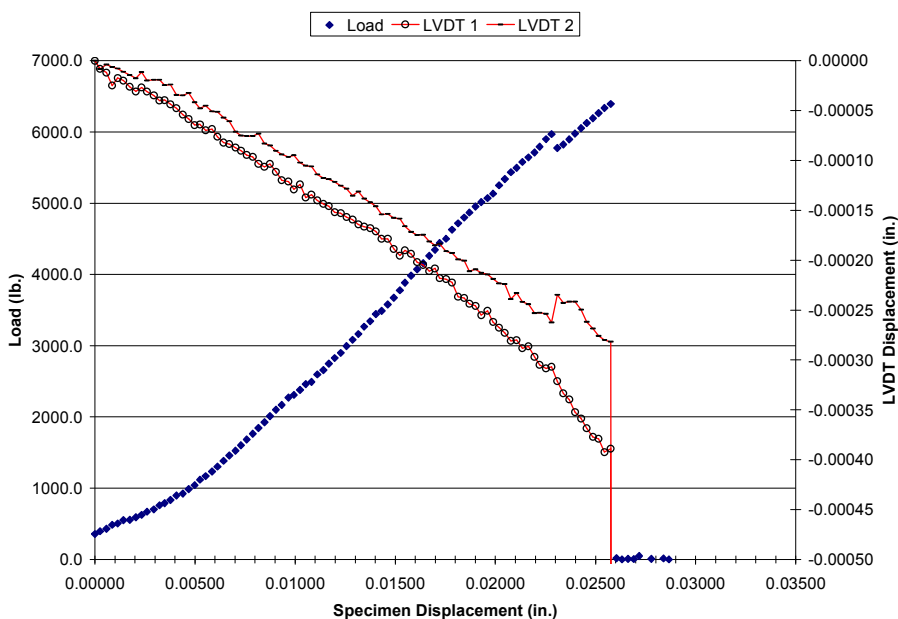


Figure 5.8: Typical experimental measurements for test #11 illustrating the relationship between load, horizontal wedge displacement and the measured LVDT displacement at the notch for a specimen with a 2.83” (D/3) notch at maturity of 18 equivalent age hours

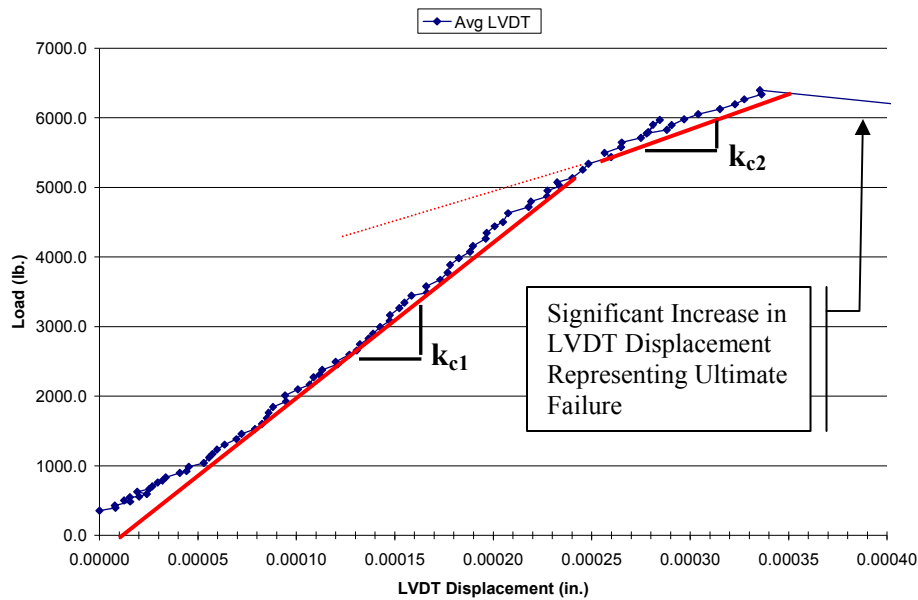


Figure 5.9: Typical experimental measurements for test #11 illustrating the relationship between load and the average measured LVDT displacement at the notch for a specimen with a 2.83'' (D/3) notch at maturity of 18 equivalent age hours

5.2.2 Pre-peak Stable Crack Growth

In a displacement controlled test a sudden decrease in the load typically corresponds to a release of energy due to the rapid growth of a crack. It should however be noted that, as described in the previous section, a stable crack growth can occur before the peak load is reached in a material like concrete. One method that is commonly used to assess the extent of crack growth in a material is to measure the change in compliance or stiffness (as shown in Figure 5.9). If an elastic body with a constant geometry is loaded and unloaded the compliance remains the same, however it can be assumed that if the crack grows, the compliance would increase (or the stiffness would decrease). This is illustrated by Equation 5.4 where an increase in compliance of the cracking region corresponded to a decrease in the force that is required to maintain equilibrium at a given displacement since it is easier to deform the specimen around the crack.

In describing the behavior of the specimens tested, it is helpful to divide the specimen into geometries in which the notch is equal to or greater than D/3 and the

geometries where the notch is less than $D/3$. In specimens with a notch that was equal to or greater than $D/3$ (“deep” notches) there were no sudden decreases in the load versus specimen displacement response until ultimate load of the specimen was reached and immediate failure was observed. The measured LVDT displacement data generally showed a continual increase until ultimate failure was reached, at which time a sudden change in the LVDT was observed. Figure 5.10 shows a load versus horizontal specimen displacement response for test 20 which contained a 2.83” ($D/3$) notch and was tested at maturity of 30 equivalent age hours. From this figure it can be seen that after seating (i.e., the application of a load up to about 1000 lb) the load increases at a relatively constant rate and there are no abrupt or distinct changes in the curve until the point where the load suddenly decreases when a crack propagates unstably. It should be noted however that the LVDT’s begin to show fluctuations in readings at approximately 90% (5800 lb) of the peak load. Unfortunately, this is a specimen in which LVDT #2 exhibited the ‘sticking behavior’ and as such it can not be used for analysis.

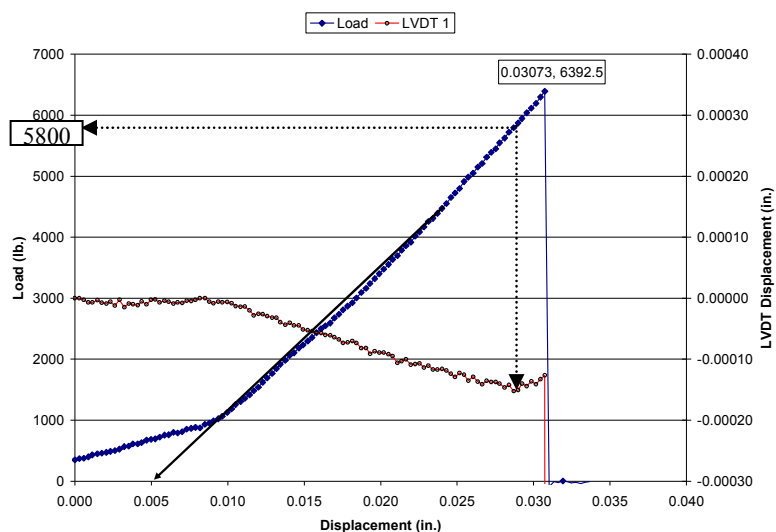


Figure 5.10: Experimental results for specimen 20: load versus specimen displacement and LVDT versus specimen displacement (2.83” ($D/3$) @ 30 eq. age hours)

Figure 5.11 shows a load versus horizontal displacement response for specimen 22 which contained the largest notch (i.e., 4.25" (D/2)) and was tested at a maturity of 29 equivalent age hours. The load versus horizontal displacement for the 4.25" (D/2) showed a response that was fairly similar to that of the specimen with the 2.83" (D/3) notch in which no abrupt changes in the response were present up to the point of failure. Figure 5.12 shows the load versus LVDT displacement for specimen 22. Again, there does not appear to be any distinct changes in the linear relationship between load and LVDT displacement for low load levels. However, as the load begins to increase (i.e., approximately 85% of the peak load) it can be seen that the response begins to deviate from linearity. This deviation continues to increase until the maximum load is reached at which time the LVDT response rapidly increases from 0.00122 to 0.06029 which represented the ultimate failure.

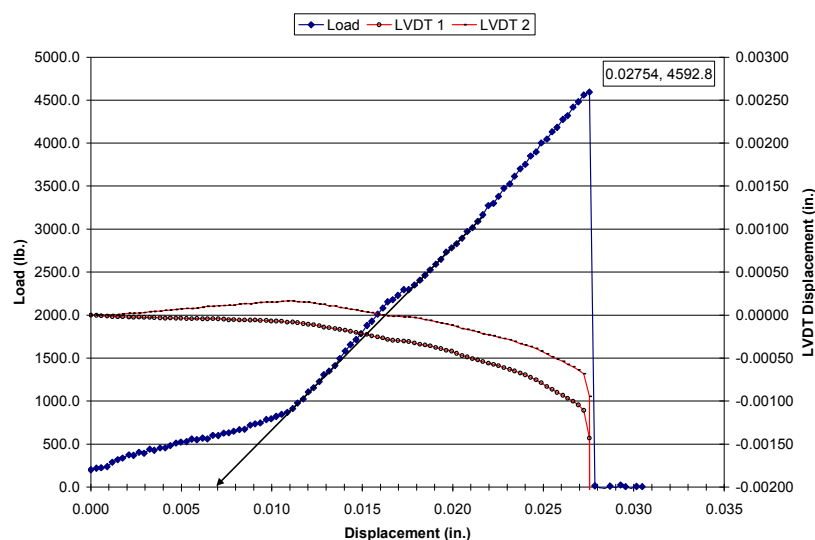


Figure 5.11: Experimental results for specimen 22: load versus specimen displacement and LVDT displacement versus specimen displacement (4.25" (D/2) @ 29 eq. age hours)

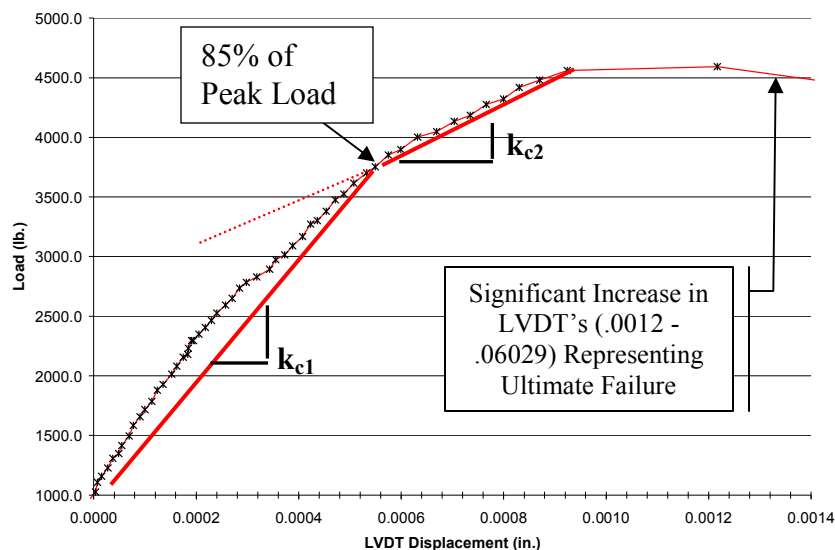


Figure 5.12: Experimental results for test 22: load versus LVDT displacement (4.25'' (D/2) @ 29 eq. age hours)

This non-linear response between the load and a displacement at the crack (or load versus crack mouth opening displacement) is a fundamental aspect of a non-linear fracture mechanics approach. Non-linear fracture mechanics in concrete is used to describe pre-peak crack growth which occurs prior to the specimen reaching the peak load. While we will discuss the concept of a fracture process zone, many people quantify the pre-peak crack extension using changes in compliance to determine the 'effective length of crack extension' in models like those of Jenq and Shah (1985) and Nathalambi Karihaloo and (1986). These models can be used to illustrate the stable crack growth that occurs prior to the peak load.

While Figure 5.10 through Figure 5.12 represented the typical response in all of the 2.83'' (D/3) and 4.25'' (D/2) load versus specimen displacement curves at later ages (i.e., ages greater than 15 equivalent maturity hours). A different response was typically observed with the smaller notched specimens (i.e., notches less than 2.83'' (D/3)). These shorter notched specimens exhibited a significant, sudden decrease in the load prior to the immediate loss of load carrying capacity that occurred at peak. This distinct drop in load before ultimate failure will be called the 1st peak load in this report. An example of the

distinct drop in the load versus specimen displacement is illustrated in Figure 5.13. It can be seen in this figure that after reaching a value of approximately 85% of the peak load, the load decreases suddenly. This decrease in load corresponds to a sudden change in the LVDT response that may signify some quasi-stable crack growth. It should however be noted that while the crack may grow, the crack does not appear to propagate completely through the depth of the specimen. Rather, it appears that the crack grows unstably to a specific length, then stops, until the load is increased to a point at which the crack would again grow unstably.

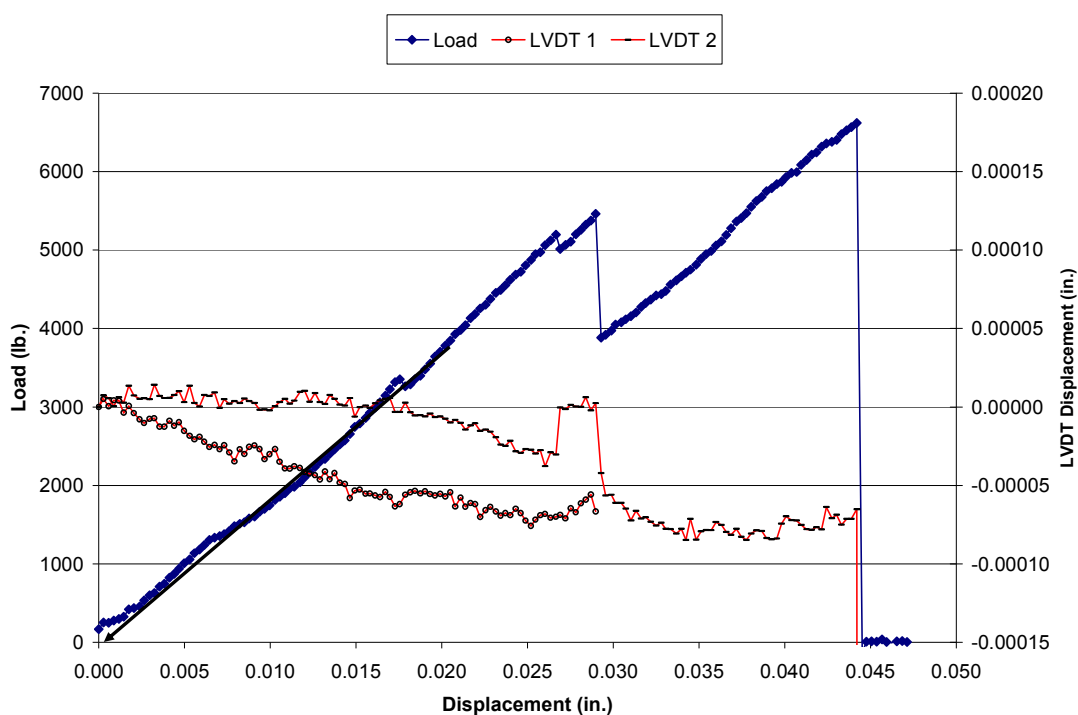


Figure 5.13: Experimental results for specimen 33: load versus specimen displacement and LVDT displacement versus specimen displacement (2.00" (D/4.25) @ 38 eq. age hours)

It is speculated that this distinct drop in the load curve represents quasi-stable crack growth since the specimen is loaded in a displacement control mode. As the length of the crack increases, the specimen becomes more compliant. Therefore, if the displacement is

relatively fixed, the extension of the crack decreases the stiffness causing the load level and corresponding crack driving energy to dramatically reduce. After the crack stops growing in this unstable fashion, the overall displacement of the specimen must once again be increased until enough energy is stored in the specimen to cause the crack to grow again.

In the further examination of why this behavior is not seen in the 2.83" (D/3) and 4.25" (D/2) specimens we can consider the influence of the fracture process zone (FPZ). It should also be noted that the heterogeneous nature of concrete causes an inelastic zone to form around the tip of a crack. This inelastic zone is called the fracture process zone and is defined by the development of microcracking that is caused by differences in the stiffness of aggregates and paste at the tip of the crack along with many complicated toughening mechanisms. Some of these mechanisms include aggregate bridging, microcracking, crack tip blunting, and crack tip branching (Shah et al., 1995). Figure 5.14 shows a conceptual illustration of the fracture process zone. It can be imagined that at the notch and where the crack is relatively wide stresses can not be transferred across the crack. As the crack width becomes smaller, normal stresses can be transferred or bridged across the crack due to aggregate interlock and friction. Ahead of this bridging zone, there is a region of microcracking.

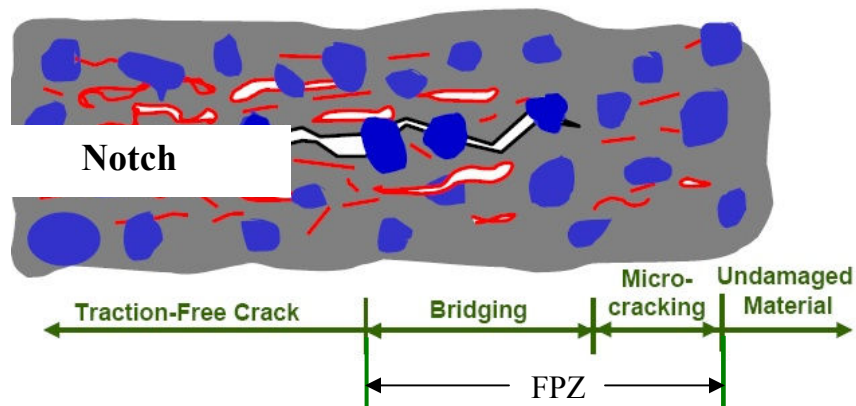


Figure 5.14: Hypothetical fracture process zone

Laser interferometry (Castro-Montero et al., 1990) has shown that at the peak load the fracture process zone ahead of the crack tip is basically a constant size regardless of the length of the crack and depends on the geometry and size of the structure. It can be envisioned that specimens with the 2.83" (D/3) and 4.25" (D/2) notch have a fracture process zone that may be nearly fully developed across the depth of specimen as the peak load is reached. However for the case of the shallower notches (i.e., 2" (D/4.25) and smaller) the fracture process zone does not be developed across the entire section depth. Therefore it may be possible to think that a crack may open suddenly but not propagate fully across the specimen because the fracture process zone is required to fully develop before the ultimate failure can occur. Figure 5.15 shows a conceptual illustration of how the fracture process zone may occupy a different percentage of the cross section depending on the notch size.

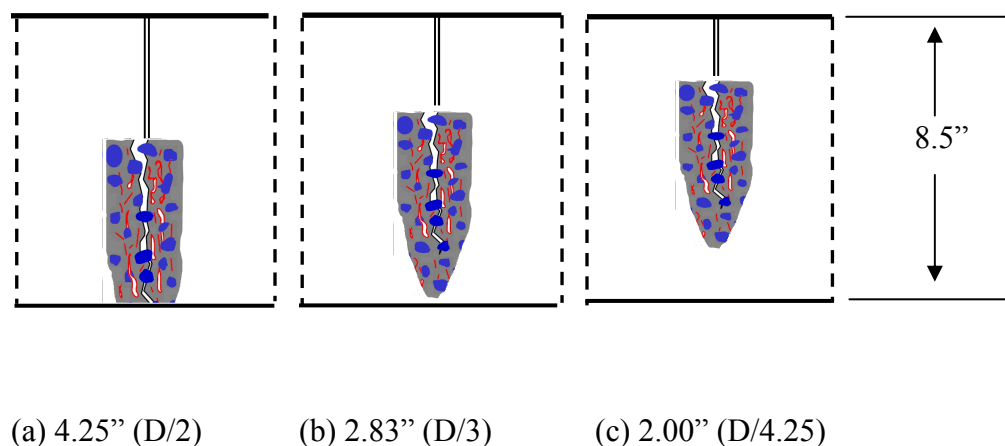


Figure 5.15: A conceptual illustration of the size of fracture process zone and its relation to the size of the initial flaw (notch)

Figure 5.16 shows a plot of the horizontal specimen displacements at the point of maximum load versus the maturity of the specimen (it should be noted that this displacement takes into consideration the seating correction that was explained in section 5.2.1.1). From this figure it appears that the 1st peak displacements occurred at a significantly lower displacement than their corresponding peak displacement. And it

could be concluded that in general, the 1st peak in the case of shallow notches and the displacements measured at ultimate load in the case of deep notches occurred at similar displacements between 0.014" and 0.040". This data would suggest that initial cracking is largely dependent upon the specimen displacement irrespective of notch depth.

The tensile loads at the point of crack initiation (1st cracking) for specimens with different notch depths are compared in Figure 5.17. It can be seen that the specimens with the 4.25" (D/2) notch have a slightly lower ultimate load in comparison to the 2.83" (D/3) data as one may expect. In addition this Figure 5.17 shows the ultimate load. The data at both ultimate and initial is at or below the data from the D/3 specimens. It should be noted that this trend may not initially be expected. A possible explanation for this behavior may be due to the fact that the load or displacement at the time of cracking may be mainly attributed to the shape of the notch tip.

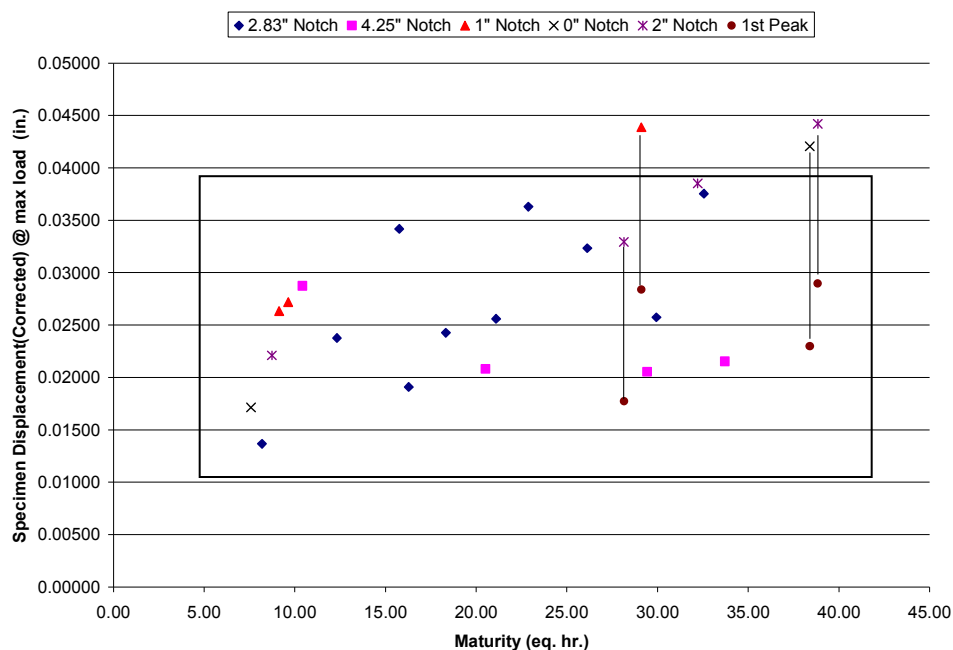


Figure 5.16: Corrected specimen displacement versus maturity for all tests

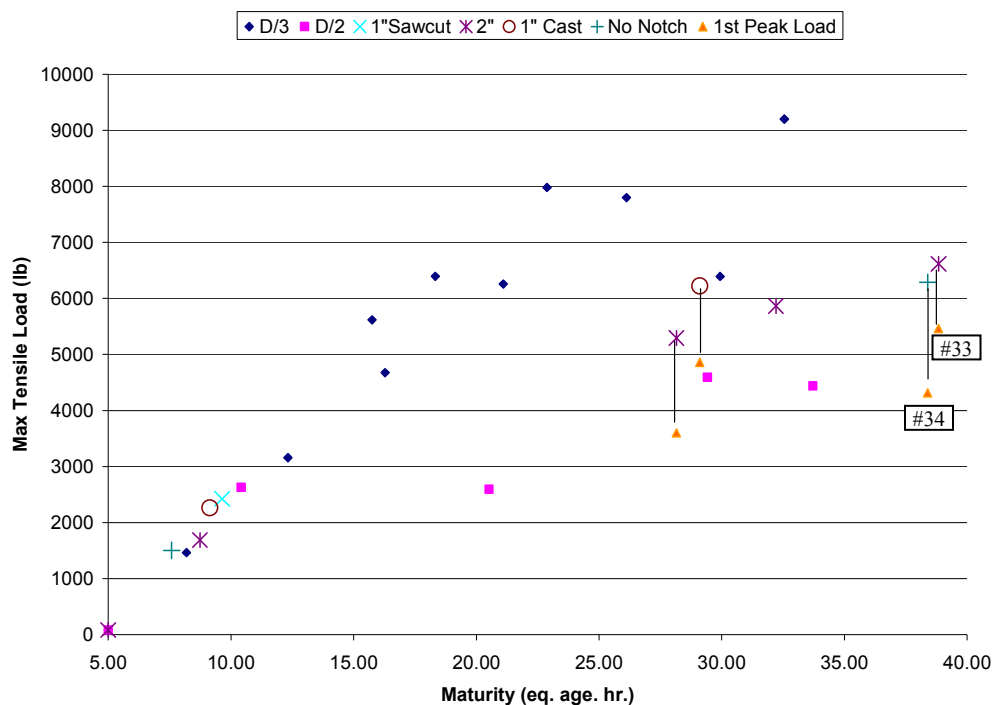


Figure 5.17: Ultimate tensile load versus maturity for all specimens (including load at 1st peak displayed in load versus specimen displacement curve for shallow notches)

It may be suggested that the lower strength for the small notched specimens may be attributed to the influence of residual stresses caused by thermal contraction. The temperature drop from maximum to the final temperature at the time of testing was shown in Table 5.1 and is re-tabulated in Table 5.2.

The maximum temperature drop can be used to estimate the thermally induced residual stress. The coefficient of thermal expansion was estimated to be (6.0×10^{-6} strain/ $^{\circ}\text{F}$) and the modulus of elasticity was estimated based on the compressive strength ($E = 57000\sqrt{f'c}$) at a maturity of 30 equivalent age hours. The thermal stress is estimated by assuming that the stress can simply be computed using the theory of elasticity assuming that the formwork does not permit the specimen to move freely. From Table 5.2 it should be noted that specimen numbers 33 and 34 were calculated to have the highest thermally induced stress levels of 175 and 213 psi respectively. If Figure 5.17 is re-examined specimen number 33 and 34 exhibit low levels of initial

cracking and maximum load relative to the others. Further studies are needed to investigate this behavior and it is suggested that testing be conducted introducing the notch at the time of testing to investigate for this effect.

Table 5.2: Thermal induced stresses

Test Number	Notch	Maturity	Temp. Drop (Max - Final)	Coefficient of Thermal Expansion	Modulus of Elasticity	Thermal Induced Stress
(#)	(in.)	(eq. age hr.)	(°F)	(1/°F)	(psi)	(psi)
34	0	38.39	10.8	6.00E-06	2.70E+06	175
24	1.00 Cast	29.10	6.3	6.00E-06	2.70E+06	102
26	2.00	28.15	7.9	6.00E-06	2.70E+06	128
29		32.21	5.7	6.00E-06	2.70E+06	92
33		38.83	13.1	6.00E-06	2.70E+06	213
14	2.83	26.12	4.1	6.00E-06	2.70E+06	66
20		29.93	6.6	6.00E-06	2.70E+06	107
31		32.55	7.3	6.00E-06	2.70E+06	119
22	4.25	29.42	5.0	6.00E-06	2.70E+06	81
32		33.72	7.5	6.00E-06	2.70E+06	121

Furthermore, the influence of thermal gradients was examined due to the temperature difference throughout the depth of the specimen. Figure 5.1 shows the temperature difference in specimen 31 between the thermocouples at 2.83" and 4.25" and displays a 4°F difference after the peak temperature. Additionally, in specimen number 32 a thermocouple was placed at 5.67" (2/3 depth) and the temperature was found to be approximately 0.5 °F less at than mid-depth (4.25") sensor throughout the time period. Therefore a proposed thermal gradient for all specimens used in this study is shown in Figure 5.18. This plot was prepared by assuming a linear temperature change with depth using the data that was recorded at the depths of 2.83" (D/3) 4.25" (D/2) and 5.67" (2D/3). Figure 5.18 demonstrates that the specimen will be inclined to curl upwards. When the specimen is restrained from curling upwards, as is the case with the specimens, tensile stresses would develop in the top of the specimen and decrease downwards in gradient fashion. Thus the maximum value of the stress would occur at the surface of the specimen and would decrease with depth. Therefore, shallower notches would have

higher stresses at their notch tips than deeper notches would before the testing occurred. This may have caused damage that lead to lower ultimate and first cracking loads which were noticed in the shallower notched specimens. Therefore two possibilities are being suggested for causing damage before loading the specimens and resulting in lower initial and ultimate loads in the shallow notched specimens. First, it is being suggested that the thermal contraction which occurred at late ages for specimen 33 and 34 lead to damage development prior to the testing and secondly, all of the shallower notches underwent larger stresses concentrations at notch tips due to the thermal gradient

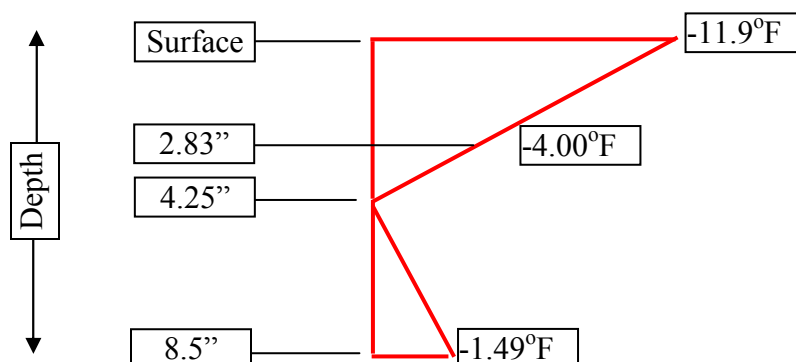


Figure 5.18: Assumed specimen temperature gradient (temperature shown as difference from mid-depth)

Previous field investigations have provided results that support the hypothesis of stable crack growth (Soares, 1997). Saw-cuts were placed in a pavement on November 8, 1991 to depths of 1" (D/12) and 3" (D/4) for a 12" pavement. No visible cracks were found in the field experiment until November 26, 1991 and many joints did not visually show any cracking. It was noted that a significant number of cracks developed after the pavement was subjected to greater temperature fluctuations in the summer months of June and July. Since the pavement had gained significant strength before the increase in visible cracking, it was suggested that cracking likely initiated at an early age but was not visible until later and larger temperature fluctuations caused the crack to propagate throughout the slab and become visible.

Other research (MODOT, 2001) has concluded that cracking often occurs more rapidly with deeper saw-cuts; however, early-entry shallow saw-cuts could provide equally adequate control of random cracking. The results from the research presented in this chapter suggested that the joints exhibited stable crack growth at an early-age that relieved stresses but these cracks did not become visible until further strain propagated the cracks to become visible.

The D/3 saw-cut depth guideline appears to have little scientific basis and was determined mostly from field experiments based on visual reference. The research provided herein showed significant stable crack growth for specimens with a notch depth less than 2.83" (D/3) which may suggest why the D/3 recommendation has become prevailing practice. It should be noted, however, that the results of the experiments suggest that crack initiation may occur at similar or lower loads for smaller notch depths. However specimens, with shallow notches, may exhibit small amounts of quasi-stable crack growth which only propagates when higher loads are applied. At these higher load levels the specimen would develop a crack that propagates through the slab thereby becoming visible to the human eye.

5.2.3 Early-age Plasticity

The second trend that was noticed from the series of testing was that there was a similar net section strength for the concrete at early ages (i.e., <15 equivalent age hours) regardless of the notch depth. Notch insensitivity is an indication of plastic behavior in a material. Figure 5.19 shows how a brittle material will create a stress concentration near the end of the notch whereas a plastic failure will be insensitive to the notch.

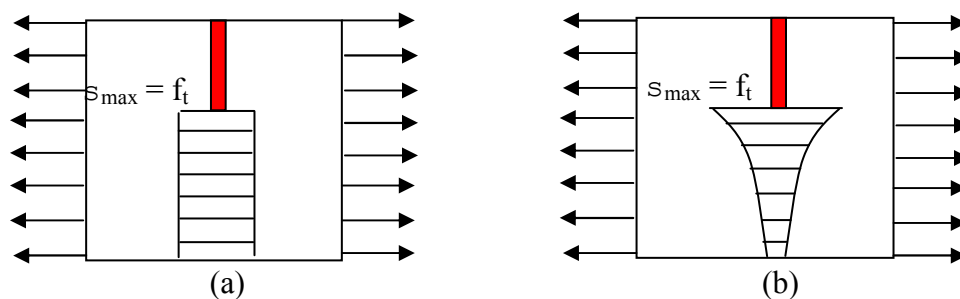


Figure 5.19: The stress distribution for (a) plastic and (b) brittle failure

In general, concrete transforms from a plastic material before “set” to a brittle material after set time where the material is capable of transferring stress throughout the continuum. Early-age crack development is largely dependent on how the mechanical properties of concrete change after set time with increased maturity. The results from this study appear to indicate that concrete may behave in a plastic behavior at very early ages after “set” time.

To further confirm the potential for a relatively ductile early behavior we can consider the observations of others. Hillerborg (Hillerborg et al., 1976) developed a material parameter to describe ‘the extent of ductility that a material may exhibit’ which he termed the characteristic length (l_{ch}). It is not the intent of this section to detail fracture mechanics and the readers are referred to a thorough summary of these properties in *Fracture Mechanics for Concrete* (Shah et al., 1995). In general, G_f is the fracture energy which can be thought of as the area under the entire stress-elongation curve. The characteristic length (l_{ch}) is considered a pure material property and is proportional to the length of the fracture process zone that occurs ahead of the crack. Equation 5.6 defines

$$l_{ch} = \frac{EG_f}{f_t^2} \quad (5.6)$$

l_{ch} where E is the modulus of elasticity, G_f is the fracture toughness, and f_t is the tensile strength. The characteristic length l_{ch} is proportional to the fracture process zone which is a figure-of-merit that is frequently used in describing the ductility of a material. In general, research work has concluded that the characteristic length (l_{ch}) decreases with age. Figure 5.20 shows a plot of characteristic length l_{ch} versus time (Peterson, 1981). Figure 5.20 shows a distinct decreasing trend in the characteristic length l_{ch} over time which shows the size of the fracture process zone is decreasing and the concrete is becoming more brittle. Similar observations were made by Ostergaard et al. (2004).

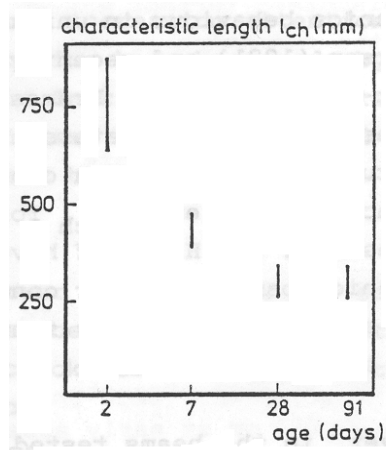


Figure 5.20: Development of characteristic length with age (from Peterson (1981))

The data from the tensile wedge test provided results that would support the hypothesis that early-age concrete responds in a ductile behavior. Early-age is a relative term and for the sake of this discussion it will refer to a maturity of less than fifteen equivalent age hours. A total of seven tests were performed between the maturities of 7-15 equivalent age hours. These included one test with no-notch, two tests with a 1.00" notch (one 1.00" notch was placed with early-entry saw), one test at 2.00" notch, two tests with a 2.83" notch, and one test with a 4.25" notch. These tests are shown in Figure 5.17 with a plot of tensile load versus maturity. The load can be converted to stress by using the net cross sectional area of the specimen. The net cross section is equal to the area of the notch subtracted from the area in the middle of the specimen (8.5"x4.5"). Based on a linear trend line (fit to the stress versus maturity data) the values of stress were normalized for an age of 10 equivalent age hours and are shown in Figure 5.21. It should be noted that in Figure 5.21 the plot for the notch depths of 1.00" and 2.00" are the average of the two tests which occurred during the early age period. From the data presented in Figure 5.21 it appears the strength at which the material fails is insensitive to the depth of the notch. Furthermore the deepest notches (4.25" and 2.83") showed the highest strengths. If the material behaved in a brittle manner an increasing notch depth would be expected to increase the stress concentration at the tip of the crack and as a result the failure load would substantially decrease as more load is applied.

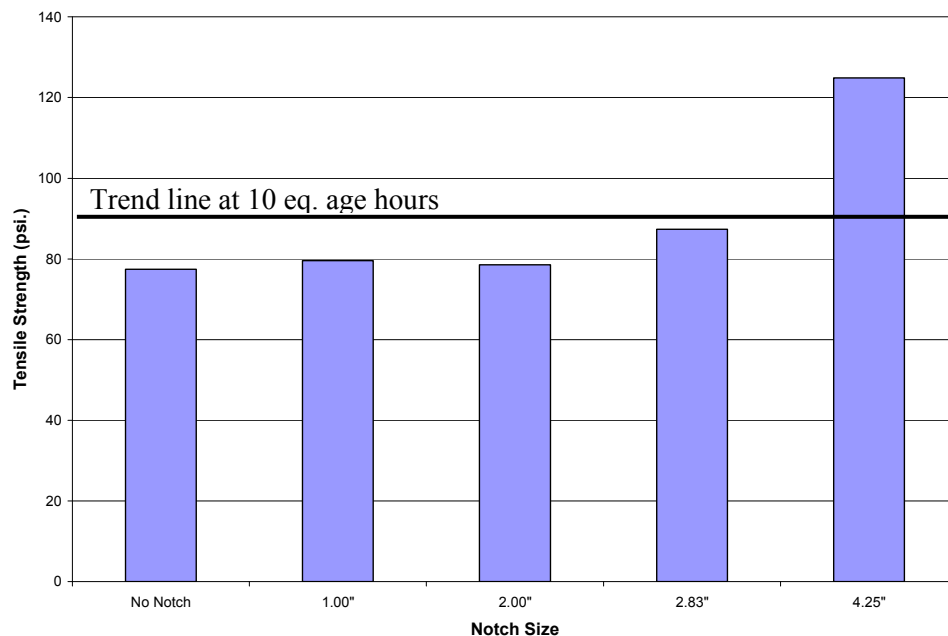


Figure 5.21: Various notch – early age data normalized for 10 equivalent age hours

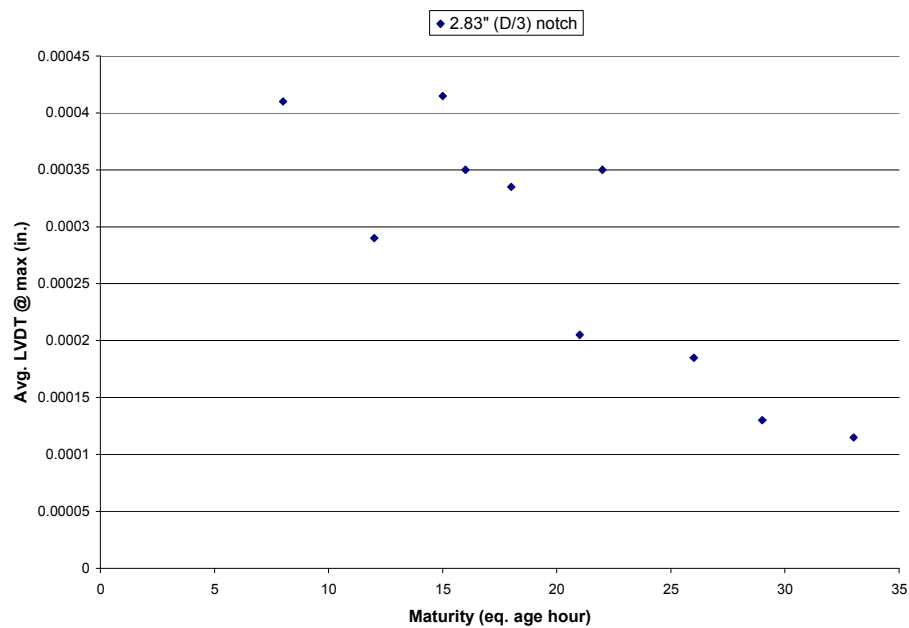


Figure 5.22: Average LVDT displacement versus maturity for the 2.83” (D/3) specimens

The hypothesis of early age plasticity is further examined in Figure 5.22 which shows the average of the two LVDT displacement values at ultimate failure for the 11 specimens which contained a 2.83" notch. The 2.83" (D/3) specimens were chosen because the largest number of tests were performed in this configuration. There is an evident decreasing trend in the LVDT displacement values as the maturity is increased. Therefore, the material has a wider crack opening at earlier ages. A wider crack opening would suggest a more compliant system with either a lower material stiffness or a large fracture process zone at the time of failure.

5.2.4. Notch Depth Propagation Probability

The third trend that was noticed in the data generated during the research was a decrease in the probability of the crack to propagate from the notch when the notch length was reduced from 2.00" (D/4.25) to the 1.00" (D/8.5") notches. All of the 2.00" notched specimens cracked from the tip of the notch whereas specimen 23 and 24 which contained 1" notches cracked at a location beside the notch tip. Specimen 23 was tested at a maturity of 9.14 and specimen 24 was tested at a maturity of 29.19 equivalent age hours. Figures 5.23 and 5.24 show pictures of each test and the paths that the cracking followed.

The depth of the saw-cut that provides adequate results in controlling random cracking is largely debated. Research by Okamoto (1994) concluded that there are too many confounding factors to develop a verified recommendation. The confounding factors included the large dependency upon the timing of the saw-cut and the wide range of environmental influences on strength and stress development. Zollinger proposed that the appropriate depth of the saw-cut is largely influenced by the time the joint is placed (Zollinger, 1993). Numerous field experiments have provided evidence that early-entry shallower saw-cuts can be just as effective as traditional D/4 to D/3 depths (MODOT, 2001). It is believed that sawing of joints at an earlier age can take advantage of larger stress gradients at the surface to initiate cracking as opposed to those as the D/4 or D/3 depth. In regards to the tensile wedge specimens, thermal gradients were discussed in section 5.2.2 of this chapter and the hygral gradient was considered to be zero due to

curing with wet burlap. Considering only the direct tension that was applied to the specimens, there was a distinct increase in the probability of cracking not occurring at the notch when notch depths were decreased from the 2" (D/4.25) to the 1" (D/8.5") notch.



Figure 5.23: Crack propagation for specimen #23 which was cast with a 1.00" (D/8.5") notch and tested at 9 equivalent age hours



Figure 5.24: Crack propagation for specimen #24 which was cast with a 1.00" (D/8.5") notch and tested at 9 equivalent age hours

In addition to 1” notches that were cast in the specimens a 1” notch was placed with a Soff-Cut x-50 early entry saw in specimen #28 15 minutes before the specimen was tested at an age of 9.64 equivalent age hours. A picture of the specimen being sawed is shown in Figure 5.25. Upon examination of the specimen the crack had developed from the notch. It is interesting to compare specimen #23 and specimen #28 which were both tested at approximately the same maturity (9 equivalent age hours) with 1.00” (D/8.5) notches. The ultimate strength and specimen displacement values were very similar for both tests even though specimen #23 did not crack from the notch tip and specimen #28 did crack from the notch tip. It should be noted that there were numerous differences between the saw-cut notch and the cast notch. First, the thickness of the x-50 saw-cut was 0.095” whereas the thickness of the cast notches was 0.125. The saw-cut notch also differed from the cast notch because it was performed 15 minutes prior to the testing of the specimen whereas the cast notches are placed when the specimen is cast. Finally, the saw-cut notches have a crack tip that consists of aggregate and paste while the placed notches have a tip that consists primarily of paste. The saw-cut test may prove that further testing is needed with 1” specimens to determine the actual decrease in probability of cracking around the notch. Of the three 1” notched specimen tests were performed two out of the three propagated at a location other than the notch. Therefore, further testing could more accurately determine the decrease in probability of a crack propagating from a 1” notch.



Figure 5.25: Introduction of the saw-cut notch using the early-entry saw

5.3 Flexural Beam Test Results

A total of fifteen flexural beams were prepared as companion beam specimens that could be tested along with tensile wedge specimens. Testing occurred within a time range of 6.8 and 71.0 hours of real time (8.2 and 87.0 equivalent age hours). Figure 5.26 shows a plot of the flexural strengths versus Arrhenius equivalent age maturity and the strength is fitted with a sigmoidal function (Equation 5.1). It can be seen that the strength develops rapidly between a maturities of 5-20 equivalent age hours.

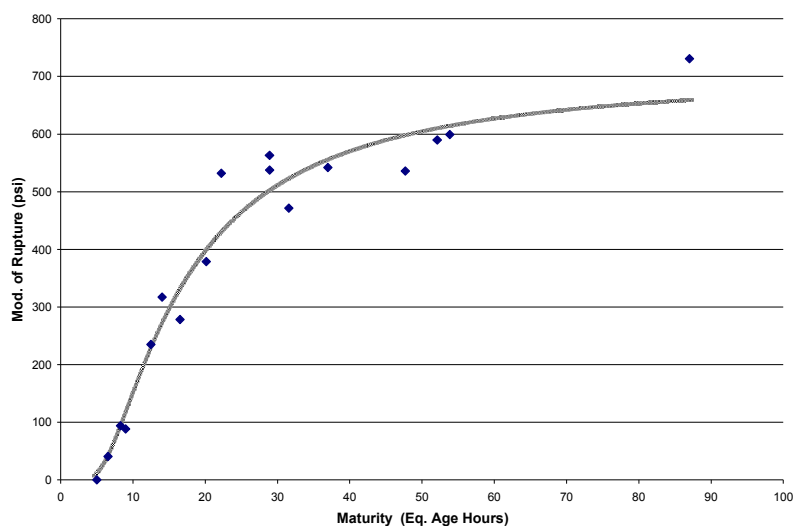


Figure 5.26: Flexural strength versus maturity fitted with sigmoidal trend line

Figure 5.27 shows a comparison of the strengths determined using the tensile wedge (2.83" (D/3) notch) and the strengths determined from the flexural tests. In addition, Figure 5.27 also shows a plot of the tensile strength as a percentage of flexural strength on the secondary vertical axis. This percentage is computed from the sigmoidal trend lines. The relationships between the flexural beams and tensile wedge specimens reveals an increasing trend before the approximate age of 12 equivalent age hours, which was called the transition point, and a consistent relationship of approximately 0.59 – 0.63 (average of 0.62) after 10 equivalent hours.

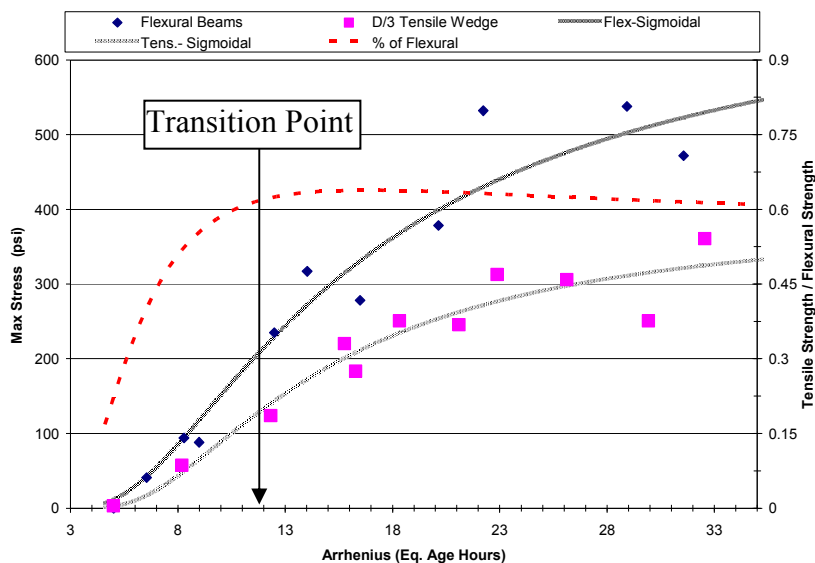


Figure 5.27: Comparison of tensile wedge strength and flexural strength

Before examining the data in greater detail, a comparison of the ratio between splitting tensile and flexural strength can be performed using equations provided by ACI. The ACI (ACI 318, 2002) equation for flexural strength (f'_r) is shown in Equation 5.7 and the ACI equation for splitting tensile strength (f'_{sp}) is shown in Equation 5.8.

$$f'_r = 7.5\sqrt{f'_c} \quad (5.7)$$

$$f'_{sp} = 6\sqrt{f'_c} \quad (5.8)$$

It should be noted that both equations are dependent on the square root of the compressive strength (f'_c). The relationship between these equations simply predicts that the splitting tensile strength is 80% of the flexural strength. The reasons for this behavior can be explained by the fact that concrete develops micro-cracking at the bottom of the flexural beam and the linear assumption of stress and strain actually overestimates the stress distribution. This behavior is illustrated in Figure 5.28.

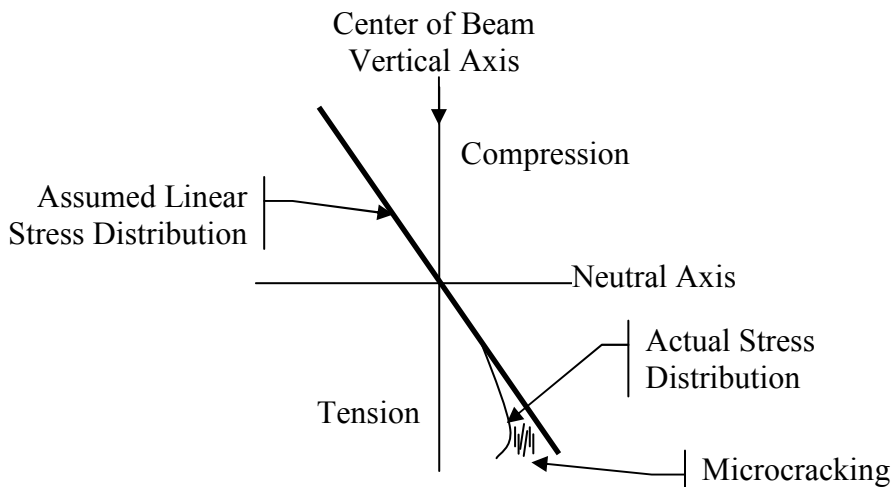


Figure 5.28: Actual and assumed stress distribution in concrete specimen tested in flexure

Several other factors should be considered when interpreting the results which show a much lower ratio of these strengths. First, Equation 5.8 was developed based on splitting tensile strength results, and therefore does not give direct tensile strength values. It has been suggested that splitting tensile strengths are 5-12% higher (Mindess, 2003) than direct tensile strength. In addition, the general influence of the notch needs to be considered and was discussed in section 1 of this chapter. Basic fracture mechanics demonstrates the ability of the notch to create a stress concentration which can lower the recorded ultimate stresses. Considering these factors, the ratio of 0.62 between flexural and tensile wedge strengths appears reasonable. It should further be noted that if the moment resistance of a purely elasto-plastic material was computed using linear theory, the extreme fiber strain would be approximately 50% higher than the actual plastic strain. As previously noted, the experimental results appear to indicate that the material behaves plastically at early ages (before 15 equivalent age hours) and as such, this would provide an explanation for why the relationships between the flexural beams and tensile wedge specimens is approximately $2/3$ of the ratio which is shown after 12 equivalent age hours.

5.4 Early-age Shrinkage Test Results

The early-age shrinkage tests were performed using four specimens, of which two were autogenous and two were exposed to two sided drying. Figure 5.29 plots the average values of strain versus the age in hours. In general the specimens behaved as expected with the two sided drying specimens shrinking more than the completely sealed (autogenous) specimens. Autogenous shrinkage occurs in low w/c (i.e., < 0.42) concrete. This data was measured to assess the potential development of residual stresses from autogenous shrinkage. Further work will be needed to more fully characterize early age volumetric movements. Specifically, it is proposed that tests are conducted using continual length change measurement and procedure to evaluate the influences of temperature.

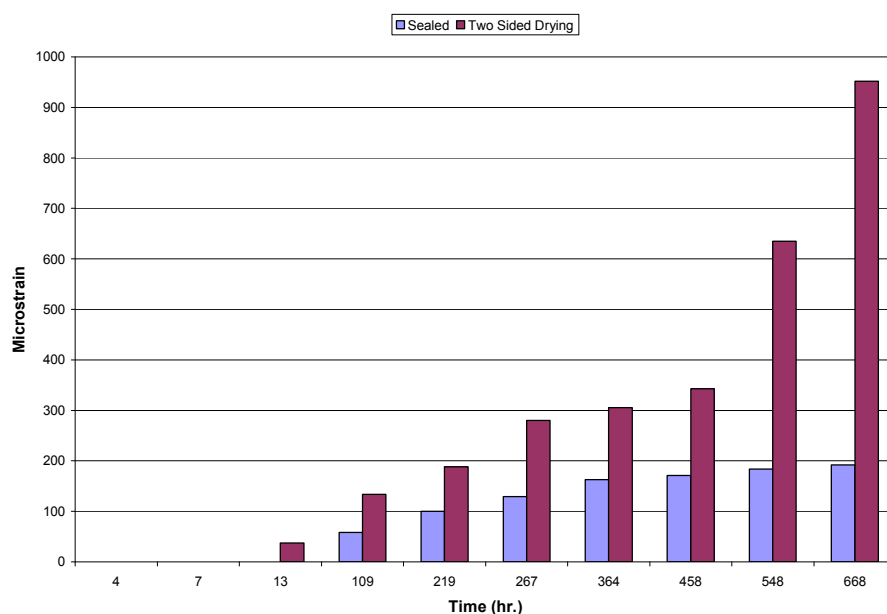


Figure 5.29: Micro-strain versus time for sealed and two sided drying shrinkage specimens

5.5 Compressive Cylinder Test Results

Early-age compressive strength testing was also performed. The compressive tests were used to develop an early-age strength versus maturity curve which could be compared to the flexural strength development. This was determined since earlier research developed saw-cutting guidelines based on compressive properties. Thirteen 6” x 12” cylinders were tested at real time hours of 5 to 30 which equates to equivalent age maturity hours of 6 to 60. The compressive tests are plotted as a function of maturity in Figure 5.30.

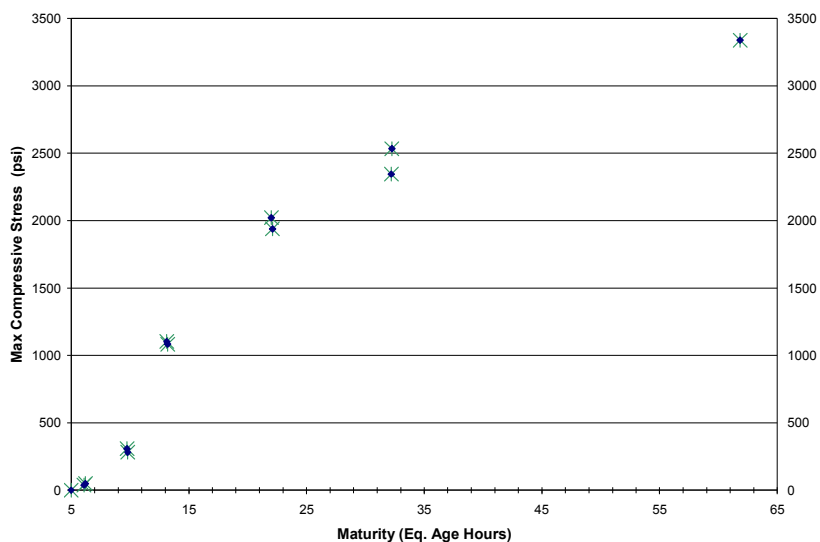


Figure 5.30: Early age 6”x12” compressive strength versus maturity

Previous related work has suggested a compressive strength of 500 psi was the minimum compressive strength required to perform an adequate saw-cut with a conventional saw. Specifically research by Okamoto (1993) determined the earliest age for saw-cutting based on cement content, aggregate type, and aggregate shape. Based on the research by Okamoto a recommendation for a “good” saw-cut (level “4” see Chapter 1) based on raveling (taking into consideration the laboratory mixture design) would occur at a compressive strength of 620 psi. If flexural strength is to be used as a guideline for saw-cutting it is imperative that there be a valid relationship between

flexural and compressive strengths during the relevant early-age window. Figure 5.31 shows the compressive and flexural data fitted with a sigmoidal trend lines. The sigmoidal equation was explained in section 1 of this chapter and is often used to fit early-age maturity versus strength plots. The trend lines provided coefficients of determination (R^2) values of 0.99 and 0.96 for the compressive and flexural data respectively. The trend line equations were formulated to present the flexural strength ($f'r$) as function of the compressive strength ($f'c$) in Equation 5.9. In Equation 5.9 the subscript of “c” and “f” represent compressive and flexural strengths respectively. The coefficients for Equation 5.9 are shown in Table 5.3.

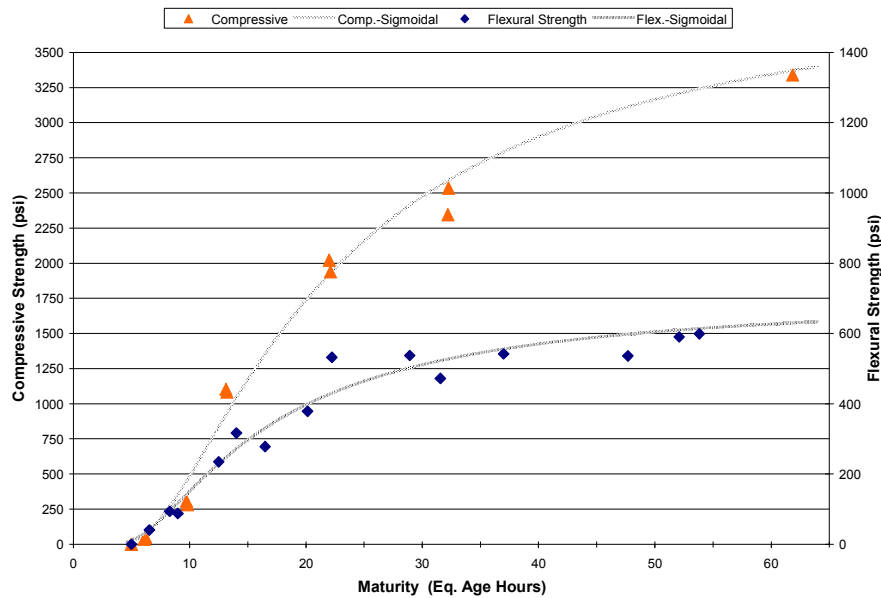


Figure 5.31: Compressive and flexural strength plots

$$f'r = \frac{S_{\infty f}}{e^{\left(\frac{\tau_f}{\tau_c} * \left(\ln \left(\frac{S_{\infty c}}{f'c} \right) \right)^{\frac{1}{\alpha_c}} \right)^{\alpha_f}}}$$
(5.9)

Table 5.3: Sigmoidal trend line constants

	Compressive	Flexural
S_{∞}	4101	708
t	17.82	13.59
a	1.31	1.41

Figure 5.32 examines the maturity age from 5 to 30 equivalent age hours using the same trend lines as Figure 5.31. Using the trend lines we can estimate that a flexural strength of 183 psi corresponds to a compressive strength of 620 psi based on the maturity (i.e., 11.0 equivalent age hours).

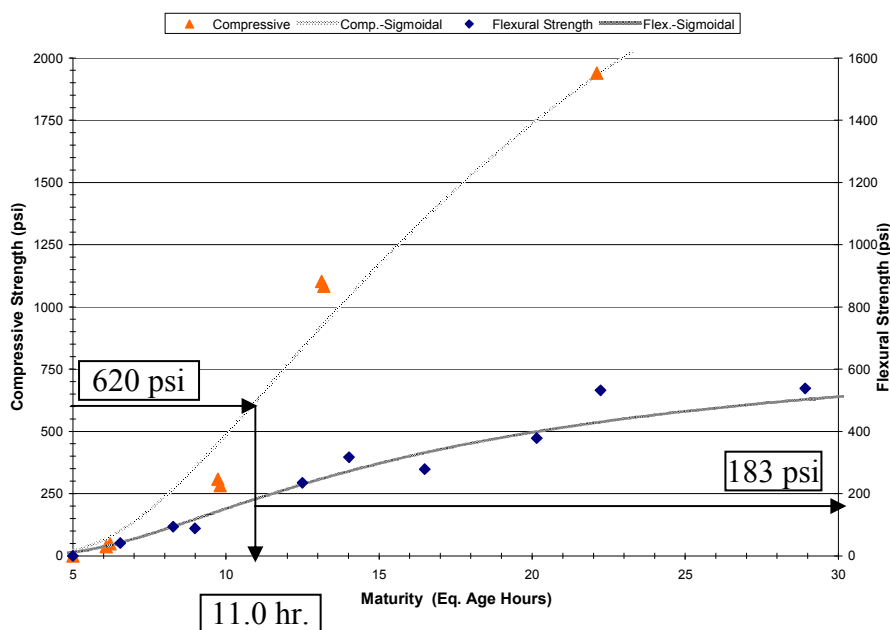


Figure 5.32: Flexural strength conversion from raveling guidelines based on compressive strength

The common ACI equation for converting compressive to flexural strength (Equation 5.7) was also considered for converting the guidelines based on compressive strength to flexural strength. A wide range of data has showed that Equation 5.7 is the lower bound of flexural strengths therefore it commonly under predicts flexural strength and conversely over predicts compressive strength. Figure 5.33 shows the predicted

compressive strength using the flexural data and Equation 5.7. It is clear that the equation does not provide an accurate conversion for the later ages but the equation proves to fit the data from 0 to 15 equivalent age hours which is shown in Figure 5.34. Figure 5.34 shows that for a compressive strength of 620 psi Equation 5.7 would predict a flexural strength of 187 psi at a maturity of 11.1 hours. This can be compared to the predicted 183 psi and 11.1 hours which was determined in Figure 5.32 using the best fit sigmoidal trend lines. The age where the equation is accurate (0 to 15 equivalent age hours) proves to be the age where previous saw-cutting guidelines based on compressive strength (Okamoto, 1993) occur. Due to the prevalent use of flexural beam testing in Indiana for concrete pavements, specifically ITM 402, it may be beneficial to provide early-age guidelines based on flexural strength. The results for this mixture show that Equation 5.7 is justified to convert compressive strength to flexural strength at these low compressive strengths (< 1500 psi compressive) and corresponding early-ages (0 to 15 equivalent age hours).

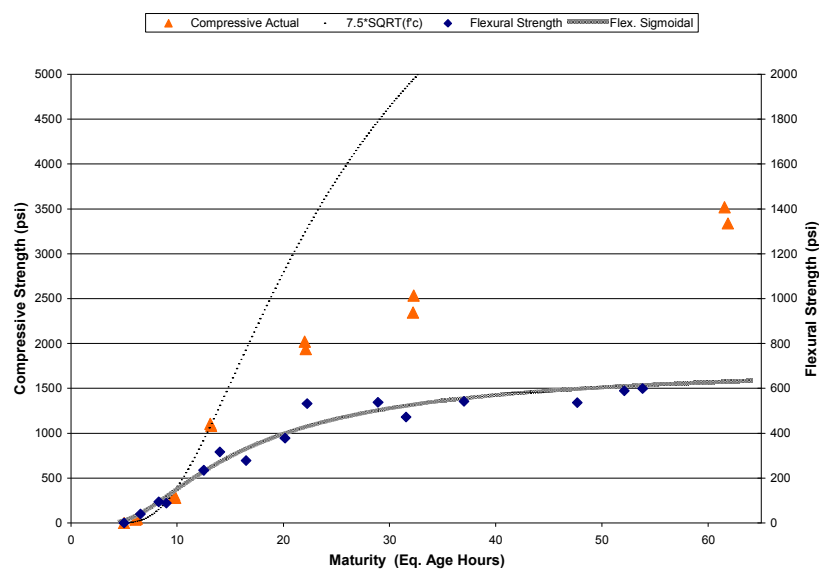


Figure 5.33: Equation 5.7 used to convert flexural to compressive strength for 0-60 equivalent age hours

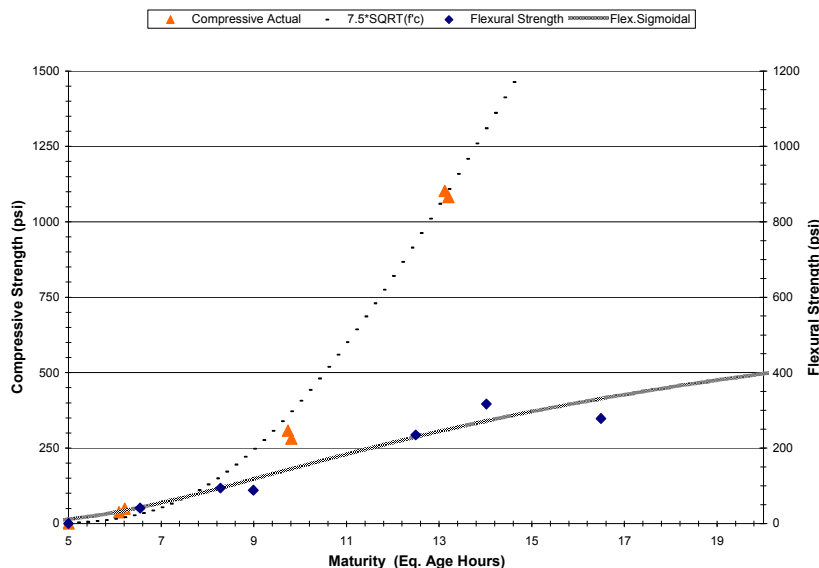


Figure 5.34: Equation 5.7 used to convert flexural to compressive strength for 0-20 equivalent age hours

5.6 Split Cylinder Test Results

Split cylinder tests were performed to determine the variation in tensile strength that may be expected at an early age. This variation was then compared to values that were obtained using the tensile wedge test. A total of eight split cylinder tests were tested at an age of 27 real time hours which equates to a maturity of 45 equivalent age hours. The average strength of the eight cylinders was 440 psi with a standard deviation of 46 psi and coefficient of variation of 10.5%. The high strength value was 506 psi and the low strength was 381 psi. It is suggested that the values obtained from the laboratory testing are higher than those referenced in AASHTO potentially due to the use of a larger maximum size of aggregate (1") which can increase the variability of tensile testing and the maturity at which the testing occurred. The maturity of the mixture at the time of testing (45 eq. age hr.) is very near the knee point identified in previous research that occurs when the aggregates begin to fracture (Barde et al., 2003). At this point the testing would prove to be sensitive to the type of aggregate and have a high coefficient of variation. Further splitting tensile testing may reveal different coefficients of variation

before and after the knee point. Figure 5.35 shows a normal probability density function for the average (m) and standard deviation (s).

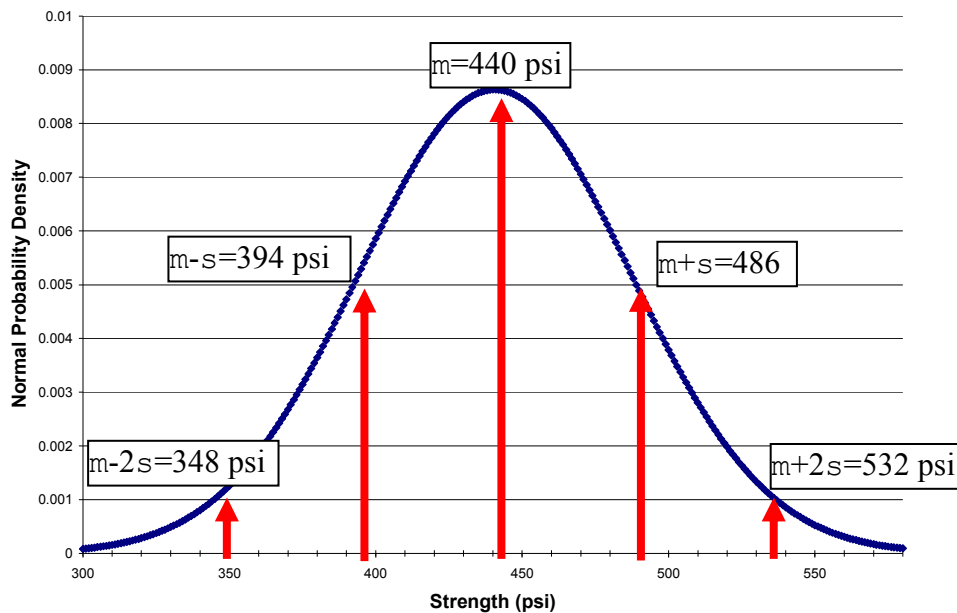


Figure 5.35: Normal probability density for splitting tensile tests

5.7 Mortar Set Time

The mortar set time test produced an equivalent age maturity at initial and final set time of 5.0 and 6.6 hours which equates to 3.0 and 4.0 hours real time respectively. For this report the initial set time of 5.0 equivalent age hours was considered the point at which mechanical strength began developing and was used as initial maturity M_0 for fitting all plots and relevant equations.

5.8 Early-entry Saw Test

Four early-entry saw-cuts were performed with the earliest saw-cut being performed at a maturity of 6.25 equivalent age hours. None of the saw-cuts revealed any raveling at the joint. Table 5.5 shows the real time and equivalent age maturity times for

Table 5.4: Soff-cut early entry saw test

Saw-Cut	Real Time	Maturity
(#)	(Hr.)	(Eq. Age Hr.)
1	3.75	6.25
2	5.00	8.75
3	6.50	12.56
4	7.90	17.32

four saw-cuts. It can be concluded that the early-entry technology can perform saw-cuts at halfway between initial and final set time set time as determined by ASTM C 403 without any significant raveling. Using the plot for the early-age compressive data, it was found out that a maturity of 6.25 eq. hours corresponds to a compressive strength of 80 psi. The constraint for early-entry sawing proves to be the ability of the concrete to support a walking person for which an average person can apply a 100 psi stress. The general guidelines for conventional saw-cutting are that a 500 psi compressive strength is required. Comparing the 80 psi value to 500 psi value demonstrates that early-entry saws are not applicable to the guidelines set forth by Okamoto (Okamoto, 1994) and early-entry saws need to be considered separately when defining the start of the saw-cutting window.

5.9 Summary

This chapter provided an analysis of the results from the experimental work and was intended to provide a framework that will use the maturity method to describe the time for saw-cutting. Specifically, the results from six different experimental procedures were described.

The first experimental procedure which was analyzed was the tensile wedge test, from which three specific trends were observed. The first observation which can be made from the wedge test is that before the peak load was reached the crack can propagate in a stable fashion. This stable crack growth was confirmed using the measurement of the LVDT displacement directly over the crack. In specimens with deep notches (i.e., D/3 or greater) the crack appeared to propagate unstably at the time of ultimate load. In specimens with shallow notches (i.e., notches < 2.83" (D/3)) the crack appeared to propagate in a semi-stable fashion with a sudden increase in crack length prior to the load reaching a peak value. The second observation which can be made from the tensile wedge data was that the specimens appear to be insensitive to the notch at early ages (i.e., <15 eq. age hours). The insensitivity to the notch was believed to be an indication of an elasto-plastic material response. The third trend was observed when notch depths were decreased to 1.00" (D/8.5) from 2.00" (D/4.25) when only 2 out of the 3 shallow notch specimens had crack propagation from the notch tip. Therefore a distinct increase in the probability of cracking occurring at a location other than the notch tip was observed (which could be compared to "random" cracking in pavements) in the 1.00" notches (D/8.5).

Mechanical property tests were performed including the flexural beam strength tests and compressive cylinder tests. The flexural beam results were used to develop a relationship between the tensile wedge data and to use as a reference for the tensile wedge specimens. The tensile wedge strength results for the 2.83" (D/3) notches were approximately 62% of the flexural beam results at later ages and approximately 40% at early ages as further indication of an elasto-plastic type of failure. Compressive strength testing was performed because previous research has developed saw-cutting guidelines based on compressive strength. It is currently believed that due to the prevalence of flexural testing used by INDOT it may prove beneficial to base guidelines on flexural strength. In order to evaluate the usefulness of the recommendations by Okamoto (1993) recommendations based on compressive strength, a relationship was developed between flexural and compressive strength. The ACI equation ($f'_r = 7.5\sqrt{f'_c}$) was only observed to be valid up to 15 eq. age hours and strengths of 1500 psi. However, this is

the range that most saw-cutting guidelines (based on early-age raveling) are determined and therefore the equation may be suitable to convert compressive to flexural strengths for saw-cutting guidelines at these ages. However, for the ages between 15 to 60 equivalent hours the ACI equation greatly over predicted compressive strength (conversely under predicted flexural strength). Split cylinder tests were performed at a single age to determine the early-age tensile variability of the mixture. The coefficient of variation was high (10.5%) relative to referenced tests in AASHTO. This high coefficient of variation may have been due to a large maximum size of aggregate or was possibly influenced by the transition that occurs when the fracture behavior changes from cracks that grow primarily around the aggregates at early ages to cracks that propagate through aggregates at later ages. It is believed that this information will eventually be able to be used to try to assess the critical depth of the notch (or saw-cut) to minimize the potential for random cracking.

A final series of test were performed to assess whether the early-entry technology may have a value for the state of Indiana. Results indicate that these early-entry saws can perform saw-cuts at approximately halfway between initial and final set time set time as determined by ASTM C 403 without any significant raveling. This proved to be significantly earlier than conventional saws and confirmed that separate guidelines or specifications may be needed (based on raveling) for early-entry sawing procedures in comparison to conventional sawing procedures.

CHAPTER 6: LITERATURE REVIEW FOR COMPUTER MODELING: A DISCUSSION OF MATERIAL PROPERTY INPUT AS WELL AS BOUNDARY CONDITIONS

6.1 Introduction

The properties of the materials used in the analysis need to be defined. The FEMMASSE software has the ability to consider several materials, each having different parameters. Throughout this section, key models and parameters in the material database (MLS) are explained and the input values used in this project are defined. An overview of the MLS Database window is shown in Figure 6.1. The right window is called the “material property editor” (MPE) which is used to activate or deactivate the material models. The “material database viewer” (MDV) is used to observe the material properties by graphs and labels. The model parameters will be discussed in more details later in this chapter.

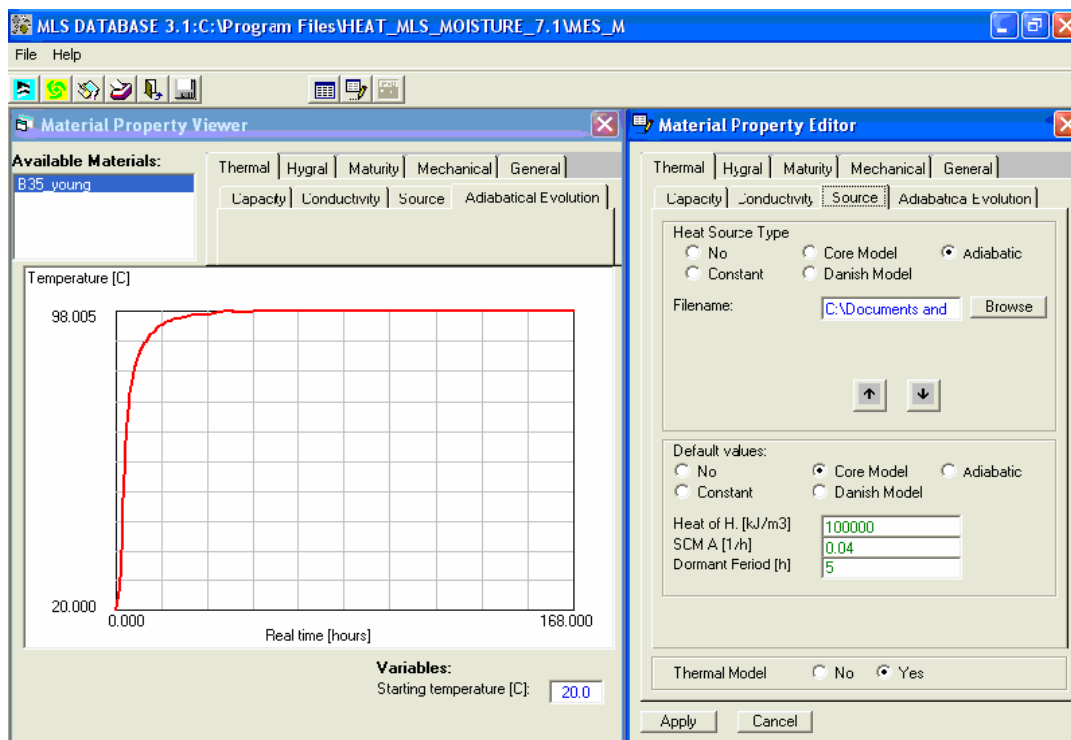


Figure 6.1: Layout of MDV and MPE windows in MLS-Database program.

6.2 Thermal Behavior of Concrete

The heat that is generated during cement hydration can raise the temperature of concrete. One way to estimate the heat of hydration is to use isothermal calorimetry. As shown in Figure 6.2, heat is rapidly released during the first few minutes after mixing the cement with water (stage 1). This heat evolves from cement hydration. The rate of heat generation remains low for a few hours. This is called dormant period (stage 2), and is due to the formation of a protective layer on the surface of cement particles. Subsequent increases in permeability of the protection layer and calcium silicate hydrate crystallization during the hydration process corresponds to the beginning of an “acceleration period” (stage 3) that is characterized by active hydration. The reaction rate then begins to decrease (stage 4). In this stage, the thickness of the hydrating layer that covers unhydrated cement particles increases, and it becomes more difficult for unhydrated particles to react with water. The final phase (stage 5), or “steady state”, is achieved within 18 to 36 hours (Mindess, 2003).

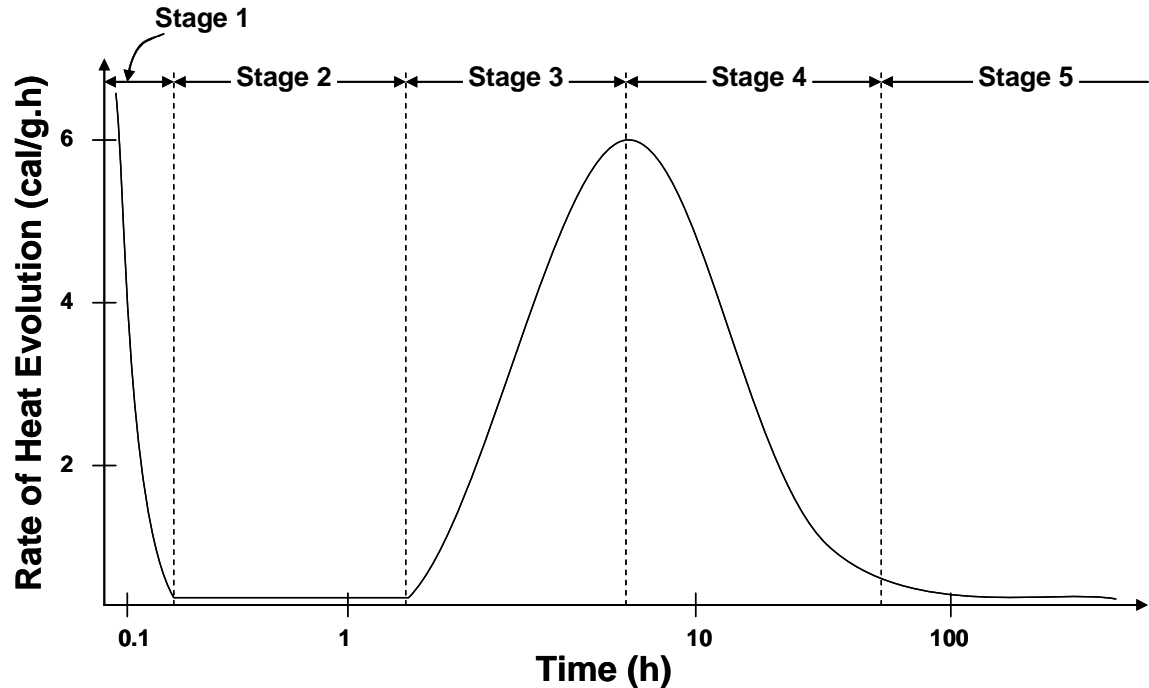


Figure 6.2: Heat evolution rate of tricalcium silicate during hydration (Mindess, 2002).

For a typical portland cement, nearly 50% of the potential heat is liberated within the first three days (Monteiro, 1995). Numerous attempts have been made to predict the temperature rise. Several factors that affect the rate of temperature rise, maximum temperature, and temperature distribution in concrete include the following:

- Rate of heat evolution,
- Total amount of heat developed,
- Composition and volume fraction of the cementitious materials,
- Concrete geometry,
- Environmental conditions such as temperature, wind, and humidity,
- Temperature of the concrete at the time of placement, and
- Aggregate type.

The rate of cement hydration is sensitive to the initial mixture temperature of the concrete as shown in the adiabatic temperature rise of Figure 6.3. It is shown that increasing the hydration temperature of concrete increases the adiabatic temperature rise

or heat of cement hydration at early ages. However, it leads to a lower long term adiabatic temperature rise of concrete.

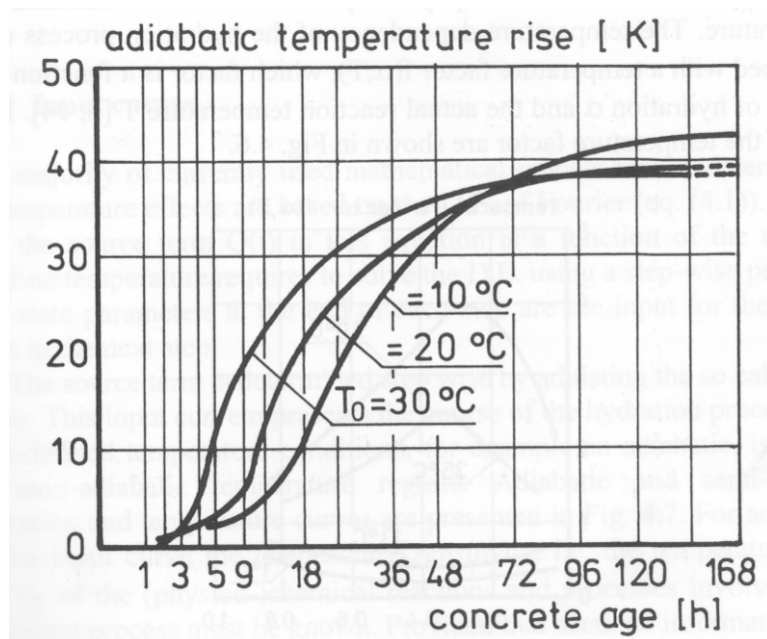


Figure 6.3: Adiabatic temperature curves as a function of mixture temperature (Springenschmid, 1999).

6.2.1 Measurement of Temperature

Many techniques have been created to determine the temperature rise (or heat of hydration) in concrete. Available testing methods for measurement of the temperature rise can be classified into three groups: isothermal (i.e., constant temperature), adiabatic (i.e., no heat loss) and semi-adiabatic (minute heat loss with a heat loss correction). The isothermal method is usually used to measure the heat generated by a pure, cement-paste sample held at constant temperature. The size of the sample makes this test difficult to conduct. In an adiabatic calorimeter, no heat is exchanged with surrounding environment. This type of calorimeter can be expensive to use. Semi-adiabatic calorimeters allow a limited heat exchange with environment. The semi-adiabatic method is commonly used in commercial applications with equipment like the Q-drum (Wang et al., 2006).

The prediction of the temperature rise in concrete is useful to engineers and designers interested in producing a durable, high-performance, concrete structure. Failure to consider the temperature rise in these materials can result in thermal cracking. The rise in the adiabatic temperature curve is directly proportional to the rate of concrete heat loss and results from cement hydration over time. This relationship enables characterization of heat generation by thermally isolated concrete, given a particular concrete-mixture proportion, and casting temperature. The type of cement, unit cement content, and initial temperature at casting are the main factors that affect the adiabatic temperature rise (Maekawa, 1999.) An example of an adiabatic temperature rise graph can be seen in Figure 6.4.

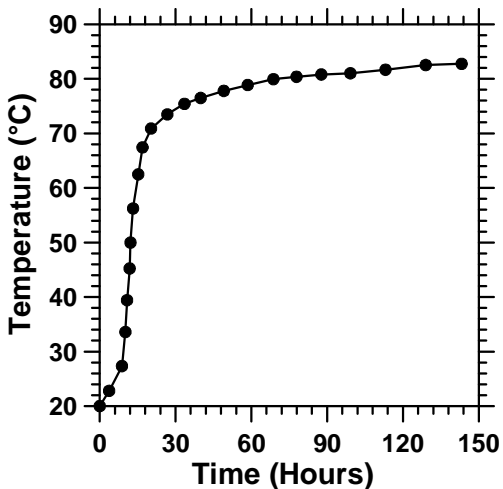


Figure 6.4: Adiabatic temperature curve for a concrete with w/c of 0.35 (Bentz, 1998).

Adiabatic calorimeters are categorized according to the insulating medium (e.g., water, air, or a heated container) used to control the specimen temperature.

Numerous efforts have been made in the recent years to develop heat models to simulate the hydration of portland cement concrete. In the next section, the models incorporated in the FEMMASSE heat simulations are discussed.

6.2.2 FEMMASSE Heat Models

The heat of hydration for a given concrete mixture can be input using the “source” tab of the MPE and the “Adiabatic Evolution” window contains a graph of the temperature versus time. The graph can also be adjusted for different starting temperatures. A layout of Adiabatic Evolution curve in MPV is shown in Figure 6.5. This graph demonstrates the adiabatic temperature rise of concrete over the first 168 hours.

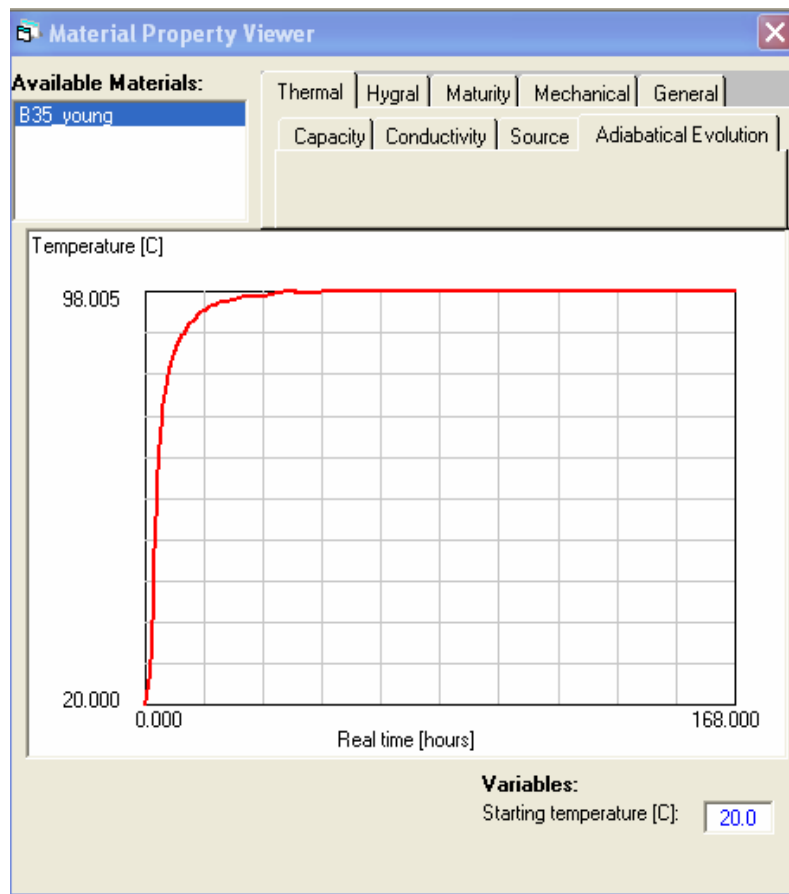


Figure 6.5: An overview of Material Database Viewer of FEMMASSE.

Five different heat source options are provided in the MLS Database. Using the option “no heat source” results in no temperature rise in the concrete due to cement hydration. However, a “constant” heat rate of hydration in ($\text{kJm}^{-3}\text{s}^{-1}$) provides an unrealistic, linear, heat-of-hydration evolution for concrete. It has been suggested that the heat-of-hydration evolution should follow a sigmoidal path (Hansen et. al., 1985).

The hydration of cement is an exothermic reaction. The degree of hydration (α), defined as the ratio of the quantity of hydrated cement to the total quantity of cement. This represents the fraction of the cement that has been hydrated, and it varies between 0% at the beginning of hydration and 100% after the hydration is completed. It is worth mentioning that a full hydration may never be achieved in reality. Van Breugel (1998) suggested that the ratio of the released heat of hydration to the total heat of hydration provides a good measure of the degree of hydration. This is shown in Equation (6.1):

$$\alpha(t) = \frac{H(t)}{H_T} \quad (6.1)$$

where, $\alpha(t)$ is the degree of hydration at time t , $H(t)$ is the released heat of hydration, and H_T represents the total heat of hydration.

6.2.2.1 Core Model

In 1956, Bernhardt suggested a hyperbolic strength-maturity function to describe the strength development of concrete with age. The American Concrete Institute adopted the same function to obtain the strength gain of concrete. This strength-maturity function is as follows:

$$S = \frac{M}{\frac{1}{A} + \frac{M}{S_\infty}} \quad (6.2)$$

where, M is maturity index, S_∞ is the ultimate strength, and A is the initial slope of strength-maturity curve.

Carino (2004) proposed an offset maturity of M_0 to modify the function as strength does not develop immediately in concrete. M_0 shifts the strength maturity graph to the right by the value of M_0 . By substituting the $A = K.S_\infty$ and including the offset value in Bernhardt equation, the following function can be obtained in which K is a constant value.

$$S = S_{\infty} \frac{K.(M - M_0)}{1 + K.(M - M_0)} \quad (6.3)$$

Knudsen considered the degree of hydration instead of strength and developed a similar function to Equation (6.3). He proposed that the hyperbolic function can be employed to describe the strength gain and any other property of concrete that is directly related to the degree of cement hydration such as heat of hydration. Consequently, the Equation (6.4) can be used to compute heat of hydration of concrete at any maturity. FEMMASSE software uses the same heat model for analysis (Shrinkage Core Model (SCM) or Core Model) as shown in Figure 6.6.

$$H(M) = H_T \frac{a(M - d)}{1 + a(M - d)} \quad M > d \quad (6.4)$$

where, $H(M)$ is the heat of hydration at maturity M , H_T is the total heat of hydration ($\text{kJ/M}^3/\text{K}$), d is the maturity offset value or the dormant period (T), and a is the model coefficient ($1/\text{T}$).

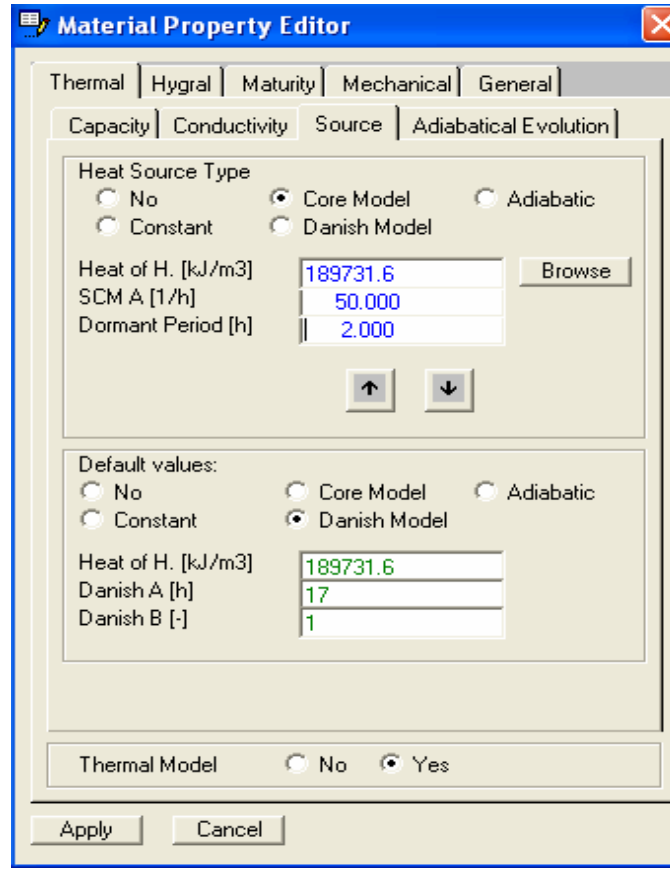


Figure 6.6: A window illustrating the Core Model (i.e., Equation 6.4).

6.2.2.2 Danish Model

Hansen and Pedersen (1985) proposed that the exponential function of Equation (6.5) can be applied to effectively define the development of the degree of hydration. This relationship produces a sigmoidal or S-shaped curve, and can be employed to describe the heat of hydration and strength gain at early ages.

$$\alpha(t_e) = \alpha_u \cdot \exp\left(-\left[\frac{\tau}{t_e}\right]^\beta\right) \quad (6.5)$$

where $\alpha(t_e)$ represents the degree of hydration at equivalent age t_e (hour), τ is the hydration time parameter in (hour), β is the hydration shape parameter (unitless), and α_u corresponds to ultimate degree of hydration (unitless).

After combining Equation (6.1) and Equation (6.5), the amount of heat released during hydration at an equivalent age t_e can be obtained from Equation (6.6).

$$H(t_e) = H_T \cdot \exp\left(-\left[\frac{\tau}{t_e}\right]^\beta\right) \quad (6.6)$$

This relationship (i.e., Equation 6.6) first proposed by Hansen describes the early parts of heat of hydration curve of concrete in which rapid heat evolution occurs. To illustrate the role of each coefficient, three curves (i.e., H1, H2, and H3) are plotted in Figure 6.7 using Hansen's function and the coefficient values displayed in Table 6.1. If the value of time parameter, τ , changes, the general shape of graph remains the same while the graph is shifted to the left or to the right. This can be observed when H1 and H3 curves are compared. The shape parameter, β , determines the shape of a curve. An increase in the β value changes the curve shape into a more S-shaped curve (i.e., a rapid increase in the middle portion of the curve followed by a relatively flat segment). Comparing the H1 and H2 curves of Figure 6.7 illuminates the role of the shape parameter in the general shape of the curve.

Table 6.1: Hansen's function coefficients for curves shown in Figure 6.7.

	τ	β
H1	1	0.4
H2	2	0.4
H3	1	1.6

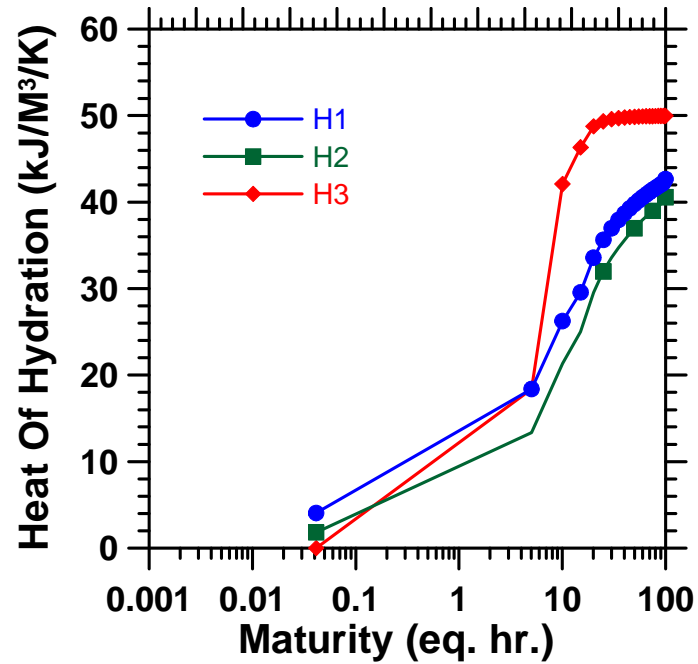


Figure 6.7: Heat of hydration curves using Hansen's function.

In FEMMASSE, Equation (6.7) (which was initially proposed by Hansen) is described as the Danish Model:

$$H(M) = H_T e^{-\left(\frac{a}{M}\right)^b} \quad (6.7)$$

where, $H(M)$ is the amount of the released heat of hydration at maturity M in (kJ/M³/K), H_T is the total heat of hydration in (kJ/M³/K), and b is the hydration shape coefficient (unitless), and a is the hydration time coefficient in (T). A layout of the Danish model in MPE is shown in Figure 6.8.

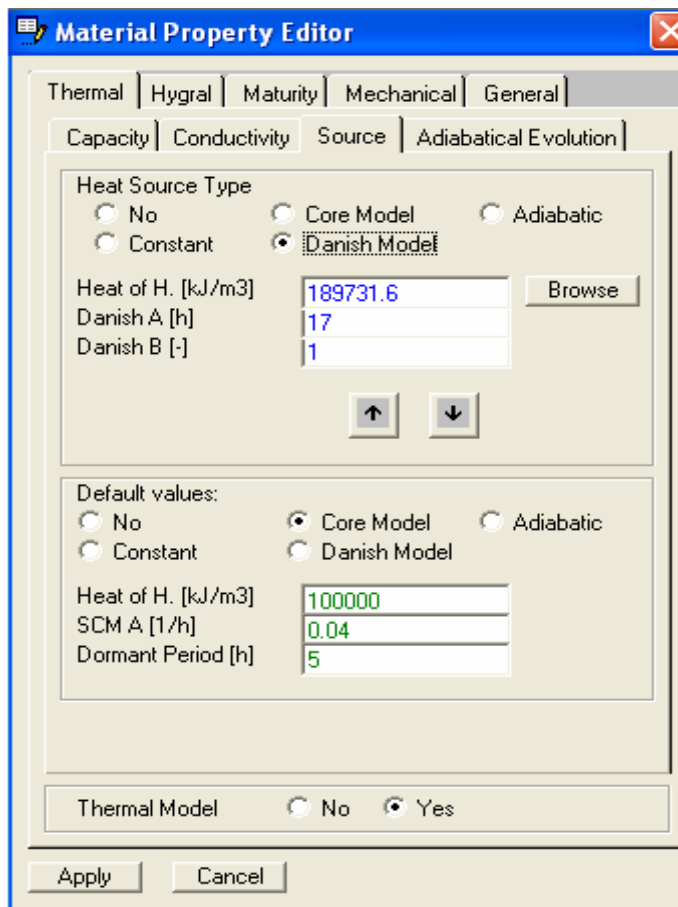


Figure 6.8: Layout of the Danish Model (available under the “Source” sub-tab).

6.2.3 Thermal Conductivity

Thermal conductivity of concrete is the ability of concrete to conduct heat through a unit volume over a unit change in temperature. Mineralogical characteristics of aggregates and moisture content are among the main factors influencing the thermal conductivity of concrete. Any rise in moisture content of concrete results in an increase in thermal conductivity of concrete as water has a higher thermal conductivity than that of air. Mindess (2003) suggests that the thermal conductivity for typical concrete varies from 1.4 (W/m.K) for a dry condition with 1% moisture to 2.4 (W/m.K) for a wet condition with 10% moisture.

In MLS Database, thermal conductivity can be set to be either moisture dependent or constant. If the thermal conductivity ($\text{Jm}^{-1}\text{K}^{-1}\text{s}^{-1}$) of concrete is set to be moisture

dependent, it will vary linearly with its moisture content. A typical layout of MLS Database window for a moisture-dependent conductivity plot is shown in Figure 6.9.

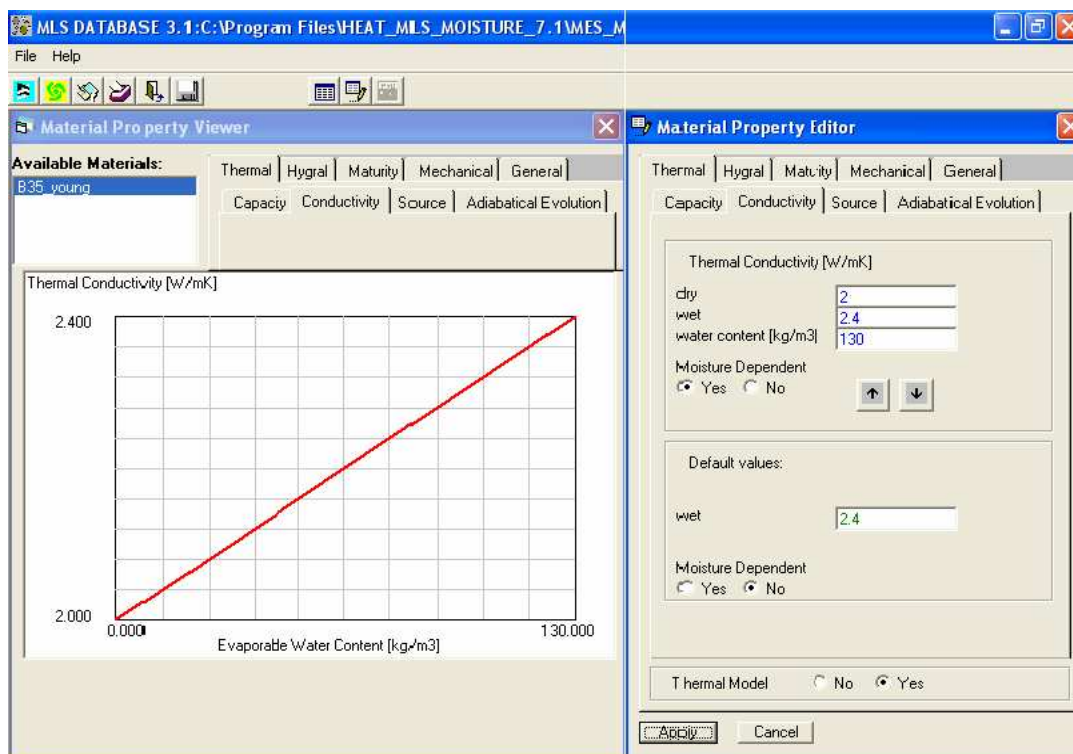


Figure 6.9: Layout of the MLS Database thermal conductivity window.

6.2.4 Thermal Capacity

Thermal heat capacity is defined as the amount of heat needed to increase the temperature of a unit mass of material by a unit degree. It depends on the water content, paste fraction, and porosity of concrete. It is known to vary from 850 to 1170 (J/kg/°C) for ordinary concrete (Springenschmid, 1998).

In MLS Database, the thermal capacity is modeled similarly to the thermal conductivity, and it can be either constant or moisture dependent.

6.3 Maturity Model

Cement hydration and concrete strength depend greatly on temperature history. Therefore, the strength development data obtained under standard laboratory conditions cannot be used directly to predict the strength development of concrete in the field.

Arrhenius derived the following empirical equation to describe the temperature dependence of the reaction rate constant, k , in homogenous chemical systems. He demonstrated that higher temperature results in an increase in the kinetic energy of molecules, and consequently an increase in reaction rate.

$$k = Ae^{\frac{-E}{RT}} \quad (6.8)$$

where, k is the rate constant of the reaction, A is the frequency coefficient related to the frequency of collisions of molecules, E is the activation energy in (J/mole), R is the universal gas constant (8.3144 J/(mole.K)), and T is the absolute temperature in (°K).

In 1977, Freiesleben Hansen and Pedersen proposed the following function based on the Arrhenius law to predict equivalent age of concrete at early ages:

$$t_e = \sum_0^t e^{\frac{-E}{R} \left[\frac{1}{273+T} - \frac{1}{T_r} \right]} \Delta t \quad (6.9)$$

where, t_e is the equivalent age at the reference temperature, T is the average temperature of concrete during time period of Δt in (°C), T_r is the reference temperature (293 °K), E represents the activation energy in (J/mole), R also represents the universal gas constant which is 8.3144 (J/(mole.K)).

The activation energy depends greatly on temperature, and plays an important role in the Hansen's function. Hansen and Pedersen proposed the following formula to predict the activation energy:

For $T \geq 20^\circ\text{C}$

$$E = 33,500 \text{ J/mole} \quad (6.10 \text{ a})$$

For $T < 20^{\circ}\text{C}$

$$E = 33,500 + 1470 (20 - T) \text{ J/mole} \quad (6.10 \text{ b})$$

Bazant (1982) proposed that the pore relative humidity “ h ” ($0 \leq h \leq 1$) influences the maturity of concrete. He proposed the following function in which the first term is Equation 6.9 and describes the effect of temperature history on maturity. The second term is an empirical function of h describing the role of relative humidity on maturity.

$$M(t) = \int_{t_{con}}^t e^{\frac{E}{R} \left[\frac{1}{T_{ref}} - \frac{1}{T+273} \right]} \left[\frac{1}{1 + (a_c - a_c h)^{b_c}} \right] dt \quad (6.11)$$

where, t is the real time, t_{con} represents time at concreting, E is the activation energy (40000 J/mole), R is universal gas constant ($8.314472 \text{ (J} \cdot \text{K}^{-1} \cdot \text{mole}^{-1})$), T_{ref} is the reference temperature ($293 \text{ }^{\circ}\text{K}$), T is the temperature at time t in ($^{\circ}\text{C}$), and a_c (≈ 5) and b_c (≈ 4) are the unit-less function coefficients which are determined experimentally.

Equation 6.11 is used in FEMMASSE software to calculate the maturity as a function of time, temperature and relative humidity. A layout of Arrhenius maturity window of MLS Database is shown in Figure 6.10.

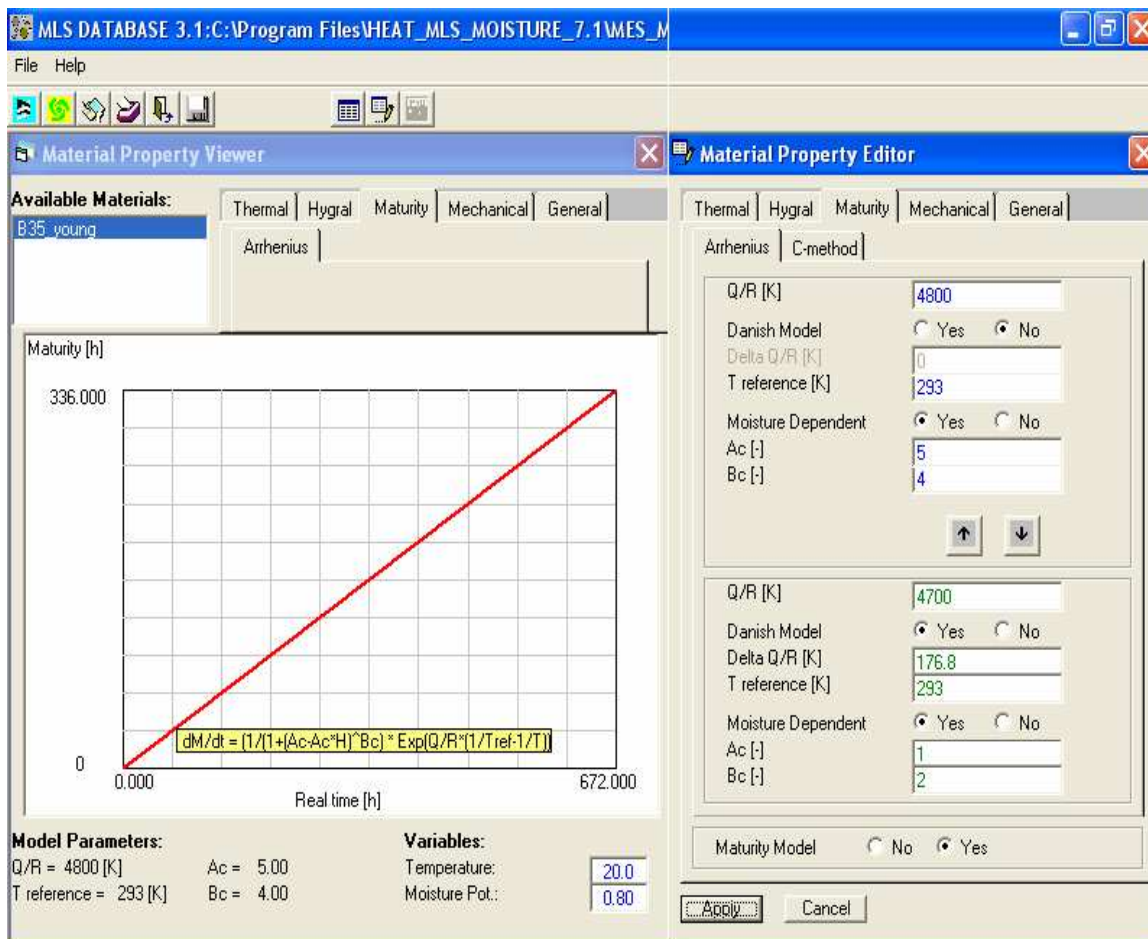


Figure 6.10: Layout of MPE and MPV windows in MLS Database after the maturity function is activated.

6.4 Hygral Behavior of Concrete

When concrete is exposed to an external environment with a lower relative humidity, water molecules start to depart the concrete surface. This phenomenon is called desorption. However, if the humidity of concrete is less than the humidity of surrounding environment, concrete begins to absorb water. The evaporation of water from the concrete surface is typically a slow process, and mainly depends on the curing time, water to cement ratio, cement type and concrete temperature (Bazant et al., 1994).

Water evaporation from the concrete surface is a diffusion-controlled process. In 1971, Bazant and Najjar proposed the following function based on the Fick's Law to predict the drying of concrete for a concrete slab:

$$\frac{\partial h}{\partial t} = \frac{\partial h}{\partial x^2} \left(D_0 \left[a + \frac{1-a}{1 + \left(\frac{1-h}{1-h_c} \right)^4} \right] \right) \quad (6.12)$$

where, D_0 is the diffusion coefficient (at 100% RH, $\approx 7.8E-7$ for a 0.30 meter slab), h is the relative humidity, x is the slab thickness, and a and h_c are coefficients (unitless) determined by experiment ($a \approx 0.05$ and $h_c \approx 0.75$ for a 0.30 meter slab).

In FEMMASSE, Equation 6.12 is used to model the evaporation of water from the concrete at different relative humidities. Figure 6.11 shows a MLS Database layout that displays a graph of evaporable water content.

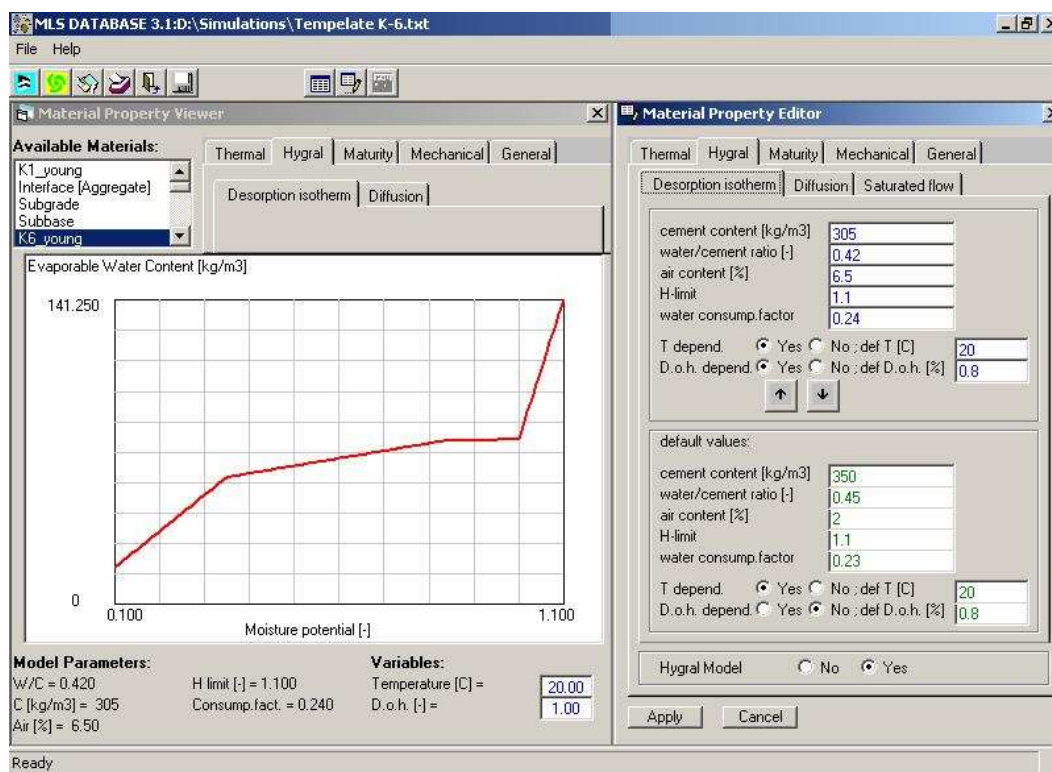


Figure 6.11: Desorption isotherm layout of MPE and MPV windows.

6.5 Time-Dependent Deformation of Concrete

6.5.1 Thermal Expansion

Thermal dilation caused by temperature changes can generate serious cracking problems in concretes exposed to differential heating or cooling. The thermal expansion is directly related to temperature changes and the coefficient of thermal expansion as shown in Equation (6.13). It should be noted that a constant coefficient of thermal expansion (CTE) of $6 \text{ E-}6 \text{ (1/}^\circ\text{C)}$ was used to model concrete thermal behavior. The equation that describes this process is

$$\Delta\varepsilon = \alpha \cdot \Delta T \quad (6.13)$$

where, $\Delta\varepsilon$ is the change in strain, ΔT is the change of temperature T ($^\circ\text{K}$ or $^\circ\text{C}$), and α is the thermal dilation coefficient in $(\text{L/L}/^\circ\text{C})$ or $(\text{L/L}/^\circ\text{K})$.

6.5.2 Autogenous Shrinkage

Autogenous shrinkage is the volume change of concrete due to self-desiccation. It is considered to be a paste property and can lead to cracking, warping, or curling of restrained concrete members. Pease (2005) measured the autogenous shrinkage for 0.30 and 0.50 w/c mortars with 55% aggregate by volume. He cured his specimens at room temperature and measured the changes in specimen length over 28 days. The reader is referred to Pease's thesis for further detail on the shrinkage measurements. Using the data obtained from his experiments, and Equation (2-1) of ACI 209.1R-05 report, the following autogenous shrinkage data were obtained and used to model the early age shrinkage of a concrete with 70% aggregate by volume and 0.42 w/c

Table 6.2: Autogenous shrinkage used in computer modeling.

Age (hr)	Autogenous Shrinkage ($\mu\epsilon$)
0	0
5	0
29	58
53	125
77	187
173	245
341	328
509	360
672	402

6.5.3 Creep and Relaxation

Concrete is a viscoelastic material that experiences both creep and relaxation, depending on its boundary conditions. The factors that influencing creep are divided into interior factors and external factors. The interior factors includes the strength, elastic modulus of aggregate, volume fraction of aggregate, maximum size of aggregate, grading and mineralogical characteristic of aggregate, water to cement ratio, and type of cement. The temperature, moisture content, and age at loading are among the external factors influencing creep (Bazant, 1988). Creep is directly related to temperature and pore relative humidity of concrete. Although creep is directly related to temperature, it is partially decreased at higher temperatures due to accelerated hydration. Moreover, the creep and relaxation of concrete not only depend on load duration, but are also highly affected by the timing of load application. This is due to the so-called “aging” effect and results from the progressive hydration reactions of concrete as well as recrystallization and polymerization of previously formed hydration products. This effect is more visible at early ages since rapid developments of the material properties affect the time-dependent deformation of concrete.

Bazant (1988) proposed that the creep response of concrete from a load increment is independent on its loading history and that the superposition principle is valid. He suggested that a parallel chain of Maxwell units composed of springs and dashpots (Figure 6.12) can be used to predict the time-dependent deformation of concrete.

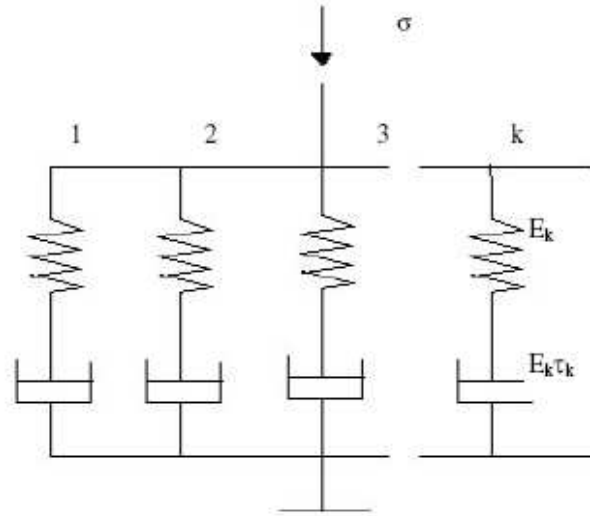


Figure 6.12: Maxwell chain model composed of spring and dashpot units (FEMMASSE manual).

Using a maturity-dependent Maxwell chain model, and assuming a constant incremental strain rate in a time interval from time t^i to time t^{i+1} , the following function is used to predict the time-dependent deformation of concrete in FEMMASSE software:

$$\sigma^{i+1} = E_{ve} A [\Delta \varepsilon^i - \Delta \varepsilon_s^i] + \sigma_c^i \quad (6.14 \text{ a})$$

where,

$$E_{ve} = \sum_{k=1}^m \left[\frac{\tau_k}{\Delta t} E_k \left(1 - e^{-\frac{\Delta t}{\tau_k}} \right) \right] \quad (6.14 \text{ b})$$

$$\sigma_c^i = \sum_{k=1}^m \sigma_k^i \cdot e^{-\frac{\Delta t}{\tau_k}} \quad (6.14 \text{ c})$$

where the σ^{i+1} is the stress at the end of time interval i , the σ_c^i represents the corrected stress at the beginning of time interval i , $\Delta \varepsilon^i$ is the total strain increment, $\Delta \varepsilon_s^i$ is the

shrinkage strain, A is a tensor containing terms of Poisson's ratio, Ek ($k = 1 \dots m$) is the stiffness of the spring in Maxwell unit k (N/mm^2), τ_k is the retardation time (hr), Δt is the duration of time interval, and m is the number of Maxwell units.

To account for the effects of the temperature and pore relative humidity on creep, Bazant proposed the following time correction factor.

$$\Delta t_c = \Delta t \left(a + (1-a)h^2 \right) e^{\frac{E}{R} \left(\frac{1}{293} - \frac{1}{T} \right)} \quad (6.15)$$

where Δt is the time interval, Δt_c is the corrected time period, E is the activation energy (J/mole), R is the universal gas constant, T is the temperature (K), h is the pore relative humidity ($0 \leq h \leq 1$) and a is the function coefficient (unitless). Bazant (1988) proposed that $a = 0.5$ can work well for concrete.

Six Maxwell chains were used to model the viscoelasticity of concrete, and Table 6.3 summarizes the elastic moduli and their distribution over the 6 Maxwell units for different retardation times and at different maturities.

Table 6.3: Maxwell chain model used in modeling the viscoelasticity of concrete.

Maturity [hr]	Elastic Modulus [MPa]	Retardation Times [hr]					
		1	10	100	1000	10000	100000
Distribution of E Over the Maxwell Units							
0	500	0	0	0.2	0.8	0	0
9	6582	0	0	0.2	0.8	0	0
18	12947	0.033	0.092	0.261	0.658	0	0
24	15841	0.029	0.110	0.145	0.600	0.114	0
48	23160	0.054	0.089	0.154	0.338	0.364	0
100	29574	0.064	0.066	0.169	0.145	0.555	0
300	33526	0.053	0.084	0.146	0.292	0.425	0
1344	36100	0.034	0.056	0.102	0.152	0.156	0.500

Figure 6.13 shows that upon loading the Maxwell file into the MLS Database, a graph of total strain versus time for different values of stress and maturity at loading is shown in MPV window.

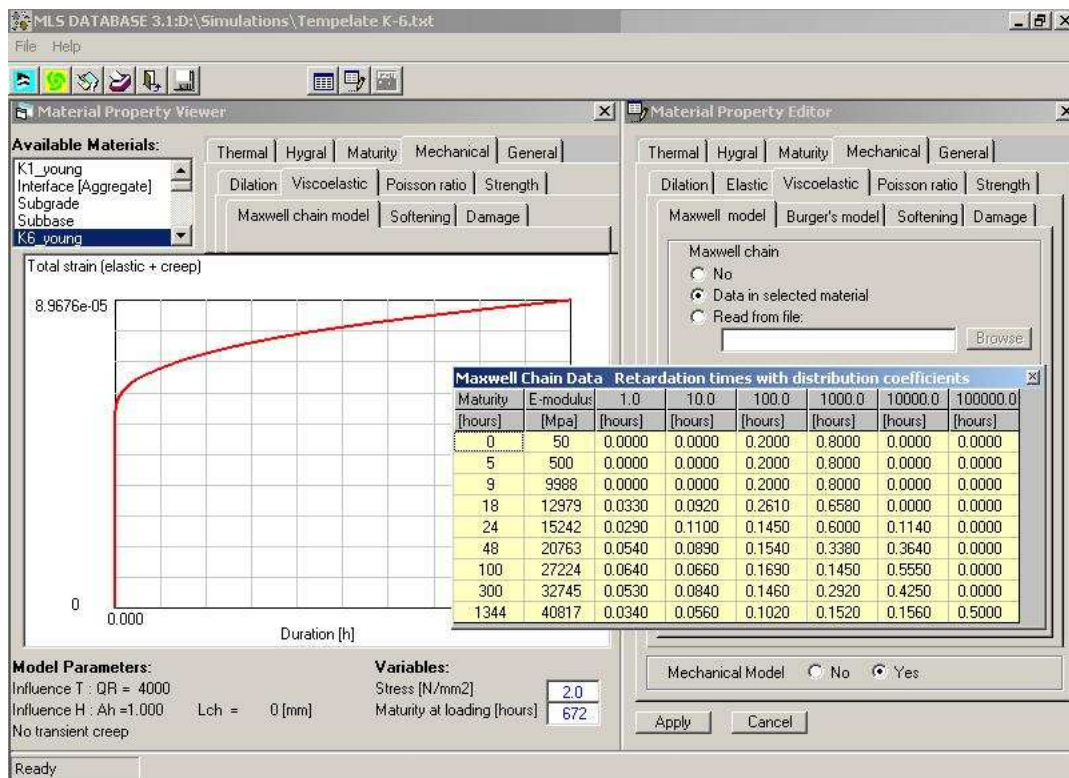


Figure 6.13: Maxwell model layout of MPE and MPV windows in MLS Database.

6.6 Stress Behavior of Concrete

6.6.1 Elastic Modulus

The dynamic modulus of elasticity is considered as the true elastic response of concrete. Its measurement involves the use of a nondestructive ultrasound pulse velocity test to obtain the stress response of concrete due to small displacements. The sensitivity of the passing time of a pulse wave (through a given length of concrete) to concrete's elastic properties is the underlying principle of this technique

Barde (2004) performed ultrasonic pulse velocity (UPV) tests to measure the development of the dynamic elastic modulus for concrete with 0.42 w/c and 70% aggregate by volume. The reader is referred to Barde's thesis for further detail on the elastic modulus measurement. Table 6.4 presents his UPV elastic modulus test results that were used in modeling.

Table 6.4: The measured UPV elastic modulus Barde (2004).

Maturity [hr]	UPV Elastic Mod [MPa]
0	500
9	9988
18	12979
24	15242
48	20763
100	27224
300	32745
1344	40817

6.6.2 Tensile Strength

The tensile strength of concrete is an important factor in the prediction of crack formation. The measured tensile strength and Hansen's function (Equation 6.5) was used to predict the 28-day tensile strength gain of concrete.

$$f'_t(t_e) = f'_{t \text{ Ultimate}} \cdot \exp\left(-\left[\frac{6}{t_e}\right]^{1.5}\right) \quad (6.16)$$

In Eq (6.16), $f'_{t \text{ Ultimate}}$ is the ultimate tensile strength (MPa), and $f'_t(t_e)$ is the tensile strength at equivalent age t_e .

Table 6.5 shows the tensile strength of concrete computed using Equation 6.16 at some selected maturities.

Table 6.5: Tensile strength values used in computer modeling.

Eqv. Age (hr)	Tensile Strength (MPa)
5	0.81
15	2.34
25	2.68
50	2.89
75	2.94
100	2.97
200	2.99
400	3.10
672	3.20

6.6.3 Compressive Strength

The measured compressive strength of concrete specimens that were presented in Chapter 5 was used in finite element analysis as shown in Table 6.6.

Table 6.6: Compression strength values used in finite element analysis.

Eq. Age (hr)	Compressive Strength (MPa)
0	0.001
5.00	0.001
6.15	0.30
9.77	2.03
13.16	7.53
22.06	13.66
32.23	16.82
61.70	23.64
84.35	27.18
168.00	34.46
672.00	40.00

6.6.4 Softening Behavior

After crack formation, a zone containing micro cracks develops at the crack tip. This zone is called the fracture process zone and controls the post-crack behavior of concrete. Hillerborg (1978) developed a model called the Fictitious Crack Model to predict the softening behavior of concrete. This model assumes a linear elastic behavior before the peak load in a uni-axial loading is reached. When the peak load is reached, a localized fracture zone develops across the entire cross section. The model suggests that fracture zone stress decreases with increasing deformation or crack width. This behavior is shown schematically in Figure 6.14.

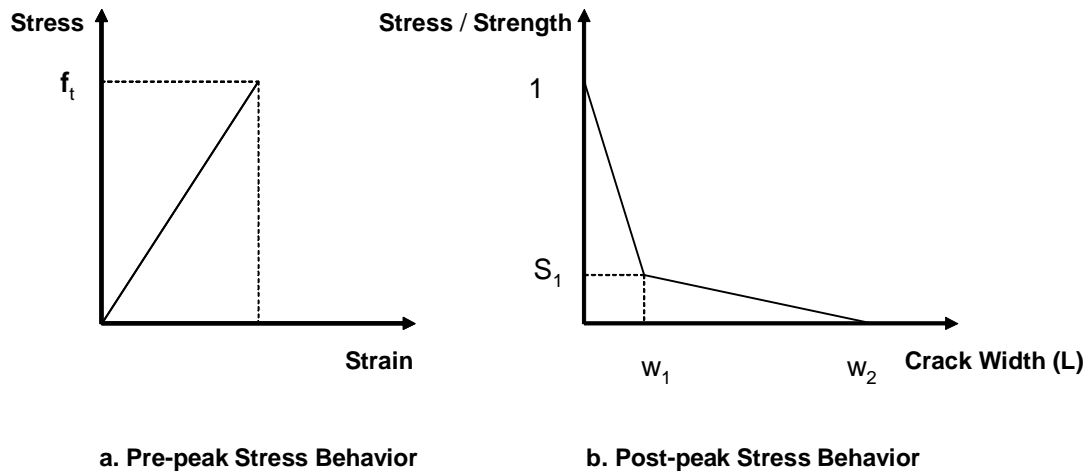


Figure 6.14: Pre-peak and post-peak behavior of concrete in a deformation control experiment.

Østergaard (2003) investigated the softening behavior of concrete, and determined the stress-crack opening relationship by performing 10 tensile wedge splitting tests. Figure 6.15 shows the measured stress-crack width results of his experiments. The middle line in this figure is the average stress-crack width, and the other two lines are boundaries on the standard deviation. The average values were used to model a bilinear softening behavior of concrete in FEMMASSE software.

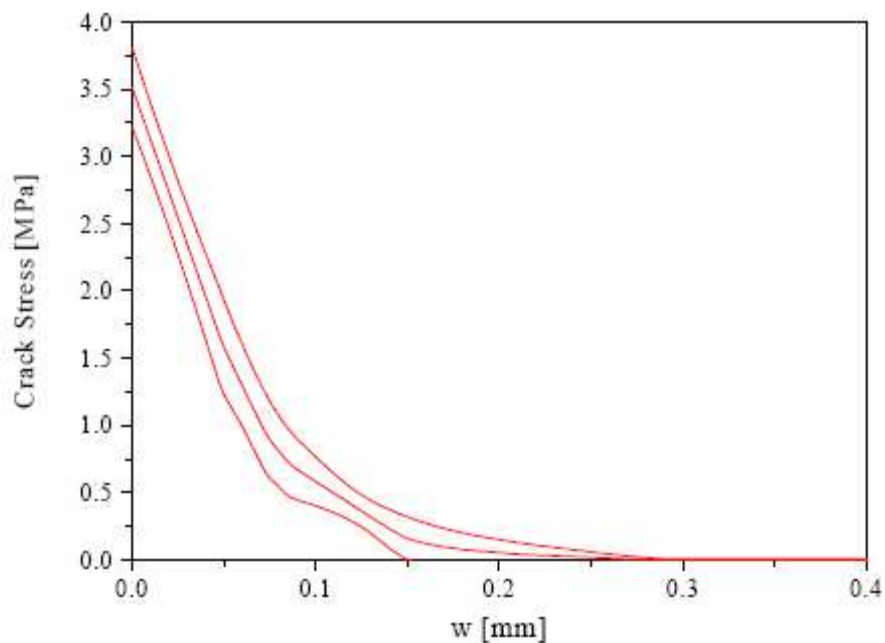


Figure 6.15: Stress-crack opening graph obtained from the wedge splitting test Østergaard (2003).

A bilinear softening model based on the Hillerborg model (1978) was used to model the softening behavior of concrete. This model requires three parameters as shown in Table 6.7. Tensile strength factor S_1 (σ/f_t) and crack width w_1 (mm) define a knee point in the stress-crack width graph and w_2 corresponds to the critical crack width at which no stress is transferred across the crack. Figure 6.16 illustrates the isotropic bilinear softening graph presented for the softening parameters shown in Table 6.7.

Table 6.7: Softening parameters used in computer simulations.

S_1 [-]	w_1 [mm]	w_2 [mm]
0.2	0.8	2.5

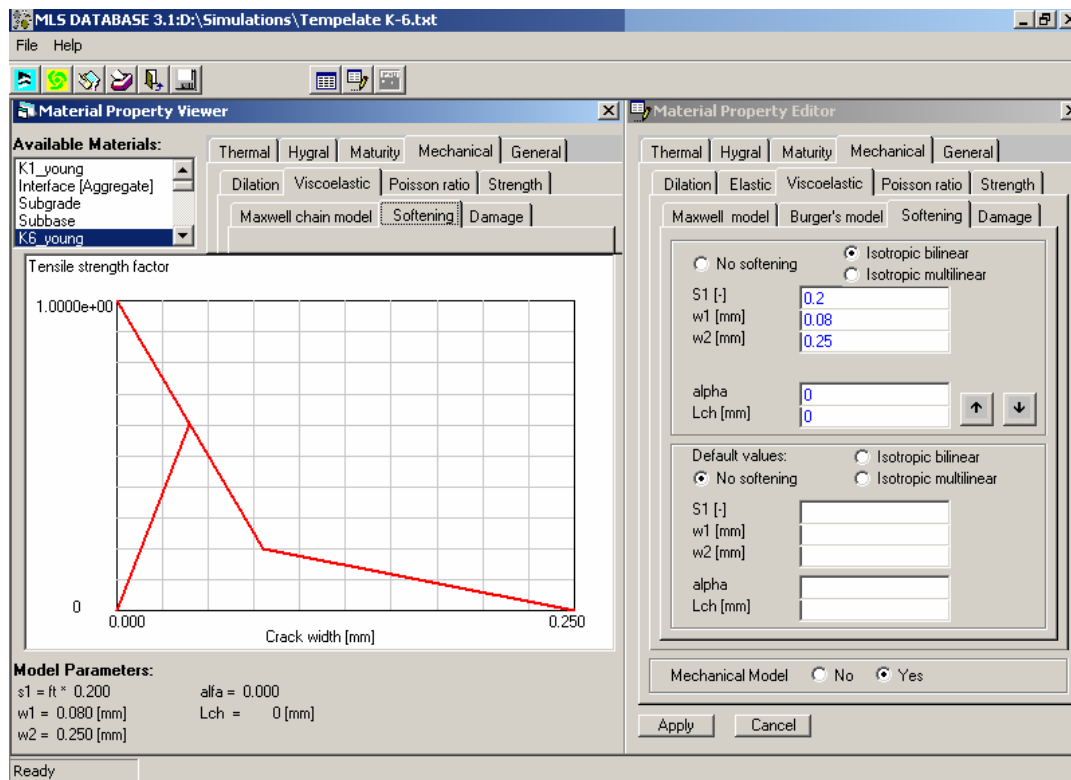


Figure 6.16: MPE and MPV layouts of the softening model window in MLS Database.

6.7 Boundary Conditions

6.7.1 Hygral Boundary Condition

The outer zone of concrete can be largely influenced by a change in the relative humidity of environment. In order to remain at equilibrium with its environment, concrete gradually loses internal water. The drying of concrete can result in volume changes, residual stress development and micro-crack development.

In FEMMASSE, a prescribed relative humidity and moisture transfer coefficient can be assigned to create a hygral convective boundary condition for any macro. The program assumes a zero moisture flux if no value is assigned. A layout of the hygral boundary condition window is shown in Figure 6.17. Note that two boundary modes of evaporation and water pressure are available for each boundary. When the evaporation

option is selected, a moisture transfer coefficient and surrounding relative humidity function must be defined for each defined time period.

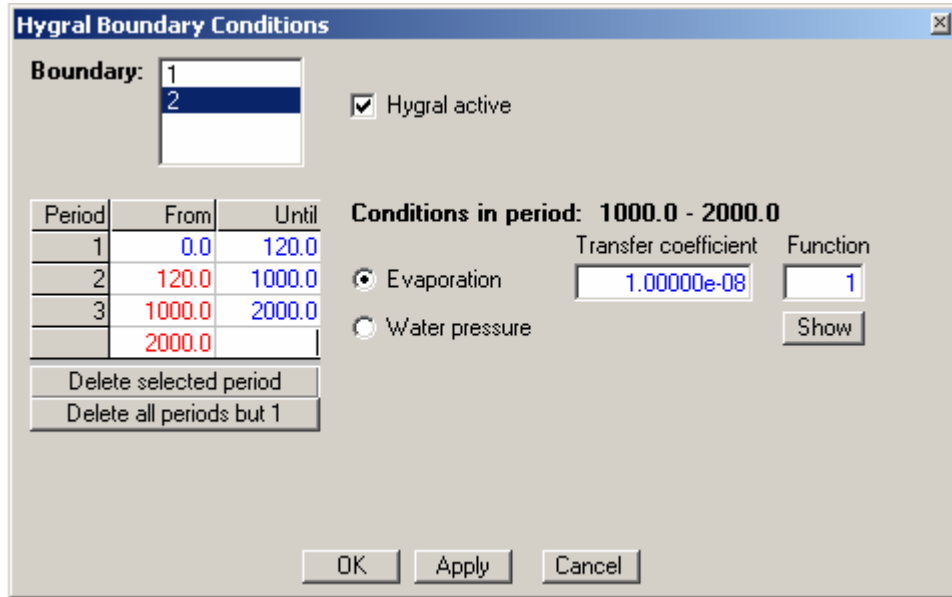


Figure 6.17: Layout of the hygral boundary property window.

The following relationship is used in the software to estimate the moisture variation at the macro boundaries:

$$q_c = b(H - H_e) \quad (6.17)$$

where q_c is the moisture flux through and perpendicular to boundary C (ms^{-1}), H is the relative humidity at boundary C (unitless), b is the moisture transfer coefficient (ms^{-1}), and H_e represents the external or environmental relative humidity (-).

6.7.2 Thermal Convection Boundary Condition

The following function is used in FEMMASSE software to consider the convection of heat of concrete through its boundaries:

$$\vec{q}_B = a(T - T_e)_B \quad (6.18)$$

where q_B is the heat flux normal to boundary B , a is the heat transfer coefficient, and T_e is the outside temperature.

FEMMASSE software uses the following two functions to estimate the convection coefficient at a given wind speed for uncovered surfaces.

$$a_{conv} = 5.6 + 4.0v_{wind} \quad v_{wind} \leq 5m/s \quad (6.19 a)$$

$$a_{conv} = 7.2 \times v_{wind}^{0.78} \quad v_{wind} > 5m/s \quad (6.19 b)$$

6.7.3 Subbase and Subgrade

Subbase is a foundation of compacted materials layer placed on a prepared subgrade. The subbase and subgrade also play a role in heat transfer in the concrete. This influences the thermal gradient and thermal stress development in the concrete.

In modeling the pavements, a single layer of subbase was placed over a deep layer of subgrade. The following table summarizes the properties of each layer.

Table 6.8: The subbase and subgrade properties.

Material	Heat Capacity (kJ/m ³ K)	Thermal Conductivity (W/m/K)	Density (kg/m ³)	CTE (μ 1/C)	Poison Ratio
Subbase	1450	2	1800	5	0.40
Subgrade	1000	1	1700	5	0.35

The friction between the pavement and the subbase is also an important factor in pavement movement and random cracking development. As such, a friction layer was defined between the subbase and the pavement. It should be noted that a shear stiffness of 30 (N/mm³), and a friction angle of 45° was defined to model this layer (Haung, 1993).

6.8 Summary

This research in large part involves in the determination of the time and depth of saw-cut taking into consideration the various environmental conditions and constituent materials. The finite element software, FEMMASSE, was employed to determine the time and depth of saw-cut for a given concrete material. This chapter has described the general property of the materials, boundary conditions, and the functions incorporated in the FEMMASSE software. The accuracy and significance of the functions used in the analysis has been shown by many over the past decades.

CHAPTER 7: SIMULATION OF SAW-CUTTING IN CONCRETE PAVEMENTS USING FINITE ELEMENT ANALYSIS: AN OVERVIEW OF TYPICAL MODEL DEVELOPMENT INPUTS AND OUTPUTS

7.1 Introduction

Saw-cutting is used to control cracking in concrete pavements. Currently however, paving construction crews do not have sufficient tools to determine the optimal time at which saw-cutting should be performed. If the saw-cut is placed too early, spalling and raveling of joints may occur. Alternatively if the saw-cut is placed too late, the risk for micro-cracking and random cracking increases.

This chapter provides an overview of the steps involved in using a computer modeling as a method to simulate the effect of saw-cutting in concrete pavements. The FEMMASSE software will be used to perform simulations of concrete pavements at early ages to simulate the influence of saw-cutting depth, slab thicknesses, timing of construction operations, and environmental conditions (relative humidity, wind speed, and temperature). In addition to discussing the model geometry and input parameters, the simulation outputs will be discussed.

7.2 General Modeling Approach

7.2.1 Description of the FEMMASSE Software Used in Computer Simulations

This study used the finite element software program FEMMASSE (Finite Element Modules for Materials Science and Structural Engineering). FEMMASSE was selected for this study since it enables:

- Hydration to be considered in the simulation thereby enabling the material properties to be updated throughout the simulation based on the use of a maturity function. In addition temperature rise can be predicted due to the heat of hydration.
- Non-linear fracture mechanics, creep, and stress relaxation to be considered in the simulation,
- Construction sequencing to be directly simulated by enabling a saw-cut to be placed during a simulated construction sequence.
- Temperature, moisture content, and wind speed to be directly assessed to compute the temperature and moisture at each point of the pavement at each time during the simulation.

The FEMMASSE software enables the stress, displacement, moisture condition, temperature, and cracking to be calculated throughout the pavement section for different material properties, mechanical boundary conditions, construction sequences, and environmental boundary conditions.

7.2.2 The Development of a Pavement Model Inputs

A model was developed to simulate concrete pavement behavior at early ages. This model considers a two-dimensional pavement section (with unit thickness) that is mechanically restrained at either end. This pavement is supported in the vertical direction on a subbase which rests on a subgrade. The concrete was allowed to hydrate over time. The simulation was begun at the time of casting and a saw-cut was introduced in the pavement as hydration proceeded. Finally, different thermal, wind, and moisture boundary conditions are applied. Details on the modeling inputs are described in the following section.

7.2.2.1 The Pavement Geometry

A pavement section was considered that contained the saw-cut (note: the saw-cut will be added at any specified time) at the center of the pavement as shown in Figure 7.1. The length of the pavement was considered to be 5.4 meters (18 feet) based on the

Indiana Department of Transportation (INDOT) Manual for Concrete Paving (published on 3/01/2005) to simulate the distance between the saw-cuts in the field. This enabled the pavement to be simulated from the mid-panel of each pavement section around the saw-cut. For the baseline case, a pavement thickness of 380 mm (15 inches) was used. However, the thickness of concrete pavement was varied from 254 mm (10 inches) to 432 mm (17 inches).

7.2.2.2 The Subbase and Subgrade

Based on section 302 of the INDOT specifications, a 225 mm (9 inches) thick subbase was defined below the concrete pavement. The drainage level of the subbase and the separation layer of the subbase were considered as a single composite level for simulations.

The pavement and subbase were placed on a 2300 mm (90.5 inches) deep subgrade. The thickness of the subgrade was chosen to be large enough to act as a heat sink (i.e., the lower boundary did not influence the temperature development). The initial temperature of the subgrade was assumed to be 13°C (55.4°F) (Bentz, 2000).

7.2.2.3 The Saw-cut Geometry

A saw-cut could be introduced in the concrete pavement at any time during the simulation analysis. For the majority of simulations, a D/3 saw-cut was placed at the mid-span of the slab. The depth of the saw-cut was also varied to investigate the effect of different saw-cutting depths on pavement behavior. The width of the slab was considered to be a unit thickness of 1000 mm. The width of the saw-cut is considered to be 4 mm (1/8 inches) based on Chapter 3 of INDOT guidelines and INDOT standard drawing of “E 503-CCPJ-06” on concrete pavement construction.

7.2.2.4 The Mechanical Boundary Conditions

The slab ends were restrained from moving in x-direction, but were allowed to move freely in “y” and “z” directions as shown in Figure 7.1.

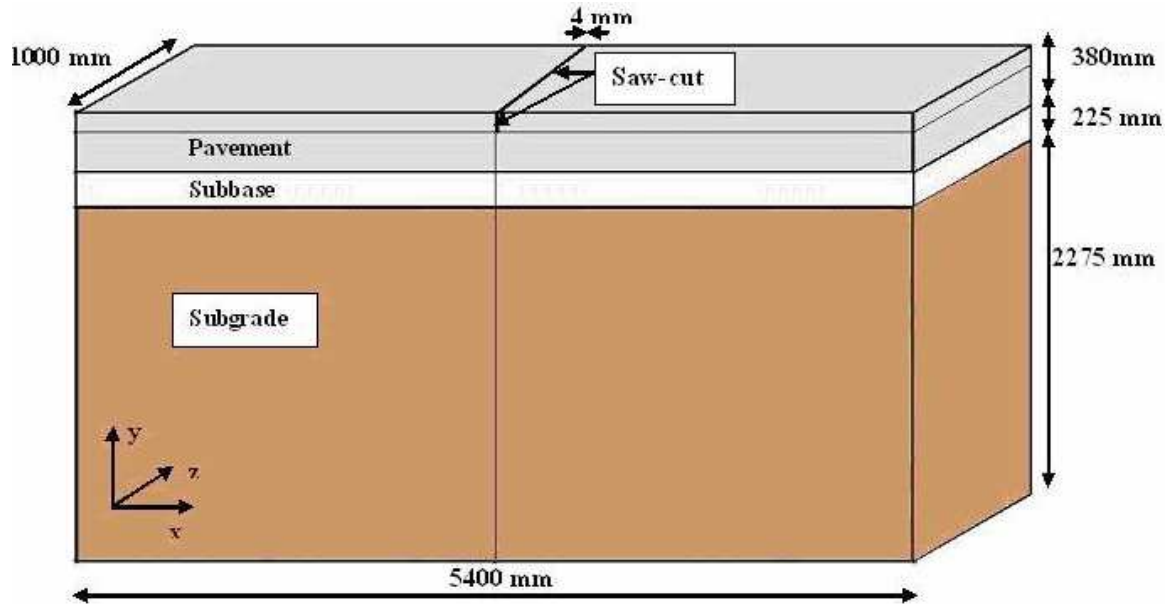


Figure 7.1: A schematic illustration of the finite element model used in analysis consisting of pavement, subbase, and subgrade.

7.2.2.5 The Environmental Boundary Conditions

The FEMMASSE software enables users to specify various ambient temperature and relative humidity functions. For the majority of simulations, a sinusoidal ambient temperature function was used where the ambient temperature fluctuated between 18 and 30 °C with a mean temperature of 24°C as shown in Figure 7.2. It was assumed that the minimum temperature occurs at 4:00 am, and paving operation (and computer simulation) starts at 7:00 am when the temperature is approximately 20°C. It should be noted that for some simulations, the time at which the paving operation was started was varied.

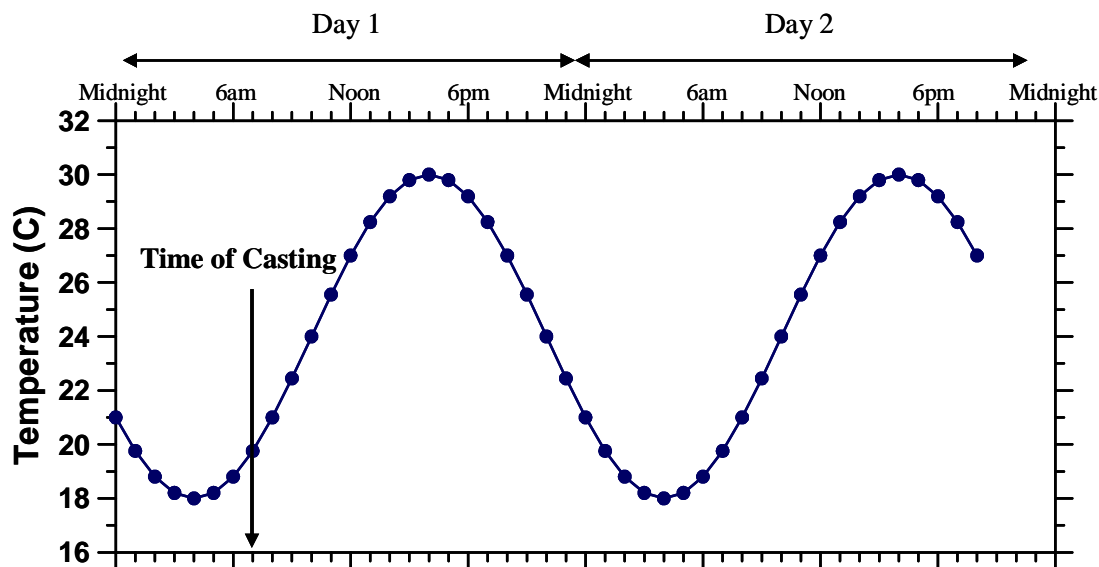


Figure 7.2: Baseline case ambient temperature function.

A constant relative humidity of 75% was used for the base line simulation case. This is about the mean relative humidity experienced in State of Indiana. The surface evaporation rates of concrete covered with curing compound at room temperature and in 50% relative humidity chamber were measured to be 4.3×10^{-7} m/s (1.4×10^{-6} ft/s) during the first 14 hours and 3.4×10^{-8} m/s (1.1×10^{-7} ft/s) throughout later times.

For the majority of simulations, the wind speed was considered to be of 10 m/s (0.33 ft/s). It should be noted that environmental boundary conditions were only defined for the surface of the pavement. It was assumed that the sides and bottom of the model were completely sealed to simulate the field conditions of the material.

7.3 The Data Inputting for Computer Simulation

The FEMMASSE software provides a user friendly preprocessing software to gather the model input. First, the concrete slab, subbase and subgrade are defined. Second, the ambient temperature, relative humidity, and support conditions are assigned to the boundaries. Third, the finite element mesh is created as explained. Fourth, the computational time steps and the intervals for simulation output are defined. Fifth, now that all necessary inputs have been provided, the computation can be started. While the computation is performed, the maximum and minimum values of several quantities

including stress, displacement, and temperature can be observed on the screen during the computation. Finally, when the analysis ends, the results can be viewed and downloaded. The Figure 7.3 provides a summary of the sequence of activities performed in the FEMMASSE software.

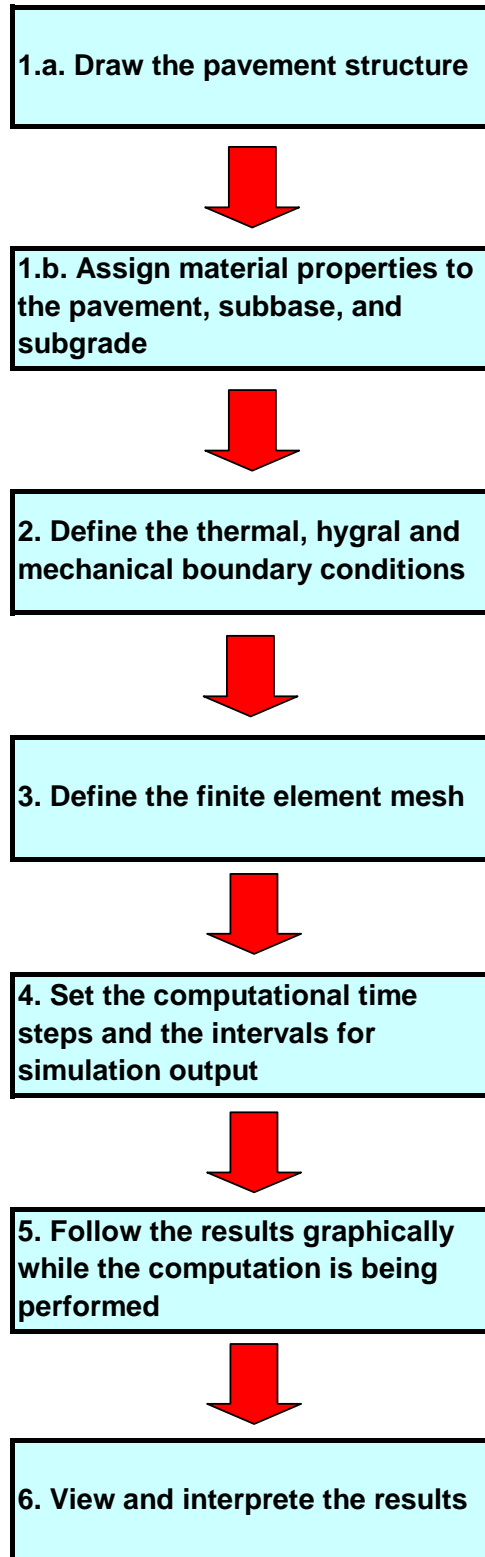


Figure 7.3: Series of actions to be performed in FEMMASSE software (FEMMASSE manual).

7.3.1 Drawing the Slab, Reinforcement, Subbase and Subgrade

Upon opening the FEMMASSE software and loading the material property file (which was discussed in Chapter 6), the software design panel is displayed which is shown in Figure 7.4. The design panel consists of two sections; the left side of the screen contains design panel tools while white panel located on the right side is where the objects (pavement sections) are drawn. The design panel tools are shown in greater detail in Figure 7.5. These panel tools are used to draw pavement sections and to assign boundaries, loads, support conditions, and reinforcements.

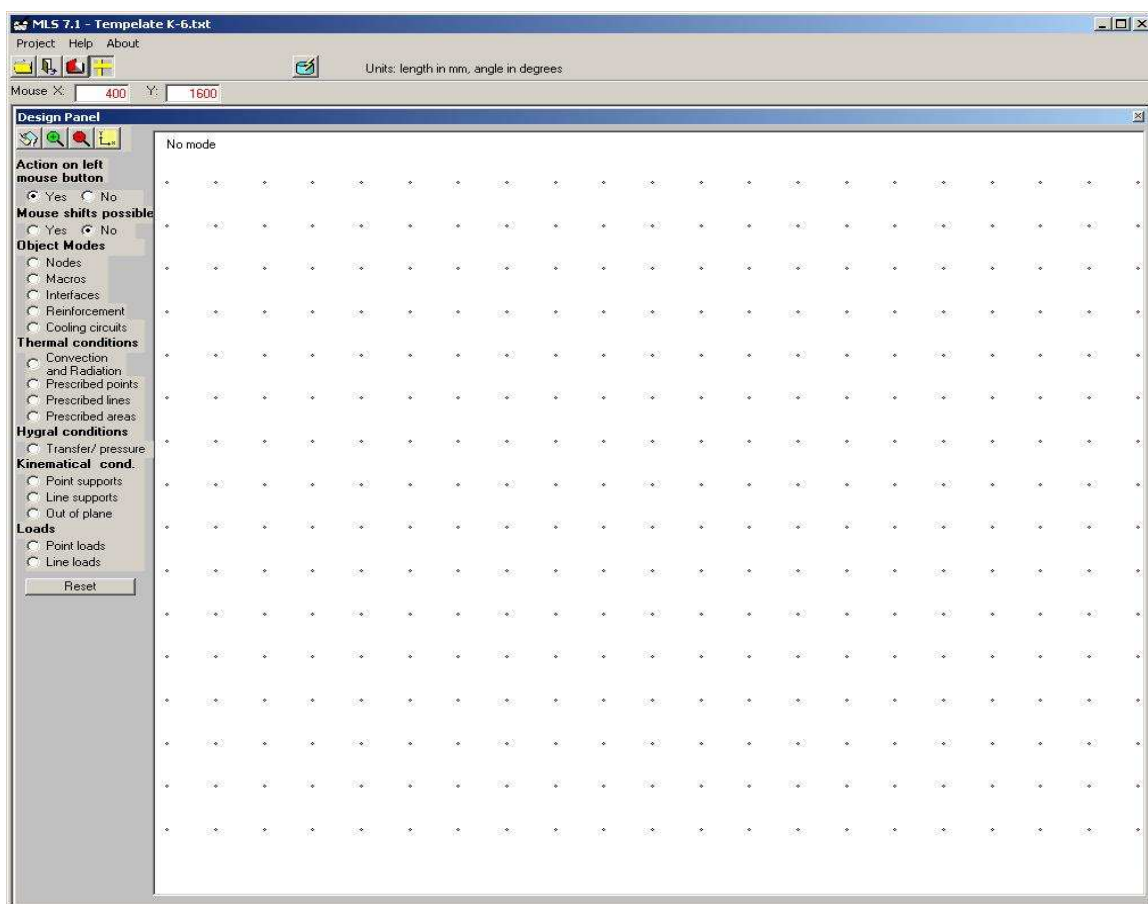


Figure 7.4: Main window of FEMMASSE.

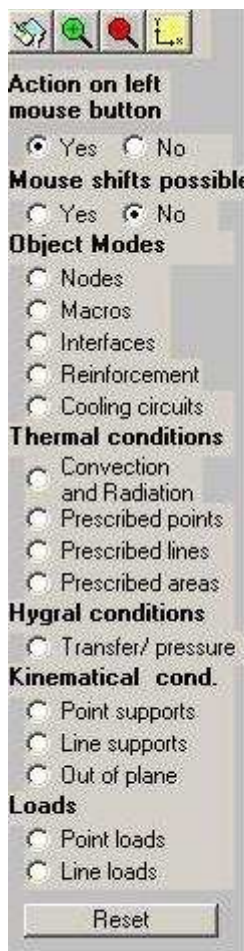


Figure 7.5: Design panel tools of FEMMASSE.

By selecting the macros from the panel tools, quadrilateral objects, called macros, can be drawn. The macros define the dimensions and properties of a material. The macros are drawn by assigning four points in the design panel. Right clicking on the macros opens a “macro property” window in which the initial conditions of macro and the material type can be adjusted. As shown in Figure 7.6, the macros appear at the time of the value inserted in the “present from” field of this window. Similarly, they are ignored at points of time after the time value inserted in the “until” field. As such, time of saw-cut introduction can be specified in the “until” field of the macro property window for the macro that represents the saw-cut. The values shown in Figure 7.6 are the values used for macros representing the concrete pavements.

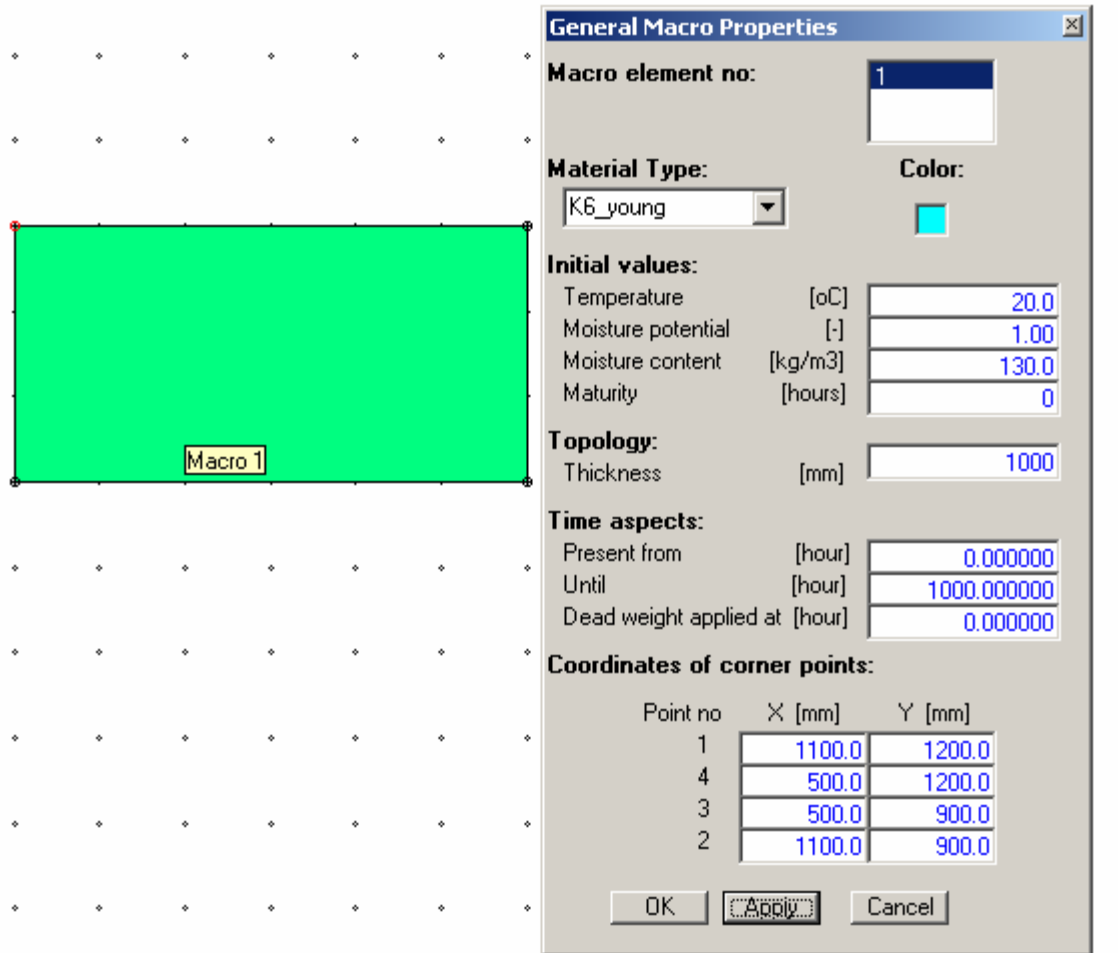


Figure 7.6: General macro properties window.

In order to simulate saw-cutting in the pavement at any time, six macros were defined which represent the concrete pavement as shown in Figure 7.7. Three more macros were defined for the subbase, and three more macros were defined for the subgrade as shown in Figure 7.7. The initial temperature of the pavement and subbase were assumed to be the same and equal to the ambient temperature at the time of casting. The dead weight of the concrete was applied from the time the concrete was placed. Figure 7.7 illustrates the configuration of the macros used in forming the pavement, subbase, and subgrade.

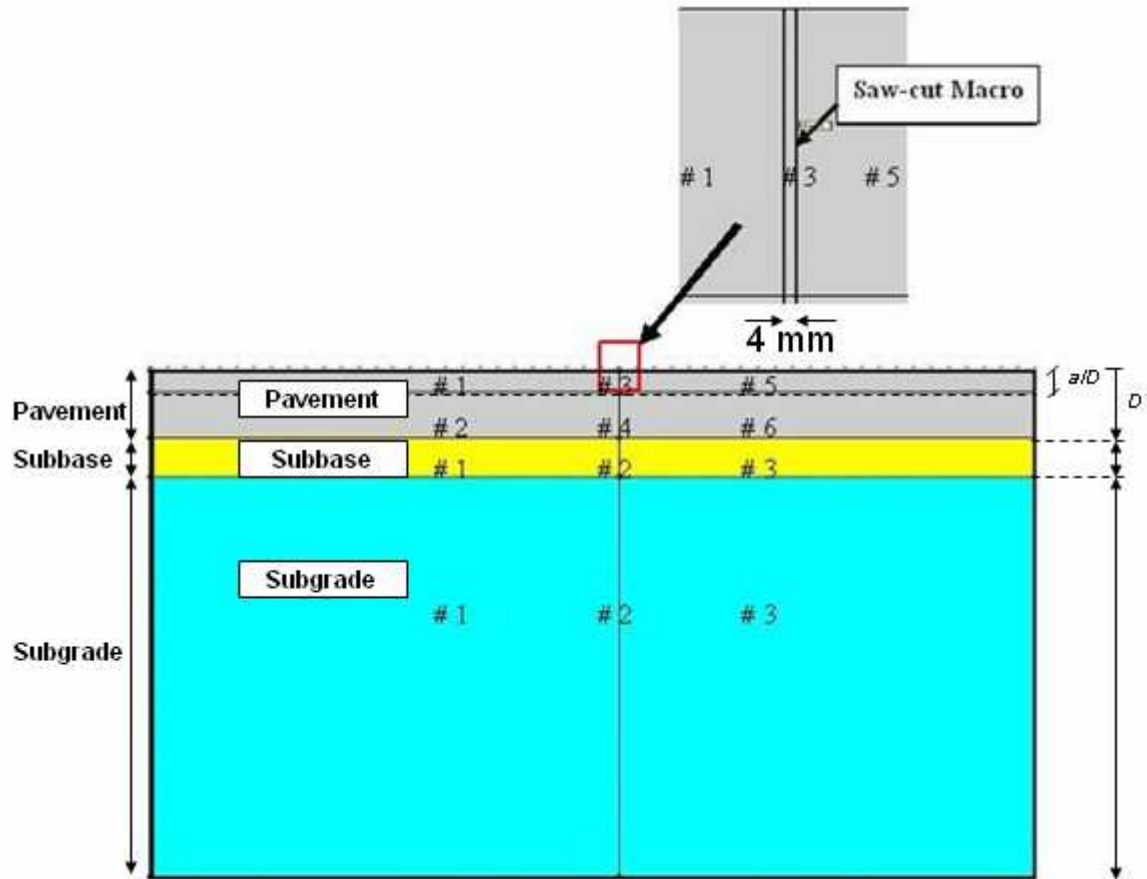


Figure 7.7: Pavement model with magnified saw-cut macro.

7.3.2 Defining the Thermal Boundary Conditions

The thermal boundaries were assigned using the “Convection and Radiation” option shown in Figure 7.8. The side and bottom boundaries were sealed, and a constant heat transfer coefficient of 45 (W/m²K) was assigned to surface boundaries. This transfer coefficient was calculated based on the wind speed of 10 (m/s). The ambient temperature function was also specified.

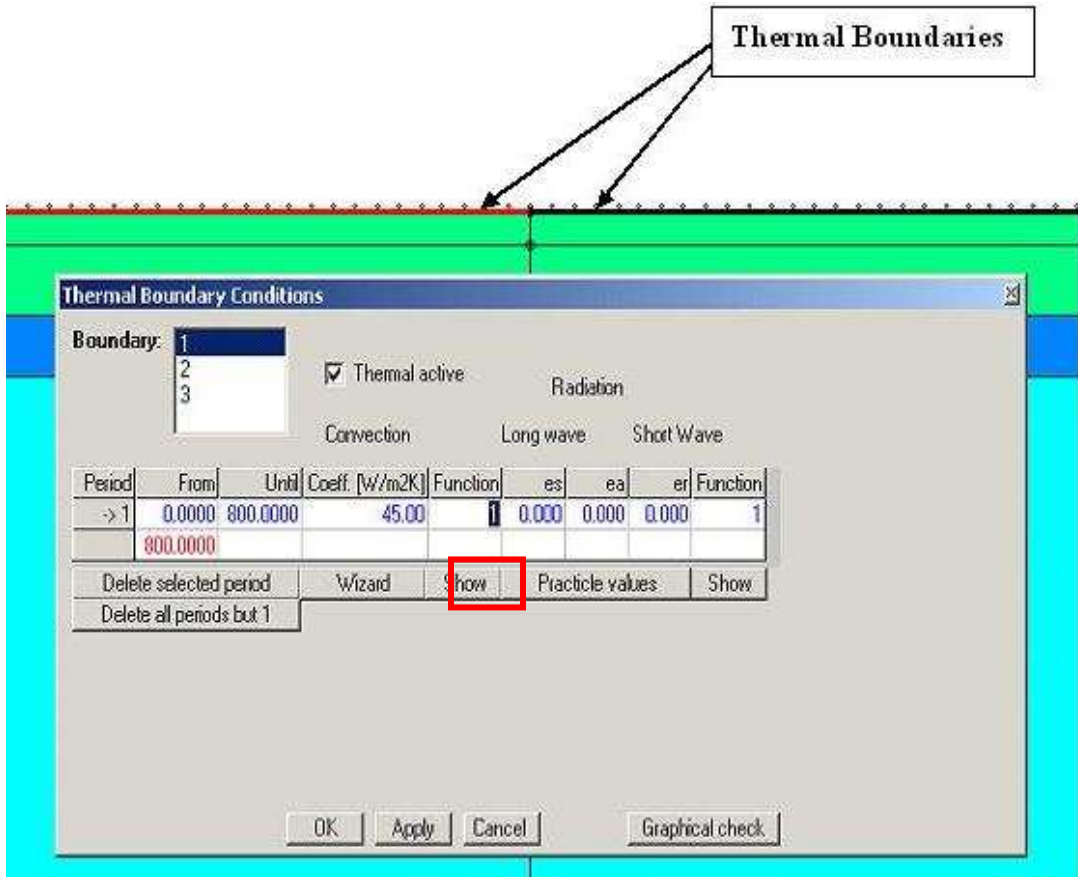


Figure 7.8: Window used to assign thermal boundary properties window.

7.3.3 Defining the Hygral Boundary Conditions

Similar to the thermal boundaries, hygral boundary conditions can be. Figure 7.9 shows the window for selecting transfer coefficients which can be set for different time periods.

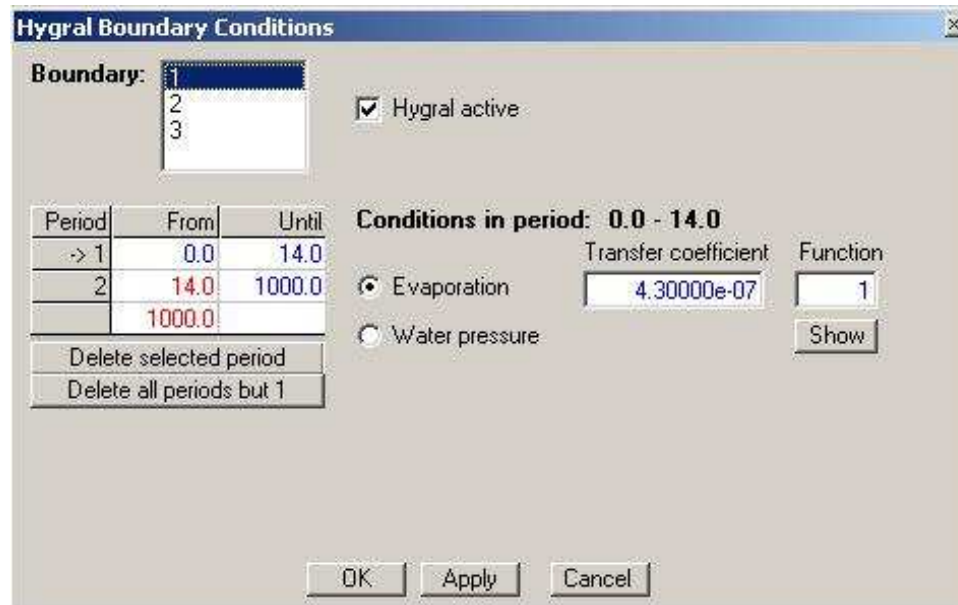


Figure 7.9: Hygral boundary conditions window.

7.3.4 Defining the Mechanical Boundary Conditions

The mechanical boundaries were assigned to the sides of the model. This was done using the line support option under “kinematical conditions” in panel design tools. Rollers were used to restrain the slab ends from moving in x-direction, but allowing them to move freely in “y” and “z” directions as shown in Figure 7.10. It should be noted that each slab side is completely restrained using line support, but only one restraint is shown in the model.

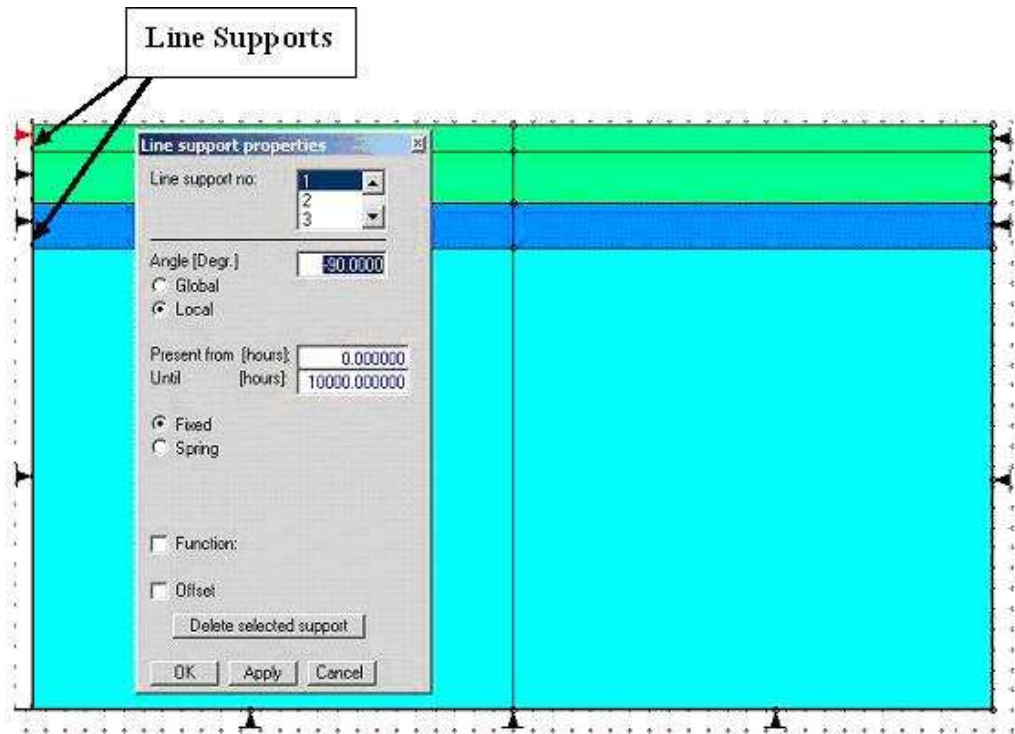


Figure 7.10: Model support conditions.

7.3.5 Defining the Finite Element Mesh

After drawing the macros, setting the initial conditions, and assigning the boundary conditions; a finite element mesh was defined as shown in Figure 7.11. The sides of macros are divided into a number of elements as determined by the “number of subdivisions” field. As shown in Figure 7.12, higher numbers of elements were assigned to the pavement than the subbase and subgrade. Figure 7.13 shows the magnified mesh close to the saw-cut. As shown in Figure 7.12 and 7.13, the mesh close to the saw-cut was more refined. The total number of 4644 elements and 4810 nodes were created to mesh the model.

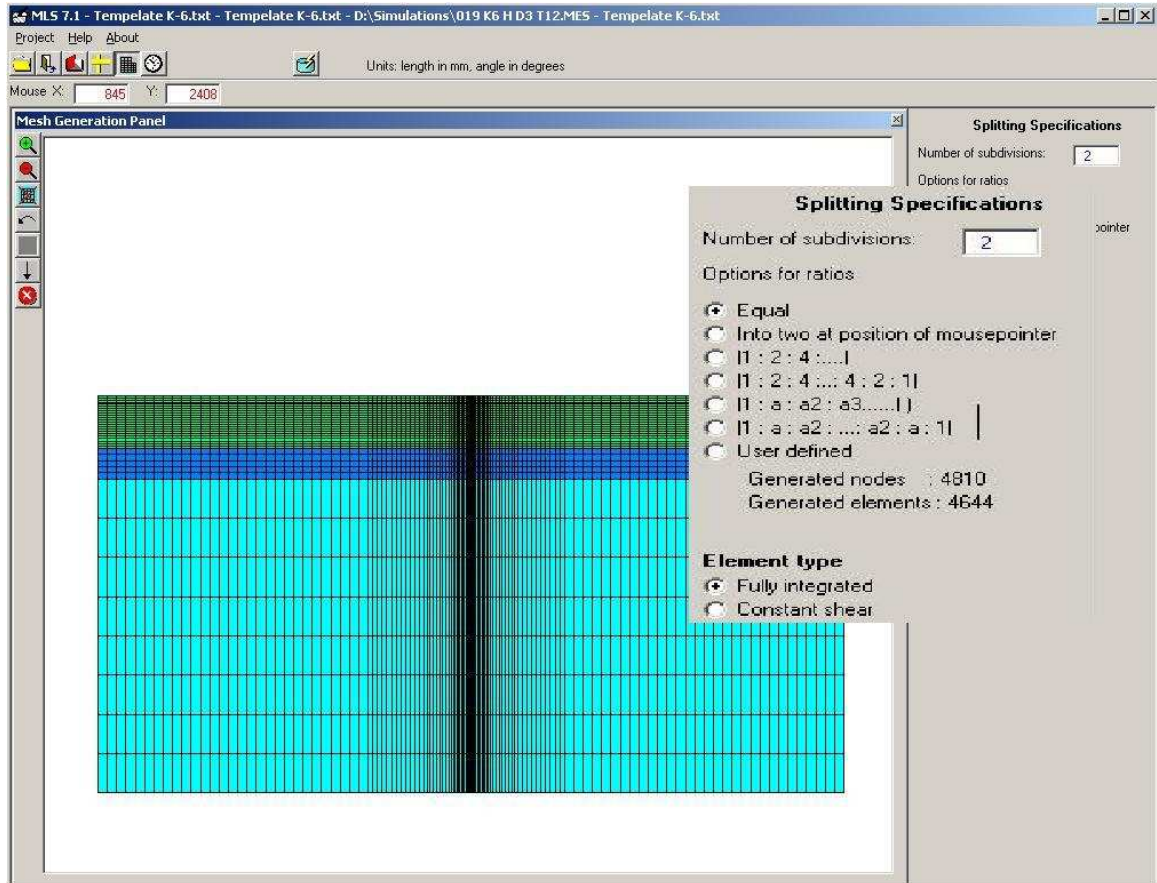


Figure 7.11: Applying the finite element mesh to the model.

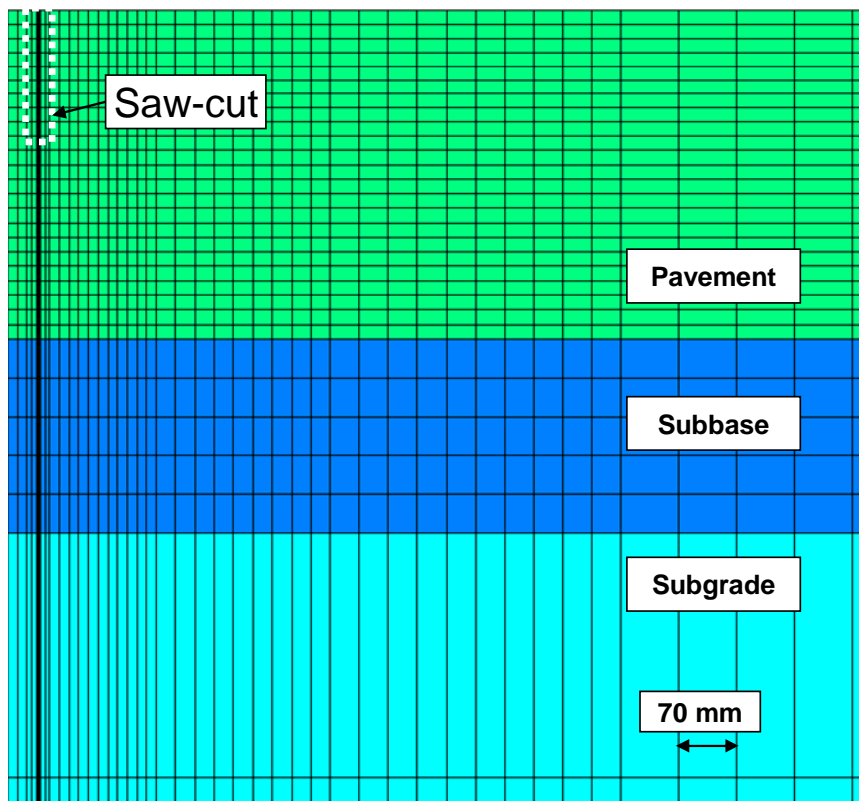


Figure 7.12: The finite element mesh of model.

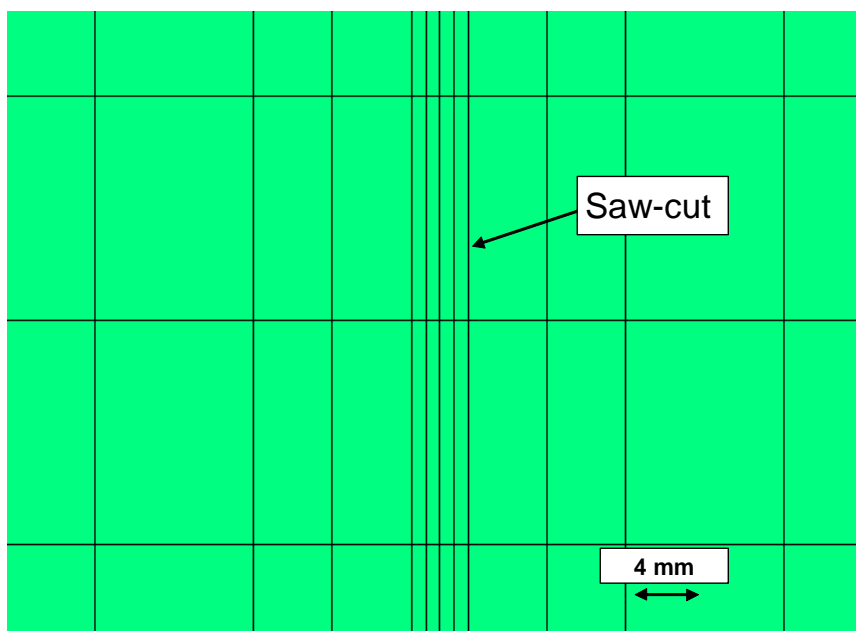


Figure 7.13: Elements of the model close to the saw-cut.

7.3.6 Determining Computational Time Steps and Storage Frequency

The computational time steps and time steps for storage of the computational results are then defined. As in any non-linear analysis the computational time step size plays an important role in stability control of the system. A time increment of 0.25 hours and output storage time of one hour were selected. However, a smaller time step and a data storage time of 0.1 hour were used when the system became unstable.

7.4 Viewing the Computed Results

After the computation process ends, the results can be viewed as defined in the following sections.

7.4.1 Viewing Contour Plots of the Simulation Results

In the contour plot option, the value of a range of some physical property or quantities (e.g., stress level) is represented by colors. For example, Figure 7.14 illustrates a contour plot of principal stresses at 23.3 hours. As shown by the legend, the blue color represents the smallest value of stress (-0.33 MPa) while the red color describes the maximum value (2.862 MPa). The colors between these limits provide a description of stress distribution in the contour plot. The contour plots can also be viewed at different times.

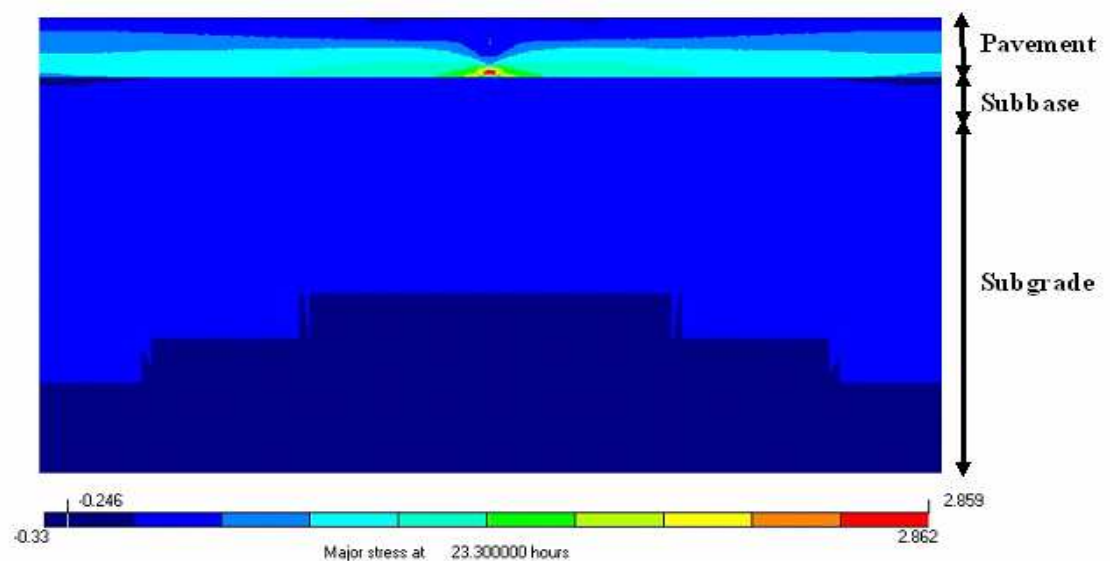


Figure 7.14: Contour plot of principal stresses at 23.3 hours.

The FEMMASSE software provides contour plots for various quantities including temperature, relative humidity, maturity, tensile strength, compressive strength, displacement in x-direction, displacement in y-direction, principal major stresses, principal minor stresses, normal stresses, end reactions, and damage (reduction in stiffness).

The temperature distributions for the baseline condition at 6 hours, 12 hours, 18 hours, and 23.3 hours are illustrated in Figure 7.15, Figure 7.16, Figure 7.17, and Figure 7.18 respectively. It should be noted that analysis stopped at 23.3 hours as through cracking is completed at this time. The pavement temperature increases rapidly due to heat of hydration, while the heat is dissipated through the surface and bottom of the pavement. Consequently, the center of pavement has higher temperature, and since the coefficient of heat transfer of surface boundary is greater than the coefficient of heat transfer of bottom boundary, the temperature of the pavement surface is lower than the temperature of the bottom of the pavement. As shown in Figure 7.15 and 7.16, during the first 12 hours there is a low temperature gradient inside the pavement; however, a temperature gradient of over 13 °C is seen in the pavement at 18 and 23.3 hours. This is a substantial temperature gradient which leads to a self restraint and thermal stress development in the pavement.

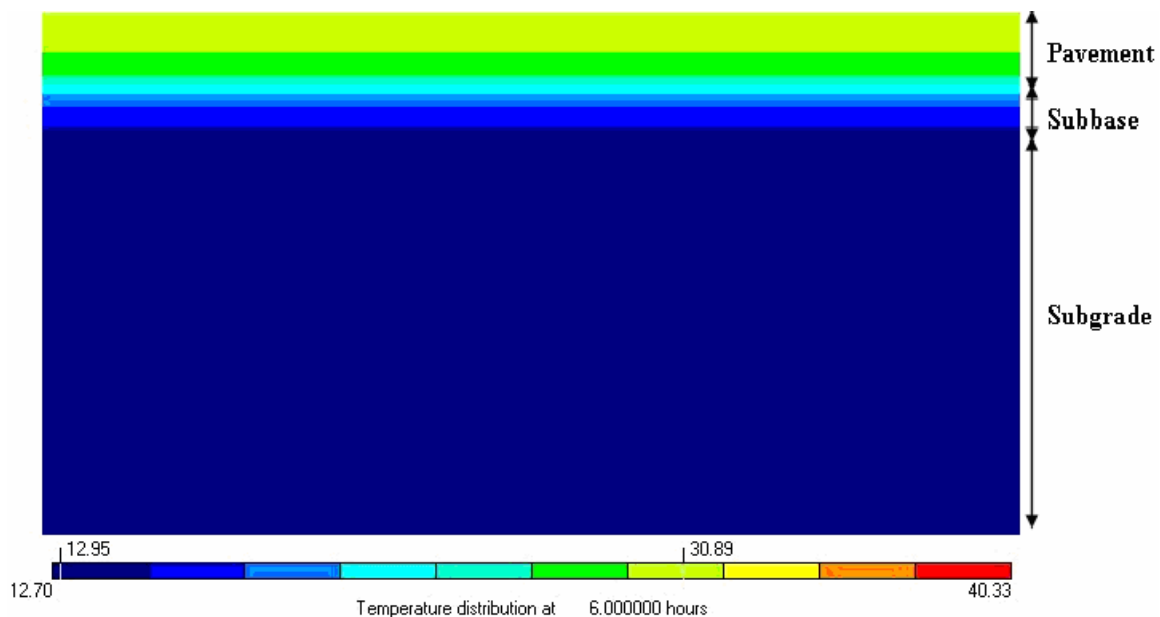


Figure 7.15: Temperature distribution contour plot at 6 hours.

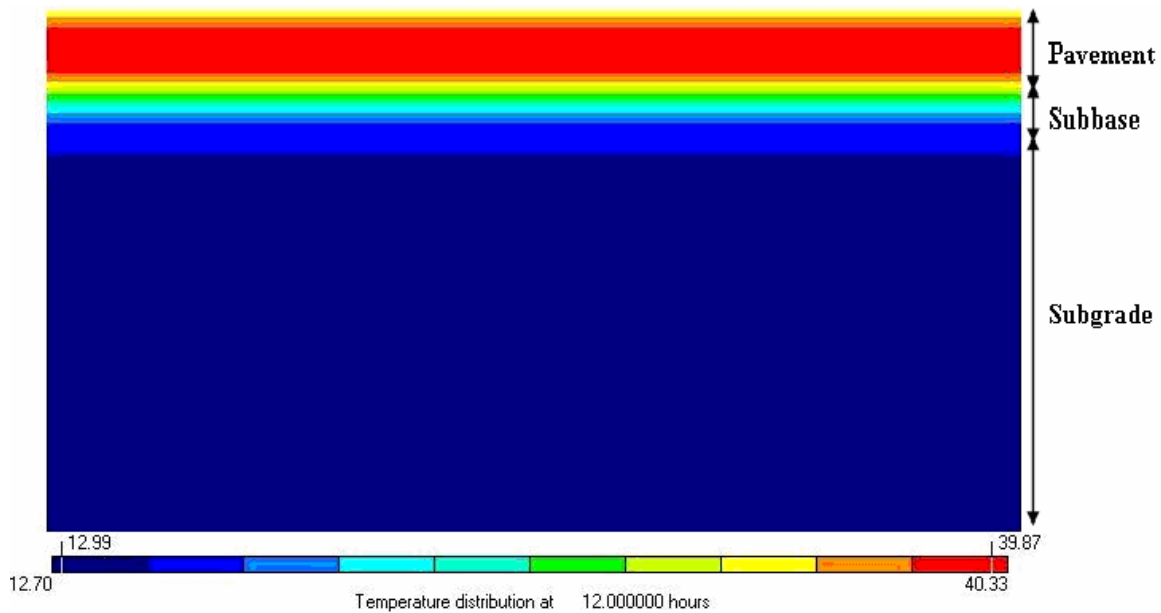


Figure 7.16: Temperature distribution contour plot at 12 hours.

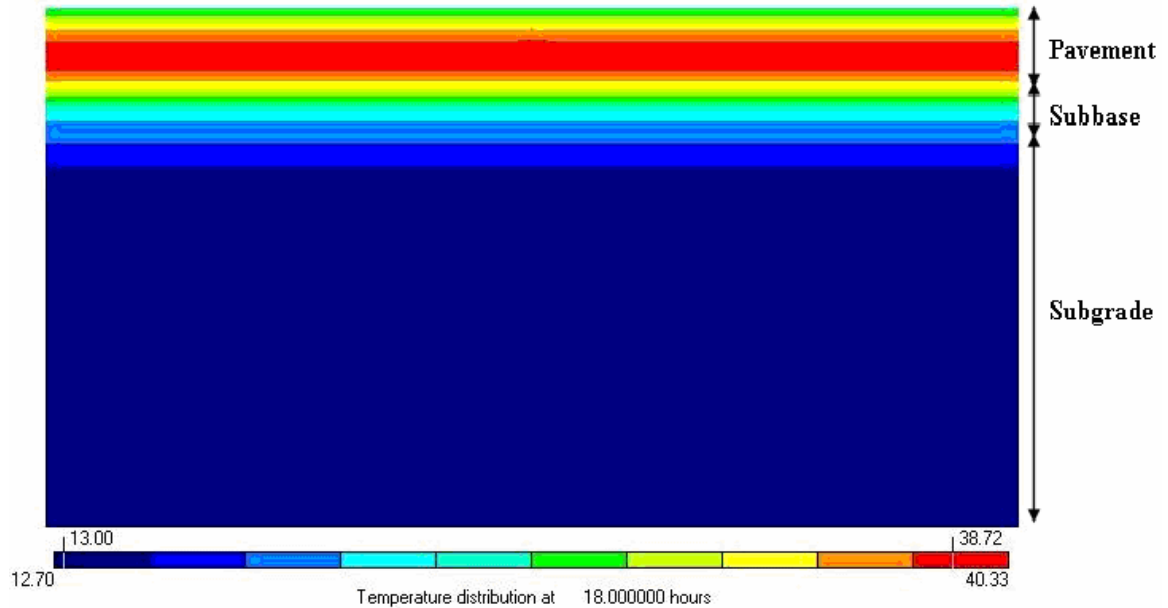


Figure 7.17: Temperature distribution contour plot at 18 hours.

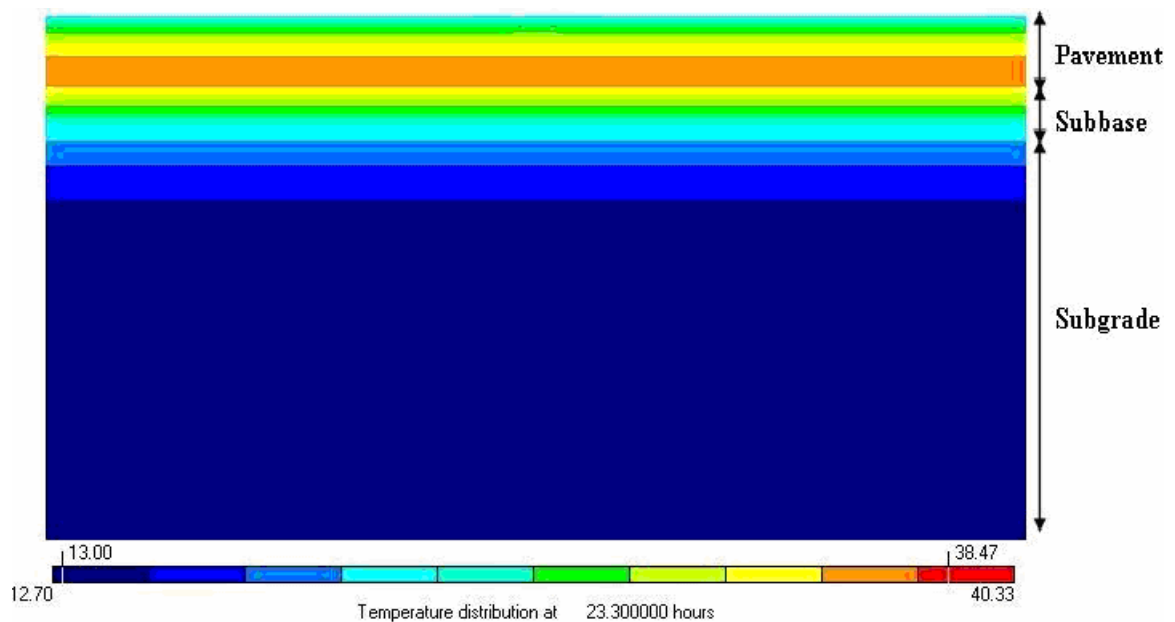


Figure 7.18: Temperature distribution contour plot at 23.3 hours.

The FEMMASSE software calculates age dependent property using a material maturity which is based on the Arrhenius maturity function. Figure 7.19 through Figure 7.22 illustrate the maturity development in the pavement at 6, 12, 18, and 23.3 hours. Since the maturity depends on the temperature and time, it can be seen that the areas

experienced higher temperatures demonstrate higher maturity values. A lower maturity is experienced in the pavement close to surface and subbase than the core of the pavement. The maximum and minimum maturity values are presented in the contour plots captions.

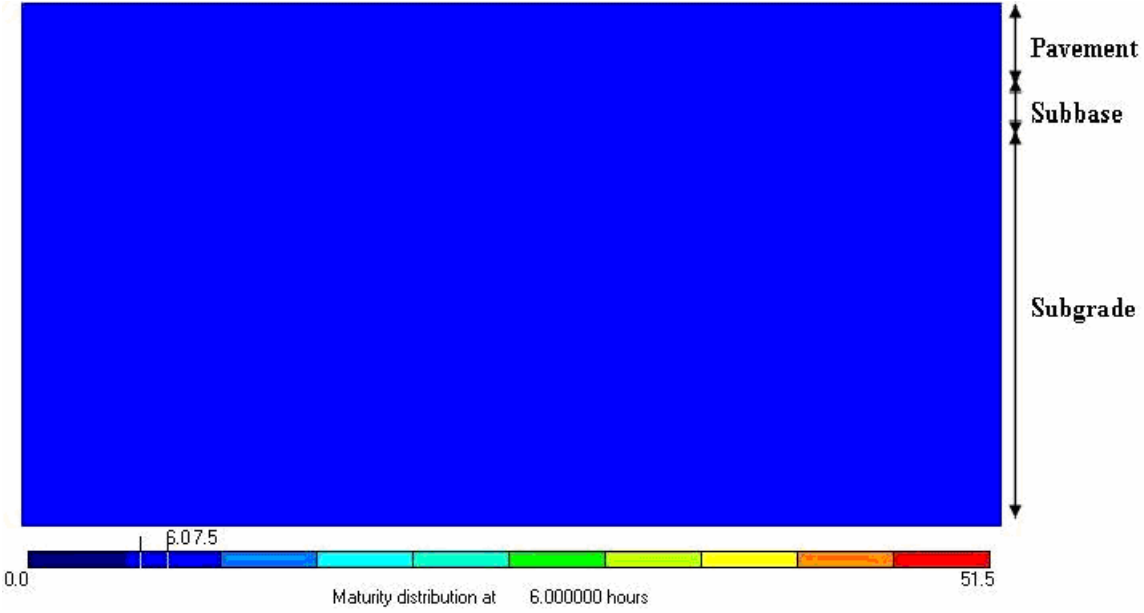


Figure 7.19: Maturity distribution contour plot at 6 hours.

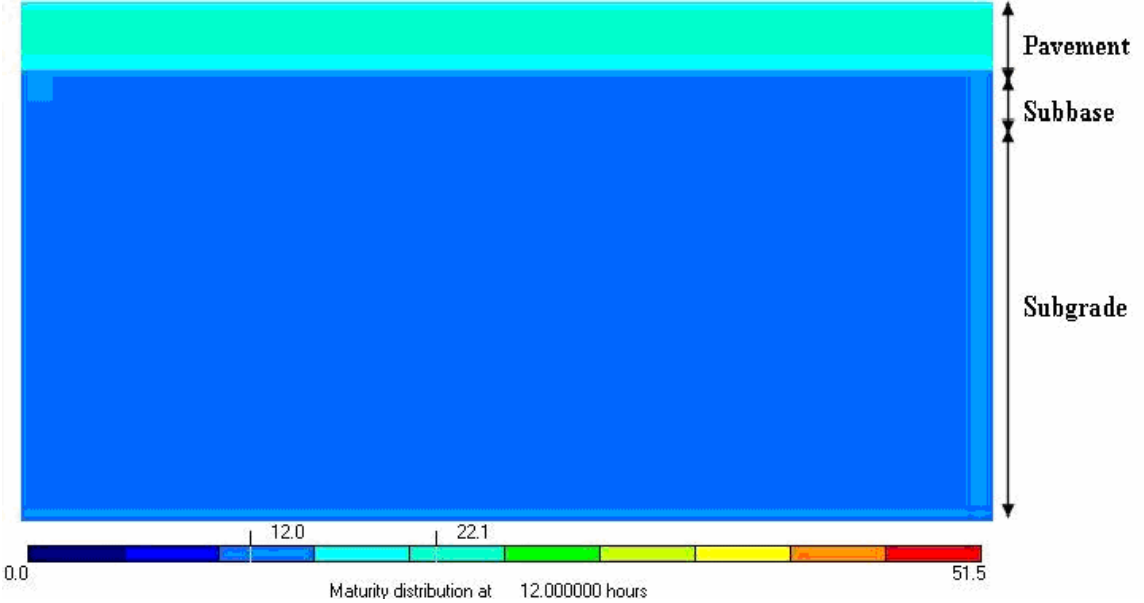


Figure 7.20: Maturity distribution contour plot at 12 hours.

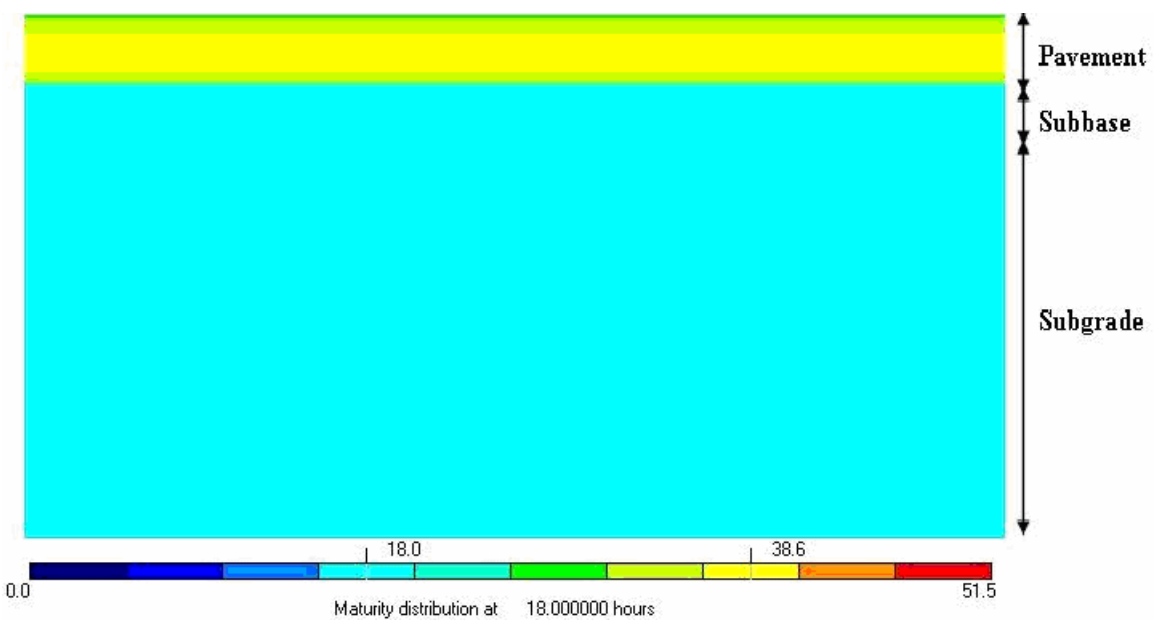


Figure 7.21: Maturity distribution contour plot at 18 hours.

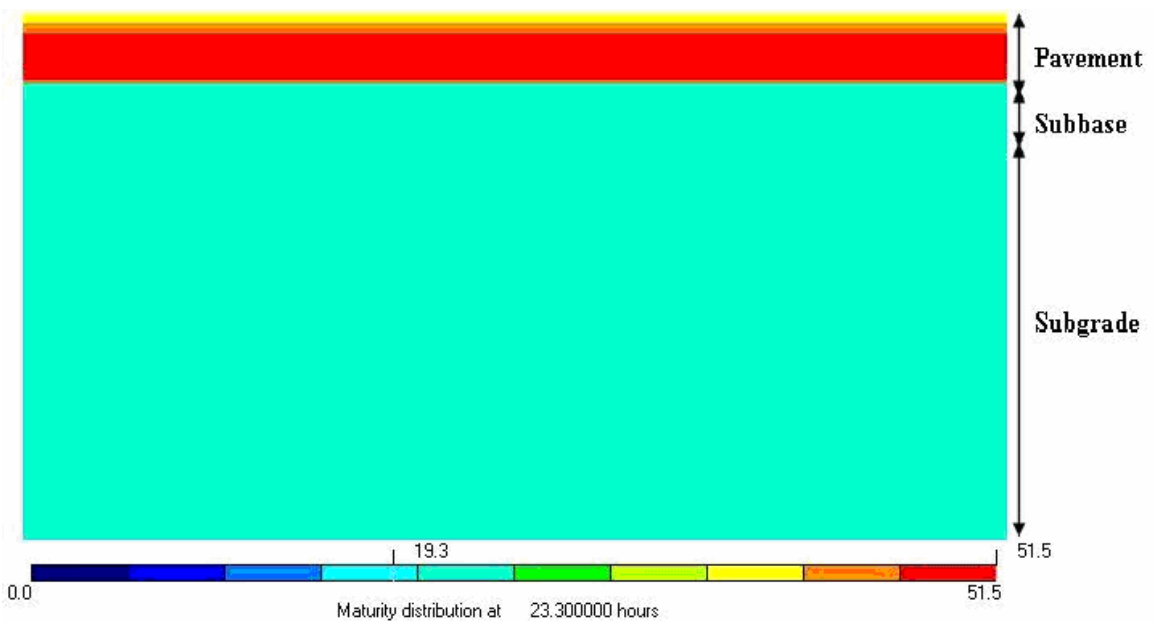


Figure 7.22: Maturity distribution contour plot at 23.3 hours.

Figure 7.23 through 7.26 illustrate the tensile strength contour plots at 6 hours, 12 hours, 18 hours, and 23.3 hours. The areas with higher temperature intensities have higher maturities, and consequently they also have a higher tensile strength. However, since the majority of the strength gain occurs in the first 6 to 18 hours when the

temperature gradient is small, the pavement strength is relatively uniform. The maximum and minimum tensile strengths (in MPa) experienced in the pavement are provided in the following figures' legends.

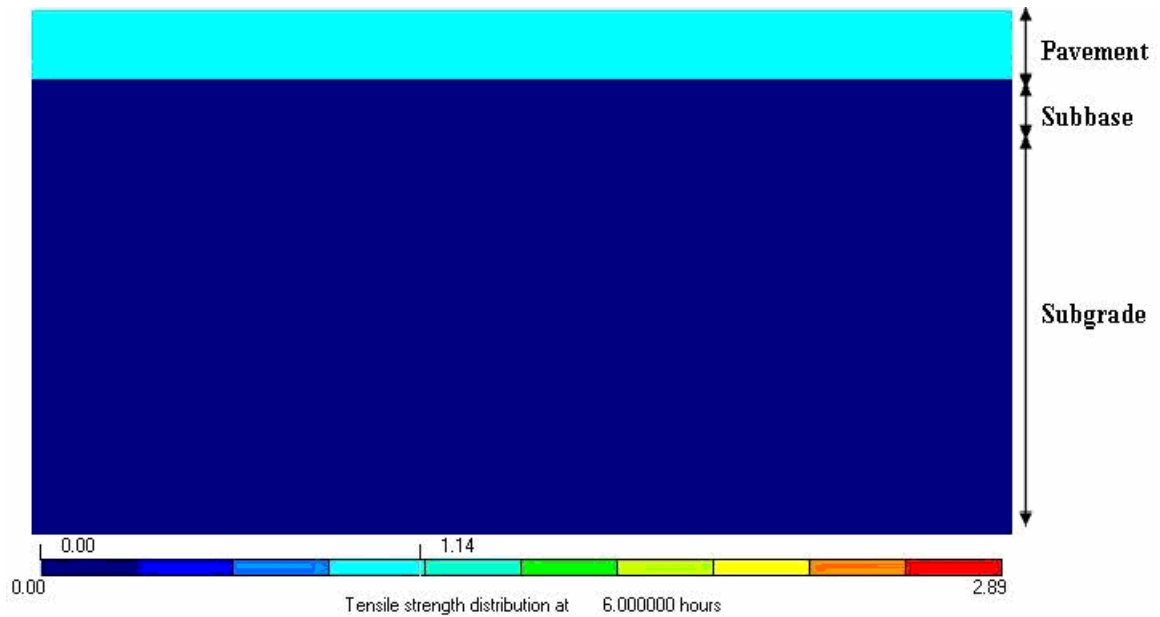


Figure 7.23: Tensile strength distribution contour plot at 6 hours.

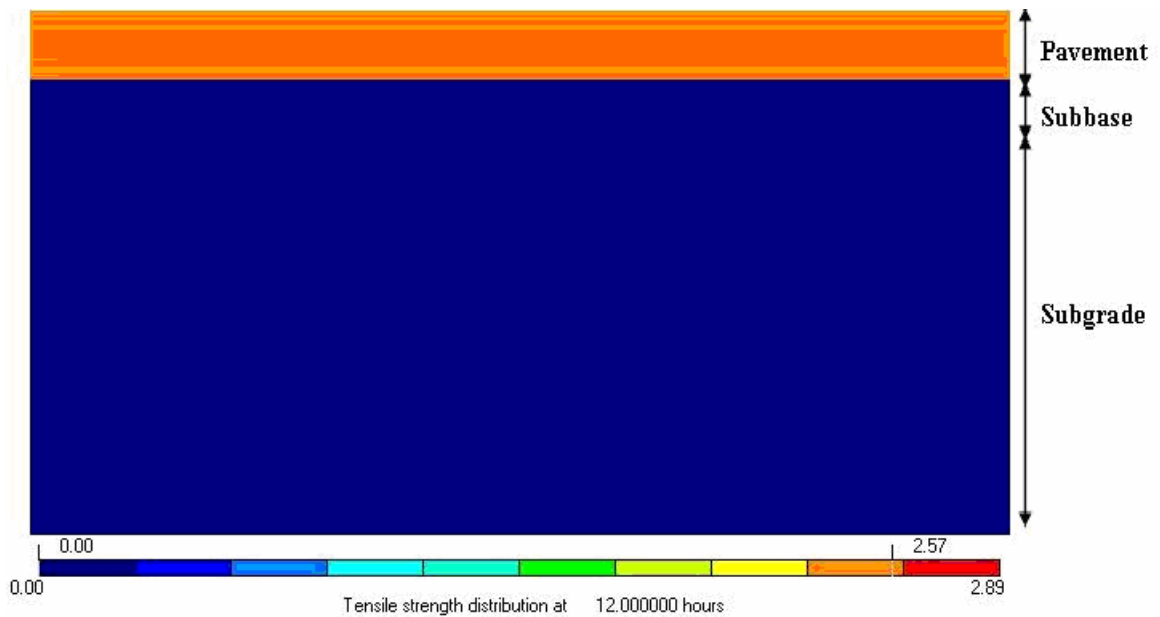


Figure 7.24: Tensile strength distribution contour plot at 12 hours.

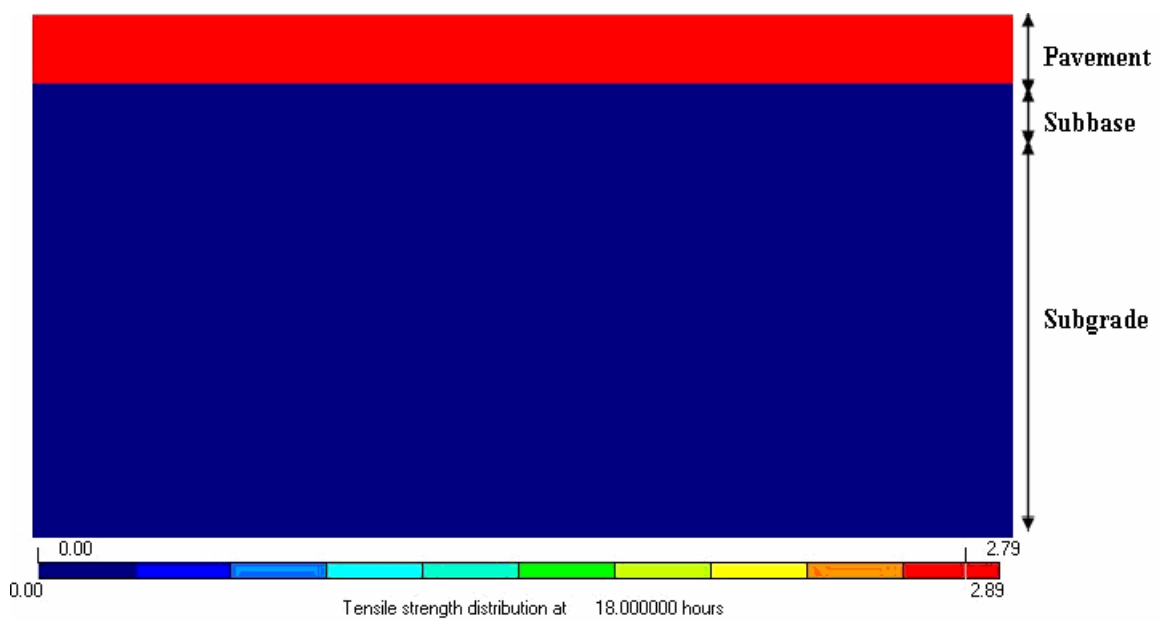


Figure 7.25: Tensile strength distribution contour plot at 18 hours.

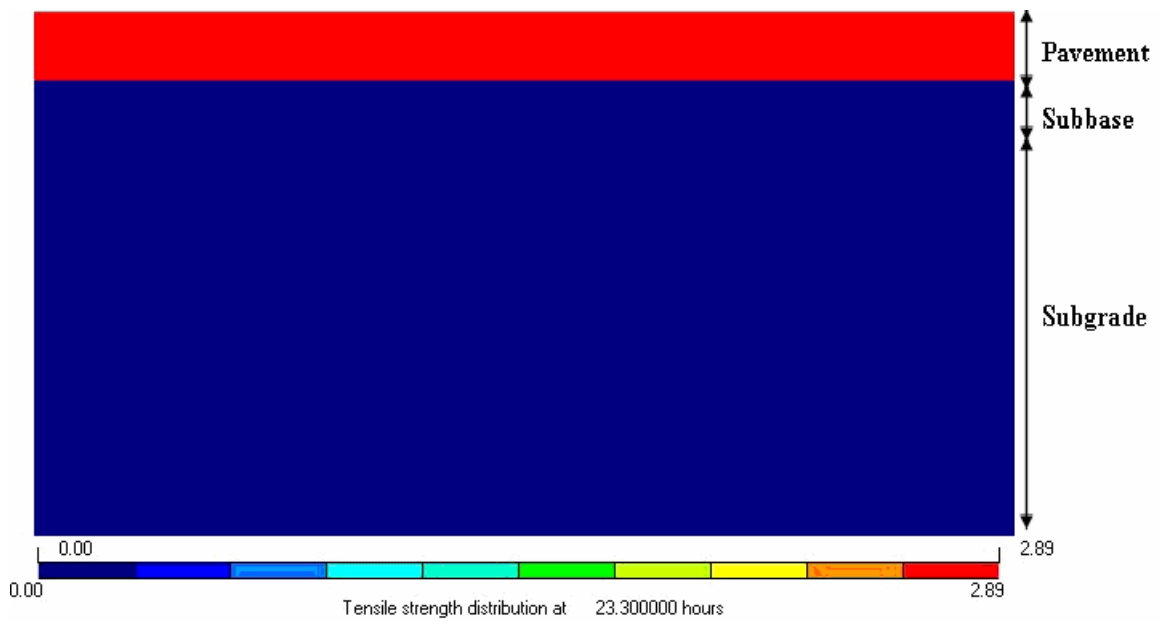


Figure 7.26: Tensile strength distribution contour plot at 23.3 hours.

Figures 7.27, 7.28, 7.29, 7.30, and 7.31 illustrate the contour plots of the principal major stresses experienced in the pavement at different ages (i.e., 6, 12, 13, 18, and 23.3 hours). The stress level in the pavement is low (e.g., < 0.2 MPa) in the first 12 hours. As shown in Figure 7.29, the stress level is still less than 2.0 MPa around the tip of the saw-

cut at 13 hours. This can be due to the low elastic modulus, high stress relaxation, heat of hydration, low thermal stresses, and shrinkage at early ages. It is seen that at 18 hours a high stress concentration begins to develop at the tip of the notch. At ages above 18 hours, stress concentration moves toward the bottom of the pavement as the crack propagates through the pavement. It should be noted that for this case through cracking occurs at 23.3 hours when the computation stops. It should be noted that the maximum stress is experienced at the tip of the crack which is designated by the red stress concentration area.

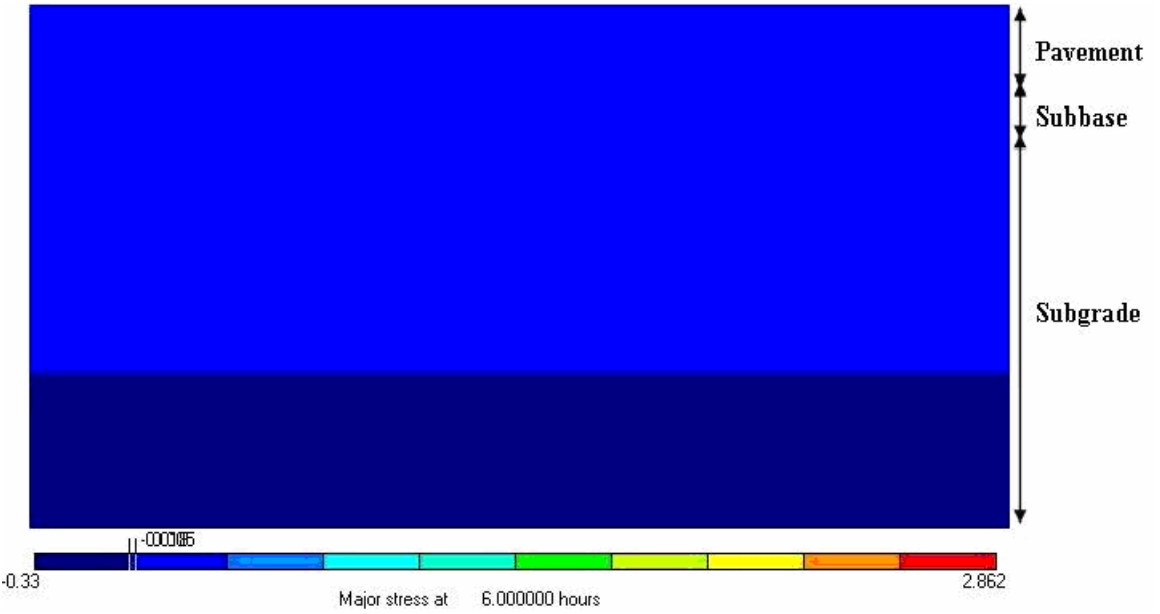


Figure 7.27: Principal stress distribution contour plot at 6 hours.

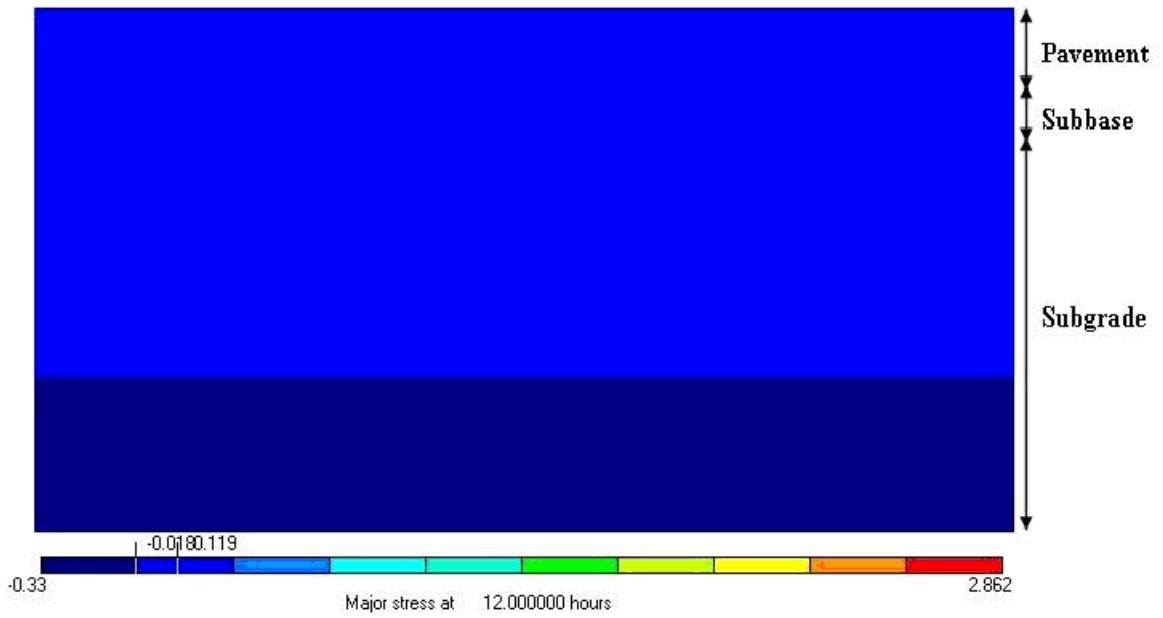


Figure 7.28: Principal stress distribution contour plot at 12 hours.

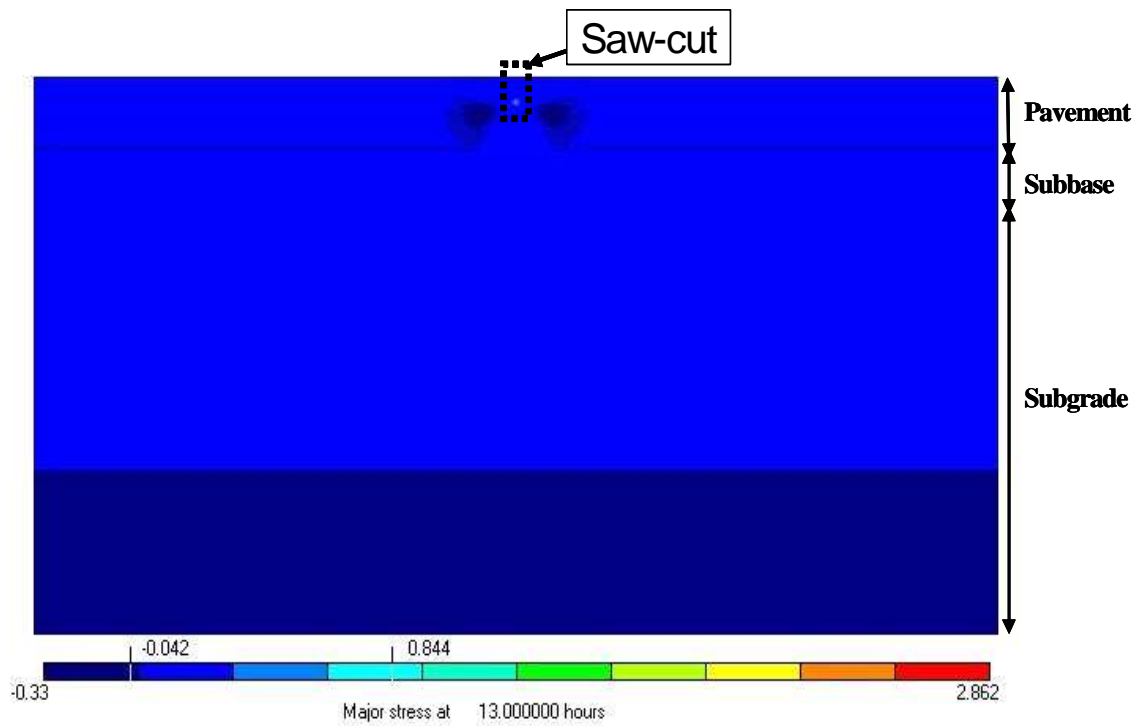


Figure 7.29: Principal stress distribution contour plot at 13 hours.

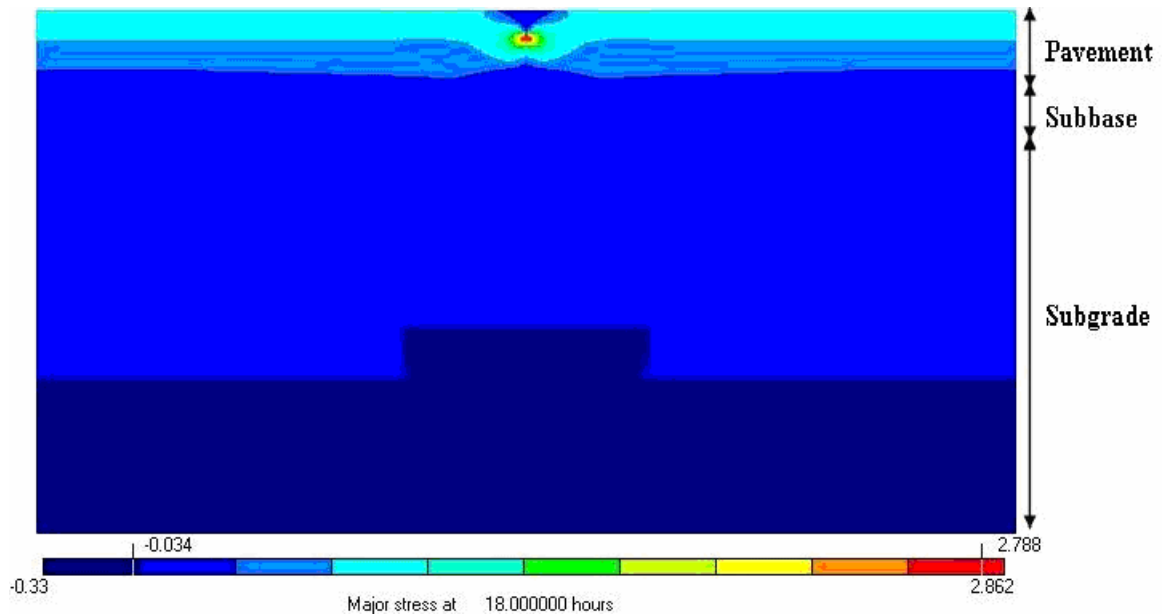


Figure 7.30: Principal stress distribution contour plot at 18 hours.

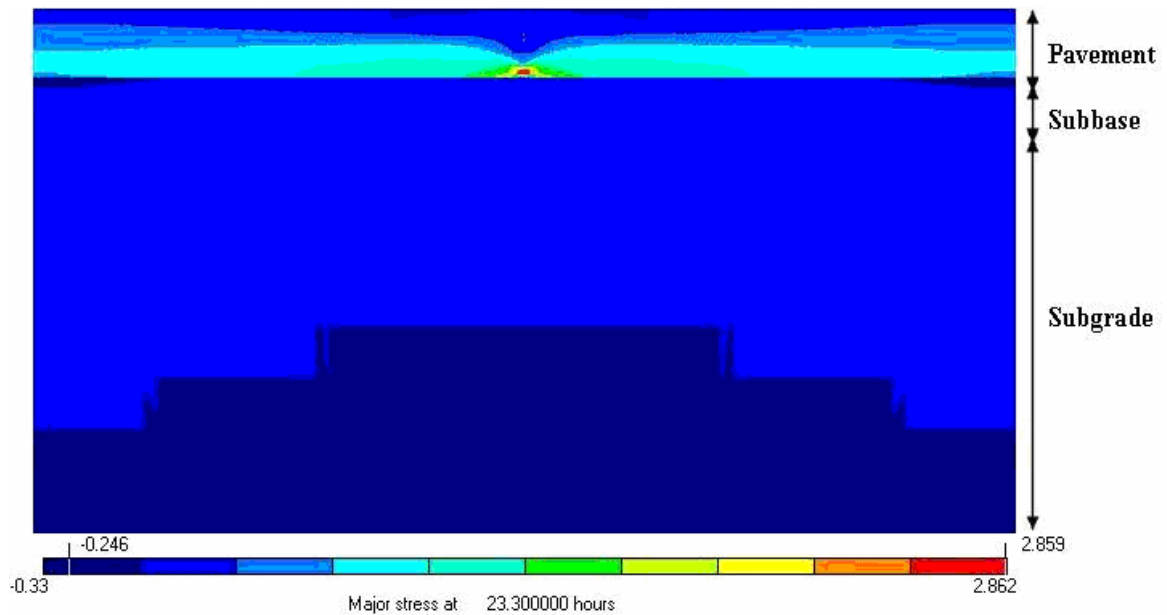


Figure 7.31: Principal stress distribution contour plot at 23.3 hours.

The pavement end reaction can also be monitored. Figures 7.32, 7.33, and 7.34 illustrate the support reaction. As the support reactions at the first 12 hours show compressive forces, the reaction contour plot at 6 hours is not presented here. As the

stress in the pavement increases, the end reaction develops. The reaction force moves toward bottom of the pavement as through cracking occurs.

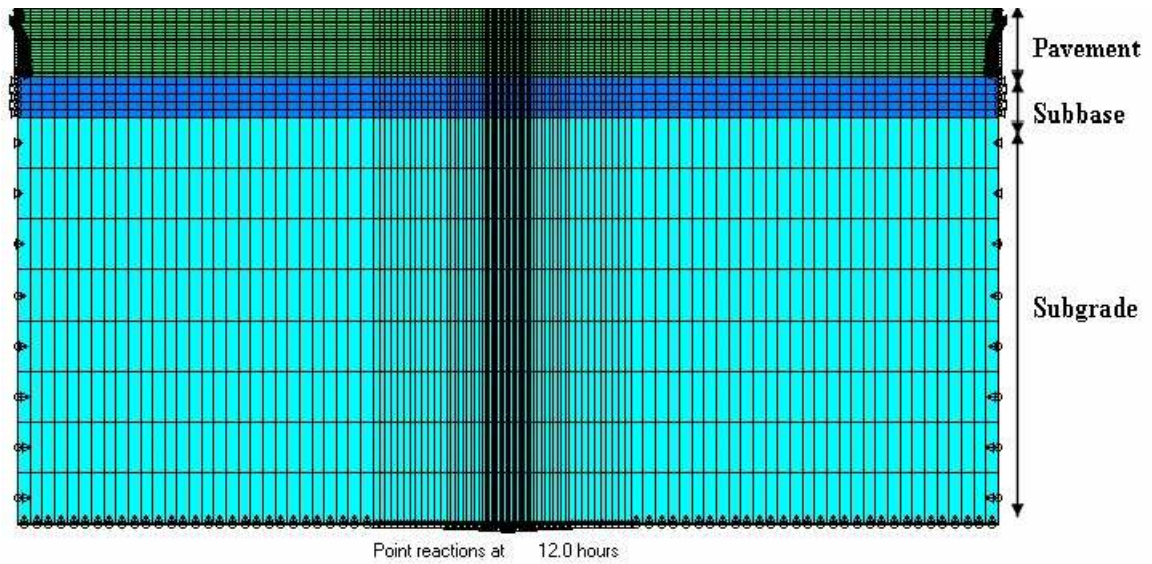


Figure 7.32: End reaction plot at 12 hours.

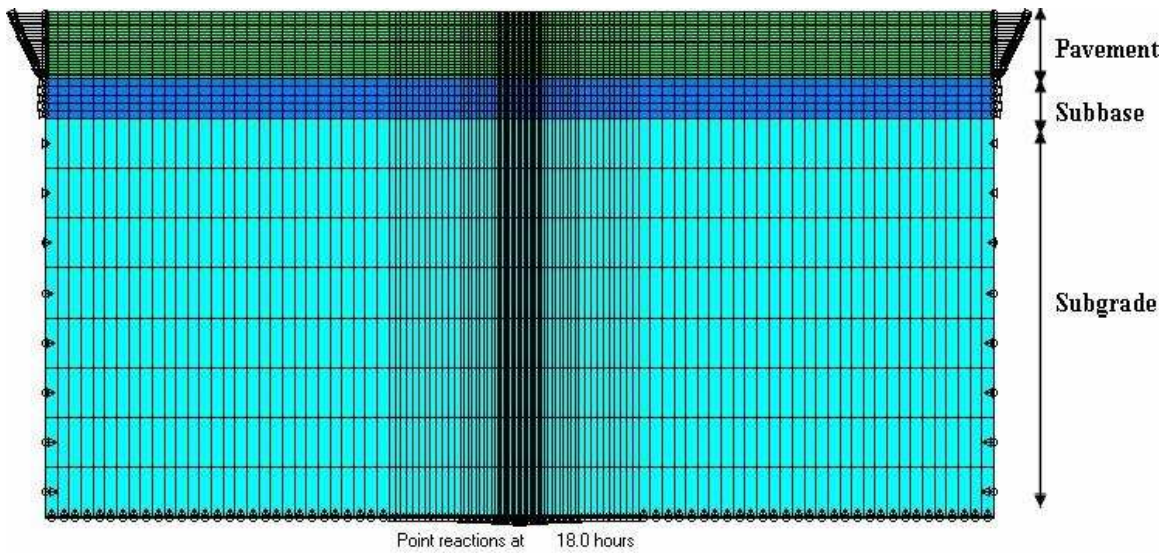


Figure 7.33: End reaction plot at 18 hours.

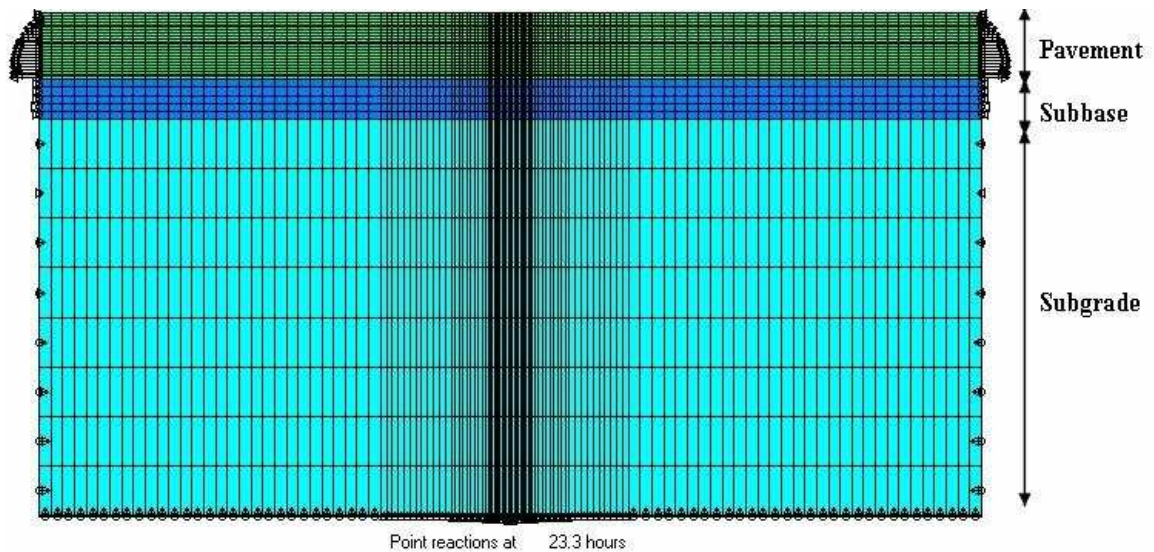


Figure 7.34: End reaction plot at 23.3 hours.

The reaction forces along one end of pavement were plotted in Figure 7.35. As shown in Figure 7.35, compressive forces, developed by high pavement temperatures due to heat of hydration development, were exerted on the pavement at or before 12 hours. However, tensile forces develop at later ages. The reaction forces are extremely higher close to surface of the pavement at 18 hours. This provides driving force to initiate cracking at the tip of the saw-cut. As the crack propagates through the pavement, the peak reaction forces move toward the bottom of the pavement.

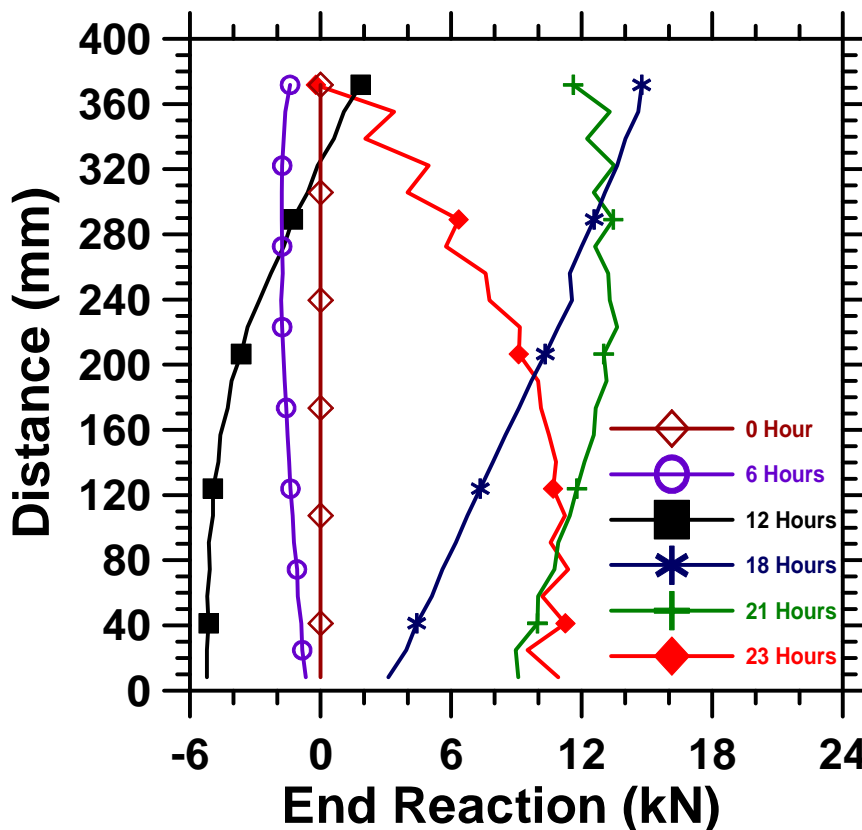


Figure 7.35: The graphs of end reactions of pavement at various hours. The distance on “y” axis is measured from the bottom of pavement.

The damage parameter produces a measure of the reduction in concrete stiffness that occurs due to cracking. When the damage parameter is zero, it means that the concrete is undamaged while a damage parameter of one relates to a concrete that lost its entire stiffness. This parameter can be used to designate the cracking path in a pavement. For this example (the baseline case), the damage intensities are negligible before 21 hours as the crack propagation is small. For purpose of illustration, the damage distribution contour plot at 21 hours and 23.3 hours are illustrated in Figure 7.36 and Figure 7.37 respectively.

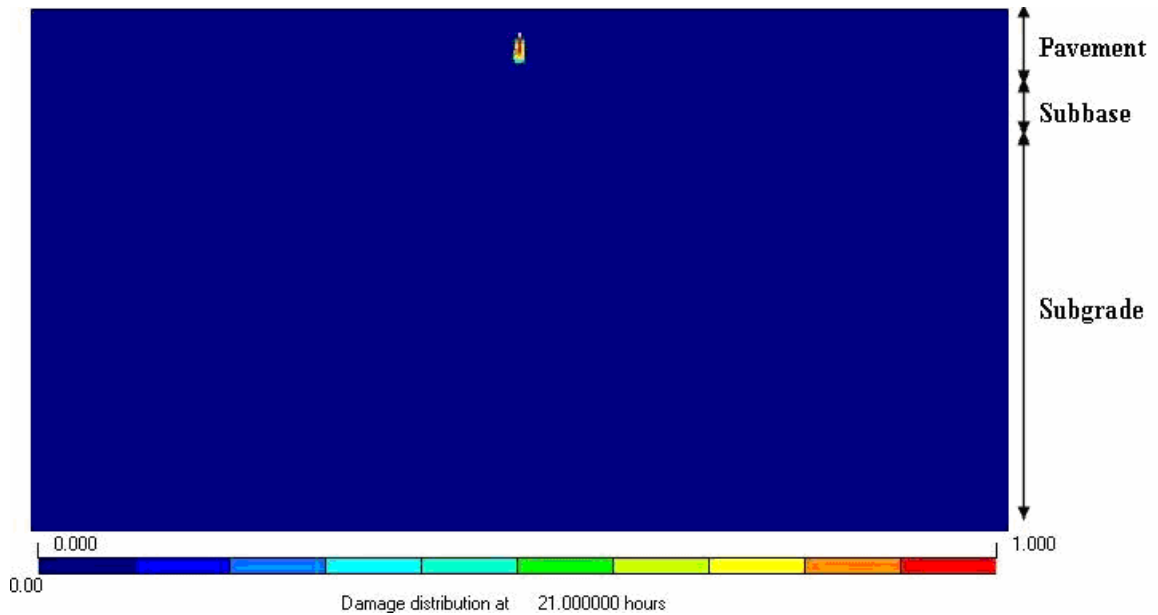


Figure 7.36: Damage distribution contour plot at 21 hours.

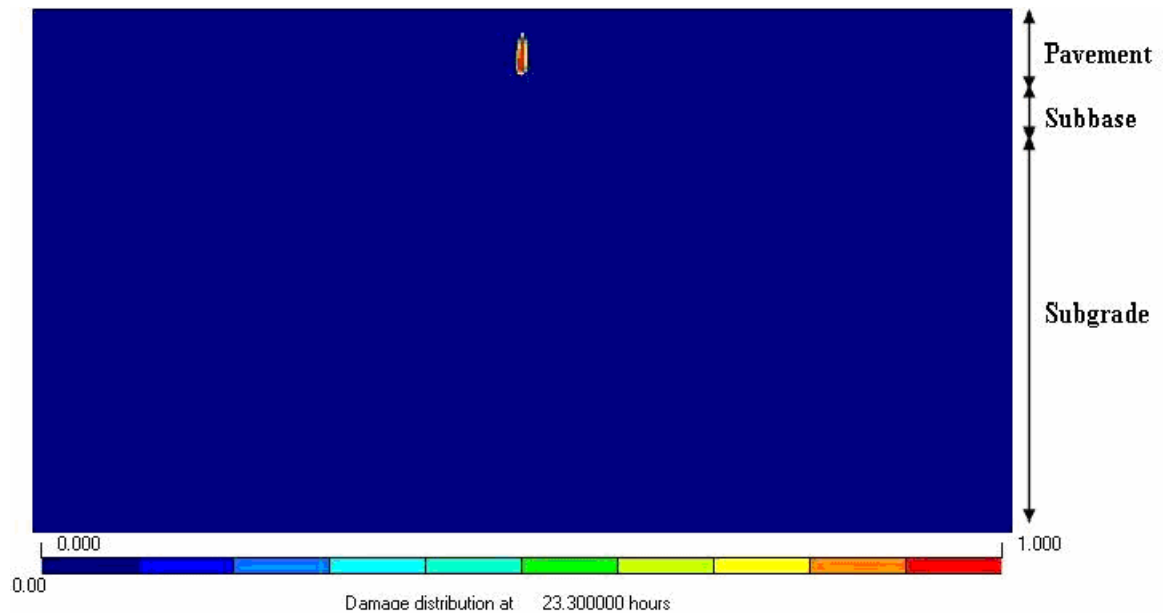


Figure 7.37: Damage distribution contour plot at 23.3 hours.

Figures 7.38, 7.39, 7.40, 7.41, and 7.42 illustrate the contour plots that represent the displacement in x-direction. As discussed earlier, major crack propagation occurs after 21 hours, and therefore the displacement before cracking is small. However, the crack propagation and opening result in rapid increase in the displacement as shown in Figure 7.41 and Figure 7.42.

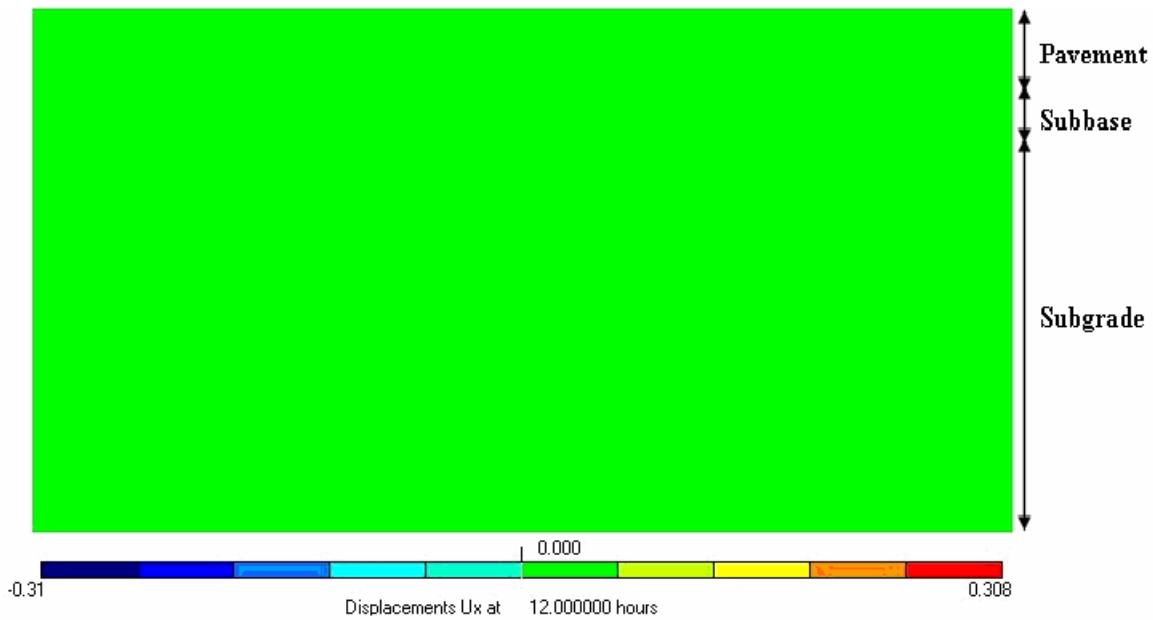


Figure 7.38: X-direction distribution contour plot at 12 hours.

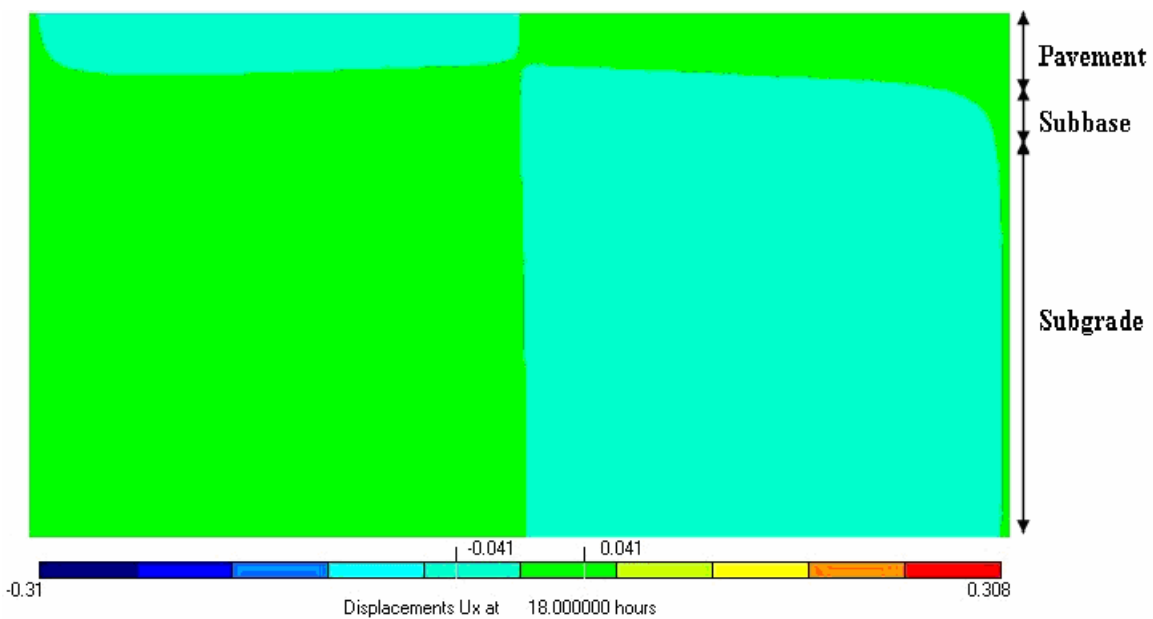


Figure 7.39: X-direction distribution contour plot at 18 hours.

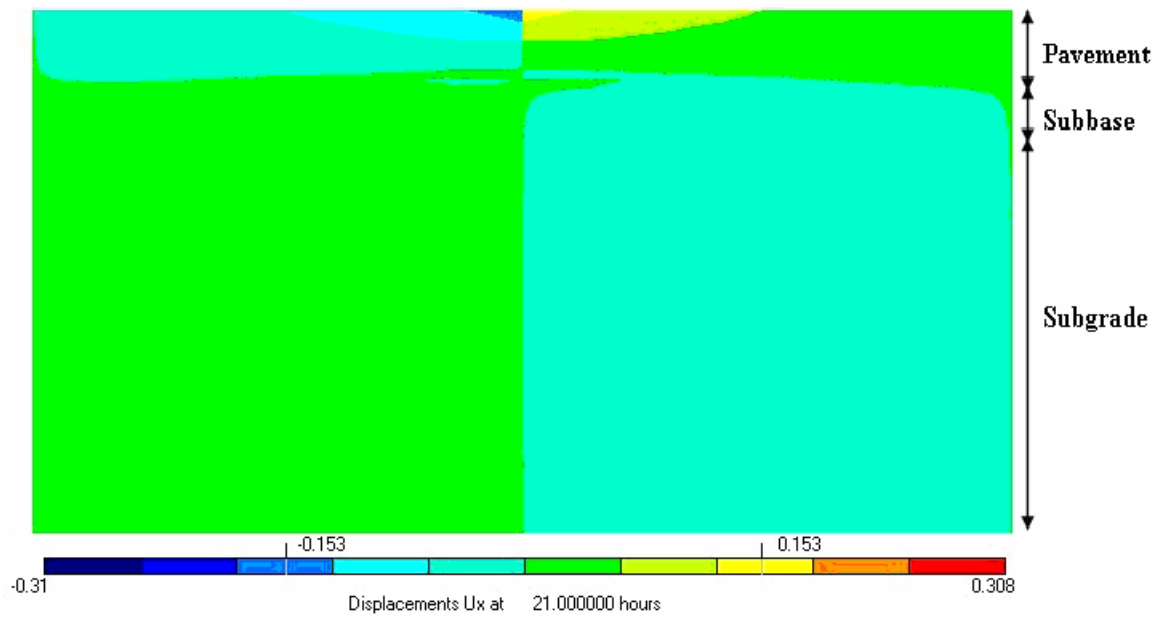


Figure 7.40: X-direction distribution contour plot at 21 hours.

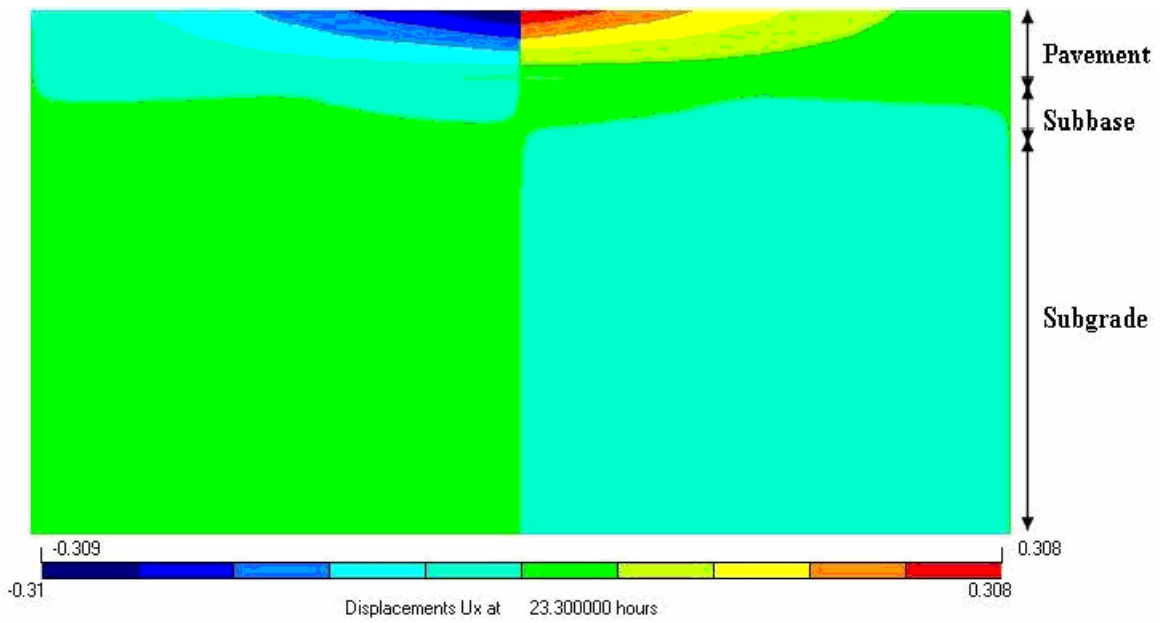


Figure 7.41: X-direction distribution contour plot at 23.3 hours.

7.4.2 Line Cuts in Contour Plots

Line cuts are used to obtain the values of one of aforementioned quantities (i.e., principal major stress, displacement, temperature, tensile strength, and maturity) along a defined line at a particular time. A plot of some quantities (e.g., stress) versus the

distance along the line will be displayed on the right side of the result panel. Figure 7.42 illustrates a magnified contour plot which was shown in Figure 7.42 in which a vertical line cut passing through the saw-cut was defined. The graph shown on the right side of the result panel illustrates the principal stress and tensile strength values below the saw-cut at 23.3 hours. The green line represents the principal stress along the line and the red line is the tensile strength.

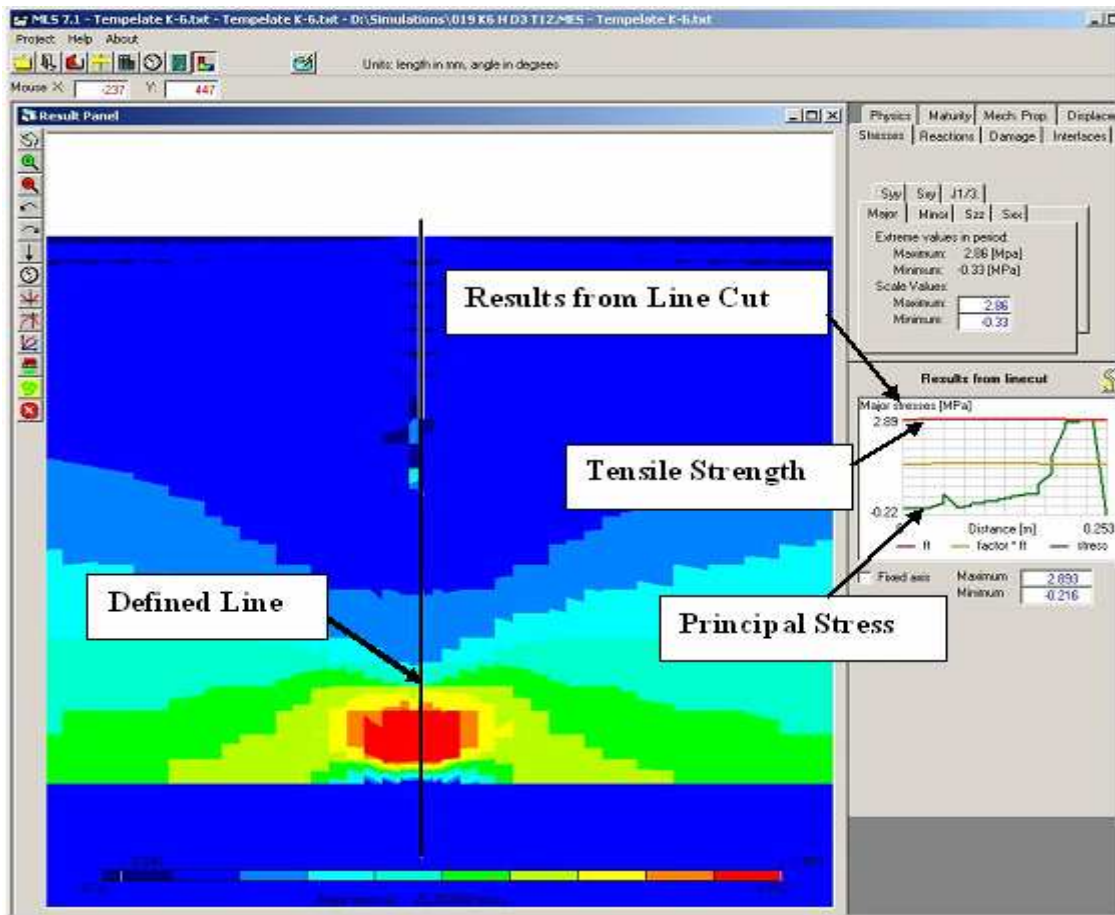


Figure 7.42: Contour plot of principal stresses at 23.3 hours with a defined line cut passing through the joint.

7.4.3 Data History of Quantities at Selected Points

The values of selected quantities at selected points can be obtained at each time increment. The time history of quantities at that point can be viewed, can also be saved in a text file.

Using the history plot option of the result panel, the values of temperature, maturity, tensile strength, compressive strength, principal stress, stress in x-direction and damage (reduction in stiffness) at the tip of the notch were determined for each simulation. As explained in the following section, the quantities were then processed and analyzed for each simulation.

7.5 Processing the Simulation Results

As it was noted earlier, the history plots of selected points were obtained as text files. The text data were then imported to Micro Soft Excel to be processed. In the following subsections, the data processing of selected quantities will be explained.

7.5.1 Pavement End Reactions and Stresses

To obtain the end reaction or support reaction of pavements, the reaction contour plot tab was selected. Figure 7.43 shows the defined elements of the model. One point was defined at each end element of the pavements. Then the reaction forces of all the pavement end elements were added together to obtain the total end reaction of the pavement at each time. This total force was then divided by the cross sectional area of the pavement (i.e., 380 mm high by 1000 mm wide) to calculate the average end stresses at each time increment. It should be noted that as shown in Figure 7.35, the end reaction is not uniformly distributed.

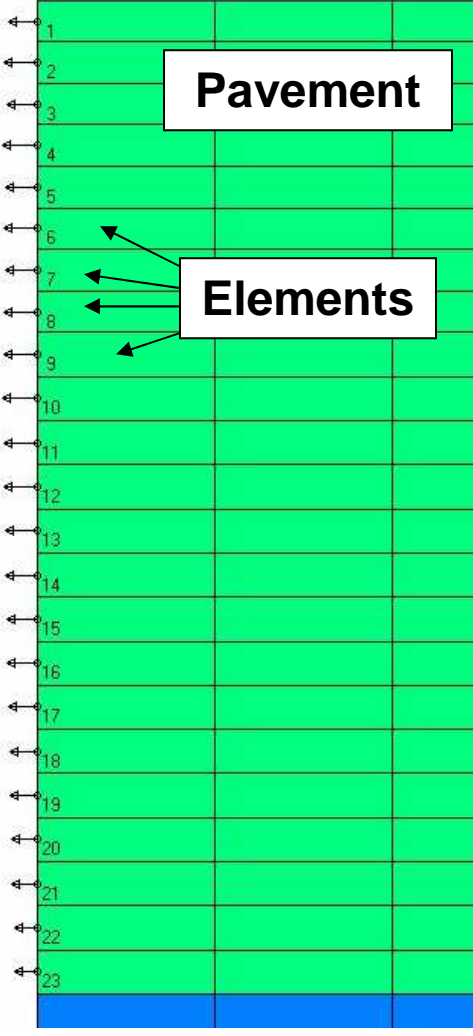


Figure 7.43: Left end finite elements of pavement.

7.5.2 Average Tensile Strength

The combined effects of the heat of hydration the dissipation of heat from the top and bottom surfaces of pavements, and ambient temperature fluctuations can create non-uniform temperature distribution in the pavement. Since the rate of concrete property development depends on the concrete temperature, different parts of a pavement may have different material properties at any age (maturity) depending on their distance from the pavement boundaries. Therefore, a single point measurement of a property such as tensile strength cannot be representative of the entire depth. To alleviate this issue, ten equal-distance history points were defined across the depth of the pavement. Then the

average tensile strength of pavement at each time increment was obtained. This value is used in cracking potential and stress behavior analysis.

7.5.3 Crack Width Opening Displacement

As it was discussed earlier, FEMMASSE enables displacement in X and Y directions at any time to be calculated. However, only the x-direction displacement is considered in this study as it enables the crack width at the tip of the saw-cut to be calculated. As shown in Figure 7.44, two history points were defined at the tip of the saw-cut, and the displacements at two points were saved. As the pavement cracks opens, each side of saw-cut moves in opposite direction (i.e., the left side has a negative and the right side has a positive x-direction displacement). The difference in the calculated x-direction displacement would result in crack tip opening displacement (CTOD). Figure 7.45 illustrates the graph of CTOD calculated at the tip of the saw-cut for the baseline case simulation.

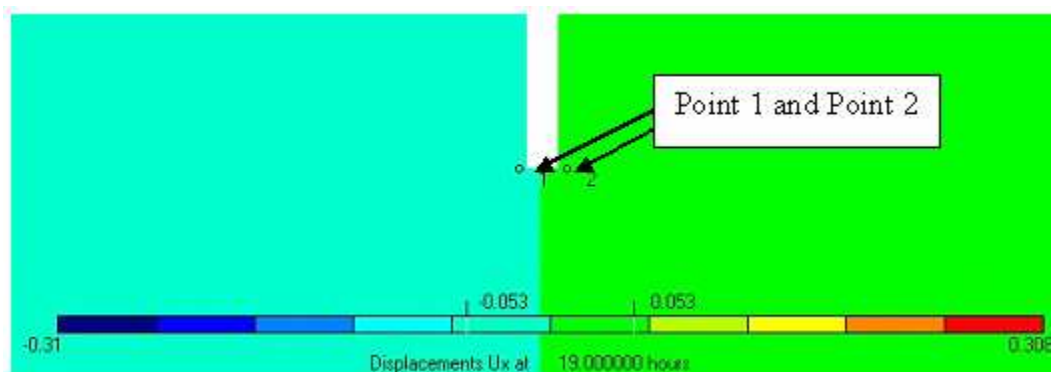


Figure 7.44: X-direction displacement contour plot.

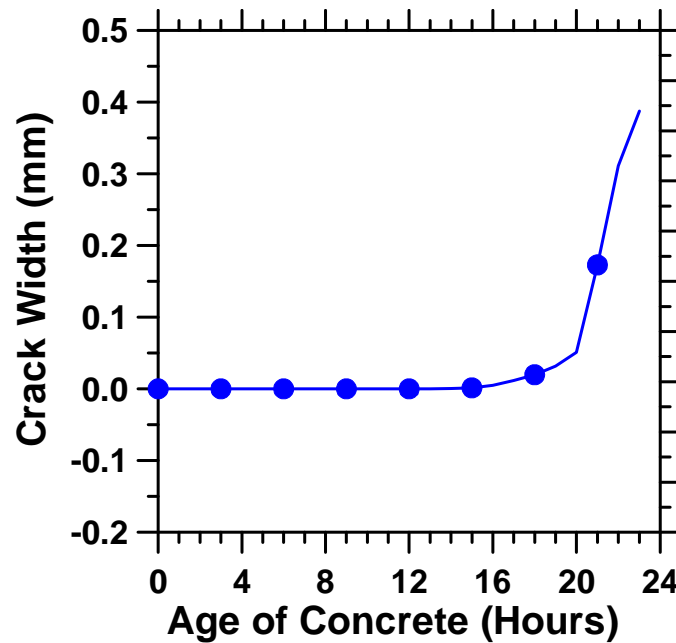


Figure 7.45: Measured CTOD versus time at the tip of saw-cut.

7.5.4 Cracking Potential

Obtained the average end stresses (reactions) and average tensile strengths throughout of pavement over a range of time increments enables the cracking potential factor to be calculated. The cracking potential is obtained by dividing tensile stress by the tensile strength, and ranges from zero to one; zero indicates no potential for cracking, and one implies that the stress equal the strength at cracking. It should be noted that negative stresses, corresponding to compressive stresses, were considered to be zero in cracking potential calculations as the main cracking force in pavement cracking in this study is the tensile stresses.

7.6 Conclusion

In this chapter, the general modeling approach used in this study was discussed. The model's geometry, initial material conditions, environmental and thermal boundary conditions such as ambient temperature functions, mechanical boundary conditions, and meshing were explained in detail. Moreover, the available ways to view the simulation output was also described. Finally, the data processing approach of simulation output that were used in data analysis were discussed.

For each simulation, the history graphs of temperature, maturity, tensile strength, compressive strength, principal stress, stress in x-direction, damage (reduction in stiffness), and CTOD at the tip of the saw-cut were plotted as function of time. These graphs can be viewed in Appendix A. The history graphs plotted for the baseline case are shown in Figure 7.46.

In the following chapter, the simulation results and data analysis will be discussed in details.

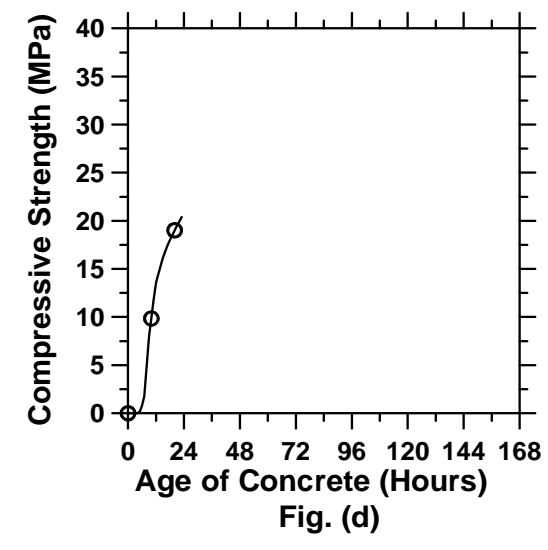
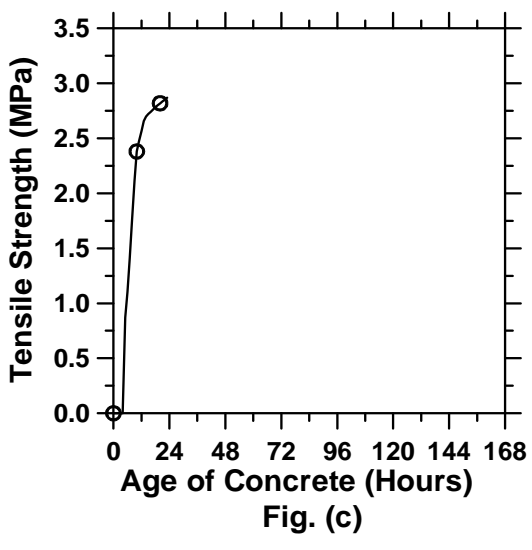
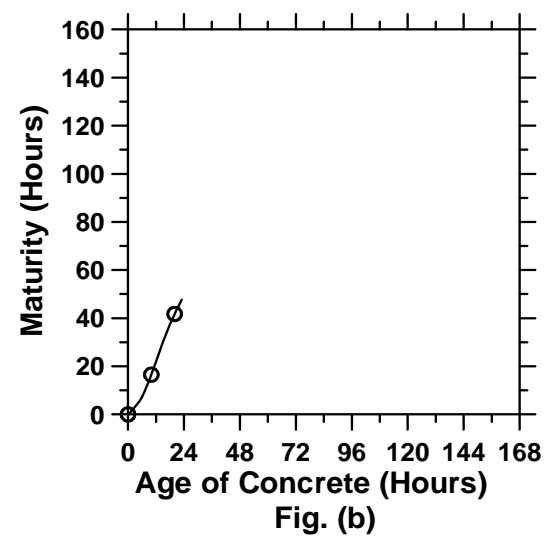
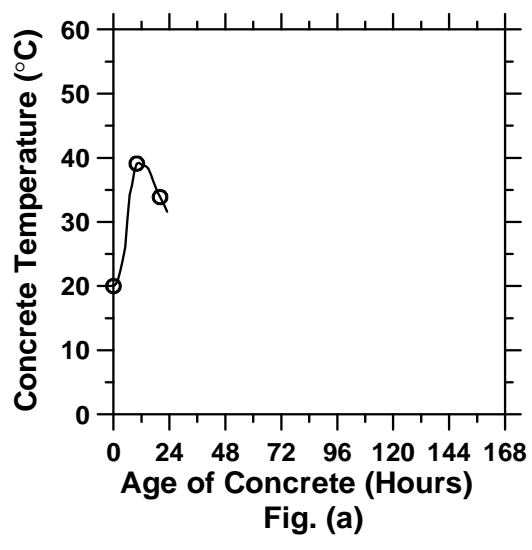


Figure 7.46: History graphs of selected quantities calculated at the tip of the saw-cut
(cont'd).

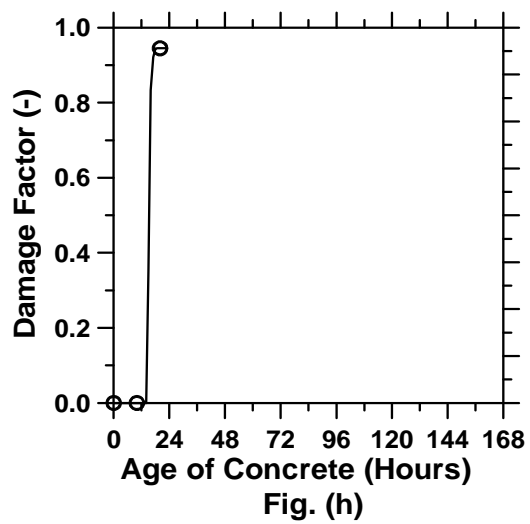
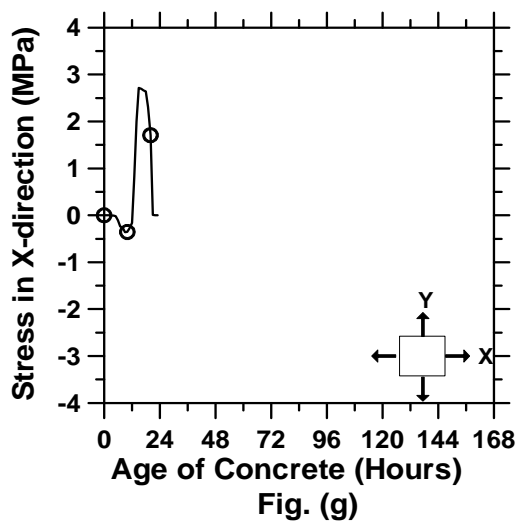
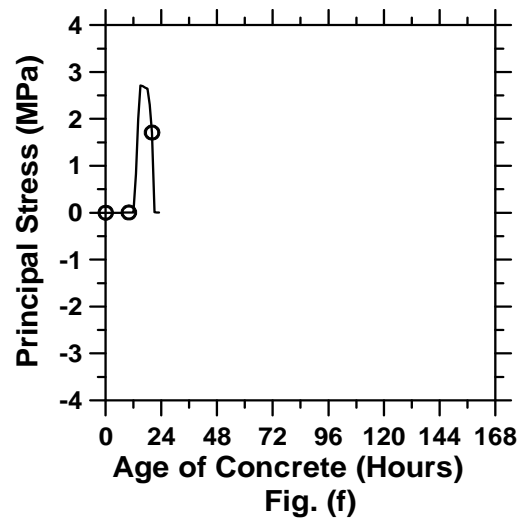
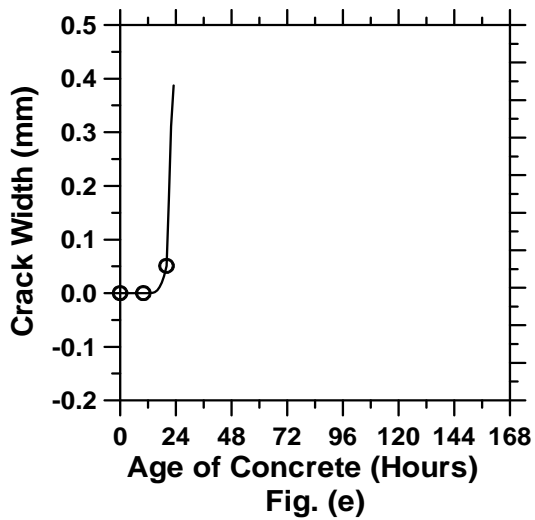


Figure 7.46: History graphs of selected quantities calculated at the tip of the saw-cut.

CHAPTER 8: FINITE ELEMENT SIMULATIONS OF CONCRETE PAVEMENTS

8.1 Introduction

Joints are placed in portland cement concrete pavements at early ages to create a weakened plane that enables a crack to form in a controlled manner. This placement reduces residual stresses that are developed in the pavement. The cracking behavior of concrete is influenced by environmental conditions, concrete mixture properties, and subgrade conditions. The prediction of the correct saw-cut time window is needed not only to minimize the risk of raveling, but also to reduce the random cracking potential of pavements. The determination of an appropriate saw-cut depth has been proven to be crucial in minimizing the risk of random cracking and in increasing the long term performance of the concrete pavements. This study employs a non-linear fracture mechanics approach to determine the appropriate saw-cut depth and time.

This chapter describes computer simulations that investigate the influence of the depth and time of saw-cut on stress and cracking behavior of concrete. Various factors influencing the saw-cutting time window and depth of saw-cuts were also considered.

8.2 Saw-cut Depth

This section describes computer simulations performed to determine the appropriate saw-cut depth that minimizes the risk of random cracking. To achieve this goal, more than eighty simulations have been performed with different saw-cut depths and saw-cut timing. It should be noted that for each simulation, the corresponding graphs of temperature, maturity, tensile strength, compressive strength, principal stress, stress in x-direction, damage, and crack tip opening displacement at the tip of the saw-cut are presented in Appendix A.

8.2.1 Computer Simulations to Investigate the Effect of Saw-cut Depth

The cracking behavior of pavements with saw-cut depths of $D/2$, $D/3$, $D/4$, $D/6$, $D/8$, and $D/100$ was investigated. In addition, the saw-cut timing was varied. In order to model the pavement behavior when no saw-cut is applied, a $D/100$ saw-cut was used. A computer simulation was also performed with no saw-cut placement. The list of simulations performed to investigate the influence of saw-cut depth on pavement cracking behavior is illustrated in Table 8.1.

Unless noted otherwise, the temperature function was considered to be the same as the baseline case periodical ambient temperature function discussed in section 7.2.2.5. The wind speed and RH were also maintained constant at 10 (m/s) and 75% respectively. The depth of the pavement (D) was considered to be 380 mm (15 inches). However, the depth and the time of the saw-cut were varied as shown in Table 8.1.

Table 8.1: List of simulations that consider saw-cut depth and time.

		<i>Time of saw-cut Introduction (Hours)</i>															
		0	6	9	12	15	18	19	20	21	22	23	24	30	36	48	60
<i>Depth of Saw-cut</i>	<i>D/2</i>	■	■	■	■	■	■	■	■	■	■	■	■	■	■	■	■
	<i>D/3</i>	■	■	■	■	■	■	■	■	■	■	■	■	■	■	■	■
	<i>D/4</i>	■	■	■	■	■	■	■	■	■	■	■	■	■	■	■	■
	<i>D/6</i>	■	■	■	■	■	■	■	■	■	■	■	■	■	■	■	■
	<i>D/8</i>	■	■	■	■	■	■	■	■	■	■	■	■	■	■	■	■
	<i>D/100</i>	■	■	■	■	■	■	■	■	■	■	■	■	■	■	■	■
	<i>D/100</i>	■	■	■	■	■	■	■	■	■	■	■	■	■	■	■	■

8.2.2 Analysis of the Simulation Results

8.2.2.1 Crack Tip Opening Displacement and Stresses at the Saw-cut Tip

For quasi-brittle materials such as concrete, the strain-softening response of materials after the peak load comes from aggregate interlock and the micro-crack regions that are developed in the fracture process zone at the crack tip (Shah et al., 1995). As shown in Figure 8.1, the saw-cut length a is considered to be a traction-free (i.e., stress

free) region. The fracture process zone includes a bridging region, aggregate interlock, and microcracks.

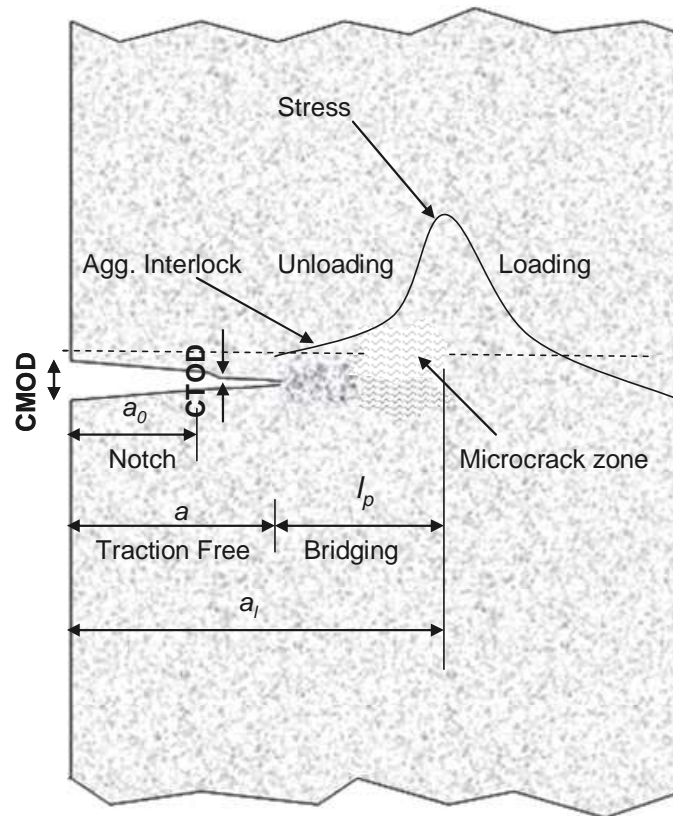


Figure 8.1: Fracture process zone crack growth of concrete.

As shown in Figure 8.2, the crack mouth opening displacement (*CMOD*) is the displacement measured on surface of specimen across the crack while the crack tip opening displacement (*CTOD*) is the displacement measured at the tip of crack. In this work, *CTOD* will describe the opening at the bottom of the saw-cut. These parameters, and consequently the cracking behavior of the materials, are related to the initial saw-cut length, a_0 , and the effective crack length, a_l . The load-displacement curves shown in Figure 8.2 are used to describe *CMOD* and *CTOD* behaviors of concrete as the crack grows. Upon loading to load level P_I , the material behaves elastically and the crack does not grow. The *CMOD* increases proportionally to the load P_I , but *CTOD* remains in the elastic range. Up to this point, the material behaves in a linear elastic fashion. When the

load level is increased to P_2 , micro cracks appear and the fracture process zone starts to develop at the saw-cut tip. As reflected by the $CTOD$ quantity, the crack consequently starts to open. It should be noted that, upon further loading, the crack will grow to a critical length (i.e., $a = a_c$ and $CTOD = CTOD_c$) which corresponds to the peak load. Following the peak load, unstable cracking growth takes place. The crack grows as the load decreases and results in the softening behavior.

In general, the load-crack opening graphs can be divided into three main regions. The elastic region (region one) can be described as the region before the load level P_I is reached. The stable region (region two) occurs between load level P_I and P_C (i.e., peak load). Finally, the unstable region (region three) that occurs after the peak load level is passed (i.e., post peak softening).

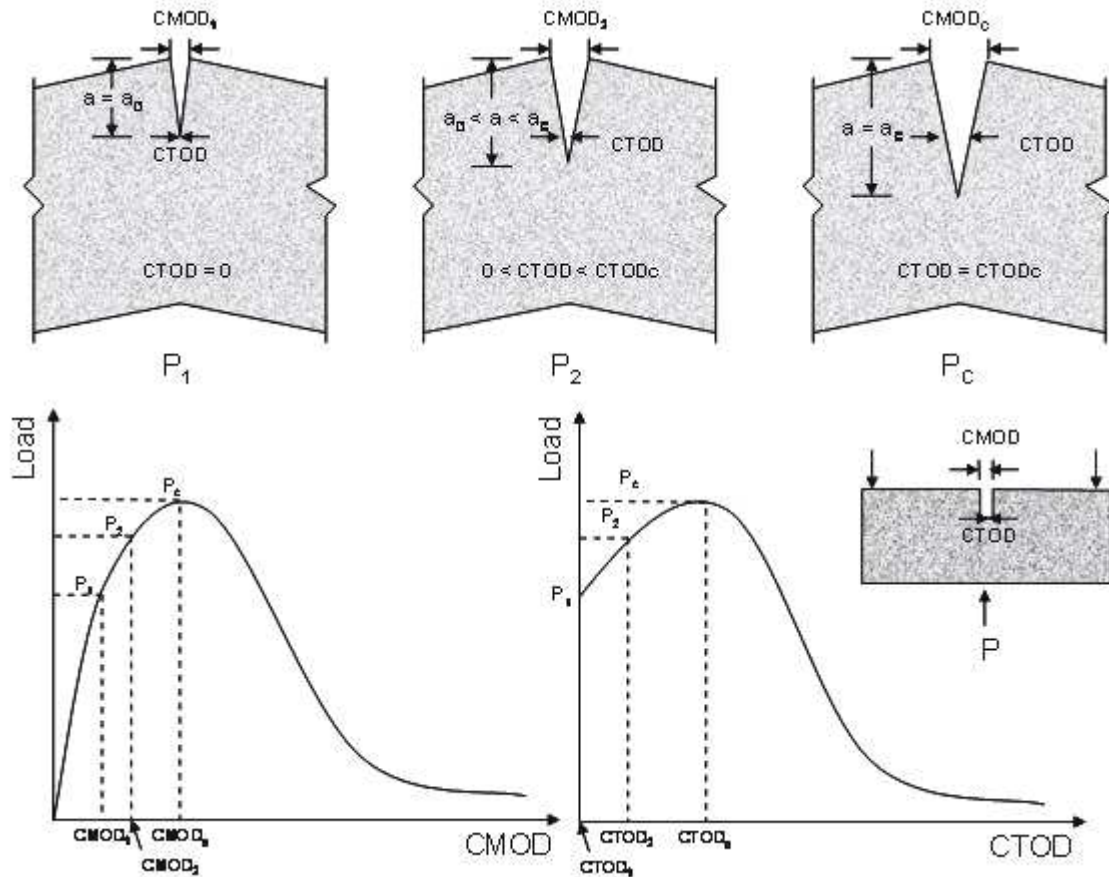


Figure 8.2: Cracking behavior of concrete under different stages of load (Shah et al., 1995).

To illustrate the softening behavior of quasi-brittle materials such as concrete, Figure 8.3 was prepared. In Figure 8.3, the average end stress of the concrete with three different crack lengths is shown. The peak stress along with the plane of the crack moves down as the crack grows from 1 to 2 to 3. At stage 3, a large portion of crack plane is stress free as the crack approaches the bottom.

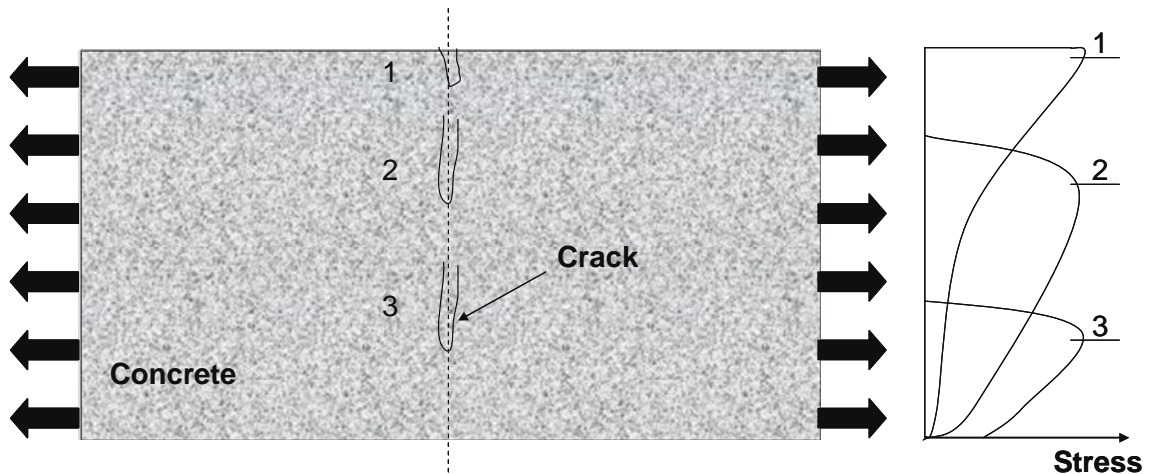


Figure 8.3: Stress response of concrete at different crack positions (Shah et al., 1995).

The same behavior can be seen in Figure 8.3. Figure 8.3 shows the average end stress of a pavement after a saw-cut depth of $D/3$ was introduced at 12 hours. The compressive forces are experienced at early ages as thermal expansion of pavement is restricted. At 12 hours, as the heat of hydration is dissipated through the surface, and concrete shrinkage increases with tensile stresses developing near the surface, the lower portion of the slab remains warmer in compression. At 18 hours, the tensile forces increase significantly and a maximum residual stress is experienced at the surface. As the fracture process zone develops and the crack propagates from the tip of saw-cut, the maximum force moves toward the bottom. Finally, at 23 hours the area close to the surface is stress free and the peak force is near the bottom.

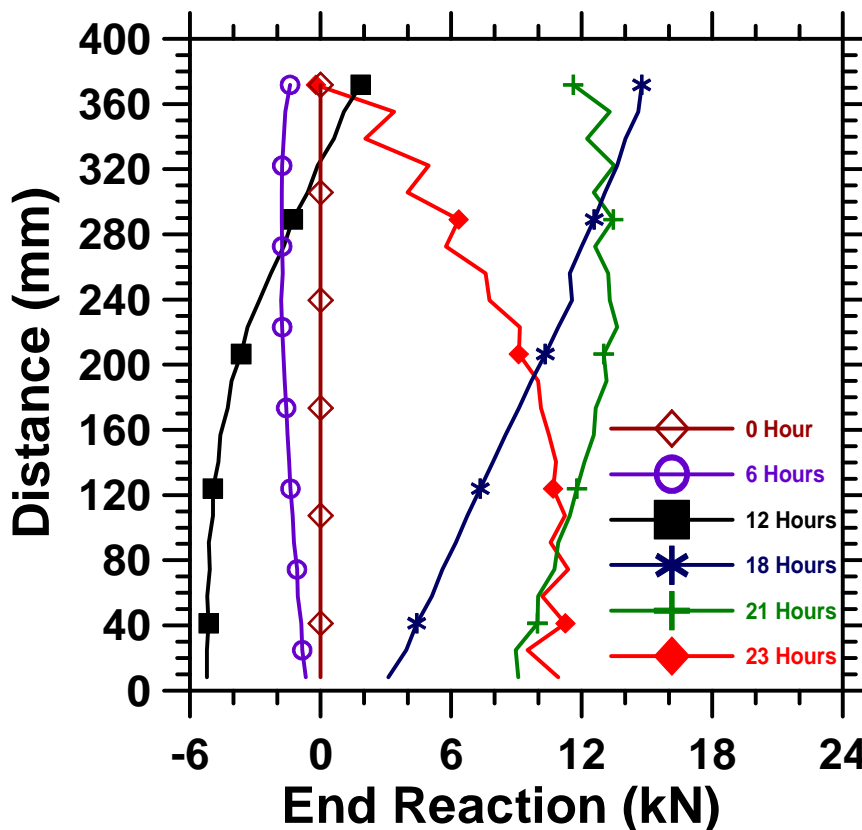


Figure 8.4: Average end reactions of pavement at various hours. Distance is measured from the bottom of the pavement.

Hillerberg (1978) proposed a crack model to describe concrete fracture. He proposed that the softening behavior of concrete can be described by a stress-crack separation displacement figure like the one shown in Figure 8.5. The area under the entire softening post-peak stress elongation curve represents the work (energy) that is released to separate two new surfaces. It should be noted that the amount of stored energy is directly related to the rate of energy release when a crack propagates. Shah et al. (1995) recommended that the propagation of a crack can be either stable, stationary, or unstable depending on the rate of energy release and the amount of stored energy. In stable crack propagation, the crack grows only when the applied load or displacement increases. Unstable cracking occurs at constant or decreasing applied load. Stationary crack growth is a critical state in between. Figure 8.5 shows the normalized stress-crack width of concrete.

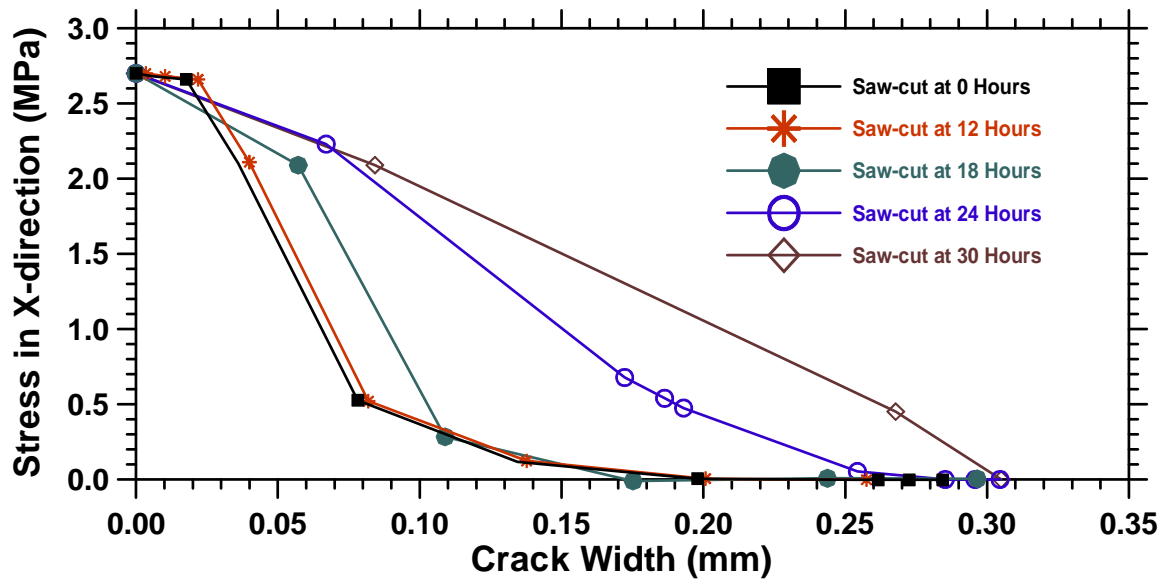


Figure 8.5: Post-peak stress crack width curves of concrete.

Computer simulations of pavements over a range of saw-cut depths ($D/2$, $D/3$, $D/4$, $D/6$, and $D/8$) and times of saw-cut application were performed. The residual stresses at the tip of saw-cut and crack tip opening displacements are compared in Figure 8.6 and Figure 8.7.

Figure 8.6 illustrates tensile strength and stresses in the x-direction, both of which are measured at the tip of the saw-cut for a pavement with a saw-cut depth of $D/2$ and introduced at 0, 12, 18, 24, and 30 hours. As shown in Figure 8.6 during an initial time period, the concrete remains insensitive to saw-cut introduction (0 hour to 12 hours), and only compressive stresses are developed. The insensitivity of concrete to saw-cut introduction can be explained by the elastic-plastic nature of concrete during this time period. The same behavior was seen from the tensile wedge experiments as explained in Chapter 5. The compressive stress development in the pavement can be attributed to the restriction of thermal expansion due to a rise in heat of hydration. As the pavement has higher heat loss through its surface boundary, temperatures near the surface of the concrete is lower than the temperatures near the bottom of the pavement. Tensile stress also begins to develop as this surface cooling begins to occur. The surface of the pavement begins to shrink while the bottom of the pavement is still in expansion state

and continue to expand. The restraint causes the residual stress development in the pavement. The temperature gradient across the pavement causes the pavement to tend bend upward. The saw-cut reduces the stiffness of the pavement. In addition, the introduction of a saw-cut during the first 6 hours results in a gradual increase in tensile stresses and CTOD and consequently stabilizes cracking growth.

As concrete hydrates, shrinkage overcomes the expansion that has resulted from the temperature rise in the concrete, and results in the development of tensile stresses in the pavement after 12 hours. At this stage, the concrete begins to illustrate saw-cut sensitivity. The introduction of the saw-cut results in a rapid increase in local stress at the tip of the saw-cut that rapidly approaches the tensile strength and results in cracking. After the cracks form, the residual stresses begin to decrease. When the saw-cut is introduced at 30 hours, the residual stress in the pavement is close to the concrete strength. This initiates nearly instant crack propagation at the addition of the saw-cut as shown by the nearly vertical rise and drop in residual stress. It should be noted that the storage time of the computations was chosen to be one hour. The stress rise and decrease in these cases occurs in less than one hour for saw-cuts applied at 18, 24, and 30 hours. As such, the maximum stresses that reach the tensile strength were not captured in the output despite the fact that they occur in the simulations.

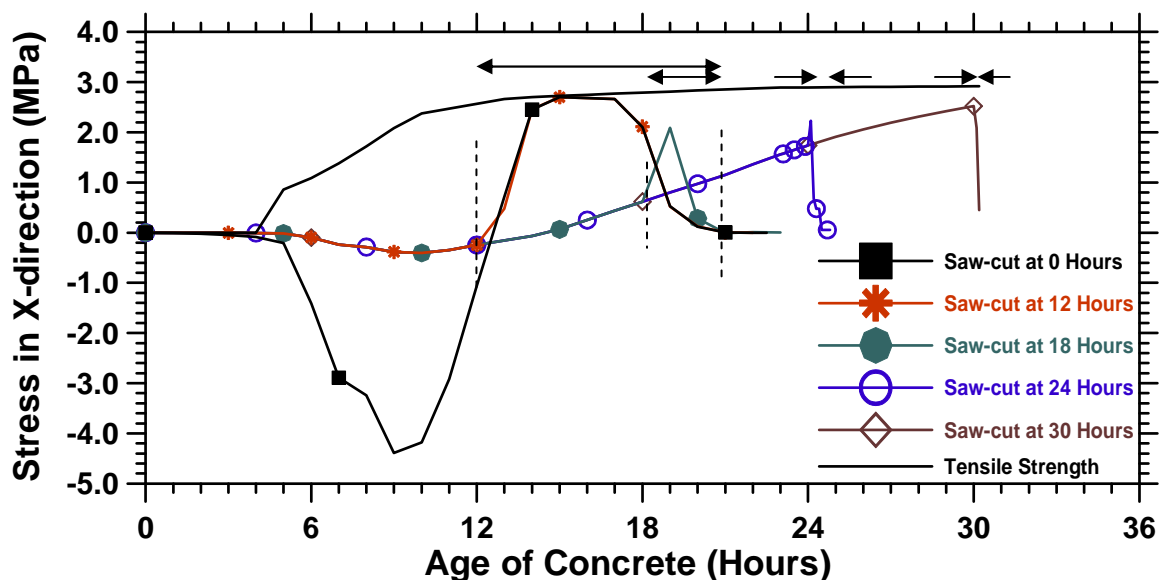


Figure 8.6: Tensile strength and stress at the tip of D/2 saw-cuts.

As shown by the dashed lines in Figure 8.7, the CTOD graphs for saw-cuts which were applied during the first 12 hours are divided into three regions. In region one (the elastic region), the COTD remains in the elastic range for the first 15 hours. This period corresponds to the development in pre-peak tensile stresses. During this period, concrete deforms elastically and no crack propagation is experienced. After the elastic region ends, the stable cracking begins to occur in region 2. This region is characterized by the development of the fracture process zone at the tip of the saw-cut. The CTOD begins to increase in a non-linear and stable fashion. The unstable region (region three) starts at 18 hours. In this region, the CTOD increases rapidly as stress decreases. Figure 8.8 compares the crack tip opening displacements (CTOD) of pavements with saw-cut depths of $D/2$ that were introduced at 0, 12, 18, 24, and 30 hours. As discussed previously, the measured CTOD can be used to investigate the cracking behavior of the saw-cut in pavements. It is seen that as the saw-cut is applied at later ages, the region 2 begin to disappear, and the rate of crack opening in the unstable cracking region increases.

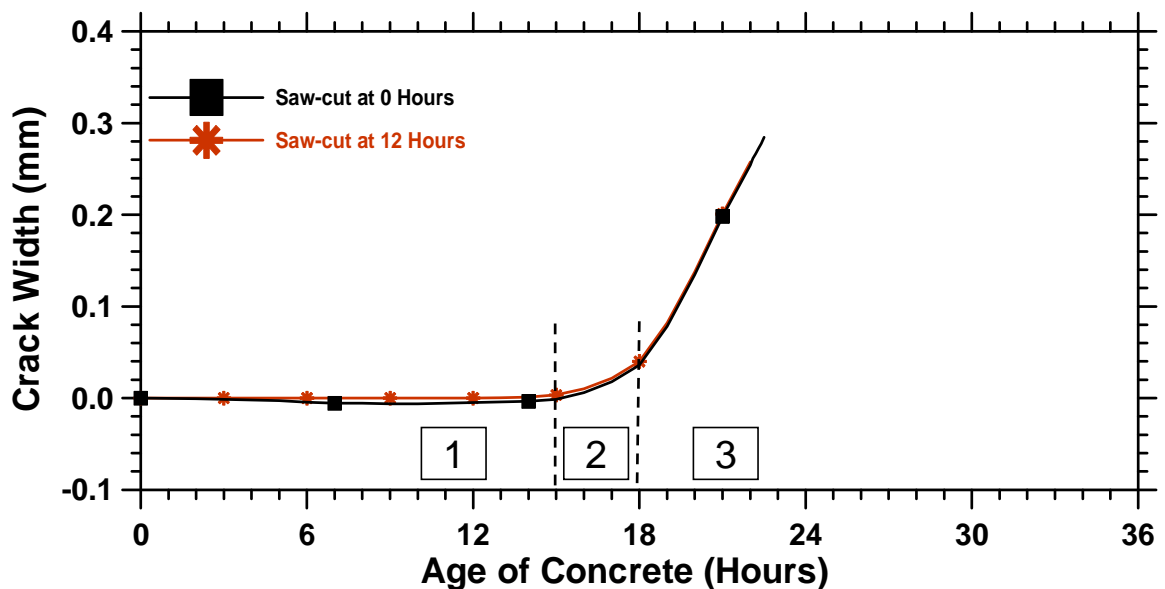


Figure 8.7: CTOD for pavements with $D/2$ depth of saw-cut applied at 0 and 12 hours.

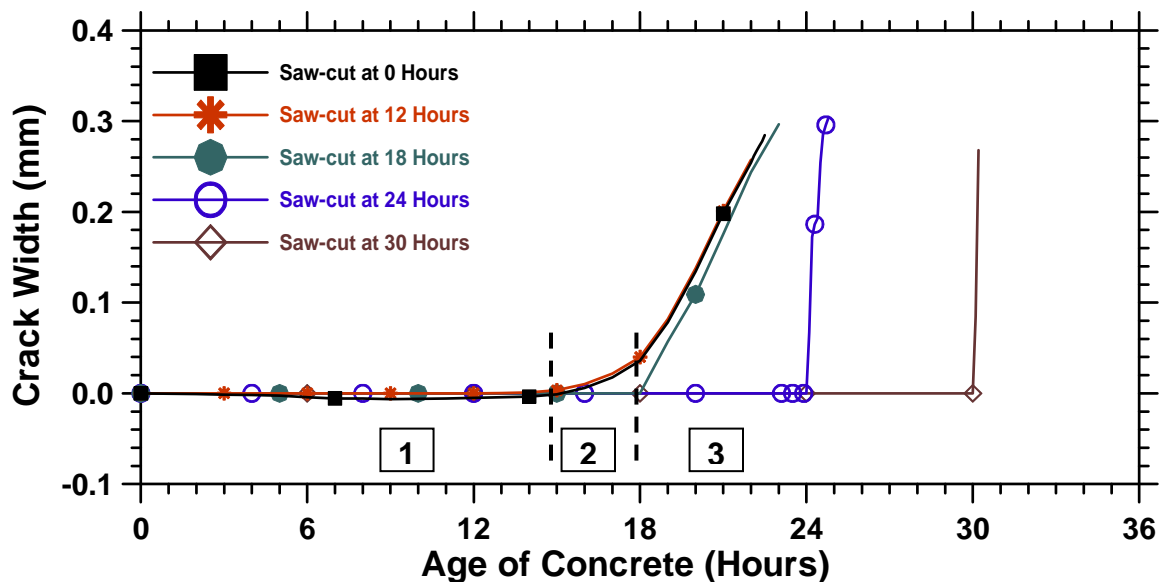


Figure 8.8: CTOD for pavements with D/2 saw-cuts.

The tensile strength and stress at the tip of saw-cuts for pavements with D/3 saw-cuts introduced at 0, 12, 18, 24, and 30 hours are shown in Figure 8.9. It should be noted that a similar stress behavior between the pavements with D/3 depths of saw-cut and the pavements with D/2 depths of saw-cuts was observed.

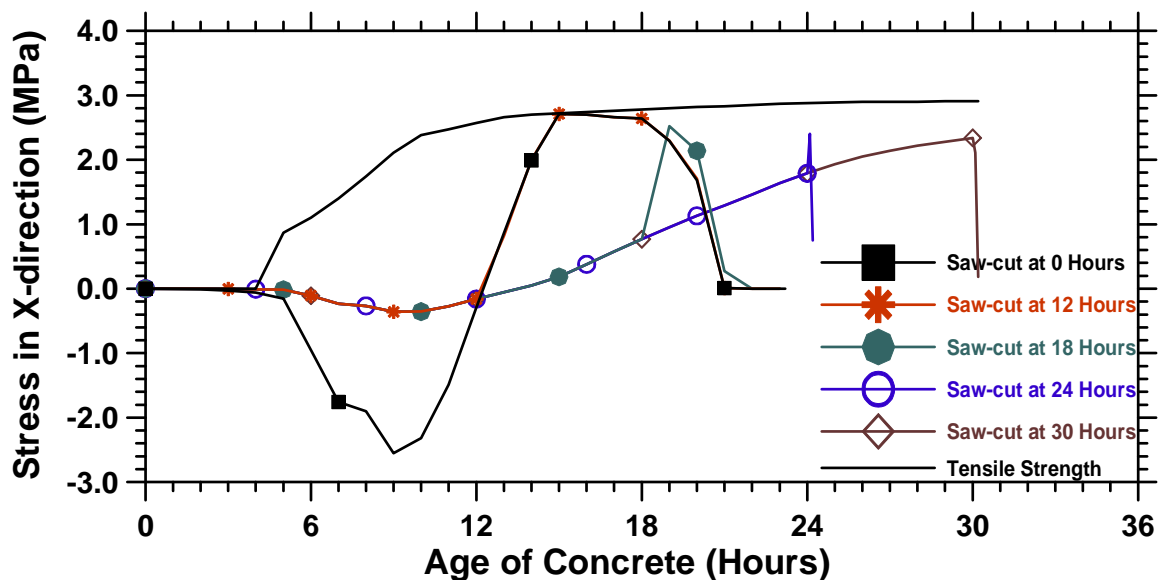


Figure 8.9: Tensile strength and stresses at the tip of D/3 saw-cuts.

Figure 8.10 shows stress contour plots for a saw-cut of D/3 that is introduced at 12 hours. The legend can be used to describe the stress level in the pavement. It should be noted that the negative values in the legend correspond to compressive stresses while positive values indicate tensile stresses. The bottom of the pavement is under slight compression initially while the top surface experiences tensile stresses. Later, after the saw-cut introduction, a fracture process zone begins to develop at the tip of saw-cut. For example, at 18 hours a large fracture process zone, designated by high stress concentration area, develops at the tip of the saw-cut. The crack then begins to grow, and the crack tip reaches the bottom of the pavement at 24 hours while the upper half of the pavement is stress free.

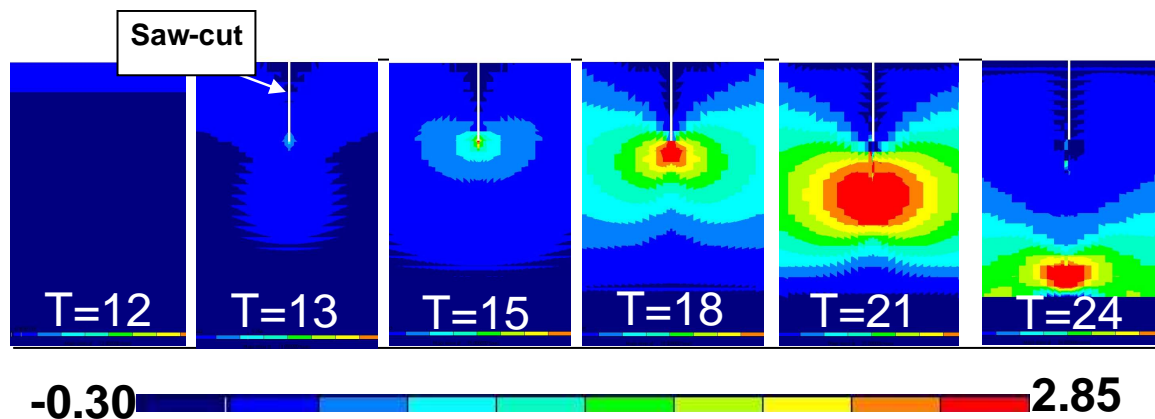


Figure 8.10: Contour plots of stresses at different times for a pavement with D/3 saw-cut introduced at 12 hours.

Figure 8.11 illustrates CTOD behavior of pavements with a saw-cut depth of D/3 which was introduced at 0, 12, 18, 24, and 30 hours. As shown in Figure 8.11, the pavements with D/3 saw-cuts illustrate crack opening behavior that is similar to pavements with D/2 saw-cuts (i.e., Figure 8.8). The CTOD initially remains close to zero as concrete behaves elastically. After the stress level at the tip of the saw-cut reaches the strength of the pavement (i.e., 15 hours), stable crack growth begins. As the stress level increases and reaches its critical level, unstable crack opening occurs (20 hours). However, when the saw-cut is applied to pavements with a high residual stress level, the

stable crack growth tends to disappear (i.e., the elastic CTOD behavior is followed by unstable crack propagation).

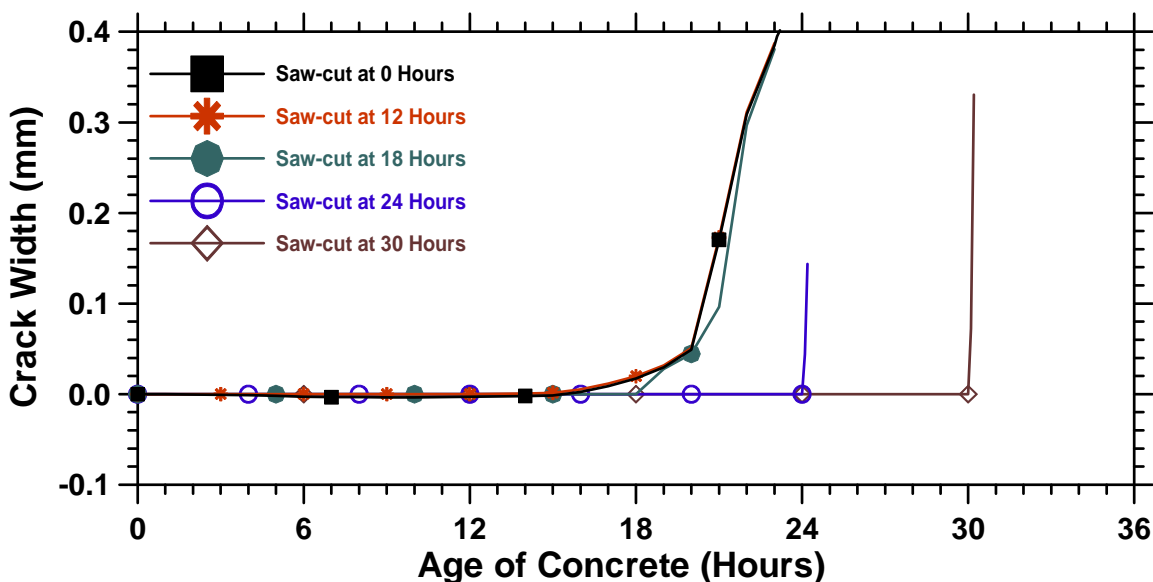


Figure 8.11: Crack tip opening displacements for pavements with a D/3 depth of saw-cut.

Figures 8.12, 8.13, 8.14, 8.15, 8.16, and 8.17 illustrate the selected stress and CTOD graphs of pavements with D/4, D/6, and D/8 saw-cut depths. Similar CTOD and stress behaviors of pavements with D/2 and D/3 saw-cut depths are observed. The pavement remains in elastic-plastic condition during the first 12 hours, and the concrete behaves elastically. If saw-cuts are applied before residual stresses reach the critical stresses, stable crack growth occurs. However, the introduction of saw-cut in pavements when the stresses are higher than the critical stress level would result in unstable cracking, and this should be avoided for field concrete.

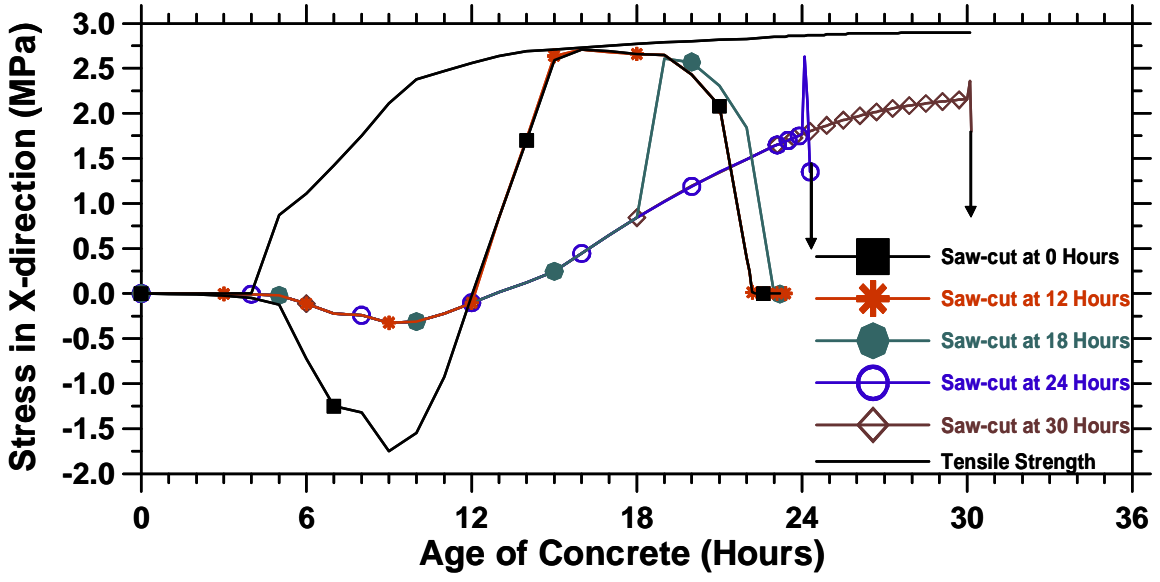


Figure 8.12: Strength and local stresses of pavements with a saw-cut depth of D/4.

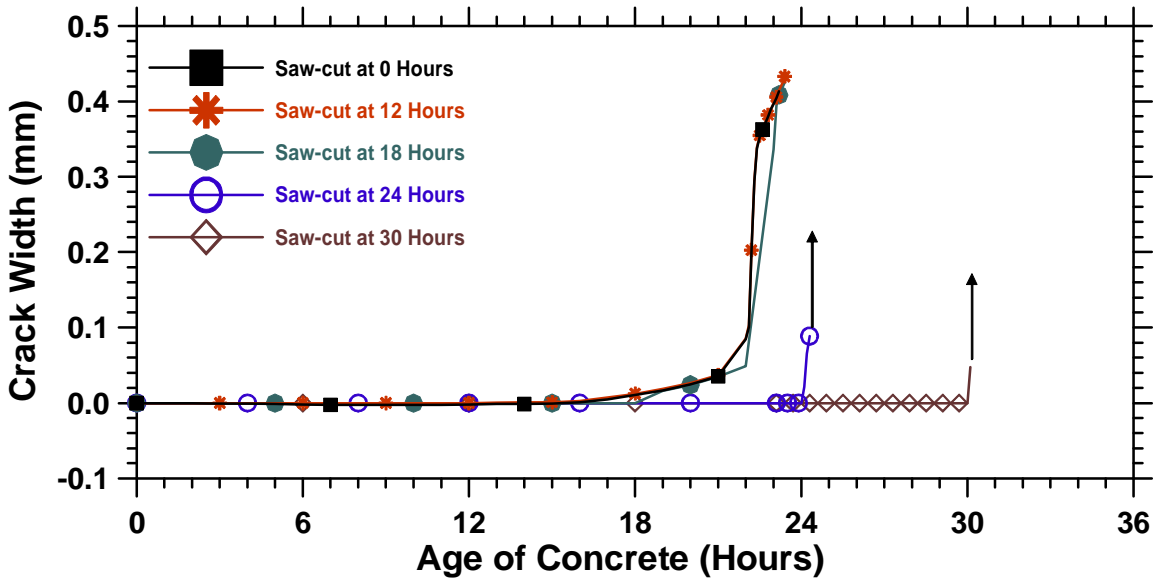


Figure 8.13: CTOD of pavements with a saw-cut depth of D/4 applied at different times.

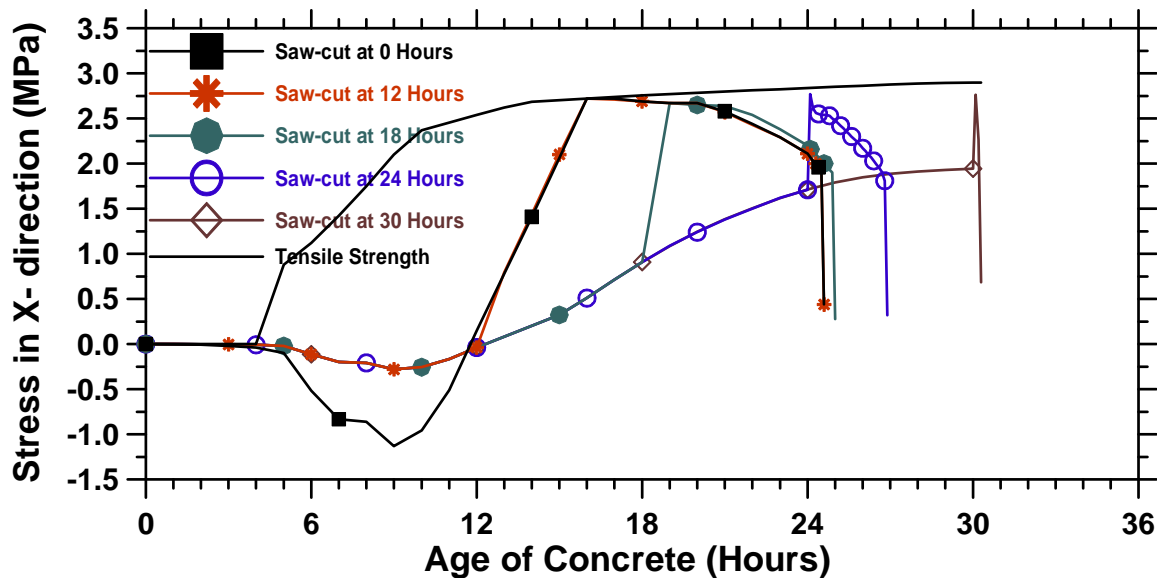


Figure 8.14: Tensile strength and stresses of pavements with D/6 saw-cuts.

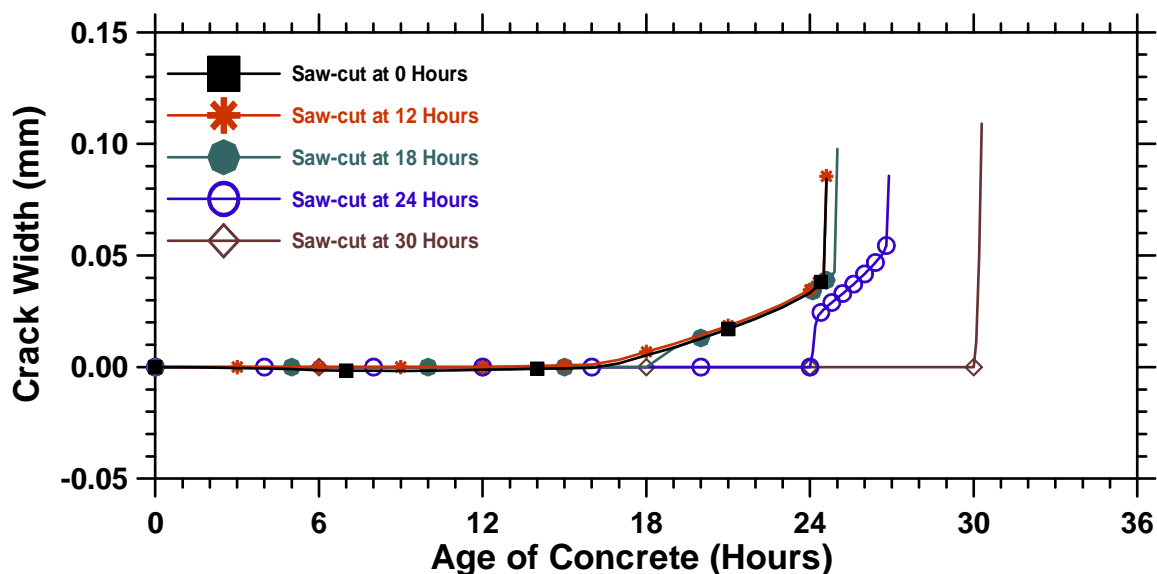


Figure 8.15: CTOD of pavements with a saw-cut depth of D/6 applied at different times.

Figure 8.16 and Figure 8.17 show the residual stresses and CTOD behaviors of the pavements with saw-cut depths of D/8 respectively. As shown in Figure 8.16, the residual stress development is reduced slightly as the ambient temperature increases. The higher ambient temperature raises the surface temperature of concrete, and causes thermal expansion to occur. The thermal expansion reduces the tensile stress of concrete mostly

near the surface and at the tip of the saw-cut. This behavior is also shown in Figure 8.17 by a relatively constant crack width. As the ambient temperature decreases, the thermal expansion of concrete tends to cease and the tensile stress of concrete drives the crack growth again.

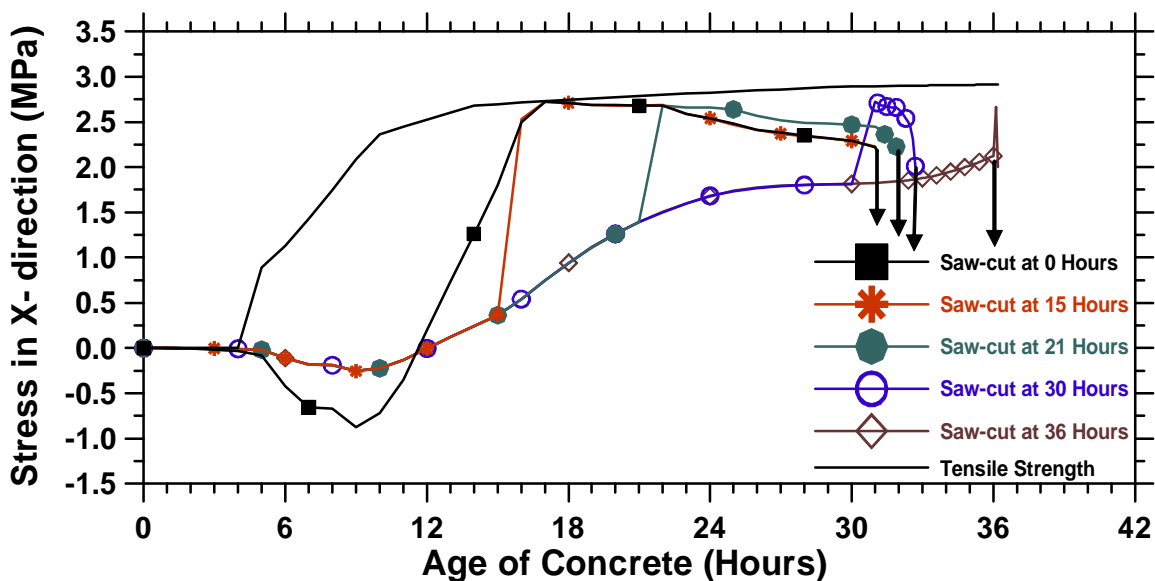


Figure 8.16: Tensile strength and stresses of pavements with D/8 saw-cuts.

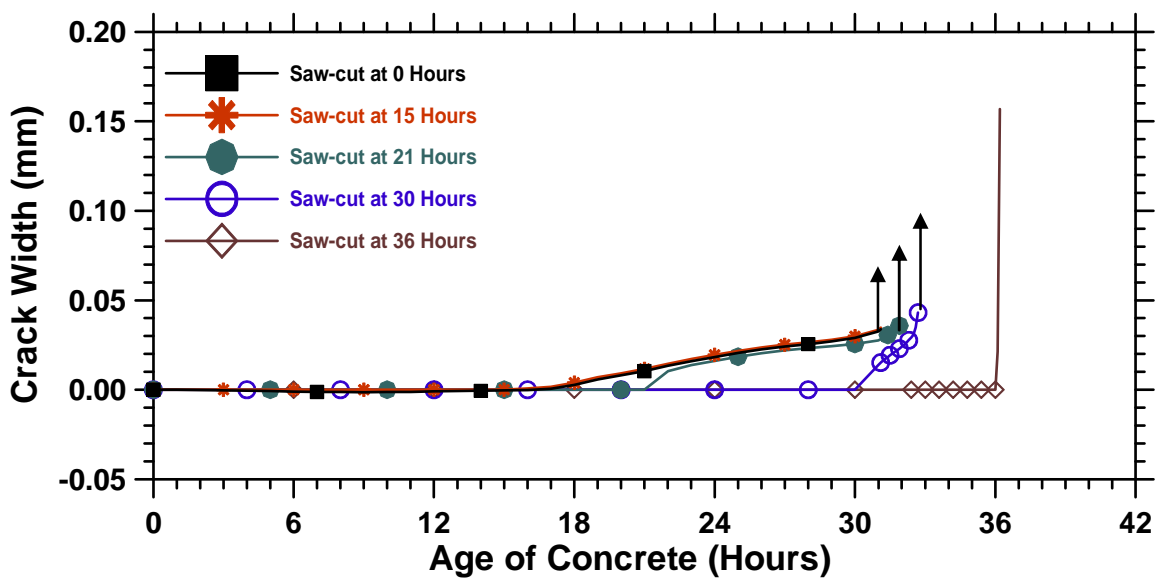


Figure 8.17: CTOD of pavements with a saw-cut depth of D/8 applied at different times.

Pavements with saw-cut depth of D/100 were used to model un-sawed pavements (D/100 represents an internal flaw). As shown in Figure 8.18, ambient temperature changes control the stress development and consequently the cracking of concrete at later ages. For example, a lower ambient temperature resulted in a higher residual stress level near the tip of the saw-cut, which was applied at 48 hours, leading to crack initiation. However, a subsequent increase in ambient temperature resulted in a decrease in residual stress level and cessation of crack opening. As the ambient temperature decreased again, the residual stress level increased, and the crack propagated.

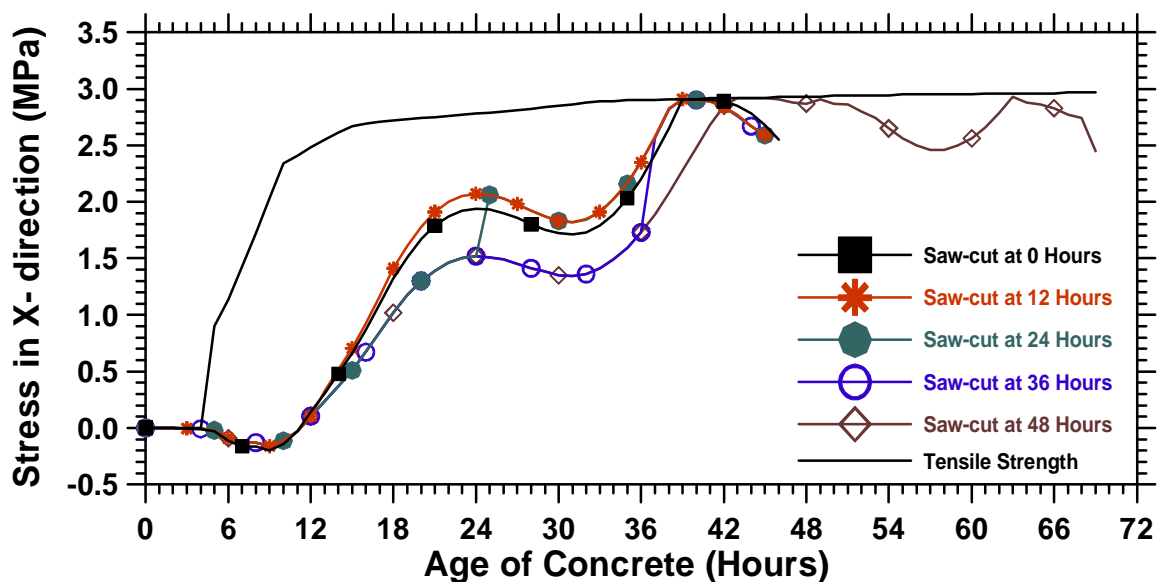


Figure 8.18: Tensile strength and stresses of pavements with D/100 saw-cuts.

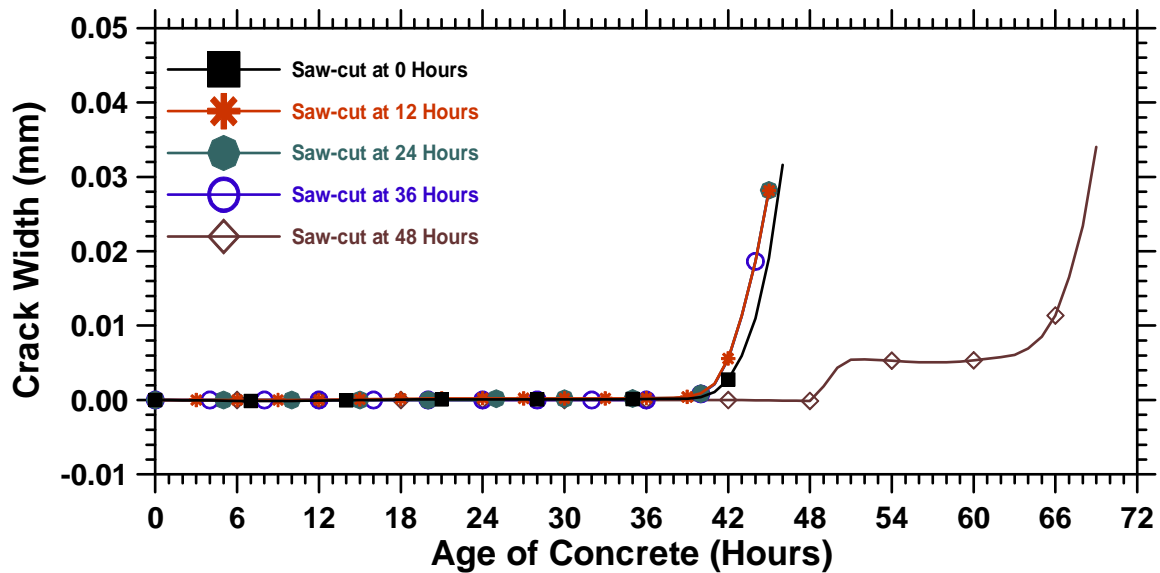


Figure 8.19: CTOD of pavements with a saw-cut depth of $D/100$ applied at different times.

8.2.2.2 The Influence of Saw-cut Depth on Pavement Cracking

“A material is considered to be notch sensitive if the presence of a notch causes a change in the net section strength (σ_{net}) of the material calculated on the basis of the reduced cross section but neglecting the stress concentration effect of the notch” (Shah et al., 1995). For quasi-brittle materials like concrete, the net section strength is reduced with an increase in notch (saw-cut) length; however, the ductile materials like metals show notch insensitivity behavior. These behaviors are summarized in Figure 8.20.

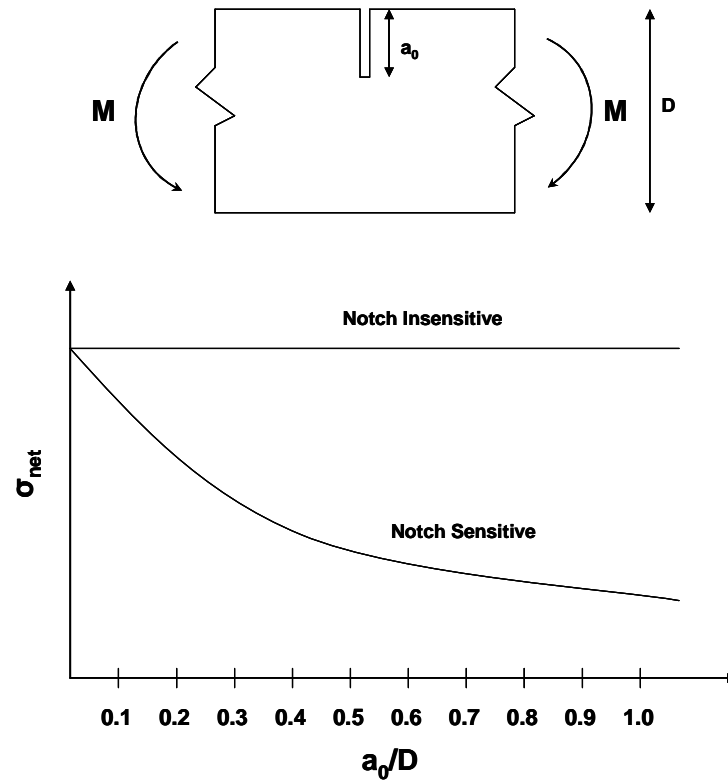


Figure 8.20: Notch sensitivity strength behavior of brittle and ductile materials
(Shah et al., 1995).

To assess the influence of saw-cut depth on stress and cracking behavior of concrete, the average end reaction and average tensile strength of pavement were obtained for each analysis. For all simulations, the average end reaction at any time was divided by the original, unnotched cross sectional area of the pavement to obtain the average end stress. The graphs of the average tensile strength and average end stress versus time were plotted for each saw-cut size. The graphs of average end stress and average tensile strength for $D/2$, $D/3$, $D/4$, $D/6$, $D/8$, and $D/100$ saw-cuts have been provided in Appendix B; however, for the purpose of explanation, only graphs of average end stress and average tensile strength for pavements with a saw-cut depth of $D/2$ are presented here in Figure 8.21. It should be noted that the solid lines (with no symbol) represent tensile strength while the solid lines with solid circles represent average end stresses.

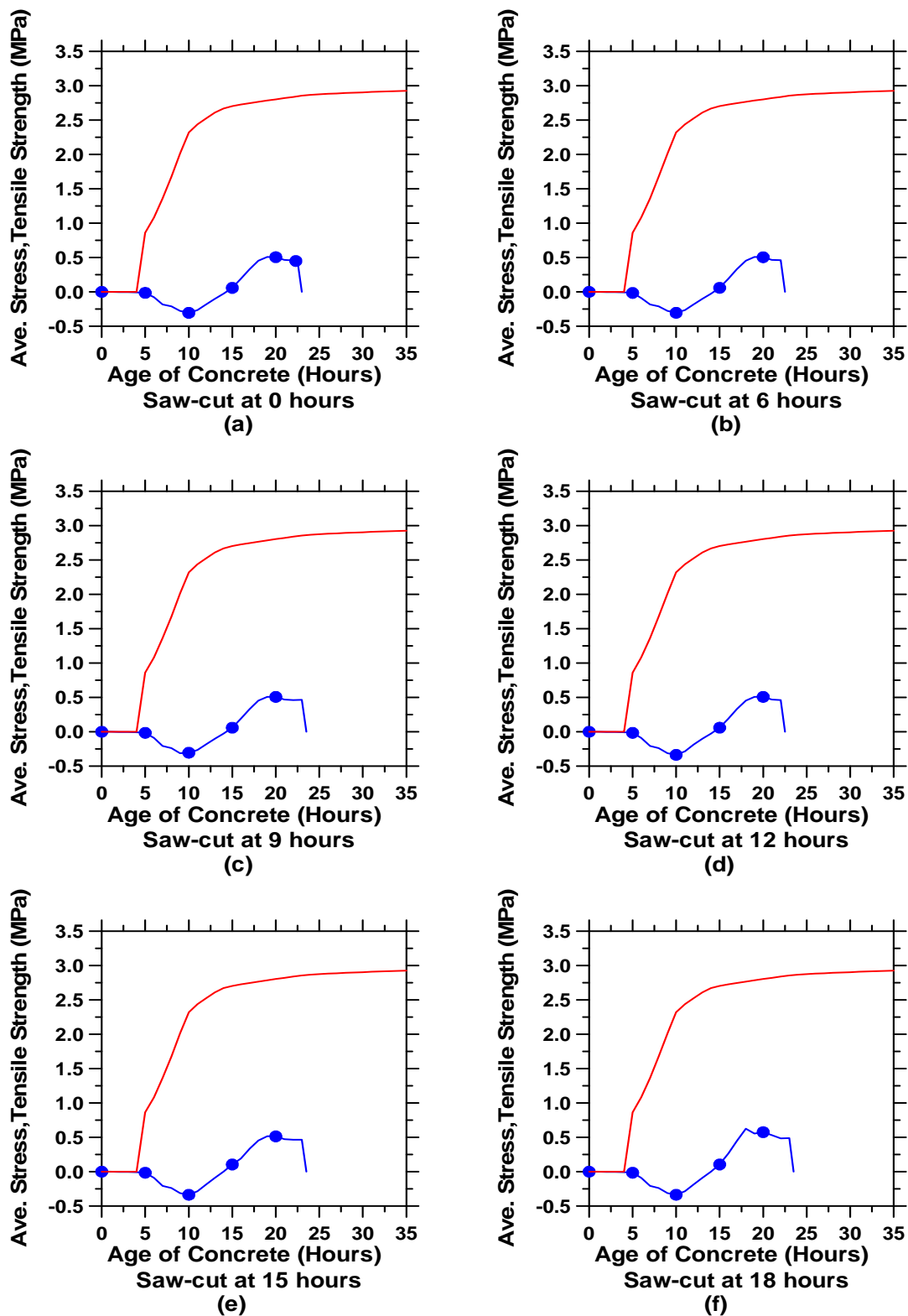


Figure 8.21: The average end stress and average tensile strength for a pavement with a $D/2$ saw-cut depth (cont'd).

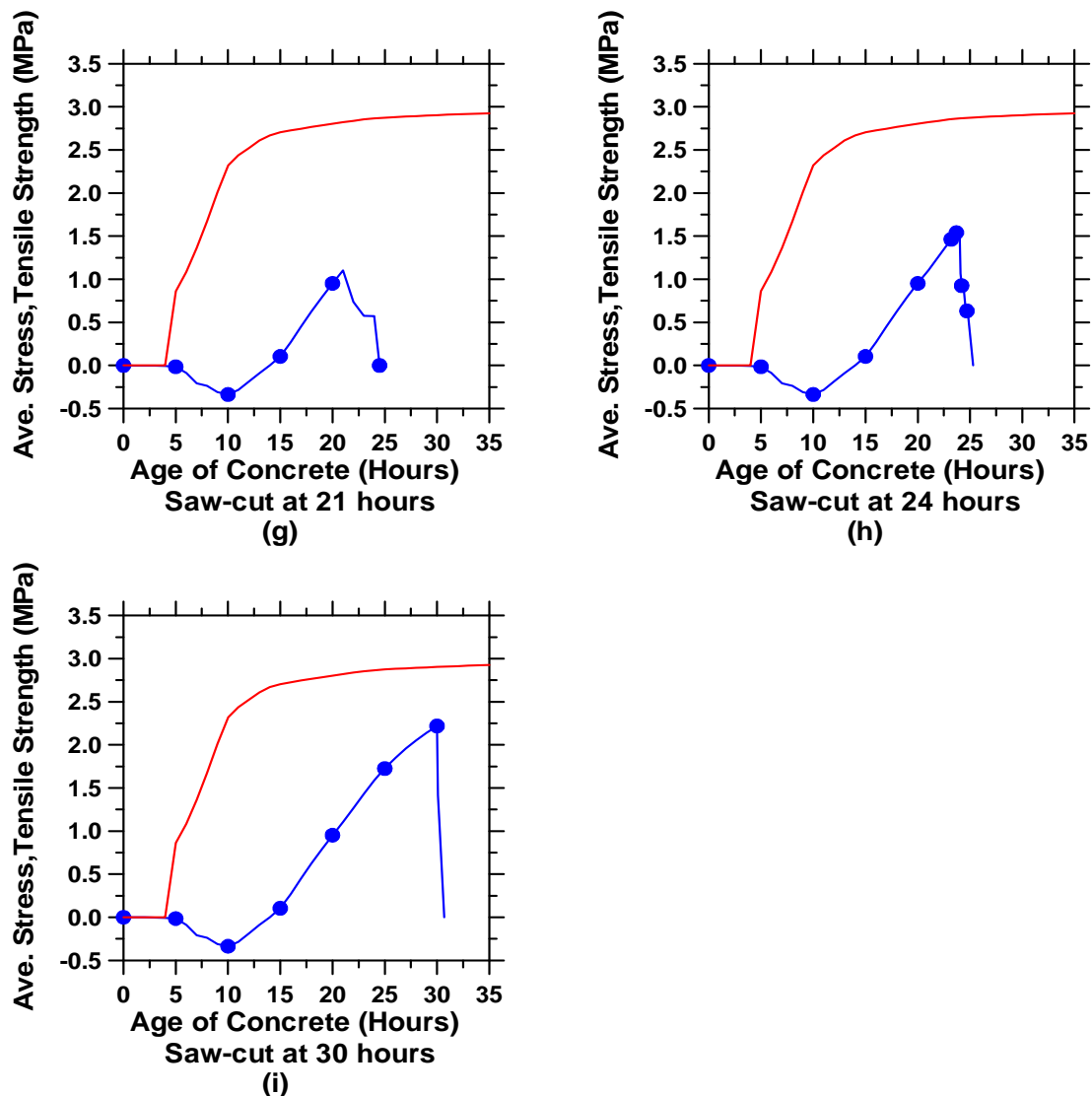


Figure 8.21: The average end stress and average tensile strength for a pavement with a $D/2$ saw-cut depth.

Figure 8.21 (a), (b), (c), (d) and (e) (i.e., saw-cuts introduced between 0 and 15 hours) show similar stress behavior although the saw-cut was applied at different times. This occurs since the saw-cut was applied during the elasto plastic state of concrete. In each of these cases, the residual stress at failure is less than the product of 0.18 (this factor will be discussed in Chapter 9) and tensile strength of concrete. When the saw-cut is introduced at later ages (i.e., between 18 and 30 hours), the residual stress are higher than $0.18f_t'$, and an abrupt reduction in stresses occurs after placement of the saw-cut.

This behavior is more pronounced in graph (i) in which the high stress level at the time of saw-cutting is followed by instant failure at the time of saw-cut introduction. In this case, it is observed that if saw-cuts are applied before 18 hours, stable crack propagation occurs. However, as saw-cuts are applied at higher stress levels, unstable cracking behavior is observed.

In order to illustrate the behavior more clearly, the average end stresses of pavements were divided by the average tensile strength of concrete at any time. The graphs representing the average end stress-to-average tensile strength ratios for different depths of saw-cut are also presented in Appendix C. However, it should be noted that in plotting these graphs, the negative values were converted to zero as they correspond to compression. Only graphs of the stress-to-strength ratios for the saw-cut depth of $D/2$ are illustrated in Figure 8.22. During the first 15 hours, the ratio remains close to zero. If the saw-cut is introduced before pavements achieve a critical stress-to-strength ratio (in this case 0.18), stable crack propagation is observed. Alternatively, if the saw-cut is applied after the critical ratio of 0.18 is reached, unstable cracking behavior is noticed. It should be noted that this ratio will be more thoroughly discussed in Chapter 9. A similar discussion can be made for other saw-cut depths. Each saw-cut size is found to have a different critical stress-to-strength ratio. The critical ratios for $D/3$, $D/4$, $D/6$, $D/8$, and $D/100$ are presented in Table 10.1. Deeper saw-cuts have smaller critical ratios, and applying a saw-cut at stress levels higher than the product of its critical stress-to-strength ratio (Φ) and the strength would result in unstable cracking. This implies that when a particular saw-cut size results in unstable cracking, a shallower saw-cut can be used to prevent unstable cracking growth at the time of saw-cut introduction.

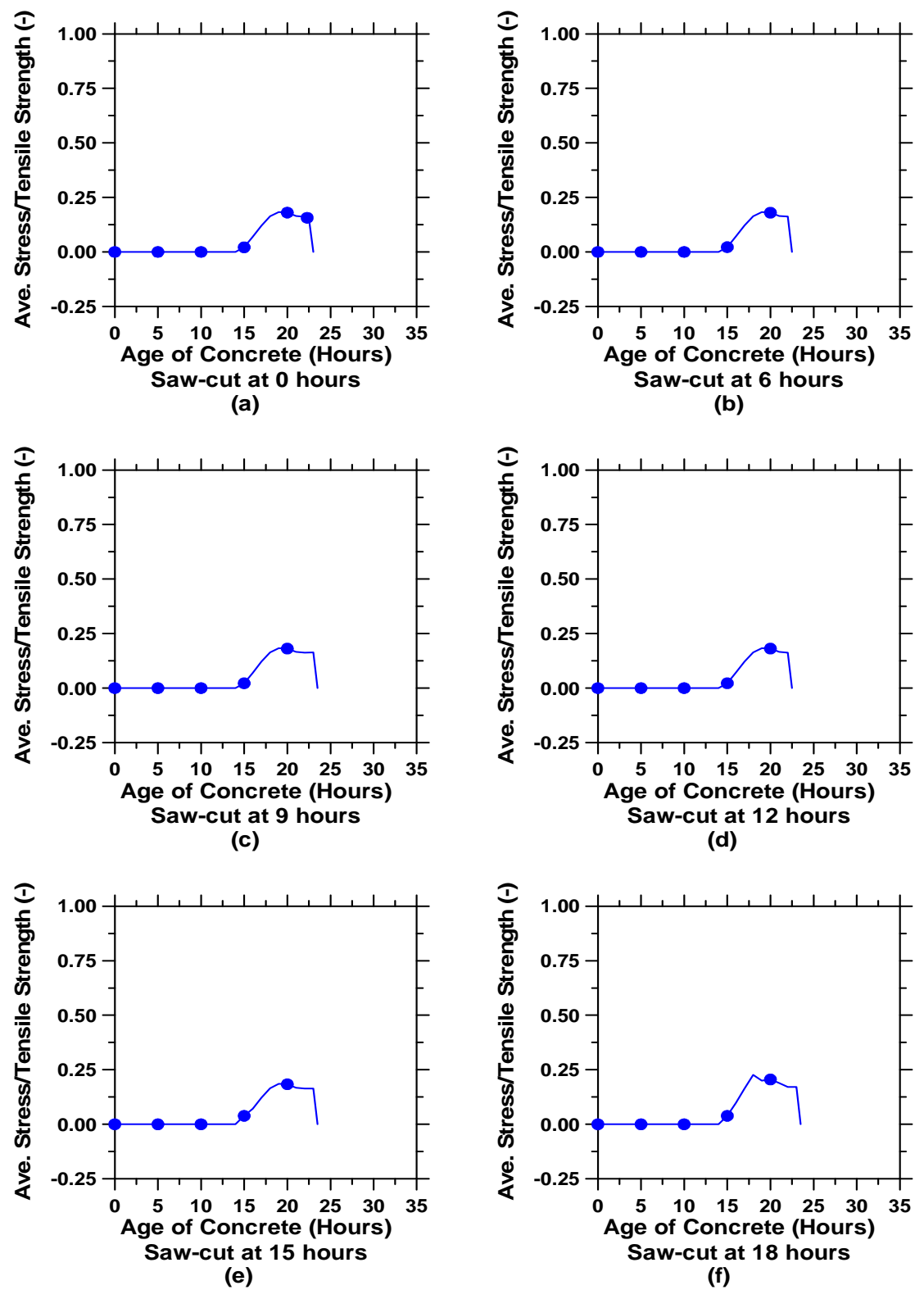


Figure 8.22: Average end stress to average tensile strength ratios for pavements with a D/2 saw-cut (cont'd).

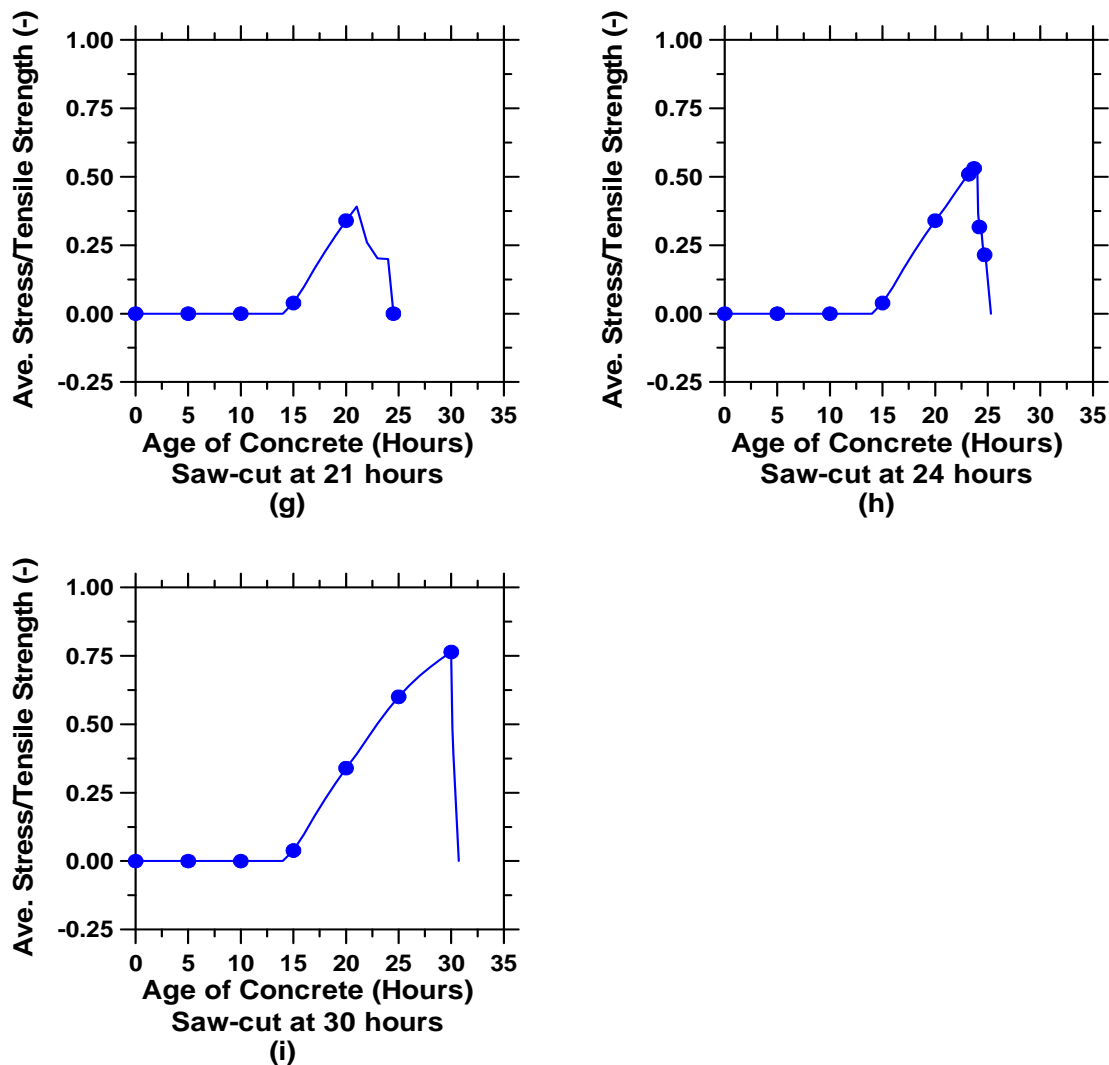


Figure 8.22: Average end stress to average tensile strength ratios for pavements with a D/2 saw-cut.

In order to estimate the appropriate depth of a saw-cut, the stress-to-strength ratios at each time point were divided by the critical stress-to-strength ratio (i.e., $\frac{\sigma_t}{f_t' \cdot \Phi}$). Numbers below one indicate stable crack propagation while numbers higher than one lead to unstable cracking behavior, which needs to be avoided.

The graphs of tensile stress/(tensile strength $\times \Phi$) for different saw-cut sizes are provided in Appendix D, and for the purpose of illustration, only graphs of tensile stress/(tensile strength $\times \Phi$) for saw-cut depths of $D/2$ are provided in Figure 8.23.

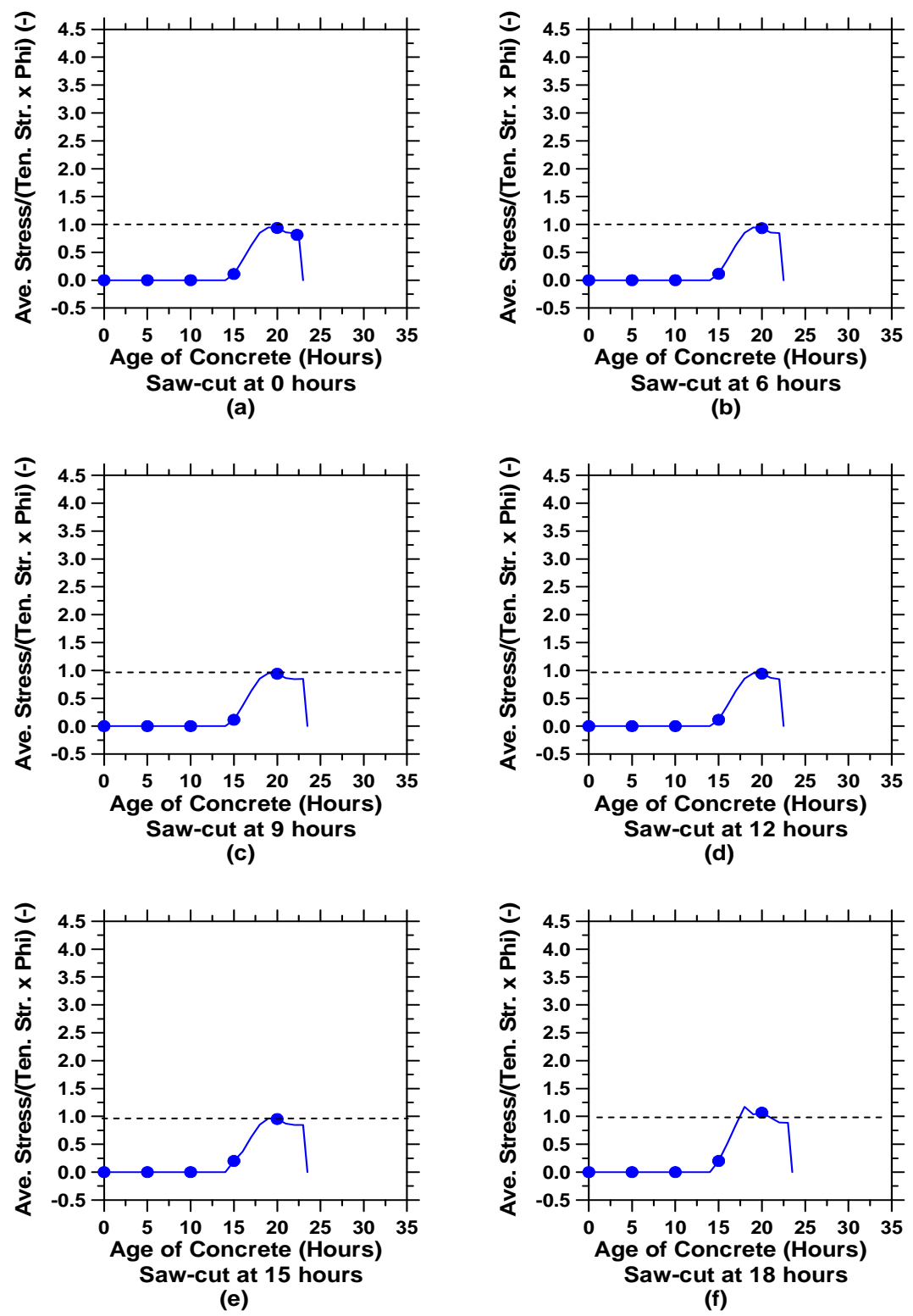


Figure 8.23: Average end stress to average tensile strength and phi ratio for a saw-cut depth of D/2 (cont'd).

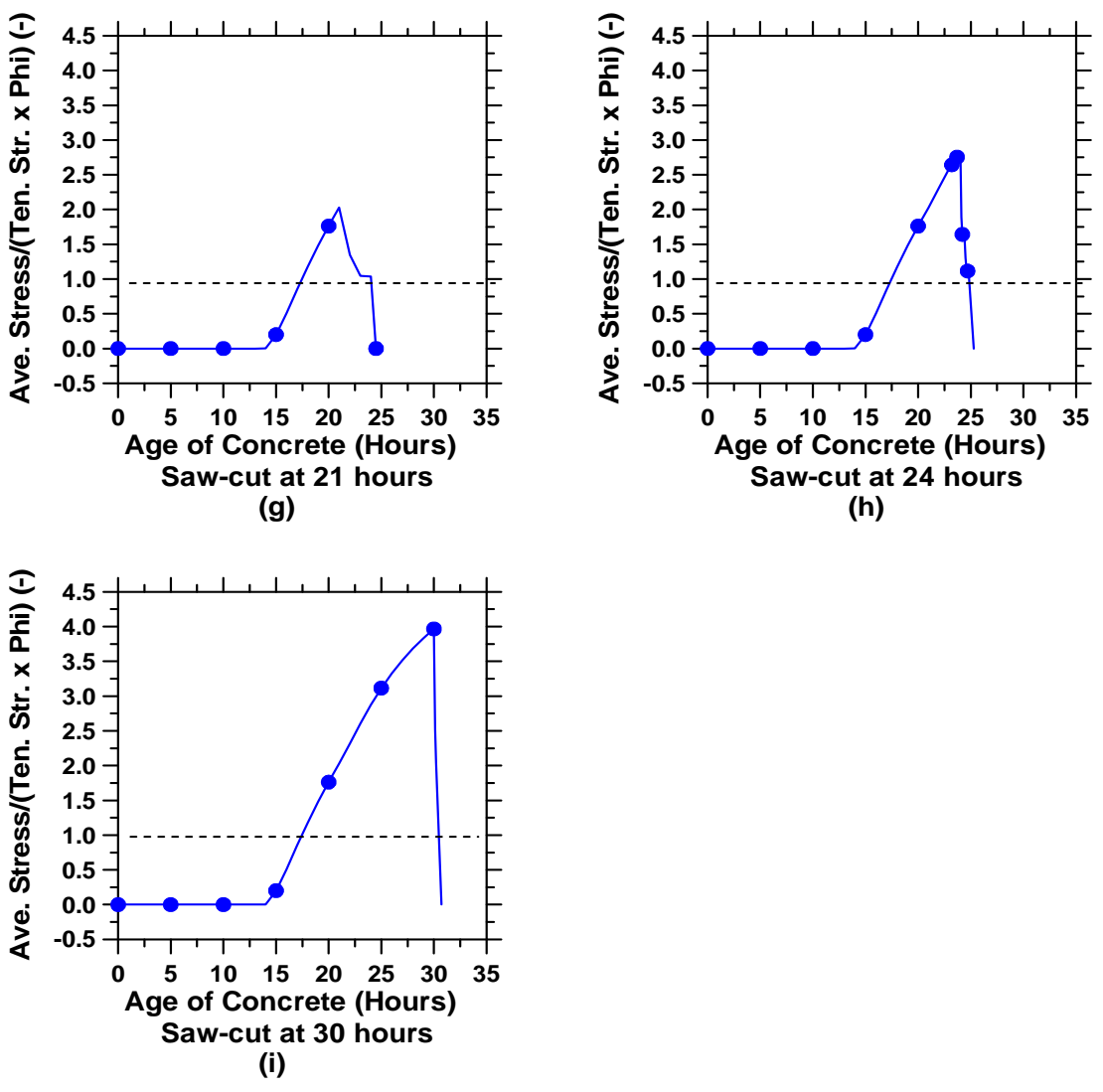


Figure 8.23: Average end stress to average tensile strength and phi ratio for a saw-cut depth of D/2.

The results shown in Figure 8.23 indicate that the ratio remains zero during the first 15 hours (in this case), and subsequently begins to increase. It is noted that pavements with saw-cuts applied before the ratio of one show similar stress behaviors (i.e., stable cracking). However, if the saw-cuts were introduced at higher ratios, a sudden drop in the ratio indicates that unstable crack propagation was observed.

8.2.3 Computer Simulations to Investigate the Effect of the Pavement Depth on the Pavements Cracking Behavior

The influence of pavement depth on cracking behavior was studied in order to determine the appropriate depth of saw-cut. The cracking behaviors of 254 mm (10 inches) thick pavements with $D/3$ and $D/8$ saw-cuts introduced at different times were initially investigated. The ambient temperature, relative humidity, boundary conditions, and wind speed were chosen as defined in section 7.2. For each saw-cut depth, the time of saw-cut introduction was varied and ranged from early saw-cuts to late saw-cuts. The behavior of 254 mm (10 inches) thick pavements with $D/2$, $D/4$, $D/6$, and $D/8$ saw-cuts were analyzed. In addition, the cracking behavior of one 305 mm (12 inches) pavement and one 432 mm (17 inches) pavement, both with a $D/3$ saw-cut applied at 12 hours, were analyzed.

8.2.3.1 Stress and Crack Opening at the Tip of a Saw-cut

Figure 8.24 illustrates the calculated stresses in x-direction at the tip of a saw-cut of depth $D/3$ which was placed at 12 hours in a 254 mm (10 inches) thick pavement. It can be seen that a 10-inch thick pavement behaves similarly to a 15 inch thick pavement (Figure 8.9). Comparing the results obtained from 10-inch and 15-inch pavements indicates that the pavement depth has an influence on the length of the initial, elastic-plastic state, pre-peak and post-peak stress development.

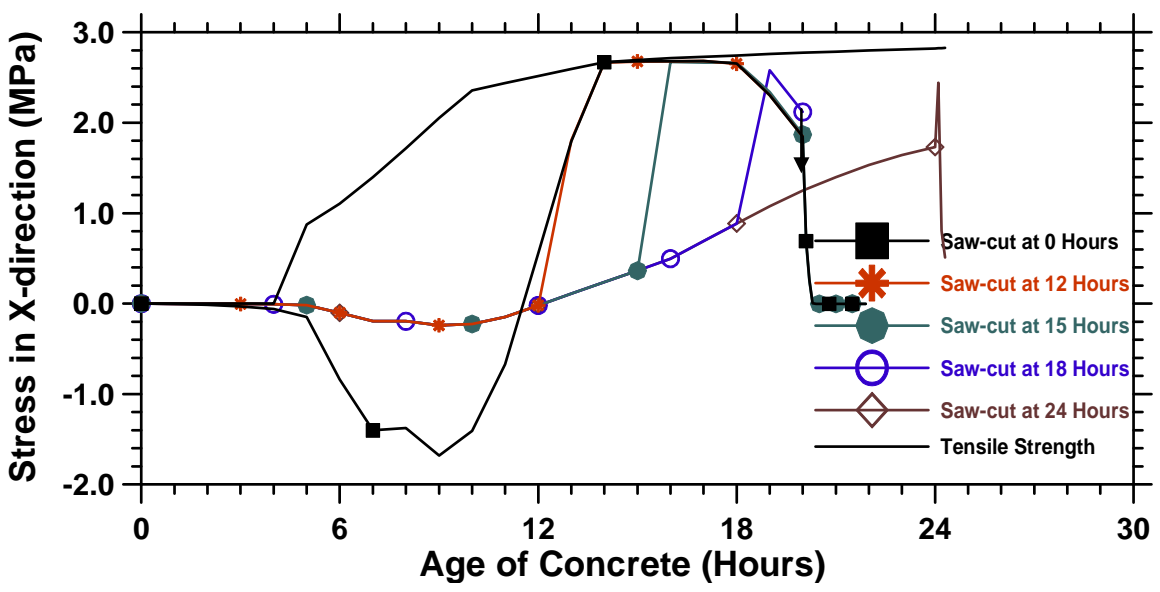


Figure 8.24: Tensile stresses at the tip of D/3 saw-cuts of 10-inch thick pavements.

The CTOD graphs of the 10-inch thick pavements with a saw-cut depth of D/3 that is introduced at 12 hours are shown in Figure 8.25. The 10-inch thick pavement with a saw-cut D/3 illustrates similar CTOD behavior to those of similar 15-inch thick pavements.

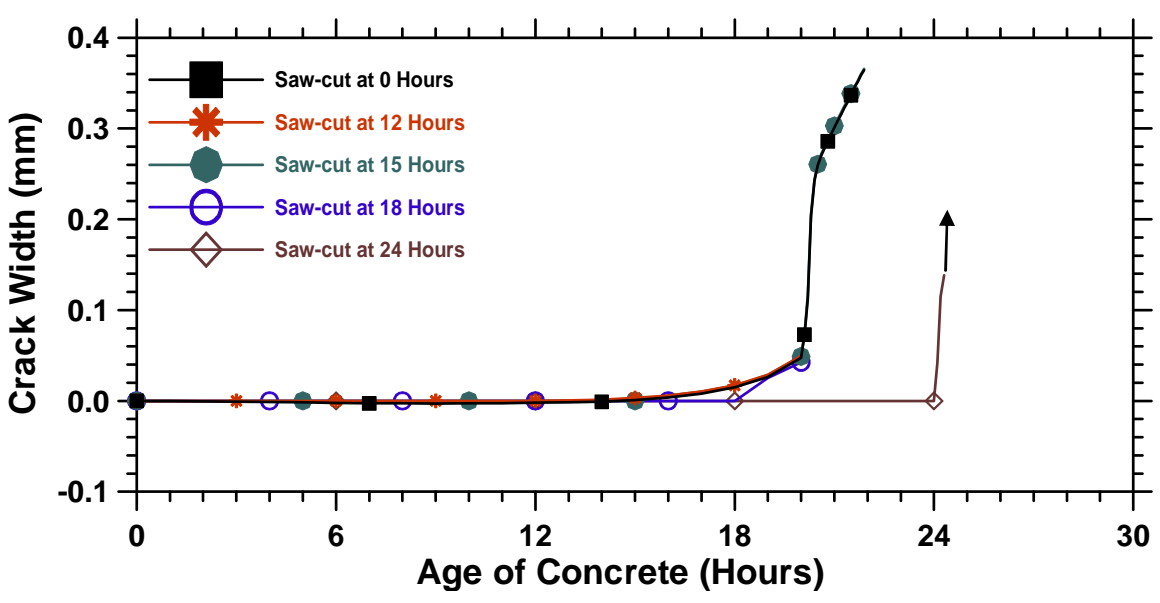


Figure 8.25: CTOD graphs of 10-inch thick pavements with saw-cut depth of D/3.

Graphs of stress in the x-direction at the tip of the D/8 saw-cut in 254 mm (10 inches) thick pavements are shown in Figure 8.26. Similar to the pavements with a saw-cut depth of D/3, an initial elastic-plastic state implies stable crack propagation. If the saw-cut is applied at a later time, unstable crack growth can occur. Comparing the 10 inch thick pavement with 15 inch thick pavements reveals that the cracking behavior of 10 inch thick pavements is more affected by ambient temperature changes than that of 15 inch thick pavements.

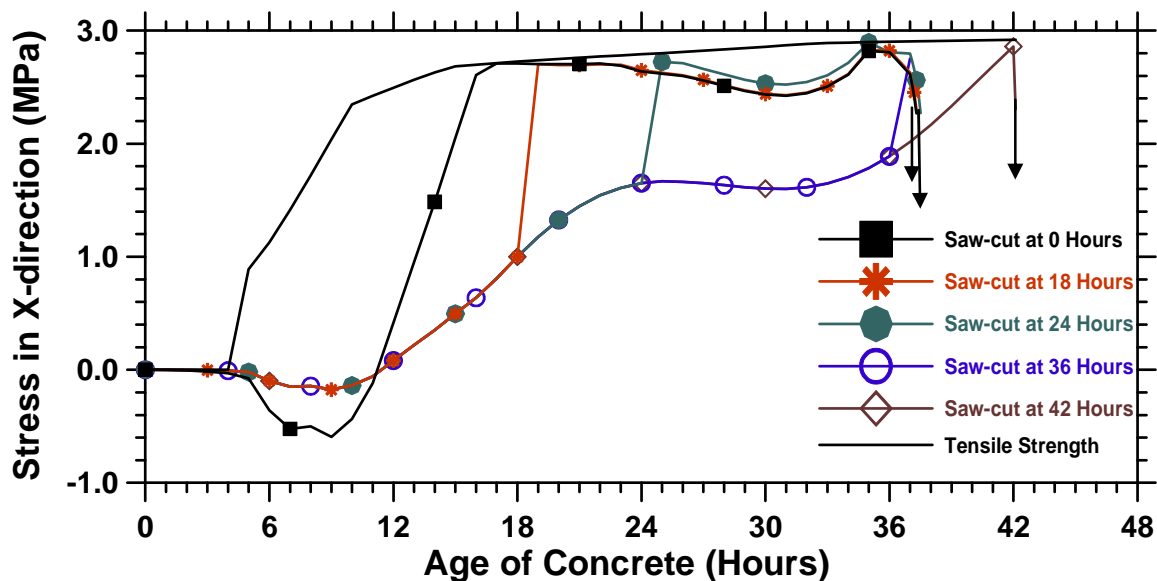


Figure 8.26: Tensile strength and stresses in x-direction of 10-inch thick pavements with D/8 saw-cuts

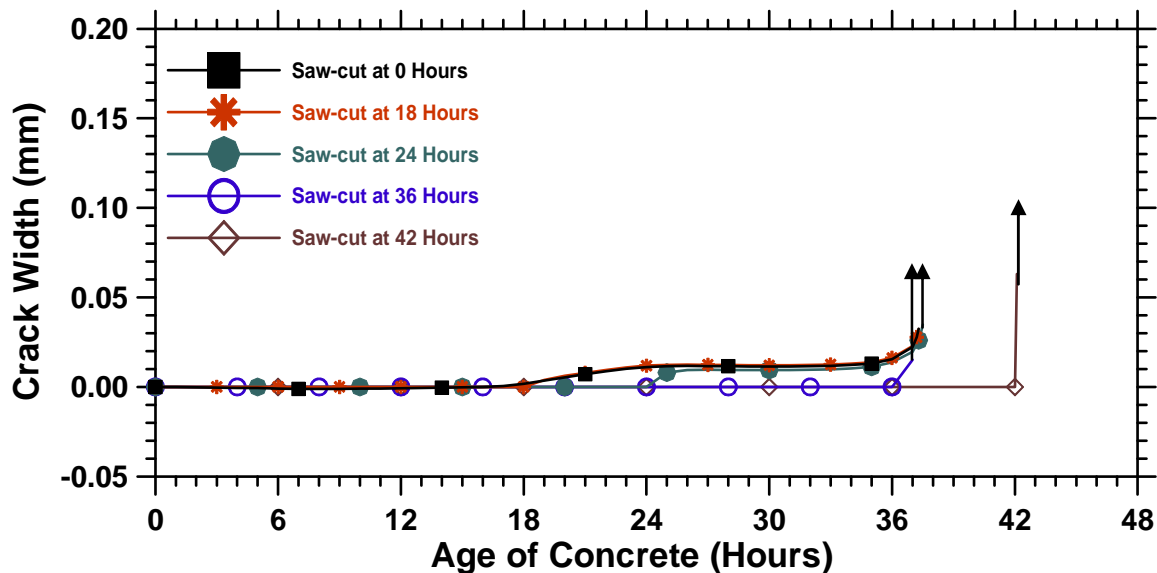


Figure 8.27: CTOD of 10-inch thick pavements with D/8 saw-cuts introduced at 12 hours.

Figure 8.28 illustrates tensile strength and stress behaviors of 10-inch thick pavements with saw-cut depths of D/2, D/3, D/4, D/6, and D/8, all of which were applied at 12 hours. Similar to 15-inch thick pavements, a higher amount of energy is needed to overcome the net strength of a 10-inch thick pavement sawed with shallow saw-cuts.

This behavior, in which the crack of deeper saw-cuts opens up earlier than the shallower saw-cuts, is also observed in Figure 8.29. In addition, as the saw-cut is decreased, stable crack propagation behavior begins to disappear.

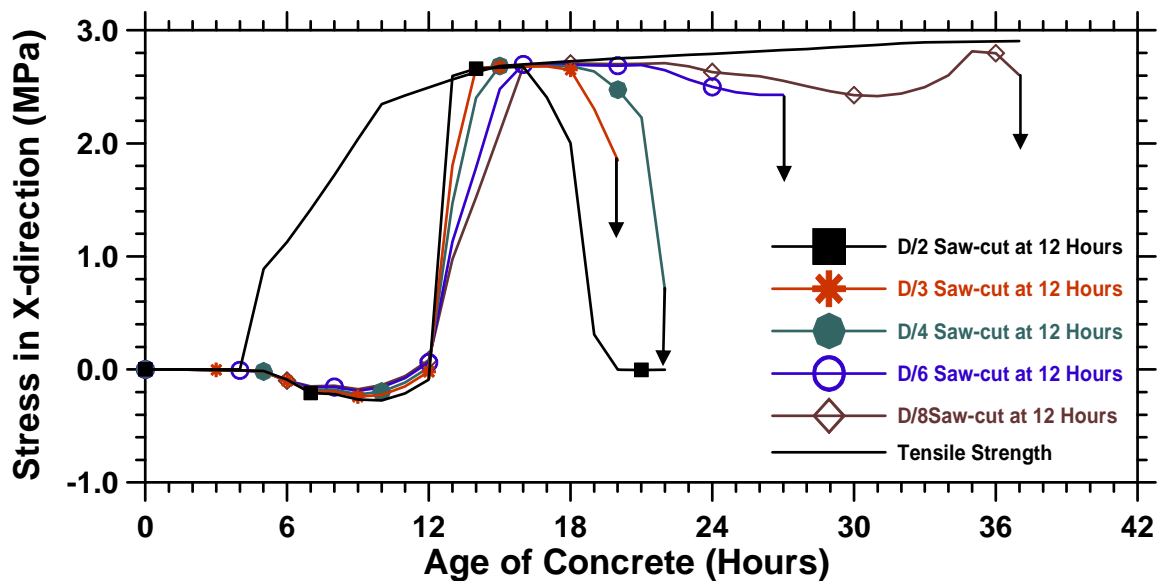


Figure 8.28: Tensile strength and stresses in the x-direction for 10-inch thick pavements.

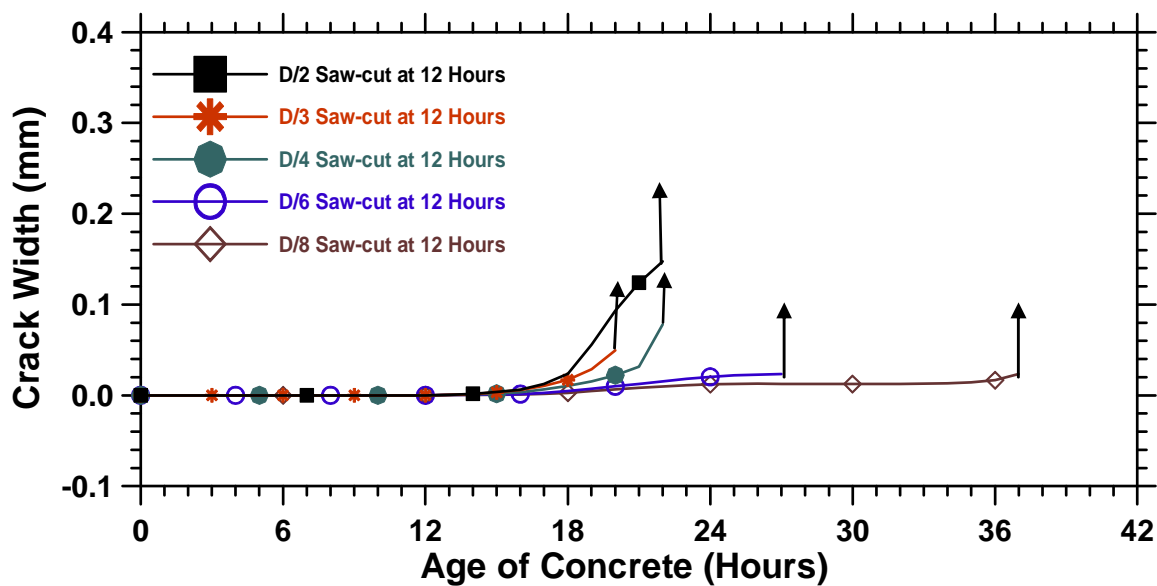


Figure 8.29: CTOD graphs of 10-inch thick pavement with different saw-cut depths.

To further illustrate the effect of the depth of pavement on the cracking behavior of pavements, pavements with different depths, but with the same saw-cut depth of D/3 applied at 12 hours, were analyzed. As shown in Figures 8.30 and 8.31, only a small variation exists between the tensile stresses and CTOD for different depths of pavements.

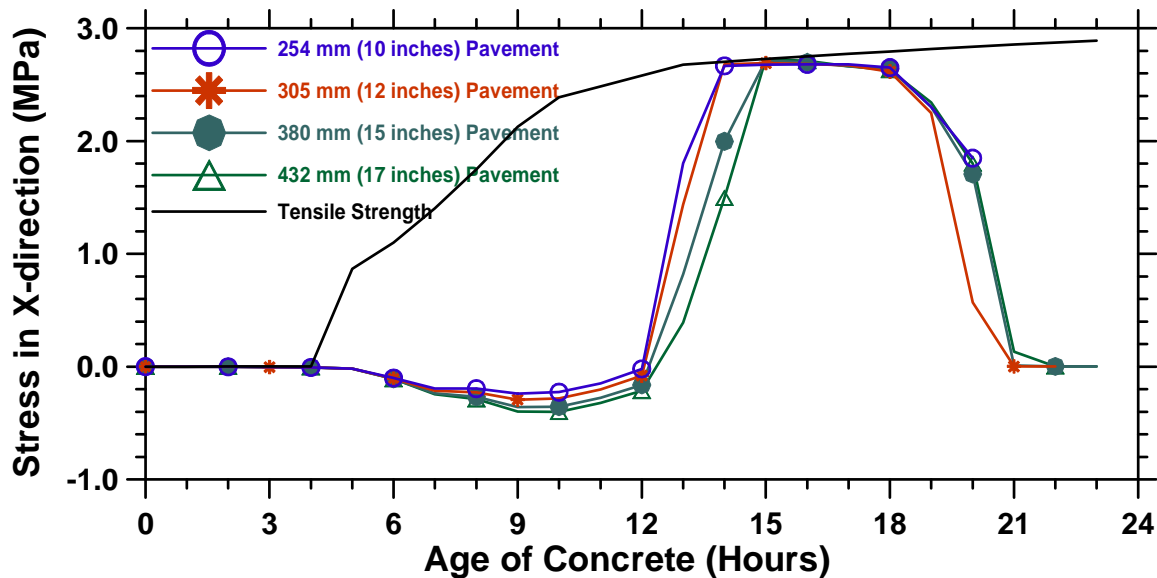


Figure 8.30: Tensile strength and stresses in x-direction of 10-inch thick pavements with different saw-cut depths.

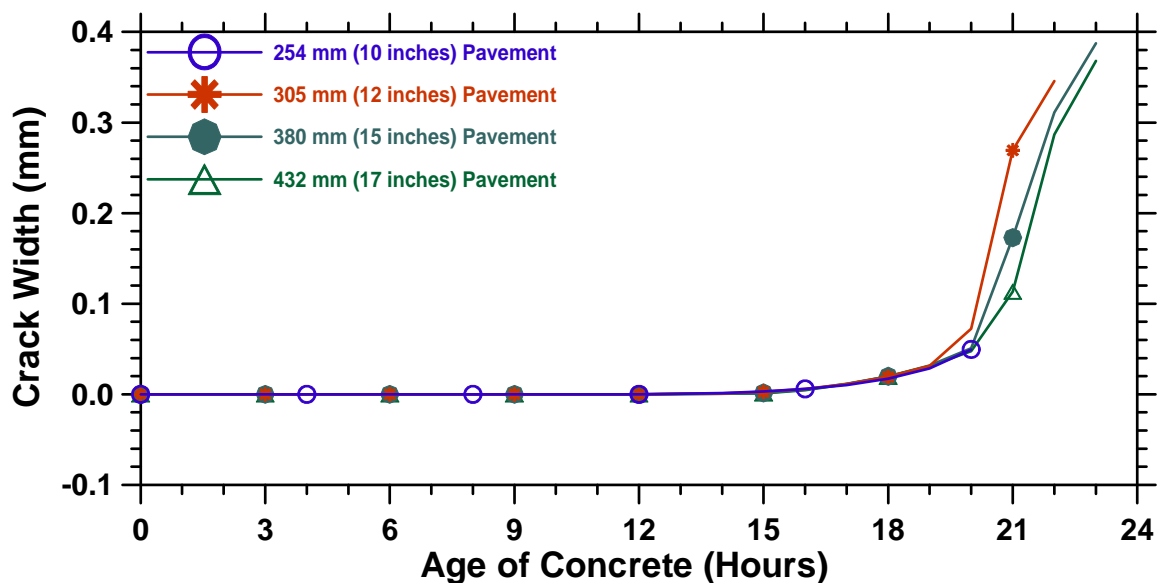


Figure 8.31: CTOD behaviors of 10-inch thick pavements with different saw-cut depths.

8.2.3.2 The Influence of the Depth of Pavements on the Cracking Behavior of Pavements

To determine the influence of the depth of pavement on the cracking of pavements, the average end reaction and average tensile strength of 10-inch thick pavements with saw-cut depths of $D/3$ and $D/8$ were obtained. The average end reaction of pavements at

any time was divided by the unnotched cross sectional area of pavement to obtain the average end stress. The graphs of average tensile strengths and average end stresses versus time for D/3 and D/8 saw-cuts are provided in Appendix B. For the purpose of explanation, only graphs of average end stress and average tensile strength of 10-inch thick pavements with saw-cut depth of D/3 are presented in Figure 8.32, in which the solid line represents the average strength and the solid lines with solid circles are the average tensile strength.

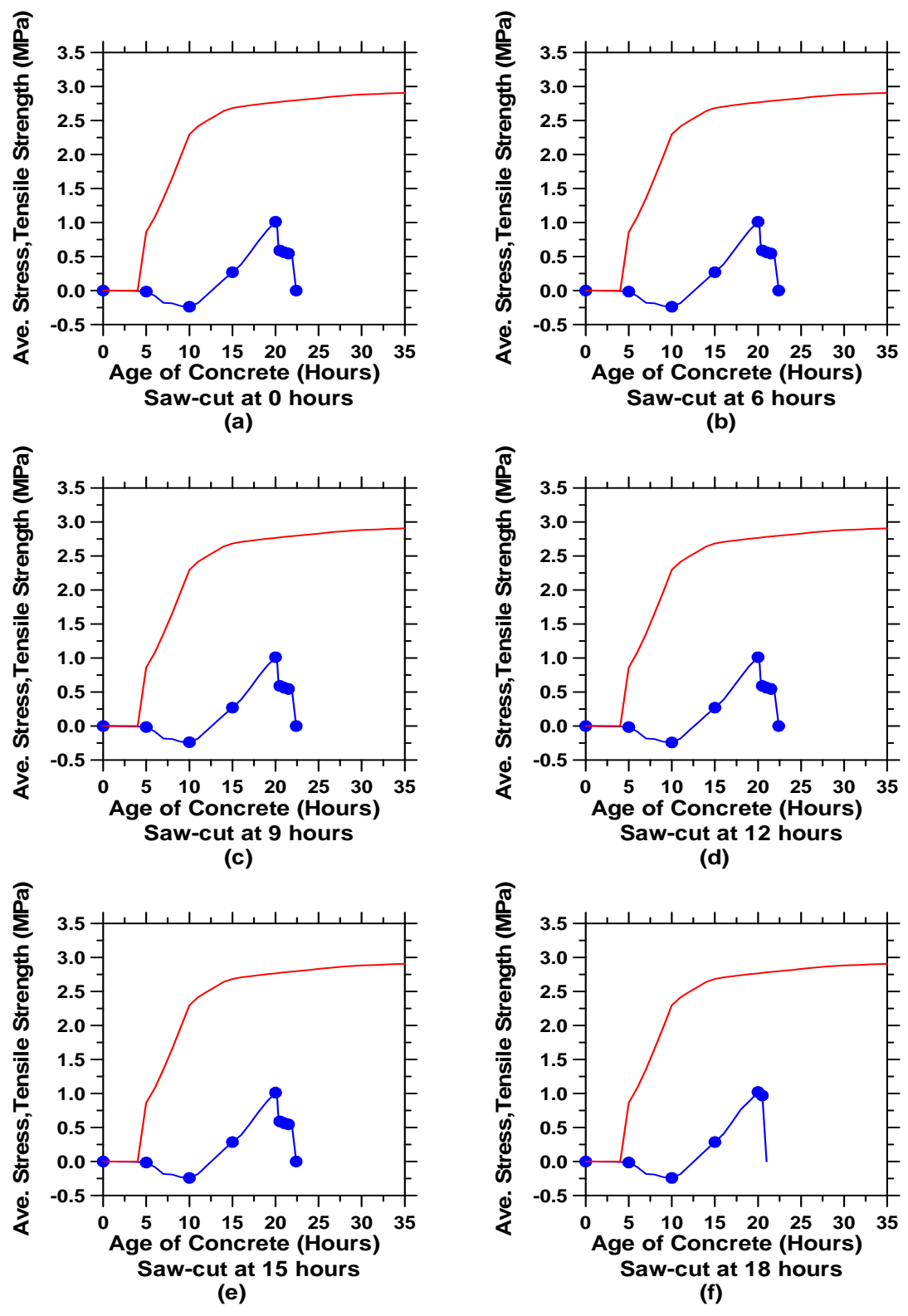


Figure 8.32: Average tensile strength and average end stresses of 10-inch thick pavements with D/3 saw-cuts (cont'd).

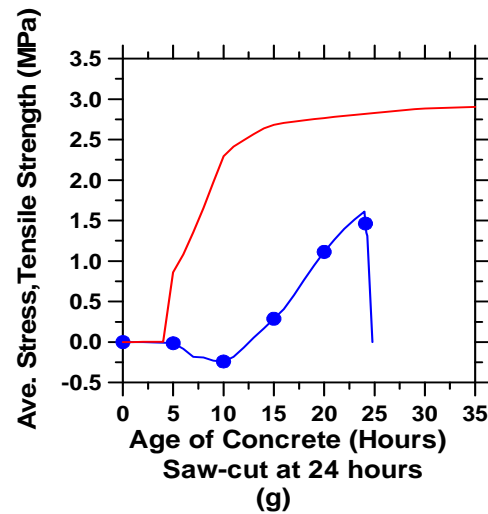


Figure 8.32: Average tensile strength and average end stresses of 10-inch thick pavements with D/3 saw-cuts.

To estimate the cracking behavior of 10-inch thick pavements, the average end stresses-to- average strength ratios for different saw-cut sizes were obtained shown in Figure 8.33. As shown in Figure 8.32, it can be concluded that 10-inch thick pavements behave similarly to 15-inch thick pavements. As tensile stresses develop in the pavement, the average end stress-to strength ratios increase reaching to a critical ratio, Φ . If saw-cuts are applied before the attaining the critical ratio, stable cracking occurs. However, unstable crack growth occurs when the saw-cut is applied after reaching the critical stress-to-strength ratio.

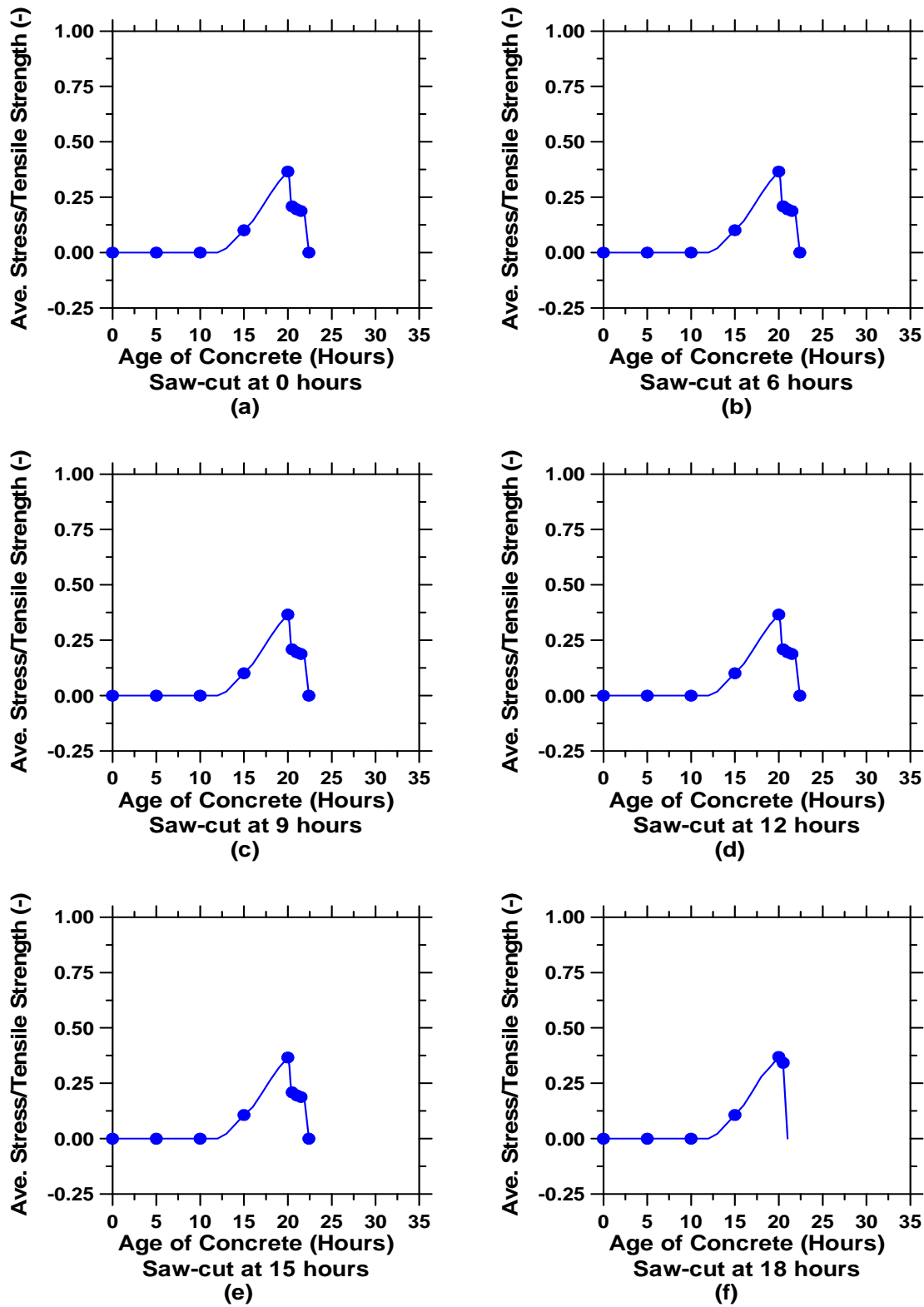


Figure 8.33: Average end stress to average tensile strength ratios of 10-inch thick pavements with D/3 saw-cuts (cont'd).

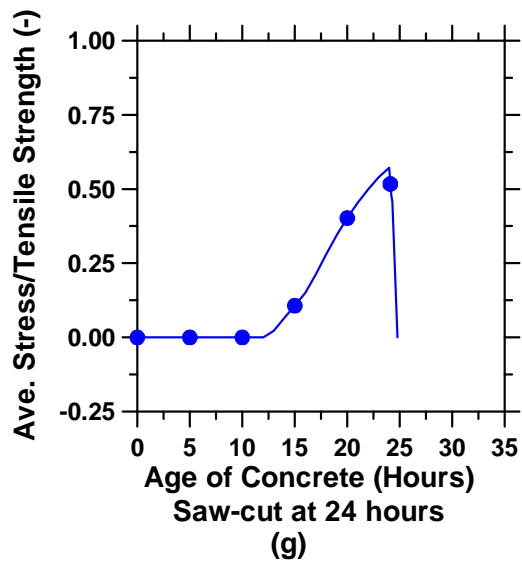


Figure 8.33: Average end stress to average tensile strength ratios of 10-inch thick pavements with D/3 saw-cuts.

To further understand the cracking behavior of pavements, the average end stresses-to-average strength ratios at any time were divided by critical stress-to-strength ratio. As shown in Figure 8.34, the introduction of saw-cut before reaching one results in stable crack propagation while the introduction of saw-cut at higher values leads to unstable crack growth. It should be noted that the graphs of tensile stress/ (tensile strength $\times \Phi$) for D/8 saw-cut are provided in Appendix D.

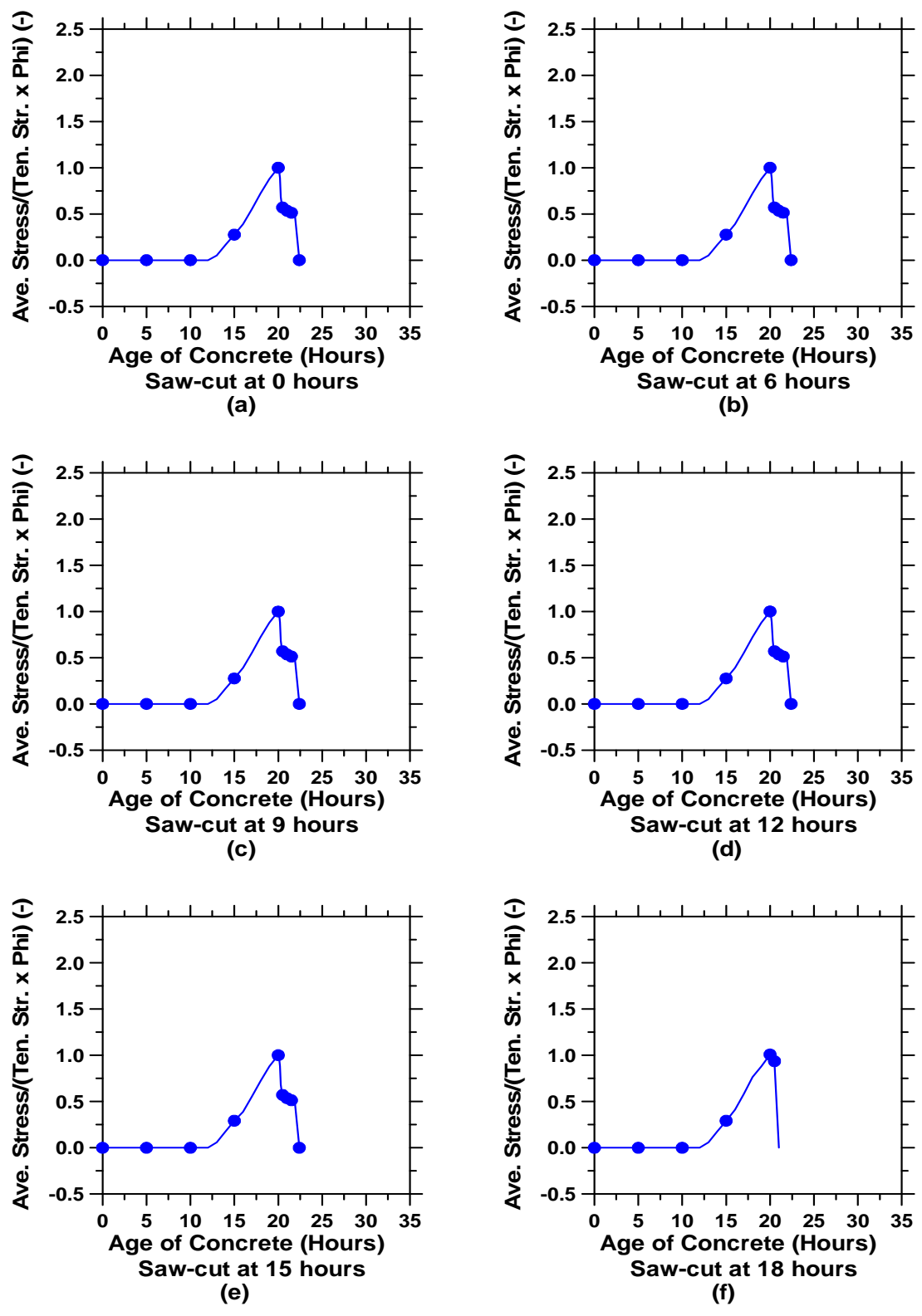


Figure 8.34: Average end stress over average tensile strength and phi of 10-inch thick pavements with D/3 saw-cut depth (cont'd).

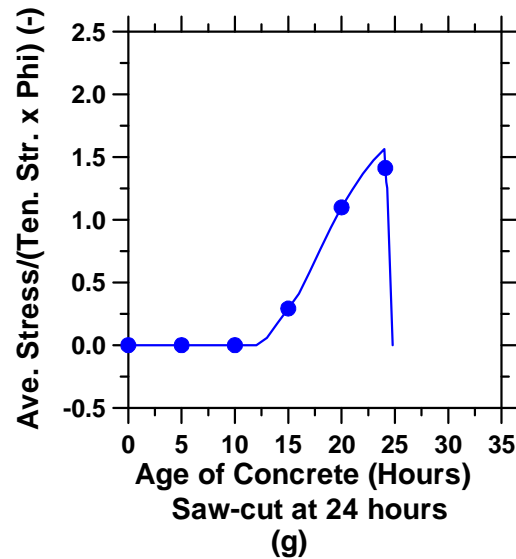


Figure 8.34: Average end stress over average tensile strength and phi of 10-inch thick pavements with D/3 saw-cut depth.

The critical stress-to-strength ratios for 10-inch thick pavements with D/3 and D/8 saw-cut depth were calculated to be 0.37 and 0.79 respectively. The similar ratios for similar 15-inch thick pavements are 0.30 and 0.78. This indicates that thinner pavements have slightly higher critical stress-to-strength ratios than thicker ones, and the difference between ratios tend to get smaller for shallower saw-cuts

8.3 Factors Influencing the Time of Saw-cut Introduction

While saw-cutting is widely used, determining the time for saw-cutting in the field is difficult and is often based on the saw-cutting operator's experience. Recently several studies have been performed to aid finishers and saw-cutting crews in determining the saw-cutting window as guidance from national agencies is limited in determining the time the saw-cut should be placed. For example, the American Concrete Institute Committee 302.1 recommends that "the joints should be sawed as soon as practical wherein the concrete should have hardened enough". This recommendation exists since sawing too early can result in raveling and spalling at the edges of the cut, while sawing too late can result in random cracking and ineffectual contraction joints that do not open or function properly. INDOT standard specification 503.03 specifies 2 to 12 hours as the

window of opportunity to saw-cut for transverse and D-1 joints and “sufficiently hardened” pavement for longitudinal joints. In cases where the joints are sawed too late the stresses can rise to a level that leads to micro-cracking (40-50% of the tensile strength) that has the potential to reduce long-term durability (Weiss et al., 2003) and (Mindess, 1981). Micro-cracking caused by late saw-cutting is related to increased water absorption and may be associated with initial damage that ultimately results in the development of ‘random’ or ‘mid-panel’ visible cracks (Weiss et al., 2003). While saw-cutting is widely used, determining the time for saw-cutting in the field is difficult and is often based on the saw-cutting operator’s experience.

Environmental conditions significantly influence the early development of stresses within the pavement. Weather conditions and fluctuations (relative humidity, temperature, precipitation, wind speed, and wind direction) all play a significant role in early age stress development and determination of the saw-cutting window. Contractors have begun using hand-held weather monitoring stations which can provide valuable information on current environmental conditions. These can be used in conjunction with the maturity method and analytical solutions for stress development to signal when saw-cutting should be performed. This information can also be used with software programs like HIPERPAV to predict the saw-cutting window effectively.

In this section, the effects of ambient temperature, mixture differences, and moisture conditions that influence the saw-cutting window are discussed. After a general introduction in each sub-section, the general modeling approach including boundary conditions, material differences, and ambient temperature, wind speed, and moisture conditions will be discussed in detail. Then the computer simulation results will be presented and compared in detail.

8.3.1 The Effect of Ambient Temperature on Cracking Behavior of Pavements

Ambient temperature can greatly affect the rate of concrete property and residual stress development at early ages. As the hydration reactions of cement are temperature dependent, ambient temperature changes can affect the rate of hydration reactions and concrete property development. The ambient temperature changes can also alter the

temperature profile and thermal gradient in pavements. The residual stresses developed due to thermal gradient can be quite significant and governs the crack opening of pavement at later ages (Thompson et al., 1987, Armaghani, 1987, Jenq et al., 1993).

In this section, the effect of constant ambient temperature on pavement cracking behavior will be followed by a discussion of the effect of periodical ambient temperatures on the cracking behavior of concrete pavements. At the end, the effect of ambient temperature on the saw-cutting time window will be discussed.

8.3.1.1 The Effect of Constant Ambient Temperature on Cracking Behavior

In field applications, a constant ambient temperature is rarely experienced. However, to investigate only the effect of different ambient temperatures on the cracking behavior of pavements, pavements with D/3 and D/8 saw-cuts at constant 4°C, 10°C, 18°C, 23°C, 30°C, and 36 °C ambient temperatures were analyzed, and the results were compared.

8.3.1.1.1 The General Modeling Approach

The ambient temperature functions influencing the top surface of pavements were defined as constant 4°C, 10°C, 18°C, 23°C, 30°C, and 36 °C. Analysis was performed with two different saw-cut depths (D/3 and D/8) both introduced at 12 hours. However, other model properties were the same as the baseline case described in section 7.2.

8.3.1.1.2 The Results and Analysis

Figure 8.35 illustrates the calculated principal stresses at the tip of saw-cuts with a depth of D/3 which were introduced at 12 hours for pavements exposed to constant ambient temperatures of 4°C, 10°C, 18°C, 23°C, 30°C, and 36°C. The ambient temperature greatly affects the saw-cutting process. The higher ambient temperatures accelerate the rate of concrete stiffening and shrinkage in the pavement, which increase the rate of residual stress development in pavements. For example, when the pavement is exposed to a 36°C ambient temperature, residual stresses start to rise after 6 hours, and reach to 65% of its strength at the time of saw-cut introduction (12 hours). It should also

be noted that at the time the saw-cut is introduced micro-cracking has already begun to occur as stress has already reached about 65% of its tensile strength. As the ambient temperature decreases, this behavior changes. It can be seen that an elastic plastic state exists for the first 32 hours for the pavement exposed to 4°C, providing a wide time window to place the saw-cut. Therefore, ambient temperature affects the rate of residual stress development which is slower at lower temperatures. Therefore, ambient temperature should be given a major role in the determination of the saw-cutting window.

The CTOD graphs of pavements at different temperatures with a saw-cut depth of $D/3$ can be viewed in Figure 8.36. As ambient temperature increases, region two or post-peak stable crack behavior starts to disappear, and unstable cracking occurs. For example, the introduction of saw-cut at 36°C causes a sudden crack opening at the time of saw-cut placement which is shown by a vertical line of crack width development. However, a gradual decrease of post-peak stresses of pavements exposed to 4°C results in gradual stable crack width opening.

As shown by the dashed line in Figure 8.36, a critical CTOD of 0.03 mm needs to be achieved before crack propagates unstably. Therefore, as discussed in section 8.2.2.1, if CTOD is between zero and $CTOD_c$ or 0.03 mm, stable crack growth occurs. However, if CTOD becomes higher than $CTOD_c$, unstable crack propagation is observed.

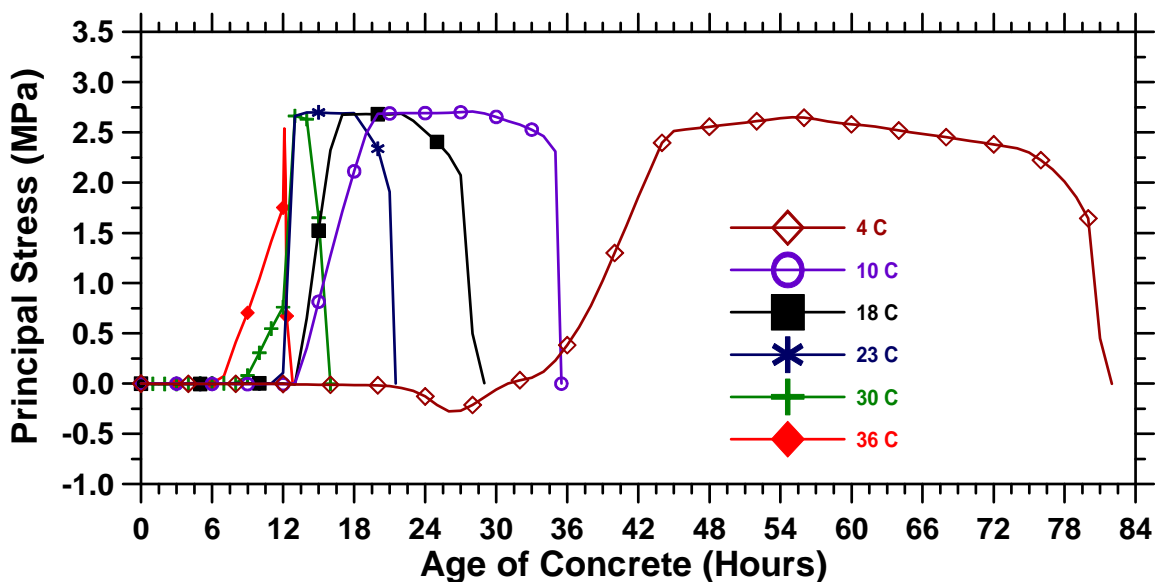


Figure 8.35: Principal stresses at the tip of $D/3$ saw-cuts introduced at 12 hours.

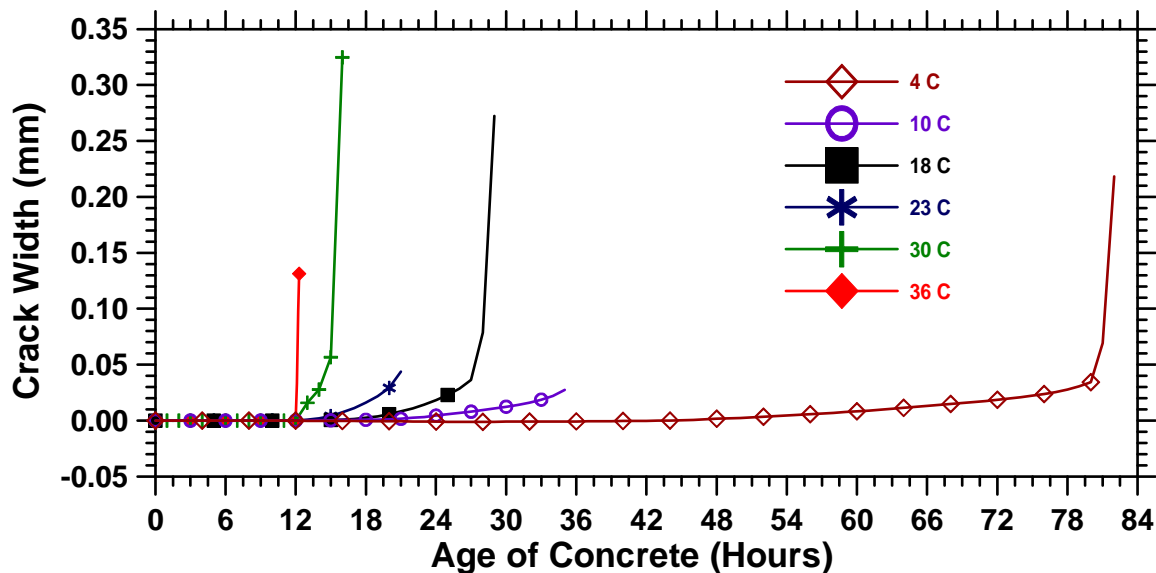


Figure 8.36: CTOD of pavements with D/3 saw-cut depth.

Figures 8.37 and 8.38 illustrate the stress and CTOD behaviors of pavements exposed to different ambient temperatures. The pavements with D/8 saw-cut depth introduced at 12 hours demonstrate similar behavior to pavements with D/3 saw-cut depth. As shown in Figure 8.37, the introduction of a saw-cut at 12 hours when the ambient temperature is 36 °C initiates unstable cracking. At this time the residual stress in pavement is approximately 50% of the tensile strength which can result in micro-crack development. As the net pavement strength is reduced by the saw-cut introduction, the stored energy is released, and the crack opens unstably. As the ambient temperature decreases, the rate of residual stress development in pavements declines, and more stable cracking occurs. This provides a wider time window to place the saw-cut.

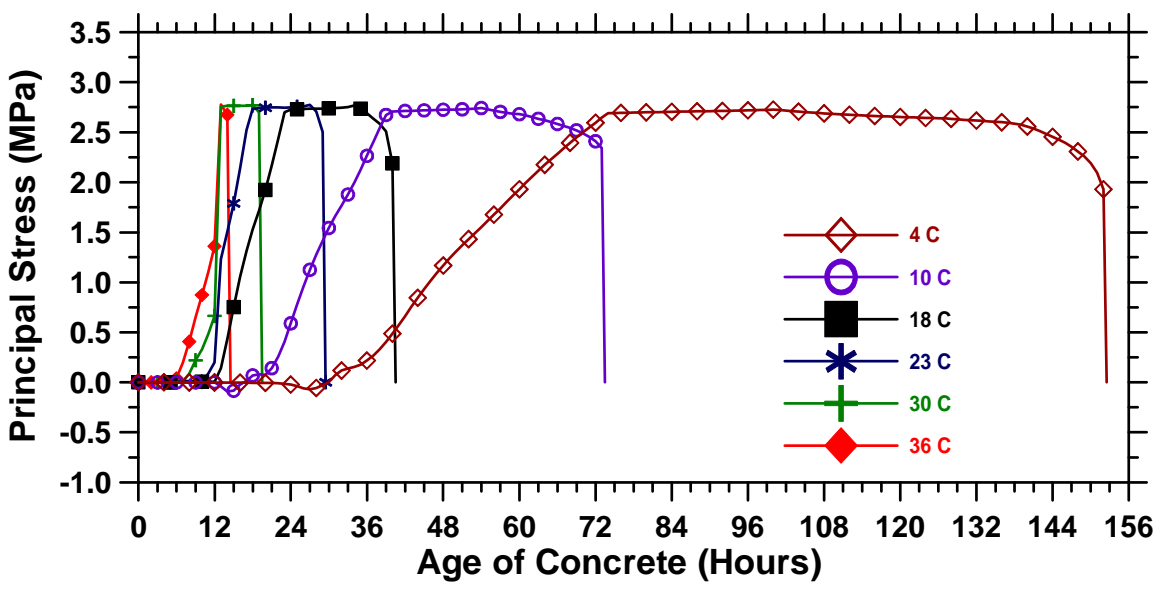


Figure 8.37: Principal stresses at the tip of D/8 saw-cut depth.

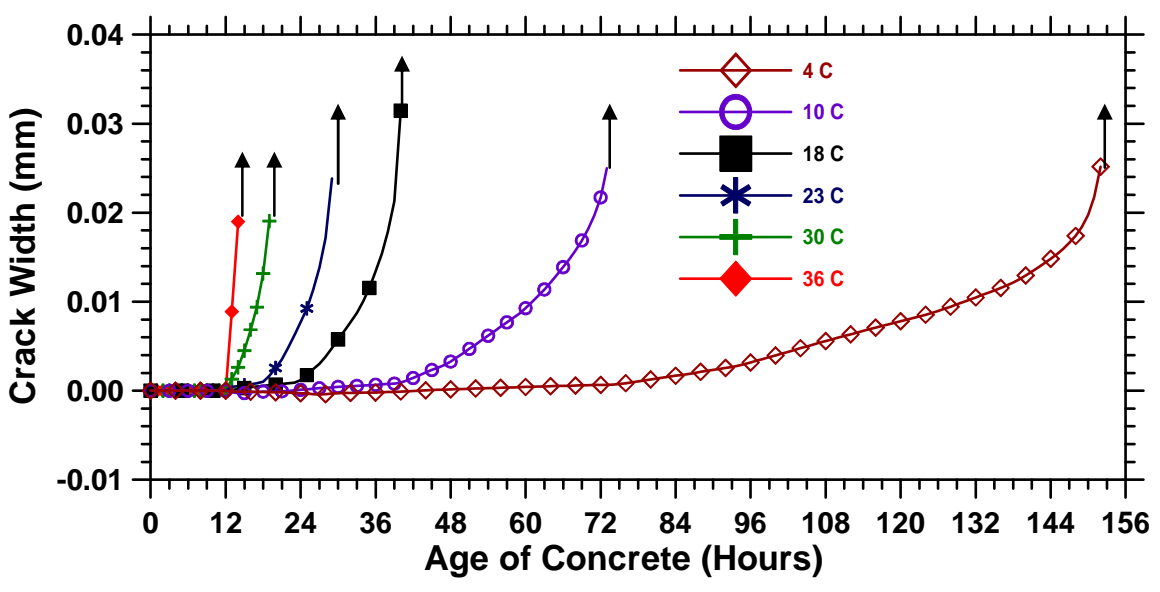


Figure 8.38: CTOD of pavements with D/8 saw-cut depth.

To further illustrate the effect of temperature on stress development, Figures 8.39 and 8.40 were prepared. As it is seen, the stresses in pavements sawed with D/3 saw-cuts increase instantly when the saw-cuts are introduced. However, stresses in pavement with D/8 saw-cuts take longer time to reach tensile strength. This can be due to the fact that to initiate cracking at the tip of pavements with saw-cut depth of D/8, more energy is

required. It should also be noted that ambient temperature greatly influences the length of elastic plastic region and post-peak stable stress behavior.

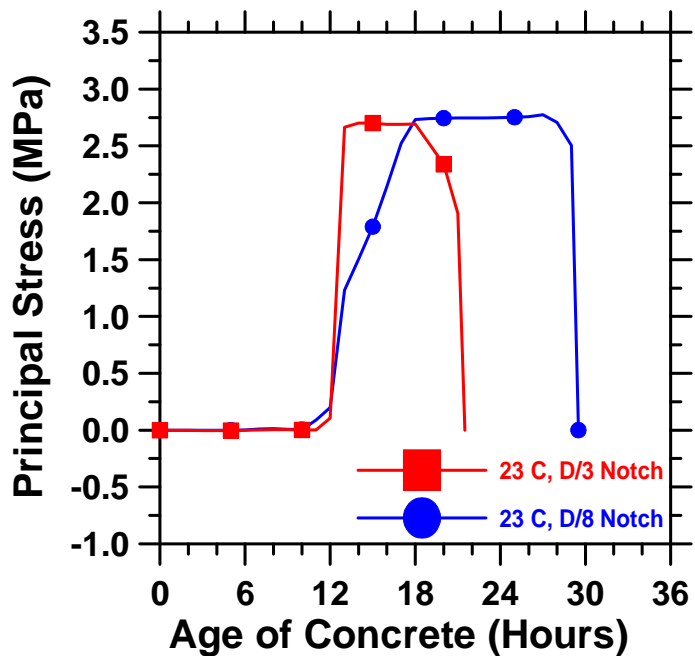


Figure 8.39: Principal stresses at the tip of D/8 and D/3 saw-cuts introduced at 12 hours for pavements exposed to 23°C ambient temperature.

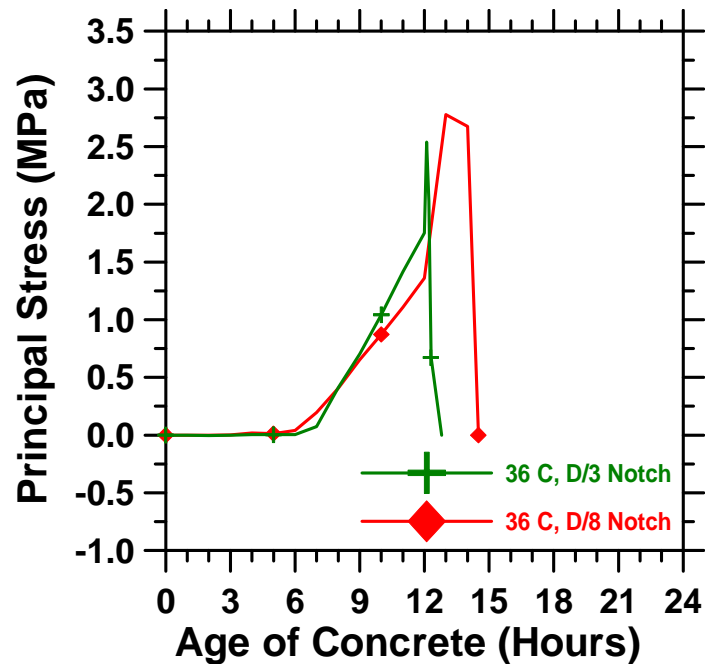


Figure 8.40: Principal stresses at the tip of D/8 and D/3 saw-cuts introduced at 12 hours for pavements exposed to 36°C ambient temperature.

The ambient temperature plays a major role in determining the time window for saw-cutting operation. While the introduction of saw-cut at certain temperature initiates stable crack propagation, the introduction of the same saw-cut at a higher temperature originates unstable crack propagation and vice versa. Therefore it is imperative to consider the ambient temperature changes when determining the saw-cutting time window.

8.3.1.2 The Effect of Periodical Ambient Temperature on Cracking Behavior

The effect of constant ambient temperatures on cracking behavior of pavements was described in previous section. However, computer simulations were performed with different sinusoidal ambient temperature functions to better understand the influence of daily ambient temperature cycling on the cracking behavior of pavements. In the following section, these ambient temperature functions are introduced.

8.3.1.2.1 The General Modeling Approach

To investigate the effect of periodical ambient temperature on saw-cutting window, three different sinusoidal ambient temperature functions were defined over the pavement's surface boundary. Two temperature functions designated with C and M are shown in Figures 8.41 and 8.42 respectively. The third function, called H , was previously defined in Figure 7.2. As it is seen, the temperature function C fluctuates between 0°C and 10°C with a mean temperature of 5°C . The M function changes between 14°C and 26°C with a mean temperature of 20°C . As already discussed, the H temperature function fluctuates between 18°C and 30°C with a mean temperature of 24°C . It is believed that these three temperature functions can effectively describe the effect of periodical ambient temperature on the cracking and stress development of pavements. The analysis (and paving) was selected to start at 7:00 a.m., which is shown in the following figures. The pavements with saw-cuts of a depth of $D/3$ were sawed at various times under different ambient temperatures. It should be noted that other model parameters were the same as the baseline case described in section 7.2.

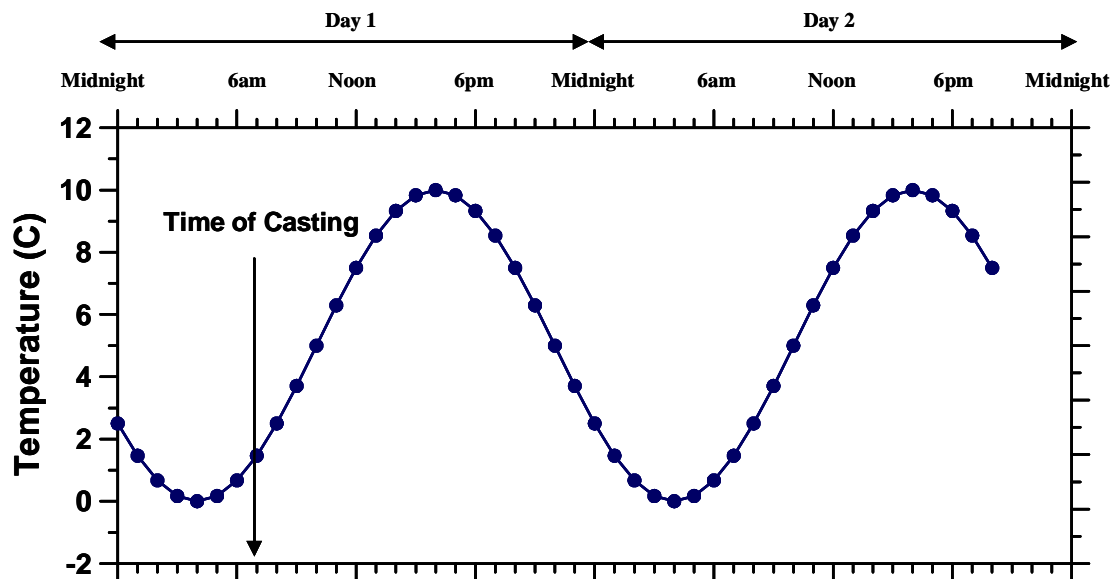


Figure 8.41: The C sinusoidal ambient temperature function.

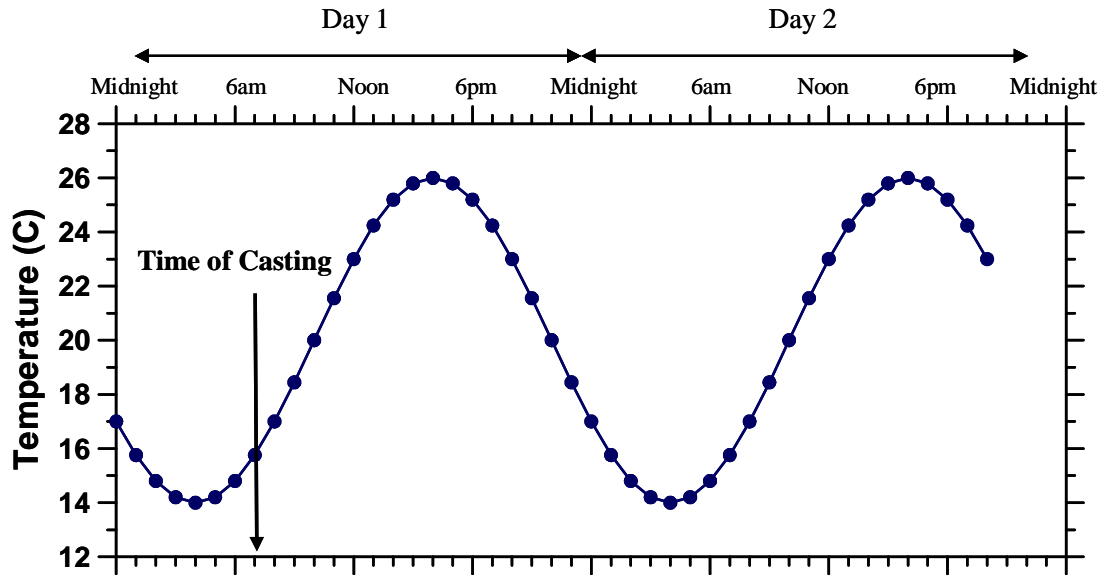


Figure 8.42: The M sinusoidal ambient temperature function.

8.3.1.2.2 The Results and Analysis

In this section, the results obtained from computer simulation investigating the effect of ambient temperature will be discussed. For simplicity, the stress and cracking behaviors of only five cases are discussed in each graph. The reader is referred to Appendix A for detailed results.

The tensile strength and principal stresses at the tip of D/3 saw-cuts which were introduced at 0, 12, 18, 24, and 30 hours for pavements exposed to H temperature function are shown in Figure 8.43. Figure 8.44 shows graphs of CTOD measured at the tip of D/3 saw-cuts which were introduced at 0, 12, 18, 24, and 30 hours for pavements exposed to H temperature function. The introduction of saw-cuts, while the pavement is in elastic plastic state, results in the same cracking behavior independent of the time of introduction. The introduction of the saw-cut after elasto plastic state results in a rapid increase in local stress. After local stress approaches the strength of concrete, crack initiates, and residual stress begins to decrease. It should be noted that the introduction of saw-cut when the residual stress level is high results in unstable cracking as shown by nearly vertical lines in Figure 8.43 and Figure 8.44.

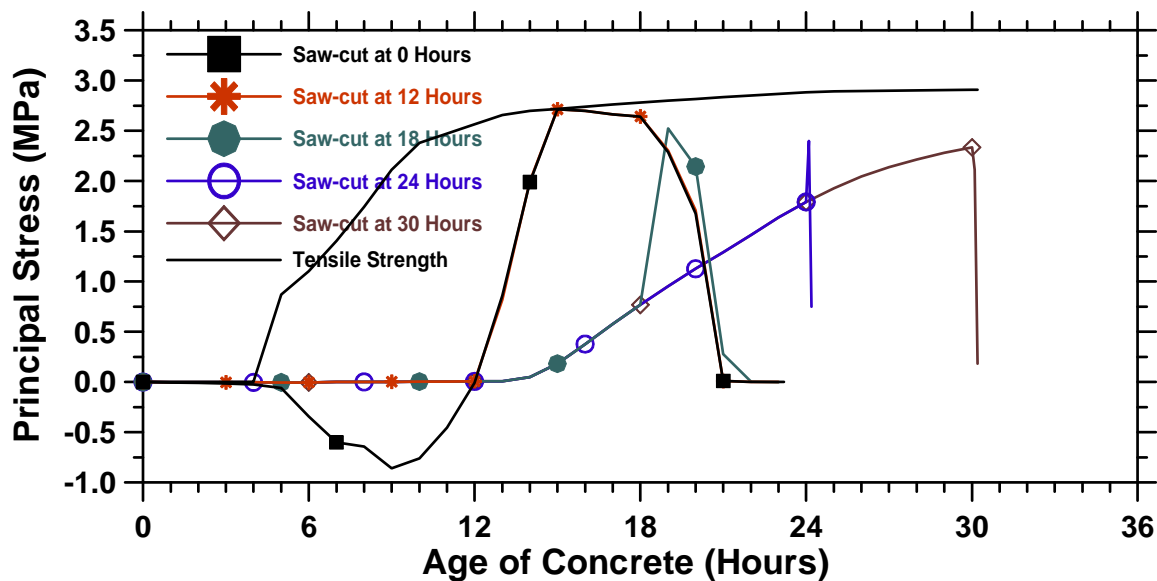


Figure 8.43: Tensile strength and principal stresses of pavements exposed to “H” temperature function.

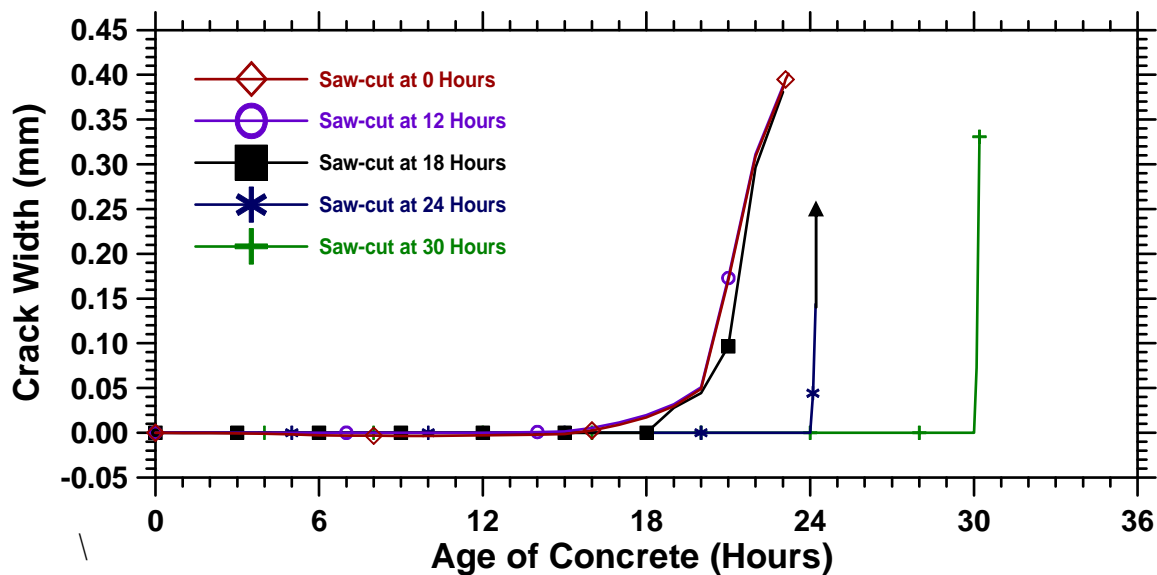


Figure 8.44: CTOD of pavements exposed to “H” temperature function.

Figure 8.45 shows the graphs of tensile strength and local principal stresses of pavements at M temperature function with saw-cut depths of $D/3$ which were introduced at 0, 12, 18, 24, and 30 hours. It is seen that the length of elastic plastic state has increased when pavements are exposed to lower ambient temperatures, and similarly, the

introduction of saw-cut results in stable cracking growth as shown in Figure 8.46. However, the pavements exposed to lower temperatures illustrate longer post-peak stable stress release region than the similar pavements exposed to *H* temperature function. In general, it can be concluded that a lower ambient temperature provides a longer saw-cutting time window.

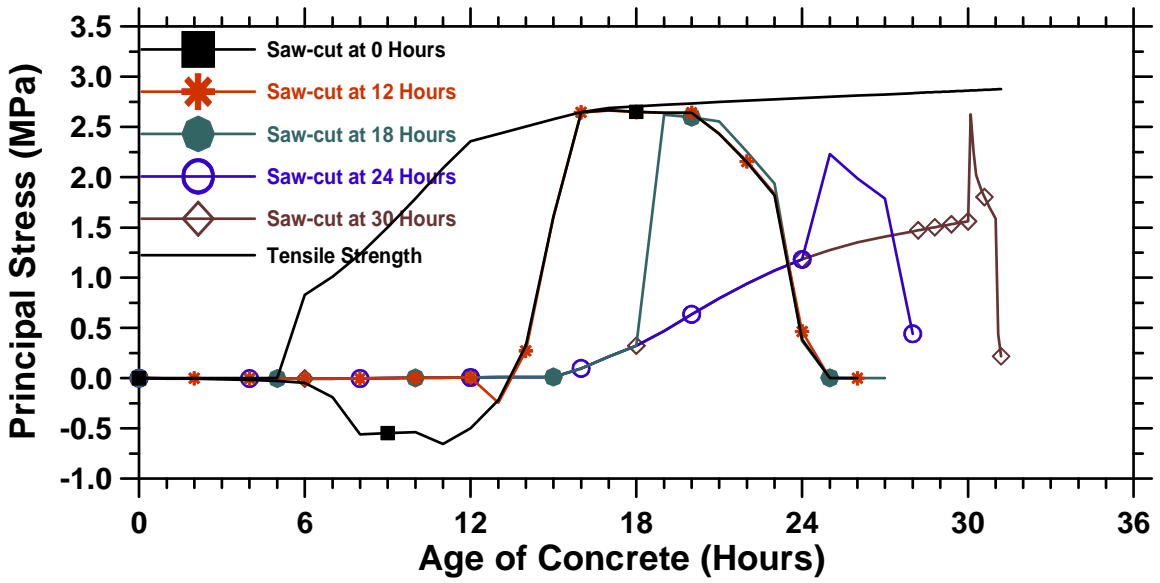


Figure 8.45: Tensile strength and principal stresses of pavements exposed to “M” temperature function.

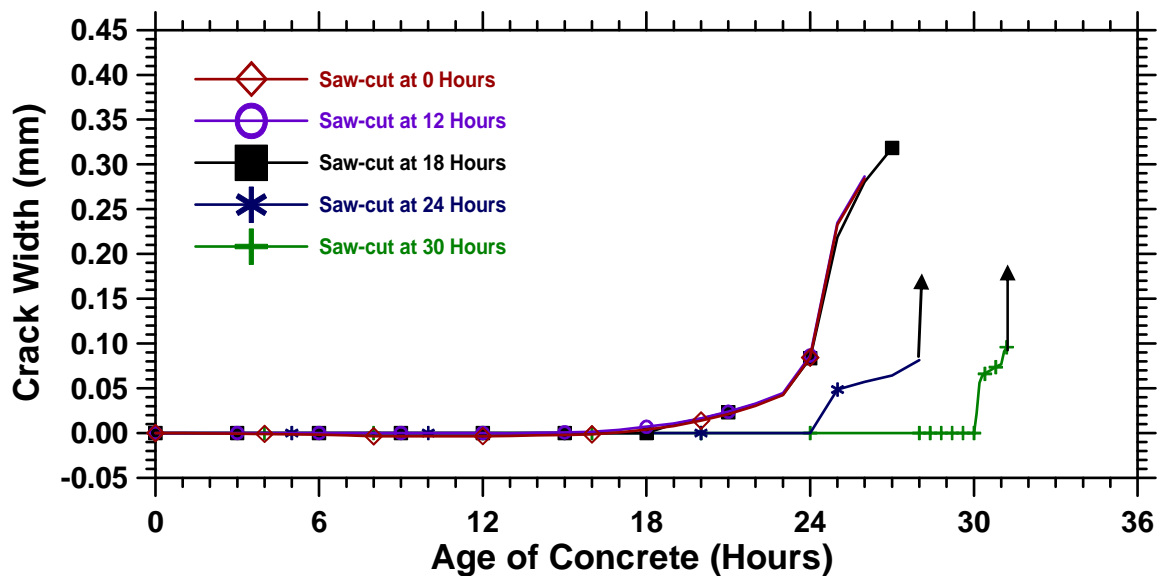


Figure 8.46: CTOD at the tip of D/3 saw-cuts of pavements exposed to “M” temperature function.

Figures 8.47 and Figure 8.48 show the graphs of local principal stresses and CTOD of pavements with D/3 saw-cut depth respectively. The saw-cuts were introduced at 0, 36, 60, 84, and 108 hours while the pavements were exposed to *C* temperature function. The concrete illustrated a longer elastic plastic state and consequently a longer saw-cutting time window. It is seen that the rate of stress development is low and stress development is controlled by ambient temperature changes. Comparing the pavements exposed to *C*, *M* and *H* ambient temperature functions, it can be concluded that the lower ambient temperatures provide a longer elasto plastic state and favor the post-peak stable stress release of pavements.

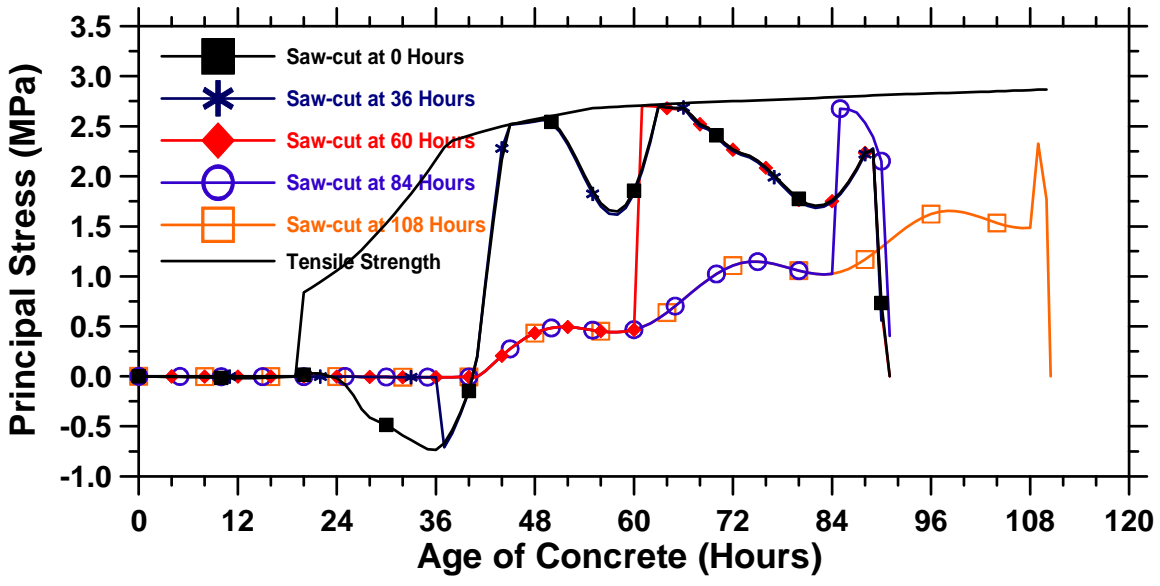


Figure 8.47: Tensile strength and principal stresses of pavements exposed to “C” temperature function.

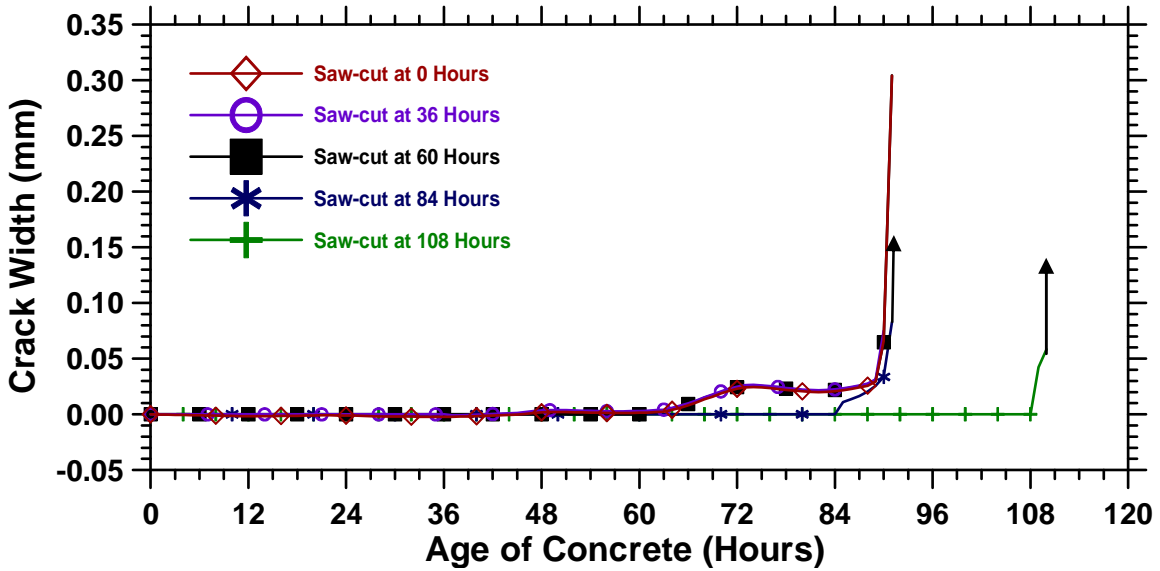


Figure 8.48: CTOD at the tip of D/3 saw-cuts of pavements exposed to “C” temperature function.

8.3.1.3 Paving at Different Times of Day

As paving operations are performed at different times of day, a series of simulations was performed to investigate how the time of casting influences the concrete cracking behavior. In the following sections, the modeling approach and the simulation results will be discussed in detail.

8.3.1.3.1 The General Modeling Approach

The model properties were considered to be the same as the baseline case model described in section 7.2. The H ambient temperature function shown in Figure 8.49 was used in the modeling and it was assumed that the coldest time of a day is 4:00 a.m. The paving (and the analysis) were started at 7:00 a.m., 1:00 p.m., 7:00 p.m., and 1:00 a.m. which are designated as 1, 2, 3, and 4 in Figure 8.49 respectively. It should be noted that a D/3 saw-cut depth was introduced in each pavement 12 hours after casting.

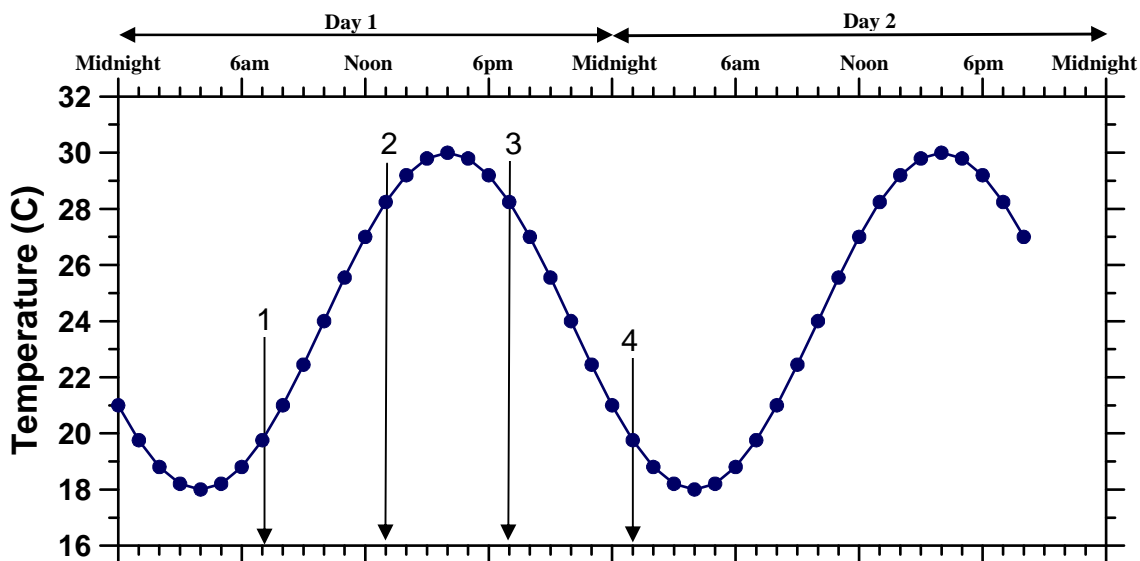


Figure 8.49: Sinusoidal ambient temperature function "H".

8.3.1.3.2 Results and Analysis

The simulation results are summarized in Figure 8.50 and Figure 8.51. As shown in Figure 8.50, the pavements cast at 1:00 p.m. and 7:00 p.m. show a shorter elastic plastic region and, an earlier residual stress development. The pavement cast at 1:00 p.m. shows an even faster residual stress release and unstable crack growth than the pavement cast at 7:00 p.m. This behavior can be explained by the fact that the pavement cast at 1:00 p.m. was exposed to higher temperatures than the pavement cast at 7:00 p.m. despite identical initial temperatures. On the other hand, the pavement cast at 1:00 a.m. was at low ambient temperature for a longer time, and shows the longest elastic plastic state. This state is followed by a stable stress behavior.

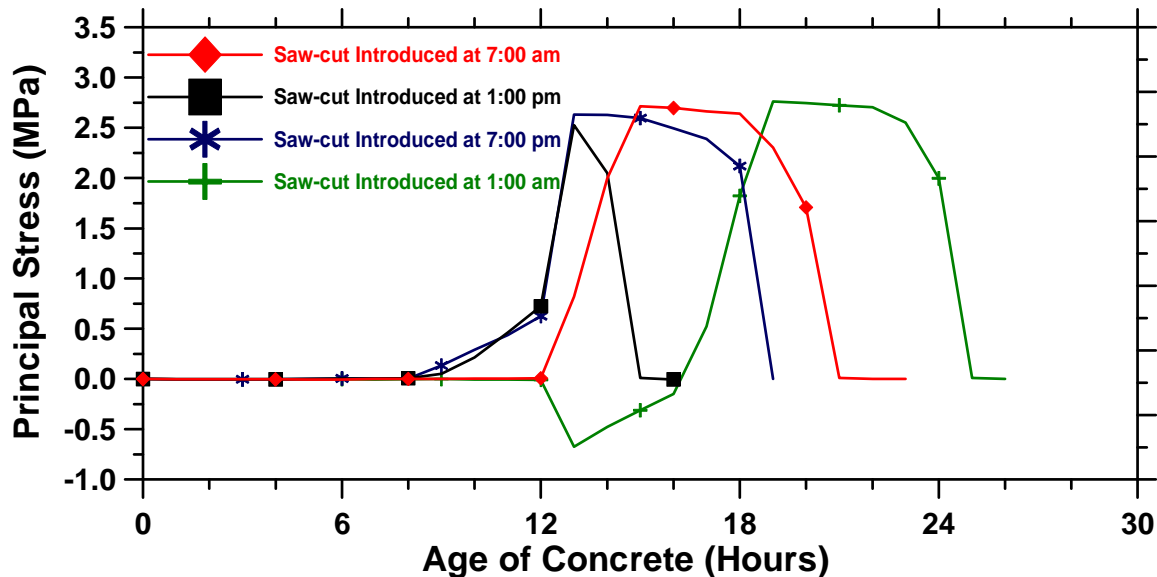


Figure 8.50: Stresses of pavements cast at different times of day.

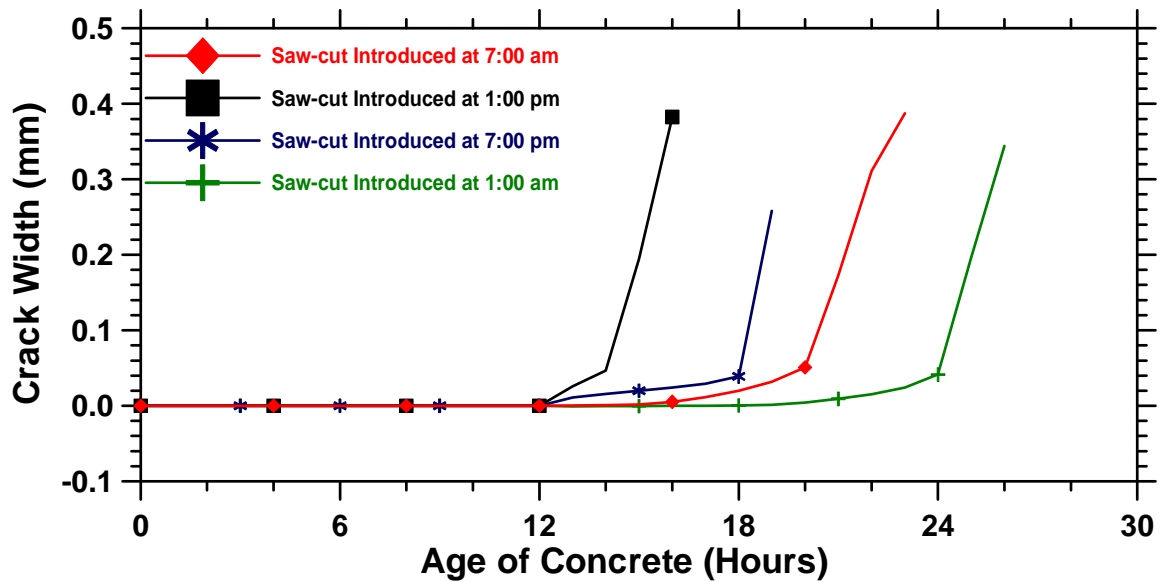


Figure 8.51: CTOD of pavements cast at different times of day.

The discussion in this section leads to the conclusion that the early ambient temperatures need special consideration in estimating the depth and time of a saw-cut. Further work is needed to better quantify the influence of early ambient temperature on cracking behavior of concrete.

8.3.1.4 Determination of the Saw-cutting Time Window

The saw-cut should be placed within a specific window of time during the construction operation. It has been determined that the ambient temperature significantly influences the saw-cutting time window (Armaghani, 1987, Jenq et. al., 1993). The ambient temperature can change the temperature profile of the pavement, and depending on the nonlinearity of temperature distribution across the depth of the pavement, the pavement can curl up, curl down, or stay flat (Armaghani et al., 1987, Thompson et al., 1987). The ambient temperature also influences the rate of strength gain and rate of chemical reaction of the concrete.

In this section the influence of ambient temperature on the saw-cutting time window is determined.

8.3.1.4.1 The Influence of the Time of Saw-cut Introduction on the Cracking Behavior of Pavements

To investigate the influence of ambient temperature on the saw-cutting time window of concrete pavements, different constant ambient temperatures were defined. The model property was considered to be the same as the baseline case defined previously in section 7.2, and the time of saw-cut introduction was varied. The influence of ambient temperature on the saw-cutting time window for pavements at 36°C with saw-cut depth of D/3 is discussed first. The cracking behaviors of pavements cured at 23°C and 10°C are then described. The average end stresses, local stresses at the saw-cut tip, and CTOD were determined for each simulation. The results are shown as a function of maturity which was measured at the D/3 distance from surface of the pavement.

Figure 8.52 illustrates the average end stresses, local stresses, and crack width openings for pavements at 36°C with D/3 saw-cut depths. As shown in Figure 8.52, the pavements experience compression during the first 30 maturity hours (in this case). When a saw-cut is made in the first 6 maturity hours, the early compression is followed by an increase in local and average end tensile stresses. The CTOD remains close to zero while local stresses approach the pavement strength. When the local stresses reach the concrete strength, cracking initiates, and CTOD begins to grow in a stable manner. When the average end stresses reach their maximum, cracks begin to grow at a faster rate and unstable crack propagation occurs. If the saw-cut is introduced when the tensile residual stress exists (after 6 maturity hours in this case), cracking initiates at a faster rate. However, applying a saw-cut when the stress levels are higher than the critical stress level (1.2 MPa in this case) results in instant crack initiation and propagation as shown by approximately vertical lines in Figure 8.52f, 8.52g, 8.52h, and 8.52i.

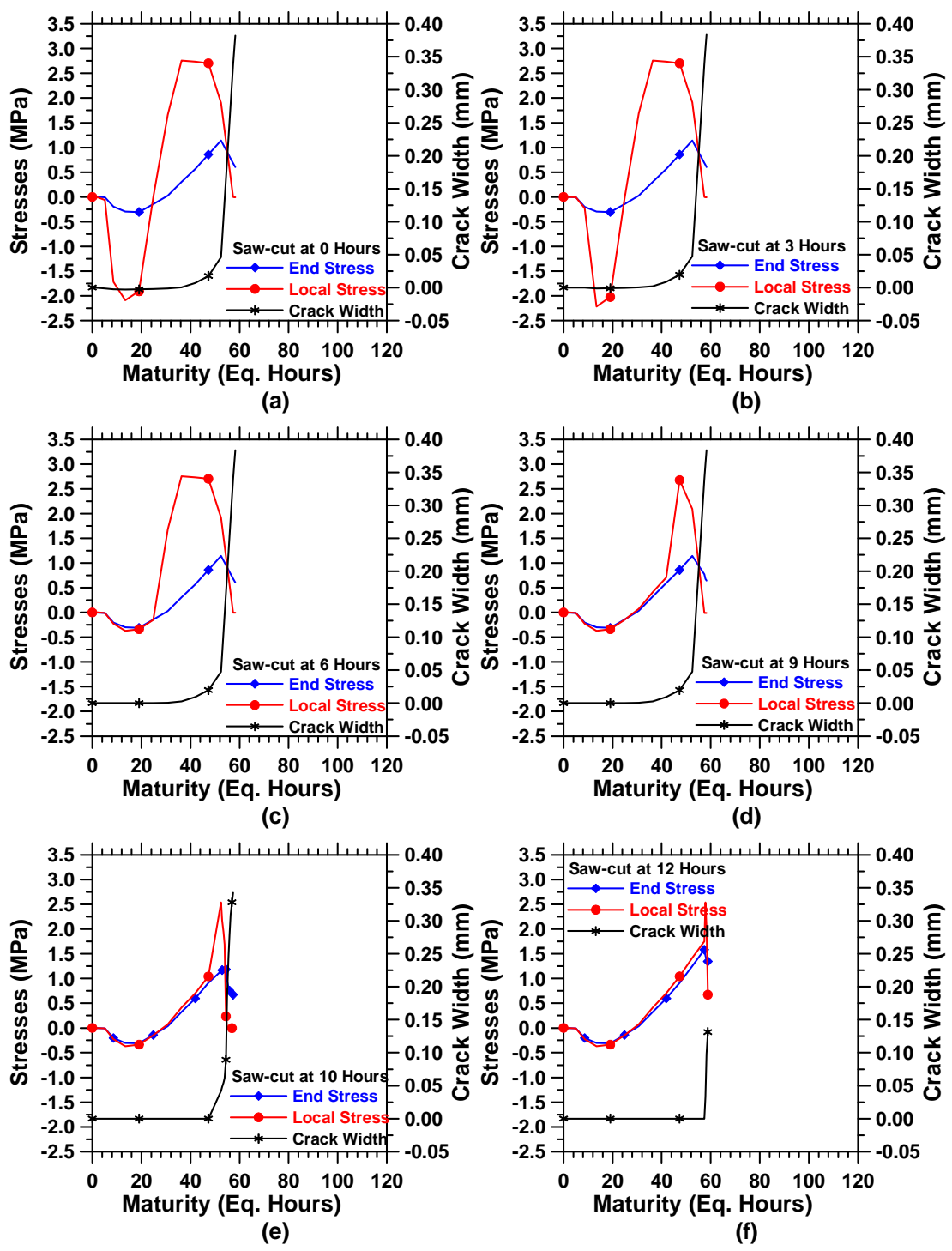


Figure 8.52: End and local stresses and crack width of pavements at 36°C with D/3 saw-cut depths (cont'd).

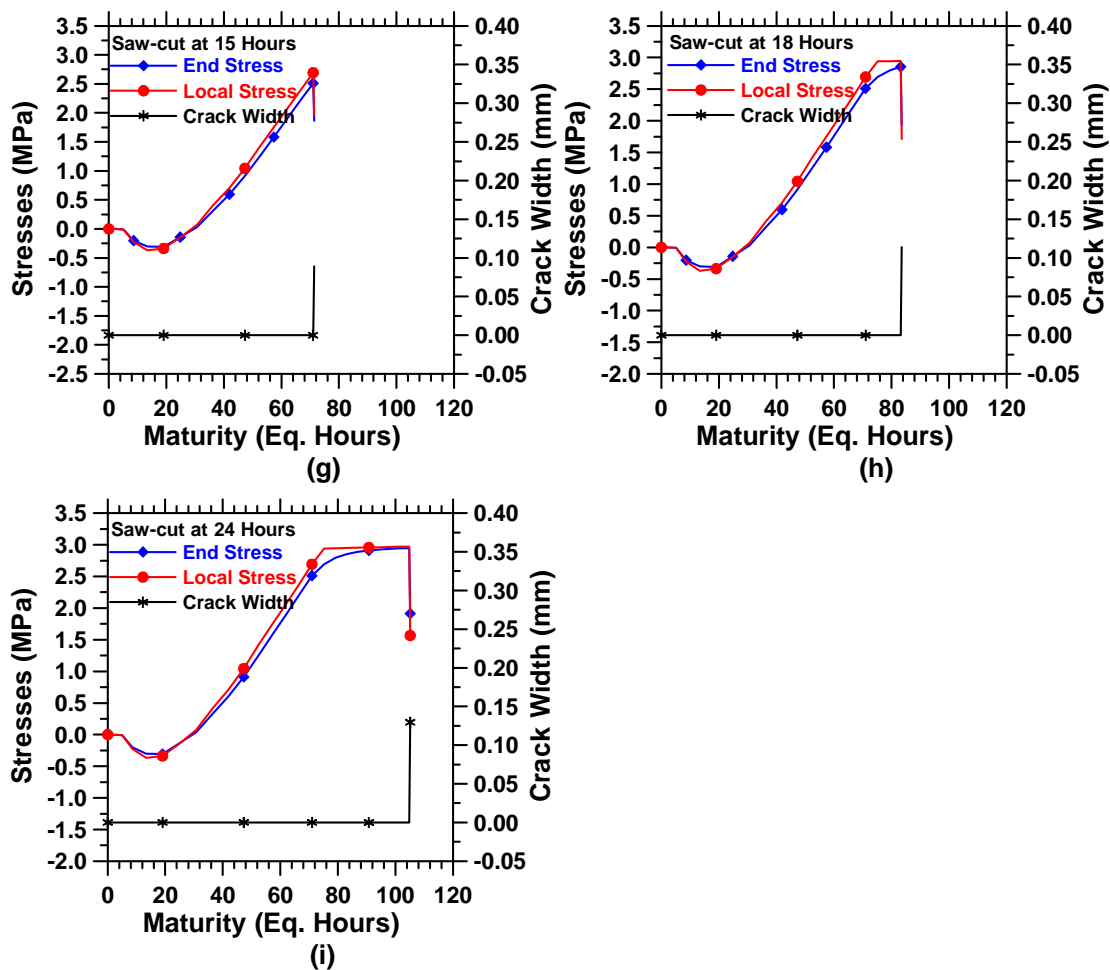


Figure 8.52: End and local stresses and crack width of pavements at 36°C with D/3 saw-cut depths.

The simulation results shown in Figure 8.52 were used to develop Figure 8.53. Figure 8.53a shows that the maturity corresponding to residual stress development is not dependent on the time of saw-cut. As a result, residual stress would be expected to develop at 23 equivalent hours irrespective of saw-cut time or geometry. For cases when the saw-cut is introduced during the first 6 hours (25 maturity hours), cracking initiates (i.e., the residual stress at the tip of the saw-cut reaches the tensile strength of concrete) at the tip of saw-cut at 36.4 maturity hours (in this case). However, for cases when the saw-cut is introduced after 6 hours, the cracks initiate at the time the saw-cut is introduced. Similarly, if the saw-cut is introduced before 10 hours in real time (47 maturity hours), the unstable crack propagation occurs at 52 maturity hours. However, if the saw-cut is

introduced at later ages, unstable crack propagation occurs as the saw-cut is applied. The through cracking line indicates the time at which the tip of the crack reaches the bottom of the pavement. As shown in Figure 8.53a, the crack initiates and propagates to the bottom of the pavement instantly if the saw-cut is applied after 12 hours (58 maturity hours). The point identified as no saw-cut indicates that the maturity at which a pavement would fail if no saw-cut were applied in the field. Figure 8.53b shows the maturity when the saw-cut was introduced.

Figure 8.53c illustrates the residual stress development. If the saw-cut is introduced at residual stress levels higher than 1.2 MPa (52 equivalent hours) for this case, an instant decrease in residual stresses is observed. This sudden drop in stress levels indicates that unstable crack propagation has occurred. Figure 8.43e shows how the time of saw-cut introduction influences the residual stress development at the saw-cut tip. Figure 8.43f shows the average end stress versus crack width behavior. The area under stress-crack width graph implies the amount of stored energy in the pavement. When the saw-cut is introduced at later ages, the area under the stress-crack width increases. The larger area under the graphs indicates a higher level of stored energy. It is worth mentioning that this energy is consumed to create two surfaces when the concrete cracks.

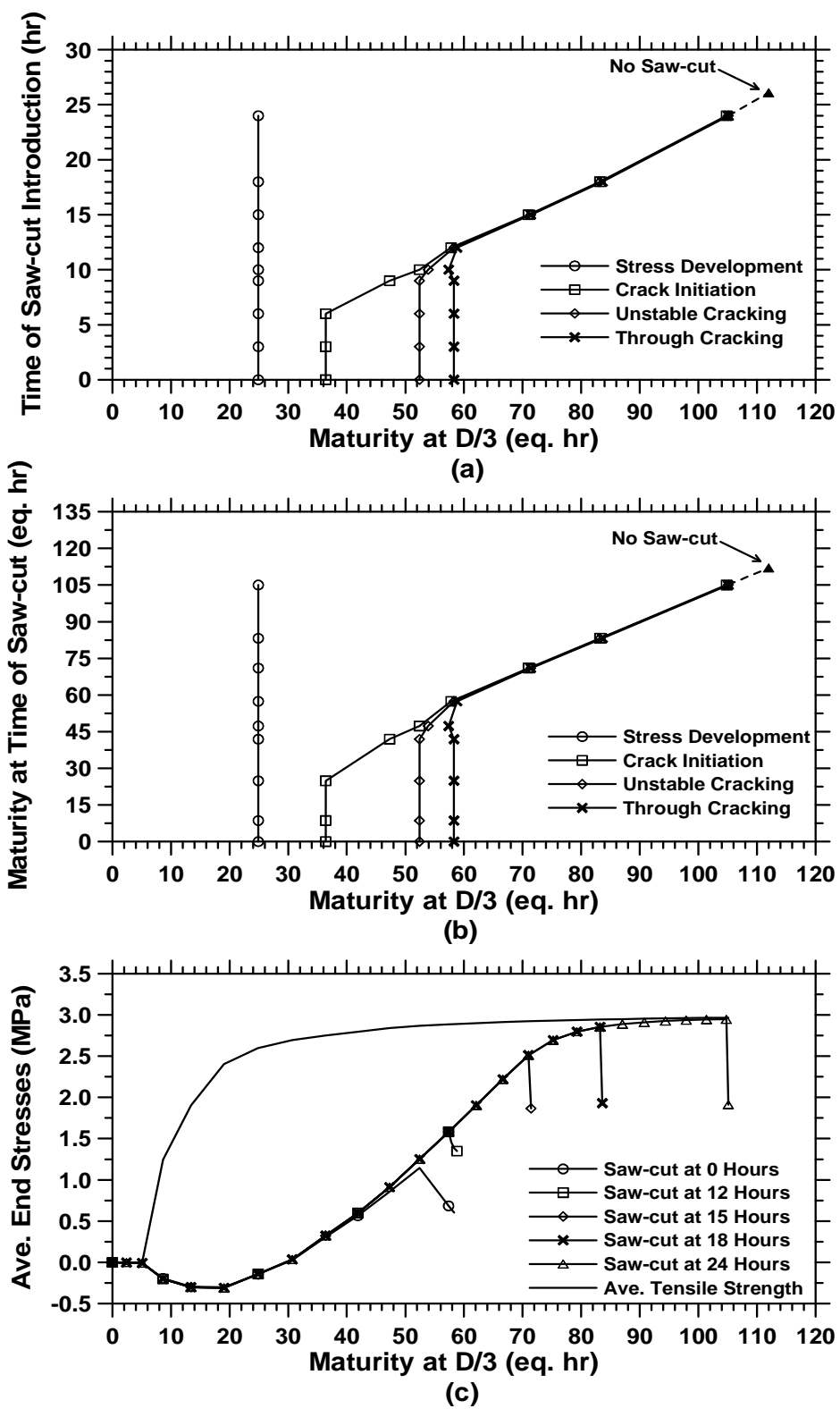


Figure 8.53: The cracking behavior of pavements with D/3 saw-cut depths cured at 36°C (cont'd).

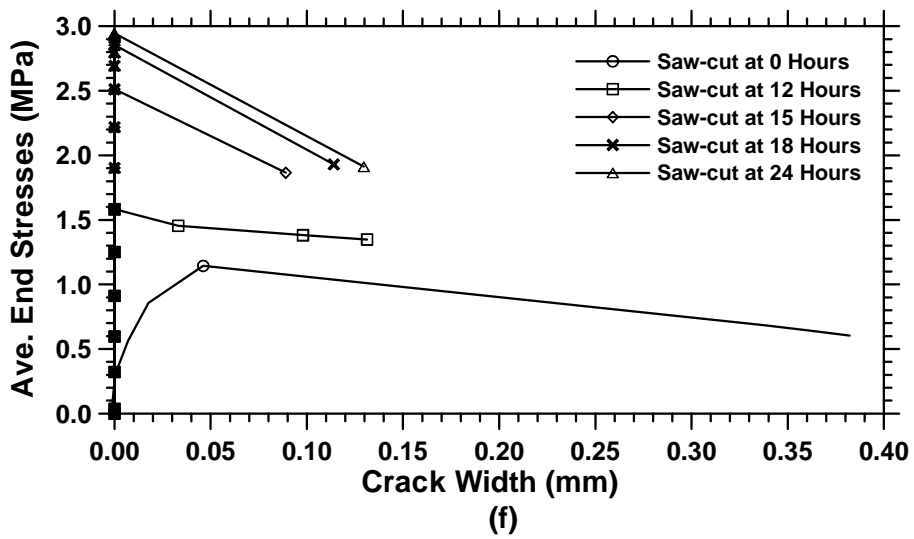
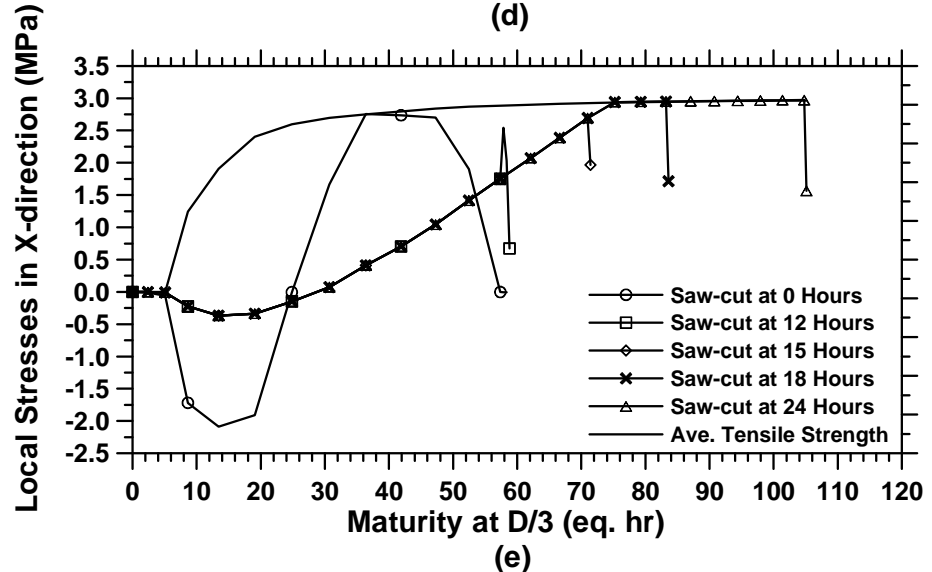
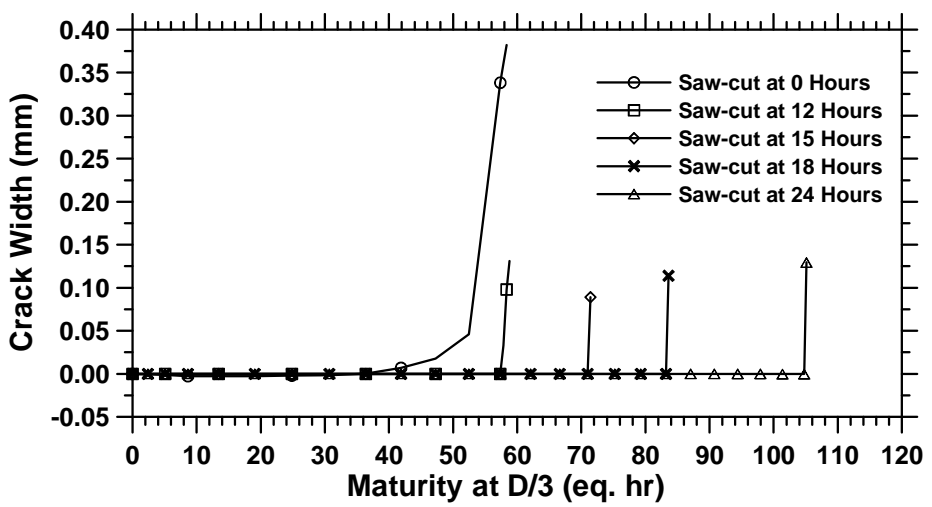


Figure 8.53: The cracking behavior of pavements with D/3 saw-cut depths cured at 36°C.

Figure 8.54 and Figure 8.55 provide the stress and cracking behaviors of concrete pavements at 23°C with D/3 saw-cut depths while Figures 8.56 and Figure 8.57 provide the stress and cracking behaviors of concrete pavements at 23°C with D/2 saw-cut depths. Figure 8.58 and Figure 8.59 provide the similar graphs for concrete pavements at 10°C with D/3 saw-cut depths. Figure 8.60 and Figure 8.61 present the stress and cracking behaviors of concrete pavements at 23°C with D/8 saw-cut depths. These pavements showed similar trends in behavior to the pavements at 36°C with D/3 saw-cut depths.

It should be noted that through cracking of pavements with D/8 saw-cut depths tend to happen soon after the unstable cracking. The reason that unstable cracking happens in a much shorter time period is likely due to the higher amount of stored energy in the pavements as shown in Figure 8.57f and 8.61f. It has been determined that the rate of energy release would also be higher for pavements with shallow saw-cut depths. As such, the pavements with shallow saw-cut depths have higher rates of crack propagations.

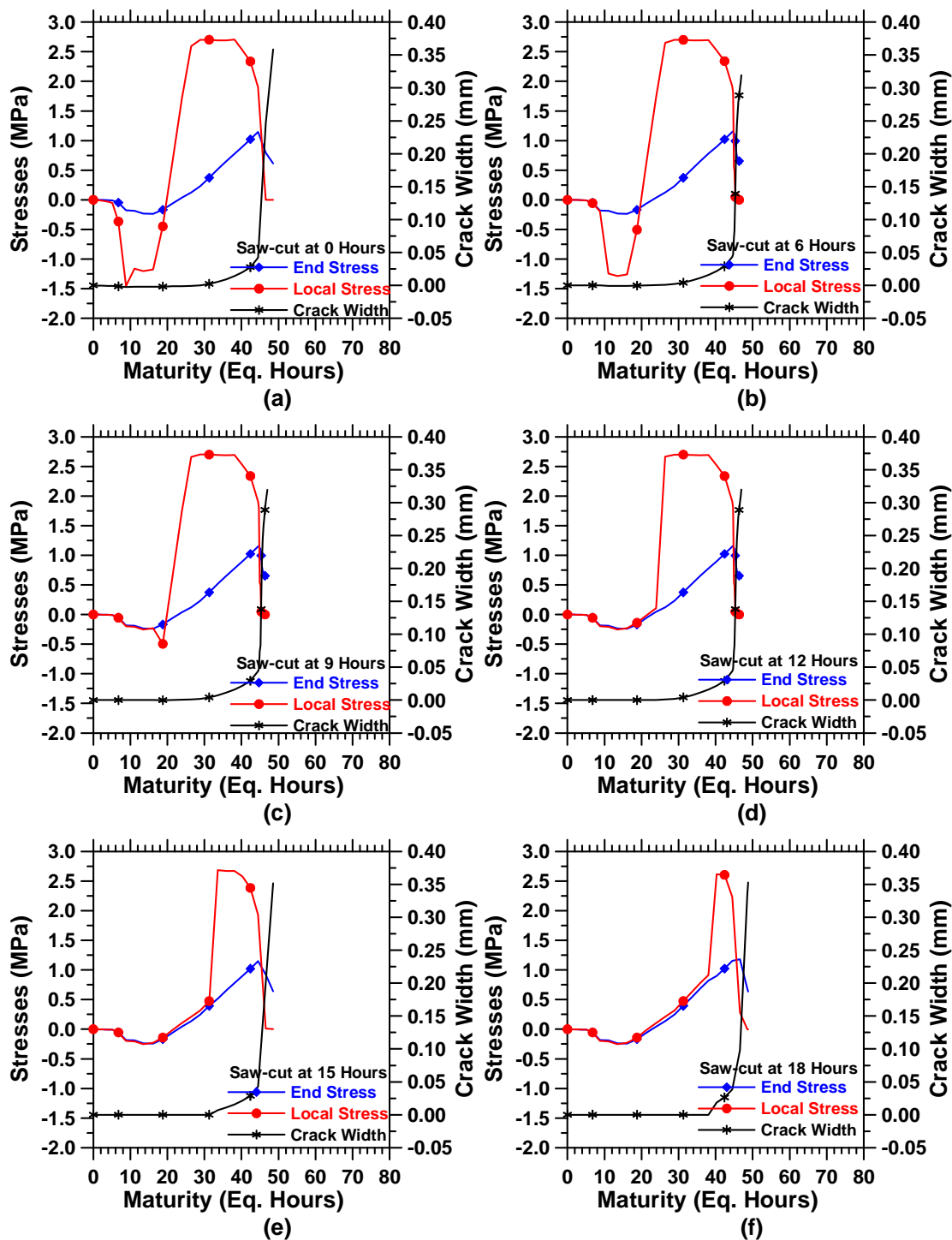


Figure 8.54: End and local stresses and crack width of pavements at 23°C with D/3 saw-cut depths (cont'd).

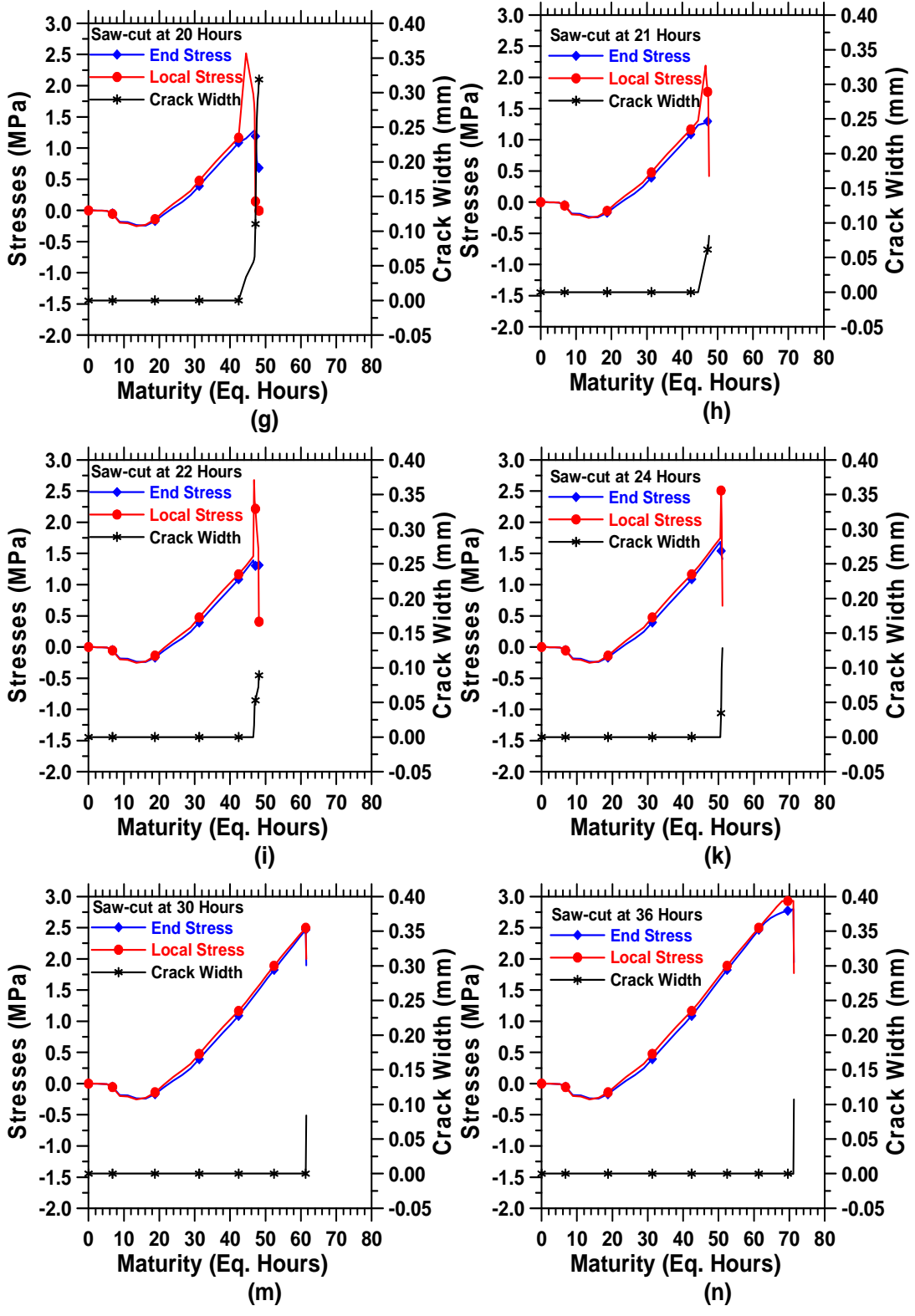


Figure 8.54: End and local stresses and crack width of pavements at 23°C with D/3 saw-cut depths.

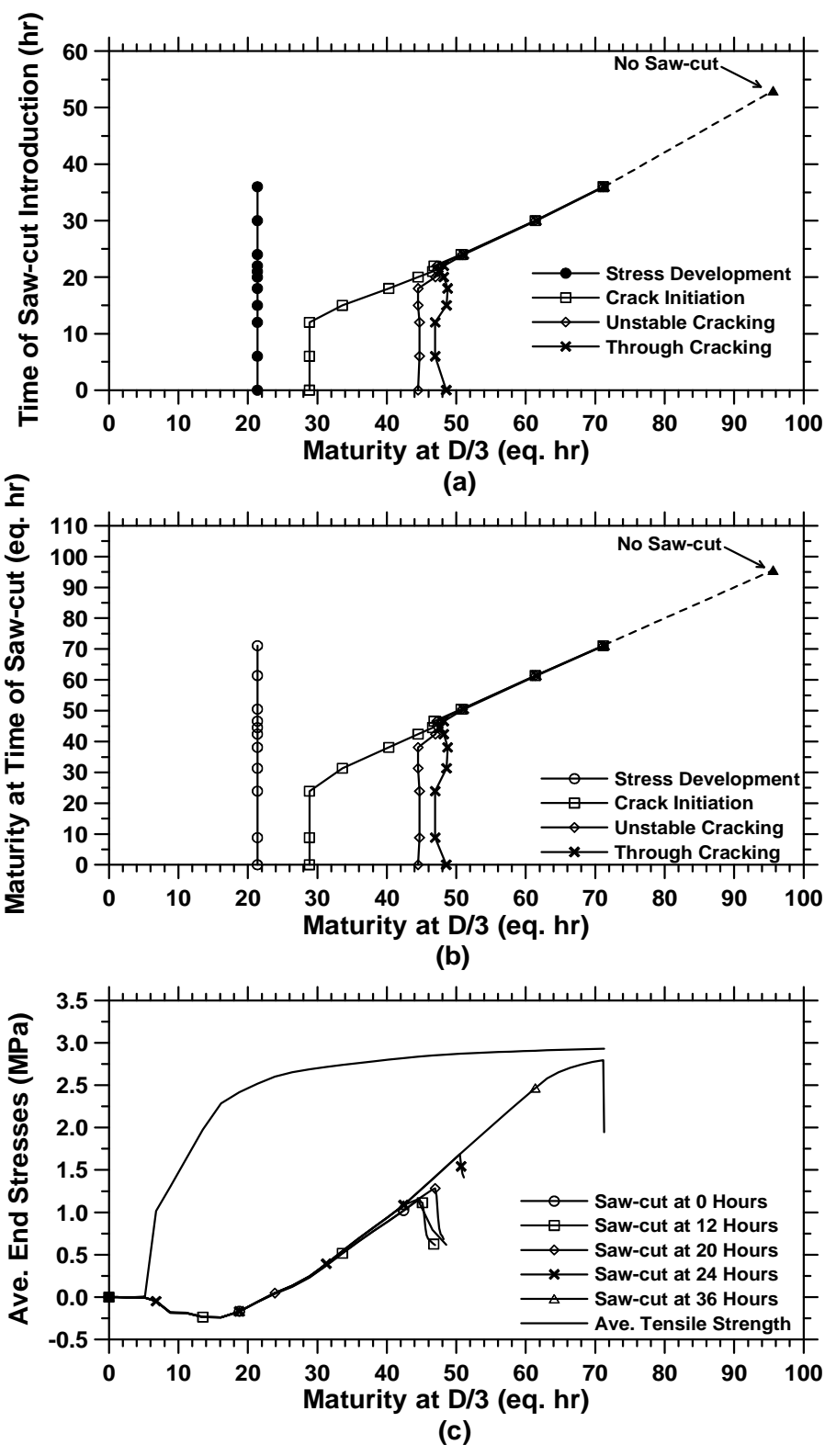


Figure 8.55: The cracking behavior of pavements with D/3 saw-cut depths cured at 23°C (cont'd).

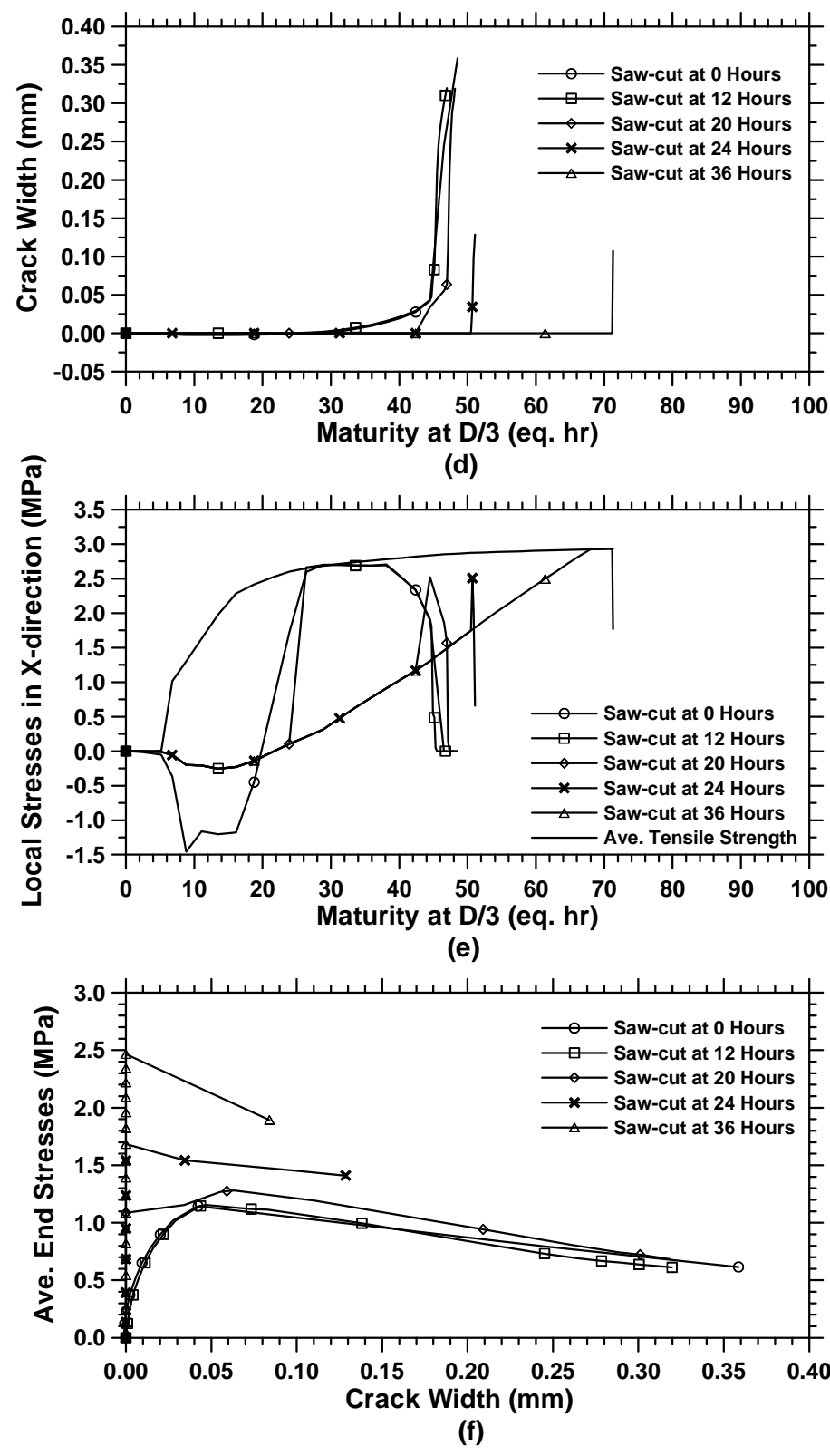


Figure 8.55: The cracking behavior of pavements with D/3 saw-cut depths cured at 23°C.

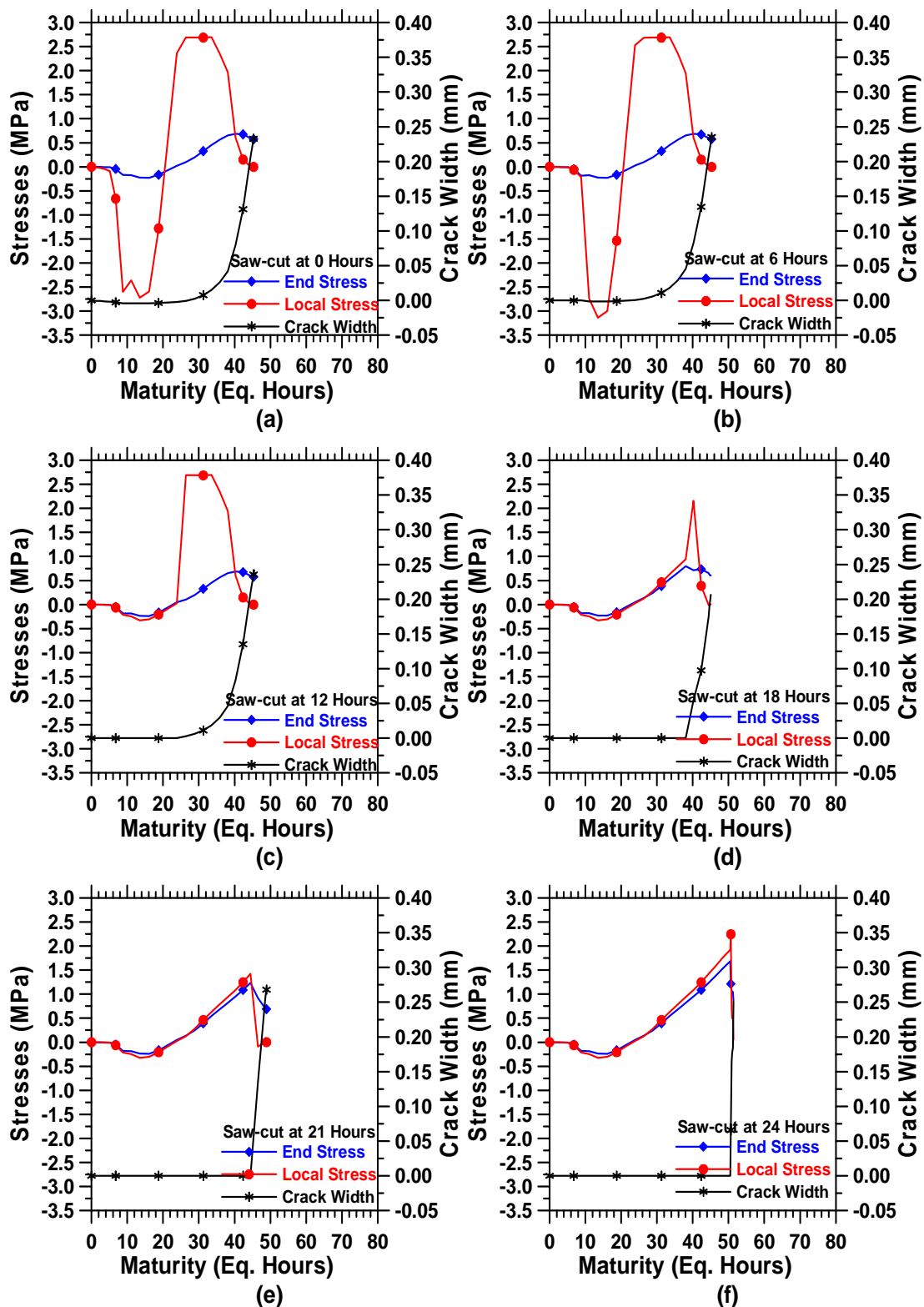


Figure 8.56: End and local stresses and crack width of pavements at 23°C with D/2 saw-cut depths (cont'd).

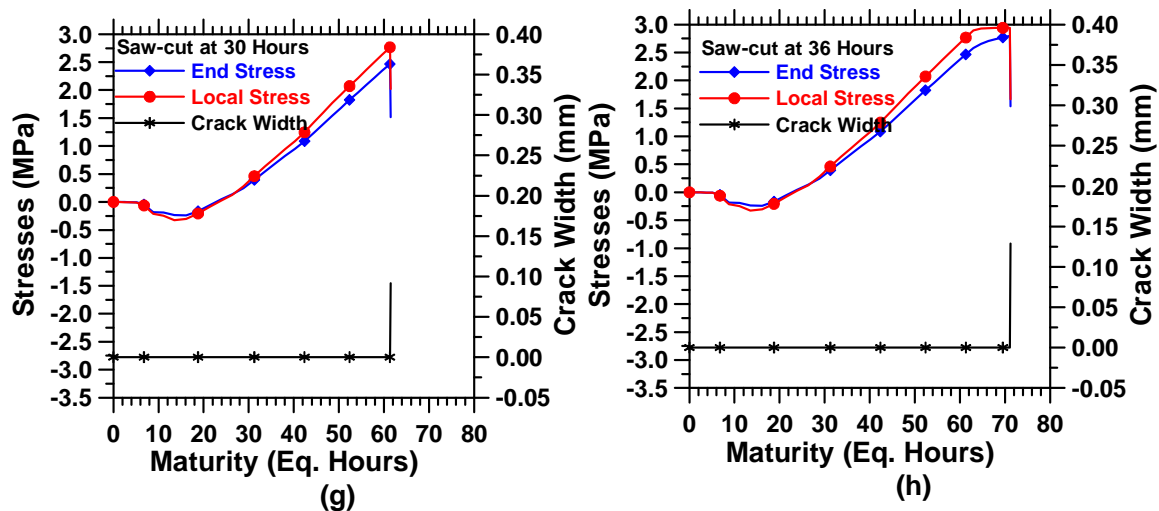


Figure 8.56: End and local stresses and crack width of pavements at 23°C with D/2 saw-cut depths.

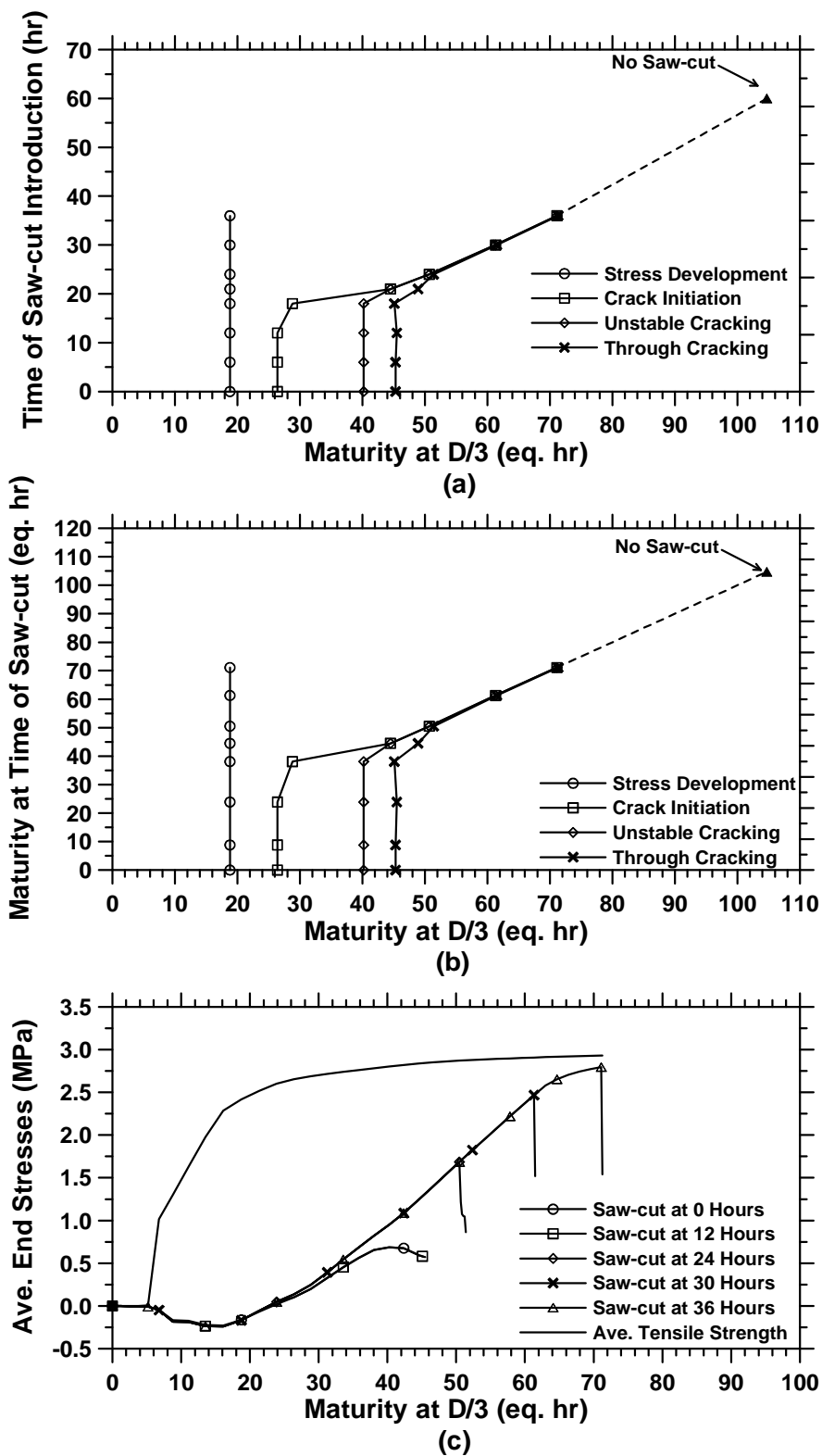


Figure 8.57: The cracking behavior of pavements with D/2 saw-cut depths cured at 23°C

(cont'd).

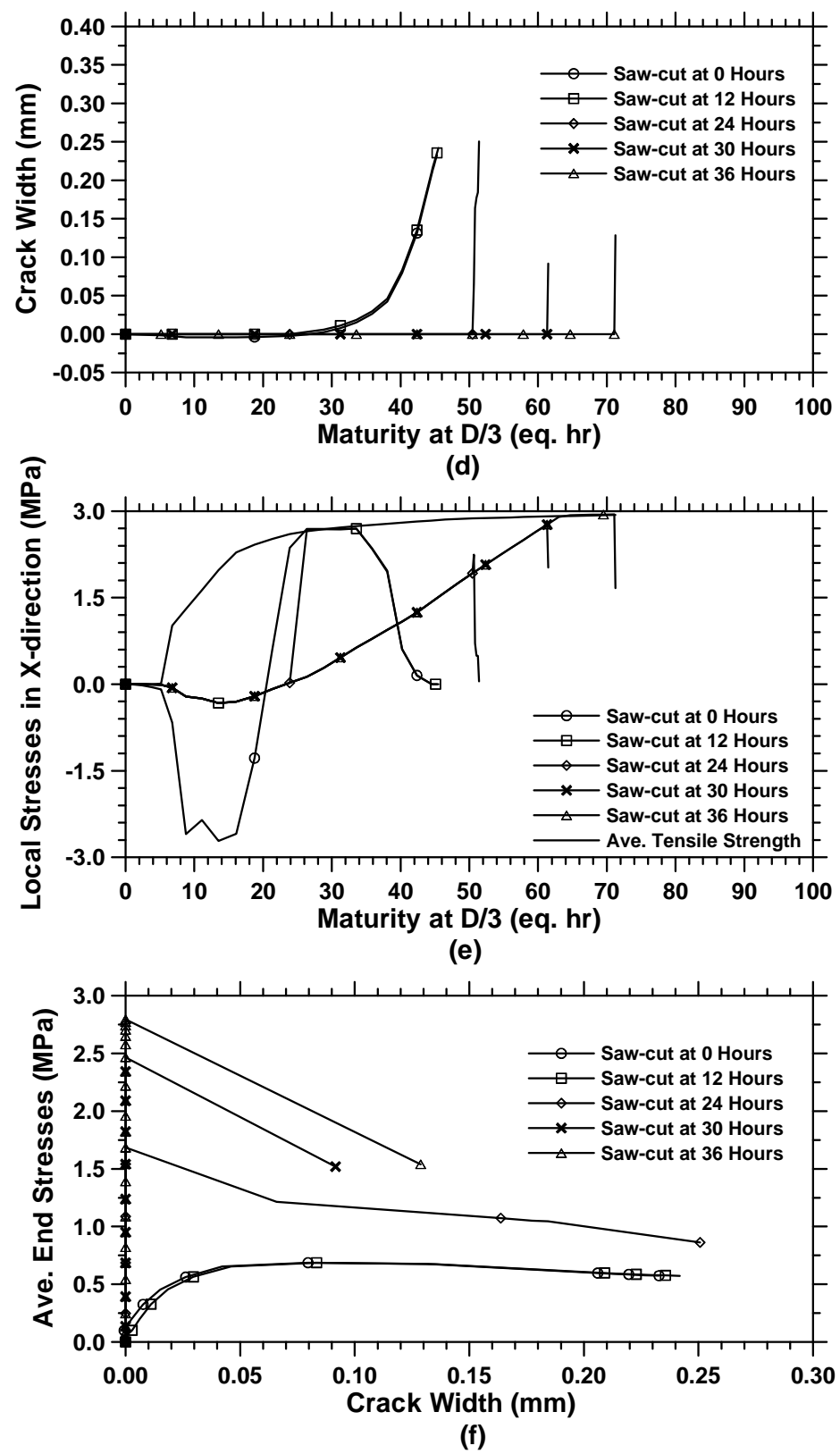


Figure 8.57: The cracking behavior of pavements with D/2 saw-cut depths cured at 23°C.

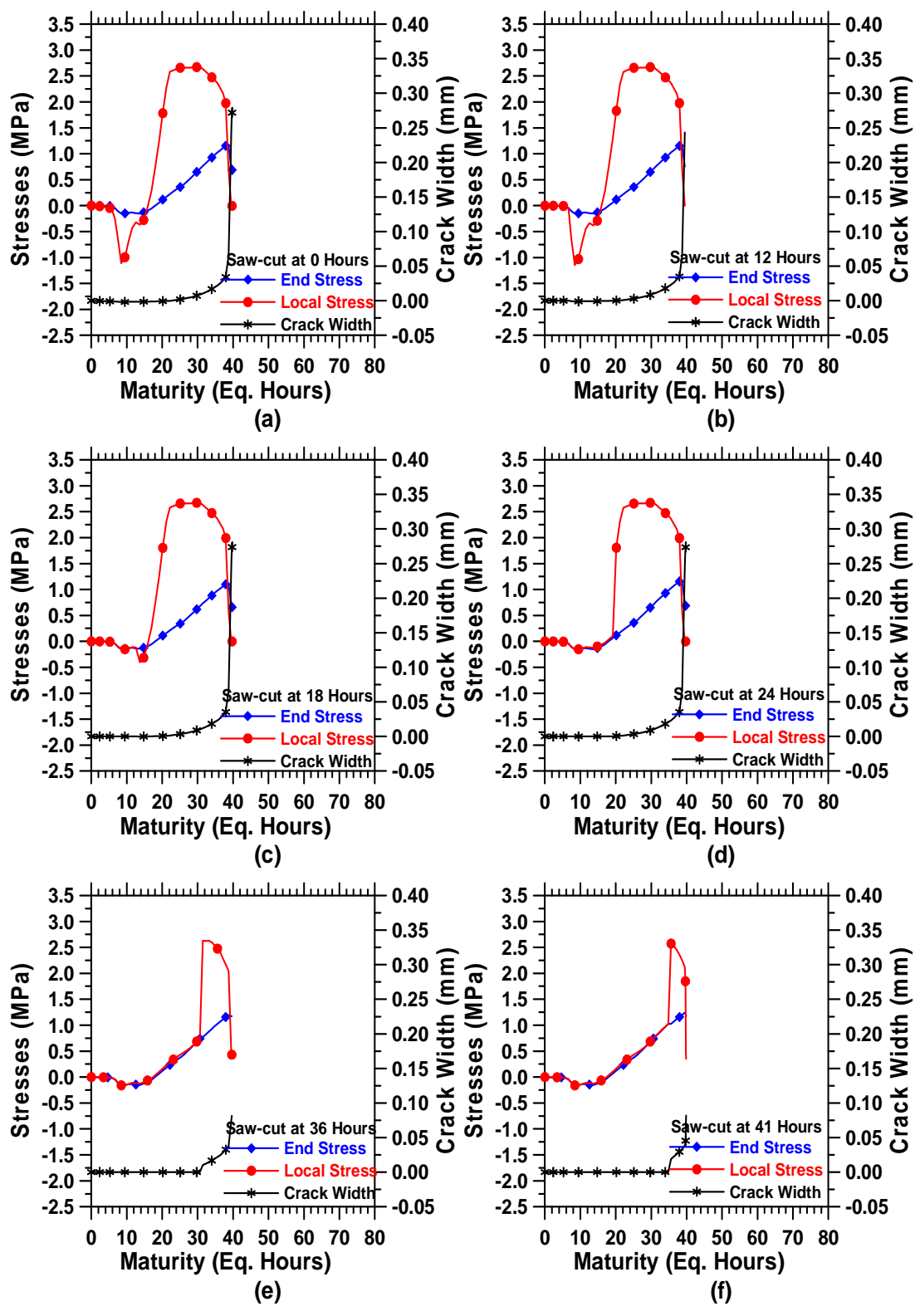


Figure 8.58: End and local stresses and crack width of pavements at 10°C with D/3 saw-cut depths (cont'd).

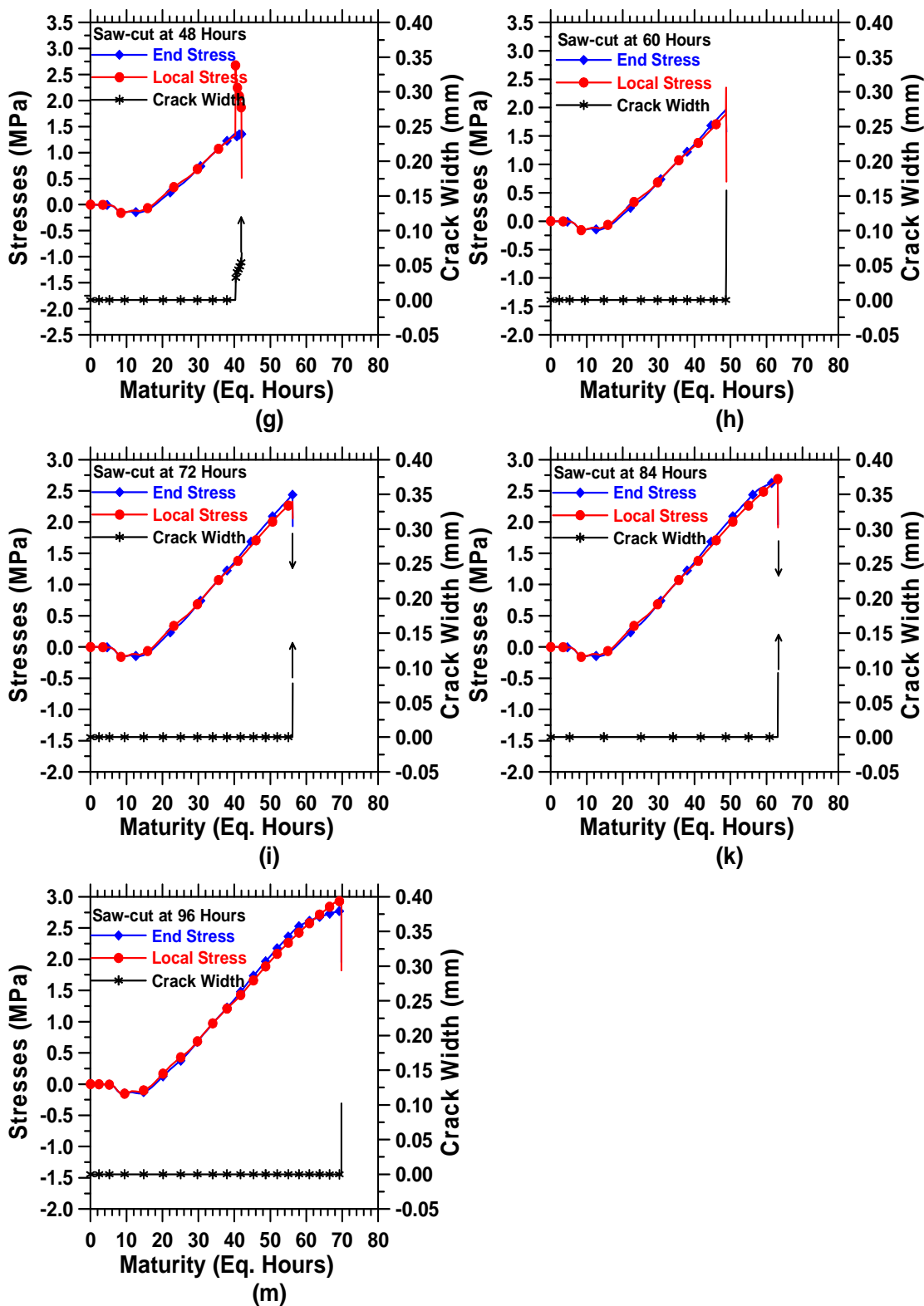


Figure 8.58: End and local stresses and crack width of pavements at 10°C with D/3 saw-cut depths.

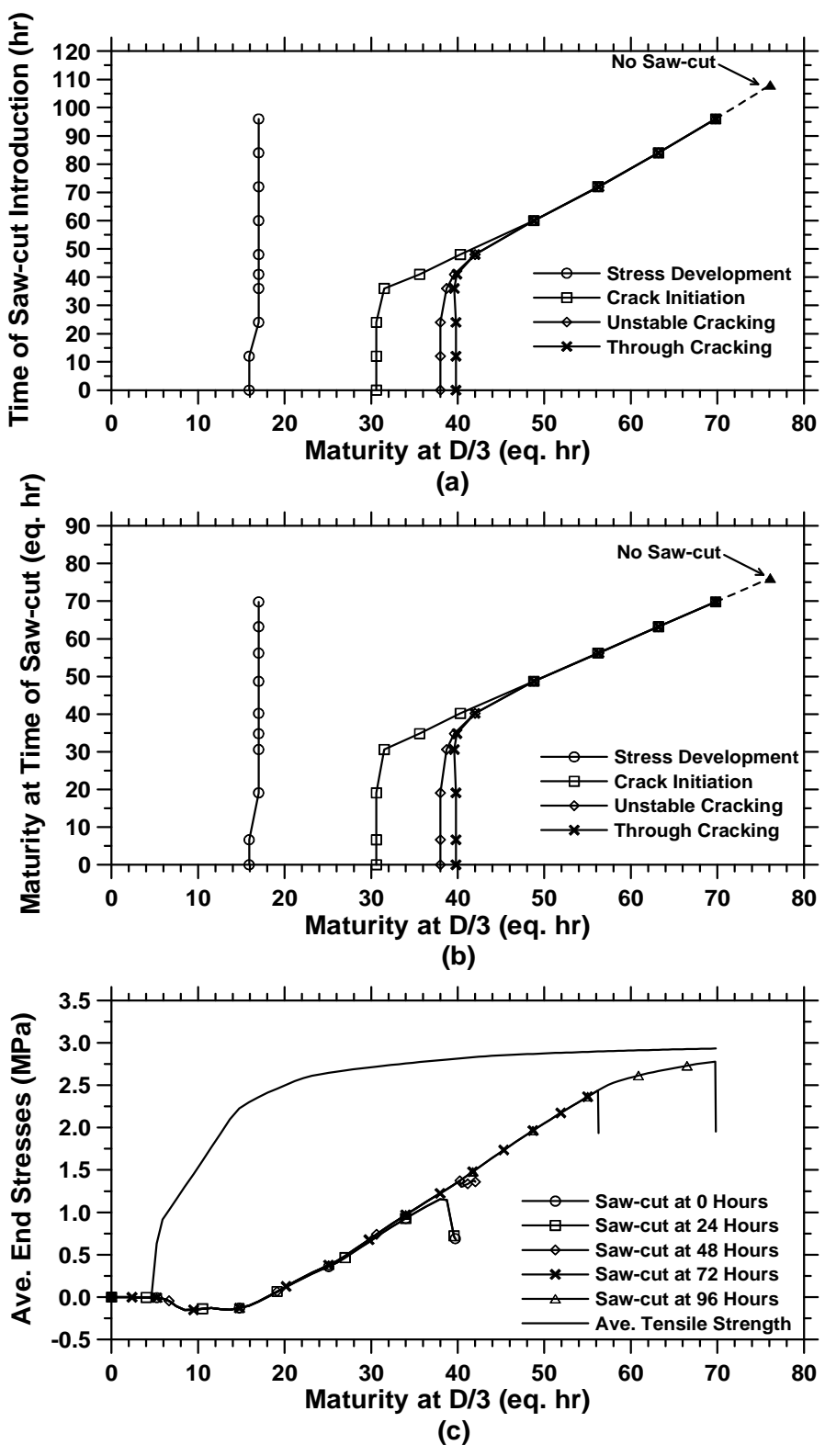


Figure 8.59: The cracking behavior of pavements with D/3 saw-cut depths cured at 10°C (cont'd).

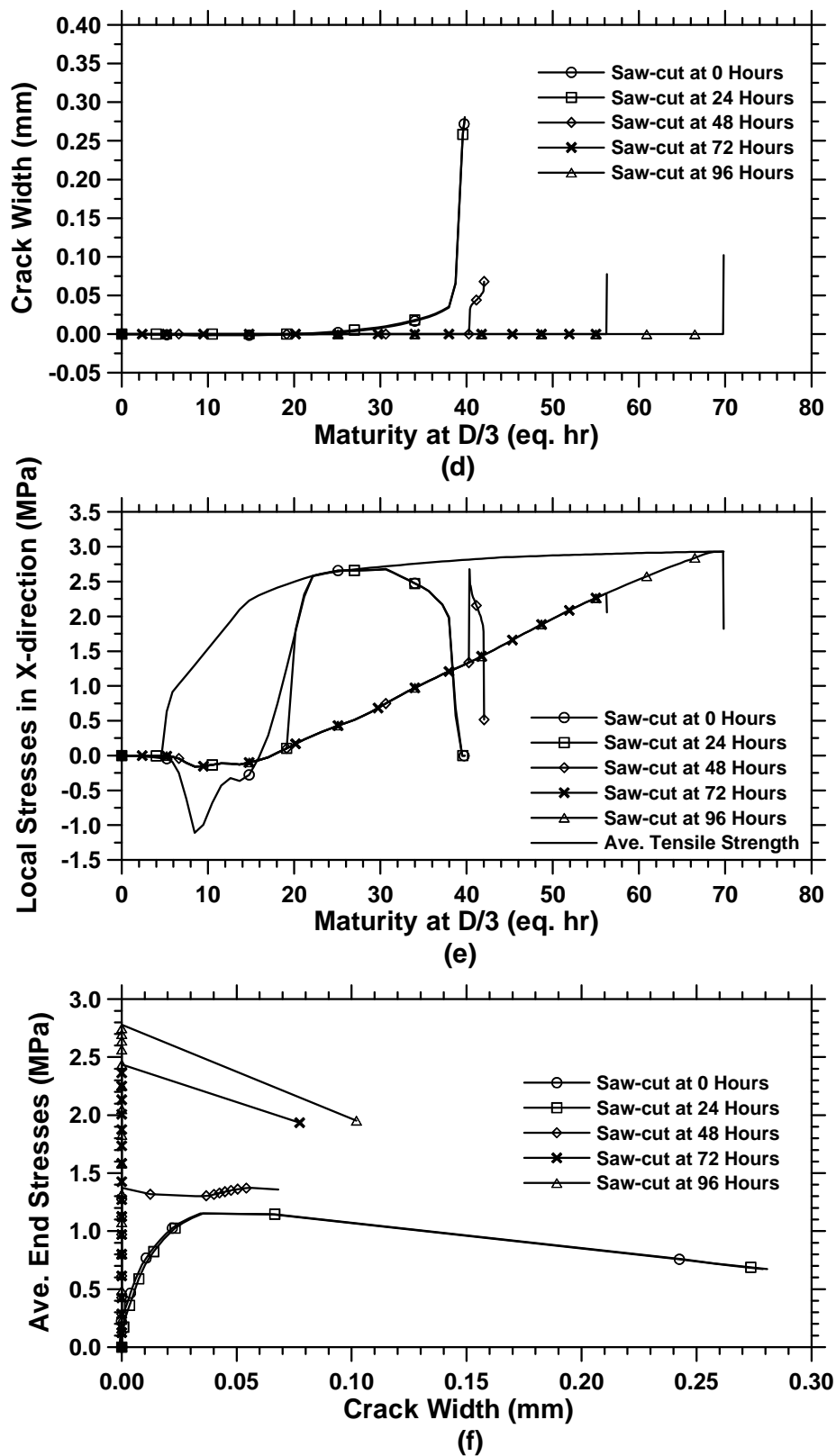


Figure 8.59: The cracking behavior of pavements with D/3 saw-cut depths cured at 10°C.

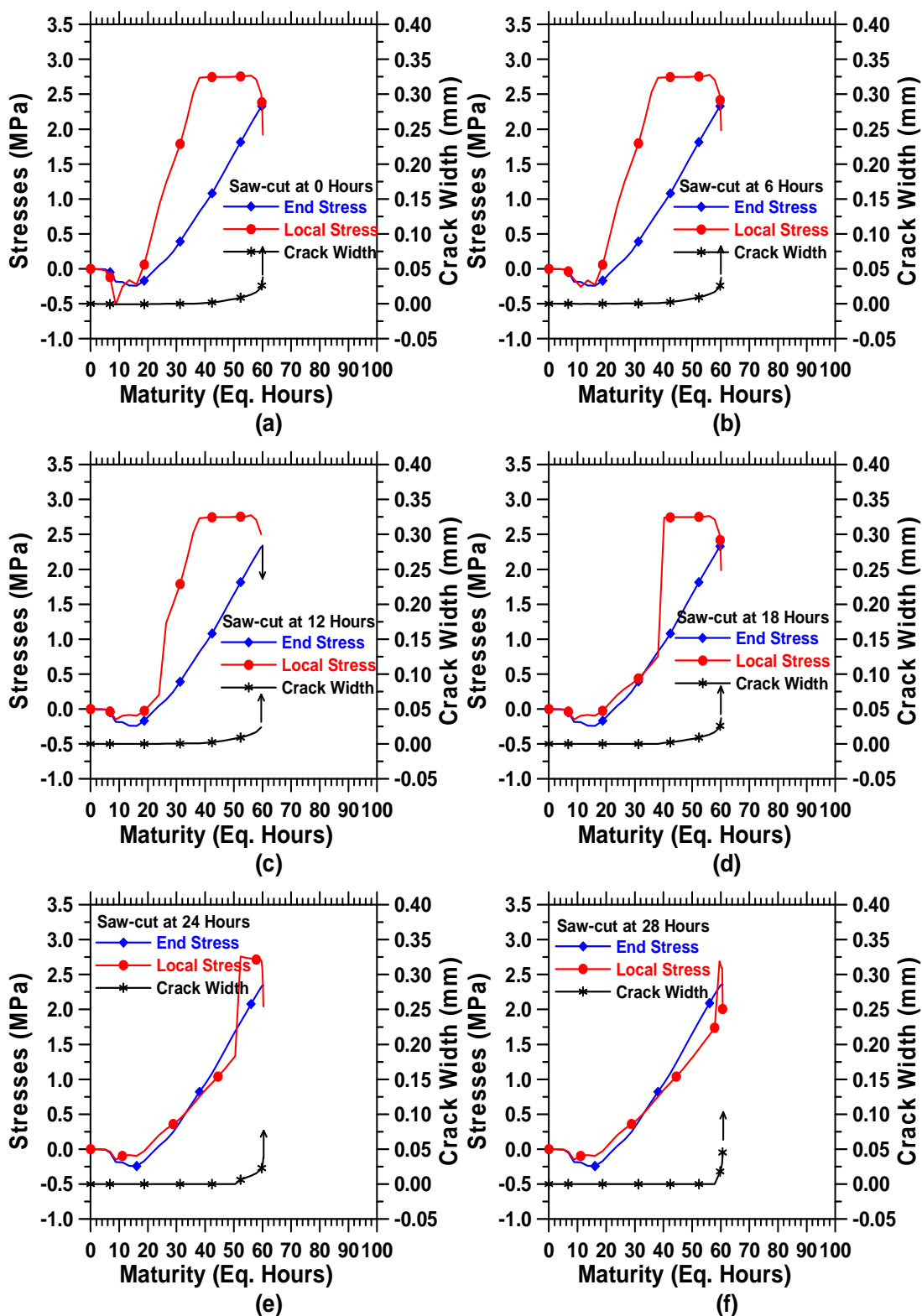


Figure 8.60: End and local stresses and crack width of pavements at 23°C with D/8 saw-cut depths (cont'd).

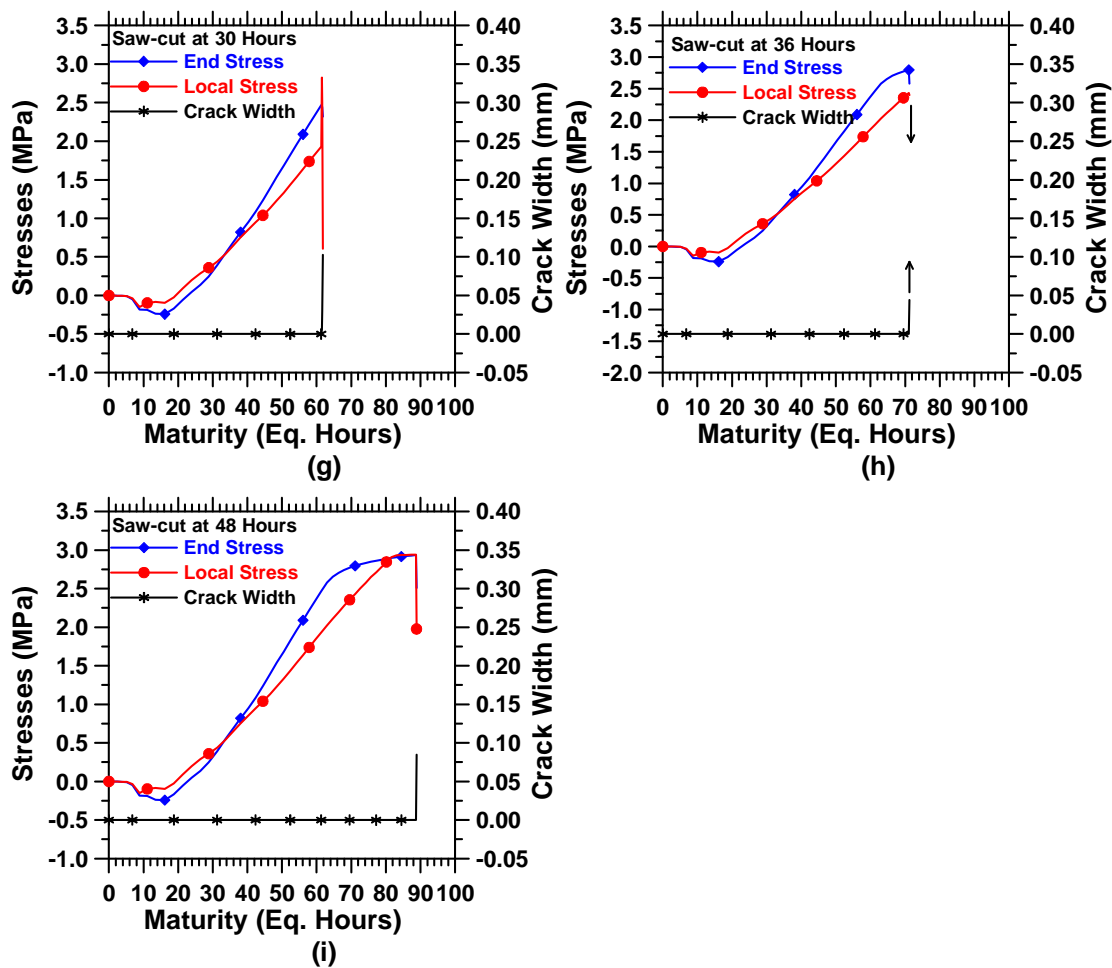


Figure 8.60: End and local stresses and crack width of pavements at 23°C with D/8 saw-cut depths.

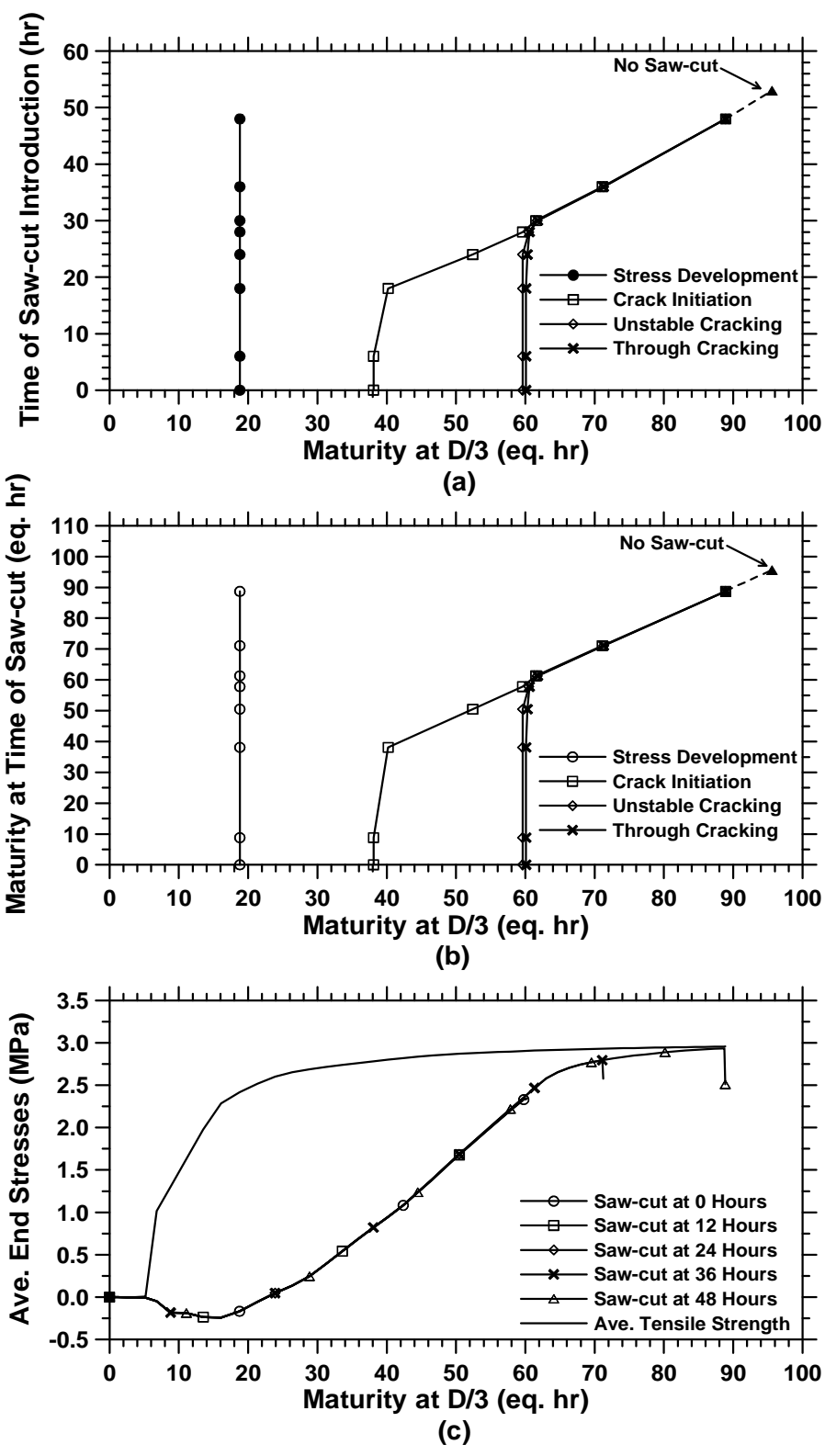


Figure 8.61: The cracking behavior of pavements with D/8 saw-cut depths cured at 23°C (cont'd).

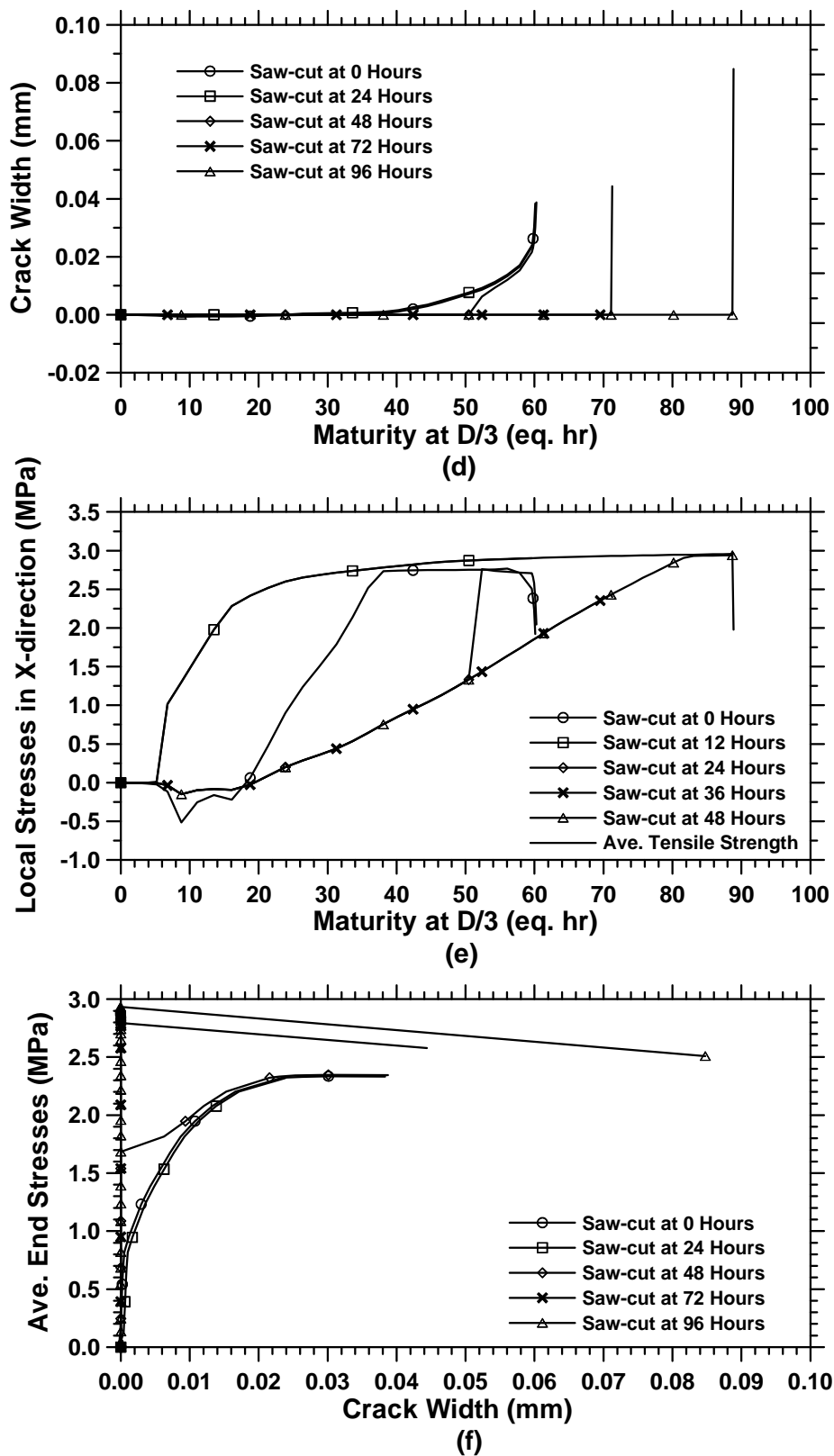


Figure 8.61: The cracking behavior of pavements with D/8 saw-cut depths cured at 23°C.

Figure 8.62 and Figure 8.63 show the crack initiation and unstable cracking maturities of pavements with D/2, D/3, and D/8 saw-cut depths respectively. It should be noted that in these simulations the saw-cuts were applied at 0 hours. The maturities at which the cracking of pavements with D/8 saw-cut depths occurs are higher than the maturities at which pavements with D/2 and D/3 saw-cut depths crack. The cracking maturities of pavements also increase at higher ambient temperatures. This can be explained by the higher thermal expansion of concrete at higher ambient temperature, and the reduced time under load that results in less stress relaxation. The expansion is thought to cancel out some of the tensile stresses developed due to chemical and drying shrinkage.

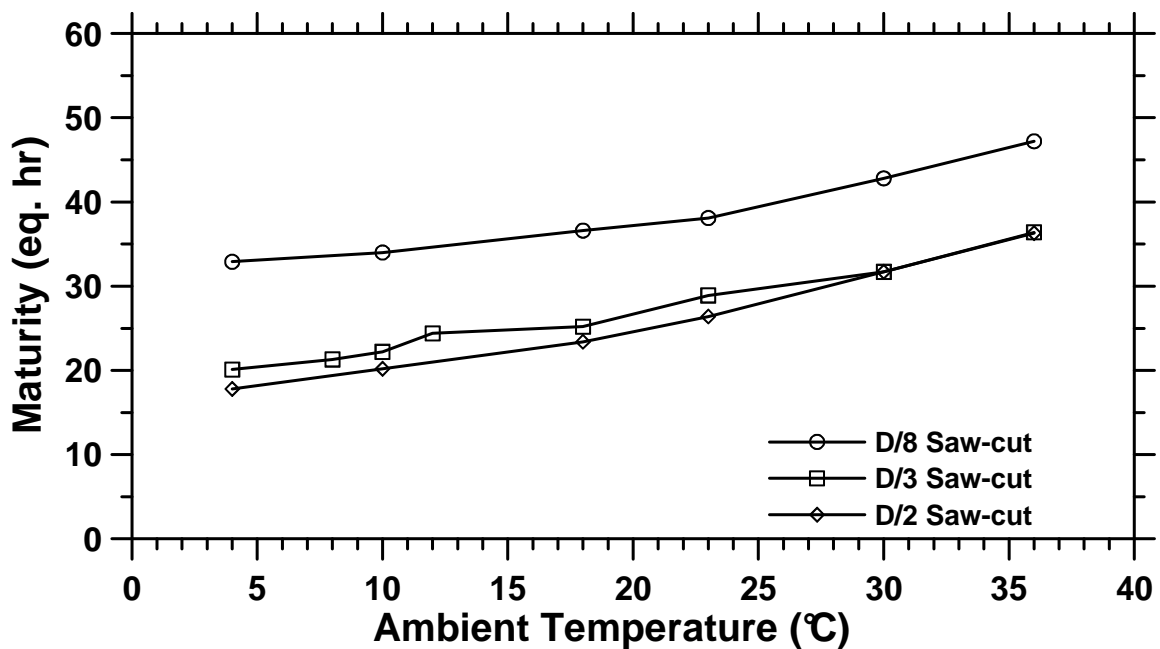


Figure 8.62: Crack initiation maturities of pavements with different saw-cut sizes and at different ambient temperatures.

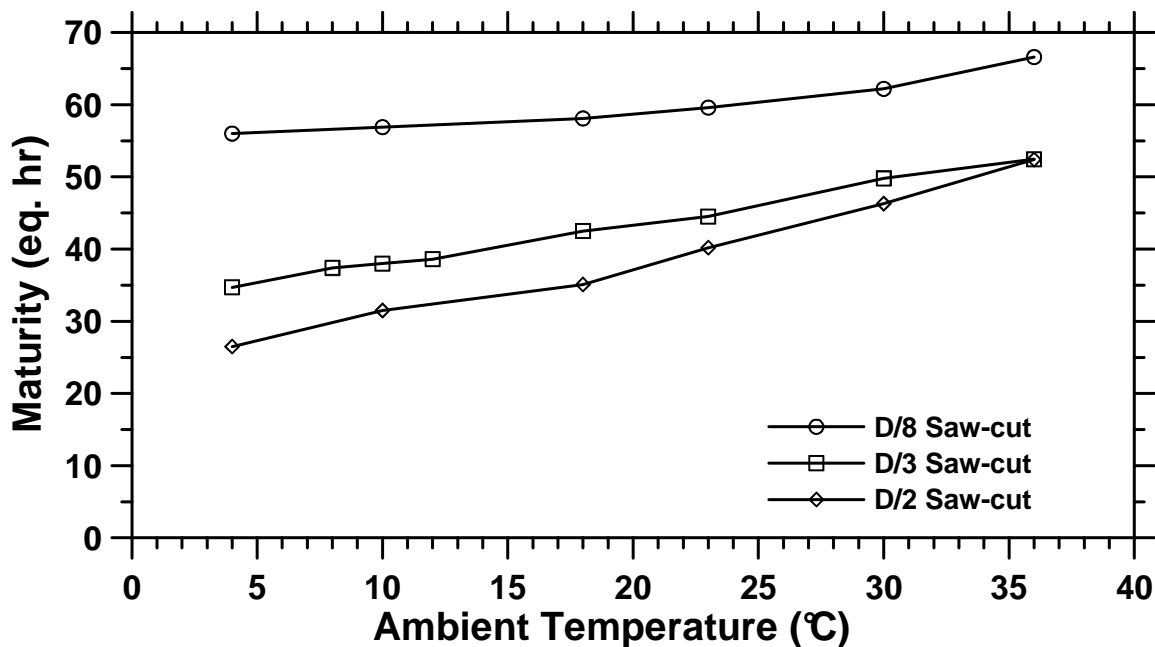


Figure 8.63: Unstable cracking maturities of pavements with different saw-cut sizes and at different ambient temperatures.

8.3.1.4.2 The Influence of the Ambient Temperature on the Cracking Behavior of Pavements

In this section, the effect of ambient temperature on the cracking and stress behaviors of concrete pavements are investigated. Pavements with D/2, D/3 and D/8 saw-cut depths which were introduced at 0 hours were modeled. Figure 8.64, Figure 8.66, and Figure 8.68 show the result of the end support reactions, local principal stresses, and crack tip opening displacements for pavements with D/2, D/3 and D/8 saw-cut depths, respectively. The results show that the pavements exposed to higher ambient temperatures experience higher thermal expansion and consequently higher compressive stress levels at early ages. The early age expansion provides a bigger time window in terms of maturity time to place the saw-cut. However, the higher ambient temperatures actually decrease the actual real time window for saw-cutting

Figure 8.65, Figure 8.67, and Figure 8.69 show that an increase in ambient temperature results in an increase in the maturity at which the residual stress development and cracking occur. To quantify the influence of ambient temperatures on the residual

stress development, the following equation was used to calculate the thermal stresses at 36.4 maturity hours for pavements at 4°C and 10°C. To obtain the ΔT , the temperature at the set time was subtracted from the temperature at 36.4 maturity hours. The temperature difference was then multiplied by the coefficient of thermal expansion (0.000006 (1/°C)) and modulus of elasticity of concrete at 36.4 maturity hours (18002.5 MPa) to estimate the thermal stresses in concrete. A small difference between the residual stresses and calculated thermal stresses of 0.28 MPa is attributed to the variation in elastic modulus and relaxation of concrete. Table 8.2 summarizes the calculation process.

$$\sigma_T = \alpha \cdot \Delta T \cdot E \quad (8.1)$$

Table 8.2: Calculation of thermal stresses.

Ambient Temp. (°C)	Maturity (eq hr)	Real Time (hr)	Residual Stress (MPa)	Temp. (°C)	Temp. at Set (°C)	ΔT (°C)	Thermal Stress (MPa)	$\Delta\sigma_{\text{resid}}$ (MPa)	$\Delta\sigma_{\text{temp}}$ (MPa)
10	36.4	43	1.07	17.06	13.60	3.46	0.37		
36	36.4	8	0.30	53.10	39.88	13.22	1.43	0.77	1.05

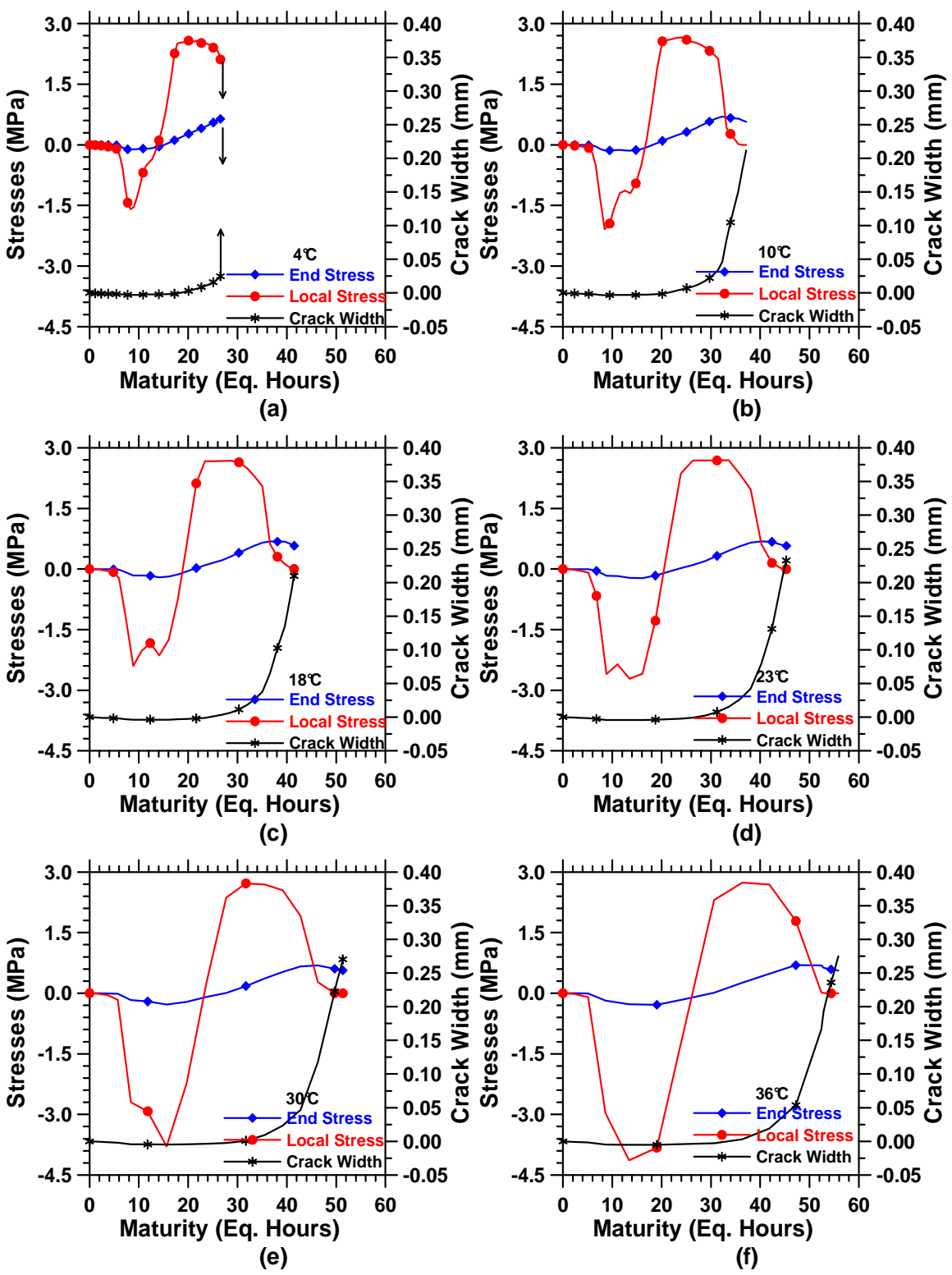


Figure 8.64: End and local stresses and crack width of pavements with D/2 saw-cut depths cured at different ambient temperature.

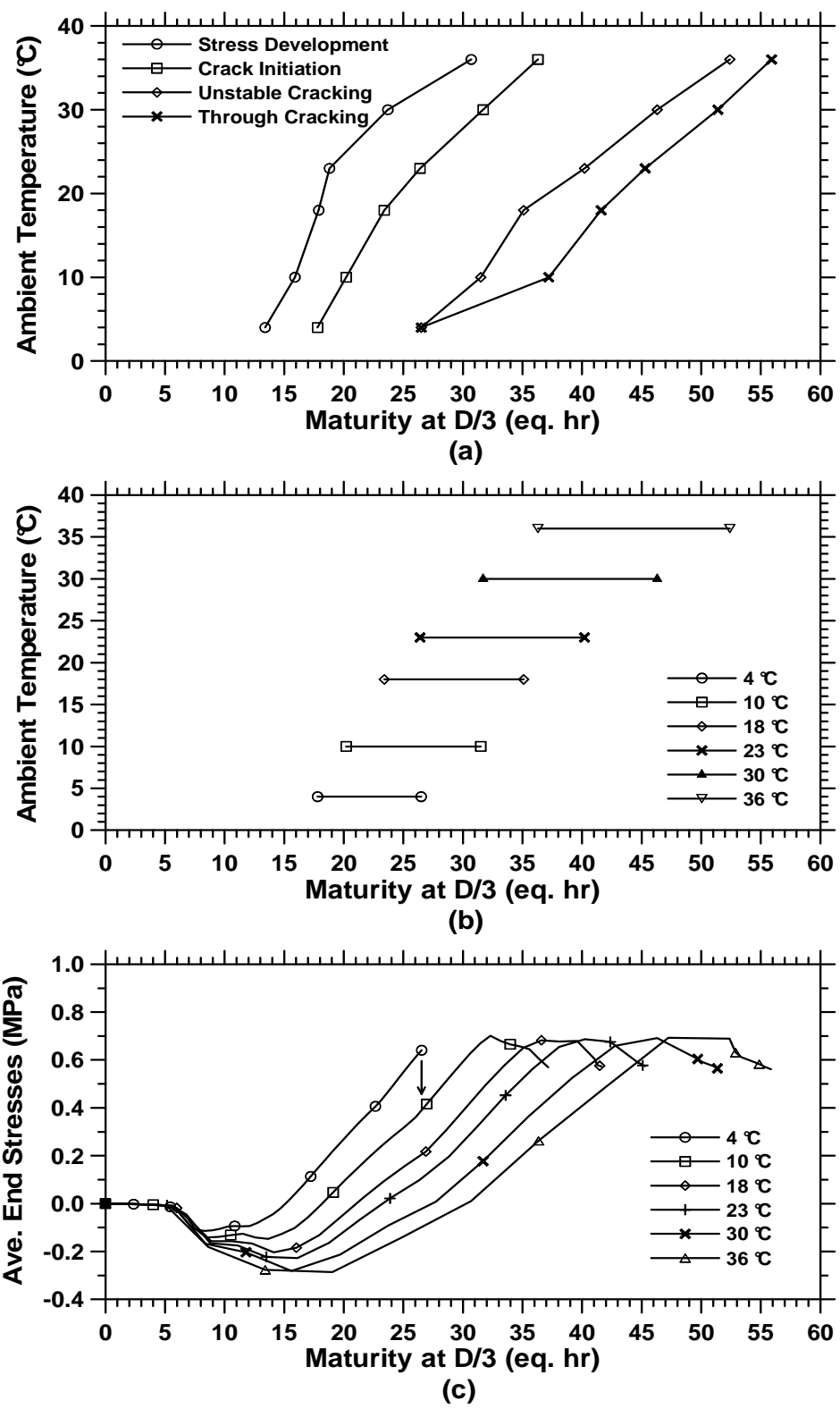


Figure 8.65: The cracking and stress behavior of pavements with D/2 saw-cut depths cured at different ambient temperatures (cont'd).

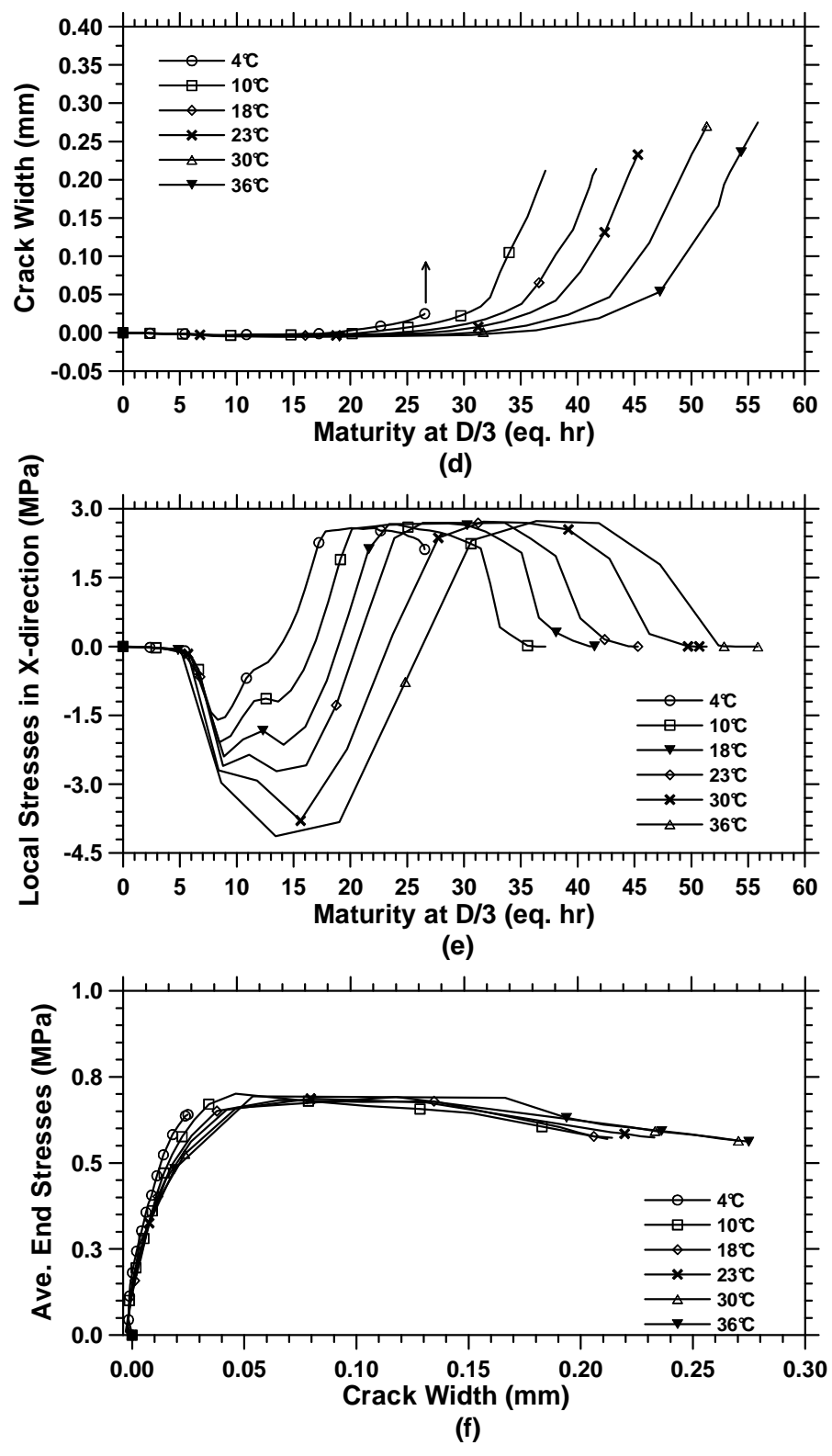


Figure 8.65: The cracking and stress behavior of pavements with D/2 saw-cut depths cured at different ambient temperatures.

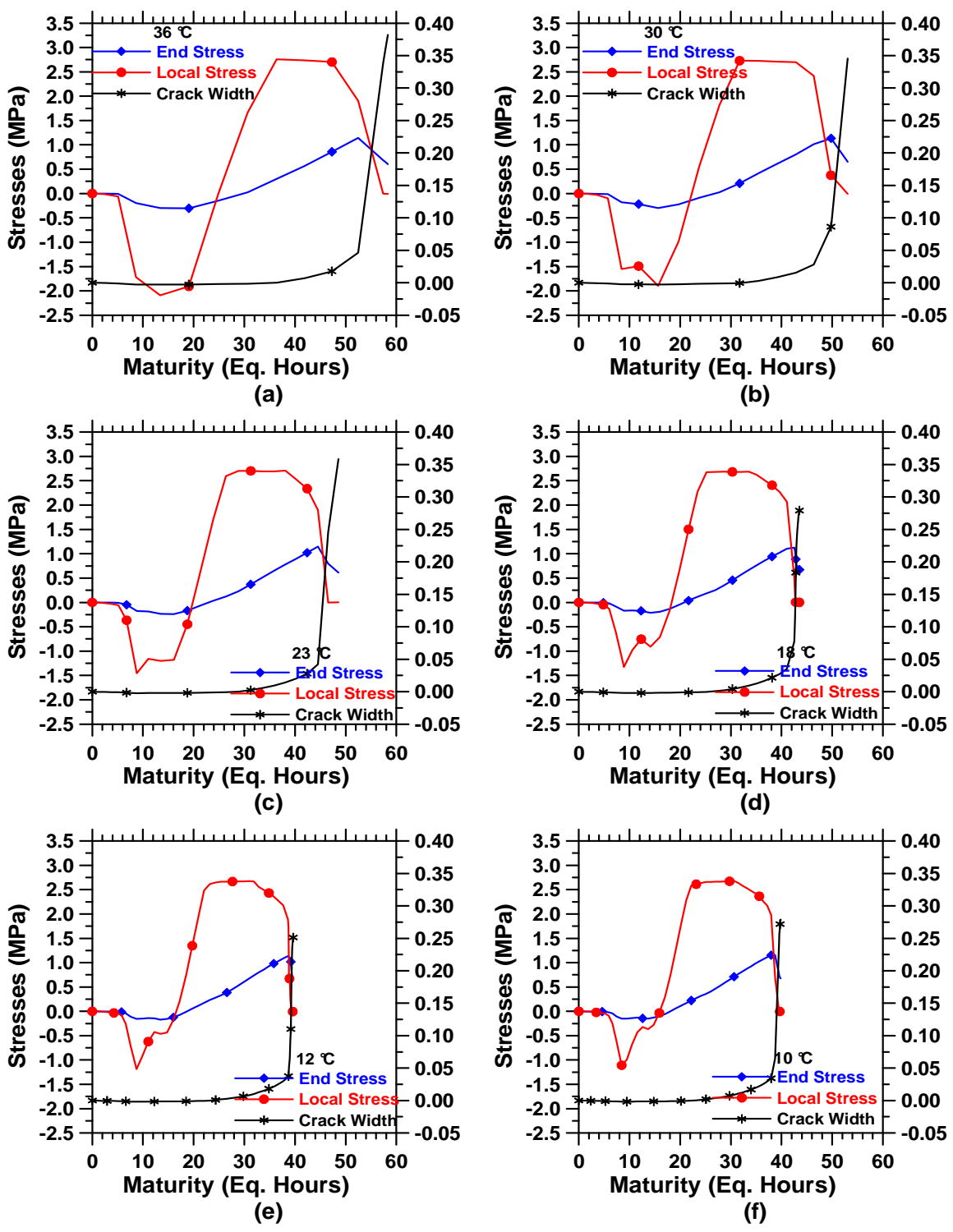


Figure 8.66: End and local stresses and crack width of pavements with D/3 saw-cut depths cured at different ambient temperatures (cont'd).

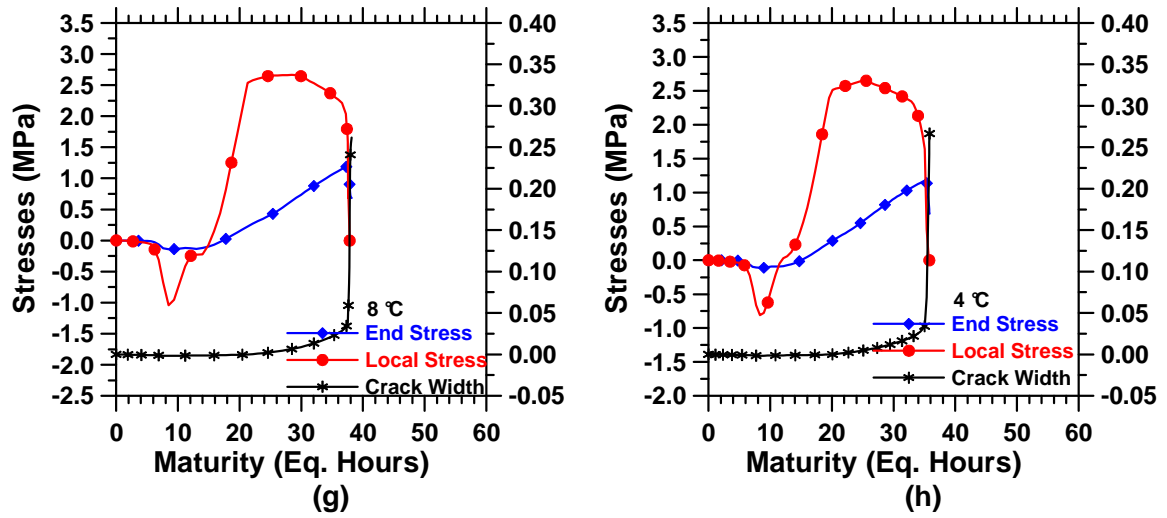


Figure 8.66: End and local stresses and crack width of pavements with D/3 saw-cut depths cured at different ambient temperature

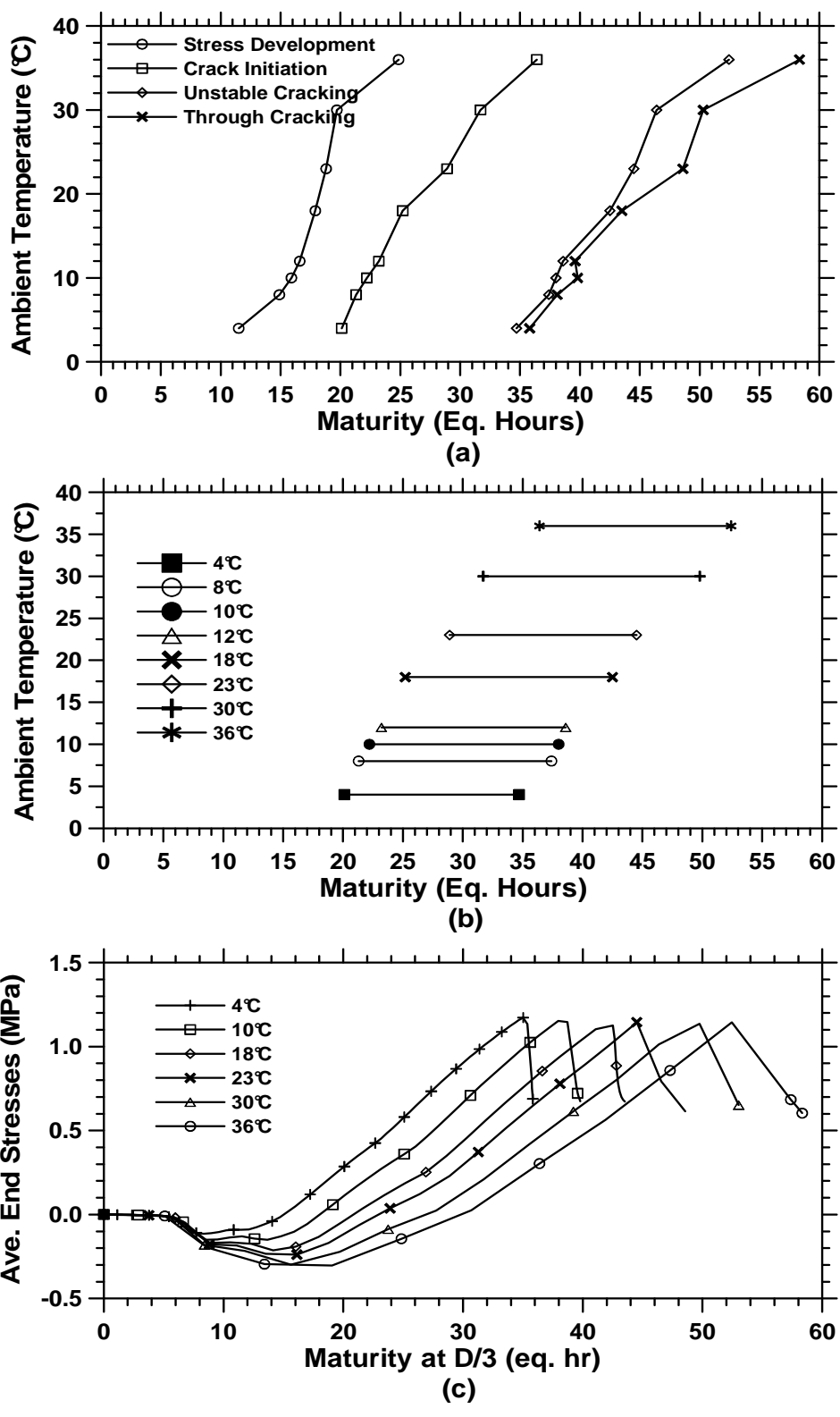


Figure 8.67: The cracking and stress behavior of pavements with D/3 saw-cut depths cured at different ambient temperatures (cont'd).

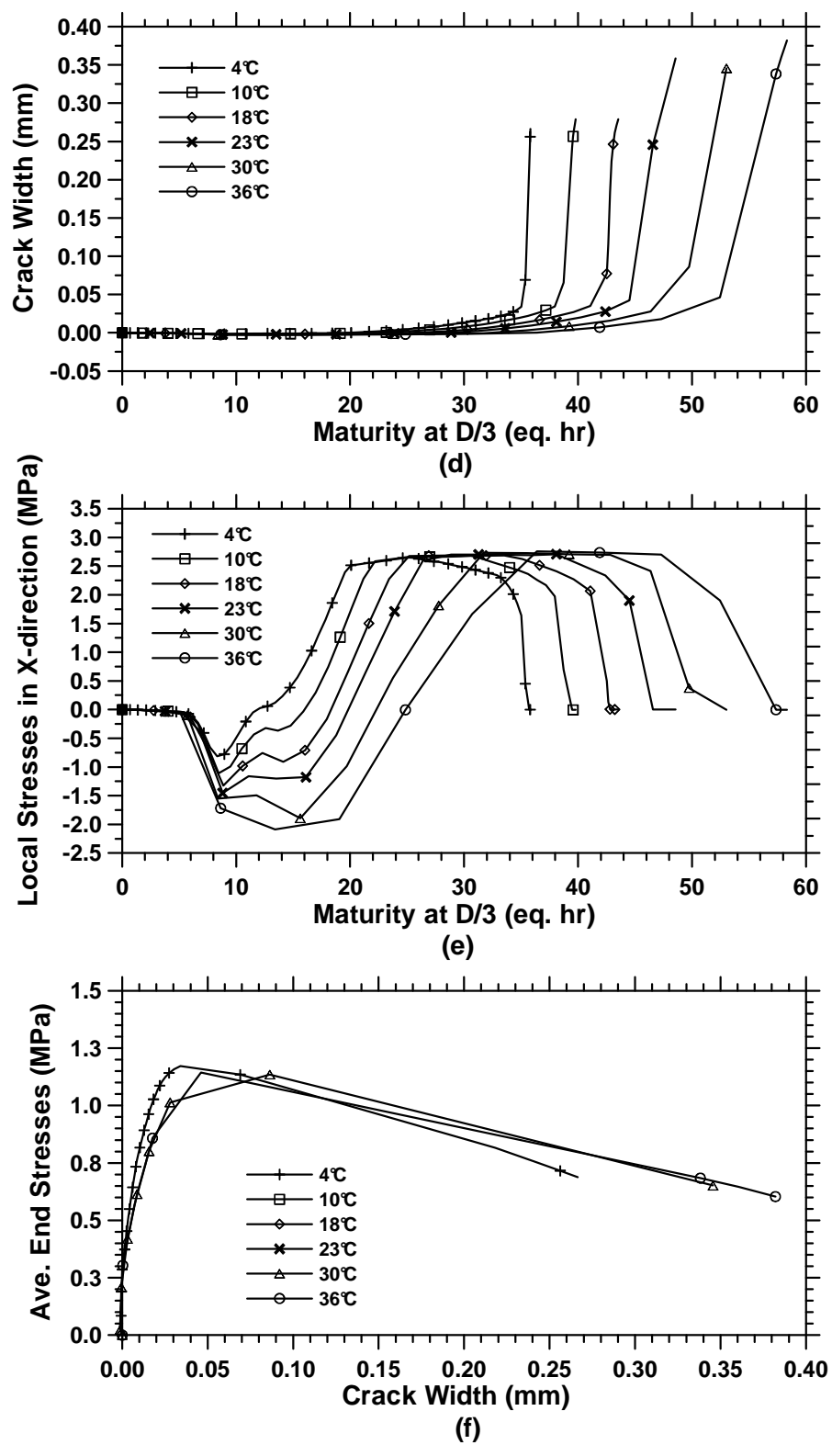


Figure 8.67: The cracking and stress behavior of pavements with D/3 saw-cut depths cured at different ambient temperatures.

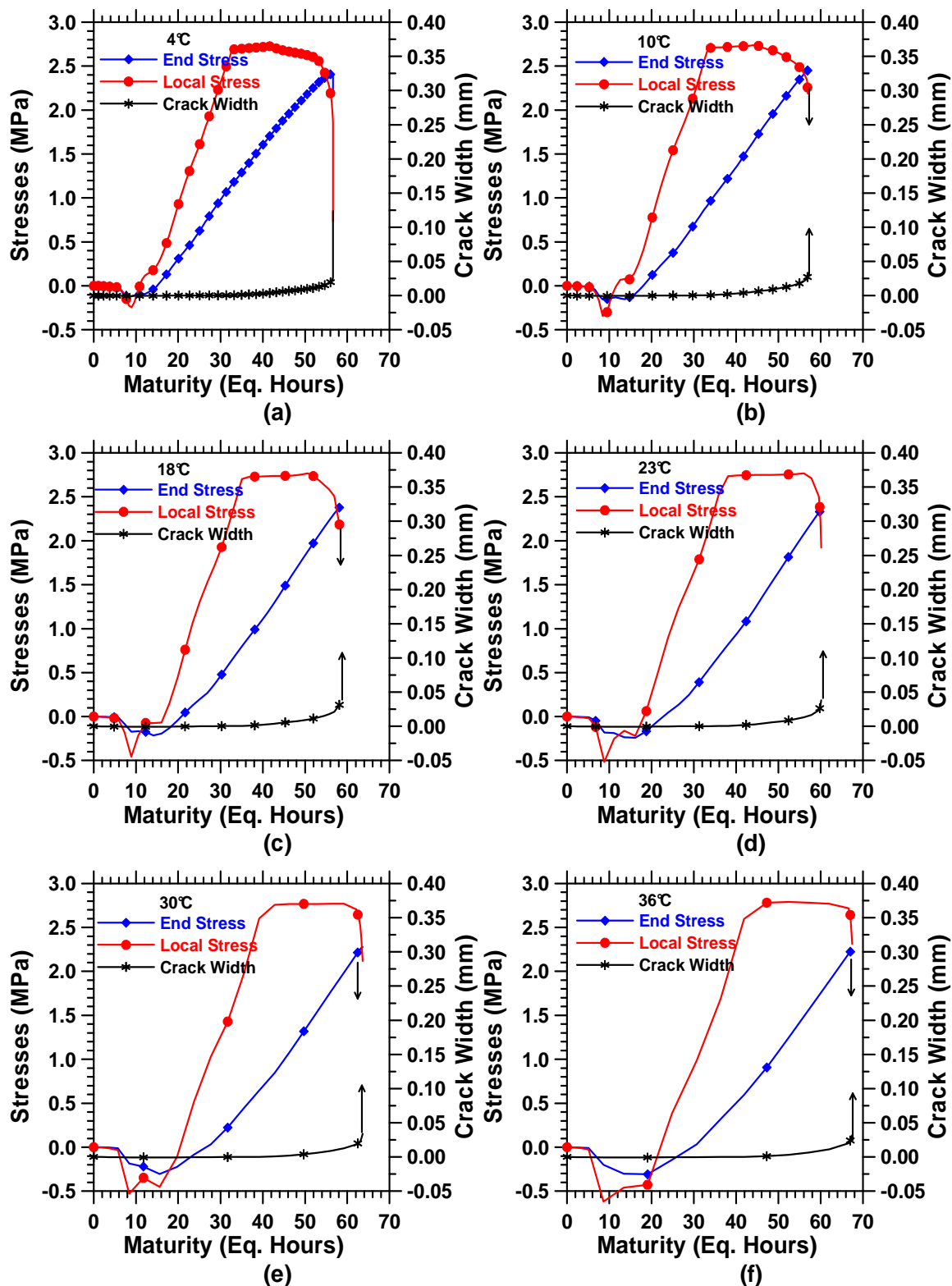


Figure 8.68: End and local stresses and crack width of pavements with D/8 saw-cut depths cured at different ambient temperatures.

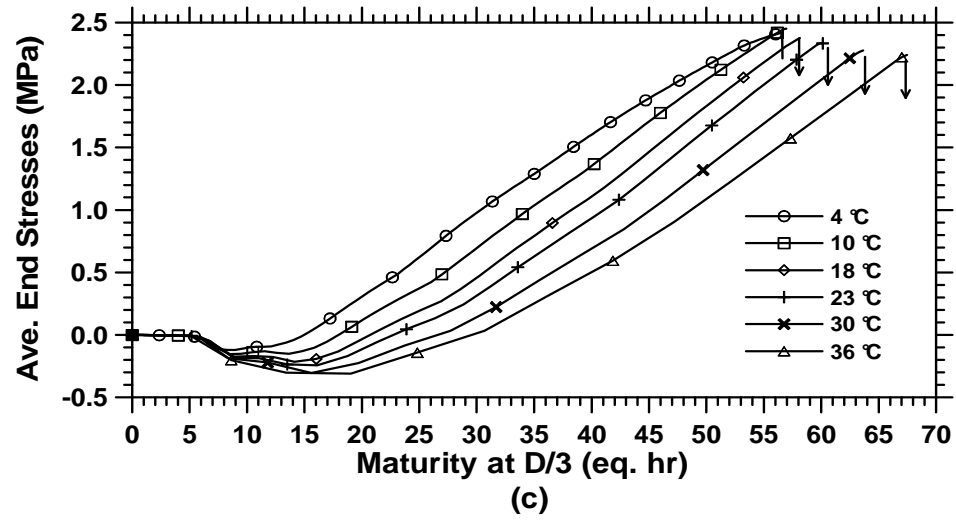
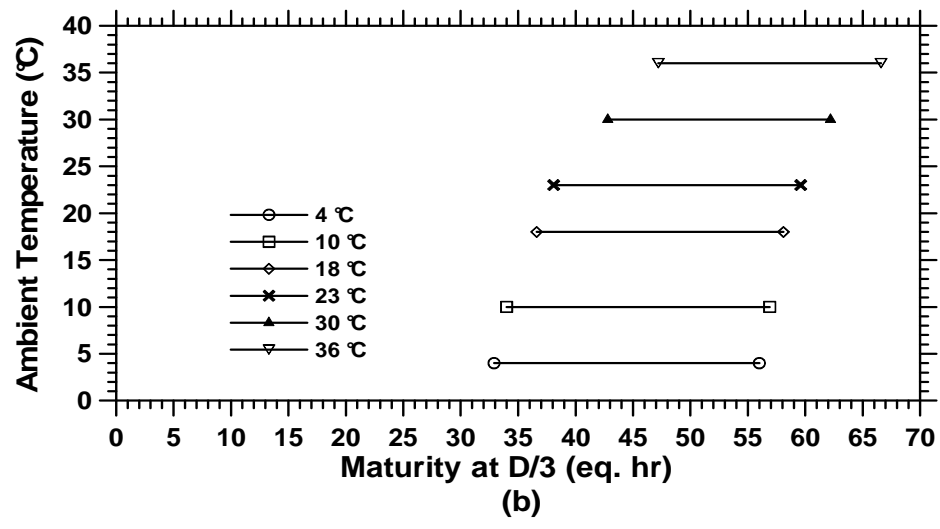
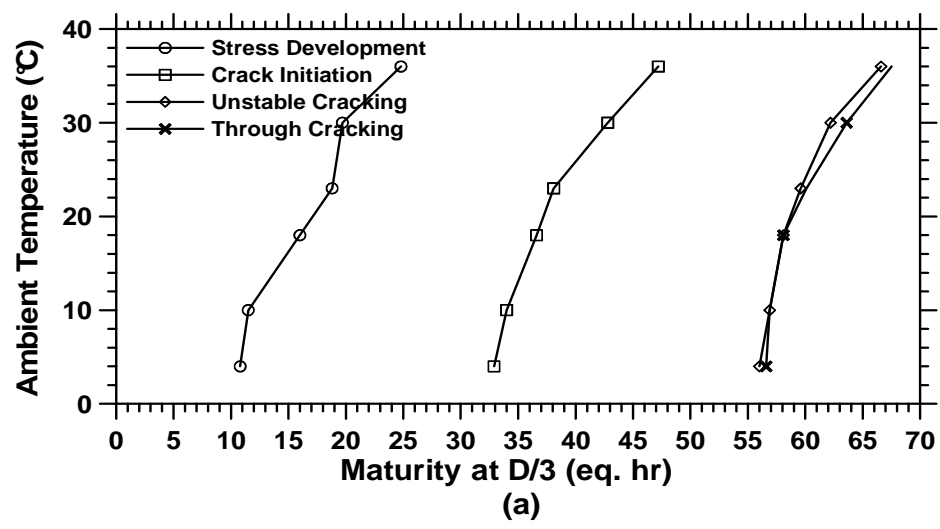


Figure 8.69: The cracking and stress behavior of pavements with D/8 saw-cut depths cured at different ambient temperatures (cont'd).

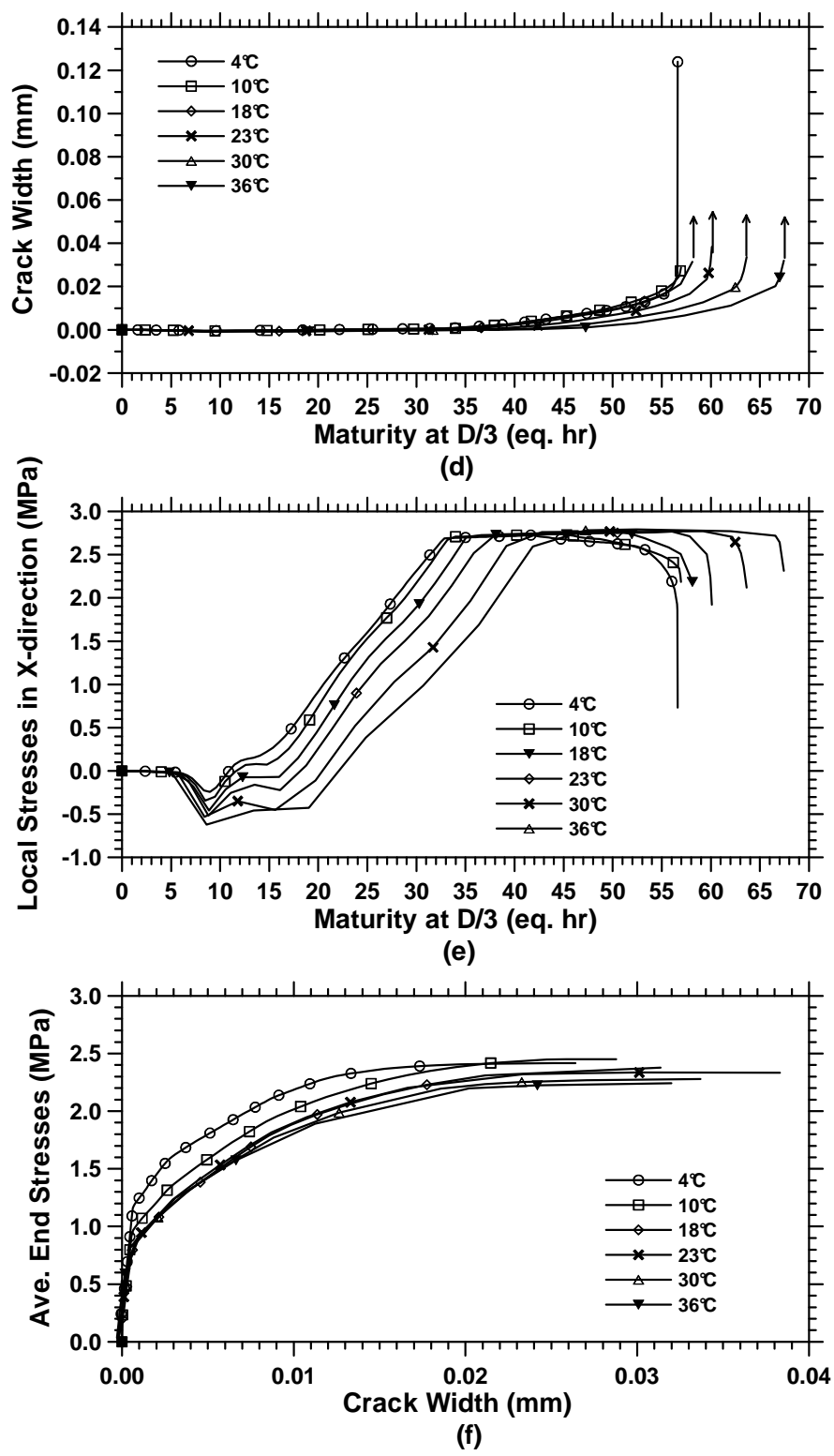


Figure 8.69: The cracking and stress behavior of pavements with D/8 saw-cut depths cured at different ambient temperatures.

8.3.1.4.3 The Influence of the Saw-cut Depth on the Saw-cutting Time Window

To illustrate the effect of saw-cut depth on the saw-cutting time window, Figure 8.70 was prepared. As shown in Figure 8.70, the stress development maturities remain relatively constant irrespective of the size of a saw-cut. However, maturities of cracking increase as the saw-cut to depth ratios decrease. Therefore, deep saw cuts need to be placed sooner than shallow saw cuts.

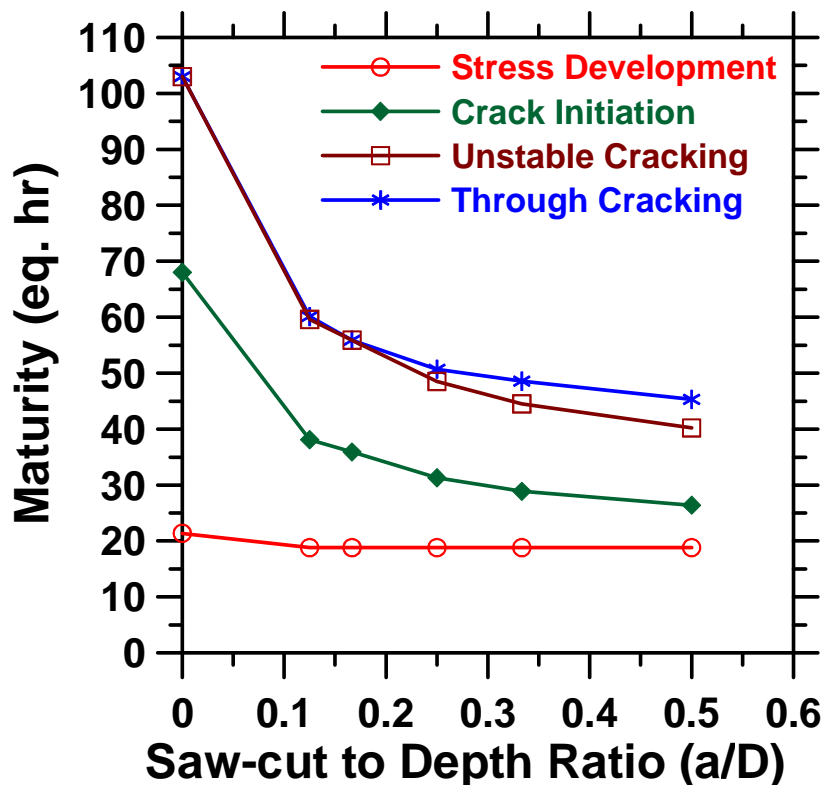


Figure 8.70: The cracking behavior of pavements at 23°C.

8.3.2 The Influence of Rate of Reaction on the Time of Saw-cut Introduction

Changes have been taken place over the last few decades to utilize mixtures that are capable of obtaining higher earlier strengths; however, these materials are more prone to cracking and can be more susceptible to weather fluctuations. In addition, the use of supplemental cements has become prevalent. Although using supplemental cements has various benefits including higher long-term strength and increased durability they often delay early strength gain and make the saw-cutting window more difficult to determine.

The complex effects of mixtures that develop strength rapidly, and slow strength development material containing supplemental cements need further investigations.

8.3.2.1 The General Modeling Approach

To investigate the effect of rapid setting and slow setting concrete mixtures on saw-cutting of pavements, two different material files were developed. Figure 8.71 illustrates the three adiabatic temperature rise curves for these mixtures. The initial and final temperature of mixtures is the same, and only the rate of temperature development differs.

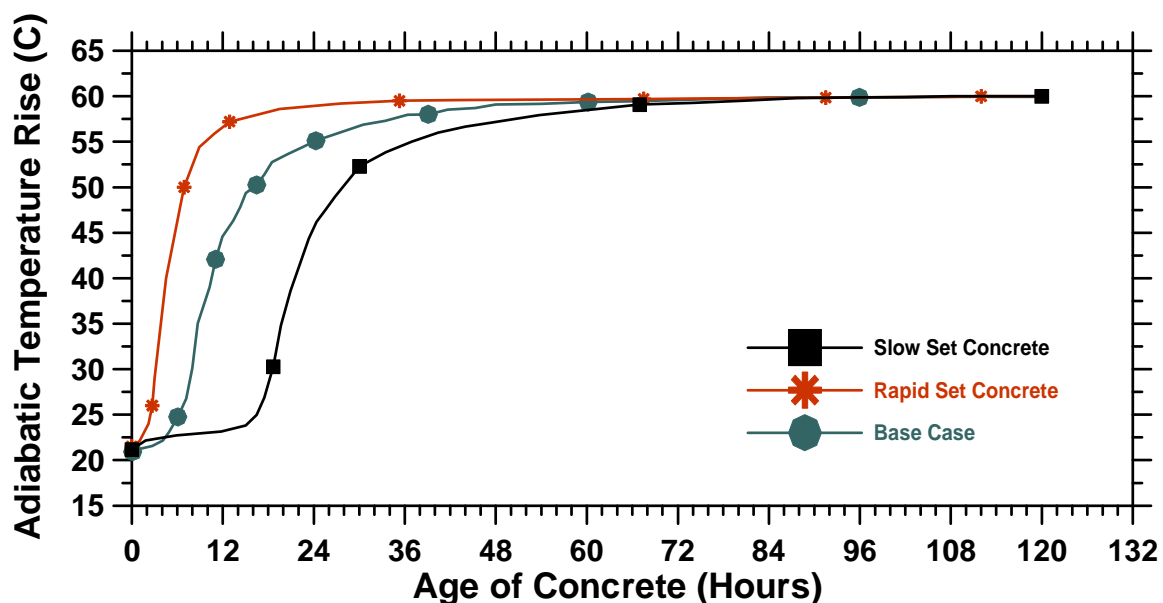


Figure 8.71: Three adiabatic temperature rise curves used in computer simulations.

The other model properties were kept the same as the baseline case model described in section 7.2. In this analysis, D/3 saw-cuts were introduced to pavements at different times, and the calculated results will be discussed in detail in the next sections.

8.3.2.2 The Behavior of the Pavement Built with Rapid Setting Concrete

Figures 8.72 and 8.73 illustrate calculated stresses and CTOD at the tip of saw-cuts which were applied at 0, 6, 12, 18, and 24 hours. Comparing these results with the

baseline case results, a shorter elastic plastic state and a higher rate of residual stress development are observed in pavements built with rapid setting materials.

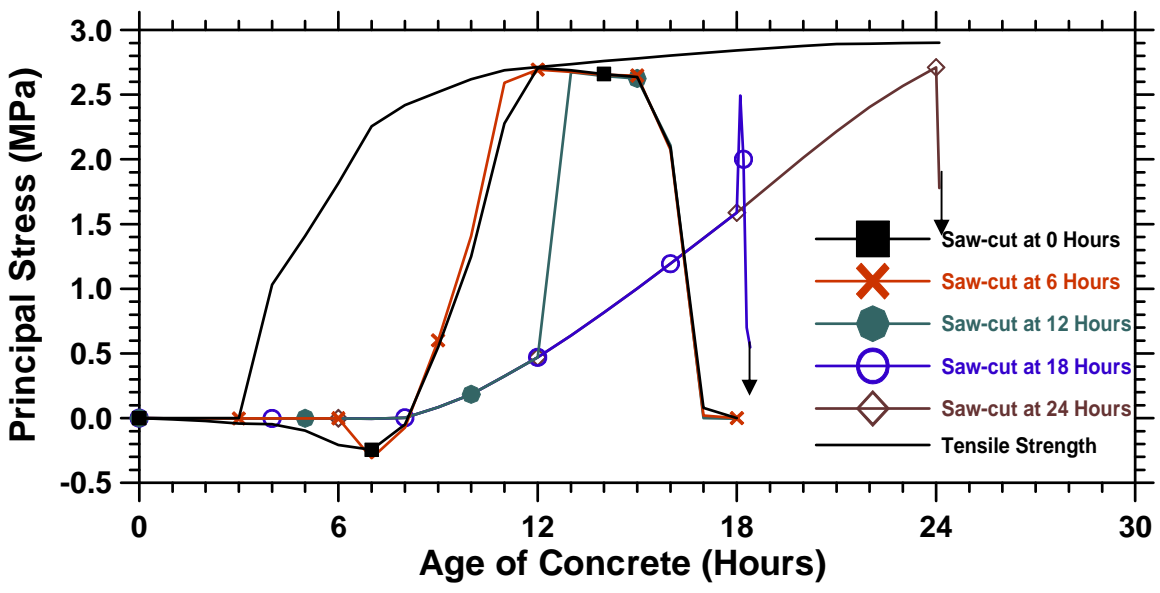


Figure 8.72: Stresses at the tip of saw-cuts for pavements built with rapid-set concrete.

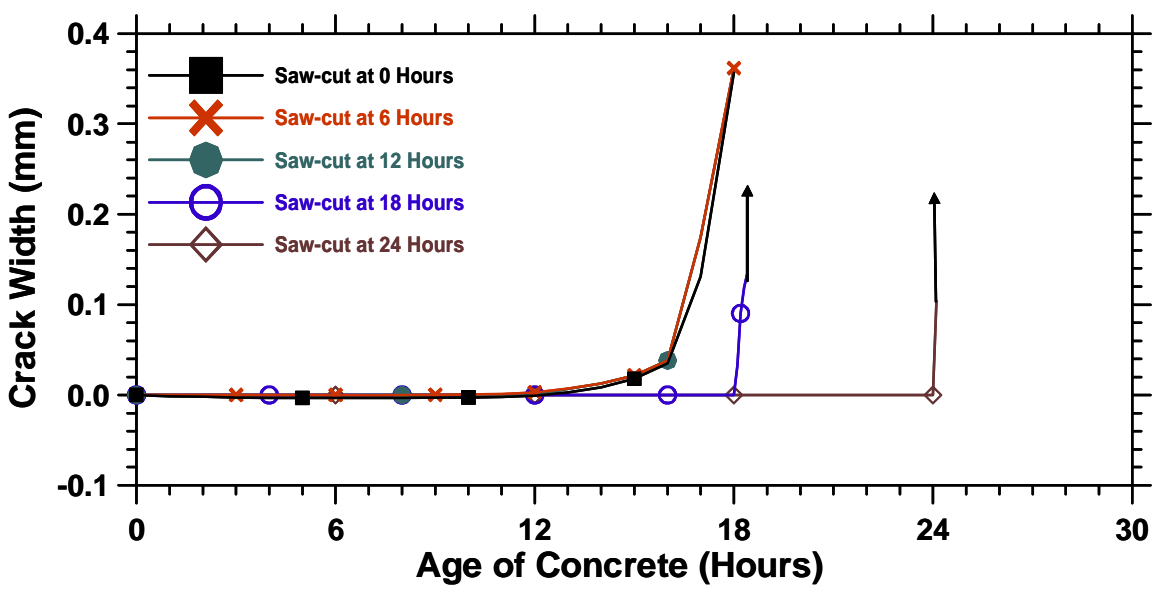


Figure 8.73: CTOD of pavements built with rapid-set concrete.

8.3.2.3 The Behavior of Pavement Built with Slow Setting Concrete

Figure 8.74 and 8.75 demonstrate the stress and CTOD calculated at the tip of the saw-cuts which were applied at 0, 6, 12, 18, and 24 hours for slow-set concrete mixture. Comparing stresses and CTOD of slow-set concrete pavements with pavements built with regular and rapid-set concrete, a longer elastic plastic state, and a slower rate of stress development is observed for slow-set concrete pavements.

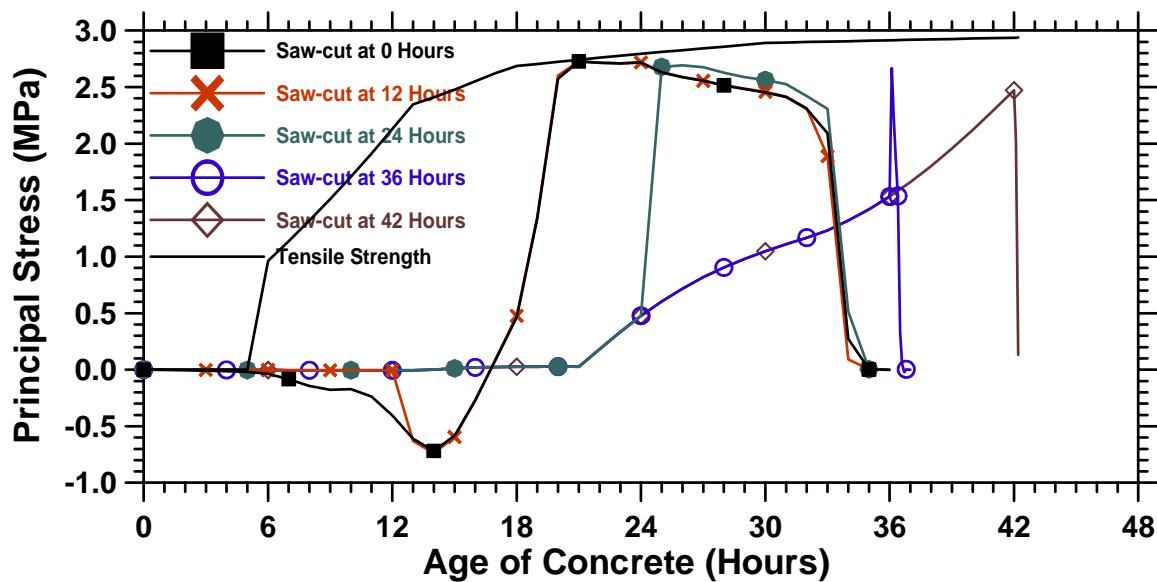


Figure 8.74: Stresses of pavements built with slow-set concrete.

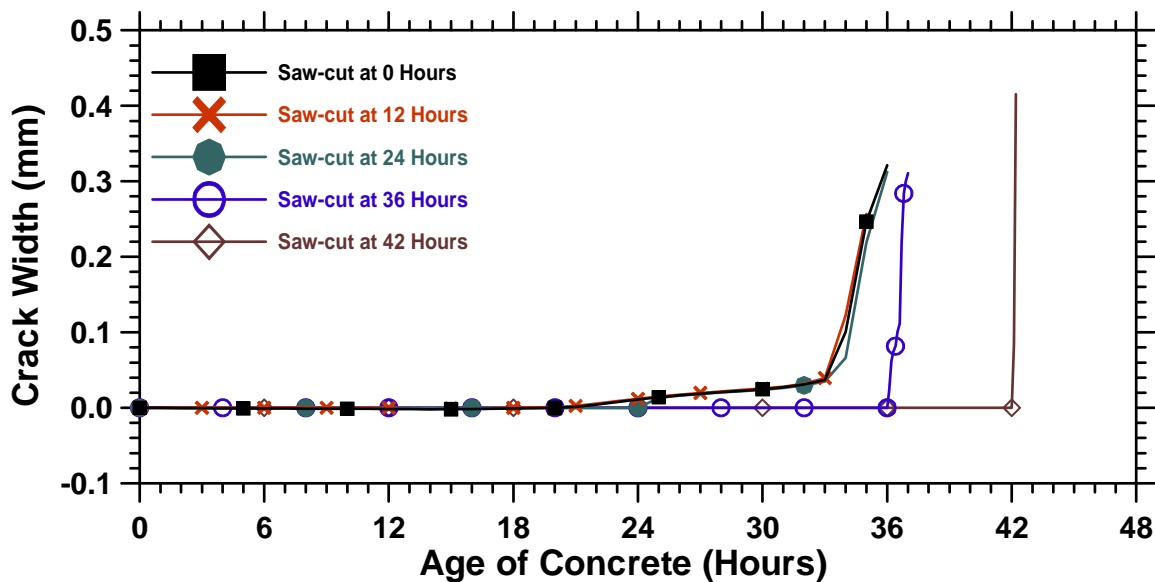


Figure 8.75: CTOD of pavements built with slow-set concrete.

8.3.2.4 The Comparison and Discussion

To investigate the effect of concretes with different reaction rates on stress and cracking behavior of pavements, Figure 8.76 was prepared. Figure 8.76 shows the stress at the tip of a D/3 saw-cut introduced at 12 hours. The rapid-set pavement has the shortest time to unstable crack propagation. A substantial difference is seen between the behavior of pavements built with rapid-set and slow-set concretes which suggests that depending upon the type of cement and amount of pozzolanic materials, the saw-cutting window varies greatly. Further research is needed to fully understand this behavior.

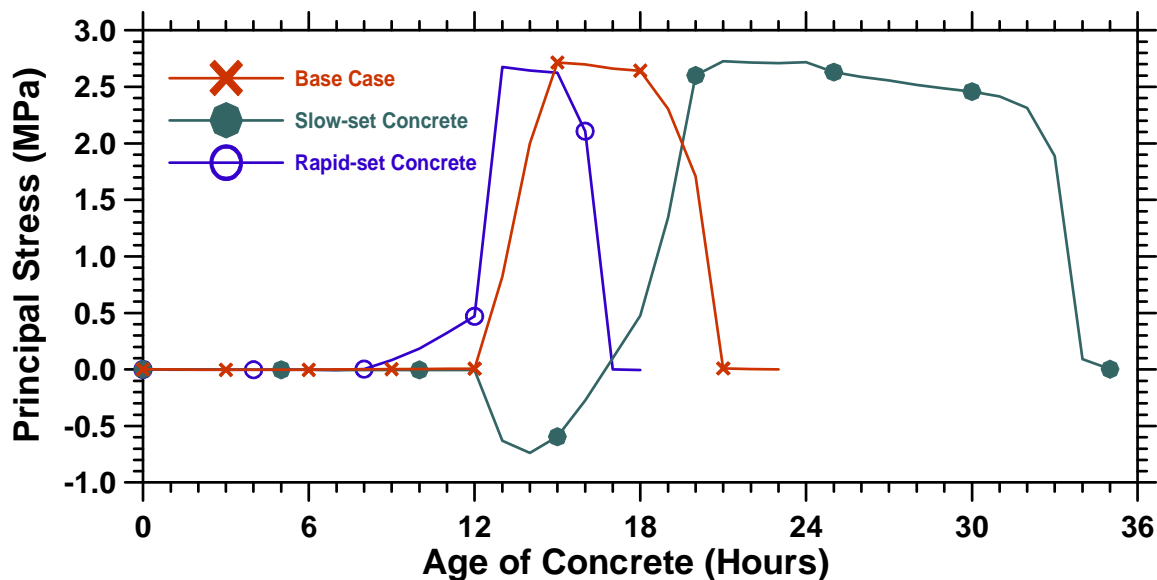


Figure 8.76: Stresses of pavements built with different types of concrete.

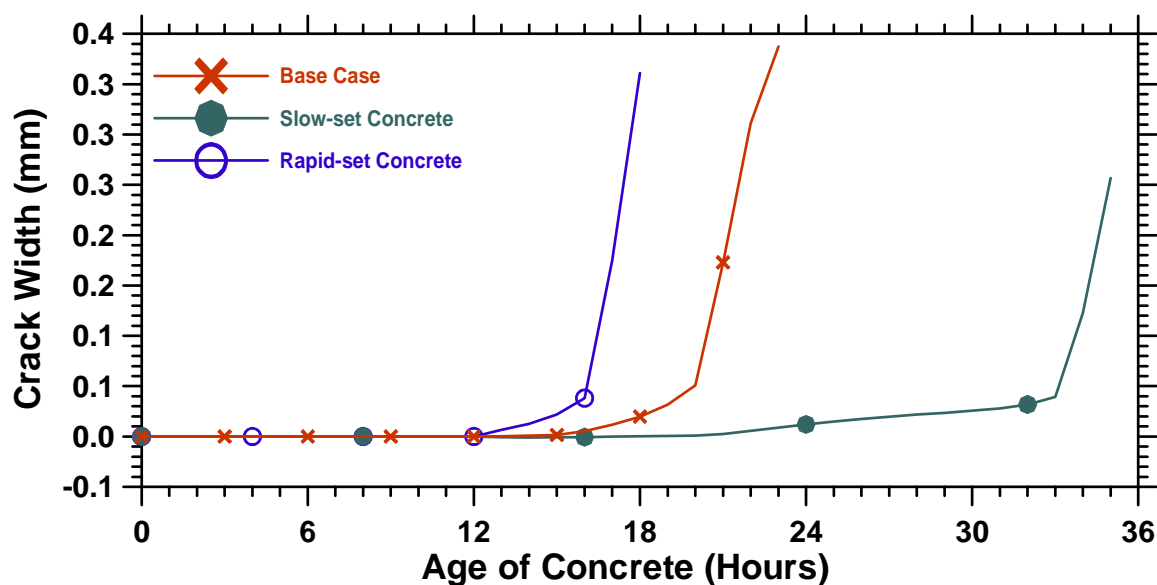


Figure 8.77: CTOD of pavements built with different types of concrete.

8.4 Summary

This chapter described a finite element analysis approach to determine the saw-cutting time and depth to minimize the risk of random cracking and micro crack development. The influence of different saw-cut depths was investigated, ranging from shallow to deep, as it relates to the cracking behavior of pavements. It was shown that

deeper saw-cuts reduce the failure stress of a pavement more than shallow saw-cuts. The introduction of a saw-cut before reaching the critical residual stress level can result in stable crack propagation while the introduction of a saw-cut at higher stress levels results in unstable crack propagation, which needs to be avoided in the field. It was also concluded that time and depth of saw-cut are two interrelated factors. The deeper saw-cuts need to be placed sooner while shallower saw-cuts have a longer saw-cutting time window. The influence of the ambient temperature on cracking behavior of concrete was determined. It was found out that higher ambient temperatures reduce the saw-cutting time window greatly while low temperatures provide a longer saw-cutting time window. In addition early age thermal expansion was found to delay in the residual stress development and cracking of concrete. It was the objective of this chapter to provide data that can ultimately be used to develop a methodology to determine the appropriate time and depth of saw-cut.

CHAPTER 9: A PROPOSED SIMPLIFIED METHODOLOGY TO DETERMINE THE TIME OF SAW-CUTTING CONSIDERING SAW-CUT DEPTH

9.1 Introduction

When a saw-cut is introduced in a concrete pavement, the classical strength of materials' approach to predict the average section stress fails to capture the increase in local stresses at the tip of the saw-cut. Consequently, a simple strength of materials solution is not applicable in analyzing pavements with a saw-cut. The net strength of a pavement varies greatly, depending on the size of the saw-cut. To investigate the influence of the saw-cut size on the maximum residual stresses that can be permitted in a concrete pavement, a fracture mechanics approach was employed. This approach simultaneously considers the applied stress, material toughness, and saw-cut depth for determining when a concrete pavement may be expected to develop random cracking. The intention of this chapter is to develop a methodology that can be used to determine the appropriate time for the placement of saw-cuts of varying depths using results obtained from hand computation or computer software that does not explicitly consider the presence of a saw-cut.

This chapter begins with an overview of a classic fracture mechanics approach. The theoretical solution for unstable cracking in a single-edge notch specimen (i.e., saw-cut) is described. The data obtained from the computer simulations of chapter 8 is compared with the simplified prediction methodology to demonstrate the applicability of the proposed design methodology. Finally, the cracking potential associated with different depths of saw-cut was determined.

9.2 Fracture Mechanics Analysis of Pavements Containing a Saw-Cut

The behavior of a concrete pavement is dependent on both the properties of the materials used as well as the geometry of the pavement. The behavior of the material can be classified as one of these classic types: brittle, ductile, or quasi-brittle. Figure 9.1 illustrates the stress-elongation response of these three material types. Figure 9.1a shows the response of a brittle material. It can be seen that in a brittle material the stress suddenly drops to zero after the peak load is exceeded. The stress-elongation behavior of a ductile material is shown in Figure 9.1b. The ductile material yields when the yield strength is reached, and the material elongates under a constant level of stress. Figure 9.1c shows the behavior of a quasi-brittle material (like concrete). The stress in quasi-brittle materials gradually decreases after reaching a peak demonstrating the softening response of the material. The quasi-brittle response can be explained by the growth and opening of cracks.

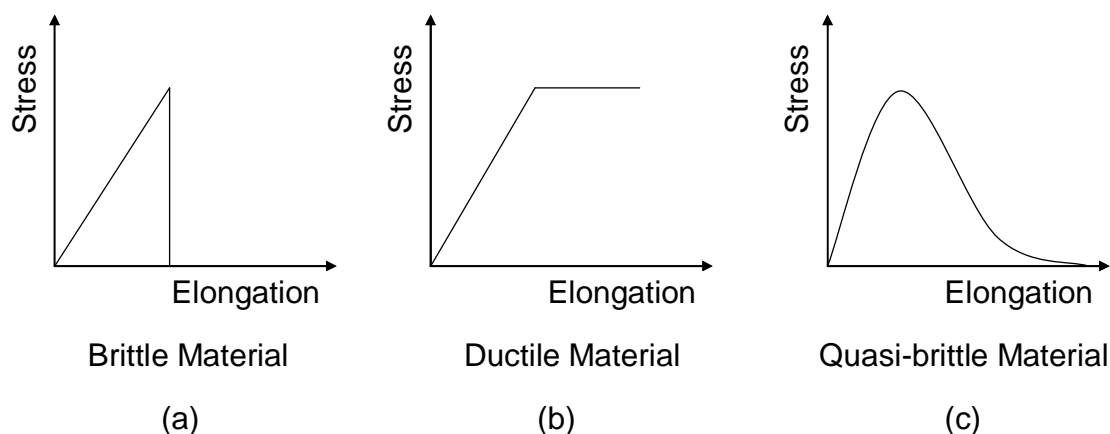


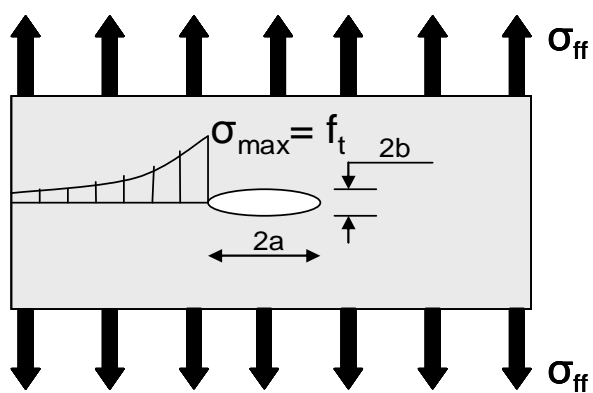
Figure 9.1: The stress-elongation behavior for different types of material: (a) brittle material, (b) ductile material, and (c) quasi-brittle material.

The failure behaviors of the different materials types with a saw-cut can be illustrated by considering a wide plate with an elliptical hole (Figure 9.2). Inglis (1913) proposed that if a tensile stress of σ_{ff} (this is commonly called the far-field stress) is applied to the wide plate, the stress that develops locally along the edge of the ellipse (σ_{max}) is greater than the far-field stress σ_{ff} . Equation 9.1 describes the relationship between σ_{ff} and σ_{max} :

$$\sigma_{\max} = \left(1 + \frac{2a}{b}\right) \sigma_{ff} \quad (9.1)$$

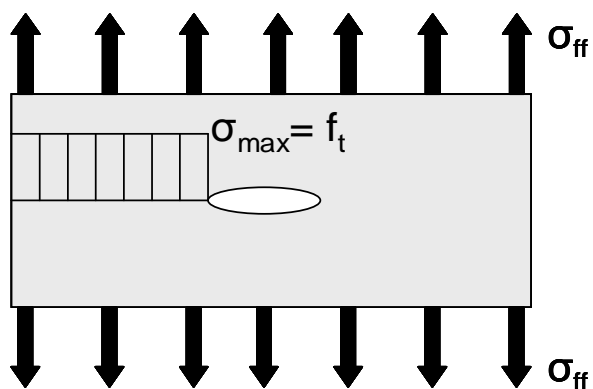
where, a and b are the long and short radii of the ellipse, respectively (Figure 9.2).

The local stresses distributions for the brittle, plastic, and quasi-brittle materials with an elliptical hole are shown schematically in Figure 9.2. For the perfectly brittle material, the stress increases as the edge of the ellipse is approached. Failure occurs when σ_{\max} reaches the material tensile strength. For the case of the ductile material (9.2b), it begins to yield when the applied stress reaches a value equal to the yield stress, and fails when the normal tensile stress in entire cross section reaches the material's tensile strength (or yield). A quasi-brittle material develops an inelastic fracture process zone near the edge of the ellipse. Consequently the normal tensile stress decreases as the edge of the material is approached. The development of this zone results in a softening behavior response.



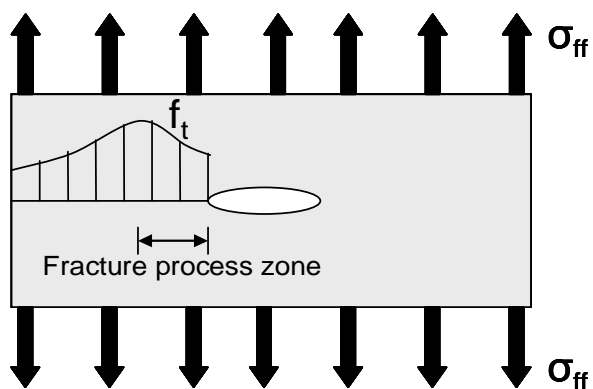
Brittle Materials

(a)



Ductile Materials

(b)



Quasi-brittle Materials

(c)

Figure 9.2: The stress distribution of different materials: (a) brittle material, (b) ductile material, and (c) quasi-brittle material.

Linear elastic fracture mechanics (LEFM) has been used to simultaneously consider the size of a flaw (a), the magnitude of the applied far field stress (σ_{ff}), and a material property that describes the resistance to cracking. This property is called fracture toughness or critical stress intensity factor (K_{IC}).

The stress intensity factor at the tip of a crack can be described by the following relationship.

$$K_I = \sigma_{ff} \sqrt{\pi a} f(\text{geom}) \quad (9.2a)$$

where, the K_I is the stress intensity factor, σ_{ff} is the far-field stress, a is the flaw size, and $f(\text{geom})$ is a geometry factor (which equals to 1.0 for a wide plate with a central notch and 1.12 for a semi-infinite plate with a single edge notch). The geometry factors for other geometries can be found in compilations such as one prepared by Tada et al. (1985).

It should be noted that at failure $K_I = K_{IC}$, where K_{IC} (the critical stress intensity factor) is a material property. Equation 9.2a can be used to predict the failure stress when the critical stress intensity factor of a material is known. Equation 9.2a can be rearranged to form equation 9.2b.

$$\sigma_{\max} = \frac{K_{IC}}{\sqrt{\pi a} f(\text{geom})} \quad (9.2b)$$

This approach illustrates that when the material property is fixed (K_{IC}), a higher tensile stress can be achieved before failure would occur as the size of the flaw (a) or saw-cut is reduced. It should be noted however, that this approach is not valid when crack length is smaller than a critical size (a_{critical}/D) as shown in Figure 9.3. In those cases (i.e., when flaw size is smaller than a critical size) failure stress is limited by the tensile strength.

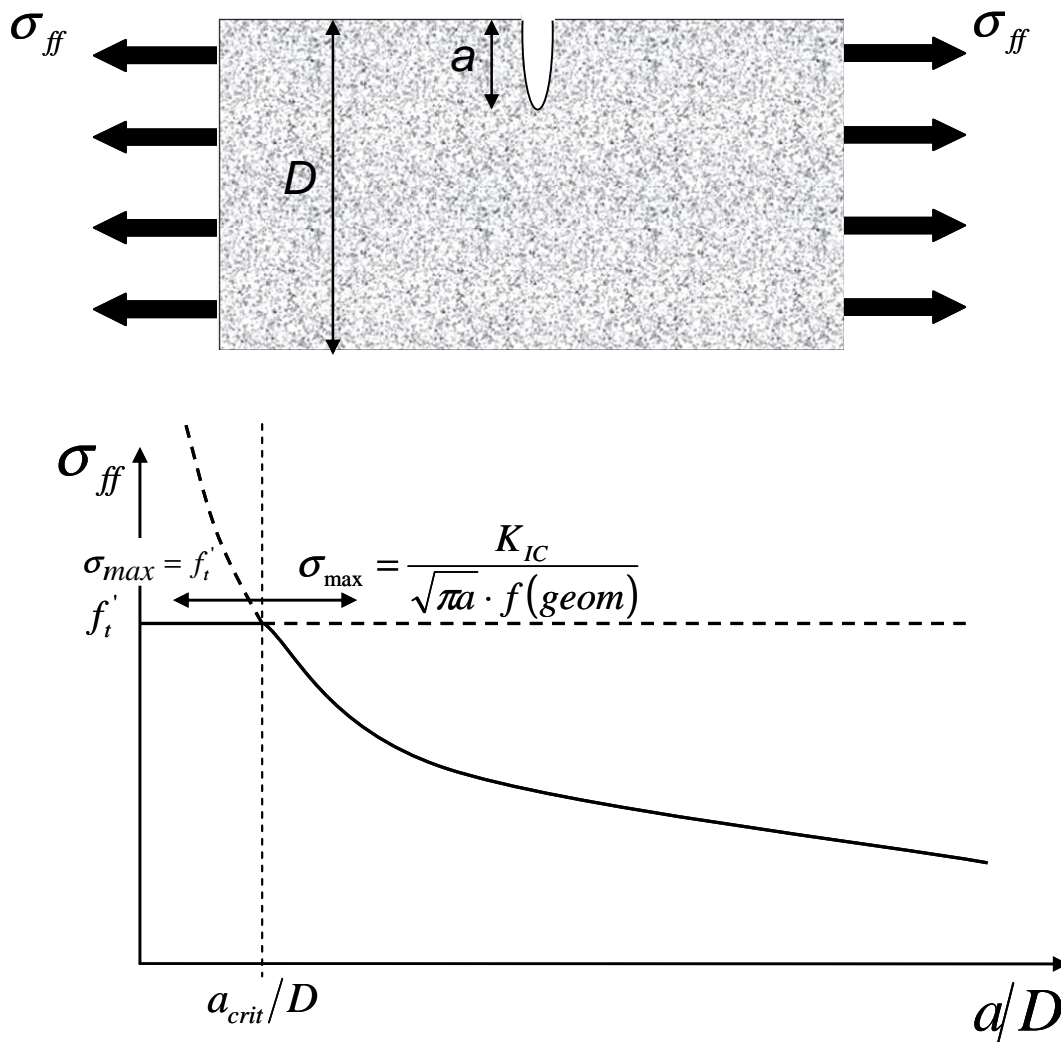


Figure 9.3: The failure stress of an infinitely large plate with a single edge notch (crack).

In this study, the cracking behavior of pavements with the use of a fracture mechanics approach was investigated. This is similar to a plate with a single edge notch under uniaxial tensile load as shown in Figure 9.4. It should be noted that the stress field in a pavement may not strictly be as uniform as illustrated due to non-uniformity in drying and temperature distribution (Weiss, 1999).

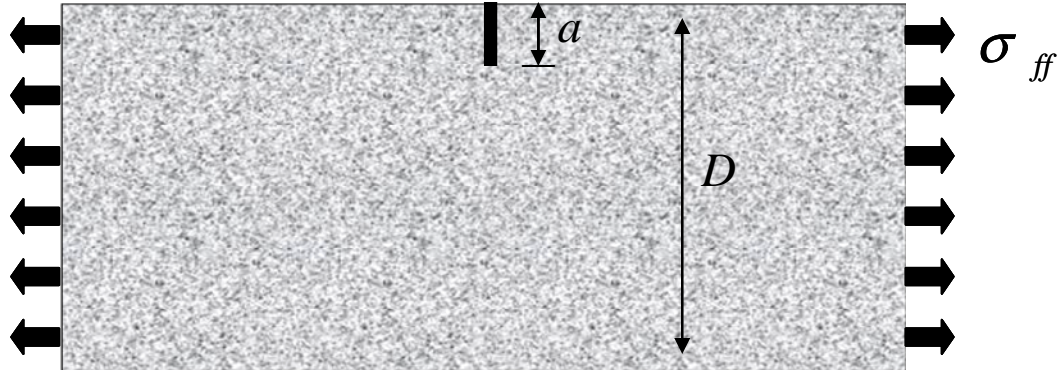


Figure 9.4: A plate with a single edge notch under uniaxial tensile.

Nevertheless the solution for a single edge notch specimen will be used in the rest of this discussion, and the equation that describes stress intensity factor, flaw size, specimen depth (D), and stress is shown below (Tada et al., 1985).

$$K_{IC} = \sigma_{\max} \cdot \sqrt{\pi \cdot a} \cdot f\left(\frac{a}{D}\right) \quad (9.3a)$$

where, the geometry function for a single edge specimen is:

$$f\left(\frac{a}{D}\right) = 1.12 - 0.231\frac{a}{D} + 10.55\left(\frac{a}{D}\right)^2 - 21.72\left(\frac{a}{D}\right)^3 + 30.39\left(\frac{a}{D}\right)^4 \quad (9.3b)$$

Equation 9.3a can be rewritten to calculate the failure stress as a function of the critical stress intensity factor (K_{IC}), notch size (a), and depth (D).

In order to simplify the process of failure stress calculations, a new parameter ($\Phi_{saw-cut}$) is introduced. This parameter is a function of geometry specifically (a/D), and is obtained by dividing the stress at the time of failure (σ_{\max}) by the tensile strength ($f_t'(t)$) as shown in Equation 9.4.

$$\Phi_{saw-cut} = \frac{\sigma_{\max}}{f_t'} = \frac{K_{IC}}{f_t' \sqrt{\pi \cdot a} \cdot f\left(\frac{a}{D}\right)} \quad (9.4)$$

9.3 A Recommendation for a Procedure to Minimize Random Cracking

For concrete, the residual stresses developed due to concrete shrinkage and thermal variations, and tensile strength vary greatly with time, especially at early-ages. While many software packages can be used to perform stress analysis on an unnotched concrete pavement, it should be remembered that a saw-cut will reduce the residual stress that is required to cause failure. It is proposed that uncontrolled cracking can occur in a concrete pavement when the residual stress exceeds the product of the tensile strength and $\Phi_{saw-cut}$ as shown in Equation (9.5b).

$$\sigma_{max} \leq f'_t(t) \cdot \Phi_{saw-cut} \quad \text{Stable cracking} \quad (9.5a)$$

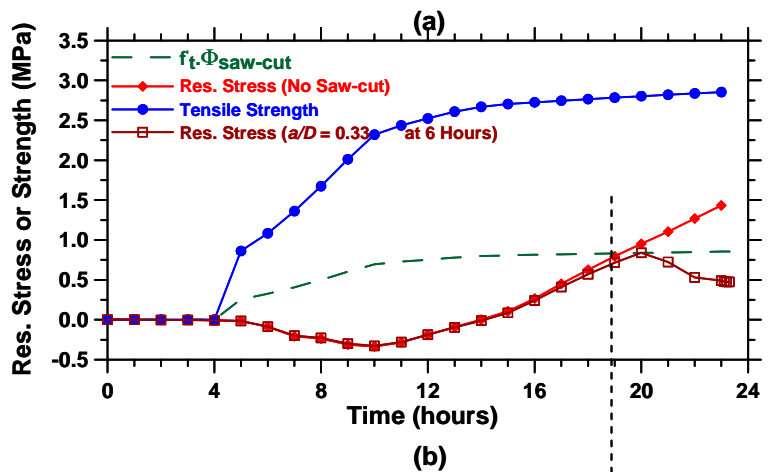
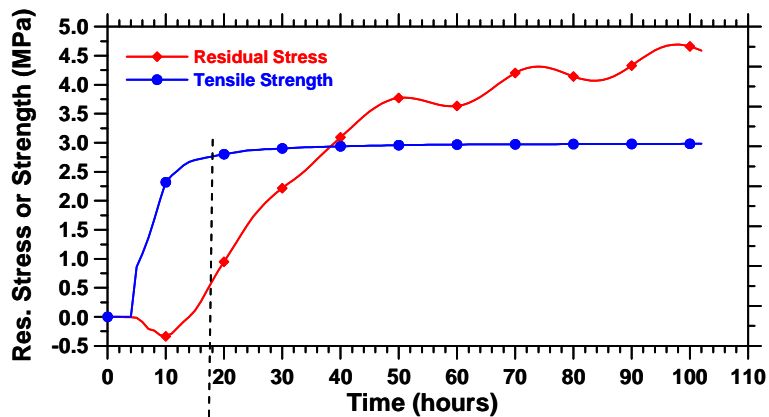
$$\sigma_{max} > f'_t(t) \cdot \Phi_{saw-cut} \quad \text{Unstable cracking} \quad (9.5b)$$

where, σ_{max} is the failure stress, $f'_t(t)$ is the tensile strength at time t , and $\Phi_{saw-cut}$ is the critical stress to strength ratio.

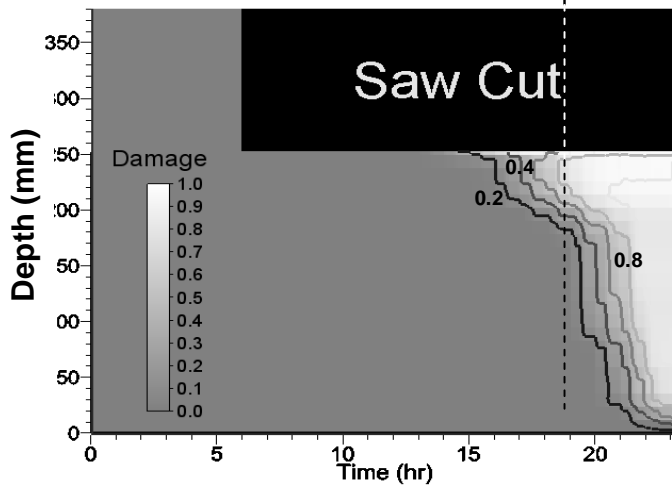
Figure 9.5a illustrates the residual stresses and tensile strength development in a concrete pavement when no saw-cut was performed. The input data and boundary conditions used in the model were the same as those used for the baseline case explained in section 7.2 of Chapter 7. It should be noted that the observed fluctuation in residual stress is due to ambient temperature fluctuations as explained in Chapter 8. Figure 9.5b illustrates the same residual stress and tensile strength developments but just for the first 24 hours. This figure also shows the stress behavior in a pavement with a saw-cut ($a = D/3$), which was introduced at 6 hours. The residual stress of pavement was released when it reached the maximum stress calculated by Equation 9.5b (i.e., $(f'_t(t) \cdot \Phi_{saw-cut})$) as shown by the dashed line. The maximum stresses calculated by Equation 9.5a can be used to create a failure envelope for any depth of saw-cut.

Figure 9.5c uses finite element results from Chapter 8 to illustrates the damage level that occurs directly below the saw-cut (using a contour plot) for the pavement cross section with a saw-cut size ($a = D/3$) which was introduced at 6 hours. The damage plot indicates crack development and growth in concrete. As shown by the vertical dashed line, the crack starts to propagate when the residual stress reaches the maximum stresses

calculated using Equation 9.5a. The introduction of a saw-cut before reaching the calculated maximum stress results in stable crack growth while unstable cracking occurs if a saw-cut is placed after the pavement experiences residual stress that is greater than that represented by a dashed line (obtained from Equation 9.5b) in Figure 9.5b.



Stable Cracking ← Unstable Cracking →



(c)

Figure 9.5: The effect of a saw-cut on the cracking behavior of concrete pavements: (a) residual stress prediction when cracking is not considered, (b) stress behavior with the introduction of saw-cut, (c) damage distribution or crack propagation of the sawed pavement.

The variable $\Phi_{saw-cut}$ can be determined for any depth of saw-cut. As a result, the residual stress at failure can be determined using Equation 9.5a. Equation (9.4) can be used to compute $\Phi_{saw-cut}$ for different saw-cut to depth ratios (a/D). Figure 9.6 compares the finite element simulation results with the theoretical solution computed using Equation (9.4). It should be noted that in this analysis the depth of pavements was considered to be 380 mm (15 inches), but the depth of saw-cut was varied. As the stress to strength ratios ($\Phi_{saw-cut}$ values) cannot be greater than 1.0 (i.e., failure stress cannot be higher than tensile strength), the stress to strength ratios greater than 1.0 have been assumed to be equal to 1.0 for a/D smaller than a critical saw-cut to depth ratio.

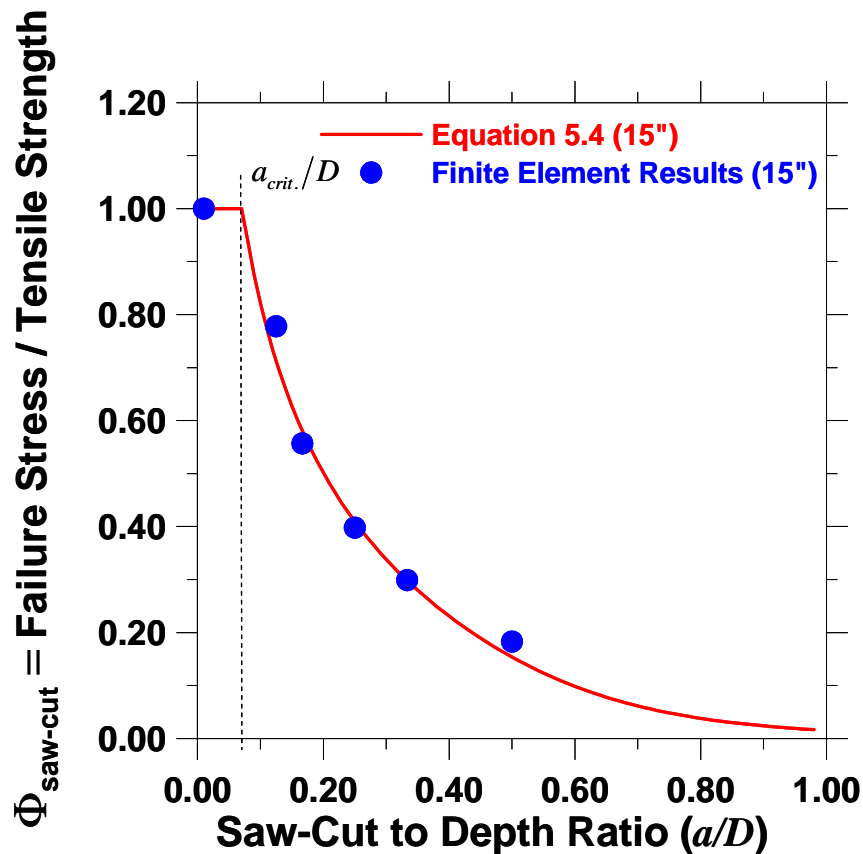


Figure 9.6: Predicted and calculated stress to strength ratios.

As shown in Figure 9.6, $\Phi_{saw-cut}$ remains 1.0 for small saw-cut to pavement depth ratios. It is only after reaching a critical saw-cut size to depth ratio of 0.08 that the

presence of saw-cut reduces the failure stress of a pavement. This value is approximately equal to the maximum size of aggregate, and it changes depending on the maximum size of aggregate (Weiss, 1999).

The variable $\Phi_{saw-cut}$ depends not only on the depth of the saw-cut and but also on the depth of the pavement. As such, the stress to strength ratios for pavements with a depth (D) of 254 mm (10 inches) were also calculated using Equation 9.4. Figure 9.7 illustrates the response for two pavement thicknesses ($D = 254$ mm and $D = 380$ mm) with the data points obtained from computer simulations presented in Chapter 8. It should be noted that the solid line and solid circles correspond to a pavement with a $D = 380$ mm while the dashed line and empty circles represent pavements with $D = 254$ mm. As shown in Figure 9.7, the pavement depth is a secondary factor that should be considered in determining the failure stress to strength ratio. As shown in Figure 9.7 the critical saw-cut size to depth ratio is seen to be approximately 0.09 (0.08 to 0.10). It should also be noted that the graphs of Figure 9.7 (i.e., Equation 9.4) can be used to successfully describe $\Phi_{saw-cut}$ for different saw-cut sizes.

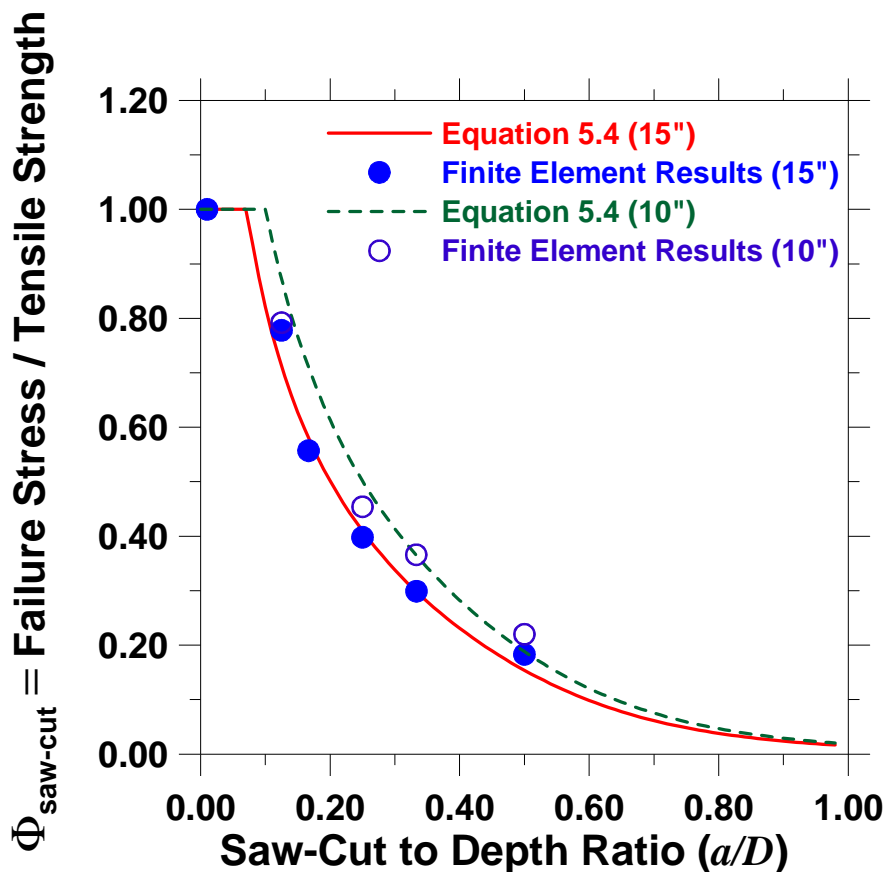


Figure 9.7: Average failure stress to tensile strength ratio for different 380 mm (15 in.) and 254 mm (10 in.) thick pavements.

Having determined the average stress to strength ratios ($\Phi_{\text{saw-cut}}$) for different saw-cut depth to pavement depth (a/D) ratios, the $\Phi_{\text{saw-cut}}$ can be multiplied by the tensile strength of concrete pavement to obtain a series of failure envelopes, each corresponding to a different depth of saw-cut. Figure 9.8 illustrates the same type of residual stress and tensile strength development as previously shown in Figure 9.5a. It can be seen that depending on the desired depth of saw-cut, the time window for saw-cutting changes as a function of different depths of saw-cut. As such, a deeper saw-cut requires earlier saw-cutting. As shown in Chapter 5, a distinct increase in probability of random cracking (i.e., cracking that may not occur at the joint) when a shallow saw-cut (such as $D/8.5$) was used.

Based on the above results, once the information on tensile strength evolution of concrete is available, failure envelopes (such as shown in Figure 9.8a) for different depths of saw-cut are determined by using Equation 9.5. Different computer software can be used to predict the residual stress development of concrete pavements considering both variable environmental conditions and material properties. If the saw-cut is applied when the residual stress is higher than its failure envelope, unstable cracking would occur. If the residual stress is high enough, then instantaneous unstable cracking occurs. Figure 9.8b shows the results obtained from finite element analysis and indicates the latest time of saw-cutting as a function of the depth of saw-cut.

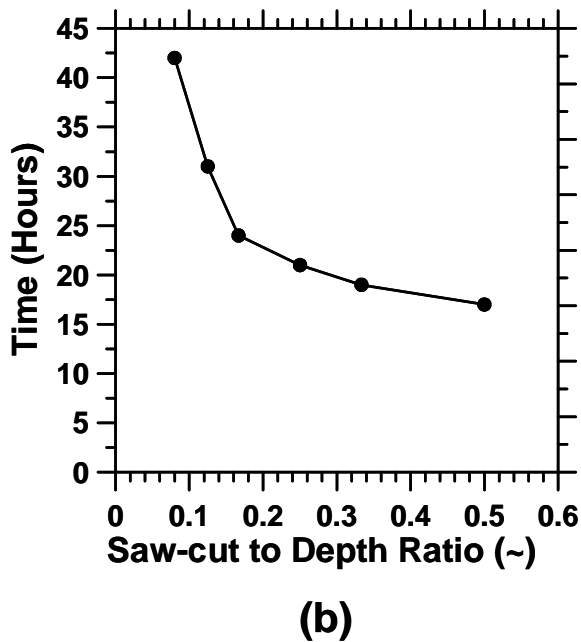
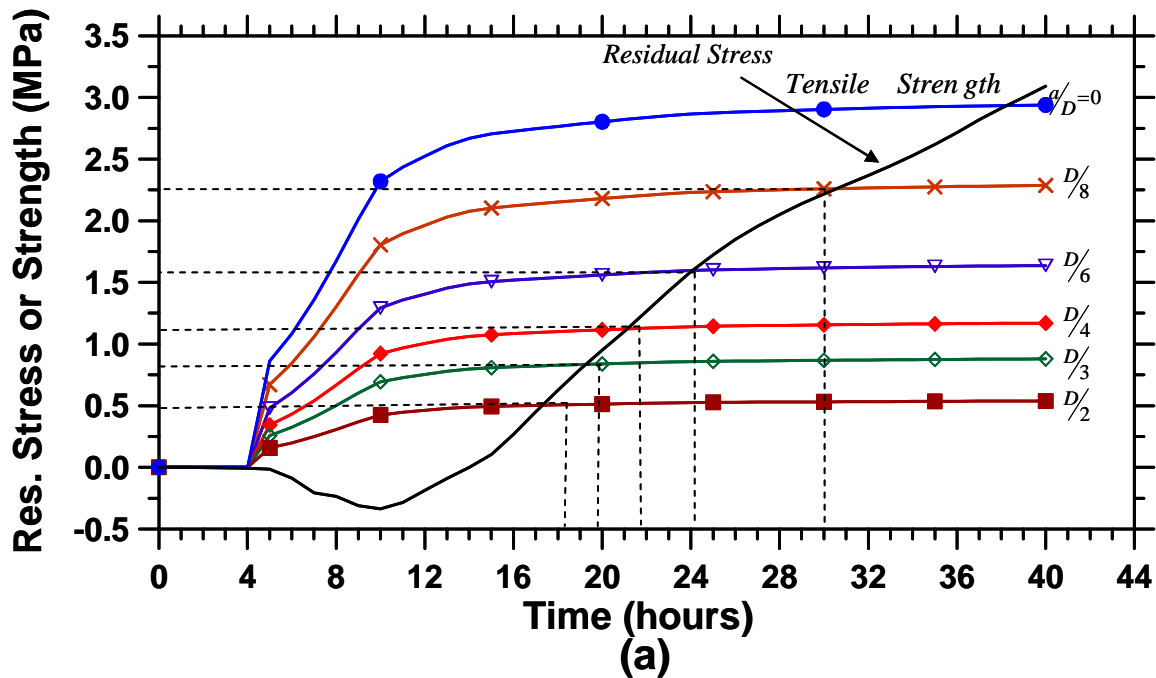


Figure 9.8: (a) The development of failure envelopes for different depths of the saw-cut, and (b) the latest time (from the time of casting) to place the saw-cut for different depths of saw-cut.

9.4 The Probability of Cracking

Monte Carlo analysis was used to assess the probability of random cracking for different concrete pavements with different saw-cut to depth ratios and variations in tensile strength and residual stress development. To illustrate how variability in stress and strength of concrete influences the time of saw-cut introduction, the tensile strength and residual stress shown in Figure 9.5a were used in a Monte Carlo analysis. Both the strength and residual stress were assumed to have a 10% variation (for most cases), and it was also assumed that the stress and strength can be described using a normal distribution. The Monte Carlo simulations used a random number generator to adjust the stress and strength to the normal distribution. The age of uncontrolled cracking was recorded for each of 10,000 simulations.

The simulations were performed for $\Phi_{saw-cut}$ values of 0.183 ($D/2$), 0.299 ($D/3$), 0.398 ($D/4$), 0.557 ($D/6$), 0.778 ($D/8$), and 1.000 ($0 = a/D$). The results, which are shown in Figure 9.9, show that the probability of cracking increases at a slower rate as the saw-cut to depth ratio decreases. It is also noted that the shape of cracking potential curves changes as the depth of saw-cut decreases. A relatively small difference is seen between the probability of cracking for $D/2$, $D/3$, and $D/4$ saw-cuts while a larger difference is observed for shallower saw-cuts.

Figure 9.10 illustrates a 5%, 25%, 50%, 75%, and 95% risk of cracking assuming 10% variability in the stress and in the strength values. Less uncertainty and variation in the time of cracking is noted in determining the cracking time of pavements when saw-cuts deeper than a $D/4$ saw-cut were used. The 2% or 5% cracking potential curves should be used to determine the latest time (from the time of casting) that a saw-cut should be introduced in practice to minimize the risk of uncontrolled cracking.

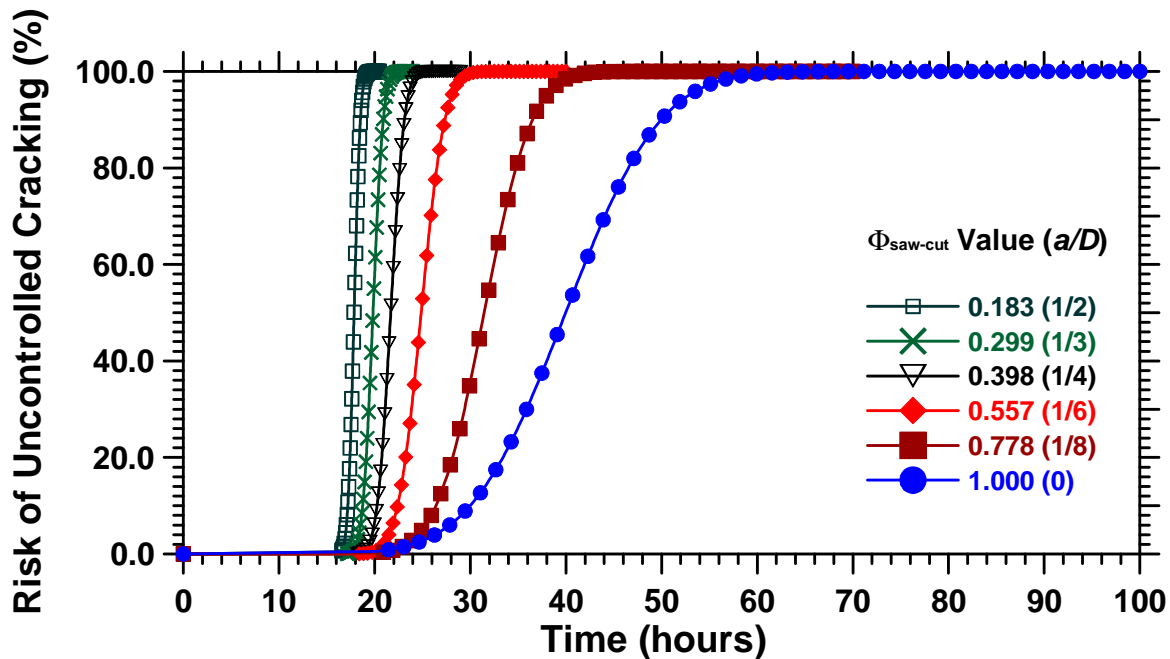


Figure 9.9: Probability of cracking for different $\Phi_{\text{saw-cut}}$, assuming 10% variability of tensile strength and residual stress.

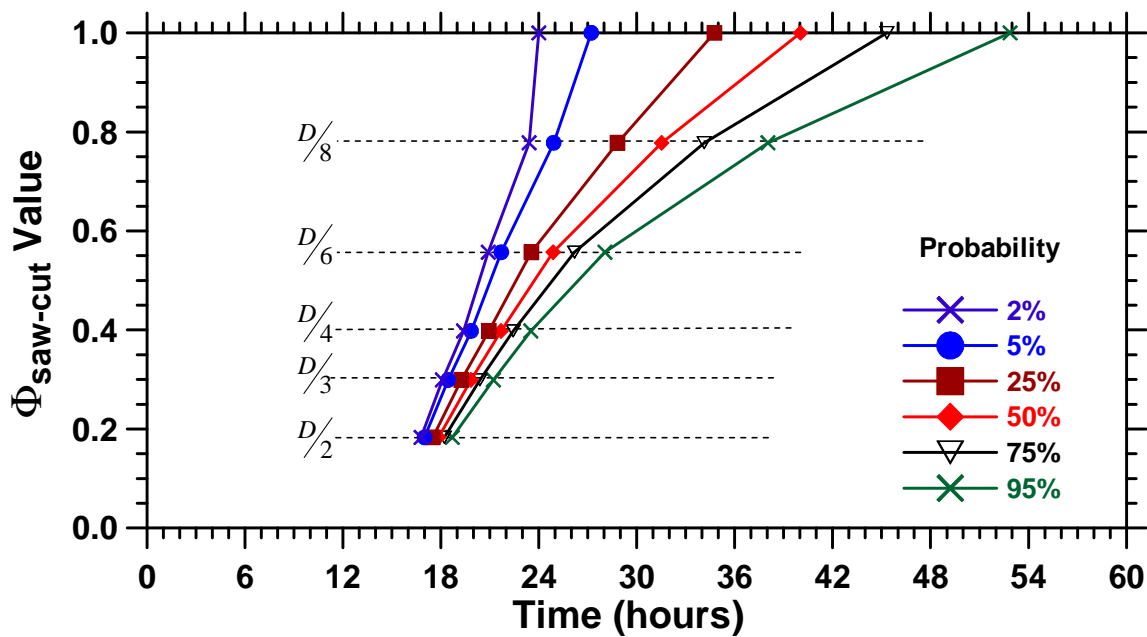


Figure 9.10: The risks of uncontrolled cracking of a given slab for different saw-cutting depths, assuming 10% variability of tensile strength and residual stress.

A second series of simulations was performed to assess how different levels of variability in residual stresses and strength development (i.e., 0%, 1%, 10%, and 20%) influence the probability of cracking (Figure 9.11). It is noted that as the variability in the stress and strength increases, the shape of the curve changes, and the time to cut can be increased or decreased depending on the assumed probability of cracking. As shown in Figure 9.11a, if the assumed probability of cracking is lower than 50% for a given variability level, the time to saw-cut will decrease. However, for the same variability level the time to saw-cut will increase if the assumed probability of cracking is more than 50%. The saw-cutting time of pavements with deep saw-cuts (i.e., $D/2$, $D/3$ and $D/4$ saw-cuts) are seen to be less susceptible to variations in tensile strength and stress. As such, the time of saw-cutting can be more reliably determined for deeper saw-cuts and lower variability of stress and strength.

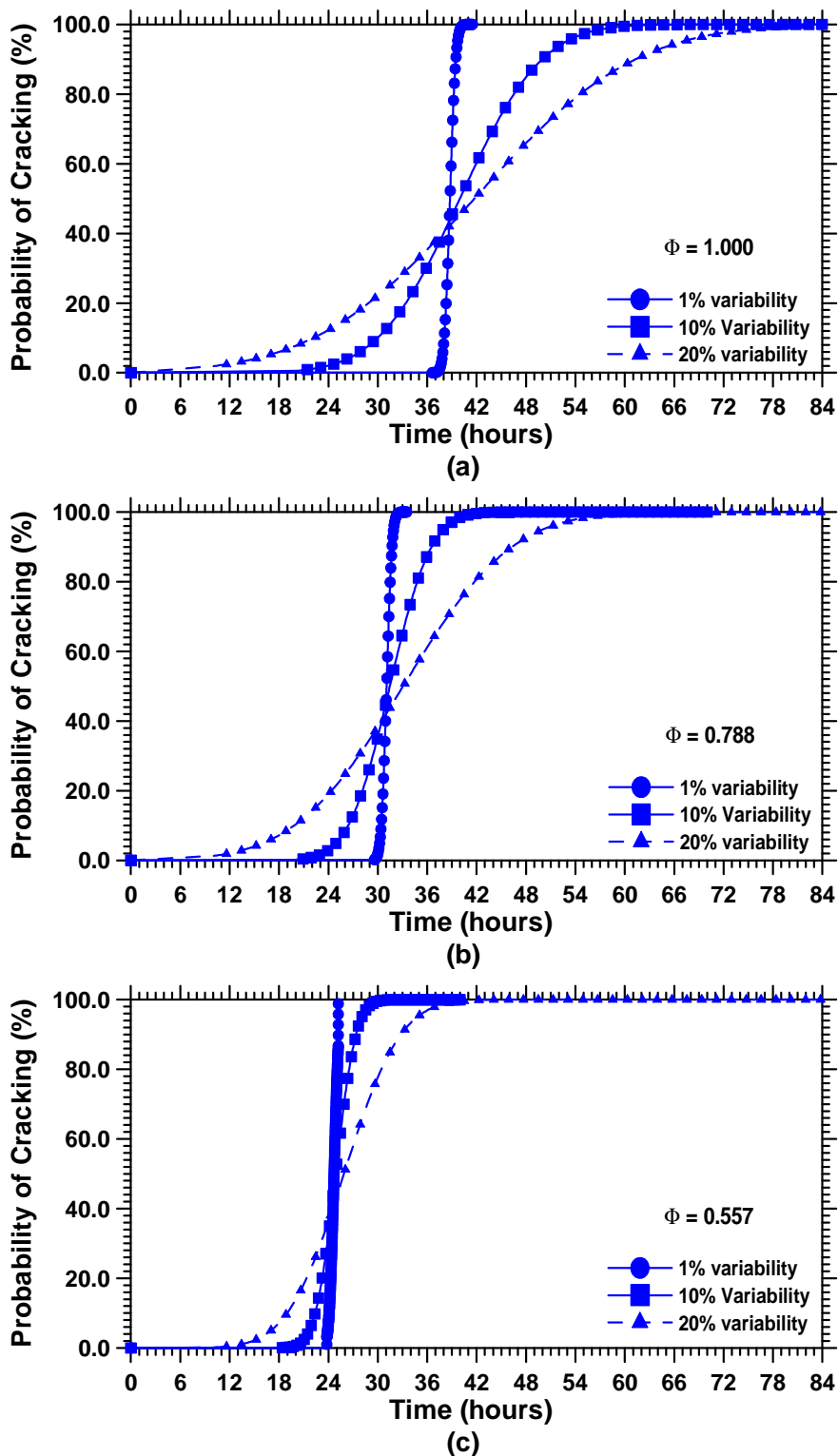


Figure 9.11: Probability of cracking for pavements, assuming 1%, 10%, and 20% variability of tensile strength and residual stress: (a) no saw-cut, (b) D/8 saw-cut, and (c) D/6 saw-cut (cont'd).

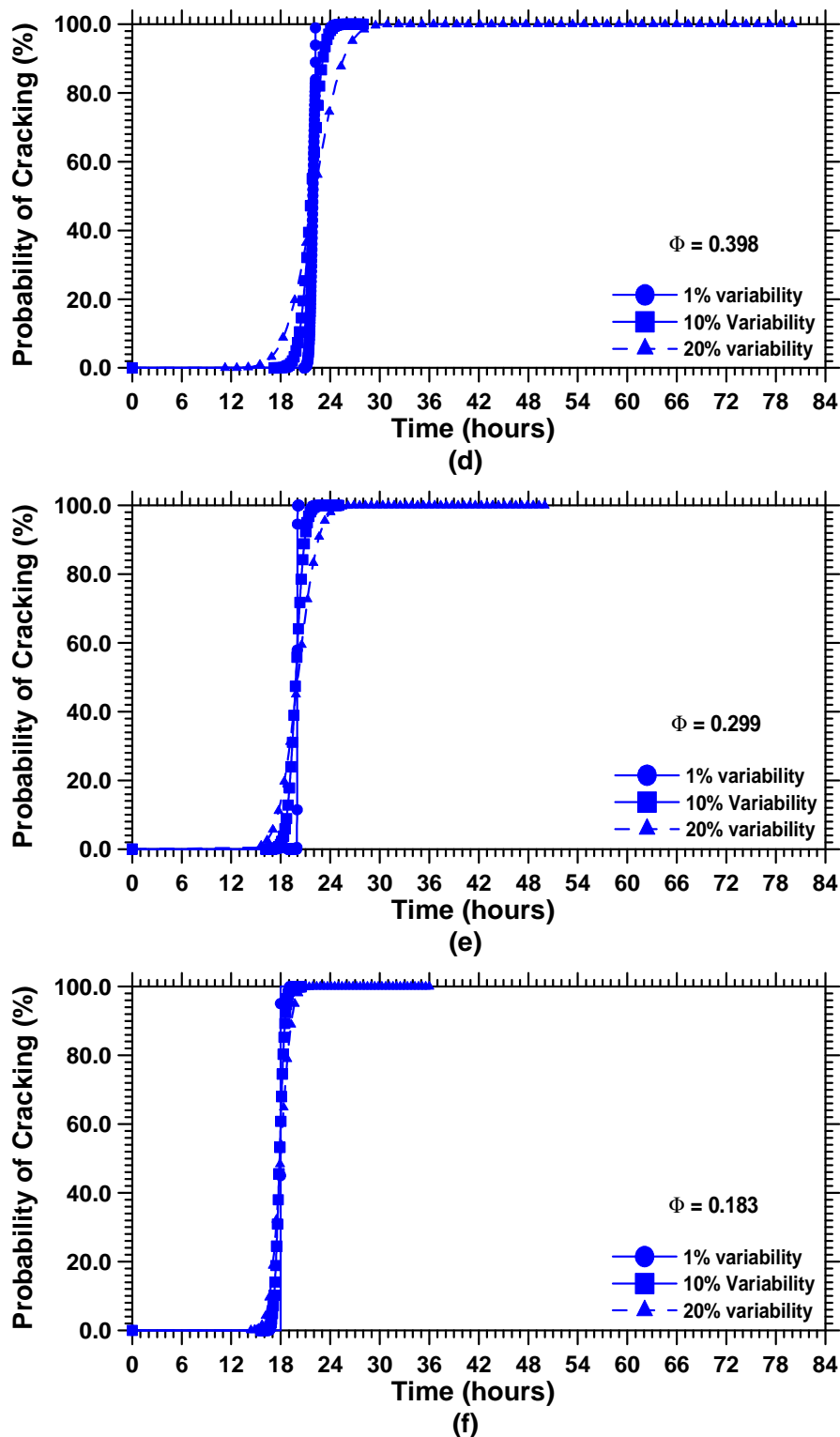


Figure 9.11: Probability of cracking for pavements assuming 1%, 10%, and 20% variability of tensile strength and residual stress: (d) D/4 saw-cut, (e) D/3 saw-cut, and (f) D/2 saw-cut.

Figure 9.12 provides an illustration of how a risk of cracking changes for different saw-cut depths as variability is introduced. Figure 9.12 is constructed using a 5% risk of cracking to show how the variability in the stress and strength of concrete influences the time of cracking. It is noted that the variability in construction only slightly influences the time of cracking for deep saw-cuts (i.e., $D/2$, $D/3$, and $D/4$). However, this is much more dramatic for shallower saw-cuts.

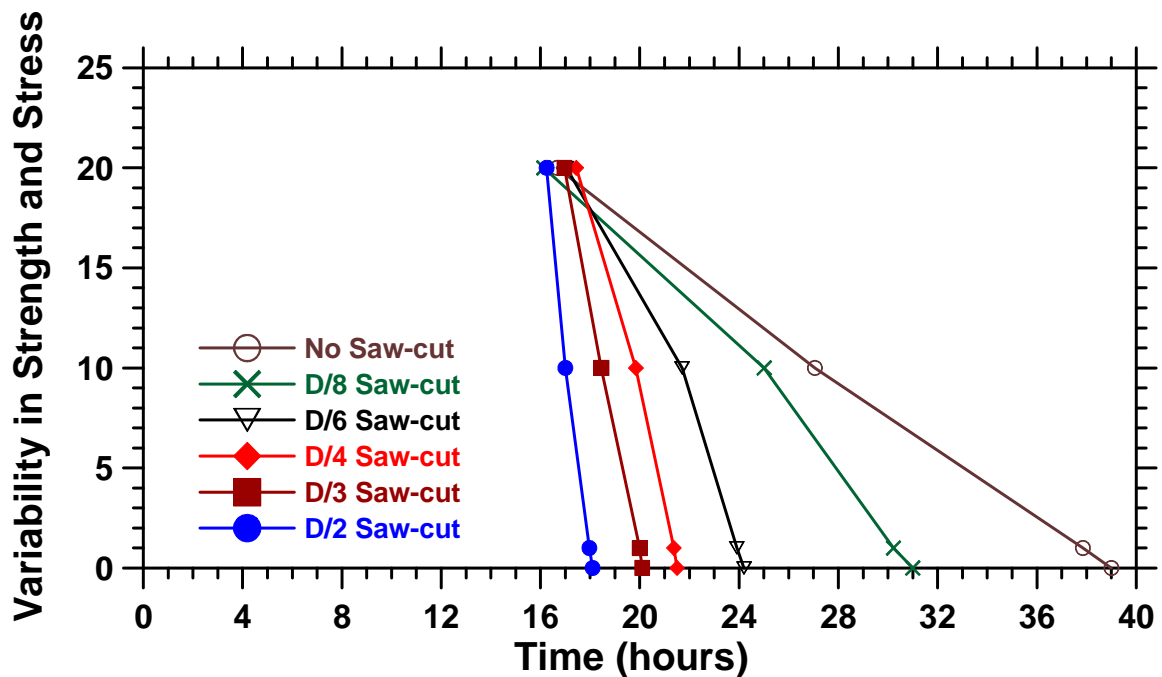


Figure 9.12: A 5% risk of random cracking considering different levels of variability of tensile strength and residual stress.

9.4 Summary

This chapter provided recommendations on determining an appropriate time for saw-cutting of pavements using different saw-cut depths to minimize the risk of random cracking. The first section provided an overview of a fracture mechanics approach. The fracture mechanics solution of a plate with a single edge notch under uniaxial tensile stress was discussed. This solution can be used to predict the stress and cracking behavior of concrete pavements when a saw-cut is introduced.

The results obtained from Equation 9.4 were compared with the results from finite element analysis of pavements with saw-cut of varying depth (i.e., D/2, D/3, D/4, D/6, D/8, and D/100). The obtained values of $\Phi_{saw-cut}$ can be determined for any saw-cut depth. The failure envelope can be developed by multiplying the tensile strength by $\Phi_{saw-cut}$ of concrete.

If a saw-cut is placed before the residual stress reaches the failure envelope (i.e., $f_t'(t) \cdot \Phi_{saw-cut}$), stable cracking occurs, and the saw-cut is placed safely. On the other hand, if the saw-cut is introduced after the residual stress exceeds the failure envelope, unstable cracking or even instant failure (i.e., chasing the crack across the pavement with the saw) would occur. This recommendation can be used in combination with stress and strength values predicted by hand (Weiss, 1999) or from computer software such as HIPERPAV software to appropriately assess the time and depth of a saw-cut.

The risk of cracking associated with different depths of saw-cut at any given time was also determined. The Monte Carlo analysis showed that the probability of uncontrolled cracking increases as the saw-cut to depth ratio decreases at any given time. It was noted that the determination of the time of saw-cutting for pavements with deep saw-cuts (i.e., D/2, D/3, and D/4) seems to be less susceptible to variability of strength and residual stress. As such the time of cracking can be more reliably determined for deep saw-cuts.

CHAPTER 10: SUMMARY AND RECOMMENDATIONS

10.1 Introduction

Contraction joints are placed in jointed plain portland cement concrete pavements and floors. These joints serve to control random cracking by providing a weakened plane that allows cracking to take place in a controlled manner at pre-specified location. Although the development of techniques to determine the time and depth of the saw-cut began with the early work of Westergaard in 1913 (Ioannides, 2005), the determination of the appropriate time and depth of the saw-cut is still a problematic task in practice. The saw-cut needs to be introduced in the pavement within a specific window of time. Sawing too early (i.e., before the concrete attains enough strength) would result in raveling and spalling at the edges of the cut. Sawing too late can result in micro crack development and random cracking. Not only is the saw-cutting time window difficult to determine, but also the appropriate depth of the saw-cut is largely debated. A shallow cut is preferred by contractors as it is introduced at a faster pace, and is more economical. A deeper cut is preferred by others to insure cracking at joint locations. Currently the field methods used for determining the timing of a saw-cut are relatively rudimentary and these rules of thumb generally do not show a good relationship with pavement performance, especially with different binder systems. Within the industry there is a wide range of specifications for saw-cut depth and timing for which no single specification has proven to be optimal. In addition, saw-cut depth and timing requirements have been further contested by the new technology of early-entry saws. The development of new, fracture-based, finite element software programs that model the introduction of a saw-cut provides one promising approach for determining the appropriate time and depth of saw-cuts.

The focus of this study was that the residual stresses can be computed based on simple rules and that these stresses can be compared to the permissible stress (i.e., either strength or critical stress from fracture mechanics) predicted from maturity concepts to define a saw-cutting depth and time window that considers the risk associated with raveling or random cracking.

The research was divided into three major components. The first component included field investigations to assess the current saw-cutting practices in Indiana. From these field investigations practical information was gained from the field which was useful in developing the laboratory testing program and for testing predictive models as they are developed. The second component of this work included laboratory testing. The laboratory testing consisted in large part of the development and commissioning of a new tensile wedge testing approach to determine the early age properties of concrete. In addition, this work included a series of more standard tests flexural beam testing, compressive cylinder testing, and splitting tensile testing for comparison with field testing. Finally, the work consisted of some preliminary approaches for assessing the potential for raveling using set-time and early entry saw-cut testing. The third component consisted of finite element analysis to assess the influence of the depth and time of saw-cut on residual stress development taking into consideration various ambient weather and environmental conditions. This work was also involved in the development of a simple methodology to compute when a saw-cut needs to be placed, using a stress development for an un-notched specimen. The following section will discuss the important findings that were obtained from this study.

10.2 A Summary of Important Findings

This section provides conclusion and recommendations which have been based upon the seven objectives that were proposed in Chapter 1.

The first objective of this work was to perform field experiments which will determine the approximate saw-cutting time window in the State of Indiana given the range of environmental and material parameters. In

addition, the field experiments will assess the potential implementation of the maturity method as a tool to assist contractors with saw-cutting.

In general, the saw-cutting window takes place between a pavement mid-depth maturity of 5 and 30 equivalent age hours (20°C) given Indiana's range of environmental conditions and current concrete pavement mixture designs. The maturity equipment should meet certain requirements for a successful implementation. In order to have an accurate maturity prediction the sensor must be capable of recording intervals of 15 minutes or shorter and be embedded at the time of or before the concrete is placed. In addition, the sensor should be of the type that it will not disrupt the construction operation with logging attachments or compromise the quality of the pavement.

Various depths were considered for the placement of the temperature sensors but it was found that there was little variation in the maturity calculations between mid-depth and the sensors placed at one-fourth of the depths. Therefore a mid-depth sensor is recommended because it has the advantages over shallower depths. A mid-depth sensor is easy to place because it can be placed on the dowel bar and basket. In addition, there are no durability concerns at mid-depth with regard to the surface of the pavement. Also, a sensor placed at mid-depth is more practical and efficient because it can be used in coordination with ITM-402. Furthermore, a single sensor placed towards the beginning 100 feet of a single day's segment of pavement placement proves adequate to determine what maturity the saw-cutting can begin at.

Master curves currently developed for ITM 402 are not suitable for saw-cutting window predictions and are likely to over-predict flexural strengths in relation to maturity at early-ages. Therefore a testing procedure that implements testing at earlier ages than ITM 402 will be required to define strengths for the saw-cutting window.

The second objective of this work was to examine the relationship between compressive, flexural, and direct tensile strength during the saw-cutting window time period.

Using the tensile wedge testing apparatus a direct tensile versus maturity relationship was established in 2.83" (D/3) notch depth configuration. This relationship

was compared to flexural beam strength and a relationship was developed. The tensile wedge strength results for the 2.83" (D/3) notches were approximately 62% of the flexural beam results at later ages and approximately 40% at early ages (i.e., equivalent ages of less than 15 hours). An additional relationship was developed between the compressive and flexural strength for the saw-cutting window. This relationship was used to convert previous saw-cutting guidelines based on compressive strength (Okamoto, 1993) to flexural strength. Further, the ACI equation $f'_r = 7.5\sqrt{f'_c}$ was an adequate approach for the relationship between compressive and flexural strengths for compressive strengths up to 1500 psi which corresponded to maturity values of less than 15 equivalent age hours. Split cylinder testing was performed at a single age to determine the early-age tensile variability of the mixture. The coefficient of variation was high (10.5%) relative to referenced tests in AASHTO. This high coefficient of variation may have been due to a large maximum size of aggregate or was possibly influenced by the transition that occurs when the fracture behavior changes from cracks that grow primarily around the aggregates at early ages to cracks that propagate through aggregates at later ages. It is believed that this information will eventually be able to be used to try to assess the critical depth of the notch/saw-cut to minimize the potential for random cracking.

The third objective of this work was to compare early-entry saws to conventional saws in terms of their timing, depth, and possible influences.

A series of tests were performed to assess whether the early-entry technology may have value for the state of Indiana. Results indicate that these early-entry saws can perform saw-cuts at approximately halfway between initial and final set time as determined by ASTM C 403 without any significant raveling. Therefore, the beginning of the saw-cutting window for early-entry saws is defined by the age at which the pavement can support the operator. This proved to be significantly earlier than conventional saws and confirmed that separate guidelines or specifications may be needed (based on raveling) for early-entry sawing procedures in comparison to conventional sawing procedures. Furthermore, the biggest advantage of early entry saws

proves to be their ability to saw at a significantly earlier age which can reduce the risks associated with random cracking. Data from the tensile wedge test and finite element analysis revealed that shallower 1" notches may significantly increase the probability of cracking at random locations. The tensile wedge data also suggested that shallower saw-cuts may initiate cracking at comparable displacements and loads to deeper notches but the initial cracking may not propagate to the bottom of the slab and may not result in the complete relief of residual stress buildup.

The fourth objective of this work was to determine how the depth of the saw-cut influences the potential for cracking considering residual stress development which can lead to random cracking.

It was determined that the probability of cracking at joint locations increases as the saw-cut to depth ratio increases. It was also noted that the deeper saw-cuts (i.e., saw-cuts greater than D/4) need to be placed sooner than shallower saw-cuts to avoid unstable crack propagation. The crackings of pavements with deep saw-cuts (i.e., D/2, D/3, and D/4 saw-cuts) are less susceptible to variability in construction. As such the time of cracking for deeper saw-cuts can be more reliably determined, thereby reducing the random cracking potential. It was also noted that when shallow saw-cuts (i.e., D/8 or shallower saw-cuts) are introduced, bottom up cracking is more likely to occur. It was shown that before the peak load was reached the crack can propagate in a stable fashion. This stable crack growth was confirmed using the measurement of the LVDT displacement directly over the crack in the tensile wedge test. In specimens with deep notches (i.e., 2.83" (D/3) or greater) the crack appeared to propagate unstably at the time of ultimate load. In specimens with shallow notches (i.e., notches < 2.83" (D/3)) the crack appeared to propagate in a semi-stable fashion with a sudden increase in crack length prior to the load reaching a peak value. The other trend was observed from tensile wedge test was that when notch depths were decreased to 1.00" (D/8.5) from 2.00" (D/4.25), only one out of three 1.00" specimens had cracks that caused failure to propagate from the notch tip. Therefore a distinct increase in the probability of cracking occurring at a location other than the notch tip was observed (which could be compared to "random" cracking in pavements) in the 1.00" notches (D/8.5).

The fifth objective of this work was to investigate the effect of the time of saw-cut introduction on residual stress development and cracking behavior of concrete pavements.

The results obtained from the tensile wedge and finite element analysis show that the specimens appear to be insensitive to the saw-cut at early ages (i.e., <15 eq. age hours). The insensitivity to the saw-cut was believed to be an indication of an elastoplastic material response. Results obtained from finite element analysis indicate that the saw-cutting time window ends when the residual stress of concrete exceeds the product of concrete strength and $\Phi_{saw-cut}$ (a factor that depends primarily on the depth of the saw-cut). The residual stress of an uncut pavement can be predicted by various numerical tools taking into consideration the ambient weather conditions and concrete material properties. This factor enables the calculation of the maximum age before unstable cracking would be expected to occur.

The sixth objective of this work was to determine the influence of ambient weather conditions and constituent materials on the saw-cutting time window.

Results showed that at early ages a high thermal expansion occurs due to the heat of hydration. This offset the tensile stress developments resulting in a delay in the residual tensile stress development and a delay in the cracking. Concrete with slower rate of hydration provides larger saw-cutting time window. On the other, a fast set material demonstrated a reduction in the saw-cutting time window.

The seventh objective of this work was to develop a methodology to explain when a saw-cut should be placed considering the depth of saw-cut.

A design methodology was developed to determine when the saw-cut needs to be placed in the pavement. The design methodology consists of comparing the residual stress (σ) with the product of the tensile strength (f_t') and $\Phi_{saw-cut}$. The time of saw-cutting can be determined as the age at which Equation (10.1) fails to be true.

$$\sigma_{(t)} \leq f'_t(t) \cdot \Phi_{saw-cut} \quad (10.1)$$

Equation 10.2 can be used to calculate the $\Phi_{saw-cut}$ for any depth while Table 10.1 provides $\Phi_{saw-cut}$ for some of the common saw-cut depths.

$$\Phi_{saw-cut} = \frac{K_{IC}}{\sqrt{\pi \cdot a} \cdot f\left(\frac{a}{D}\right)} \quad (10.2)$$

Table 10.1: $\Phi_{saw-cut}$ for selected values of saw-cut to depth ratios.

a/D		$\Phi_{saw-cut}$
1/10	0.01	1.00
1/8	0.13	0.78
1/6	0.17	0.56
1/4	0.25	0.40
1/3	0.33	0.30
1/2	0.50	0.18

REFERENCES

LIST OF REFERENCES

American Concrete Institute, Committee 318, "Building Code Requirement for Structural Concrete", Farmington Hills, MI, 2002

American Concrete Institute, Committee 228.1, "In-Place Methods to Estimate Concrete Strength", Farmington Hills, MI.

American Concrete Institute, Committee 446.1, "Fracture Mechanics of Concrete: Concepts, Models and Determination of Material Properties", Farmington Hills, MI, 1999.

American Concrete Institute, Committee 302.1, "Guide for Concrete Floor and Slab Construction", Farmington Hills, MI.

American Concrete Institute, Committee 305R-99, "Hot Weather Concreting", Farmington Hills, MI.

American Concrete Institute, Committee 224.3, "Joints in Concrete Construction", Farmington Hills, MI, 1995

American Concrete Institute, Committee 224, "Control of Cracking in Concrete Structures", Farmington Hills, MI.

American Concrete Pavement Association, "Early Cracking of Concrete Pavement – Causes and Repairs", Publication TB016P, Skokie IL, 2002 a.

American Concrete Pavement Association, "Maturity Testing of Concrete Pavements: Applications and Benefits", Publication IS257P, Skokie IL, 2002 b.

American Concrete Pavement Association, "Design and Construction of Joints for Concrete Highways", Publication TB010P, Arlington Heights IL, 1991.

Armaghani, J.M., and Richardson, J.M., "Stress Caused by Temperature Gradient in Portland Cement Concrete Pavement", Transportation Research Record, Page 7-13, 1987.

Barde, A, "Early-age Flexural Behavior of Cementitious Systems and Factors Affecting Maturity Based Predictions", Master Thesis, Purdue University, May 2004.

Barde, A., Mozotta, G., and Weiss, J., "Early Age Flexural Strength: The Role of Aggregates and Their Influence on Maturity Predictions", *Materials Science of Concrete VII*, American Ceramic Society, pp. 247-264, 2004

Bazant, Z., Najjar, L., "Drying of Concrete as a Nonlinear Diffusion Problem", *Cement and Concrete Research*, Vol. 1, Page 461-473, 1971.

Bazant, Z., "Material models for structural creep analysis", *Fourth RILEM International Symposium on Creep and Shrinkage of Concrete: Mathematical Modeling*, August 26-29, 1986.

Bazant, Z., Xi, Y., and Jennings, H., "Moisture Diffusion in Cementitious Materials, Adsorption Isotherm", *Advanced Cement Based Materials*, Volume 1, Issue 6, Pages 248-257, November 1994.

Bentz, D., "Prediction of adiabatic temperature rise in conventional and high performance concretes using a 3-D micro-structural model", *National Institute of Standards and Technology*, 1998.

Bentz, D., "A computer model to predict the surface temperature and time-of-wetness of concrete pavements and bridge decks", *NISTIR 6551*, National Institute of Standards and Technology, August 2000.

Bernhardt, C.J., "Hardening of Concrete at Different Temperatures", *Proceedings, RILEM Symposium on Winter Concreting*, Danish Institute for Building Research Copenhagen, 1956.

Brameschuber W., and Hilsdorf H.K., "Development of strength and deformability of very young concrete. Proceedings from "RILEM International Conference on Fracture of Concrete and Rock", pp 655-657, Houston 1987.

Carino, Nicholas," *The Maturity Method*", Chapter 5 of *Handbook on nondestructive Testing of Concrete*, edited by V. Malhotra and N. Carino, CRC Press, second edition, 2004.

Castro-Montero, A., Shah, S. P., and Miller, R.A., "Strain Field Measurement in Fracture Process Zone," *Journal of Engineering mechanics*, ASCE, Vol. 116, No. 11, pp. 2463-2484, 1990

Chariton, T., and Weiss, W. J., "Using Acoustic Emission to Monitor Damage Development in Mortars Restrained from Volumetric Changes," *Concrete: Material Science to Application, A Tribute to Surendra P. Shah*, ed. P. Balaguru, A. Namaan, W. Weiss, ACI SP-206, pp. 205-218, 2002.

Chojnacki, T., "Evaluation of Early Entry Sawing of PCC Pavement", Missouri Department of Transportation, RDT01-010, August, 2001.

Copeland, L.E., Kantro, D. L., and Verbeck, G., "Chemistry of Hydration of Portland Cement". Part III- Energetics of the Hydration of Portland Cement, Proc. 4th Int. Symposium on Chemistry of Cement, NBS Monograph 43, Washington, 453, 1962.

4C-Temp&Stress, "Temperature and Stress Simulation During Hardening," User Manual, German Instruments, Inc., Evanston, IL 1998.

De Schutter, G., "Thermal Properties", Page 121 to 125, Early Age Cracking in Cementitious Systems, Report of RILEM Technical Committee TC 181-EAS, RILEM Report 25, Edited by A. Bentur, July 2002.

Emborg, M., Thermal Stresses in Concrete Structures at Early Ages, Doctoral thesis, Lulea University of Technology, Lulea, Germany, 1989.

FEMMASSE, "Finite Element Modules for Material Science and Structural Engineering", MLS Version 7.1, FEMMASSE B.V., February 2004.

Freiesleben Hansen, P. and Pedersen, E. J., Maturity computer for controlled curing and hardening of concrete, Nordisk Betong, 1, 19, 1977.

Graveen, C., Weiss, W.J., Olek, J., and Nantung, T., "Implications of Maturity and Ultrasonic Wave Speed Measurements in QC/QA for Concrete", Brittle Matrix Conference No. 7, October 2003.

Hansen, F., Pedersen, E., "Curing of Concrete Structures", Report prepared for CEB, general task group number 20 "Durability and Service Life of Concrete Structures", Danish concrete and structural research institute, CEB-Guide to Durable Concrete Structures, Lausanne, December 1985.

Haug, H., "Pavement Analysis and Design", Prentice Hall, NJ, 1993

HIPERPAV, "High Performance Concrete Paving Software", Version 2.5, Transtec Inc., Austin, TX, 2004.

Hossain, A., and Weiss, W.J., ARC2 , "Automated Analysis of the Restrained Rings for Creep and Shrinkage", Purdue University.

Hillerborg, A., "A Model for Fracture Analysis", Report TVBM-3005, Division of Building Materials, Lund Institute of Technology, Lund, Sweden, 1978.

Hillerborg A, Modeer M., Petersson P.E., "Analysis of Crack Formation and Crack Growth in Concrete by Means of Fracture Mechanics and Finite Elements", Cement and Concrete Research, 6, 1976.

Hover K. – Personal Communication, 2003.

Indiana Department of Transportation, Standard Specifications, 503.03, Indianapolis, IN, 1999.

Ioannides, A., “Stress Prediction for Cracking of Jointed Plain Concrete Pavements, 1925-2000 an overview”, Transportation Research Record, No. 1919, Washington D.C., Page 47-53, 2005.

Jansen, D.C., Weiss, W.J., and Schleuchardt, S.H.F., “Simplification of the Testing and Analysis Procedure for the Two Parameter Fracture Model”, Fracture Mechanics for Concrete Materials, Farmington Hills, MI 2001.

Jenq, Y., and Shah, S. P., "Two Parameter Fracture Model for Concrete," Journal of Engineering Mechanics, Vol. 111, No. 10, pp. 1227-1241, Oct. 1985.

Jenq, Y.S., et al., “Effect of Temperature on Early Crack Formation in Portland Cement Concrete Pavements”, Transportation Research Record, n 1388, Page 35-41, 1993.

Kim, B., and Weiss, W. J., “Using Acoustic Emission to Quantify Damage in Restrained Fiber Reinforced Cement Mortars”. (To appear in Cement and Concrete Research)

Lofsjogard, M., “Investigation of the optimum time for cutting joints in concrete roads”. Proceedings from the 7th international Conference on Concrete Pavements, Vol. 1 of 3, pp. 525-537, Orlando, FL, Sept. 9-13, 2001.

Maekawa, K., Chaube, R., Kishi, T., “Modeling of Concrete Performance Hydration, Micro Structure, Formation and Mass Transport”, Chapter 7, Spon Press, London, 1999.

McCullough, B.F. and Rasmussen, R. O., “Fast-Track Paving: Concrete Temperature Control and Traffic Opening Criteria for Bonded Concrete Overlays Volume I: Final Report”, Federal Highway Administration Report FHWA-RD-98-167, Washington, 1999.

McIntosh, J.D., “Electrical curing of concrete”, Magazine of Concrete Research, 1(1), 21, 1949

McIntosh, J. D., “The effects of low-temperature curing on the compressive strength of concrete”, Proceedings RILEM Symposium on winter concreting, Danish Institute for Building Research Copenhagen, Copenhagen 1956.

Mindess, S., Young, J.F., and Darwin, D., Concrete, Prentice-Hall, Inc., 2003.

Monteiro, P. and Mehta, P., "Concrete Structure, Properties, and Materials", Second Edition, Prentice Hall, NJ, 1993.

Morabito, P., "Methods to Determine the Heat of Hydration of Concrete", Page 1 to 25, Prevention of Thermal Cracking in Concrete at Early Ages, RILEM Report 15, Edited by R. Springenschmid, London 1998.

Nallathambi, P., and Karihaloo, B. L., "Determination of Specimen Size Independent Fracture Toughness of Plain Concrete," Magazine of Concrete Research, Vol. 38, No. 135, 1986, pp. 67-76.

Neville, A., "Properties of Concrete", Fourth and Final Edition, Longman, 1995.

Missouri Department of Transportation, "Evaluation of Early Entry Sawing of PCC Pavement", Report No. RDT01-010, Jefferson City, MO, 2001.

Nurse, R. W., "Steam curing of concrete", Magazine Concrete Research 1(1), 21, 1949

Norland, R., Construction Solutions, Personal Communication, 2004.

Okamoto, P. and others, "Guidelines for Timing Contraction Joint Sawing and Earliest Loading for Concrete Pavements", Volume I and II: Final Report, FHWA-RD-91-079, FHWA, U.S. Department of Transportation, February 1994.

Østergaard, Lennart, "Early-Age Fracture Mechanics and Cracking of Concrete Experiments and Modeling", PhD Thesis, Technical University of Denmark, 2003.

Ostergaard, L., Lange, D., and Stang, H., "Early-age stress-crack opening relationships for high performance concrete", Cement & Concrete Composites, 26, pp 563-572, 2004.

Pease, Bradley, "The Role of Shrinkage Reducing Admixtures on Shrinkage, Stress Development, and Cracking", Master Thesis in Civil Engineering, Purdue University, May 2005.

Peterson P.E., "Crack growth and development of fracture zones in plain concrete and similar material", Report TVBM-1006 1989.

Plowman, J. M., "Maturity and the strength of concrete", Magazine of Concrete Research, 8 (22), 13, 1956.

Reider, K.A., "Determination of Crack Resistance Curves of Cementitious Materials from Measurements of a Wedge Splitting Test," ACI SP-201, Fracture Mechanics for Concrete Materials, Farmington Hills, MI 2001.

Saul, A. G. A., Principles underlying the steam curing of concrete at atmospheric pressure, Magazine of Concrete Research 2 (6), 127, 1951

Springenschmidt, R., "Thermal Cracking in Concrete at Early-Ages", Proceedings of the International Symposium, RILEM 25, Munich German, 1995

Springenschmidt, R., and Breitenbucher, R., "Influence of Constituents, Mix Proportions and Temperature on Cracking Sensitivity of Concrete", Page 40 – 50, Prevention of Thermal Cracking in Concrete at Early Ages, RILEM Report 15, Edited by Springenschmidt, R., London 1998.

South Carolina Department of Transportation, Standard Specifications for Highway Construction, 501.26, pg. 371, 2000.

Soares, J., and Zollinger, D., "Strength Characterization and a Basis for Saw-cutting Requirements for Jointed Concrete Pavements," Proceedings from the Sixth International Purdue Conference on Concrete Pavement Design and Materials for High Performance, Vol. 2, pp. 41-61, Indianapolis, IN, 1997.

Shah, S.P., Swartz, E., and Ouyang, C., Fracture Mechanics of Concrete, 1995.

Soff-Cut Inc., www.soffcut.com, 2004

Tada, H., Paris, P., and Irwin, G., "The Stress Analysis of Cracks Handbook", Second Edition, Paris Production, New York, USA, 1985.

Thompson, M.R., and Dempsey, B.J., and Hill, H, and Vogel, J, "Characterizing Temperature Effects for Pavement Analysis and Design", Transportation Research Record, n. 1121, 1987.

Van Breugel, K., "Prediction of Temperature Development in Hardening Concrete", RILEM Report 15: Prevention of Thermal Cracking in Concrete at Early Ages, Page 51-75, 1998.

Verbeck, G. J. and Helmuth, R. H., "Structure and physical properties of cement paste", Proceedings 5th International Symposium on the Chemistry of Cement, Tokyo, 1968.

Voigt, G.F., "Specification Synthesis and Recommendations for Repairing Uncontrolled Cracks that Occur During Concrete Pavement Construction", ACPA, April 2000.

Wang, K., et al., "Developing a Simple and Rapid Test for Monitoring the Heat Evolution of Concrete Mixtures for Both Laboratory and Field Applications", National Concrete Pavement Technology Center, Final Report, January 2006

Weiss, W. J., "Prediction of Early Age Cracking in Concrete", Northwestern University, PHD Thesis, August 1999.

Weiss, W. J., Yang, W., and Shah, S. P., "Influence of Specimen Size and Geometry on Shrinkage Cracking," ASCE - Journal of Engineering Mech. Div., 2000, 126(1), 93-101.

Weiss, W.J., Yang W., and Shah, S.P., "Using Fracture to Predict Restrained Shrinkage Cracking: The Importance of Specimen Geometry", ACI Committee 446-Fracture Mechanics, Farmington Hills, MI 2001.

Weiss, W. J. and Chariton, T., "Using Acoustic Emission to Monitor Damage Development in Mortars Restrained from Volumetric Changes," Concrete: Material Science to Application, A Tribute to Surendra P. Shah, ed. P. Balaguru, A. Namaan, W. Weiss, ACI SP-206, pp. 205-218, 2002.

Weiss, W. J., Civil Engineering 530 Properties and Production of Concrete, Fracture Mechanics Lecture, 2004.

Yang, Z., J. Weiss, and J. Olek, "Interaction between Micro-Cracking, Cracking, and Reduced Durability of Concrete: Developing Methods for Quantifying the Influence of Cumulative Damage in Life-Cycle Modeling," Final Report, FHWA/IN/JTRP-2004, Joint Transportation Research Program, School of Civil Engineering, Purdue University, May 2004.

Zollinger, D., Tang, T., and Dapeng, X., "Sawcut Depth Considerations for Jointed Concrete Pavement Based on Fracture Mechanics Analysis", Transportation Research Record 1449, TRB, National Research Council, Washington, D.C., 1993, pp. 91-100.

APPENDICES

Appendix A

For each computer simulation, the history graphs of temperature, maturity, tensile strength, compressive strength, principal stress, stress in x-direction, damage (reduction in elastic modulus), and CTOD at the tip of the saw-cut are plotted as function of time. Unless otherwise noted, the model parameters are the same as the baseline case described in section 7.2.

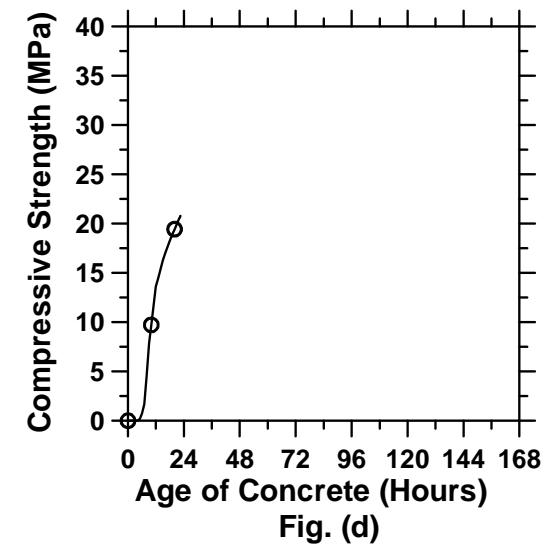
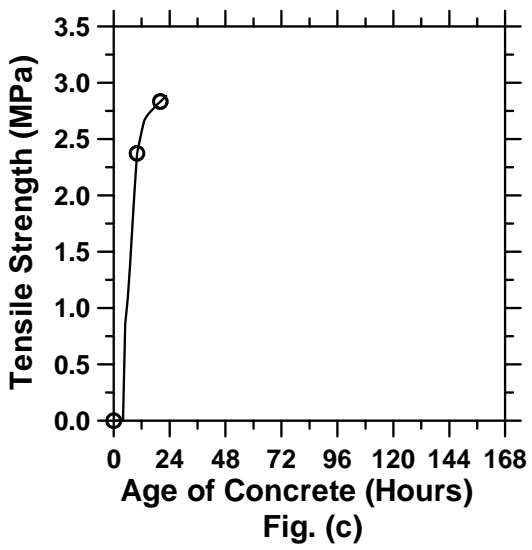
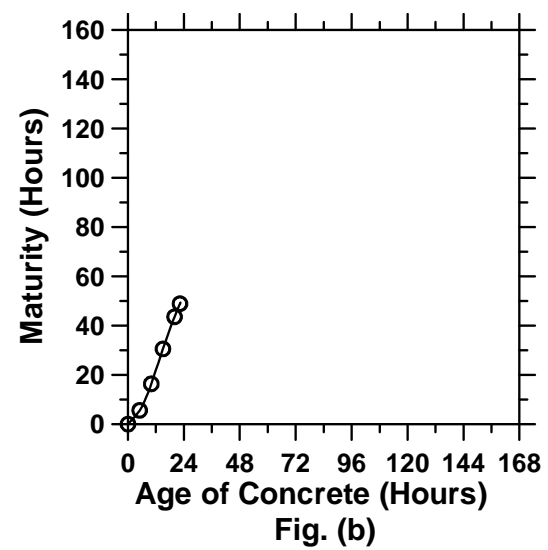
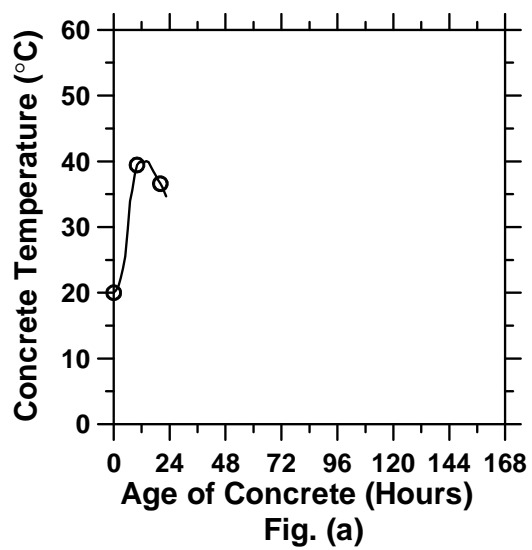


Figure A.1: Pavement with a D/2 saw-cut depth introduced at 0 hour (cont'd).

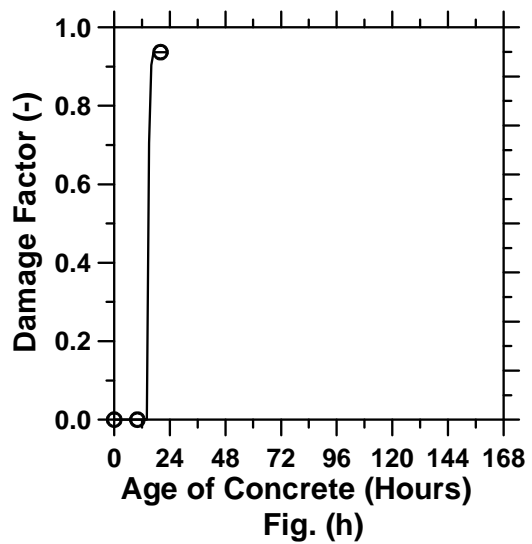
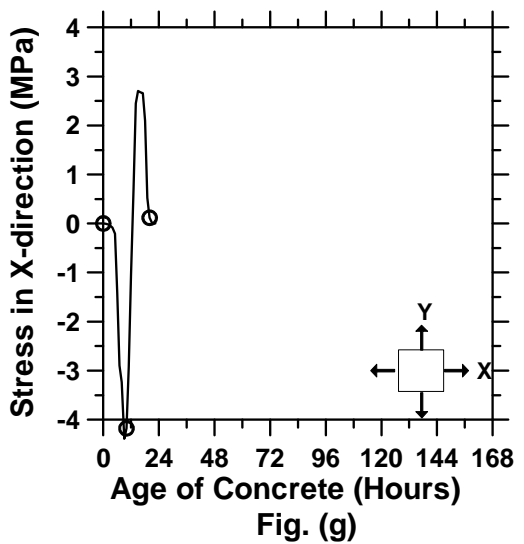
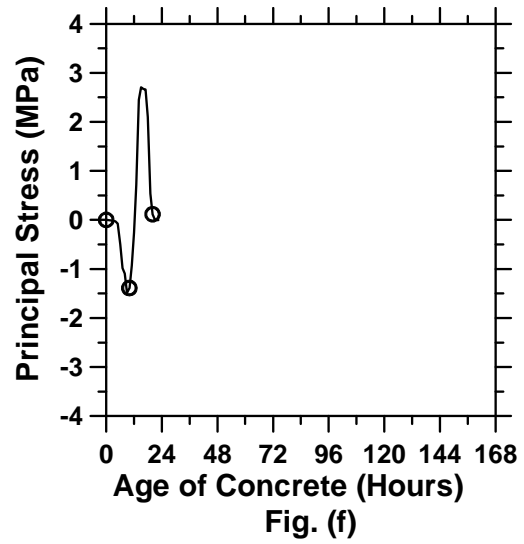
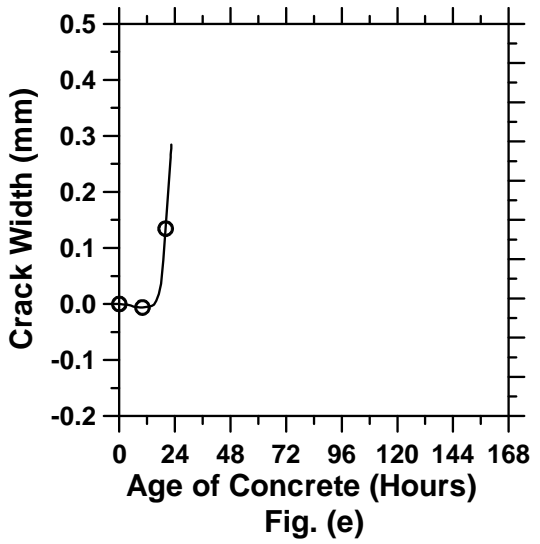


Figure A.1: Pavement with a D/2 saw-cut depth introduced at 0 hour.

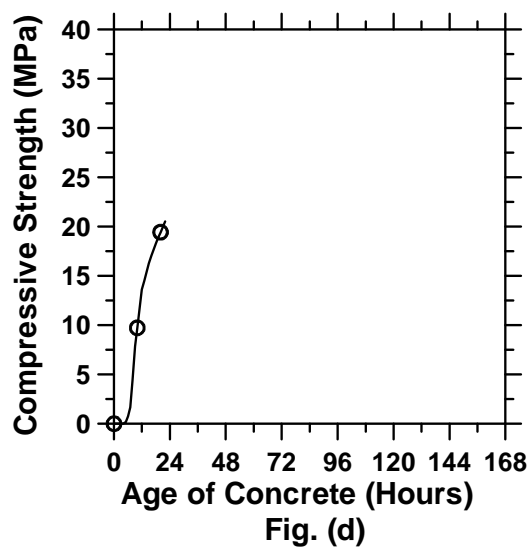
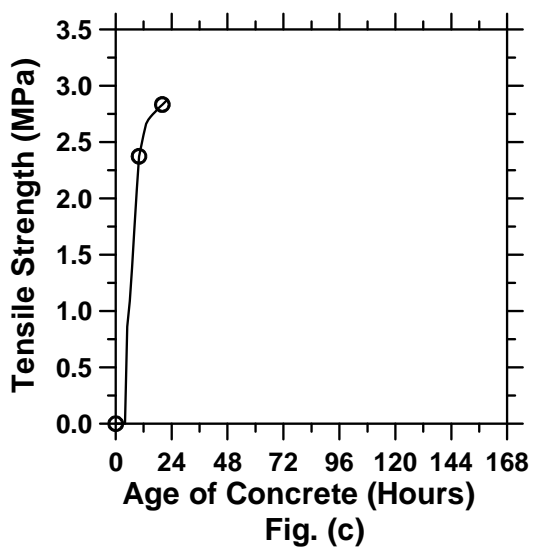
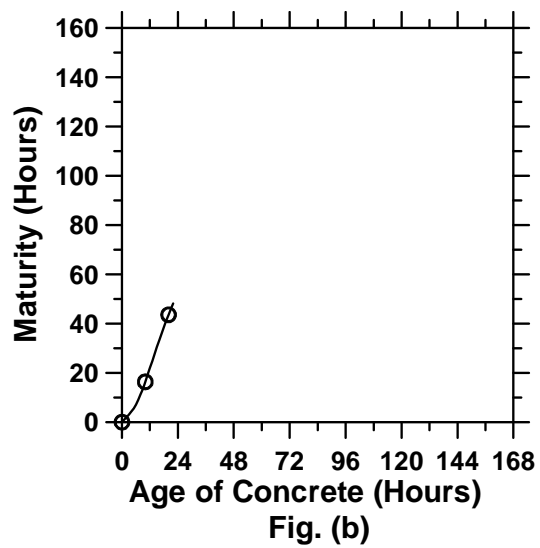
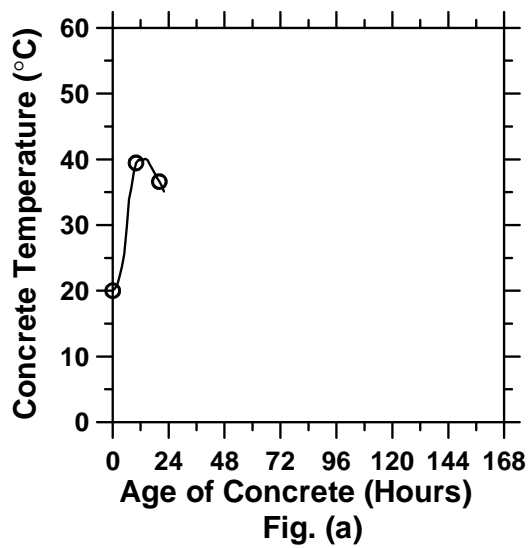


Figure A.2: Pavement with a D/2 saw-cut depth introduced at 6 hours (cont'd).

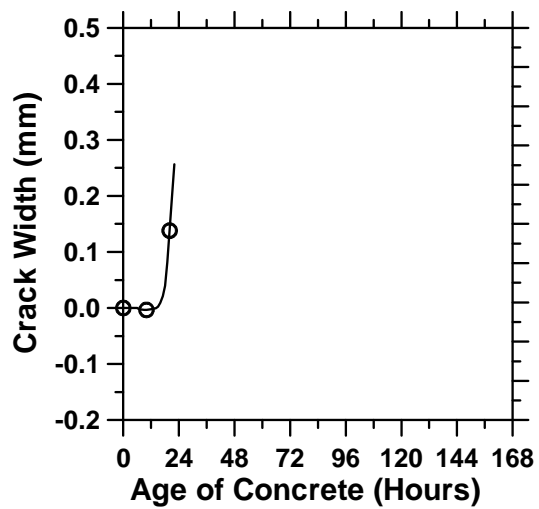


Fig. (e)

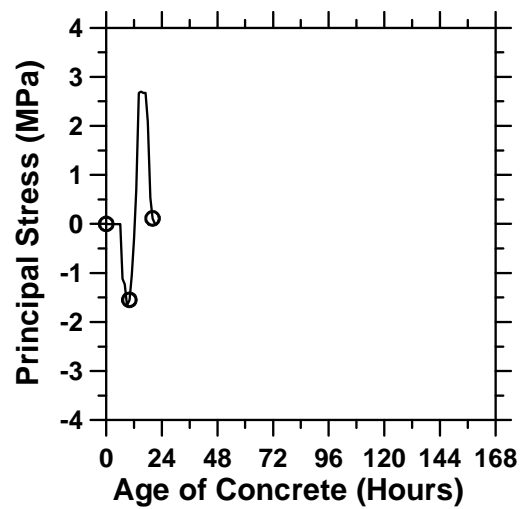


Fig. (f)

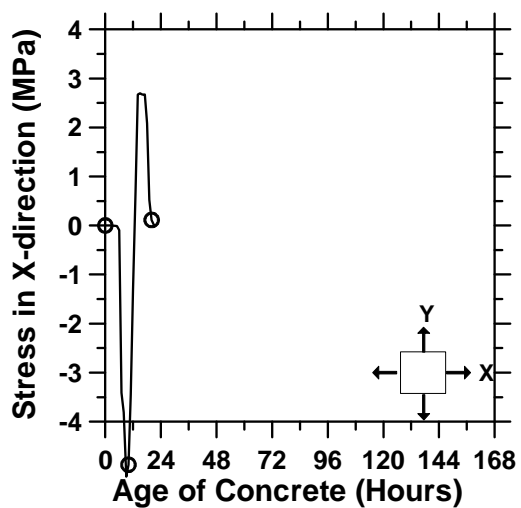


Fig. (g)

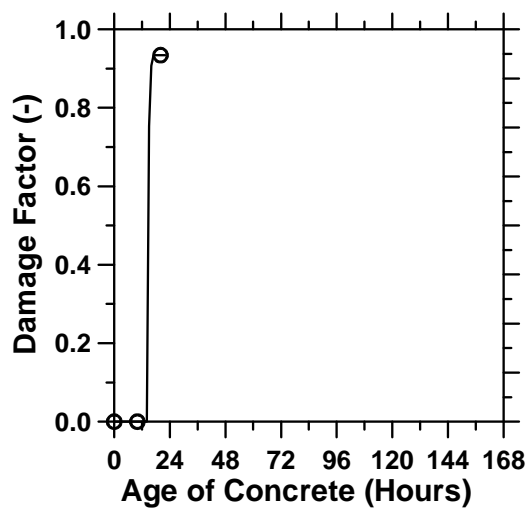


Fig. (h)

Figure A.2: Pavement with a D/2 saw-cut depth introduced at 6 hours.

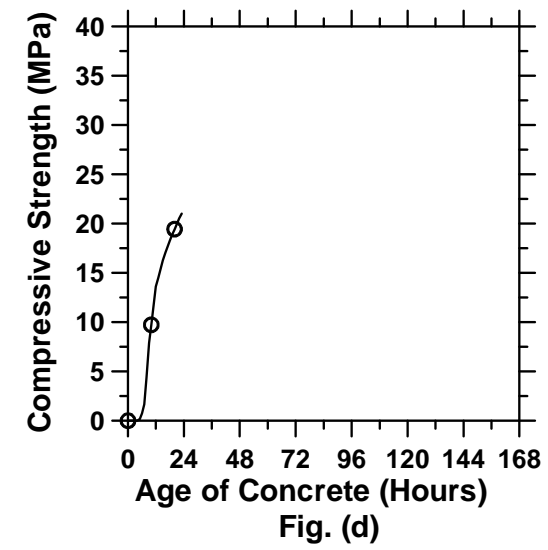
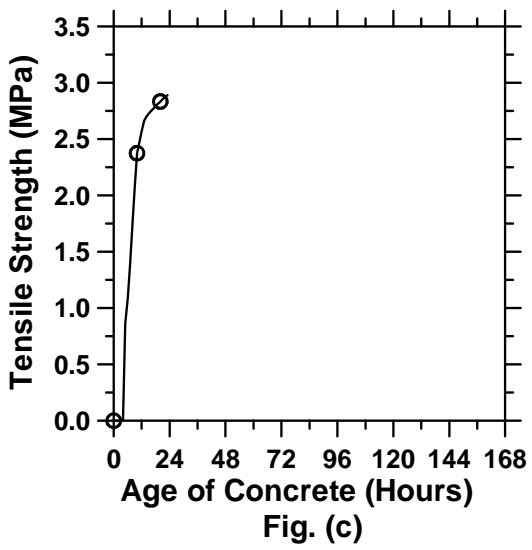
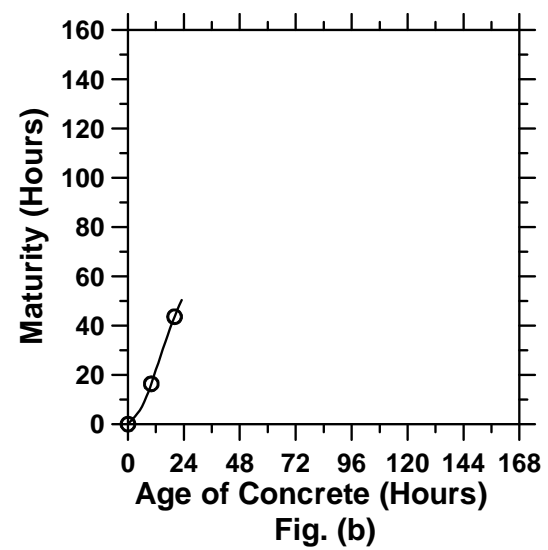
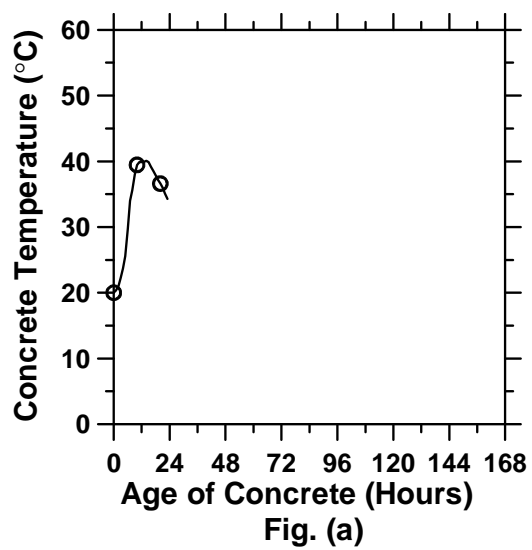


Figure A.3: Pavement with a D/2 saw-cut depth introduced at 9 hours (cont'd).

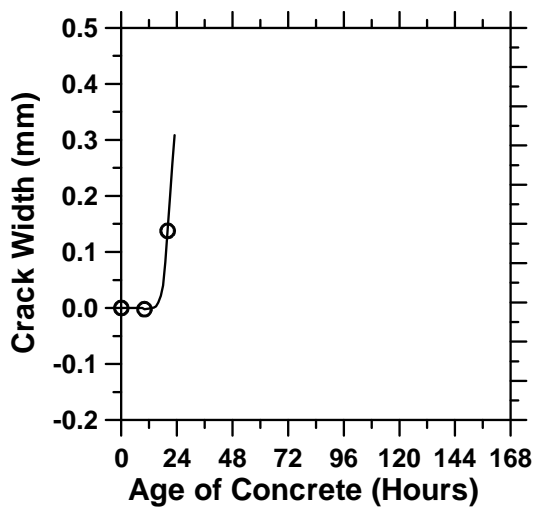


Fig. (e)

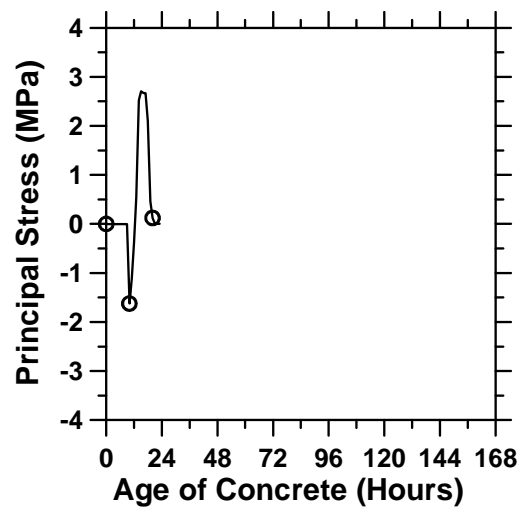


Fig. (f)

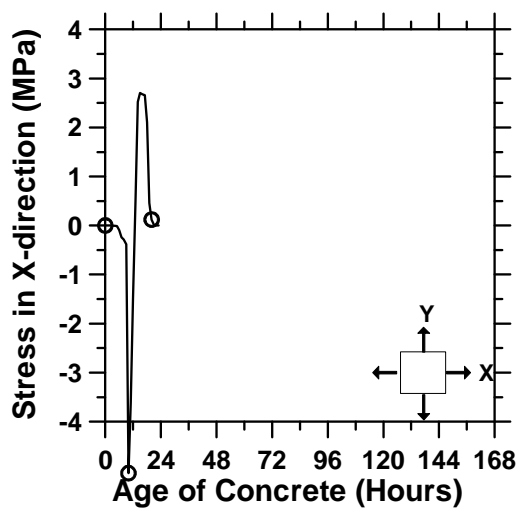


Fig. (g)

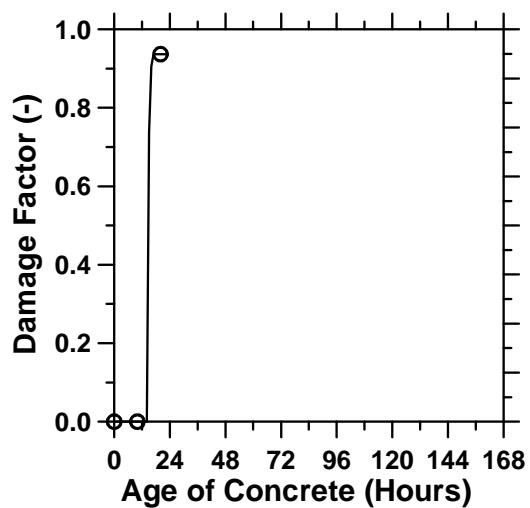


Fig. (h)

Figure A.3: Pavement with a D/2 saw-cut depth introduced at 9 hours.

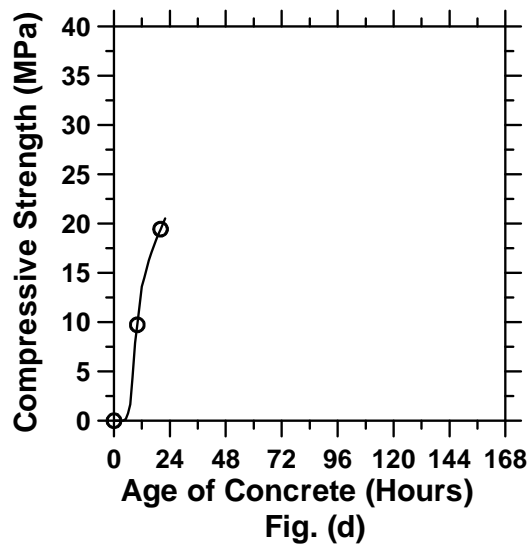
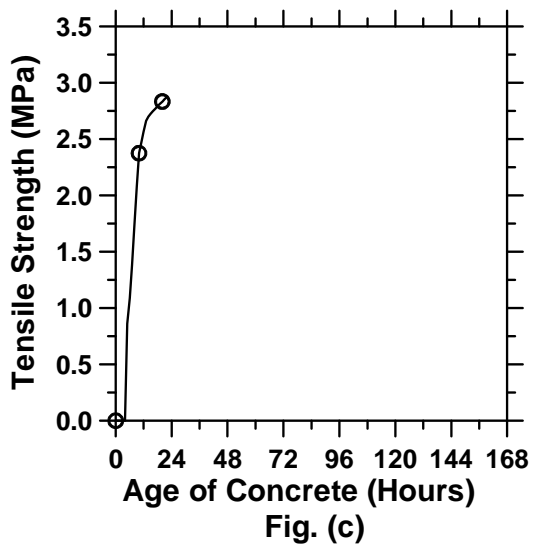
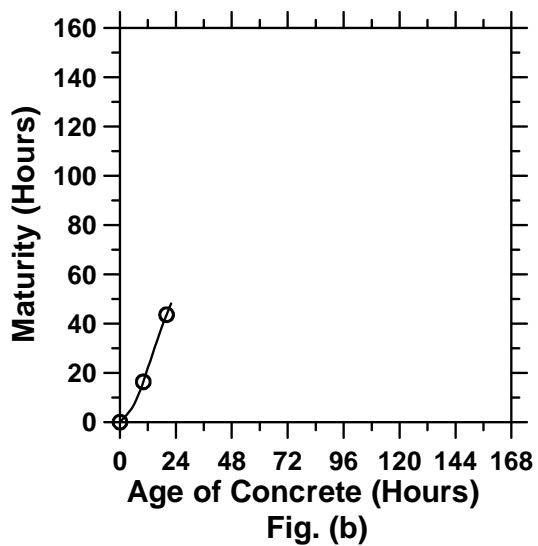
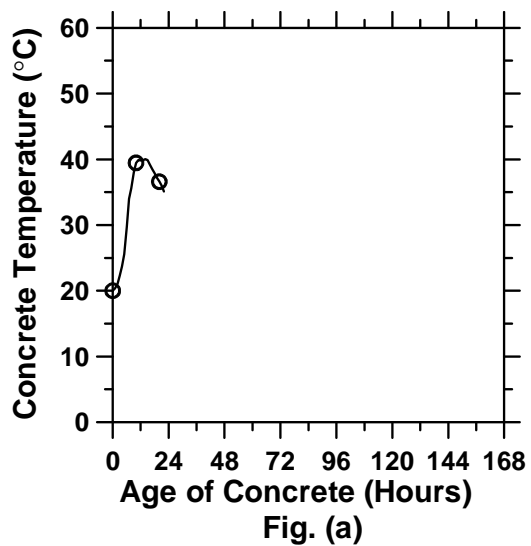


Figure A.4: Pavement with a D/2 saw-cut depth introduced at 12 hours (cont'd).

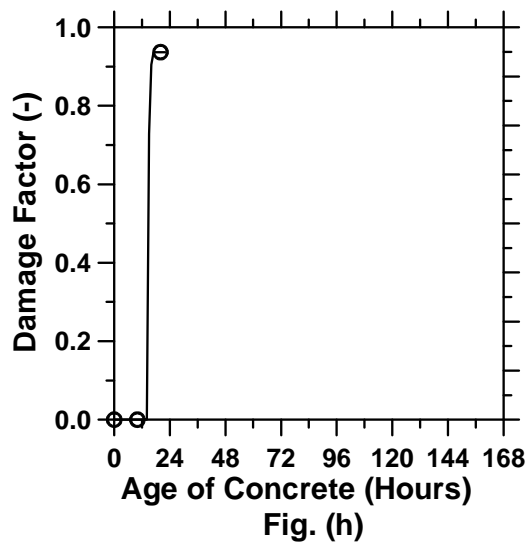
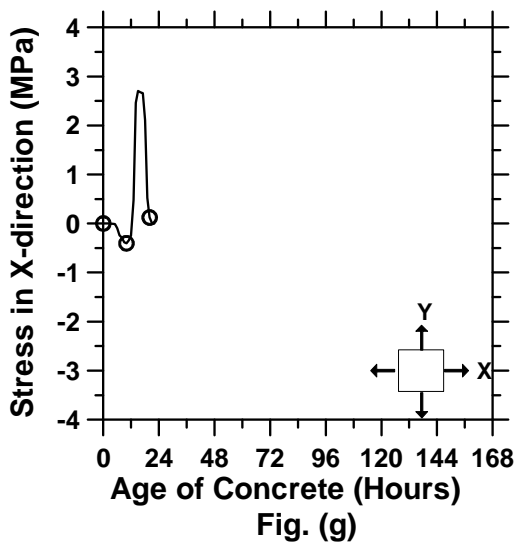
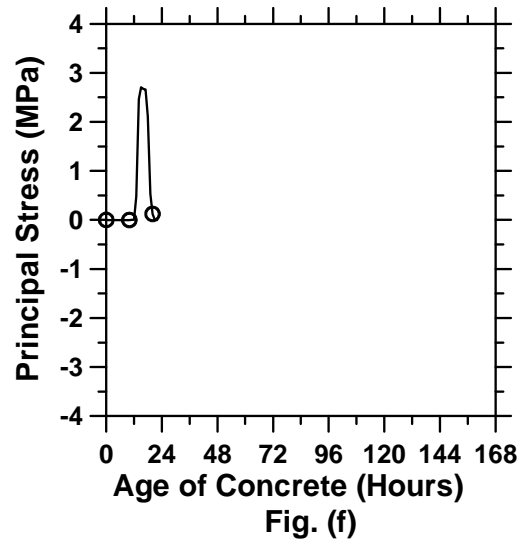
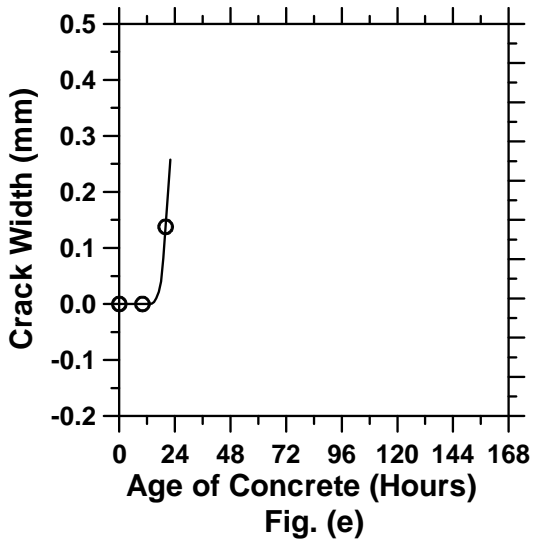


Figure A.4: Pavement with a D/2 saw-cut depth introduced at 12 hours.

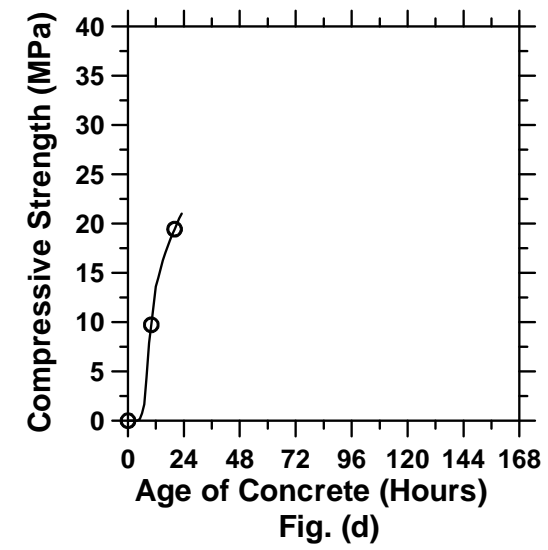
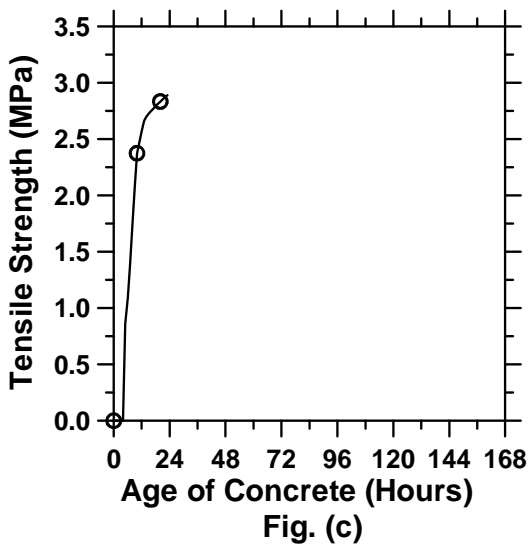
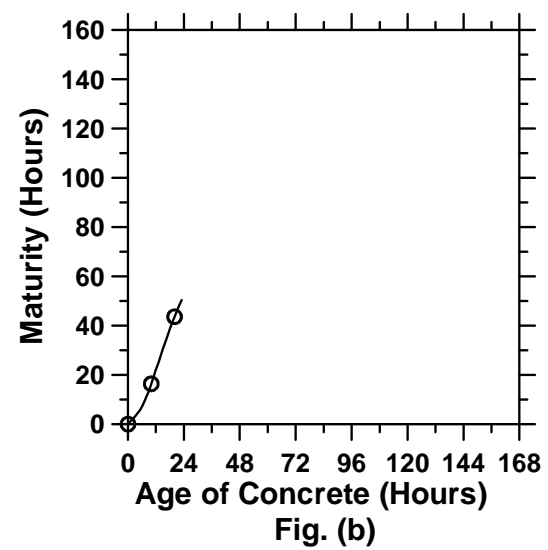
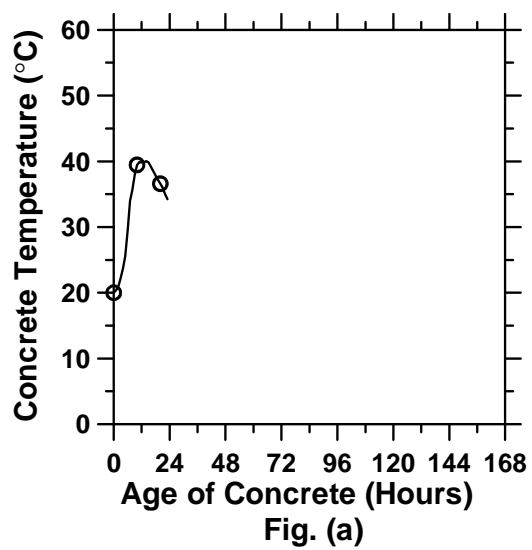


Figure A.5: Pavement with a D/2 saw-cut depth introduced at 15 hours (cont'd).

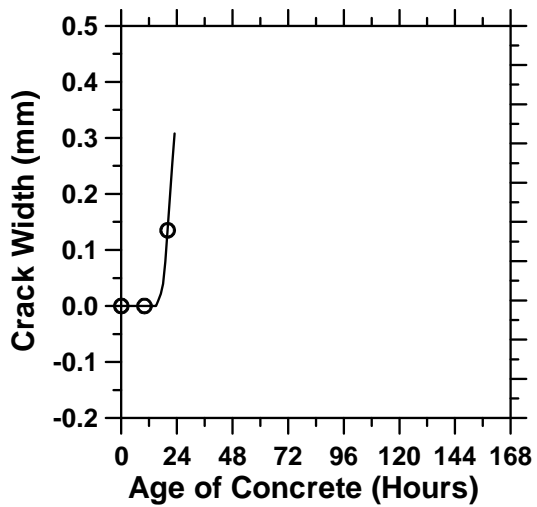


Fig. (e)

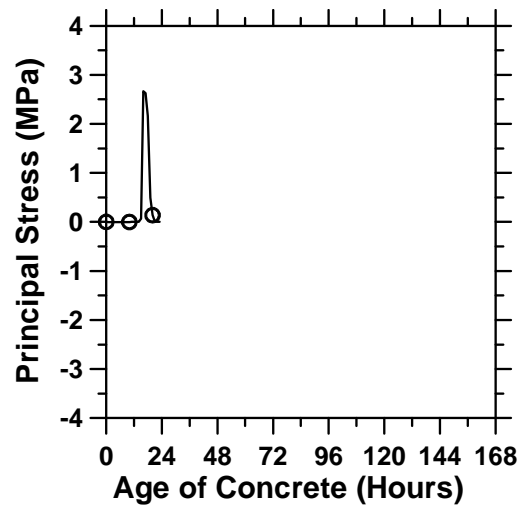


Fig. (f)

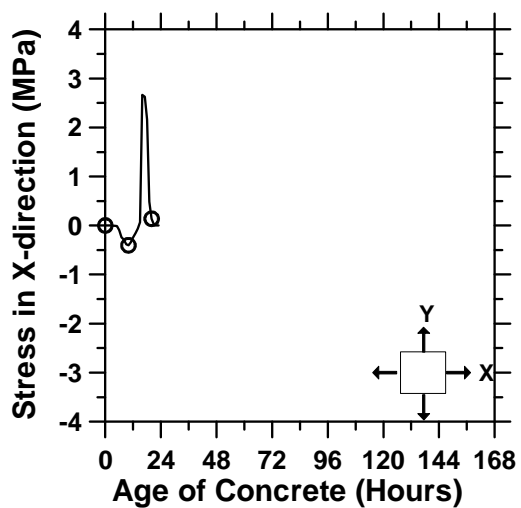


Fig. (g)

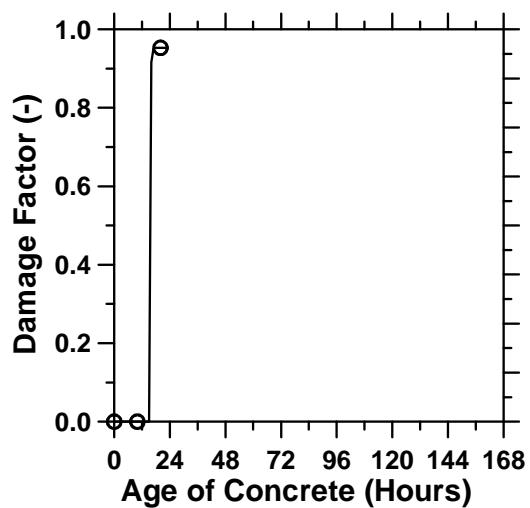


Fig. (h)

Figure A.5: Pavement with a D/2 saw-cut depth introduced at 15 hours.

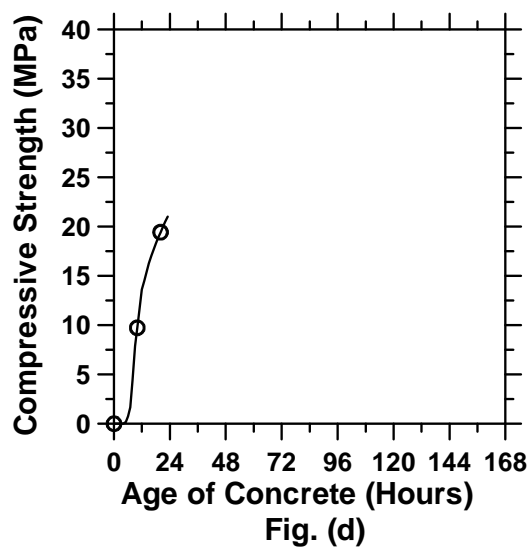
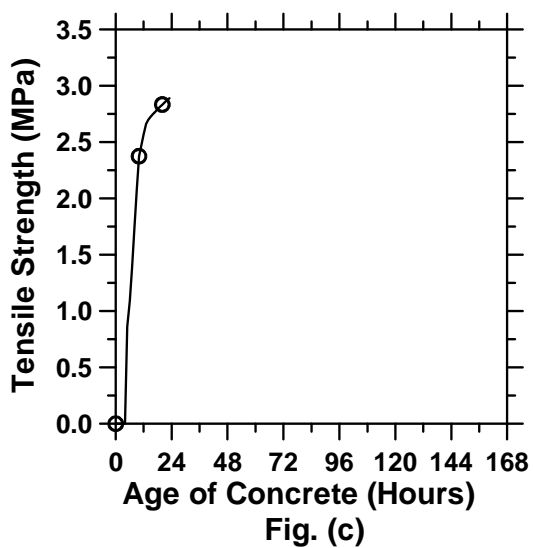
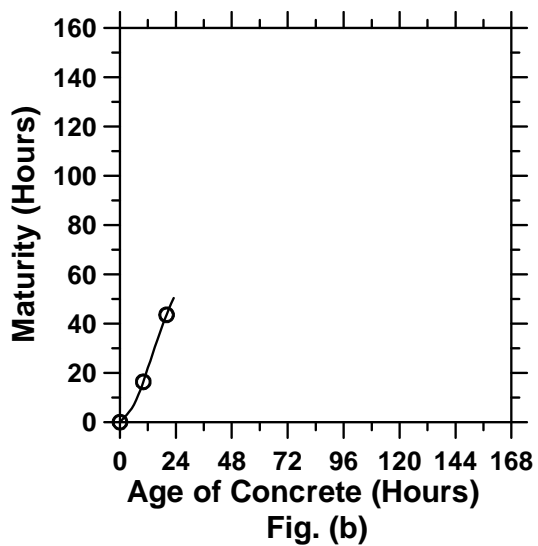
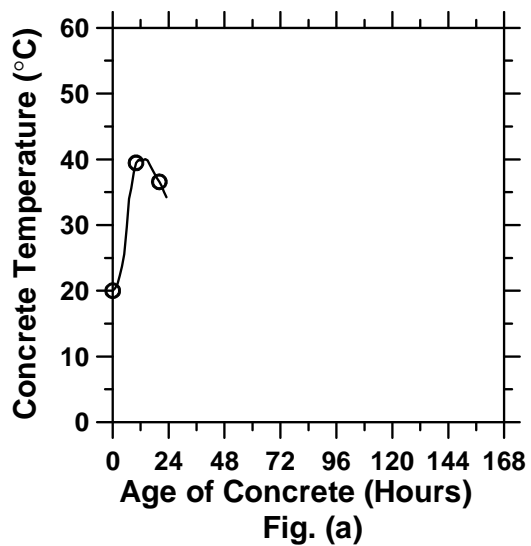


Figure A.6: Pavement with a D/2 saw-cut depth introduced at 18 hours (cont'd).

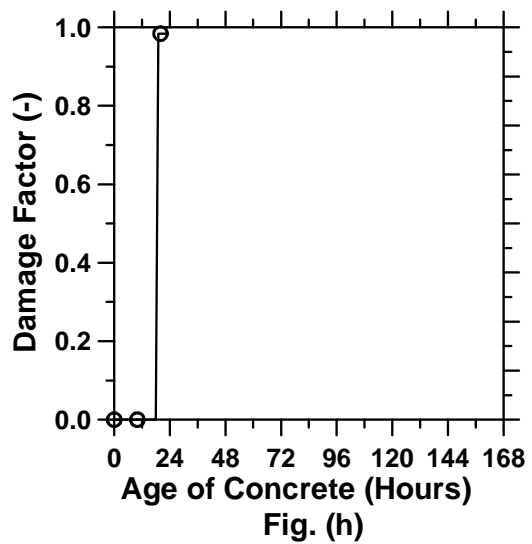
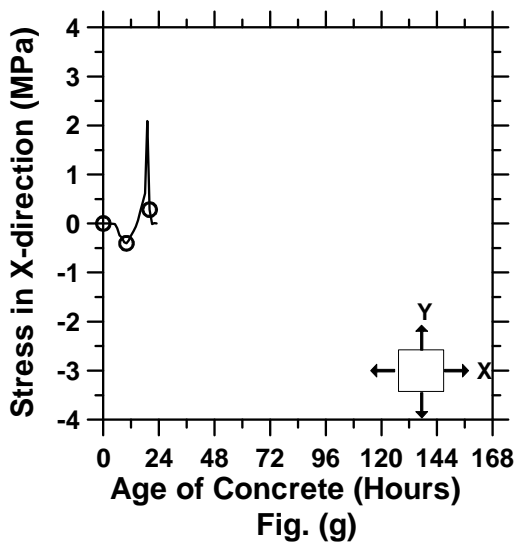
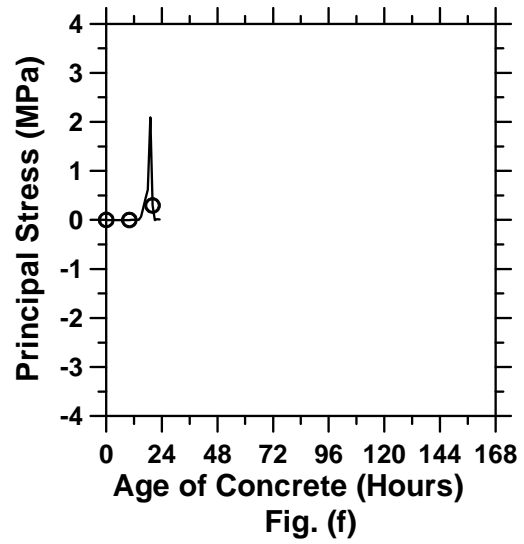
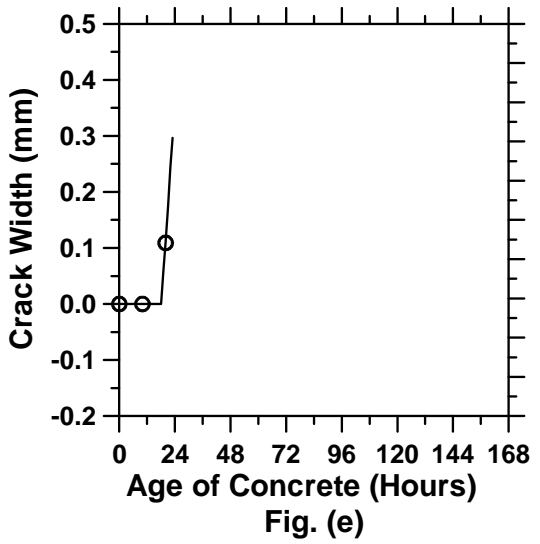


Figure A.6: Pavement with a D/2 saw-cut depth introduced at 18 hours.

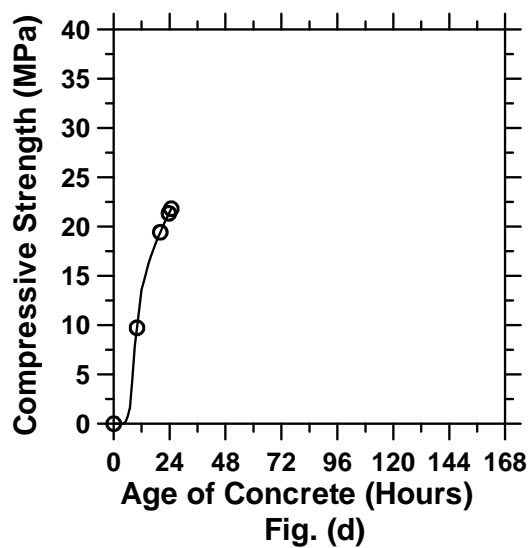
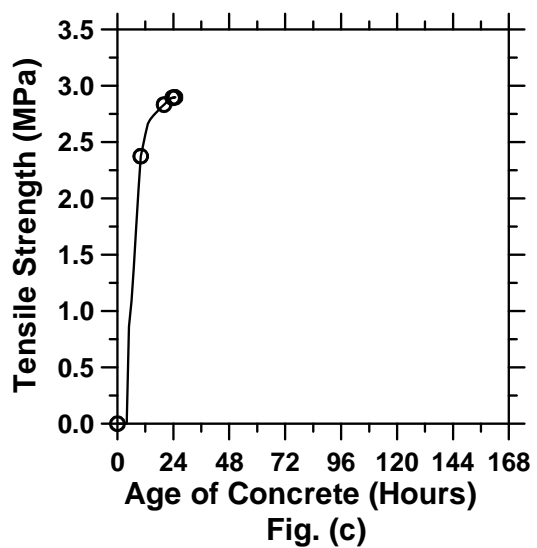
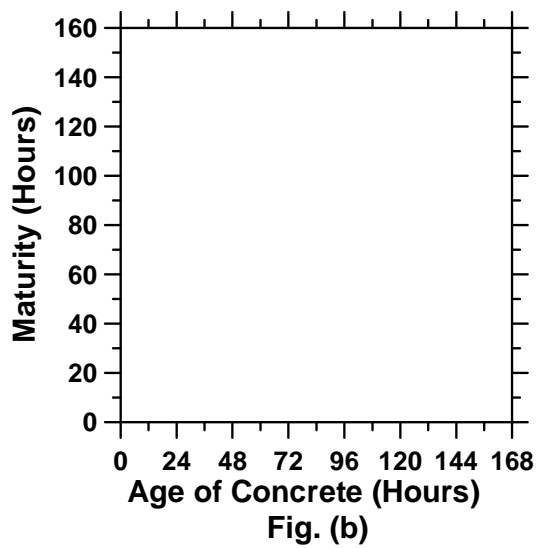
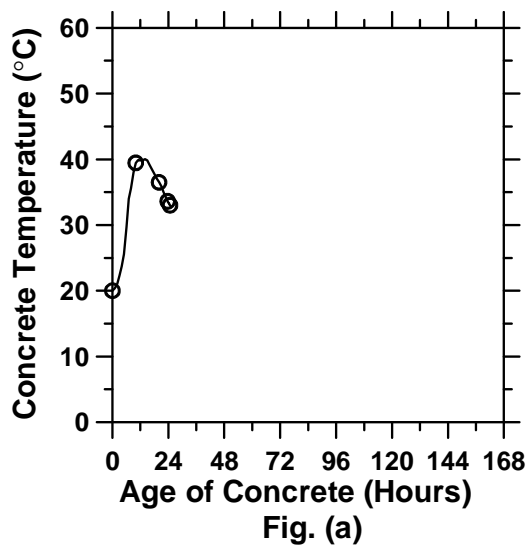


Figure A.7: Pavement with a D/2 saw-cut depth introduced at 24 hours (cont'd).

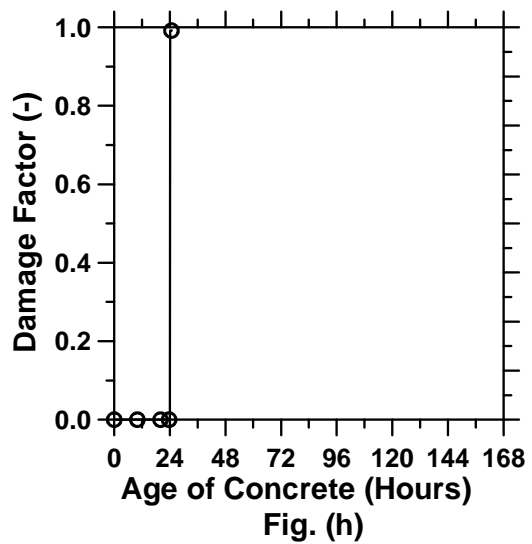
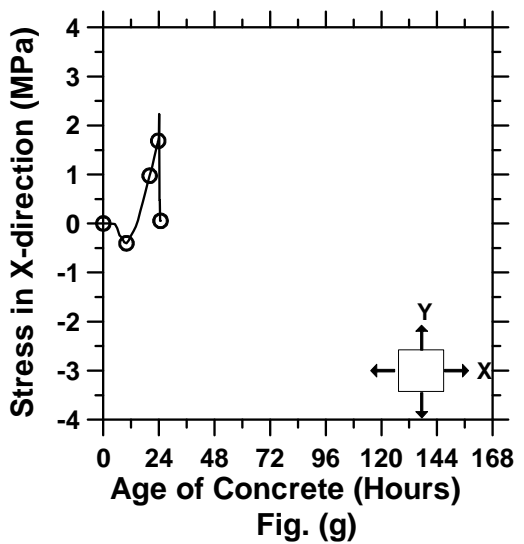
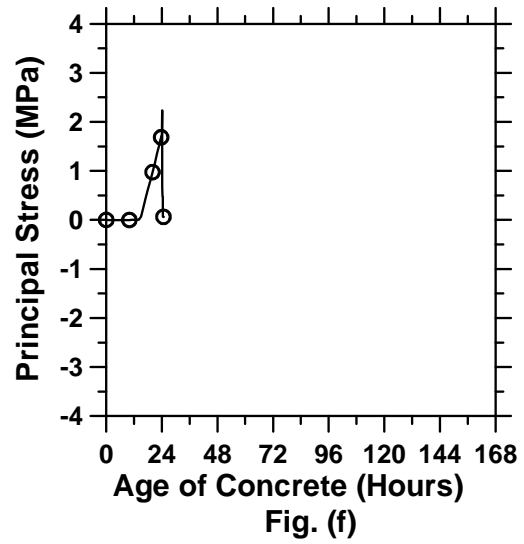
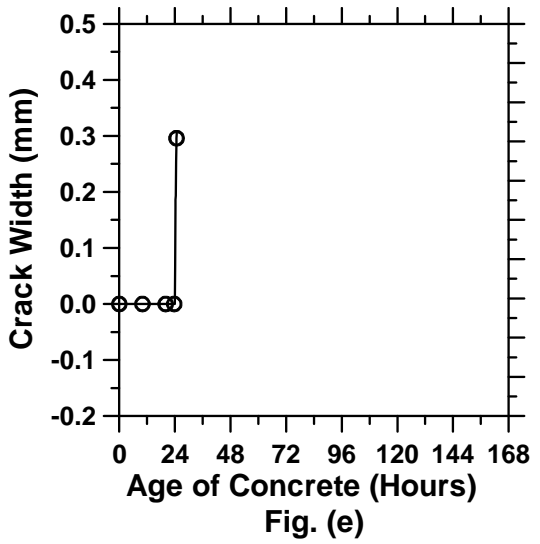


Figure A.7: Pavement with a D/2 saw-cut depth introduced at 24 hours.

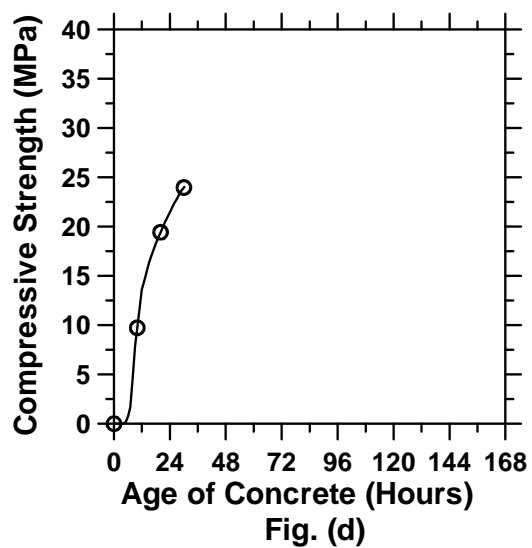
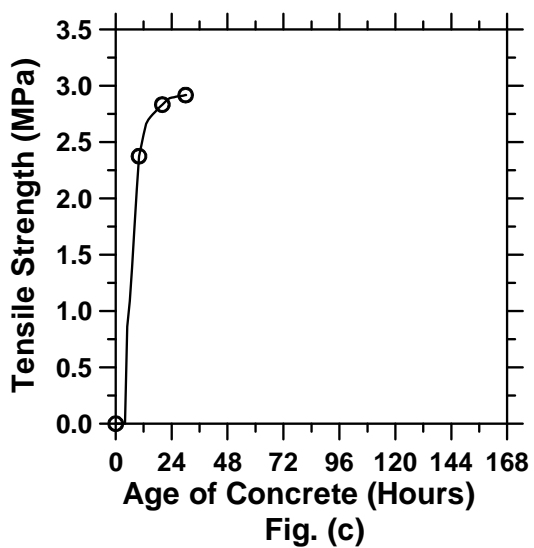
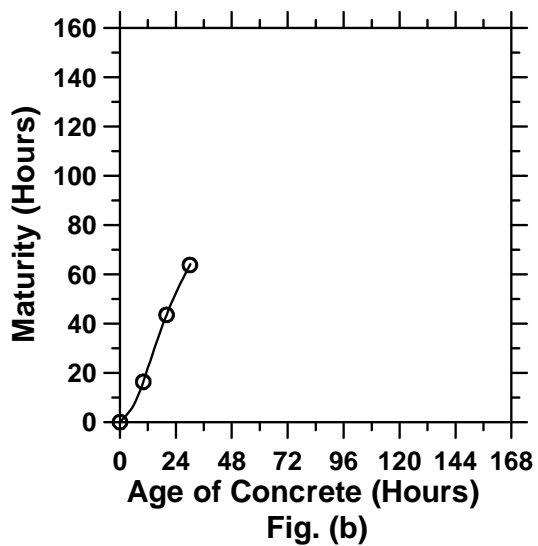
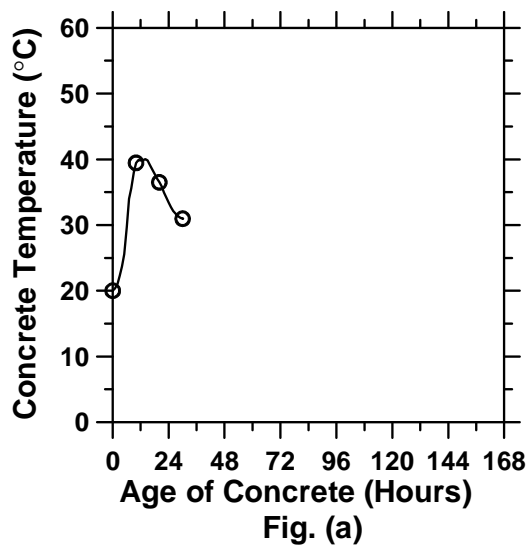


Figure A.8: Pavement with a D/2 saw-cut depth introduced at 30 hours (cont'd).

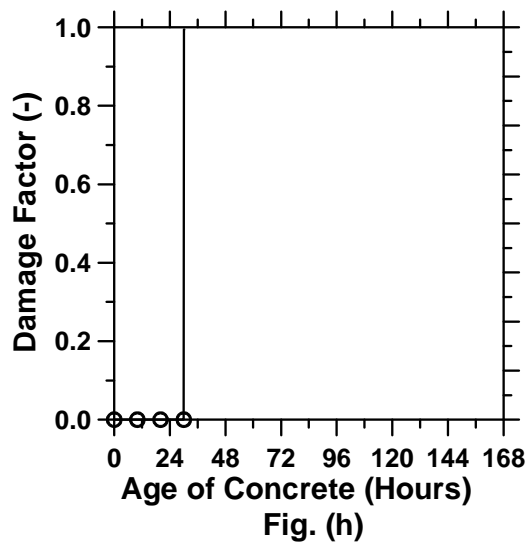
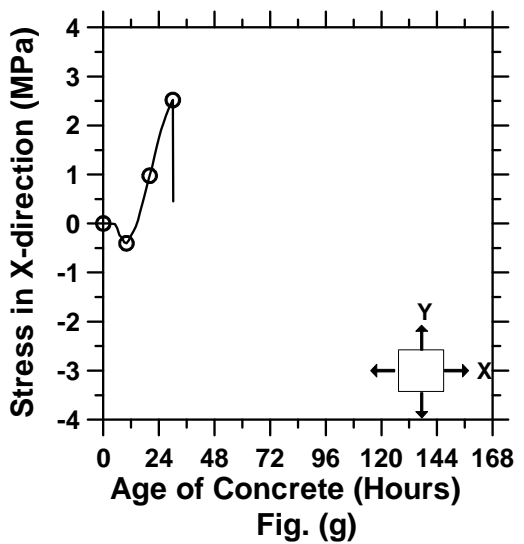
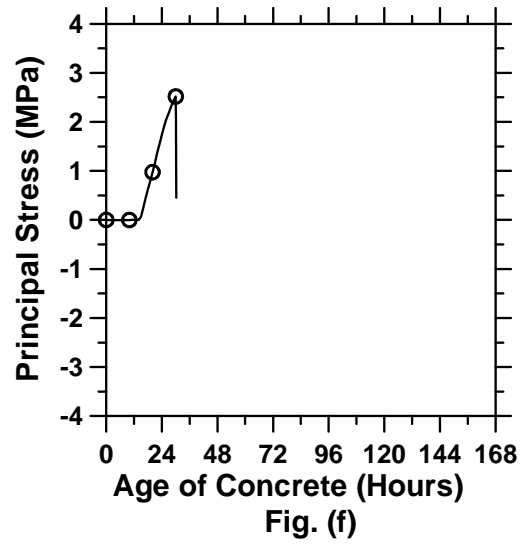
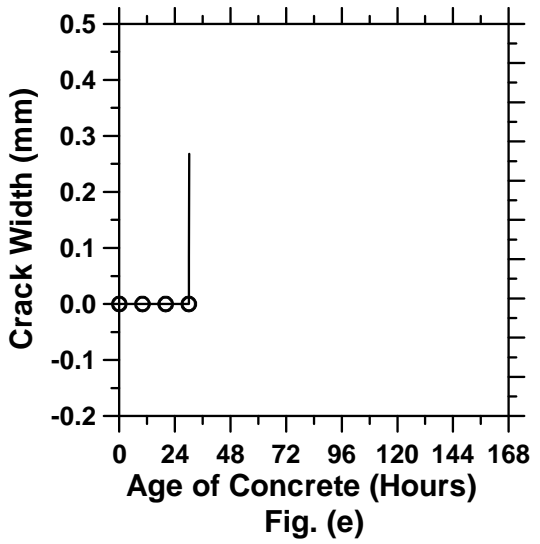


Figure A.8: Pavement with a D/2 saw-cut depth introduced at 30 hours.

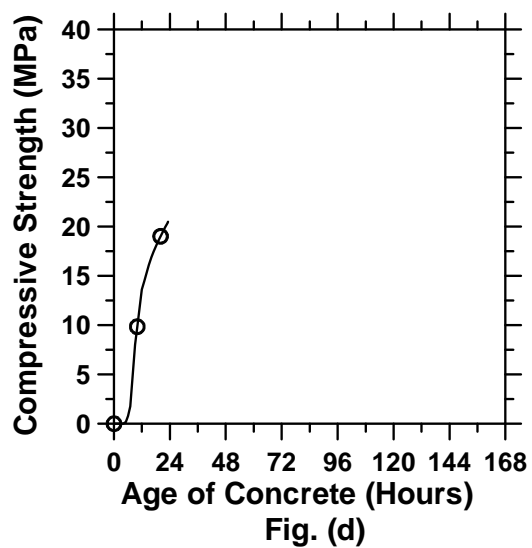
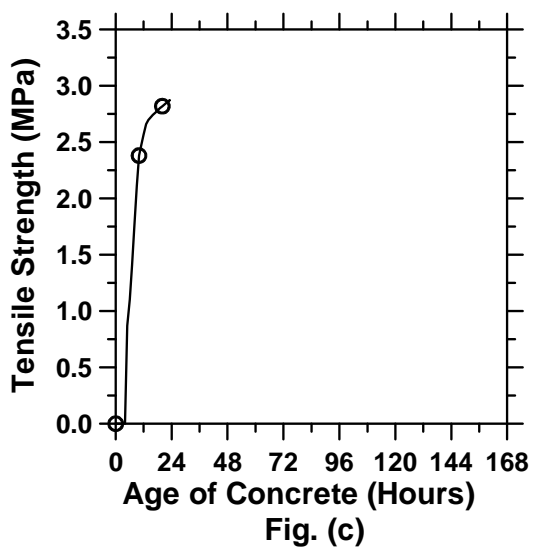
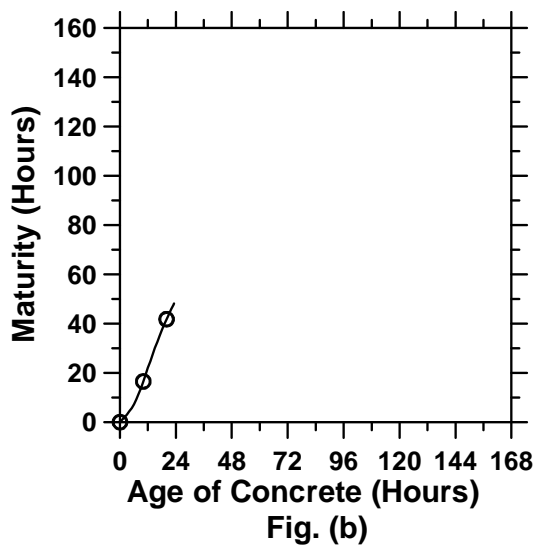
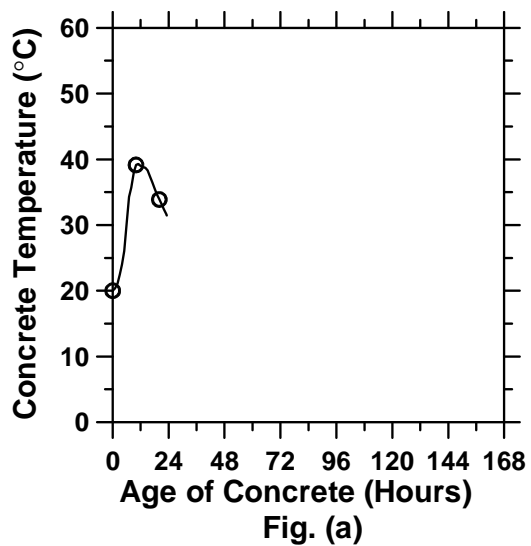


Figure A.9: Pavement with a D/3 saw-cut depth introduced at 0 hour (cont'd).

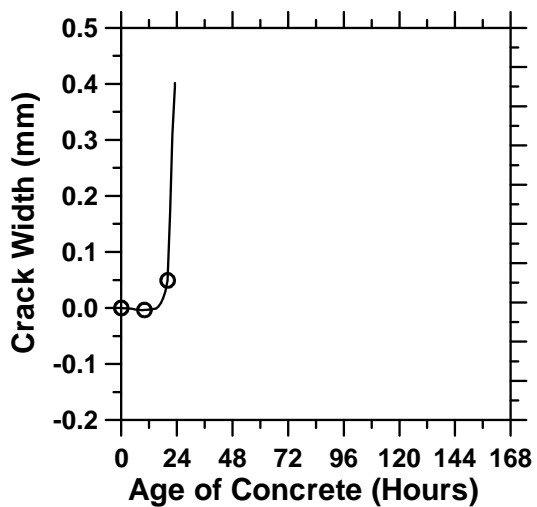


Fig. (e)

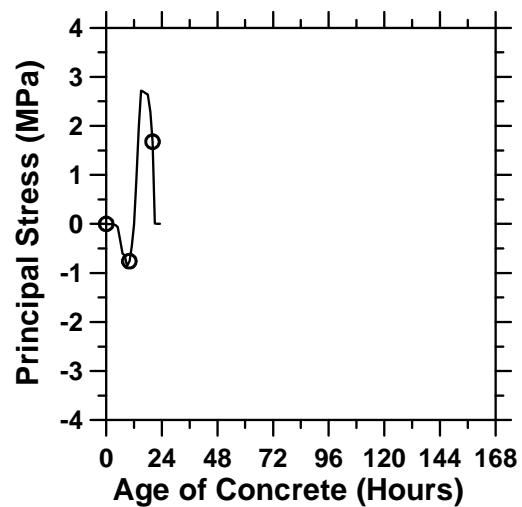


Fig. (f)

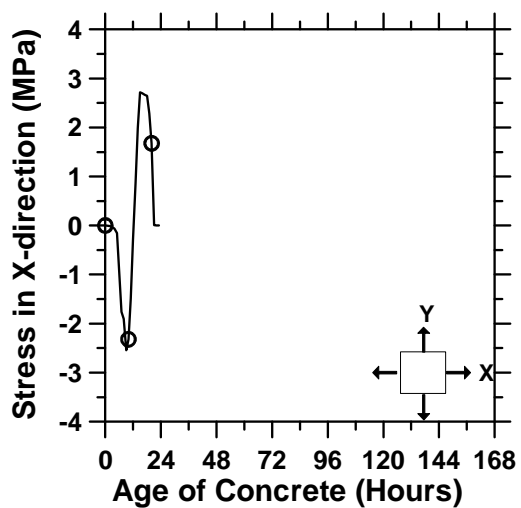


Fig. (g)

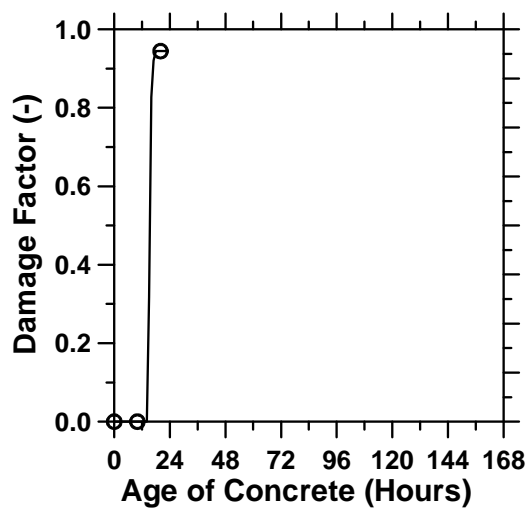


Fig. (h)

Figure A.9: Pavement with a D/3 saw-cut depth introduced at 0 hour.

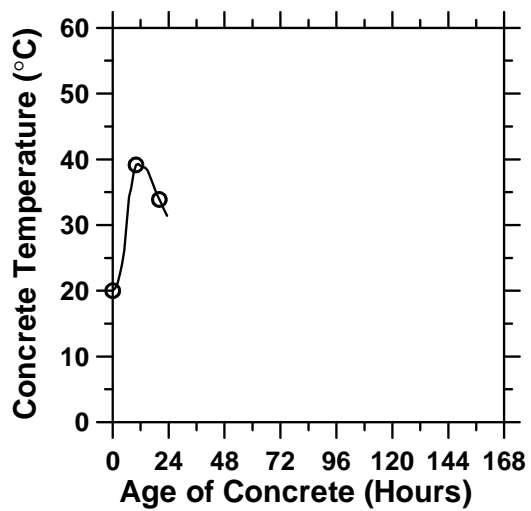


Fig. (a)

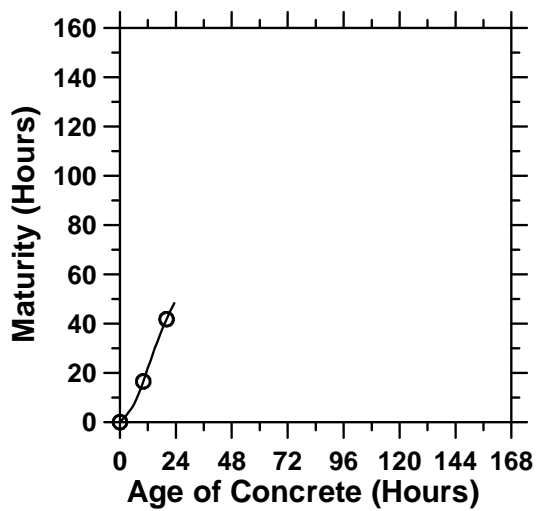


Fig. (b)

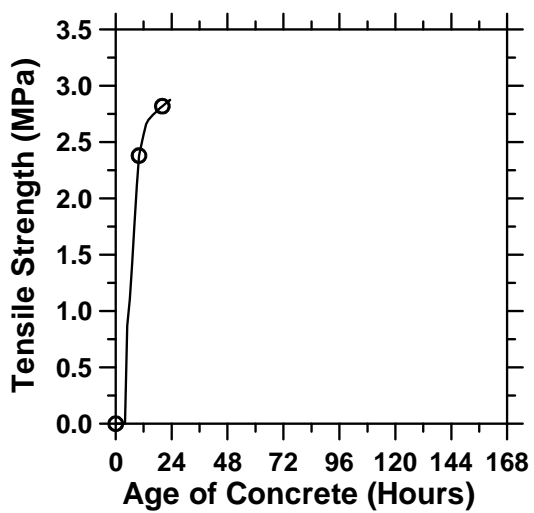


Fig. (c)

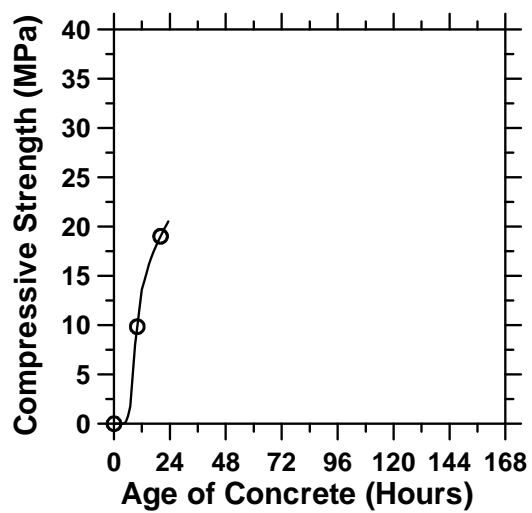


Fig. (d)

Figure A.10: Pavement with a D/3 saw-cut depth introduced at 6 hours (cont'd).

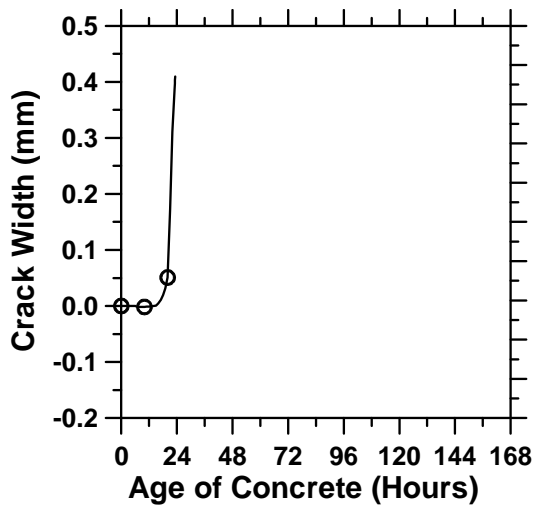


Fig. (e)

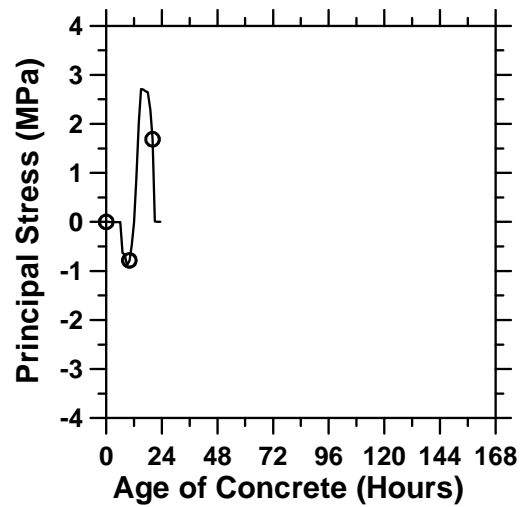


Fig. (f)

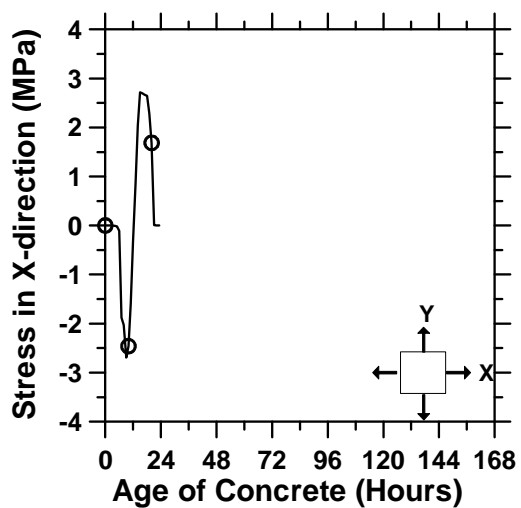


Fig. (g)

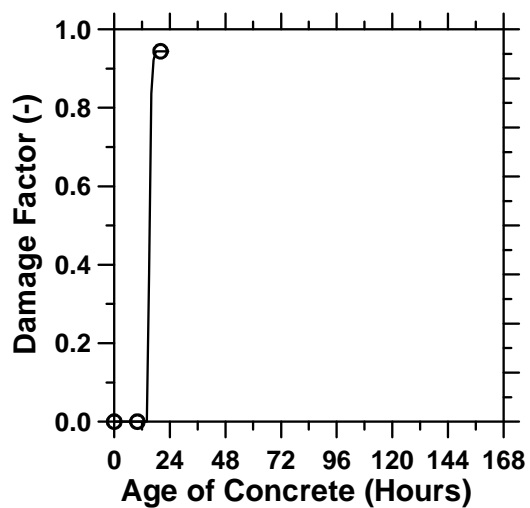


Fig. (h)

Figure A.10: Pavement with a D/3 saw-cut depth introduced at 6 hours.

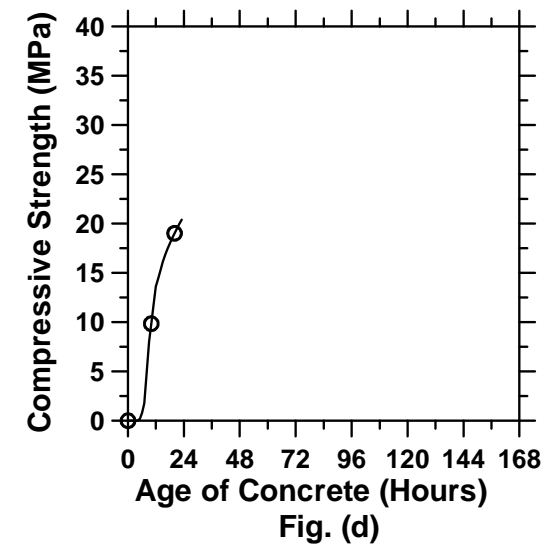
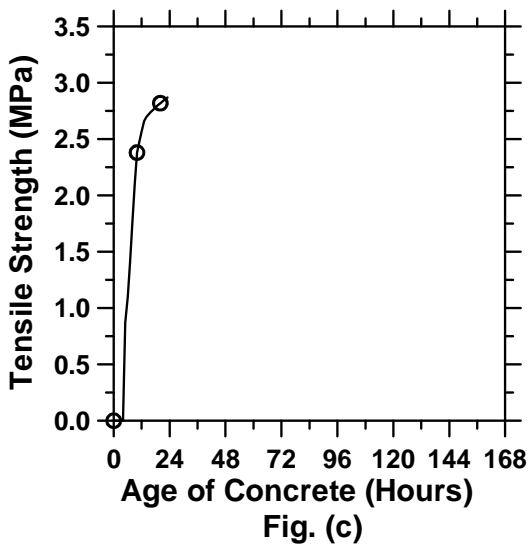
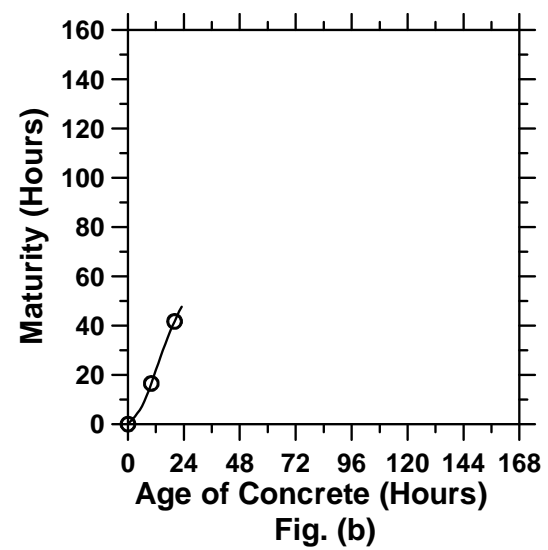
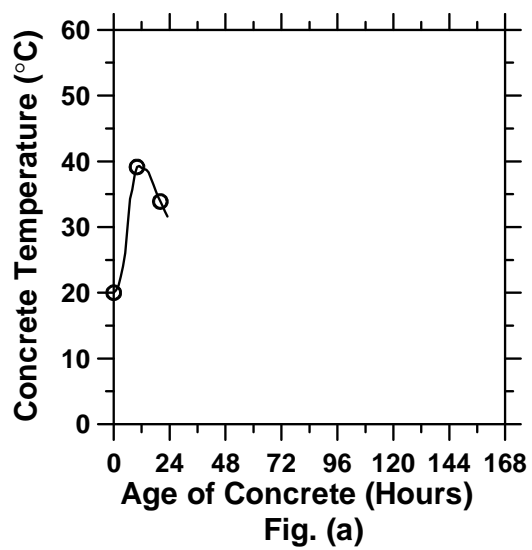


Figure A.11: Pavement with a D/3 saw-cut depth introduced at 9 hours (cont'd).

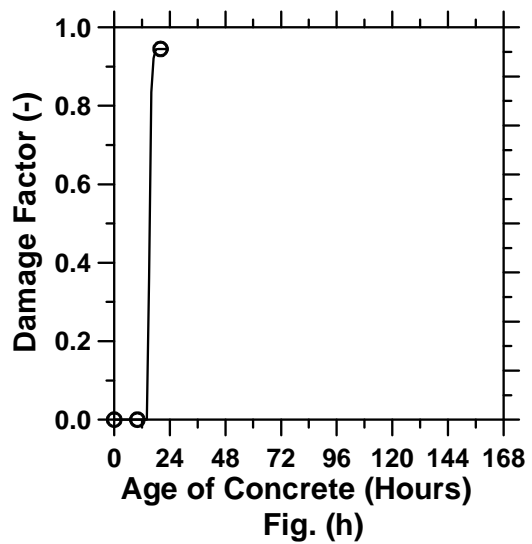
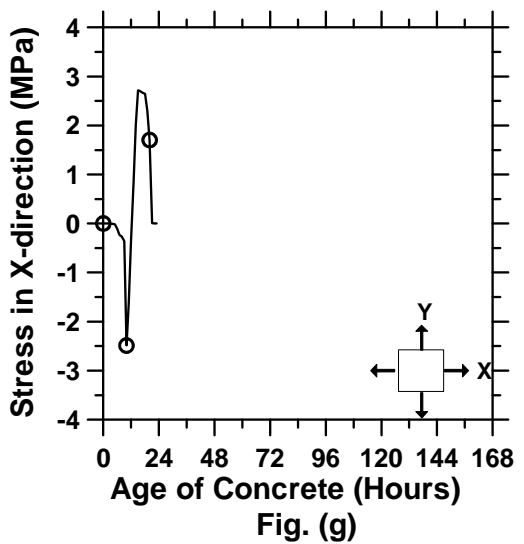
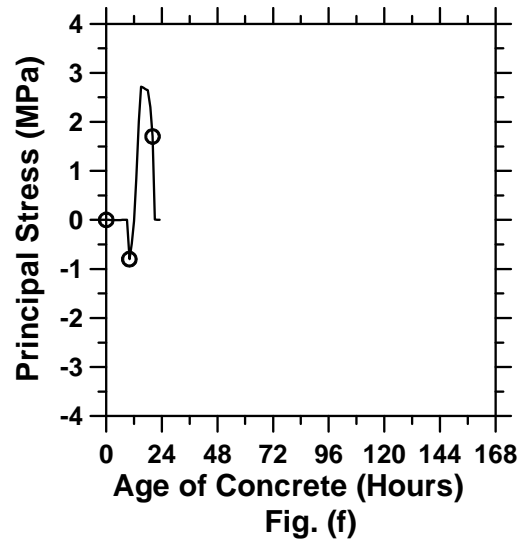
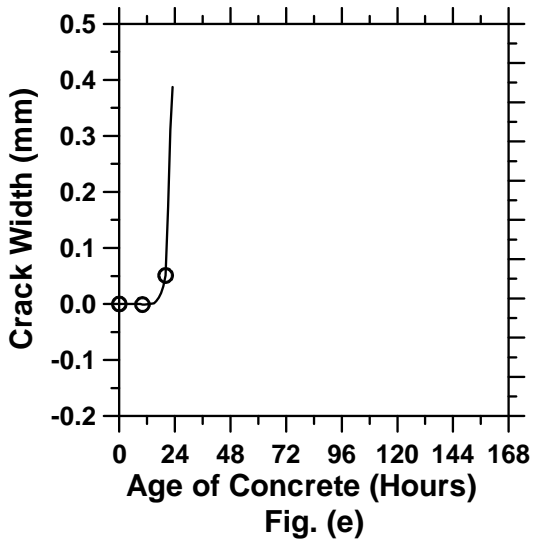


Figure A.11: Pavement with a D/3 saw-cut depth introduced at 9 hours.

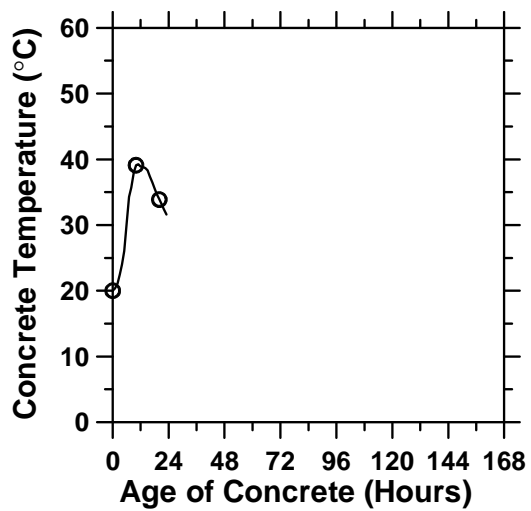


Fig. (a)

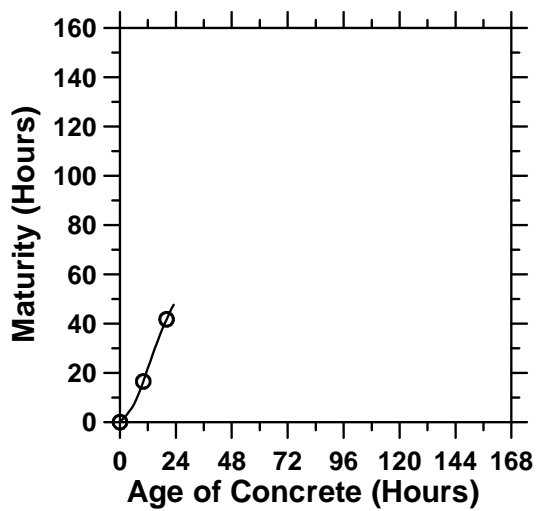


Fig. (b)

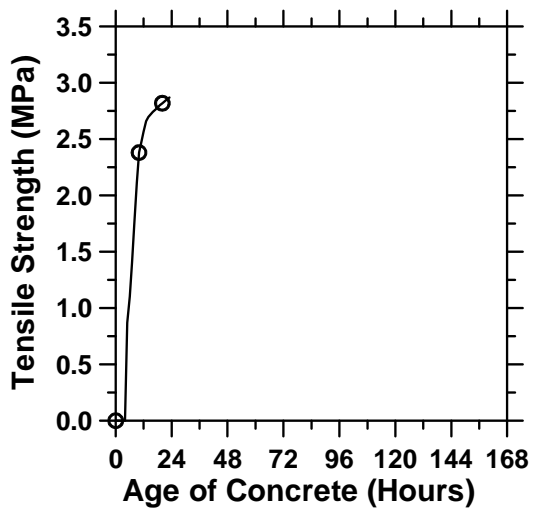


Fig. (c)

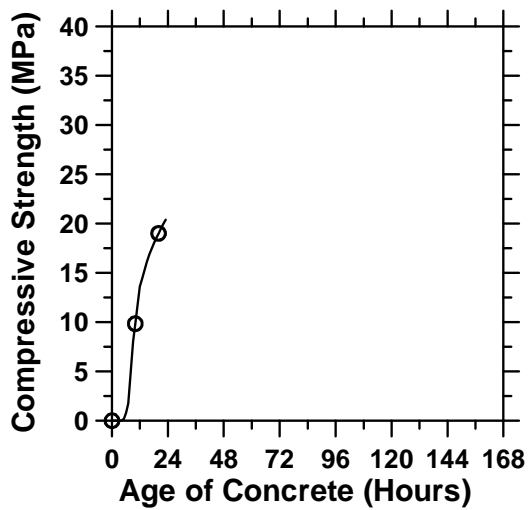


Fig. (d)

Figure A.12: Pavement with a D/3 saw-cut depth introduced at 12 hours (cont'd).

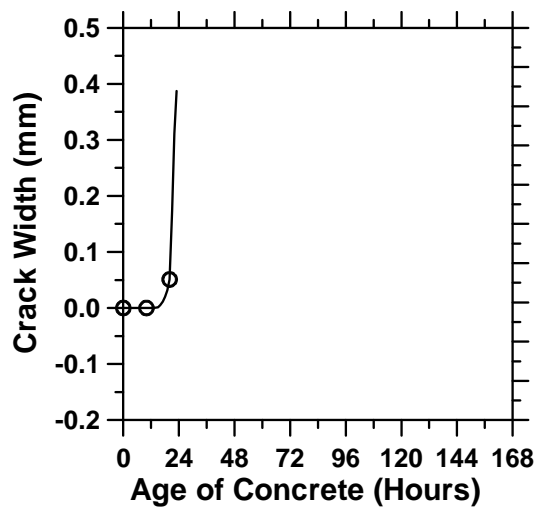


Fig. (e)

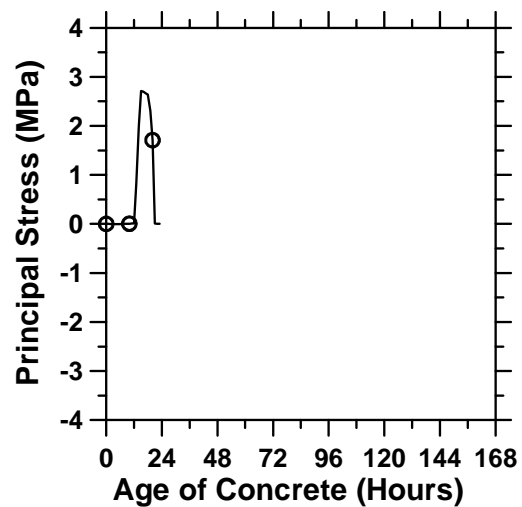


Fig. (f)

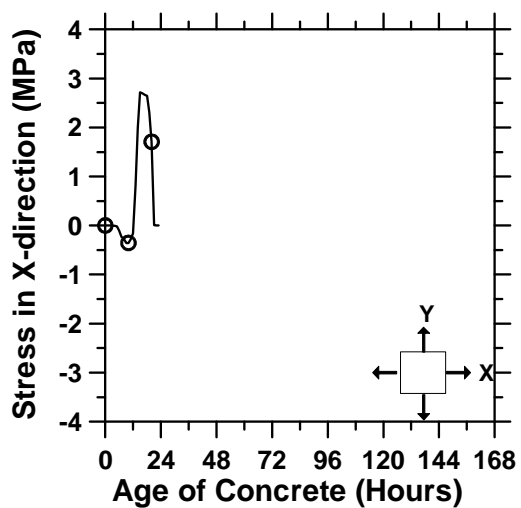


Fig. (g)

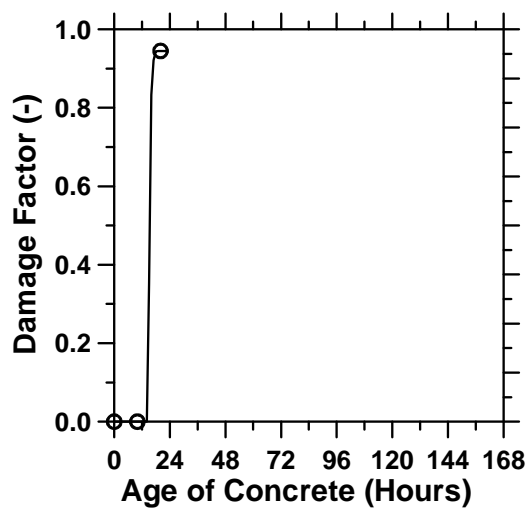


Fig. (h)

Figure A.12: Pavement with a D/3 saw-cut depth introduced at 12 hours.

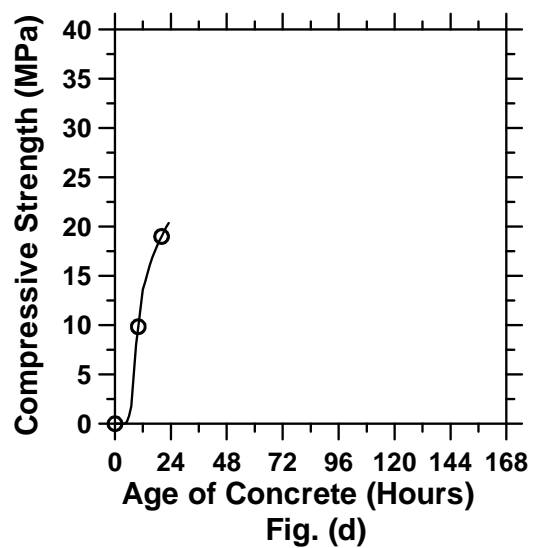
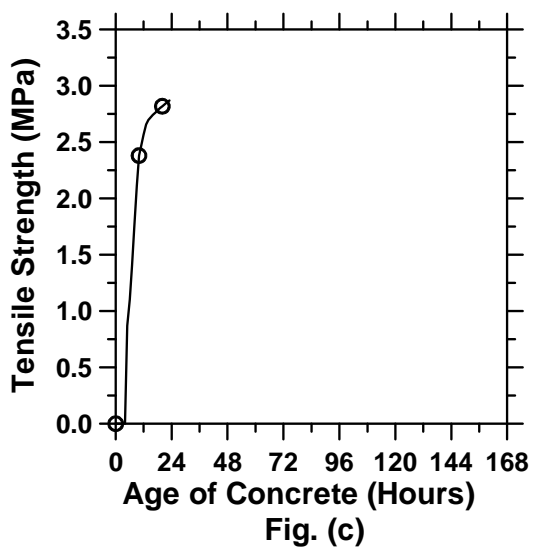
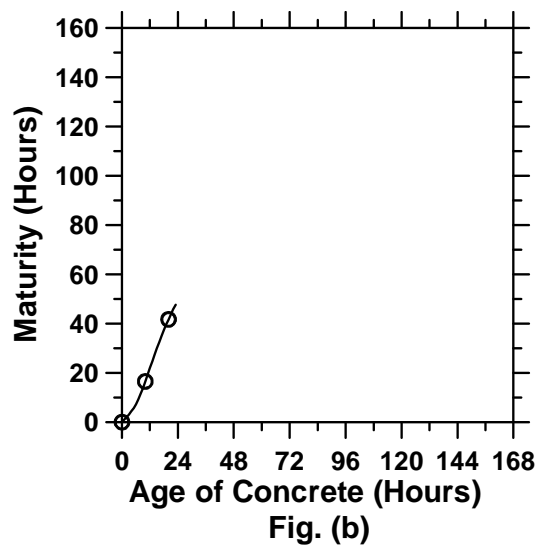
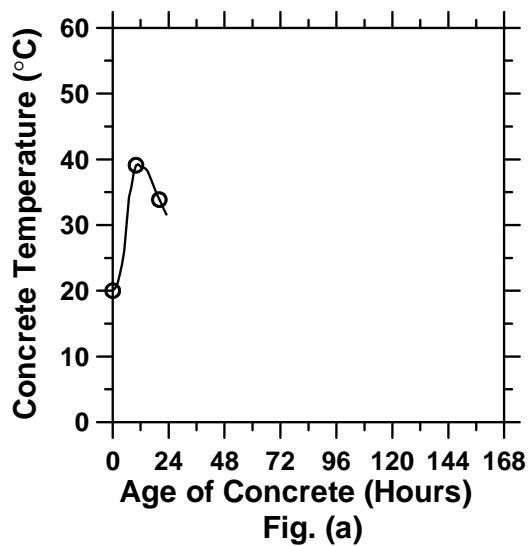


Figure A.13: Pavement with a D/3 saw-cut depth introduced at 15 hours (cont'd).

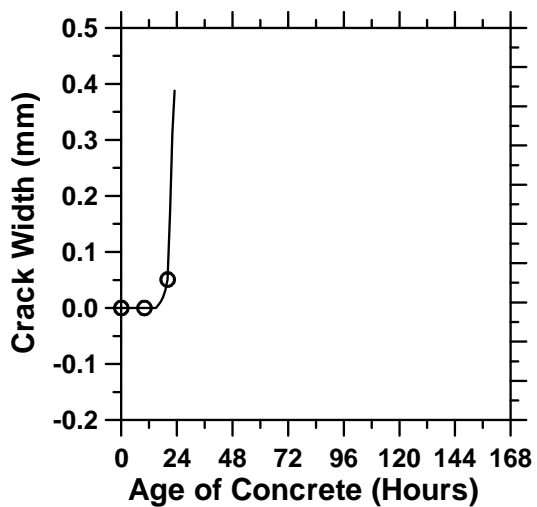


Fig. (e)

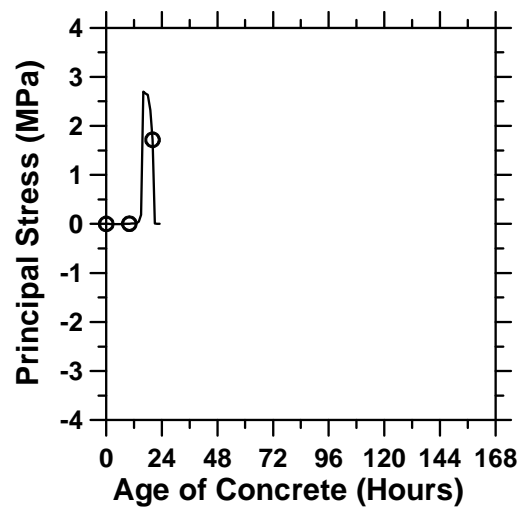


Fig. (f)

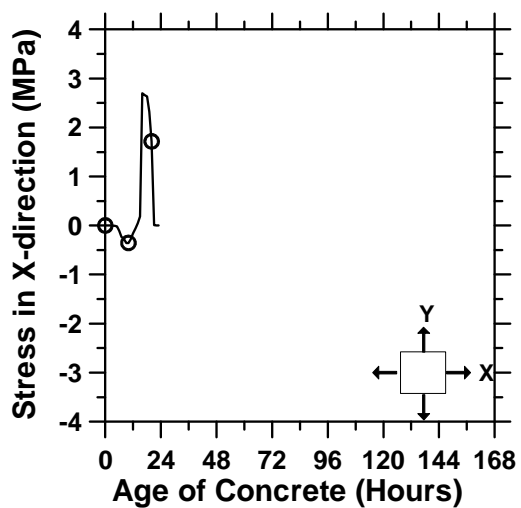


Fig. (g)

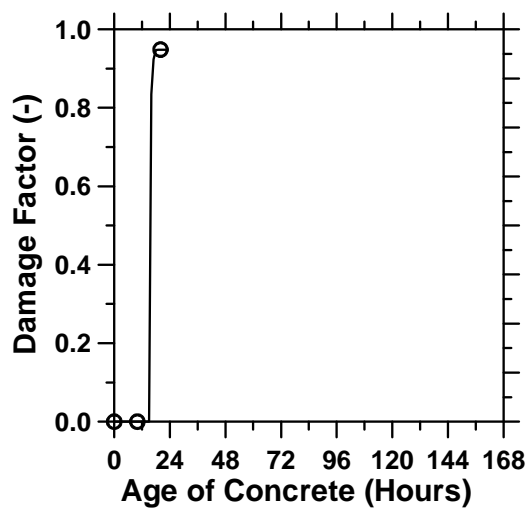


Fig. (h)

Figure A.13: Pavement with a D/3 saw-cut depth introduced at 15 hours.

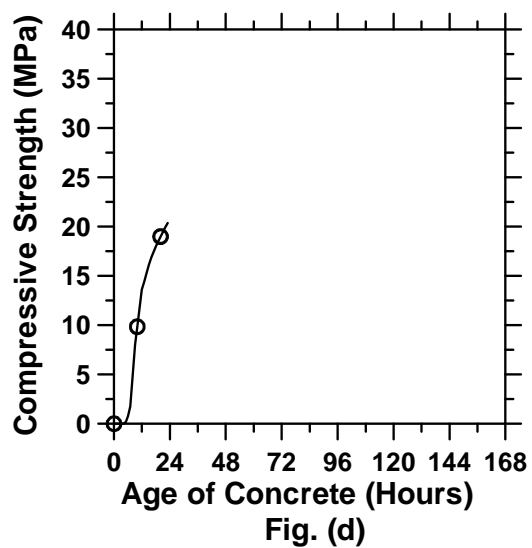
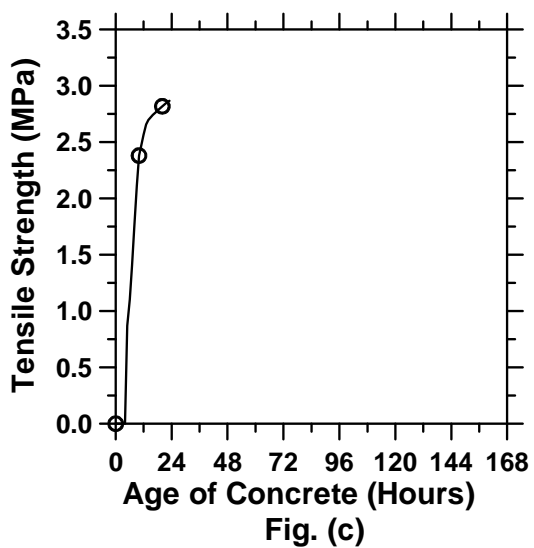
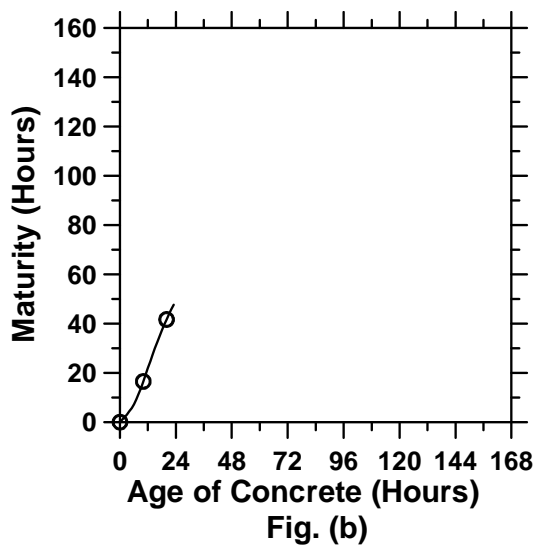
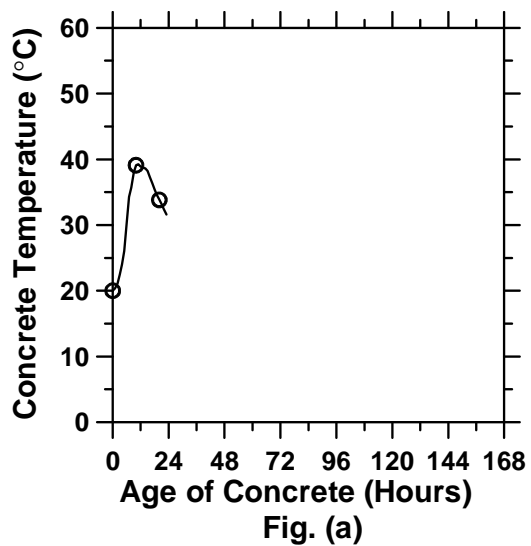


Figure A.14: Pavement with a D/3 saw-cut depth introduced at 18 hours (cont'd).

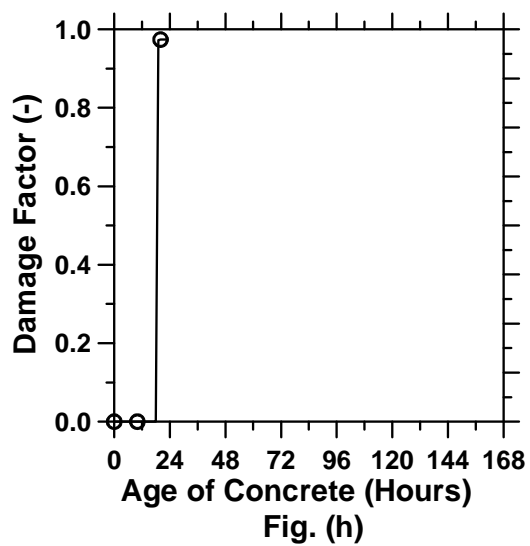
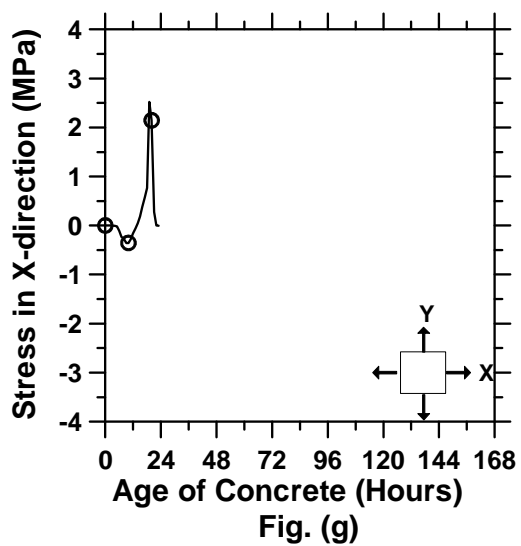
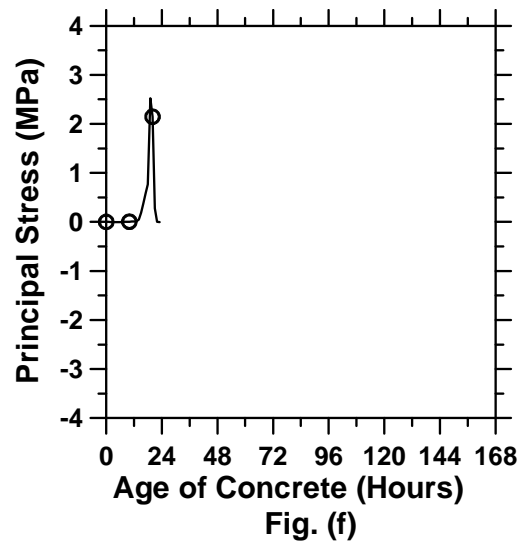
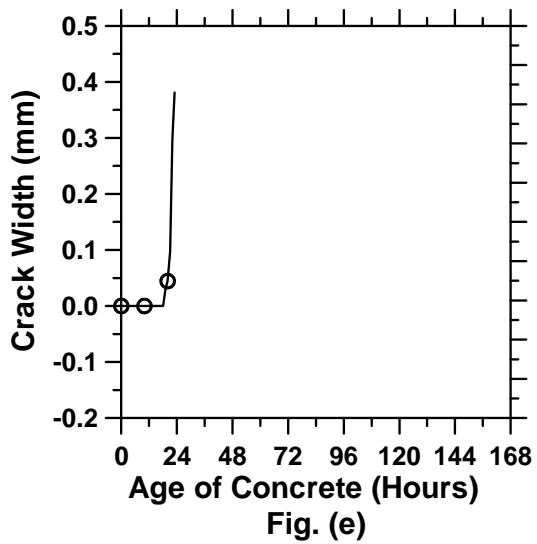


Figure A.14: Pavement with a D/3 saw-cut depth introduced at 18 hours.

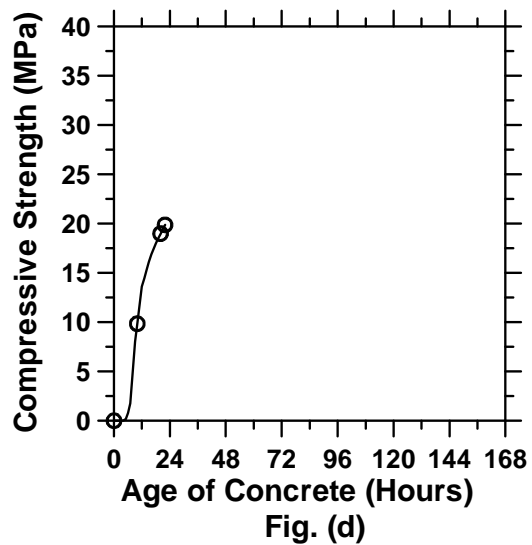
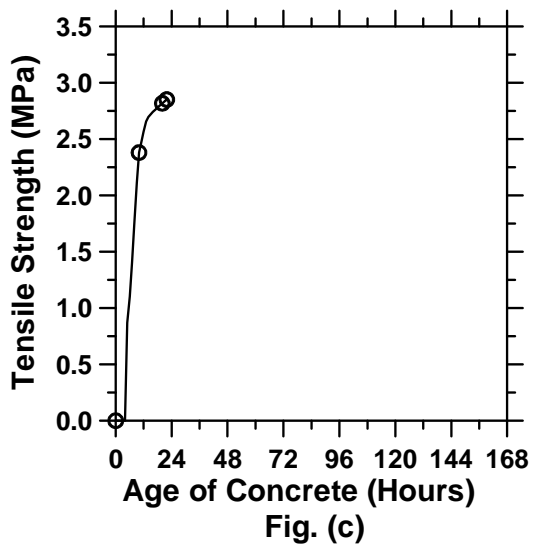
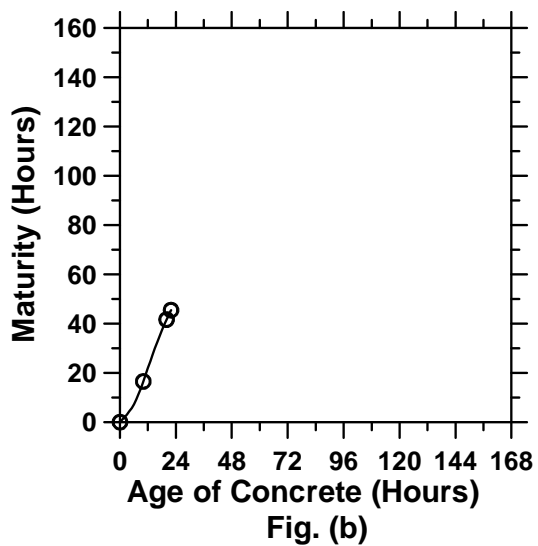
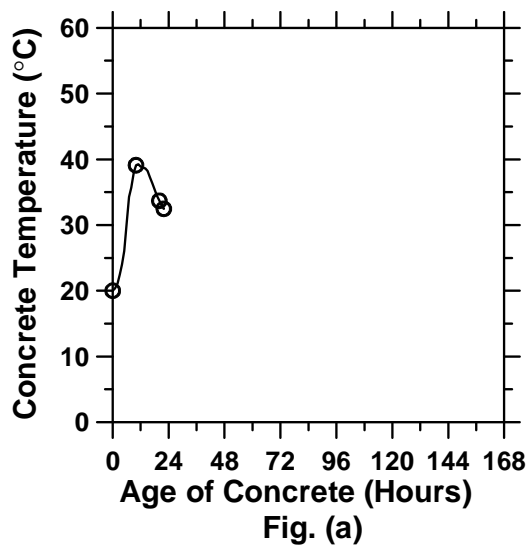


Figure A.15: Pavement with a D/3 saw-cut depth introduced at 21 hours (cont'd).

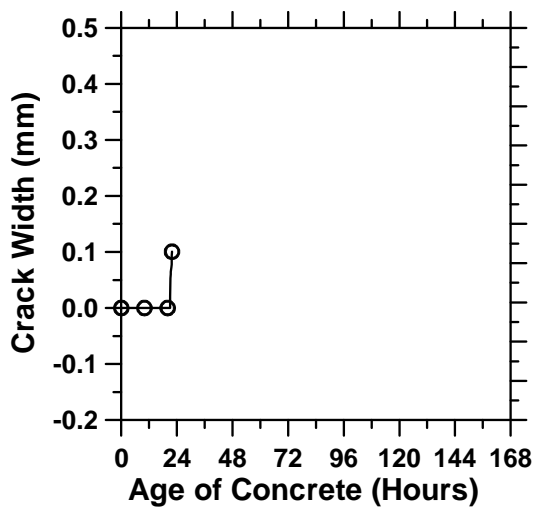


Fig. (e)

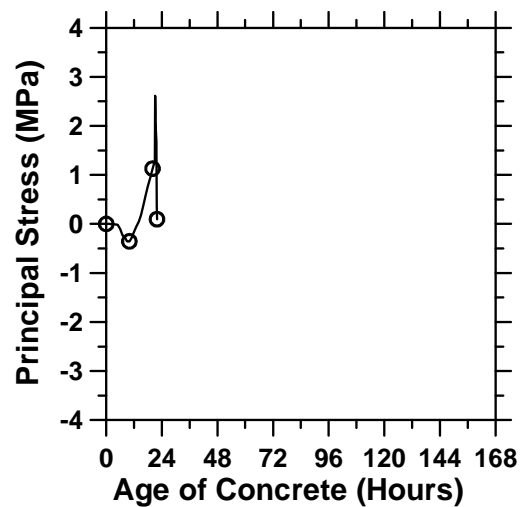


Fig. (f)

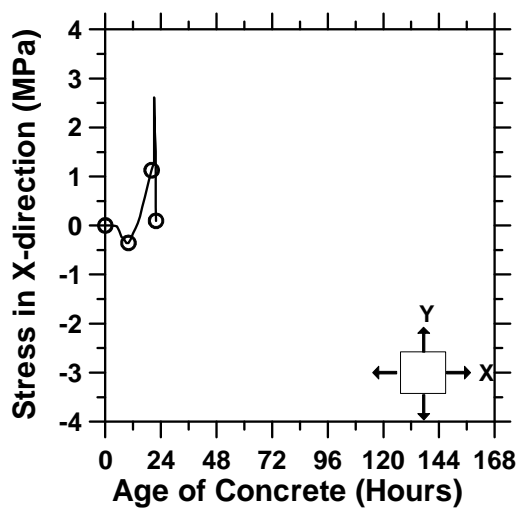


Fig. (g)

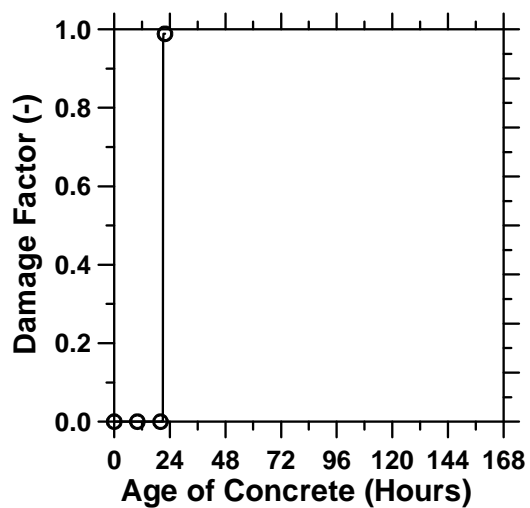


Fig. (h)

Figure A.15: Pavement with a D/3 saw-cut depth introduced at 21 hours.

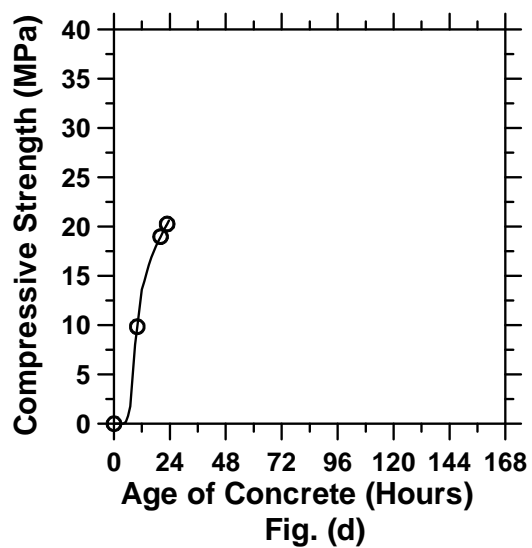
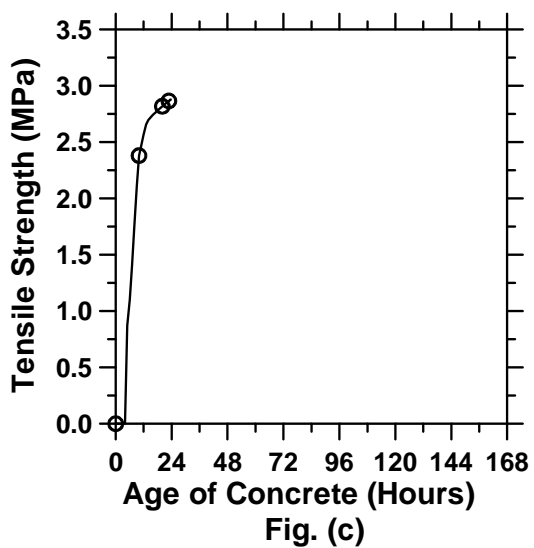
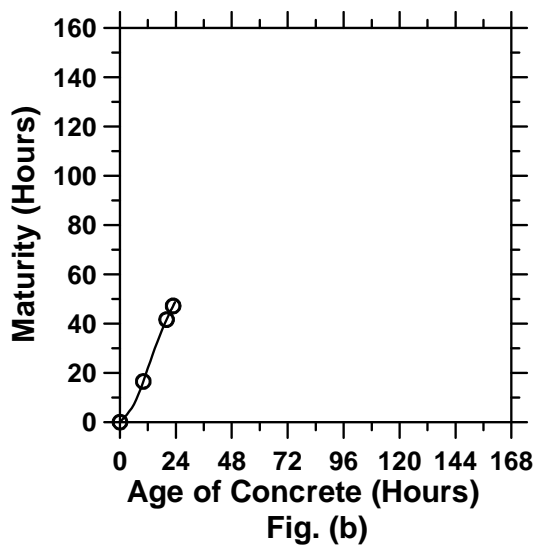
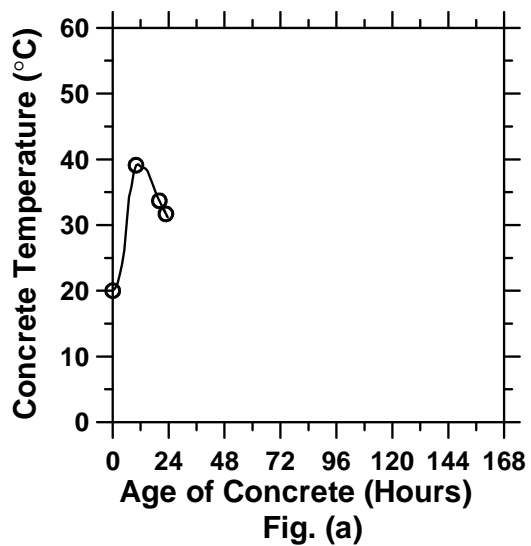


Figure A.16: Pavement with a D/3 saw-cut depth introduced at 22 hours (cont'd).

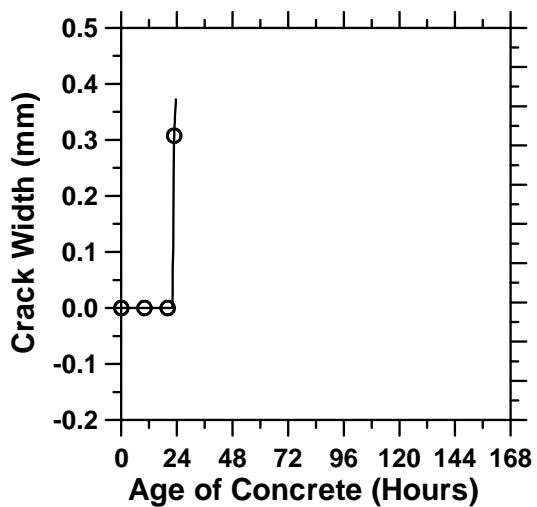


Fig. (e)

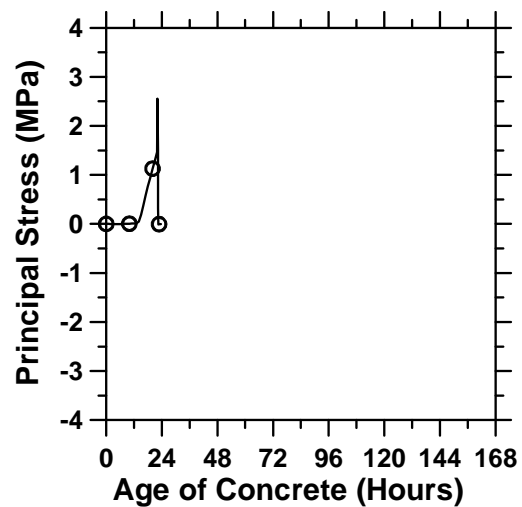


Fig. (f)

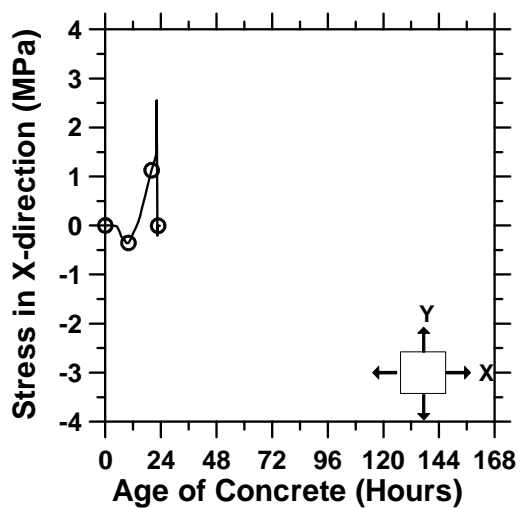


Fig. (g)

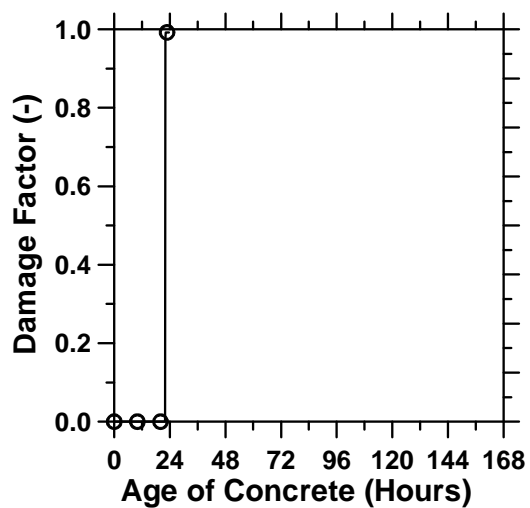


Fig. (h)

Figure A.16: Pavement with a D/3 saw-cut depth introduced at 22 hours.

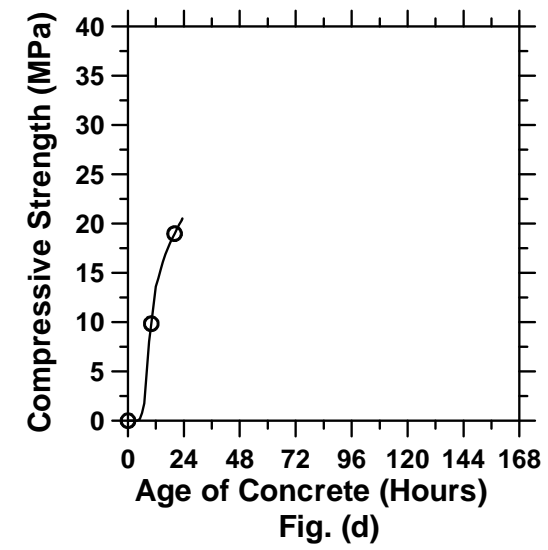
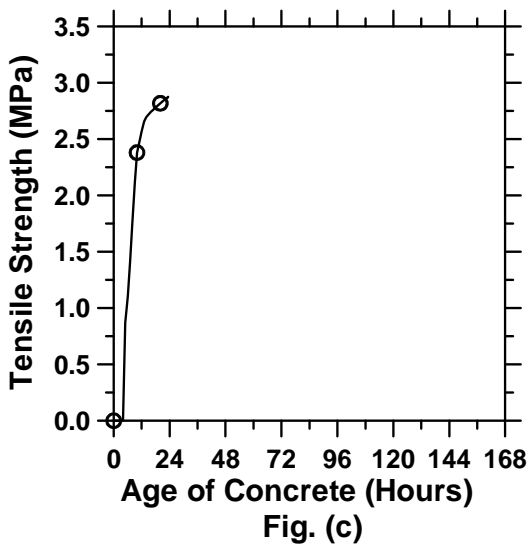
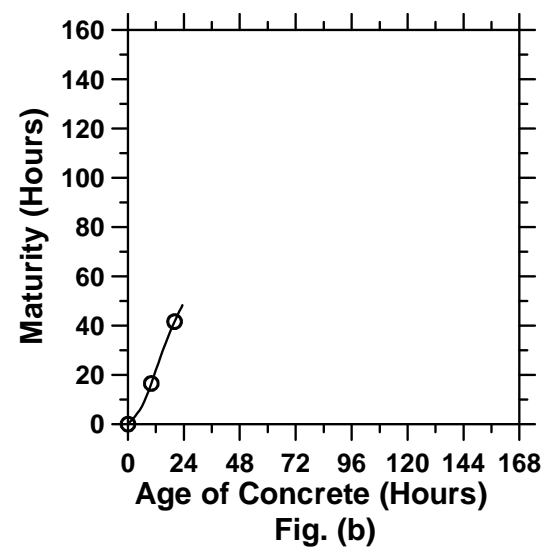
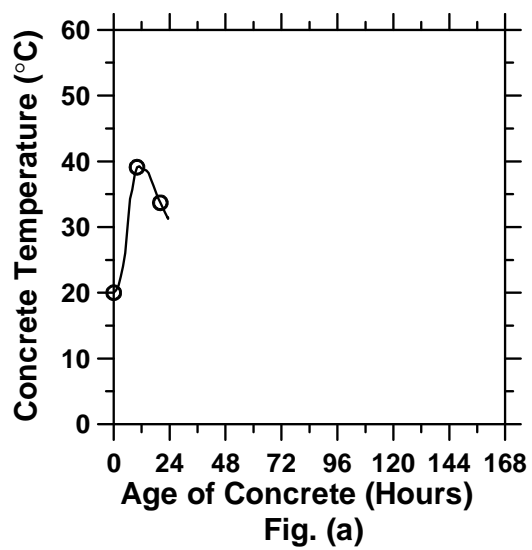


Figure A.17: Pavement with a D/3 saw-cut depth introduced at 23 hours (cont'd).

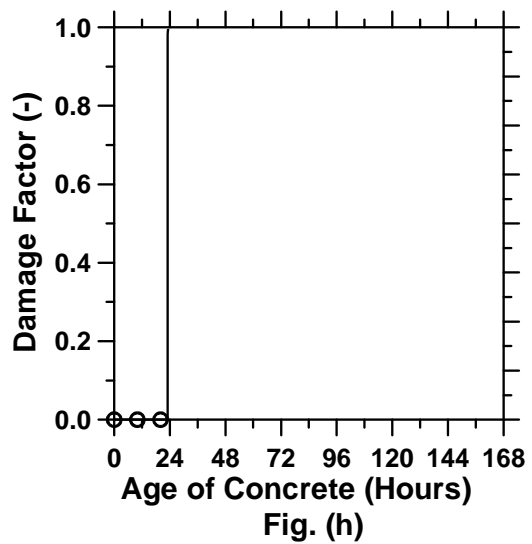
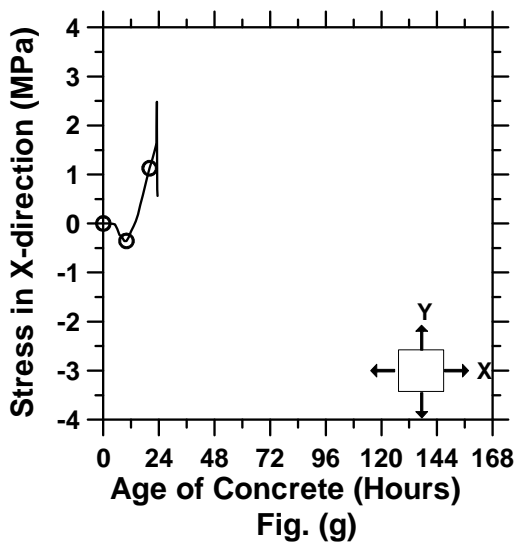
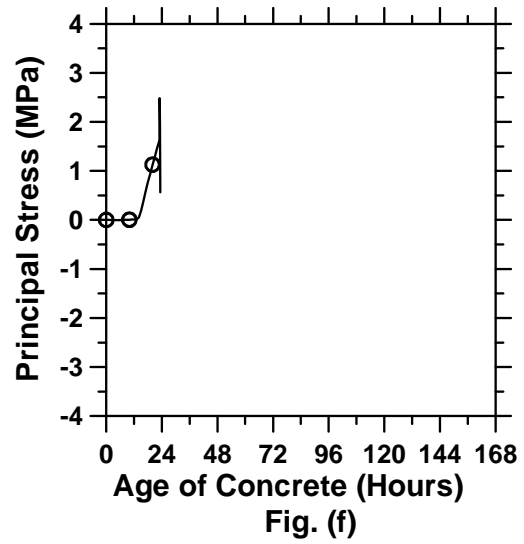
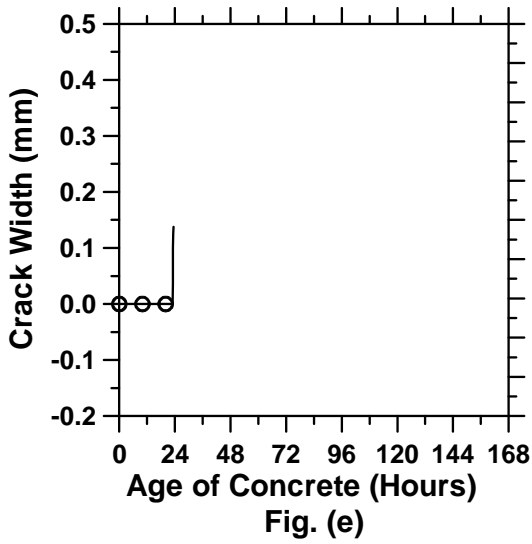


Figure A.17: Pavement with a D/3 saw-cut depth introduced at 23 hours.

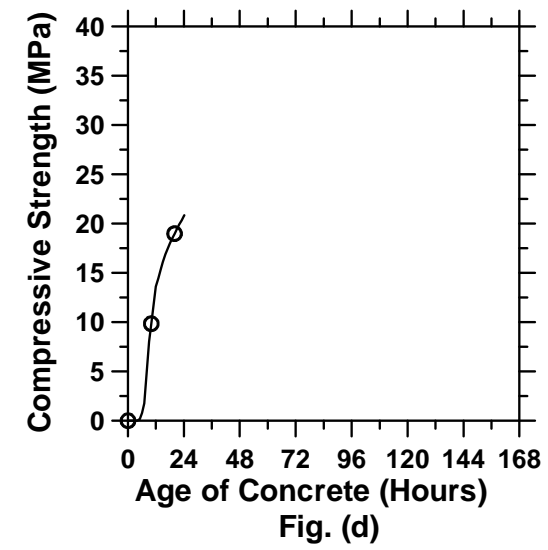
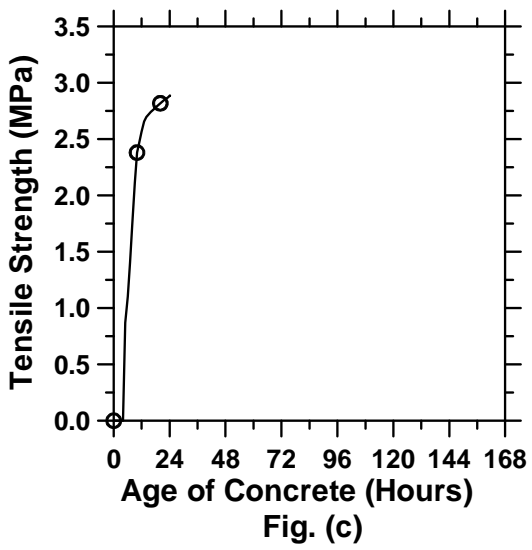
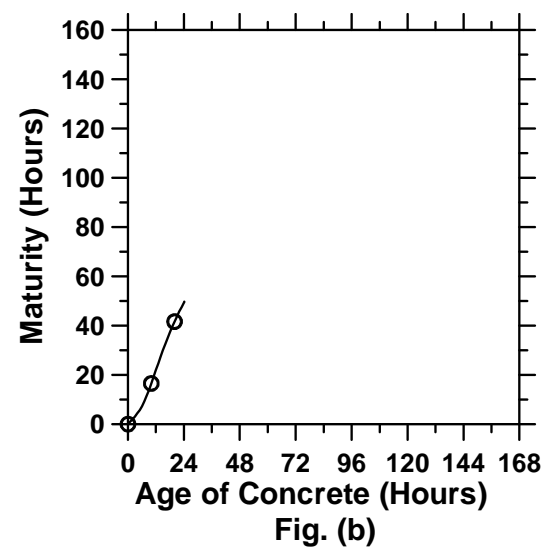
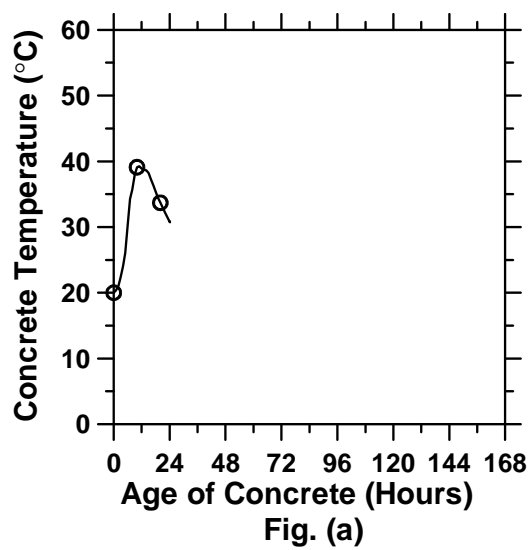


Figure A.18: Pavement with a D/3 saw-cut depth introduced at 24 hours (cont'd).

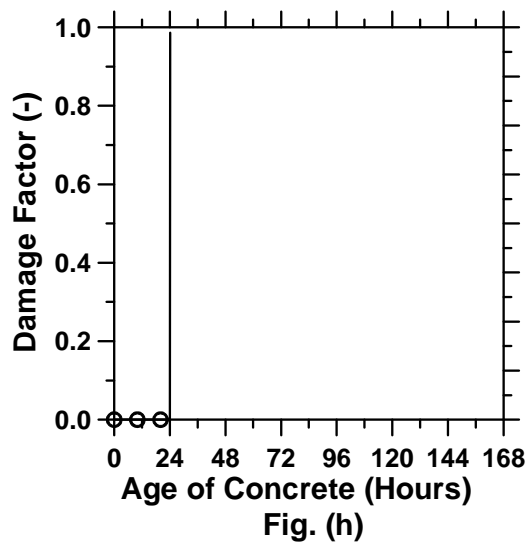
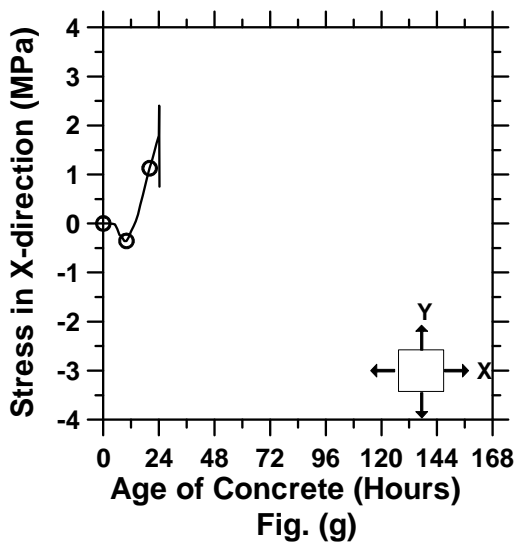
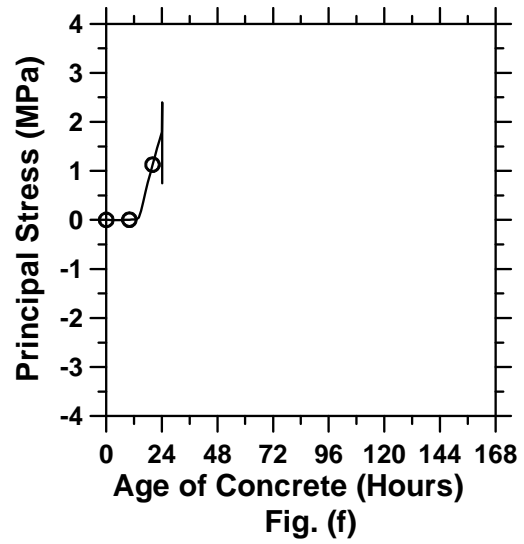
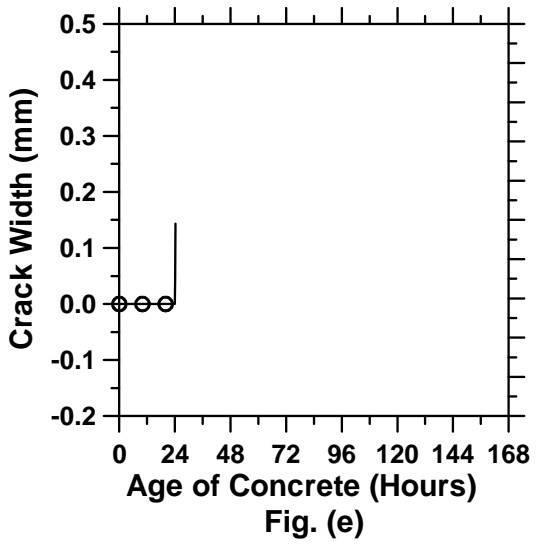


Figure A.18: Pavement with a D/3 saw-cut depth introduced at 24 hours.

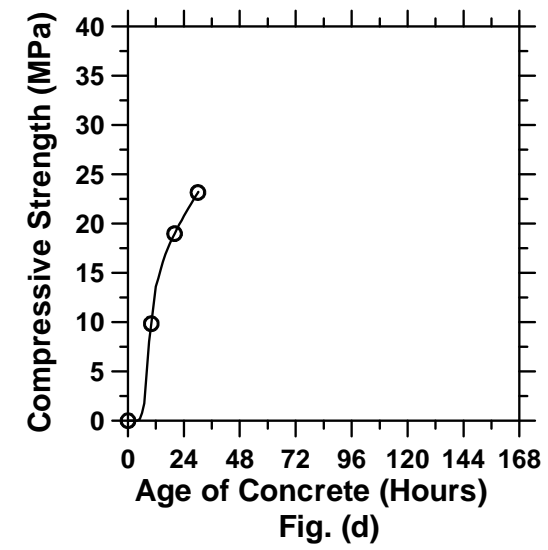
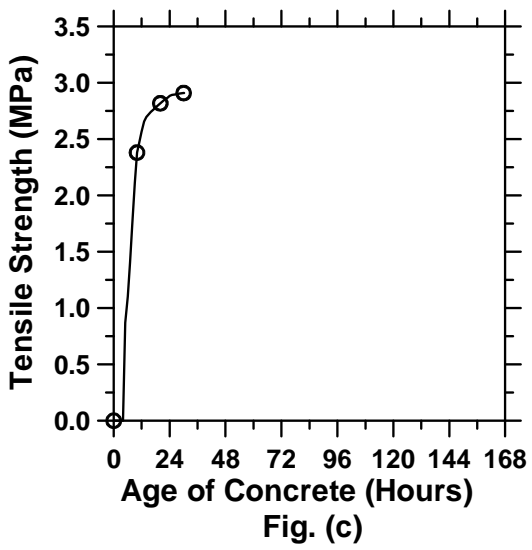
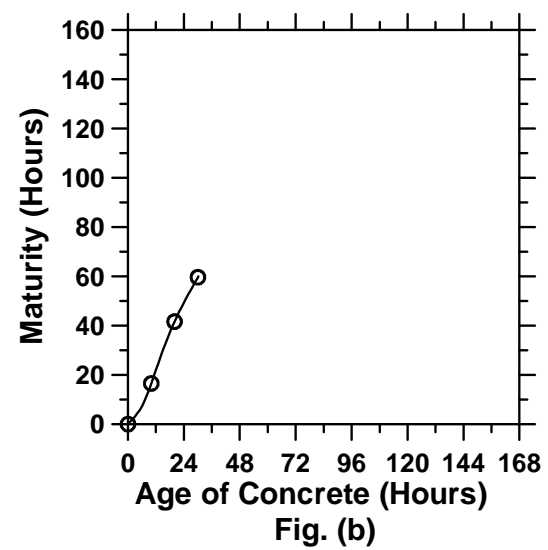
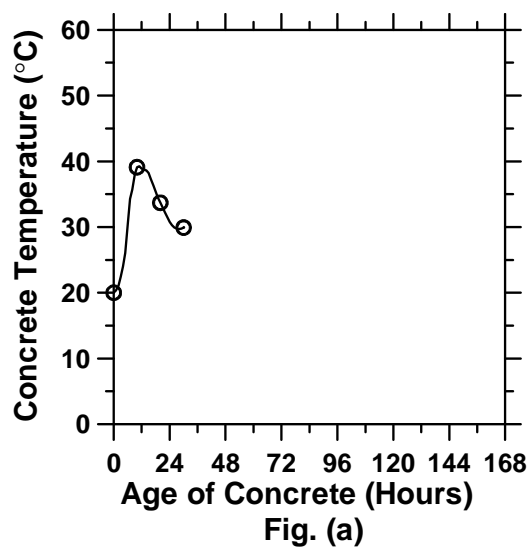


Figure A.19: Pavement with a D/3 saw-cut depth introduced at 30 hours (cont'd).

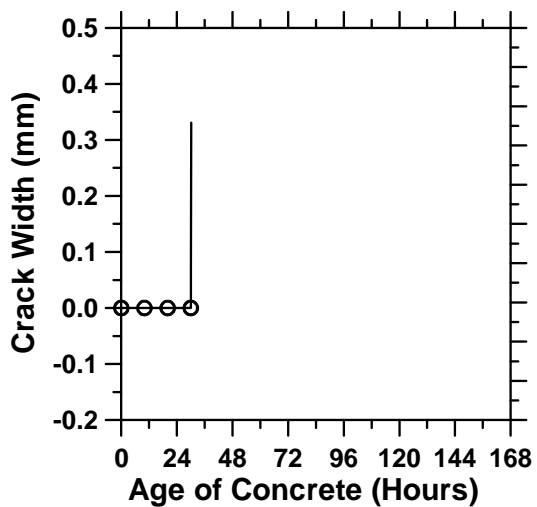


Fig. (e)

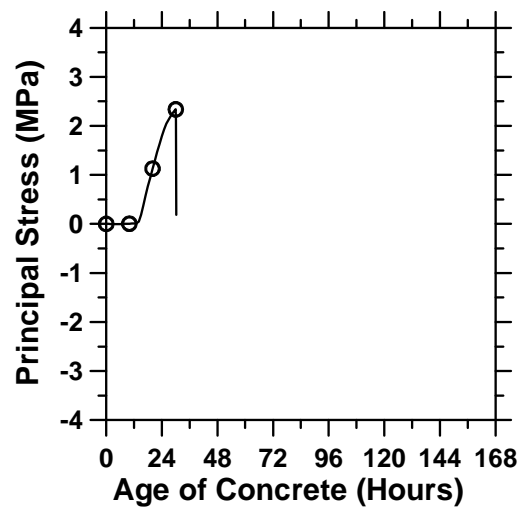


Fig. (f)

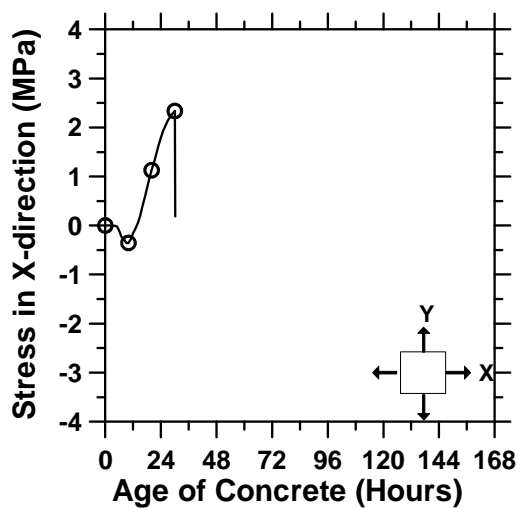


Fig. (g)

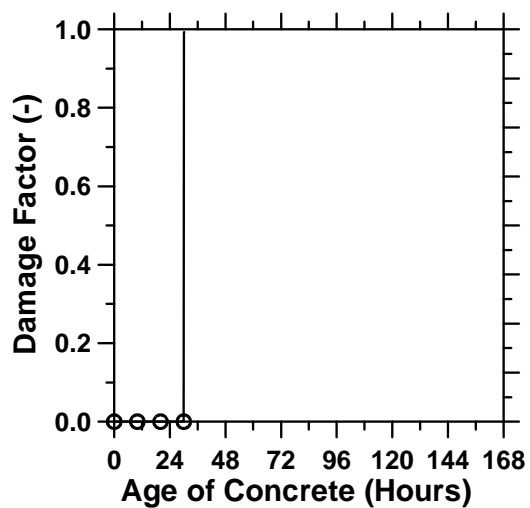


Fig. (h)

Figure A.19: Pavement with a D/3 saw-cut depth introduced at 30 hours.

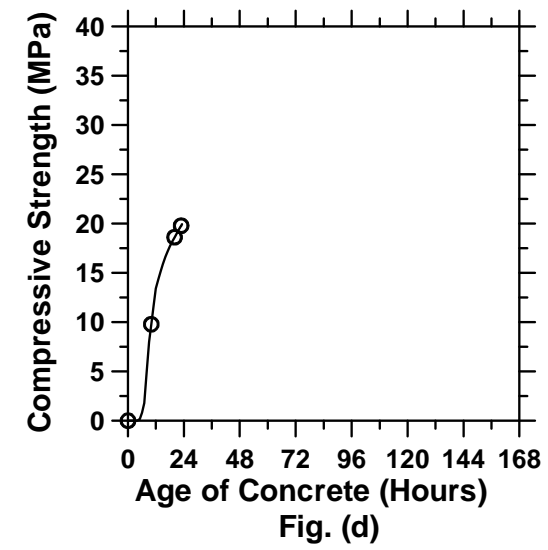
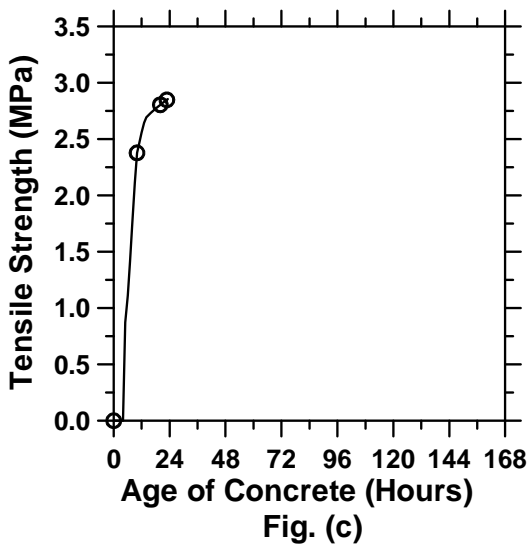
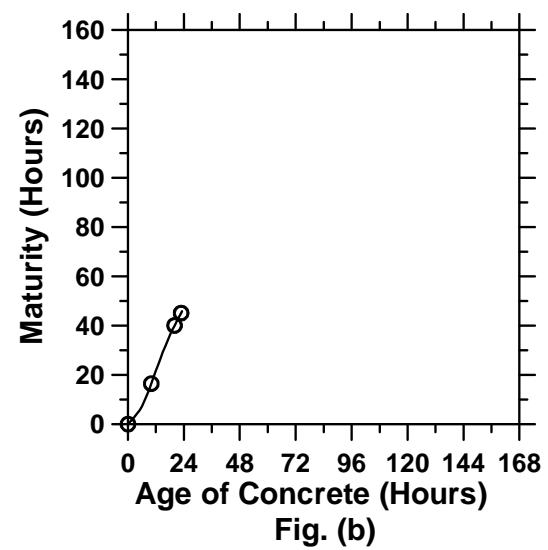
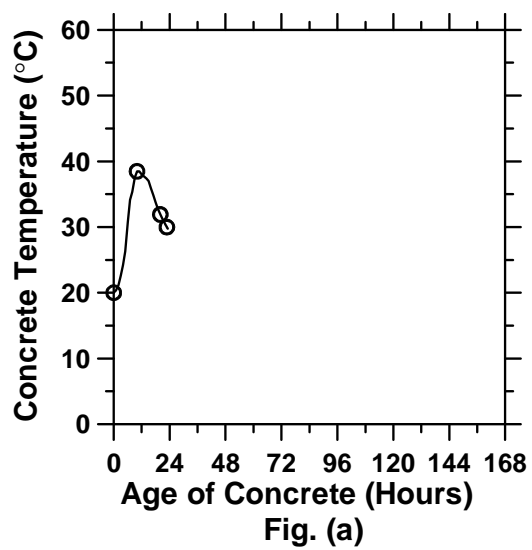


Figure A.20: Pavement with a D/4 saw-cut depth introduced at 0 hour (cont'd).

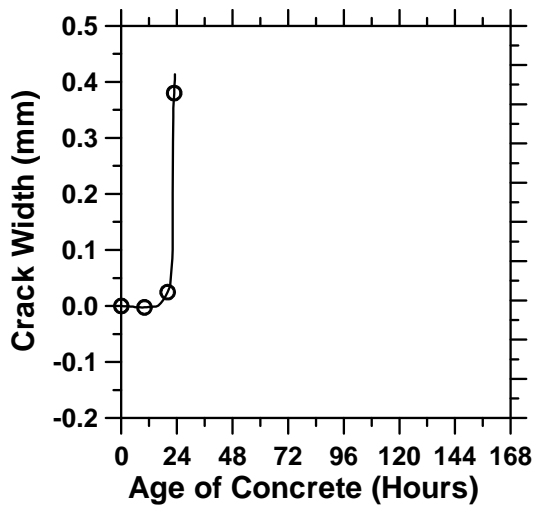


Fig. (e)

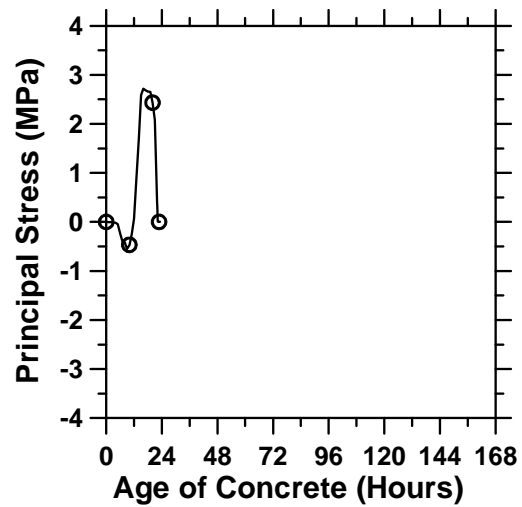


Fig. (f)

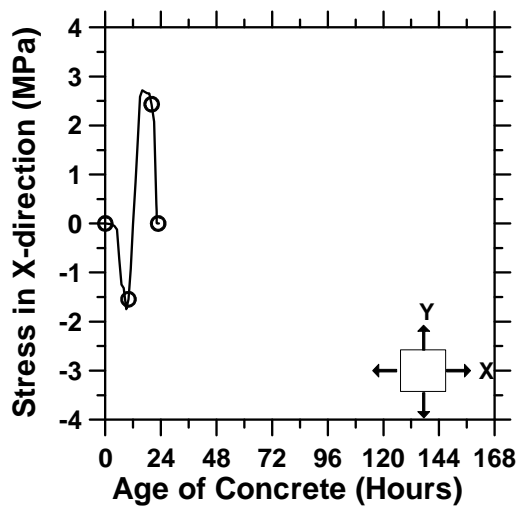


Fig. (g)

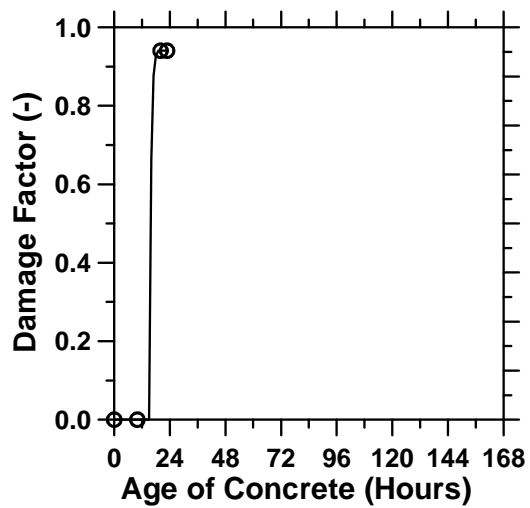


Fig. (h)

Figure A.20: Pavement with a D/4 saw-cut depth introduced at 0 hour.

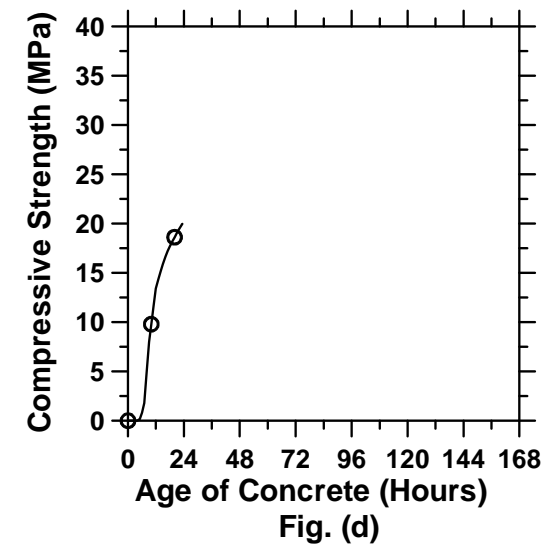
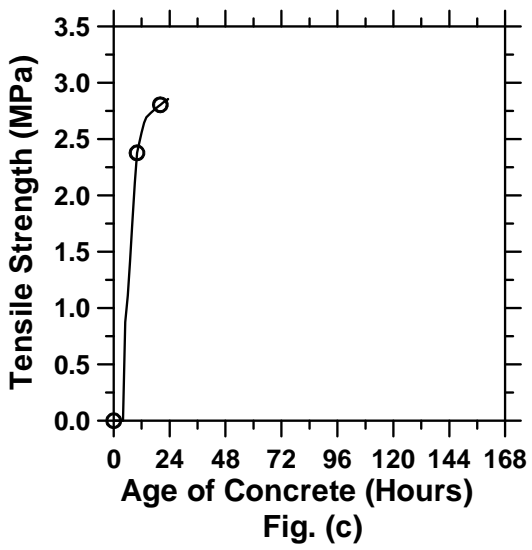
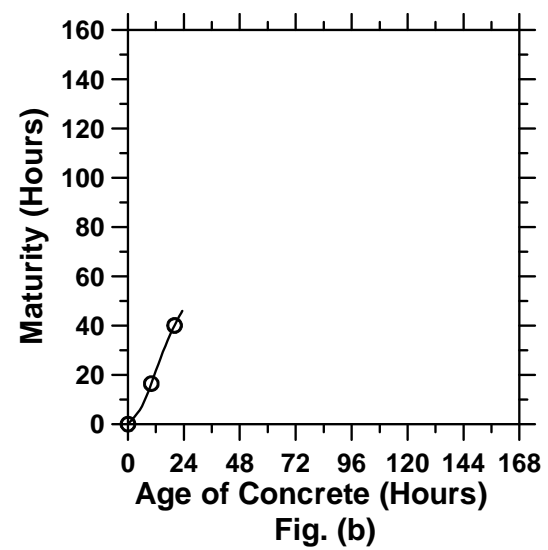
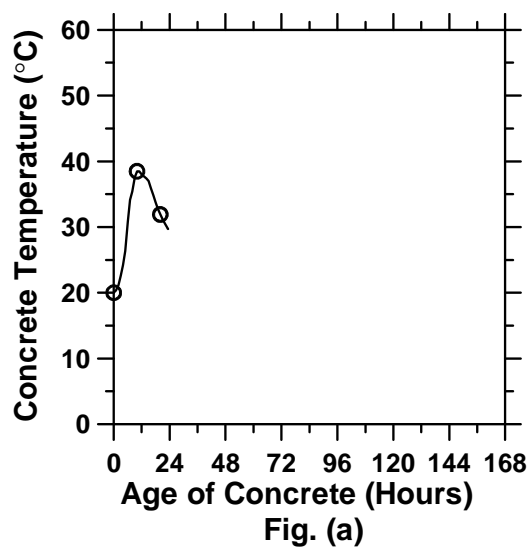


Figure A.21: Pavement with a D/4 saw-cut depth introduced at 6 hours (cont'd).

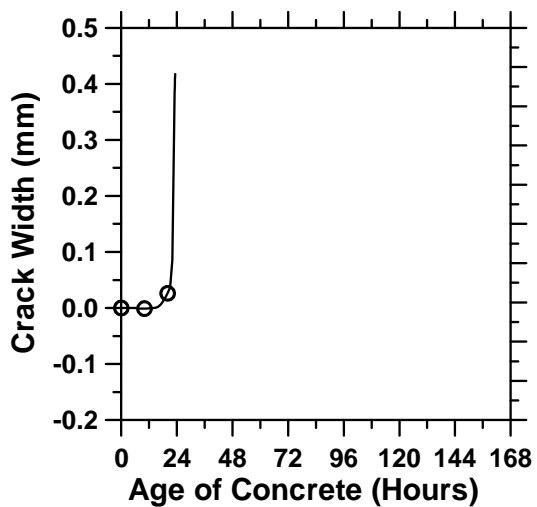


Fig. (e)

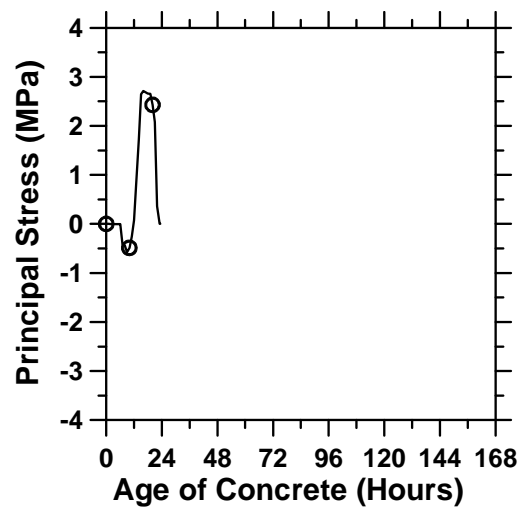


Fig. (f)

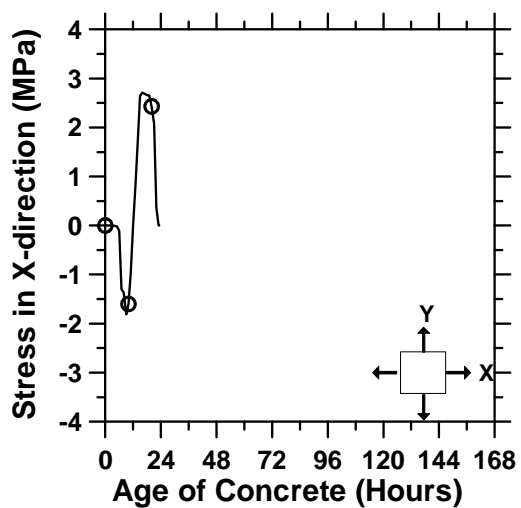


Fig. (g)

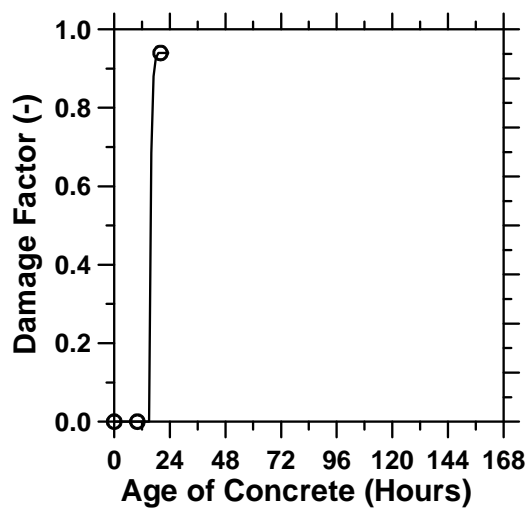


Fig. (h)

Figure A.21: Pavement with a D/4 saw-cut depth introduced at 6 hours.

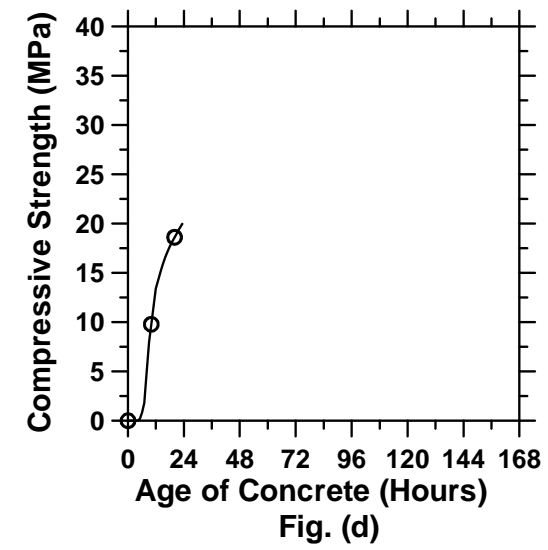
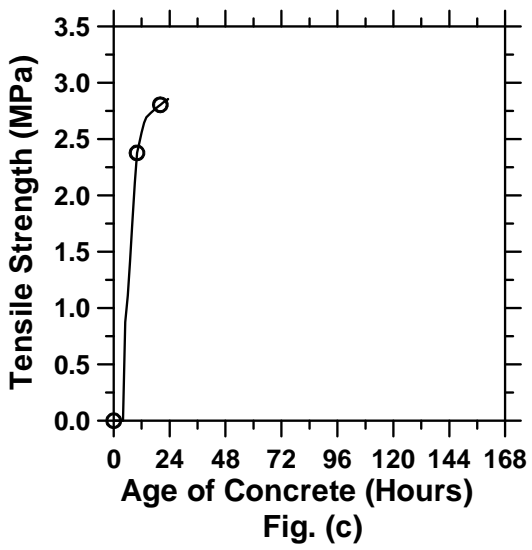
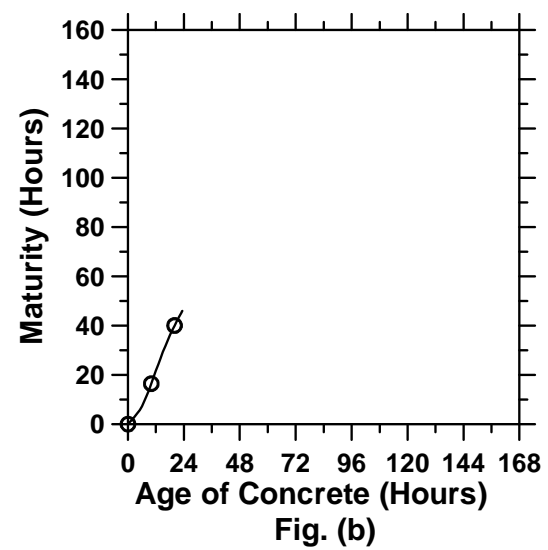
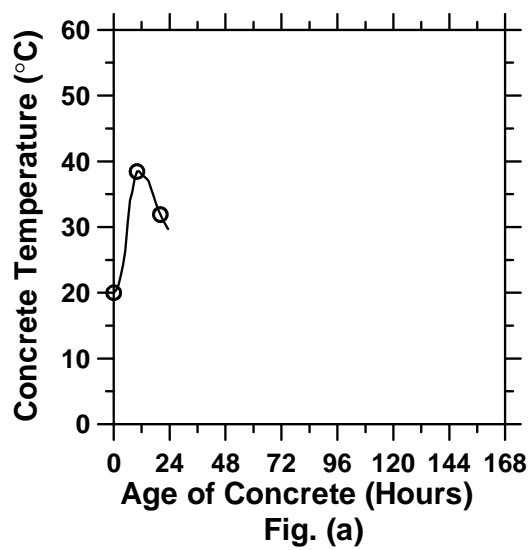


Figure A.22: Pavement with a D/4 saw-cut depth introduced at 9 hours (cont'd).

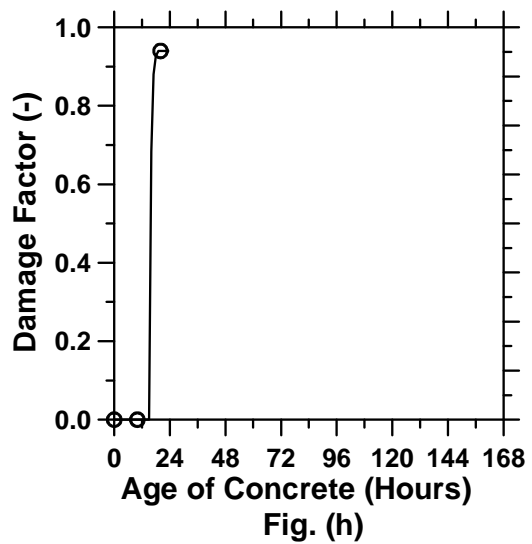
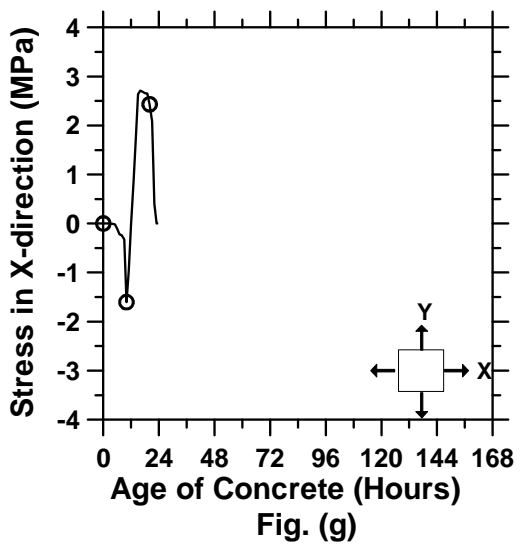
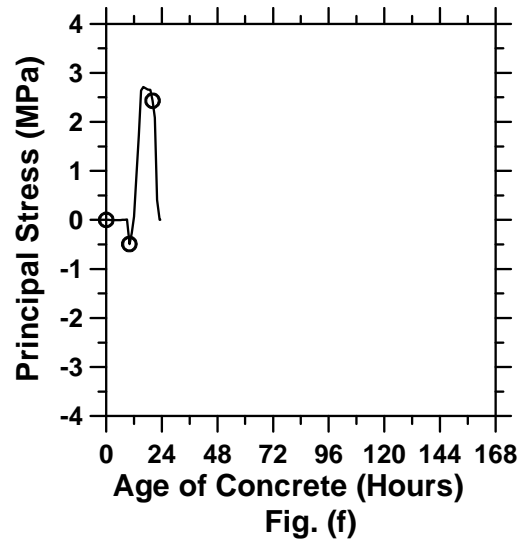
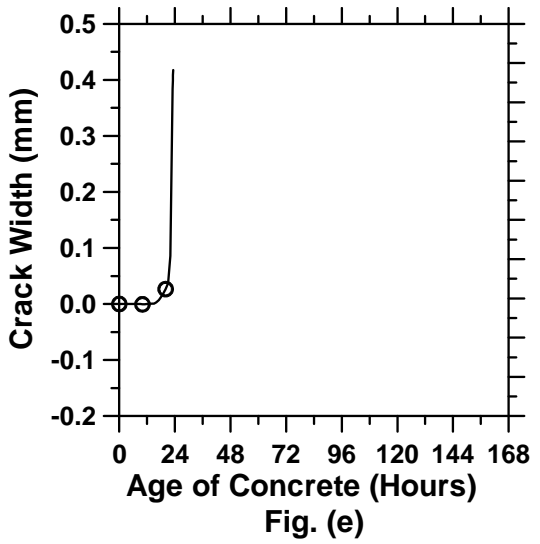


Figure A.22: Pavement with a D/4 saw-cut depth introduced at 9 hours.

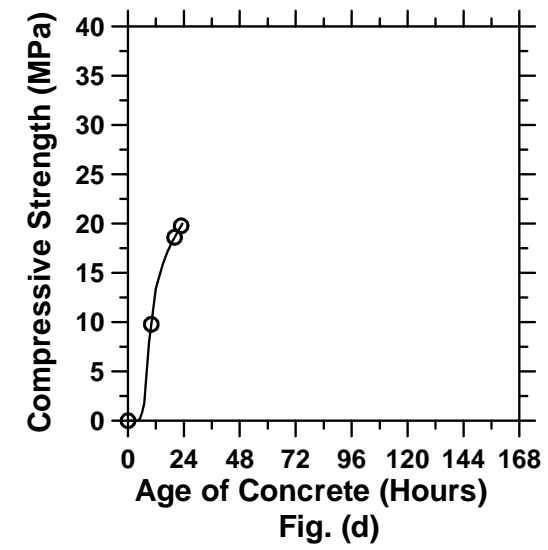
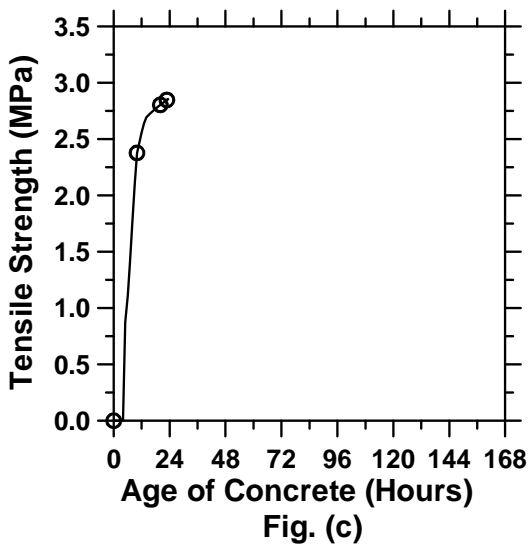
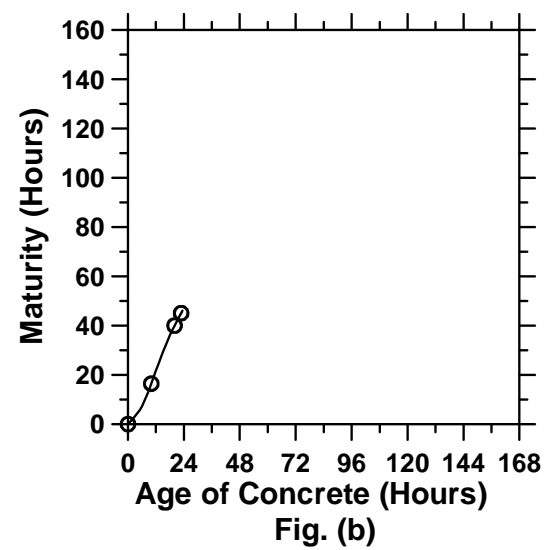
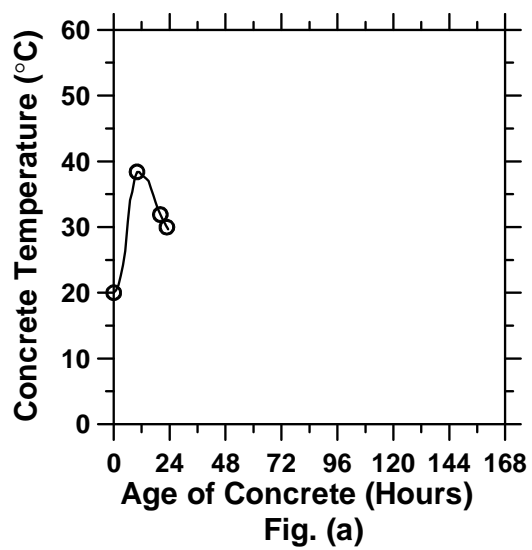


Figure A.23: Pavement with a D/4 saw-cut depth introduced at 12 hours (cont'd).

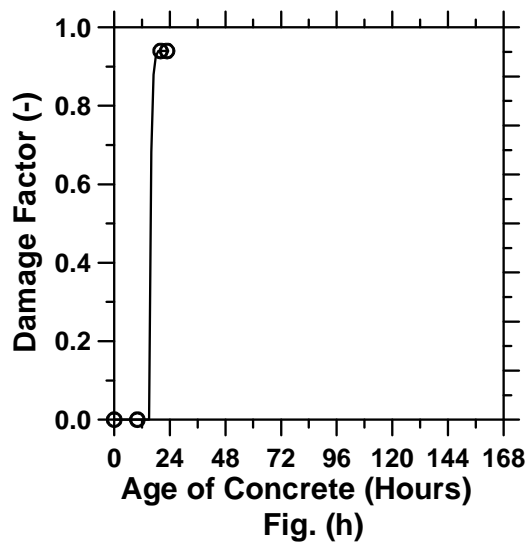
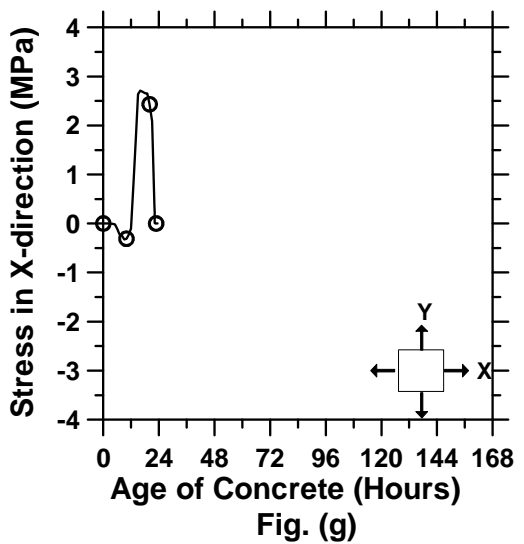
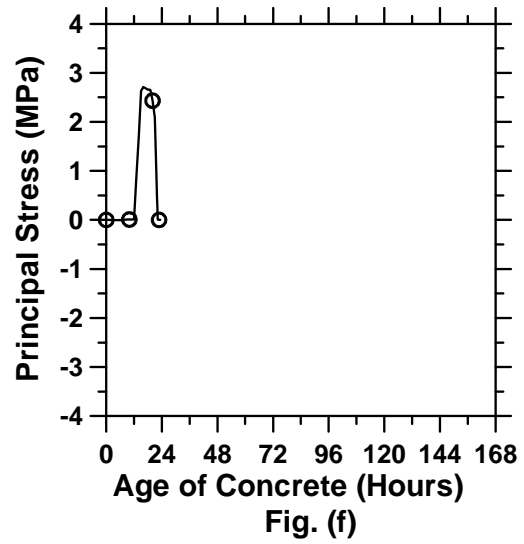
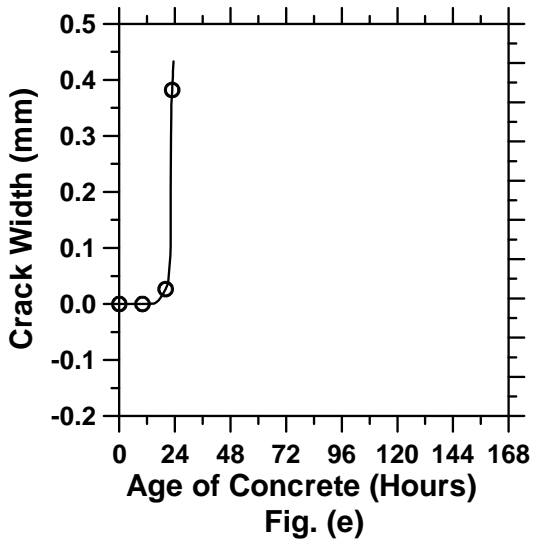


Figure A.23: Pavement with a D/4 saw-cut depth introduced at 12 hours.

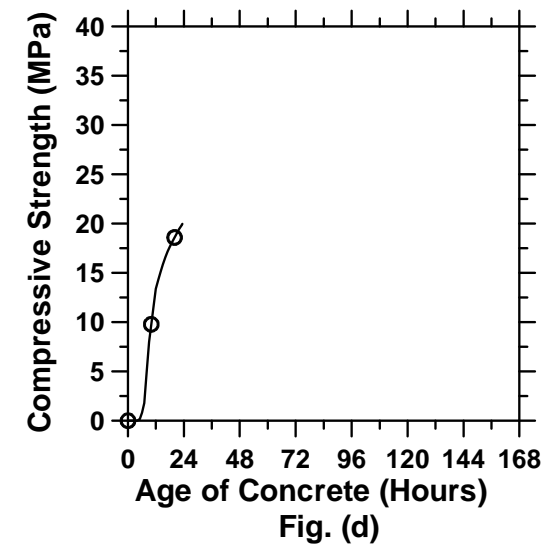
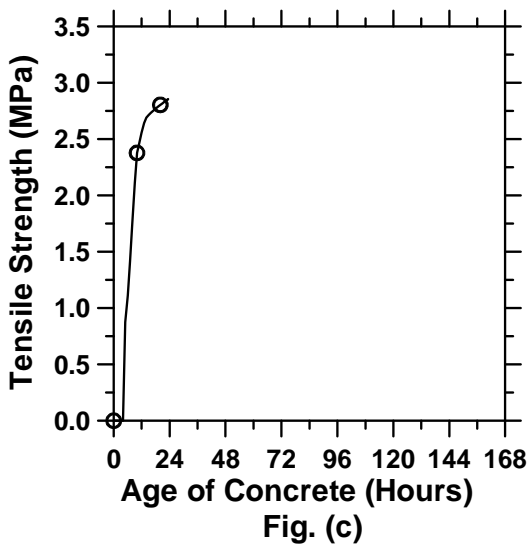
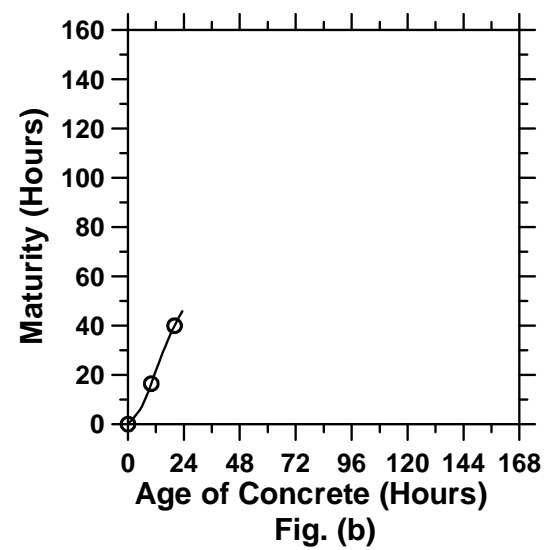
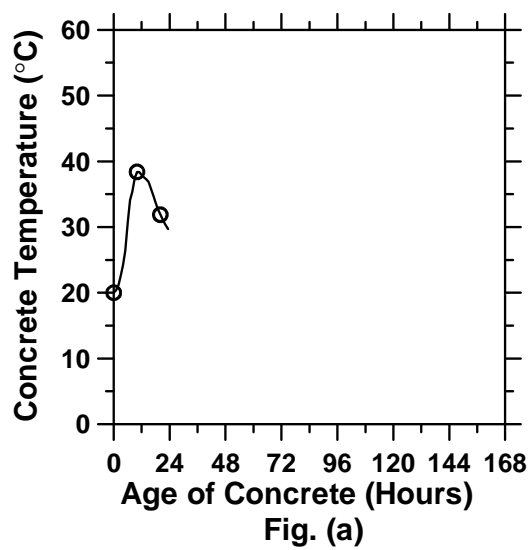


Figure A.24: Pavement with a D/4 saw-cut depth introduced at 15 hours (cont'd).

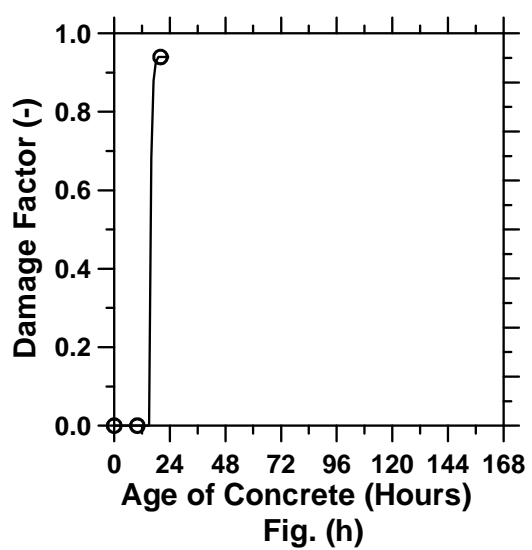
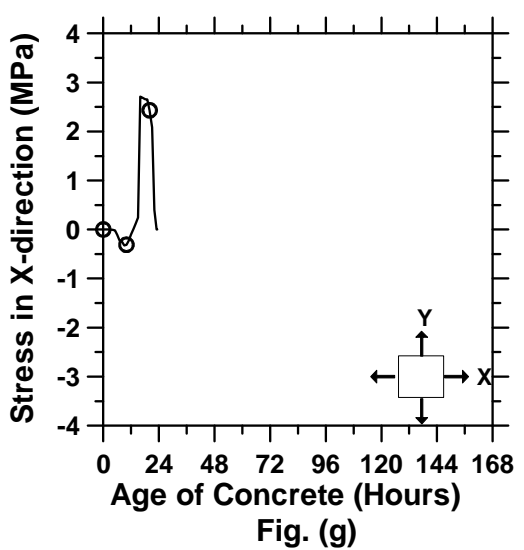
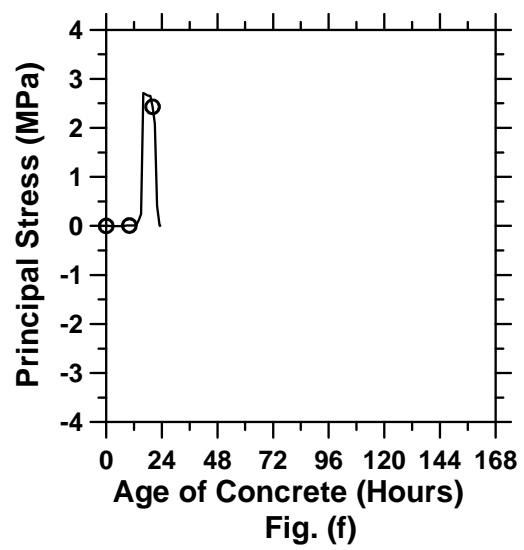
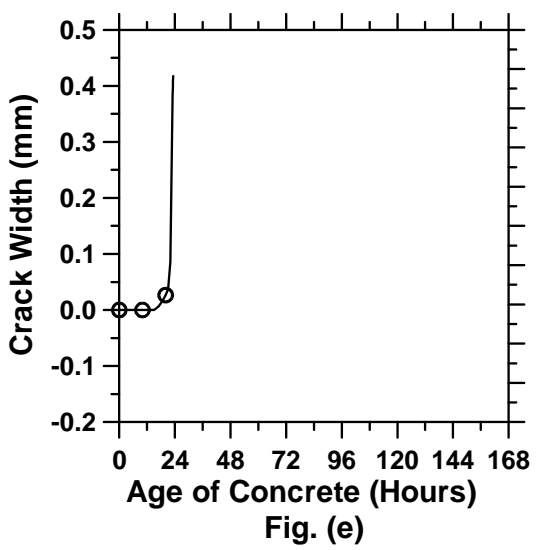


Figure A.24: Pavement with a D/4 saw-cut depth introduced at 15 hours.

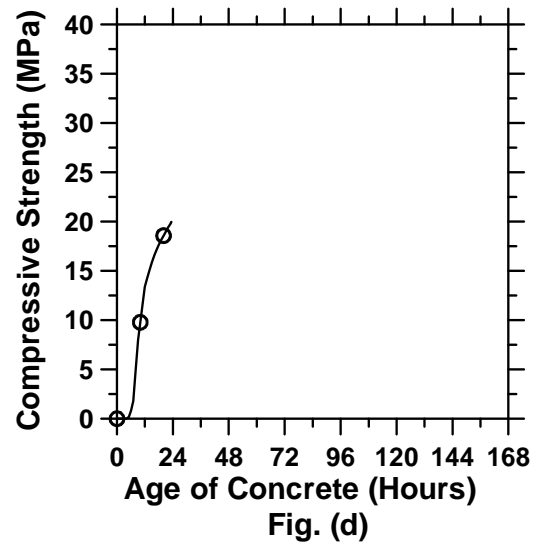
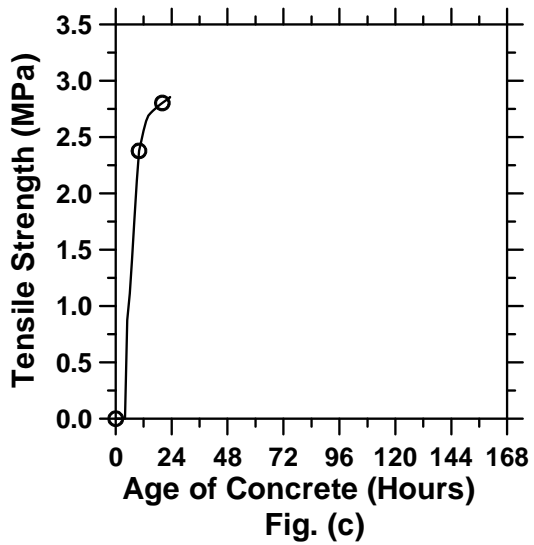
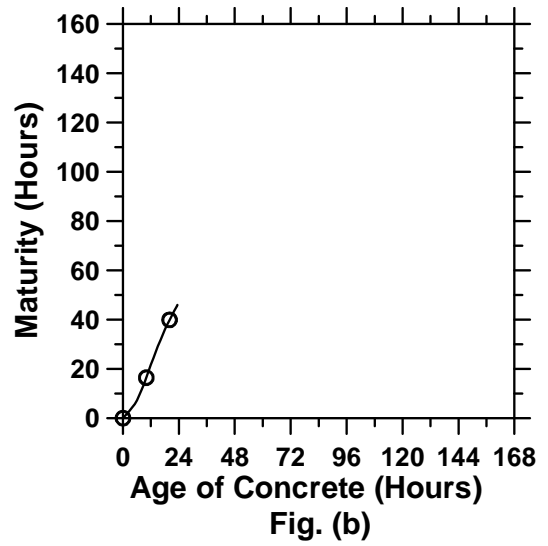
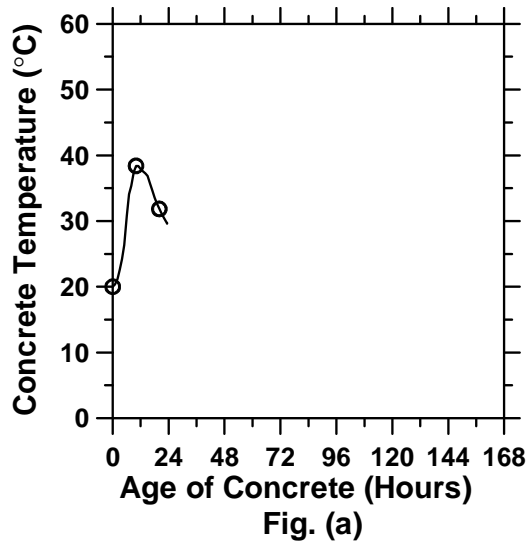


Figure A.25: Pavement with a D/4 saw-cut depth introduced at 18 hours (cont'd).

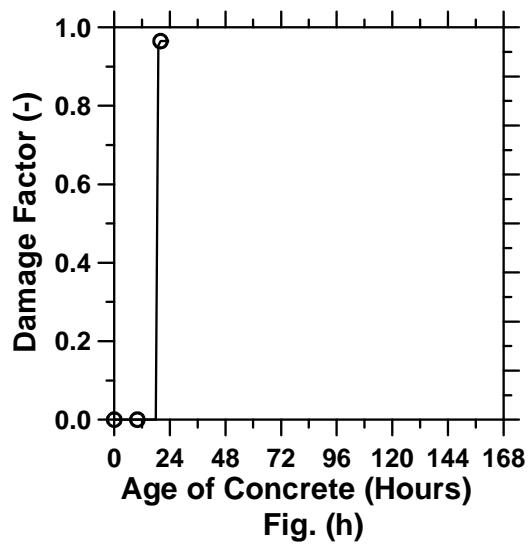
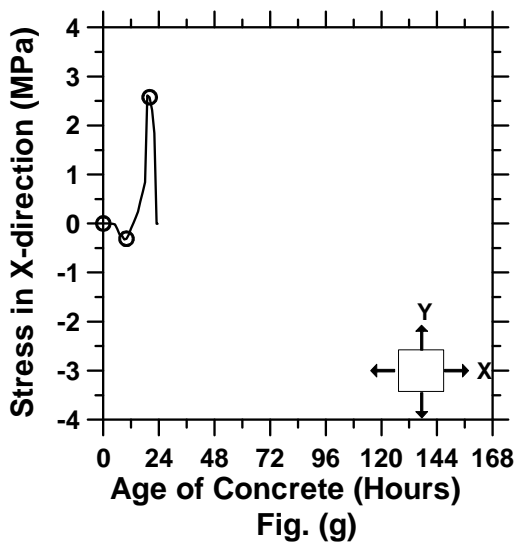
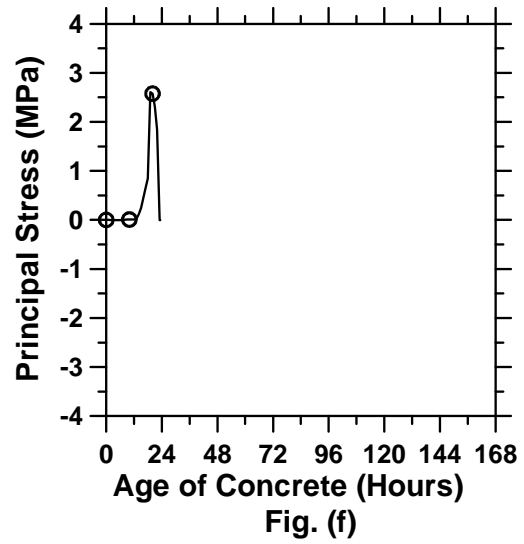
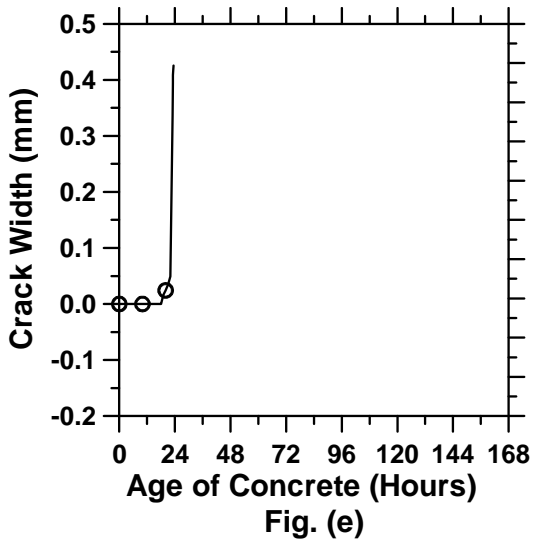


Figure A.25: Pavement with a D/4 saw-cut depth introduced at 18 hours.

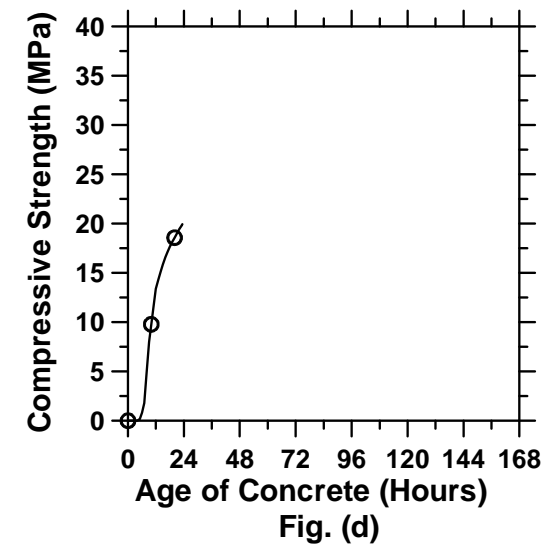
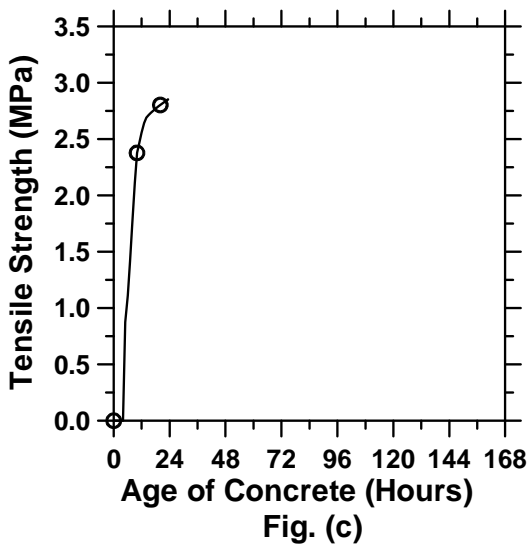
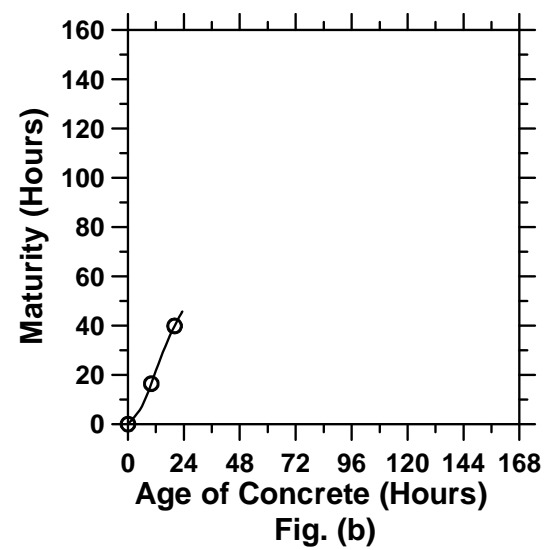
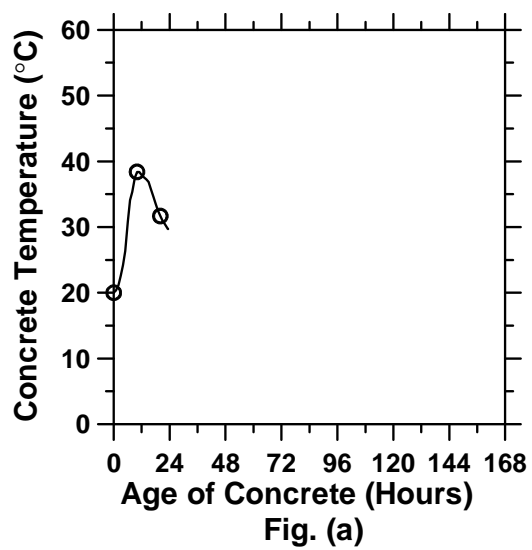


Figure A.26: Pavement with a D/4 saw-cut depth introduced at 21 hours (cont'd).

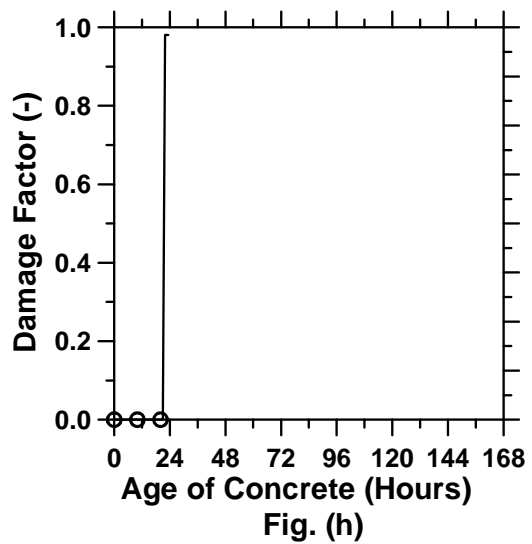
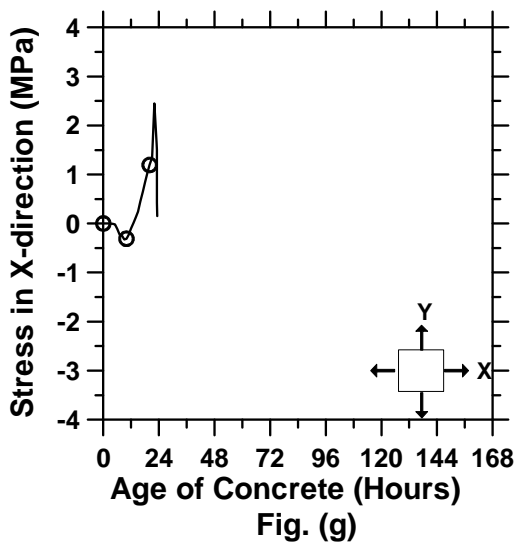
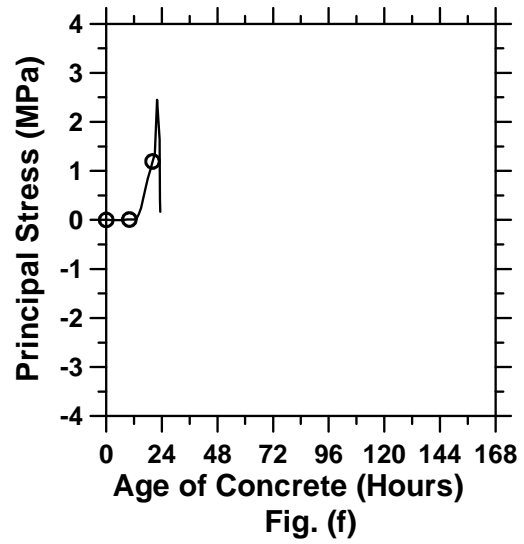
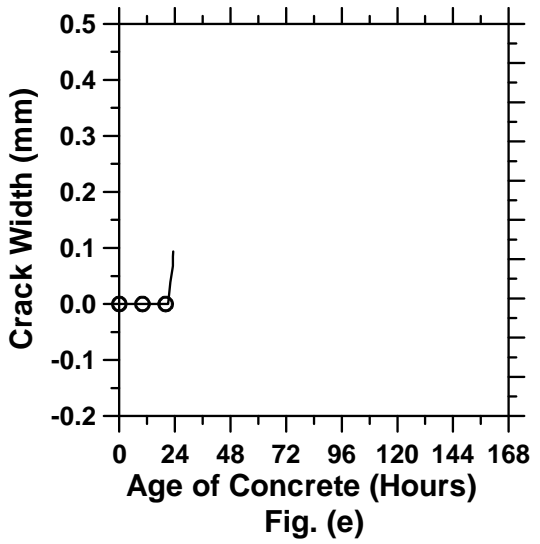


Figure A.26: Pavement with a D/4 saw-cut depth introduced at 21 hours.

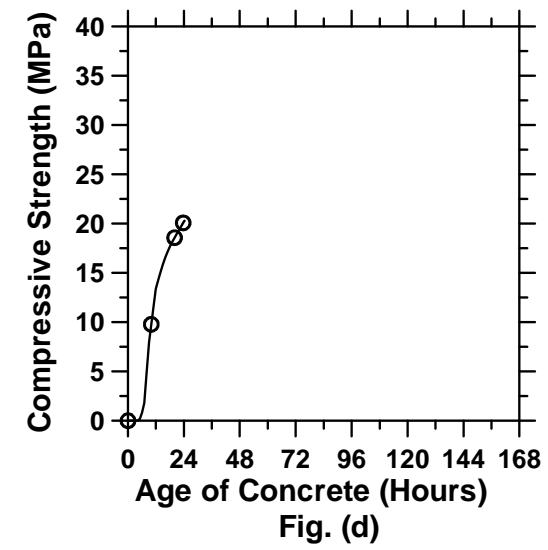
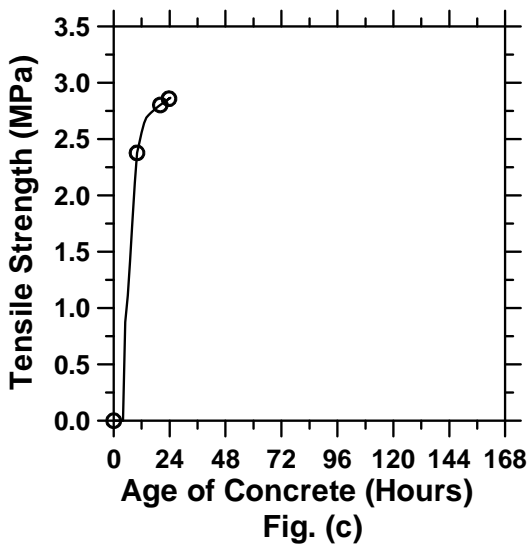
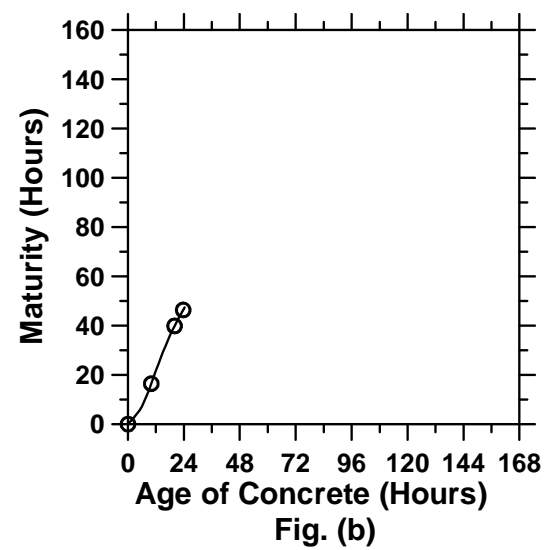
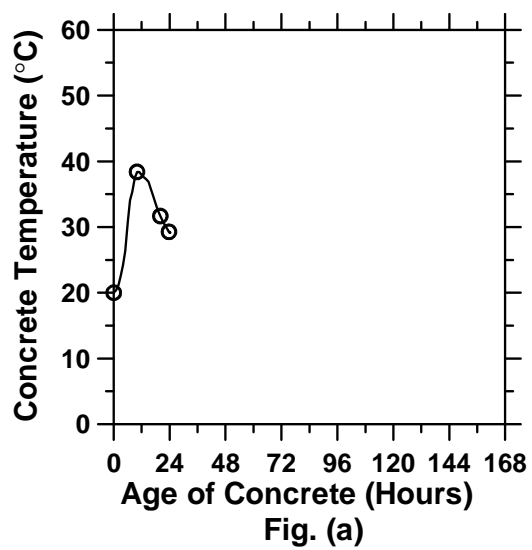


Figure A.27: Pavement with a D/4 saw-cut depth introduced at 24 hours (cont'd).

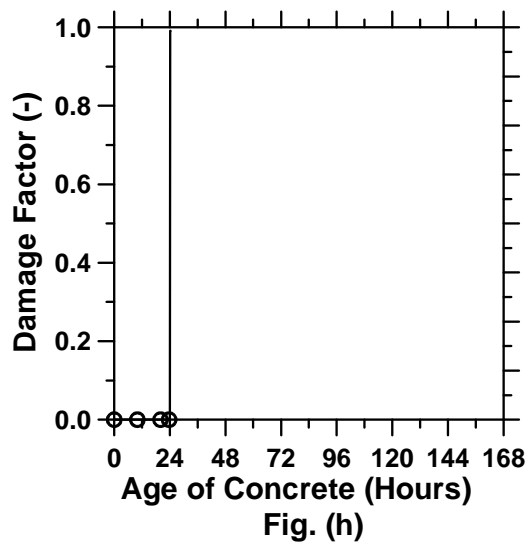
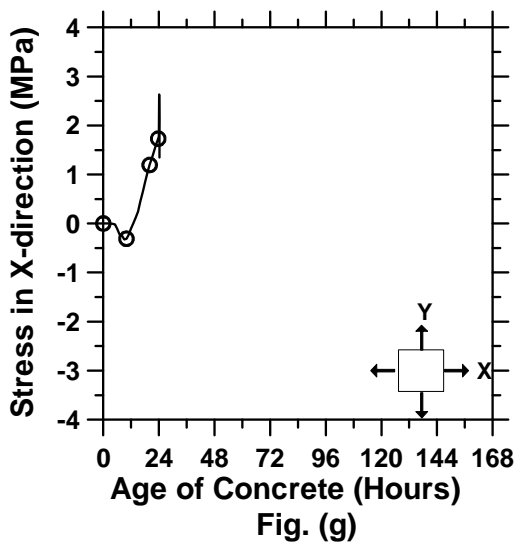
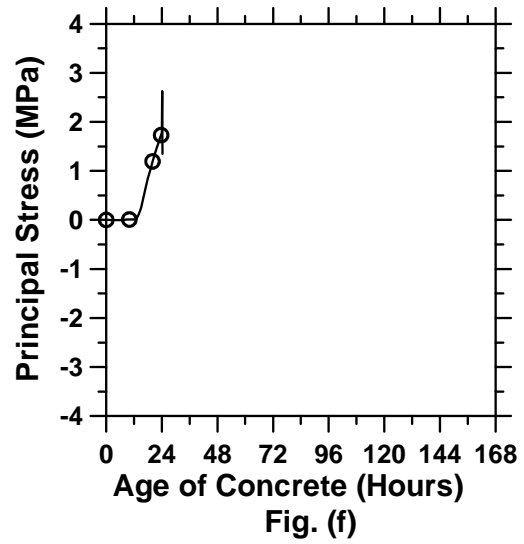
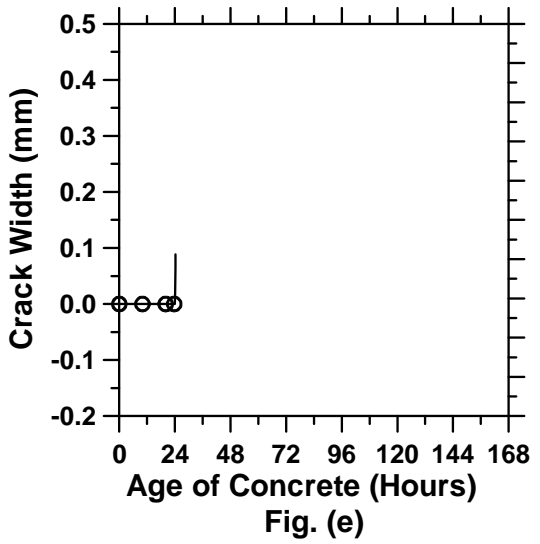


Figure A.27: Pavement with a D/4 saw-cut depth introduced at 24 hours.

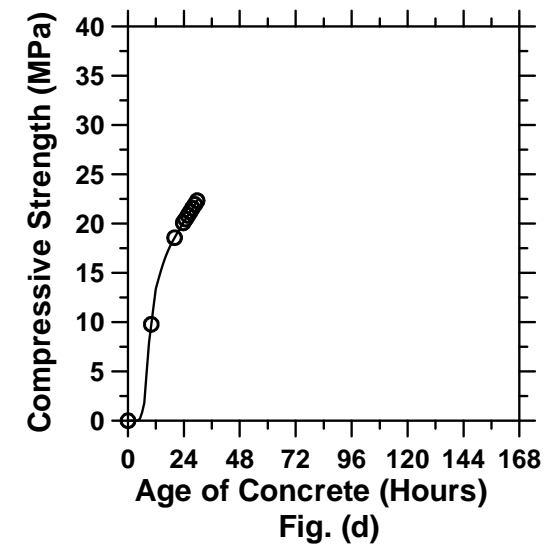
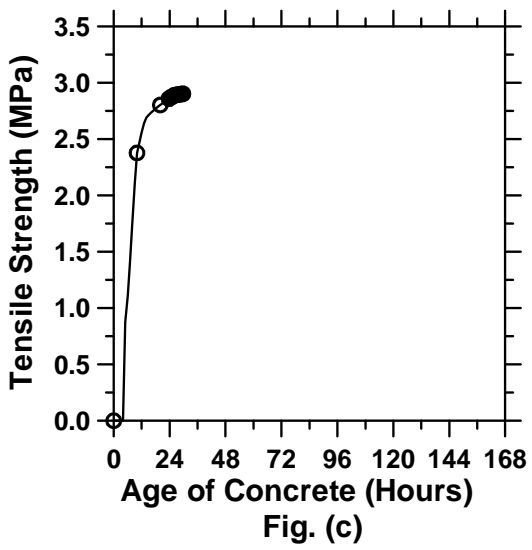
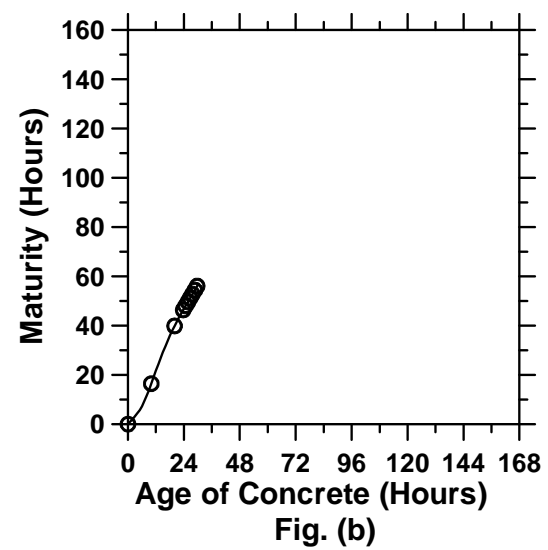
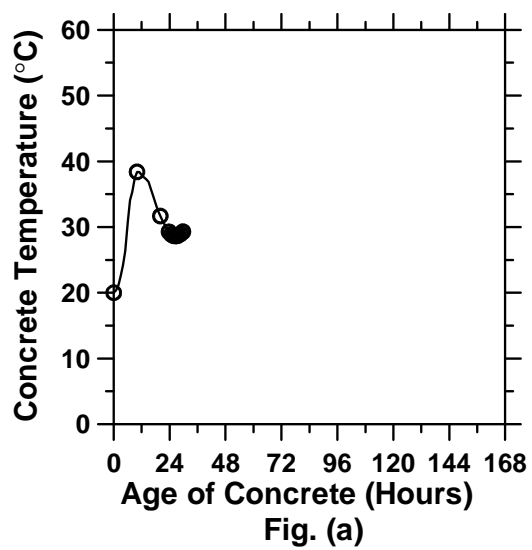


Figure A.28: Pavement with a D/4 saw-cut depth introduced at 30 hours (cont'd).

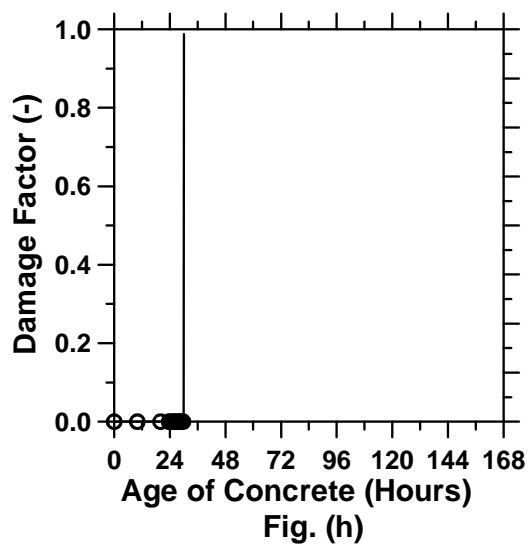
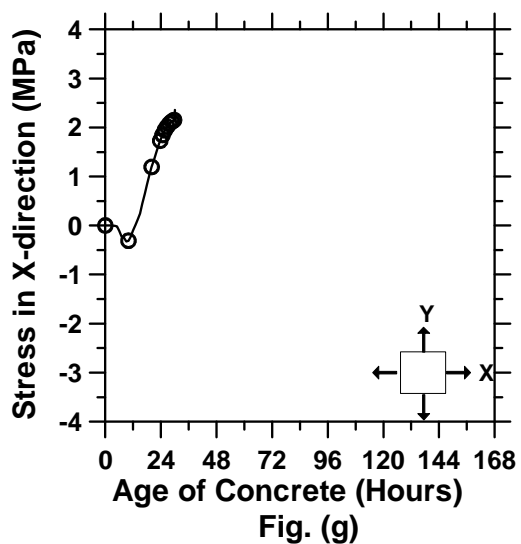
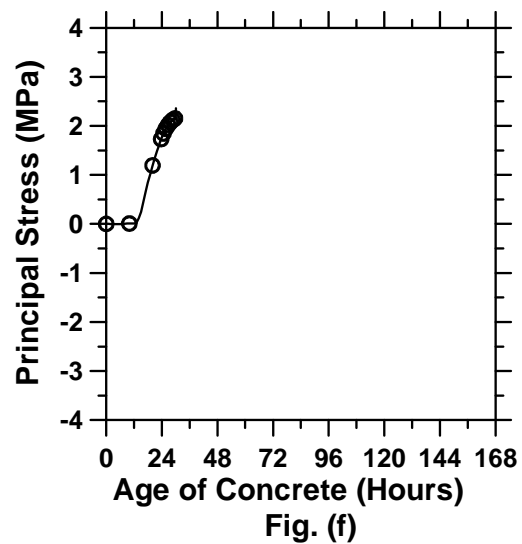
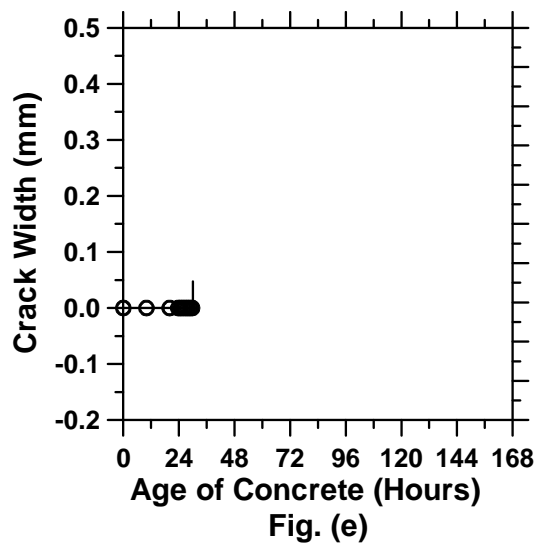


Figure A.28: Pavement with a D/4 saw-cut depth introduced at 30 hours.

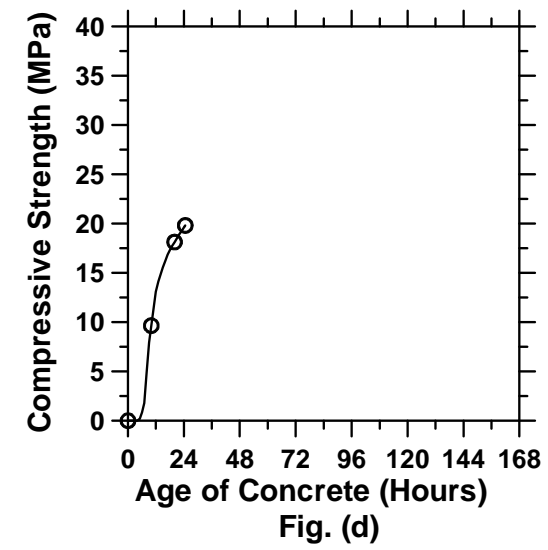
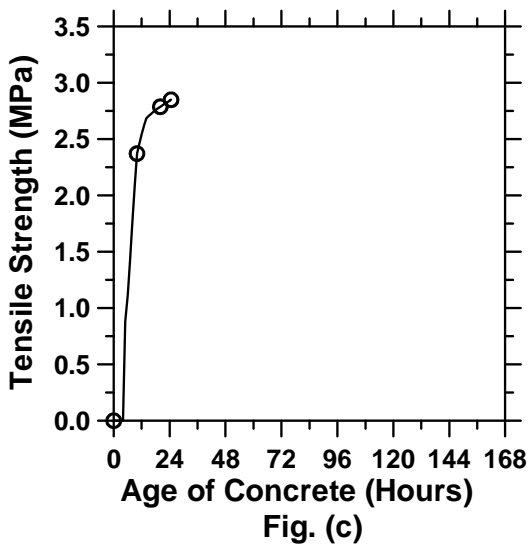
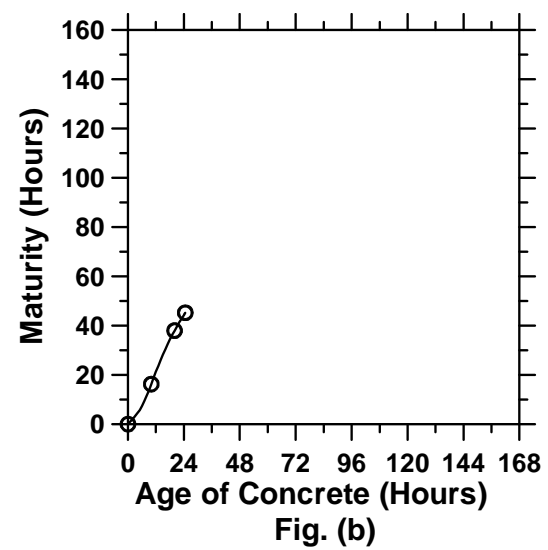
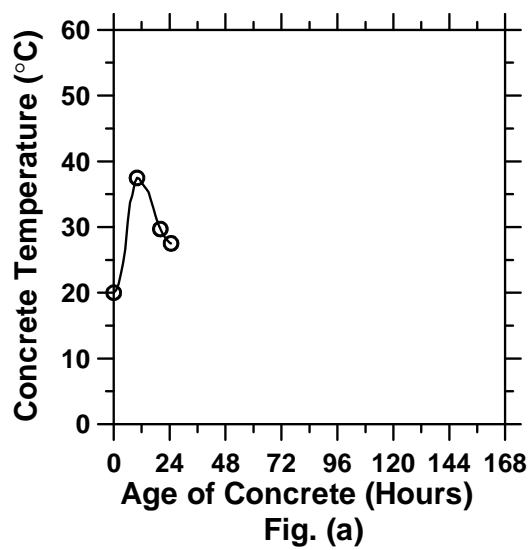


Figure A.29: Pavement with a D/6 saw-cut depth introduced at 0 hour (cont'd).

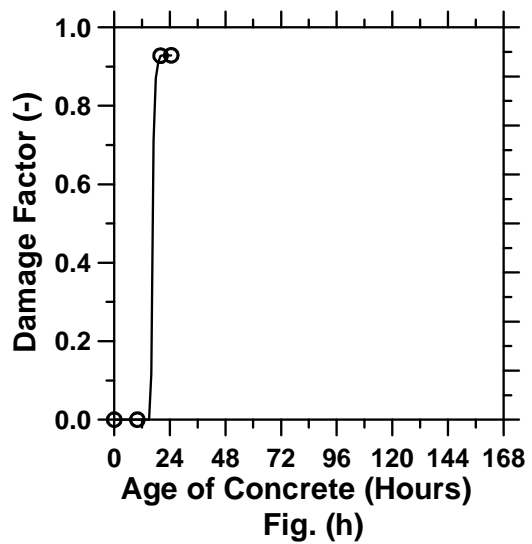
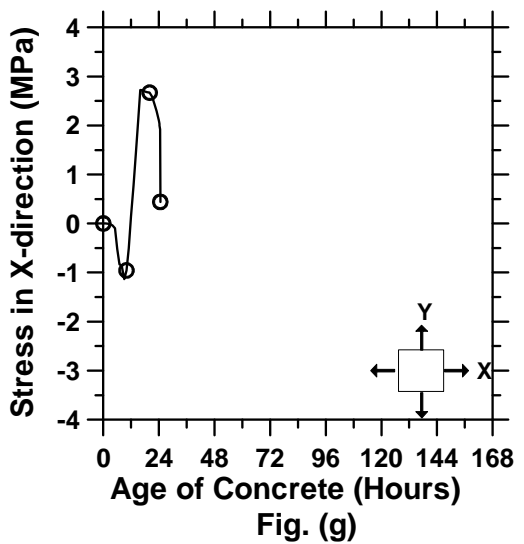
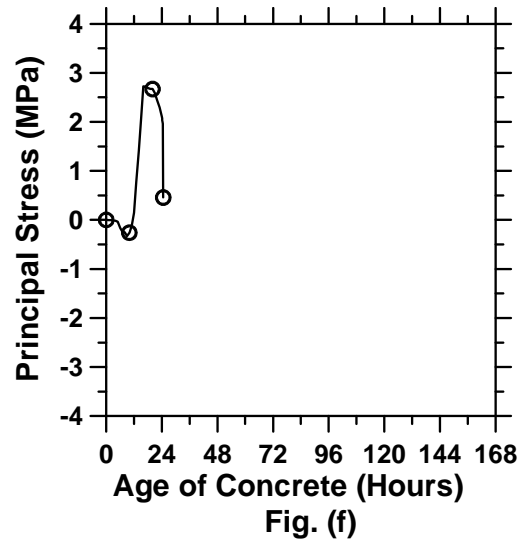
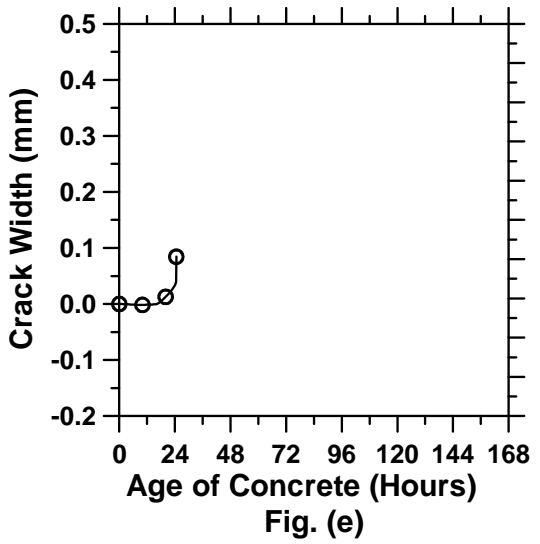


Figure A.29: Pavement with a D/6 saw-cut depth introduced at 0 hour.

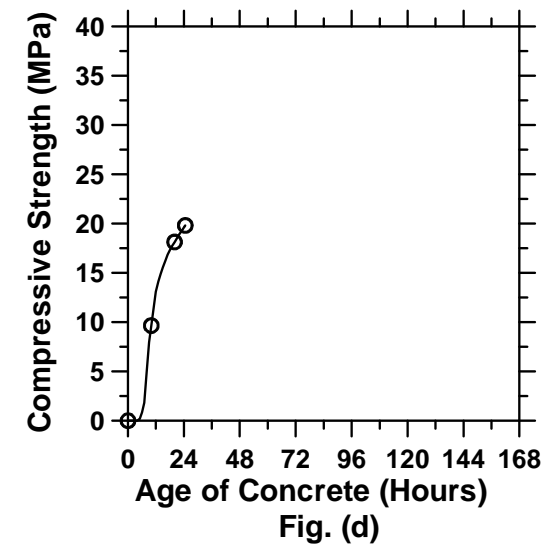
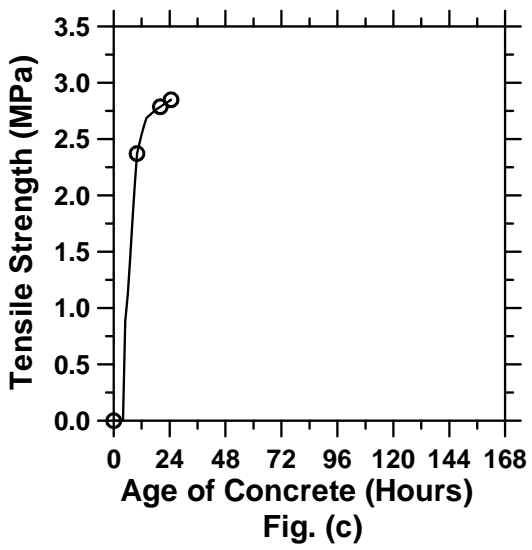
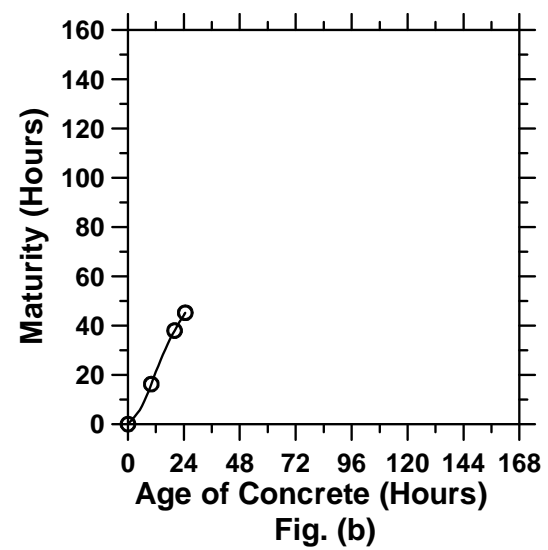
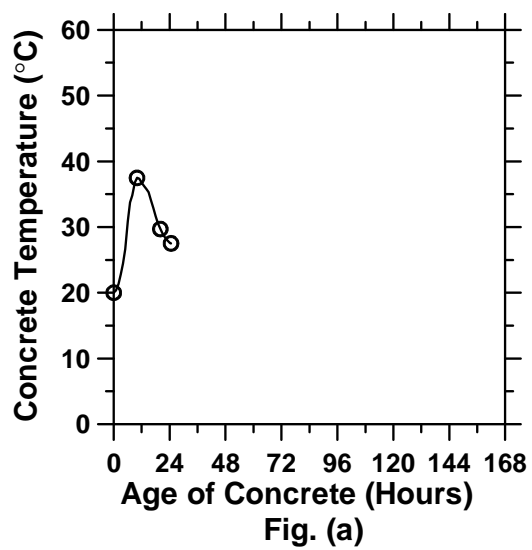


Figure A.30: Pavement with a D/6 saw-cut depth introduced at 6 hours (cont'd).

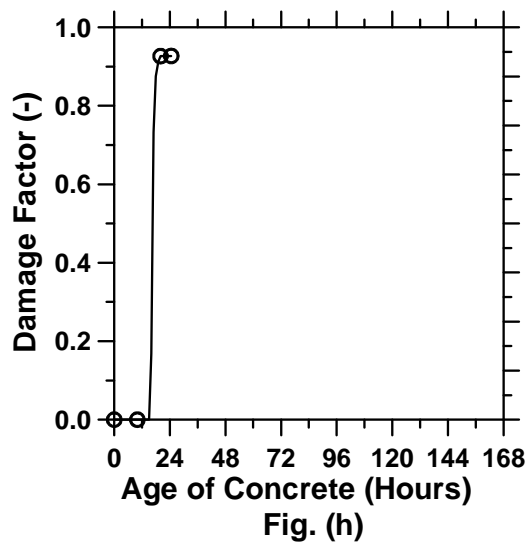
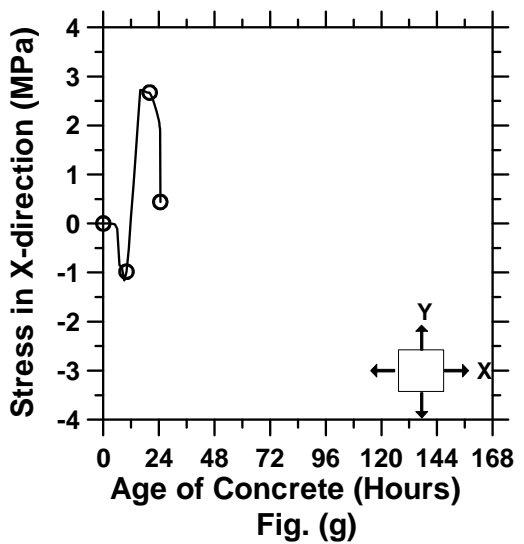
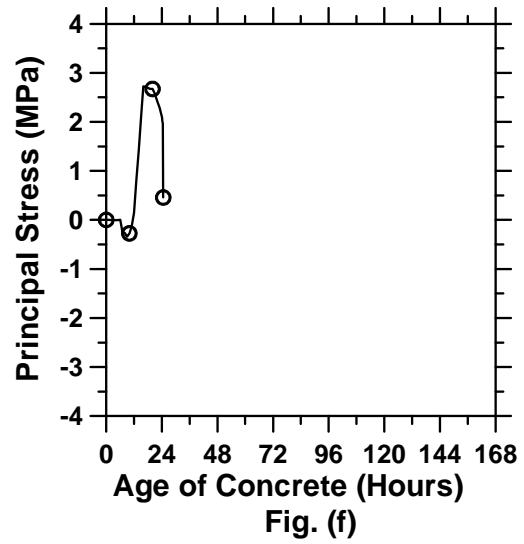
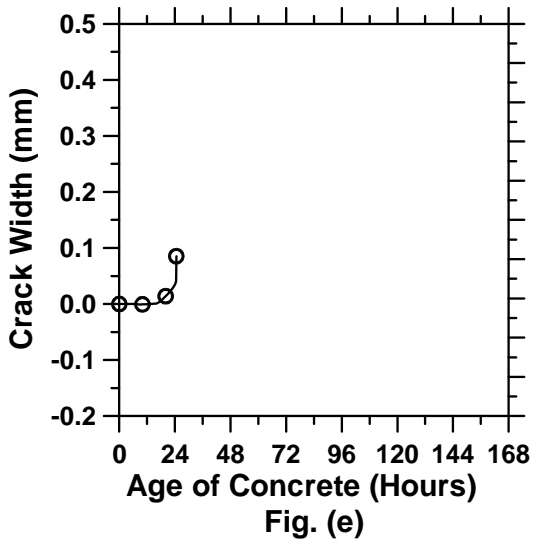


Figure A.30: Pavement with a D/6 saw-cut depth introduced at 6 hours.

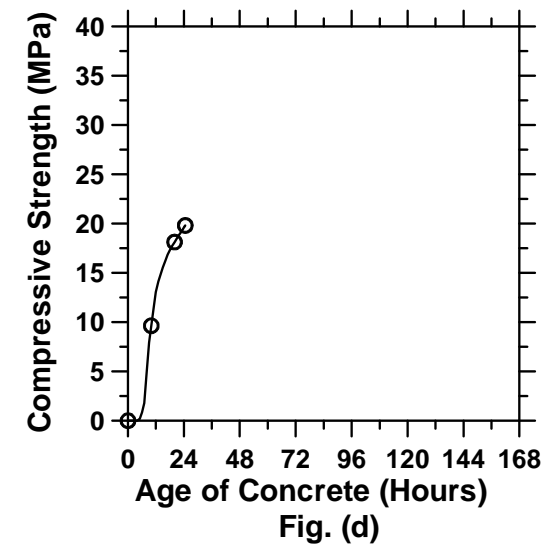
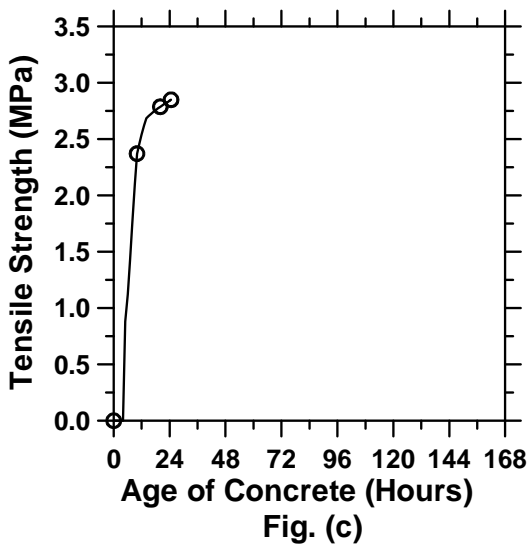
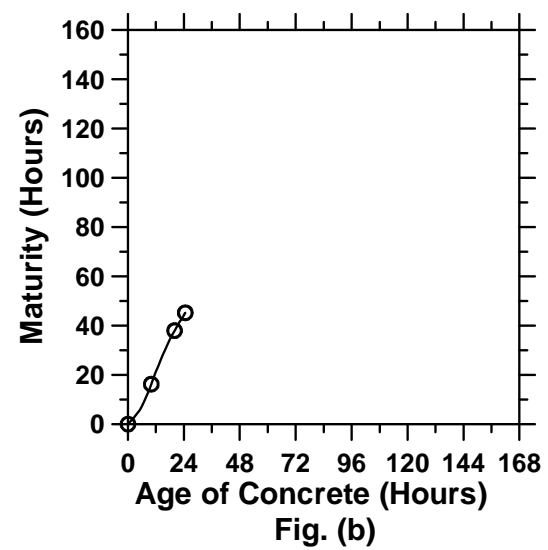
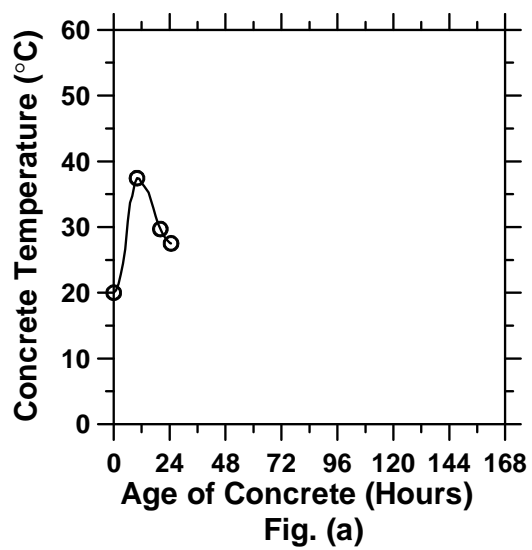


Figure A.31: Pavement with a D/6 saw-cut depth introduced at 9 hours (cont'd).

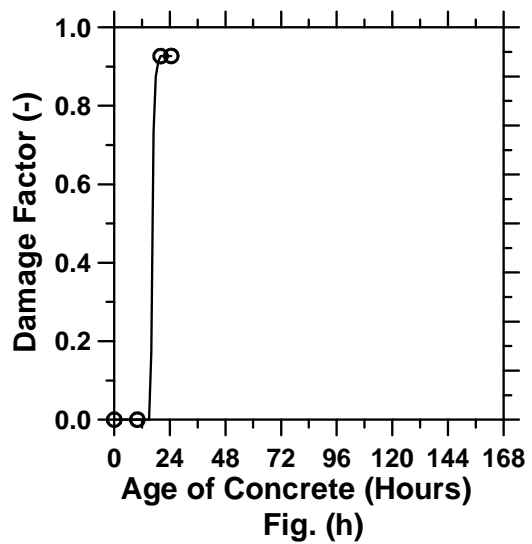
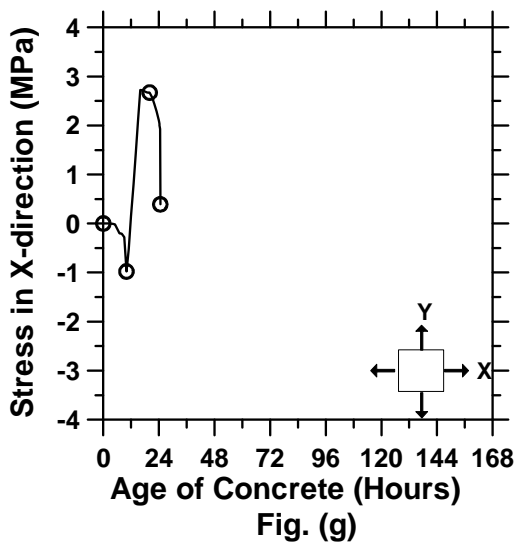
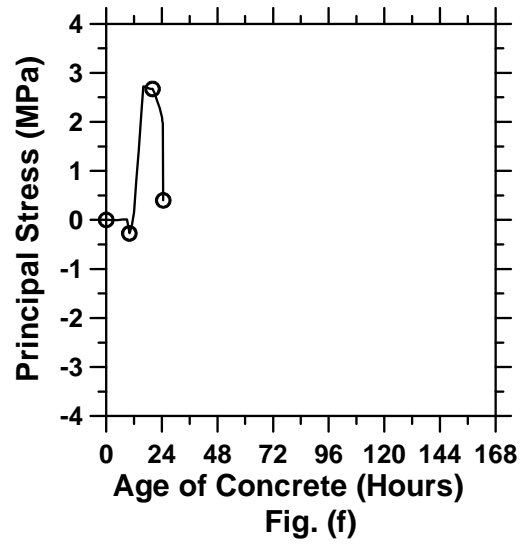
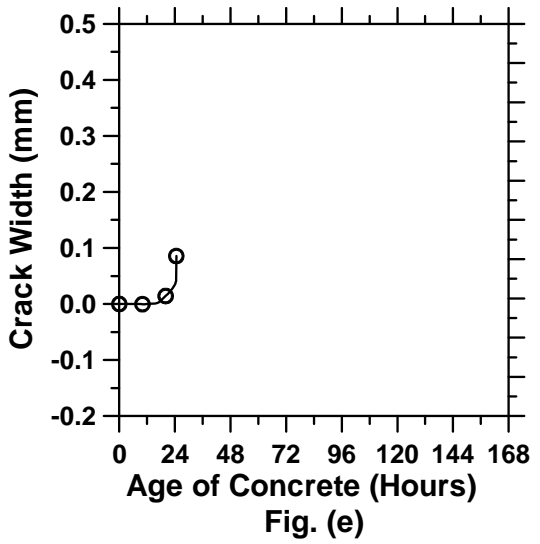


Figure A.31: Pavement with a D/6 saw-cut depth introduced at 9 hours.

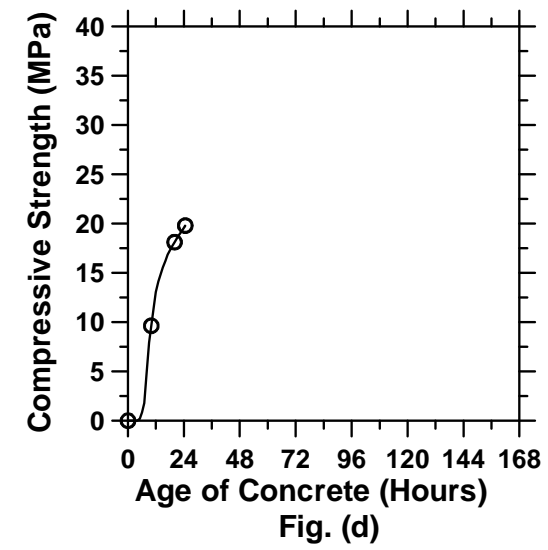
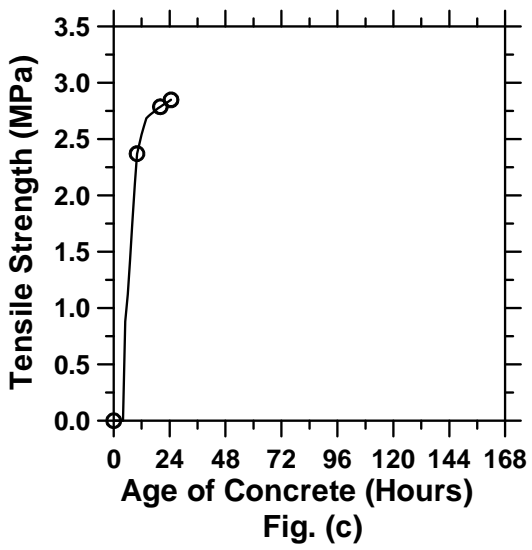
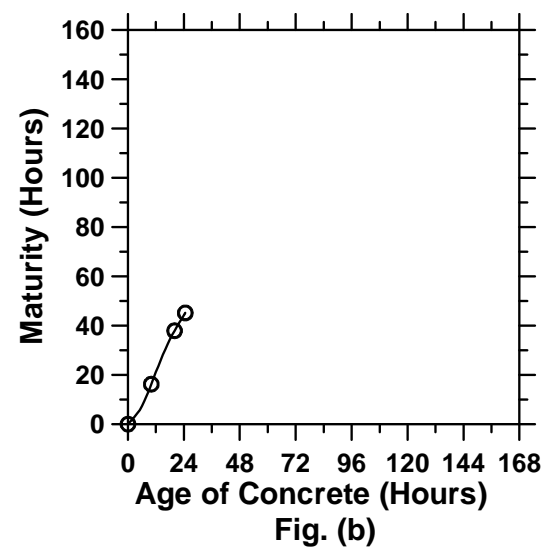
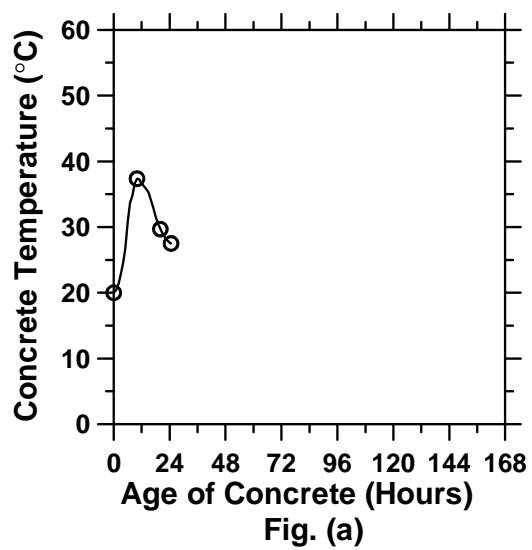


Figure A.32: Pavement with a D/6 saw-cut depth introduced at 12 hours (cont'd).

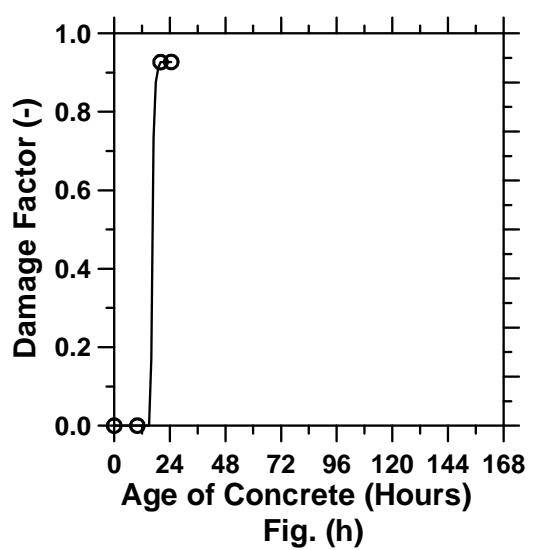
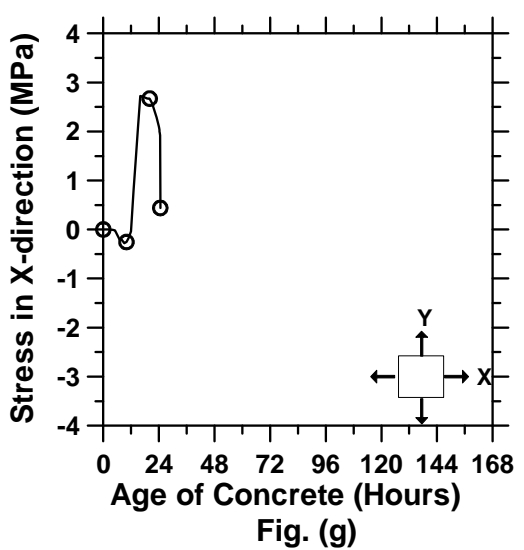
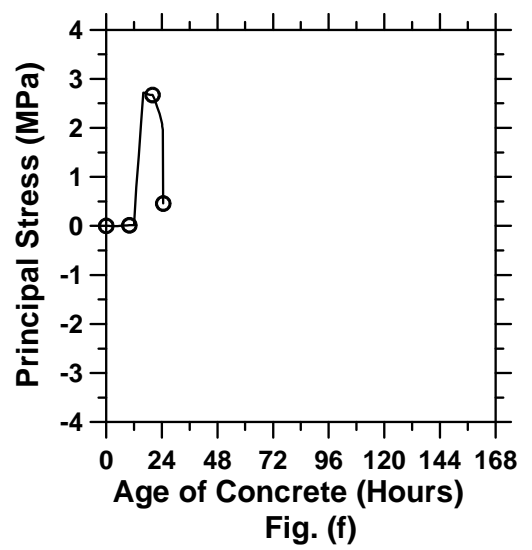
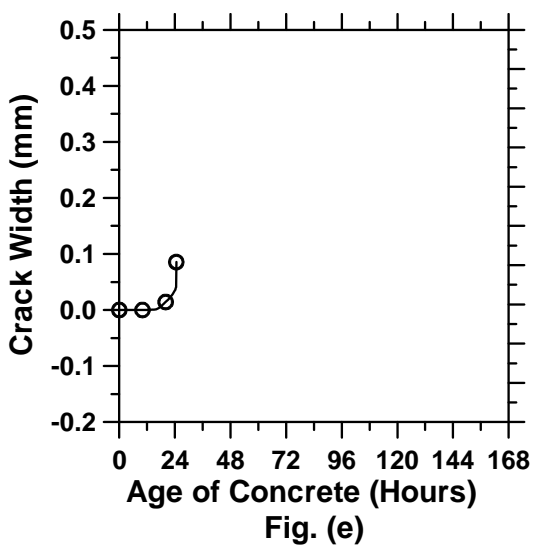


Figure A.32: Pavement with a D/6 saw-cut depth introduced at 12 hours.

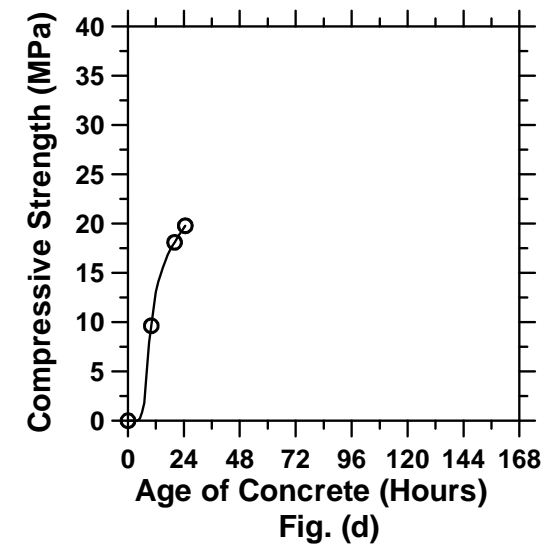
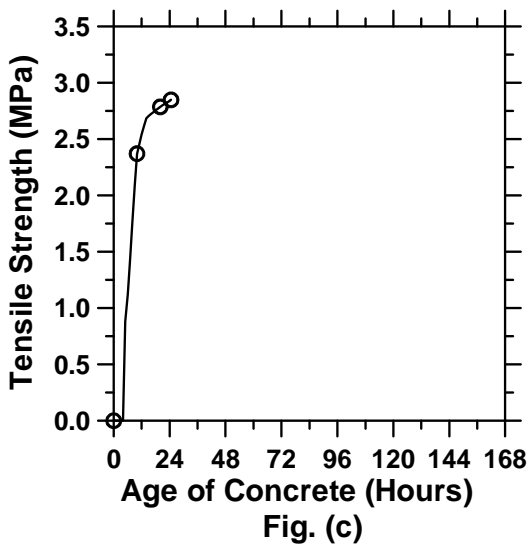
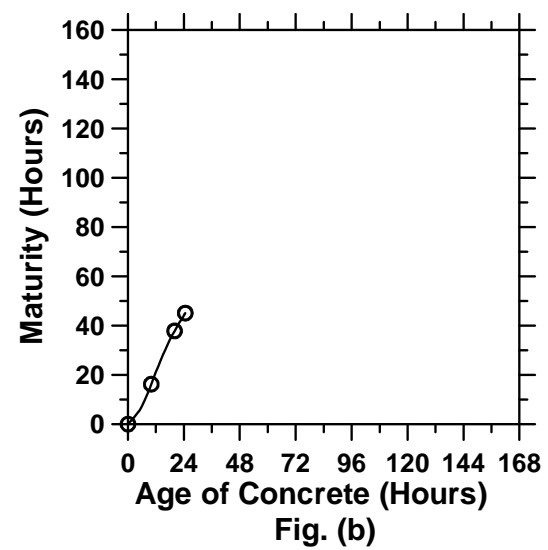
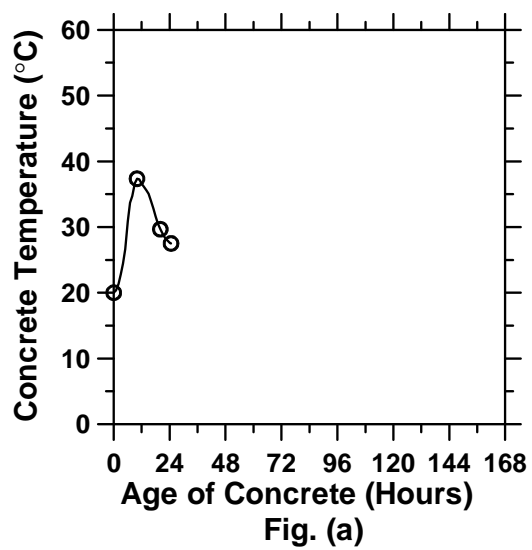


Figure A.33: Pavement with a D/6 saw-cut depth introduced at 15 hours (cont'd).

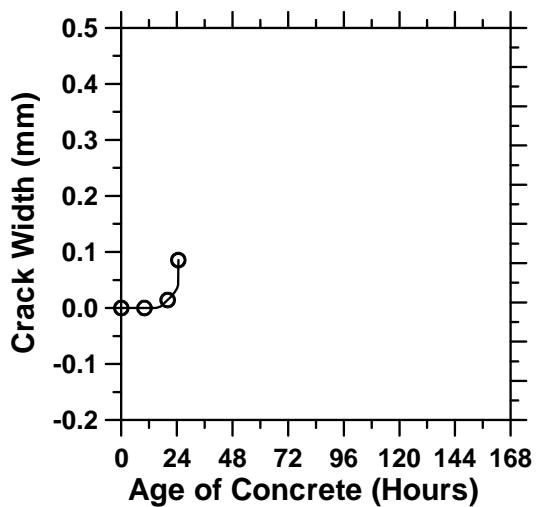


Fig. (e)

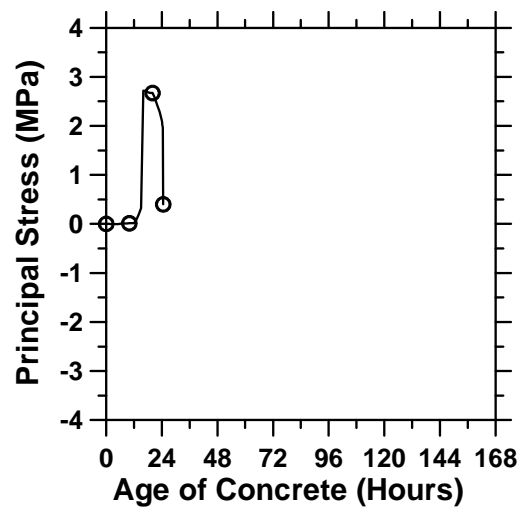


Fig. (f)

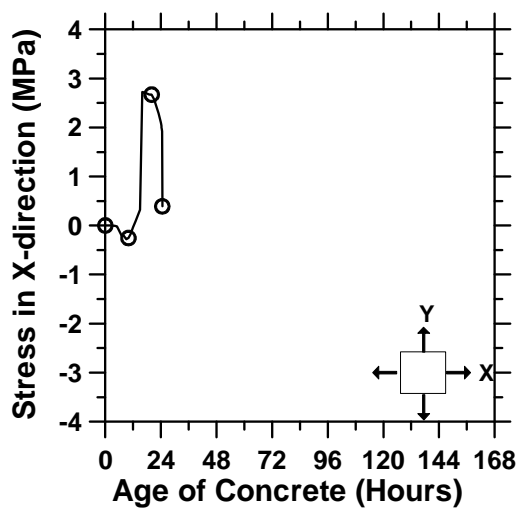


Fig. (g)

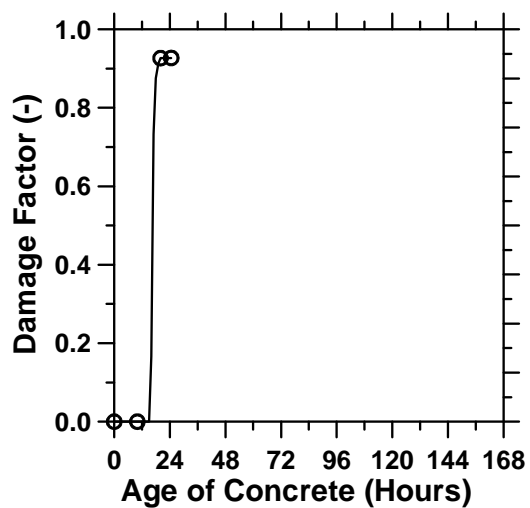


Fig. (h)

Figure A.33: Pavement with a D/6 saw-cut depth introduced at 15 hours.

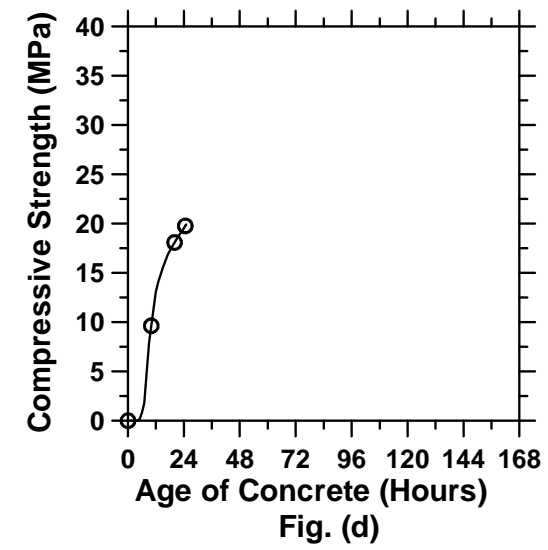
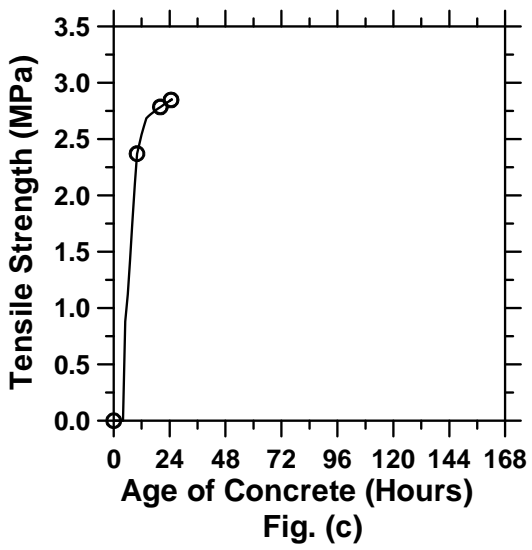
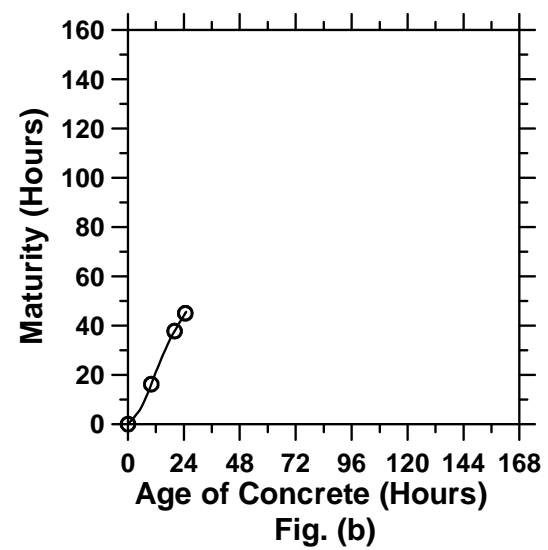
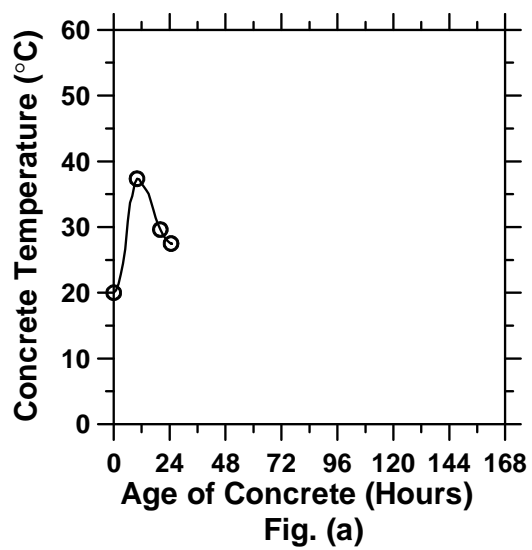


Figure A.34: Pavement with a D/6 saw-cut depth introduced at 18 hours (cont'd).

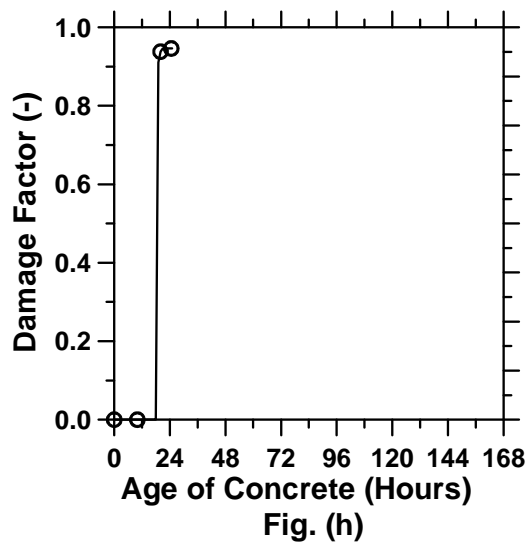
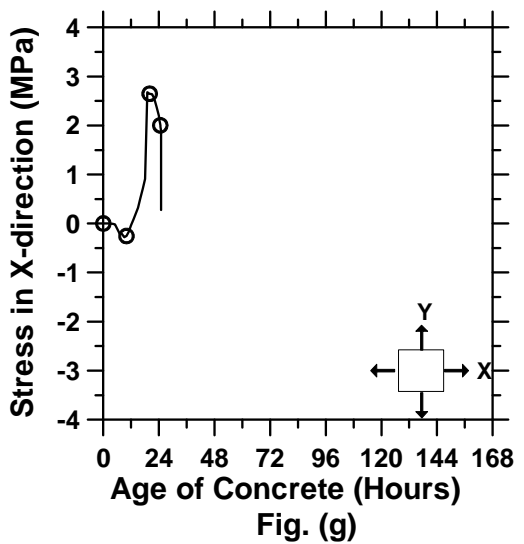
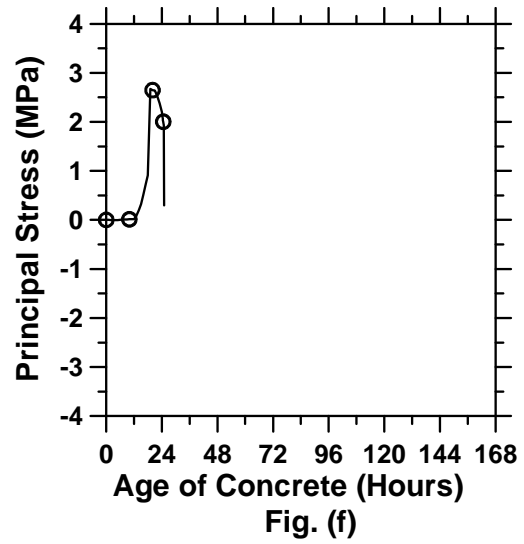
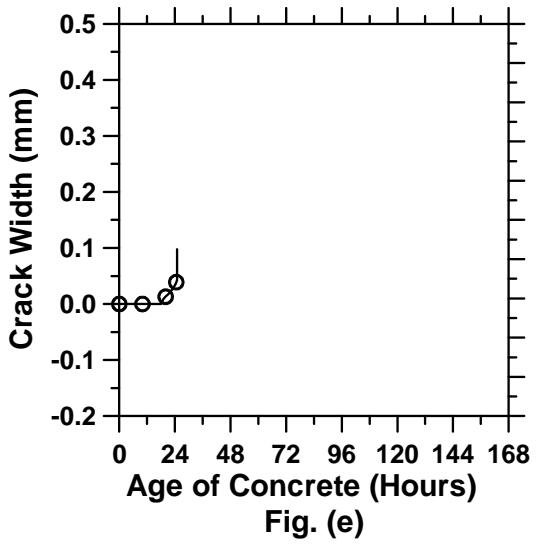


Figure A.34: Pavement with a D/6 saw-cut depth introduced at 18 hours.

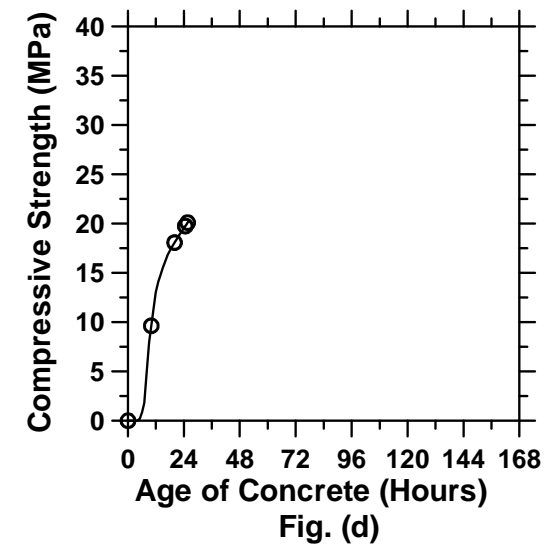
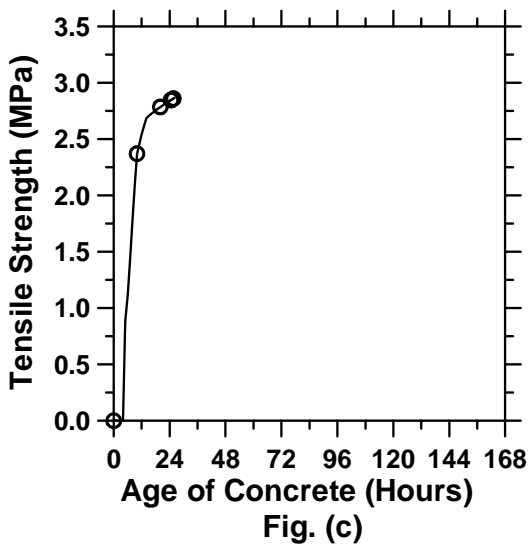
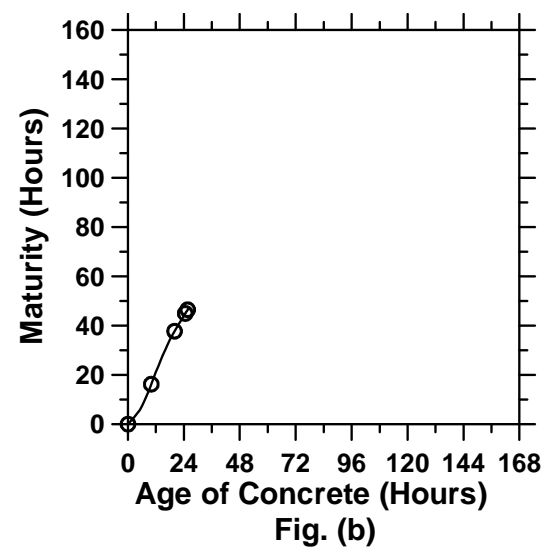
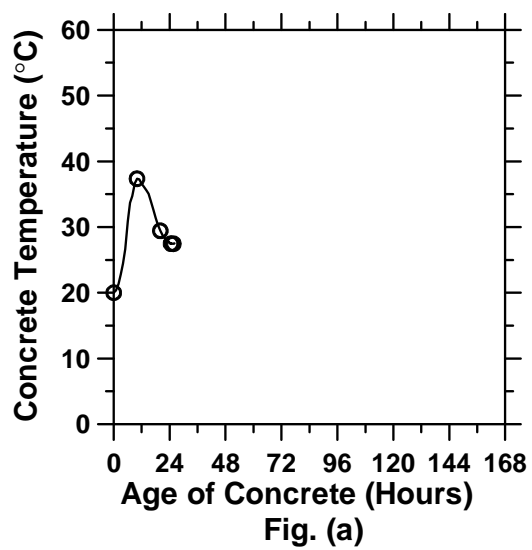


Figure A.35: Pavement with a D/6 saw-cut depth introduced at 21 hours (cont'd).

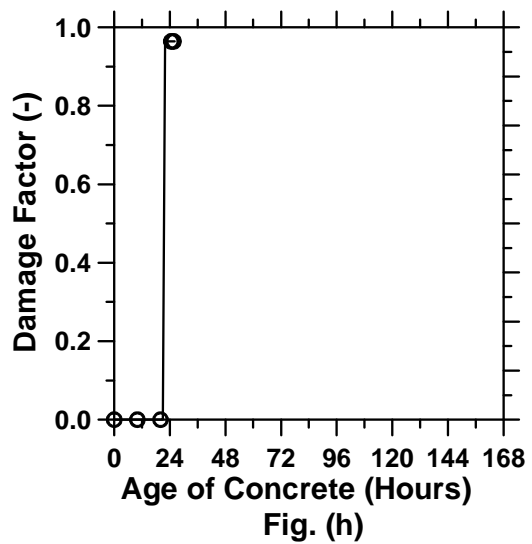
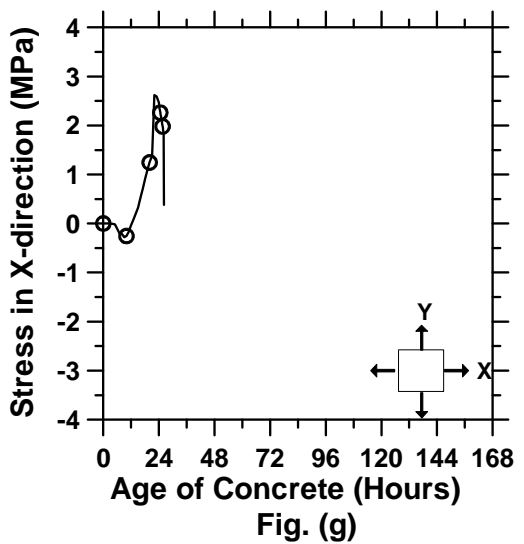
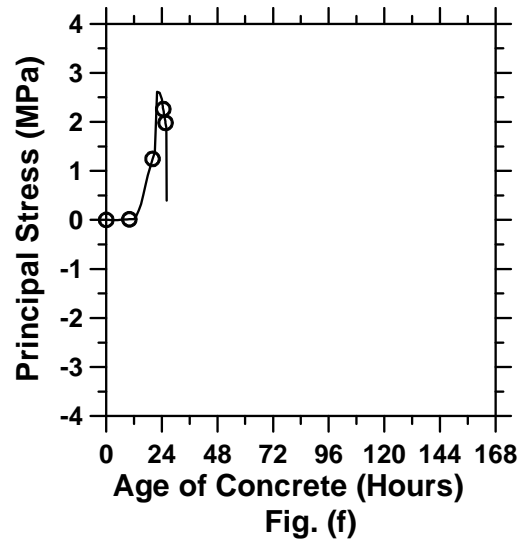
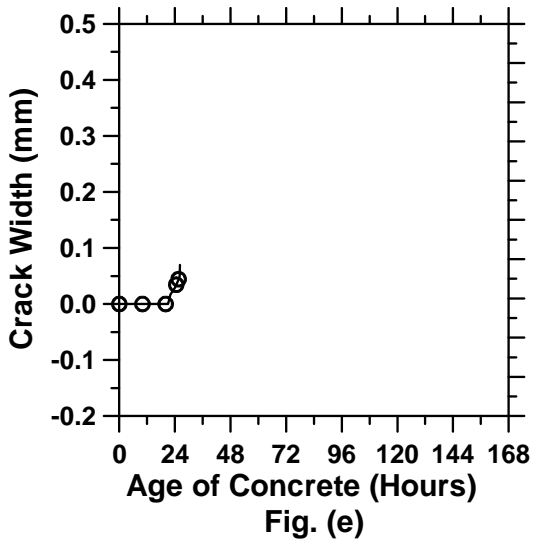


Figure A.35: Pavement with a D/6 saw-cut depth introduced at 21 hours.

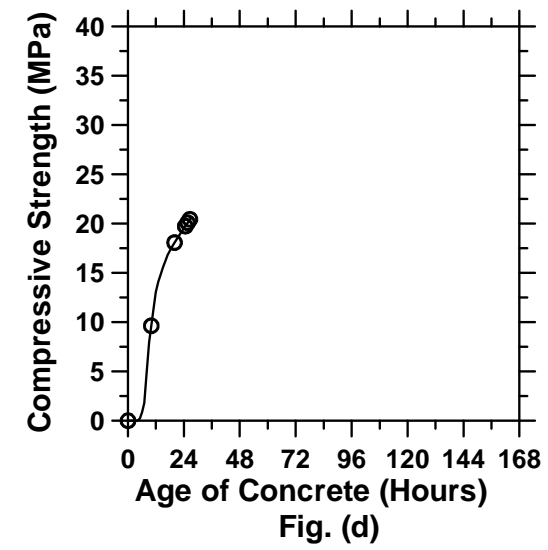
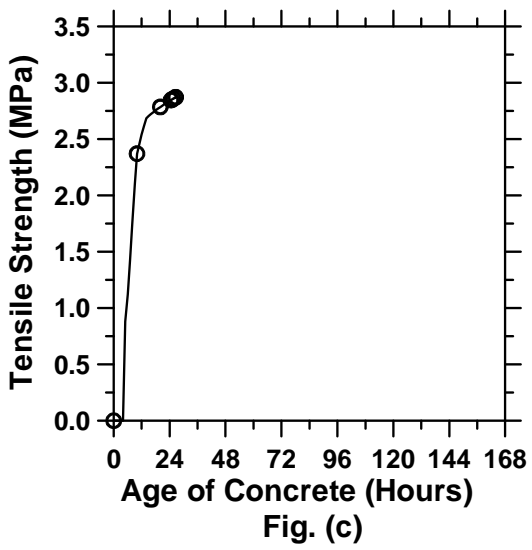
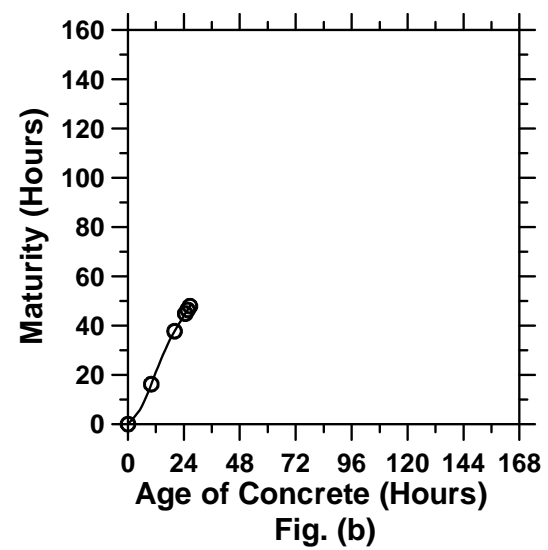
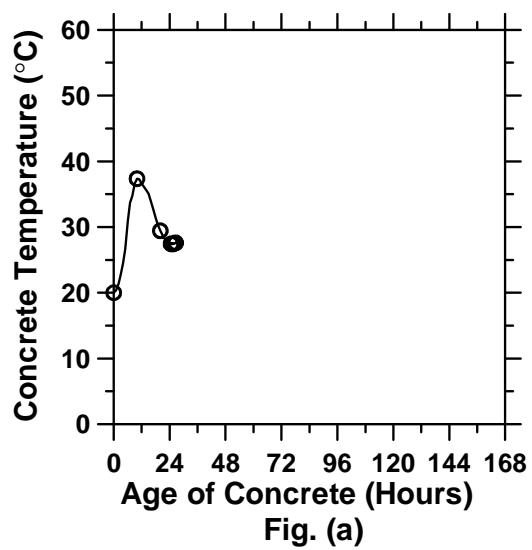


Figure A.36: Pavement with a D/6 saw-cut depth introduced at 24 hours (cont'd).

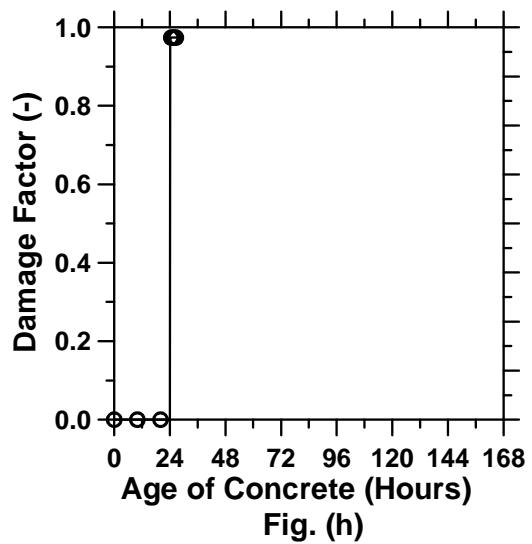
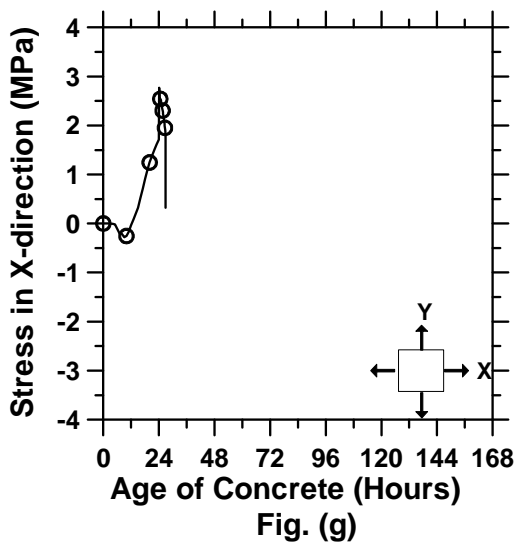
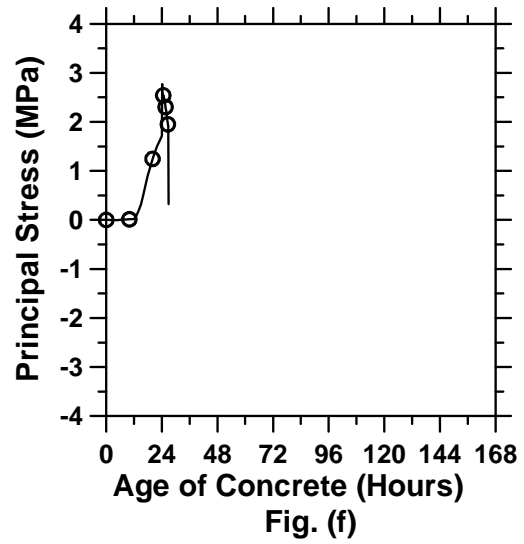
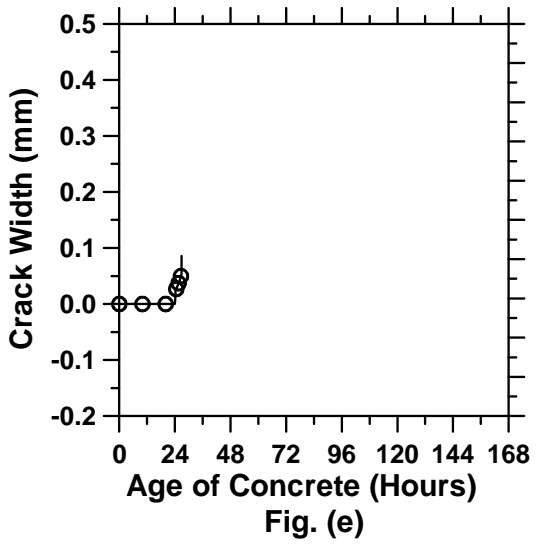


Figure A.36: Pavement with a D/6 saw-cut depth introduced at 24 hours.

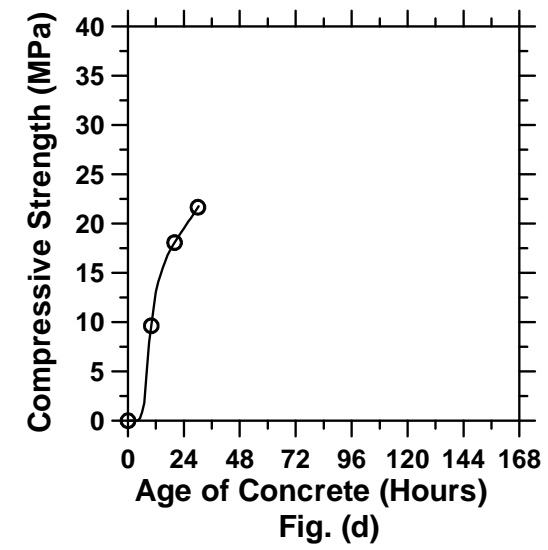
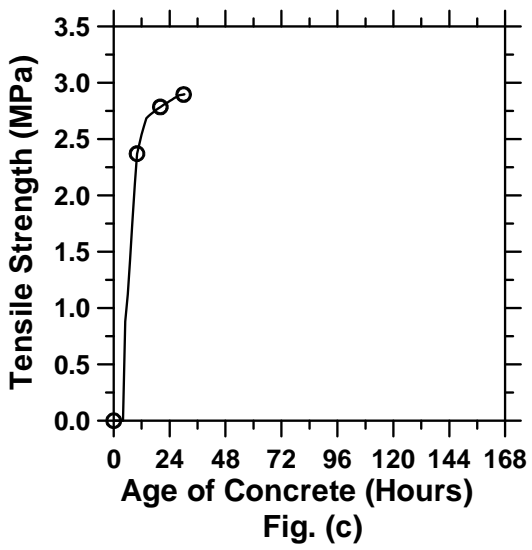
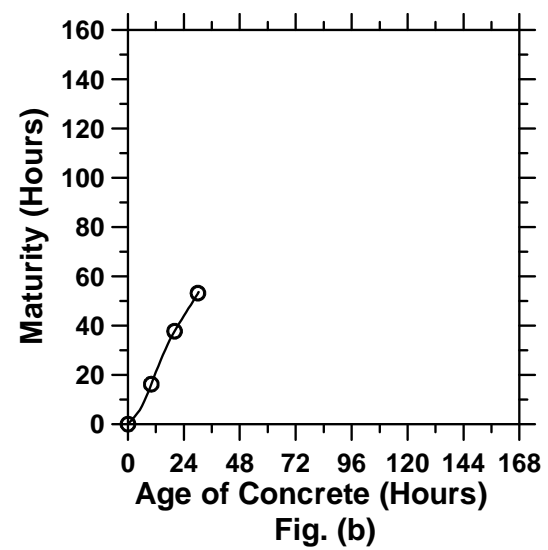
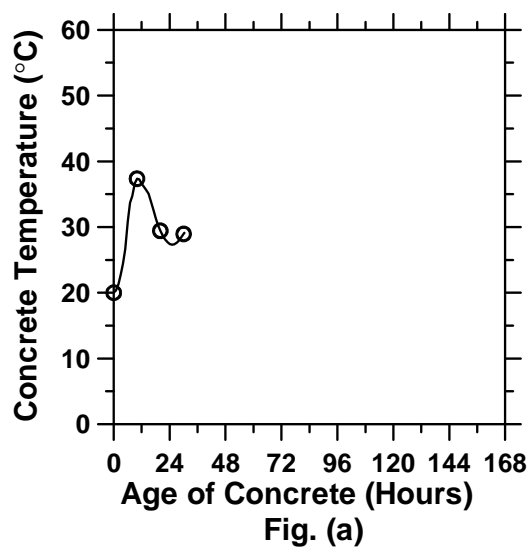


Figure A.37: Pavement with a D/6 saw-cut depth introduced at 30 hours (cont'd).

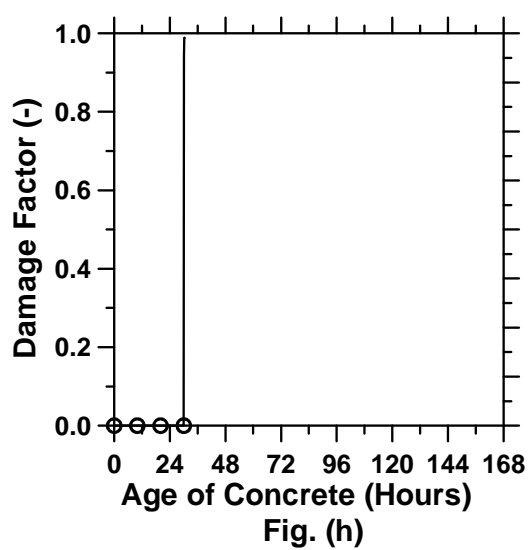
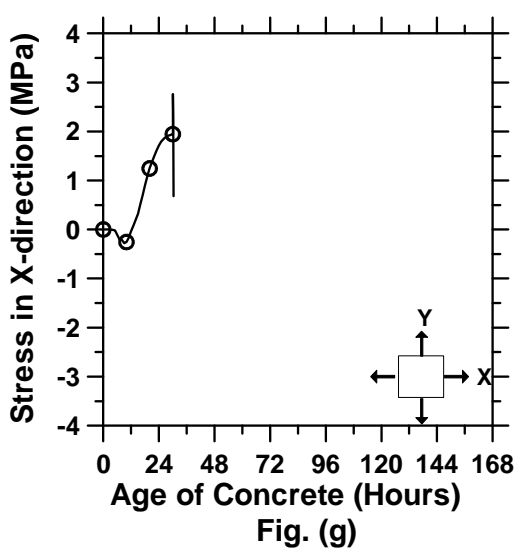
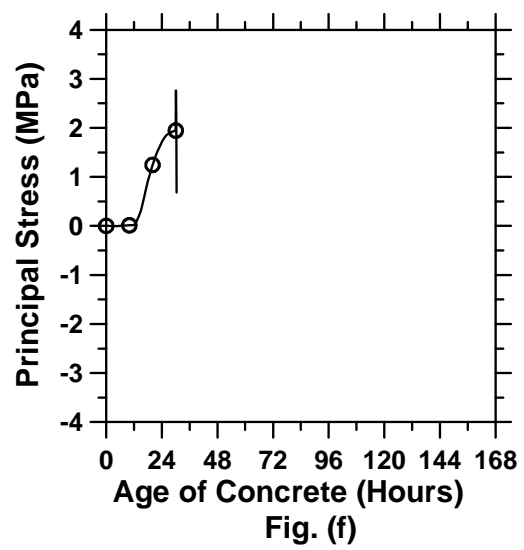
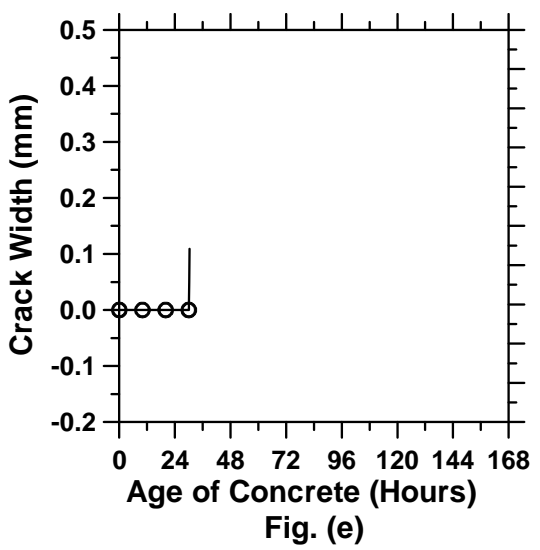


Figure A.37: Pavement with a D/6 saw-cut depth introduced at 30 hours.

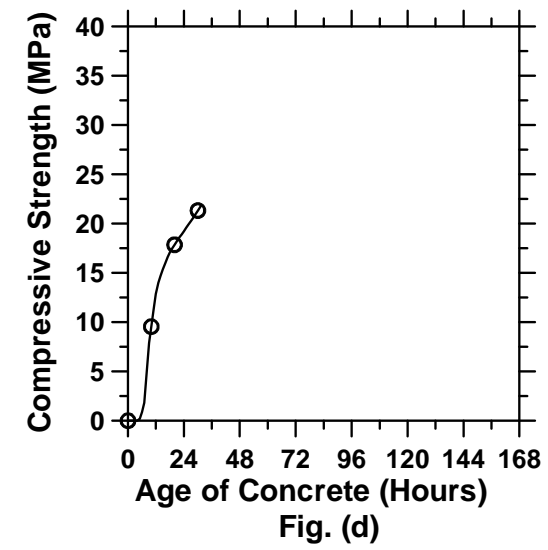
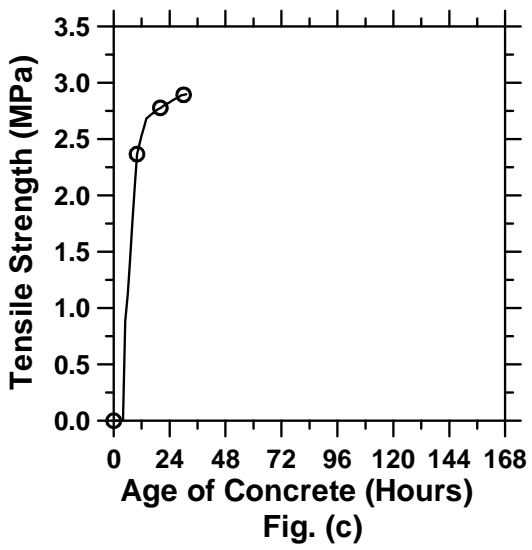
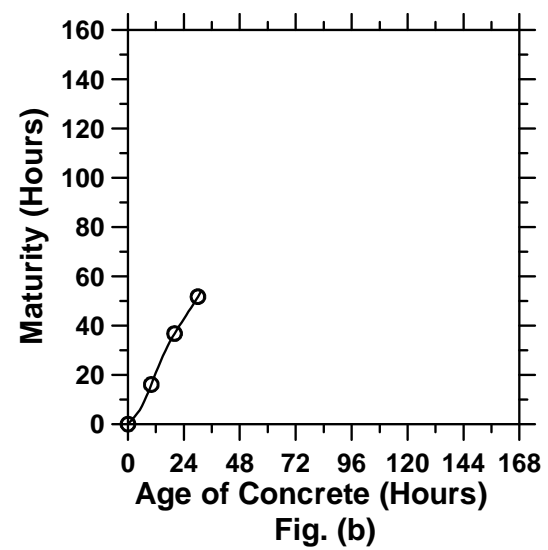
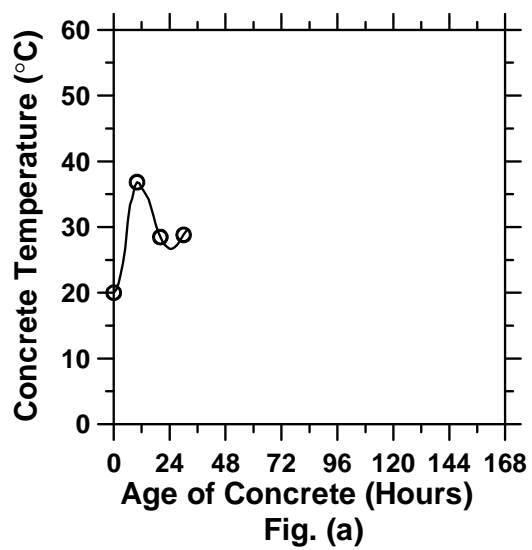


Figure A.38: Pavement with a D/8 saw-cut depth introduced at 0 hour (cont'd).

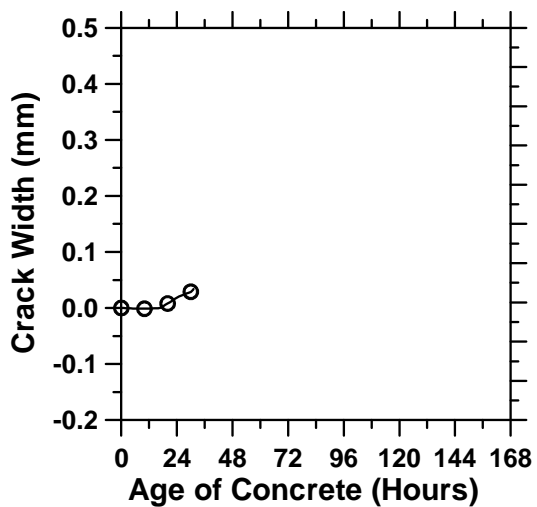


Fig. (e)

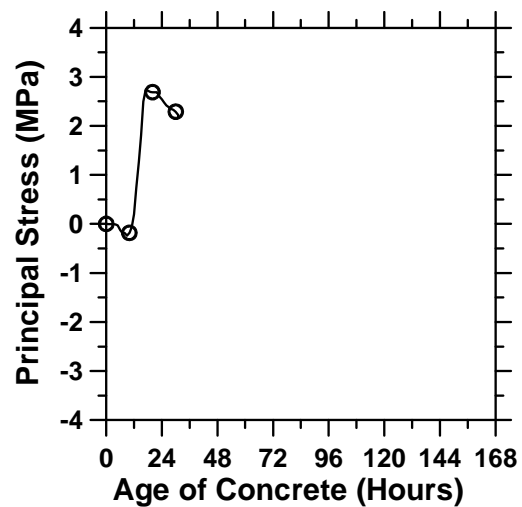


Fig. (f)

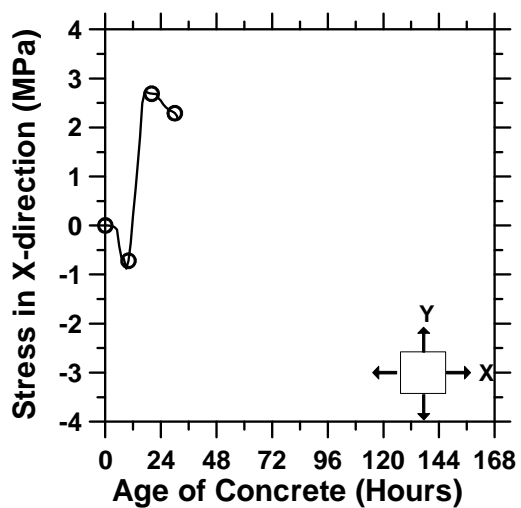


Fig. (g)

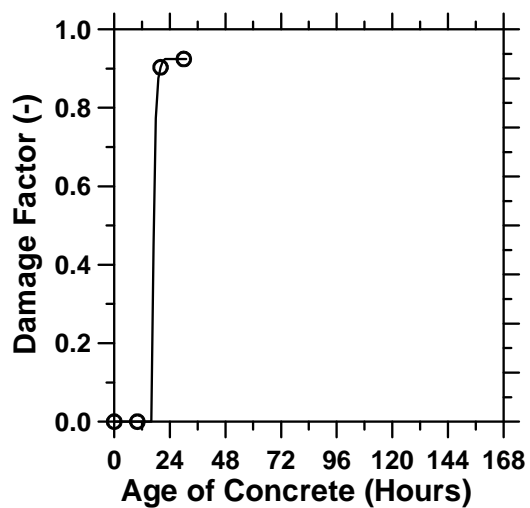


Fig. (h)

Figure A.38: Pavement with a D/8 saw-cut depth introduced at 0 hour.

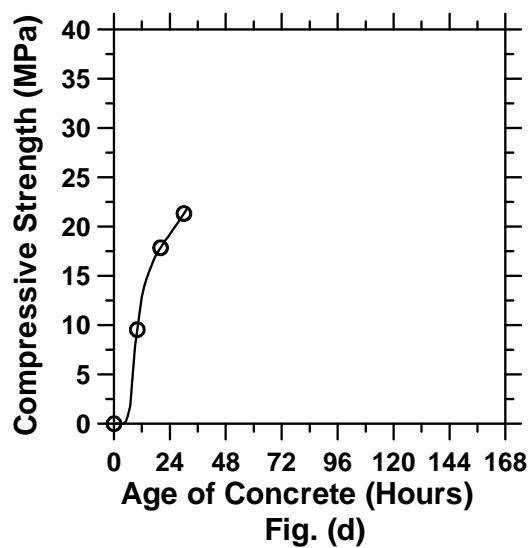
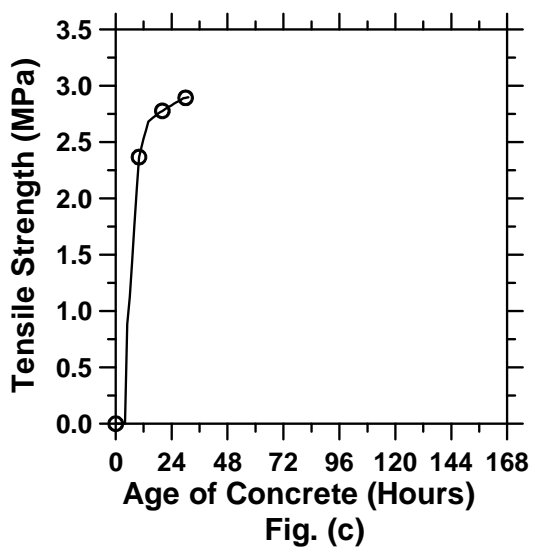
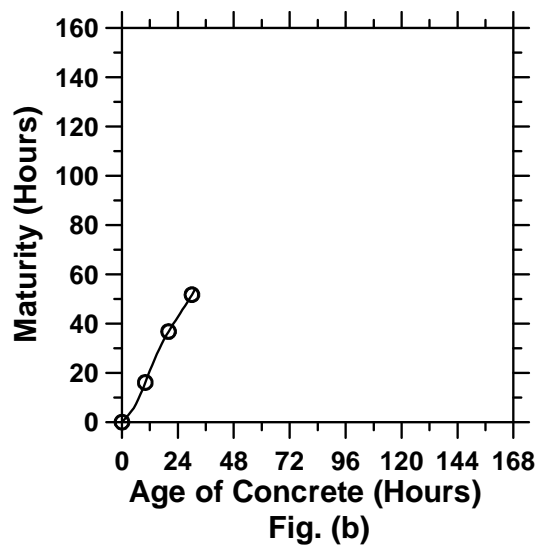
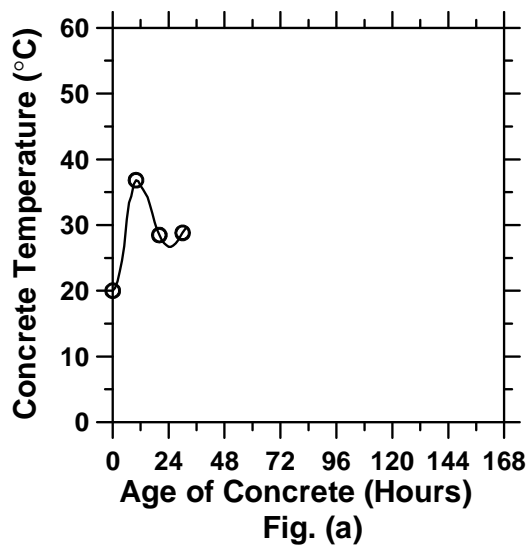


Figure A.39: Pavement with a D/8 saw-cut depth introduced at 6 hours (cont'd).

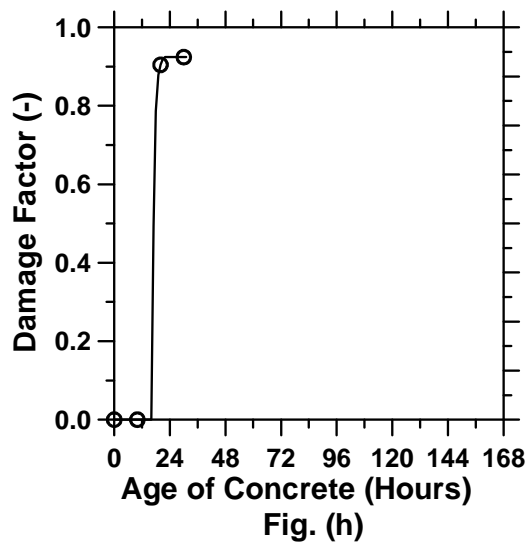
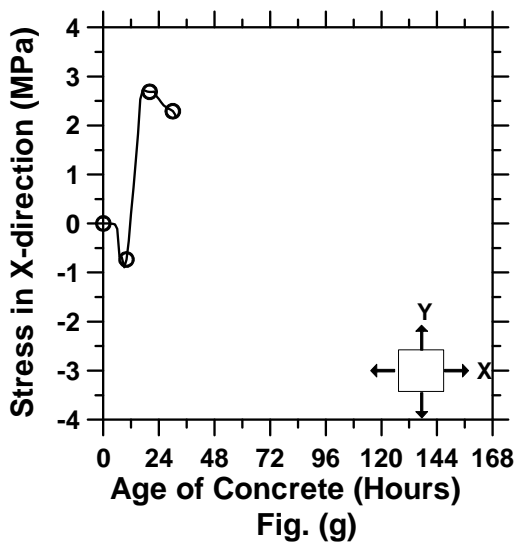
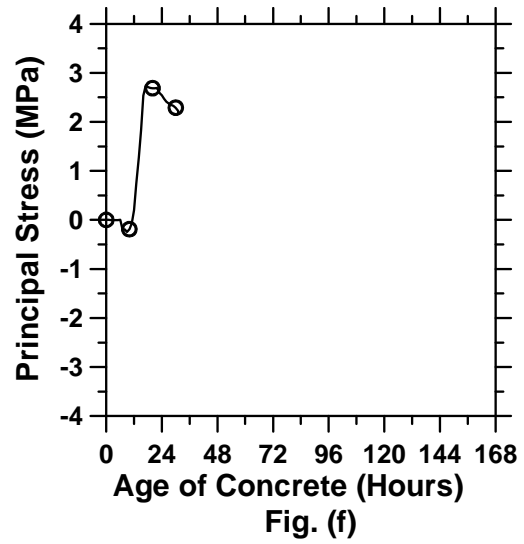
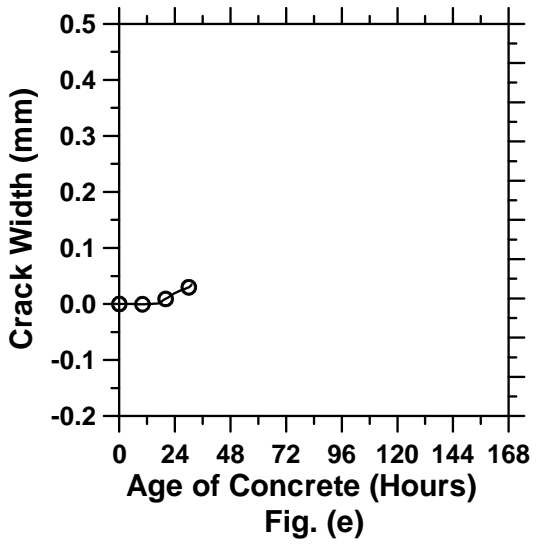


Figure A.39: Pavement with a D/8 saw-cut depth introduced at 6 hours.

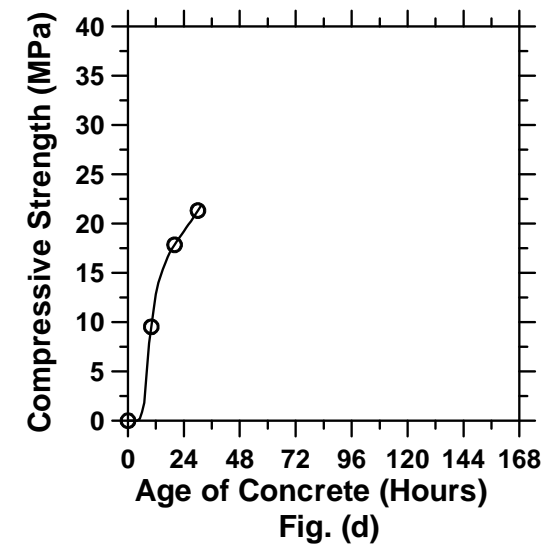
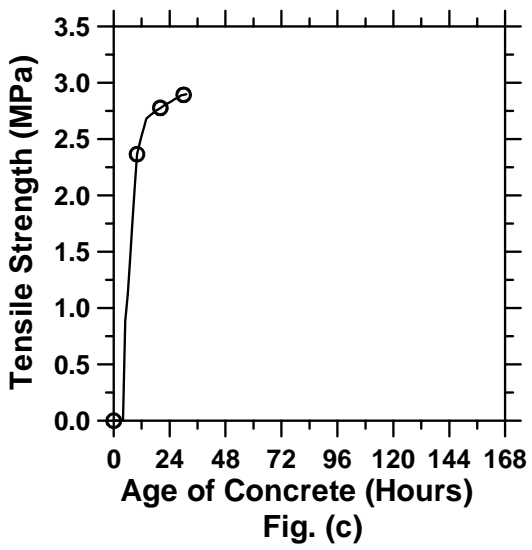
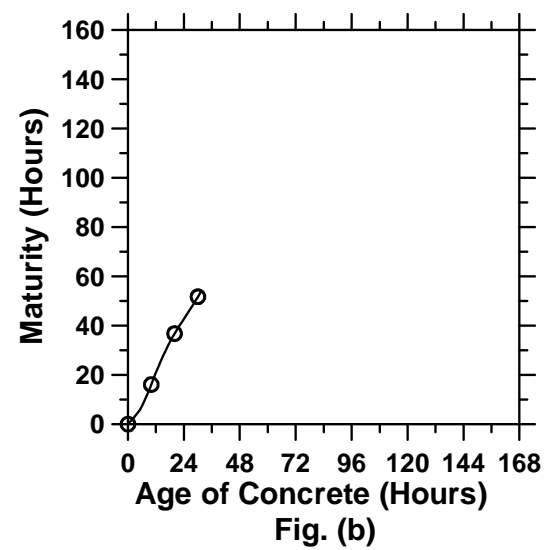
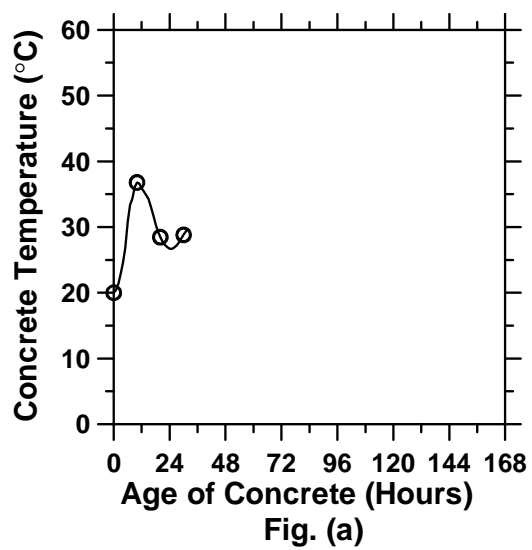


Figure A.40: Pavement with a D/8 saw-cut depth introduced at 9 hours (cont'd).

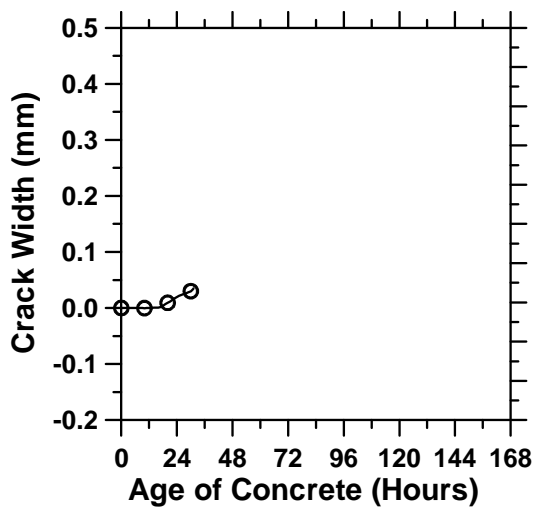


Fig. (e)

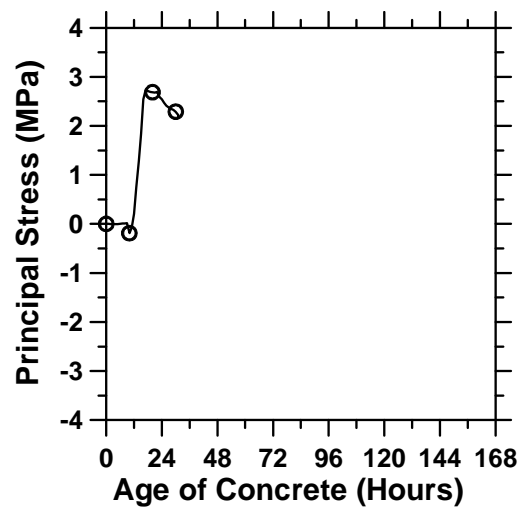


Fig. (f)

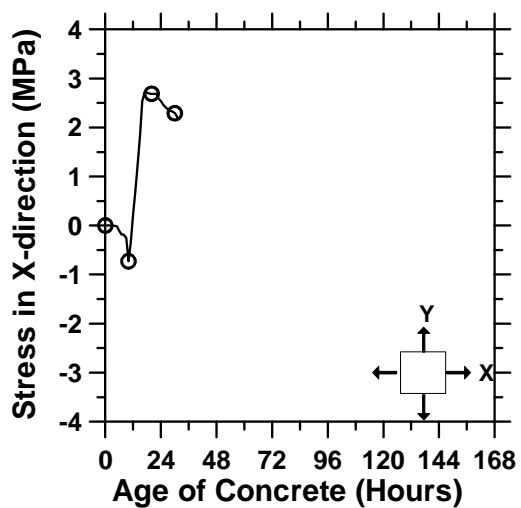


Fig. (g)

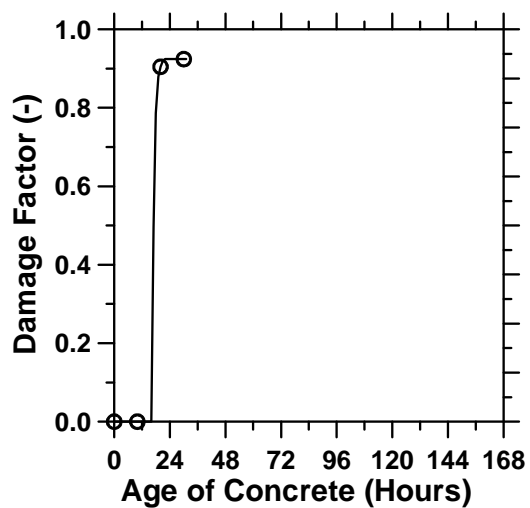


Fig. (h)

Figure A.40: Pavement with a D/8 saw-cut depth introduced at 9 hours.

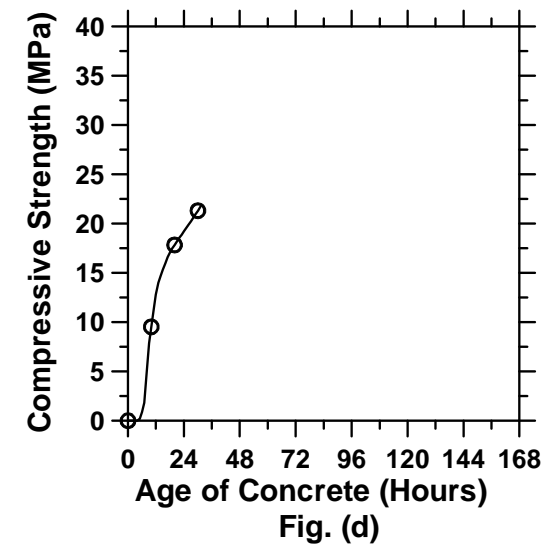
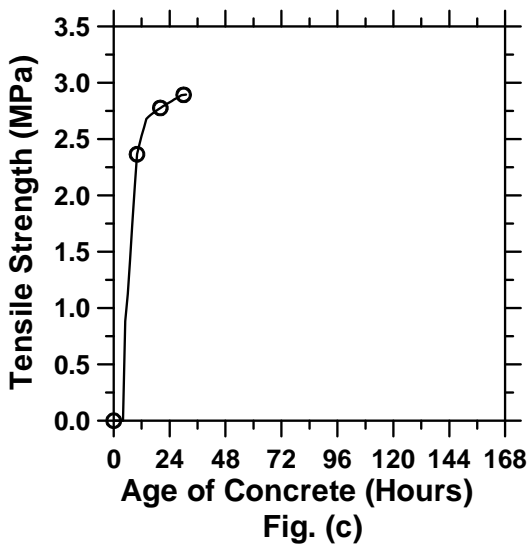
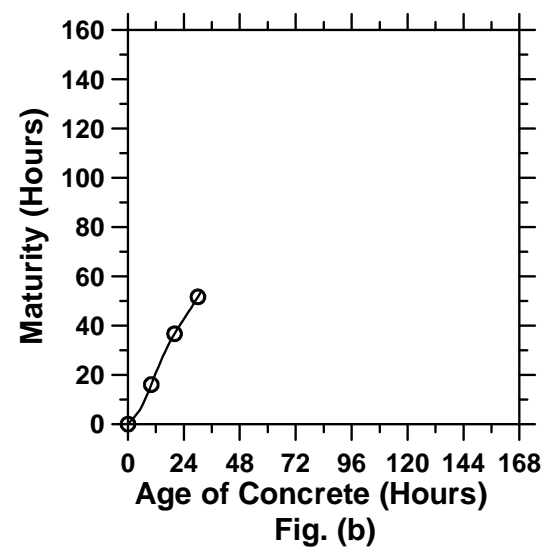
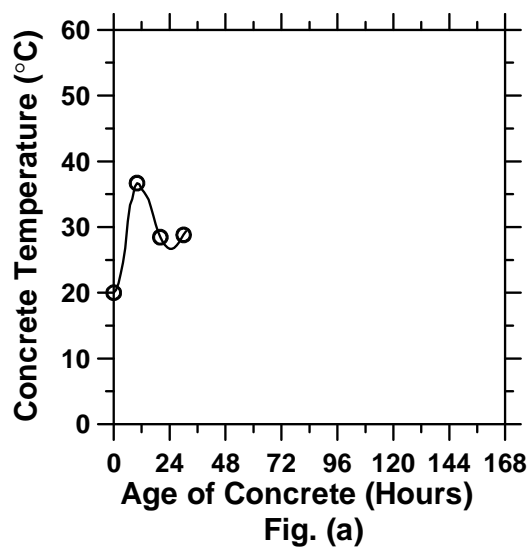


Figure A.41: Pavement with a D/8 saw-cut depth introduced at 12 hours (cont'd).

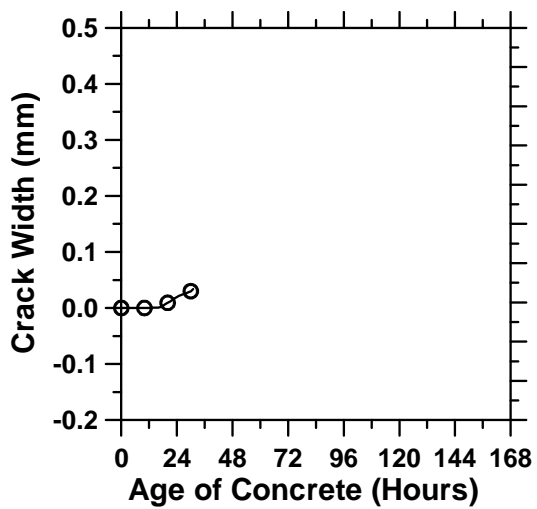


Fig. (e)

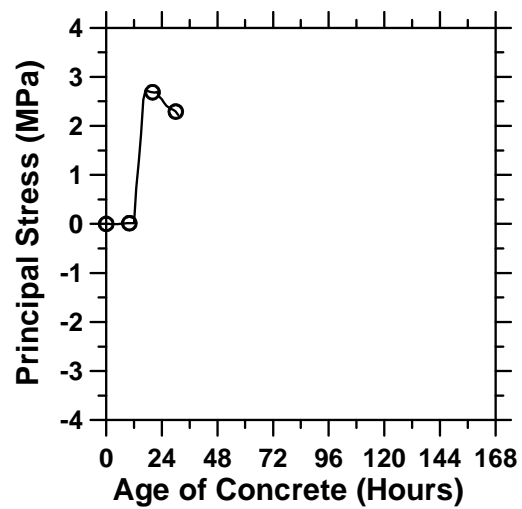


Fig. (f)

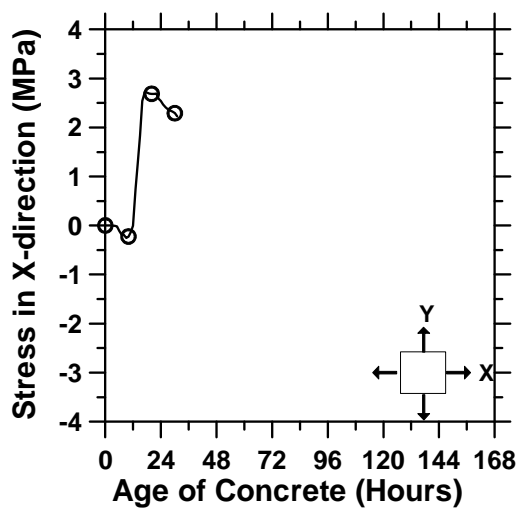


Fig. (g)

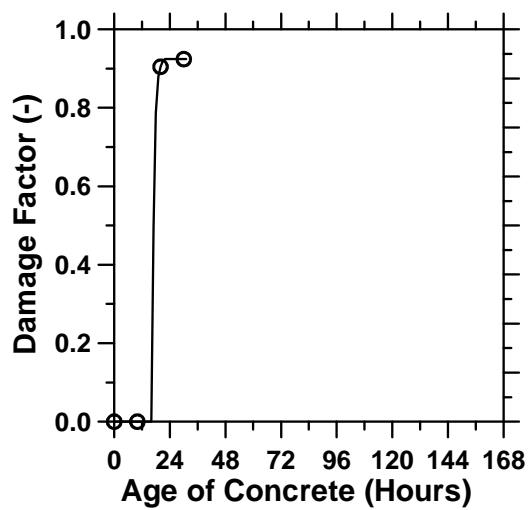


Fig. (h)

Figure A.41: Pavement with a D/8 saw-cut depth introduced at 12 hours.

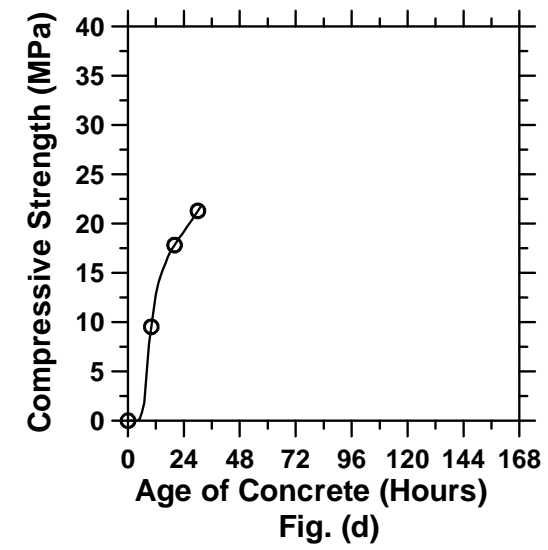
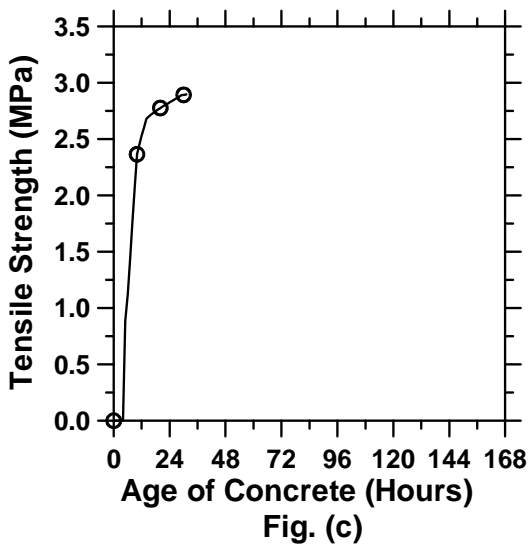
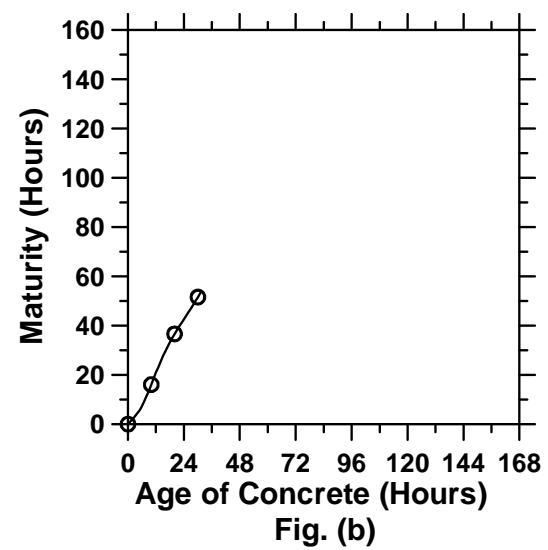
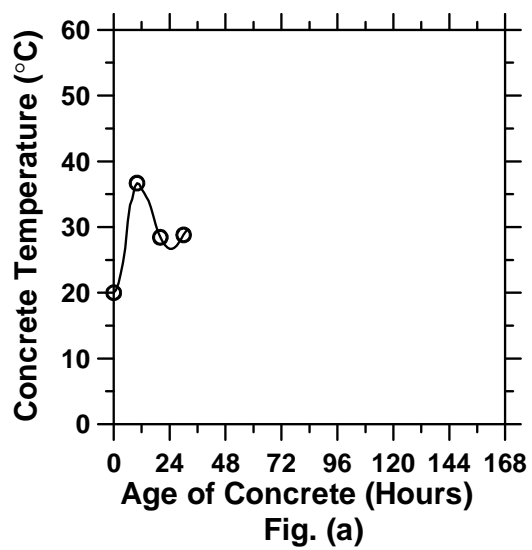


Figure A.42: Pavement with a D/8 saw-cut depth introduced at 15 hours (cont'd).

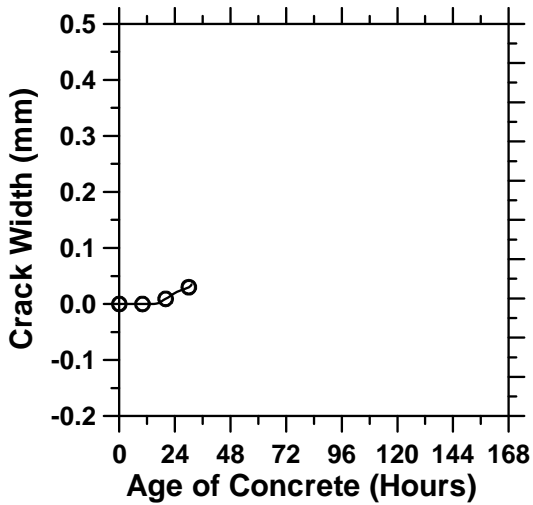


Fig. (e)

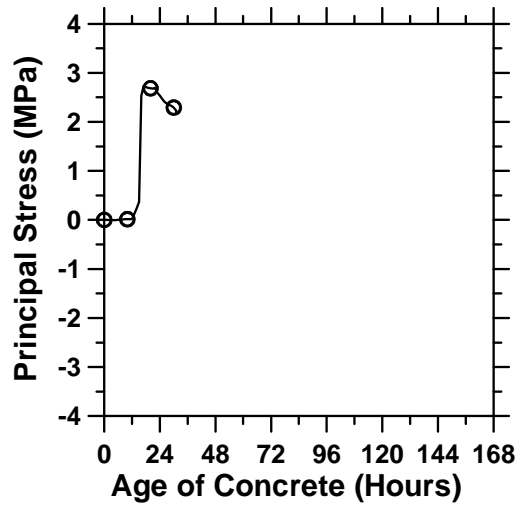


Fig. (f)

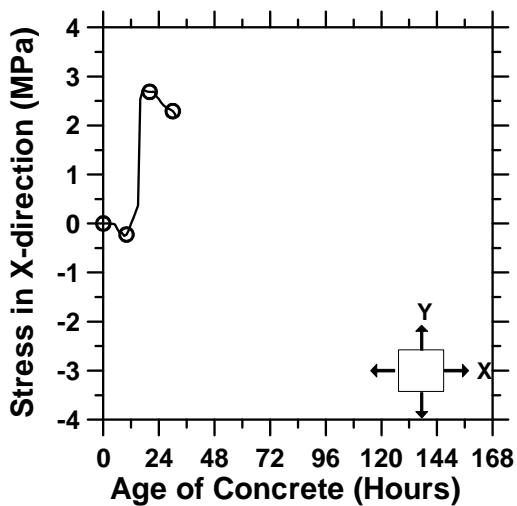


Fig. (g)

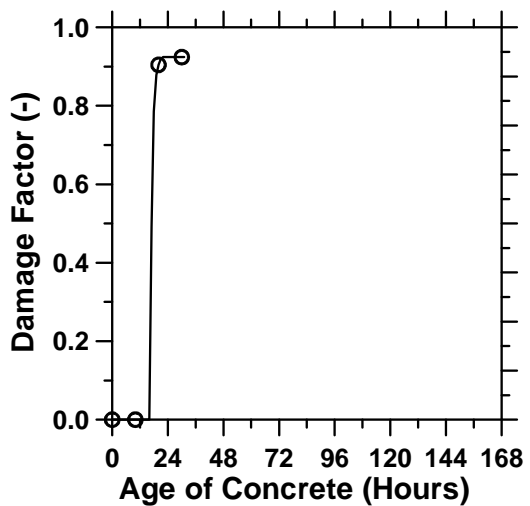


Fig. (h)

Figure A.42: Pavement with a D/8 saw-cut depth introduced at 15 hours.

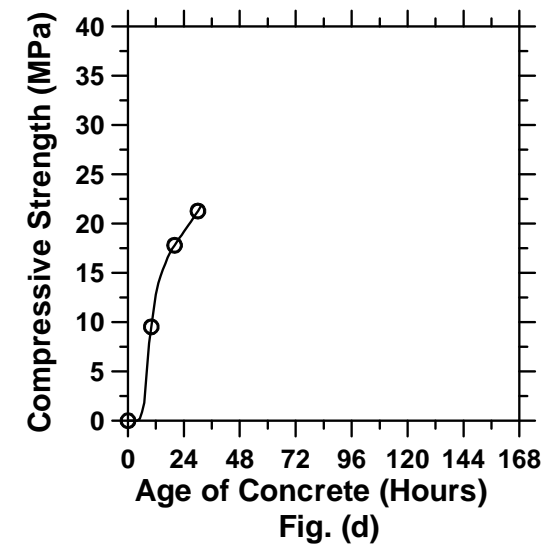
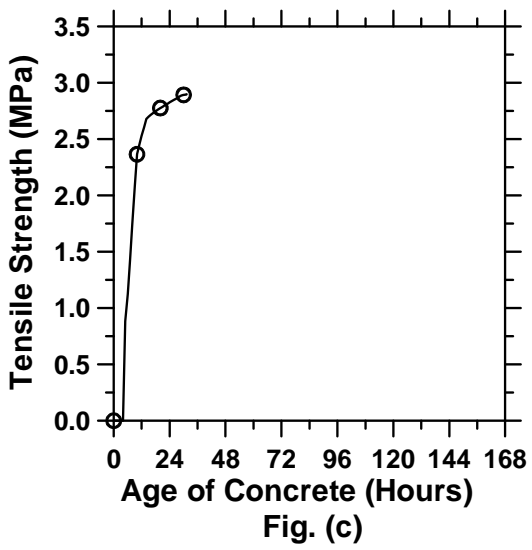
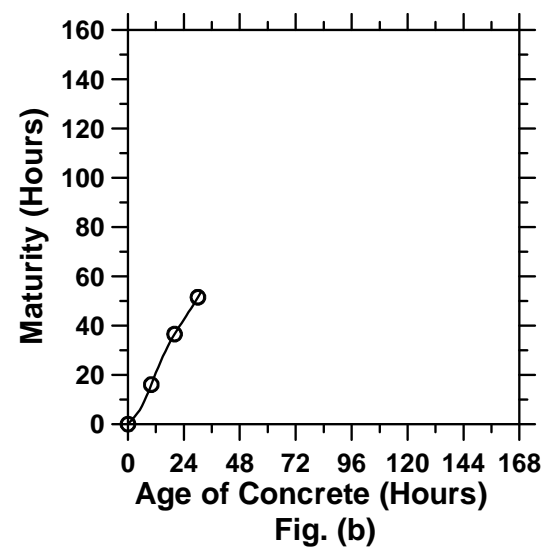
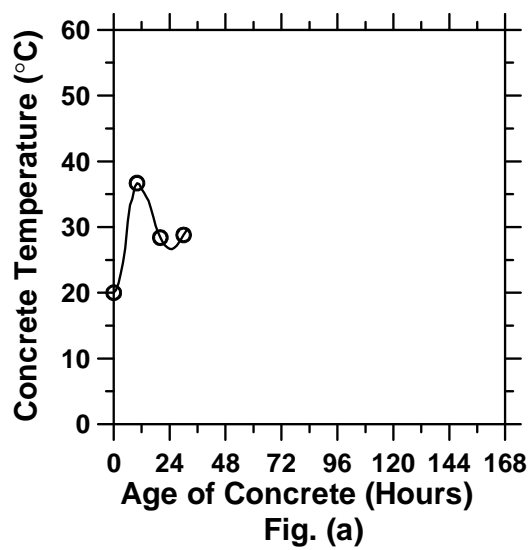


Figure A.43: Pavement with a D/8 saw-cut depth introduced at 18 hours (cont'd).

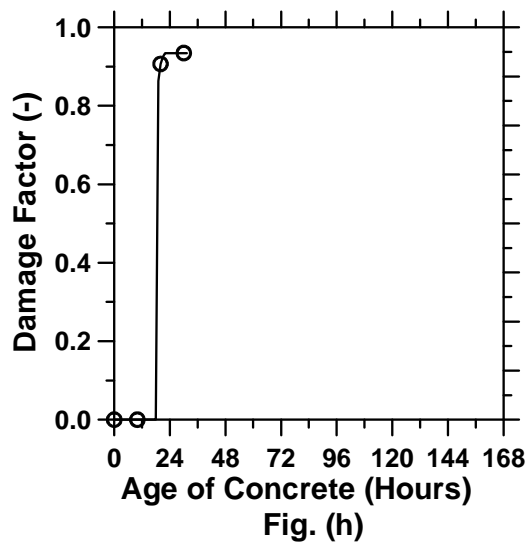
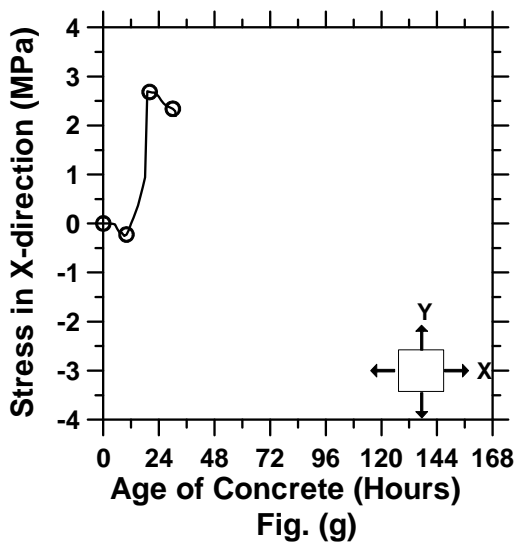
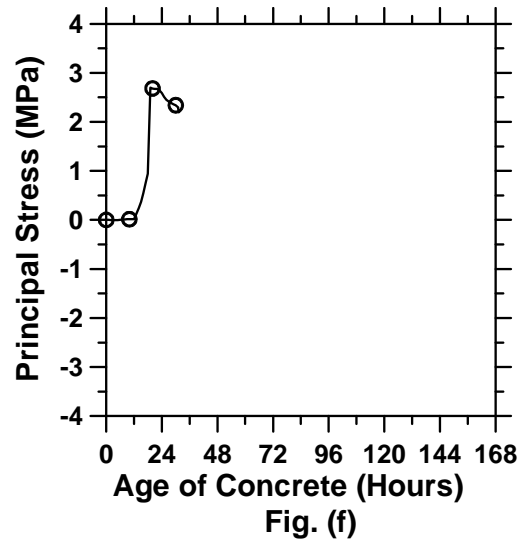
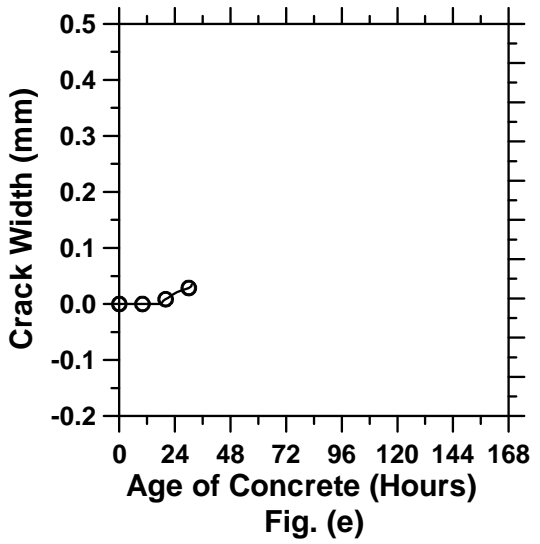


Figure A.43: Pavement with a D/8 saw-cut depth introduced at 18 hours.

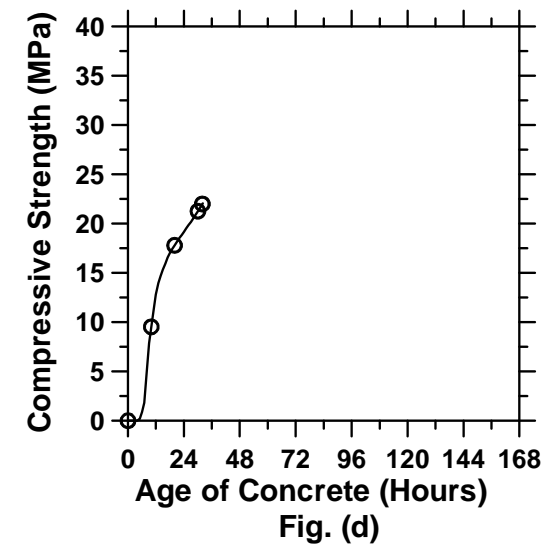
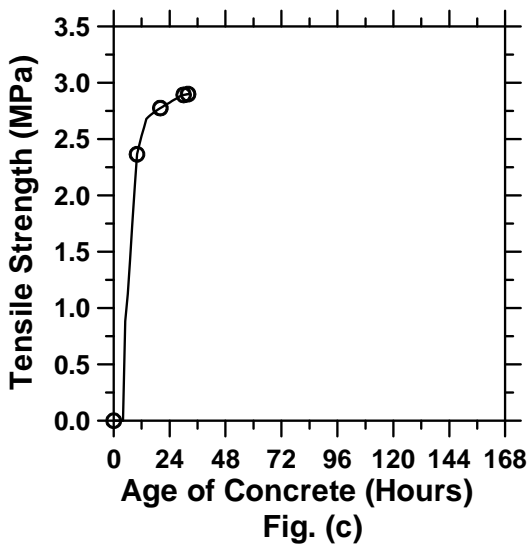
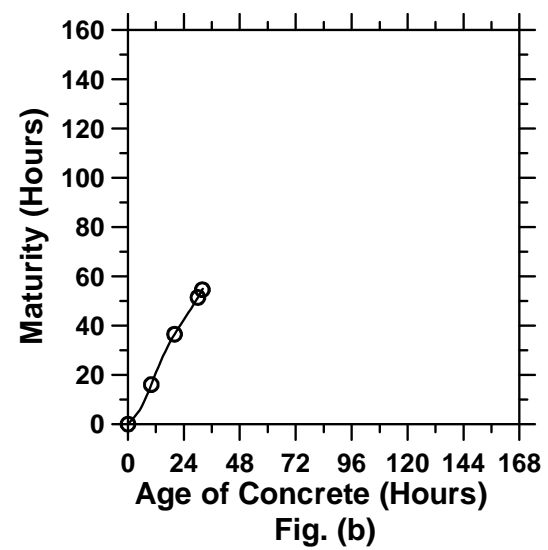
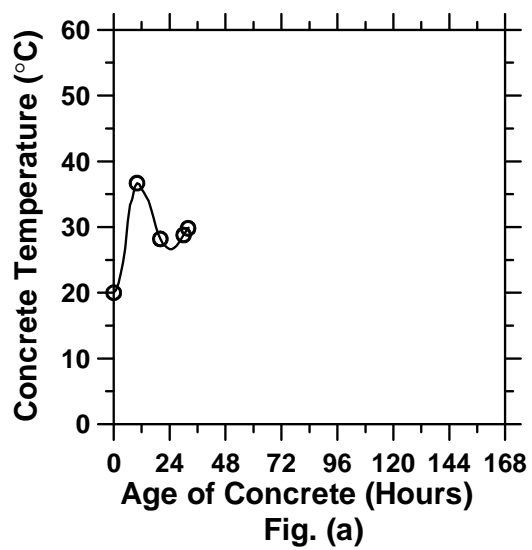


Figure A.44: Pavement with a D/8 saw-cut depth introduced at 21 hours (cont'd).

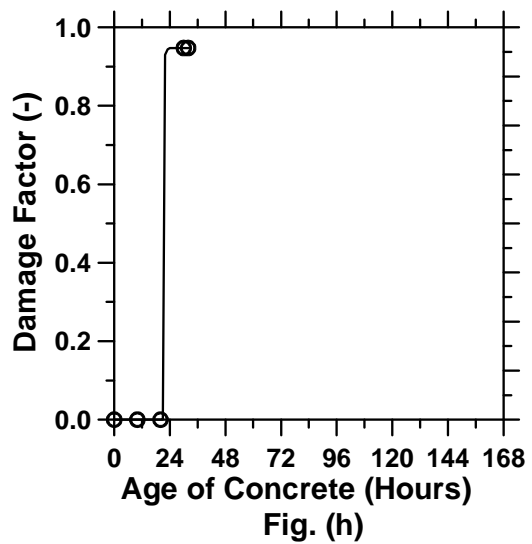
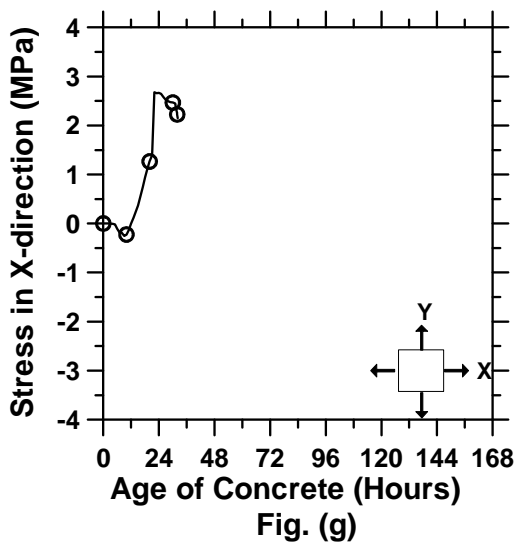
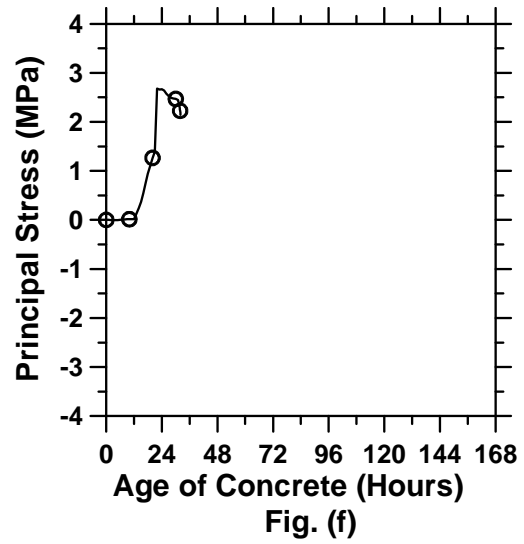
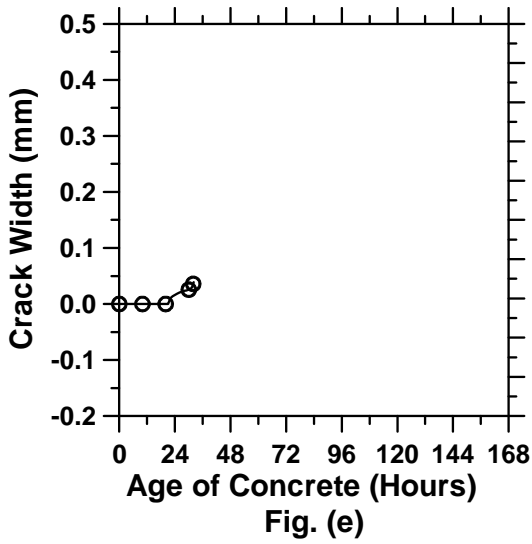


Figure A.44: Pavement with a D/8 saw-cut depth introduced at 21 hours.

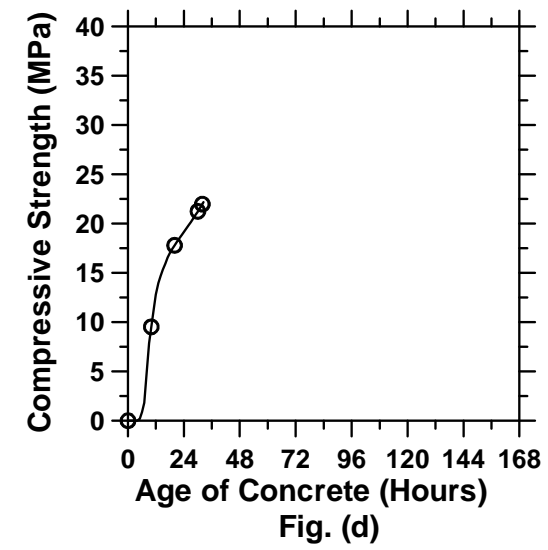
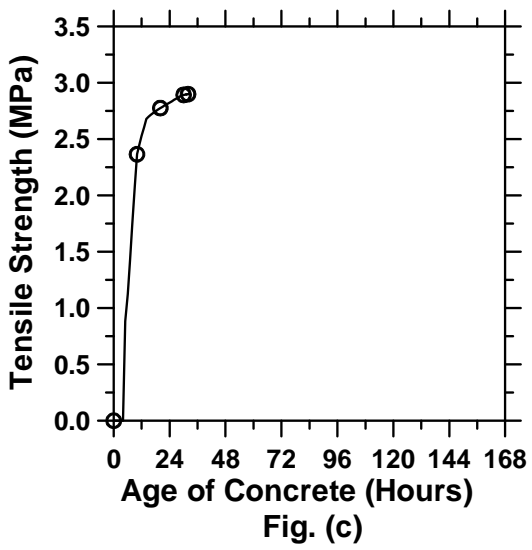
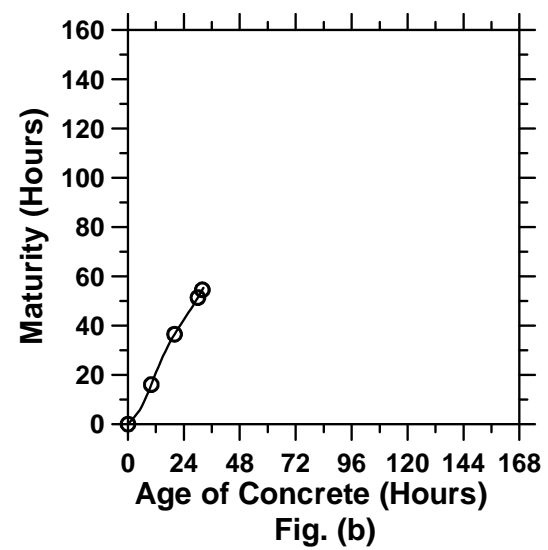
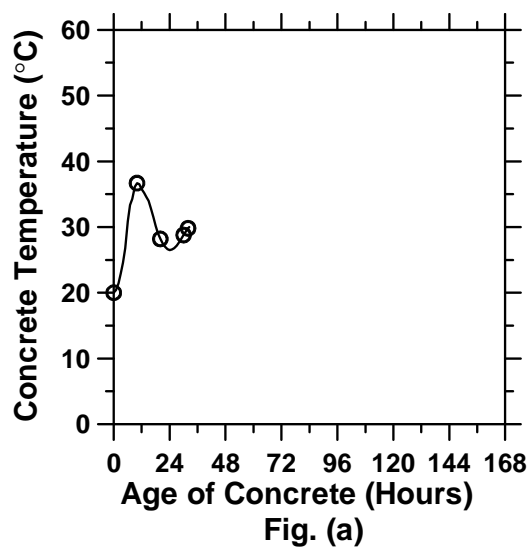


Figure A.45: Pavement with a D/8 saw-cut depth introduced at 24 hours (cont'd).

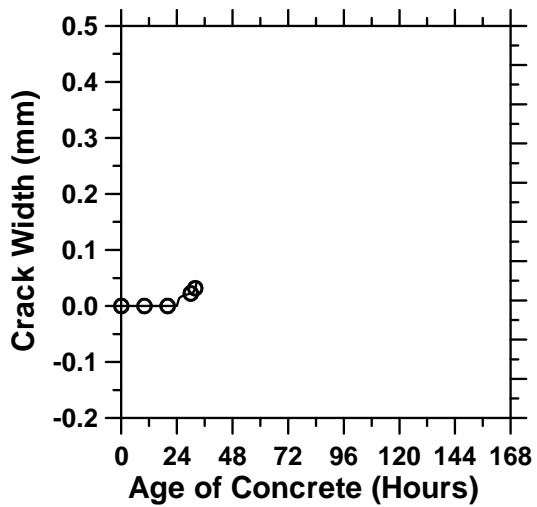


Fig. (e)

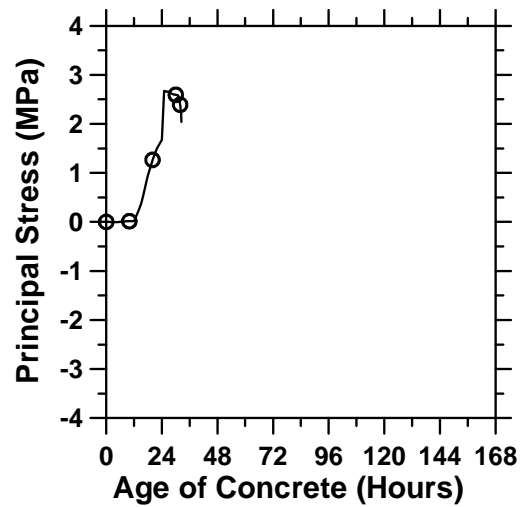


Fig. (f)

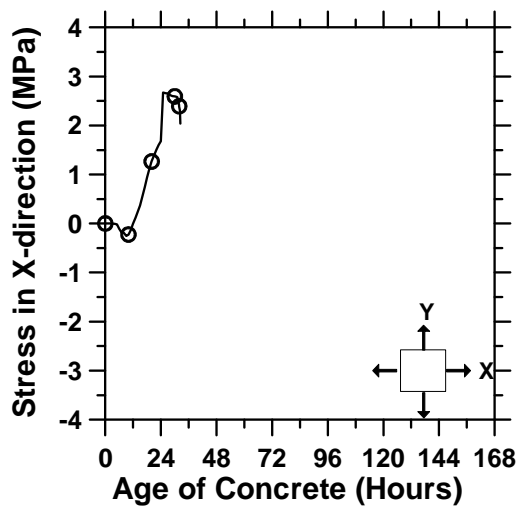


Fig. (g)

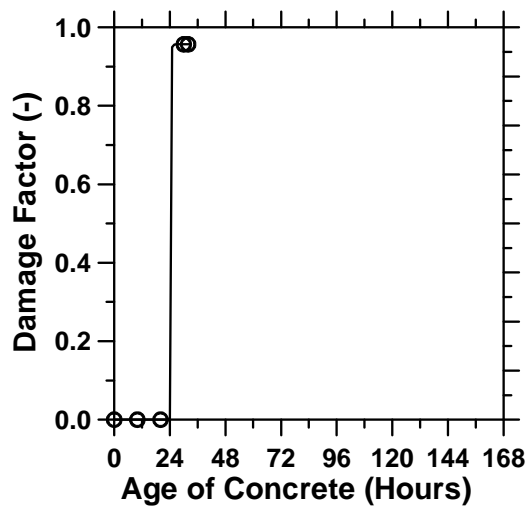


Fig. (h)

Figure A.45: Pavement with a D/8 saw-cut depth introduced at 24 hours.

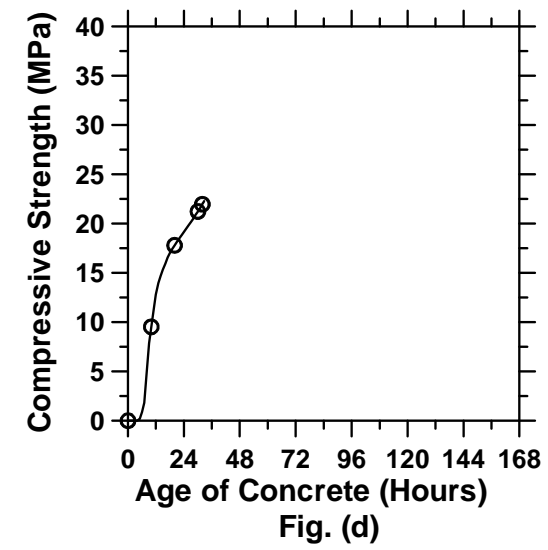
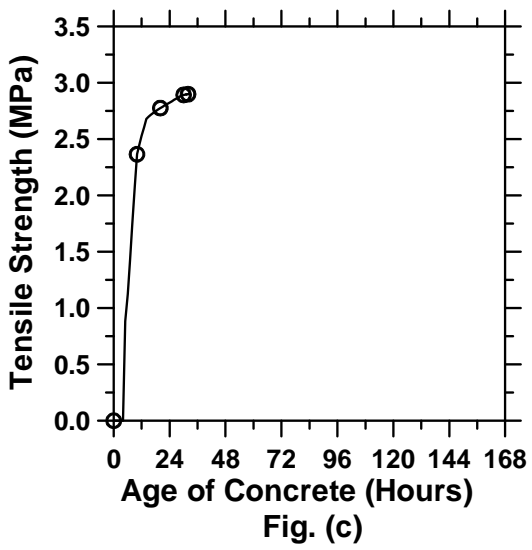
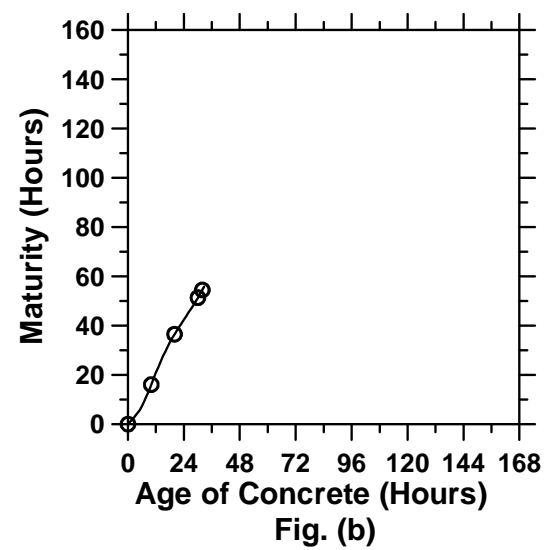
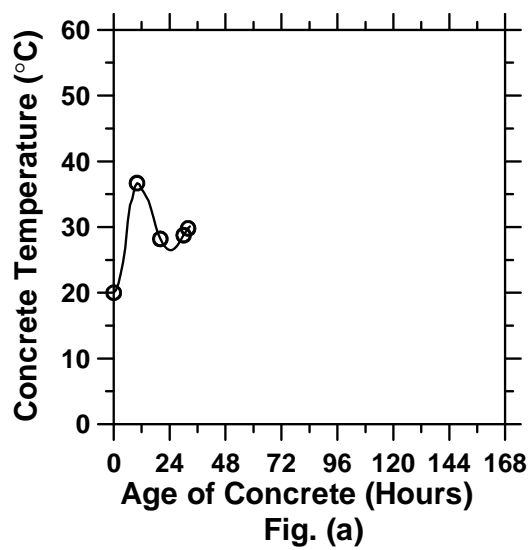


Figure A.46: Pavement with a D/8 saw-cut depth introduced at 30 hours (cont'd).

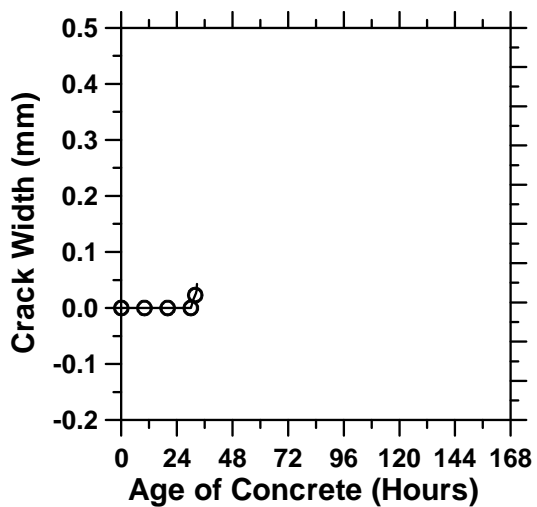


Fig. (e)

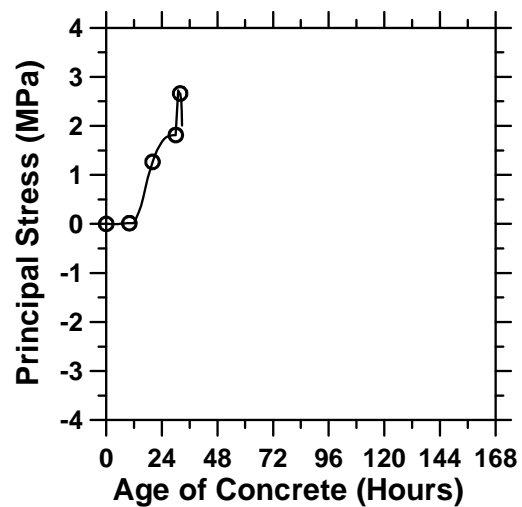


Fig. (f)

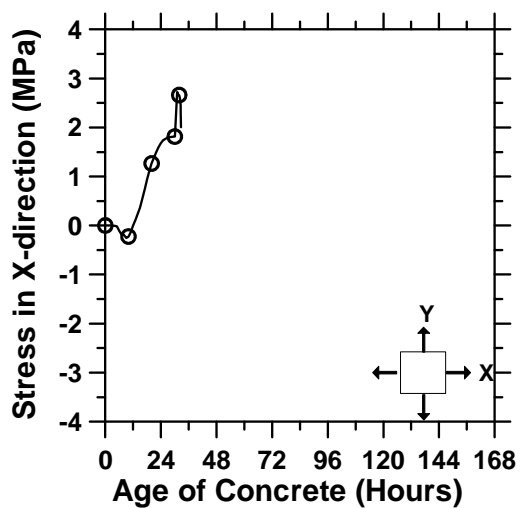


Fig. (g)

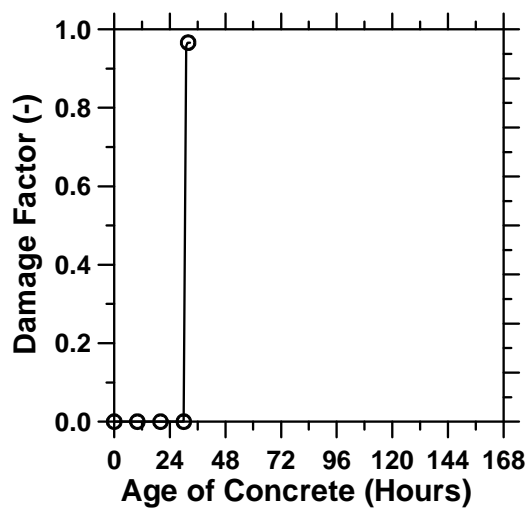


Fig. (h)

Figure A.46: Pavement with a D/8 saw-cut depth introduced at 30 hours.

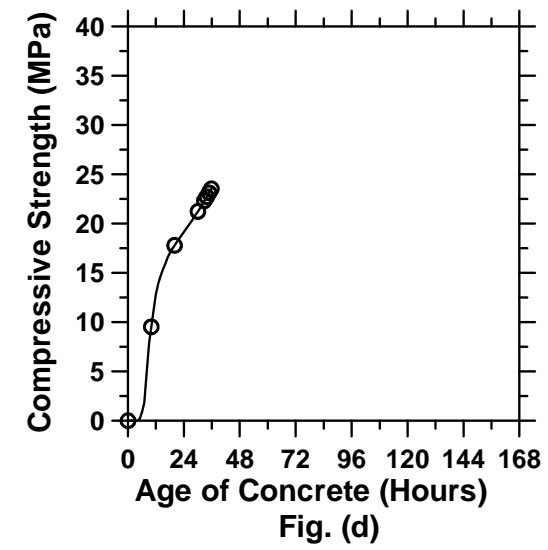
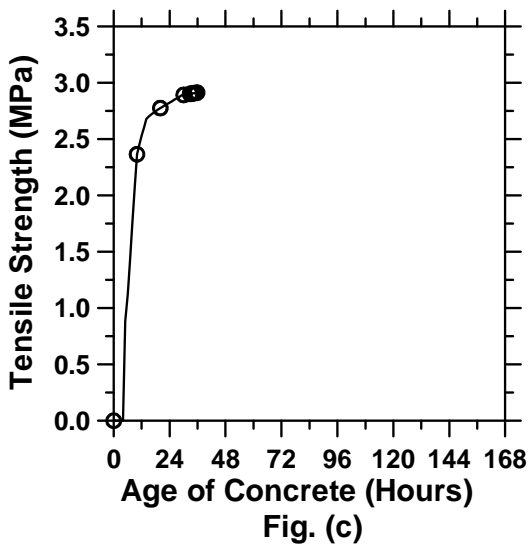
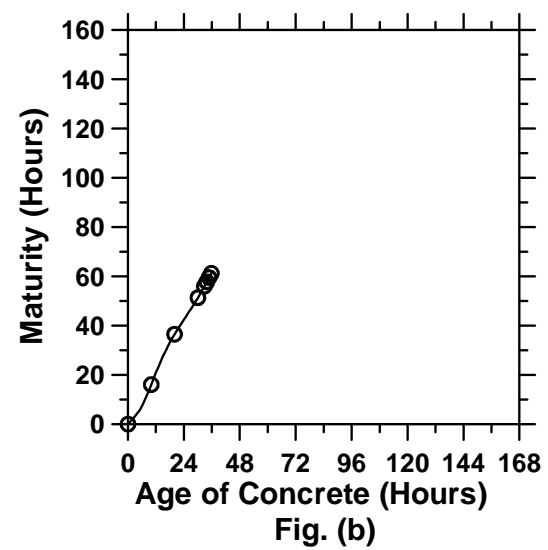
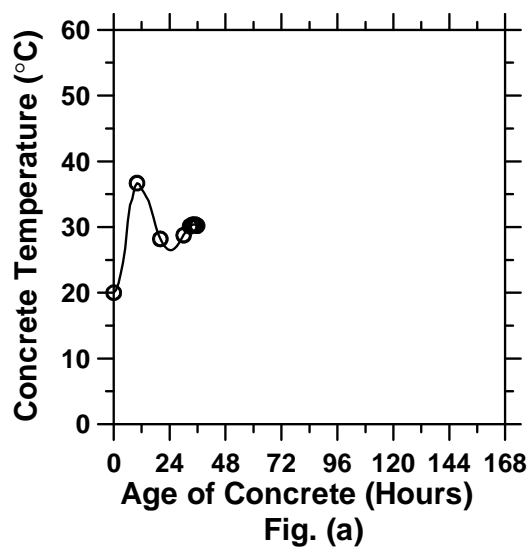


Figure A.47: Pavement with a D/8 saw-cut depth introduced at 36 hours (cont'd).

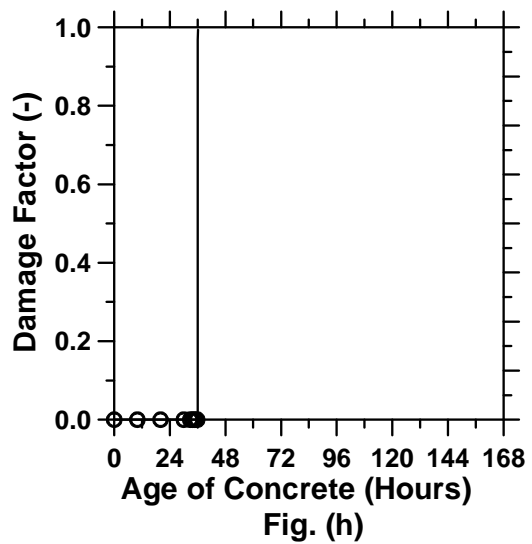
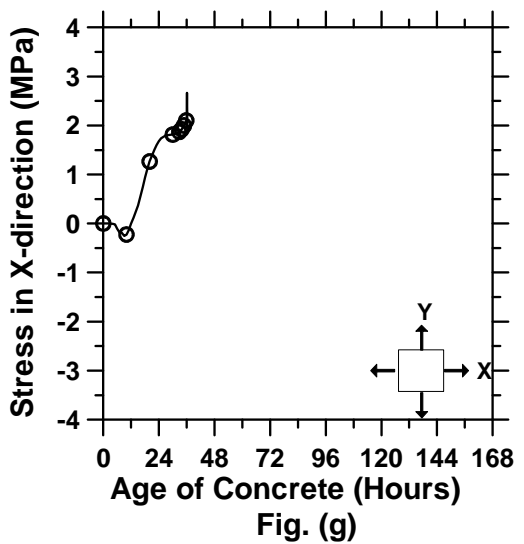
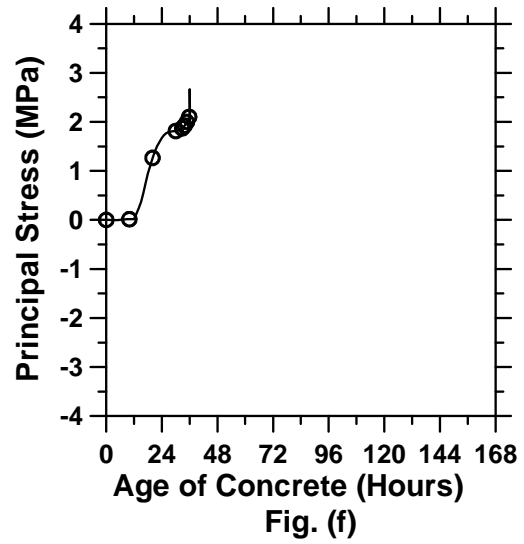
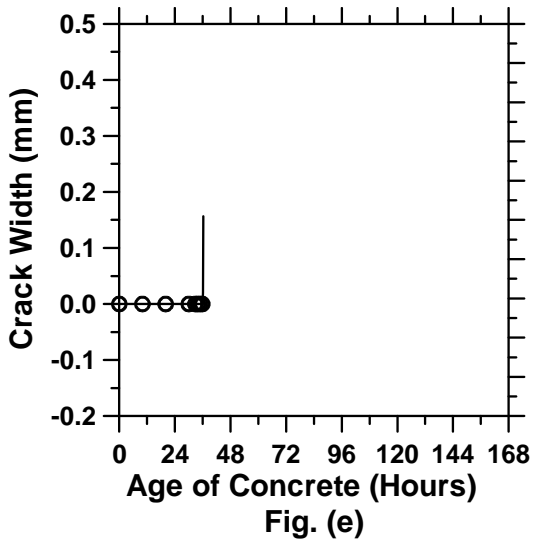


Figure A.47: Pavement with a D/8 saw-cut depth introduced at 36 hours.

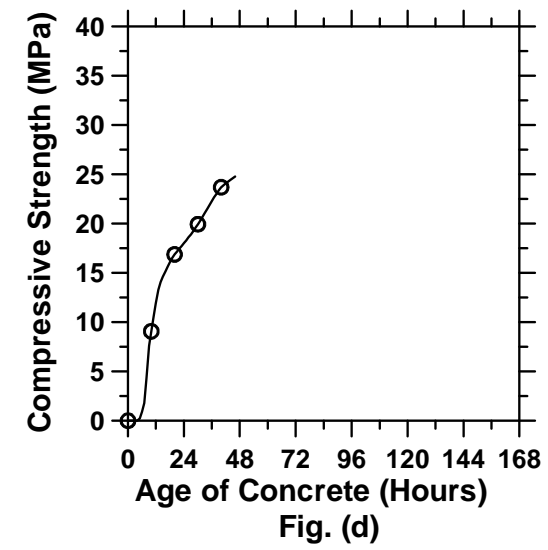
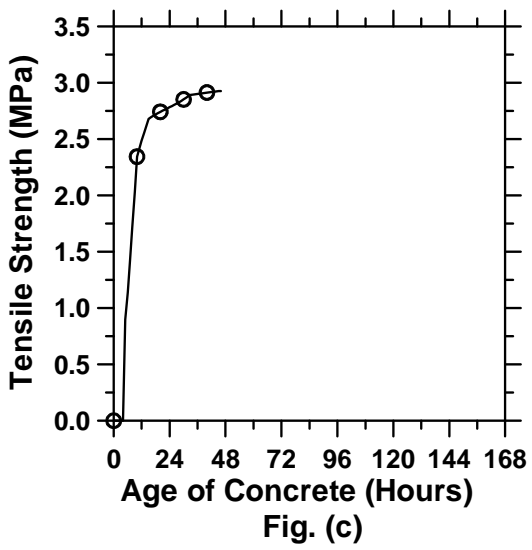
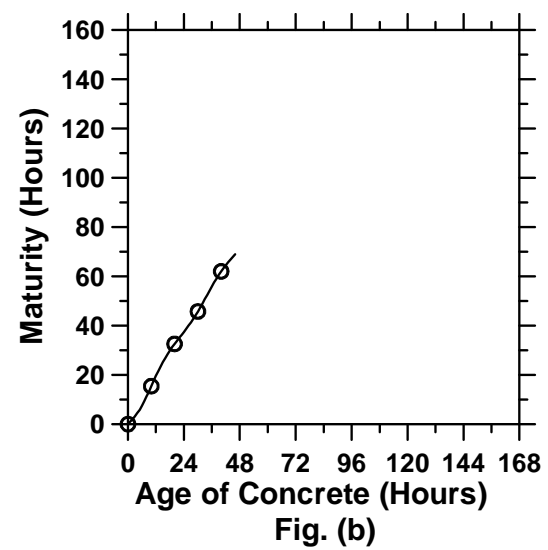
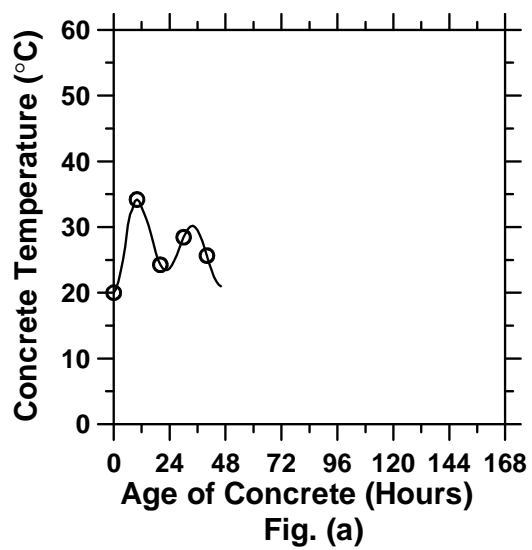


Figure A.48: Pavement with a D/100 saw-cut depth introduced at 0 hour (cont'd).

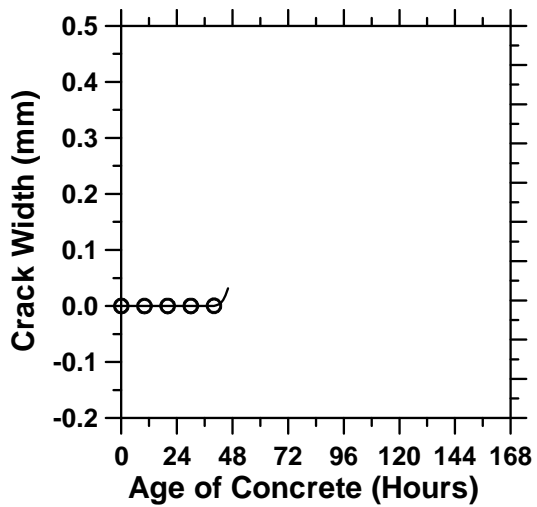


Fig. (e)

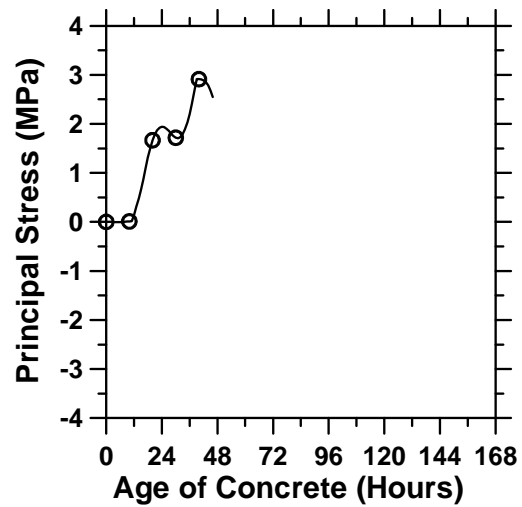


Fig. (f)

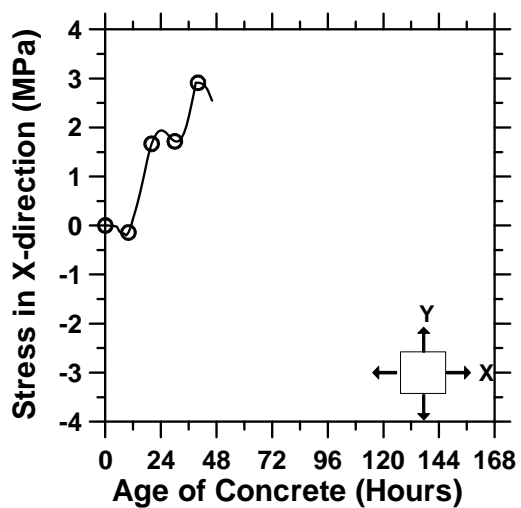


Fig. (g)

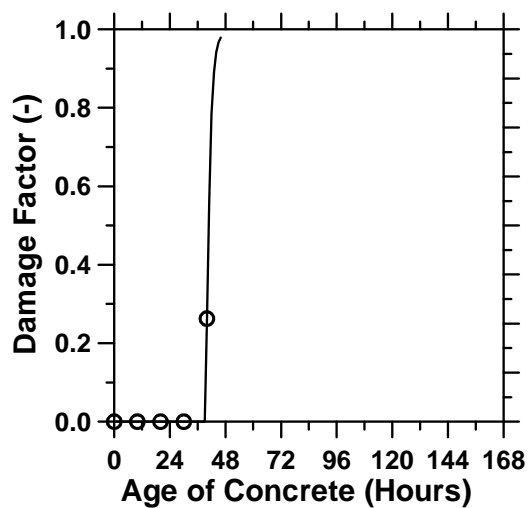


Fig. (h)

Figure A.48: Pavement with a D/100 saw-cut depth introduced at 0 hour.

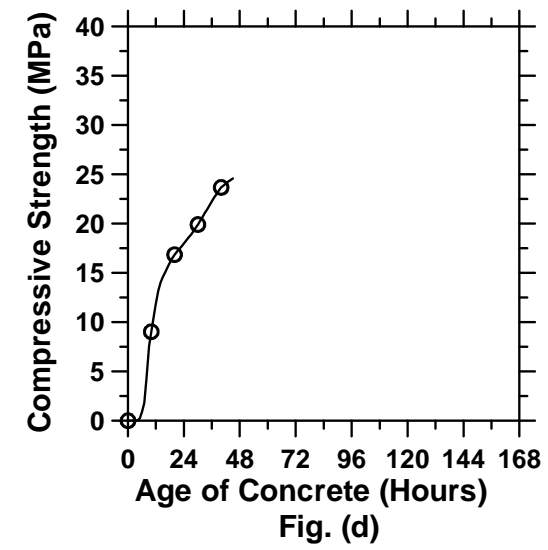
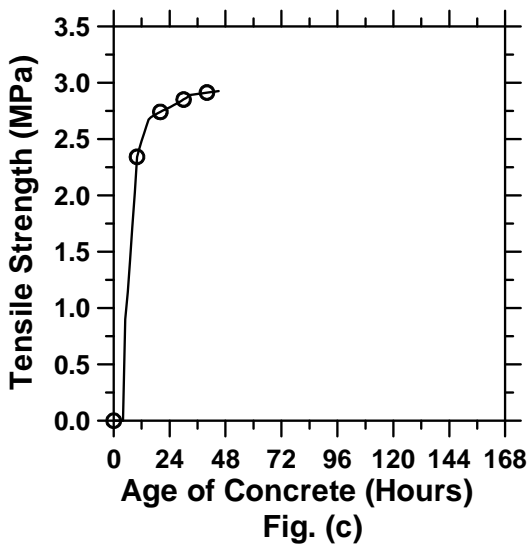
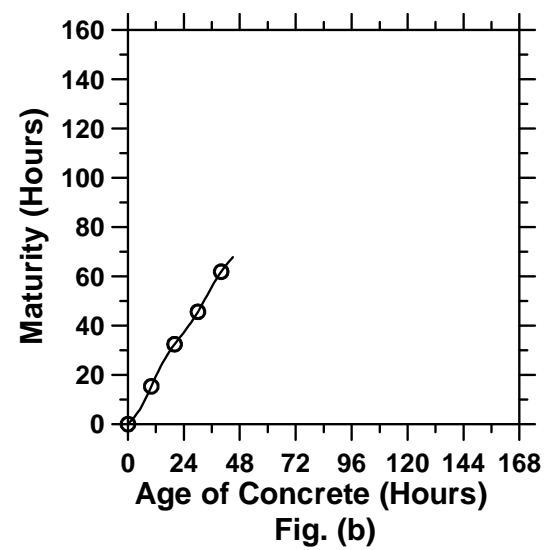
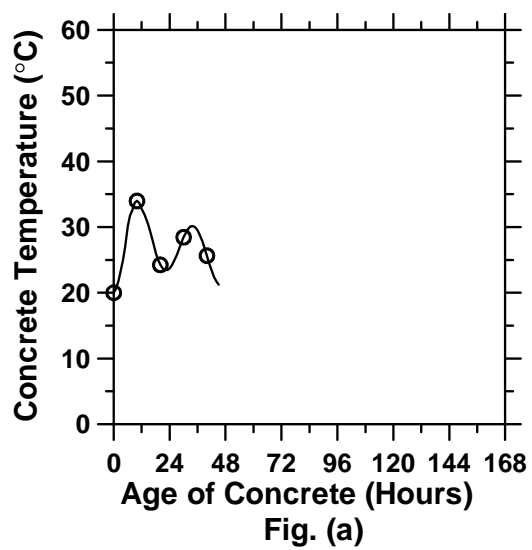


Figure A.49: Pavement with a D/100 saw-cut depth introduced at 12 hours (cont'd).

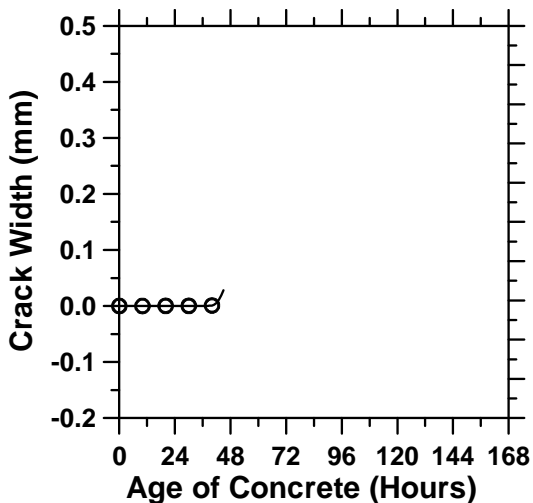


Fig. (e)

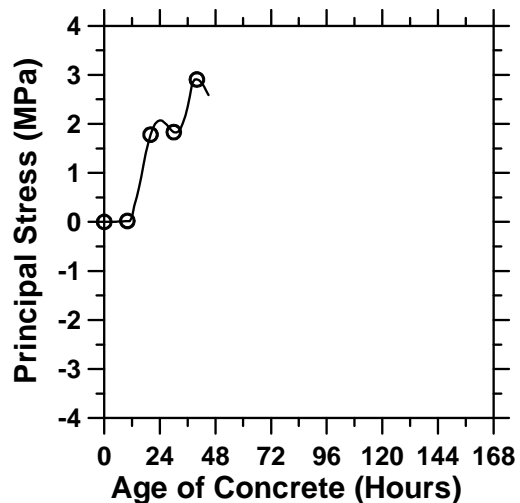


Fig. (f)

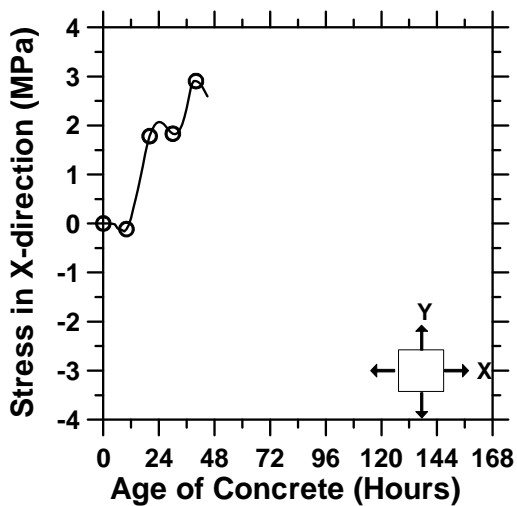


Fig. (g)

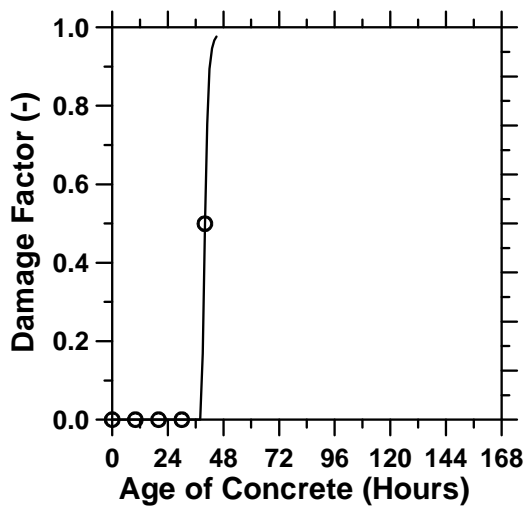


Fig. (h)

Figure A.49: Pavement with a D/100 saw-cut depth introduced at 12 hours.

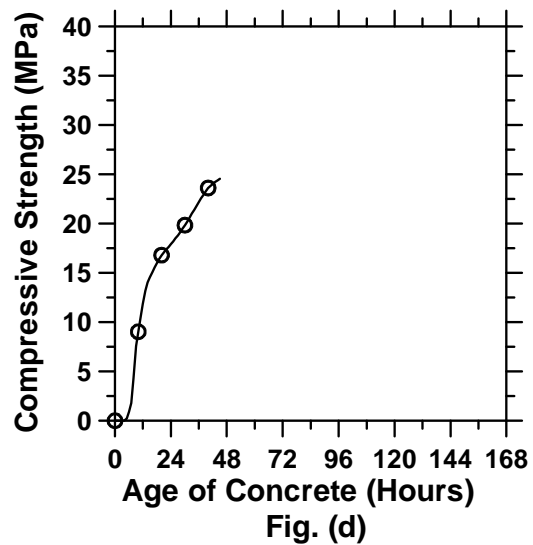
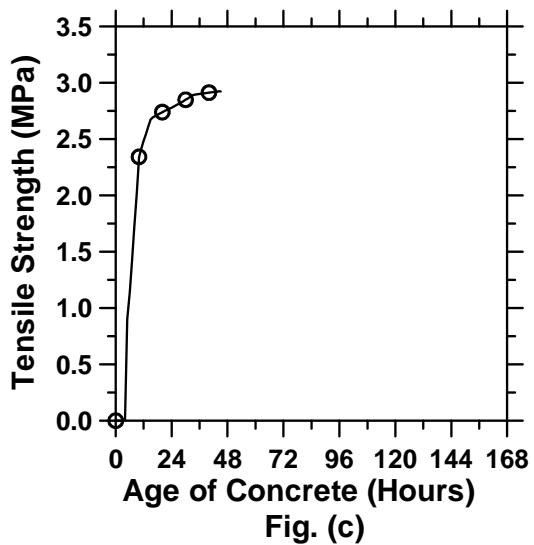
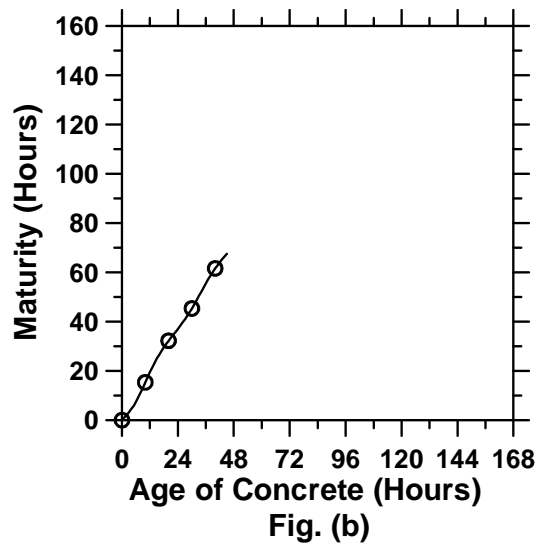
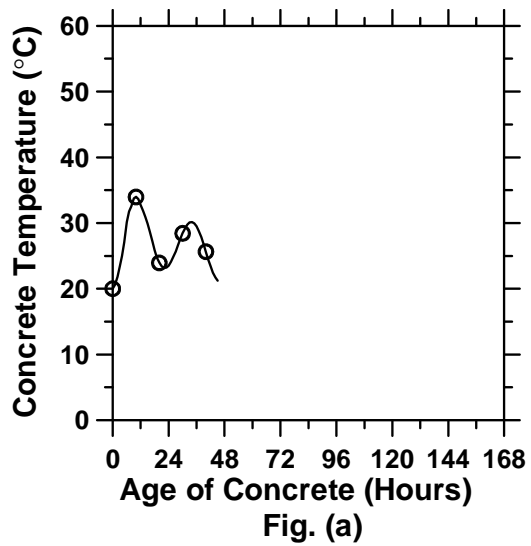


Figure A.50: Pavement with a D/100 saw-cut depth introduced at 24 hours (cont'd).

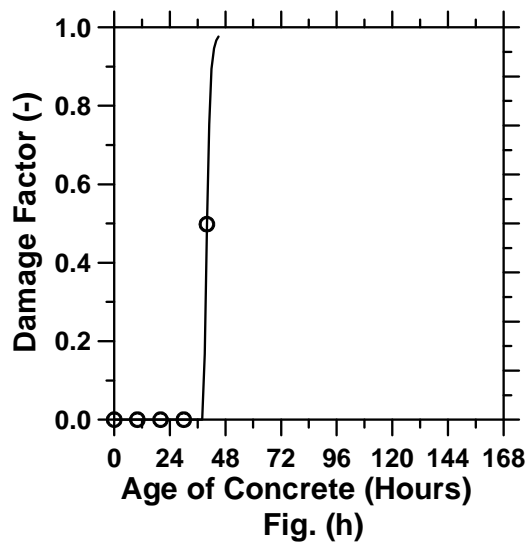
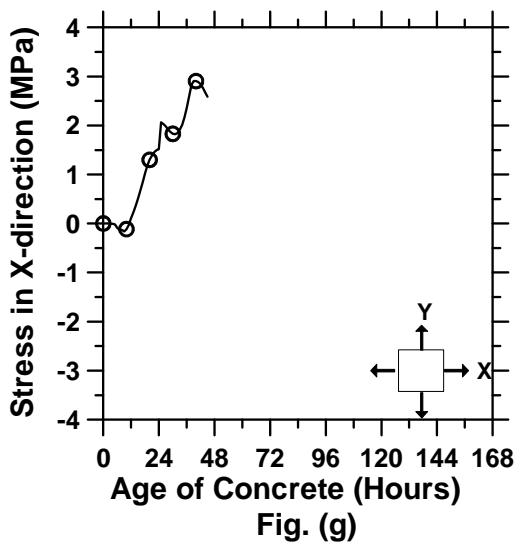
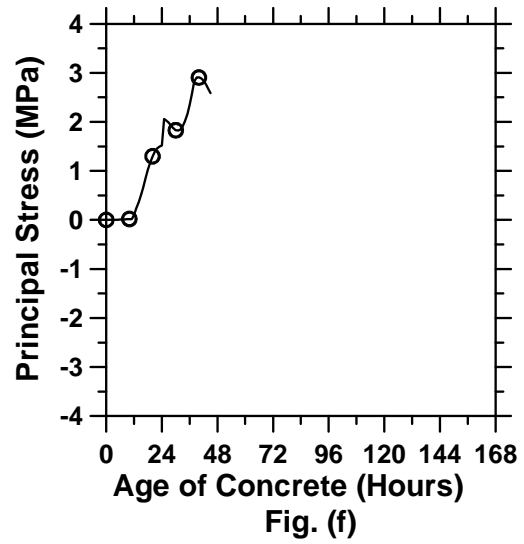
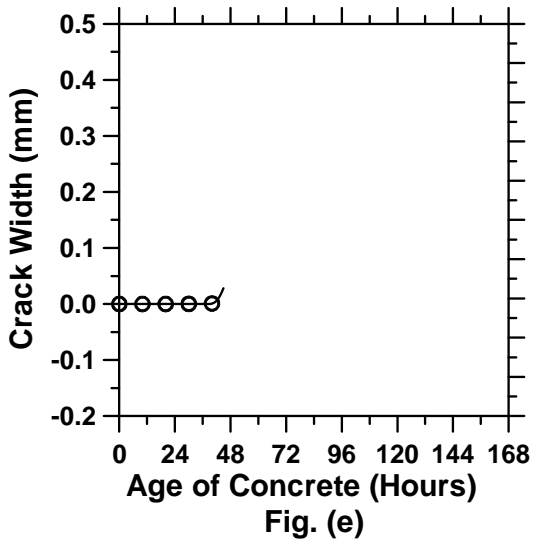


Figure A.50: Pavement with a D/100 saw-cut depth introduced at 24 hours.

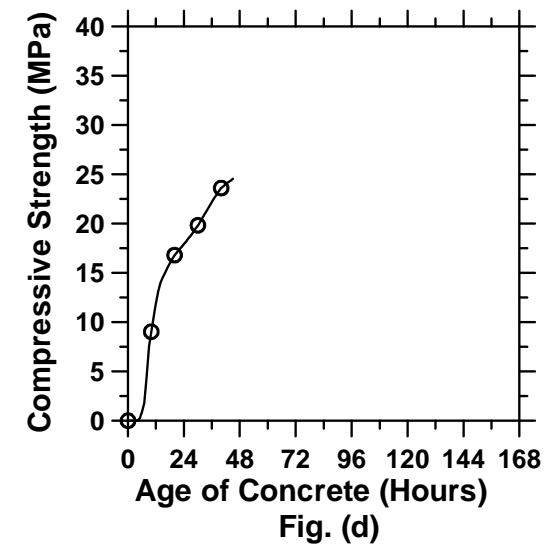
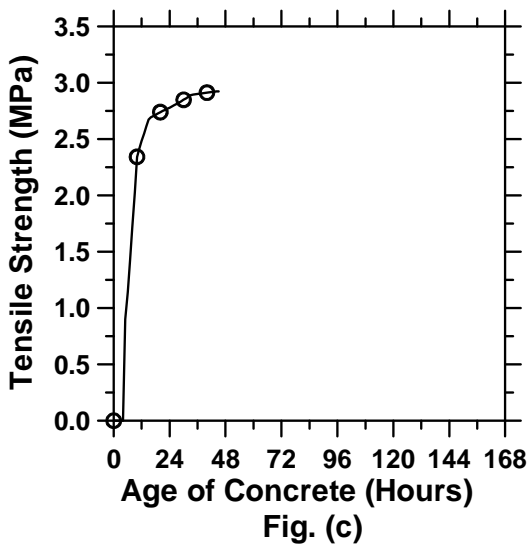
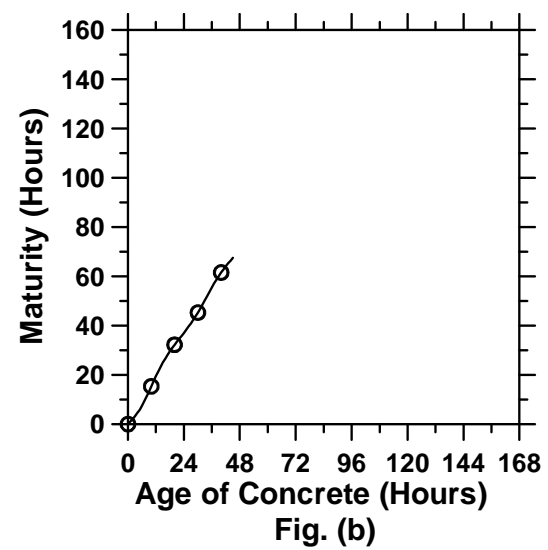
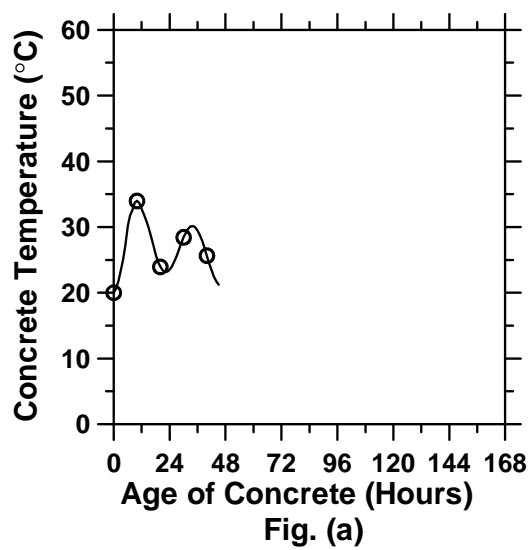


Figure A.51: Pavement with a D/100 saw-cut depth introduced at 36 hours (cont'd).

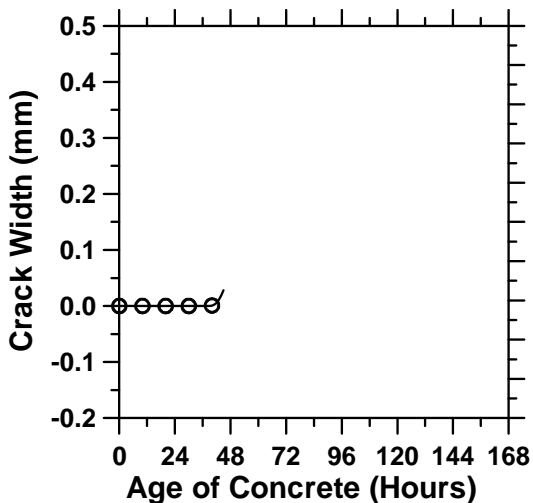


Fig. (e)

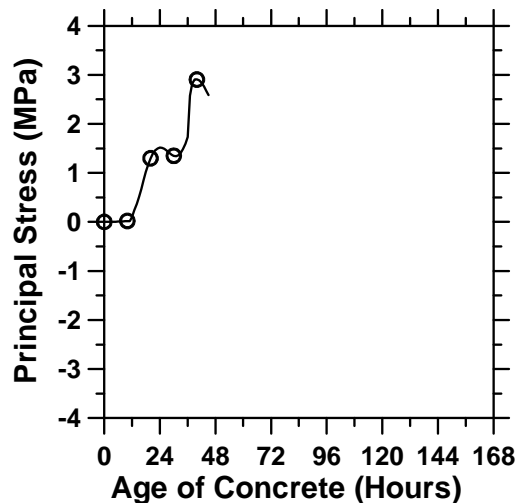


Fig. (f)

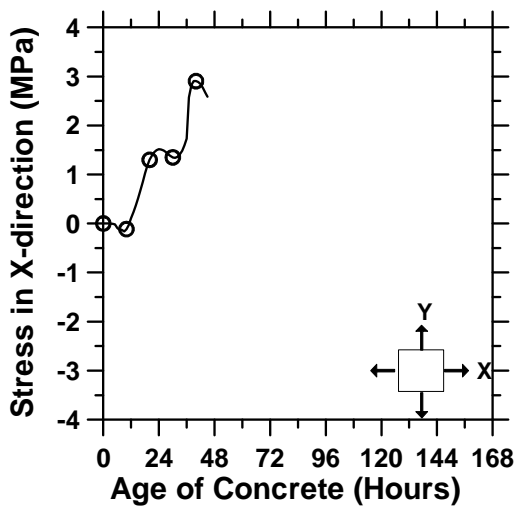


Fig. (g)

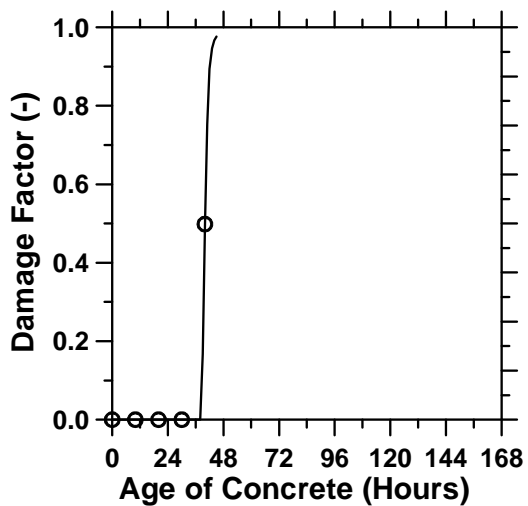


Fig. (h)

Figure A.51: Pavement with a D/100 saw-cut depth introduced at 36 hours.

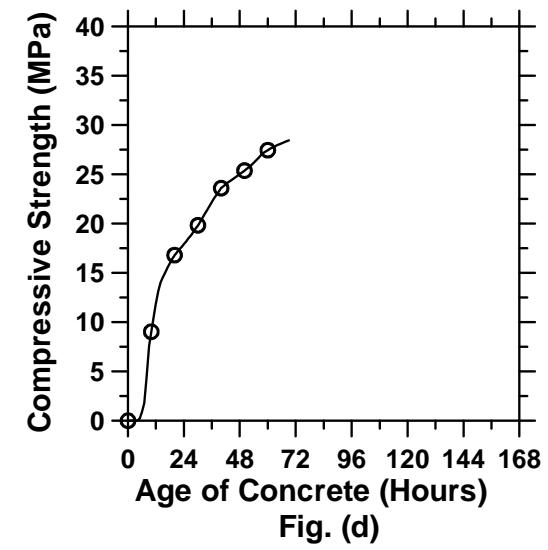
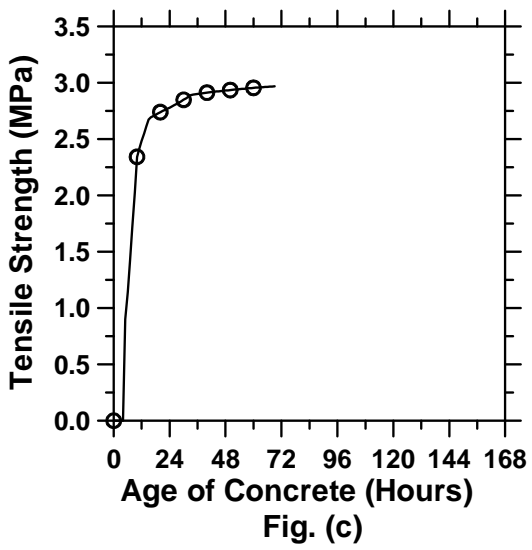
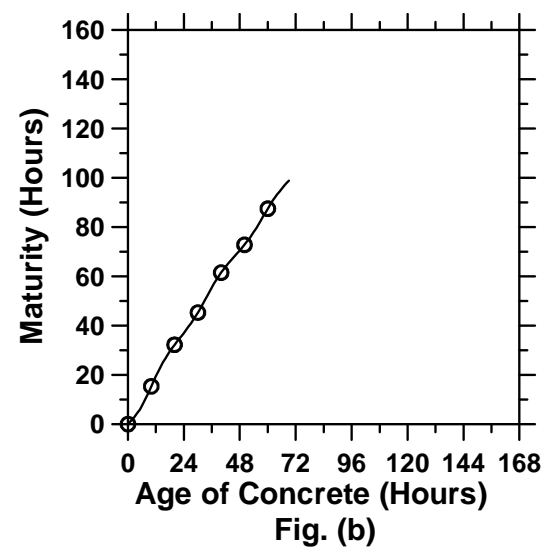
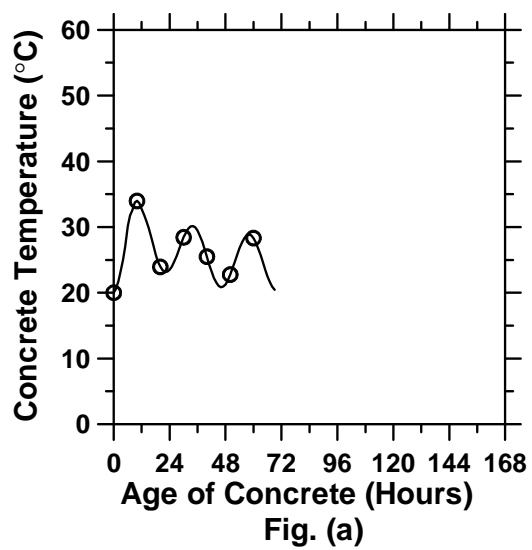


Figure A.52: Pavement with a D/100 saw-cut depth introduced at 48 hours (cont'd).

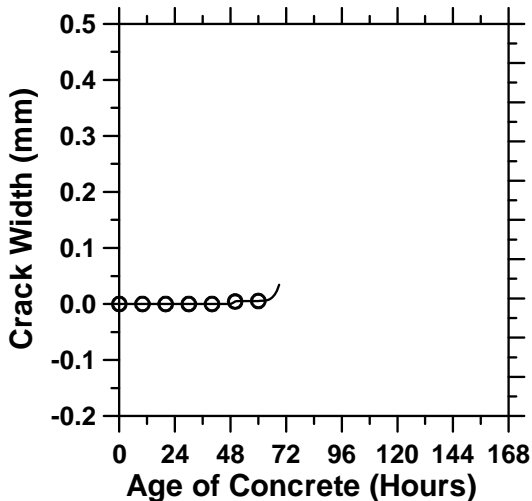


Fig. (e)

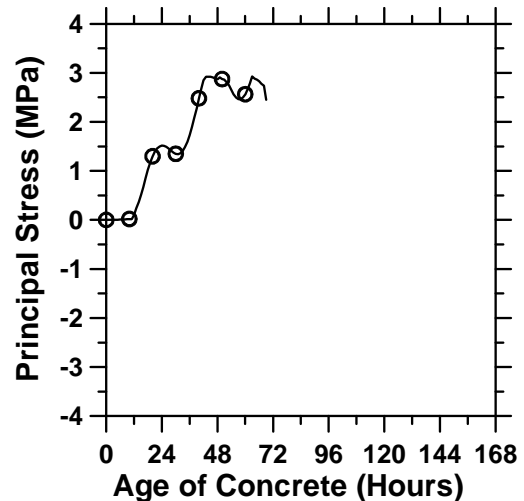


Fig. (f)

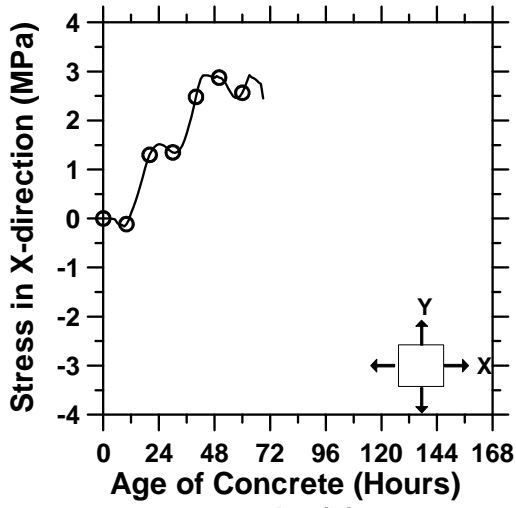


Fig. (g)

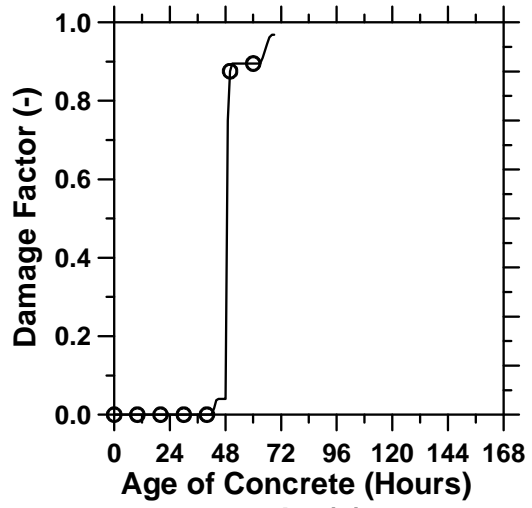


Fig. (h)

Figure A.52: Pavement with a D/100 saw-cut depth introduced at 48 hours.

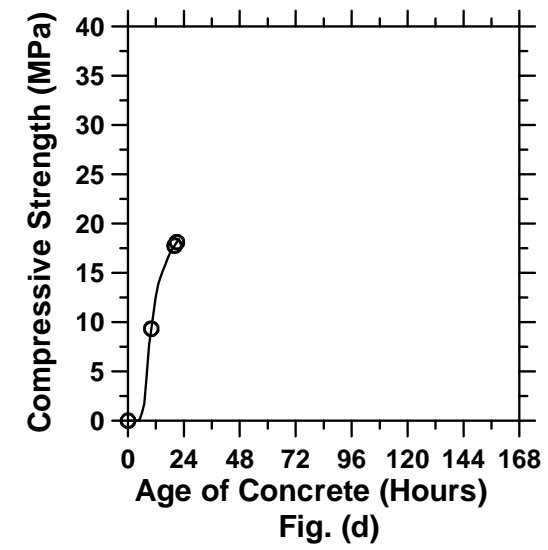
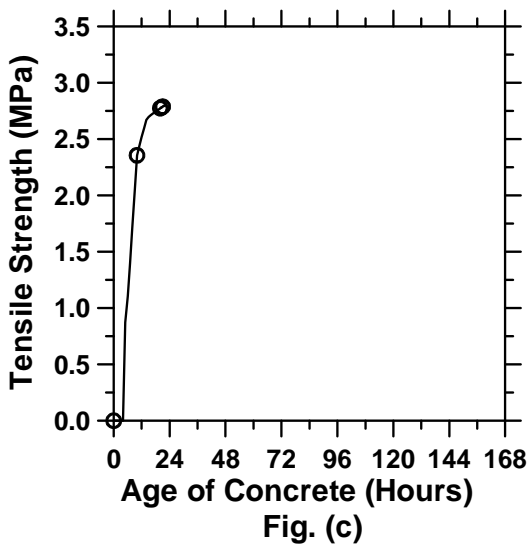
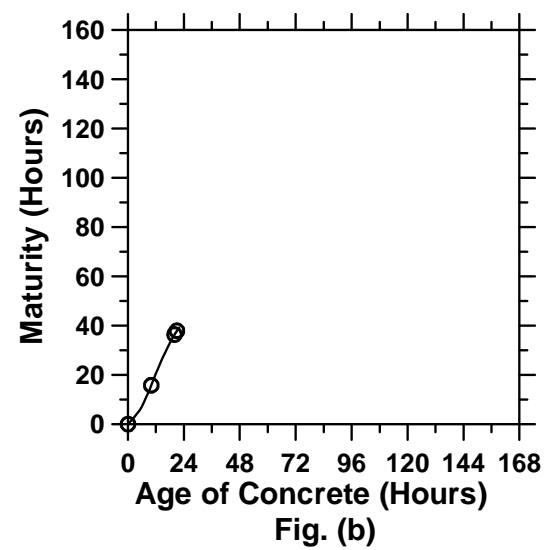
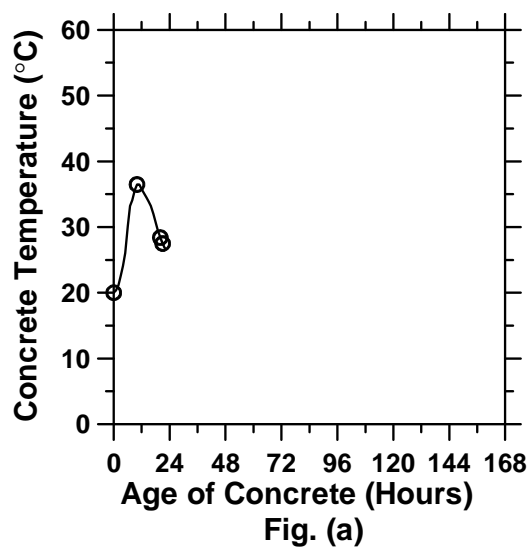


Figure A.53: 10-inch thick pavement with a D/3 saw-cut depth introduced at 0 hour
(cont'd).

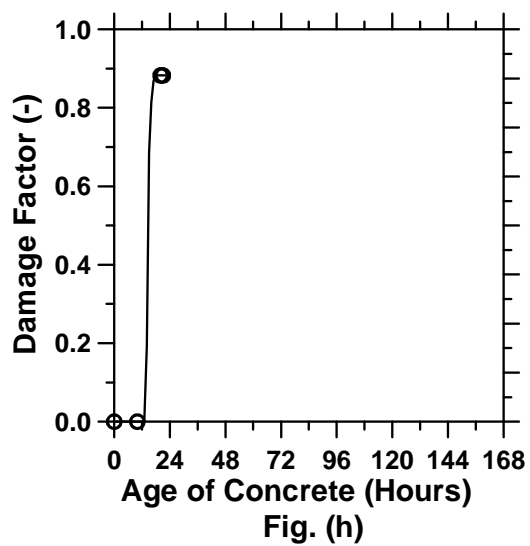
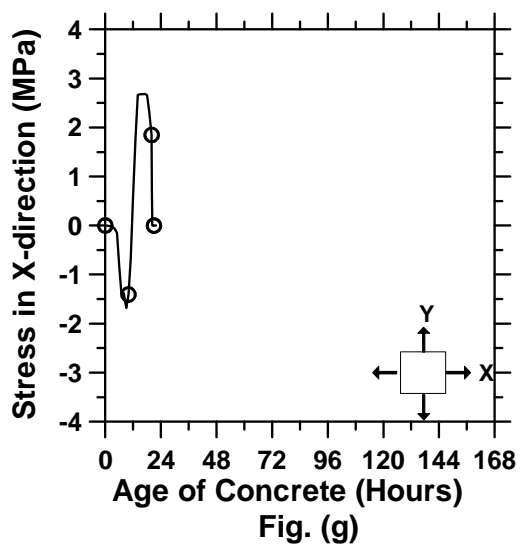
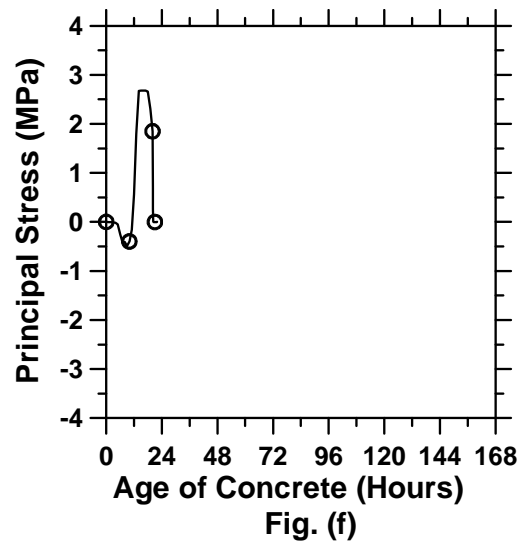
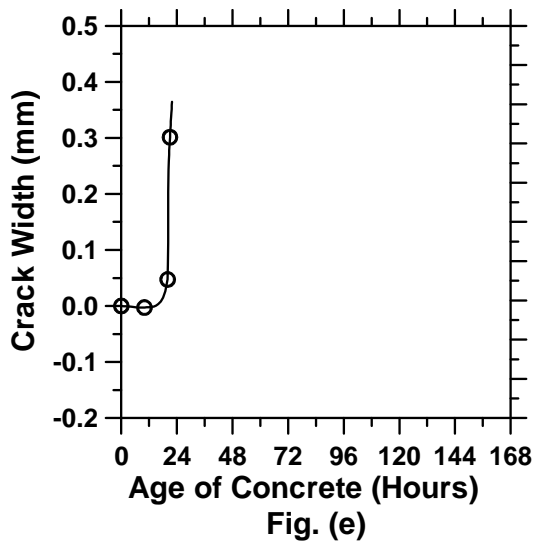


Figure A.53: 10-inch thick pavement with a D/3 saw-cut depth introduced at 0 hour.

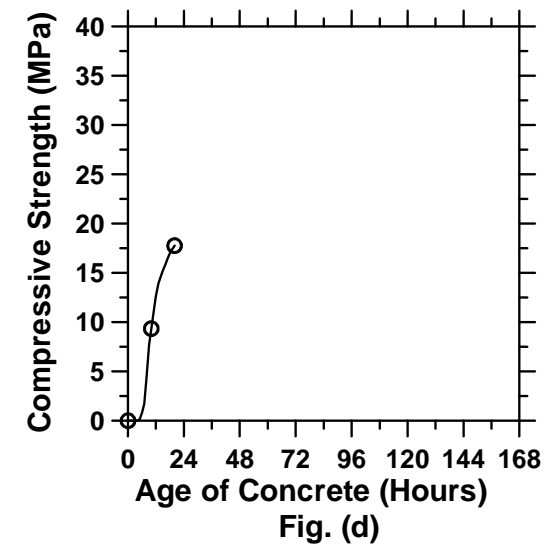
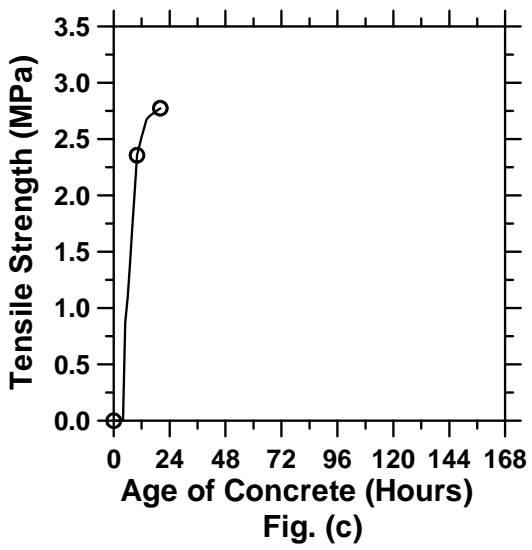
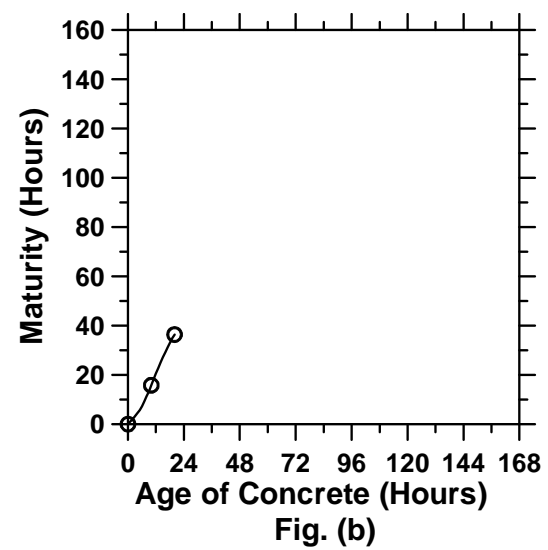
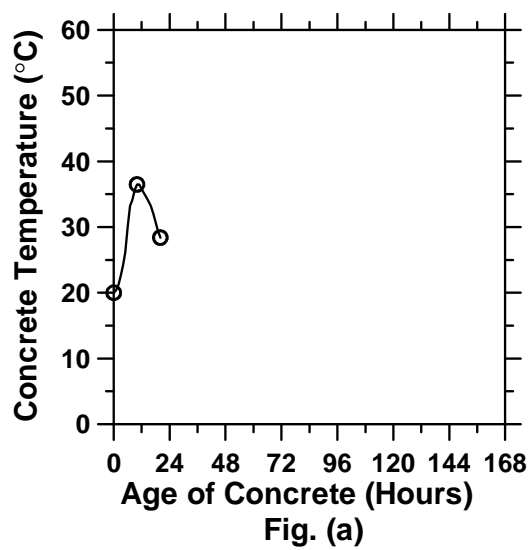


Figure A.54: 10-inch thick pavement with a D/3 saw-cut depth introduced at 6 hours
(cont'd).

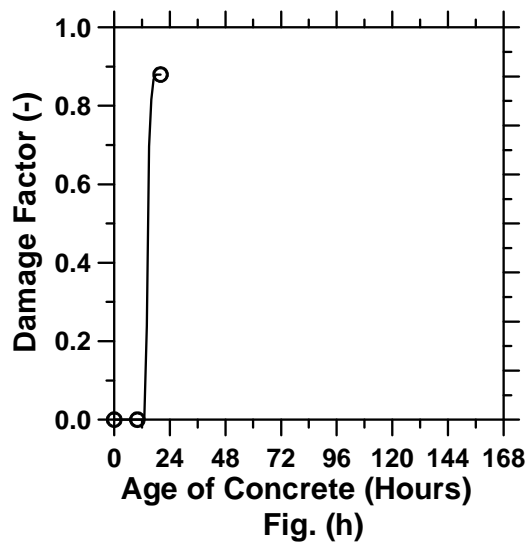
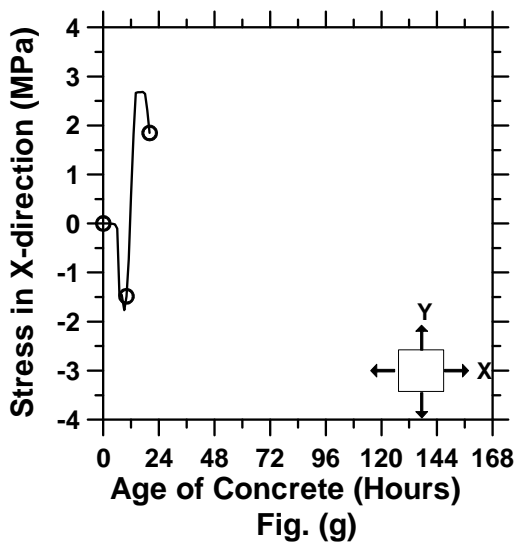
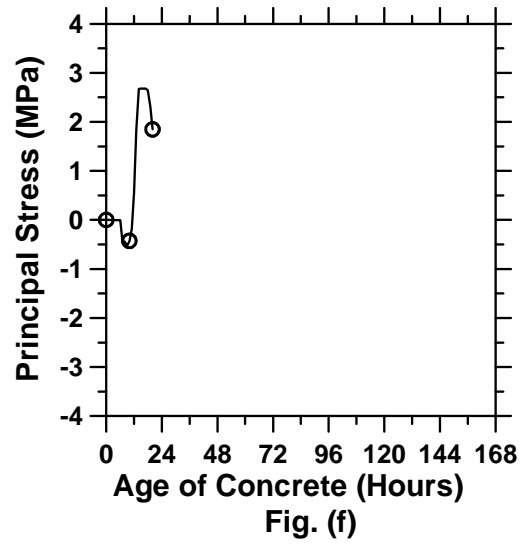
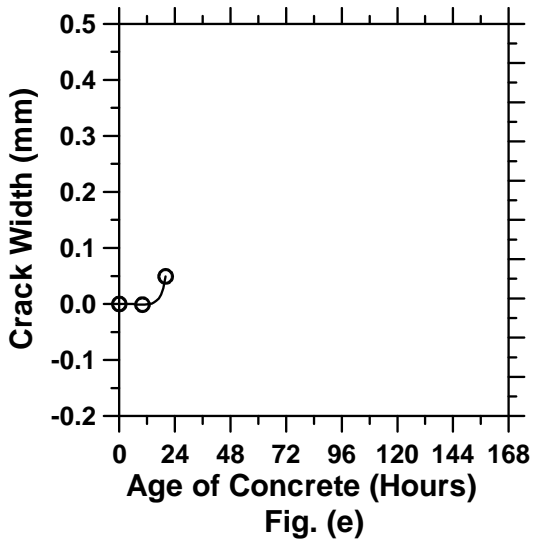


Figure A.54: 10-inch thick pavement with a D/3 saw-cut depth introduced at 6 hours.

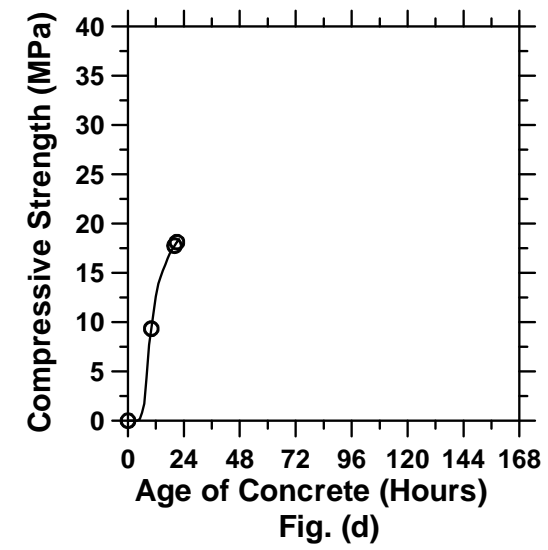
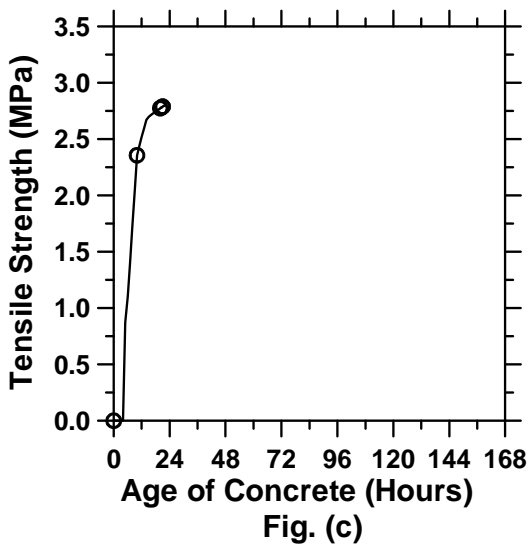
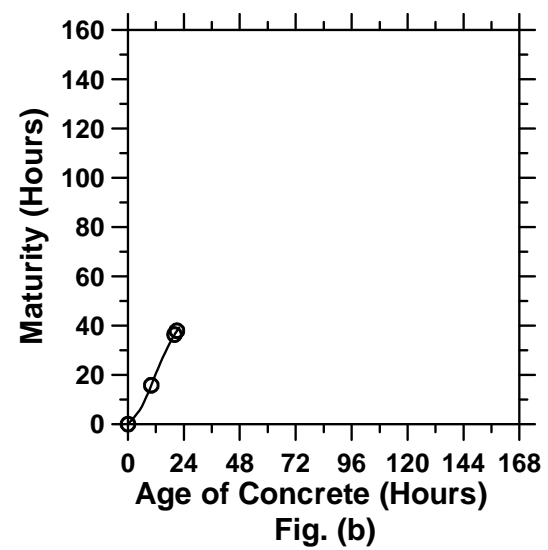
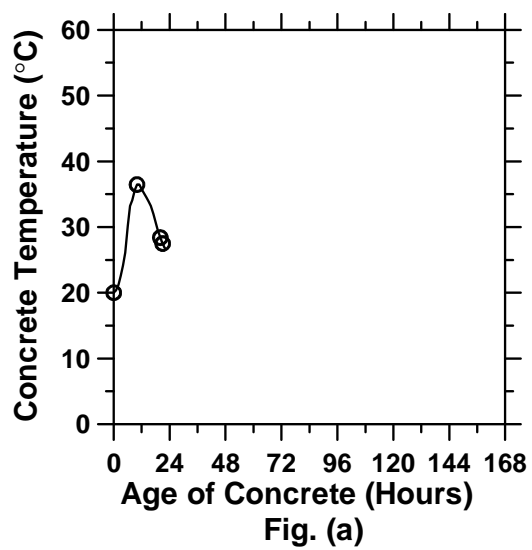


Figure A.55: 10-inch thick pavement with a D/3 saw-cut depth introduced at 9 hours
(cont'd).

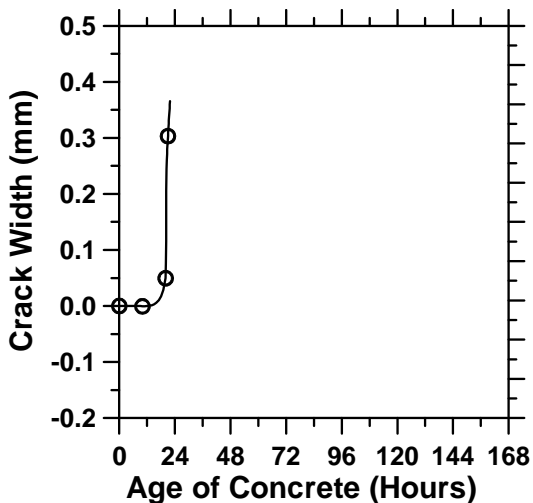


Fig. (e)

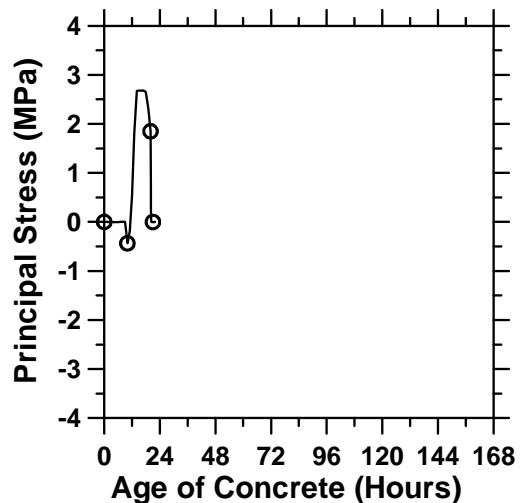


Fig. (f)

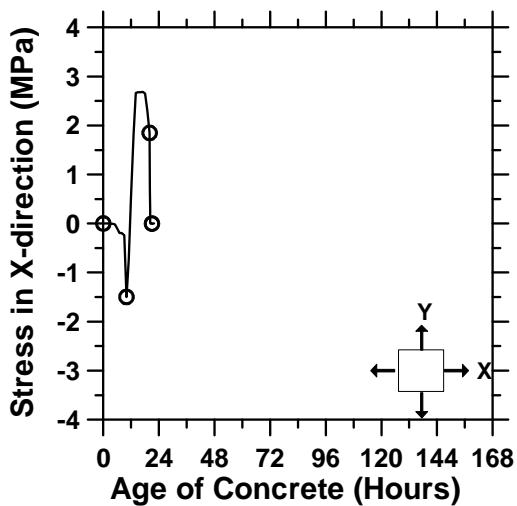


Fig. (g)

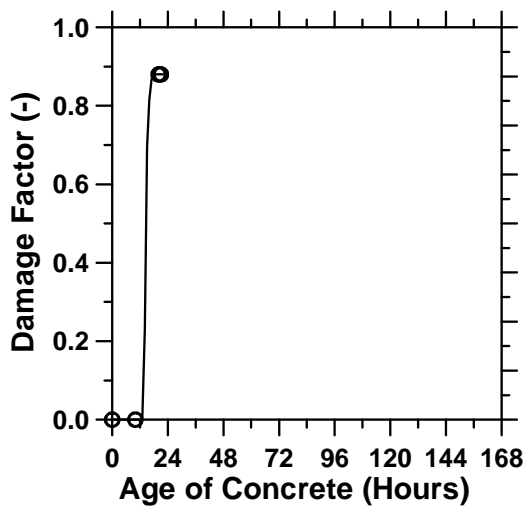


Fig. (h)

Figure A.55: 10-inch thick pavement with a D/3 saw-cut depth introduced at 9 hours.

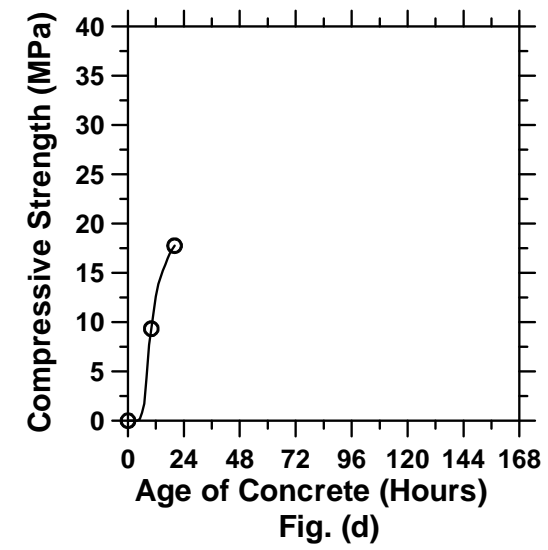
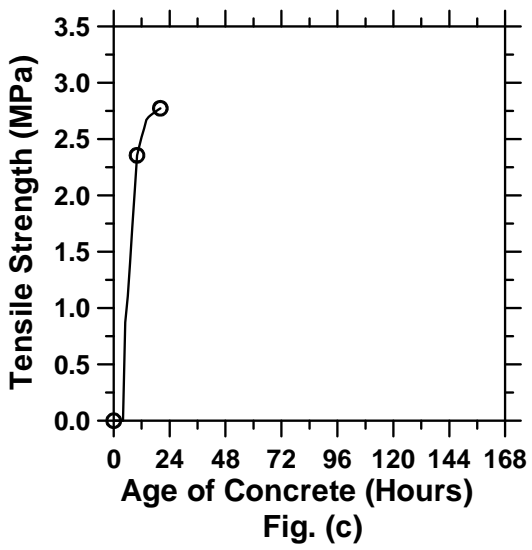
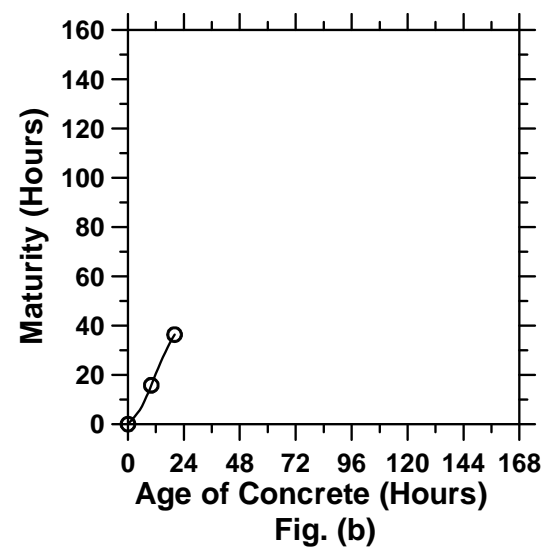
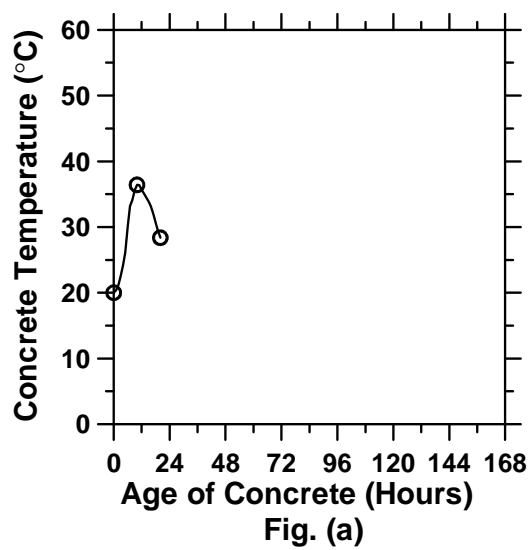


Figure A.56: 10-inch thick pavement with a D/3 saw-cut depth introduced at 12 hours
(cont'd).

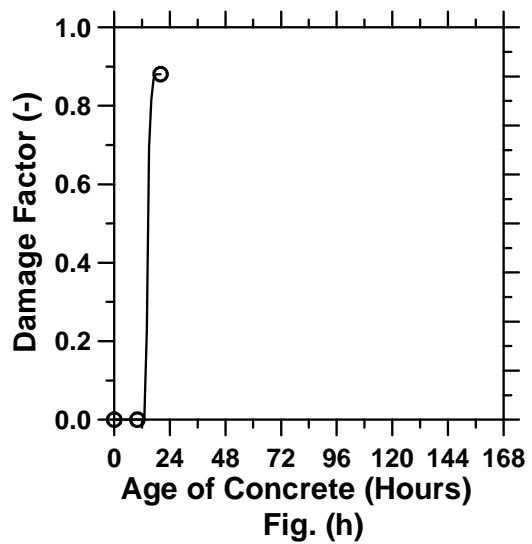
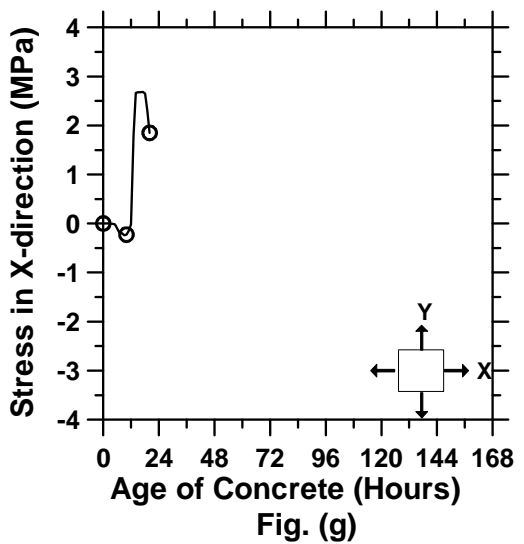
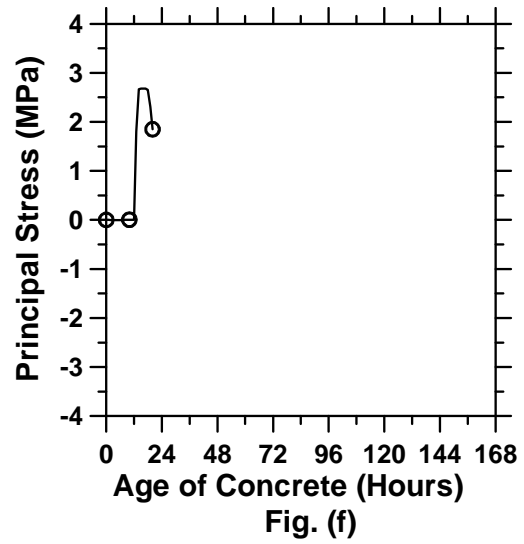
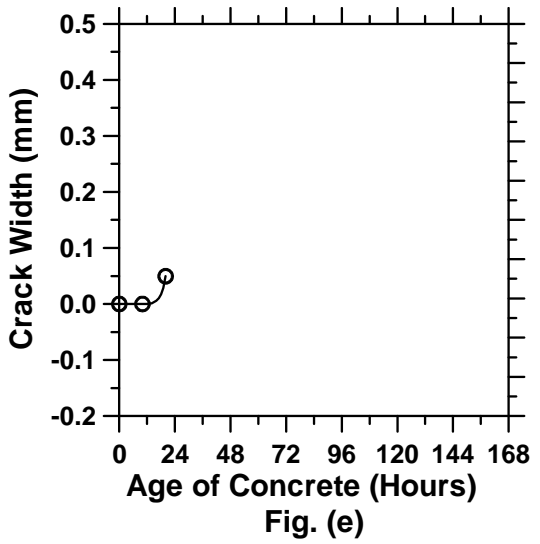


Figure A.56: 10-inch thick pavement with a D/3 saw-cut depth introduced at 12 hours.

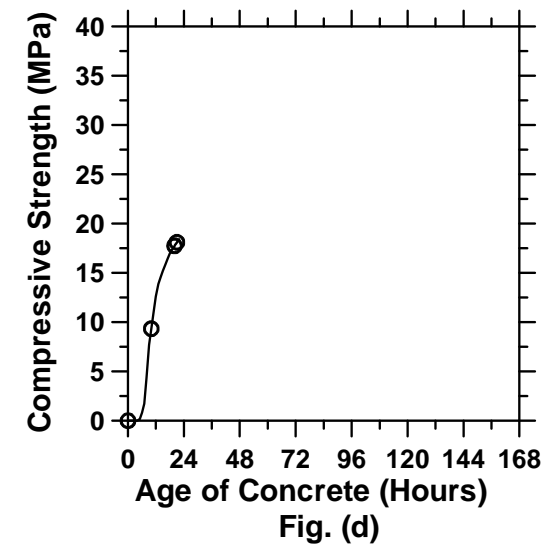
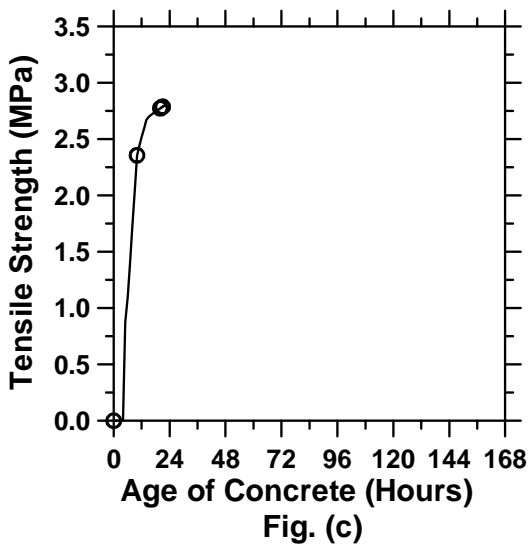
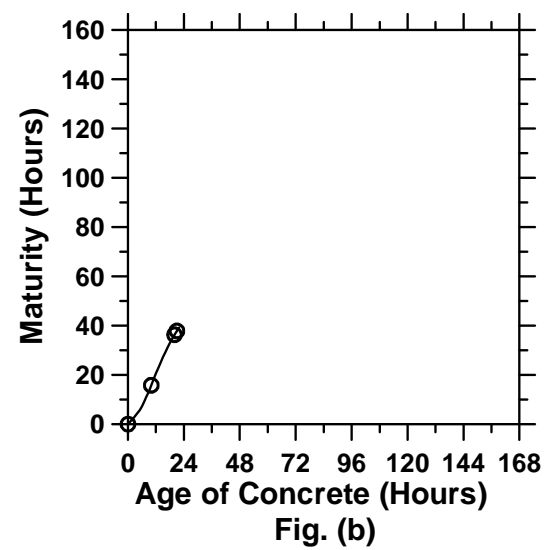
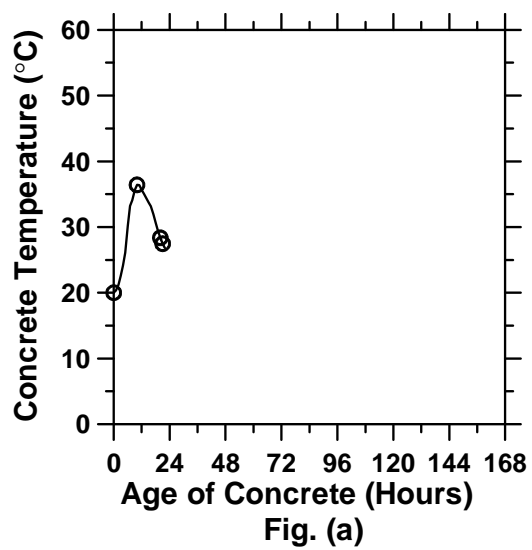


Figure A.57: 10-inch thick pavement with a D/3 saw-cut depth introduced at 15 hours
(cont'd).

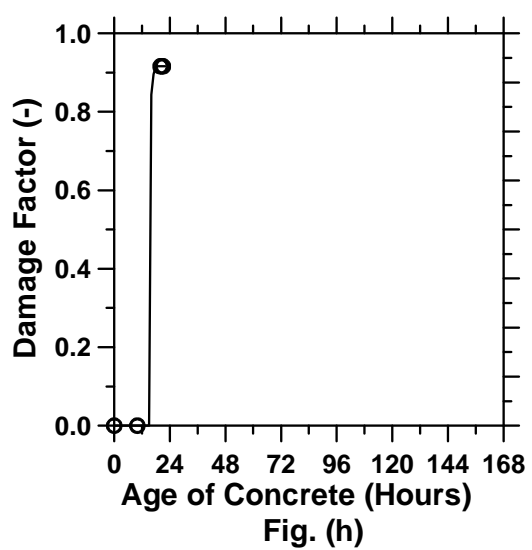
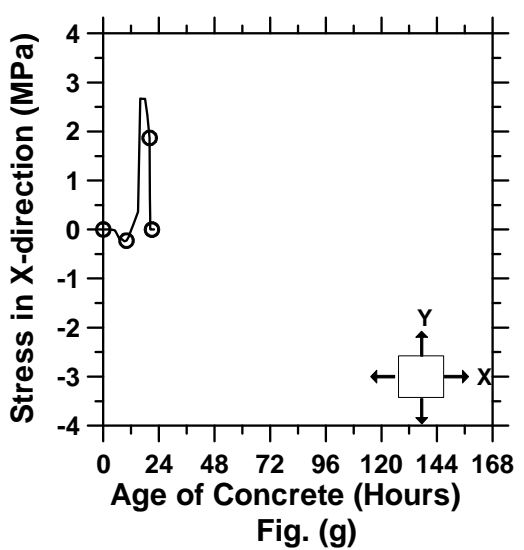
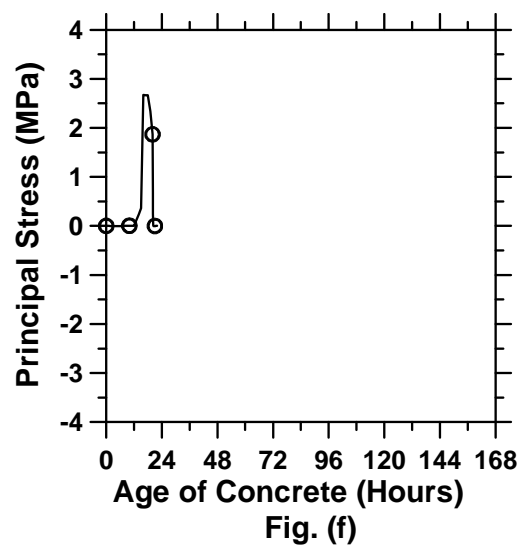
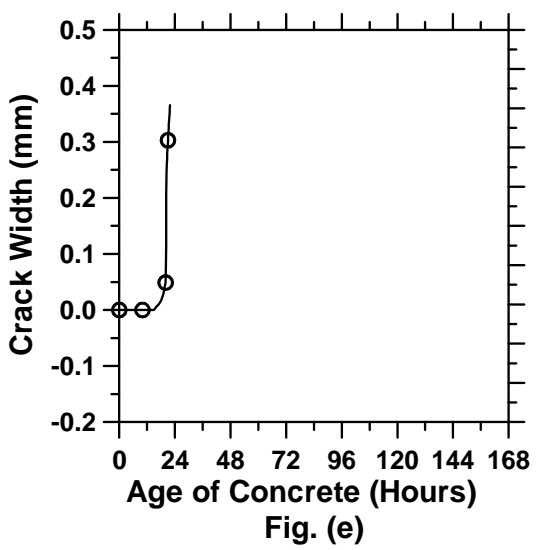


Figure A.57: 10-inch thick pavement with a D/3 saw-cut depth introduced at 15 hours.

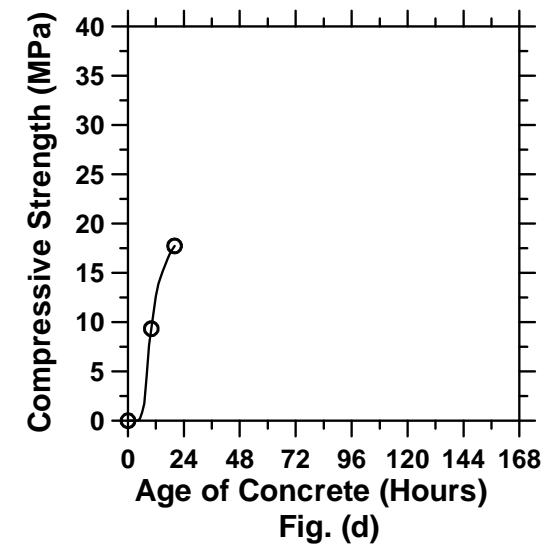
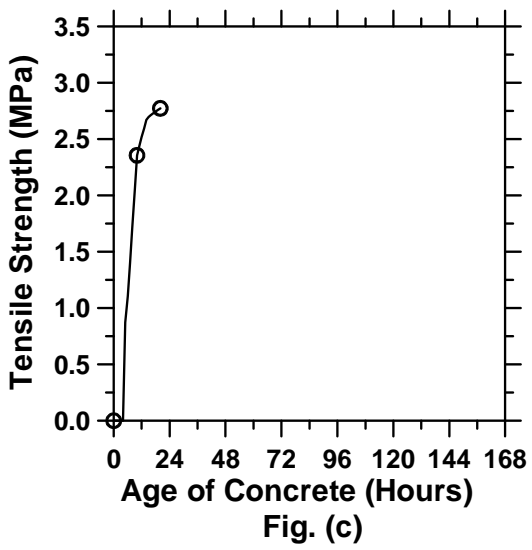
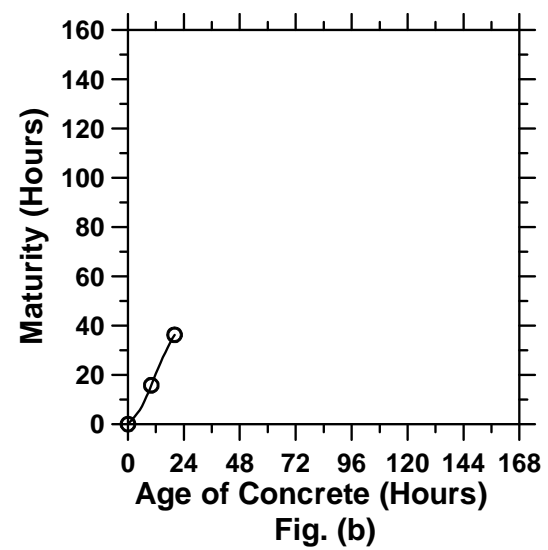
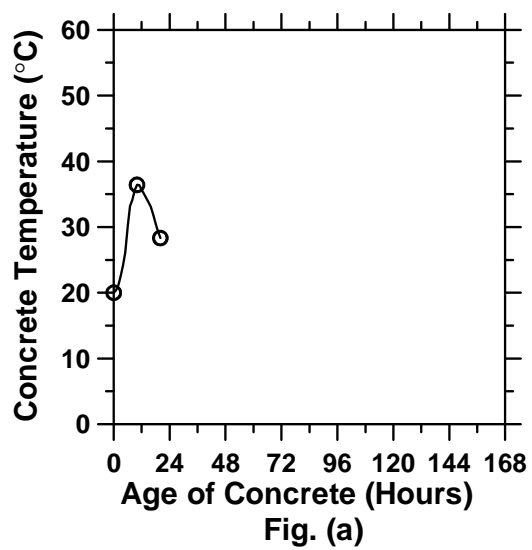


Figure A.58: 10-inch thick pavement with a D/3 saw-cut depth introduced at 18 hours
(cont'd).

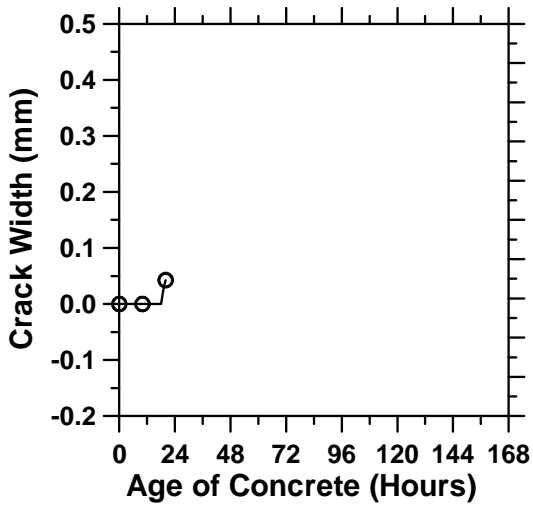


Fig. (e)

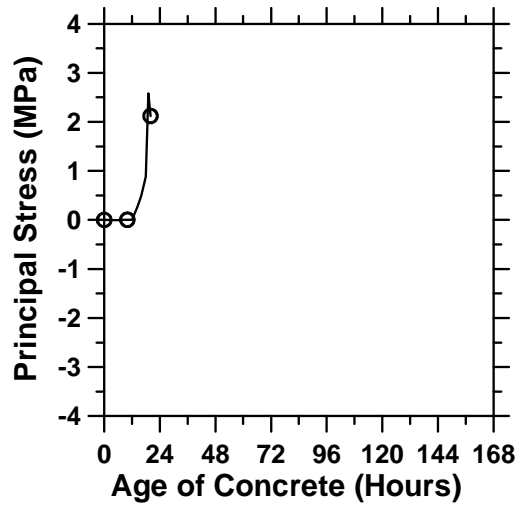


Fig. (f)

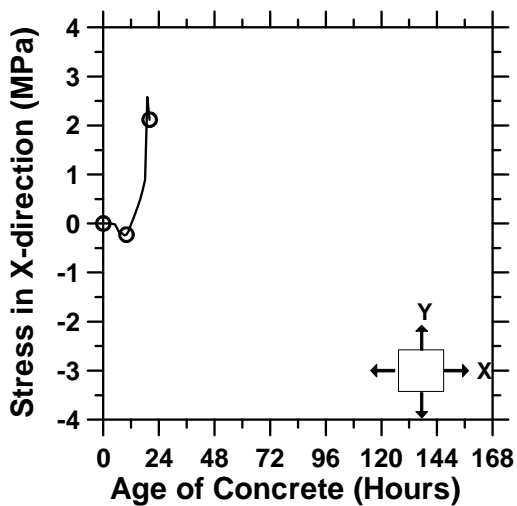


Fig. (g)

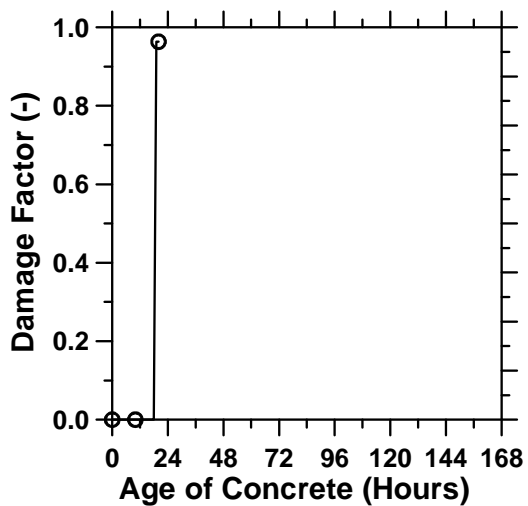


Fig. (h)

Figure A.58: 10-inch thick pavement with a D/3 saw-cut depth introduced at 18 hours.

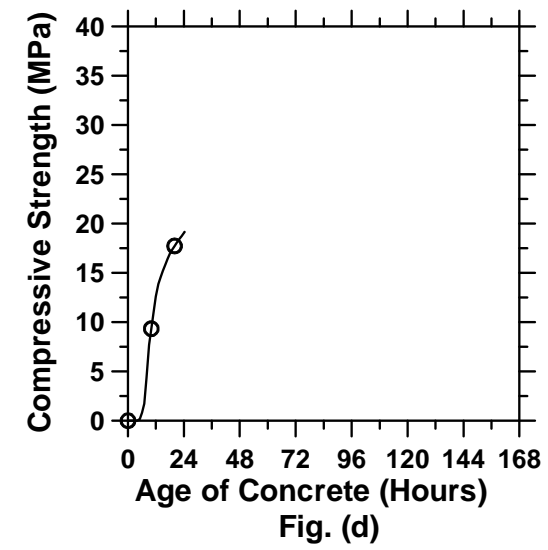
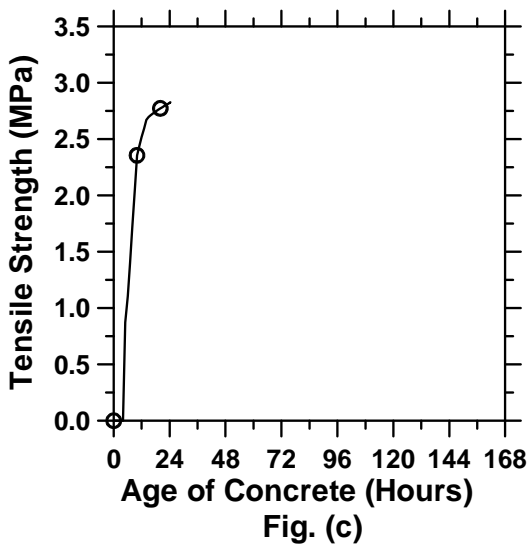
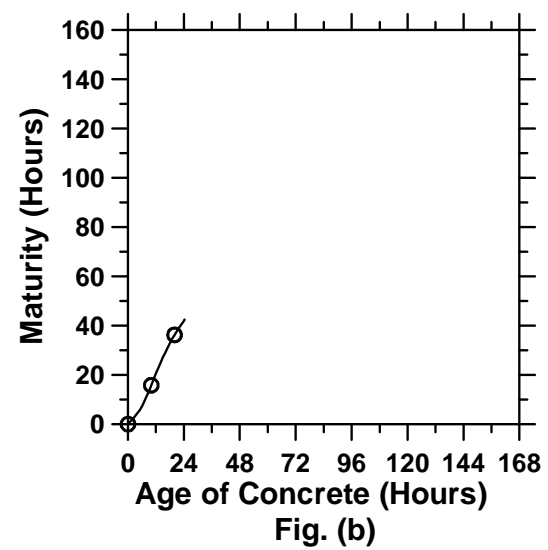
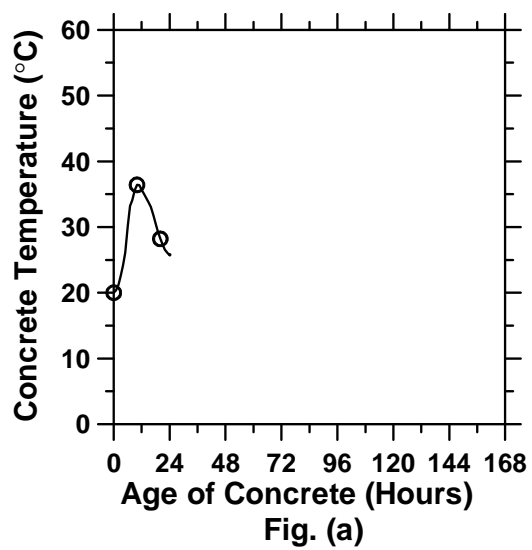


Figure A.59: 10-inch thick pavement with a D/3 saw-cut depth introduced at 24 hours
(cont'd).

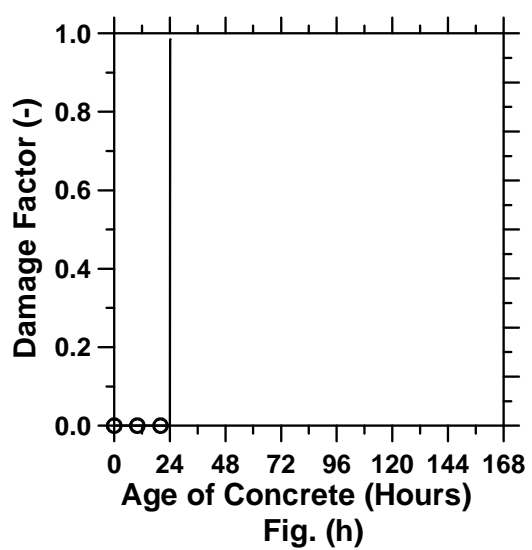
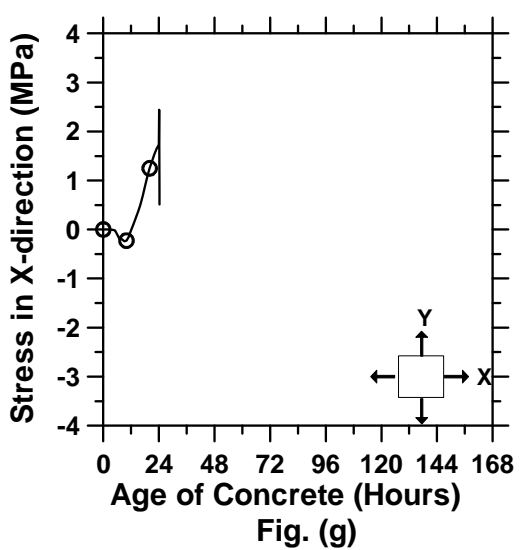
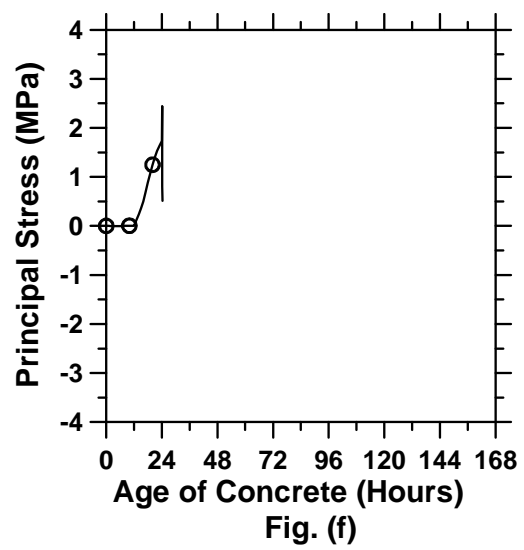
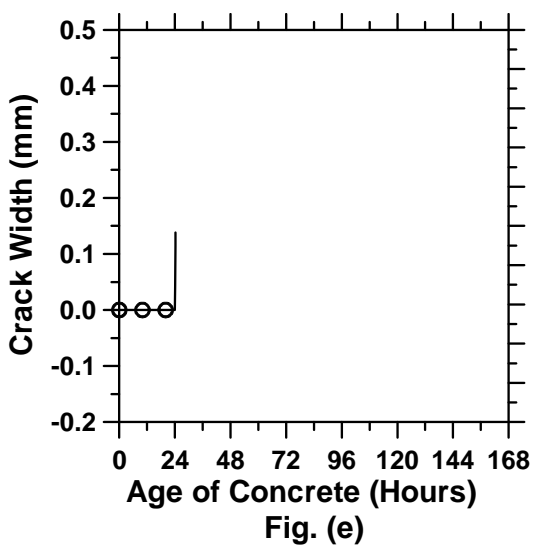


Figure A.59: 10-inch thick pavement with a D/3 saw-cut depth introduced at 24 hours.

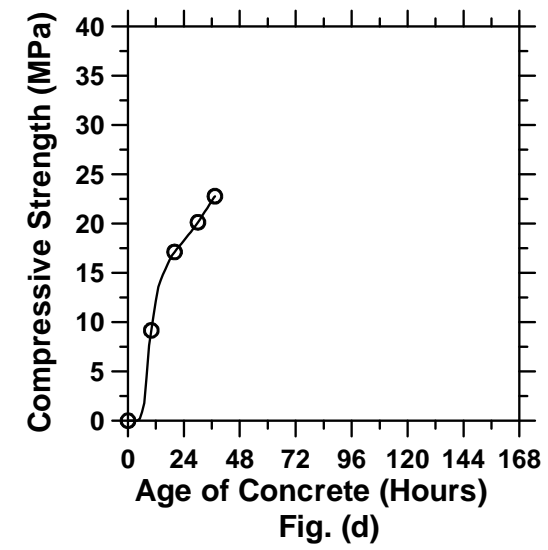
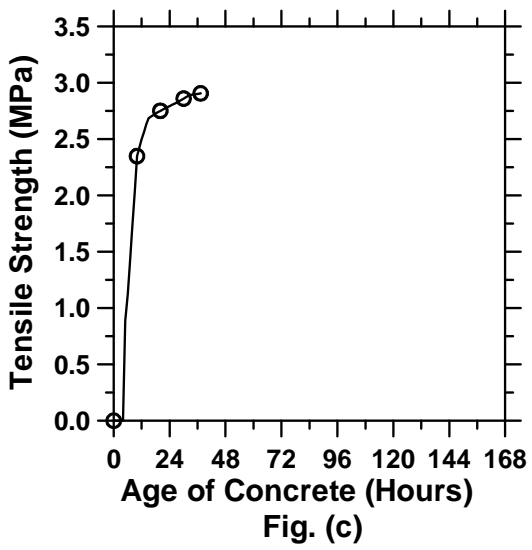
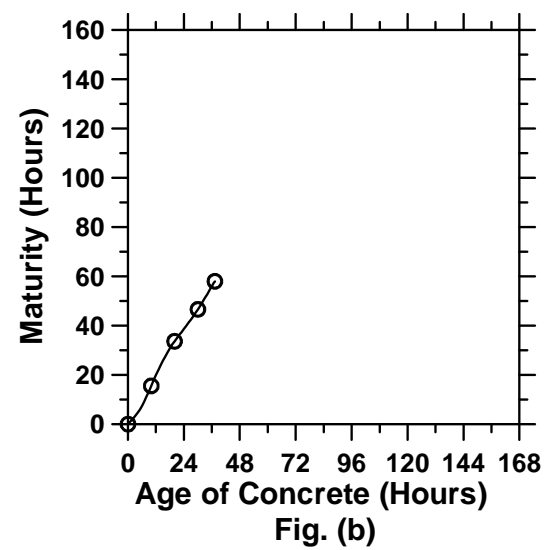
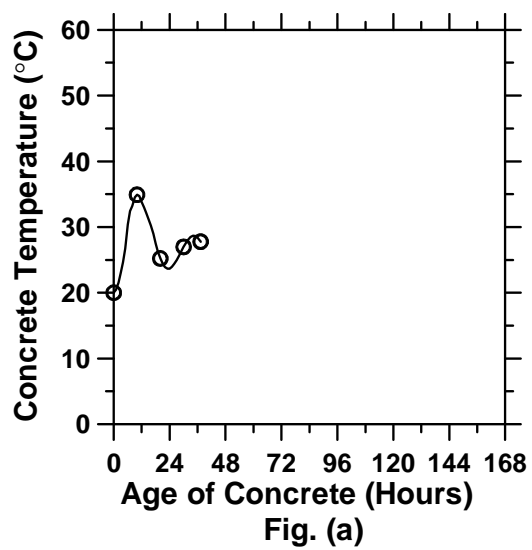


Figure A.60: 10-inch thick pavement with a D/8 saw-cut depth introduced at 0 hour
(cont'd).

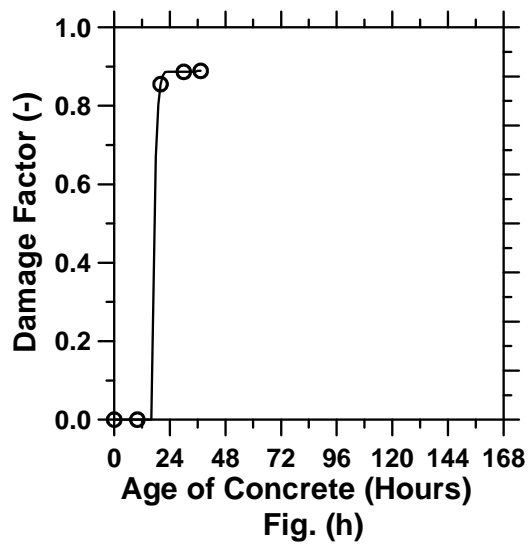
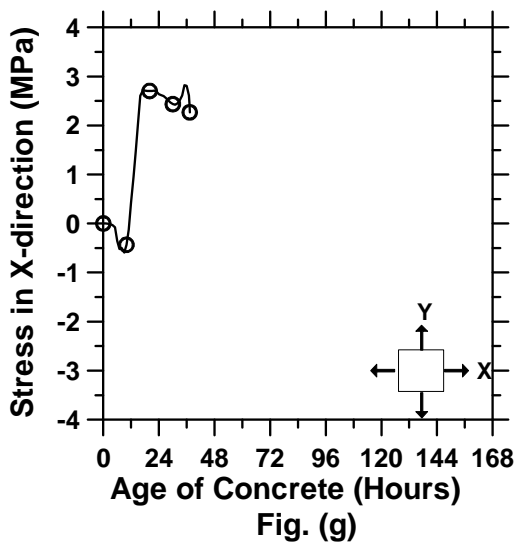
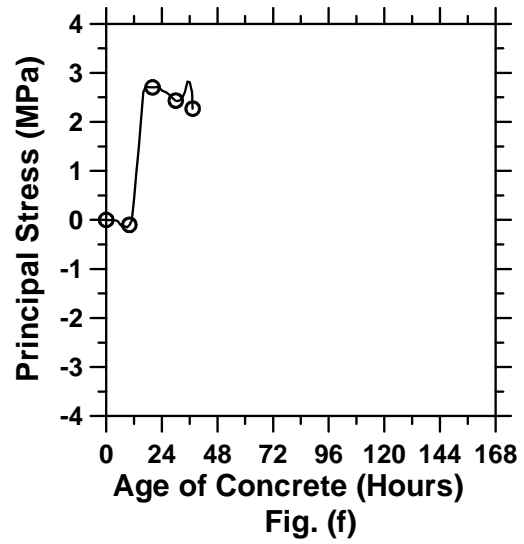
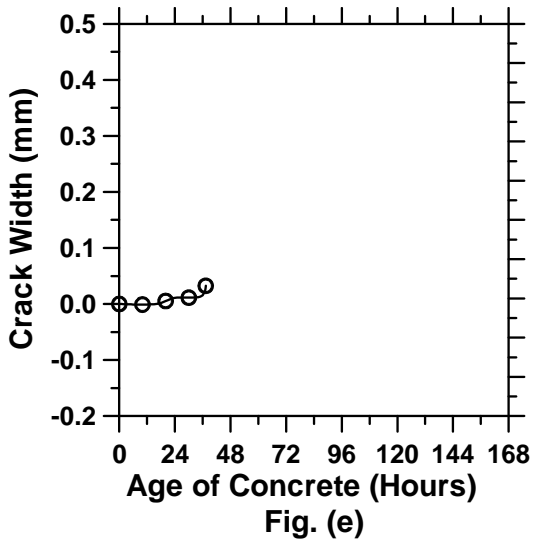


Figure A.60: 10-inch thick pavement with a D/8 saw-cut depth introduced at 0 hour.

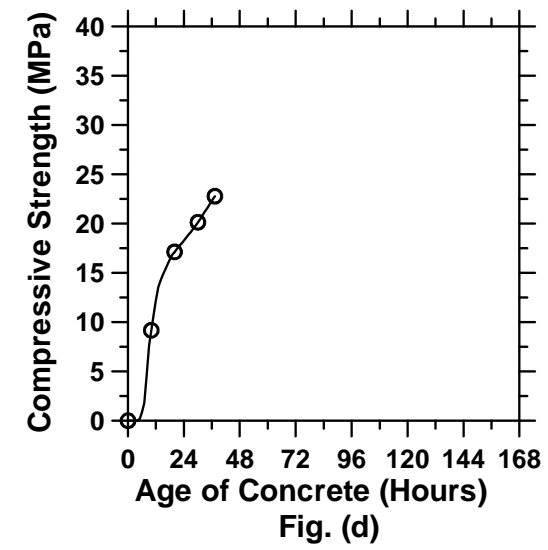
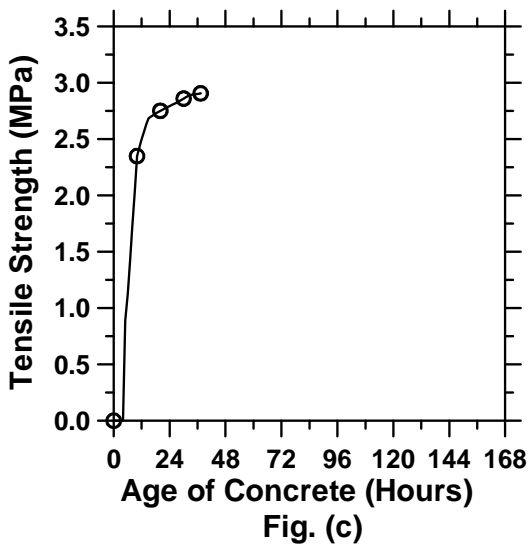
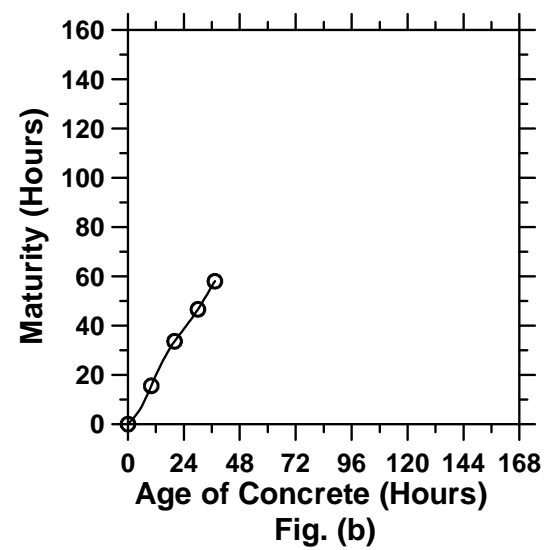
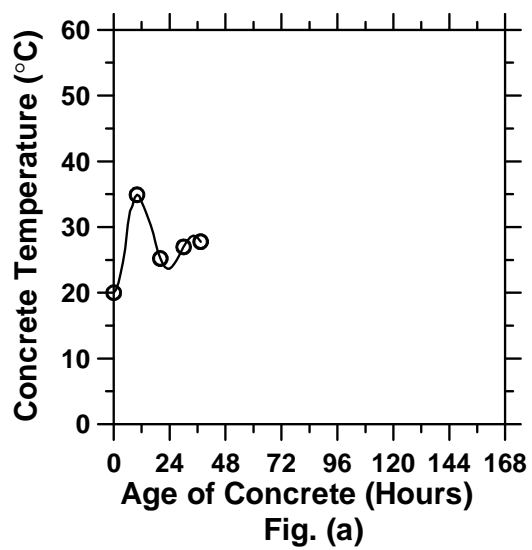


Figure A.61: 10-inch thick pavement with a D/8 saw-cut depth introduced at 6 hours
(cont'd).

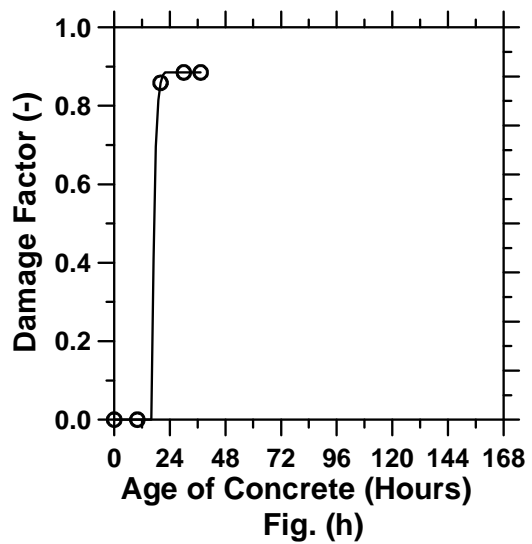
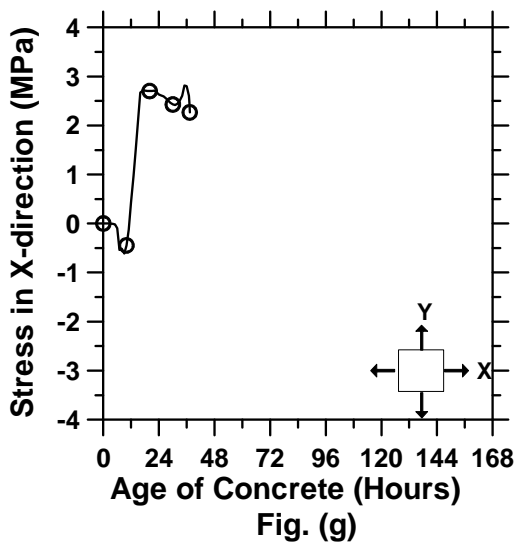
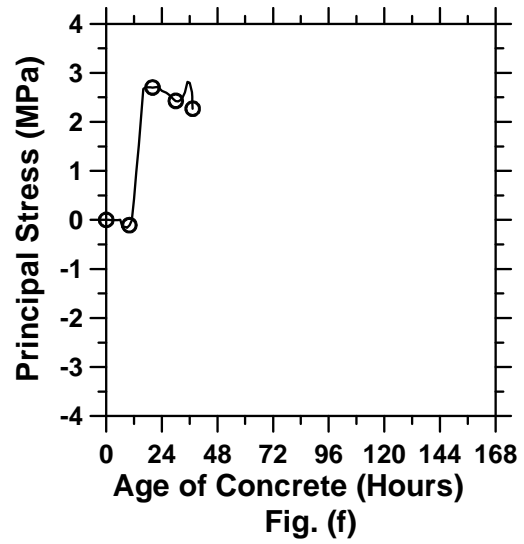
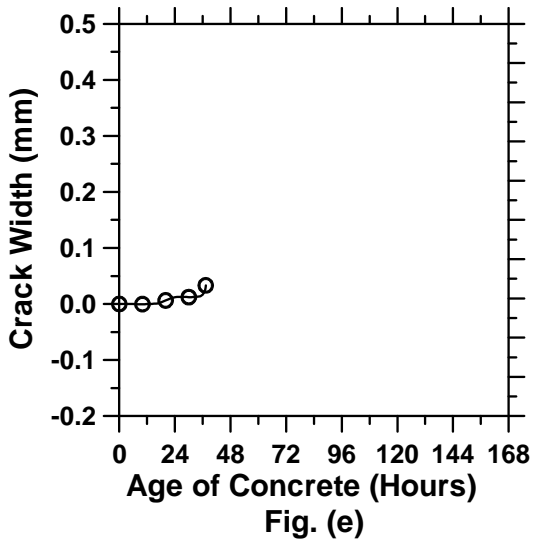


Figure A.61: 10-inch thick pavement with a D/8 saw-cut depth introduced at 6 hours.

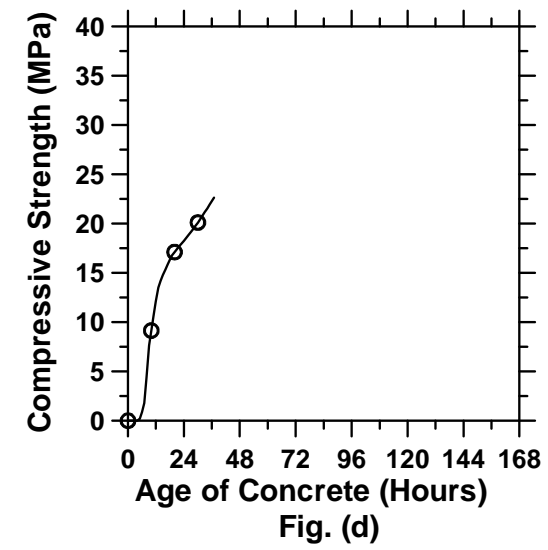
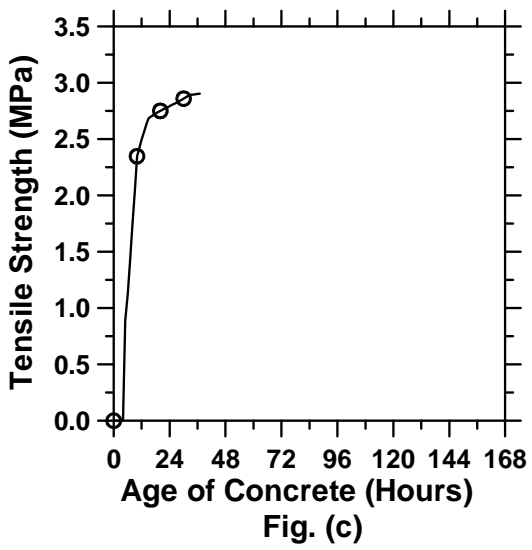
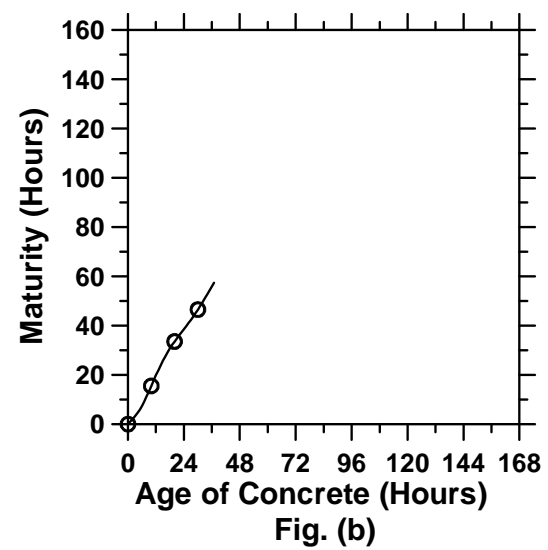
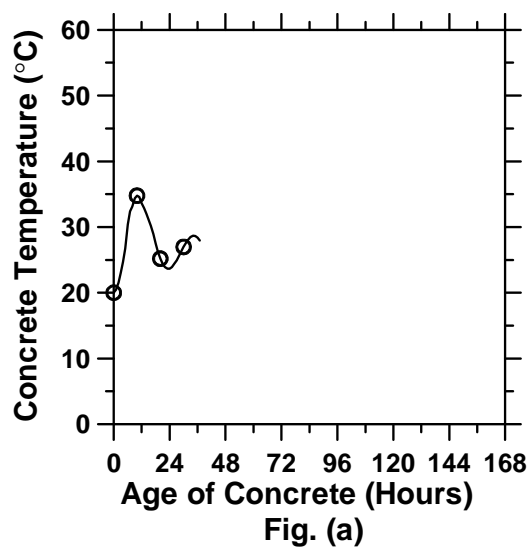


Figure A.62: 10-inch thick pavement with a D/8 saw-cut depth introduced at 12 hours
(cont'd).

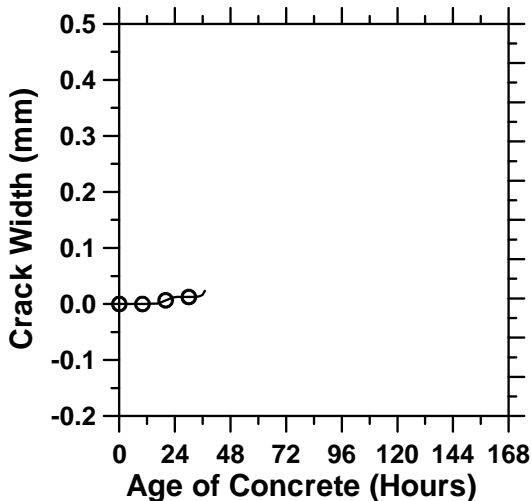


Fig. (e)

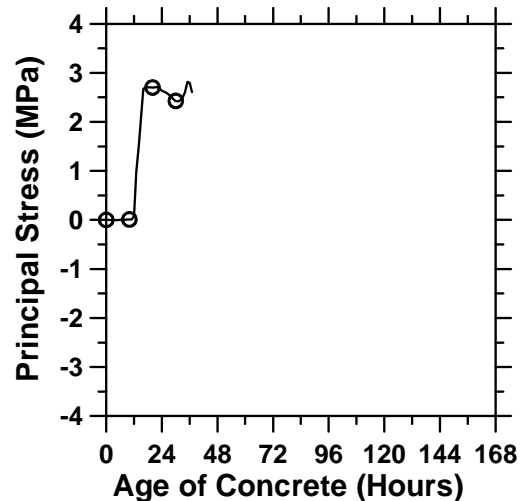


Fig. (f)

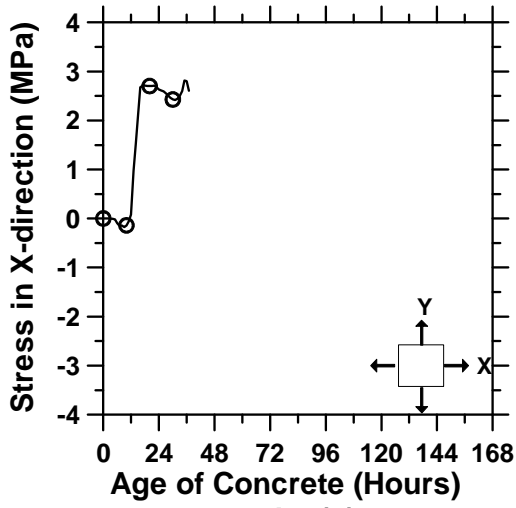


Fig. (g)

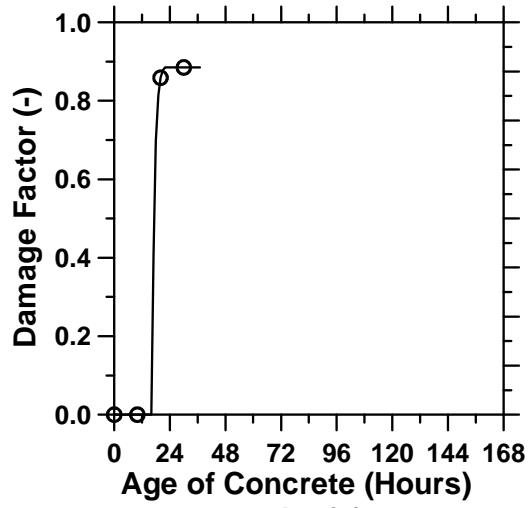


Fig. (h)

Figure A.62: 10-inch thick pavement with a D/8 saw-cut depth introduced at 12 hours.

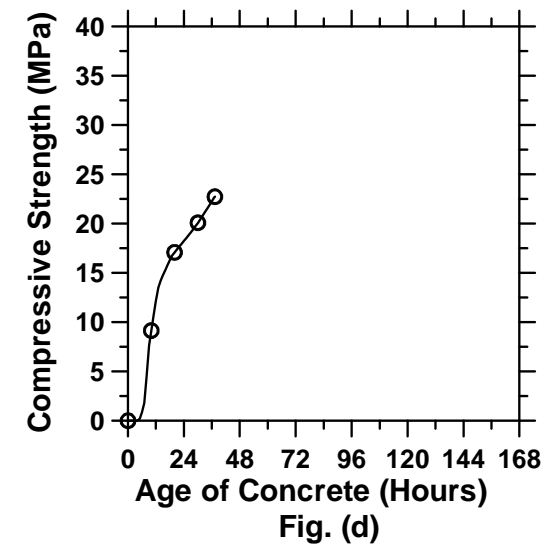
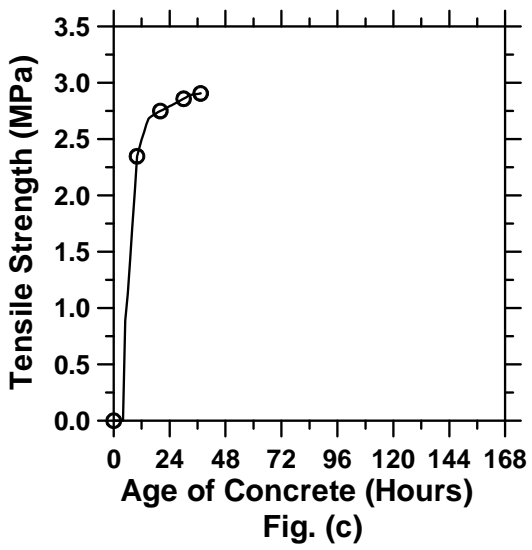
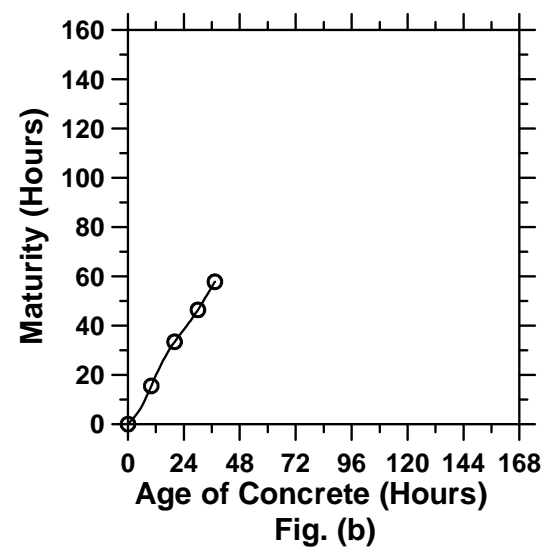
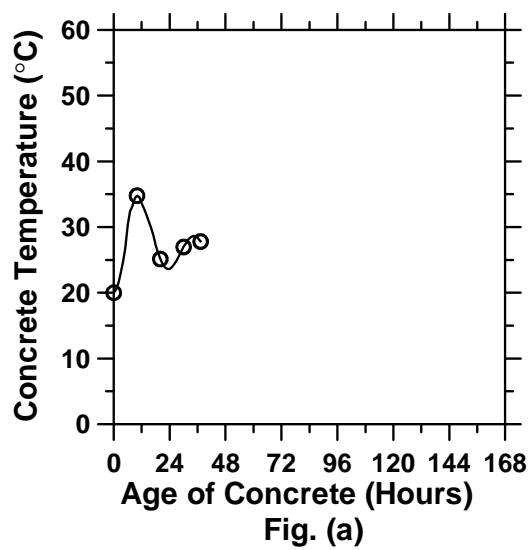


Figure A.63: 10-inch thick pavement with a D/8 saw-cut depth introduced at 18 hours
(cont'd).

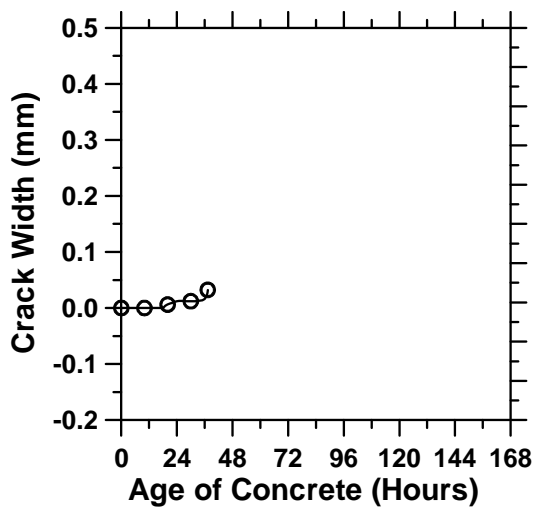


Fig. (e)

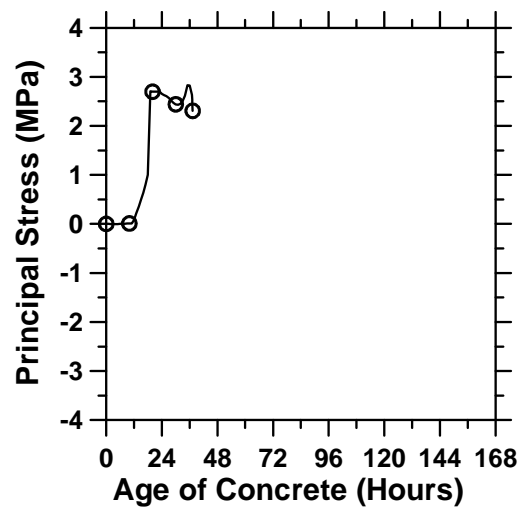


Fig. (f)

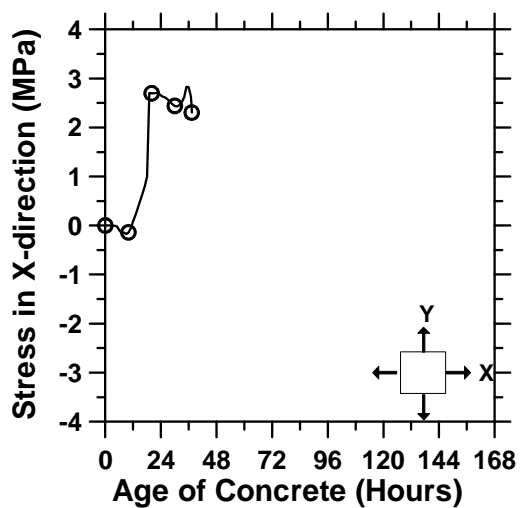


Fig. (g)

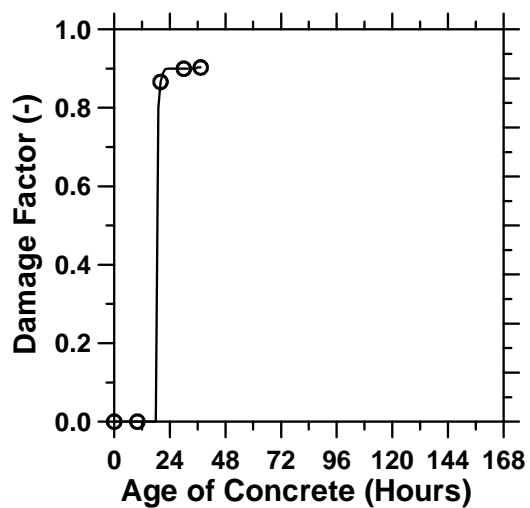


Fig. (h)

Figure A.63: 10-inch thick pavement with a D/8 saw-cut depth introduced at 18 hours.

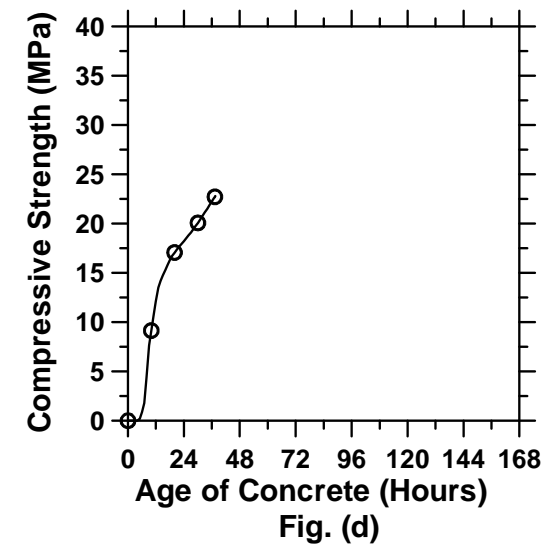
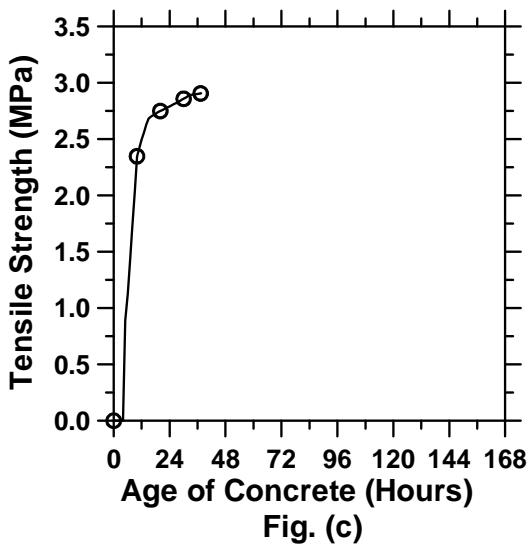
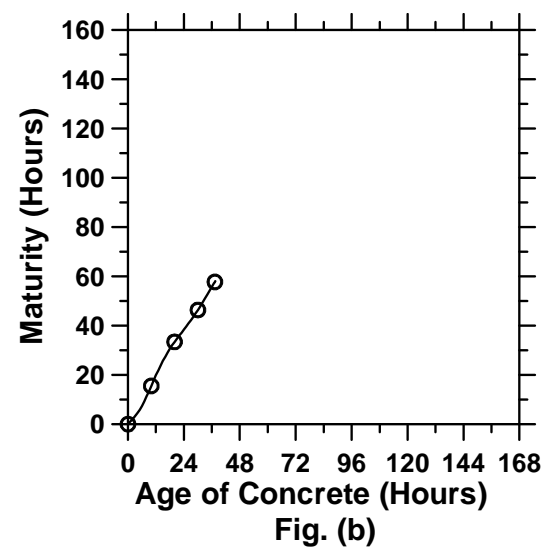
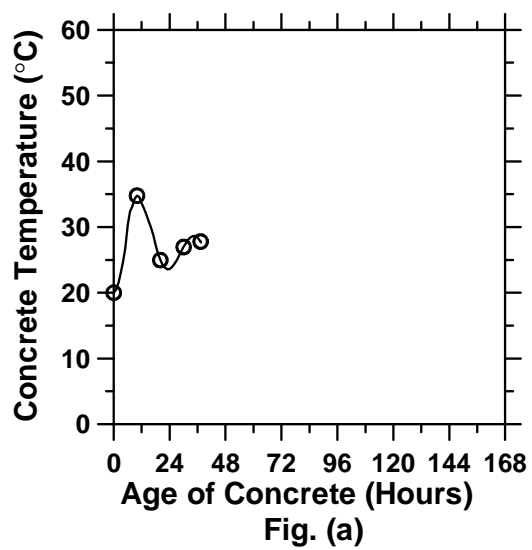


Figure A.64: 10-inch thick pavement with a D/8 saw-cut depth introduced at 21 hours
(cont'd).

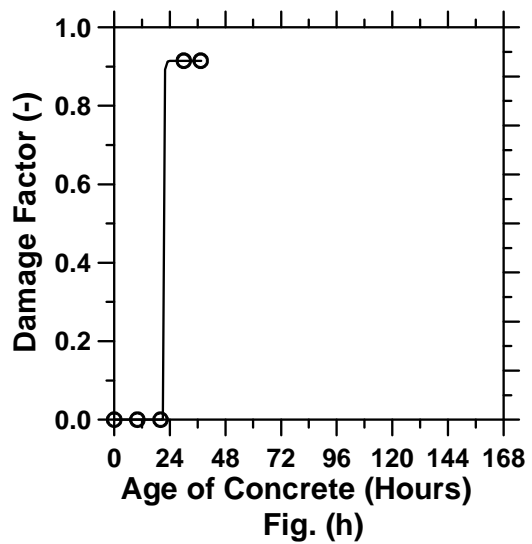
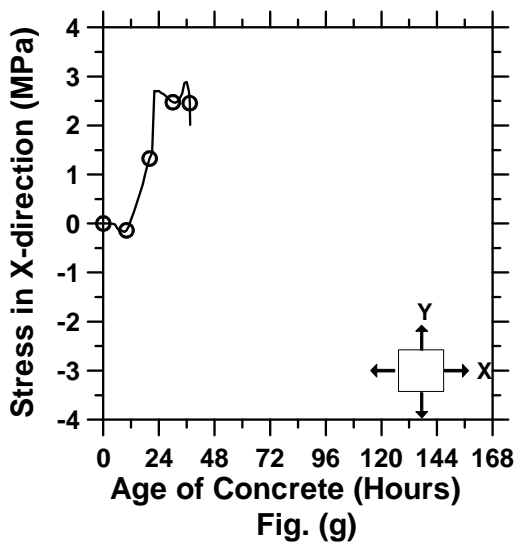
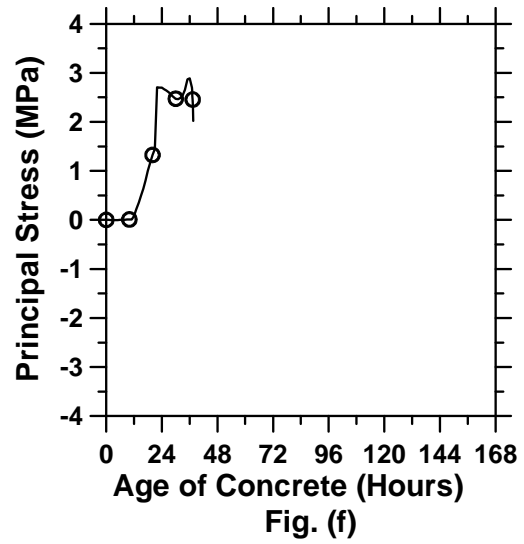
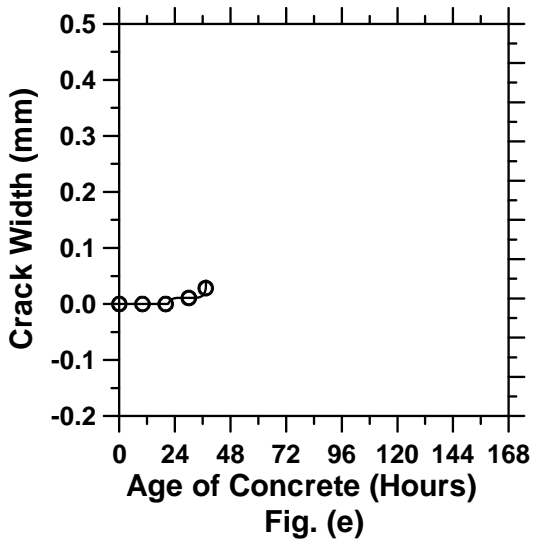


Figure A.64: 10-inch thick pavement with a D/8 saw-cut depth introduced at 21 hours.

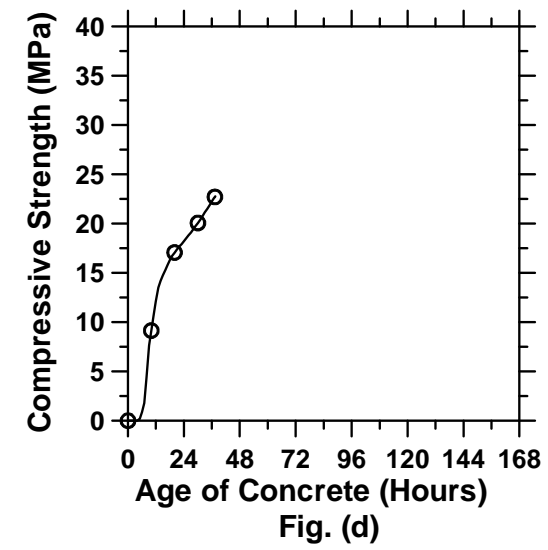
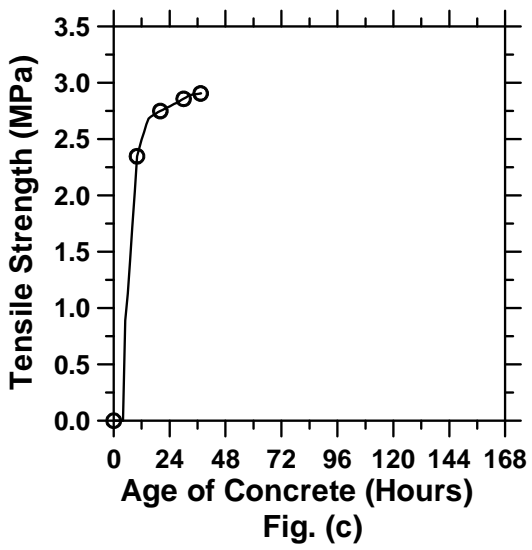
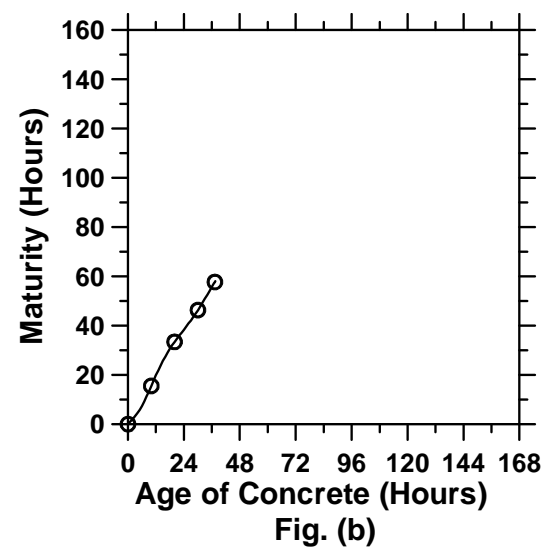
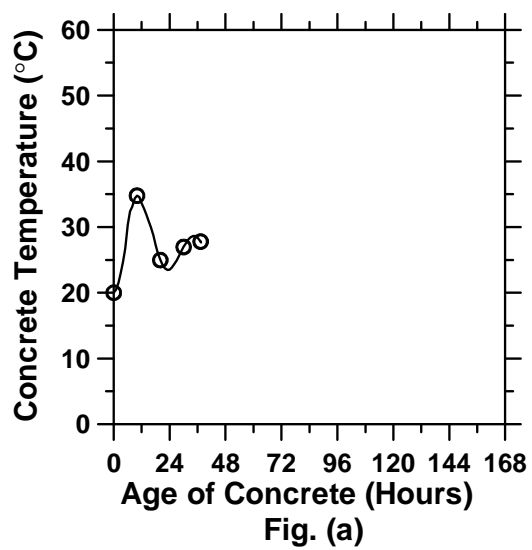


Figure A.65: 10-inch thick pavement with a D/8 saw-cut depth introduced at 24 hours
(cont'd).

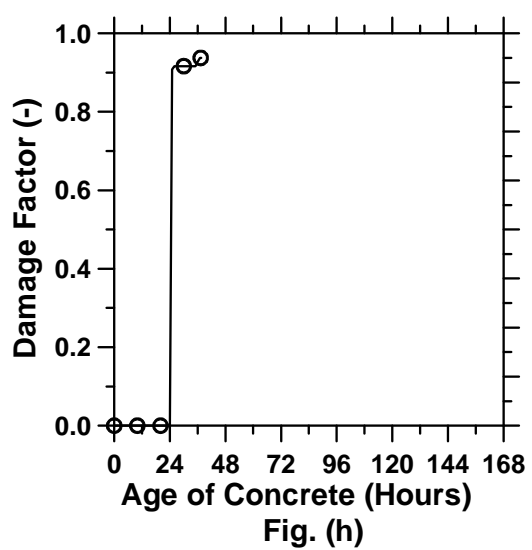
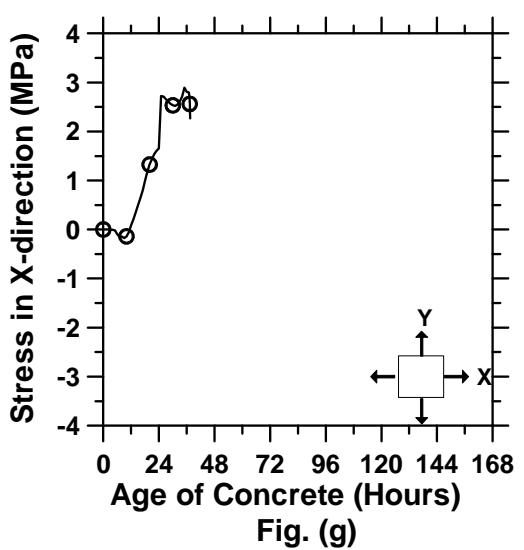
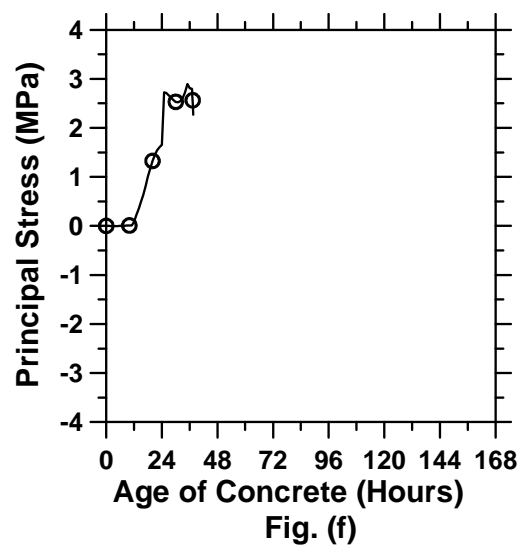
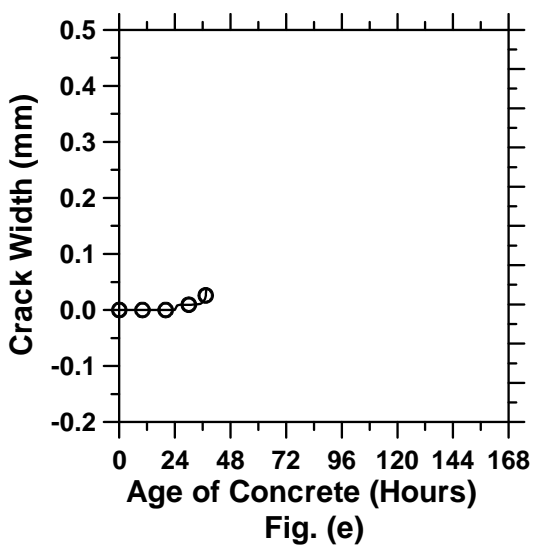


Figure A.65: 10-inch thick pavement with a D/8 saw-cut depth introduced at 24 hours.

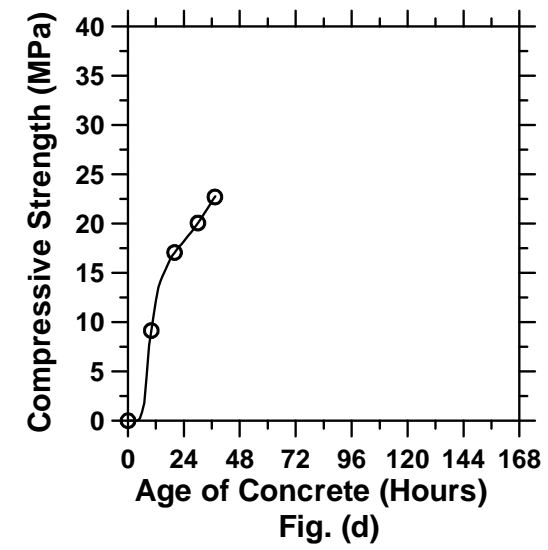
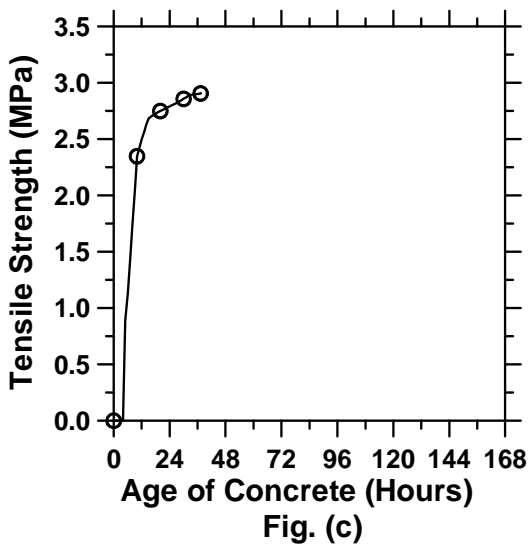
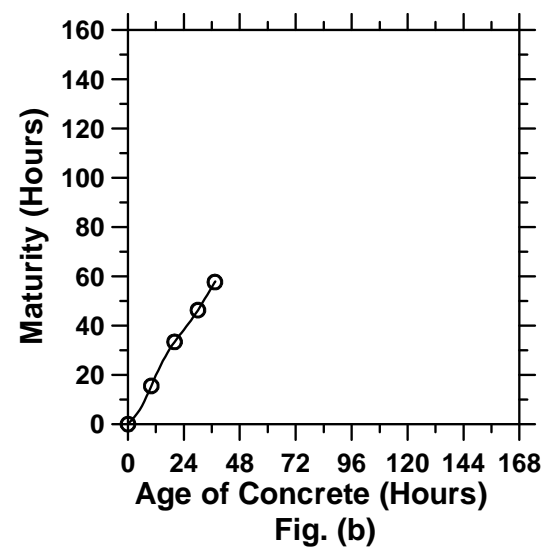
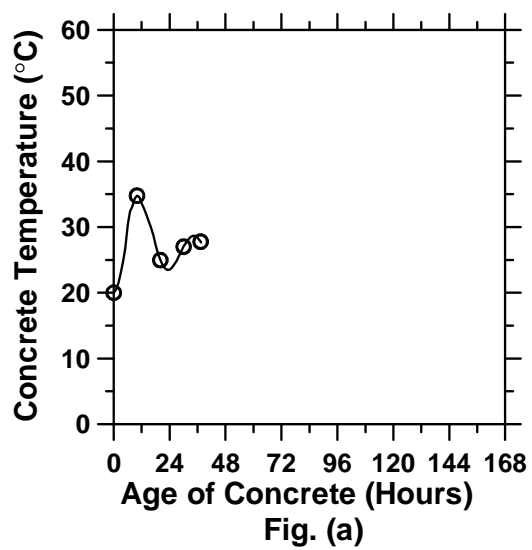


Figure A.66: 10-inch thick pavement with a D/8 saw-cut depth introduced at 30 hours
(cont'd).

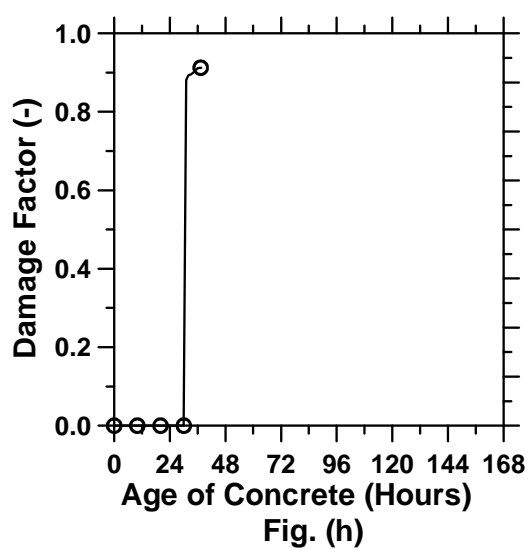
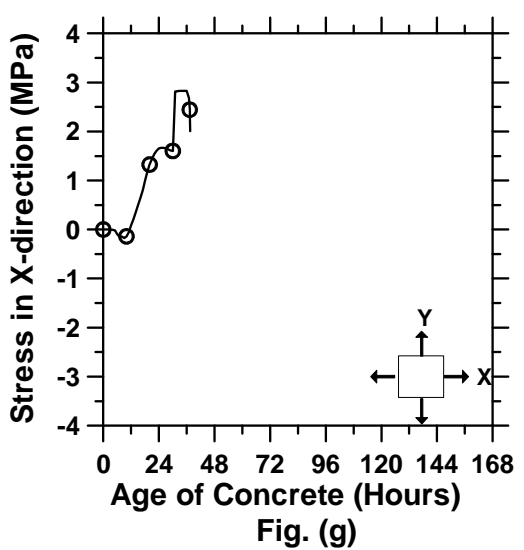
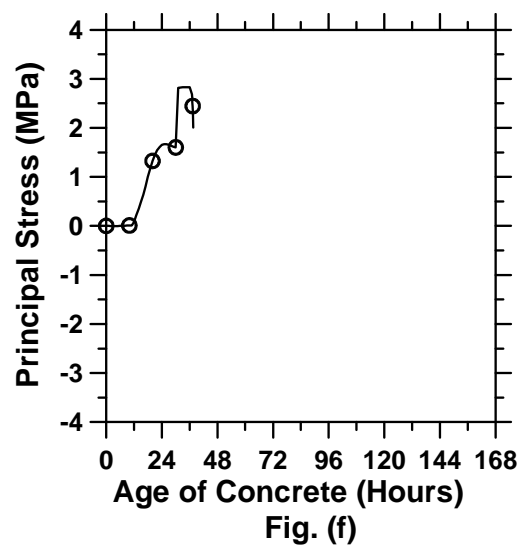
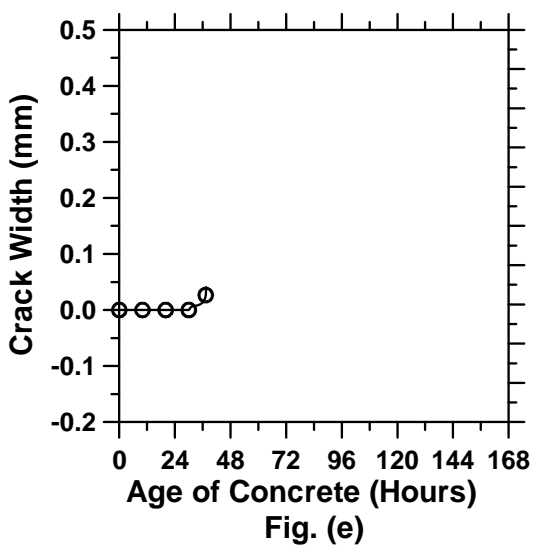


Figure A.66: 10-inch thick pavement with a D/8 saw-cut depth introduced at 30 hours.

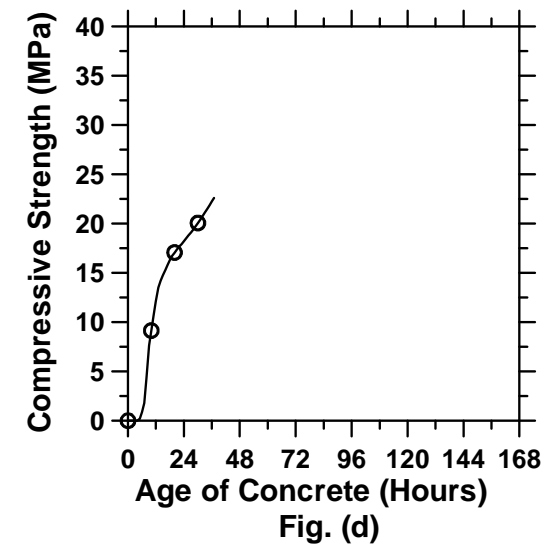
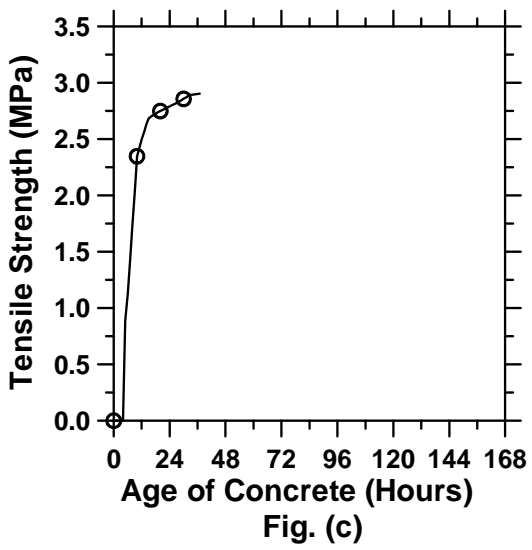
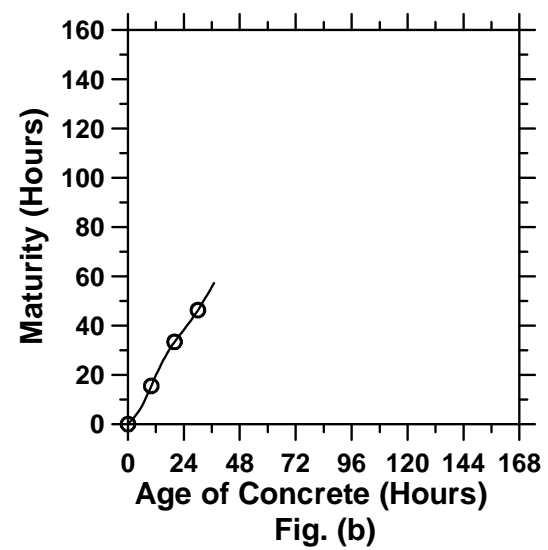
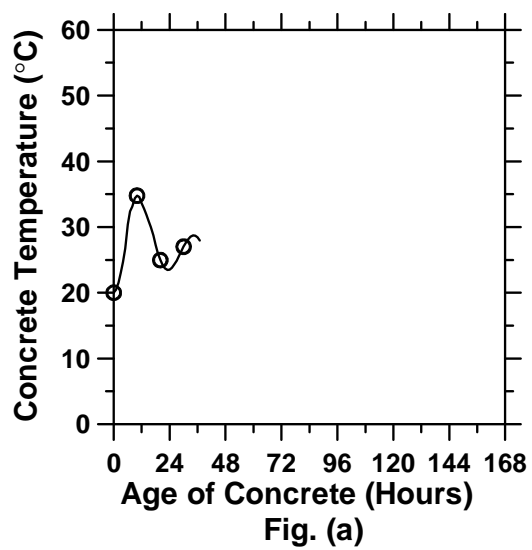


Figure A.67: 10-inch thick pavement with a D/8 saw-cut depth introduced at 36 hours
(cont'd).

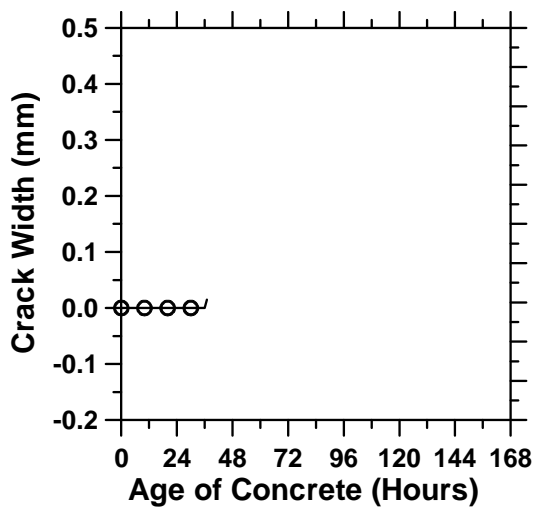


Fig. (e)

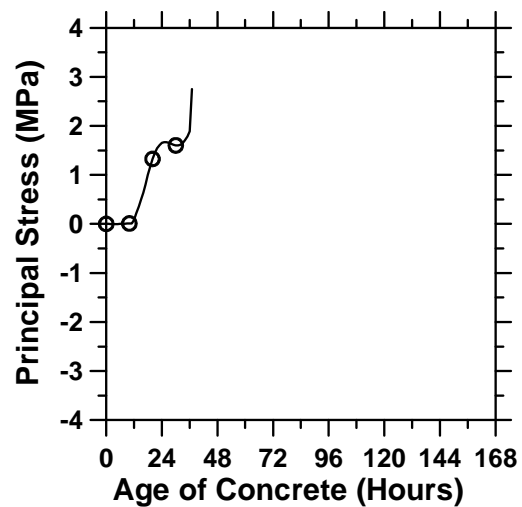


Fig. (f)

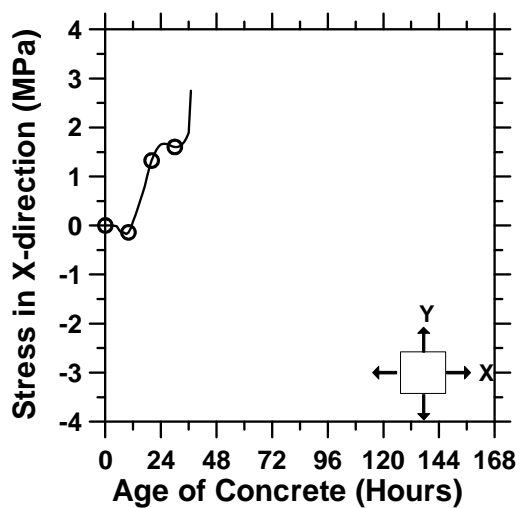


Fig. (g)

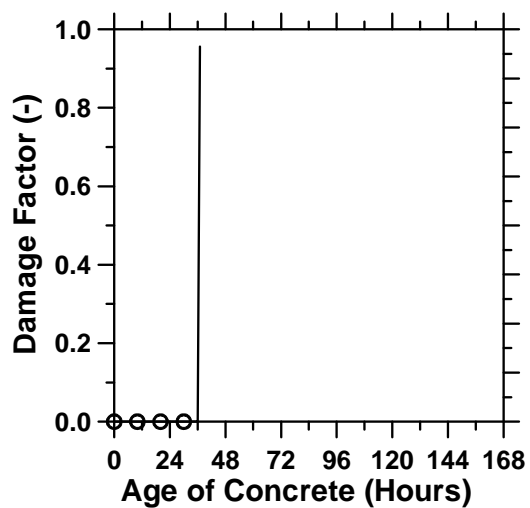


Fig. (h)

Figure A.67: 10-inch thick pavement with a D/8 saw-cut depth introduced at 36 hours.

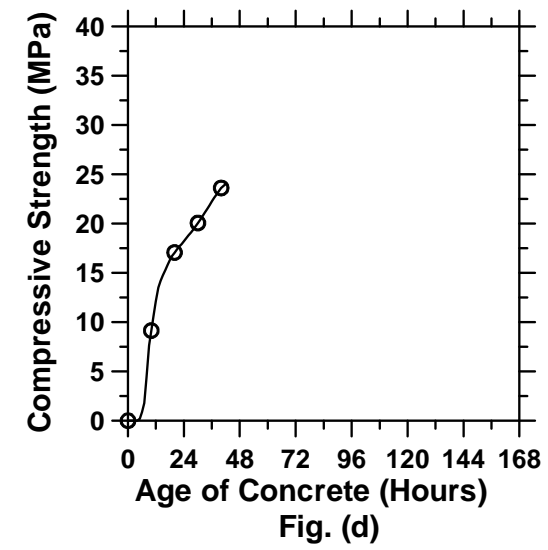
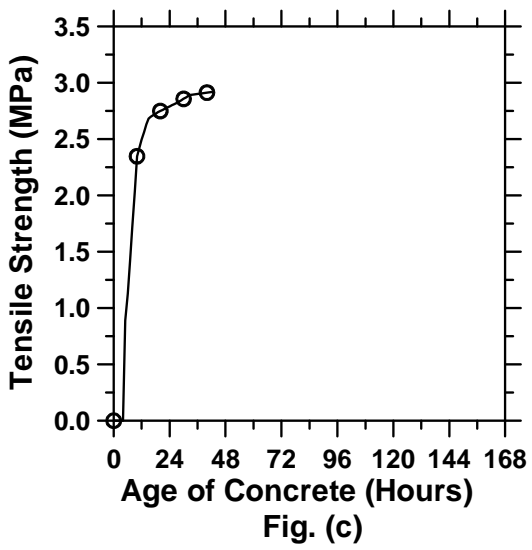
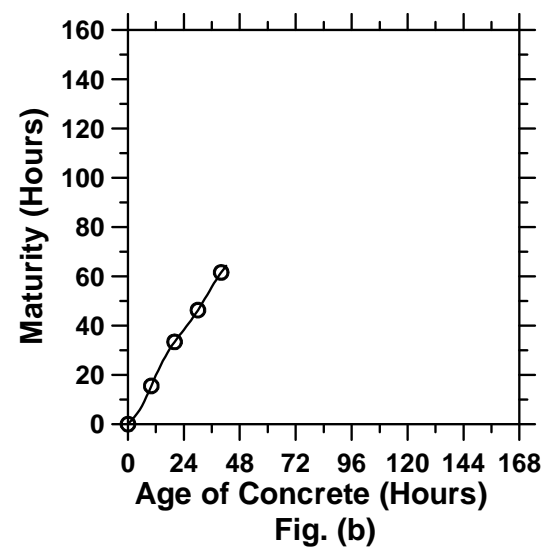
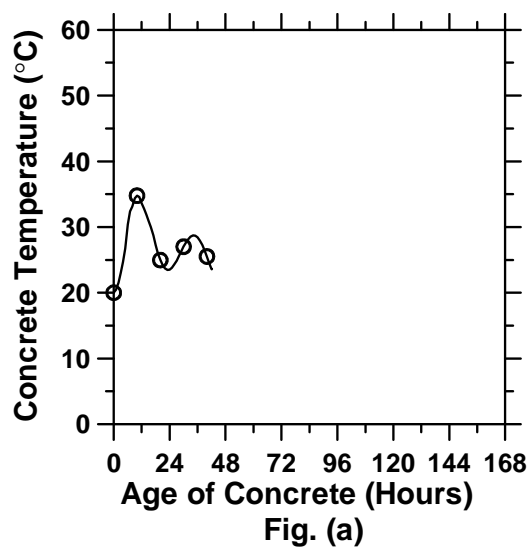


Figure A.68: 10-inch thick pavement with a D/8 saw-cut depth introduced at 42 hours
(cont'd).

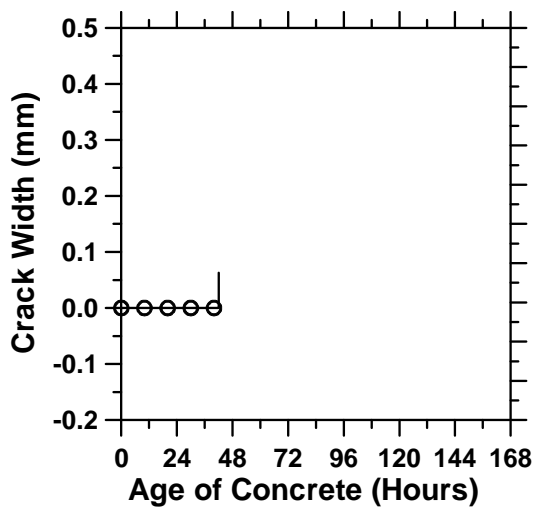


Fig. (e)

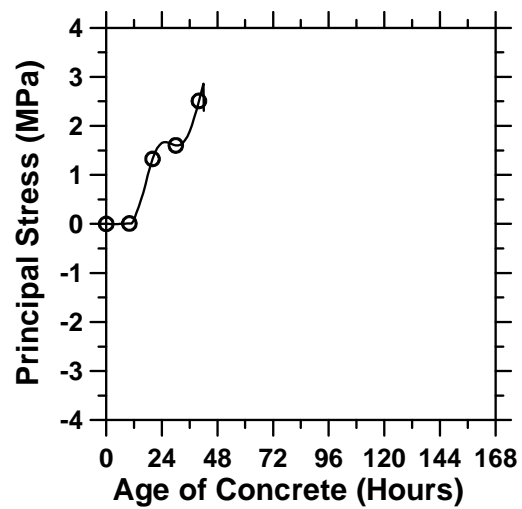


Fig. (f)

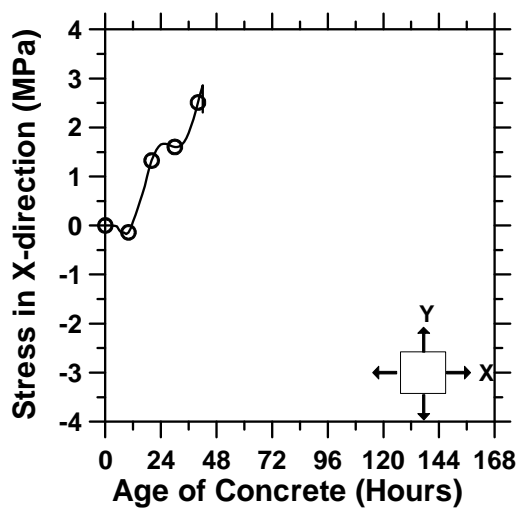


Fig. (g)

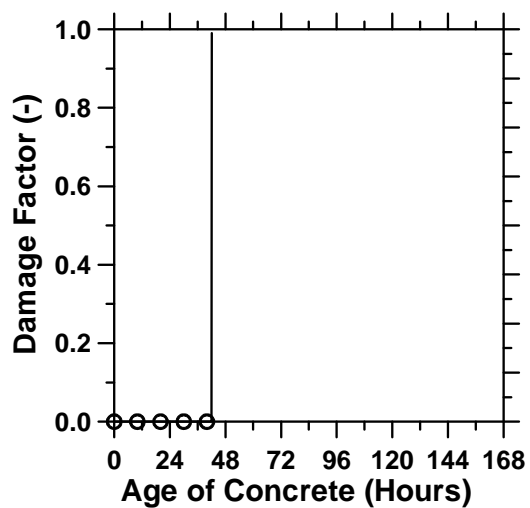


Fig. (h)

Figure A.68: 10-inch thick pavement with a D/8 saw-cut depth introduced at 42 hours.

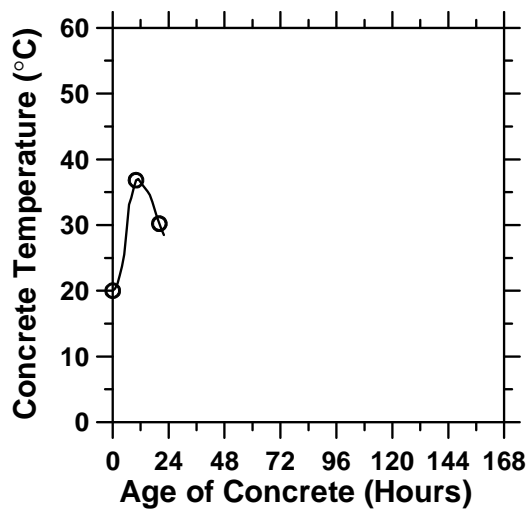


Fig. (a)

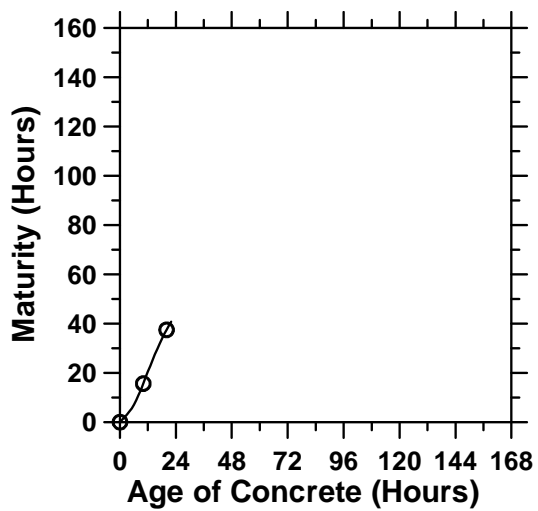


Fig. (b)

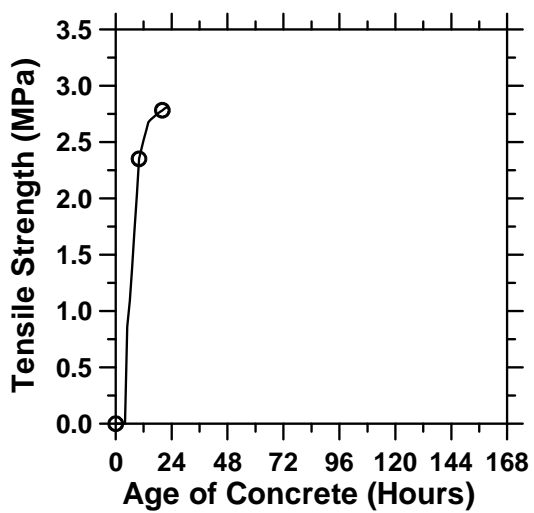


Fig. (c)

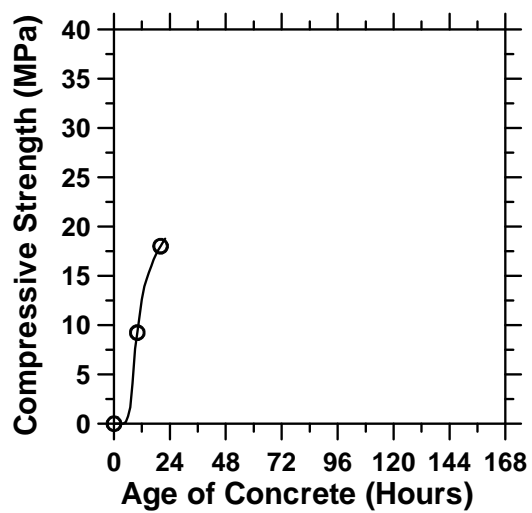


Fig. (d)

Figure A.69: 10-inch thick pavement with a D/2 saw-cut depth introduced at 12 hours

(cont'd).

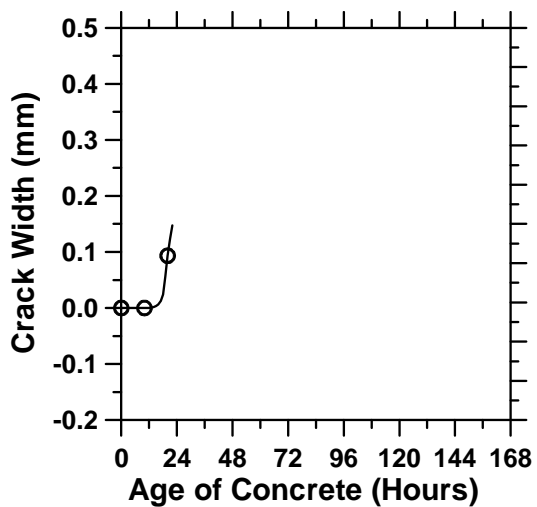


Fig. (e)

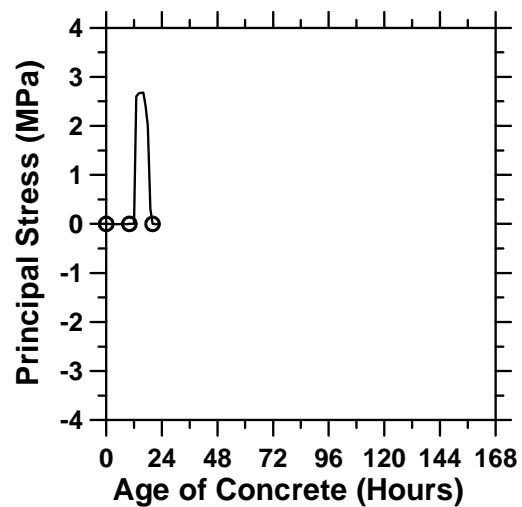


Fig. (f)

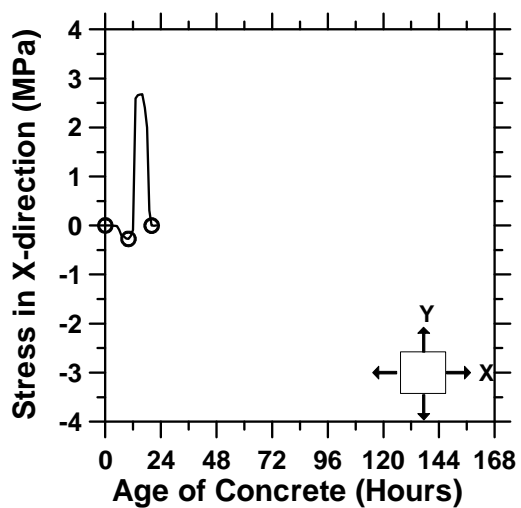


Fig. (g)

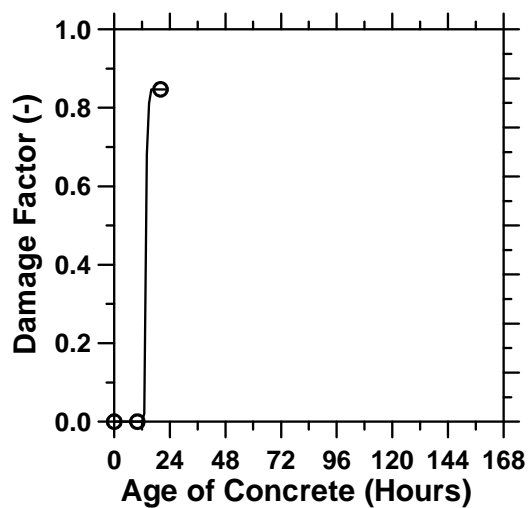


Fig. (h)

Figure A.69: 10-inch thick pavement with a D/2 saw-cut depth introduced at 12 hours.

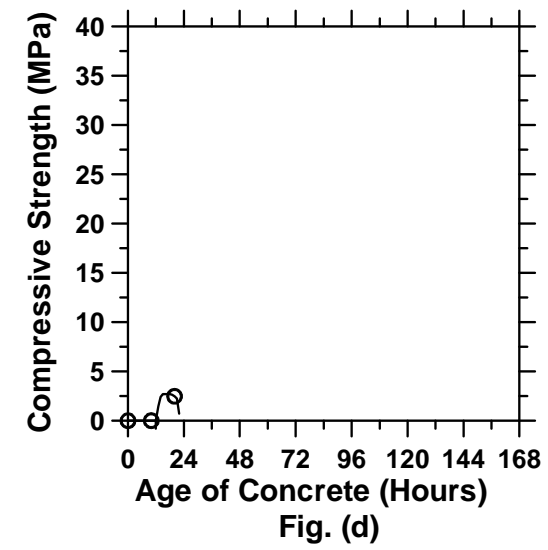
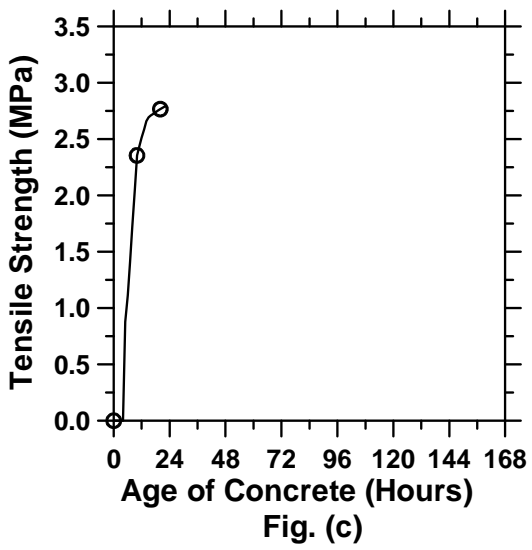
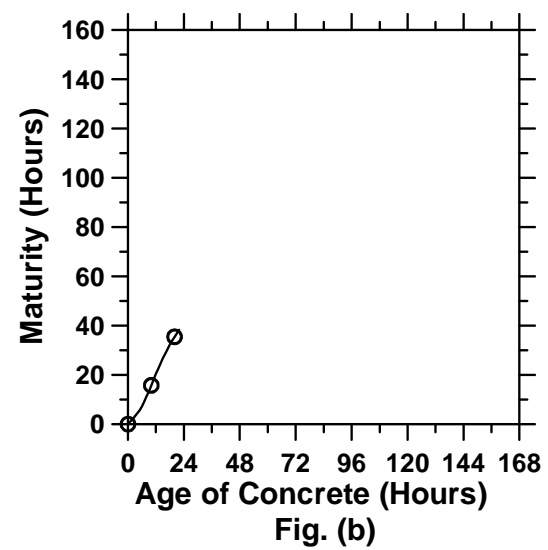
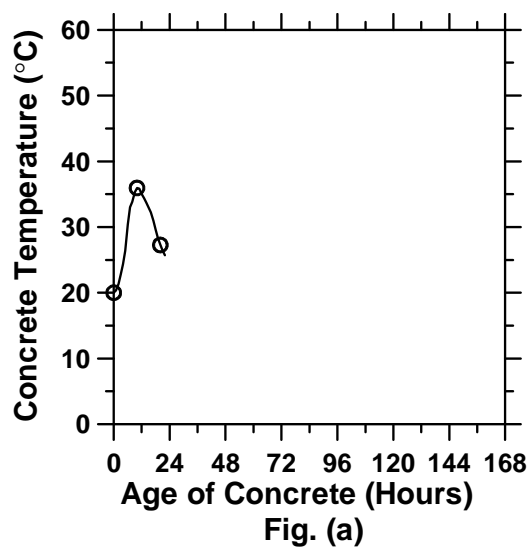


Figure A.70: 10-inch thick pavement with a D/4 saw-cut depth introduced at 12 hours
(cont'd).

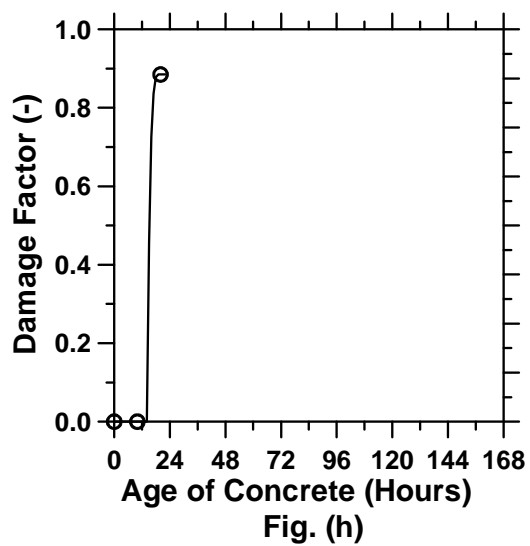
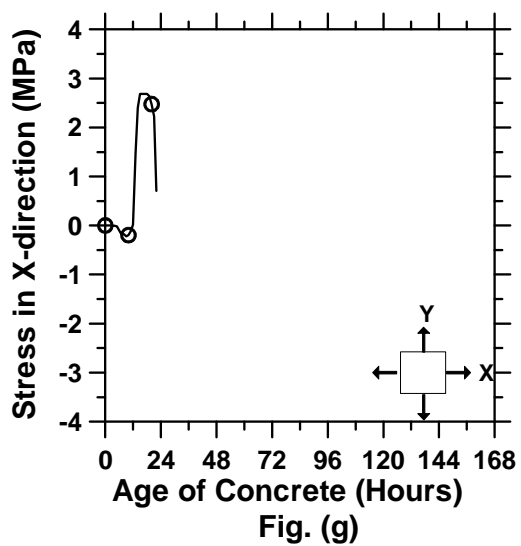
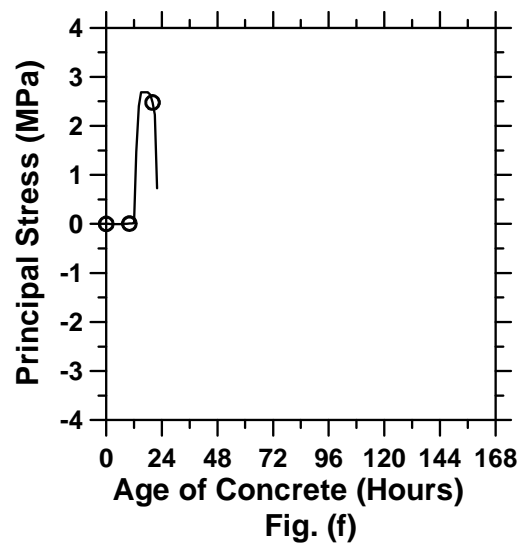
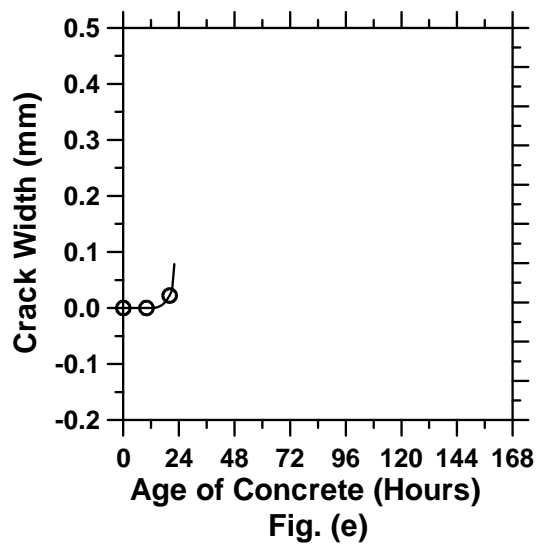


Figure A.70: 10-inch thick pavement with a D/4 saw-cut depth introduced at 12 hours.

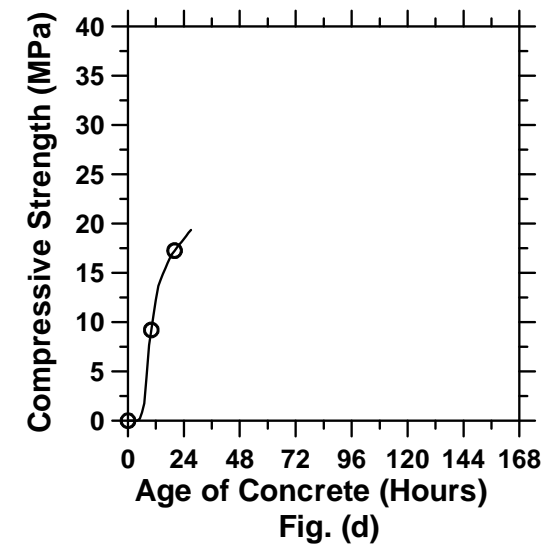
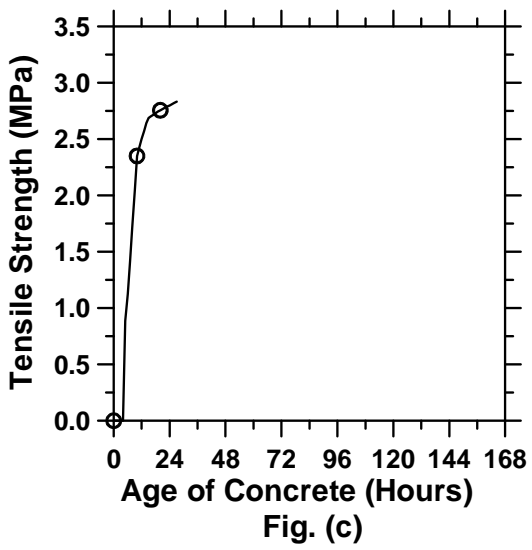
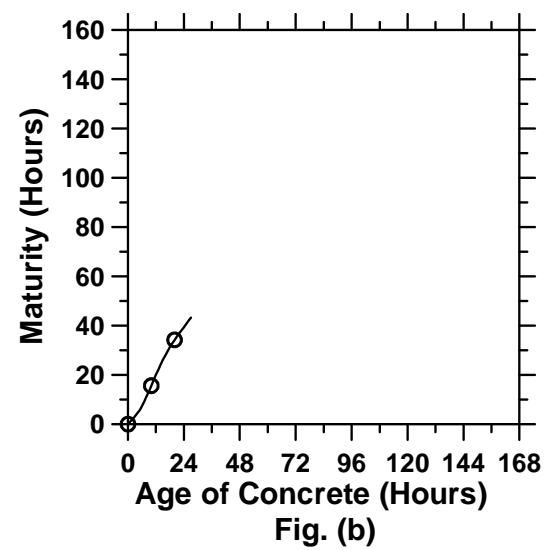
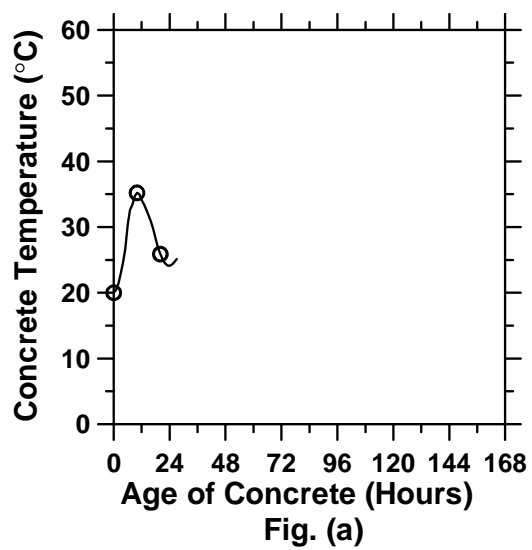


Figure A.71: 10-inch thick pavement with a D/6 saw-cut depth introduced at 12 hours
(cont'd).

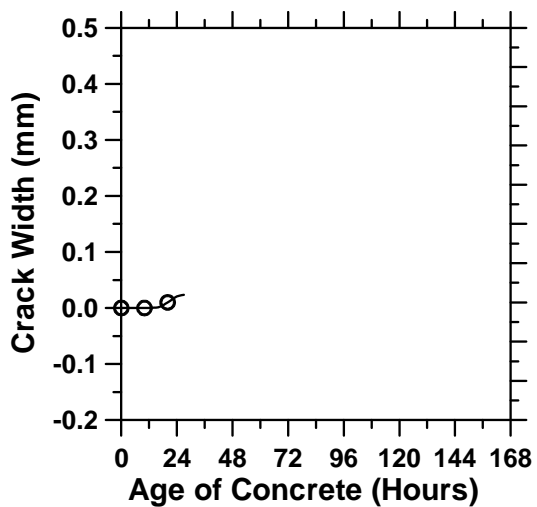


Fig. (e)

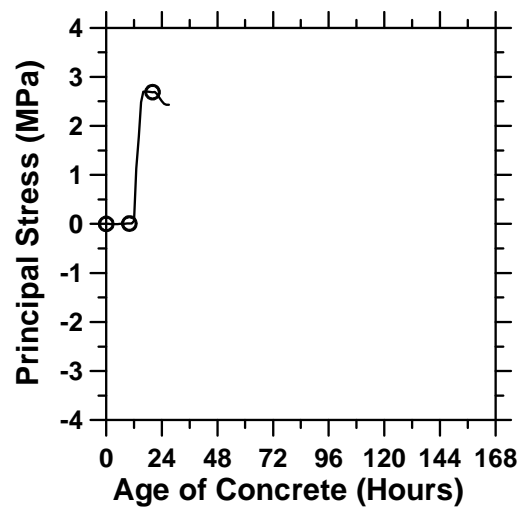


Fig. (f)

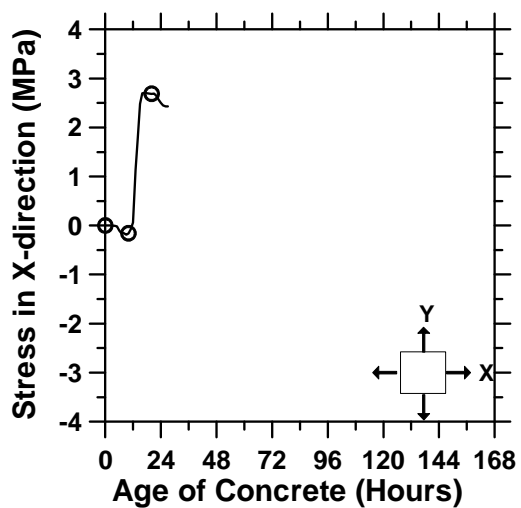


Fig. (g)

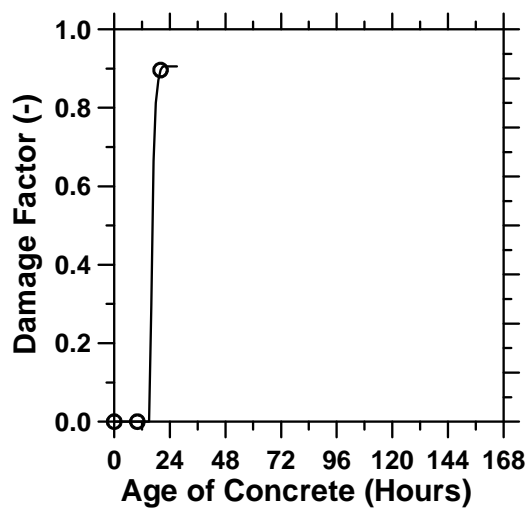


Fig. (h)

Figure A.71: 10-inch thick pavement with a D/6 saw-cut depth introduced at 12 hours.

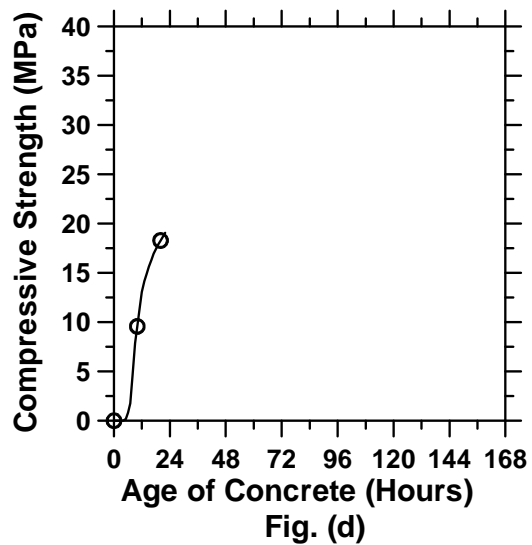
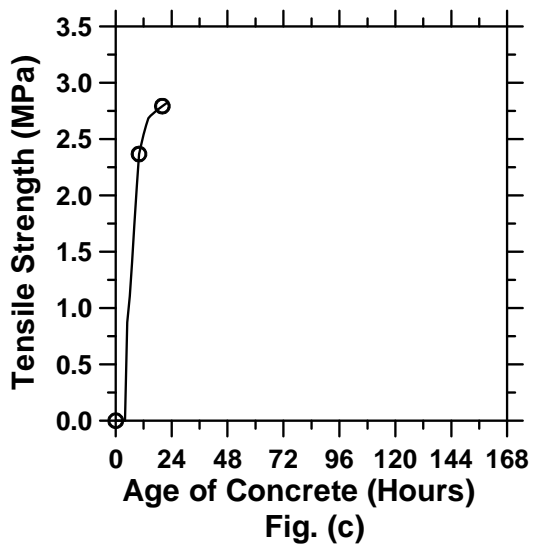
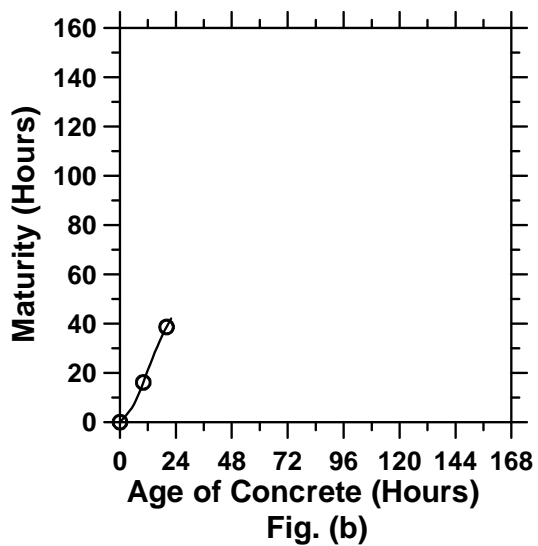
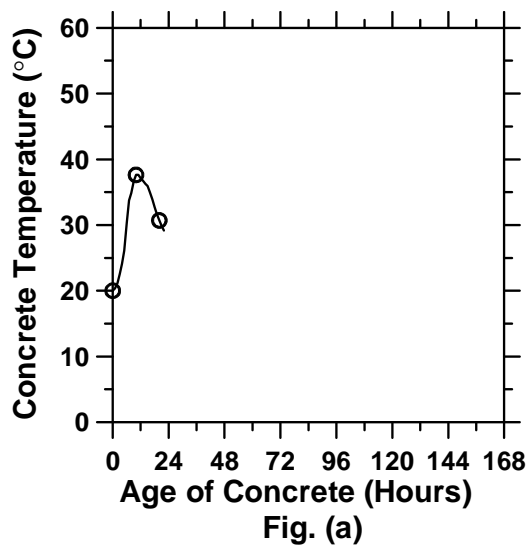


Figure A.72: 12-inch thick pavement with a D/3 saw-cut depth introduced at 12 hours

(cont'd).

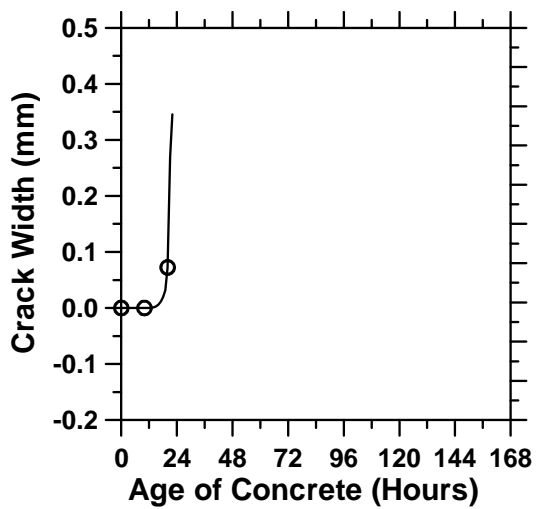


Fig. (e)

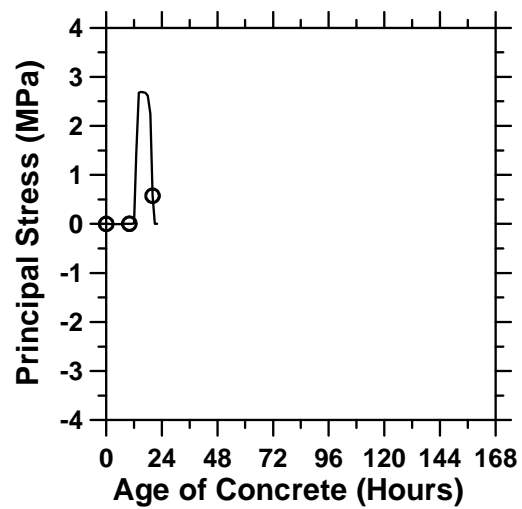


Fig. (f)

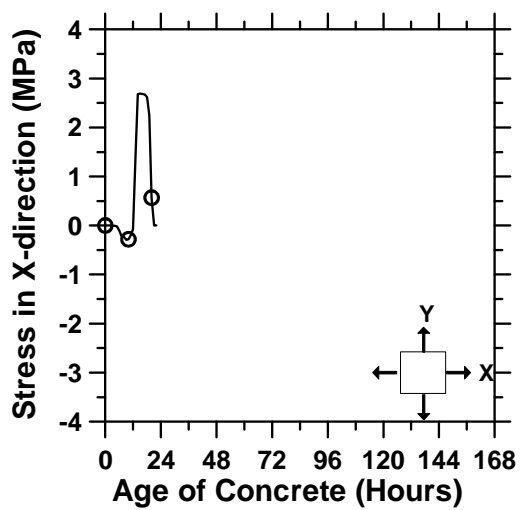


Fig. (g)

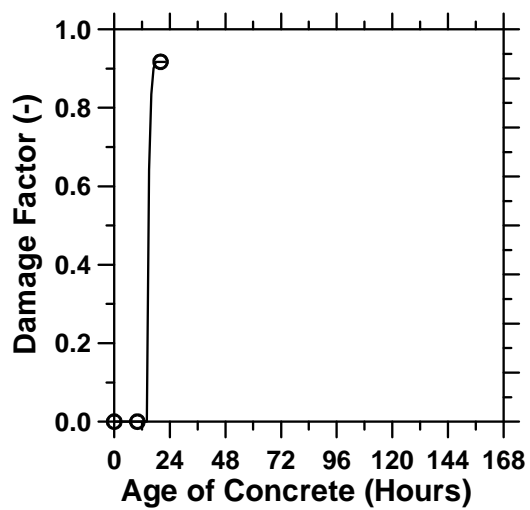


Fig. (h)

Figure A.72: 12-inch thick pavement with a D/3 saw-cut depth introduced at 12 hours.

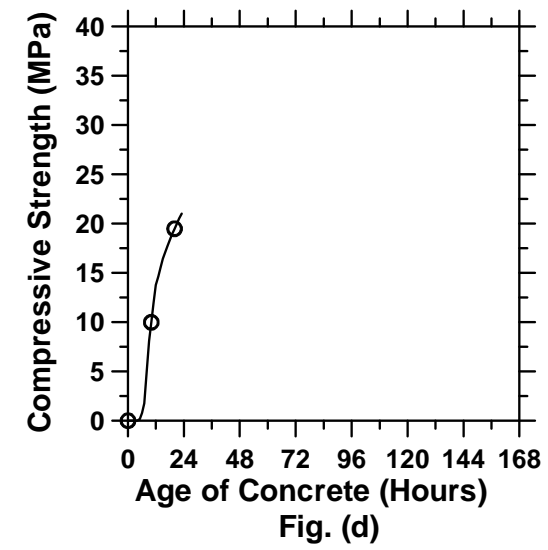
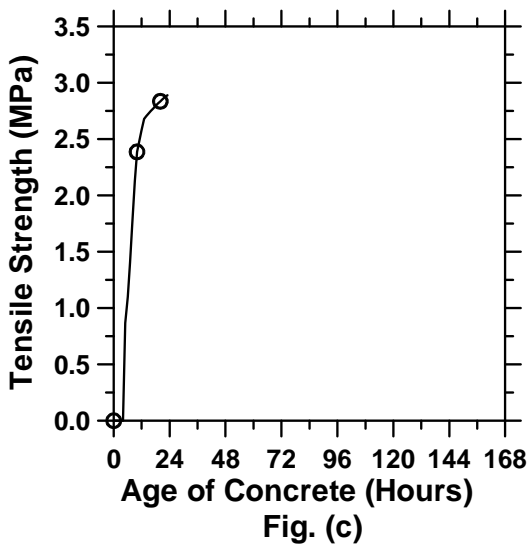
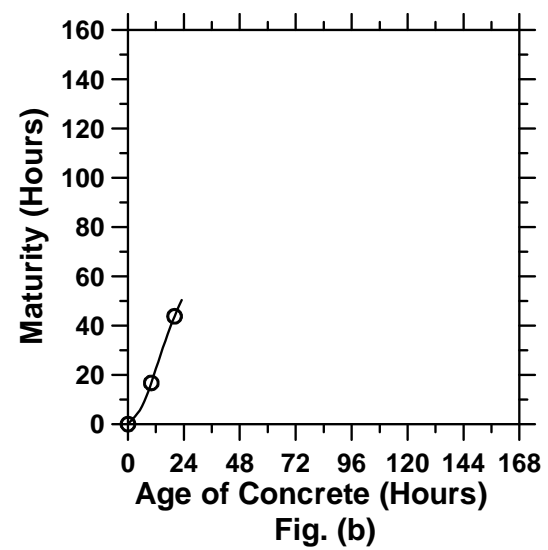
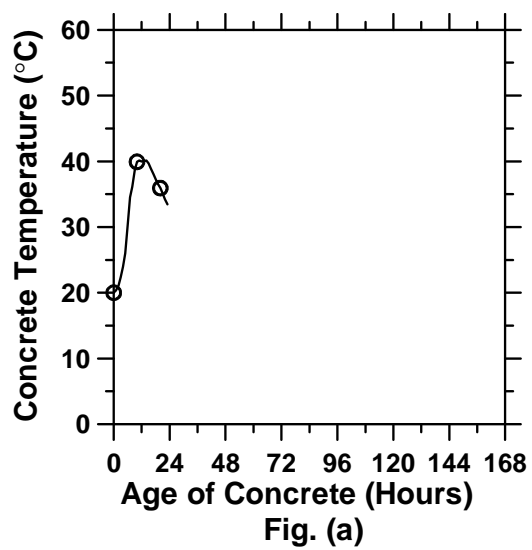


Figure A.73: 17-inch thick pavement with a D/3 saw-cut depth introduced at 12 hours
(cont'd).

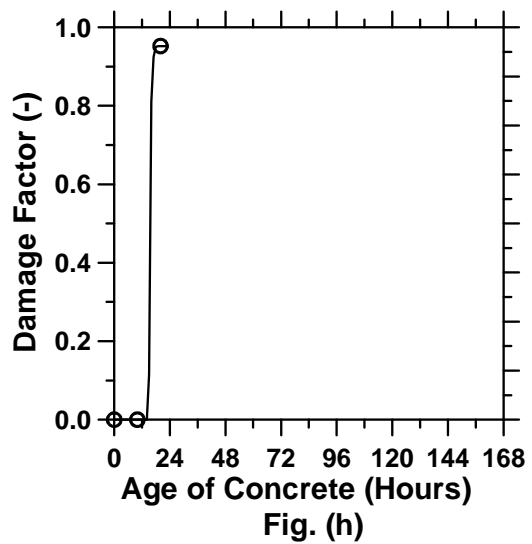
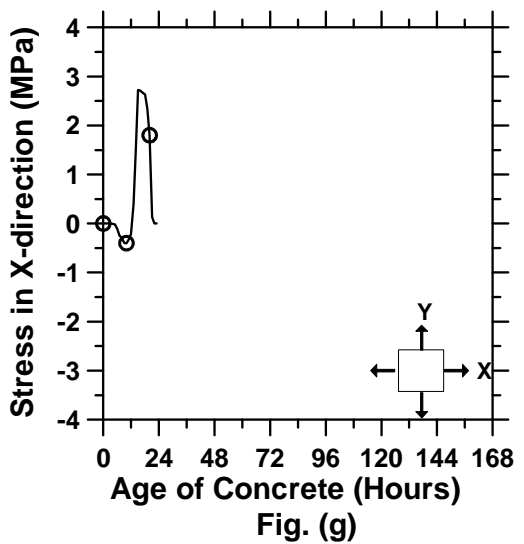
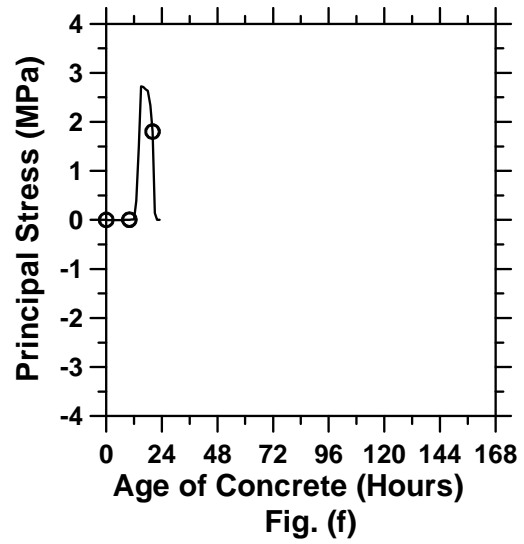
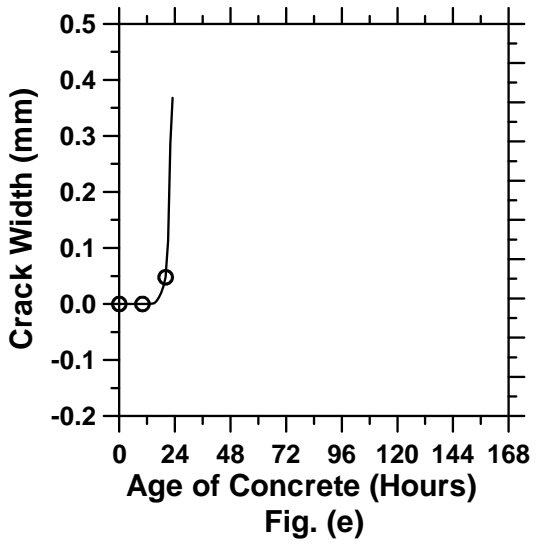


Figure A.73: 17-inch thick pavement with a D/3 saw-cut depth introduced at 12 hours.

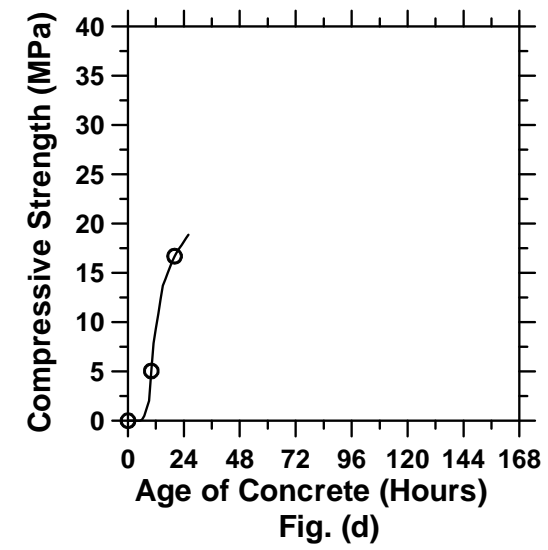
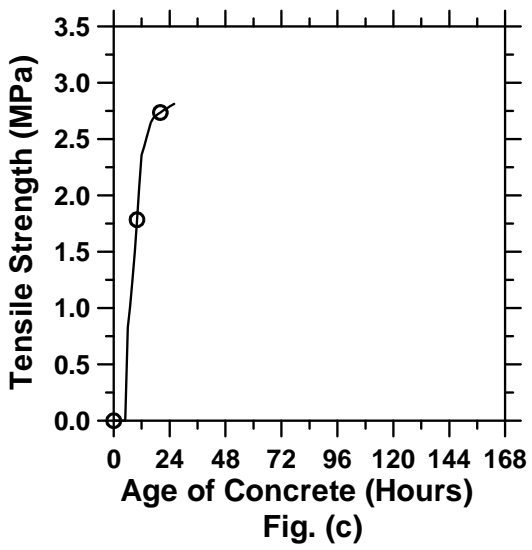
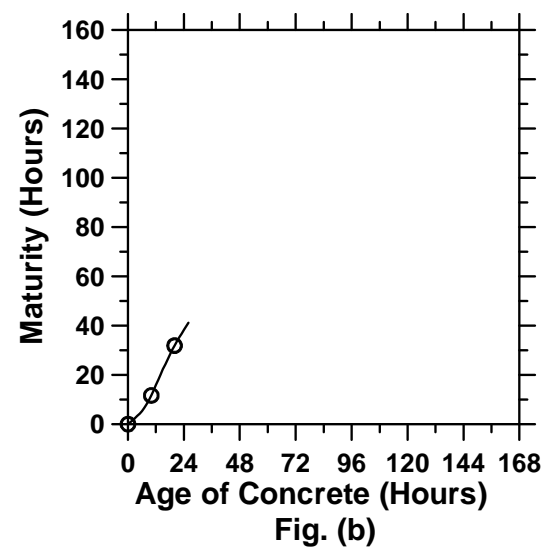
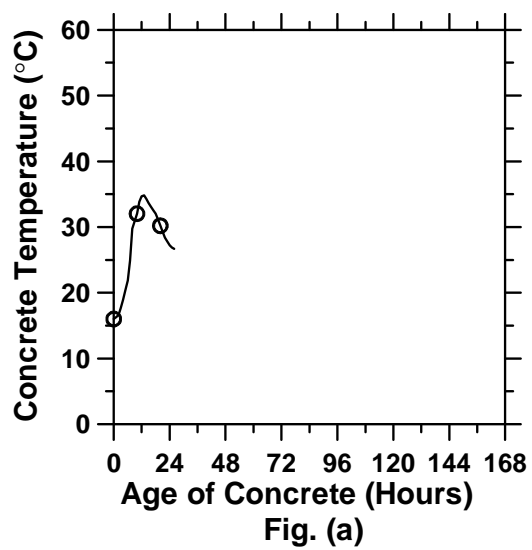


Figure A.74: Pavement cured at “M” ambient temperature with a D/3 saw-cut depth introduced at 0 hour (cont’d).

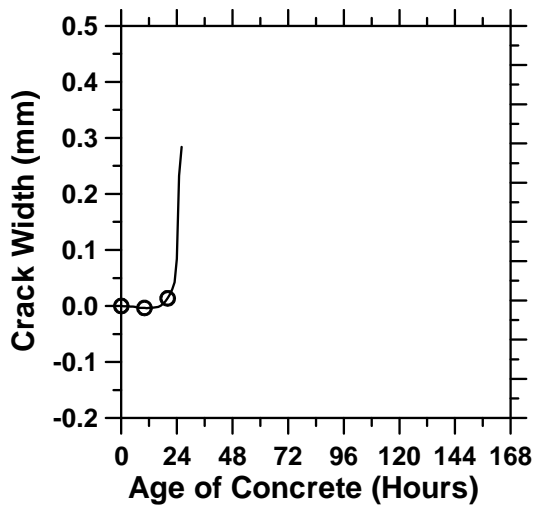


Fig. (e)

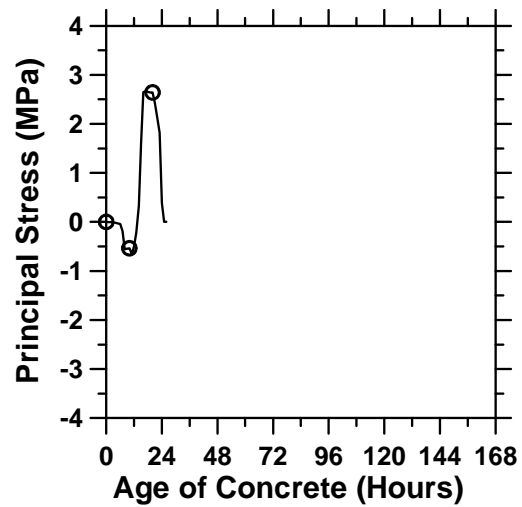


Fig. (f)

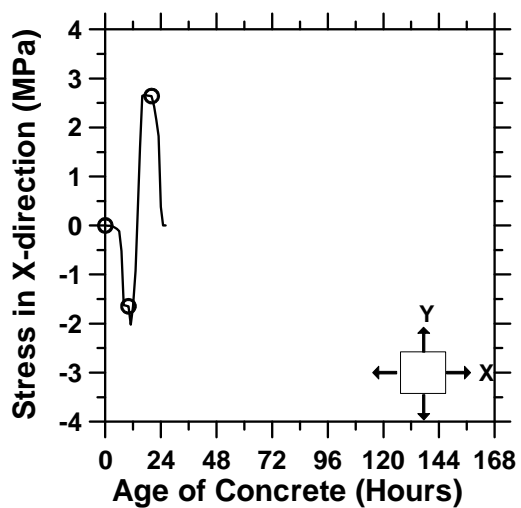


Fig. (g)

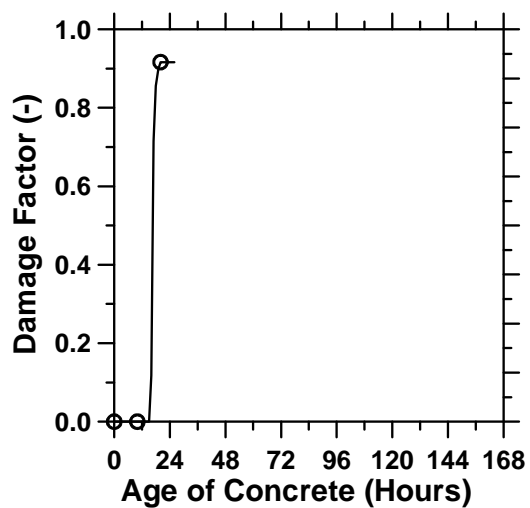


Fig. (h)

Figure A.74: Pavement cured at “M” ambient temperature with a D/3 saw-cut depth introduced at 0 hour.

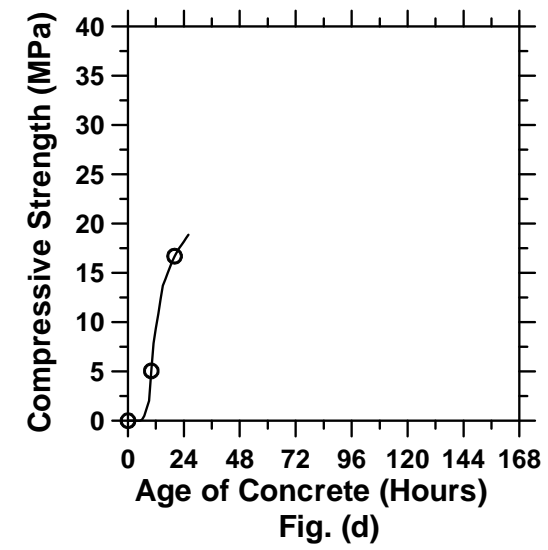
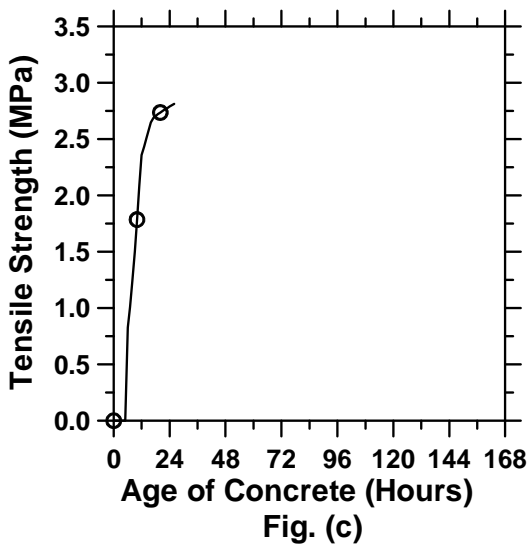
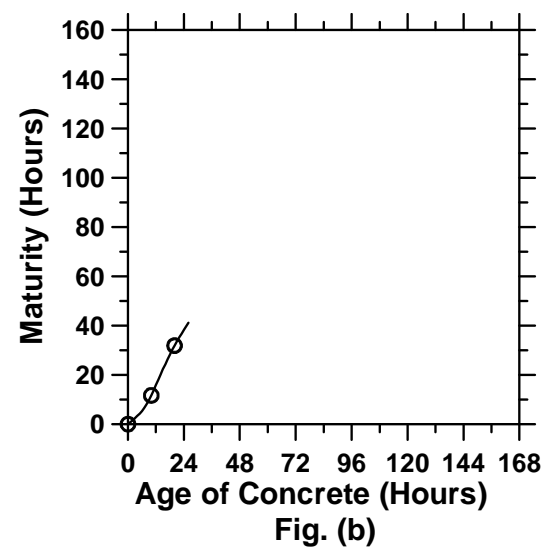
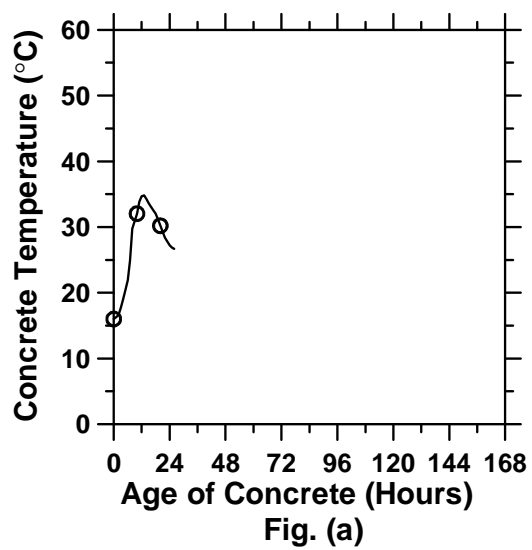


Figure A.75: Pavement cured at “M” ambient temperature with a D/3 saw-cut depth introduced at 6 hours (cont’d).

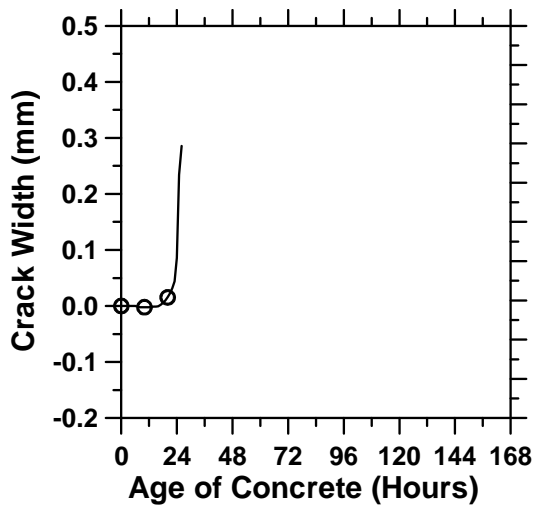


Fig. (e)

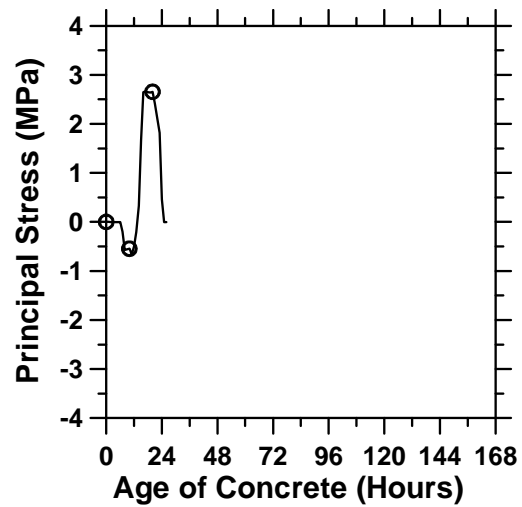


Fig. (f)

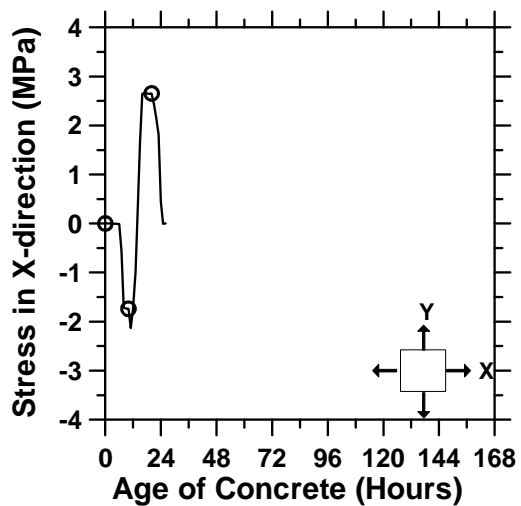


Fig. (g)

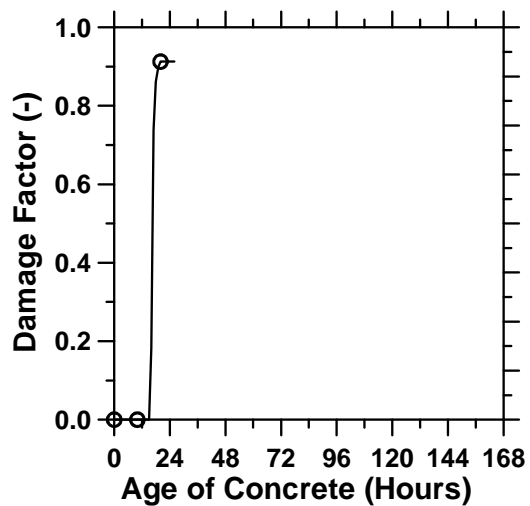


Fig. (h)

Figure A.75: Pavement cured at “M” ambient temperature with a D/3 saw-cut depth introduced at 6 hours.

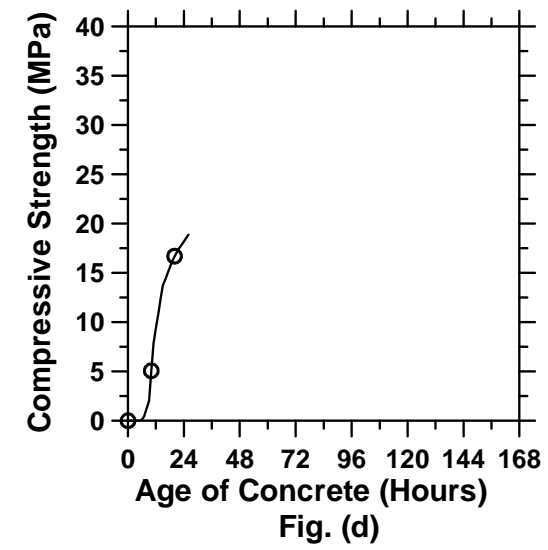
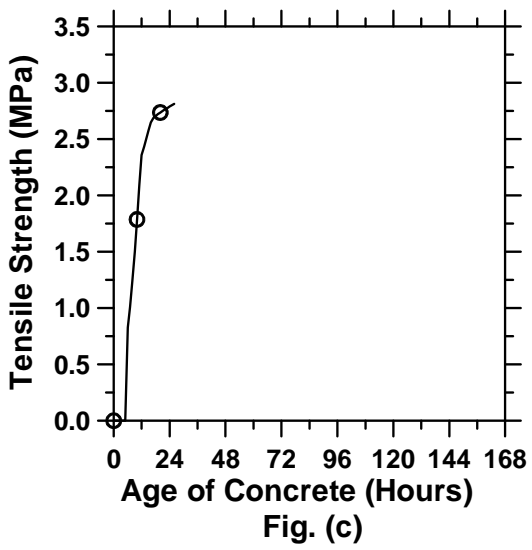
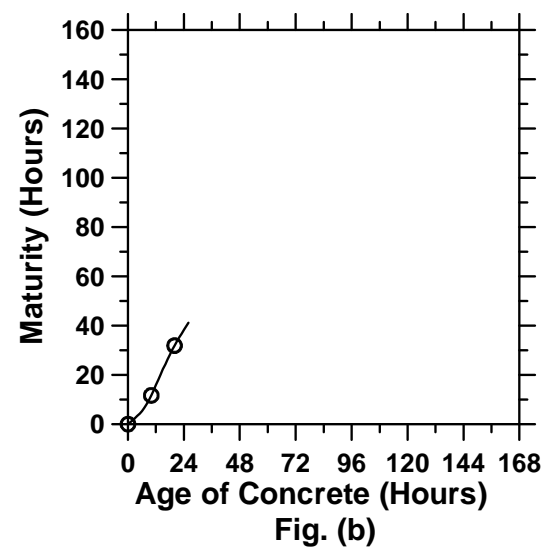
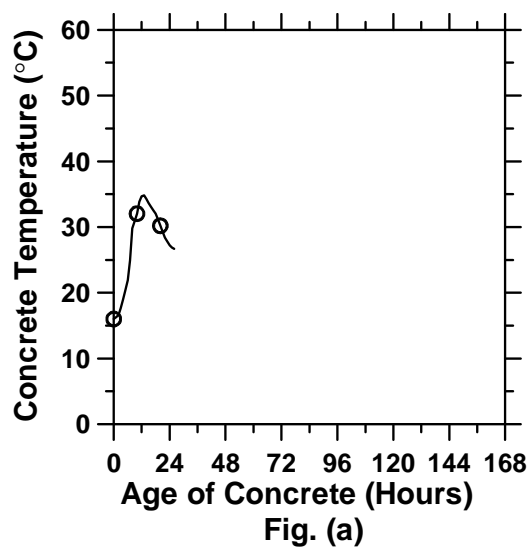


Figure A.76: Pavement cured at “M” ambient temperature with a D/3 saw-cut depth introduced at 9 hours (cont’d).

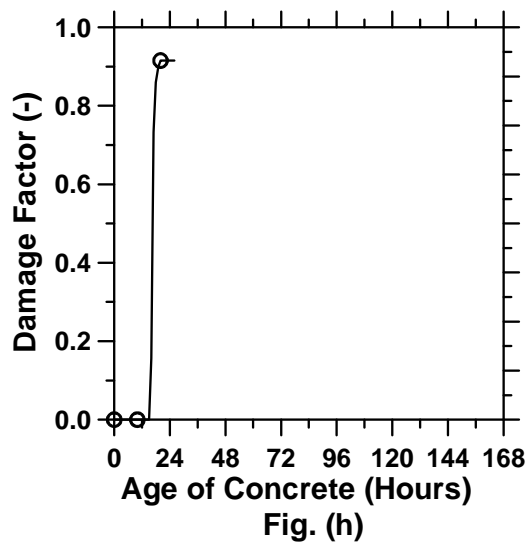
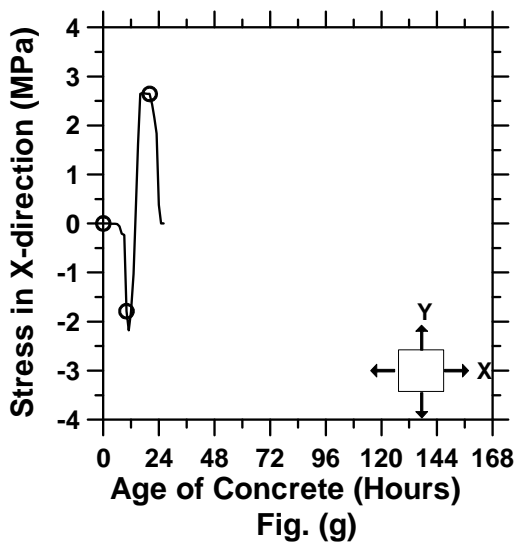
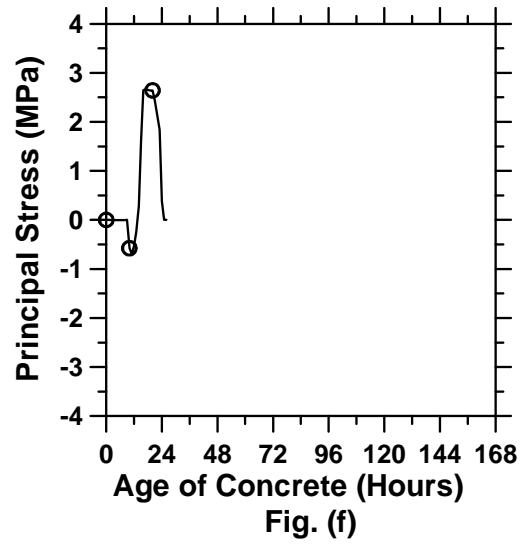
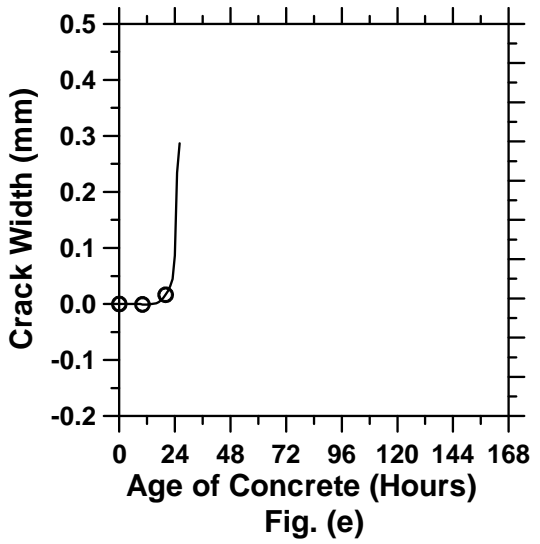


Figure A.76: Pavement cured at “M” ambient temperature with a D/3 saw-cut depth introduced at 9 hours.

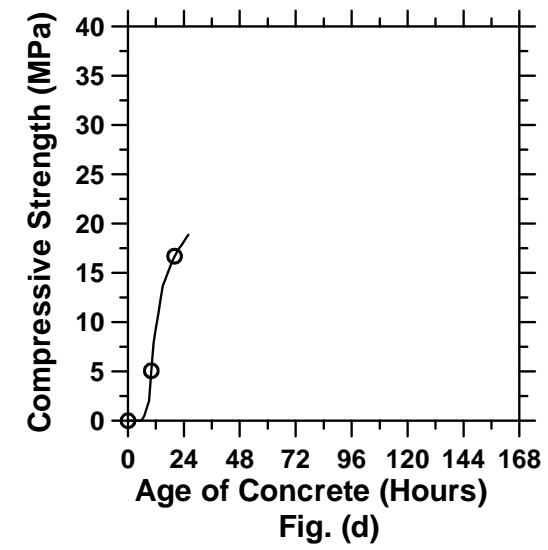
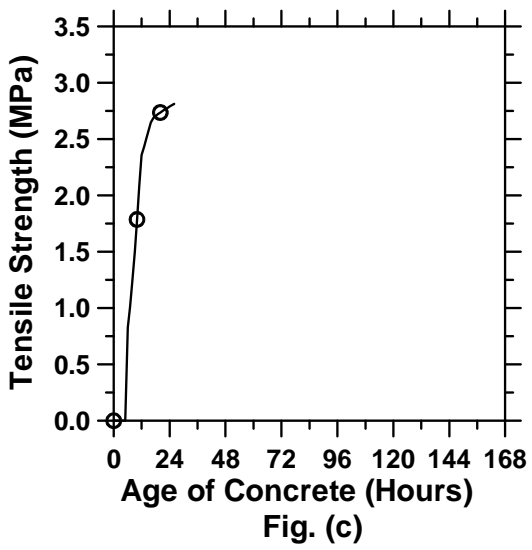
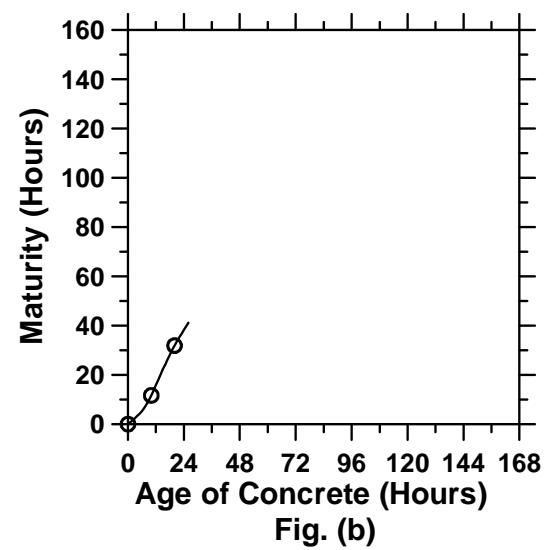
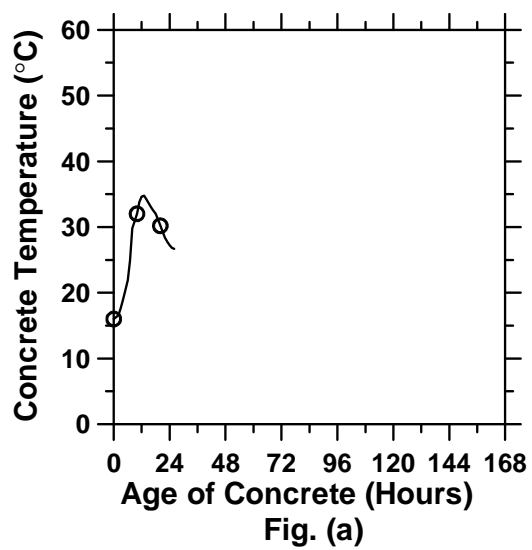


Figure A.77: Pavement cured at “M” ambient temperature with a D/3 saw-cut depth introduced at 12 hours (cont’d).

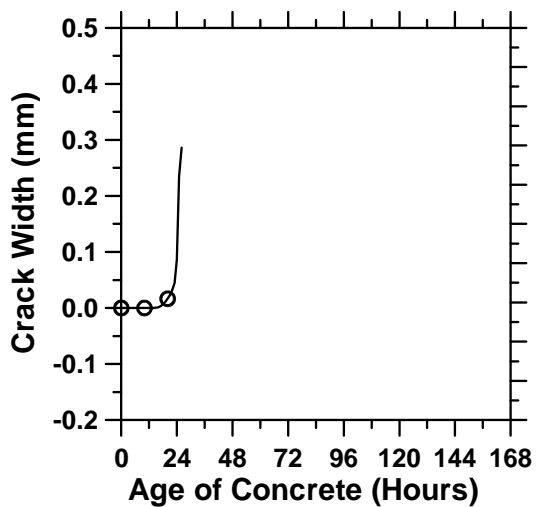


Fig. (e)

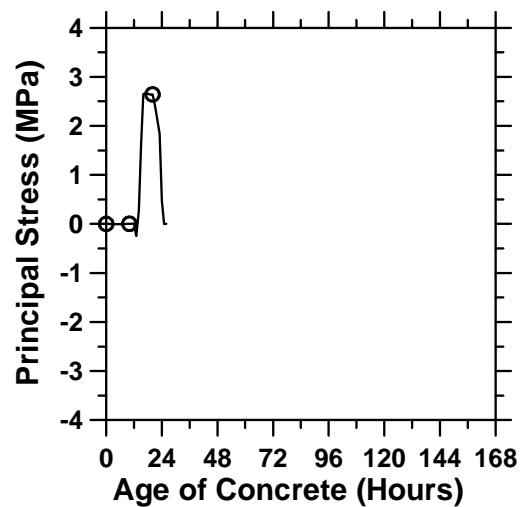


Fig. (f)

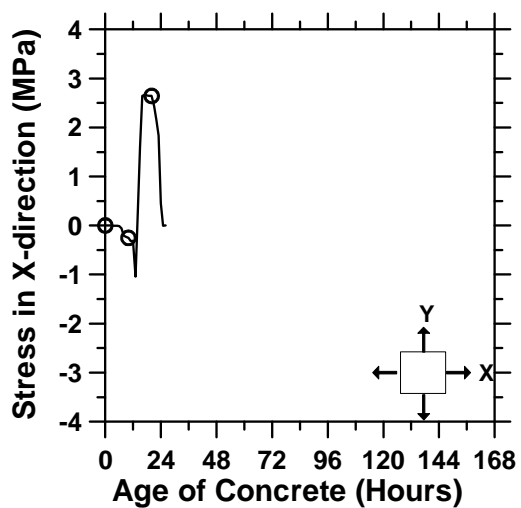


Fig. (g)

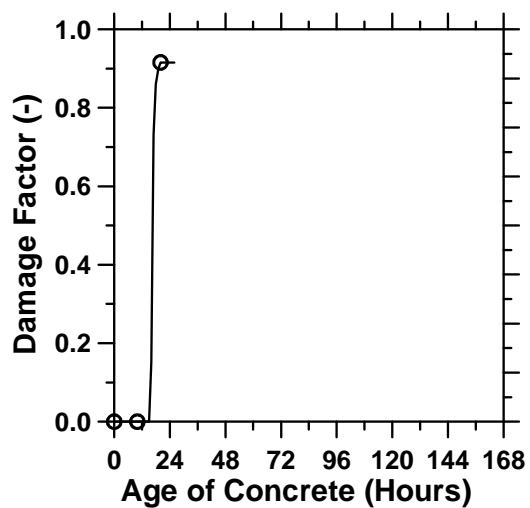


Fig. (h)

Figure A.77: Pavement cured at “M” ambient temperature with a D/3 saw-cut depth introduced at 12 hours.

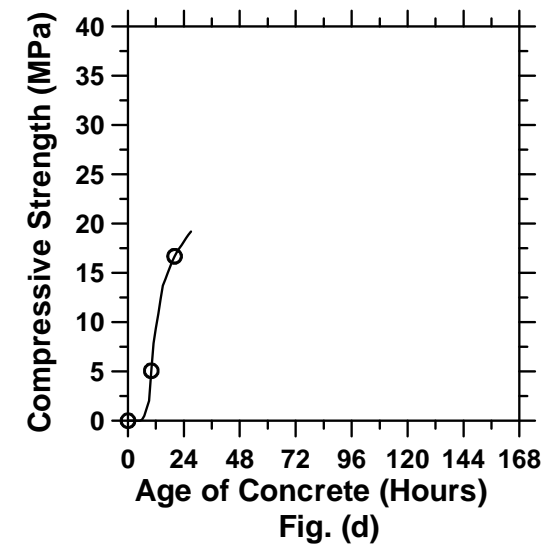
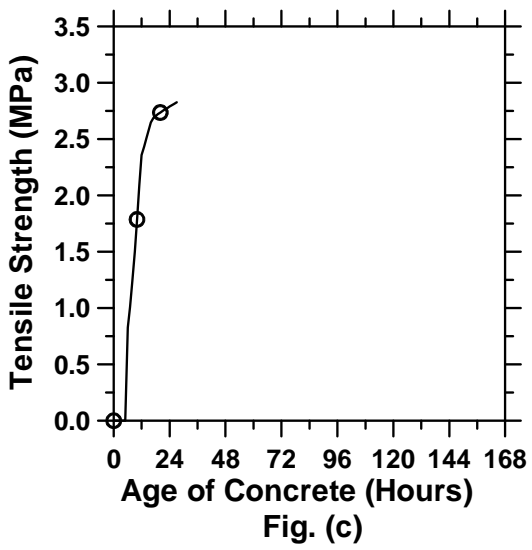
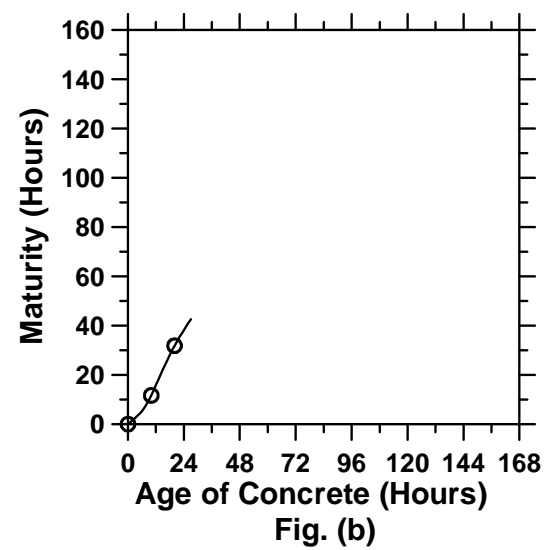
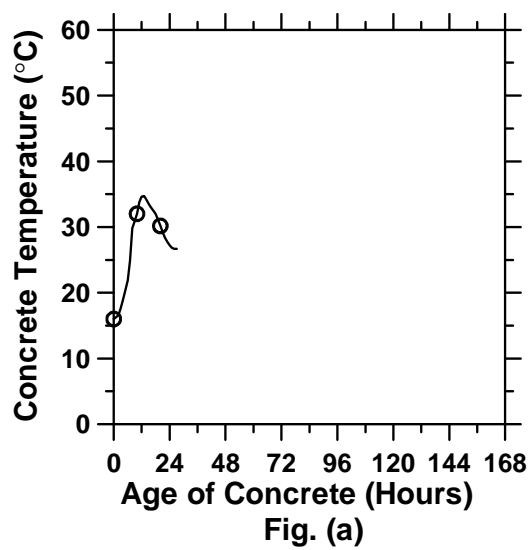


Figure A.78: Pavement cured at “M” ambient temperature with a D/3 saw-cut depth introduced at 15 hours (cont’d).

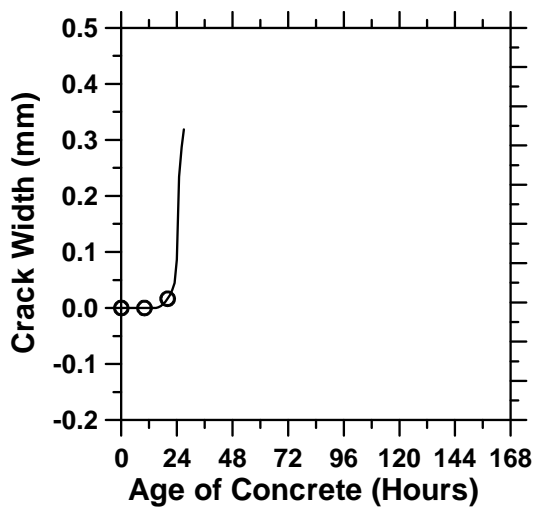


Fig. (e)

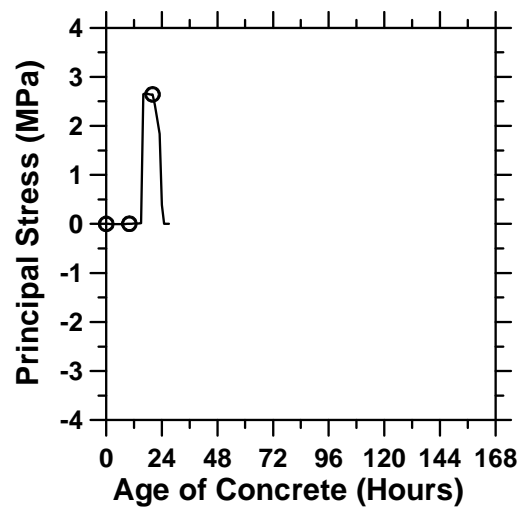


Fig. (f)

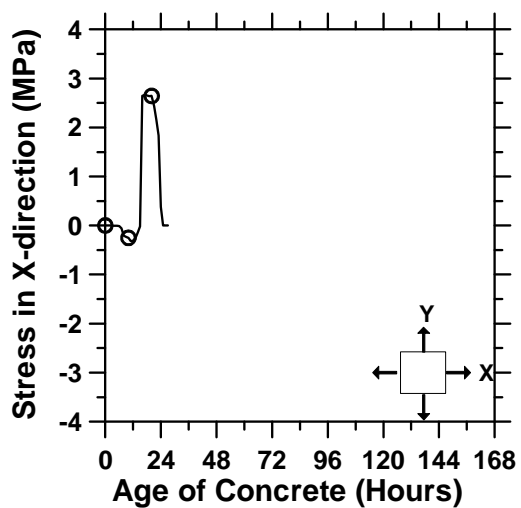


Fig. (g)

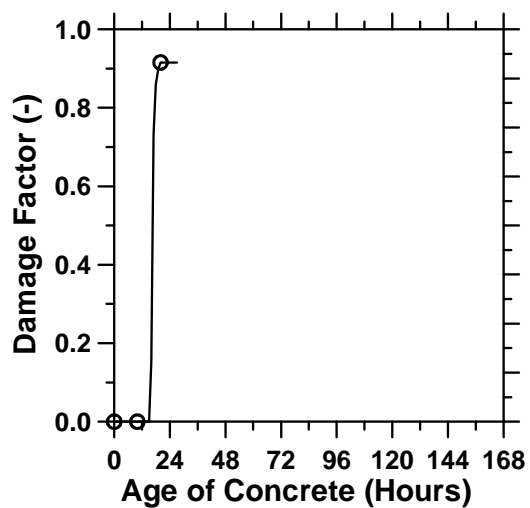


Fig. (h)

Figure A.78: Pavement cured at “M” ambient temperature with a D/3 saw-cut depth introduced at 15 hours.

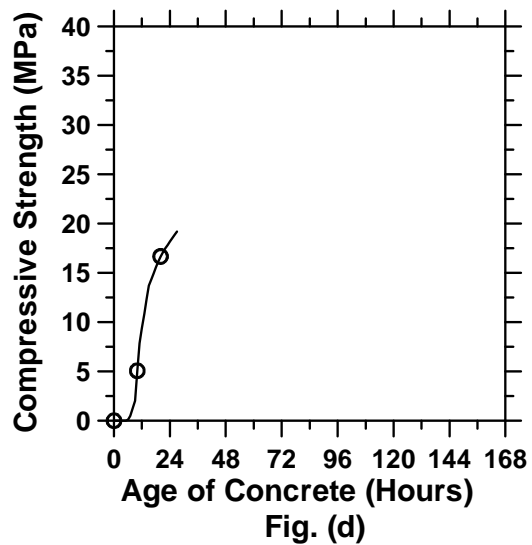
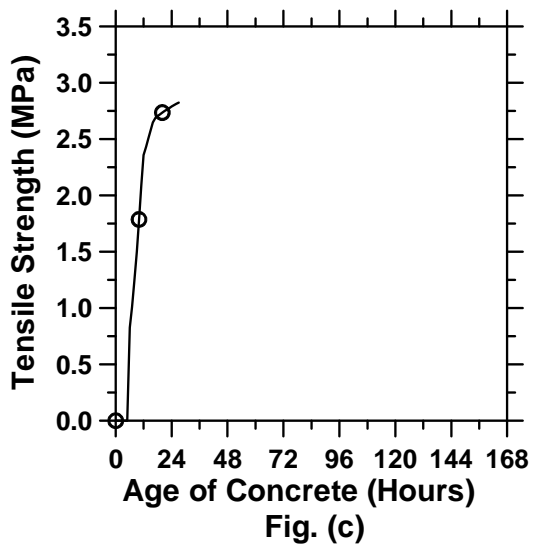
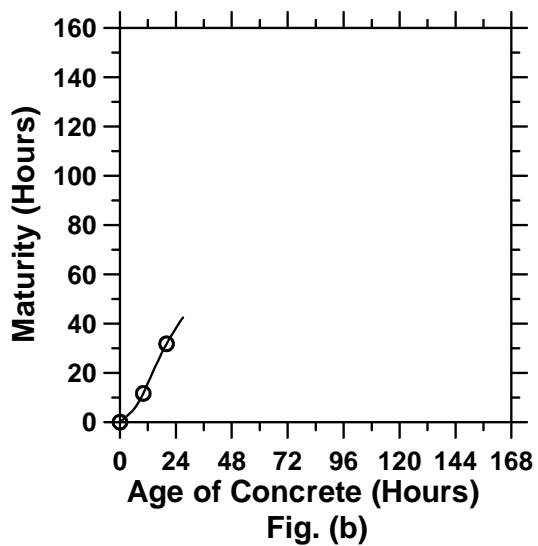
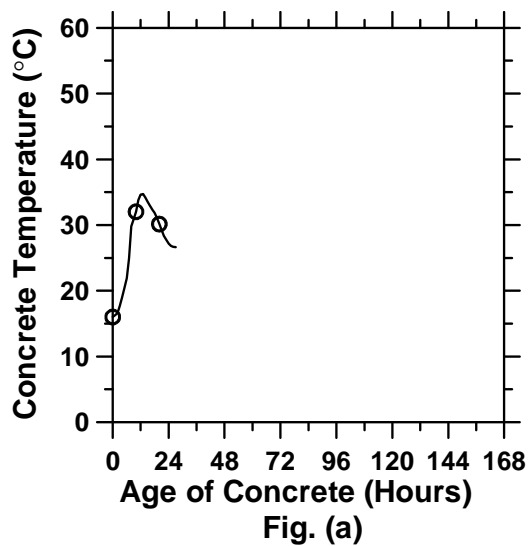


Figure A.79: Pavement cured at “M” ambient temperature with a D/3 saw-cut depth introduced at 18 hours (cont’d).

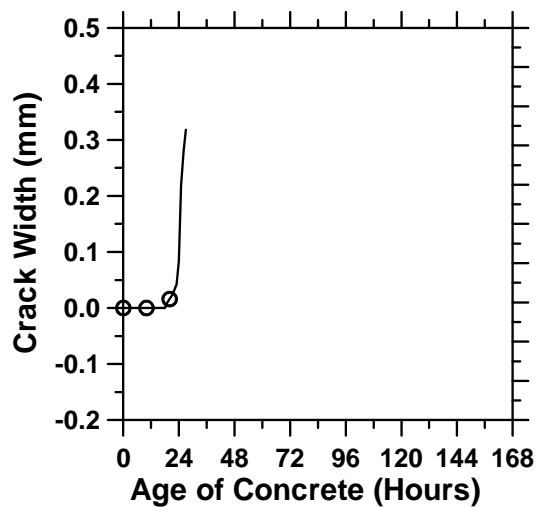


Fig. (e)

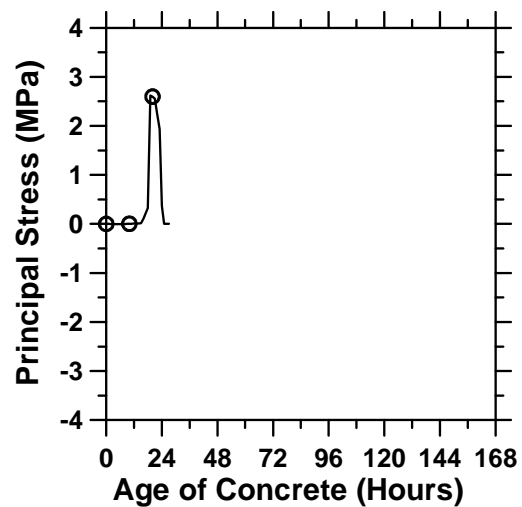


Fig. (f)

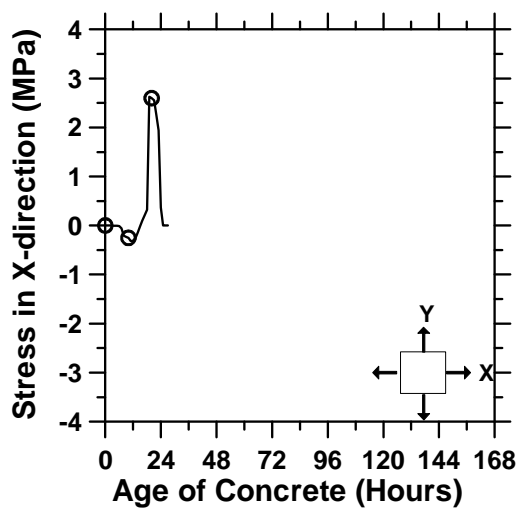


Fig. (g)

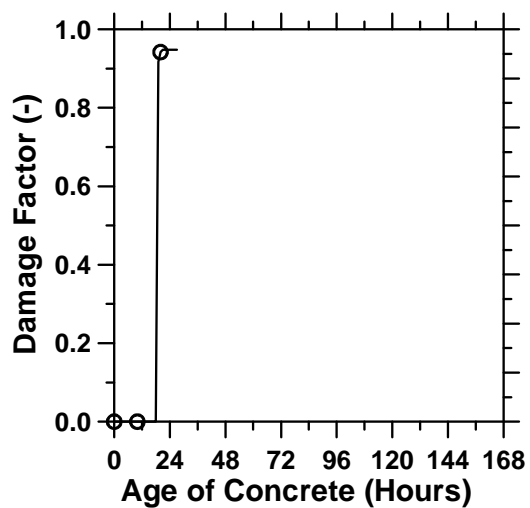


Fig. (h)

Figure A.79: Pavement cured at “M” ambient temperature with a D/3 saw-cut depth introduced at 18 hours.

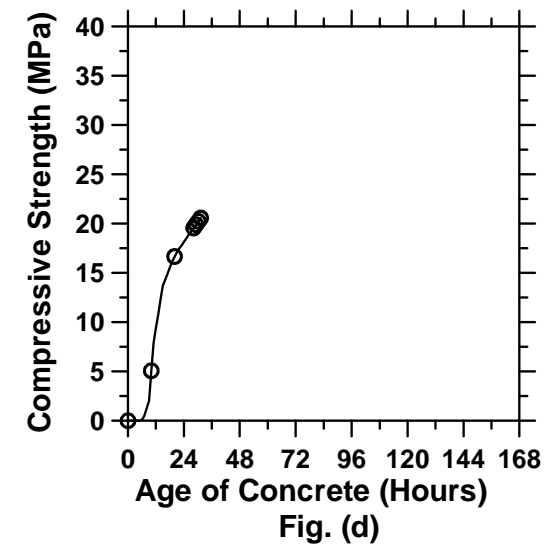
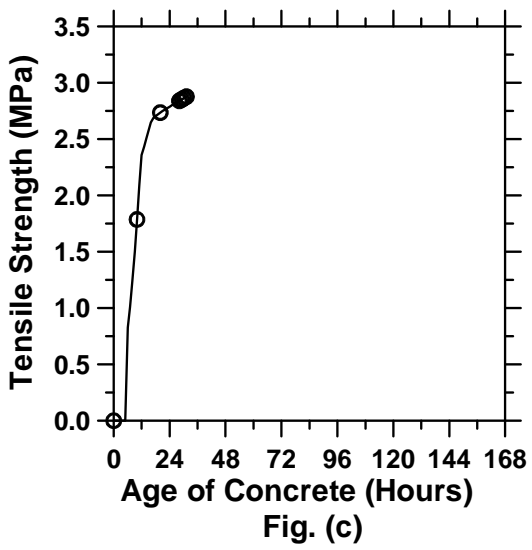
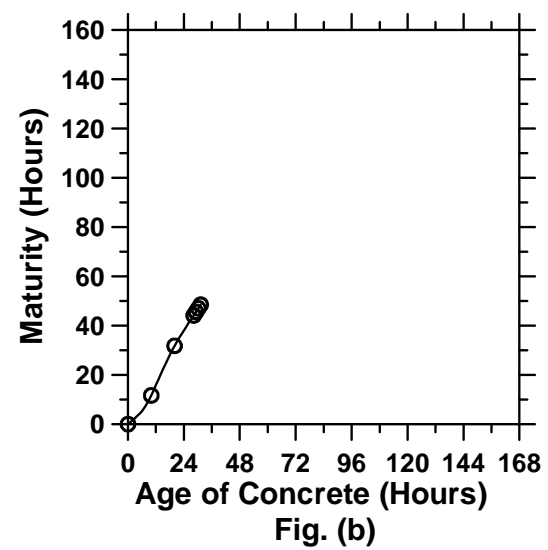
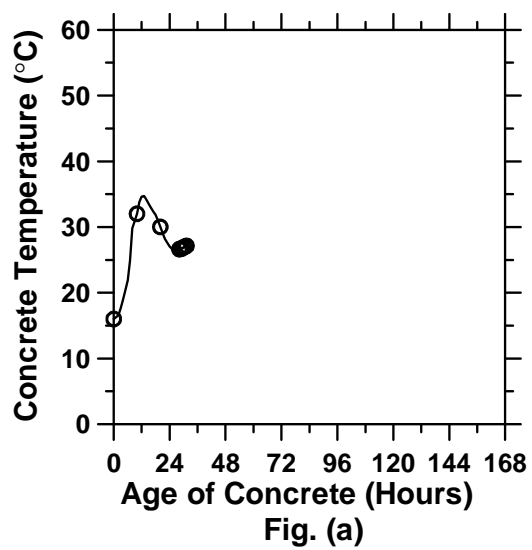


Figure A.80: Pavement cured at “M” ambient temperature with a D/3 saw-cut depth introduced at 30 hours (cont’d).

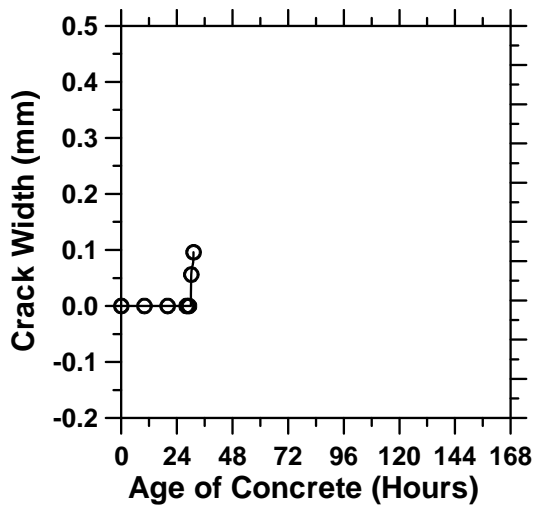


Fig. (e)

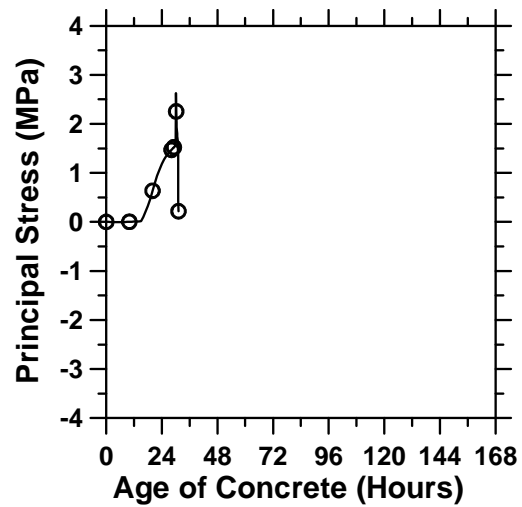


Fig. (f)

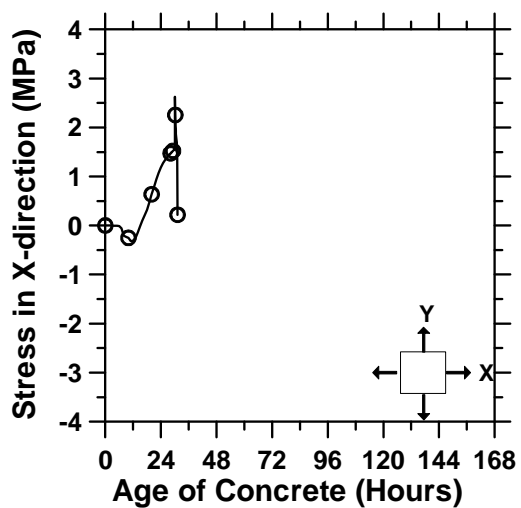


Fig. (g)

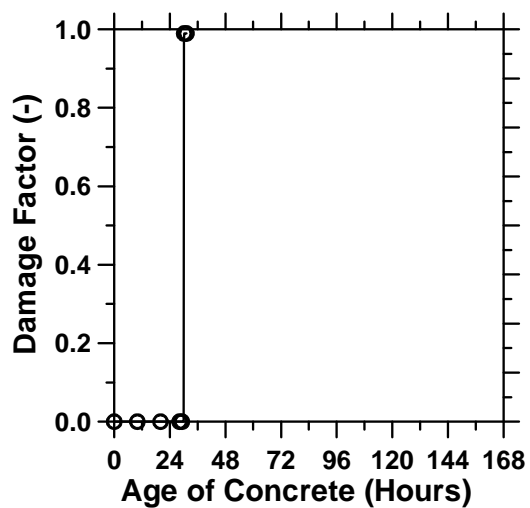


Fig. (h)

Figure A.80: Pavement cured at “M” ambient temperature with a D/3 saw-cut depth introduced at 30 hours.

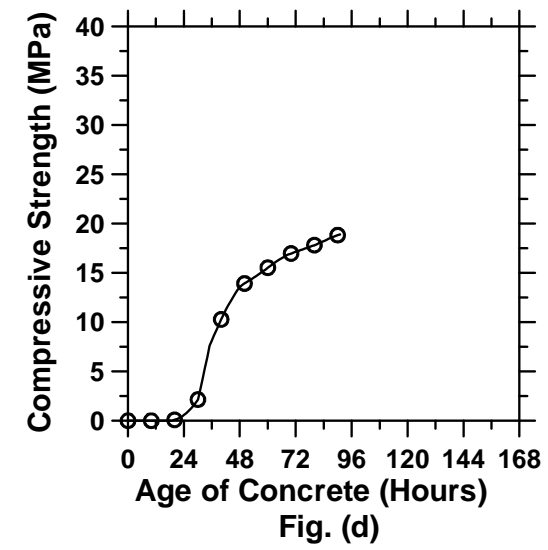
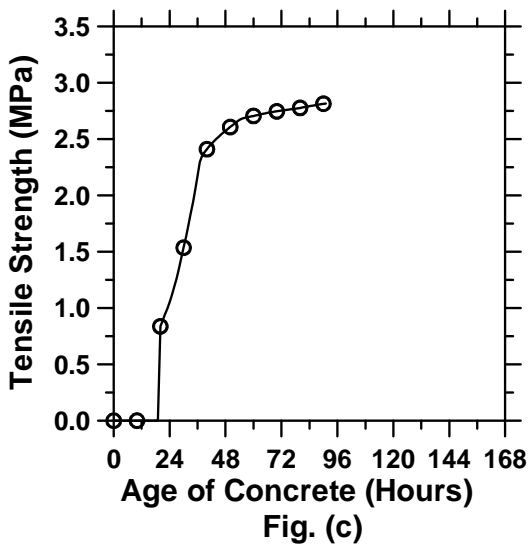
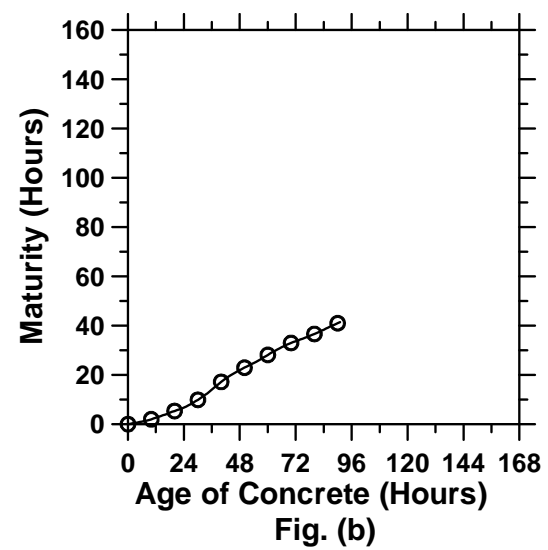
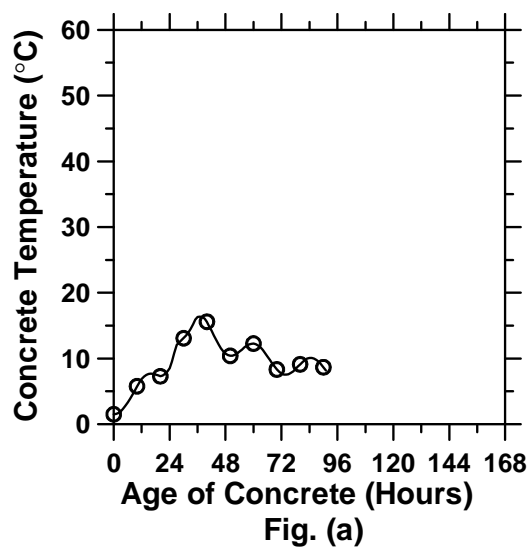


Figure A.81: Pavement cured at “C” ambient temperature with a D/3 saw-cut depth introduced at 0 hour (cont’d).

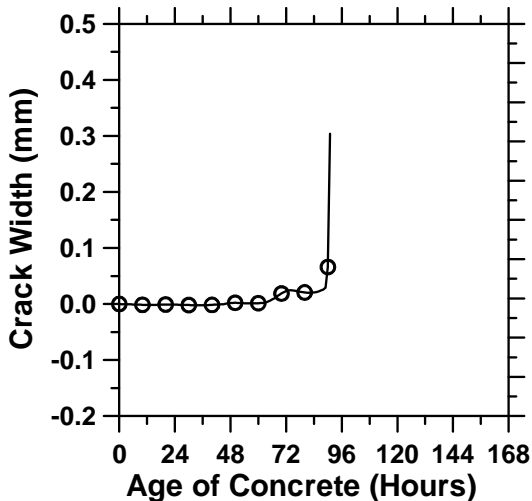


Fig. (e)

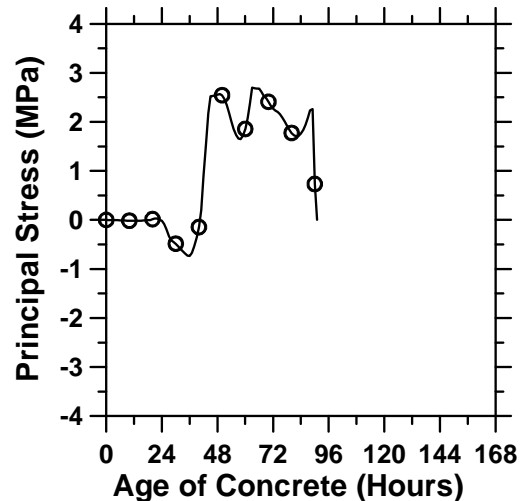


Fig. (f)

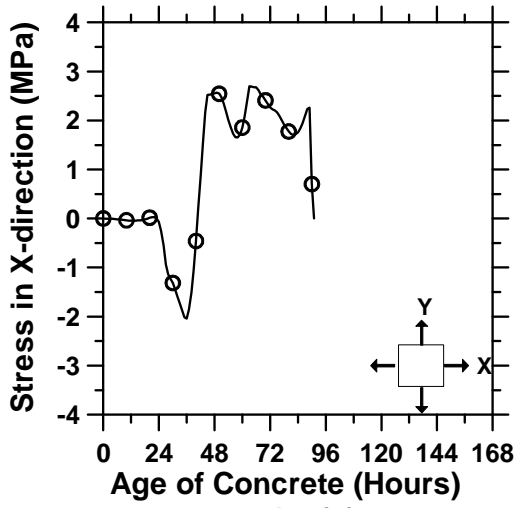


Fig. (g)

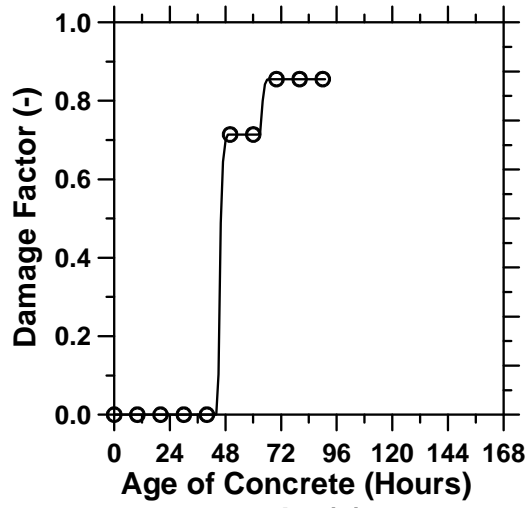


Fig. (h)

Figure A.81: Pavement cured at “C” ambient temperature with a D/3 saw-cut depth introduced at 0 hour.

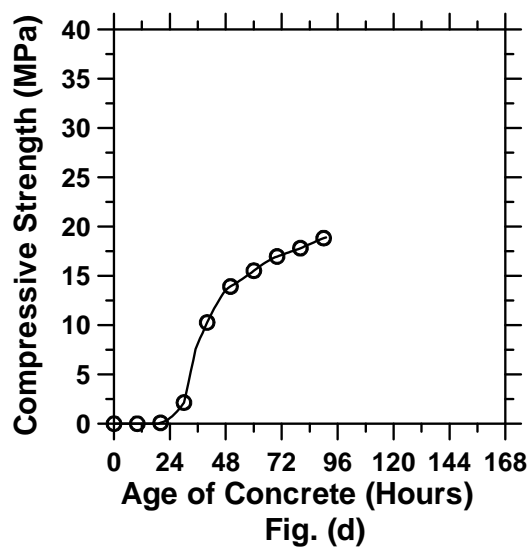
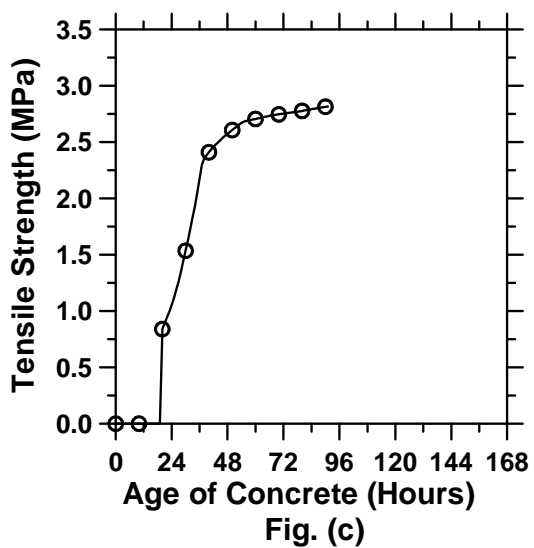
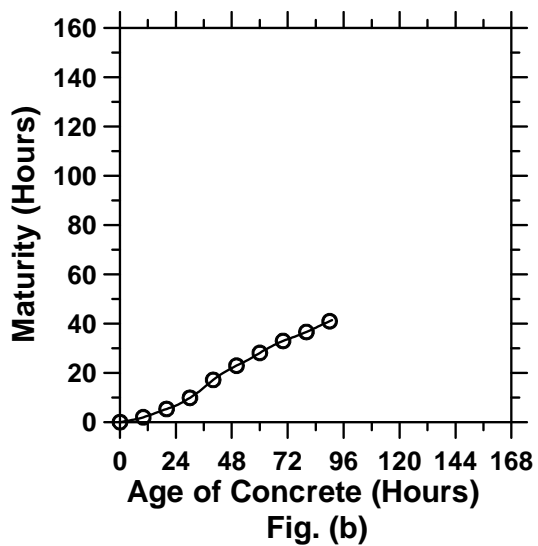
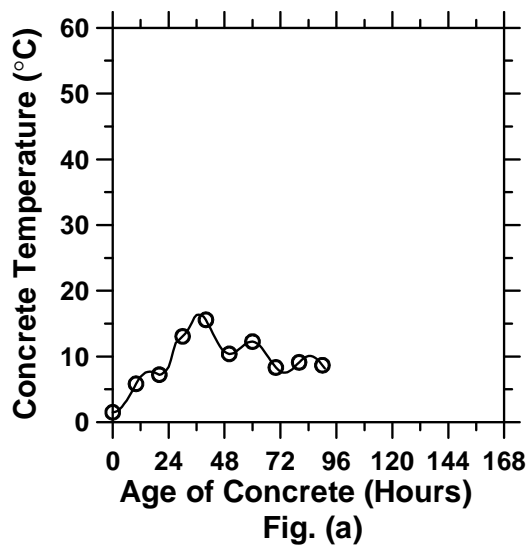


Figure A.82: Pavement cured at “C” ambient temperature with a D/3 saw-cut depth introduced at 24 hours (cont’d).

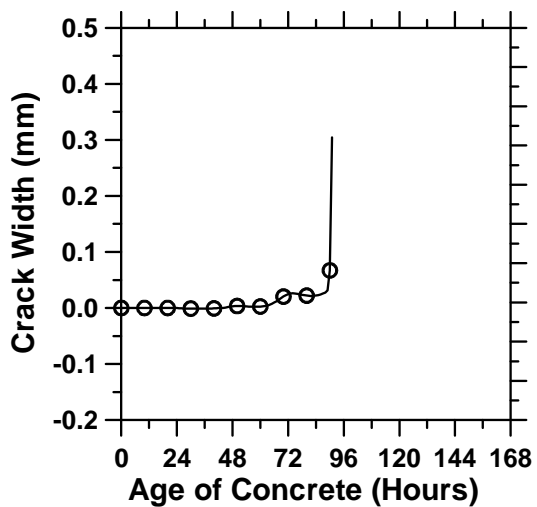


Fig. (e)

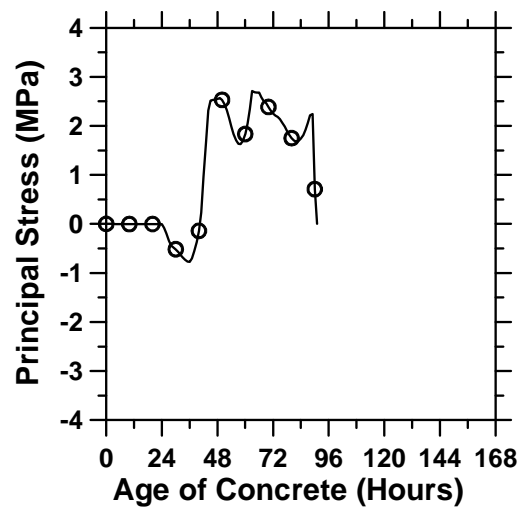


Fig. (f)

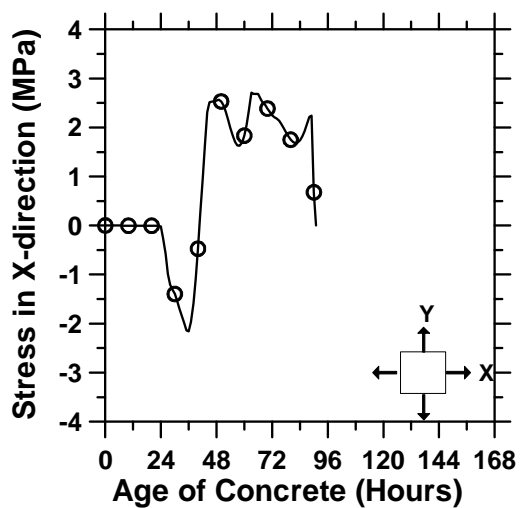


Fig. (g)

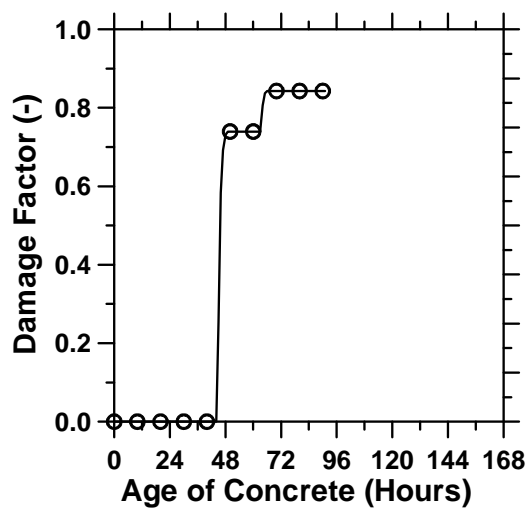


Fig. (h)

Figure A.82: Pavement cured at "C" ambient temperature with a D/3 saw-cut depth introduced at 24 hours.

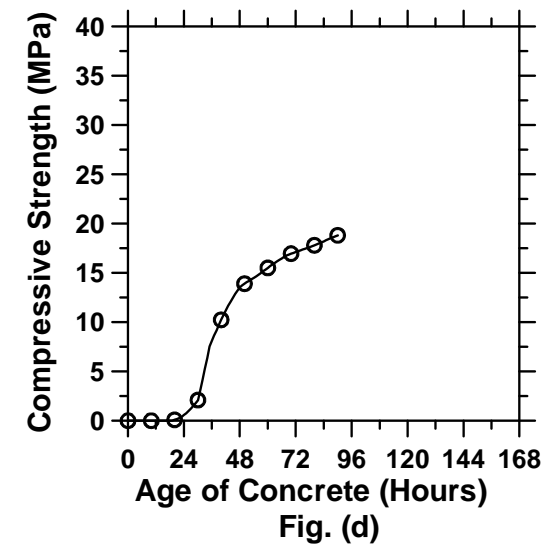
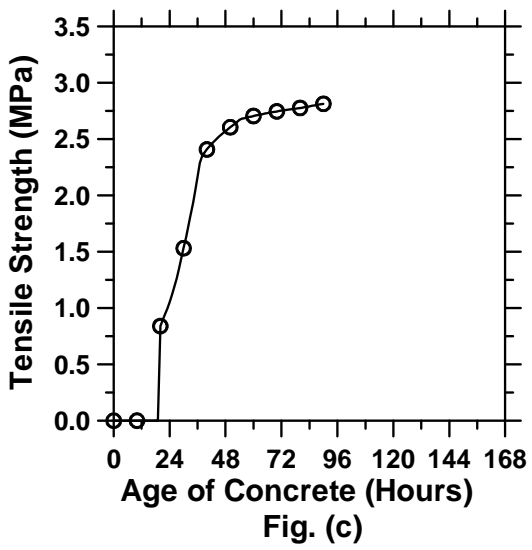
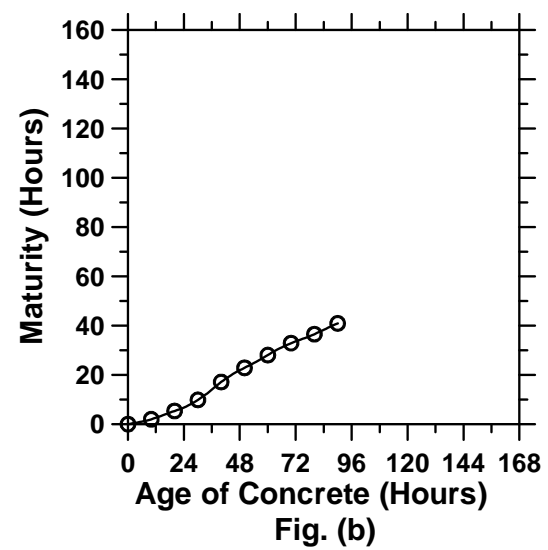
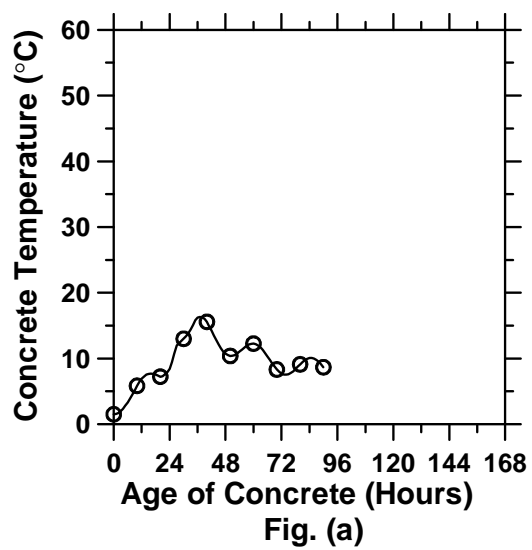


Figure A.83: Pavement cured at “C” ambient temperature with a D/3 saw-cut depth introduced at 36 hours (cont’d).

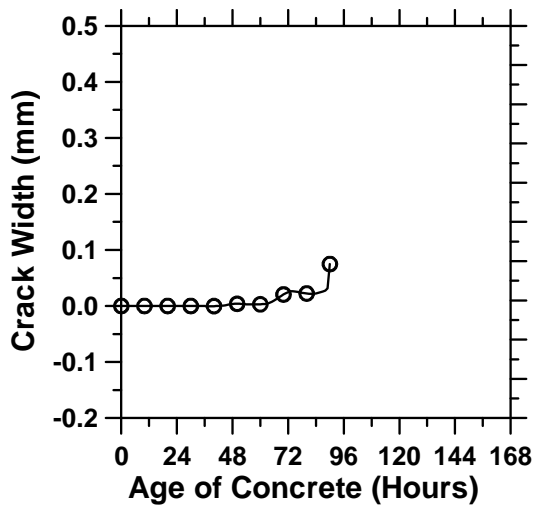


Fig. (e)

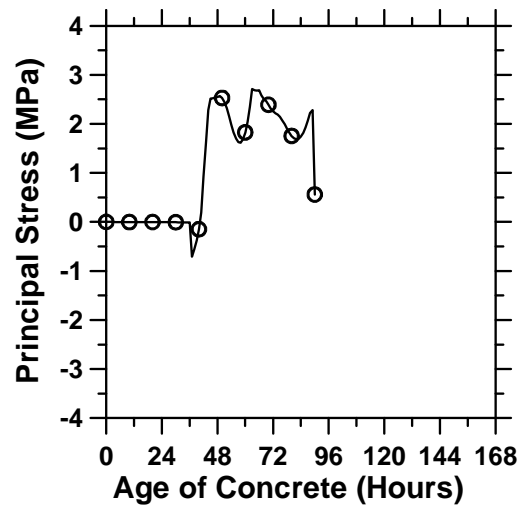


Fig. (f)

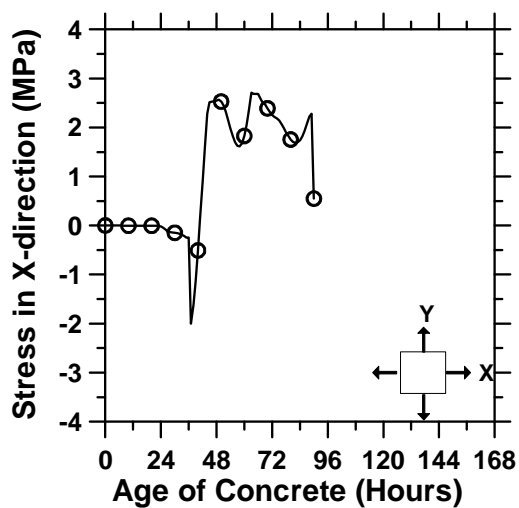


Fig. (g)

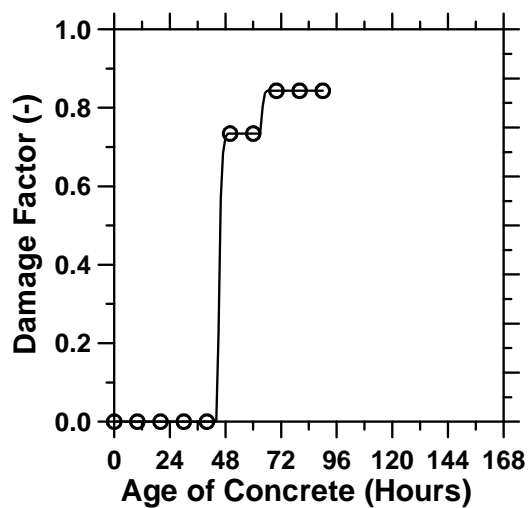


Fig. (h)

Figure A.83: Pavement cured at “C” ambient temperature with a D/3 saw-cut depth introduced at 36 hours.

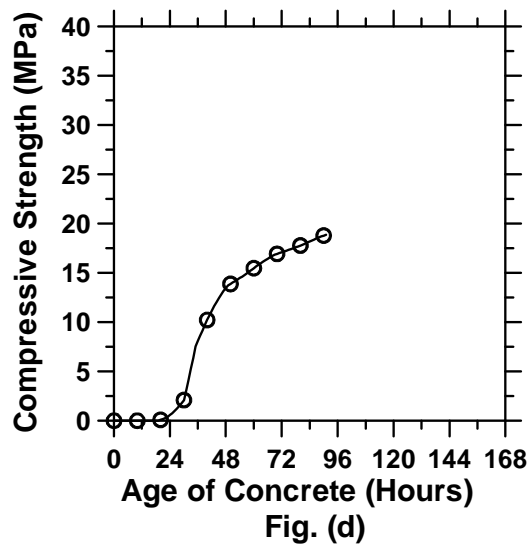
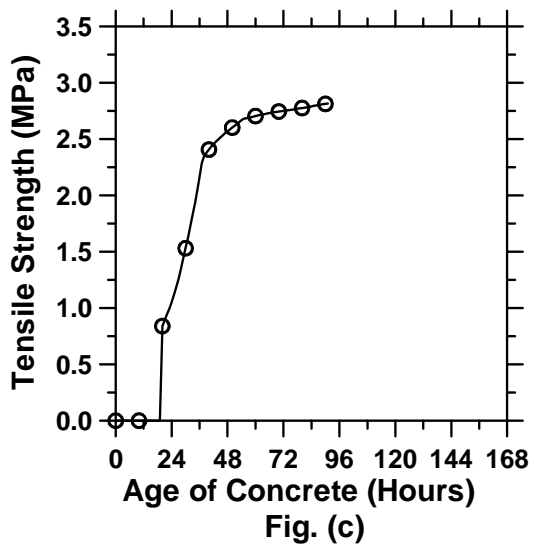
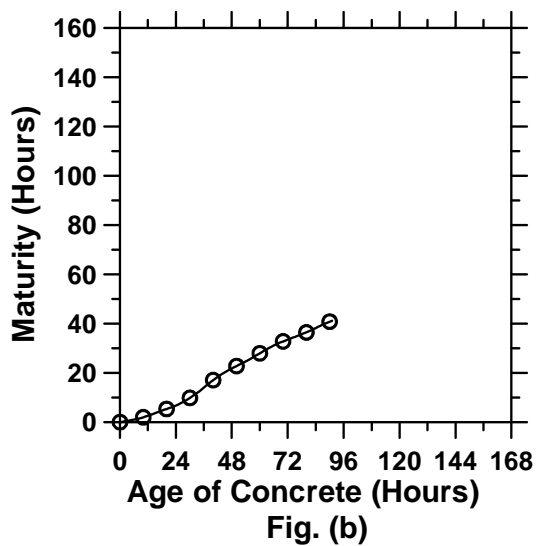
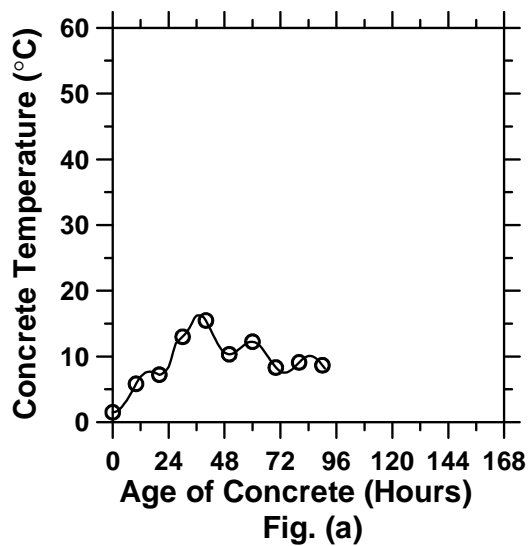


Figure A.84: Pavement cured at “C” ambient temperature with a D/3 saw-cut depth introduced at 48 hours (cont’d).

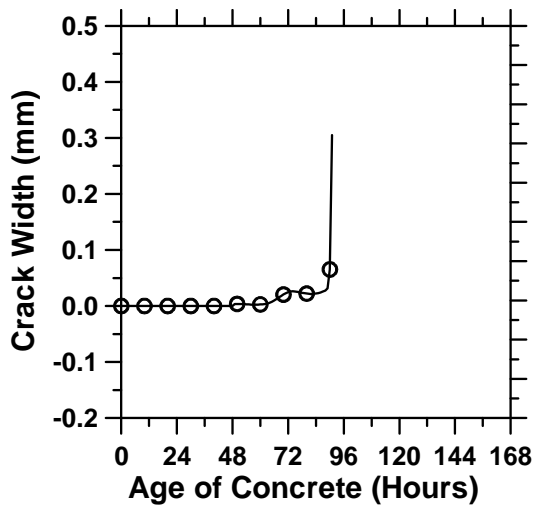


Fig. (e)

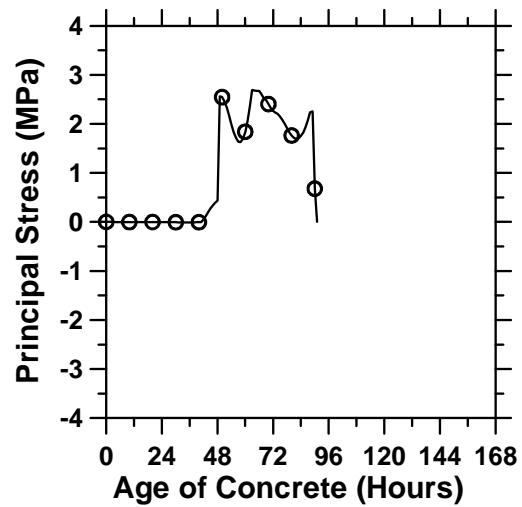


Fig. (f)

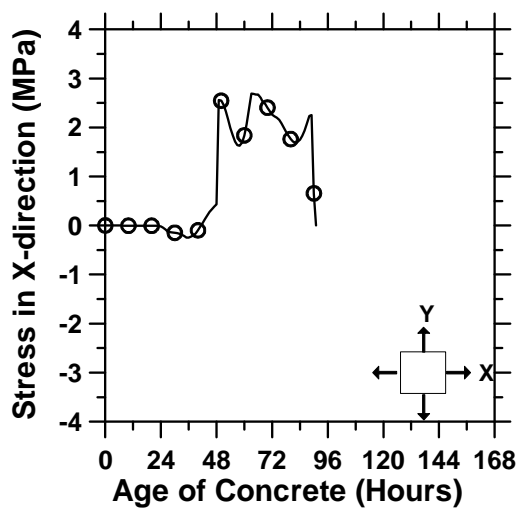


Fig. (g)

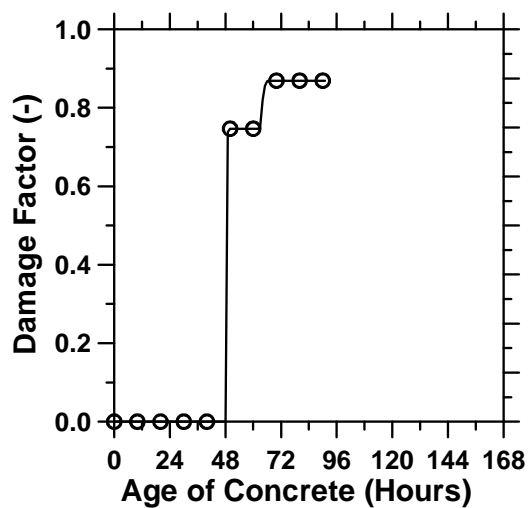


Fig. (h)

Figure A.84: Pavement cured at "C" ambient temperature with a D/3 saw-cut depth introduced at 48 hours.

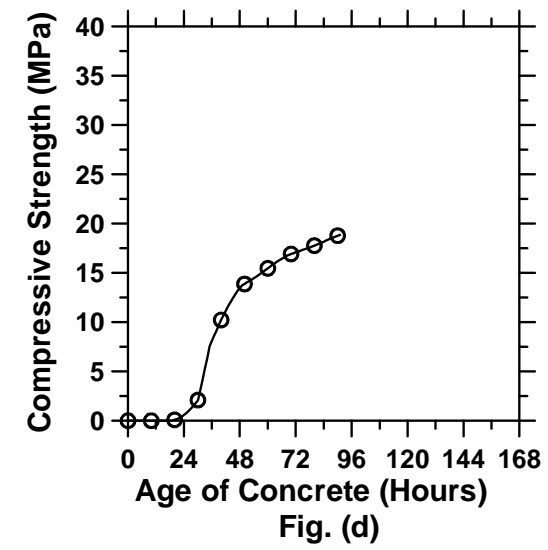
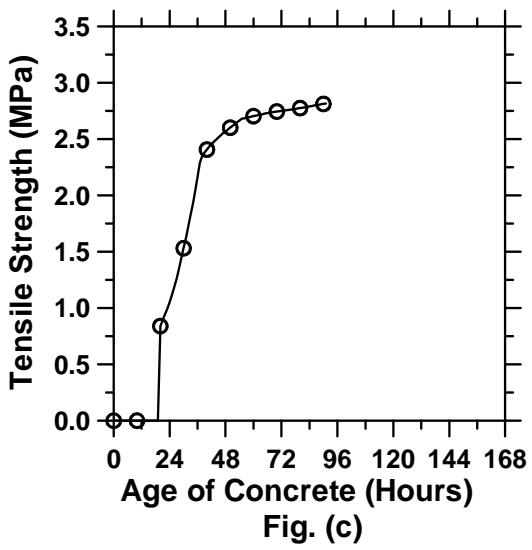
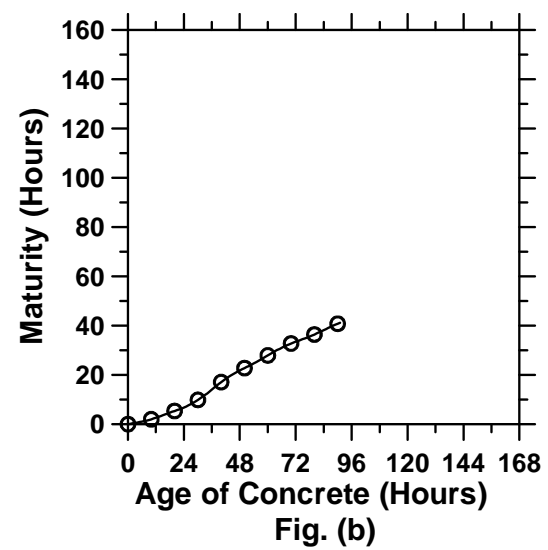
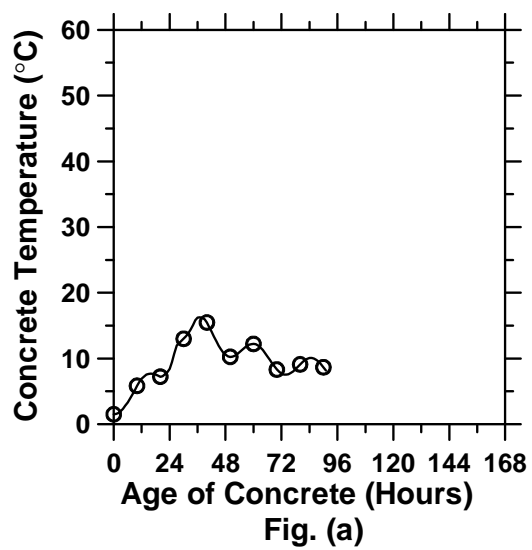


Figure A.85: Pavement cured at “C” ambient temperature with a D/3 saw-cut depth introduced at 60 hours (cont’d).

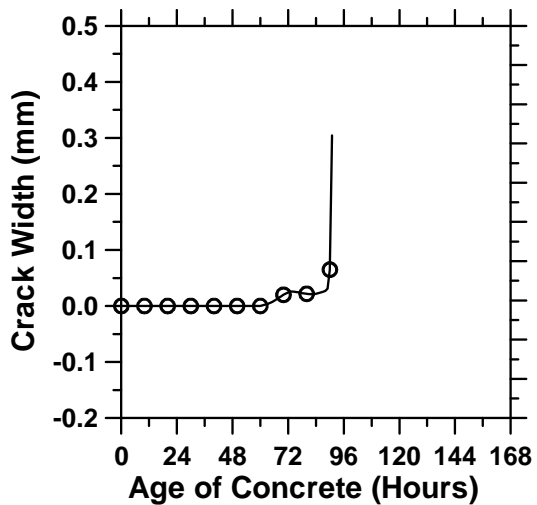


Fig. (e)

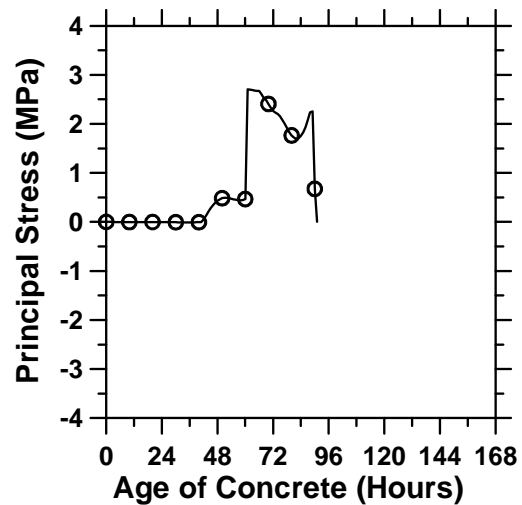


Fig. (f)

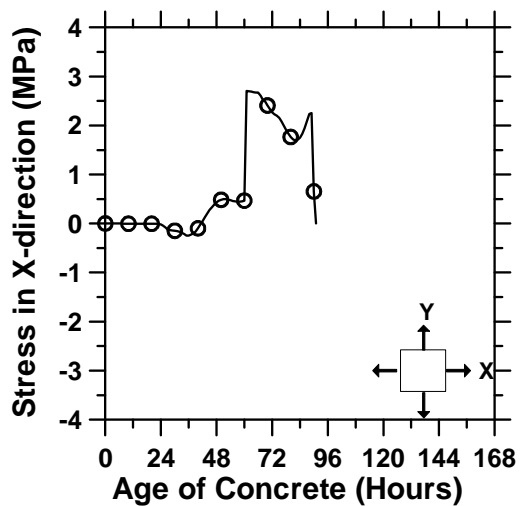


Fig. (g)

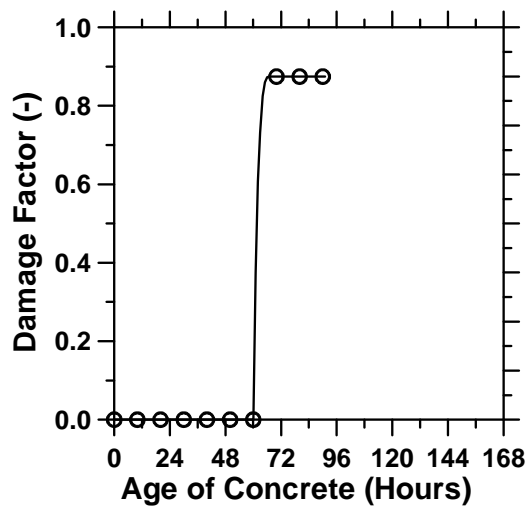


Fig. (h)

Figure A.85: Pavement cured at "C" ambient temperature with a D/3 saw-cut depth introduced at 60 hours.

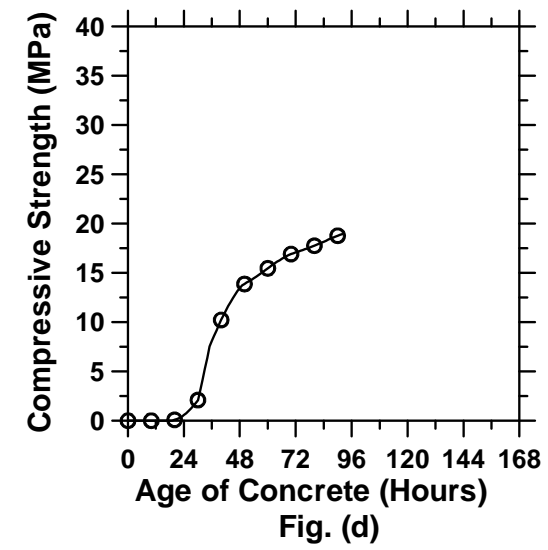
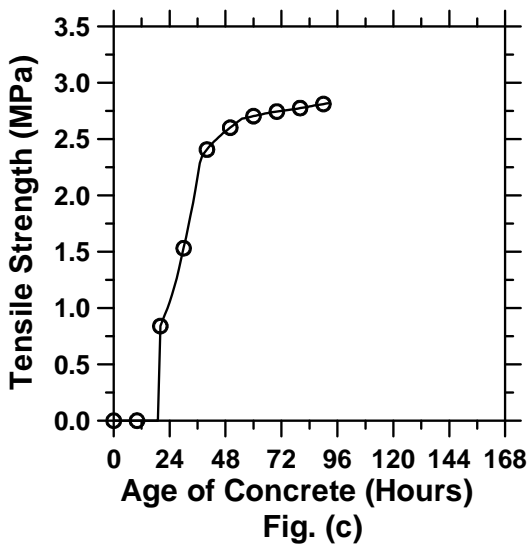
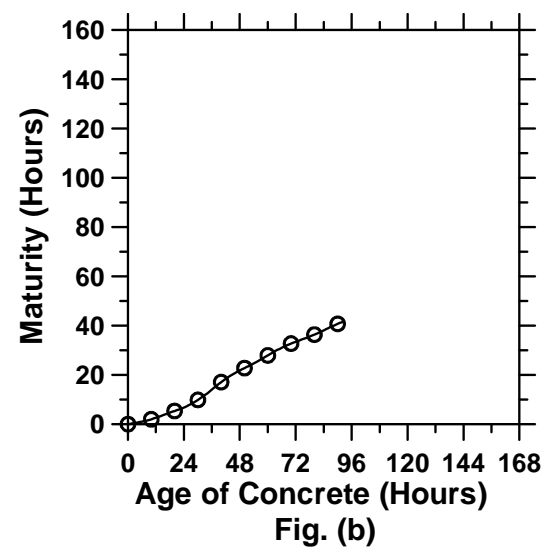
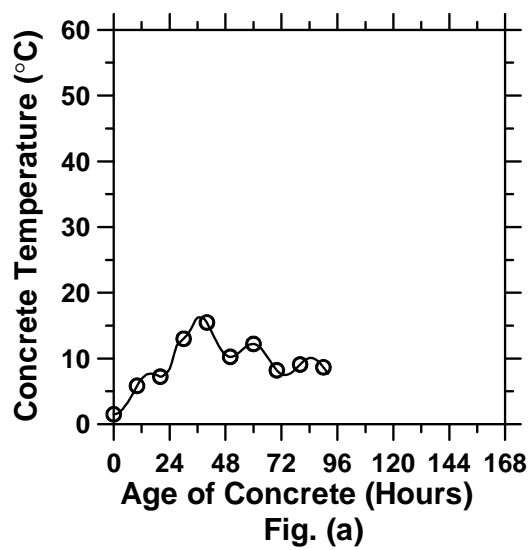


Figure A.86: Pavement cured at “C” ambient temperature with a D/3 saw-cut depth introduced at 72 hours (cont’d).

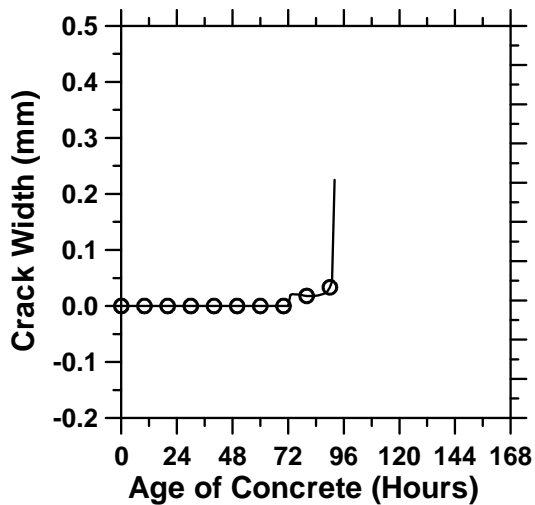


Fig. (e)

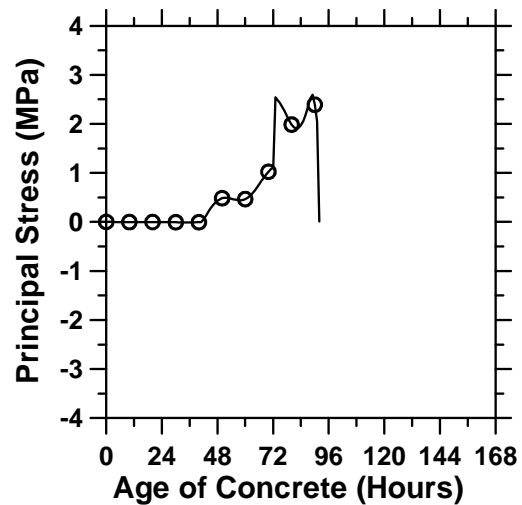


Fig. (f)

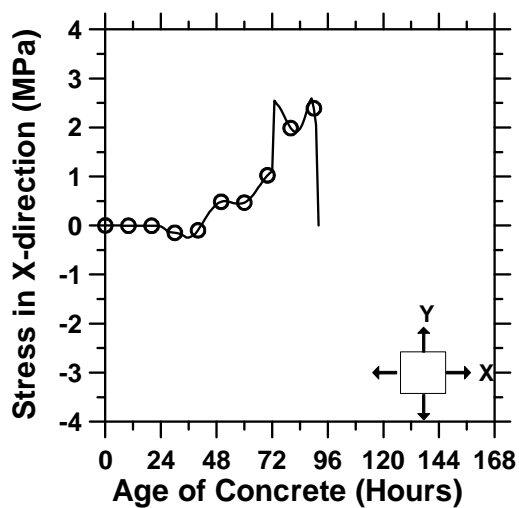


Fig. (g)

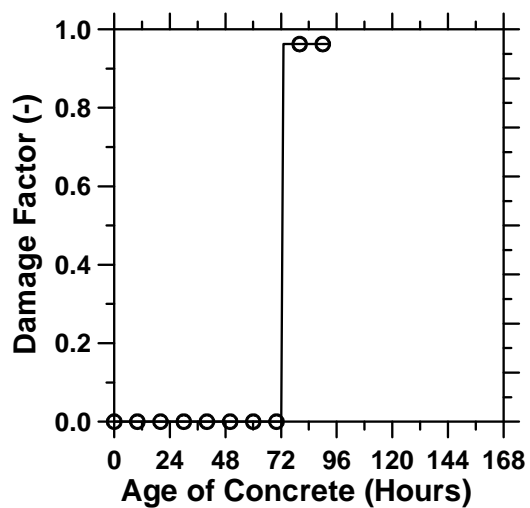


Fig. (h)

Figure A.86: Pavement cured at "C" ambient temperature with a D/3 saw-cut depth introduced at 72 hours.

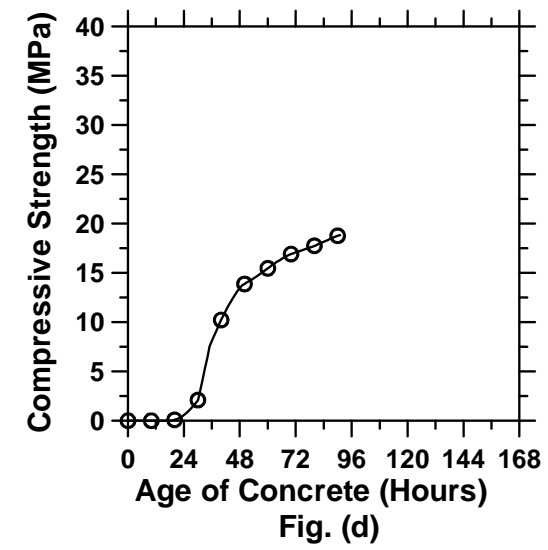
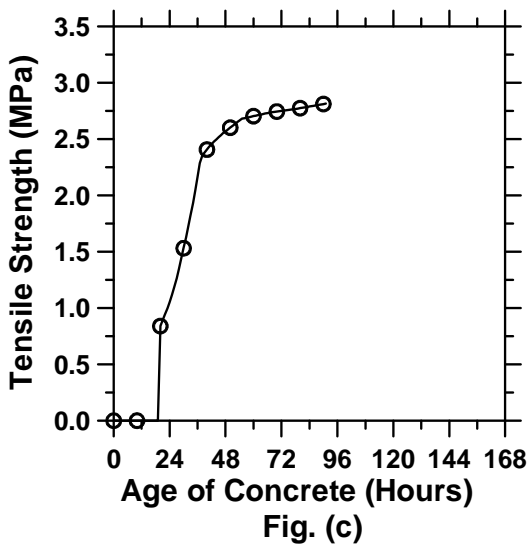
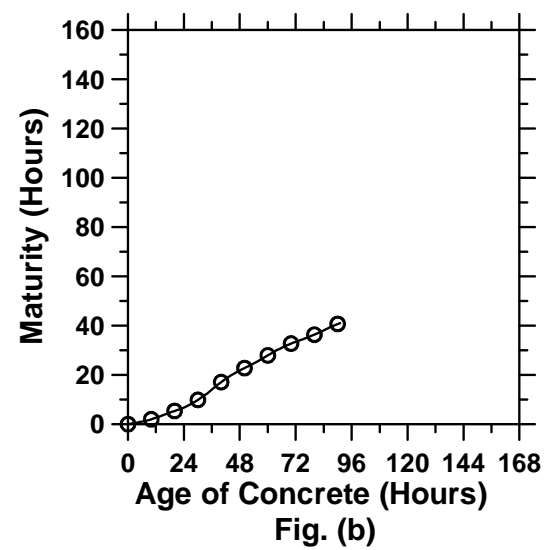
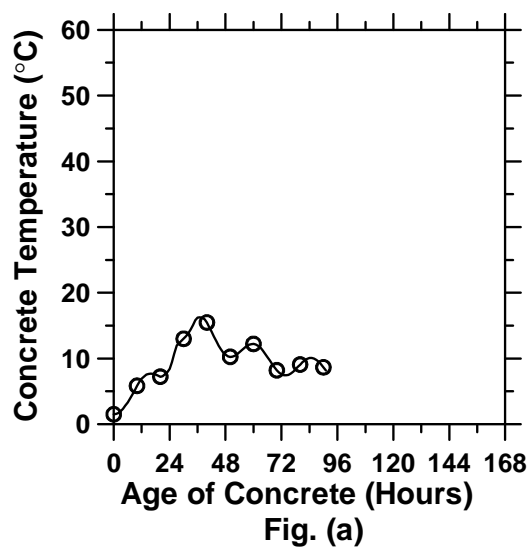


Figure A.87: Pavement cured at “C” ambient temperature with a D/3 saw-cut depth introduced at 84 hours (cont’d).

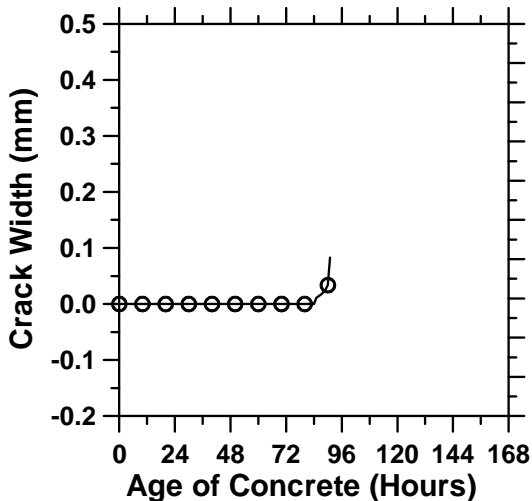


Fig. (e)

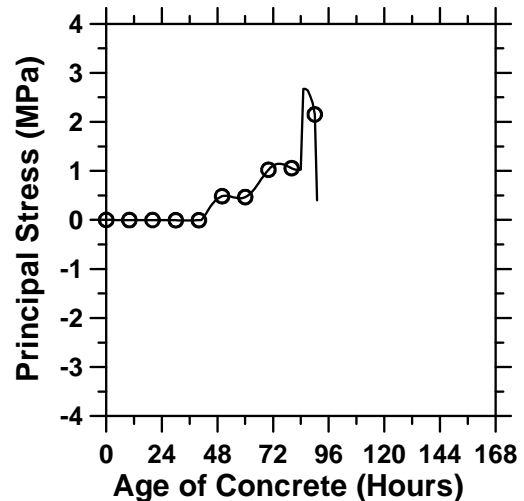


Fig. (f)

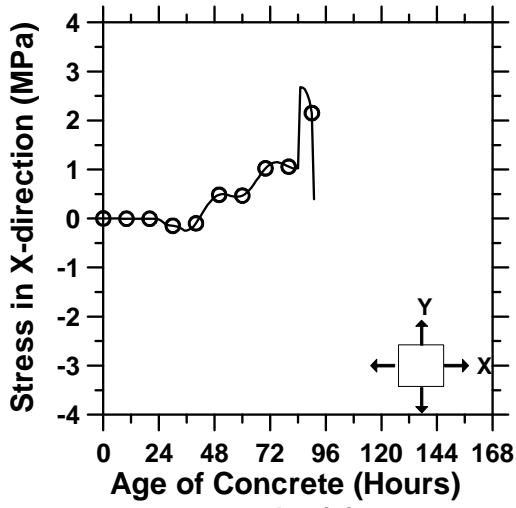


Fig. (g)

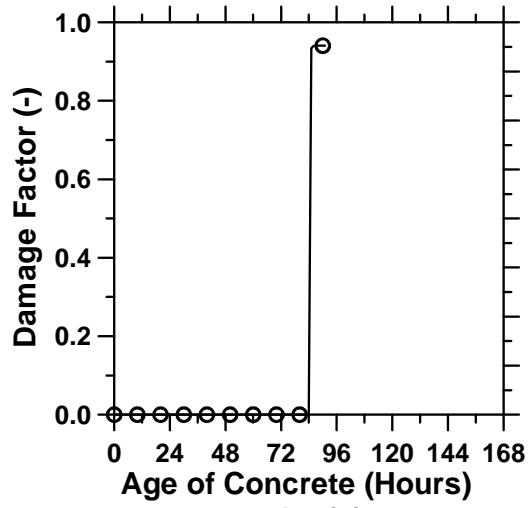


Fig. (h)

Figure A.87: Pavement cured at “C” ambient temperature with a D/3 saw-cut depth introduced at 84 hours.

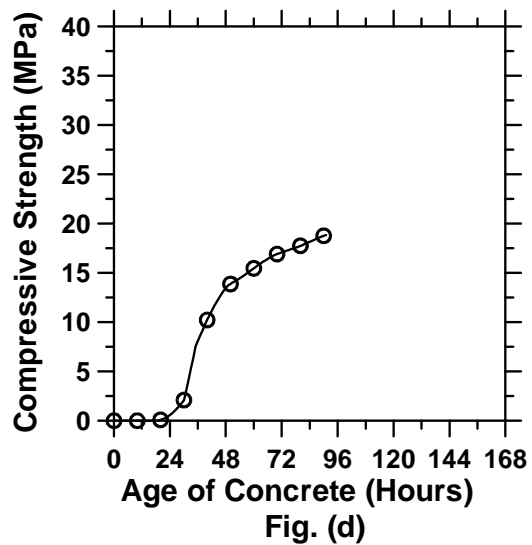
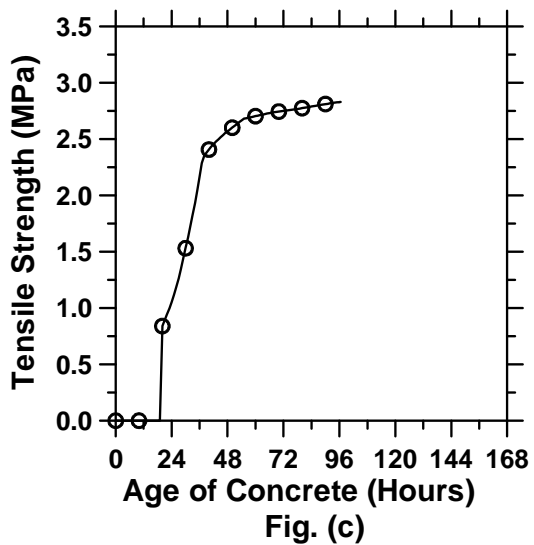
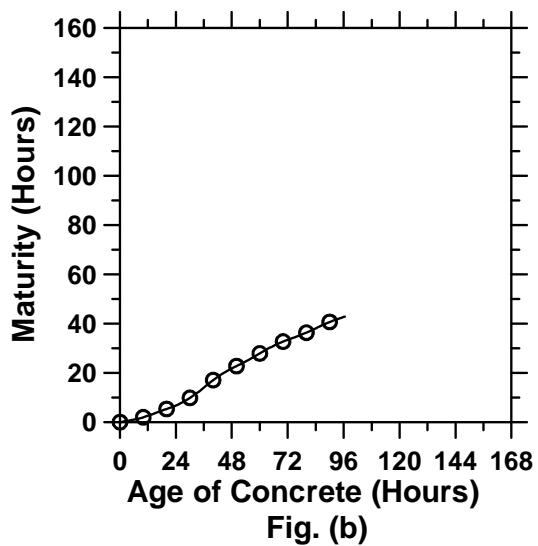
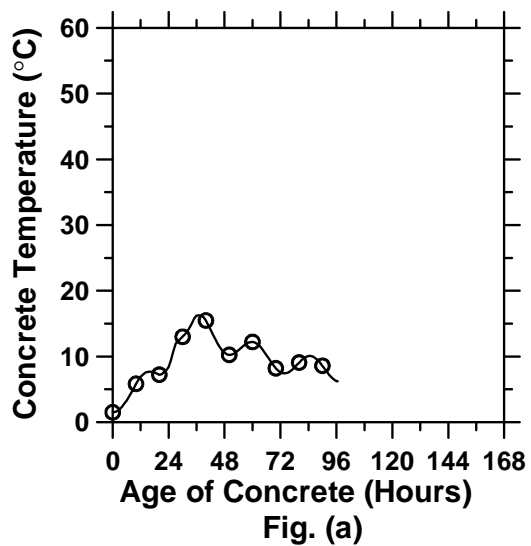


Figure A.88: Pavement cured at “C” ambient temperature with a D/3 saw-cut depth introduced at 96 hours (cont’d).

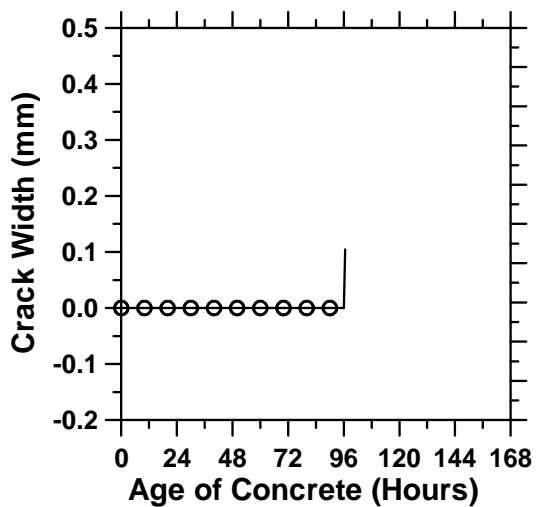


Fig. (e)

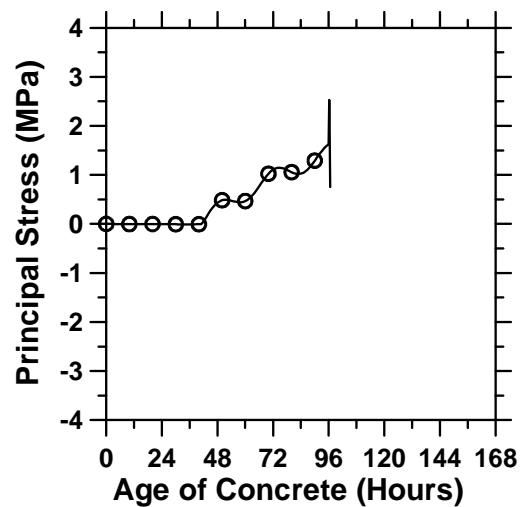


Fig. (f)

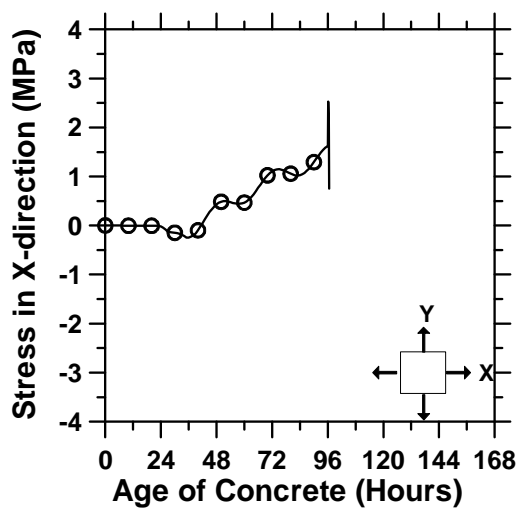


Fig. (g)

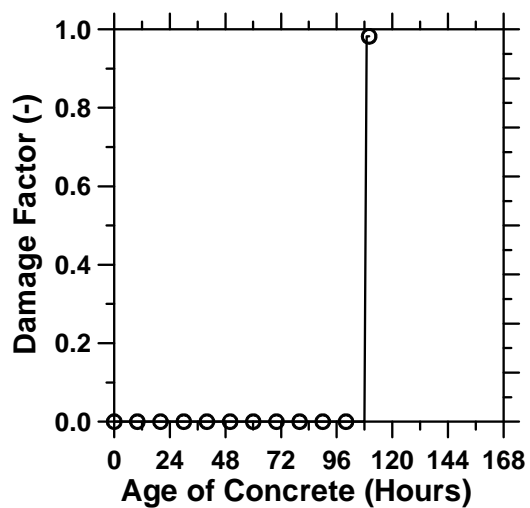


Fig. (h)

Figure A.88: Pavement cured at “C” ambient temperature with a D/3 saw-cut depth introduced at 96 hours.

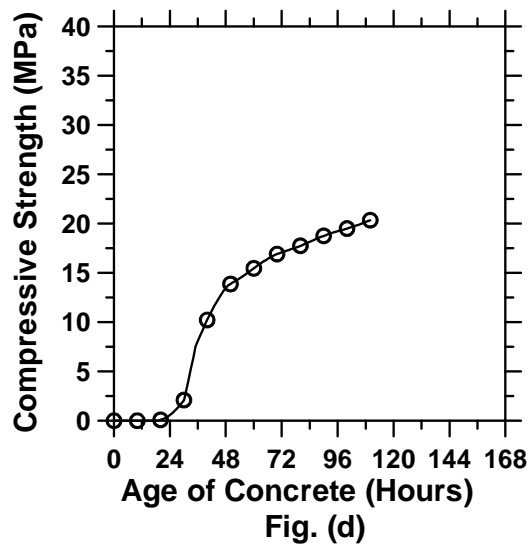
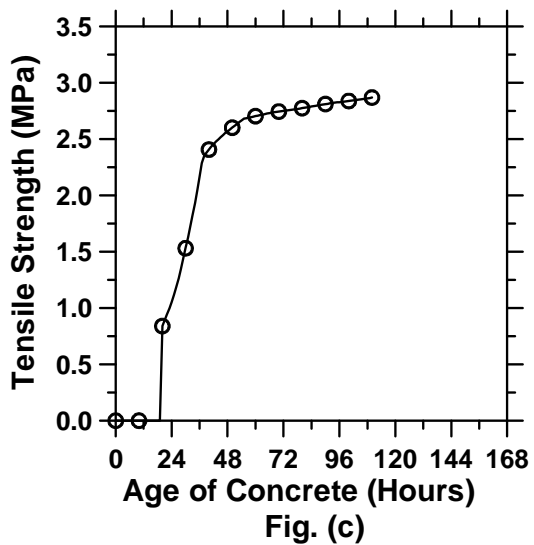
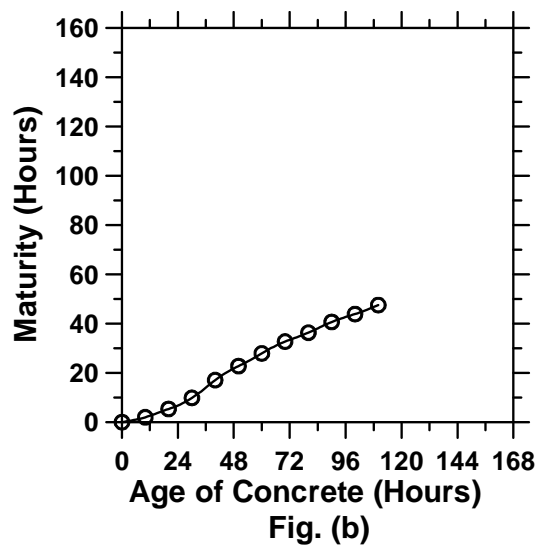
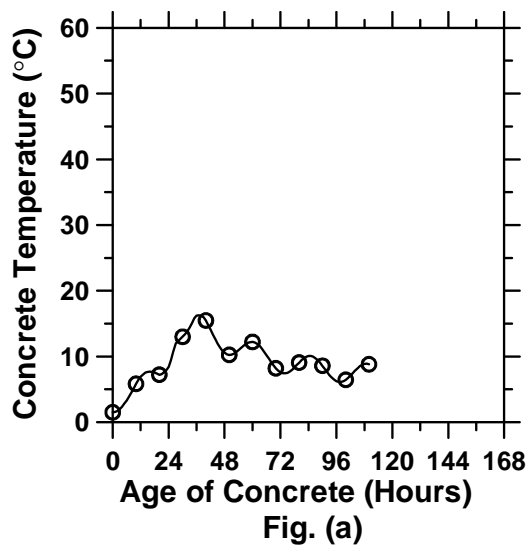


Figure A.89: Pavement cured at “C” ambient temperature with a D/3 saw-cut depth introduced at 108 hours (cont’d).

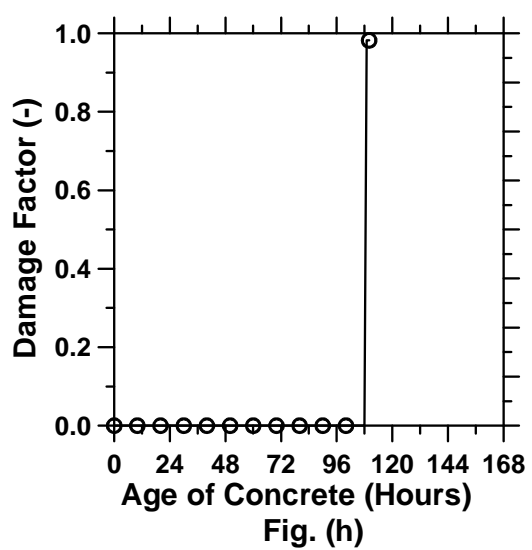
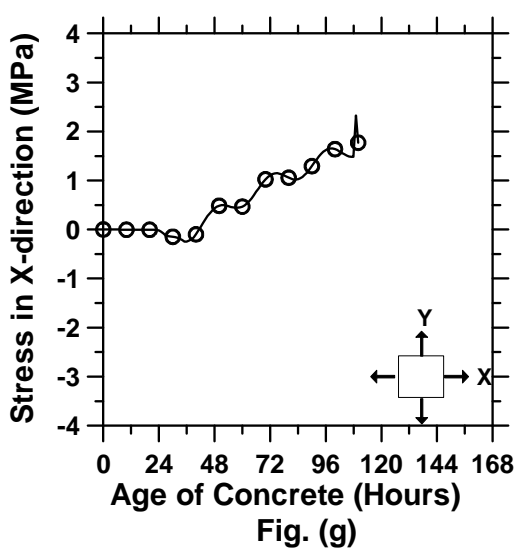
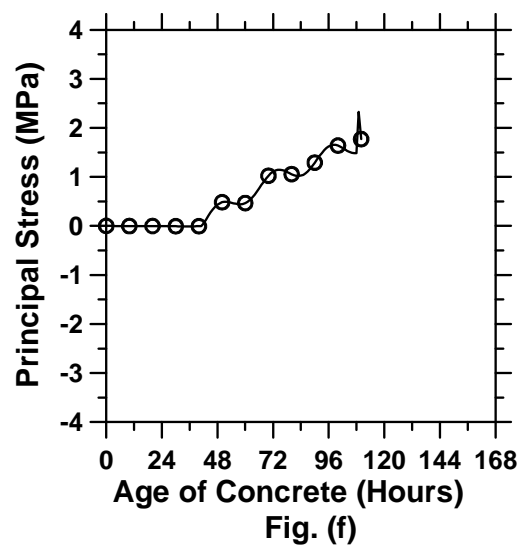
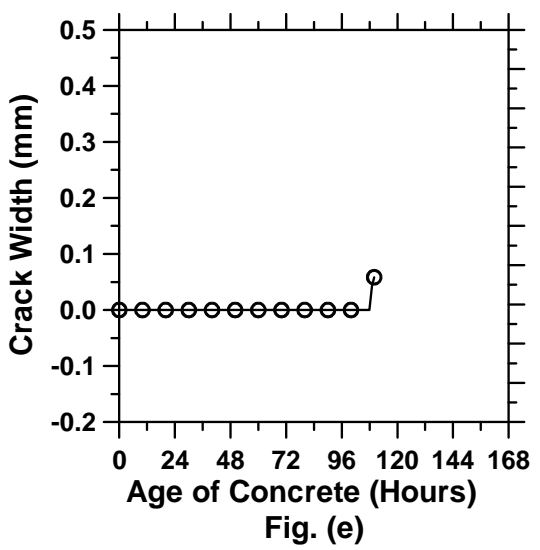


Figure A.89: Pavement cured at “C” ambient temperature with a D/3 saw-cut depth introduced at 108 hours.

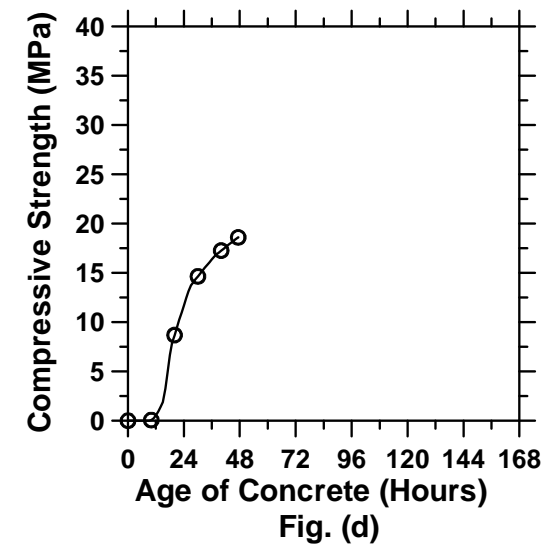
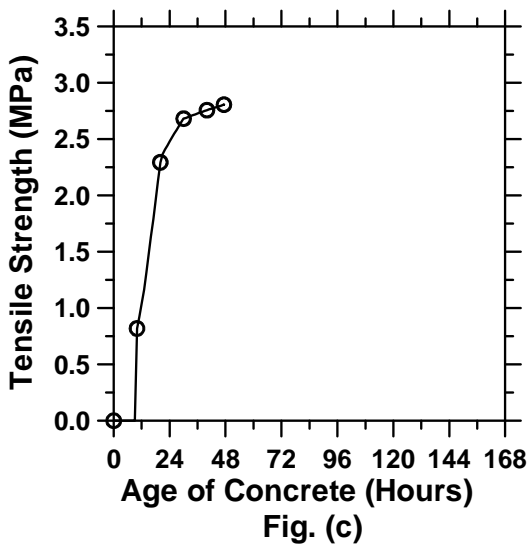
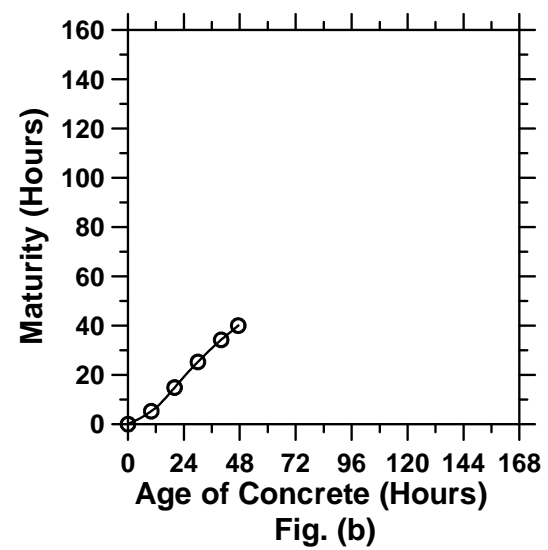
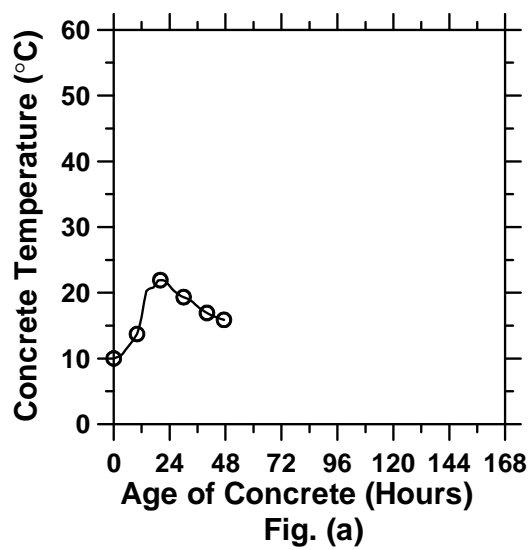


Figure A.90: Pavement cured at 10°C ambient temperature with a D/3 saw-cut depth introduced at 0 hour (cont'd).

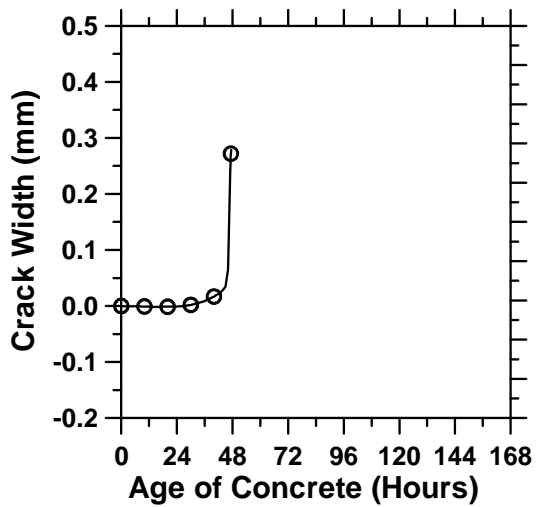


Fig. (e)

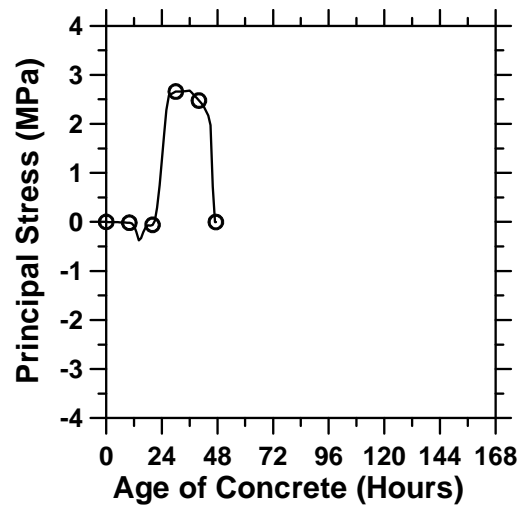


Fig. (f)

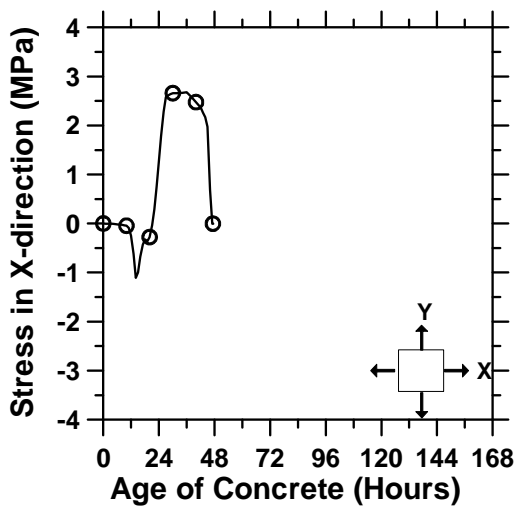


Fig. (g)

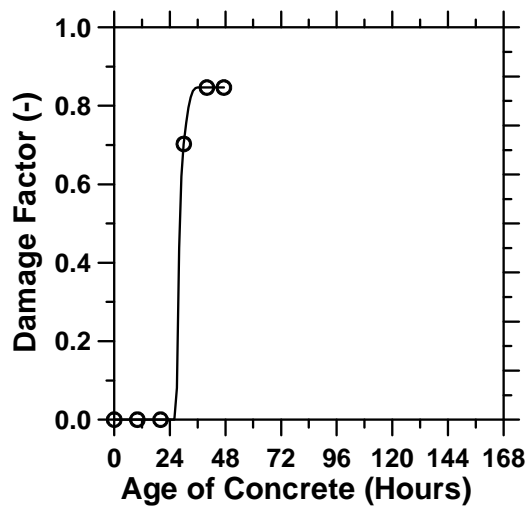


Fig. (h)

Figure A.90: Pavement cured at 10°C ambient temperature with a D/3 saw-cut depth introduced at 0 hour.

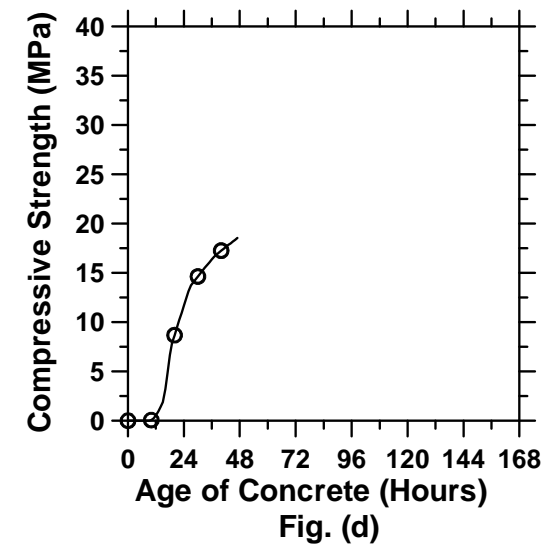
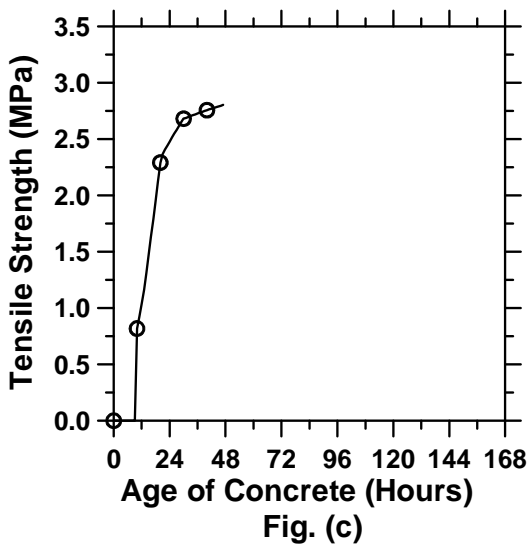
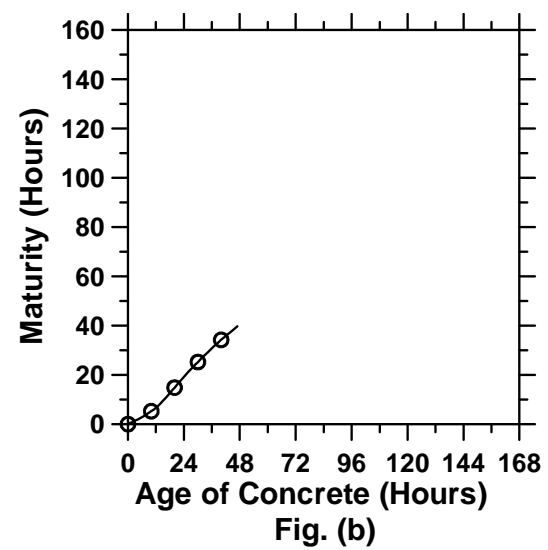
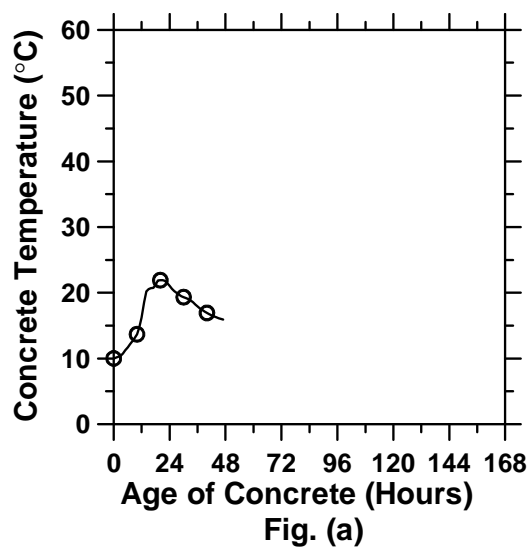


Figure A.91: Pavement cured at 10°C ambient temperature with a D/3 saw-cut depth introduced at 12 hours (cont'd).

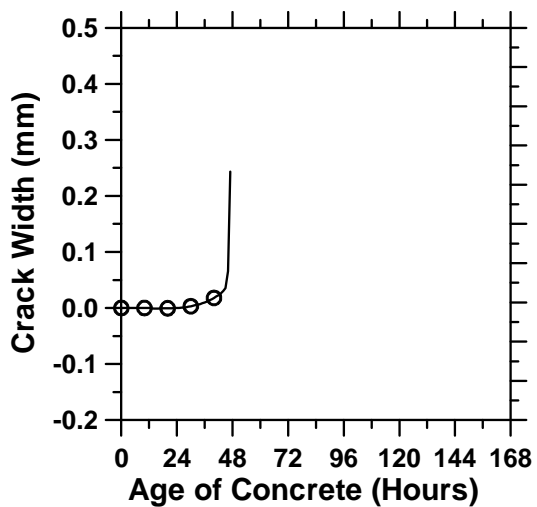


Fig. (e)

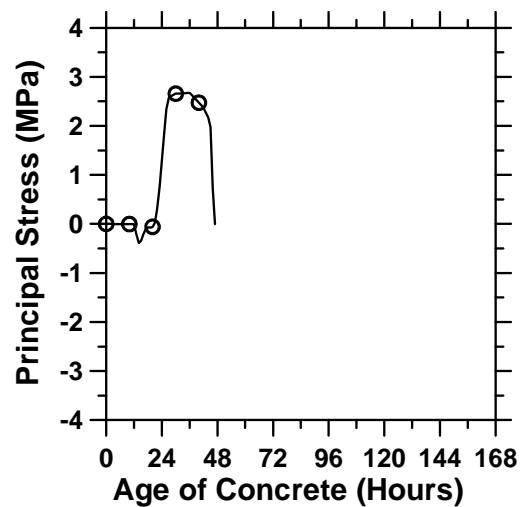


Fig. (f)

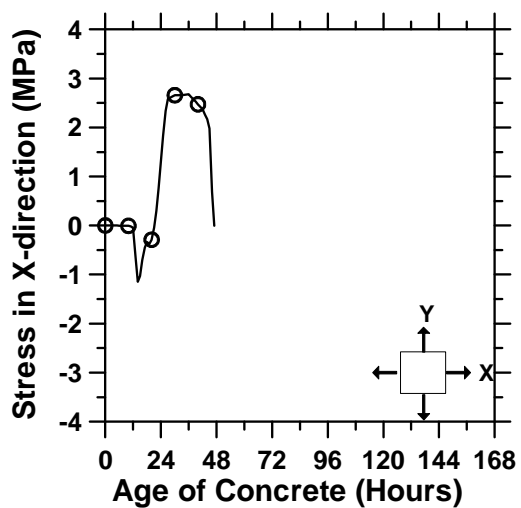


Fig. (g)

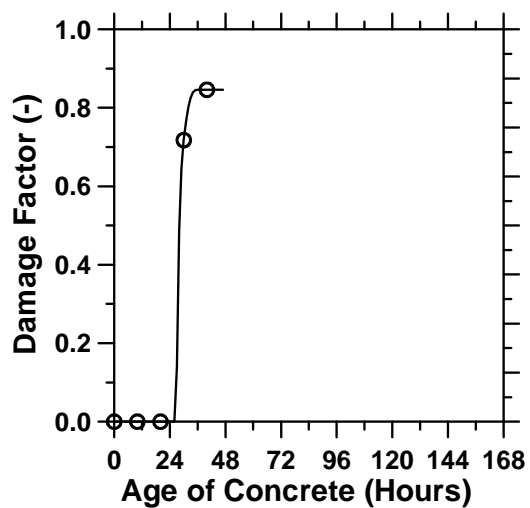


Fig. (h)

Figure A.91: Pavement cured at 10°C ambient temperature with a D/3 saw-cut depth introduced at 12 hours.

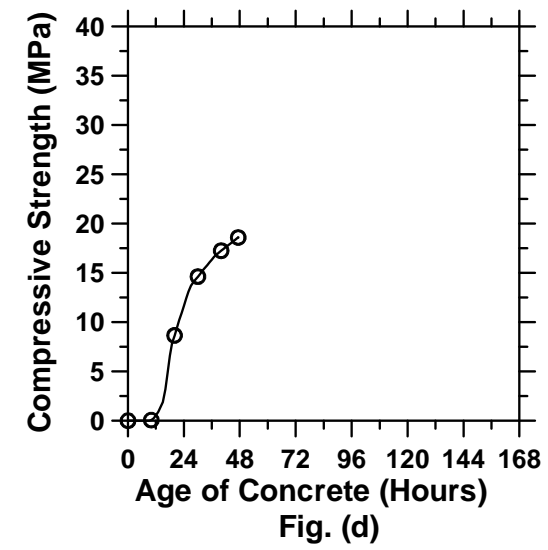
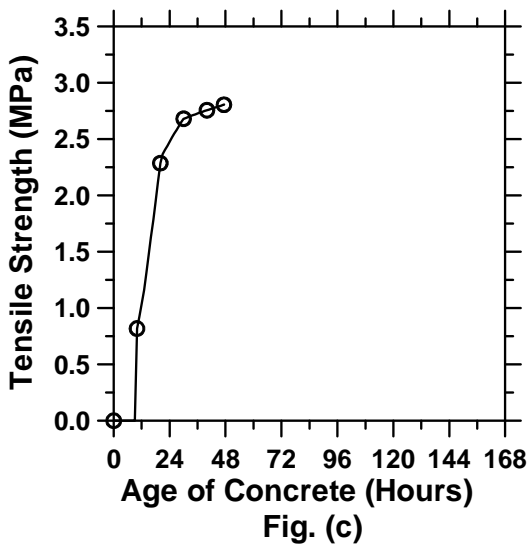
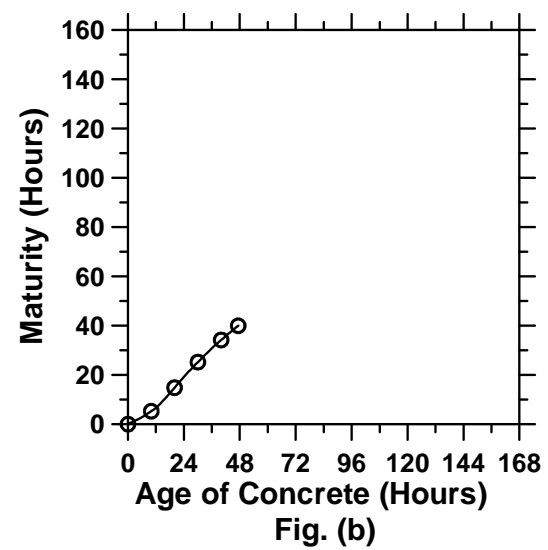
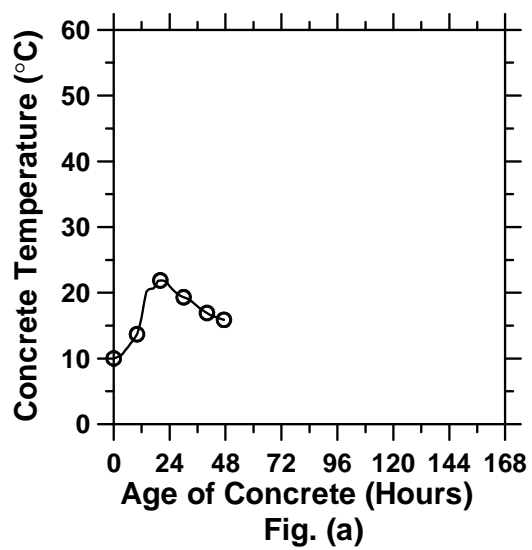


Figure A.92: Pavement cured at 10°C ambient temperature with a D/3 saw-cut depth introduced at 18 hours (cont'd).

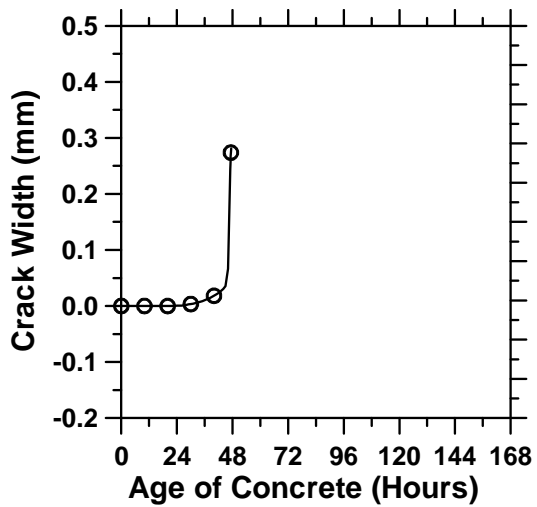


Fig. (e)

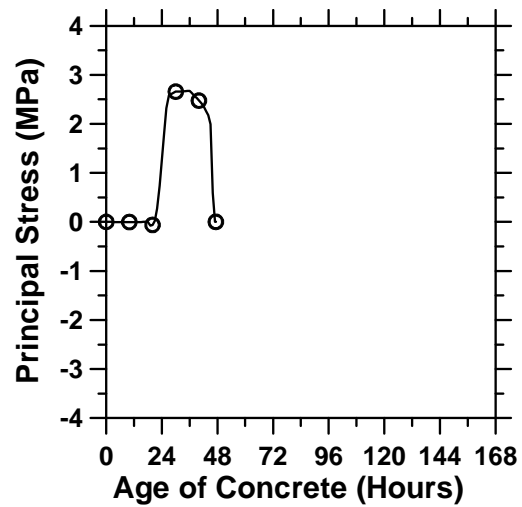


Fig. (f)

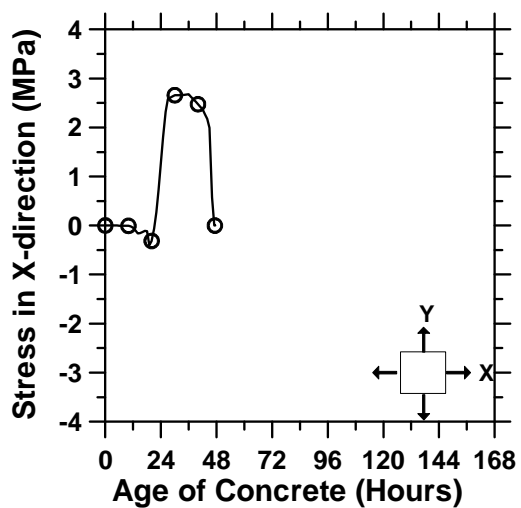


Fig. (g)

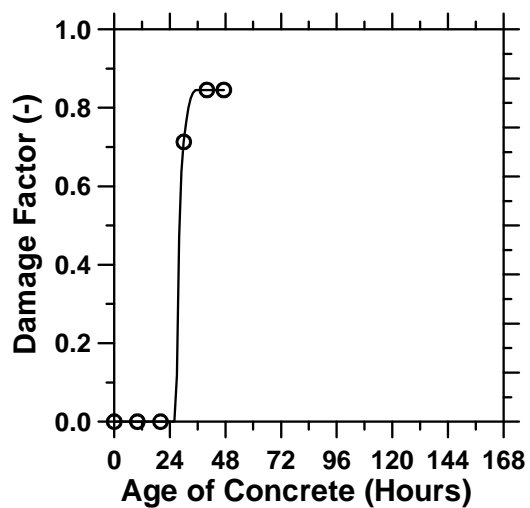


Fig. (h)

Figure A.92: Pavement cured at 10°C ambient temperature with a D/3 saw-cut depth introduced at 18 hours.

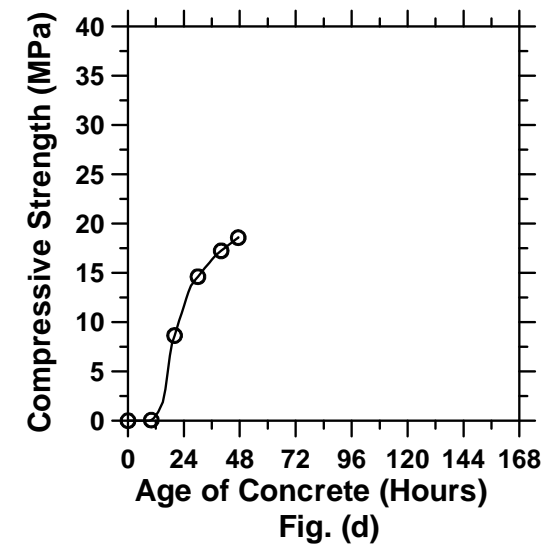
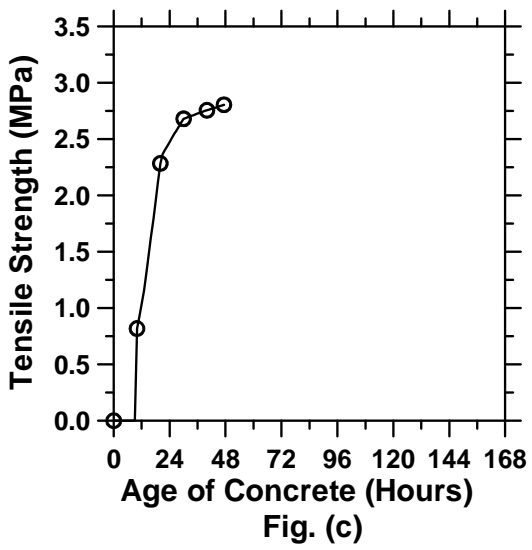
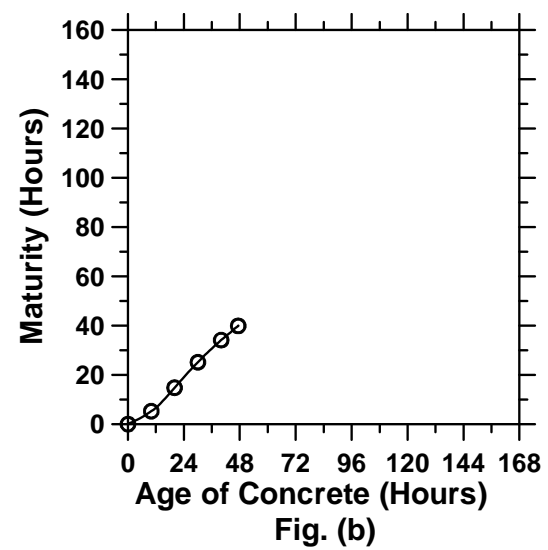
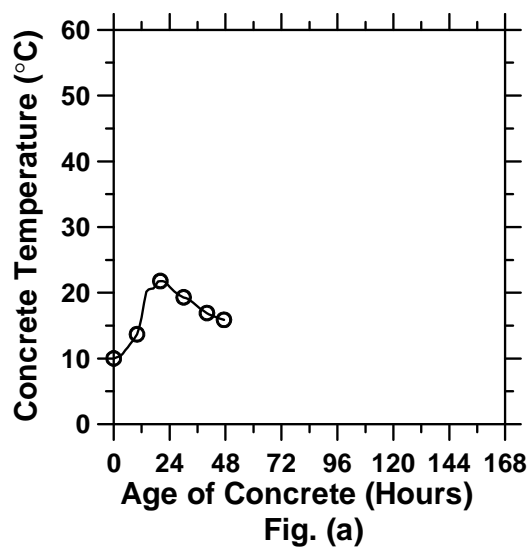


Figure A.93: Pavement cured at 10°C ambient temperature with a D/3 saw-cut depth introduced at 24 hours (cont'd).

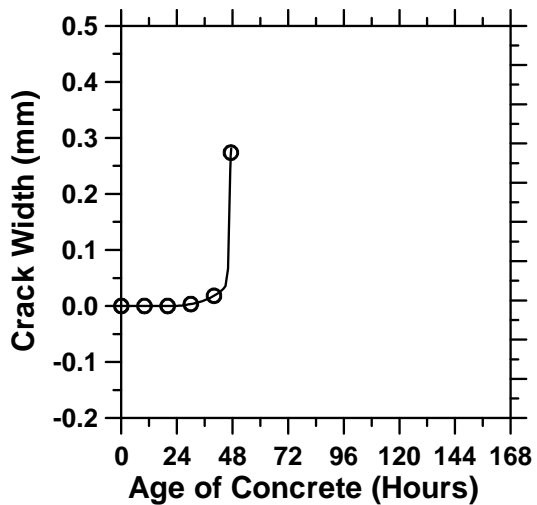


Fig. (e)

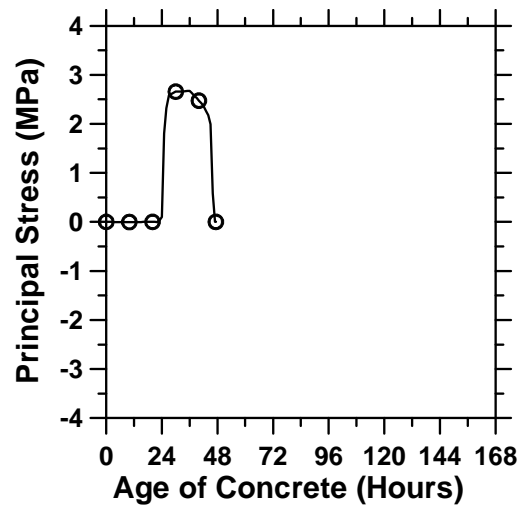


Fig. (f)

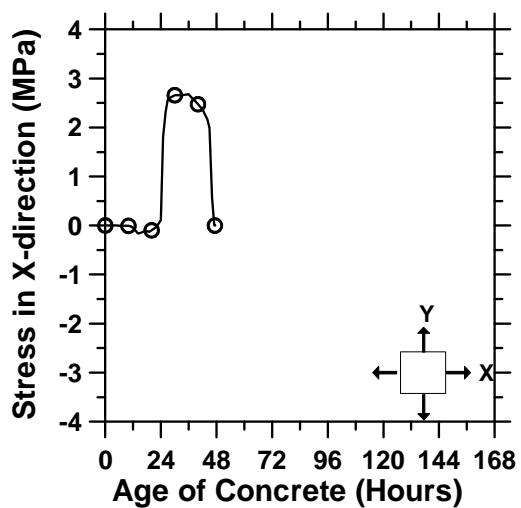


Fig. (g)

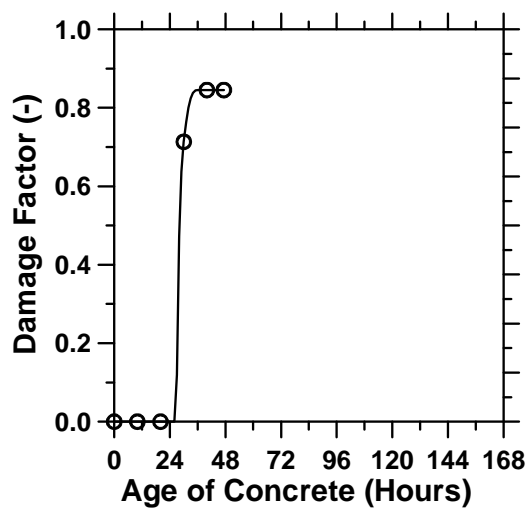


Fig. (h)

Figure A.93: Pavement cured at 10°C ambient temperature with a D/3 saw-cut depth introduced at 24 hours.

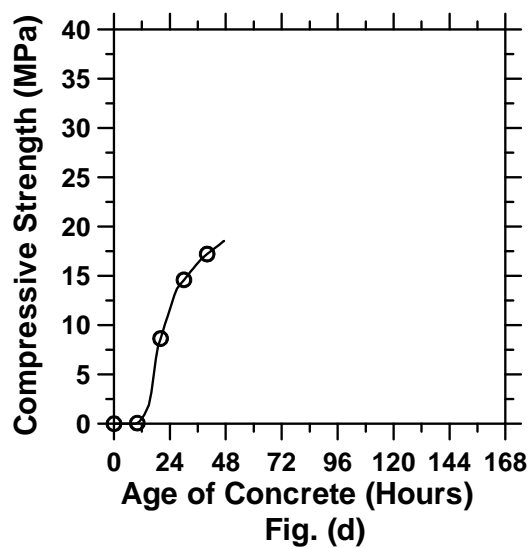
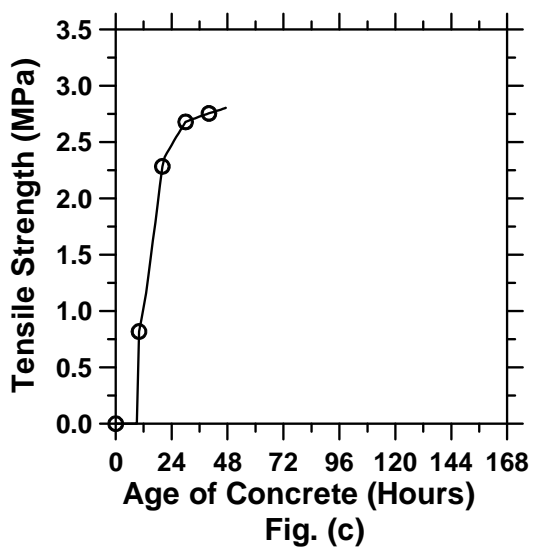
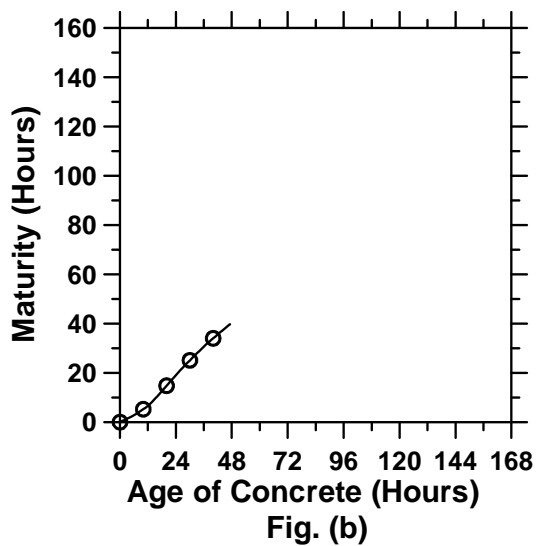
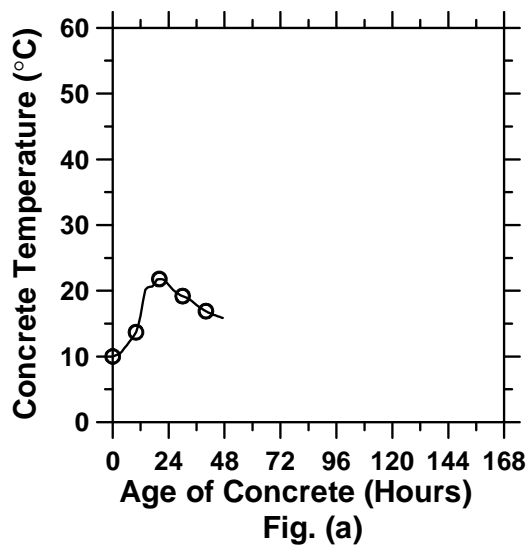


Figure A.94: Pavement cured at 10°C ambient temperature with a D/3 saw-cut depth introduced at 36 hours (cont'd).

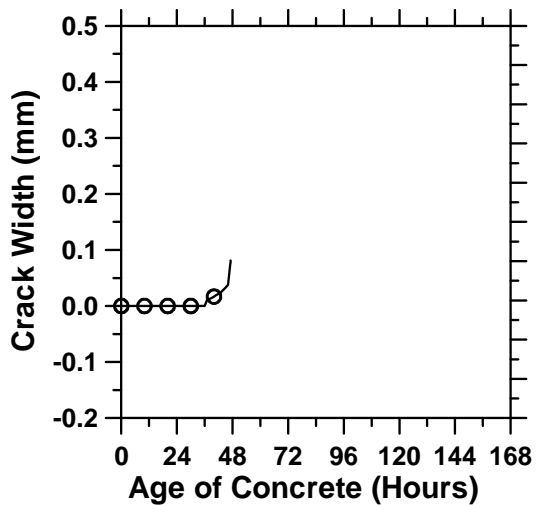


Fig. (e)

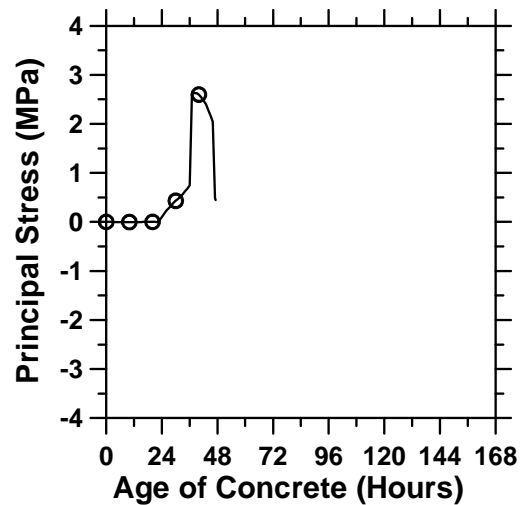


Fig. (f)

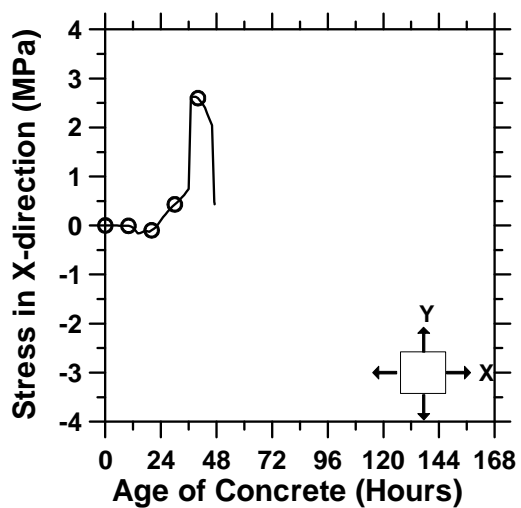


Fig. (g)

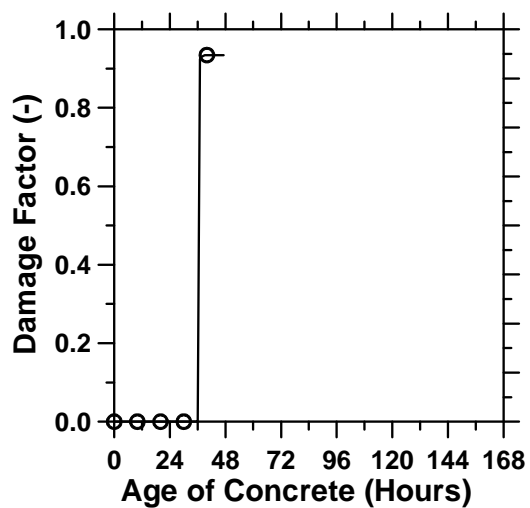


Fig. (h)

Figure A.94: Pavement cured at 10°C ambient temperature with a D/3 saw-cut depth introduced at 36 hours.

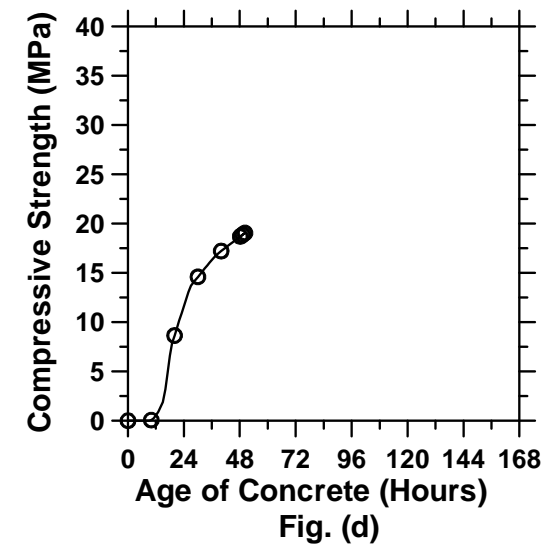
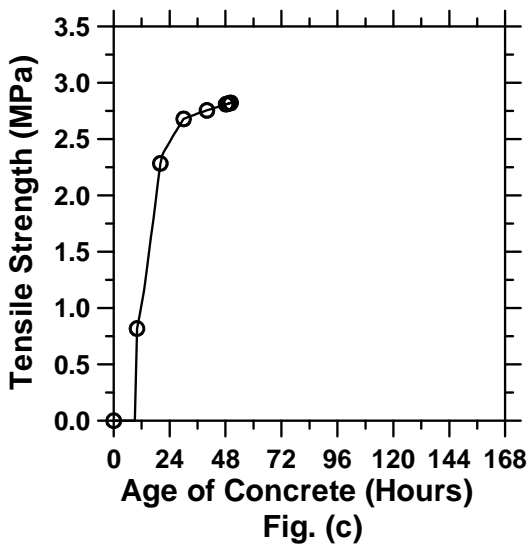
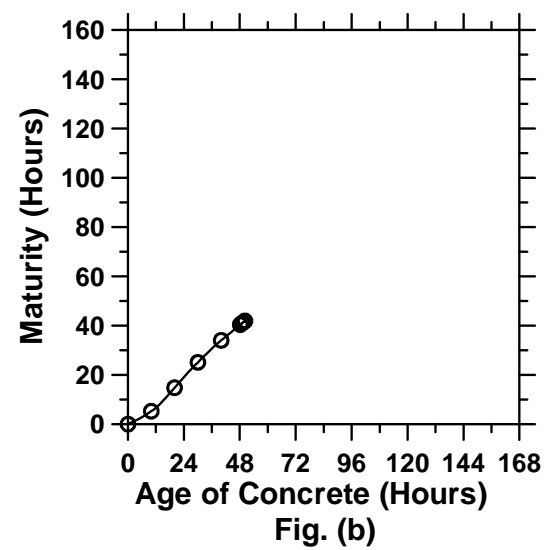
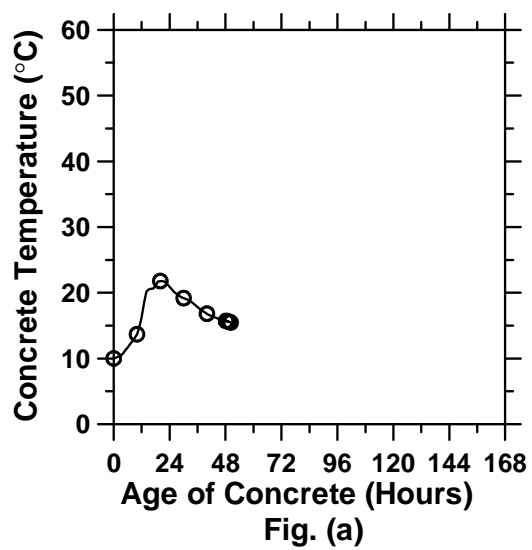


Figure A.95: Pavement cured at 10°C ambient temperature with a D/3 saw-cut depth introduced at 48 hours (cont'd).

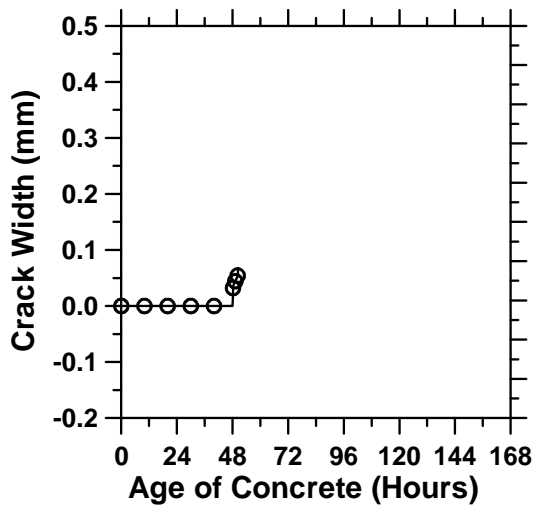


Fig. (e)

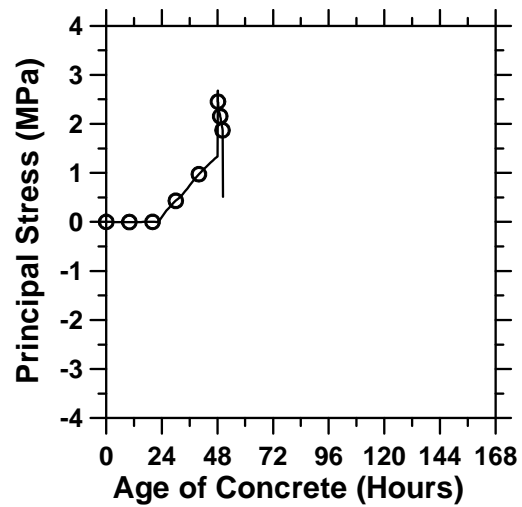


Fig. (f)

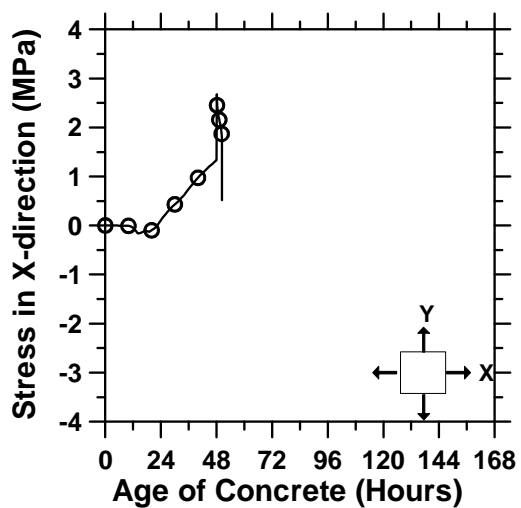


Fig. (g)

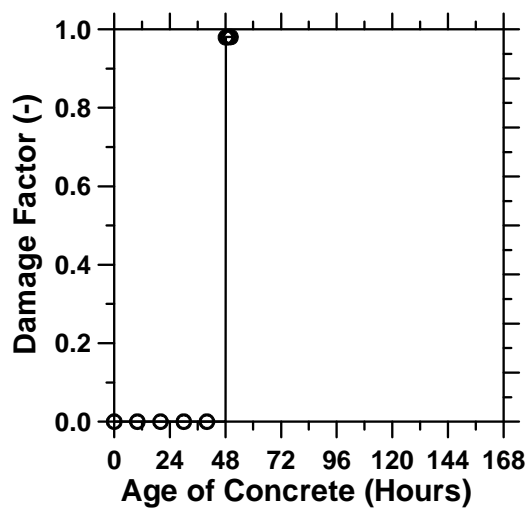


Fig. (h)

Figure A.95: Pavement cured at 10°C ambient temperature with a D/3 saw-cut depth introduced at 48 hours.

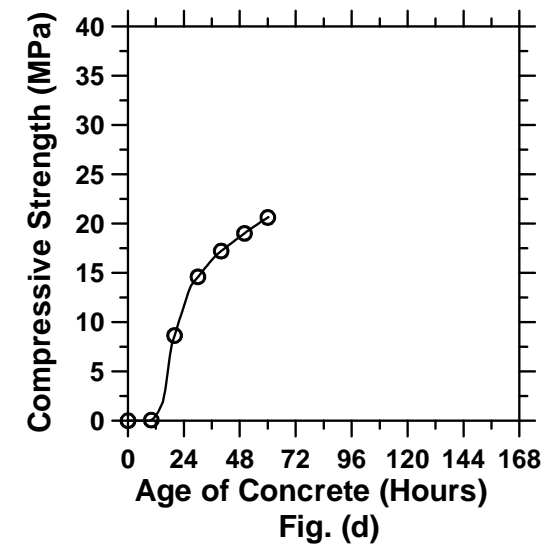
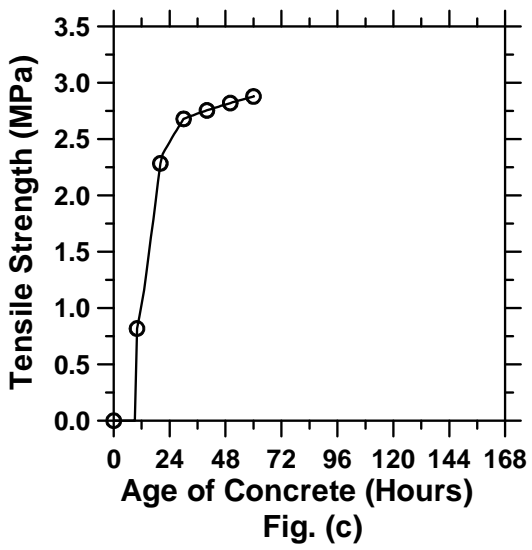
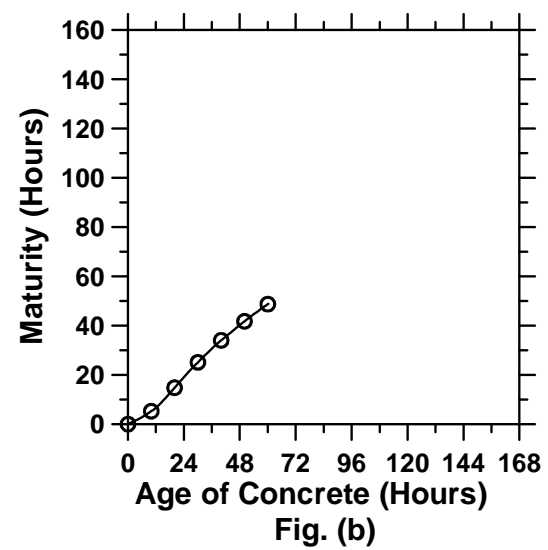
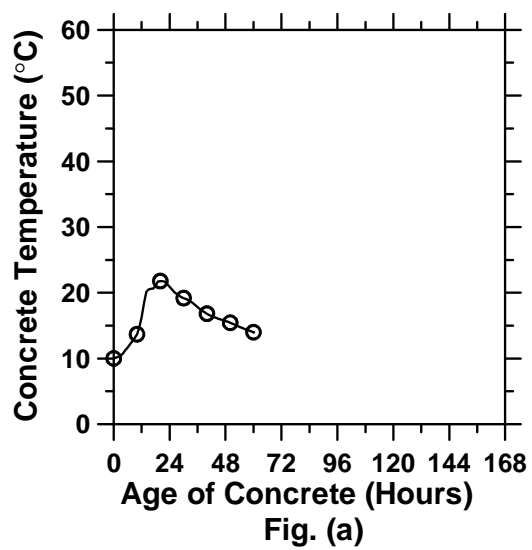


Figure A.96: Pavement cured at 10°C ambient temperature with a D/3 saw-cut depth introduced at 60 hours (cont'd).

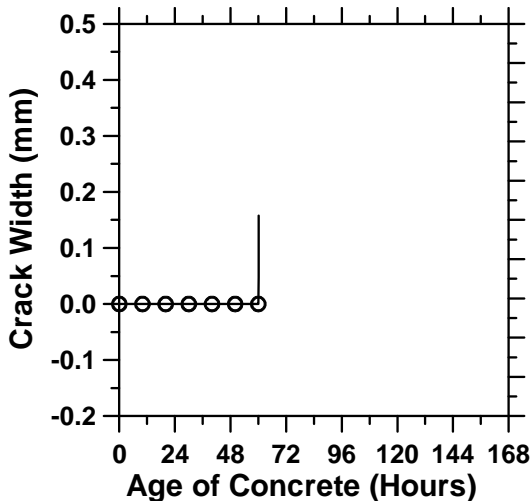


Fig. (e)

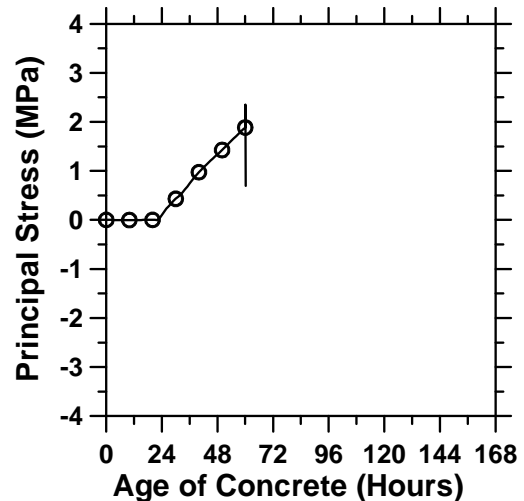


Fig. (f)

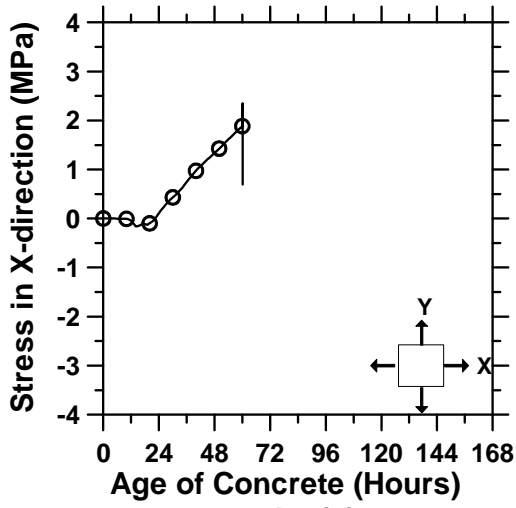


Fig. (g)

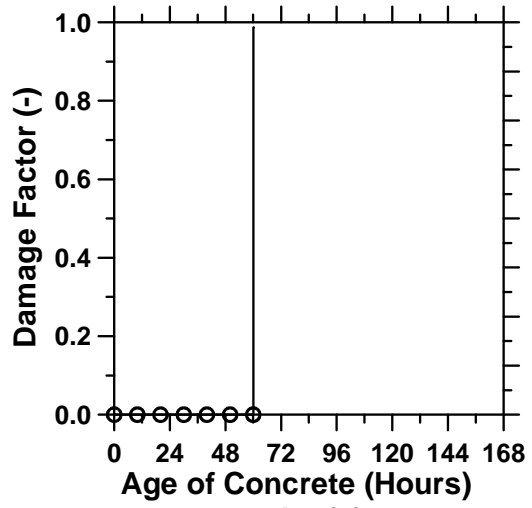


Fig. (h)

Figure A.96: Pavement cured at 10°C ambient temperature with a D/3 saw-cut depth introduced at 60 hours.

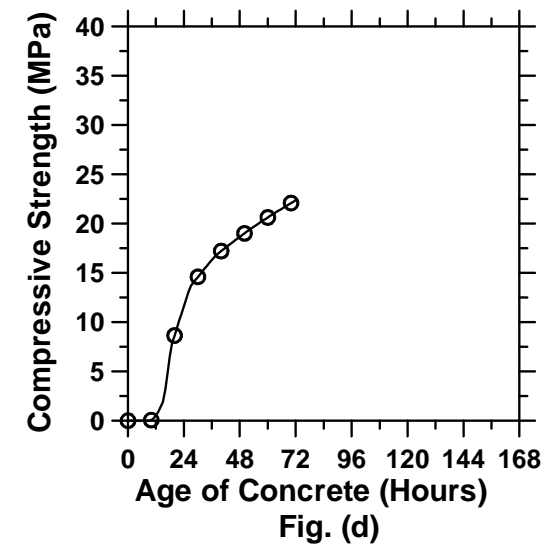
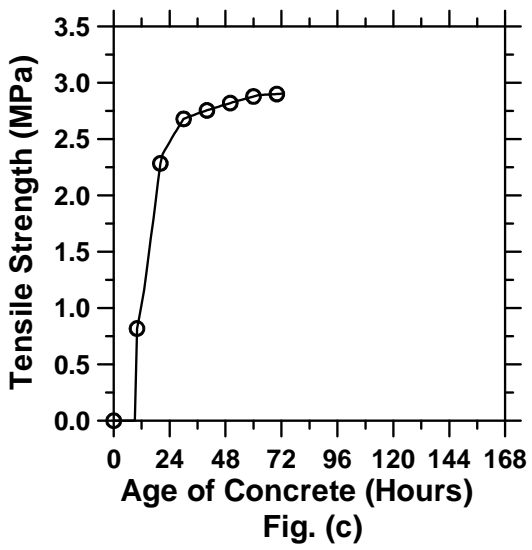
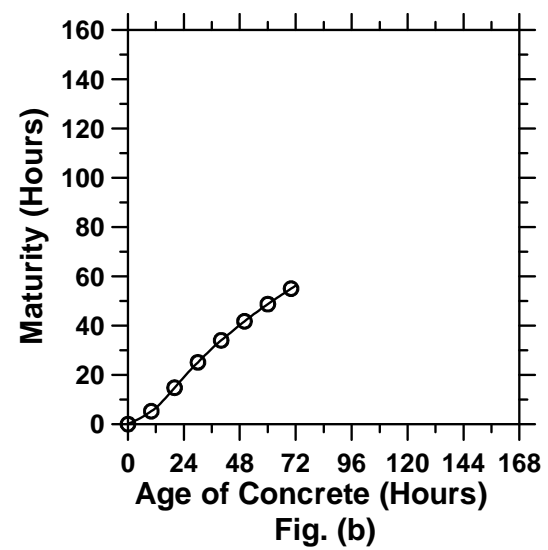
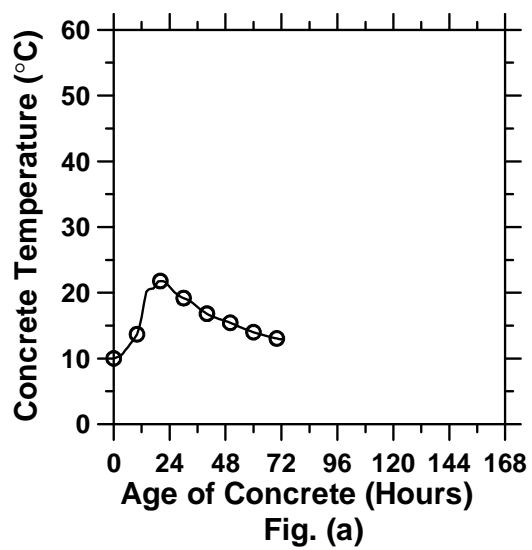


Figure A.97: Pavement cured at 10°C ambient temperature with a D/3 saw-cut depth introduced at 72 hours (cont'd).

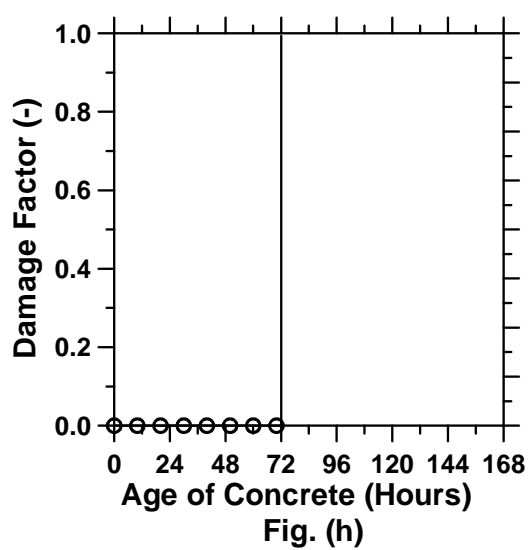
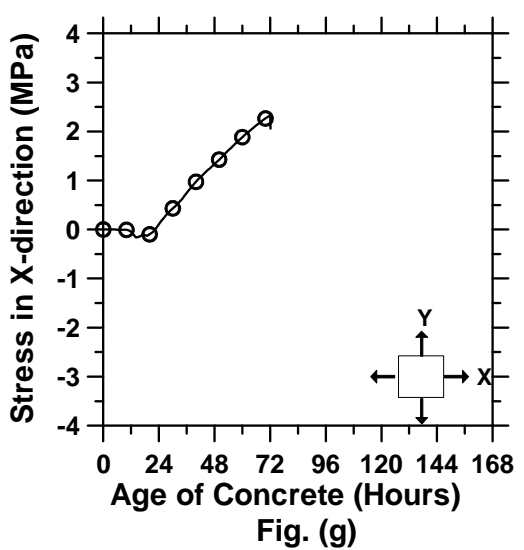
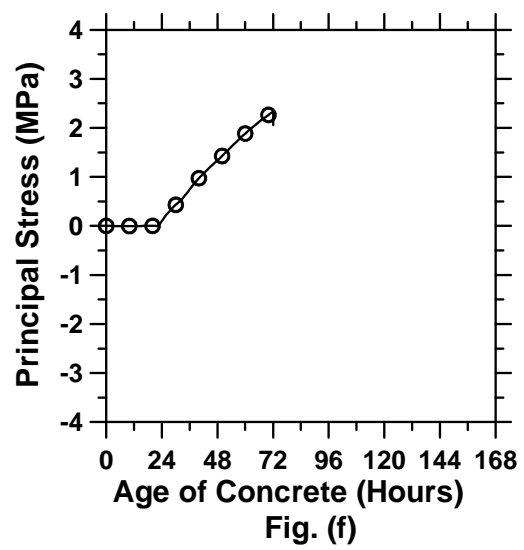
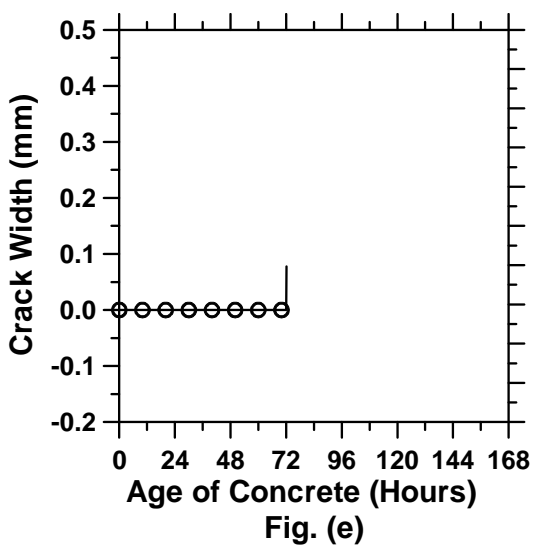


Figure A.97: Pavement cured at 10°C ambient temperature with a D/3 saw-cut depth introduced at 72 hours.

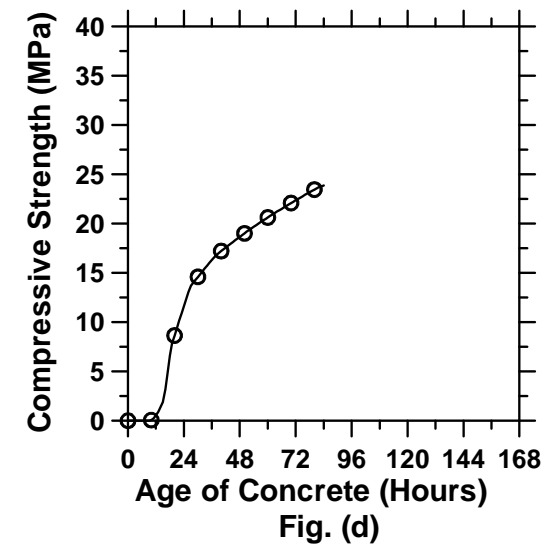
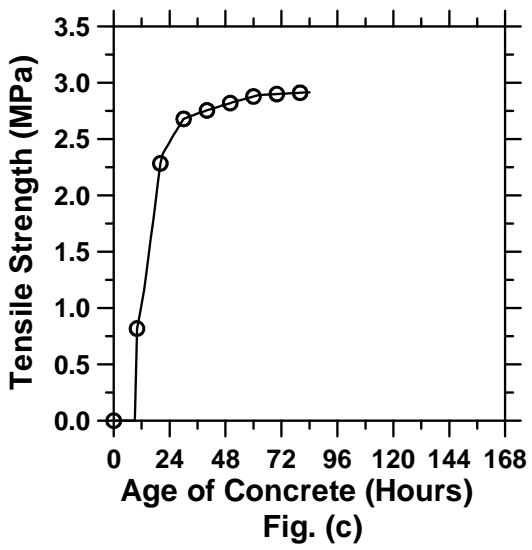
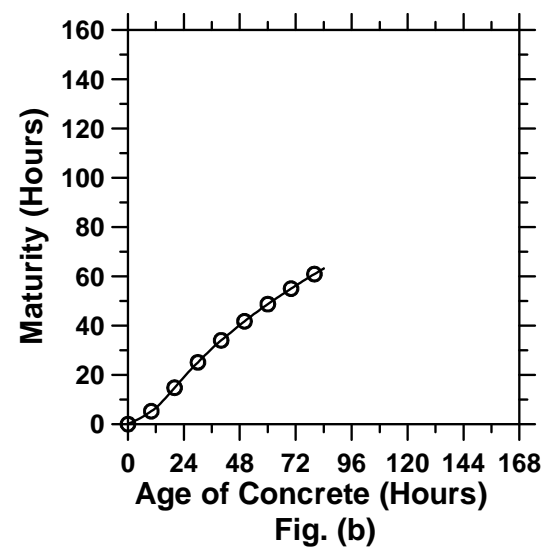
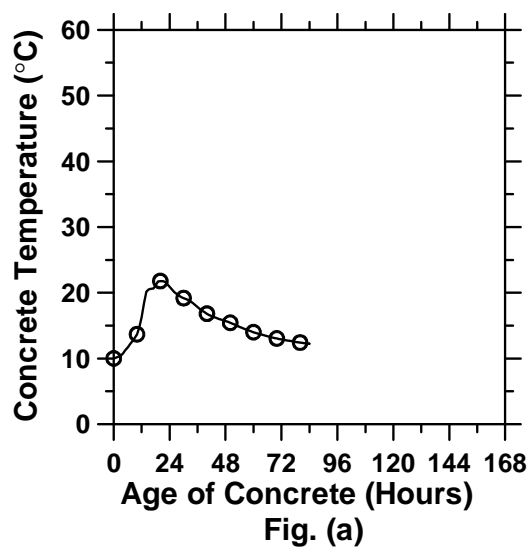


Figure A.98: Pavement cured at 10°C ambient temperature with a D/3 saw-cut depth introduced at 84 hours (cont'd).

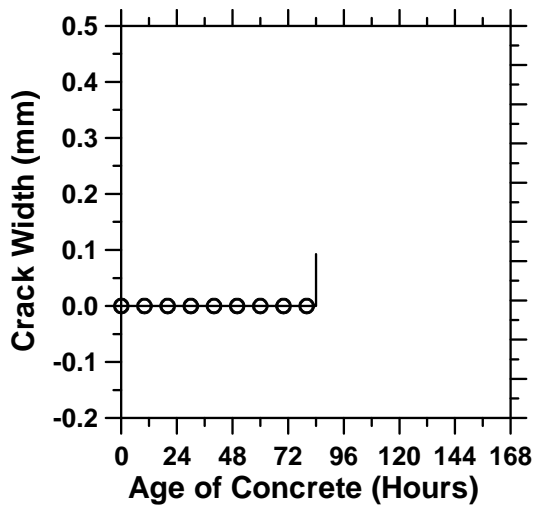


Fig. (e)

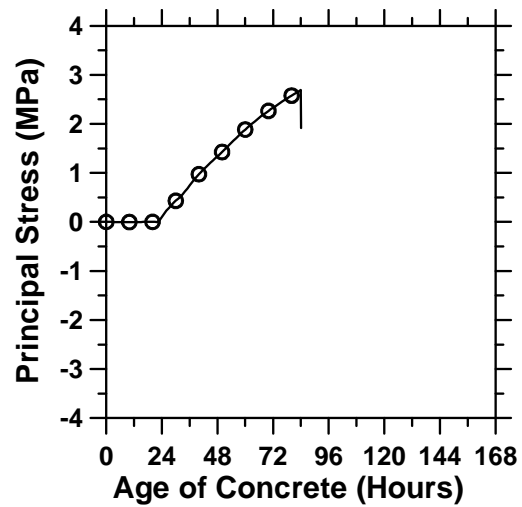


Fig. (f)

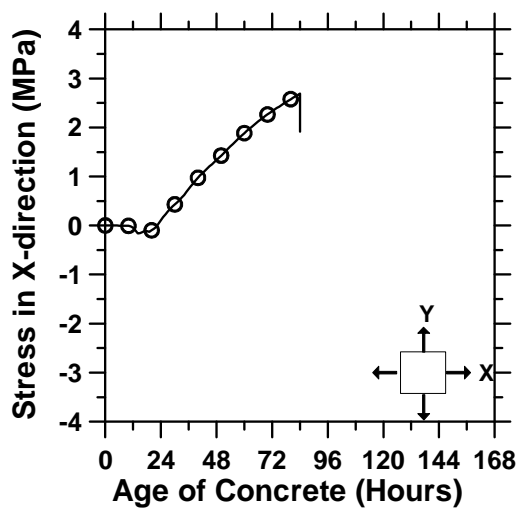


Fig. (g)

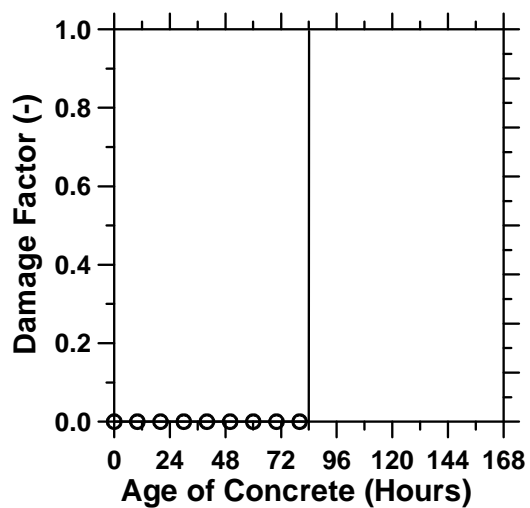


Fig. (h)

Figure A.98: Pavement cured at 10°C ambient temperature with a D/3 saw-cut depth introduced at 84 hours.

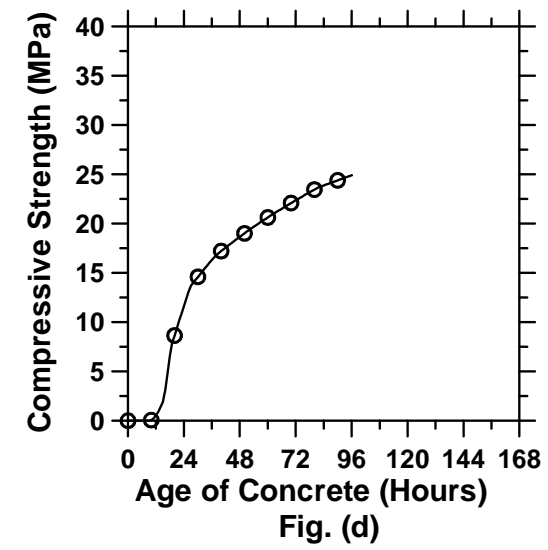
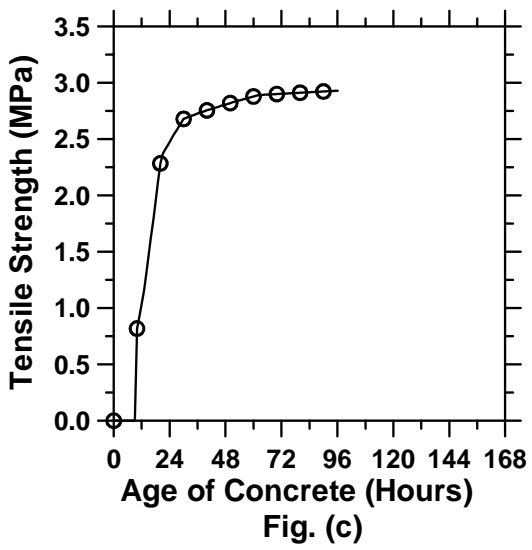
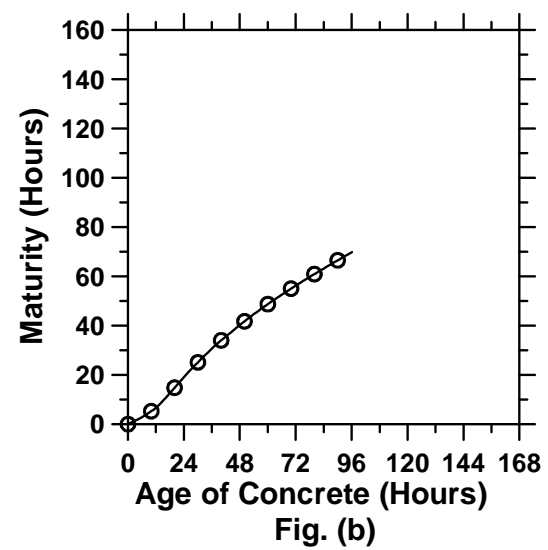
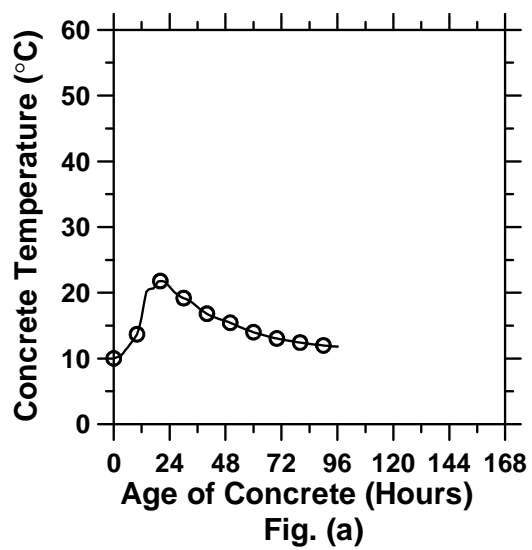


Figure A.99: Pavement cured at 10°C ambient temperature with a D/3 saw-cut depth introduced at 96 hours (cont'd).

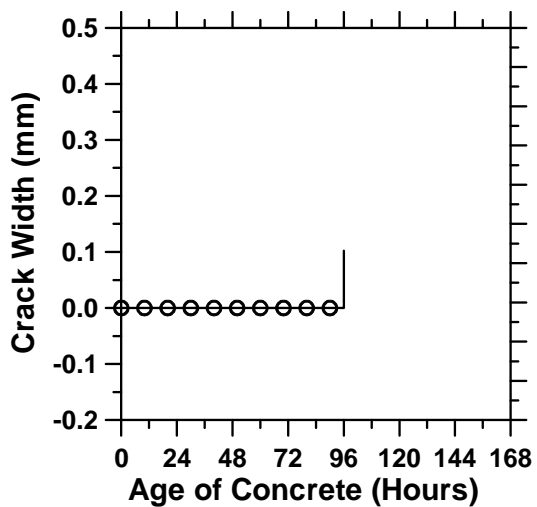


Fig. (e)

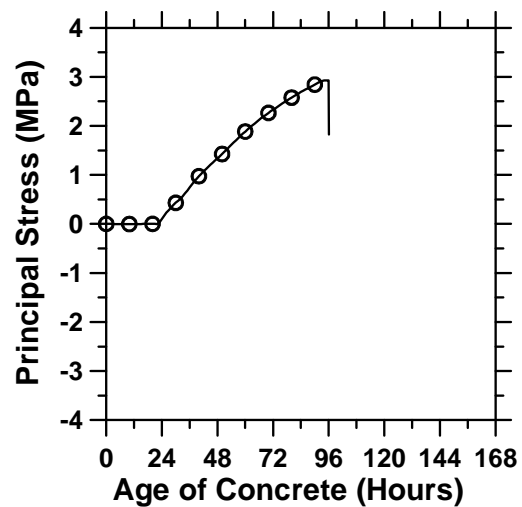


Fig. (f)

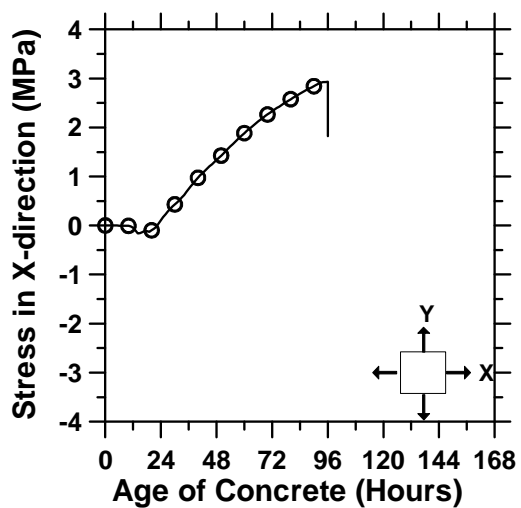


Fig. (g)

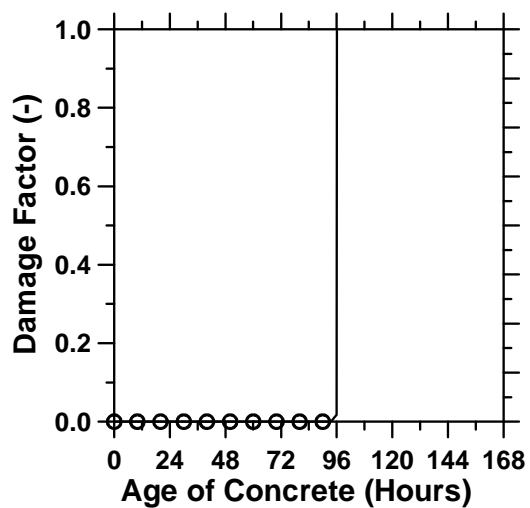


Fig. (h)

Figure A.99: Pavement cured at 10°C ambient temperature with a D/3 saw-cut depth introduced at 96 hours.

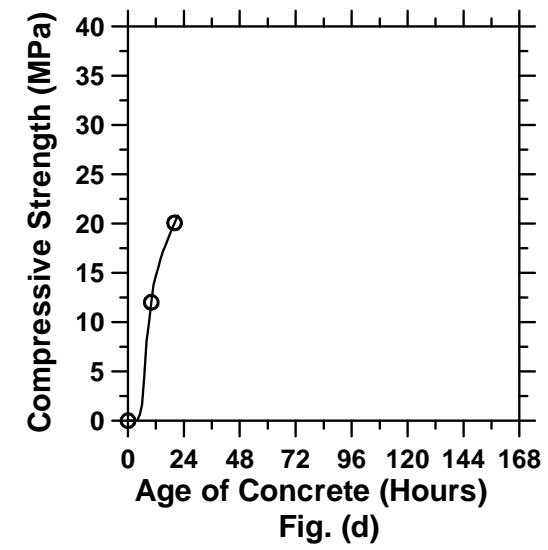
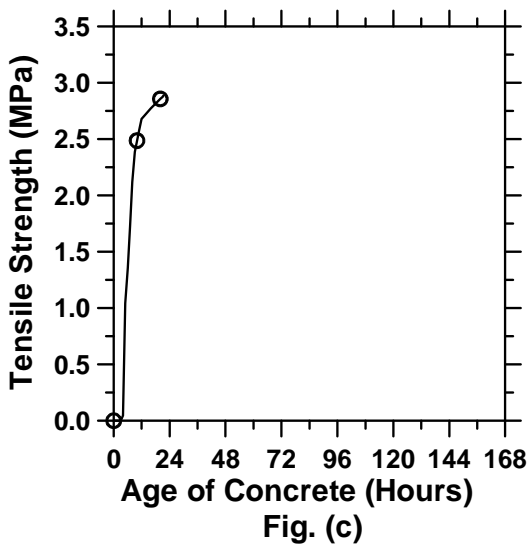
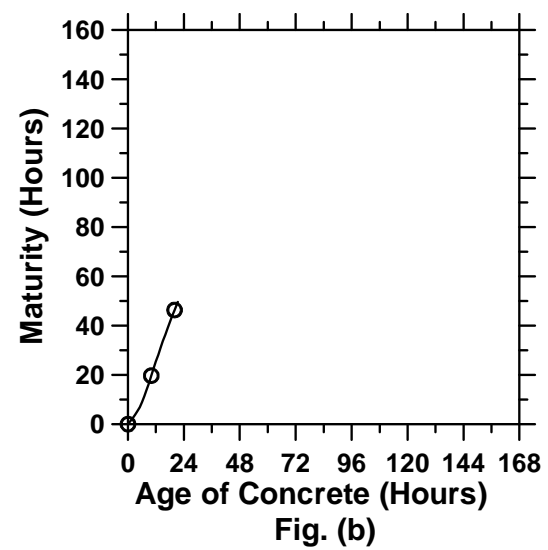
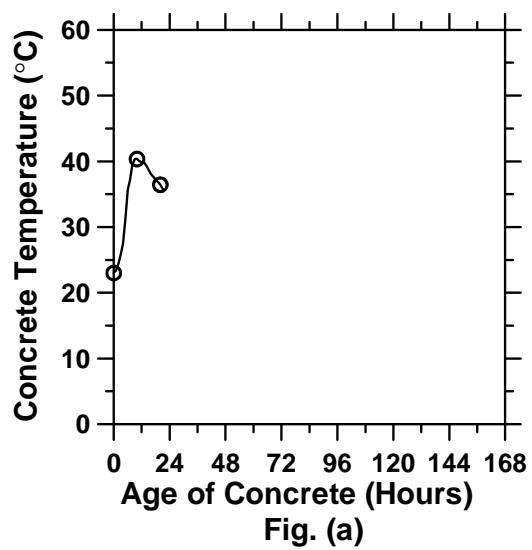


Figure A.100: Pavement cured at 23°C ambient temperature with a D/2 saw-cut depth introduced at 0 hour (cont'd).

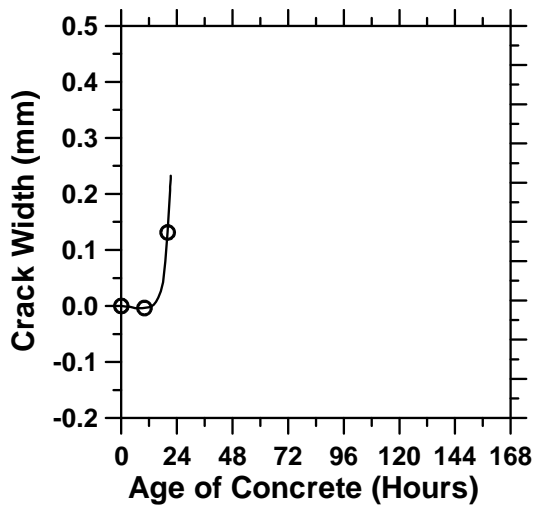


Fig. (e)

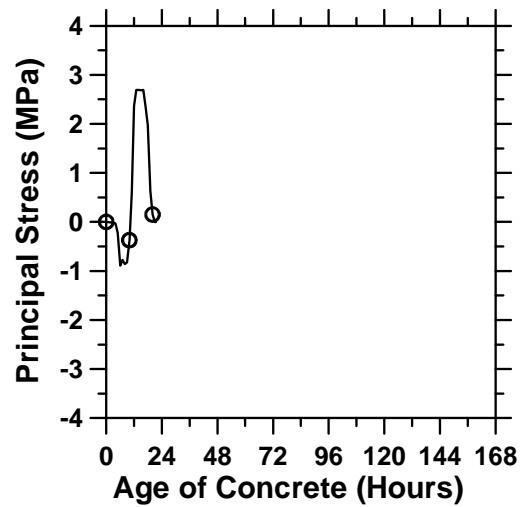


Fig. (f)

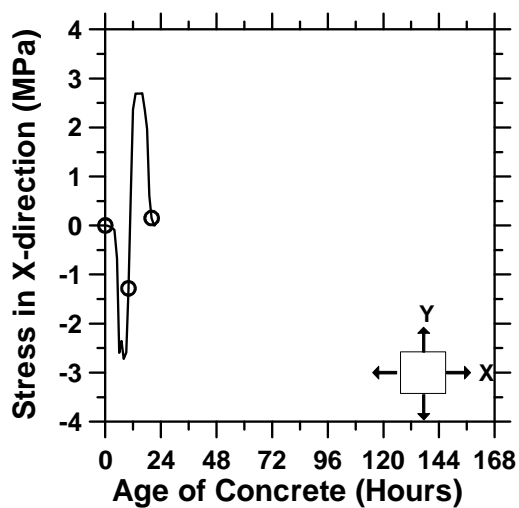


Fig. (g)

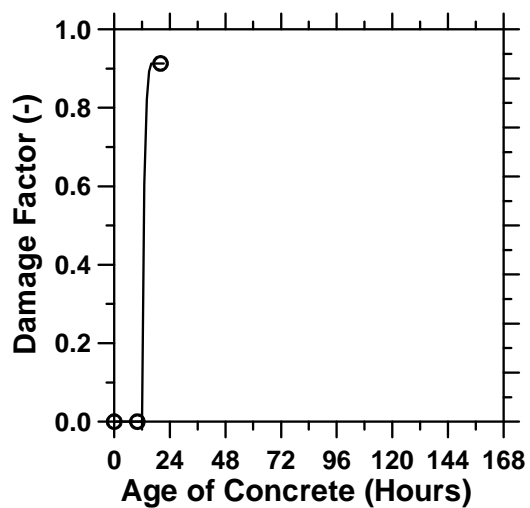


Fig. (h)

Figure A.100: Pavement cured at 23°C ambient temperature with a D/2 saw-cut depth introduced at 0 hour.

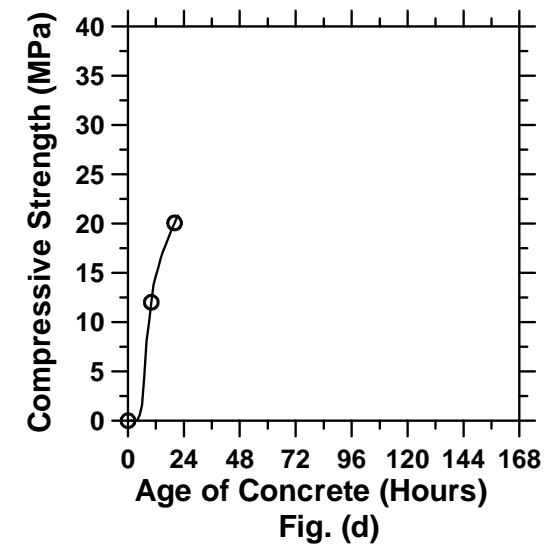
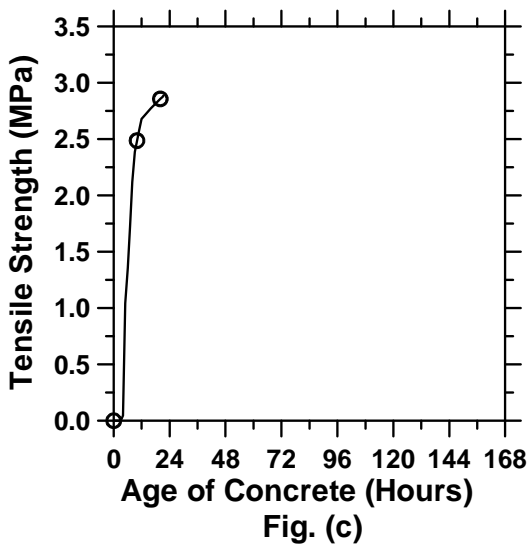
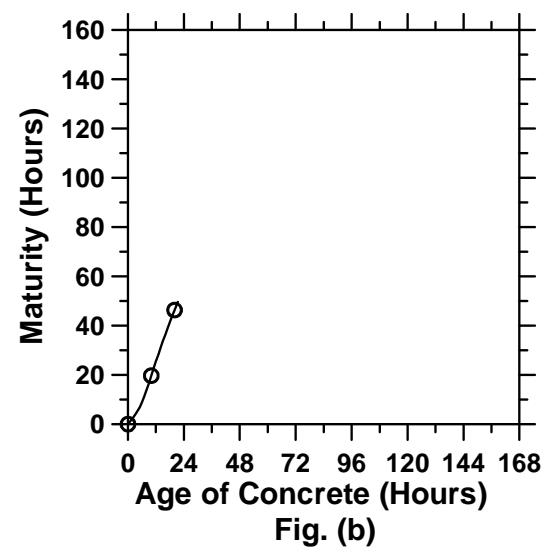
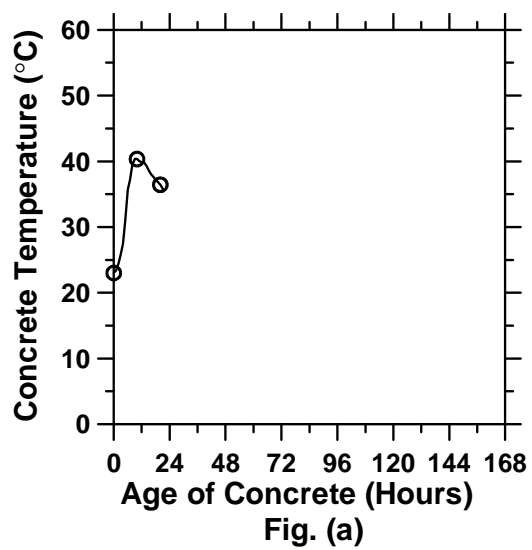


Figure A.101: Pavement cured at 23°C ambient temperature with a D/2 saw-cut depth introduced at 6 hours (cont'd).

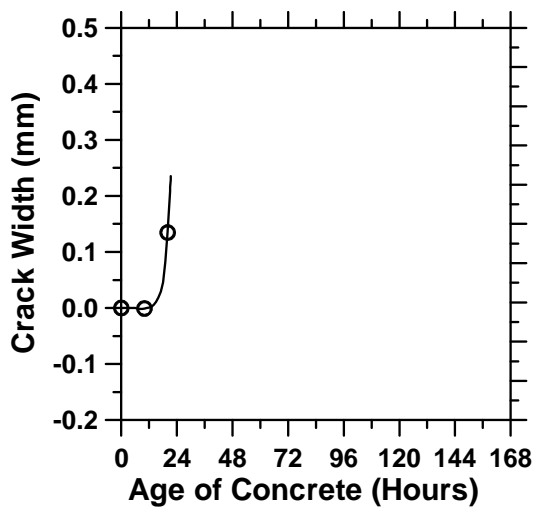


Fig. (e)

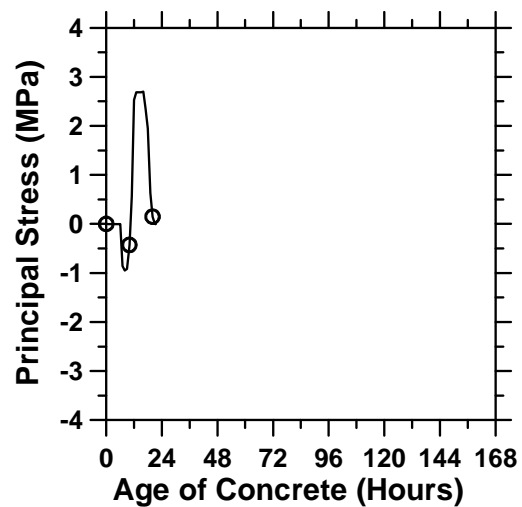


Fig. (f)

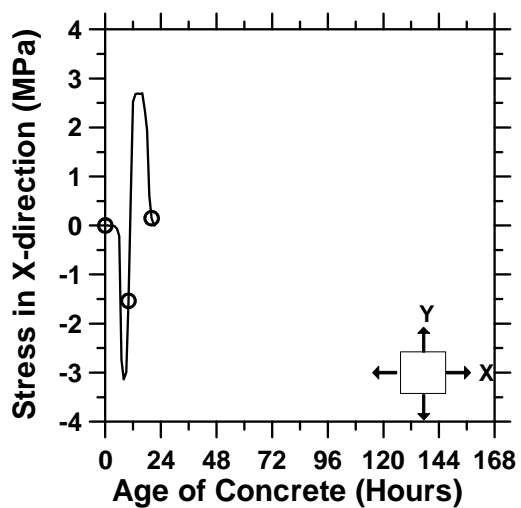


Fig. (g)

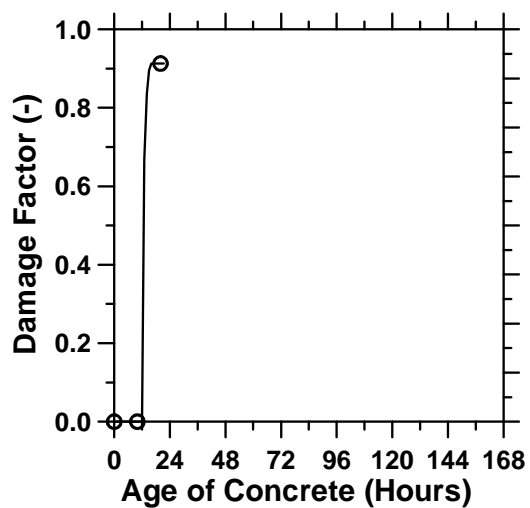


Fig. (h)

Figure A.101: Pavement cured at 23°C ambient temperature with a D/2 saw-cut depth introduced at 6 hours.

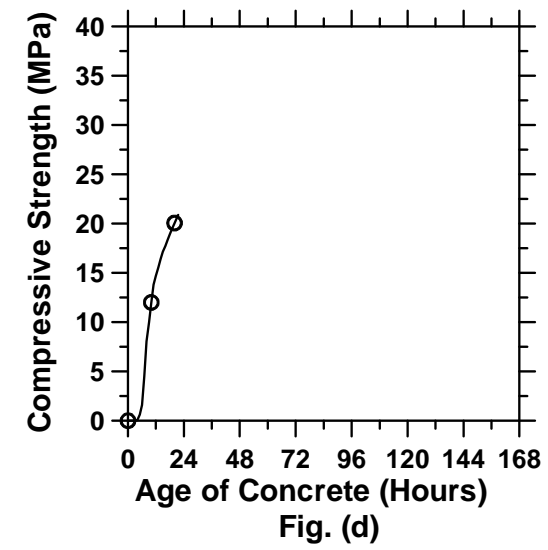
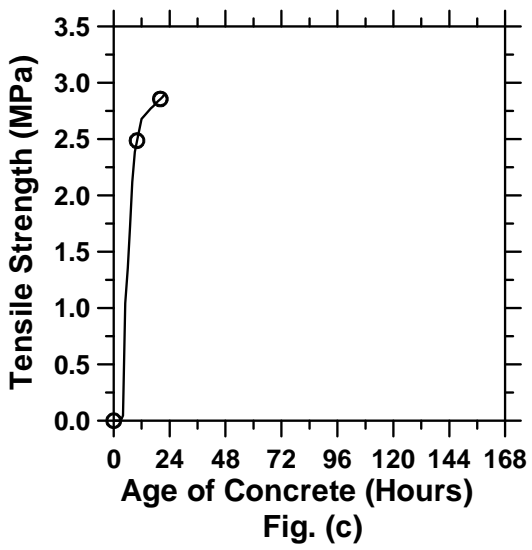
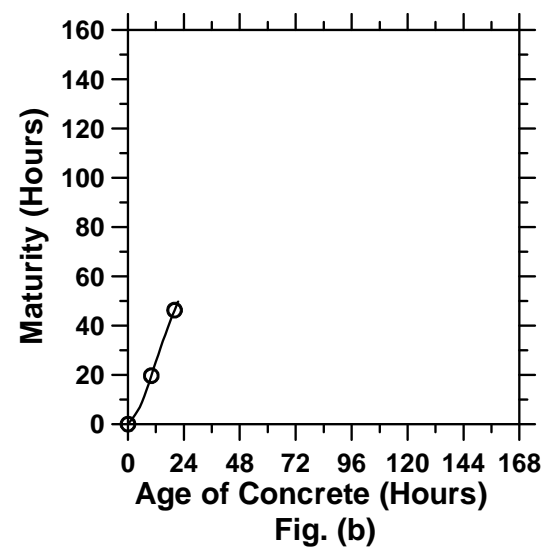
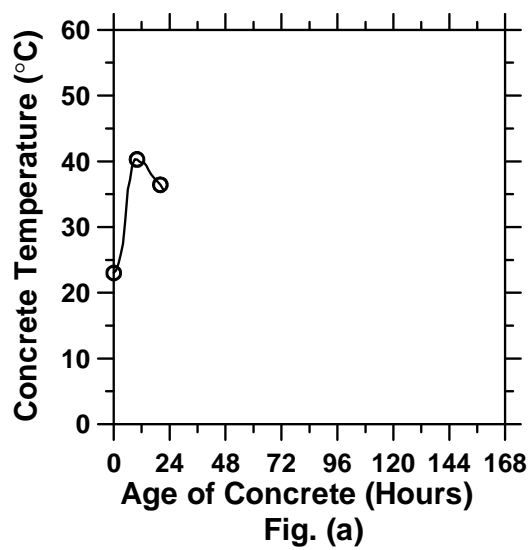


Figure A.102: Pavement cured at 23°C ambient temperature with a D/2 saw-cut depth introduced at 12 hours (cont'd).

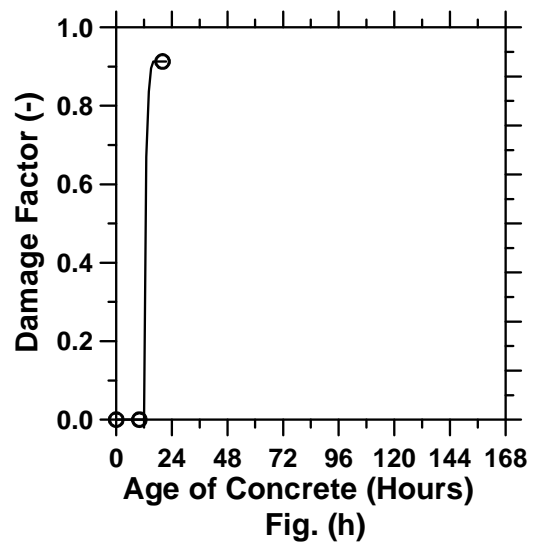
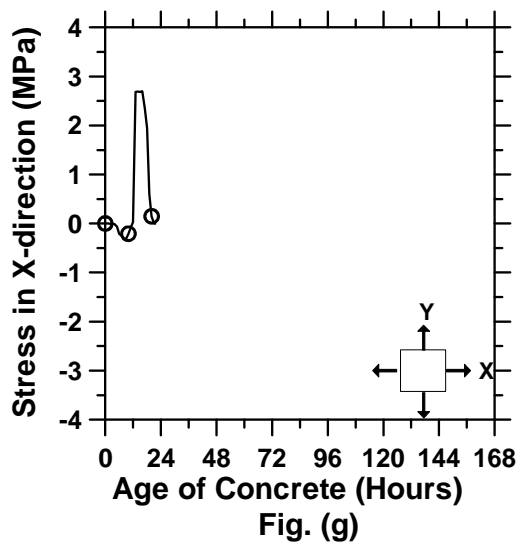
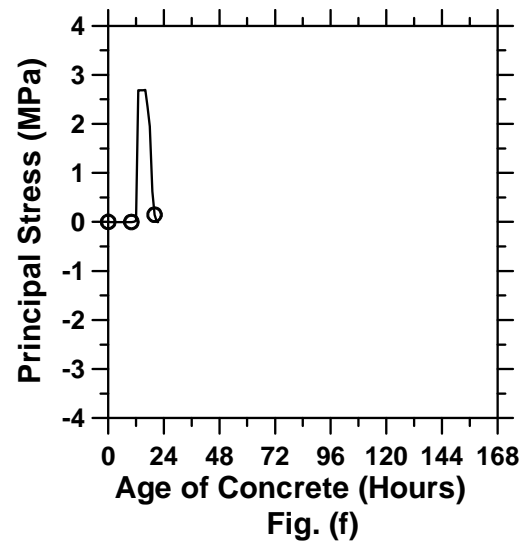
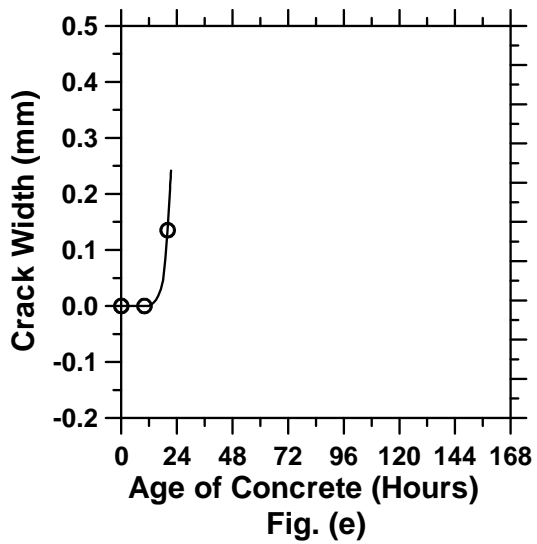


Figure A.102: Pavement cured at 23°C ambient temperature with a D/2 saw-cut depth introduced at 12 hours.

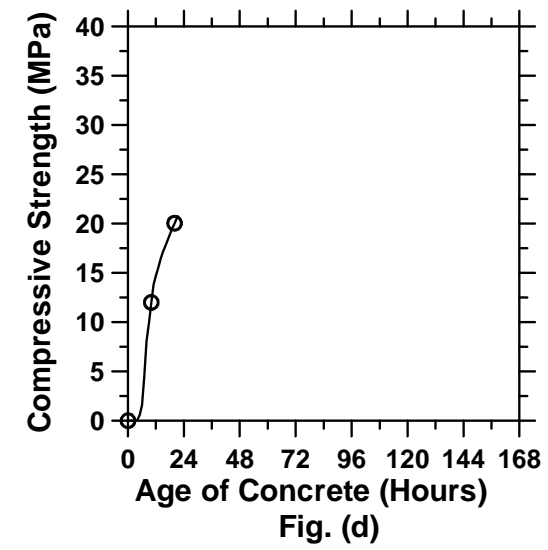
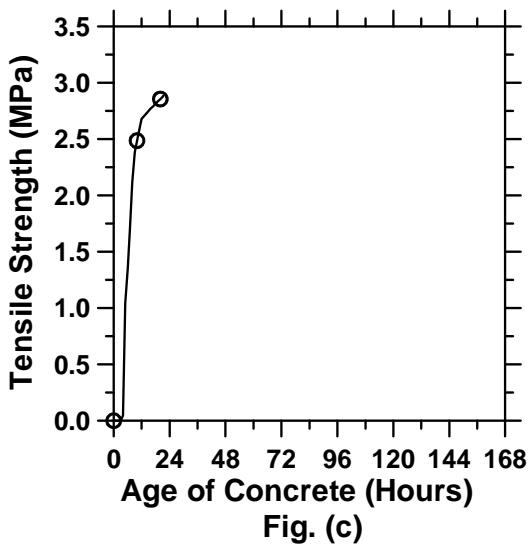
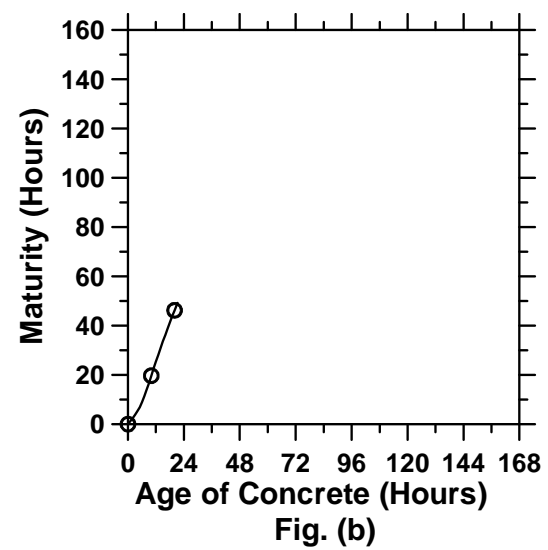
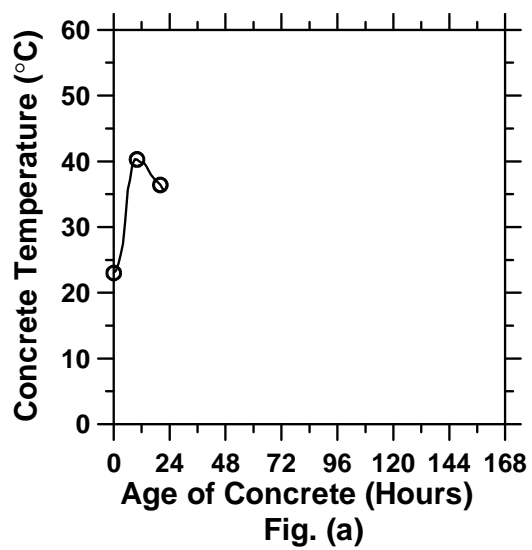


Figure A.103: Pavement cured at 23°C ambient temperature with a D/2 saw-cut depth introduced at 18 hours (cont'd).

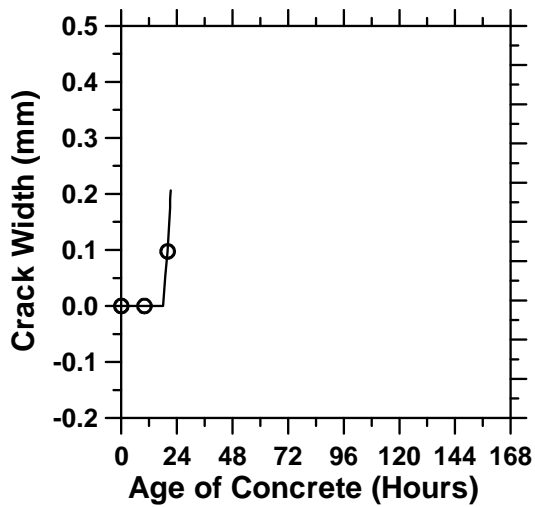


Fig. (e)

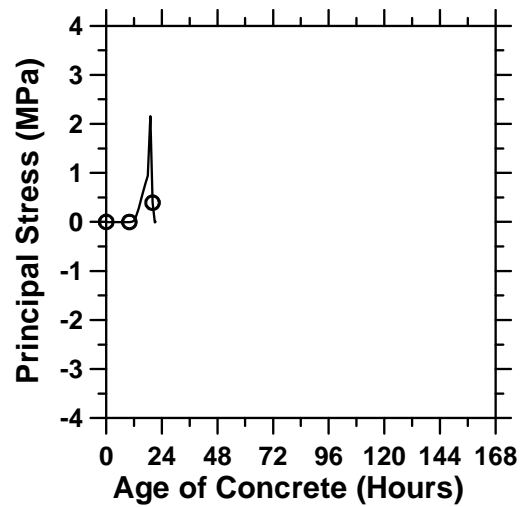


Fig. (f)

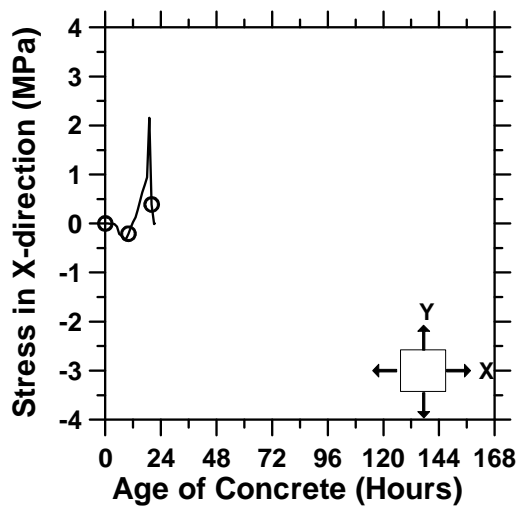


Fig. (g)

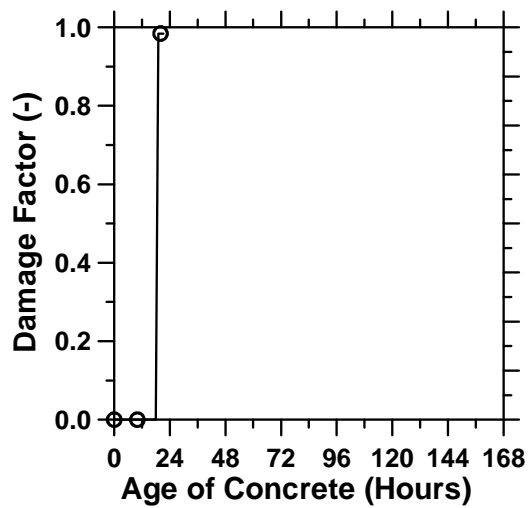


Fig. (h)

Figure A.103: Pavement cured at 23°C ambient temperature with a D/2 saw-cut depth introduced at 18 hours.

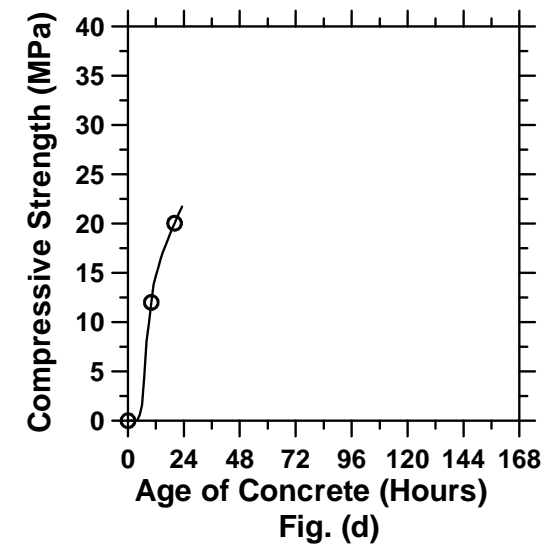
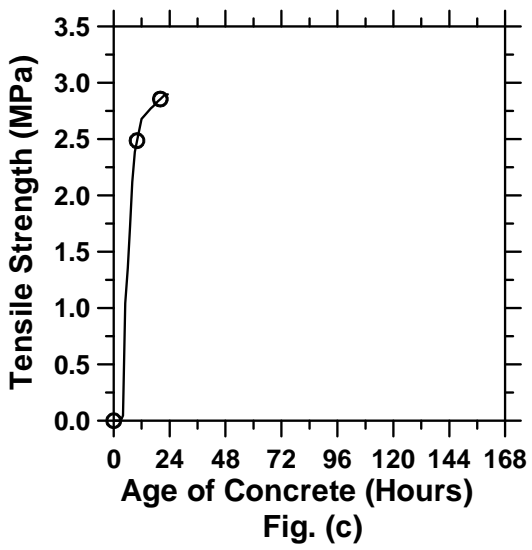
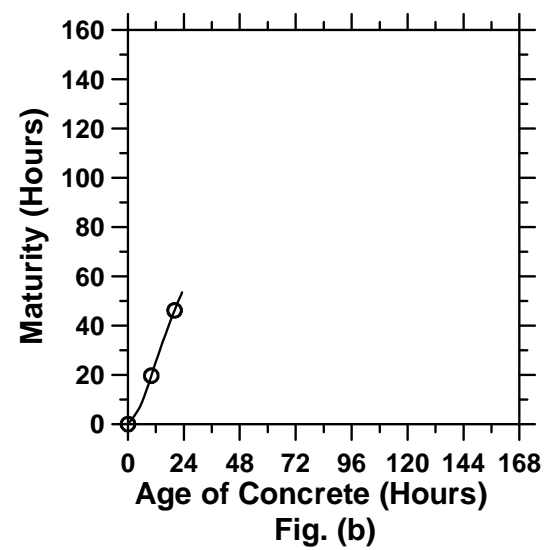
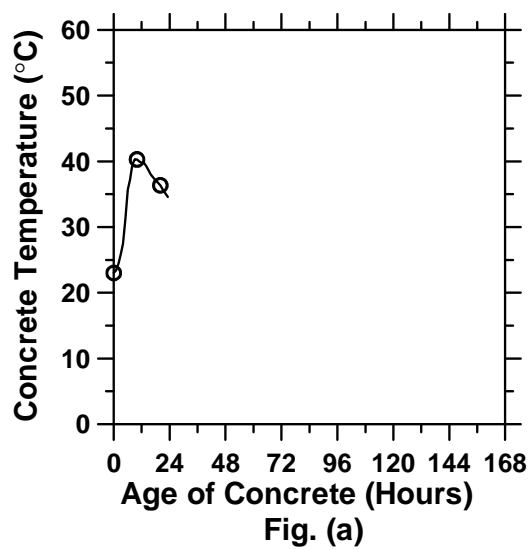


Figure A.104: Pavement cured at 23°C ambient temperature with a D/2 saw-cut depth introduced at 21 hours (cont'd).

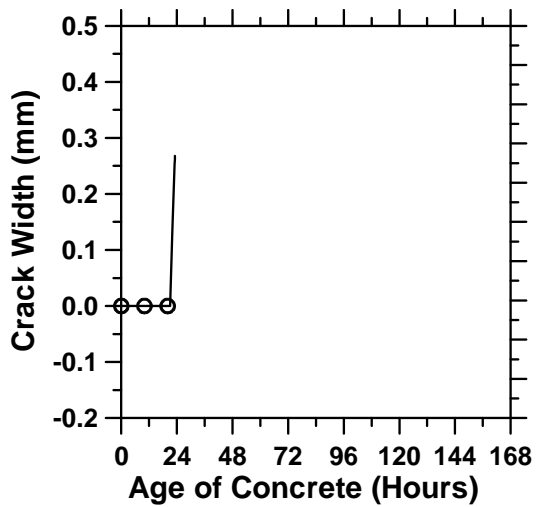


Fig. (e)

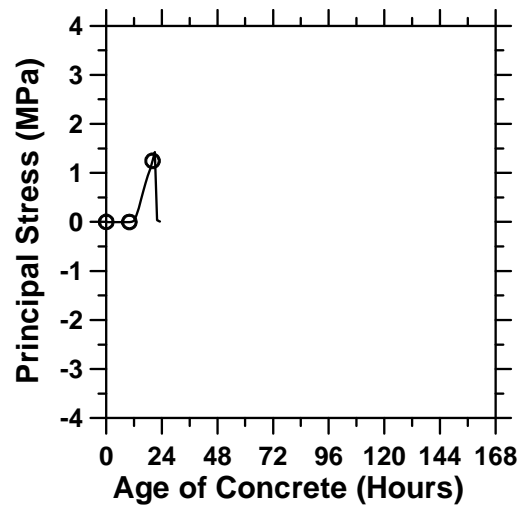


Fig. (f)

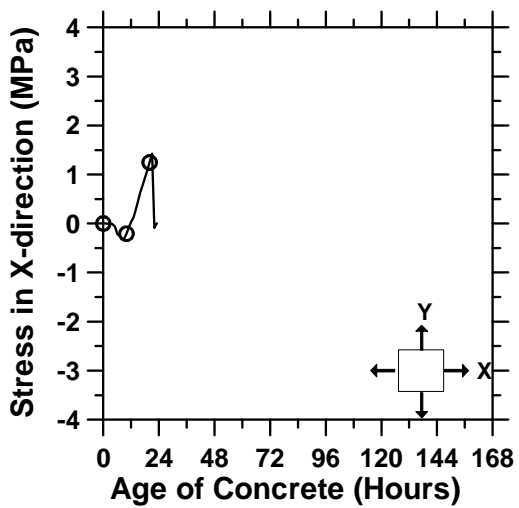


Fig. (g)

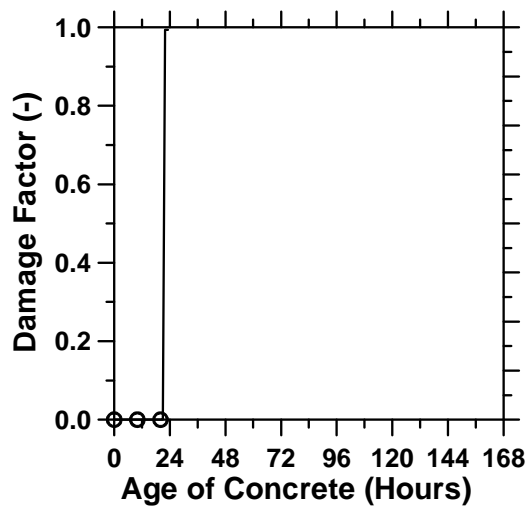


Fig. (h)

Figure A.104: Pavement cured at 23°C ambient temperature with a D/2 saw-cut depth introduced at 21 hours.

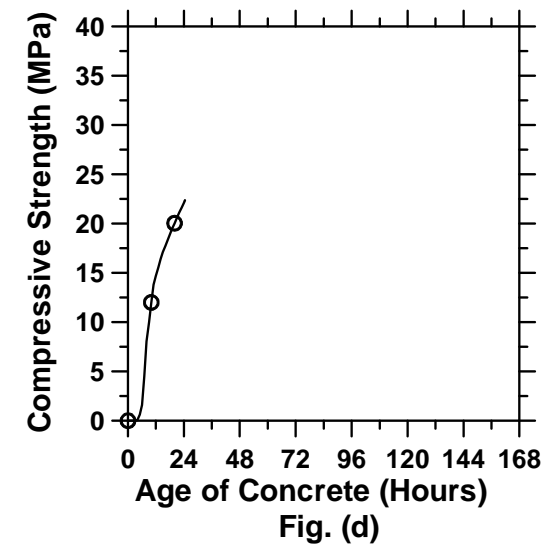
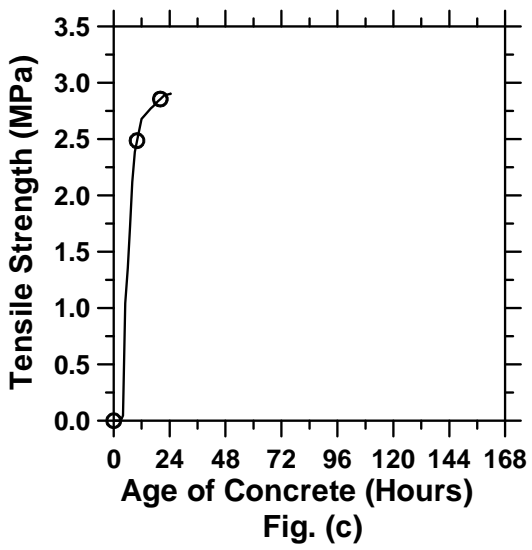
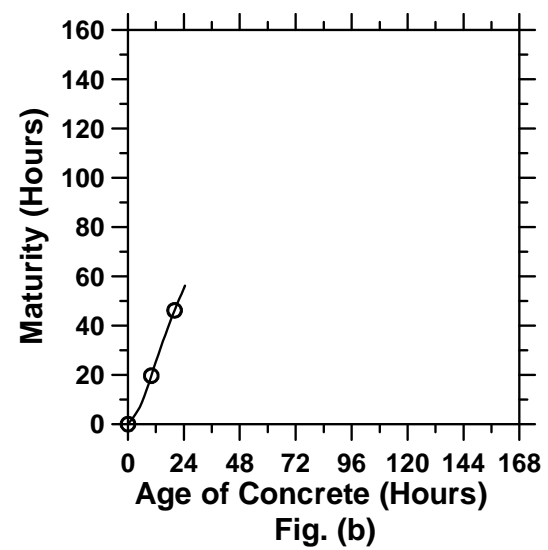
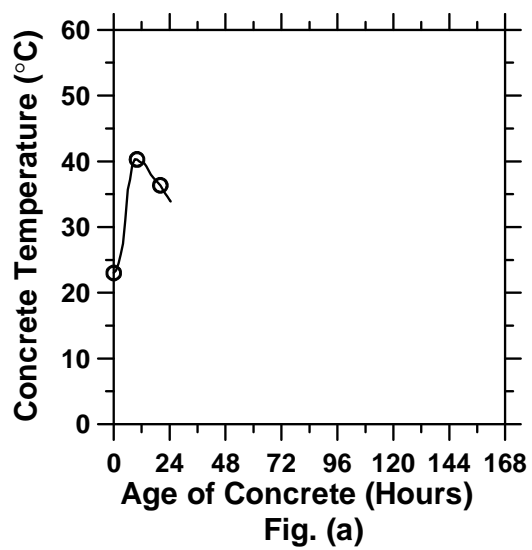


Figure A.105: Pavement cured at 23°C ambient temperature with a D/2 saw-cut depth introduced at 24 hours (cont'd).

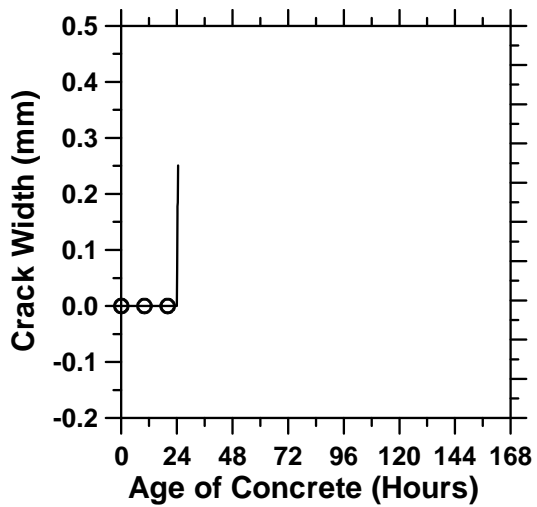


Fig. (e)

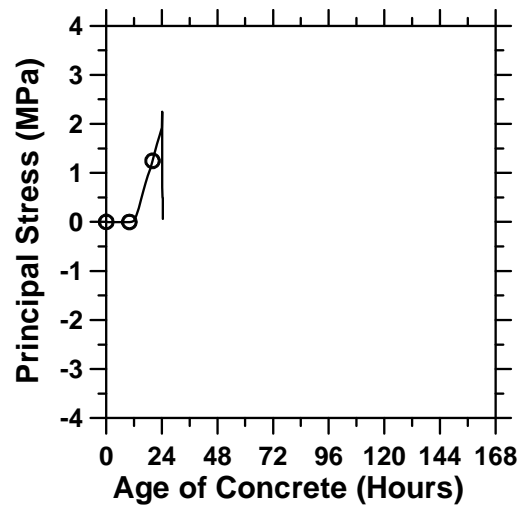


Fig. (f)

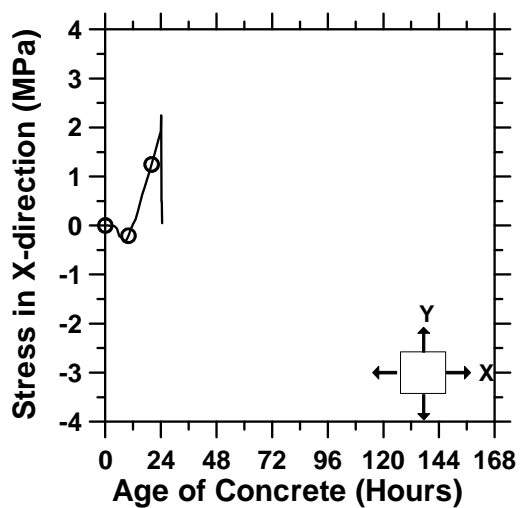


Fig. (g)

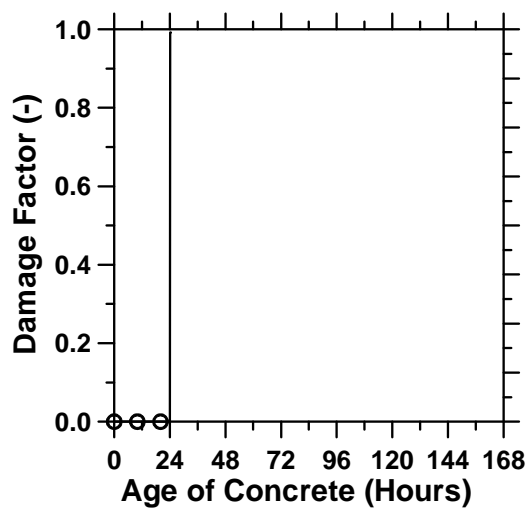


Fig. (h)

Figure A.105: Pavement cured at 23°C ambient temperature with a D/2 saw-cut depth introduced at 24 hours.

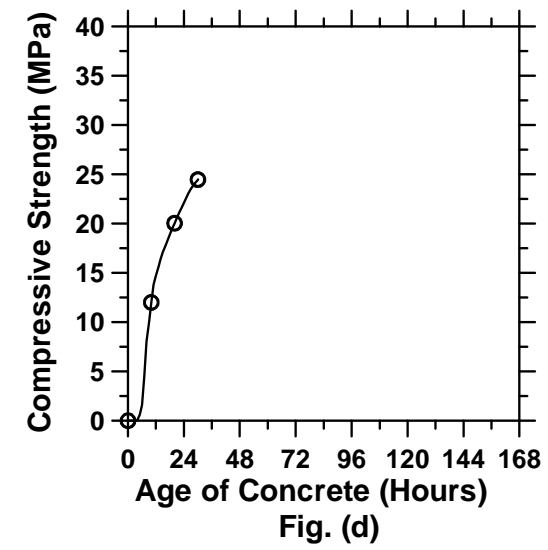
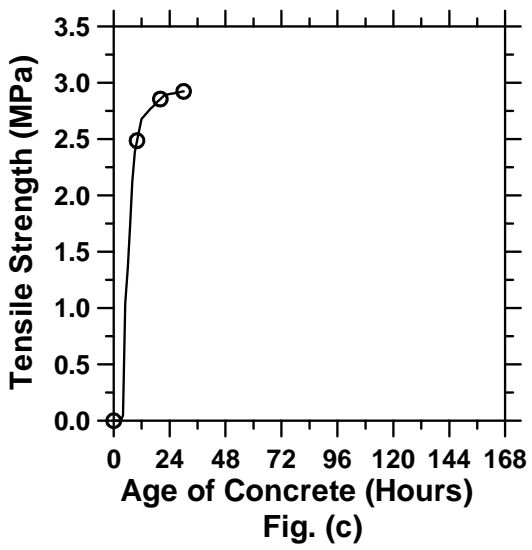
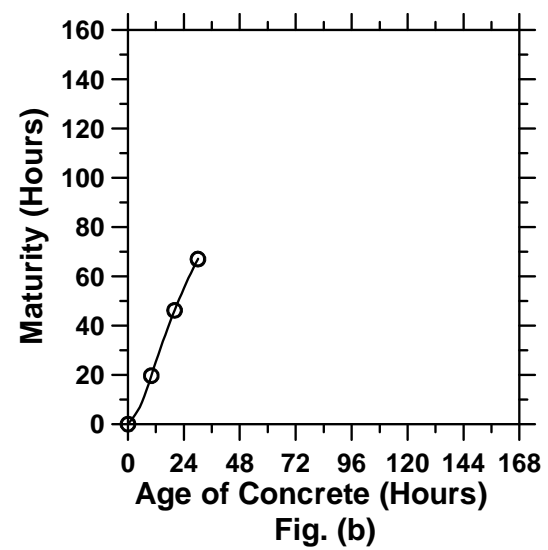
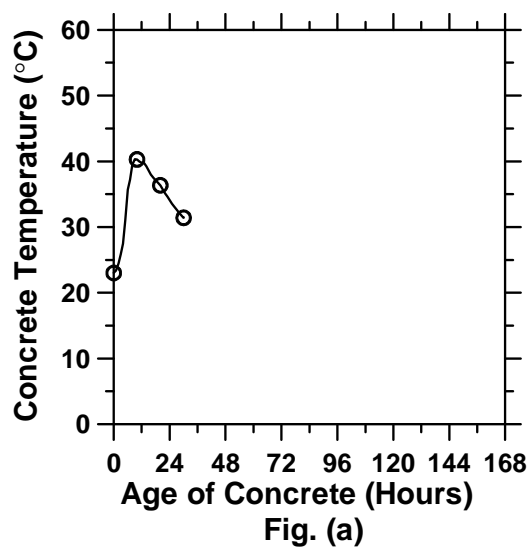


Figure A.106: Pavement cured at 23°C ambient temperature with a D/2 saw-cut depth introduced at 30 hours (cont'd).

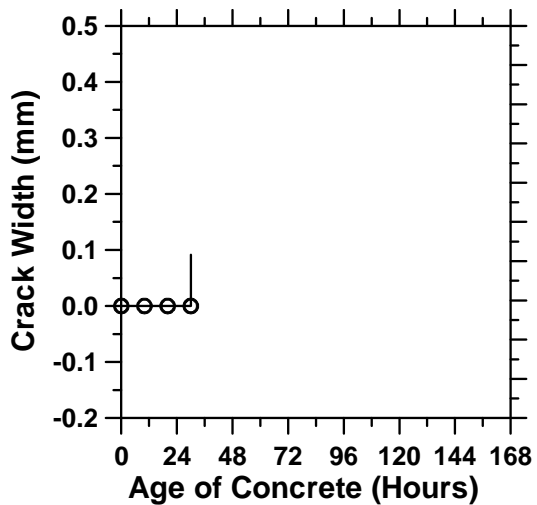


Fig. (e)

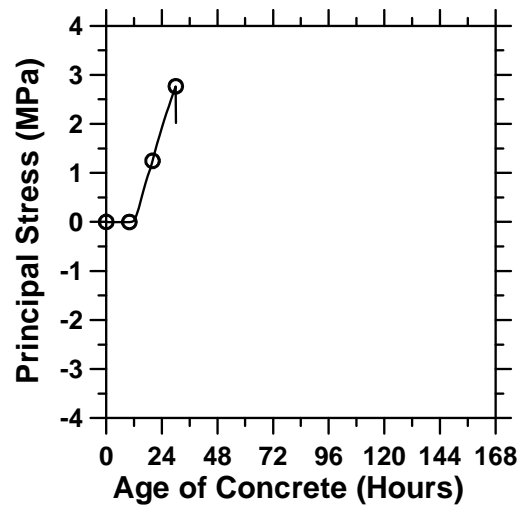


Fig. (f)

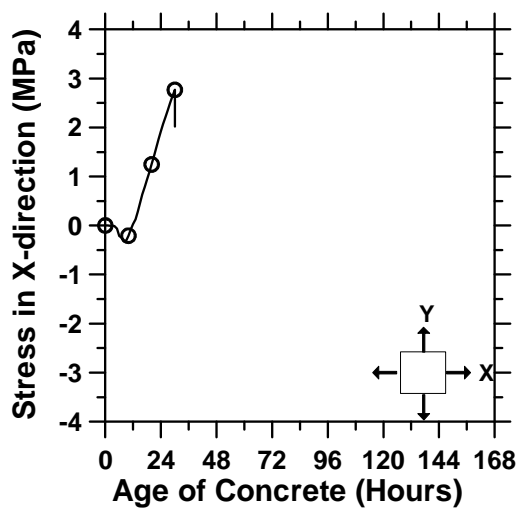


Fig. (g)

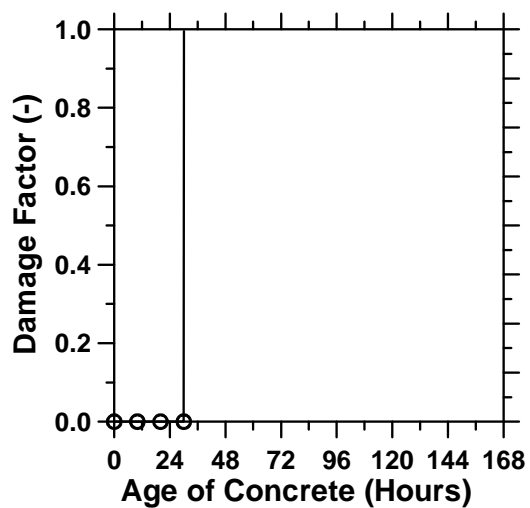


Fig. (h)

Figure A.106: Pavement cured at 23°C ambient temperature with a D/2 saw-cut depth introduced at 30 hours.

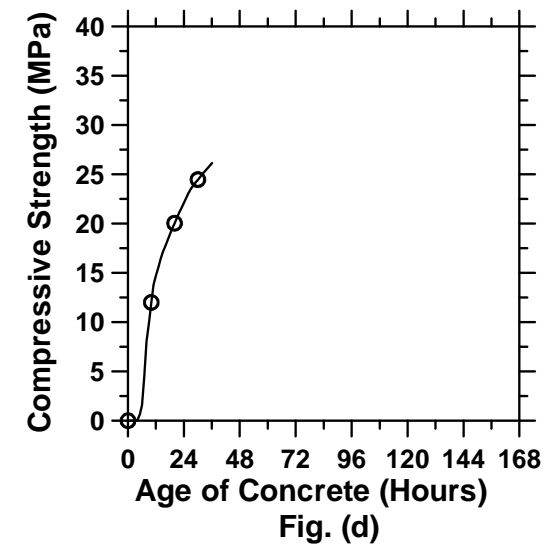
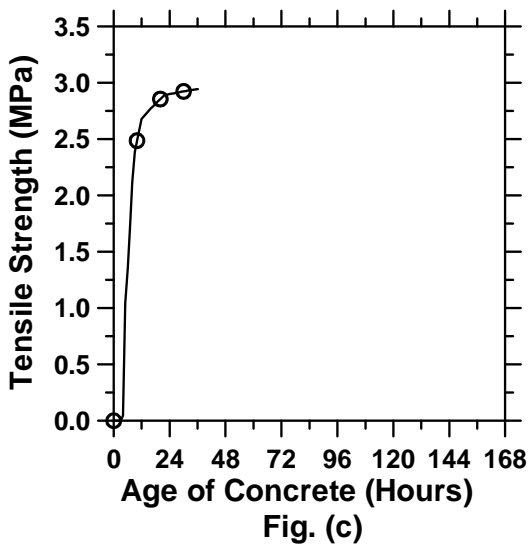
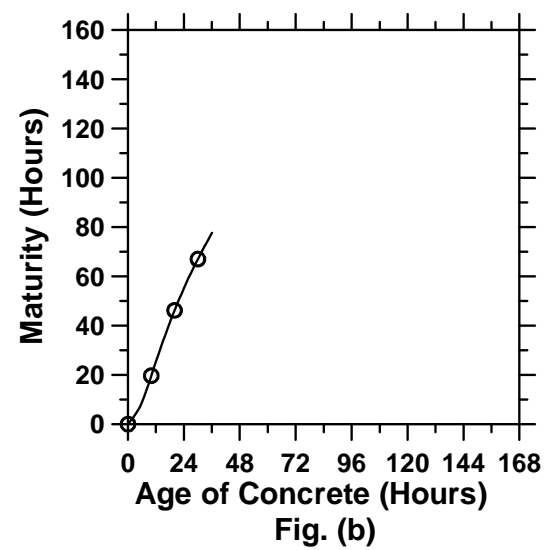
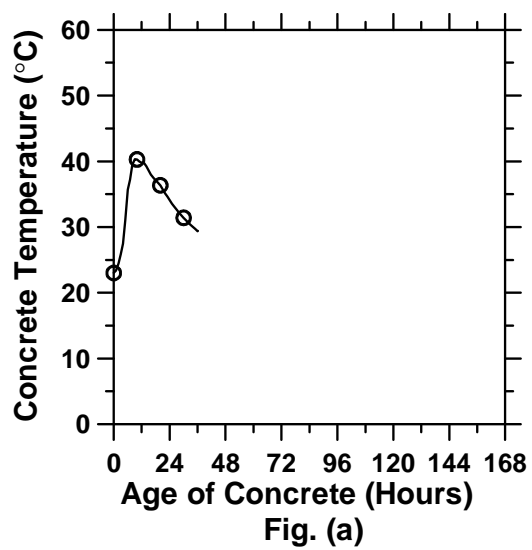


Figure A.107: Pavement cured at 23°C ambient temperature with a D/2 saw-cut depth introduced at 36 hours (cont'd).

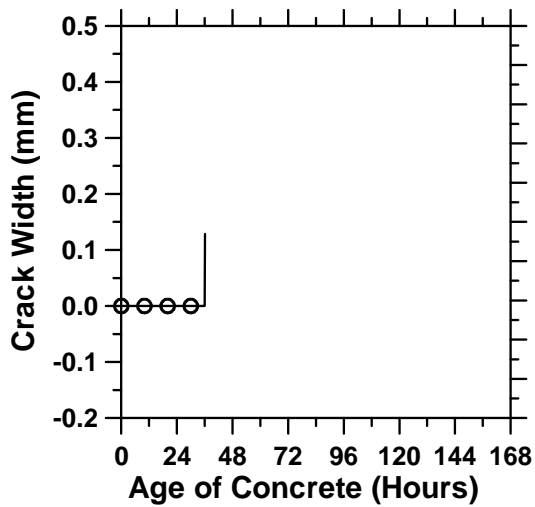


Fig. (e)

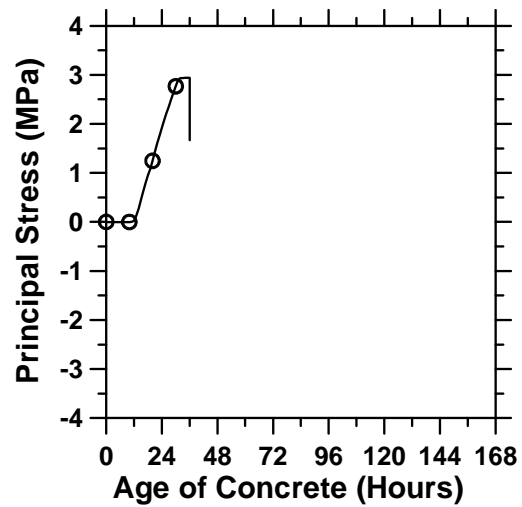


Fig. (f)

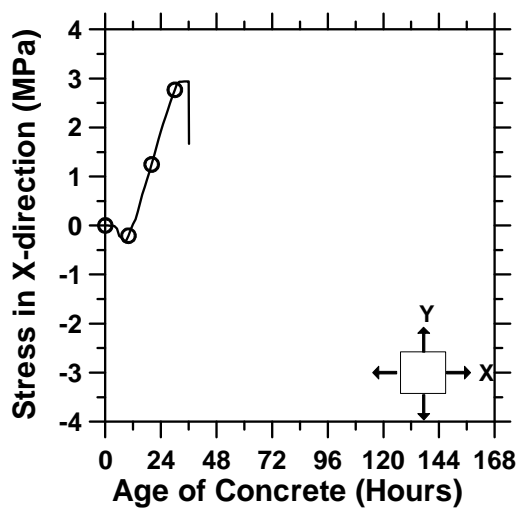


Fig. (g)

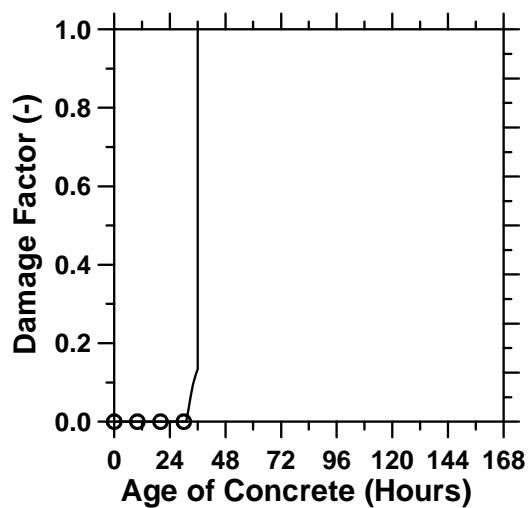


Fig. (h)

Figure A.107: Pavement cured at 23°C ambient temperature with a D/2 saw-cut depth introduced at 36 hours.

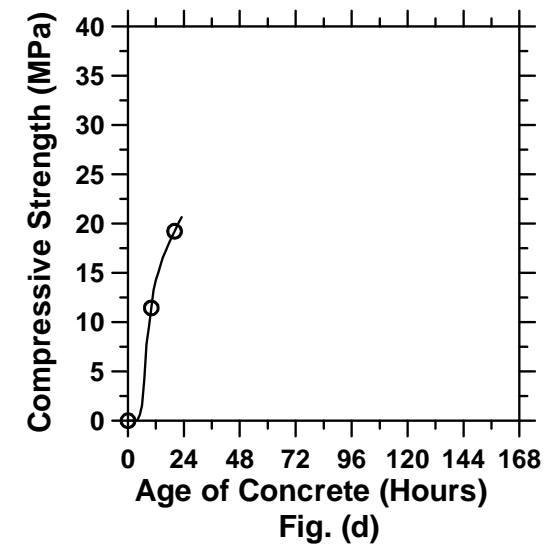
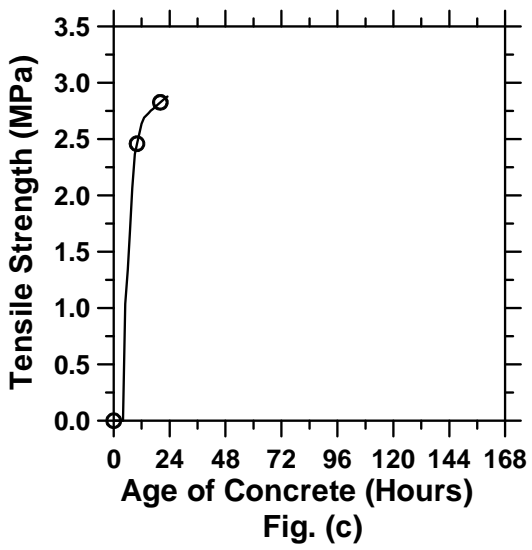
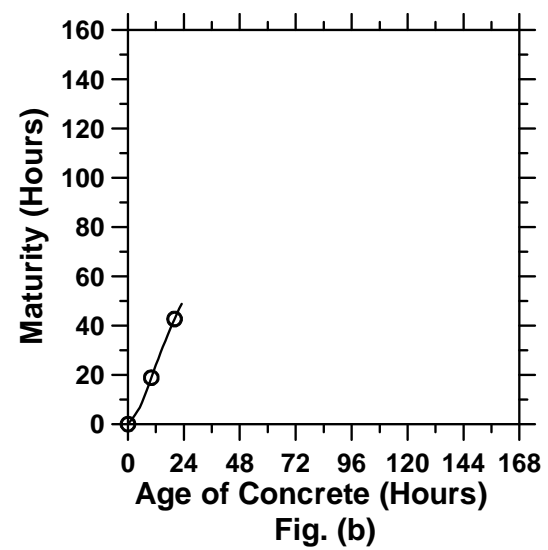
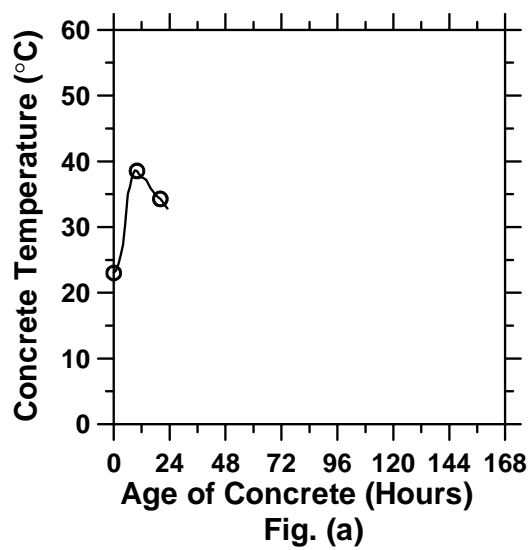


Figure A.108: Pavement cured at 23°C ambient temperature with a D/3 saw-cut depth introduced at 0 hour (cont'd).

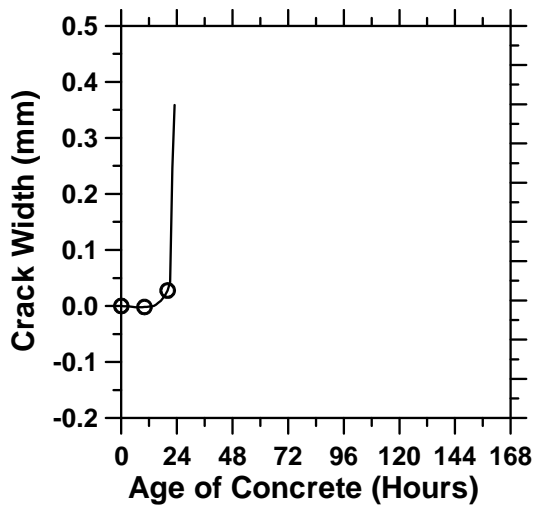


Fig. (e)

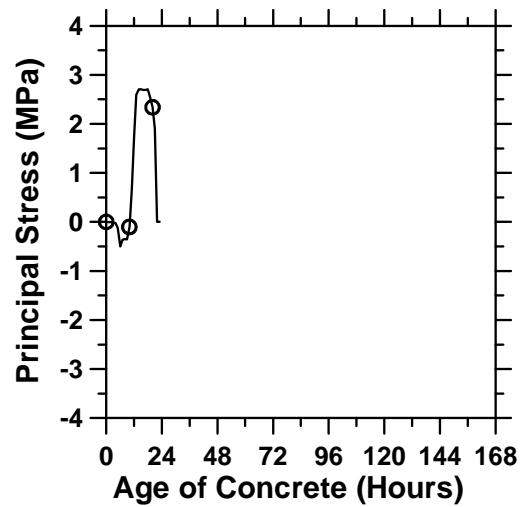


Fig. (f)

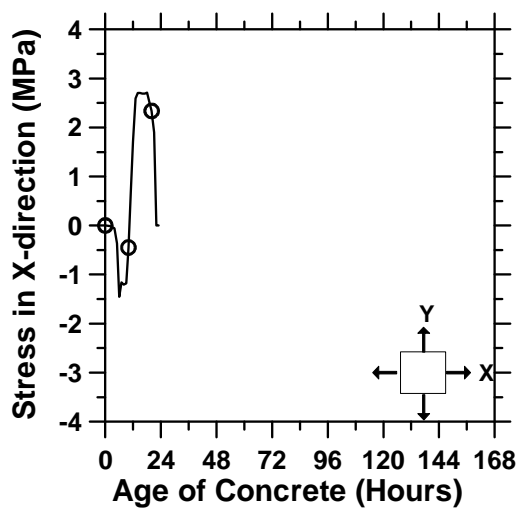


Fig. (g)

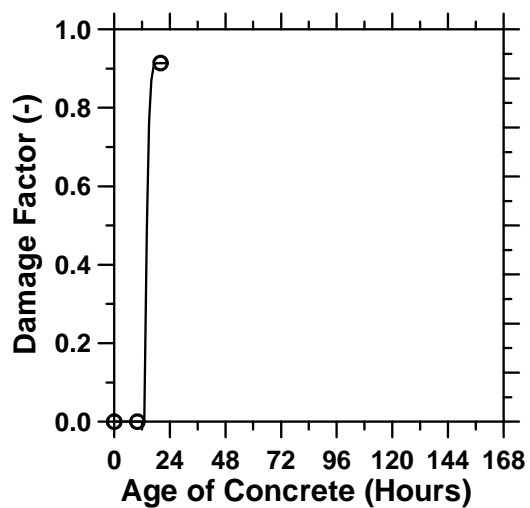


Fig. (h)

Figure A.108: Pavement cured at 23°C ambient temperature with a D/3 saw-cut depth introduced at 0 hour.

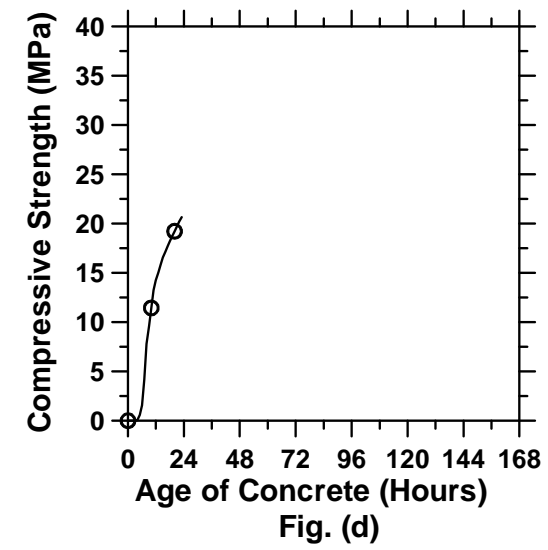
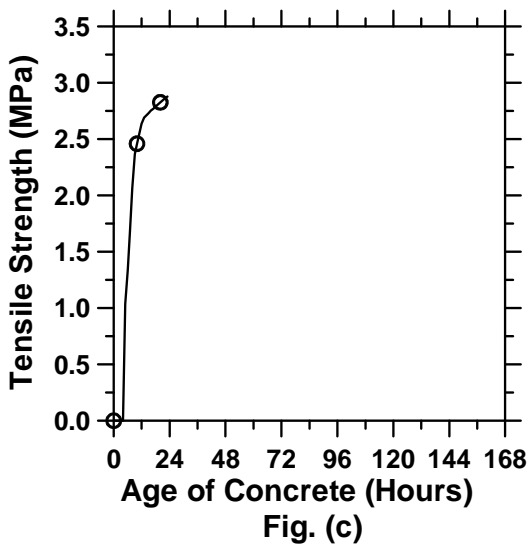
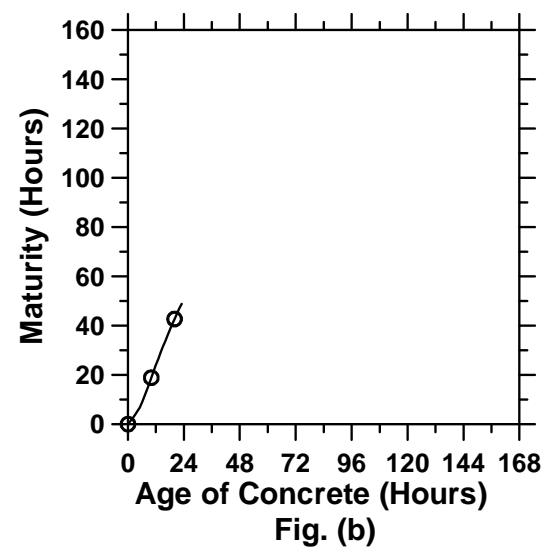
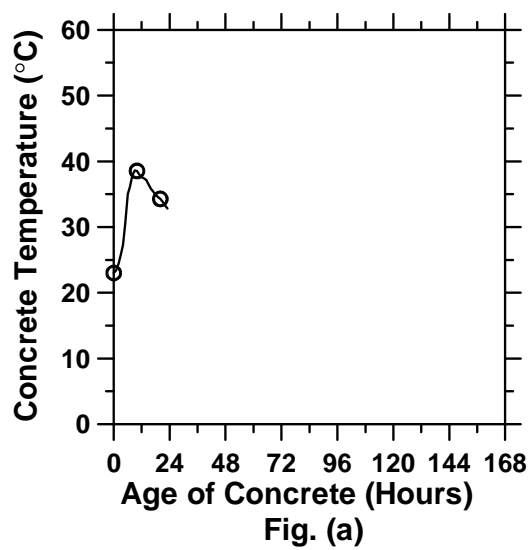


Figure A.109: Pavement cured at 23°C ambient temperature with a D/3 saw-cut depth introduced at 3 hours (cont'd).

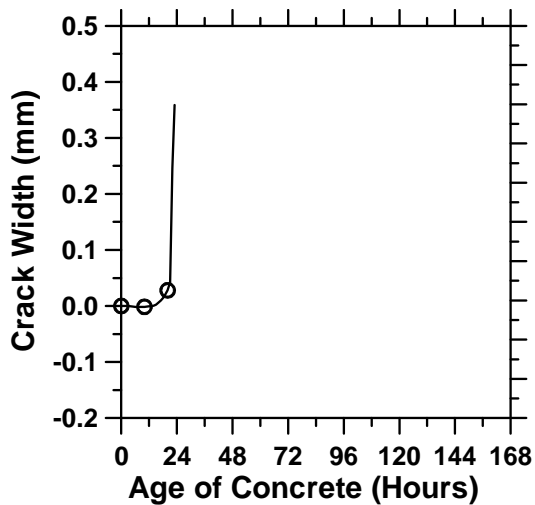


Fig. (e)

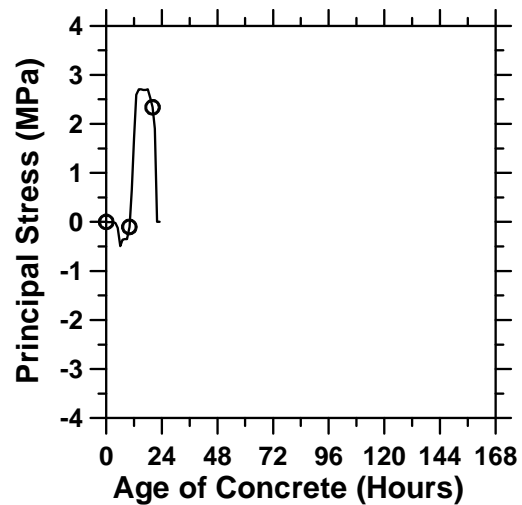


Fig. (f)

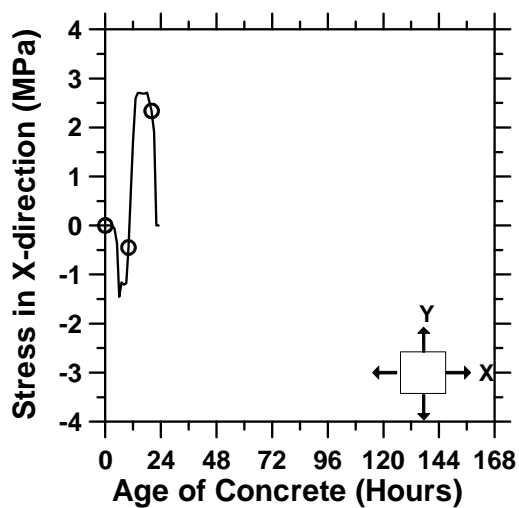


Fig. (g)

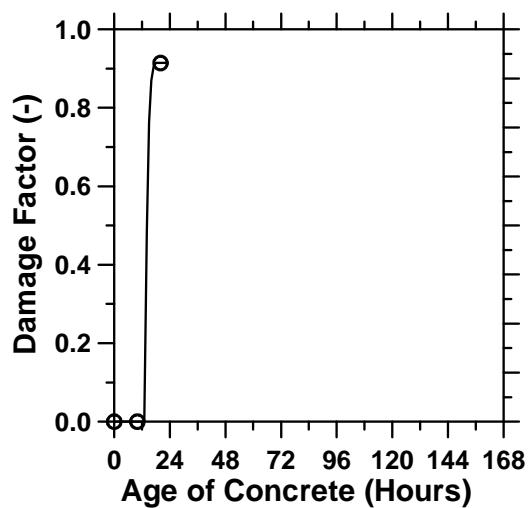


Fig. (h)

Figure A.109: Pavement cured at 23°C ambient temperature with a D/3 saw-cut depth introduced at 3 hours.

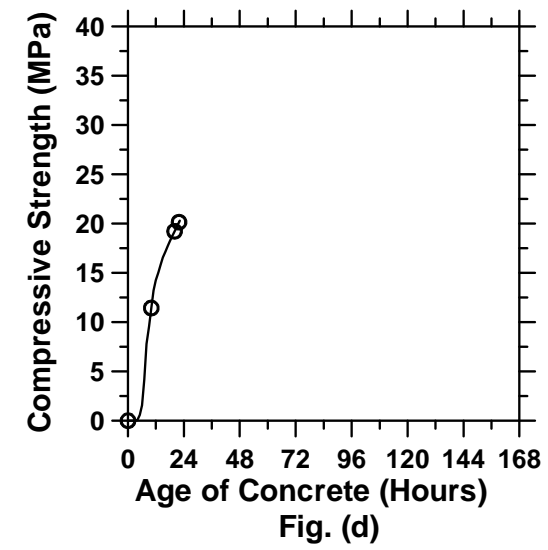
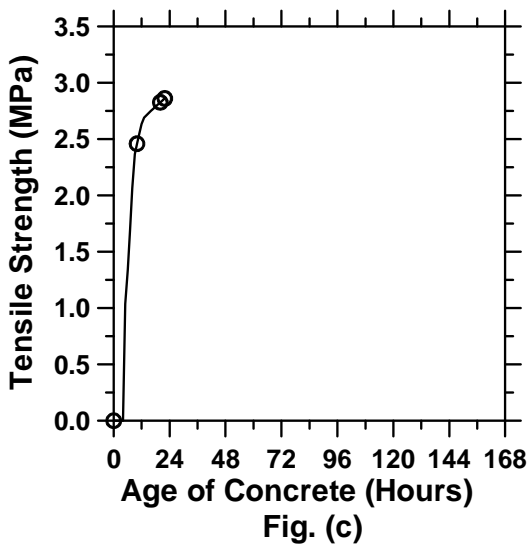
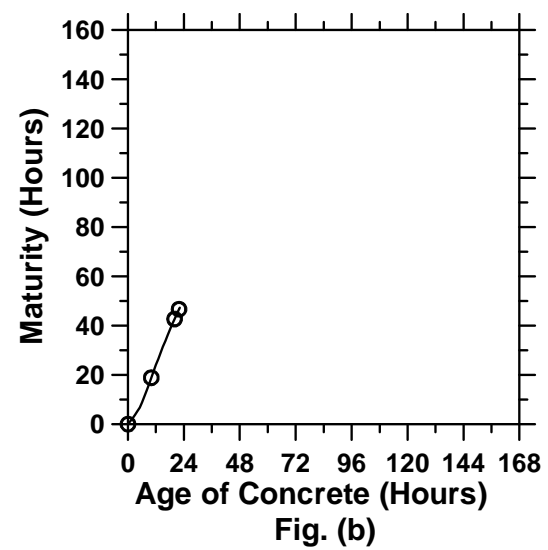
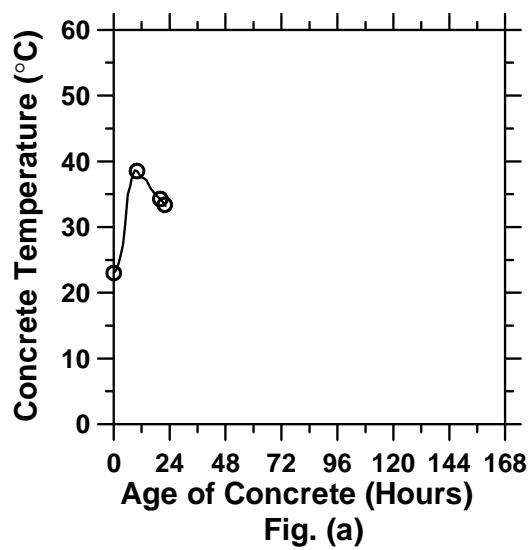


Figure A.110: Pavement cured at 23°C ambient temperature with a D/3 saw-cut depth introduced at 6 hours (cont'd).

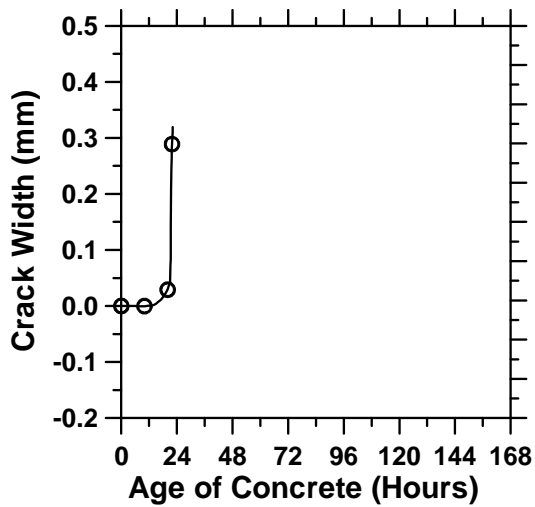


Fig. (e)

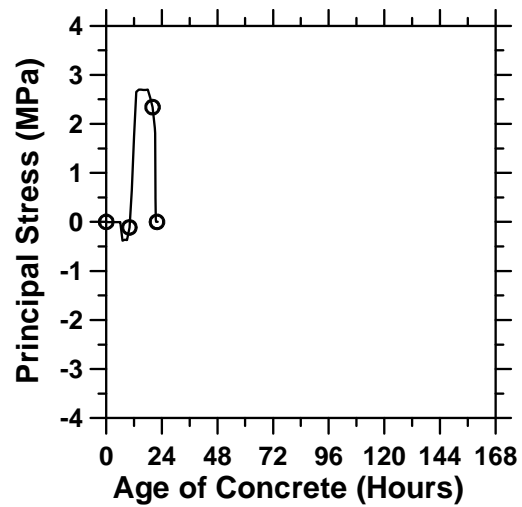


Fig. (f)

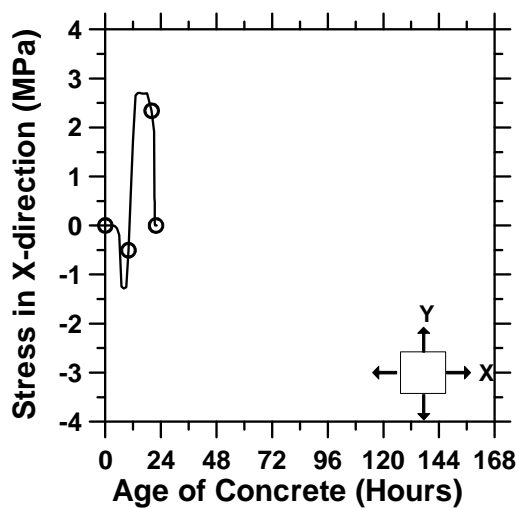


Fig. (g)

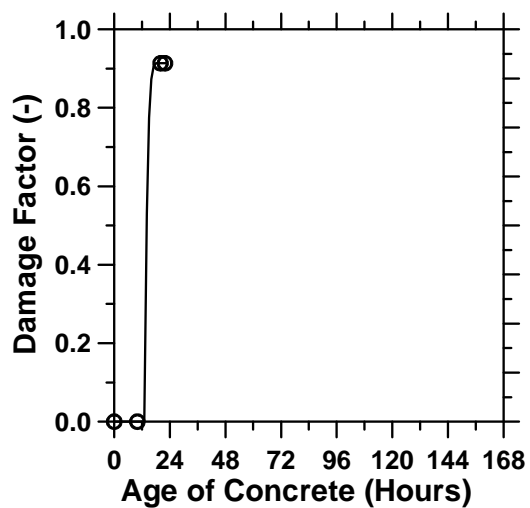


Fig. (h)

Figure A.110: Pavement cured at 23°C ambient temperature with a D/3 saw-cut depth introduced at 6 hours.

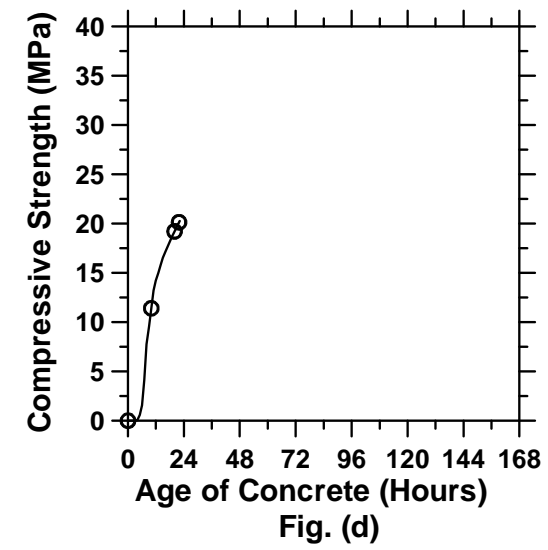
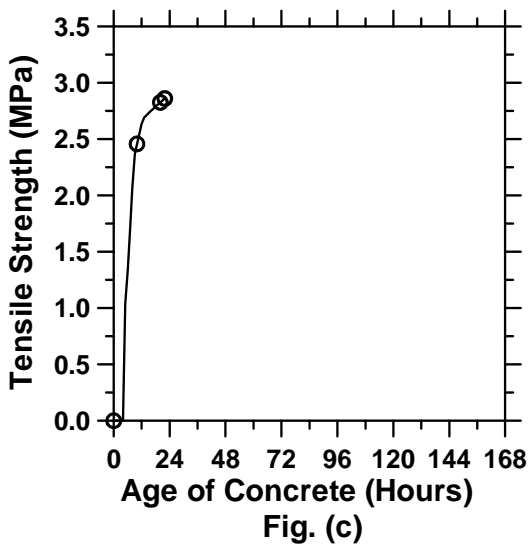
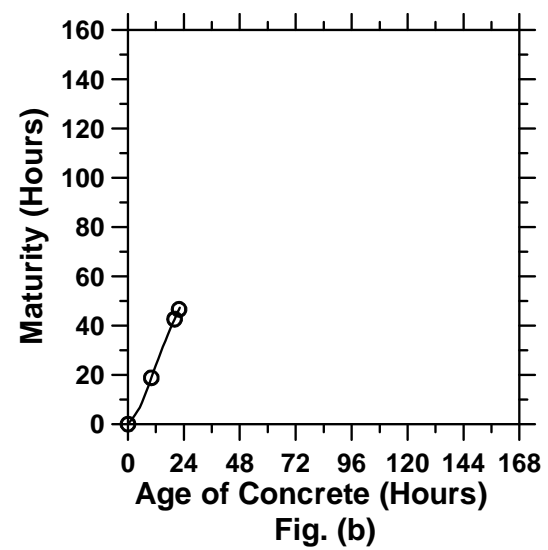
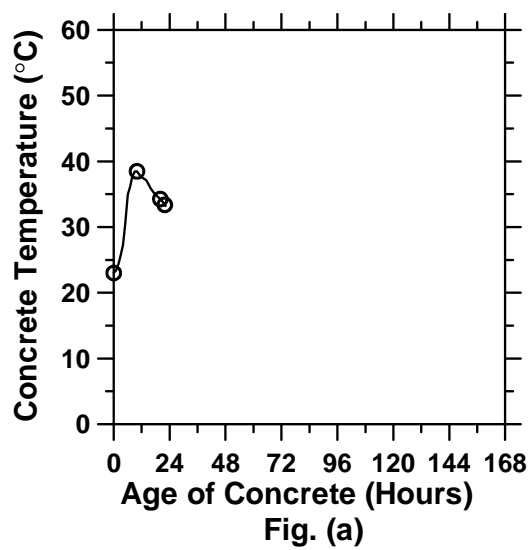


Figure A.111: Pavement cured at 23°C ambient temperature with a D/3 saw-cut depth introduced at 9 hours (cont'd).

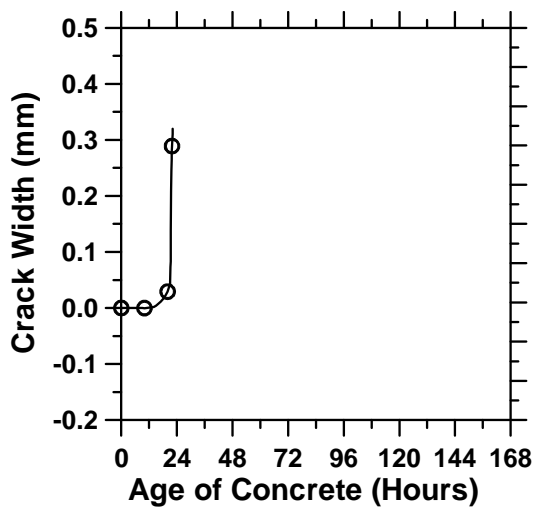


Fig. (e)

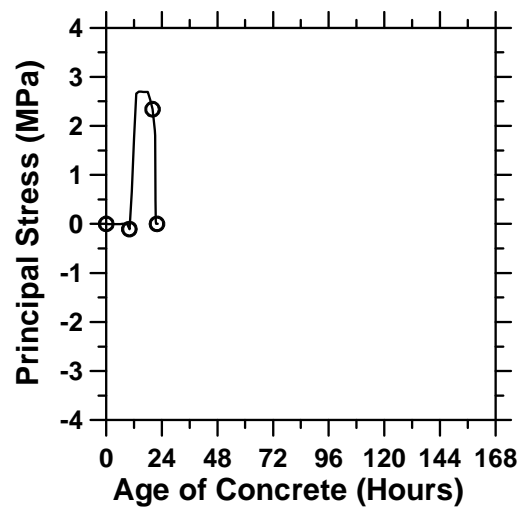


Fig. (f)

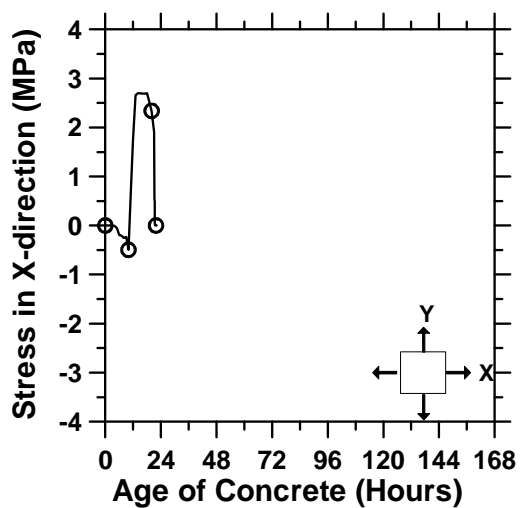


Fig. (g)

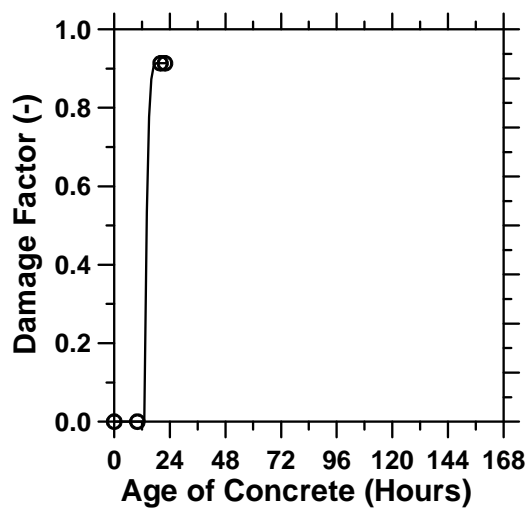


Fig. (h)

Figure A.111: Pavement cured at 23°C ambient temperature with a D/3 saw-cut depth introduced at 9 hours.

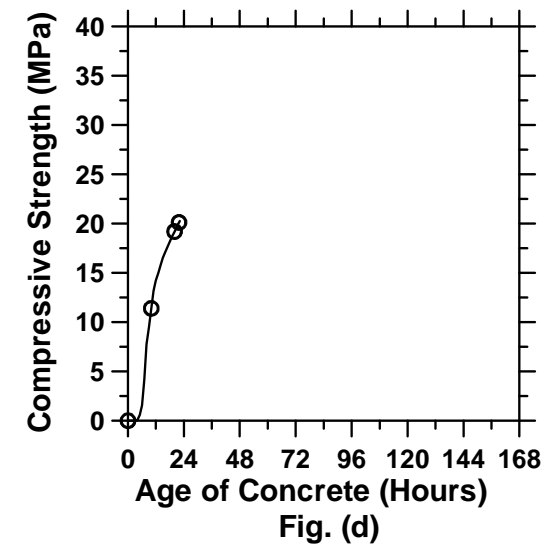
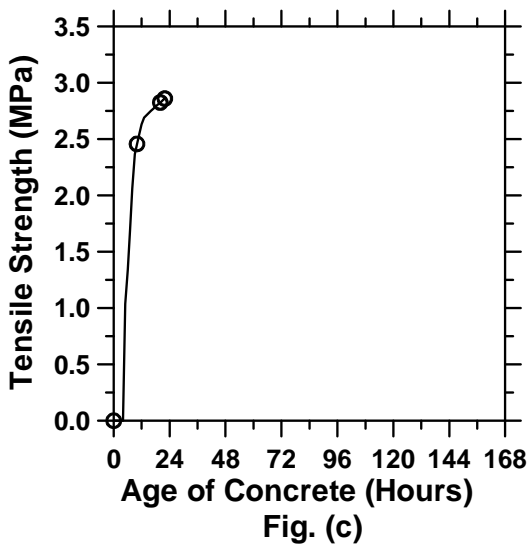
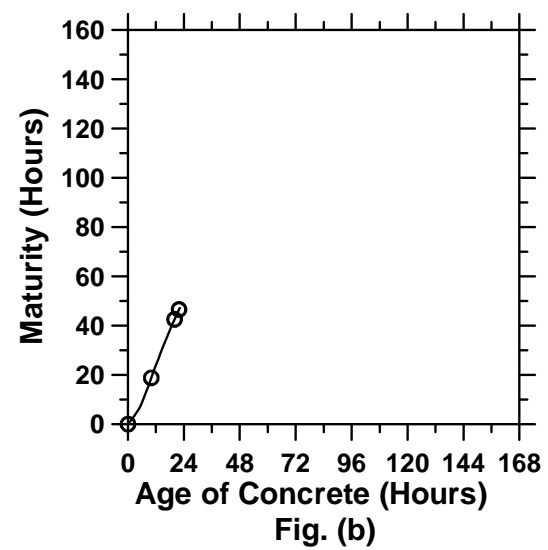
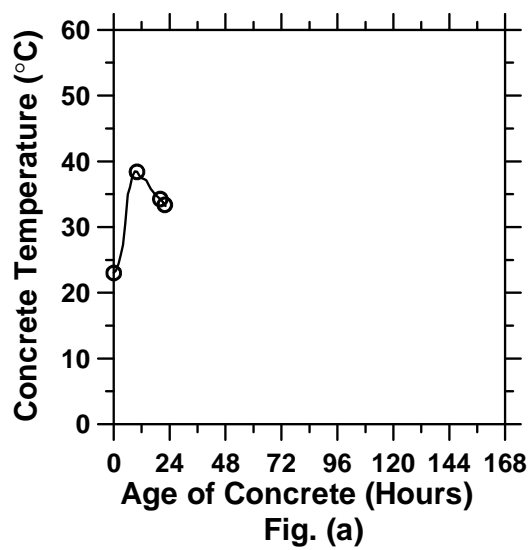


Figure A.112: Pavement cured at 23°C ambient temperature with a D/3 saw-cut depth introduced at 12 hours (cont'd).

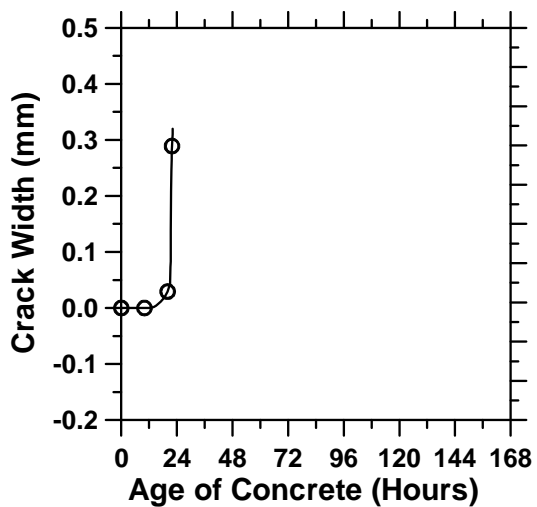


Fig. (e)

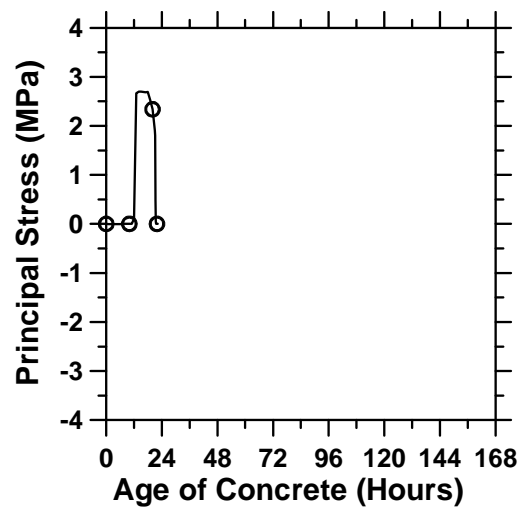


Fig. (f)

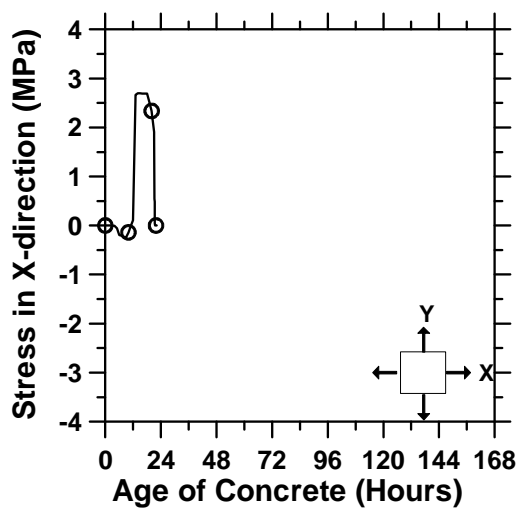


Fig. (g)

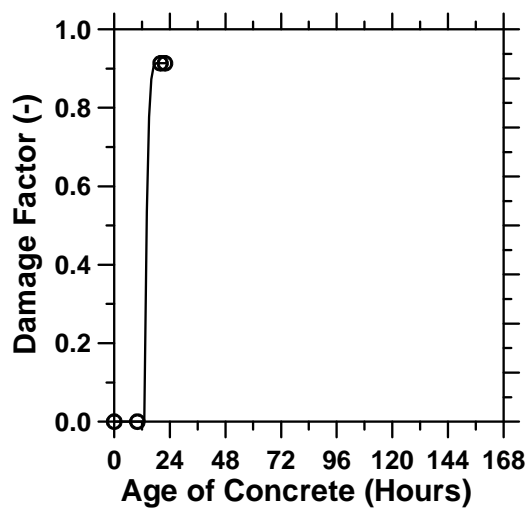


Fig. (h)

Figure A.112: Pavement cured at 23°C ambient temperature with a D/3 saw-cut depth introduced at 12 hours.

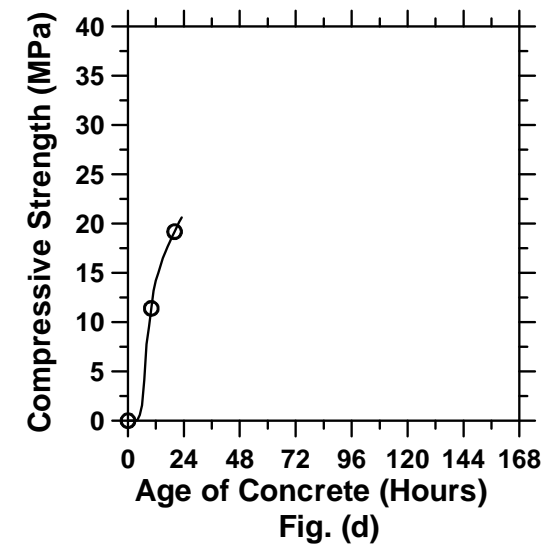
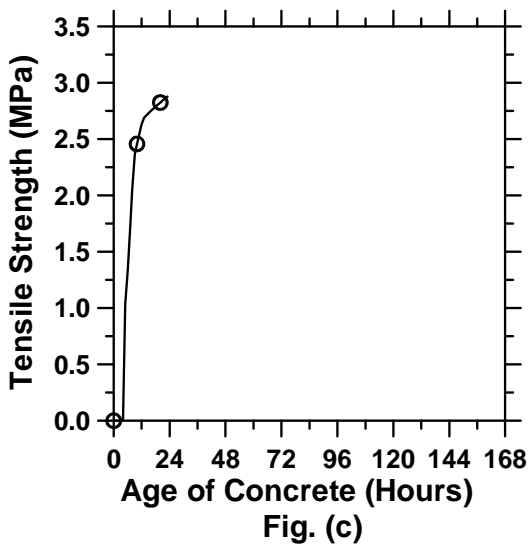
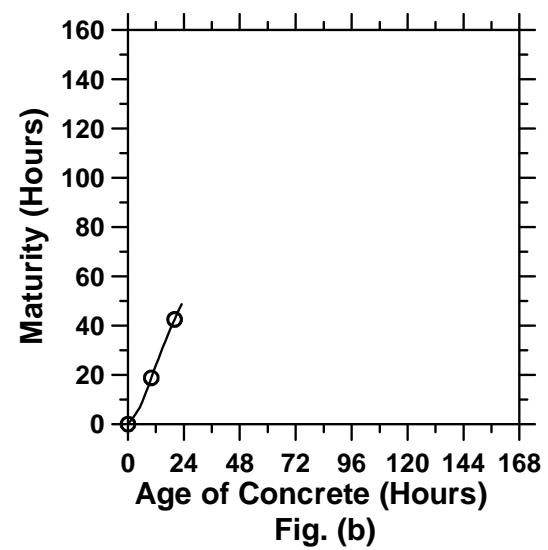
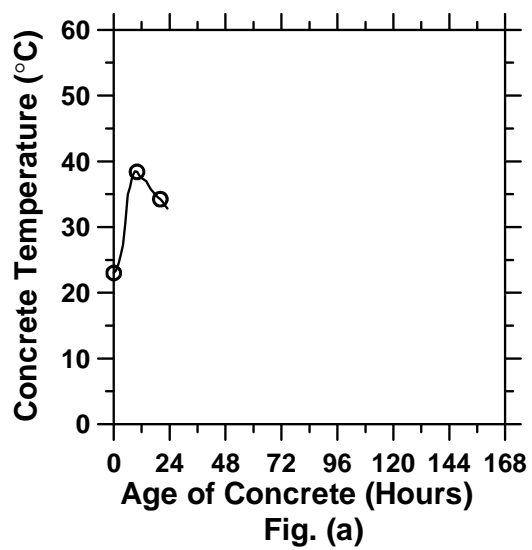


Figure A.113: Pavement cured at 23°C ambient temperature with a D/3 saw-cut depth introduced at 15 hours (cont'd).

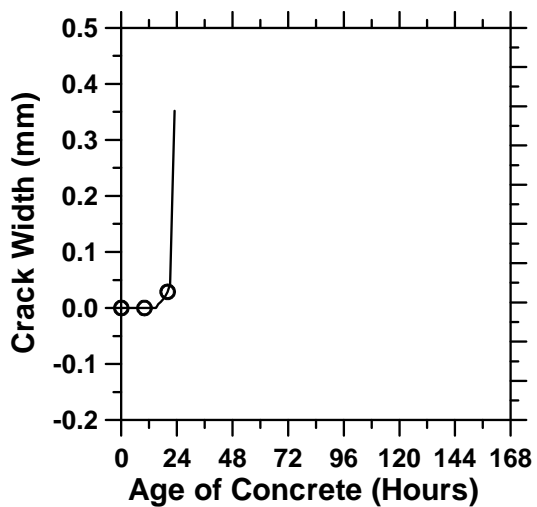


Fig. (e)

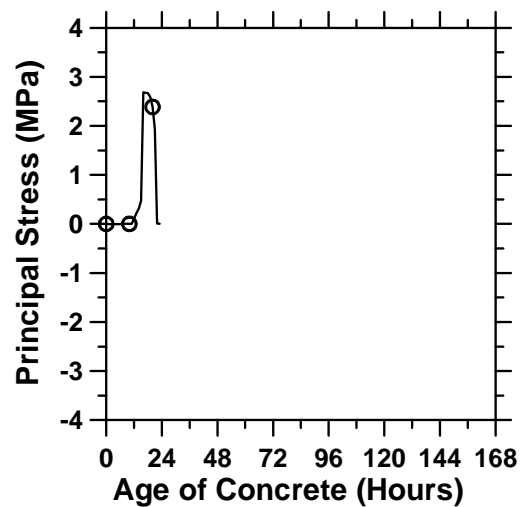


Fig. (f)

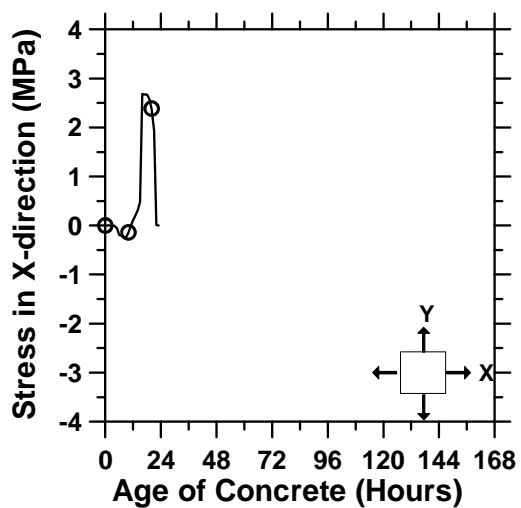


Fig. (g)

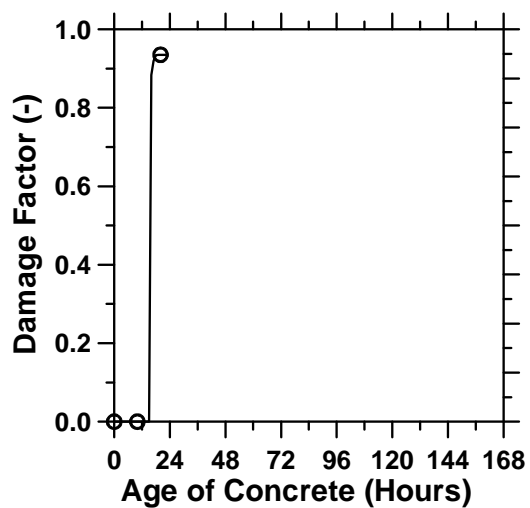


Fig. (h)

Figure A.113: Pavement cured at 23°C ambient temperature with a D/3 saw-cut depth introduced at 15 hours.

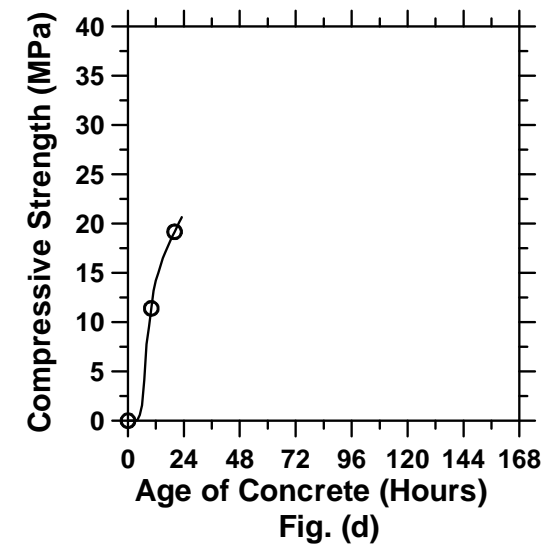
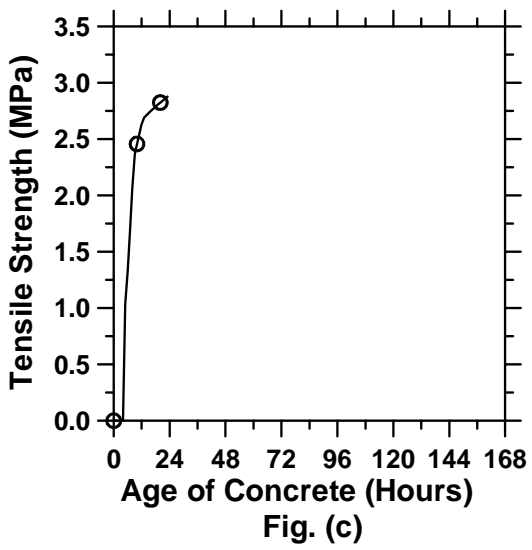
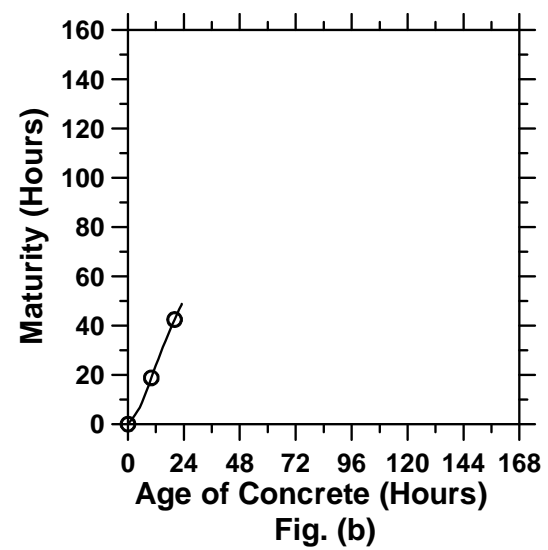
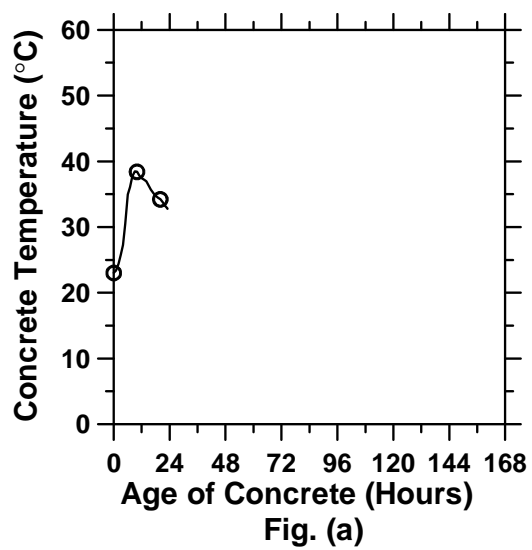


Figure A.114: Pavement cured at 23°C ambient temperature with a D/3 saw-cut depth introduced at 18 hours (cont'd).

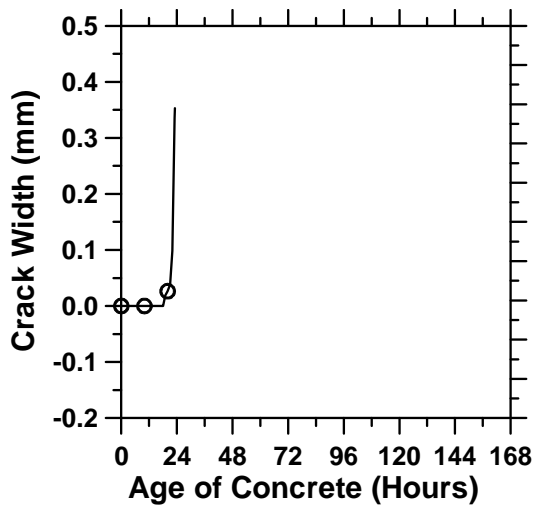


Fig. (e)

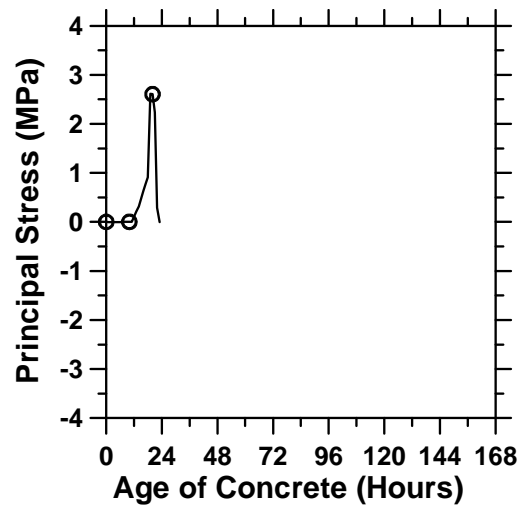


Fig. (f)

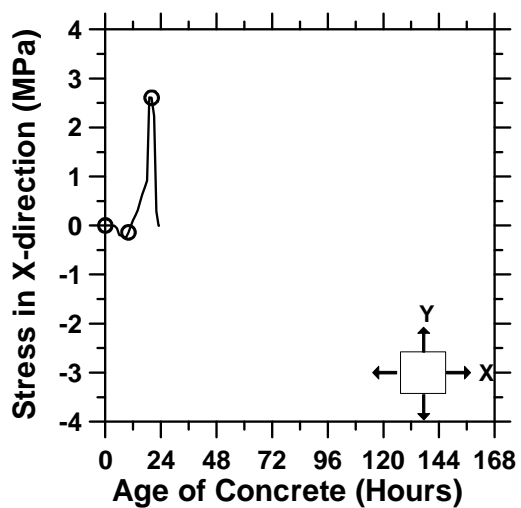


Fig. (g)

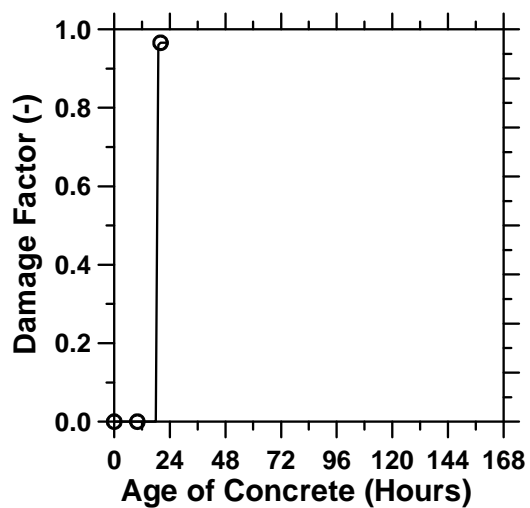


Fig. (h)

Figure A.114: Pavement cured at 23°C ambient temperature with a D/3 saw-cut depth introduced at 18 hours.

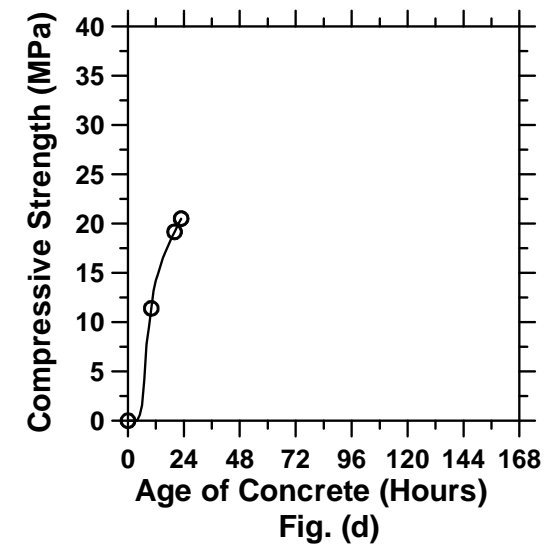
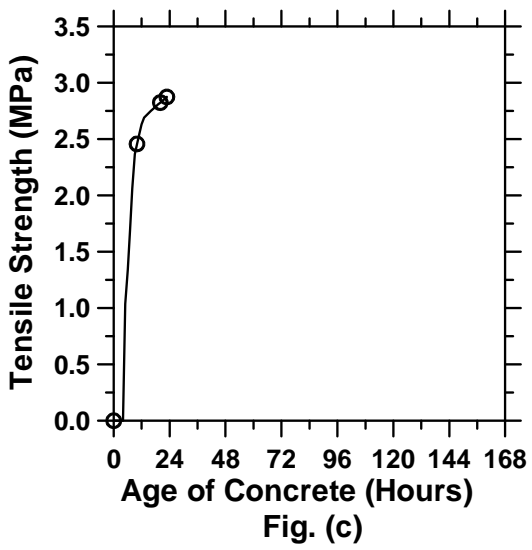
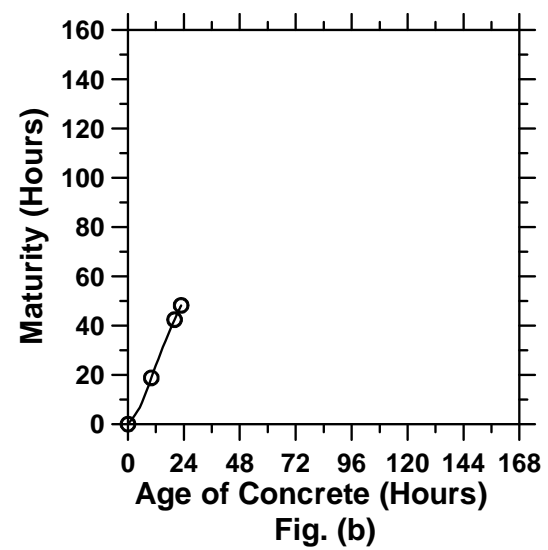
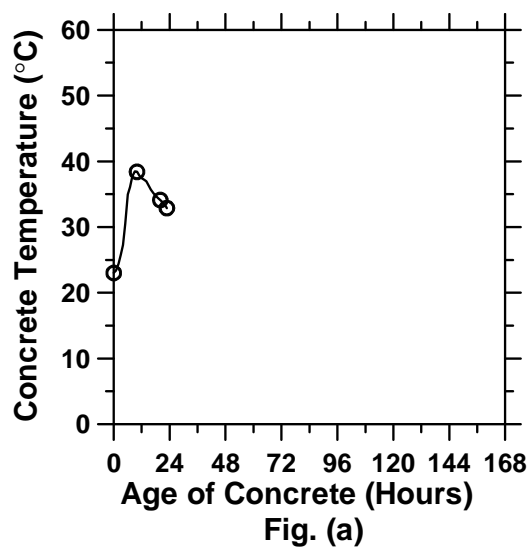


Figure A.115: Pavement cured at 23°C ambient temperature with a D/3 saw-cut depth introduced at 20 hours (cont'd).

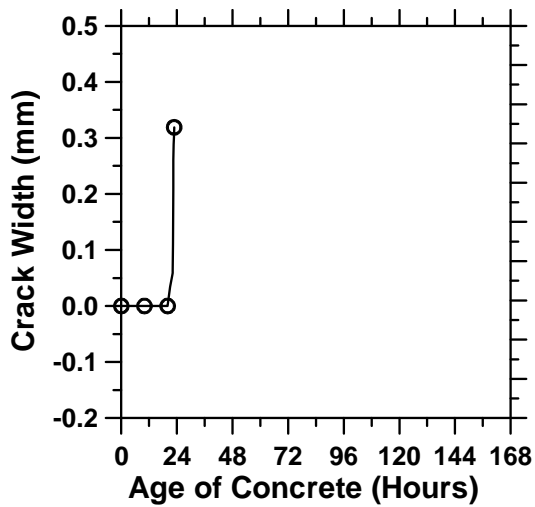


Fig. (e)

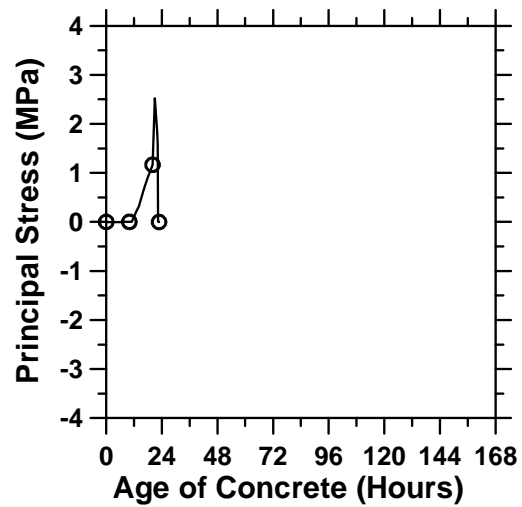


Fig. (f)

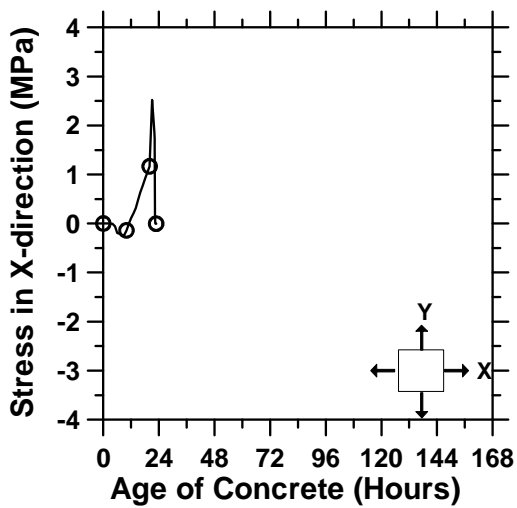


Fig. (g)

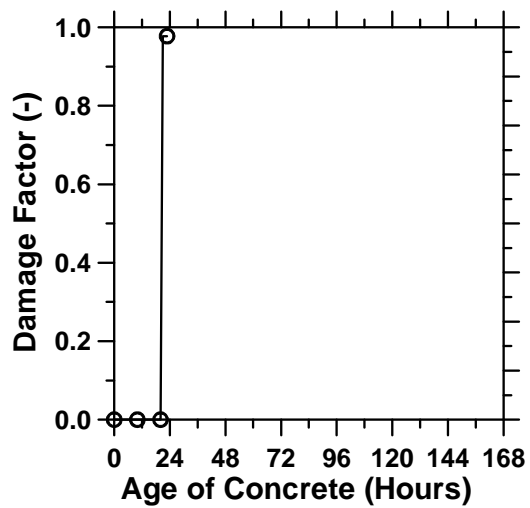


Fig. (h)

Figure A.115: Pavement cured at 23°C ambient temperature with a D/3 saw-cut depth introduced at 20 hours.

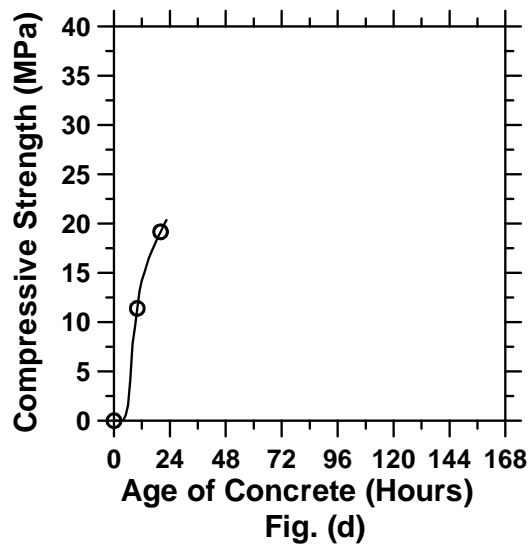
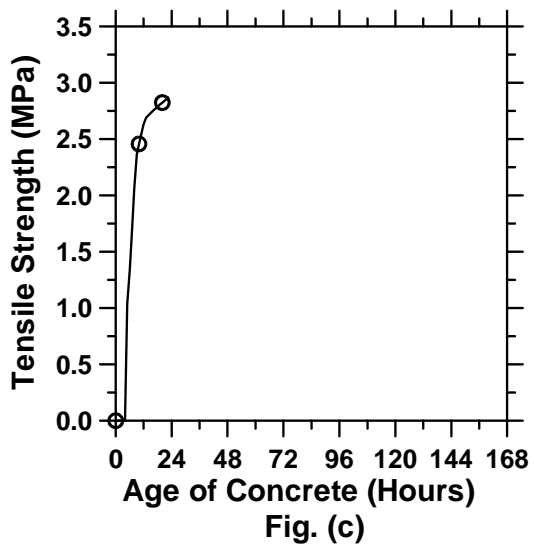
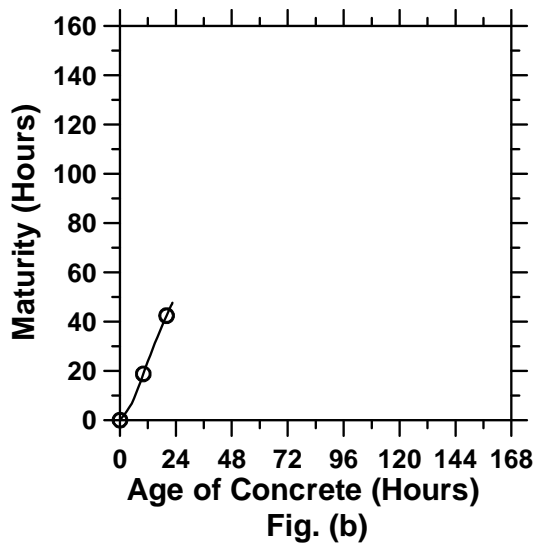
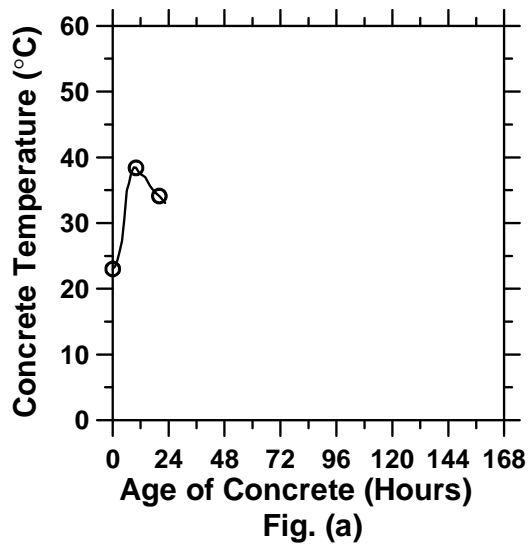


Figure A.116: Pavement cured at 23°C ambient temperature with a D/3 saw-cut depth introduced at 21 hour (cont'd).

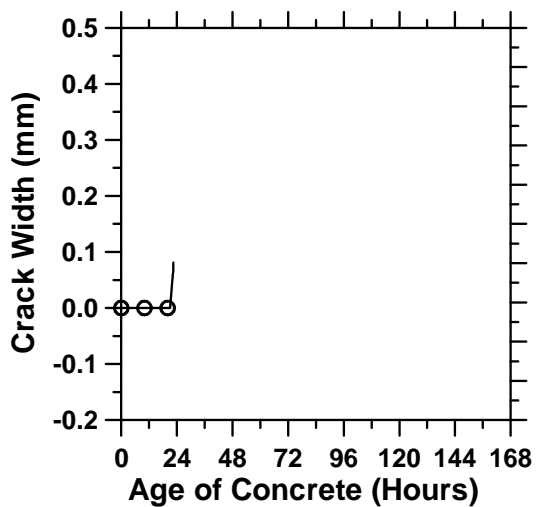


Fig. (e)

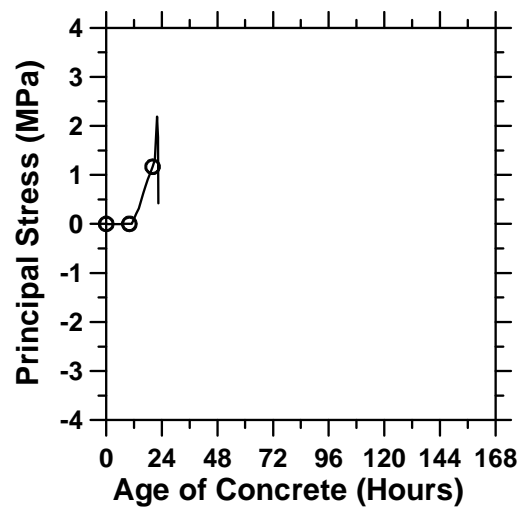


Fig. (f)

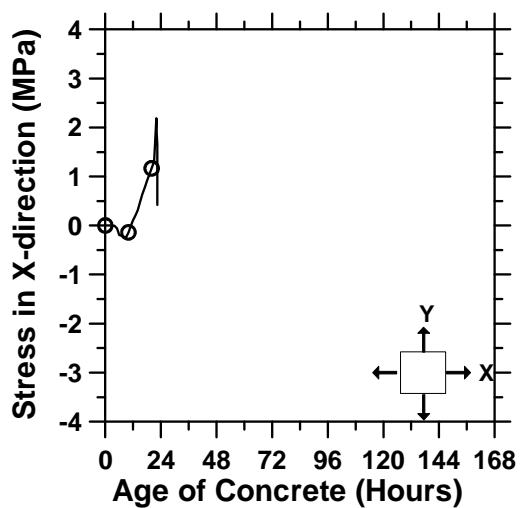


Fig. (g)

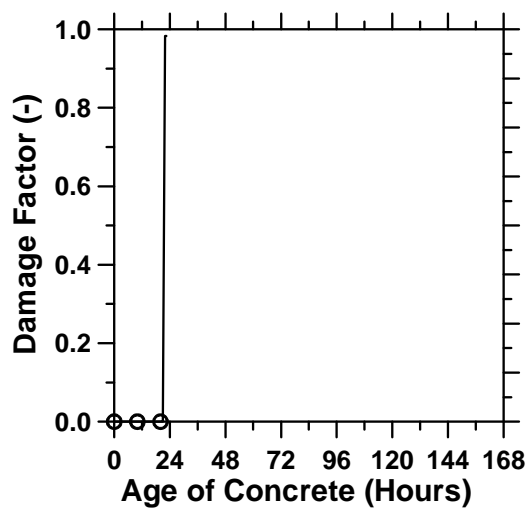


Fig. (h)

Figure A.116: Pavement cured at 23°C ambient temperature with a D/3 saw-cut depth introduced at 21 hour.

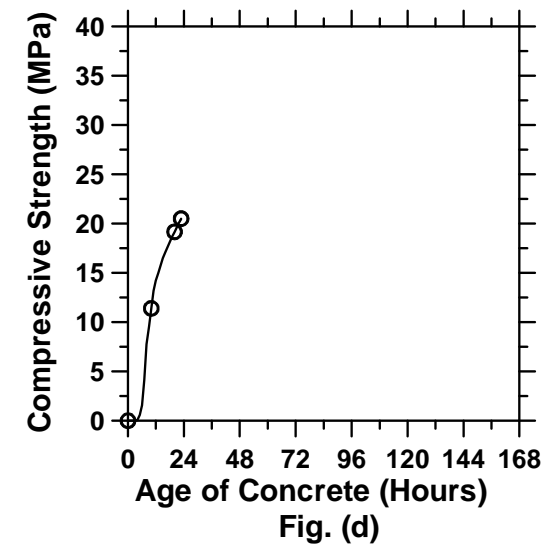
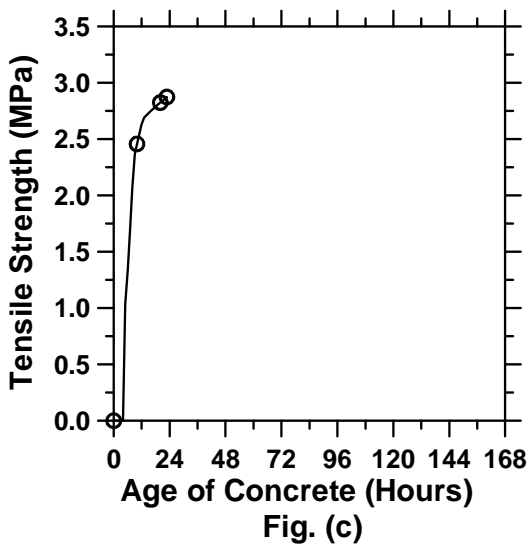
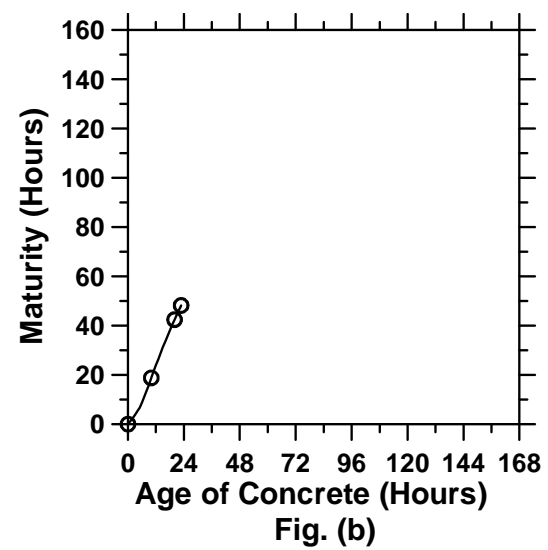
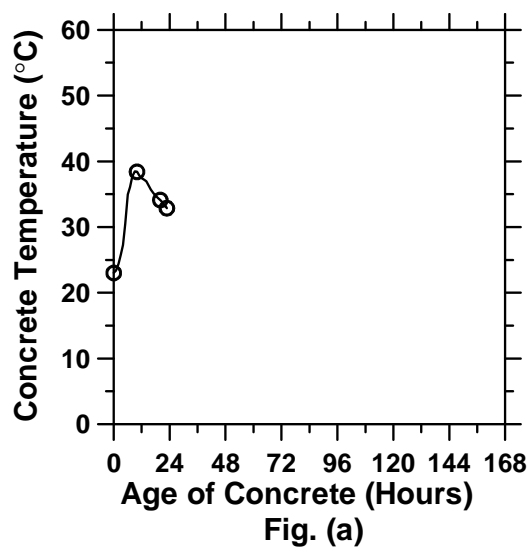


Figure A.117: Pavement cured at 23°C ambient temperature with a D/3 saw-cut depth introduced at 22 hours (cont'd).

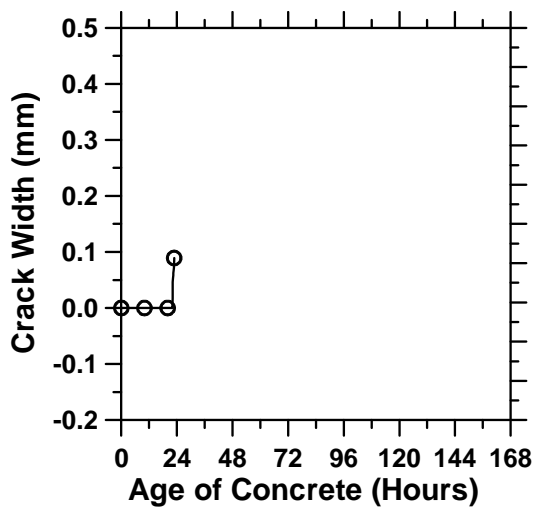


Fig. (e)

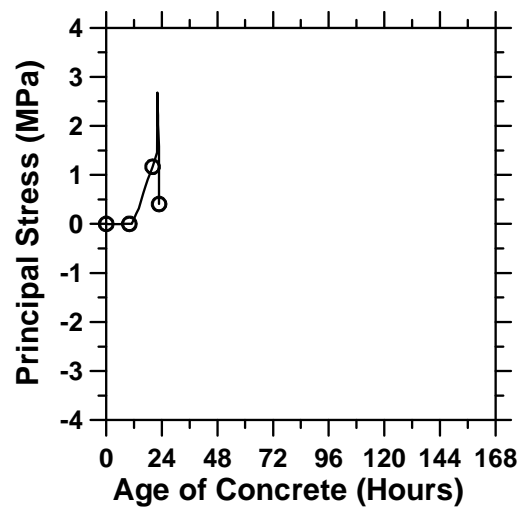


Fig. (f)

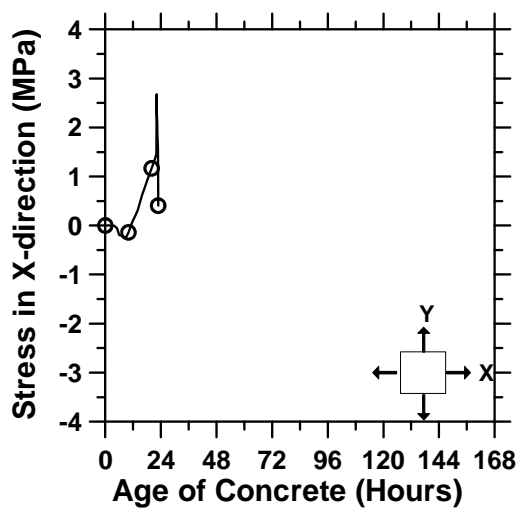


Fig. (g)

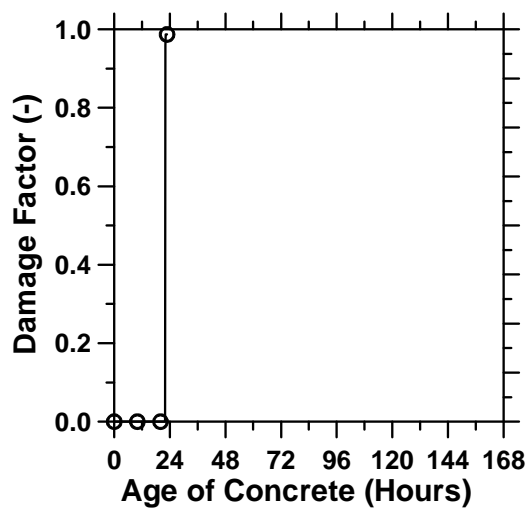


Fig. (h)

Figure A.117: Pavement cured at 23°C ambient temperature with a D/3 saw-cut depth introduced at 22 hours.

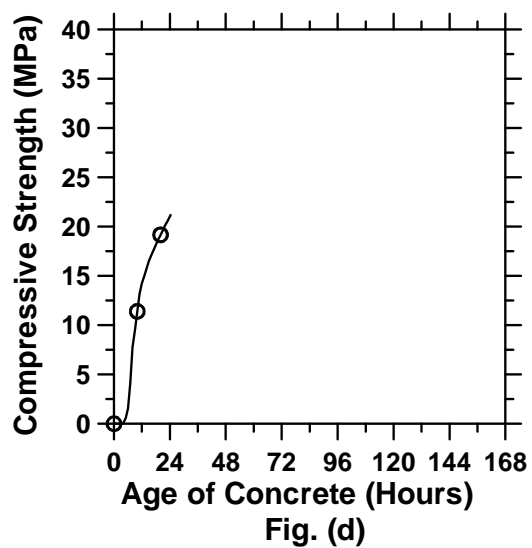
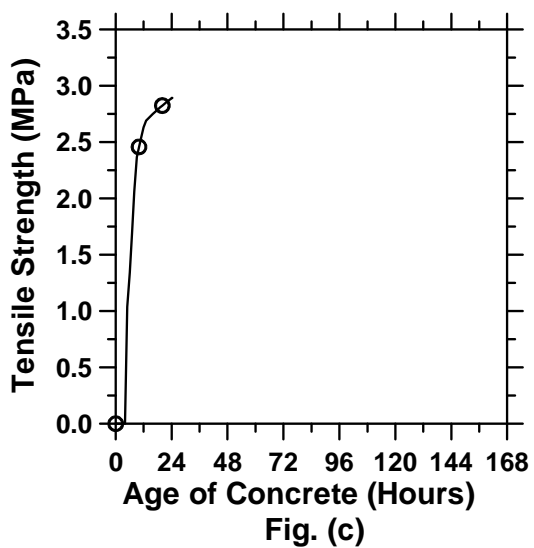
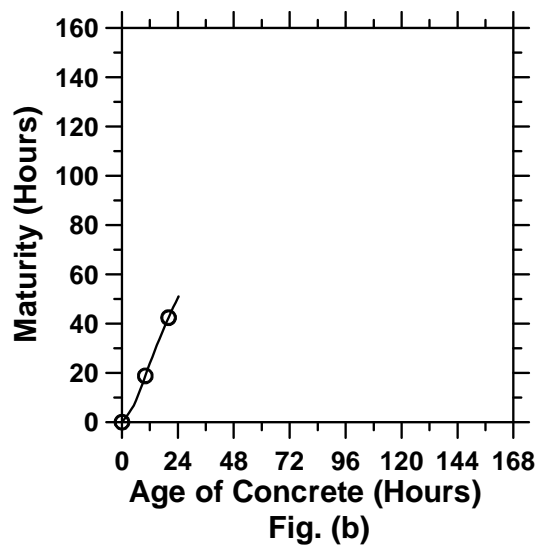
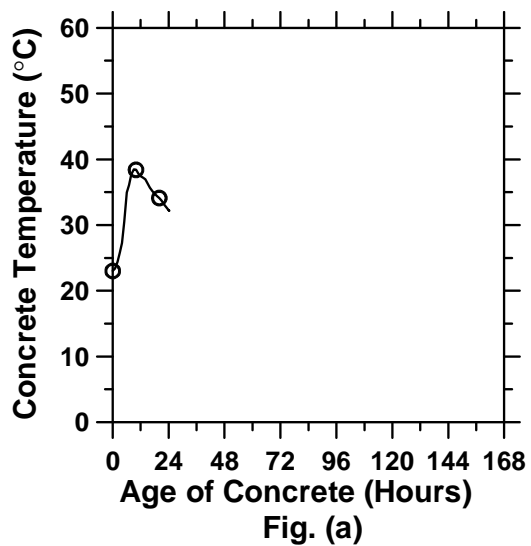


Figure A.118: Pavement cured at 23°C ambient temperature with a D/3 saw-cut depth introduced at 24 hours (cont'd).

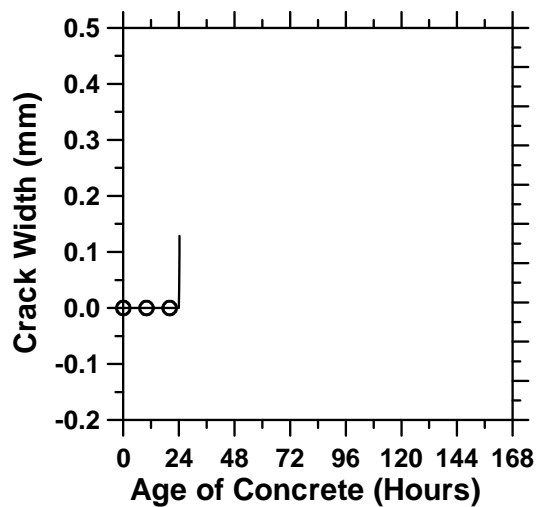


Fig. (e)

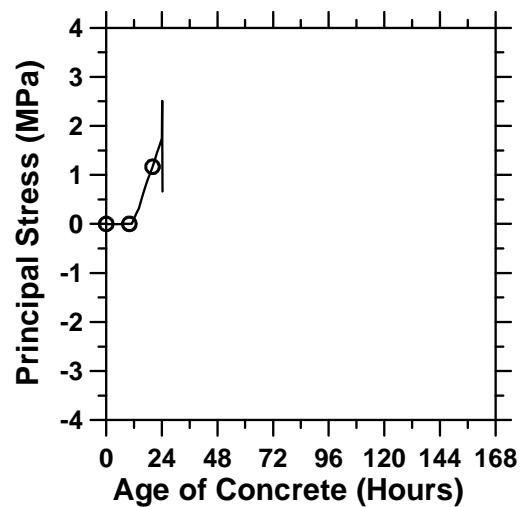


Fig. (f)

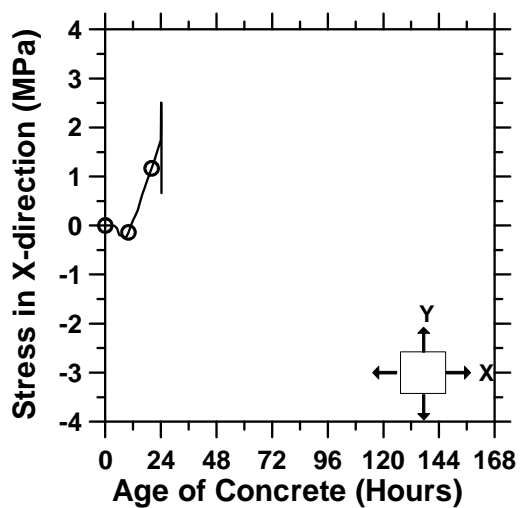


Fig. (g)

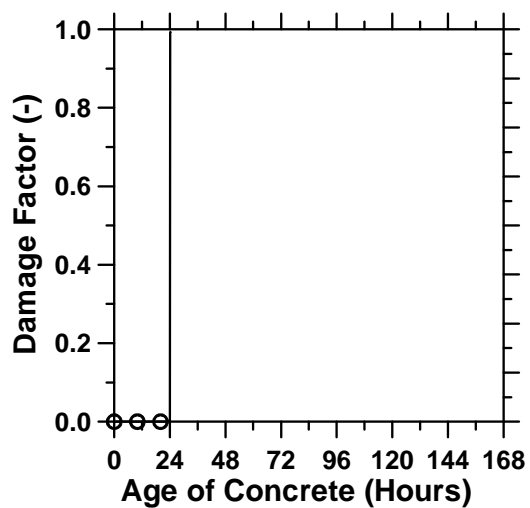


Fig. (h)

Figure A.118: Pavement cured at 23°C ambient temperature with a D/3 saw-cut depth introduced at 24 hours.

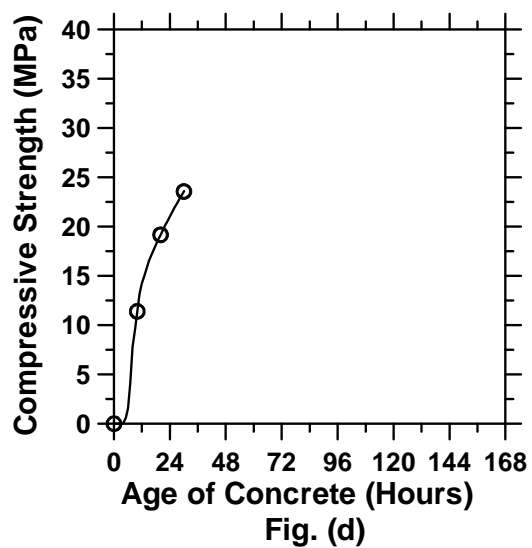
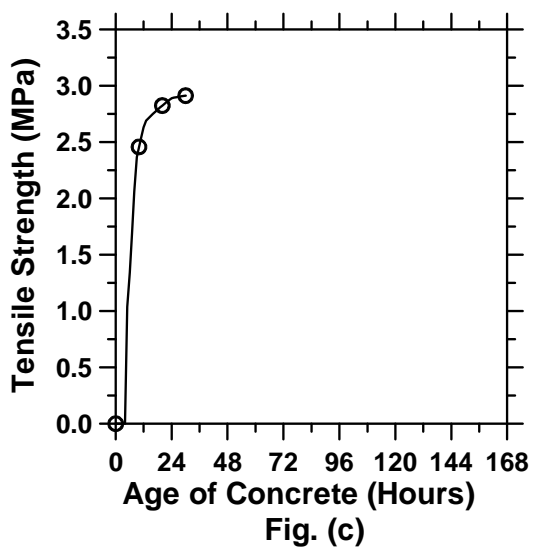
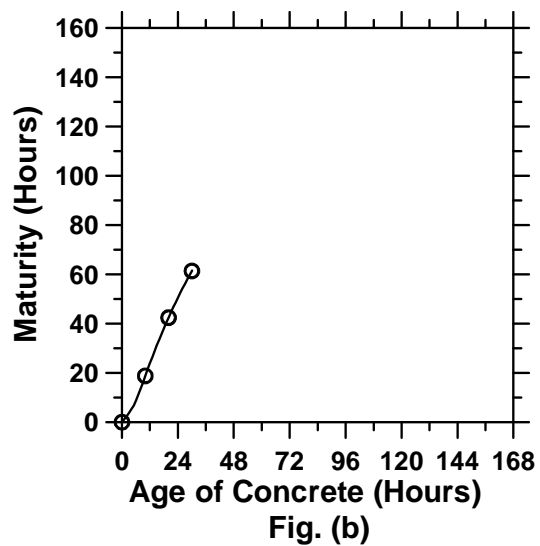
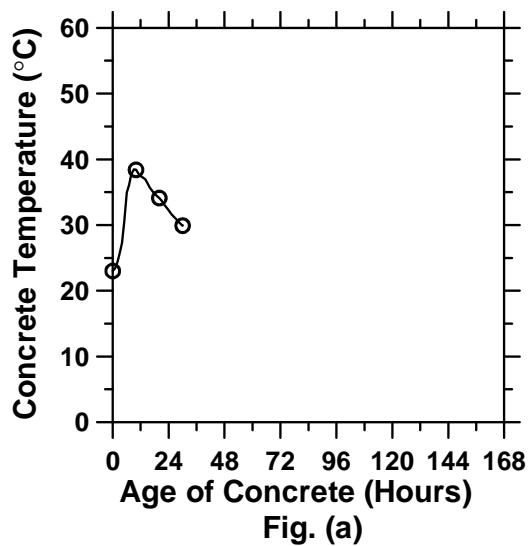


Figure A.119: Pavement cured at 23°C ambient temperature with a D/3 saw-cut depth introduced at 30 hours (cont'd).

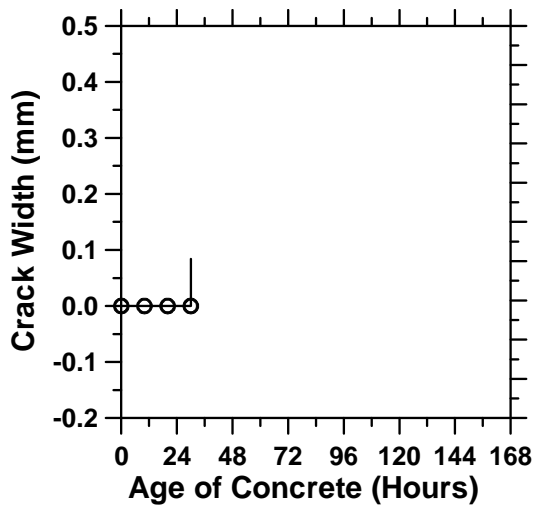


Fig. (e)

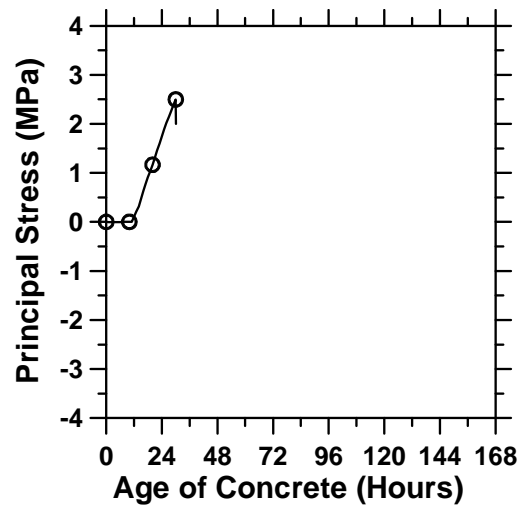


Fig. (f)

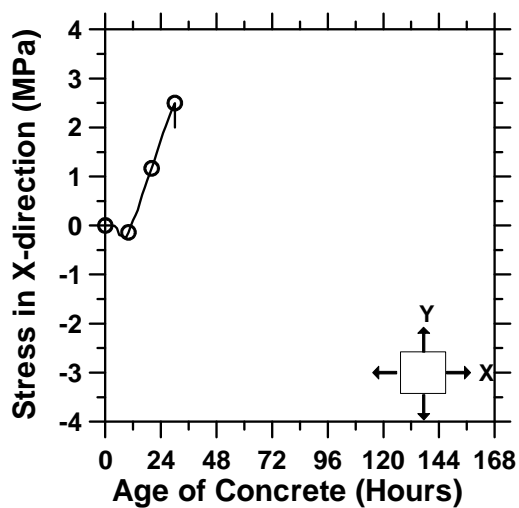


Fig. (g)

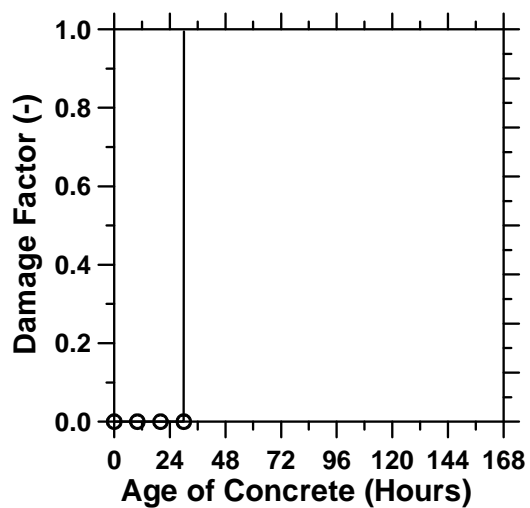


Fig. (h)

Figure A.119: Pavement cured at 23°C ambient temperature with a D/3 saw-cut depth introduced at 30 hours.

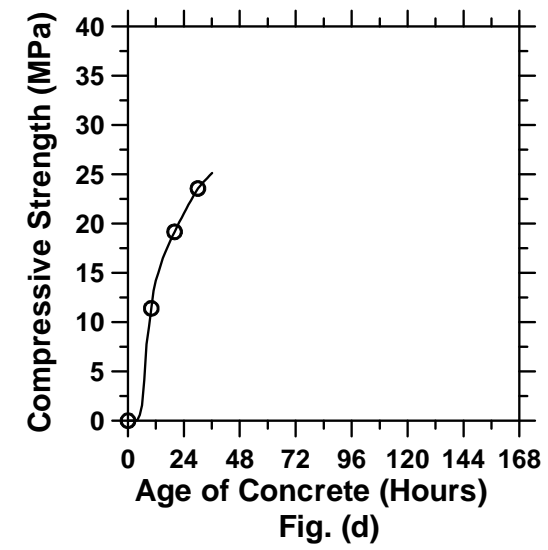
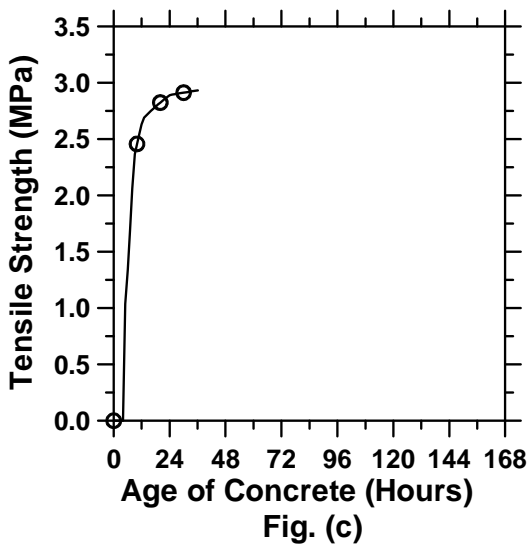
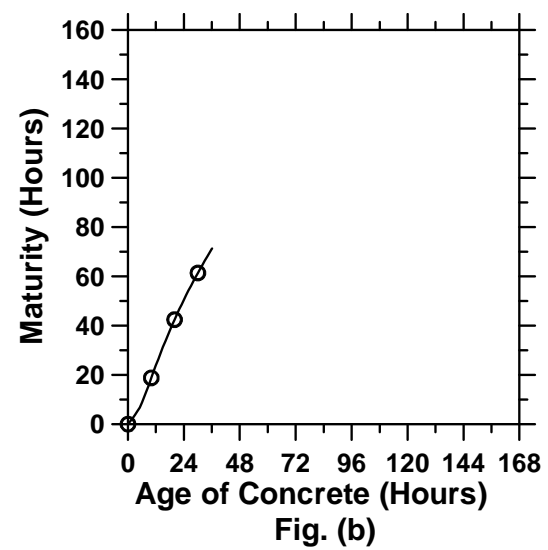
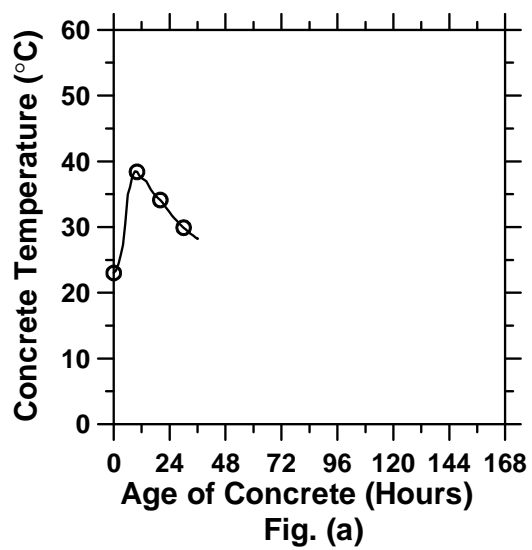


Figure A.120: Pavement cured at 23°C ambient temperature with a D/3 saw-cut depth introduced at 36 hours (cont'd).

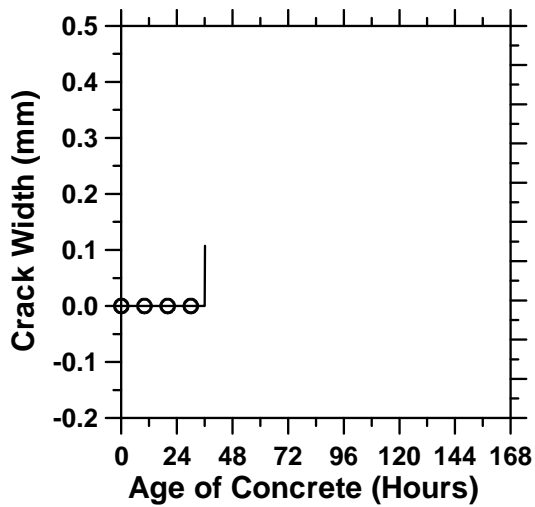


Fig. (e)

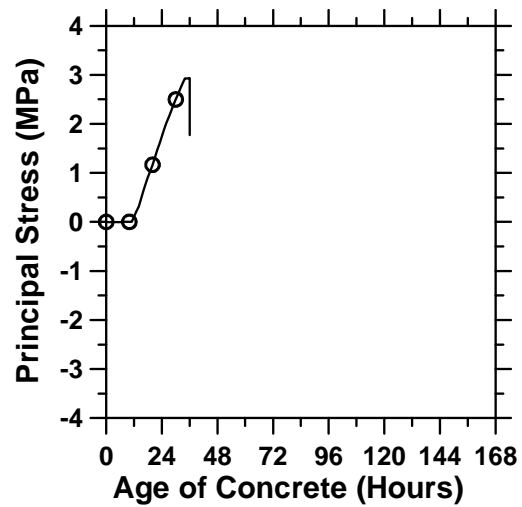


Fig. (f)

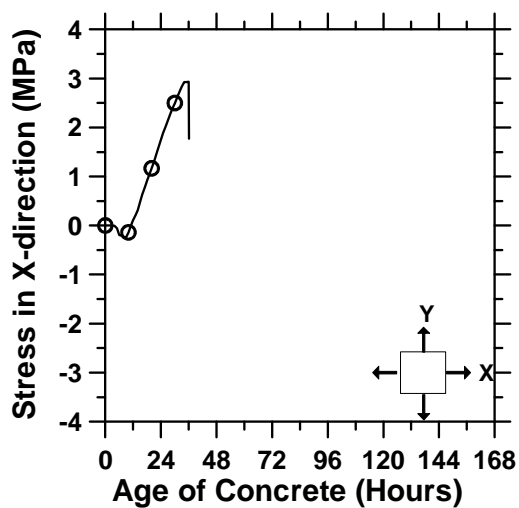


Fig. (g)

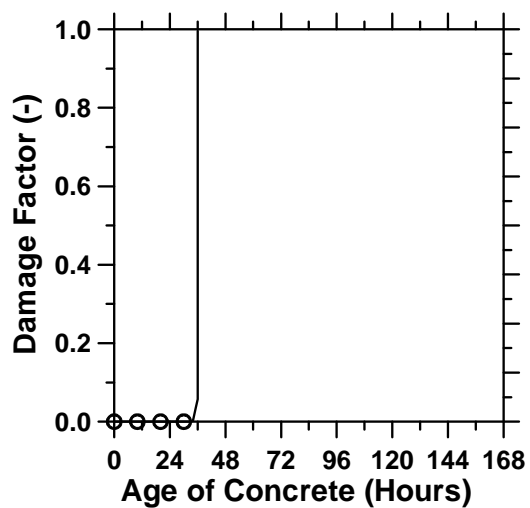


Fig. (h)

Figure A.120: Pavement cured at 23°C ambient temperature with a D/3 saw-cut depth introduced at 36 hours.

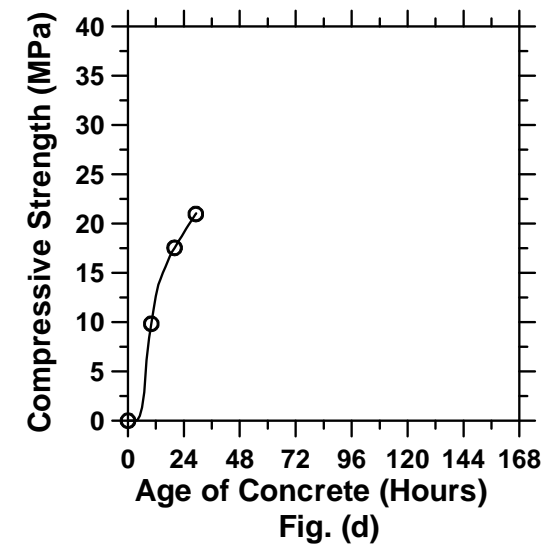
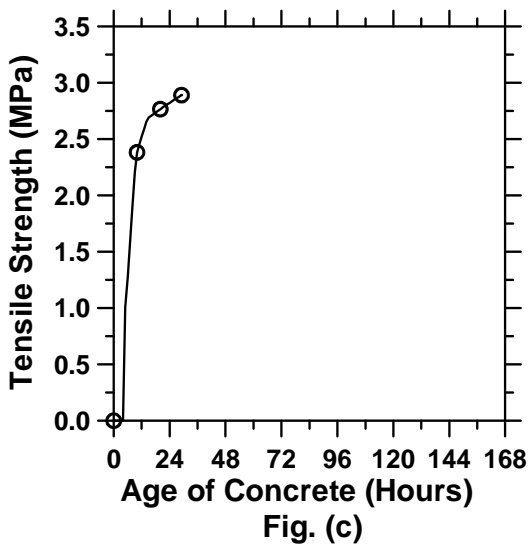
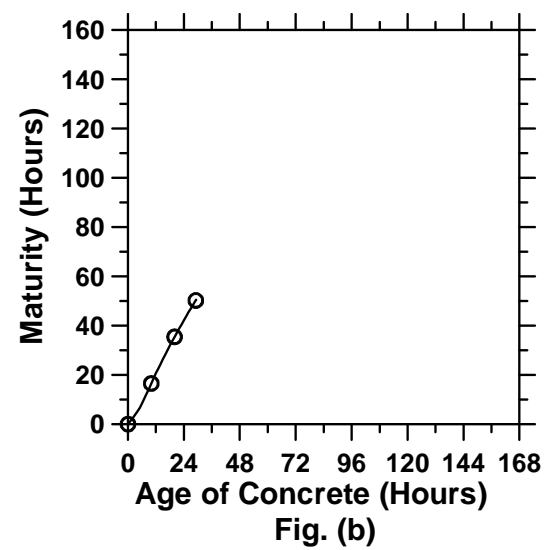
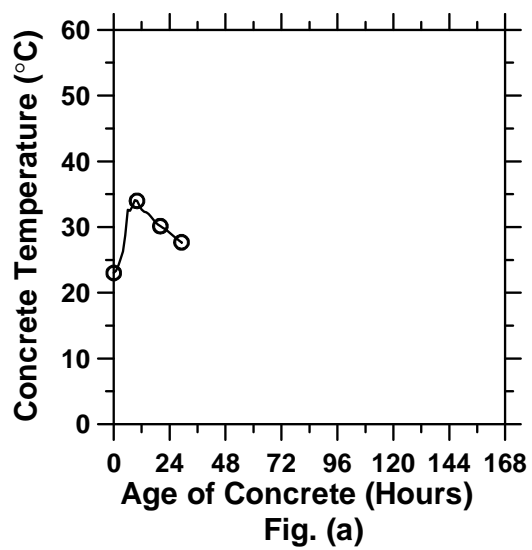


Figure A.121: Pavement cured at 23°C ambient temperature with a D/8 saw-cut depth introduced at 0 hour (cont'd).

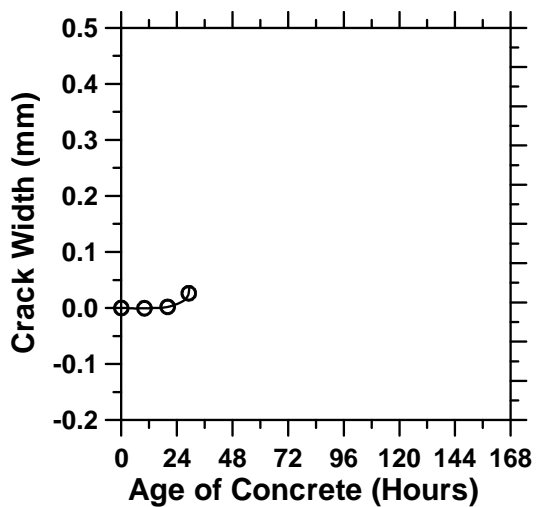


Fig. (e)

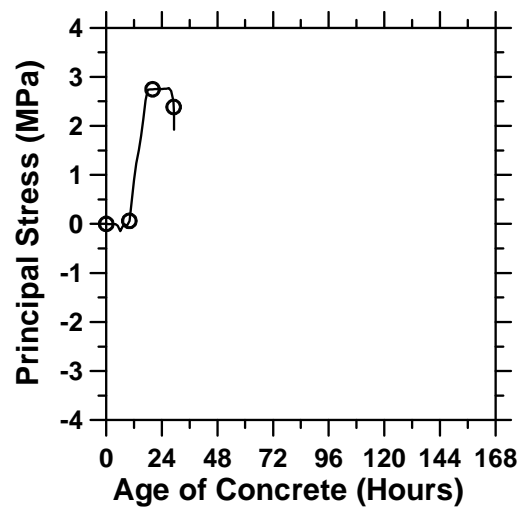


Fig. (f)

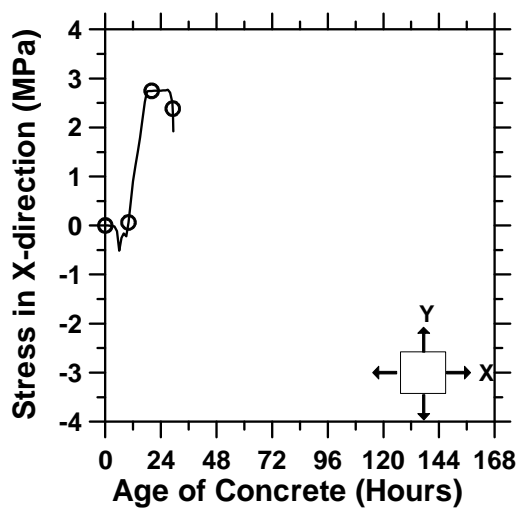


Fig. (g)

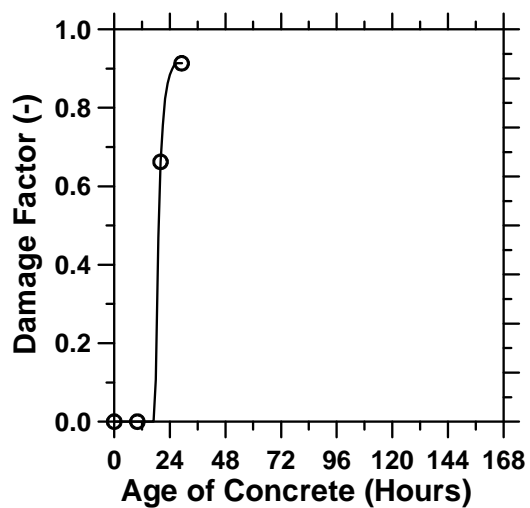


Fig. (h)

Figure A.121: Pavement cured at 23°C ambient temperature with a D/8 saw-cut depth introduced at 0 hour.

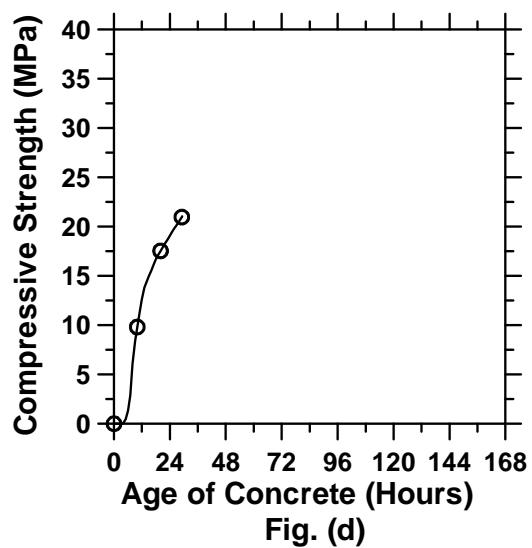
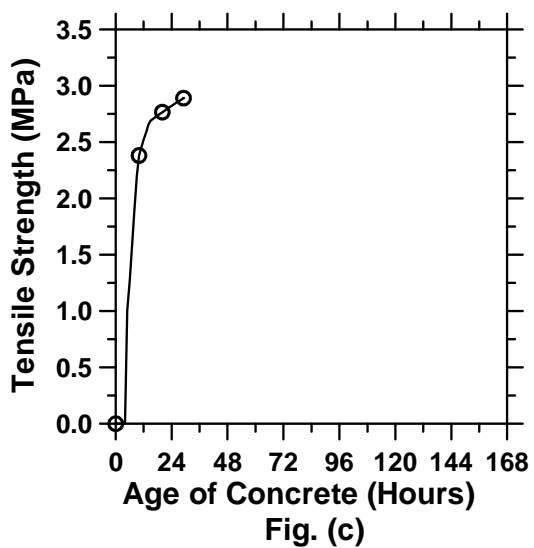
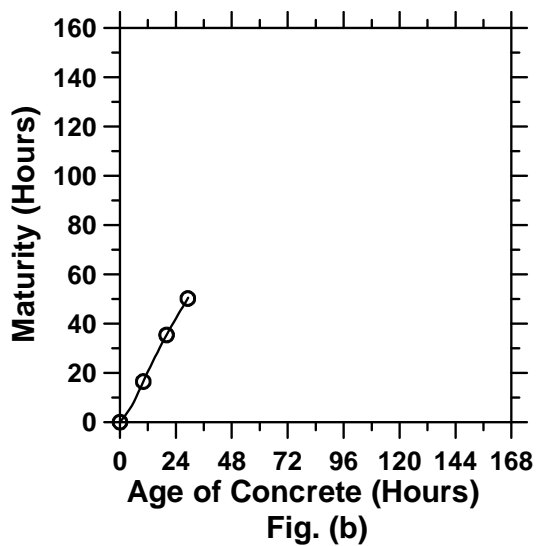
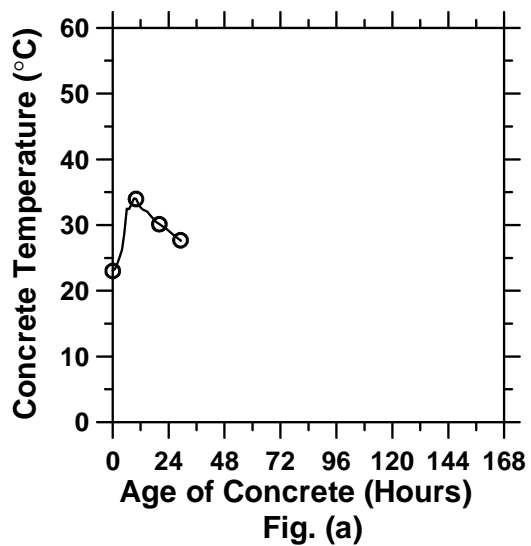


Figure A.122: Pavement cured at 23°C ambient temperature with a D/8 saw-cut depth introduced at 6 hours (cont'd).

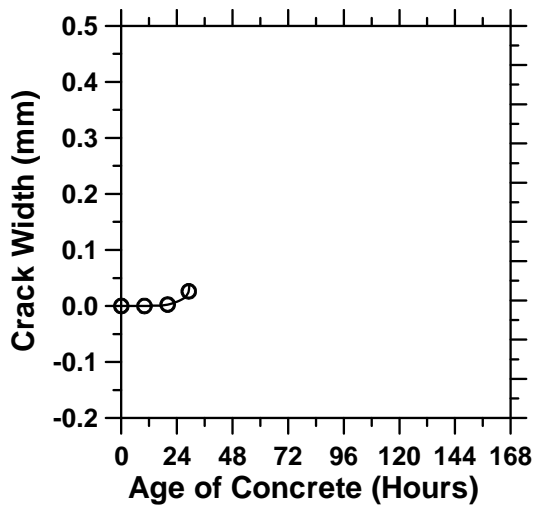


Fig. (e)

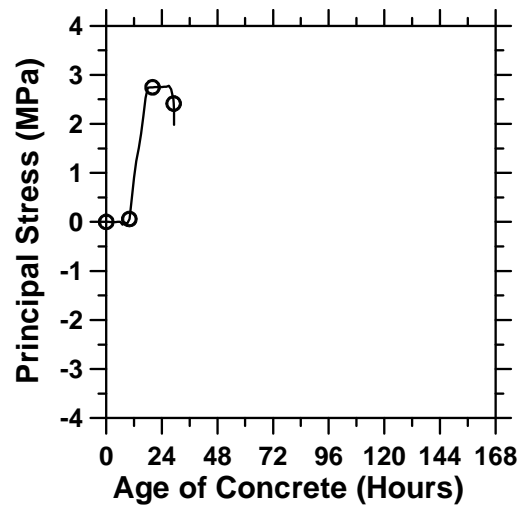


Fig. (f)

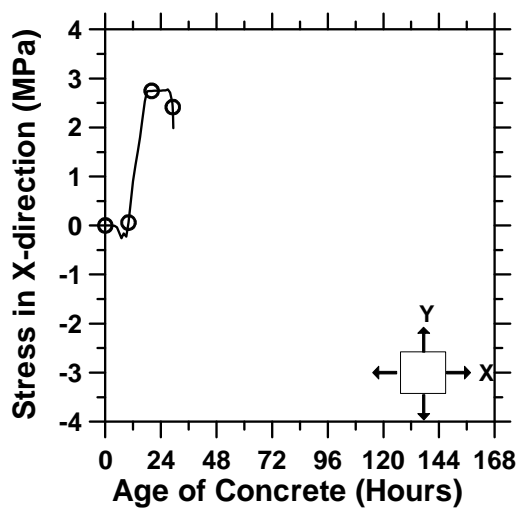


Fig. (g)

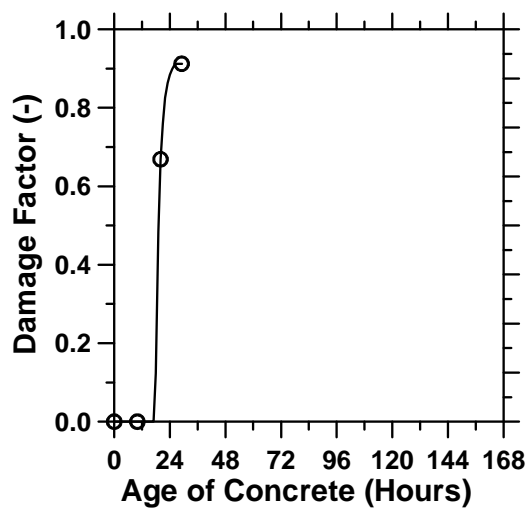


Fig. (h)

Figure A.122: Pavement cured at 23°C ambient temperature with a D/8 saw-cut depth introduced at 6 hours.

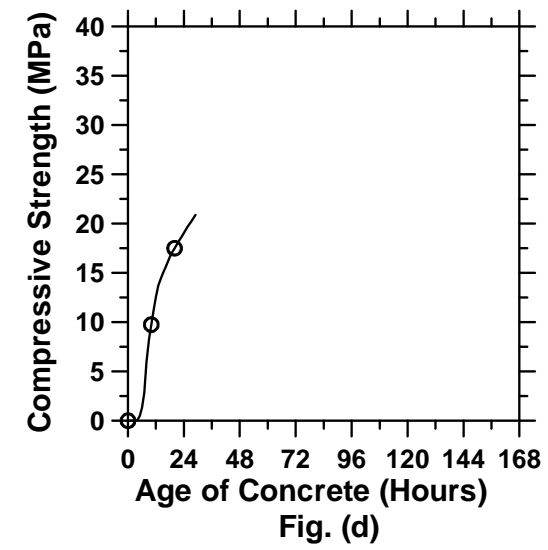
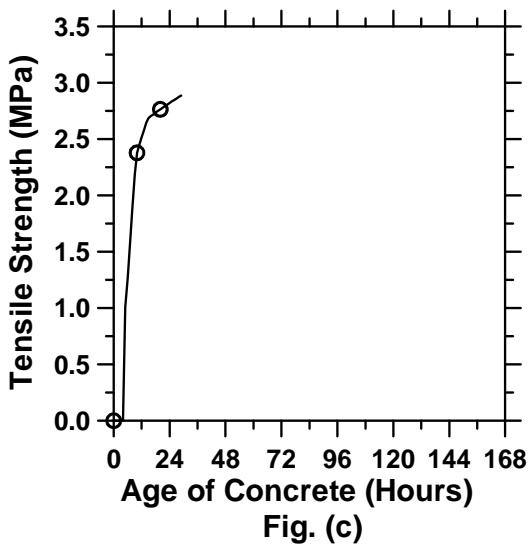
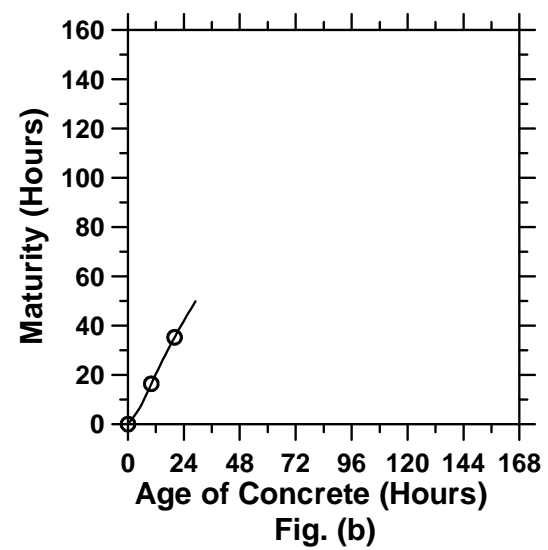
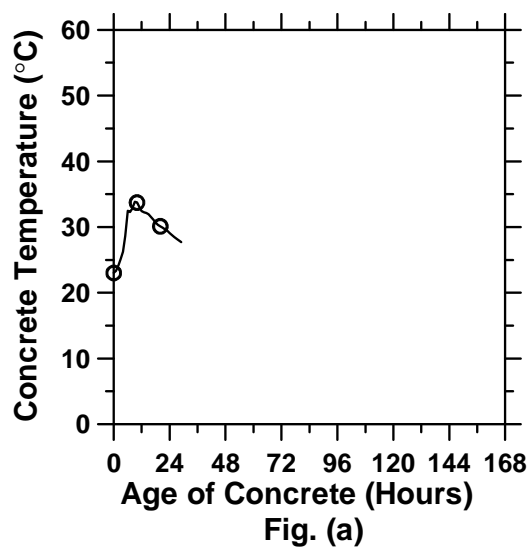


Figure A.123: Pavement cured at 23°C ambient temperature with a D/8 saw-cut depth introduced at 12 hours (cont'd).

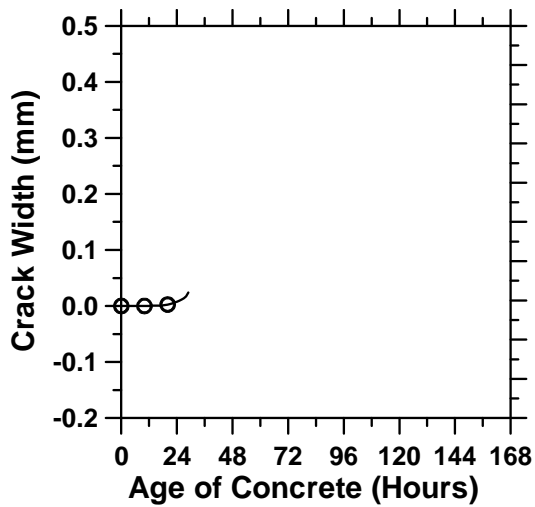


Fig. (e)

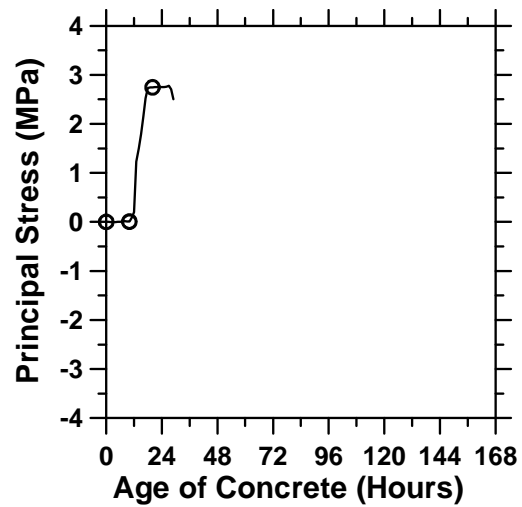


Fig. (f)

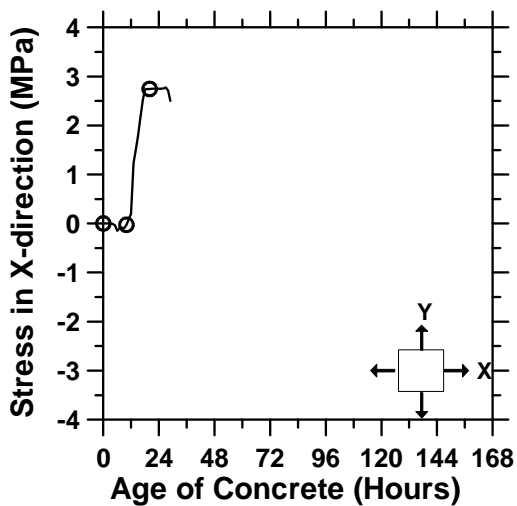


Fig. (g)

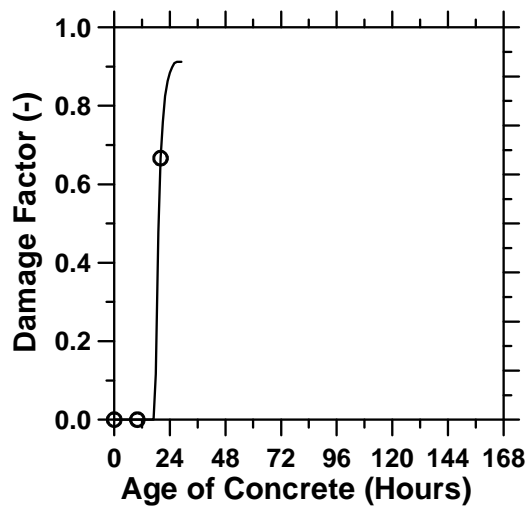


Fig. (h)

Figure A.123: Pavement cured at 23°C ambient temperature with a D/8 saw-cut depth introduced at 12 hours.

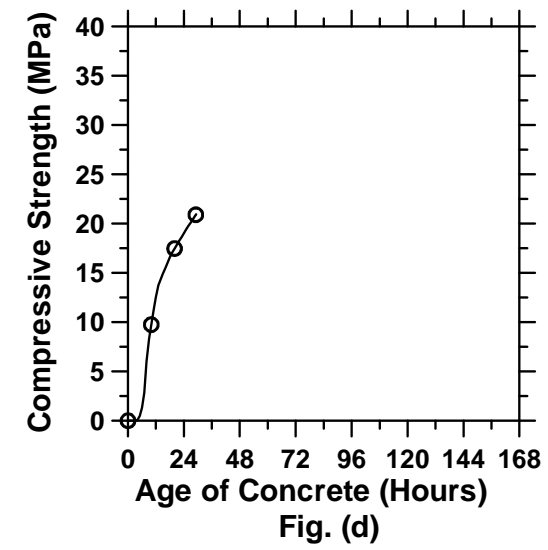
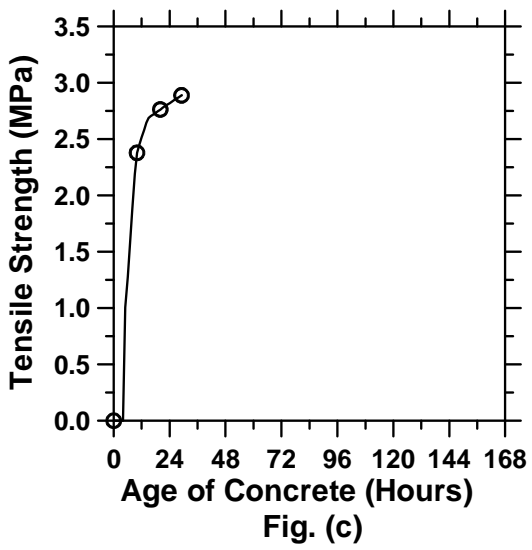
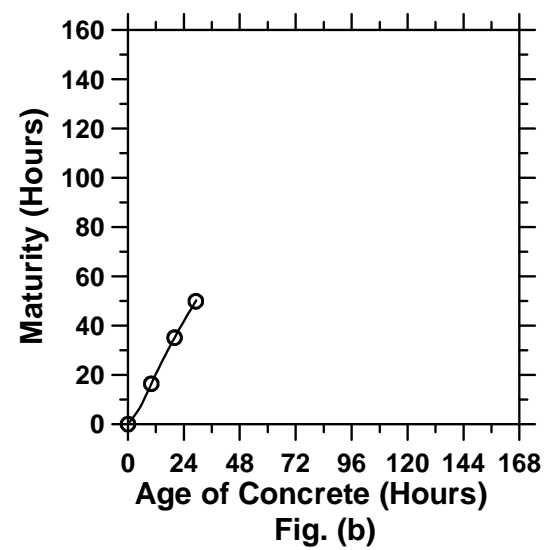
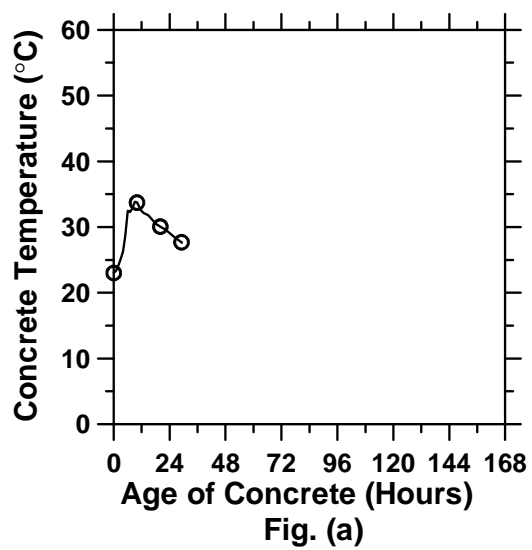


Figure A.124: Pavement cured at 23°C ambient temperature with a D/8 saw-cut depth introduced at 18 hours (cont'd).

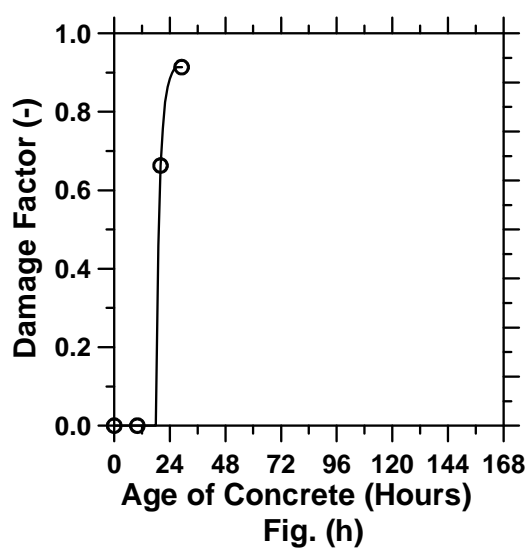
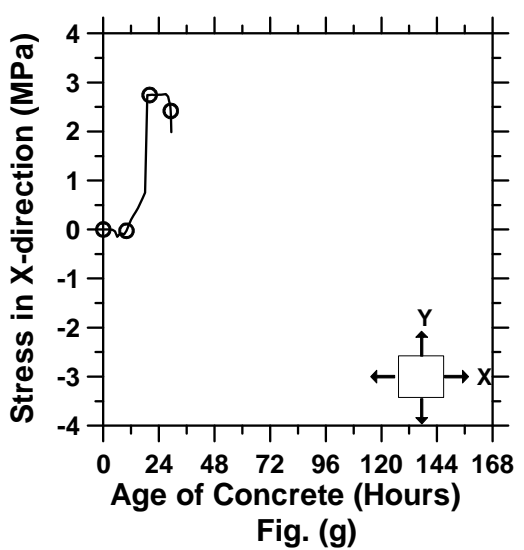
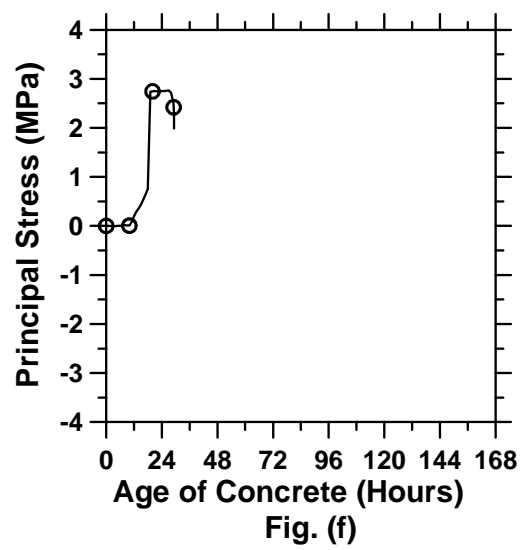
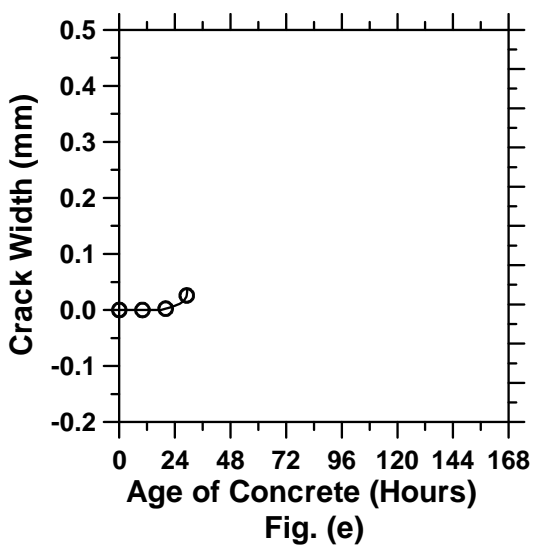


Figure A.124: Pavement cured at 23°C ambient temperature with a D/8 saw-cut depth introduced at 18 hours.

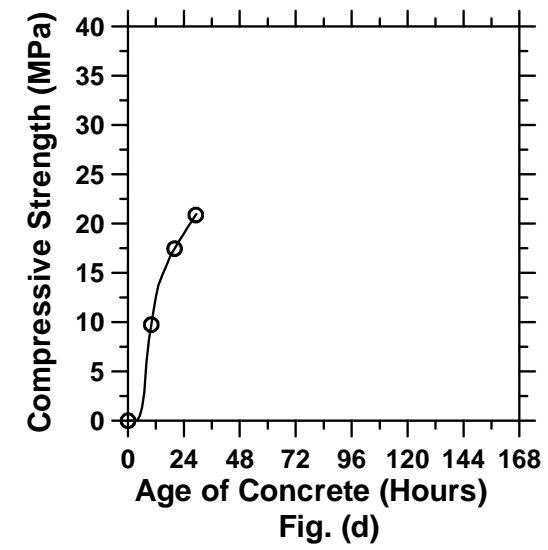
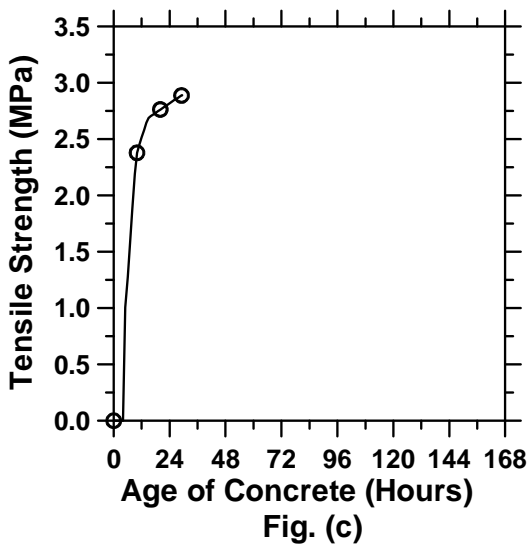
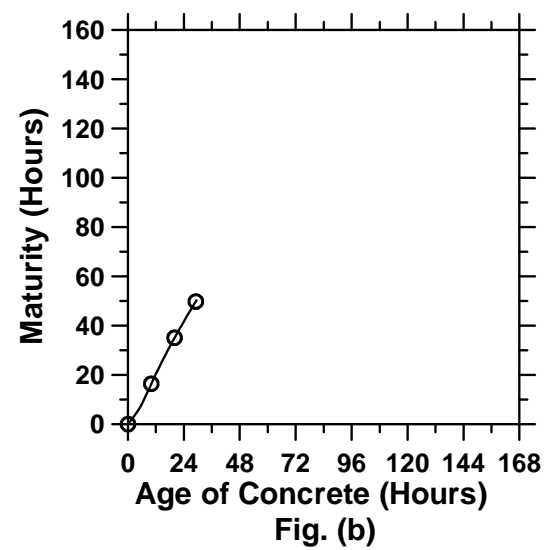
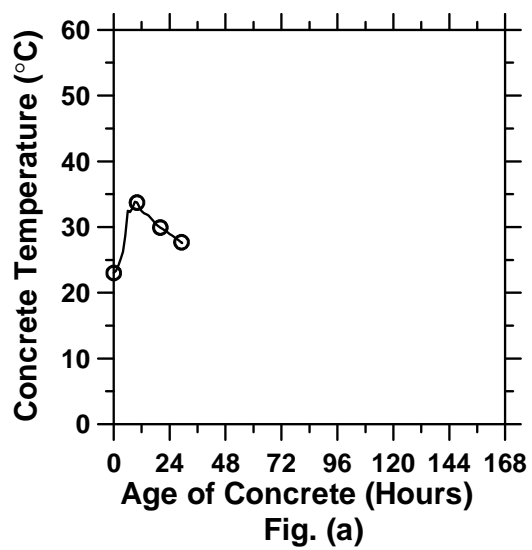


Figure A.125: Pavement cured at 23°C ambient temperature with a D/8 saw-cut depth introduced at 24 hours (cont'd).

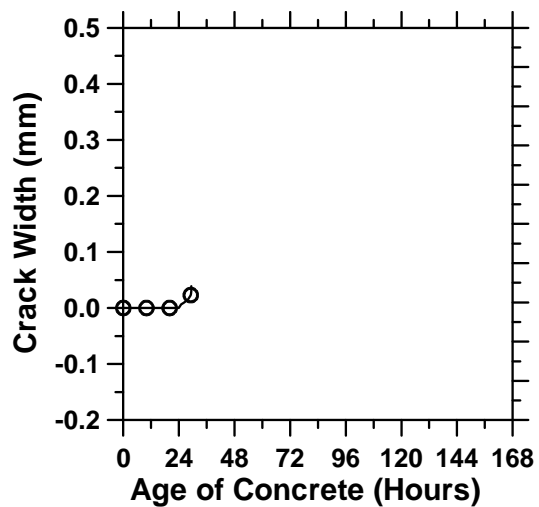


Fig. (e)

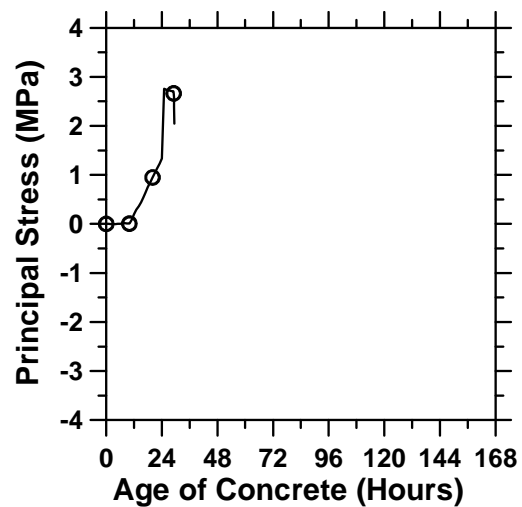


Fig. (f)

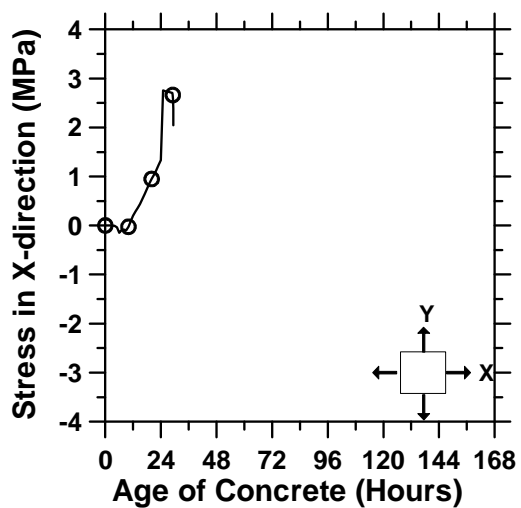


Fig. (g)

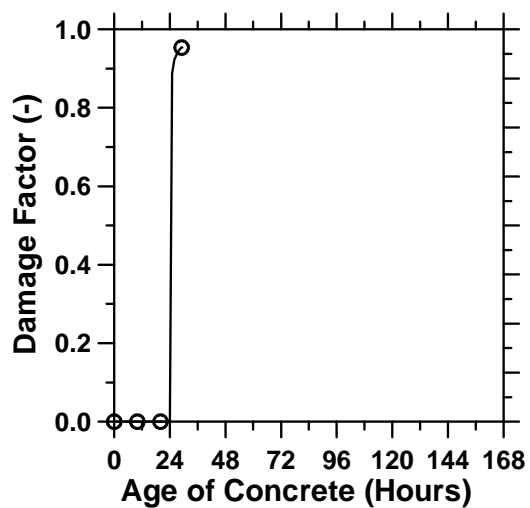


Fig. (h)

Figure A.125: Pavement cured at 23°C ambient temperature with a D/8 saw-cut depth introduced at 24 hours.

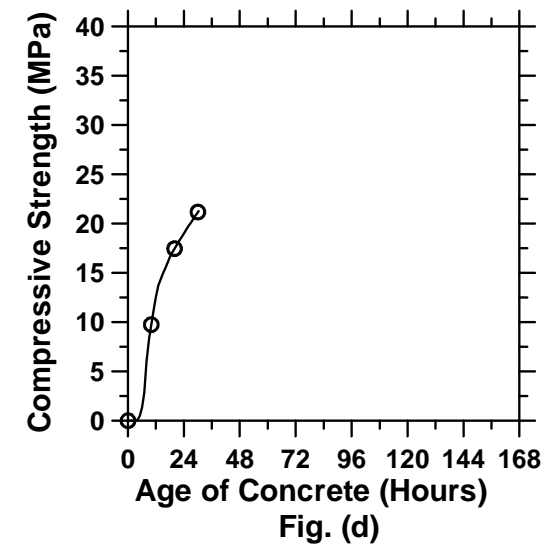
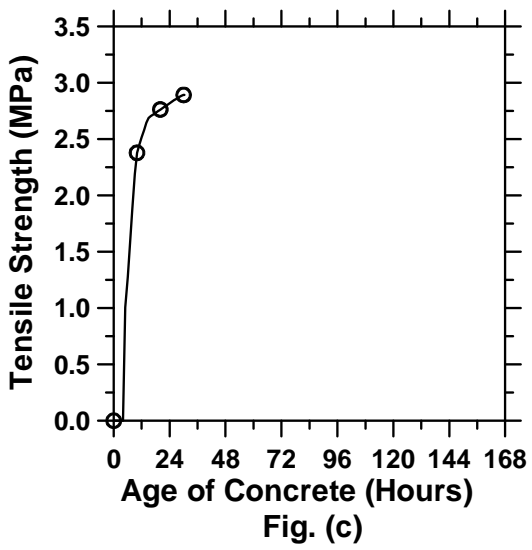
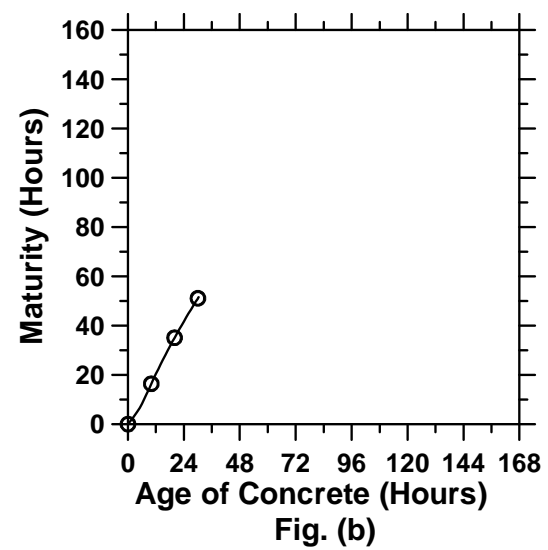
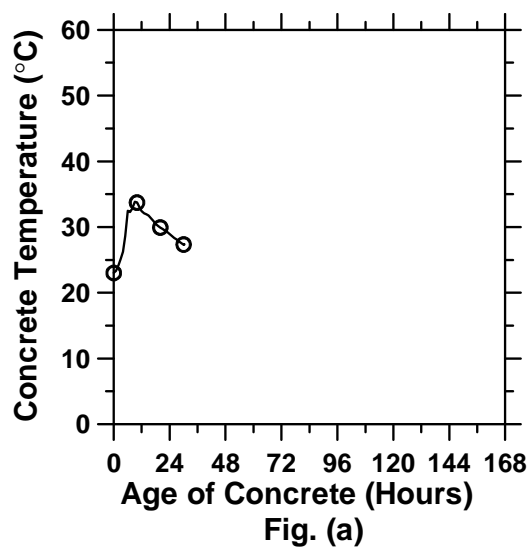


Figure A.126: Pavement cured at 23°C ambient temperature with a D/8 saw-cut depth introduced at 30 hours (cont'd).

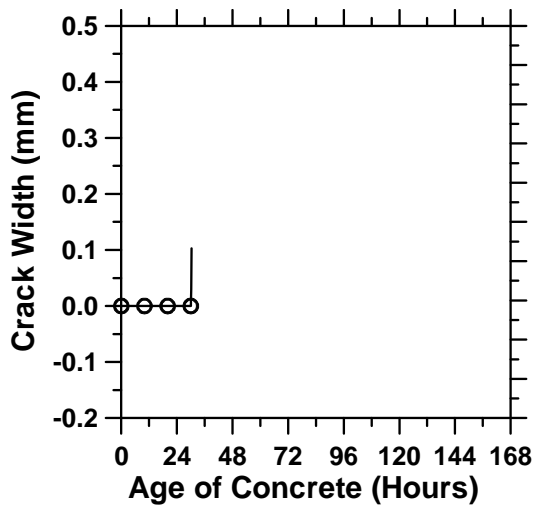


Fig. (e)

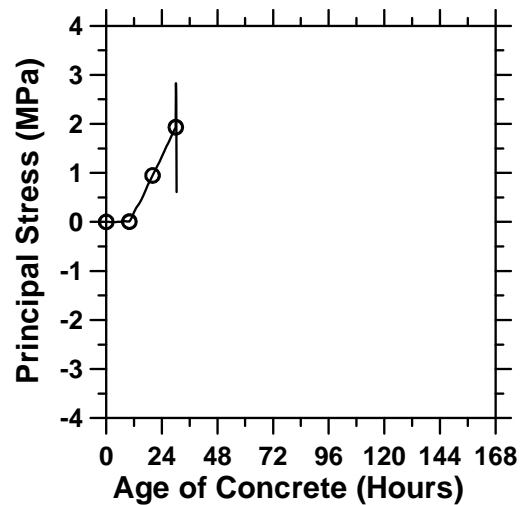


Fig. (f)

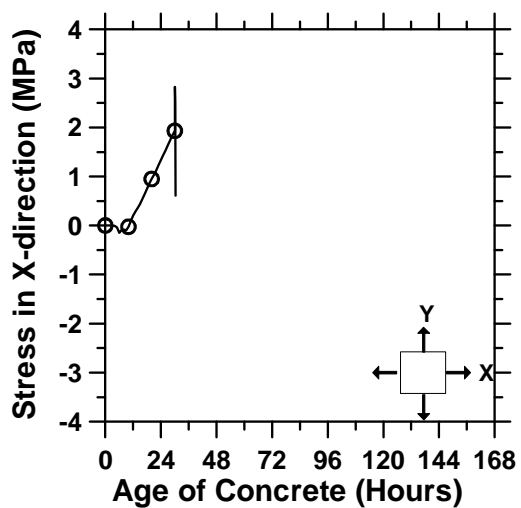


Fig. (g)

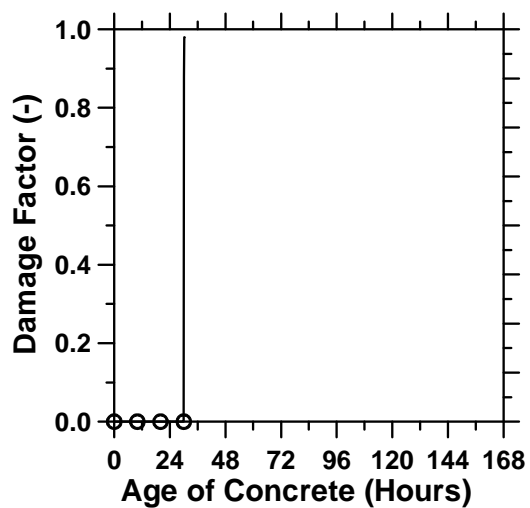


Fig. (h)

Figure A.126: Pavement cured at 23°C ambient temperature with a D/8 saw-cut depth introduced at 30 hours.

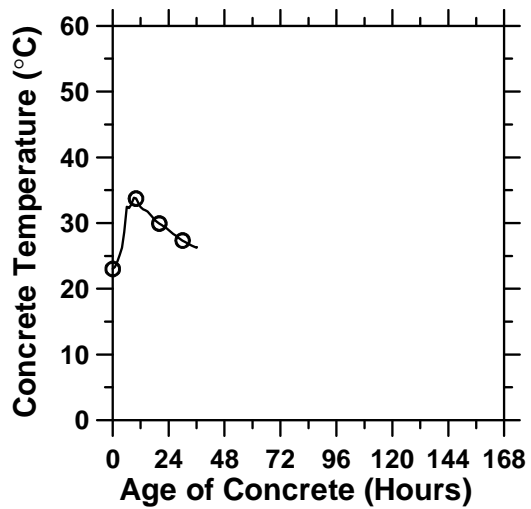


Fig. (a)

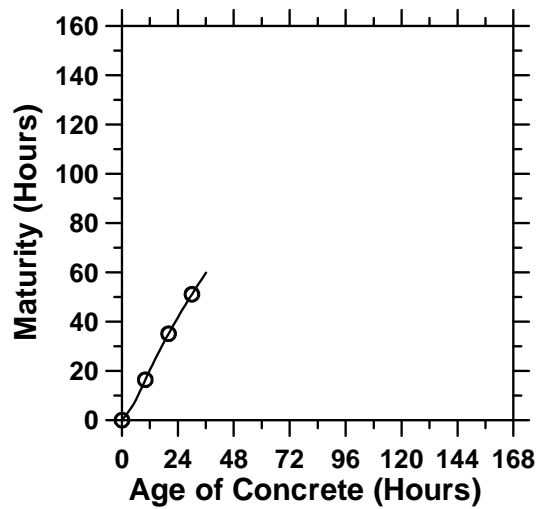


Fig. (b)

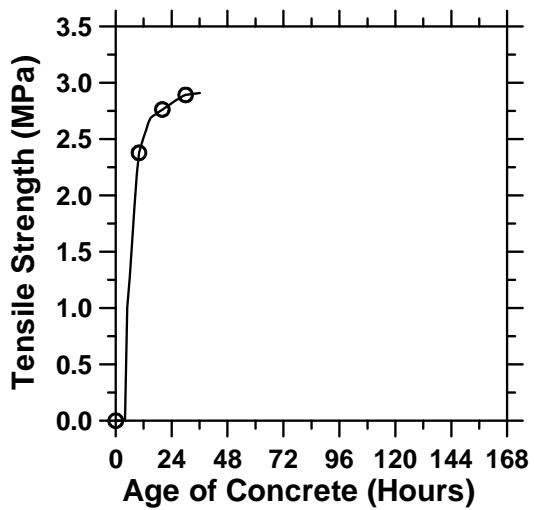


Fig. (c)

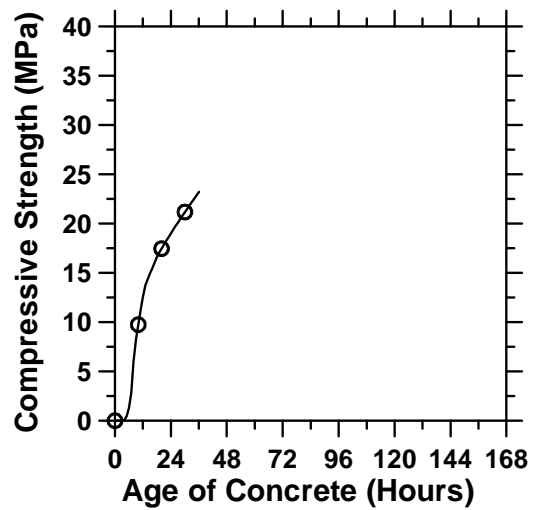


Fig. (d)

Figure A.127: Pavement cured at 23°C ambient temperature with a D/8 saw-cut depth introduced at 36 hours (cont'd).

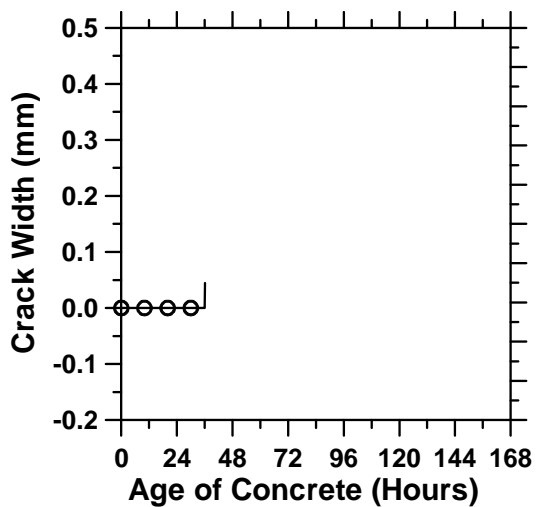


Fig. (e)

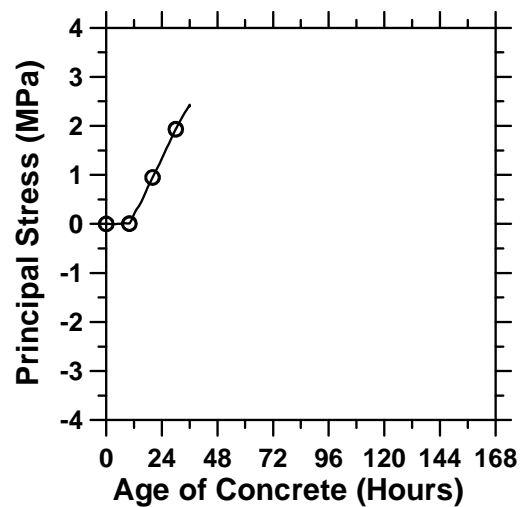


Fig. (f)

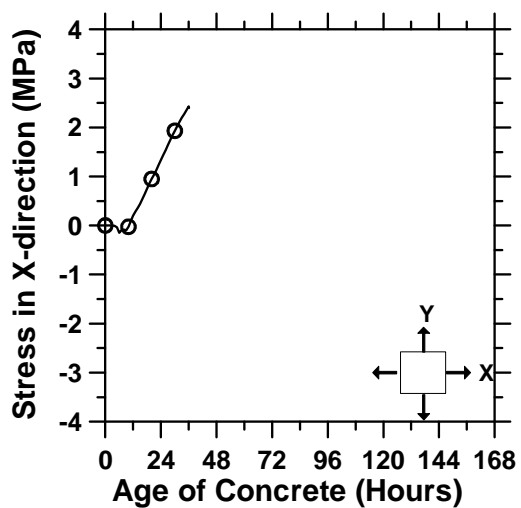


Fig. (g)

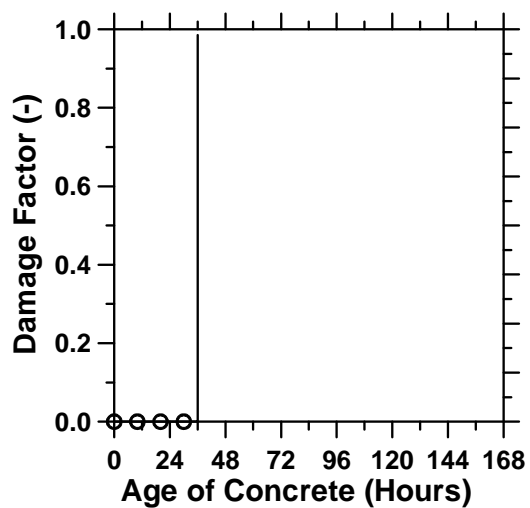


Fig. (h)

Figure A.127: Pavement cured at 23°C ambient temperature with a D/8 saw-cut depth introduced at 36 hours.

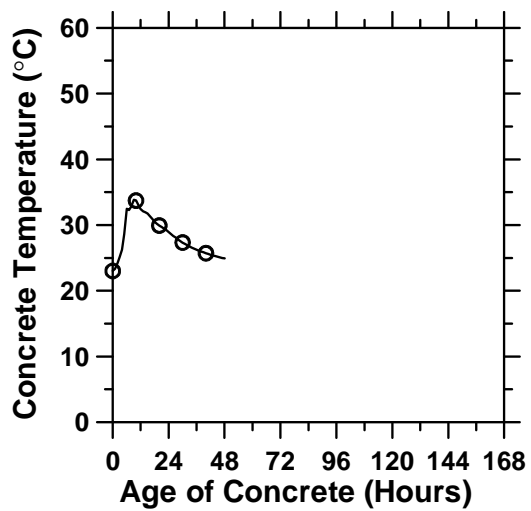


Fig. (a)

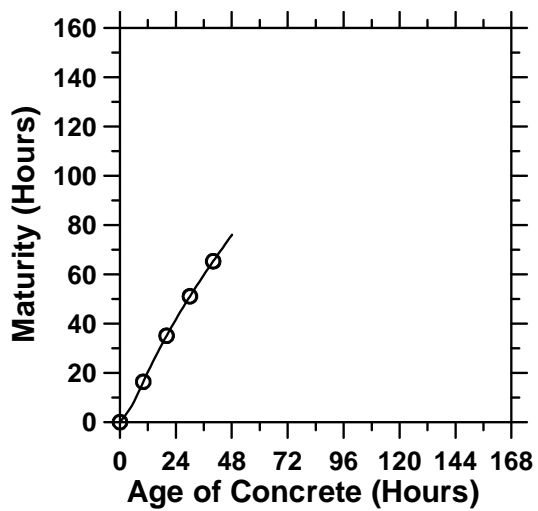


Fig. (b)

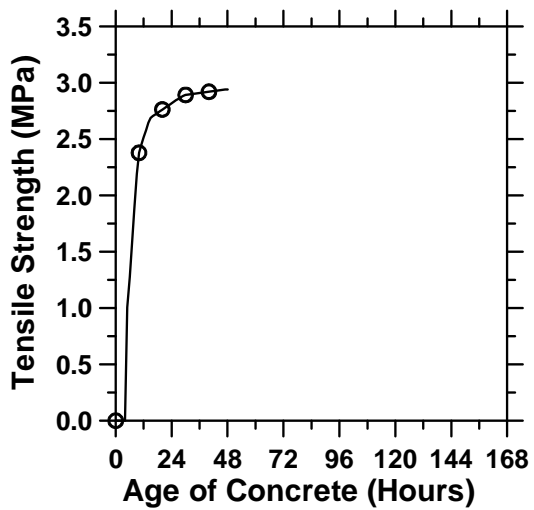


Fig. (c)

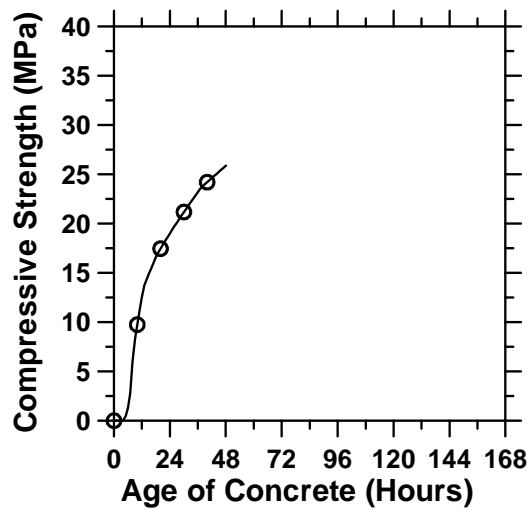


Fig. (d)

Figure A.128: Pavement cured at 23°C ambient temperature with a D/8 saw-cut depth introduced at 48 hours (cont'd).

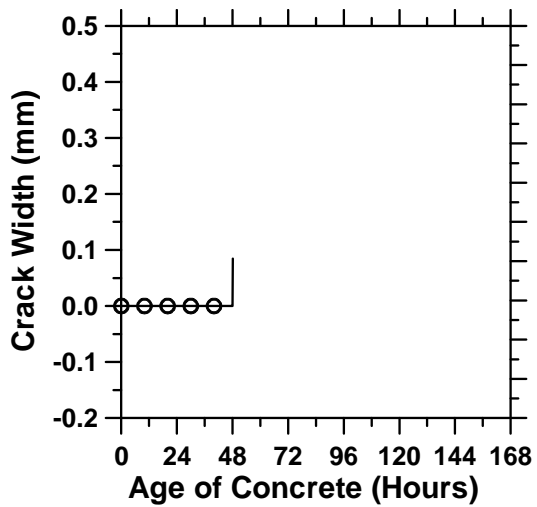


Fig. (e)

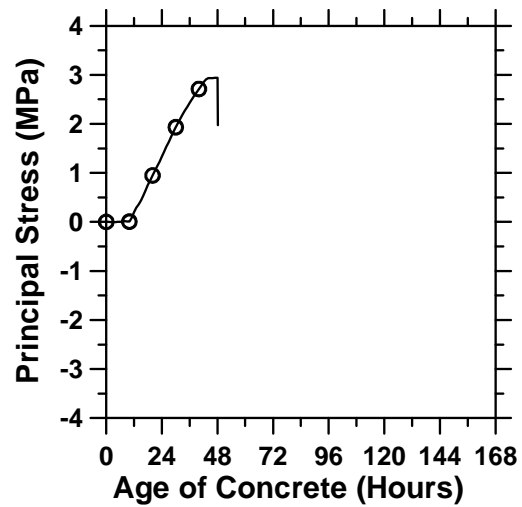


Fig. (f)

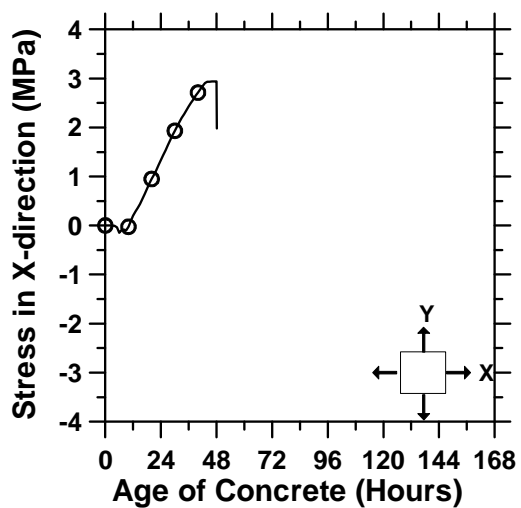


Fig. (g)

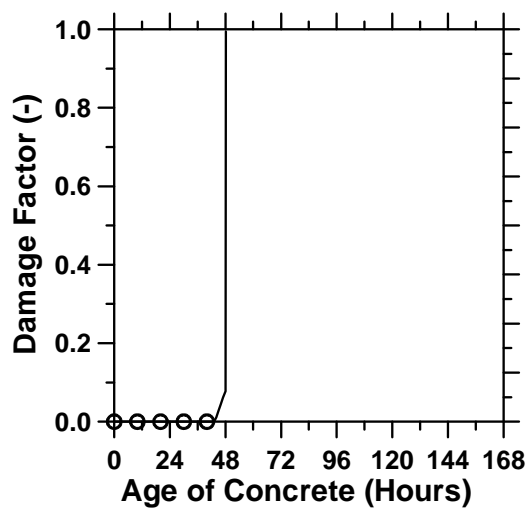


Fig. (h)

Figure A.128: Pavement cured at 23°C ambient temperature with a D/8 saw-cut depth introduced at 48 hours.

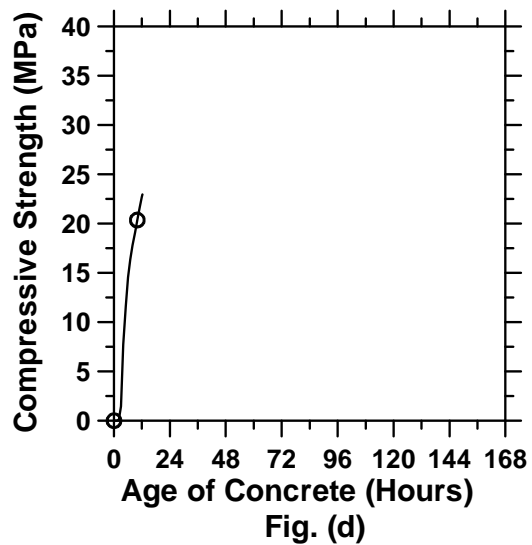
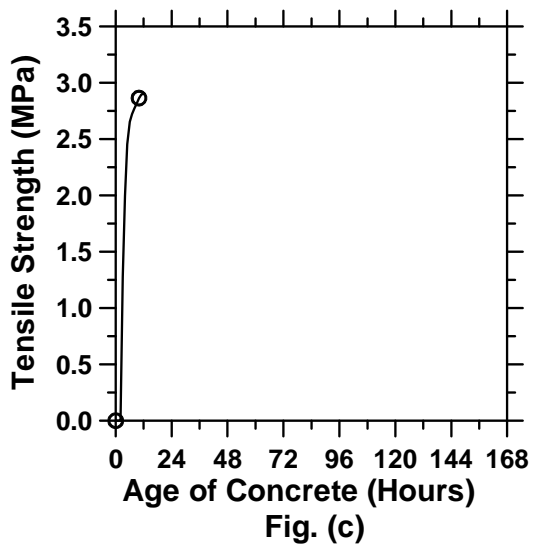
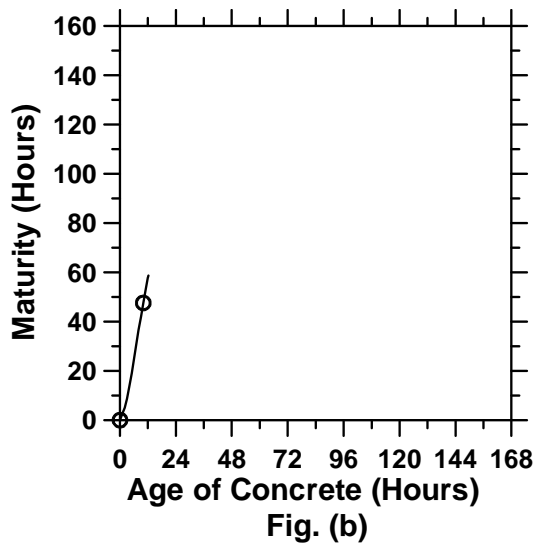
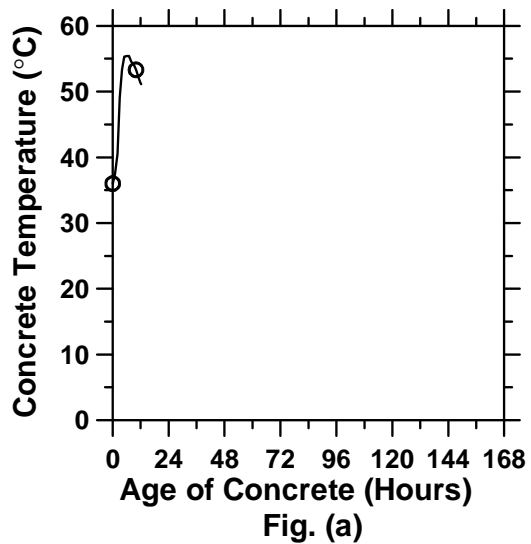


Figure A.129: Pavement cured at 36°C ambient temperature with a D/8 saw-cut depth introduced at 0 hour (cont'd).

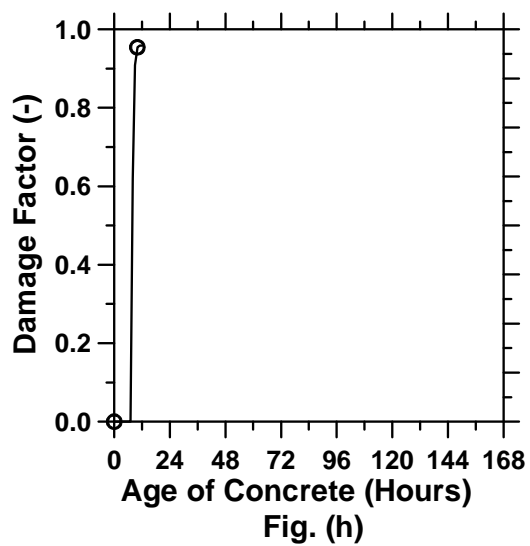
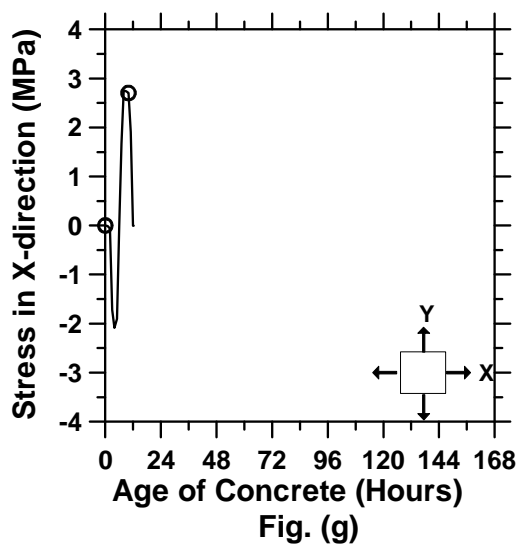
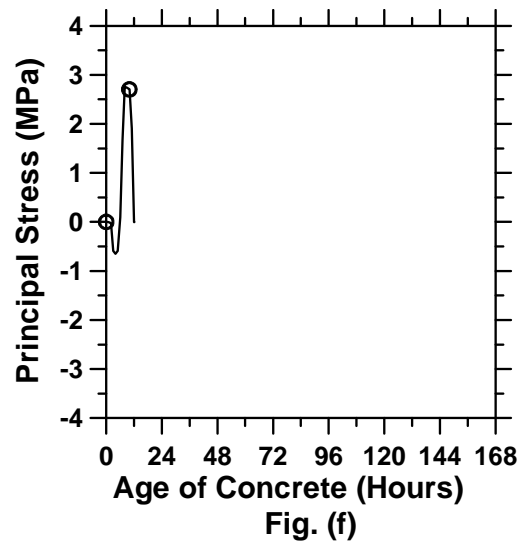
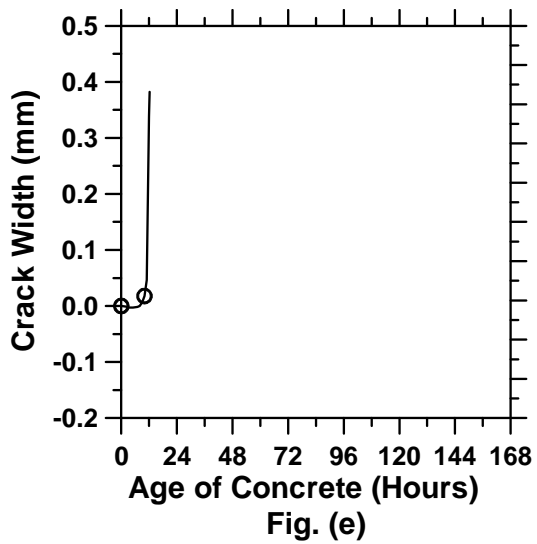


Figure A.129: Pavement cured at 36°C ambient temperature with a D/8 saw-cut depth introduced at 0 hour.

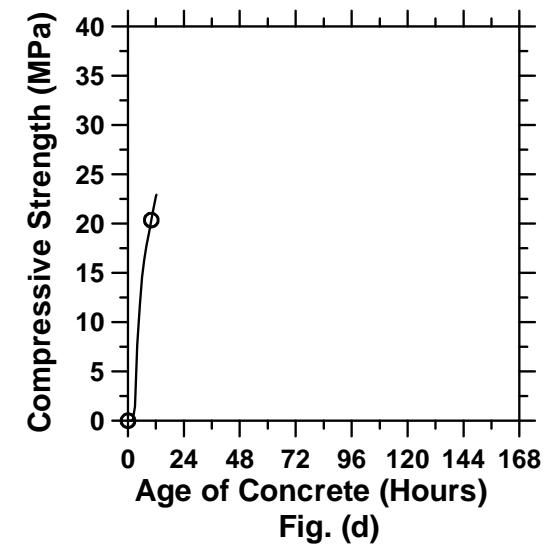
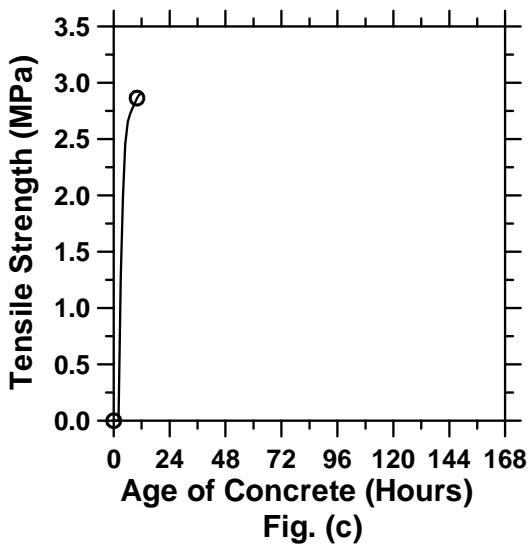
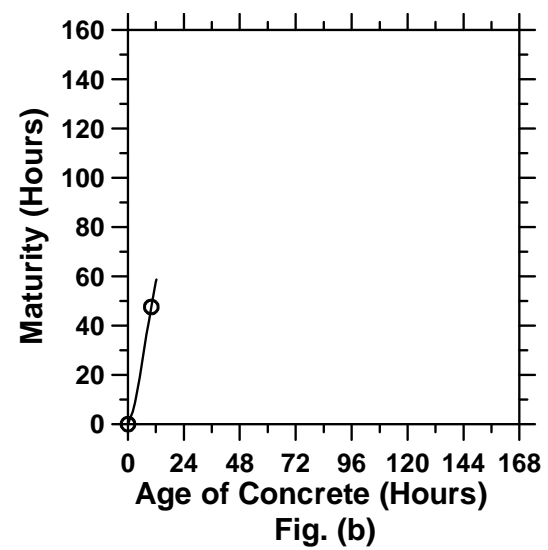
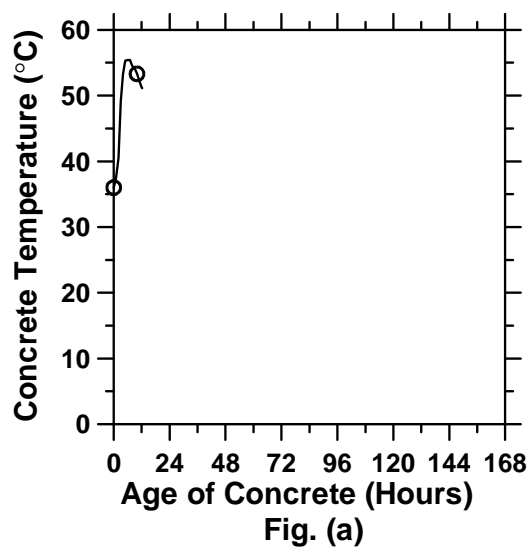


Figure A.130: Pavement cured at 36°C ambient temperature with a D/8 saw-cut depth introduced at 3 hours (cont'd).

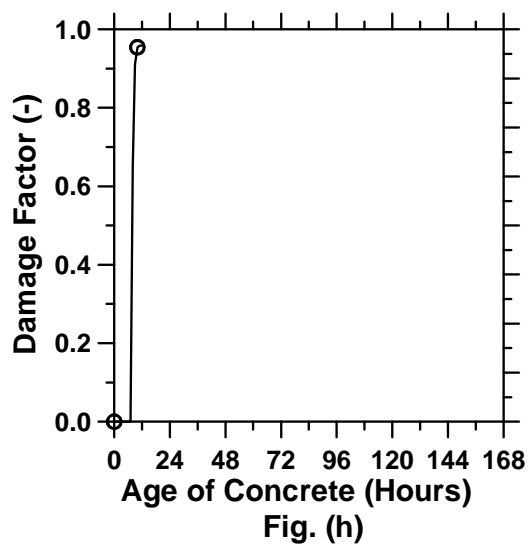
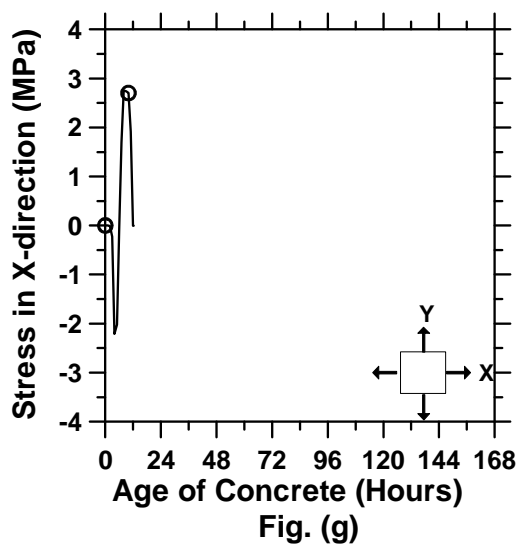
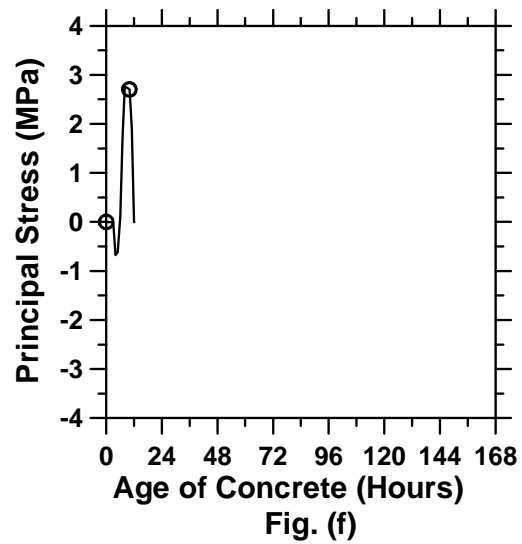
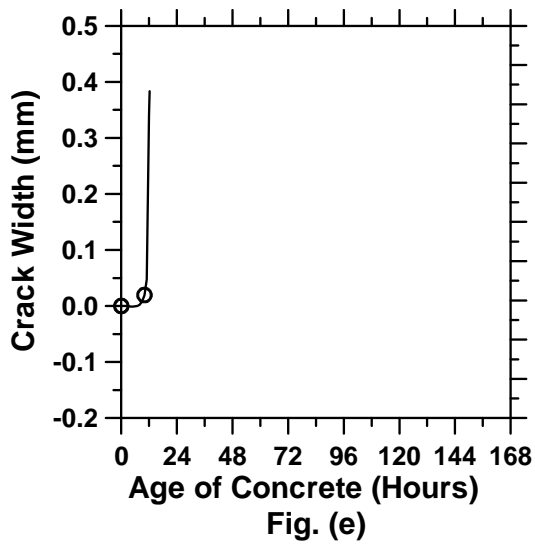


Figure A.130: Pavement cured at 36°C ambient temperature with a D/8 saw-cut depth introduced at 3 hours.

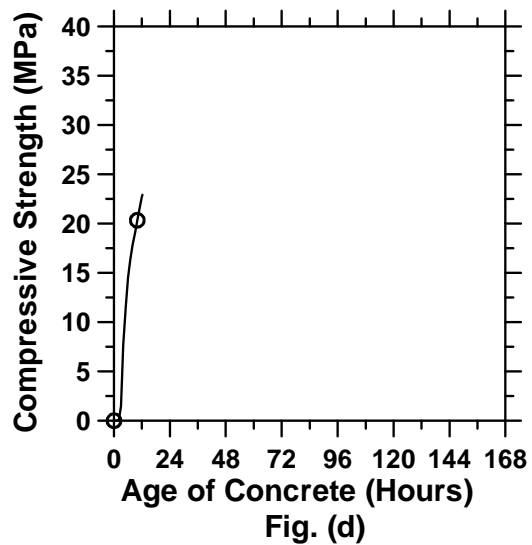
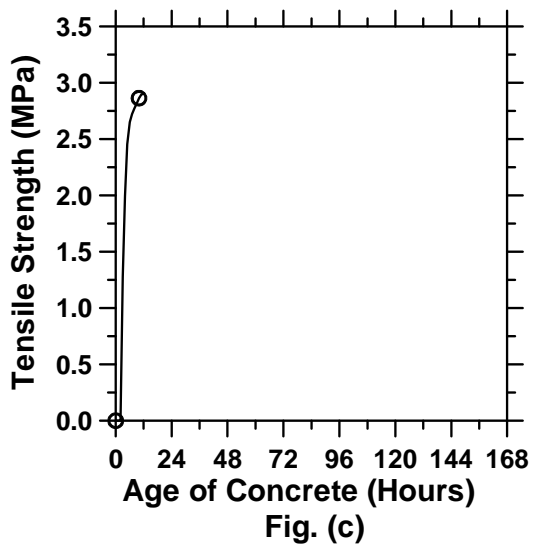
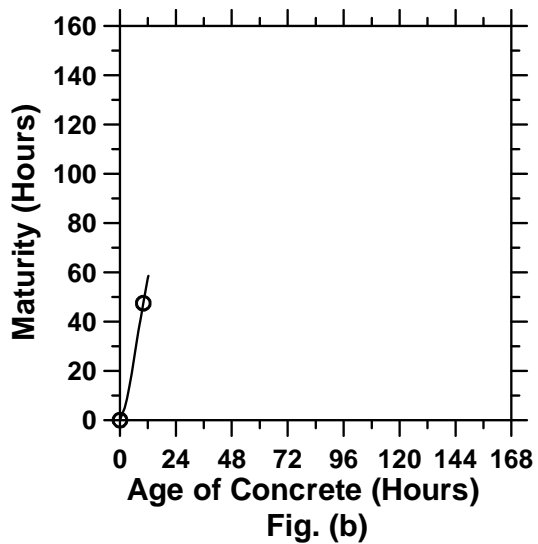
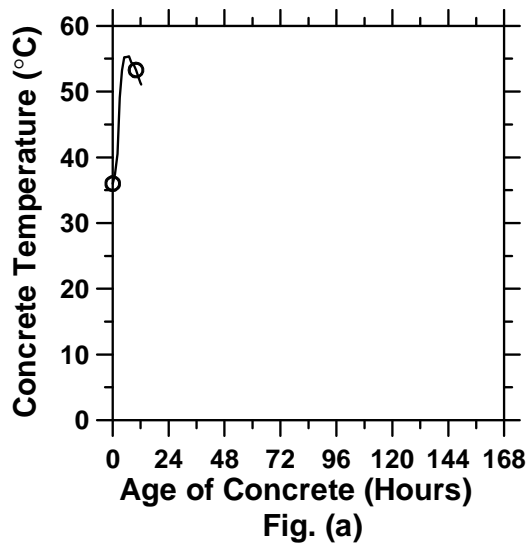


Figure A.131: Pavement cured at 36°C ambient temperature with a D/8 saw-cut depth introduced at 6 hours (cont'd).

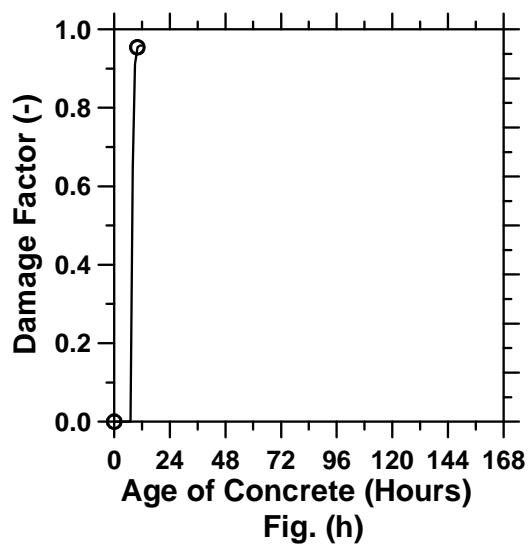
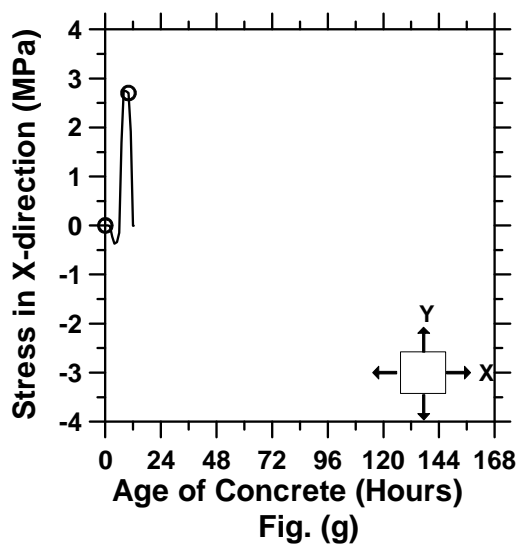
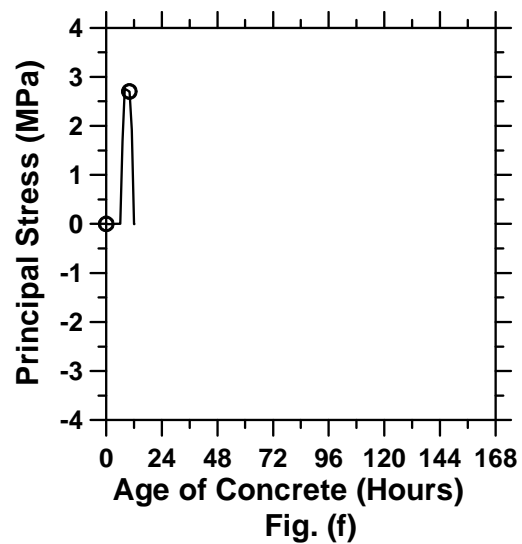
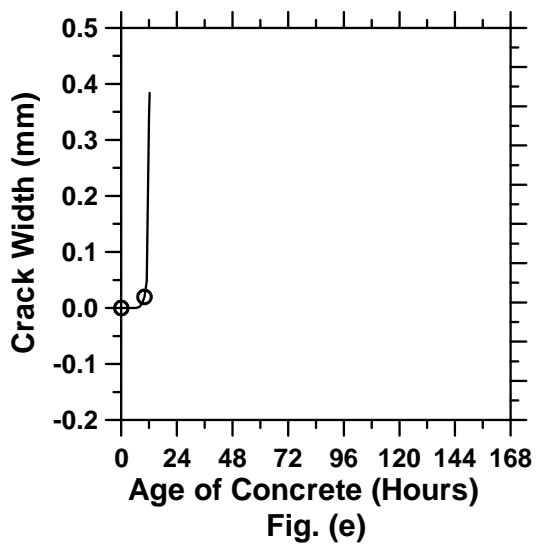


Figure A.131: Pavement cured at 36°C ambient temperature with a D/8 saw-cut depth introduced at 6 hours.

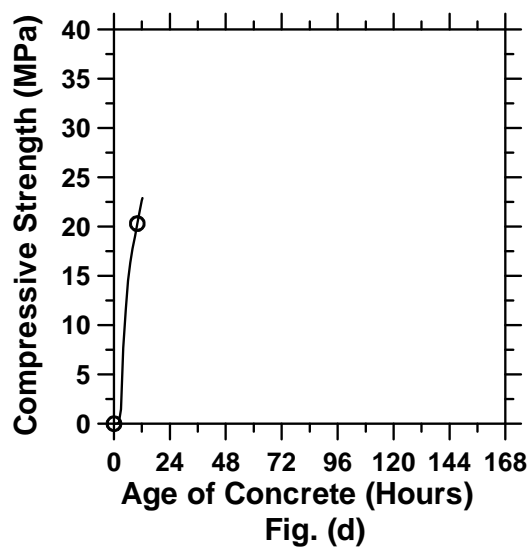
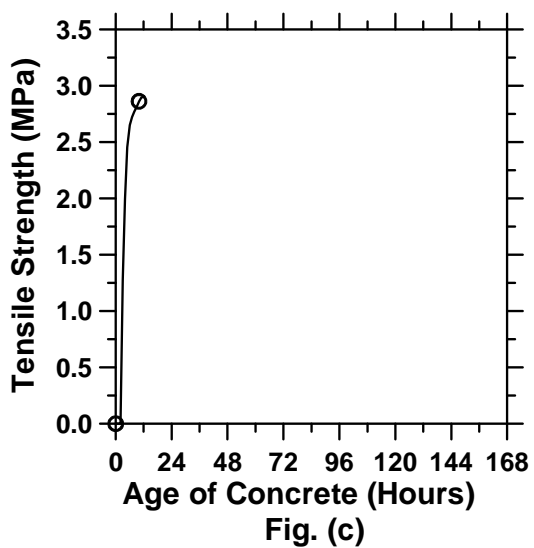
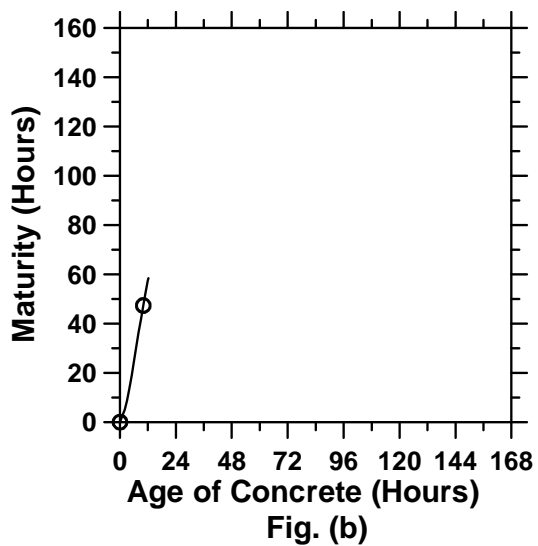
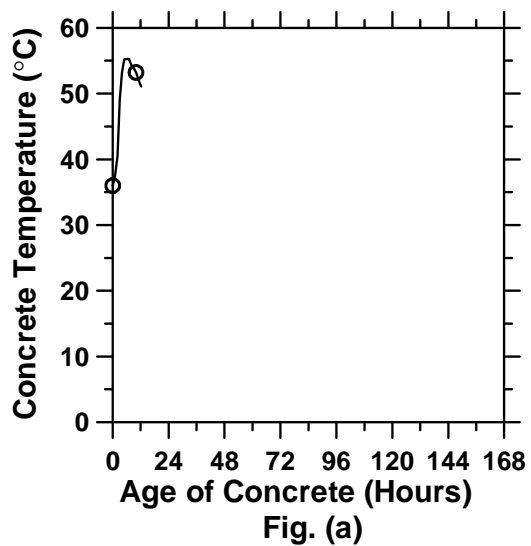


Figure A.132: Pavement cured at 36°C ambient temperature with a D/8 saw-cut depth introduced at 9 hours (cont'd).

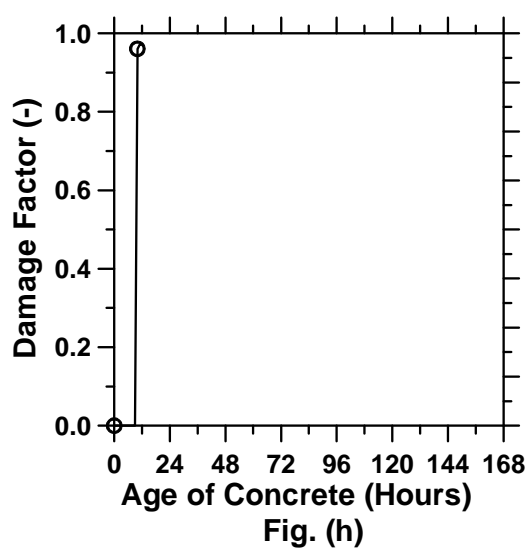
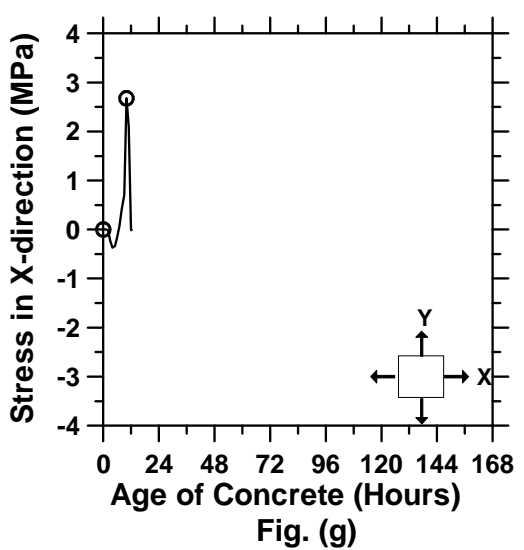
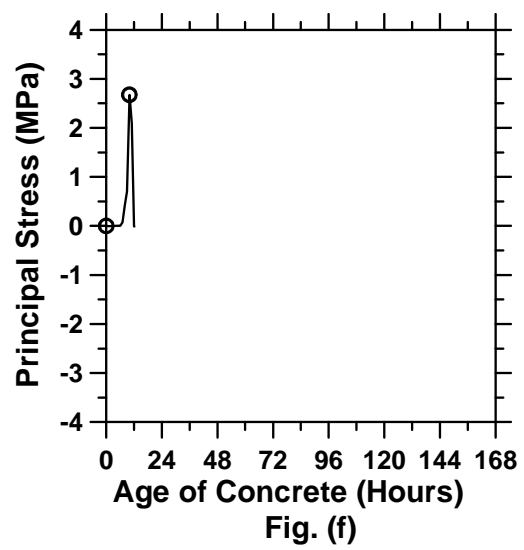
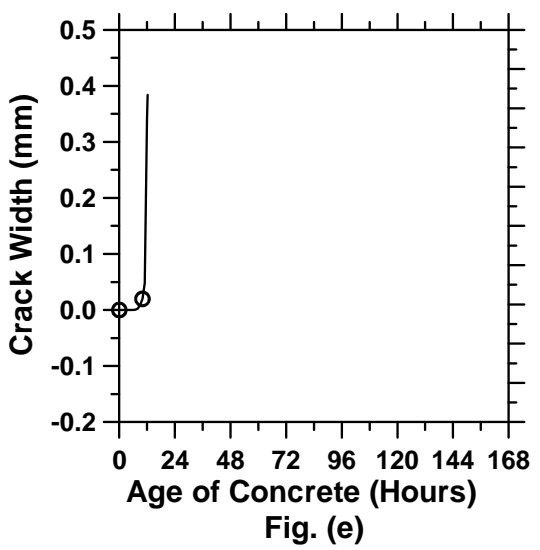


Figure A.132: Pavement cured at 36°C ambient temperature with a D/8 saw-cut depth introduced at 9 hours.

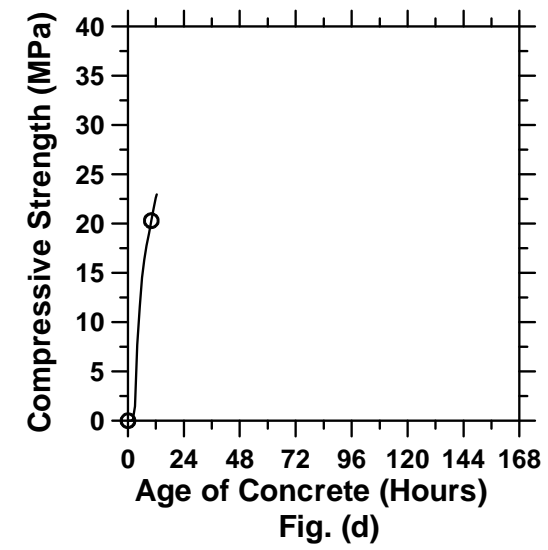
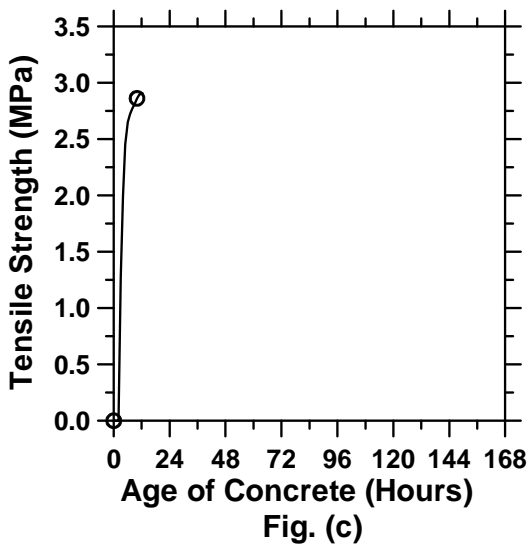
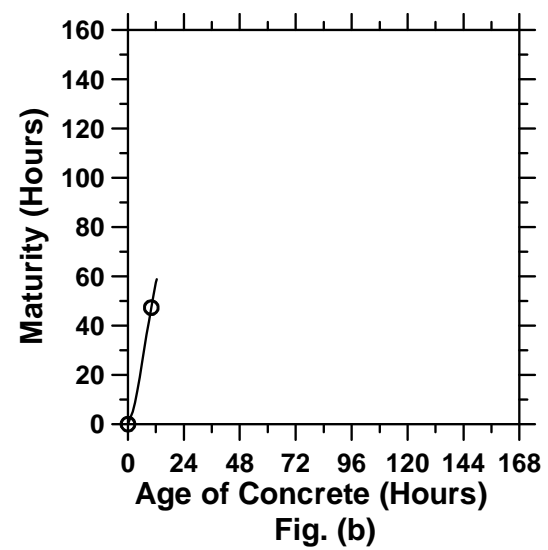
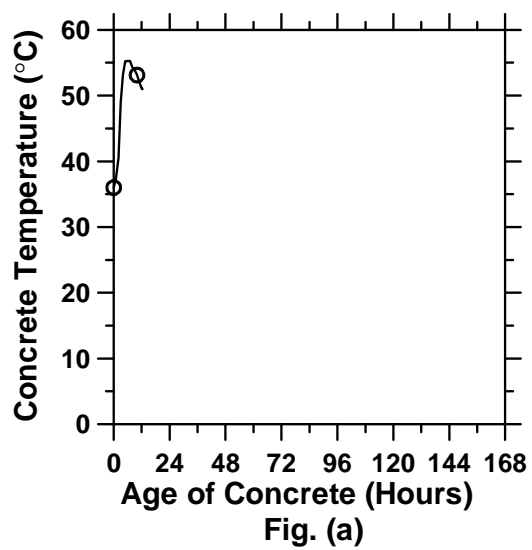


Figure A.133: Pavement cured at 36°C ambient temperature with a D/8 saw-cut depth introduced at 12 hours (cont'd).

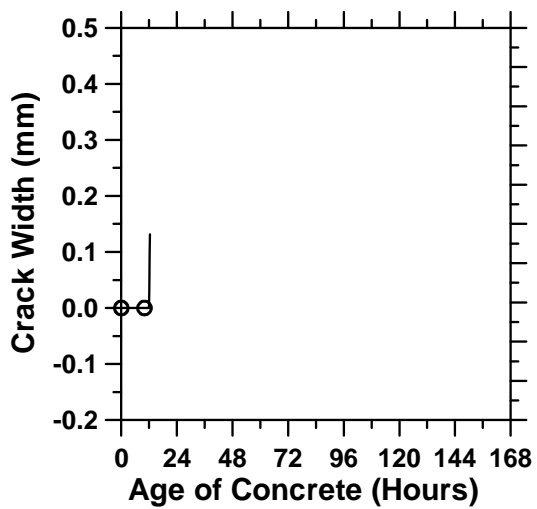


Fig. (e)

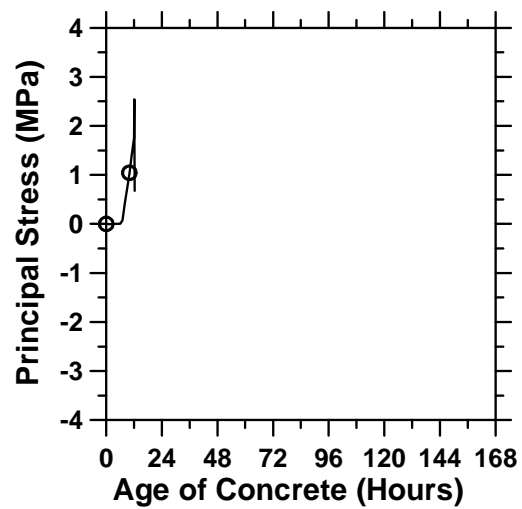


Fig. (f)

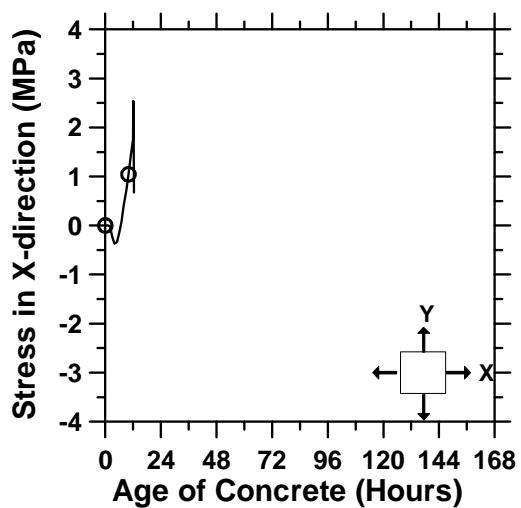


Fig. (g)

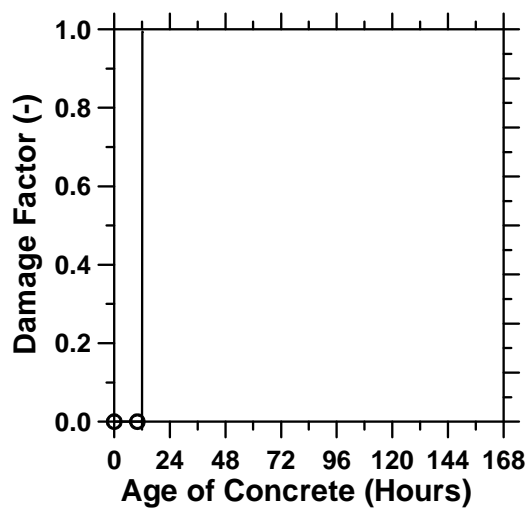


Fig. (h)

Figure A.133: Pavement cured at 36°C ambient temperature with a D/8 saw-cut depth introduced at 12 hours.

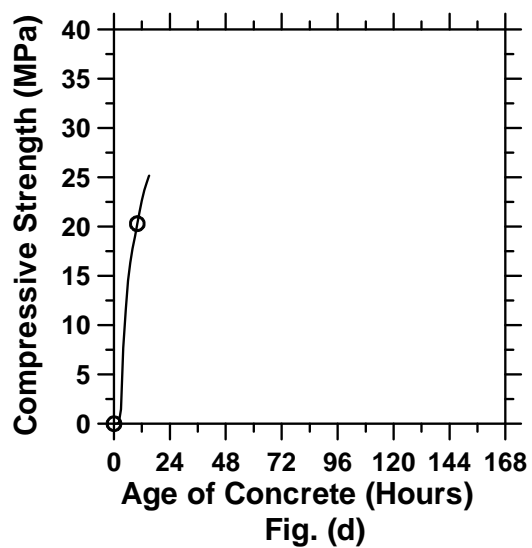
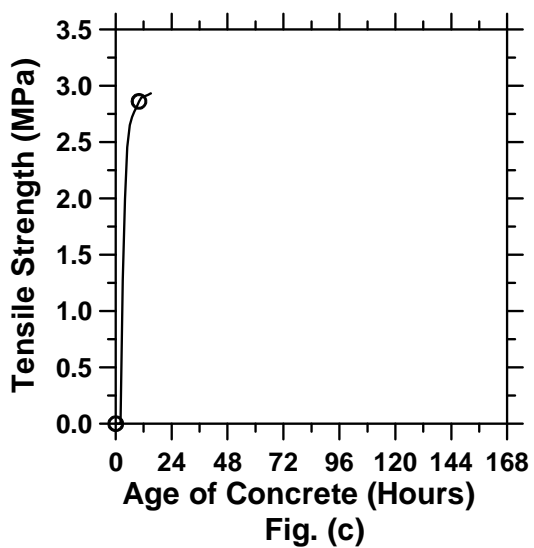
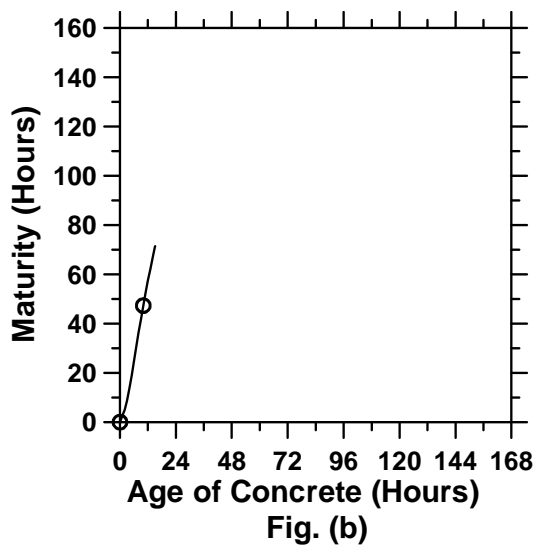
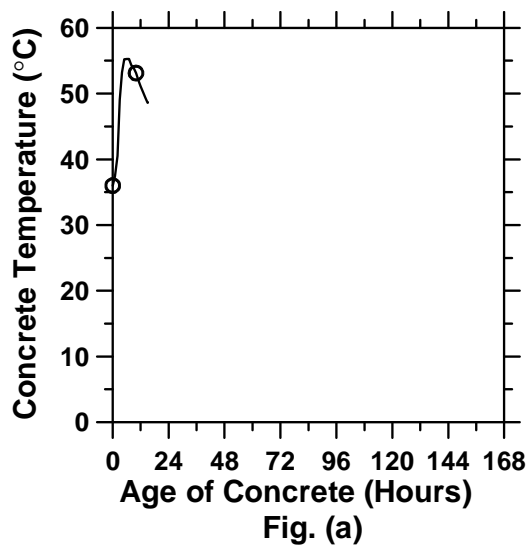


Figure A.134: Pavement cured at 36°C ambient temperature with a D/8 saw-cut depth introduced at 15 hours (cont'd).

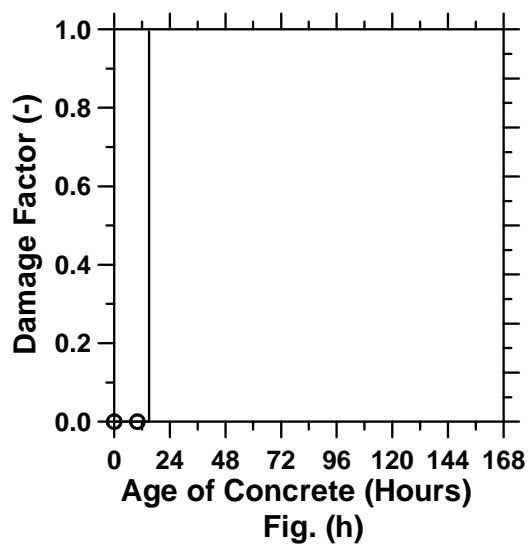
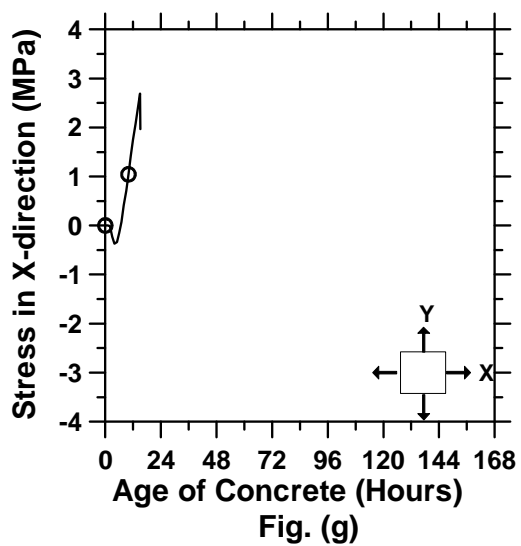
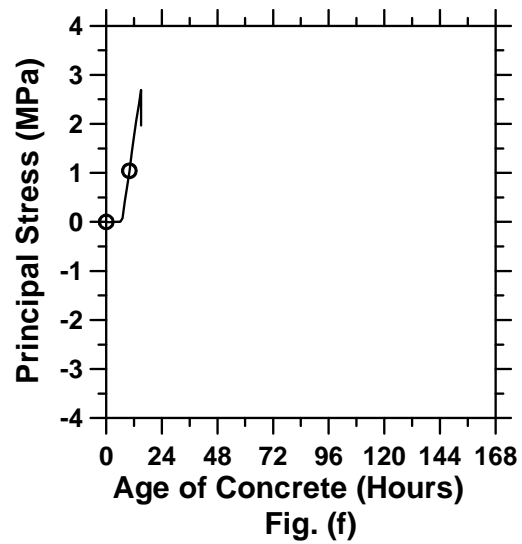
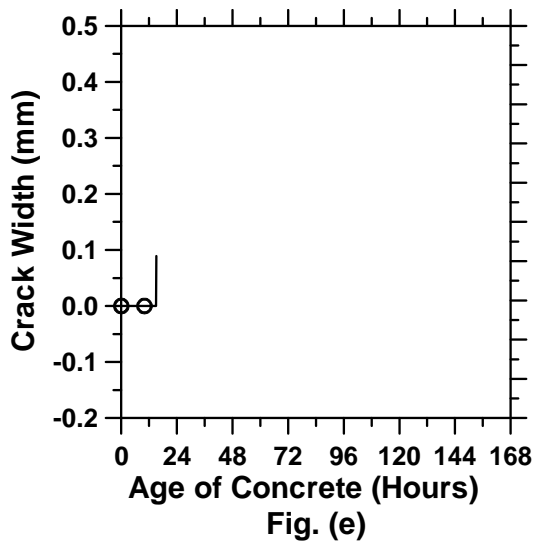


Figure A.134: Pavement cured at 36°C ambient temperature with a D/8 saw-cut depth introduced at 15 hours.

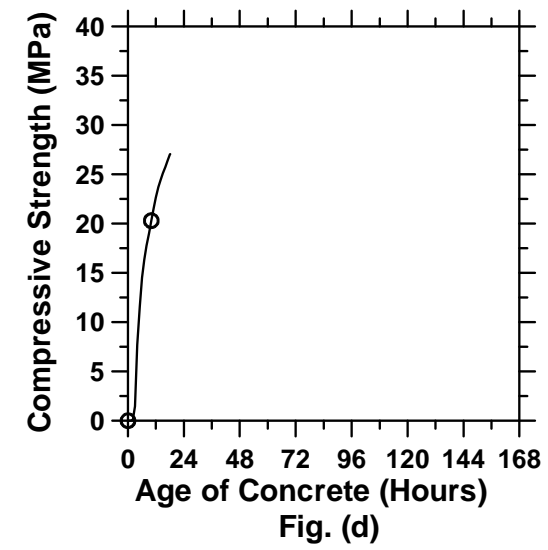
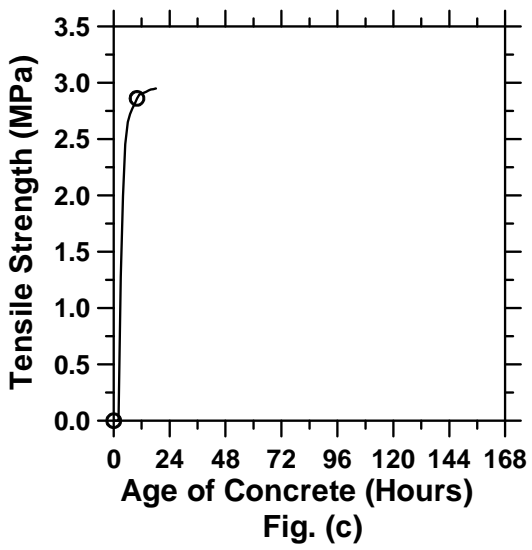
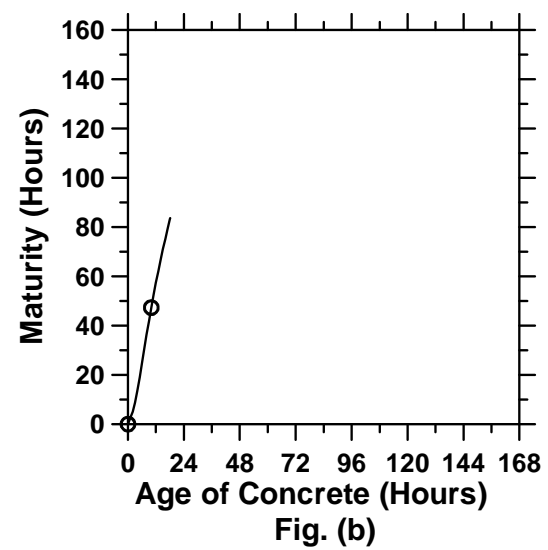
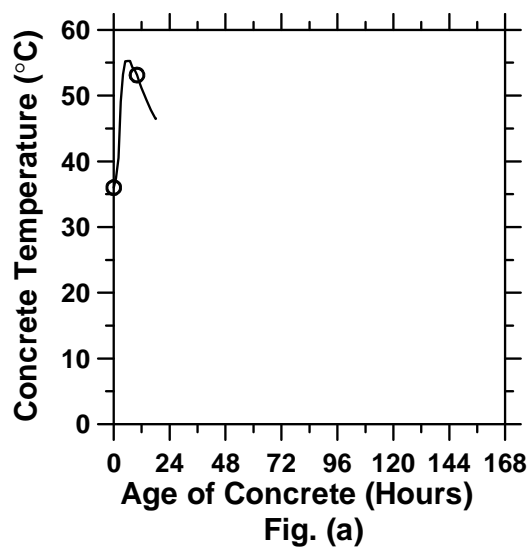


Figure A.135: Pavement cured at 36°C ambient temperature with a D/8 saw-cut depth introduced at 18 hours (cont'd).

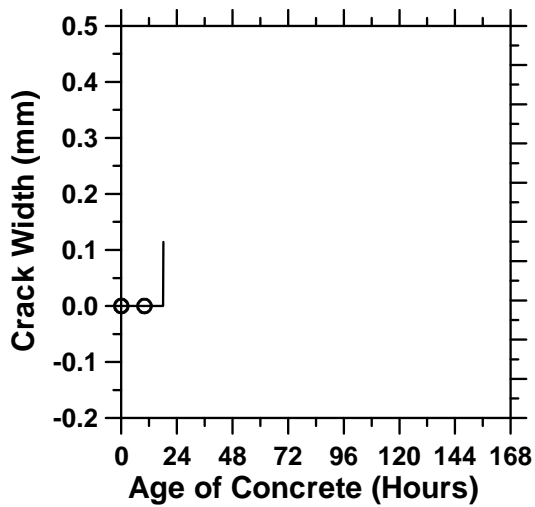


Fig. (e)

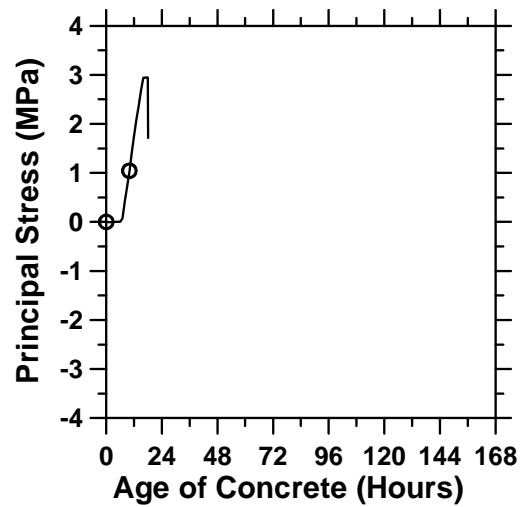


Fig. (f)

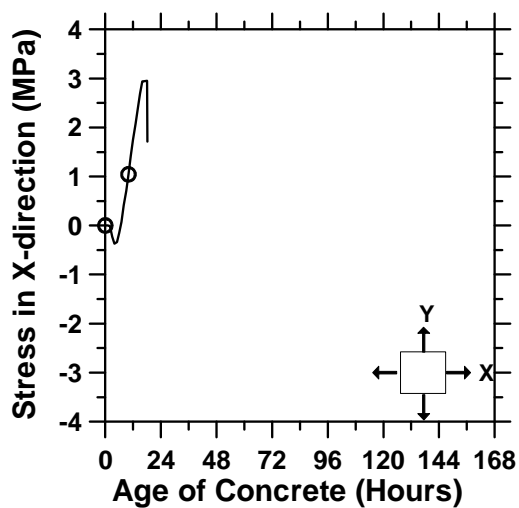


Fig. (g)

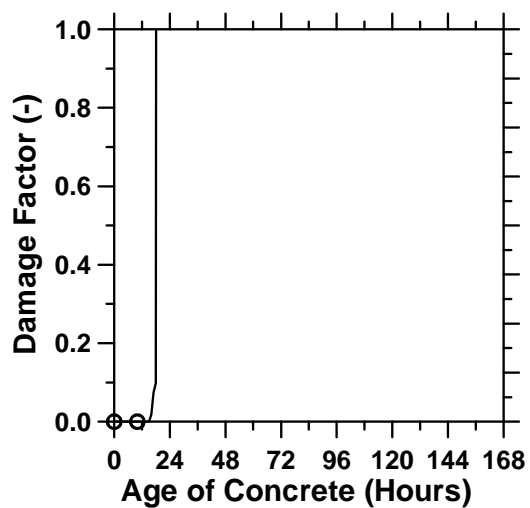


Fig. (h)

Figure A.135: Pavement cured at 36°C ambient temperature with a D/8 saw-cut depth introduced at 18 hours.

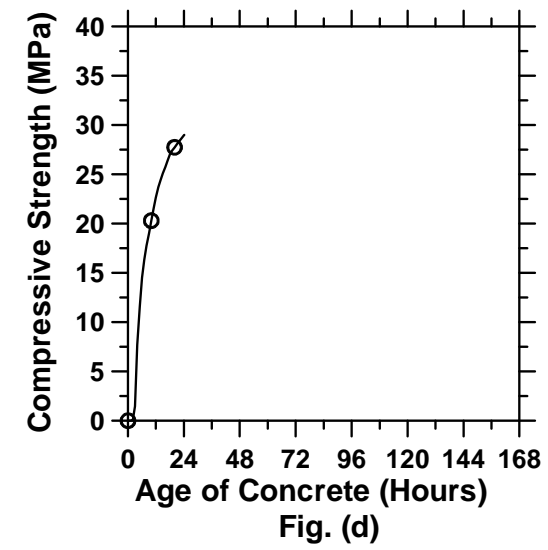
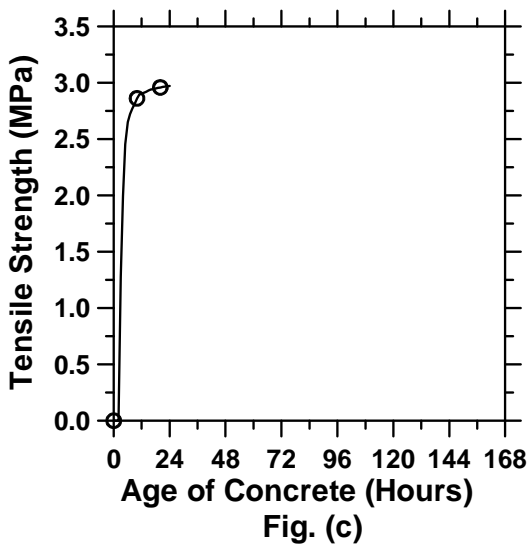
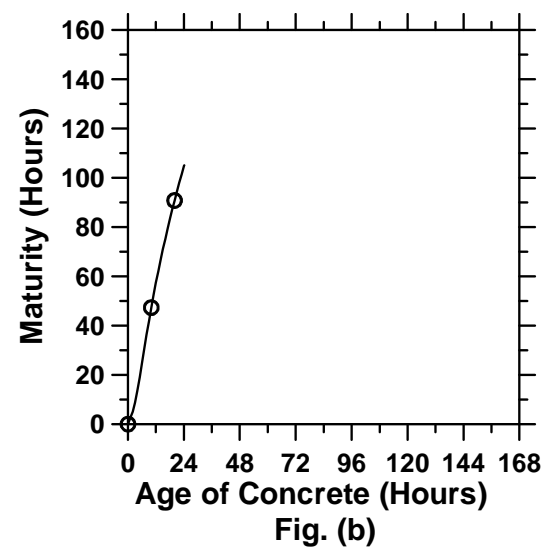
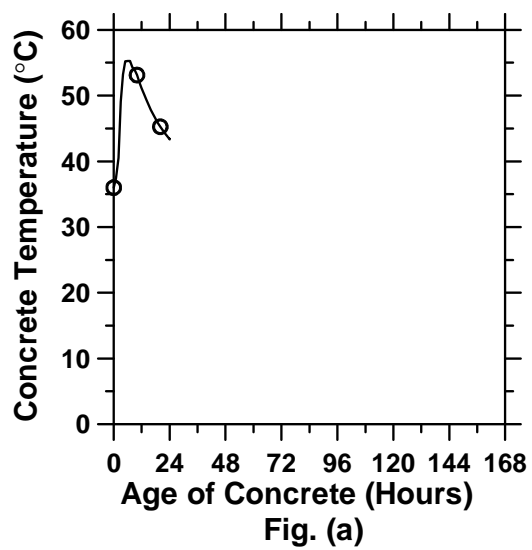


Figure A.136: Pavement cured at 36°C ambient temperature with a D/8 saw-cut depth introduced at 24 hours (cont'd).

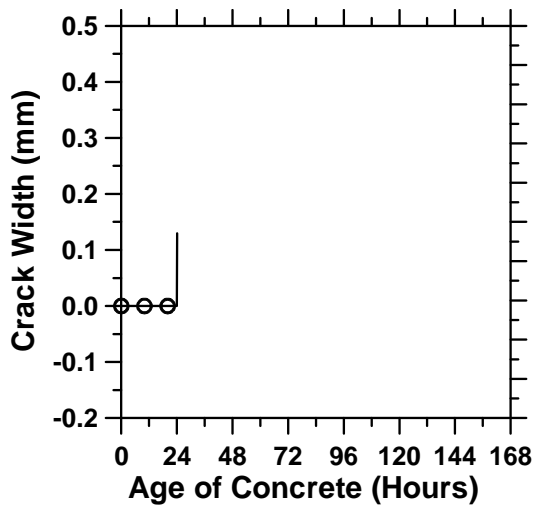


Fig. (e)

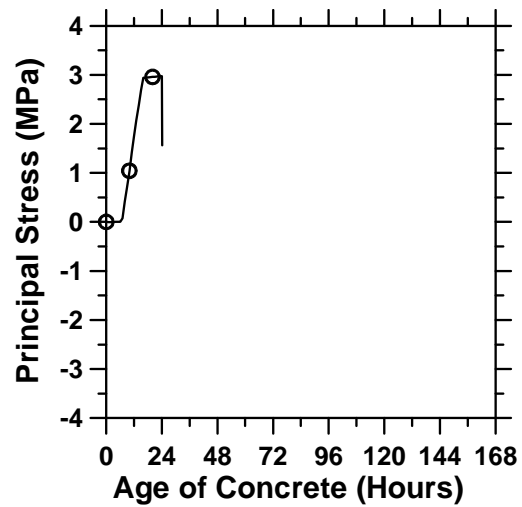


Fig. (f)

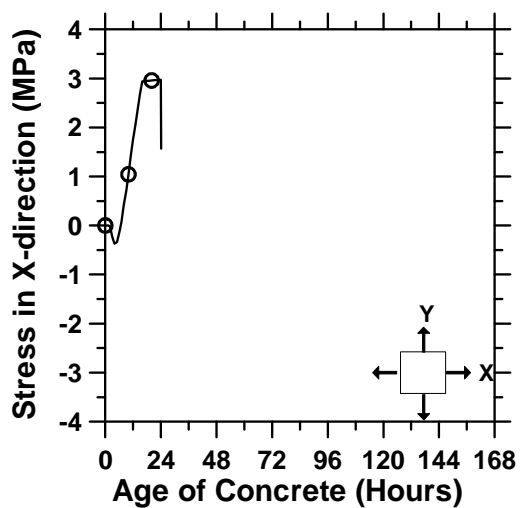


Fig. (g)

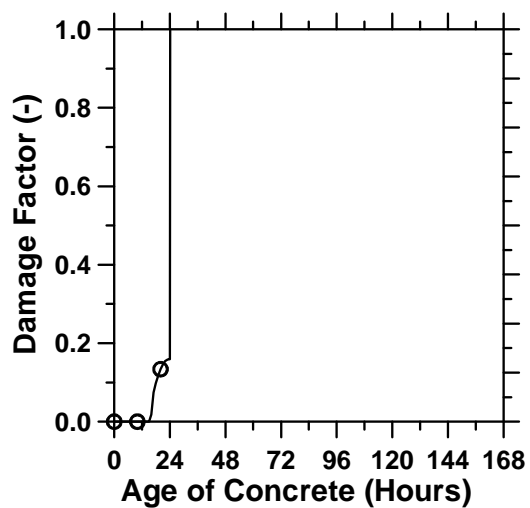


Fig. (h)

Figure A.136: Pavement cured at 36°C ambient temperature with a D/8 saw-cut depth introduced at 24 hours.

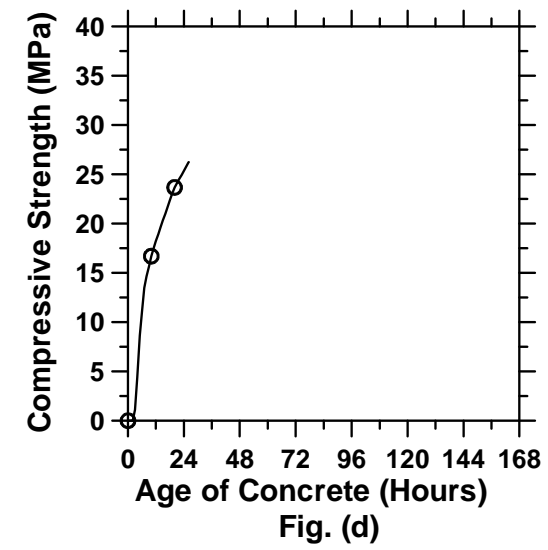
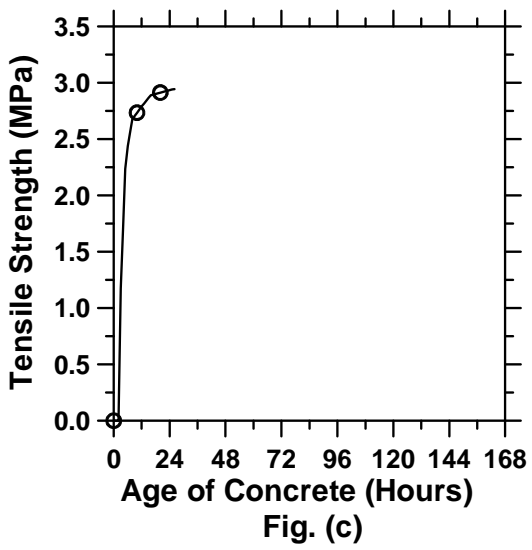
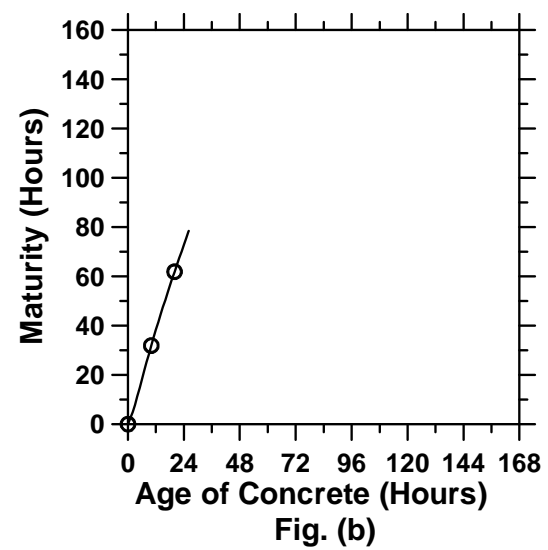
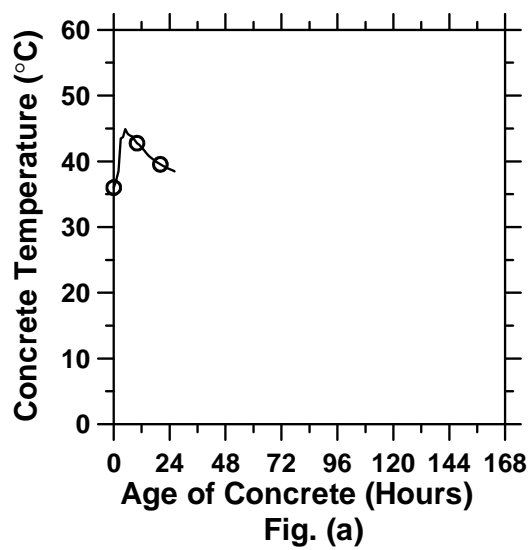


Figure A.137: Pavement cured at 36°C ambient temperature with a D/100 saw-cut depth introduced at 0 hours (cont'd).

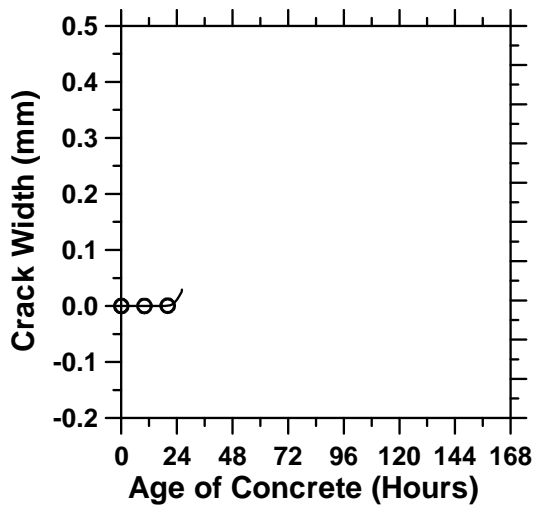


Fig. (e)

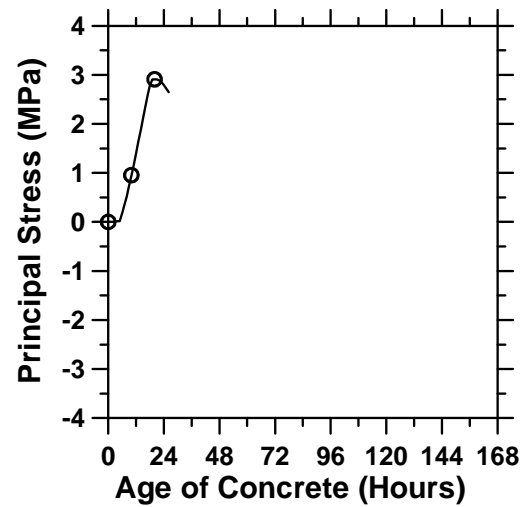


Fig. (f)

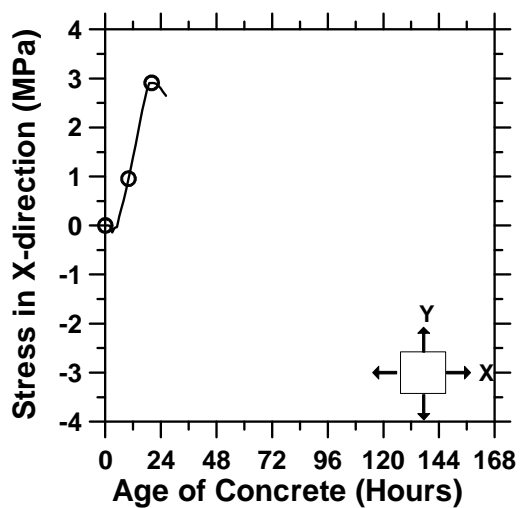


Fig. (g)

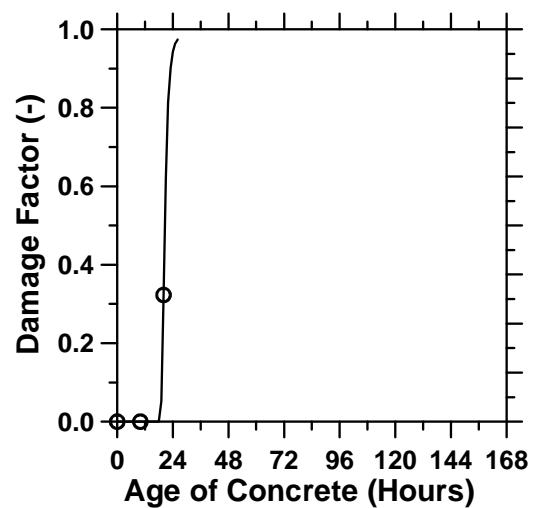


Fig. (h)

Figure A.137: Pavement cured at 36°C ambient temperature with a D/100 saw-cut depth introduced at 0 hours.

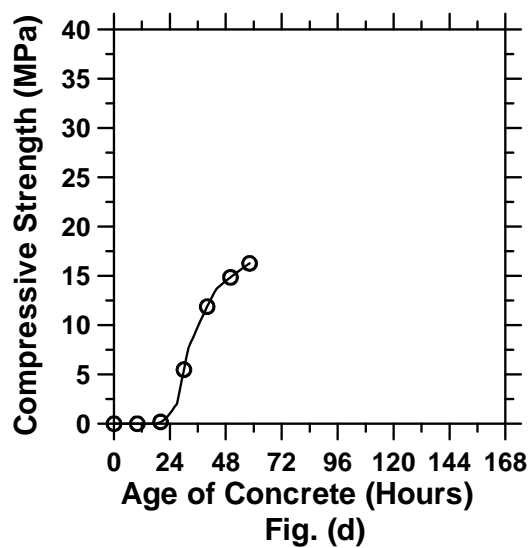
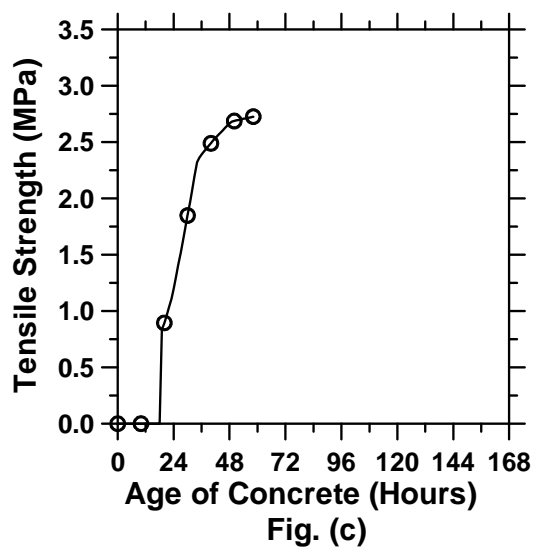
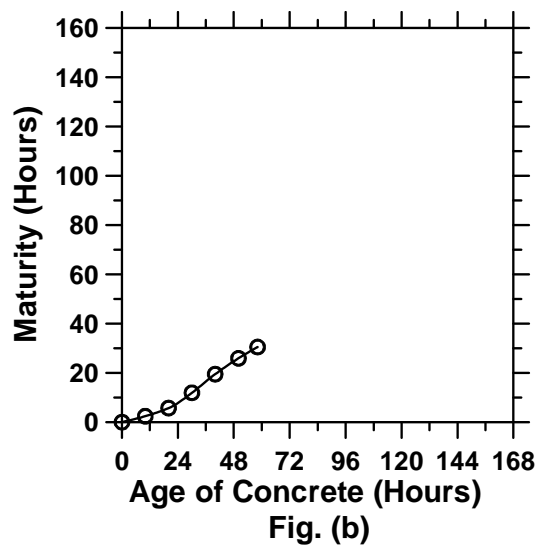
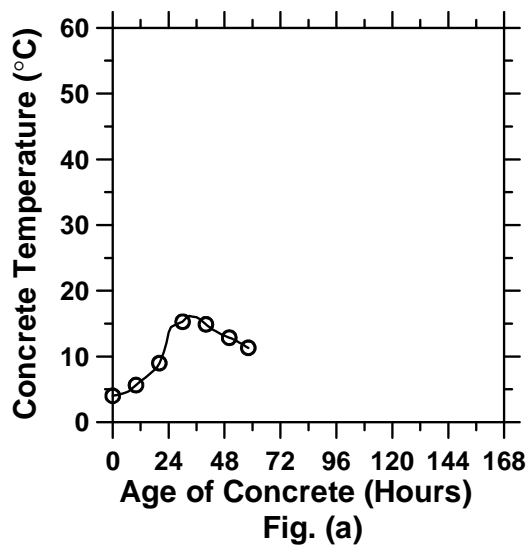


Figure A.138: Pavement cured at 4°C ambient temperature with a D/2 saw-cut depth introduced at 0 hour (cont'd).

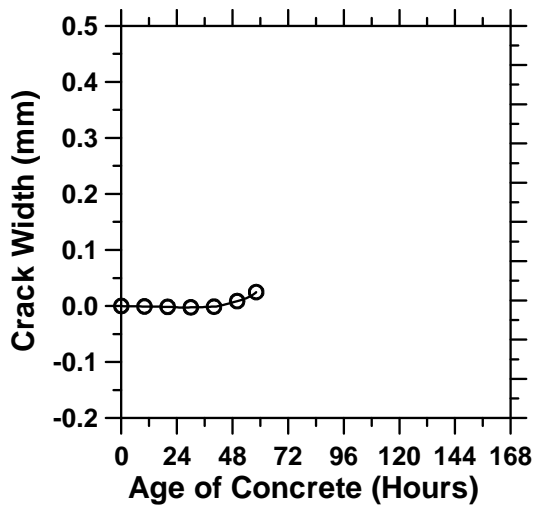


Fig. (e)

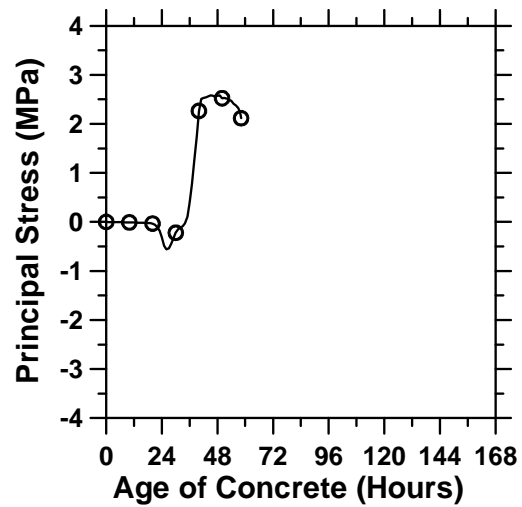


Fig. (f)

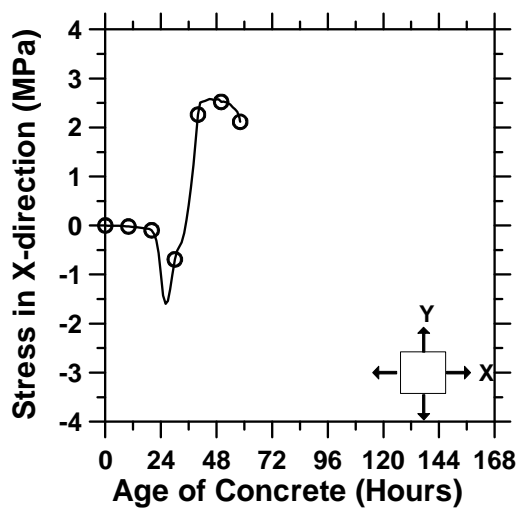


Fig. (g)

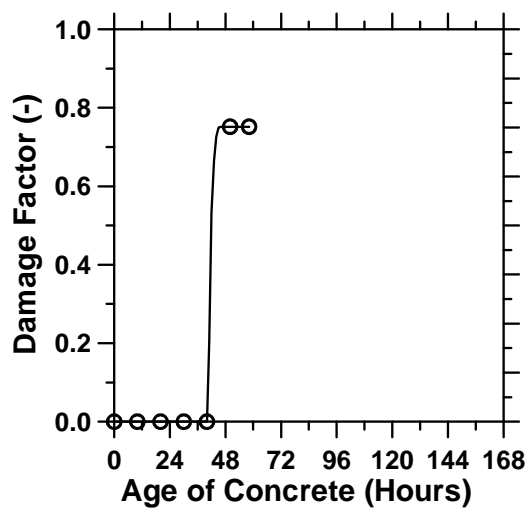


Fig. (h)

Figure A.138: Pavement cured at 4°C ambient temperature with a D/2 saw-cut depth introduced at 0 hour.

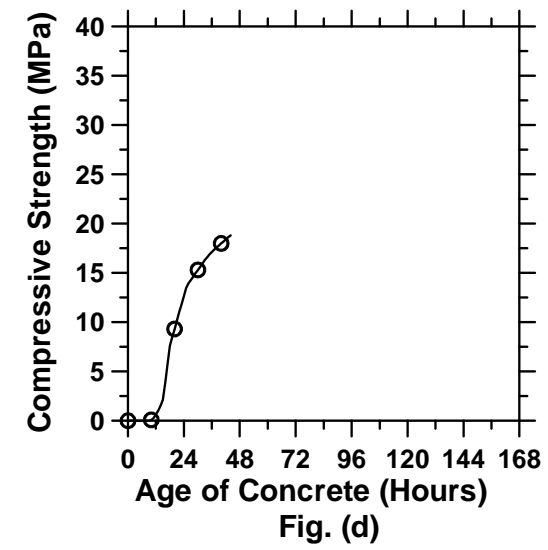
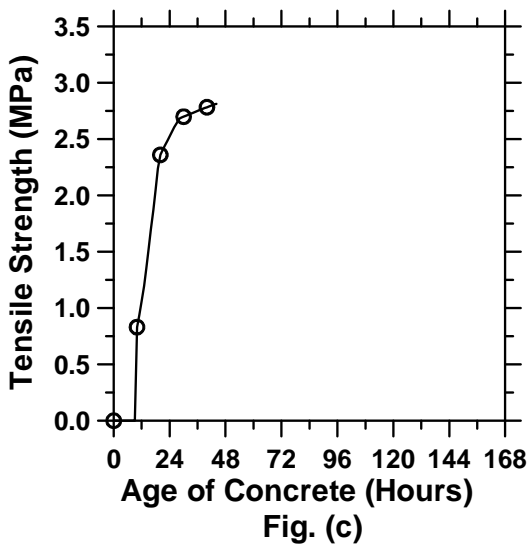
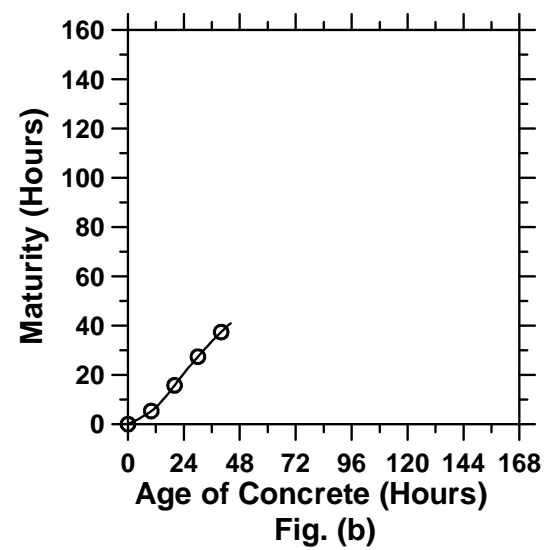
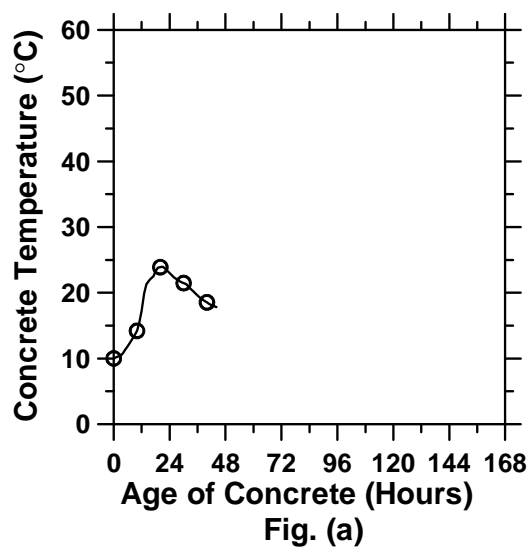


Figure A.139: Pavement cured at 10°C ambient temperature with a D/2 saw-cut depth introduced at 0 hour (cont'd).

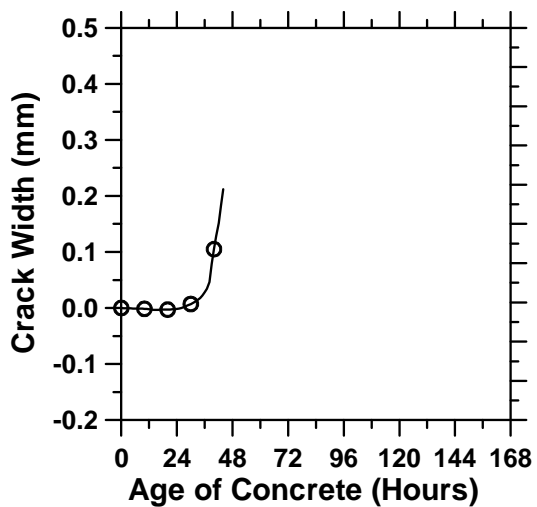


Fig. (e)

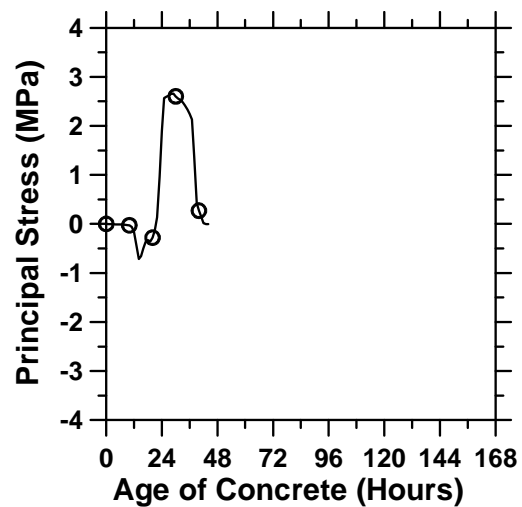


Fig. (f)

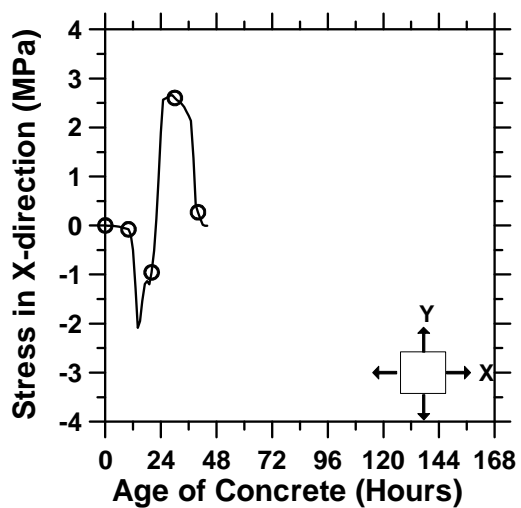


Fig. (g)

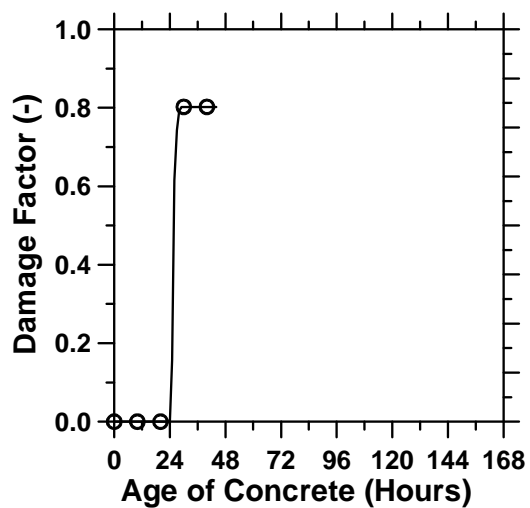


Fig. (h)

Figure A.139: Pavement cured at 10°C ambient temperature with a D/2 saw-cut depth introduced at 0 hour.

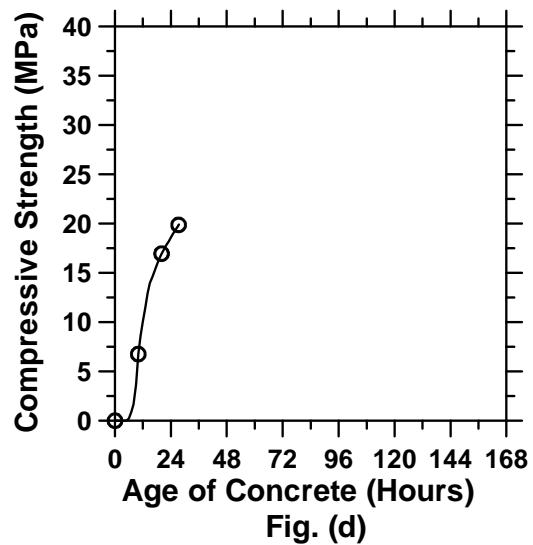
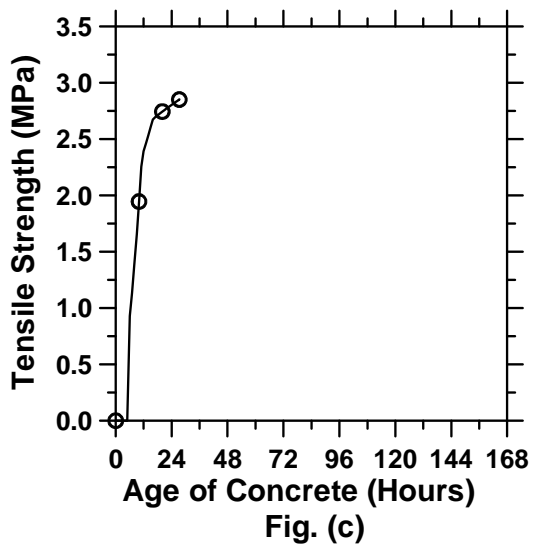
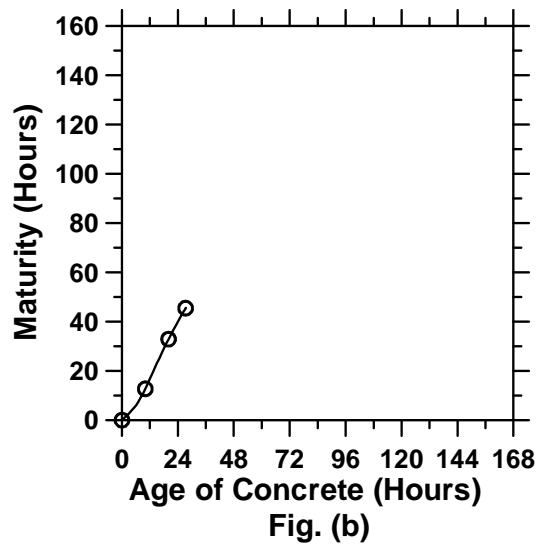
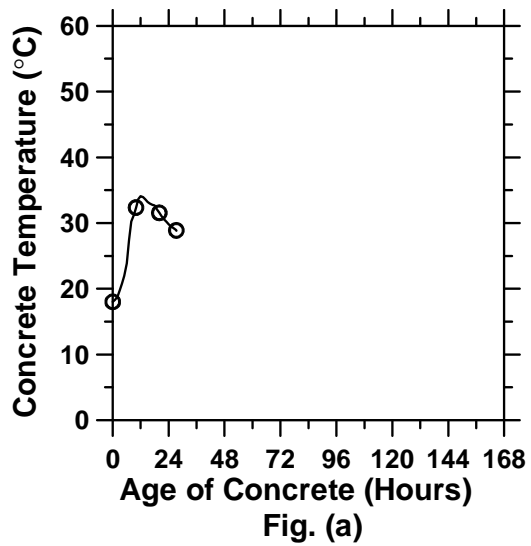


Figure A.140: Pavement cured at 18°C ambient temperature with a D/2 saw-cut depth introduced at 0 hour (cont'd).

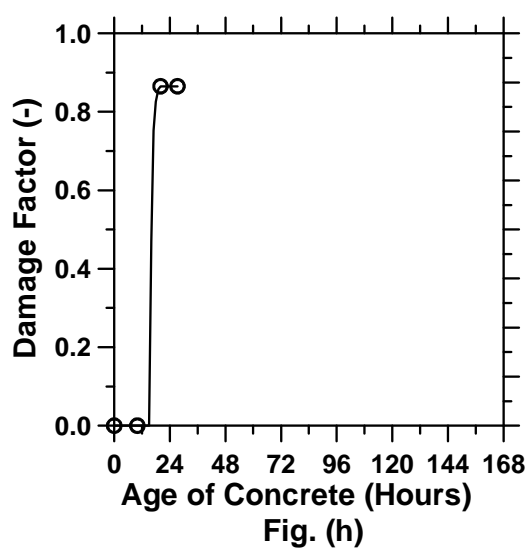
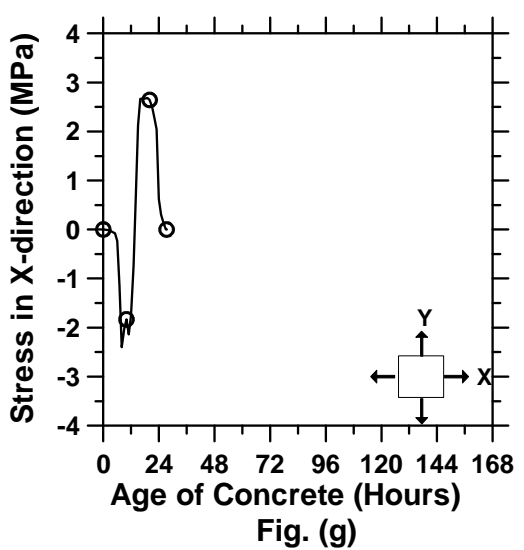
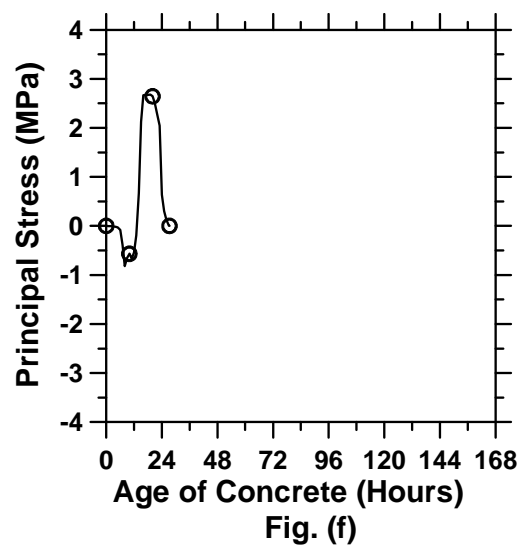
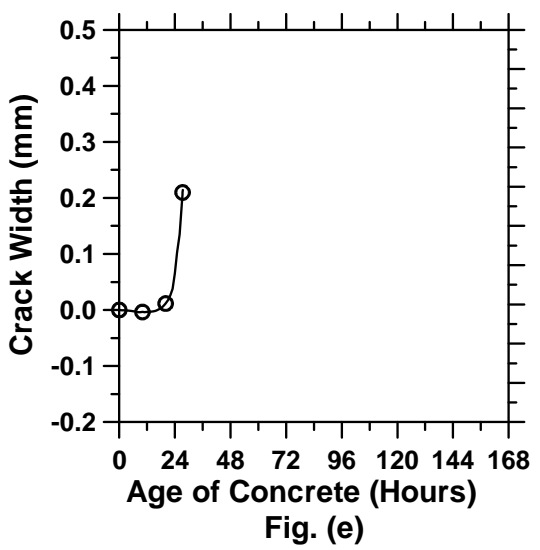


Figure A.140: Pavement cured at 18°C ambient temperature with a D/2 saw-cut depth introduced at 0 hour.

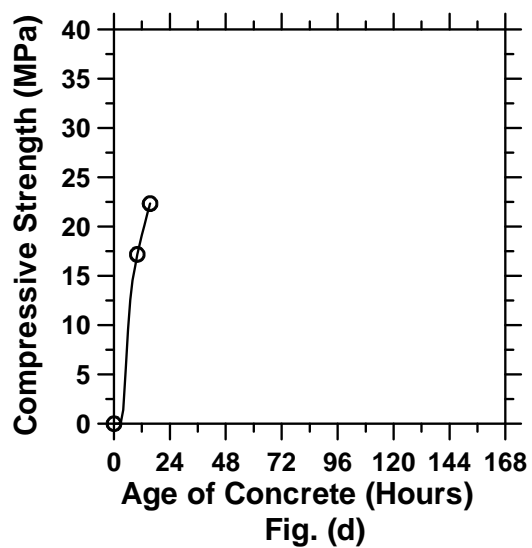
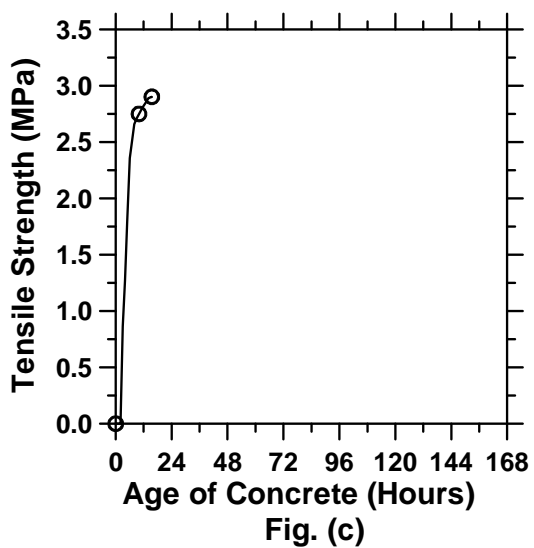
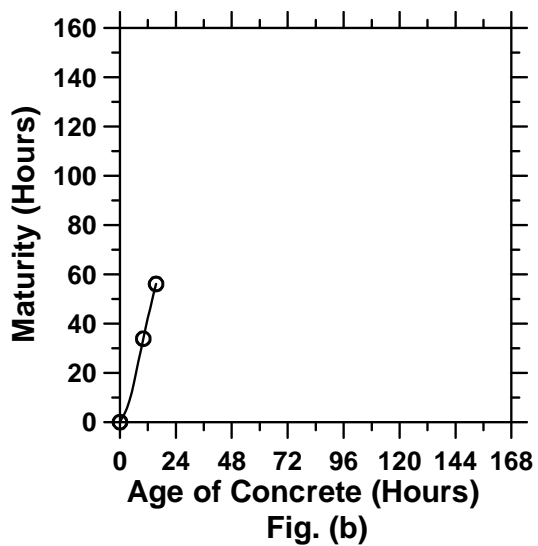
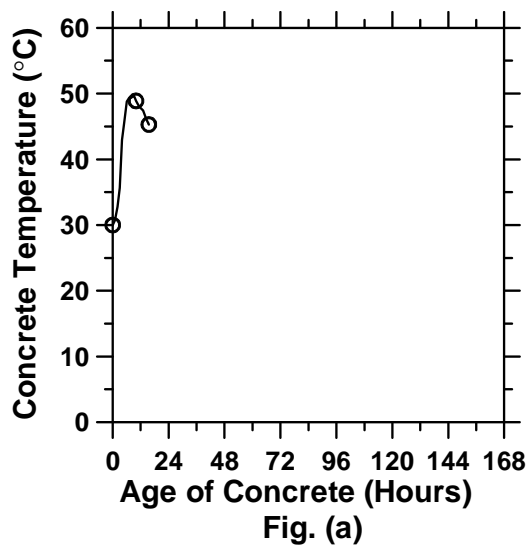


Figure A.141: Pavement cured at 30°C ambient temperature with a D/2 saw-cut depth introduced at 0 hour (cont'd).

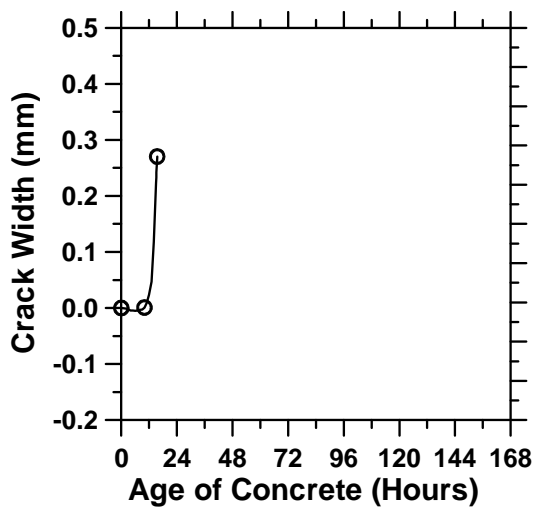


Fig. (e)

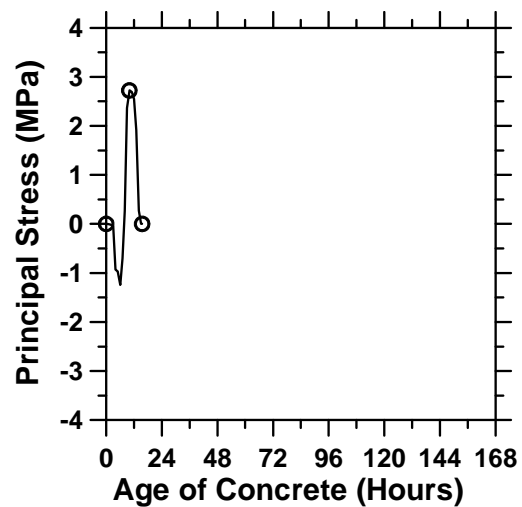


Fig. (f)

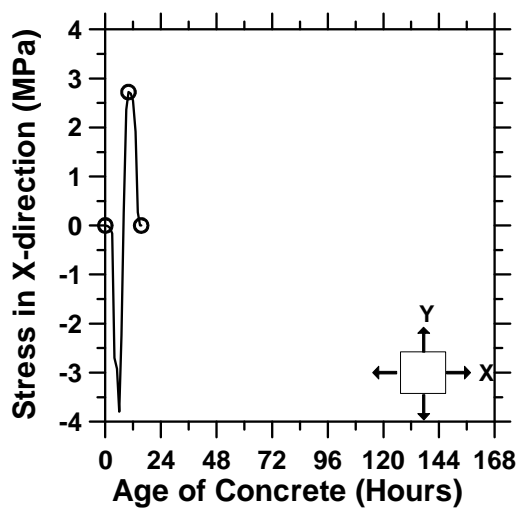


Fig. (g)

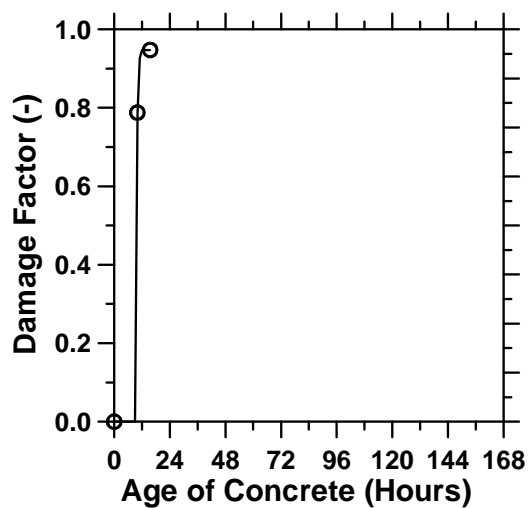


Fig. (h)

Figure A.141: Pavement cured at 30°C ambient temperature with a D/2 saw-cut depth introduced at 0 hour.

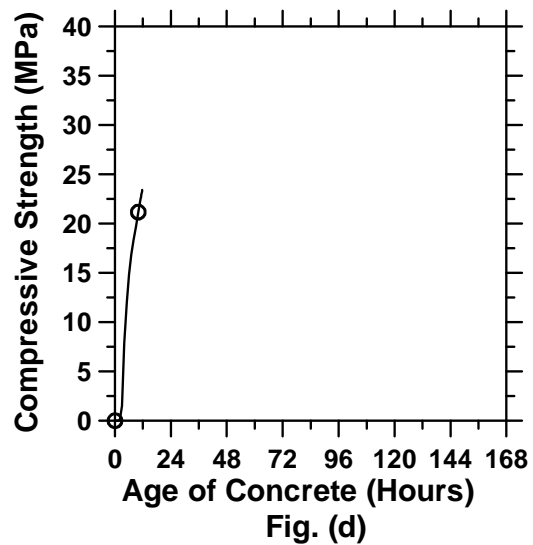
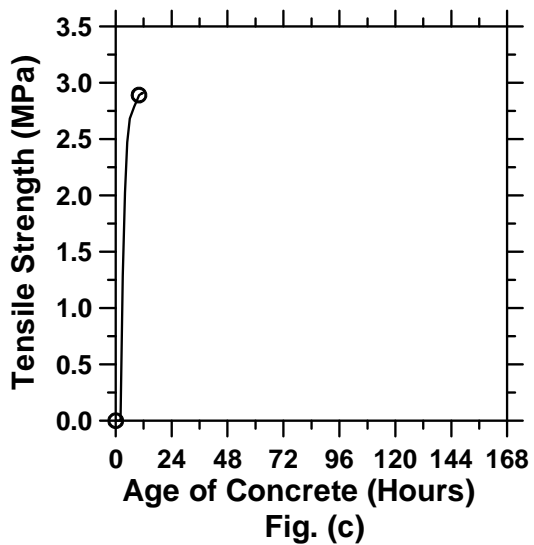
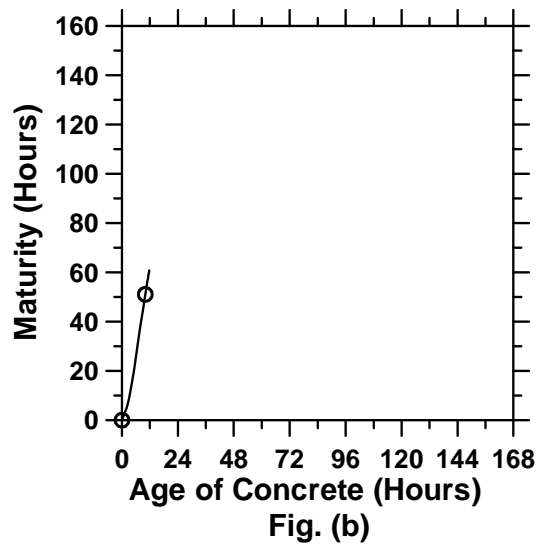
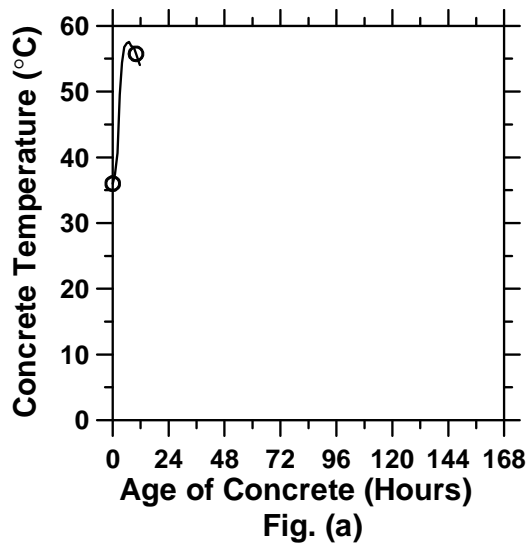


Figure A.142: Pavement cured at 36°C ambient temperature with a D/2 saw-cut depth introduced at 0 hour (cont'd).

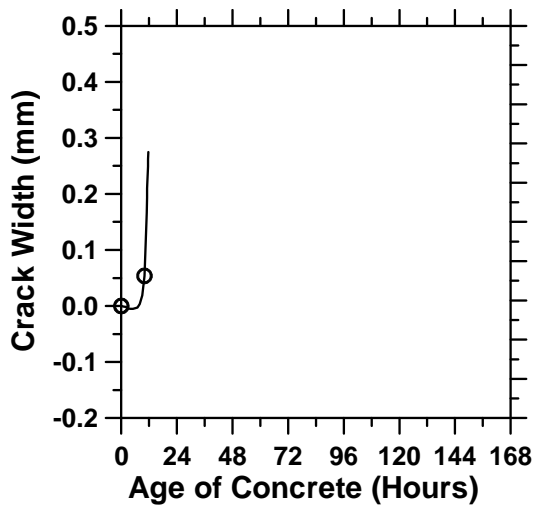


Fig. (e)

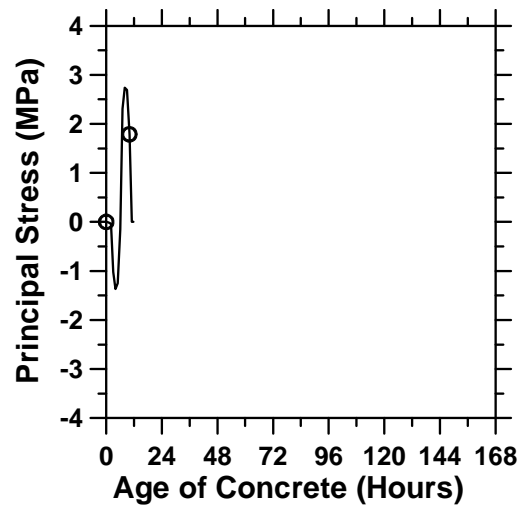


Fig. (f)

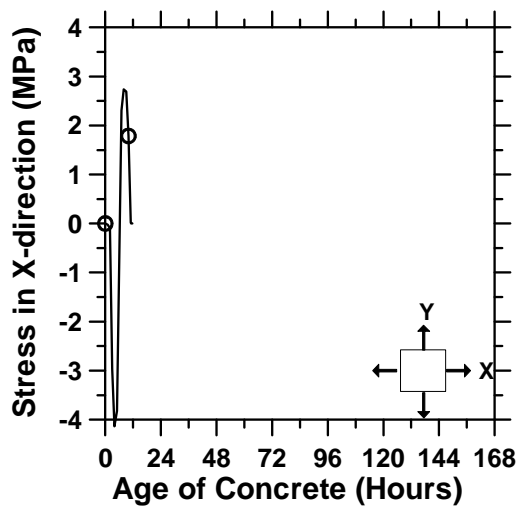


Fig. (g)

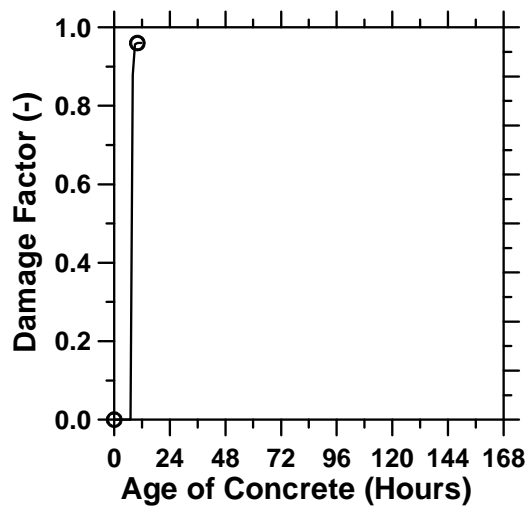


Fig. (h)

Figure A.142: Pavement cured at 36°C ambient temperature with a D/2 saw-cut depth introduced at 0 hour.

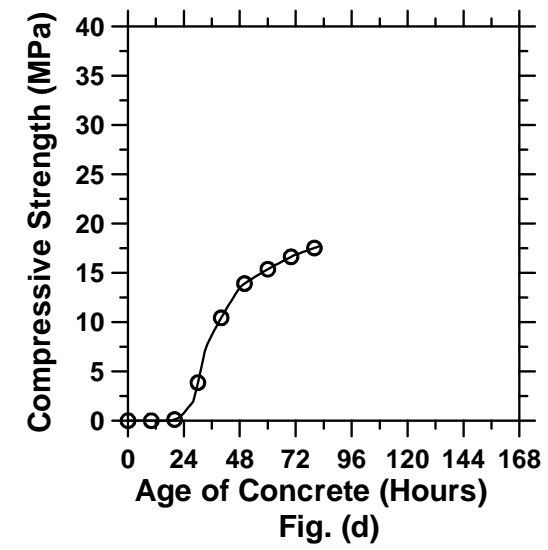
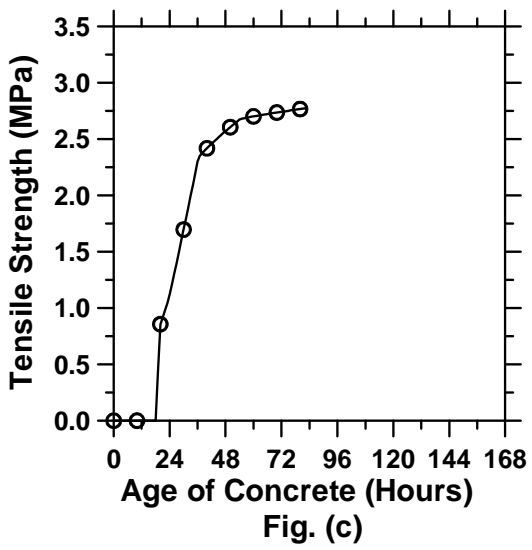
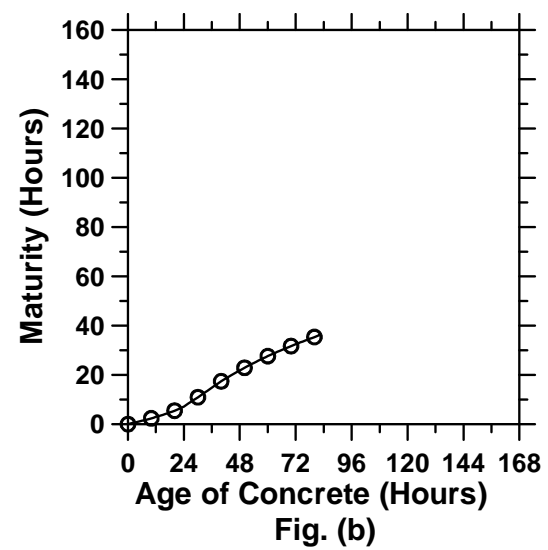
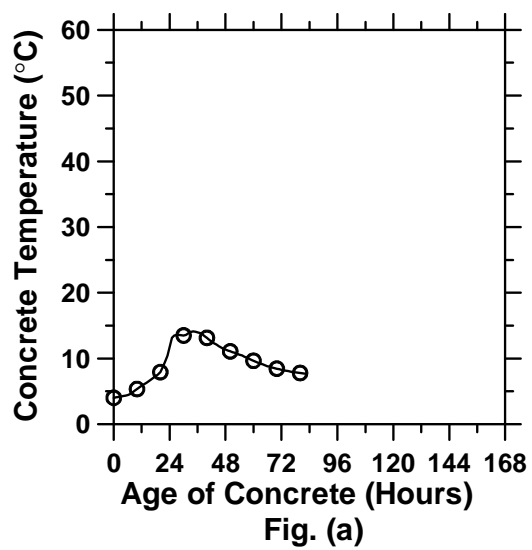


Figure A.143: Pavement cured at 4°C ambient temperature with a D/3 saw-cut depth introduced at 0 hour (cont'd).

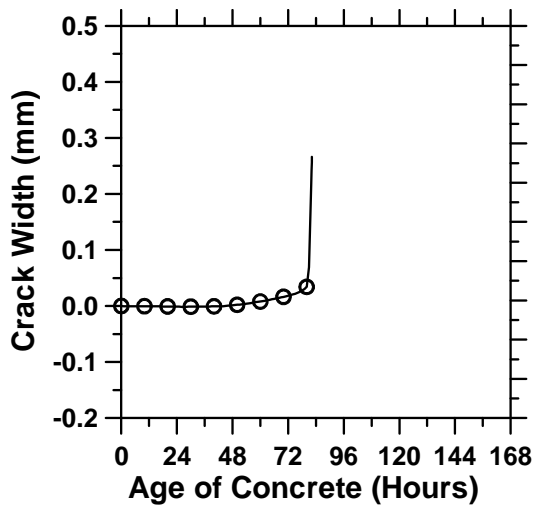


Fig. (e)

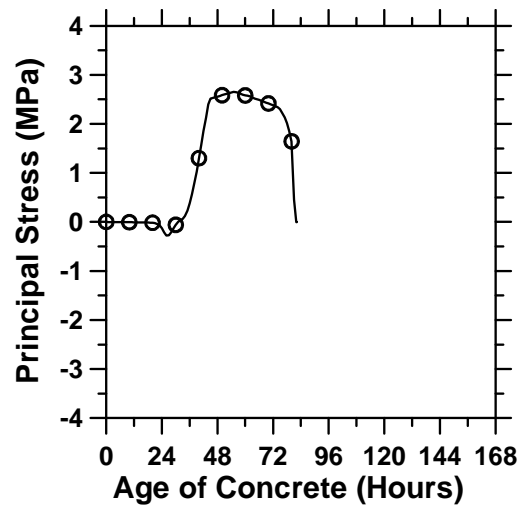


Fig. (f)

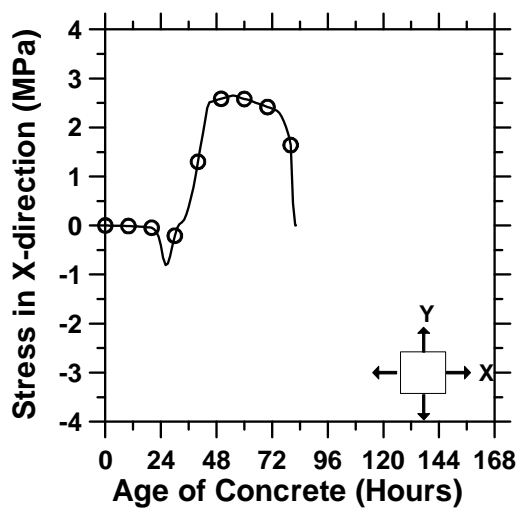


Fig. (g)

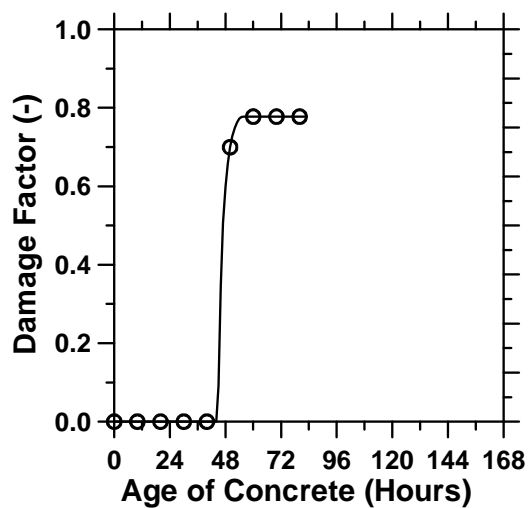


Fig. (h)

Figure A.143: Pavement cured at 4°C ambient temperature with a D/3 saw-cut depth introduced at 0 hour.

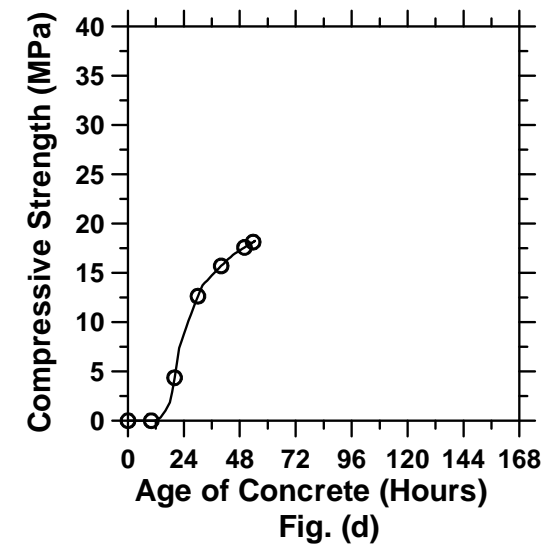
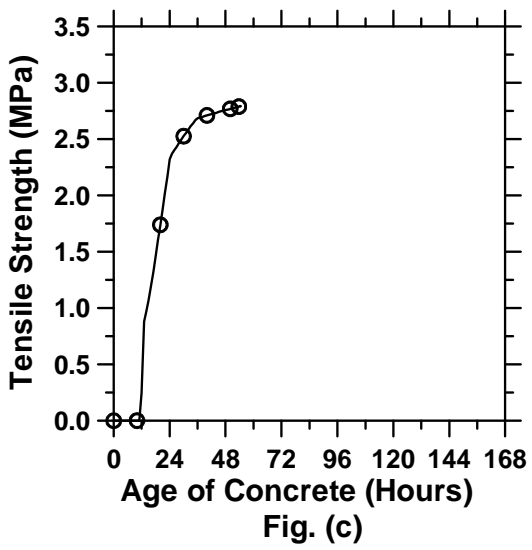
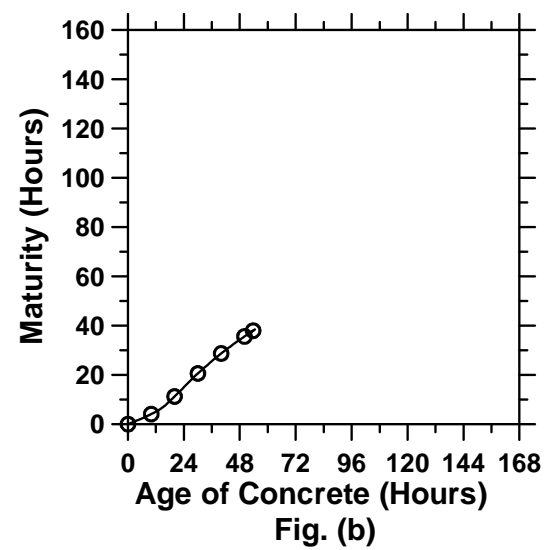
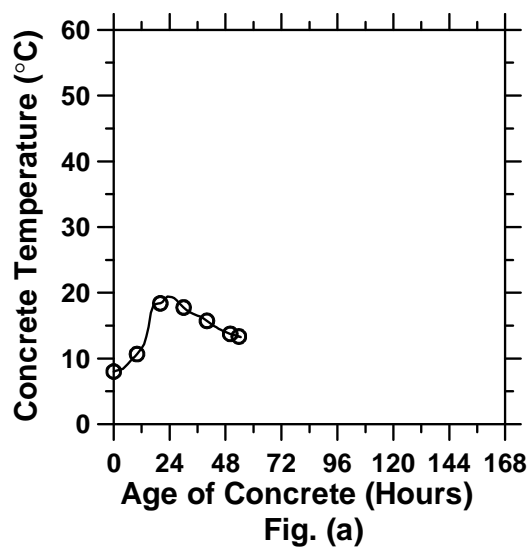


Figure A.144: Pavement cured at 8°C ambient temperature with a D/3 saw-cut depth introduced at 0 hour (cont'd).

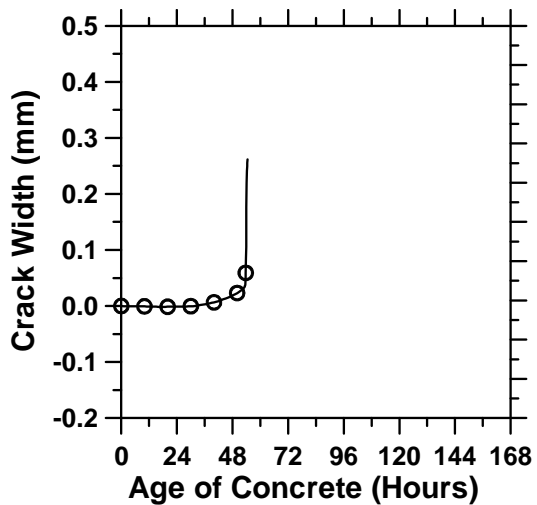


Fig. (e)

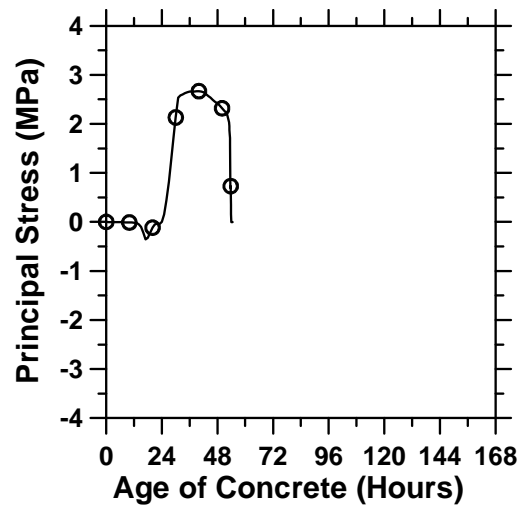


Fig. (f)

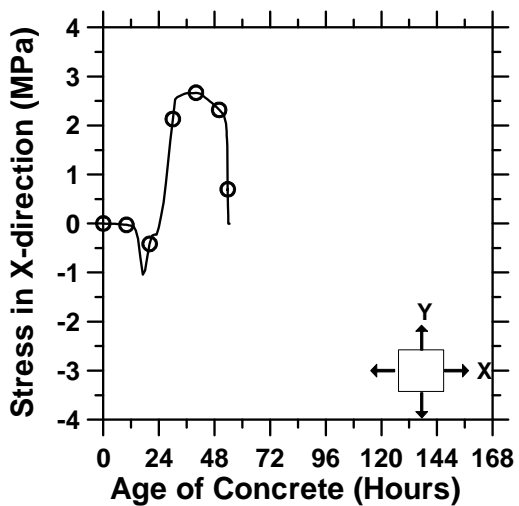


Fig. (g)

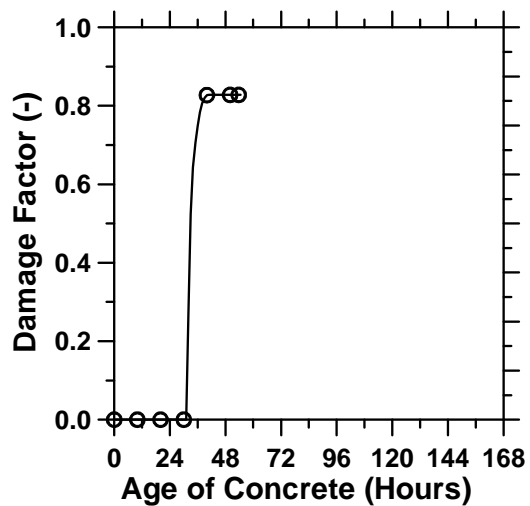


Fig. (h)

Figure A.144: Pavement cured at 8°C ambient temperature with a D/3 saw-cut depth introduced at 0 hour.

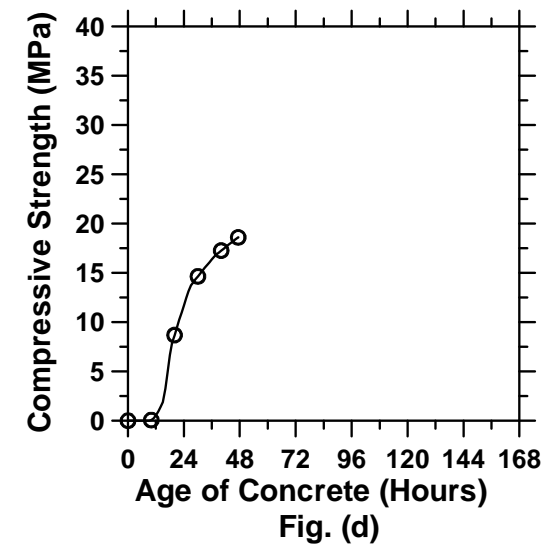
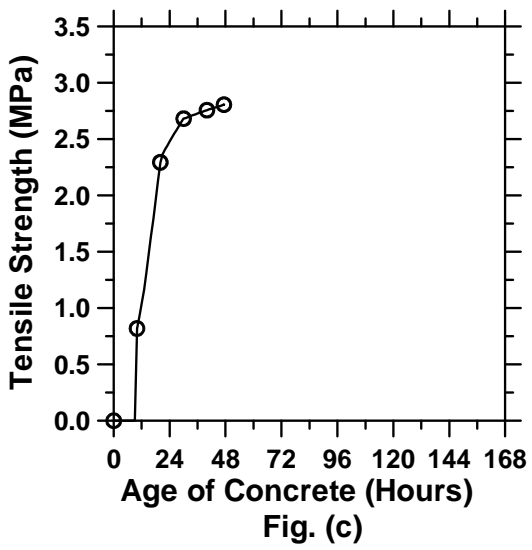
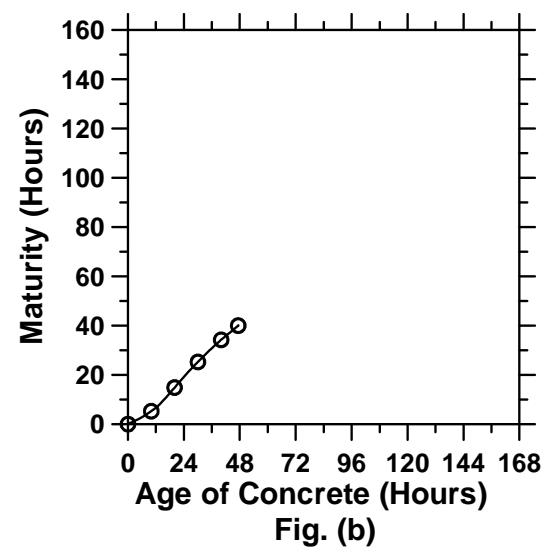
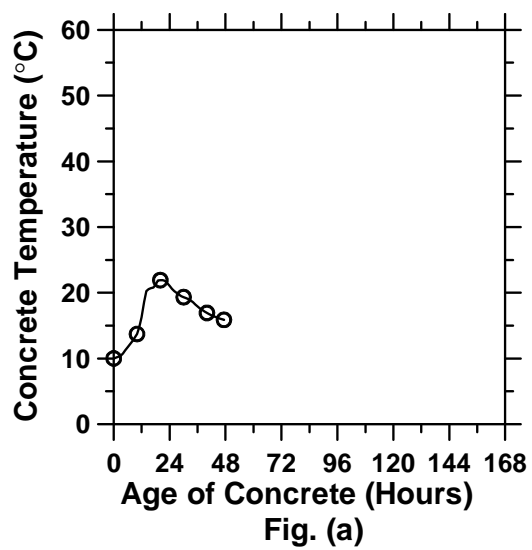


Figure A.145: Pavement cured at 10°C ambient temperature with a D/3 saw-cut depth introduced at 0 hour (cont'd).

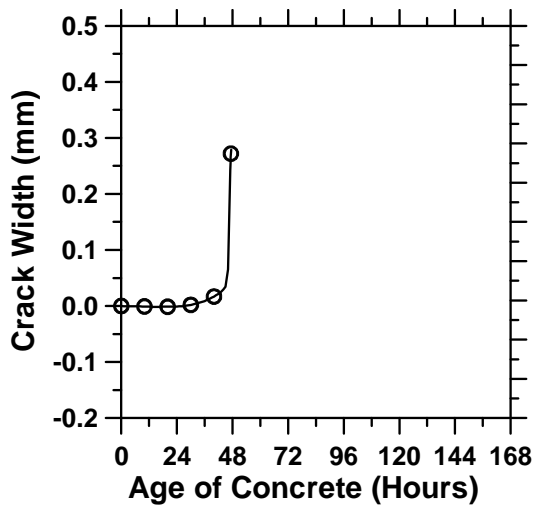


Fig. (e)

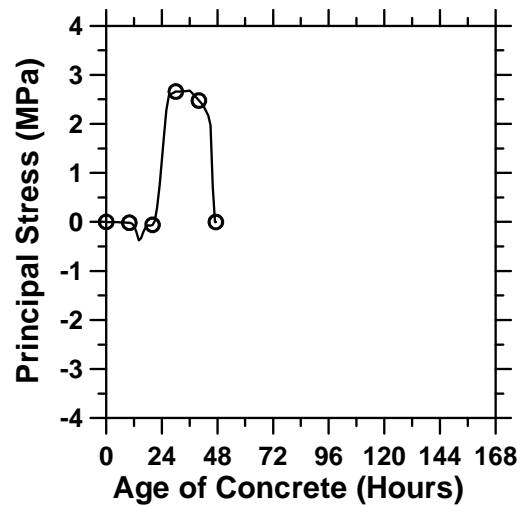


Fig. (f)

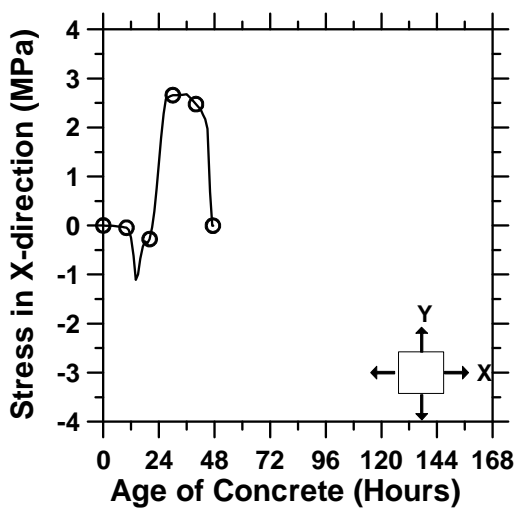


Fig. (g)

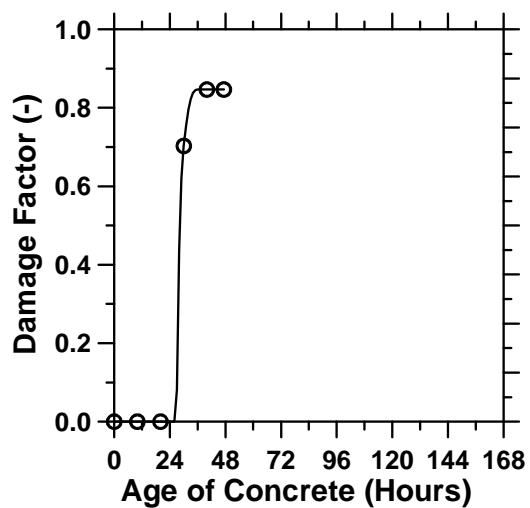


Fig. (h)

Figure A.145: Pavement cured at 10°C ambient temperature with a D/3 saw-cut depth introduced at 0 hour.

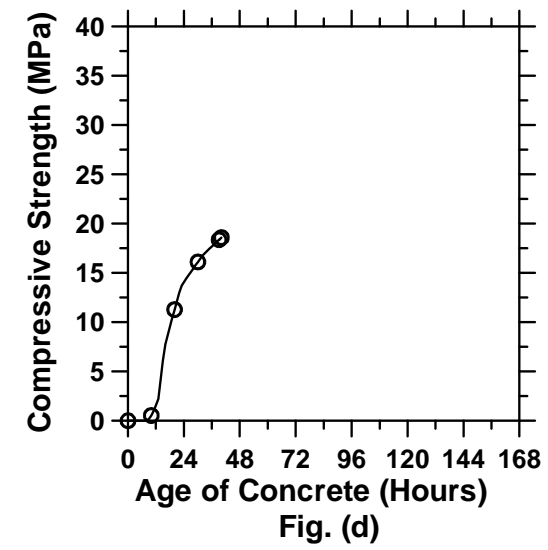
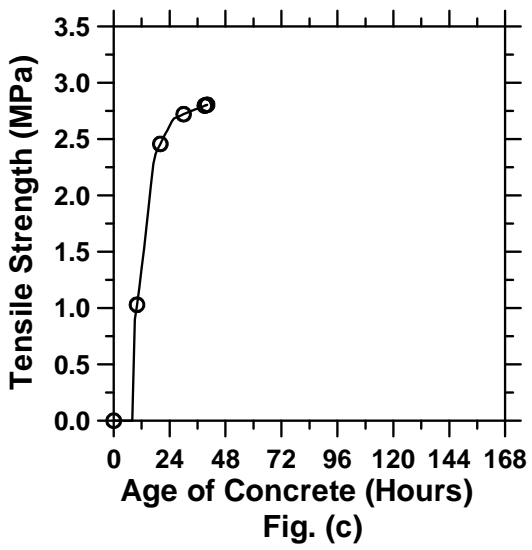
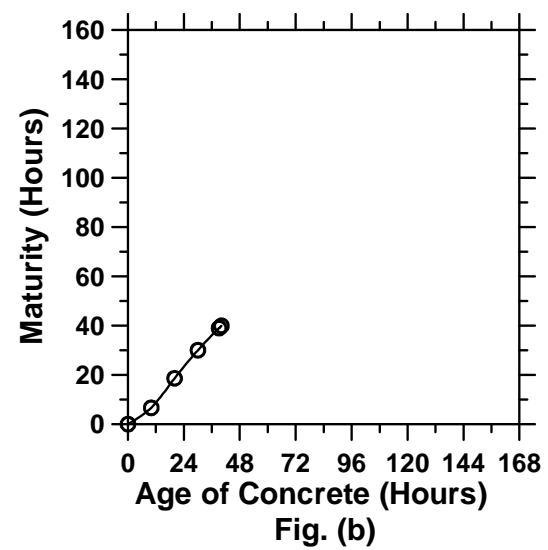
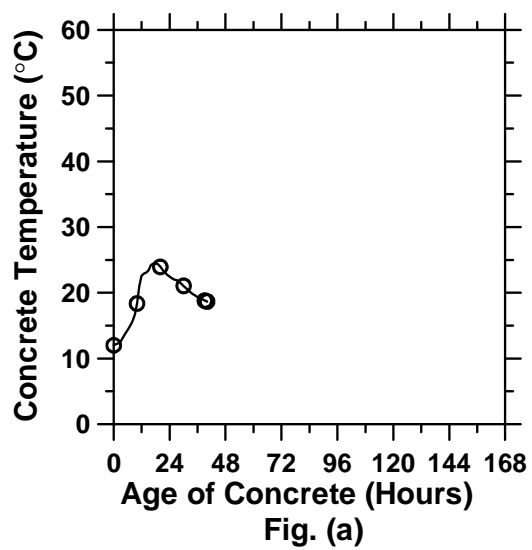


Figure A.146: Pavement cured at 12°C ambient temperature with a D/3 saw-cut depth introduced at 0 hour (cont'd).

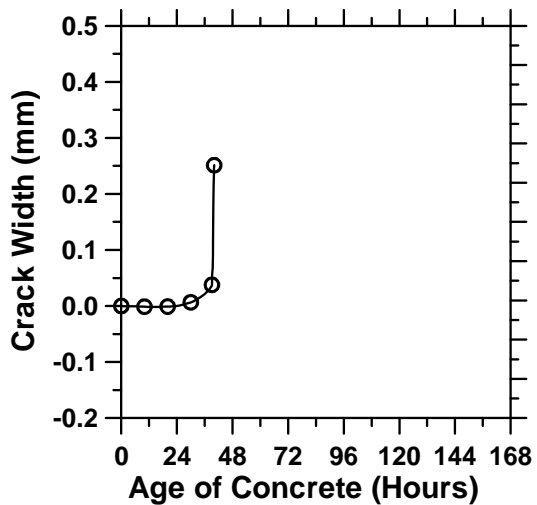


Fig. (e)

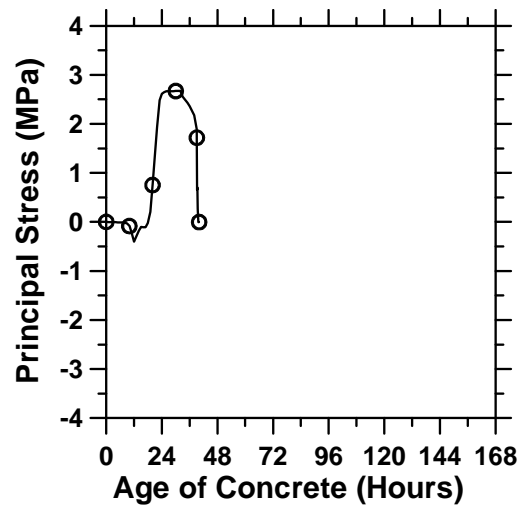


Fig. (f)

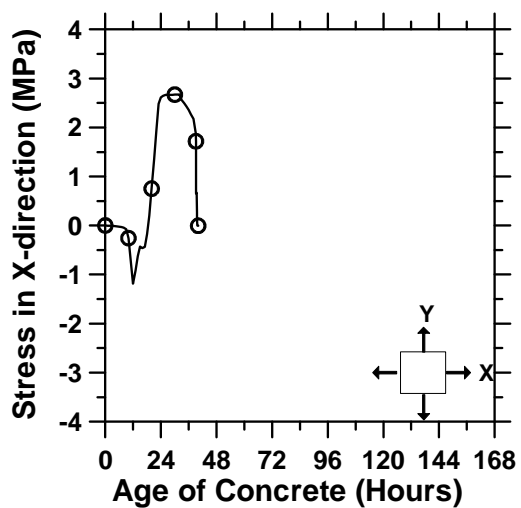


Fig. (g)

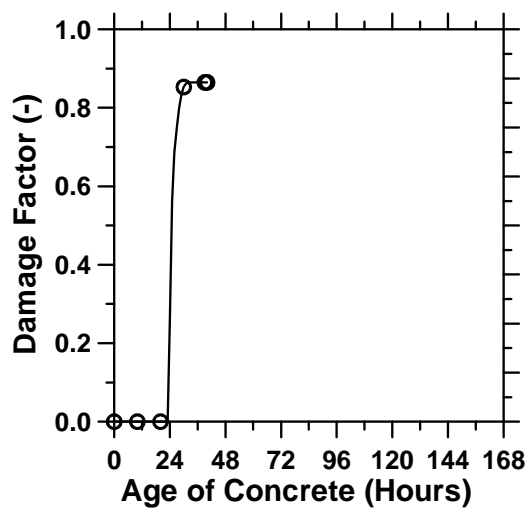


Fig. (h)

Figure A.146: Pavement cured at 12°C ambient temperature with a D/3 saw-cut depth introduced at 0 hour.

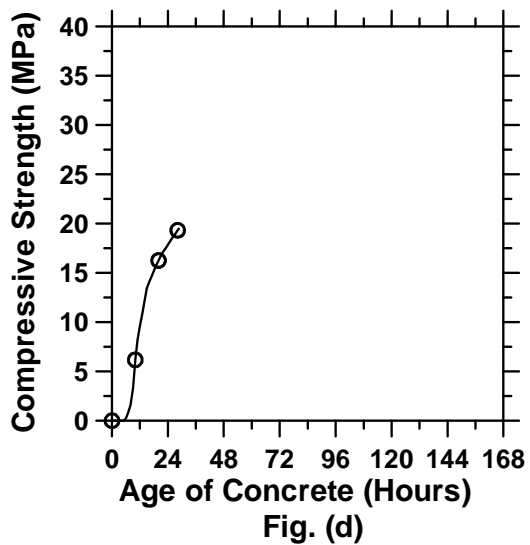
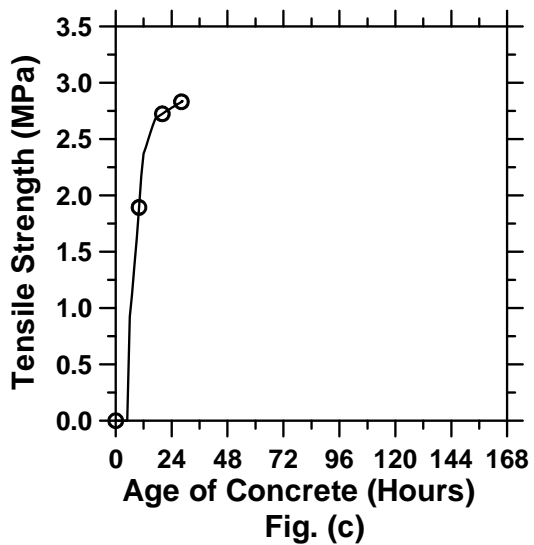
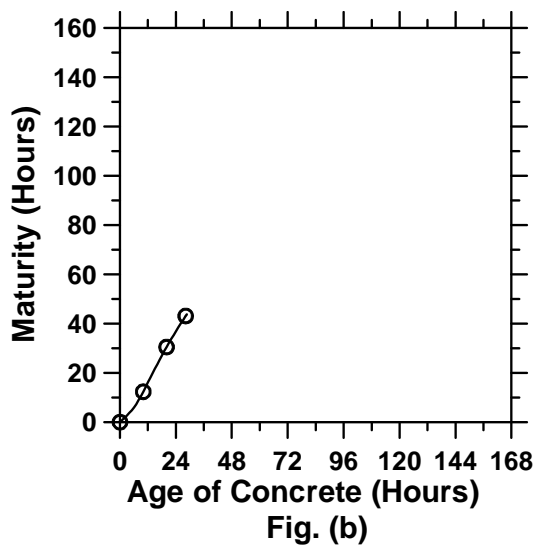
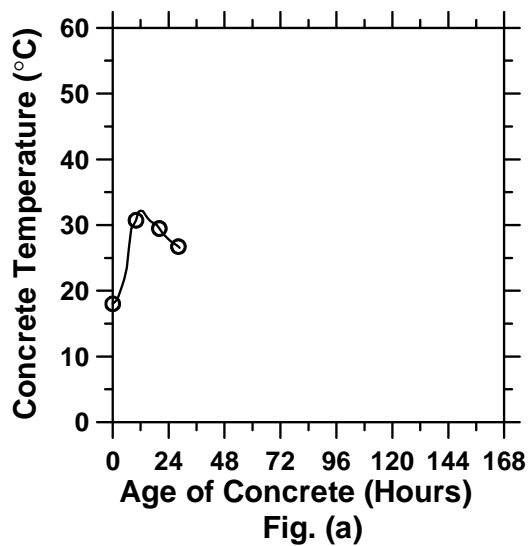


Figure A.147: Pavement cured at 18°C ambient temperature with a D/3 saw-cut depth introduced at 0 hour (cont'd).

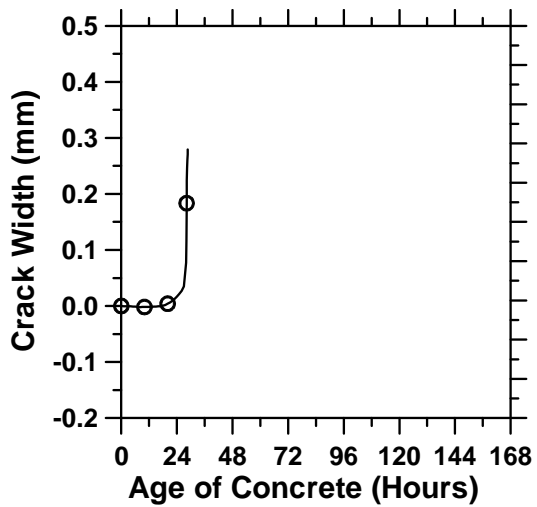


Fig. (e)

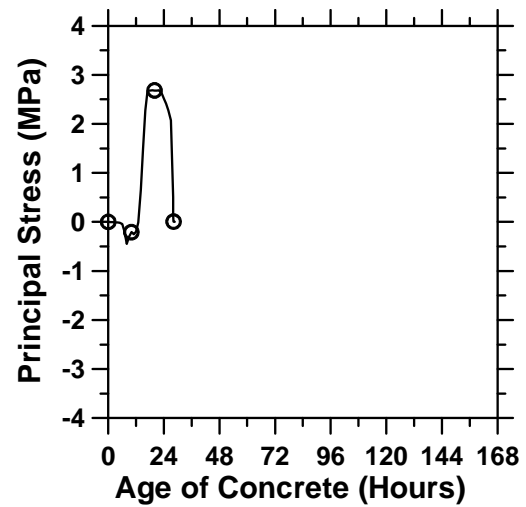


Fig. (f)

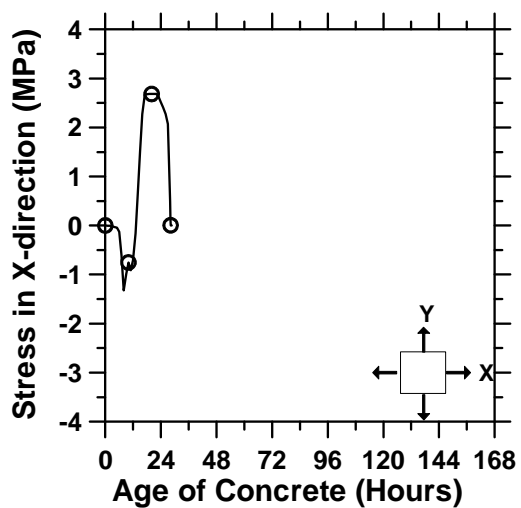


Fig. (g)

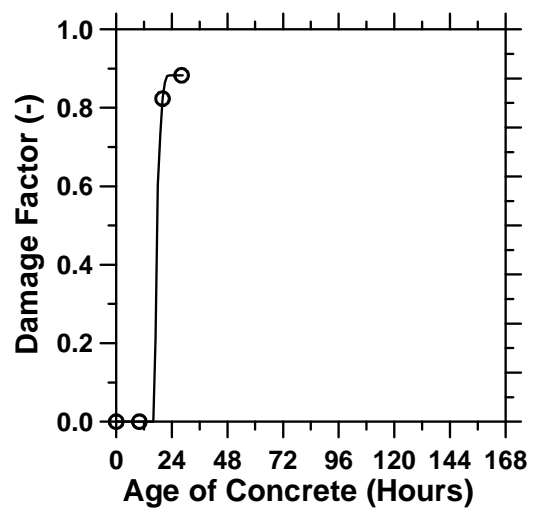


Fig. (h)

Figure A.147: Pavement cured at 18°C ambient temperature with a D/3 saw-cut depth introduced at 0 hour.

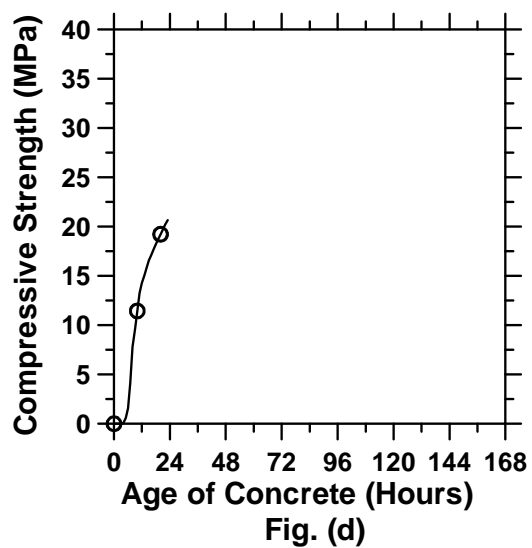
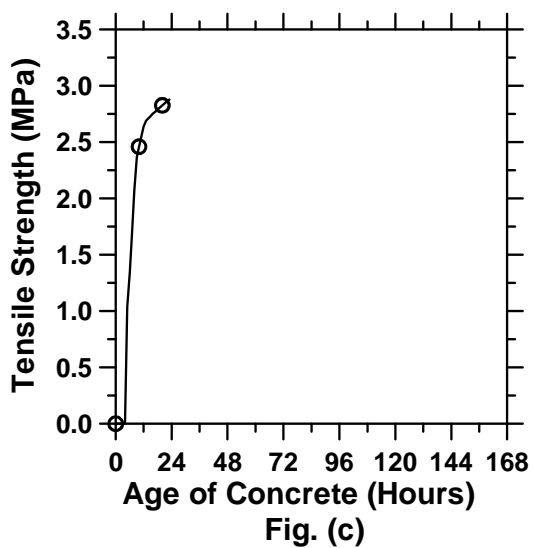
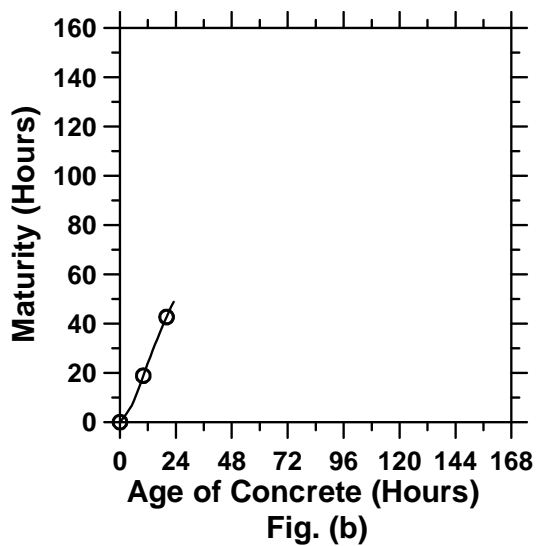
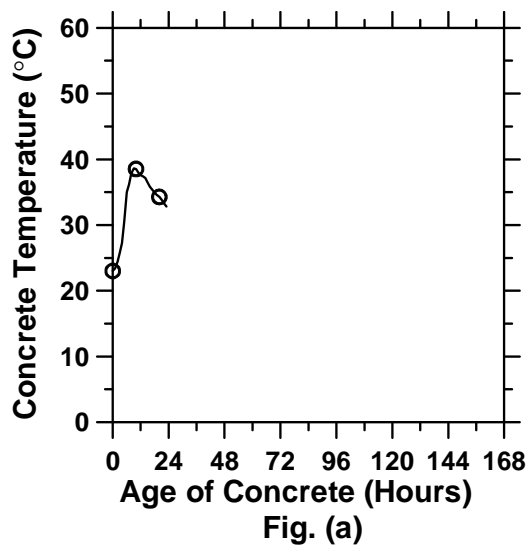


Figure A.148: Pavement cured at 23°C ambient temperature with a D/3 saw-cut depth introduced at 0 hour (cont'd).

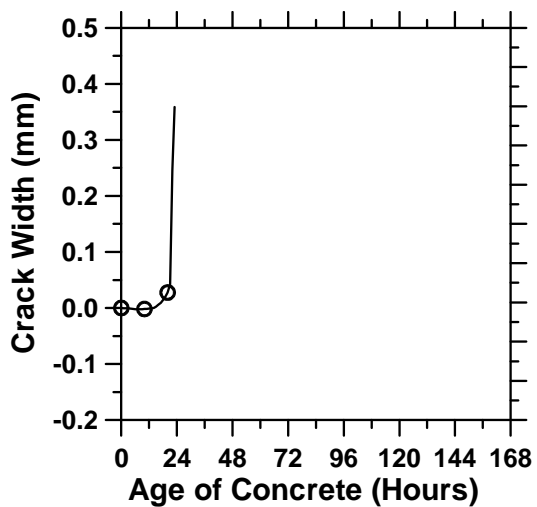


Fig. (e)

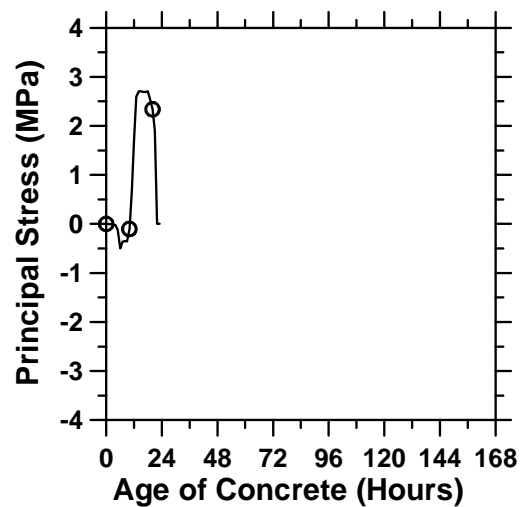


Fig. (f)

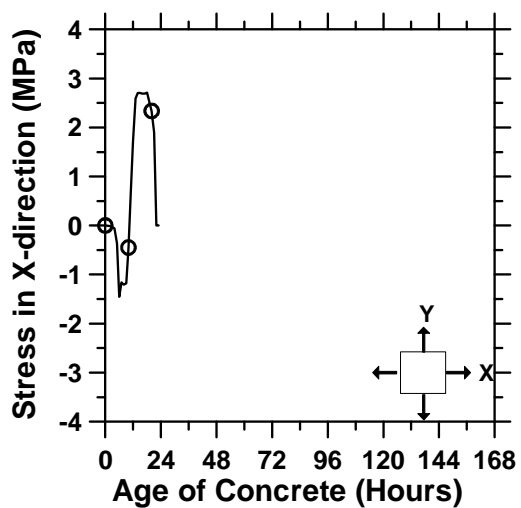


Fig. (g)

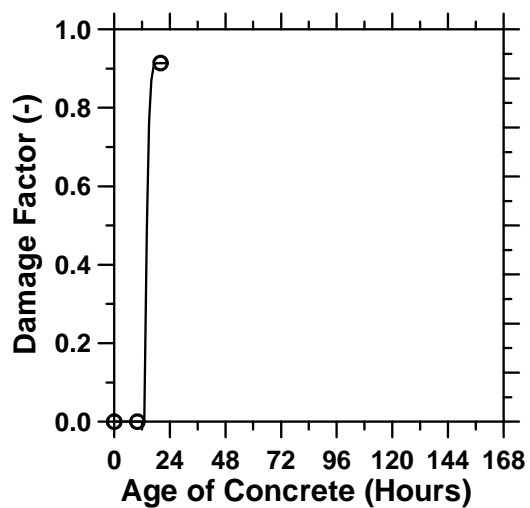


Fig. (h)

Figure A.148: Pavement cured at 23°C ambient temperature with a D/3 saw-cut depth introduced at 0 hour.

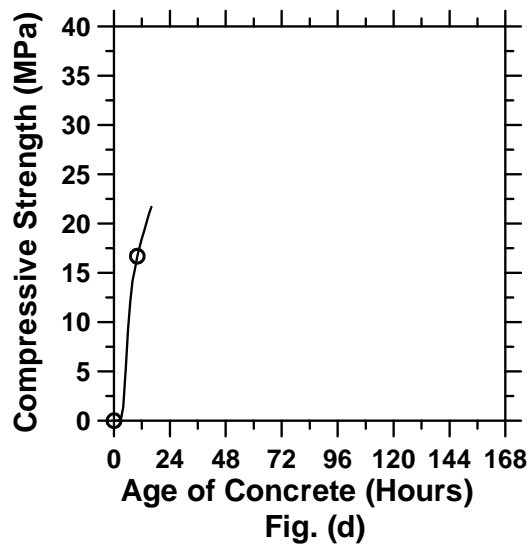
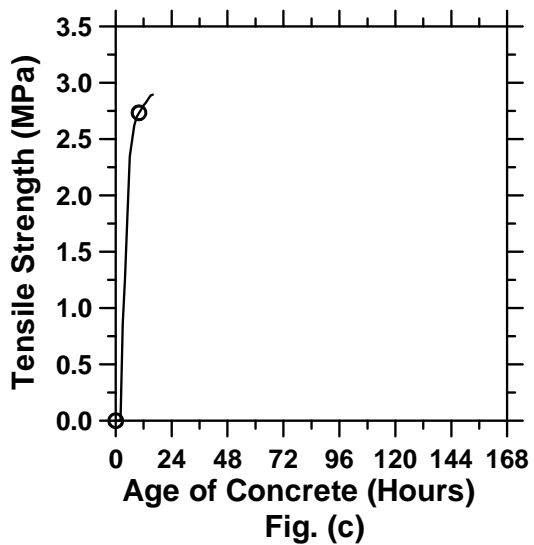
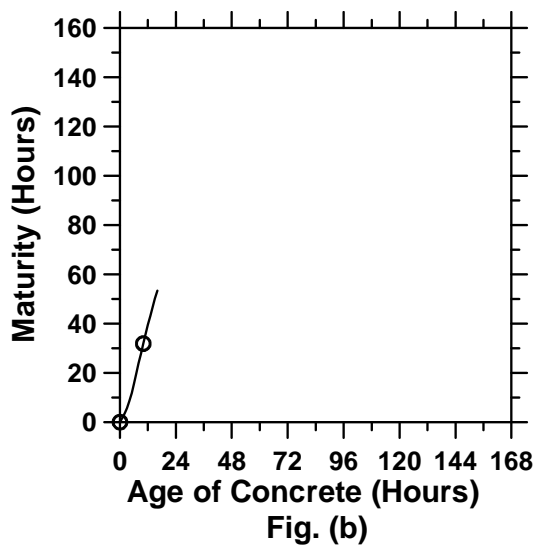
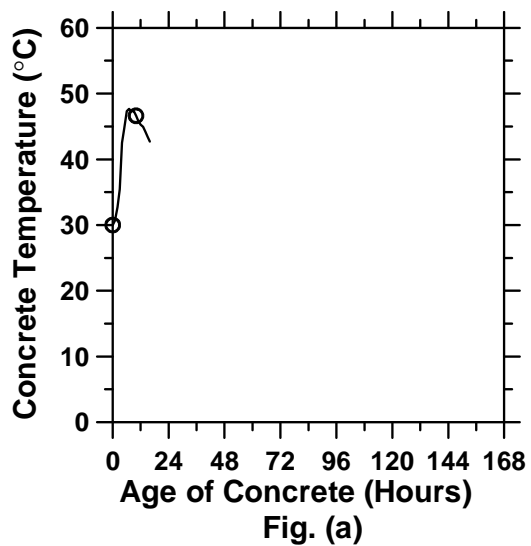


Figure A.149: Pavement cured at 30°C ambient temperature with a D/3 saw-cut depth introduced at 0 hour (cont'd).

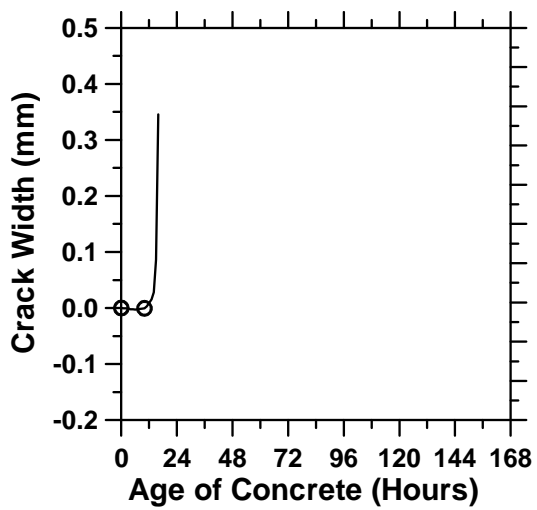


Fig. (e)

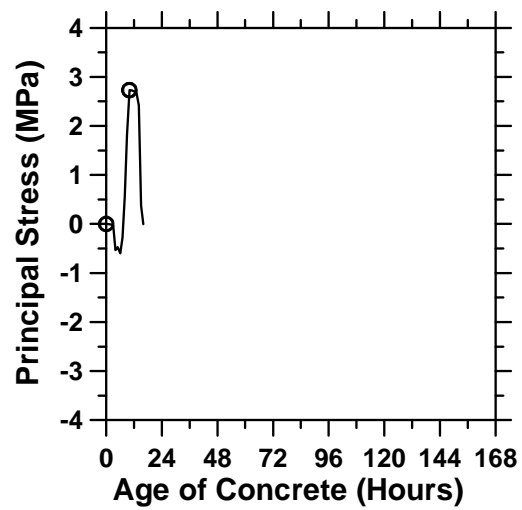


Fig. (f)

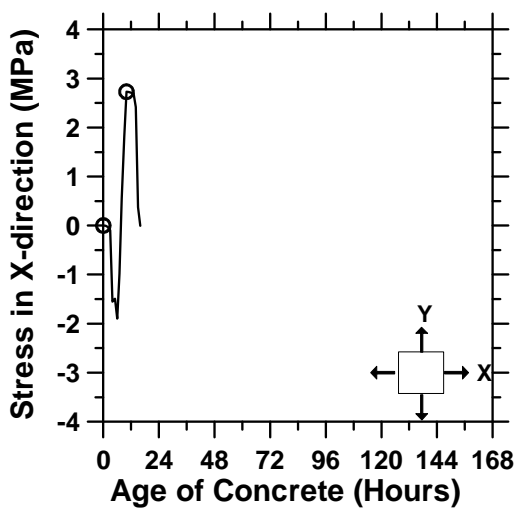


Fig. (g)

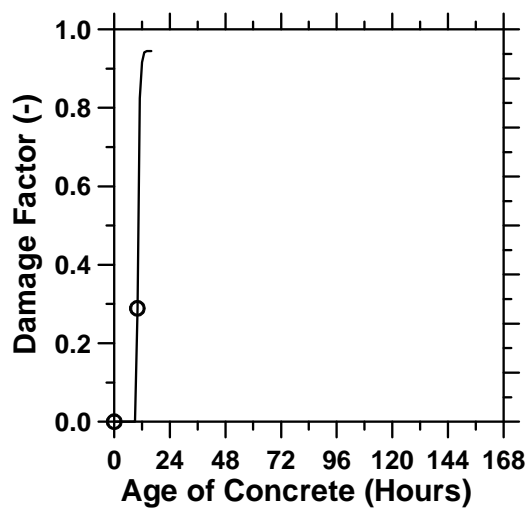


Fig. (h)

Figure A.149: Pavement cured at 30°C ambient temperature with a D/3 saw-cut depth introduced at 0 hour.

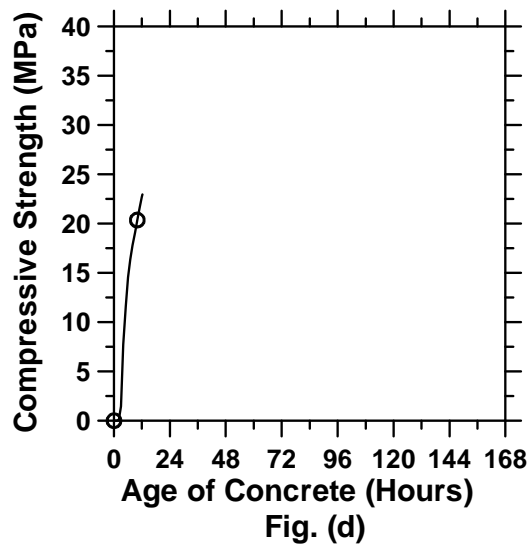
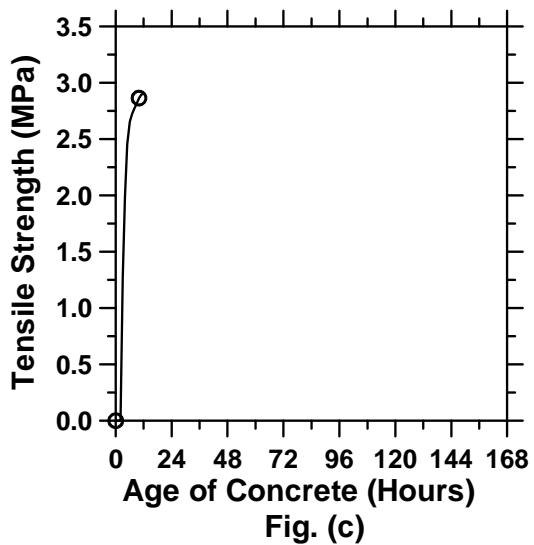
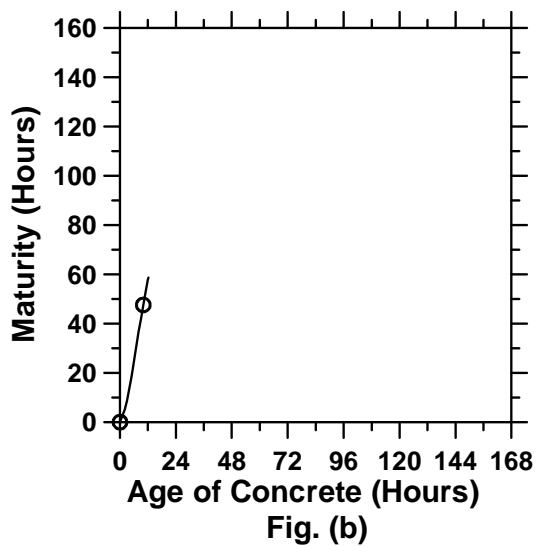
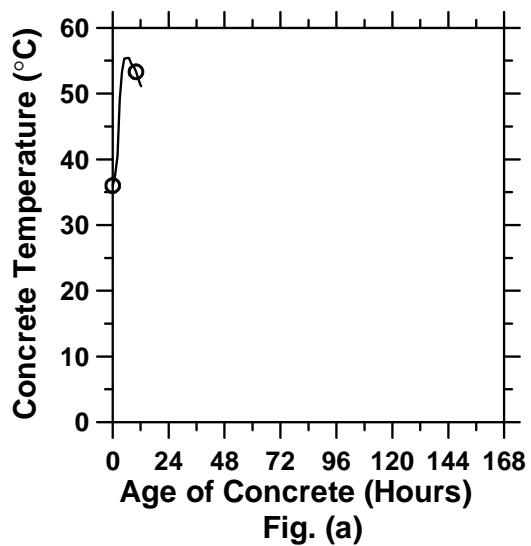


Figure A.150: Pavement cured at 36°C ambient temperature with a D/3 saw-cut depth introduced at 0 hour (cont'd).

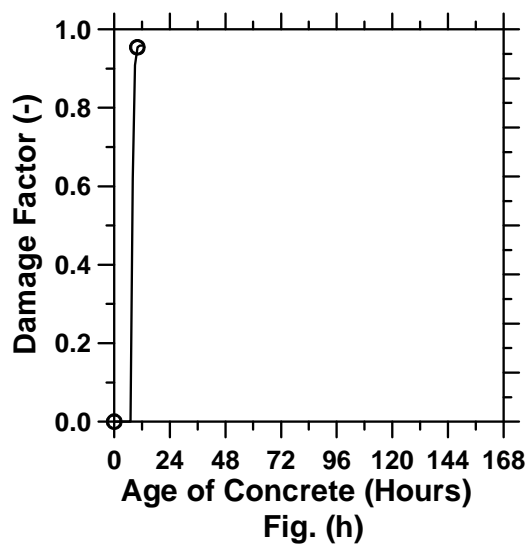
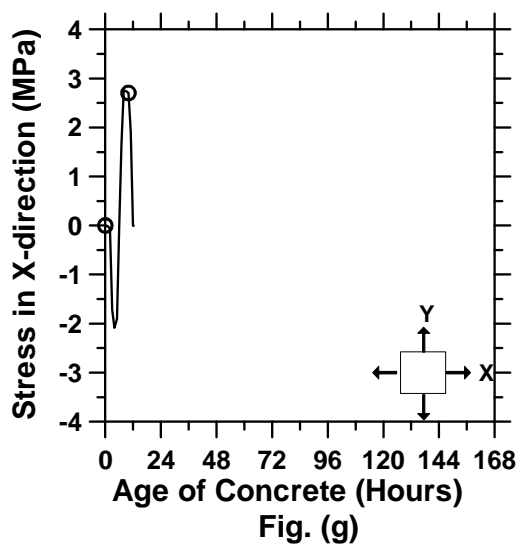
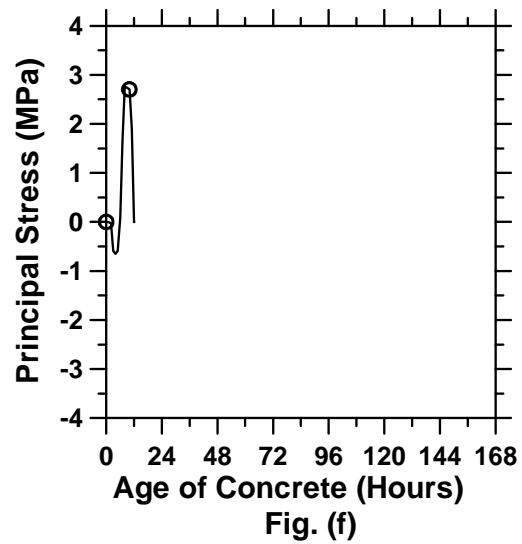
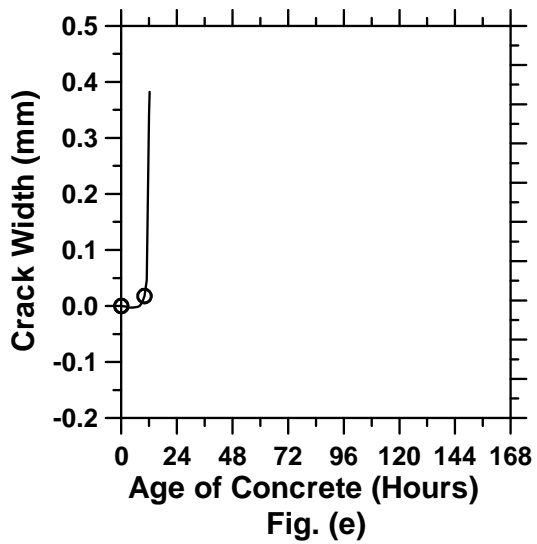


Figure A.150: Pavement cured at 36°C ambient temperature with a D/3 saw-cut depth introduced at 0 hour.

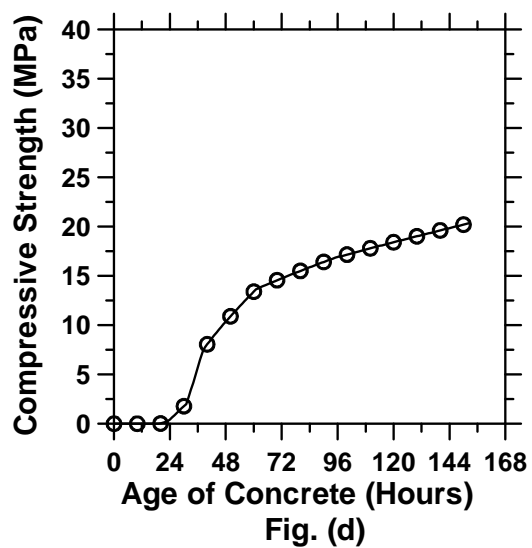
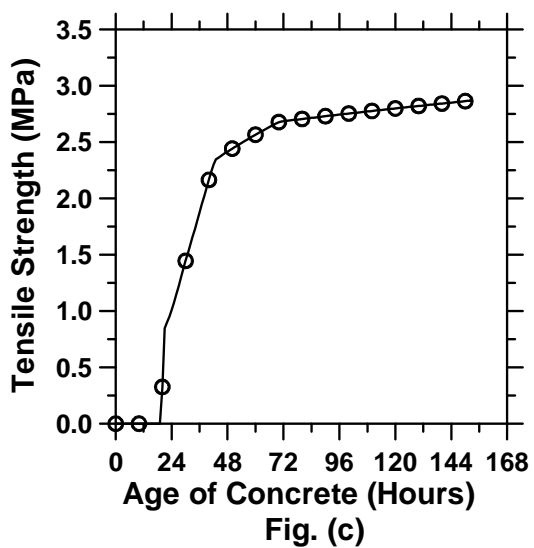
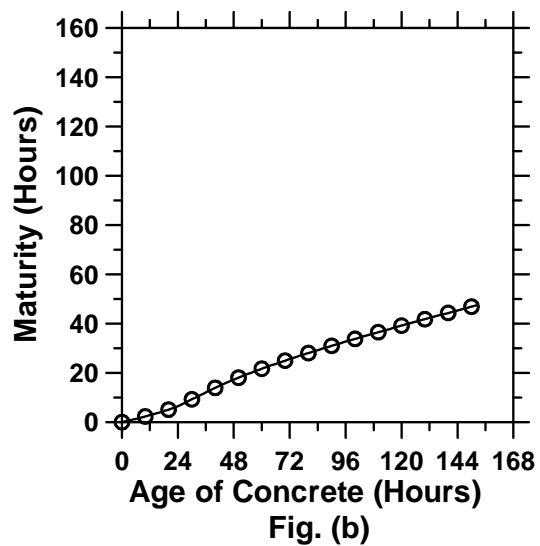
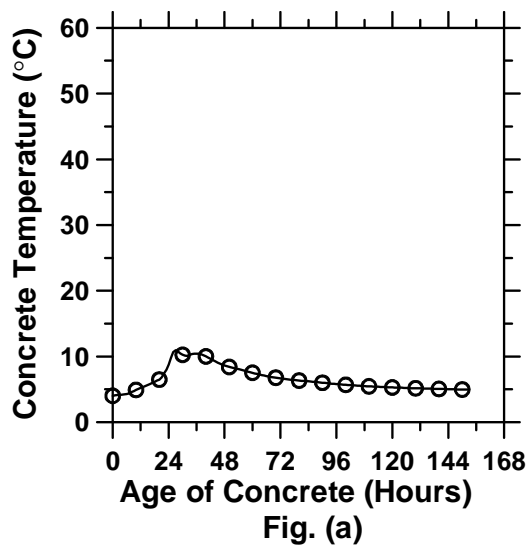


Figure A.151: Pavement cured at 4°C ambient temperature with a D/8 saw-cut depth introduced at 0 hour (cont'd).

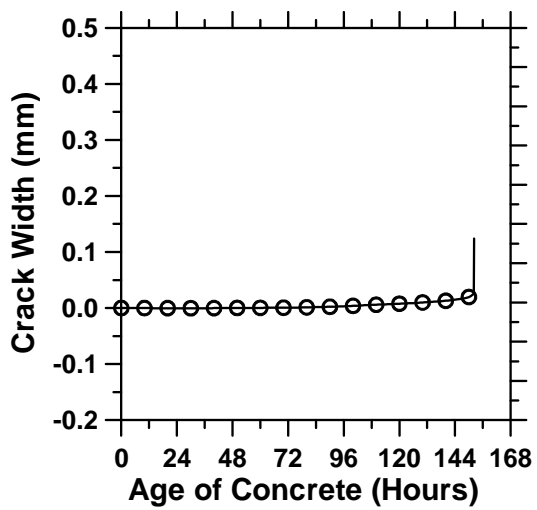


Fig. (e)

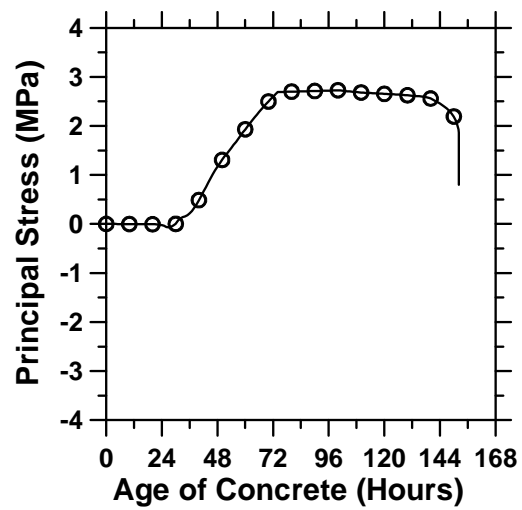


Fig. (f)

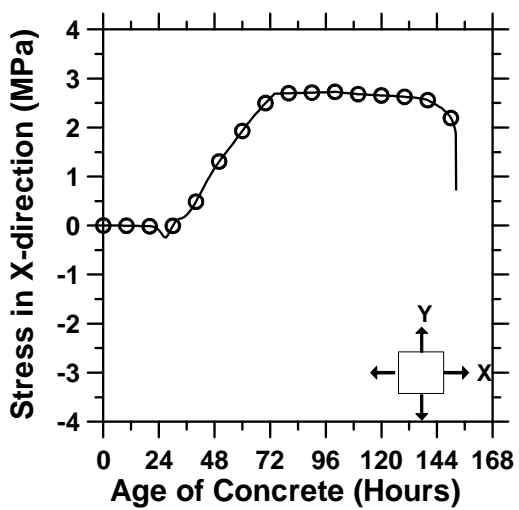


Fig. (g)

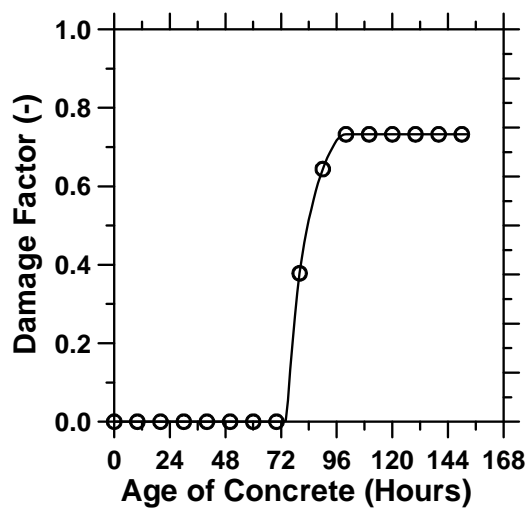


Fig. (h)

Figure A.151: Pavement cured at 4°C ambient temperature with a D/8 saw-cut depth introduced at 0 hour.

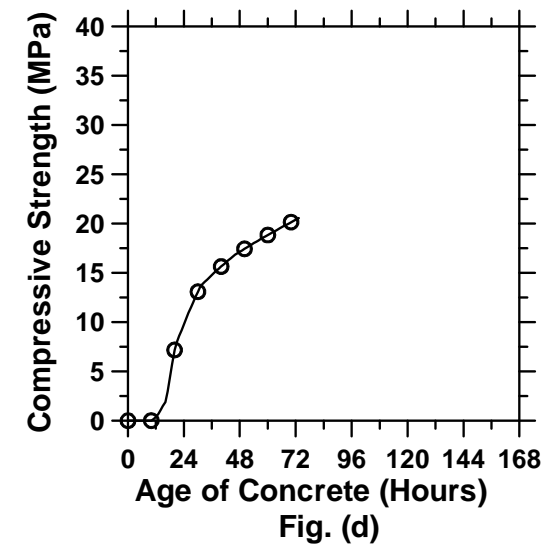
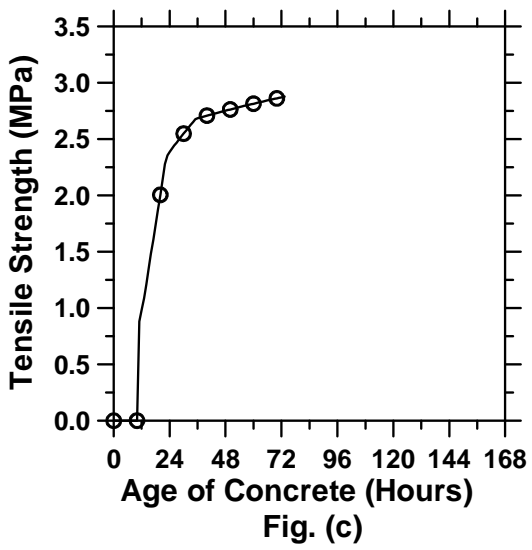
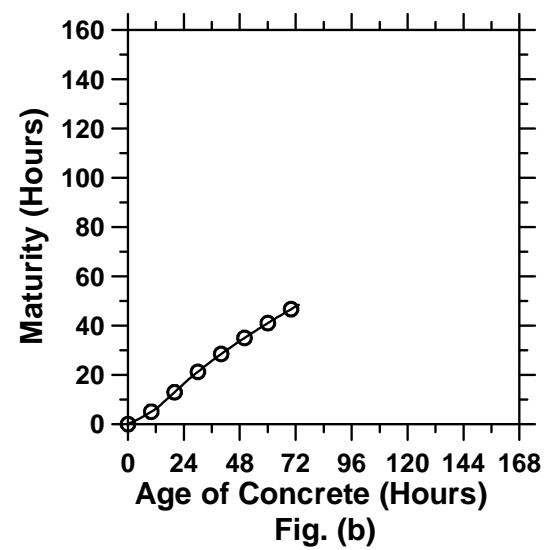
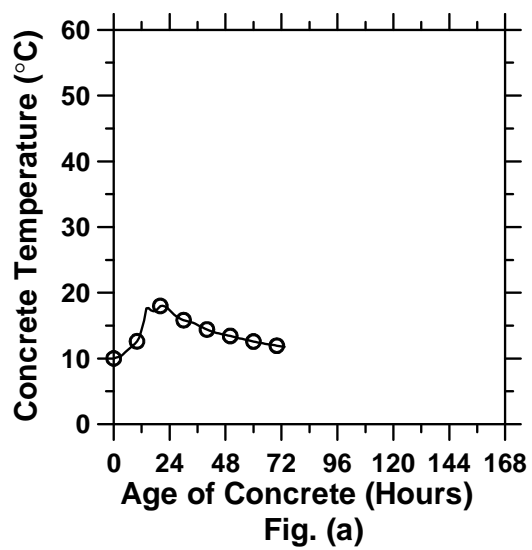


Figure A.152: Pavement cured at 10°C ambient temperature with a D/8 saw-cut depth introduced at 0 hour (cont'd).

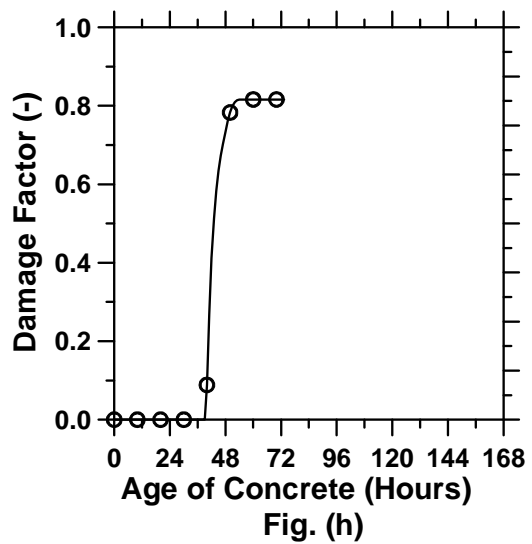
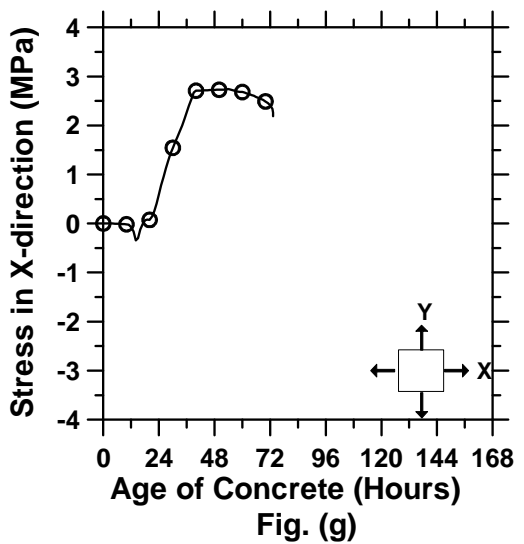
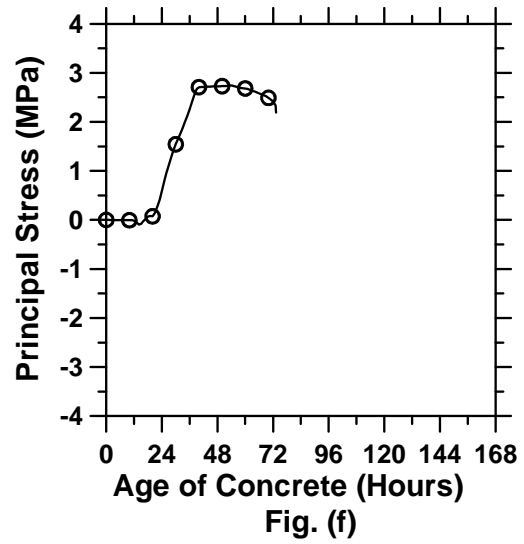
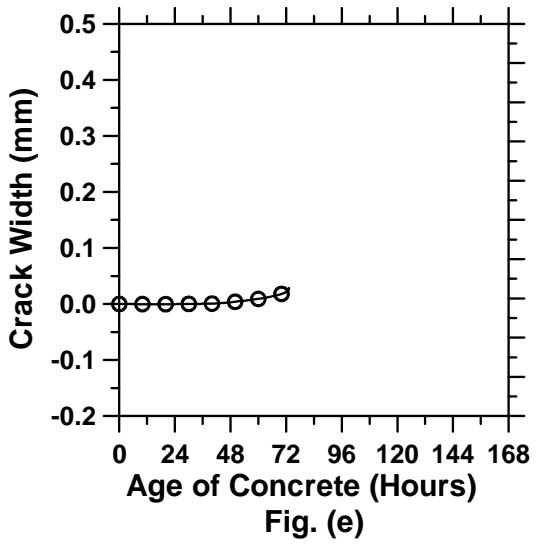


Figure A.152: Pavement cured at 10°C ambient temperature with a D/8 saw-cut depth introduced at 0 hour.

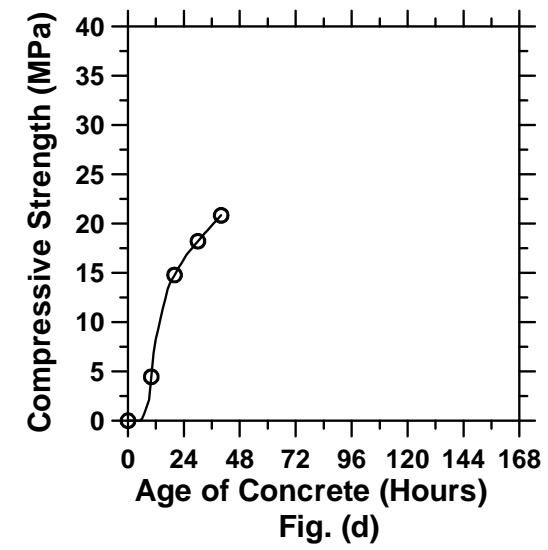
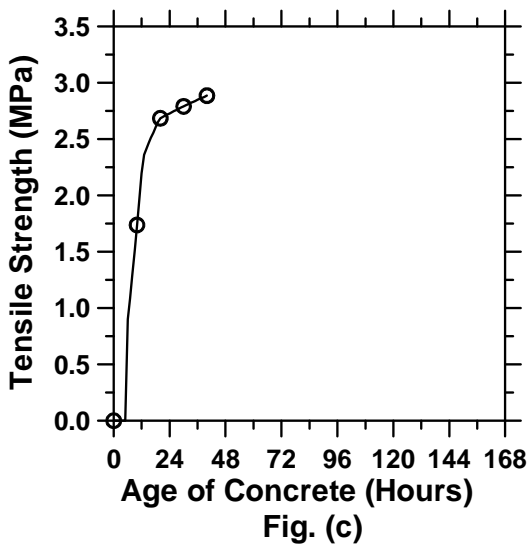
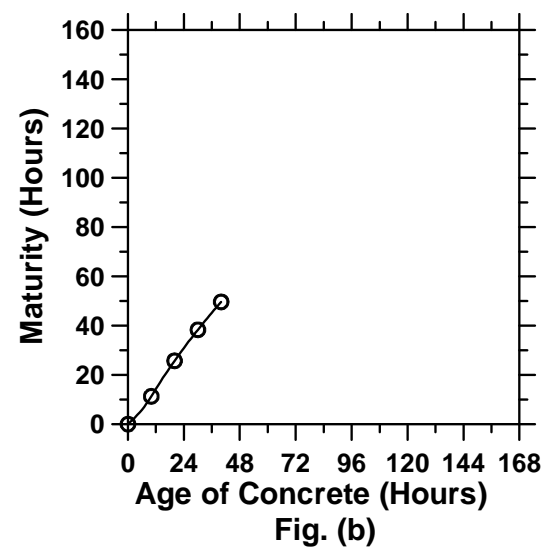
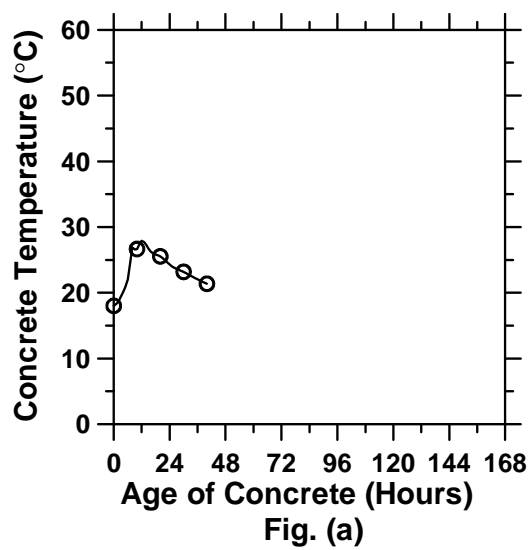


Figure A.153: Pavement cured at 18°C ambient temperature with a D/8 saw-cut depth introduced at 0 hour (cont'd).

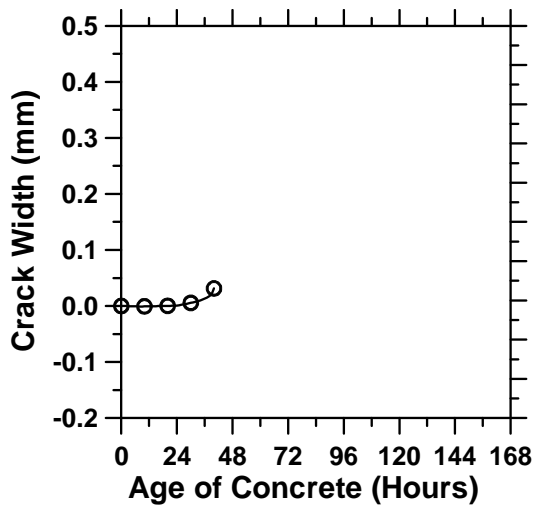


Fig. (e)

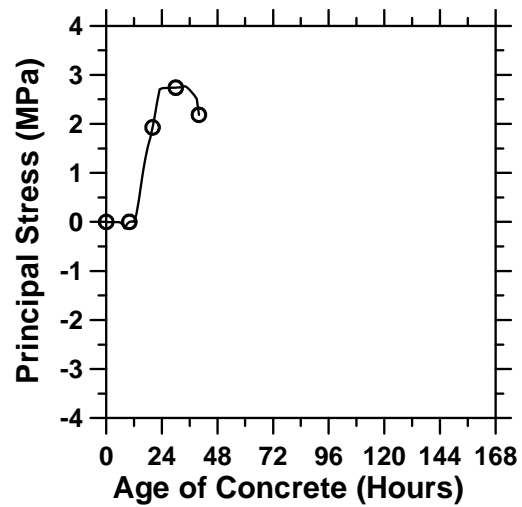


Fig. (f)

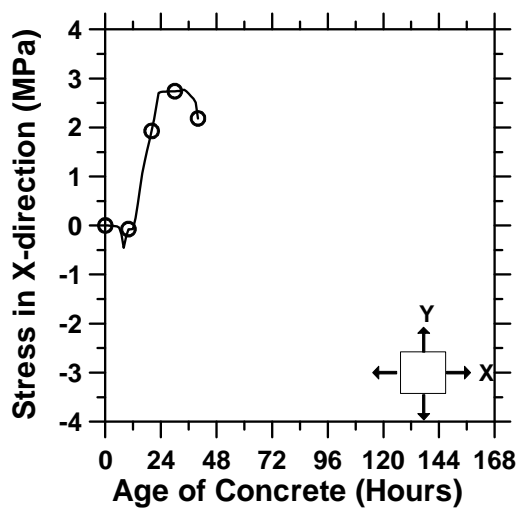


Fig. (g)

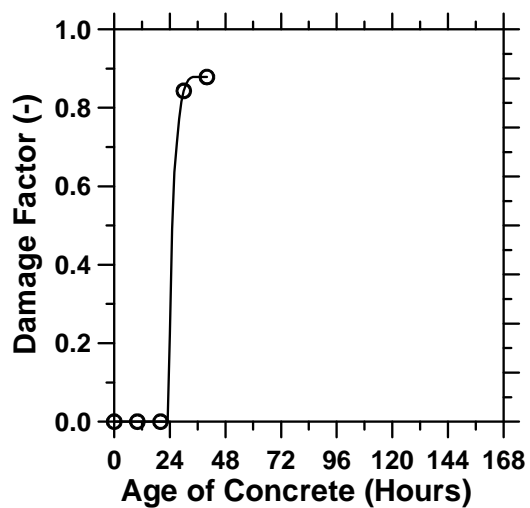


Fig. (h)

Figure A.153: Pavement cured at 18°C ambient temperature with a D/8 saw-cut depth introduced at 0 hour.

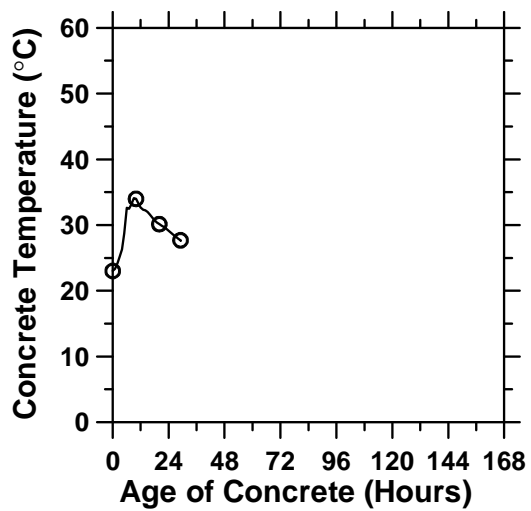


Fig. (a)

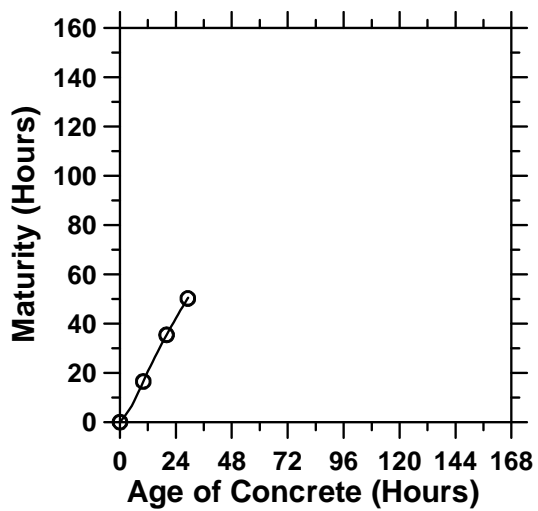


Fig. (b)

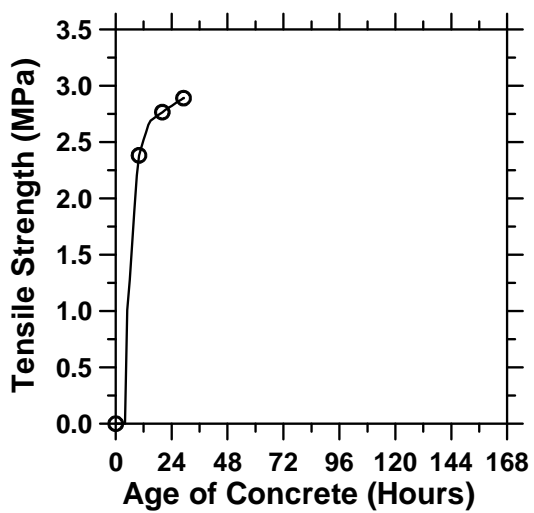


Fig. (c)

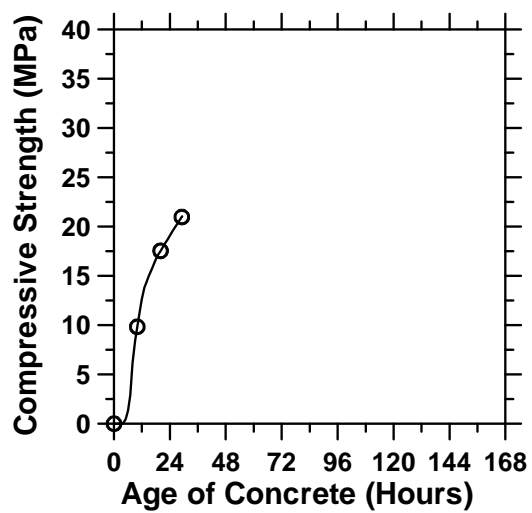


Fig. (d)

Figure A.154: Pavement cured at 23°C ambient temperature with a D/8 saw-cut depth introduced at 0 hour (cont'd).

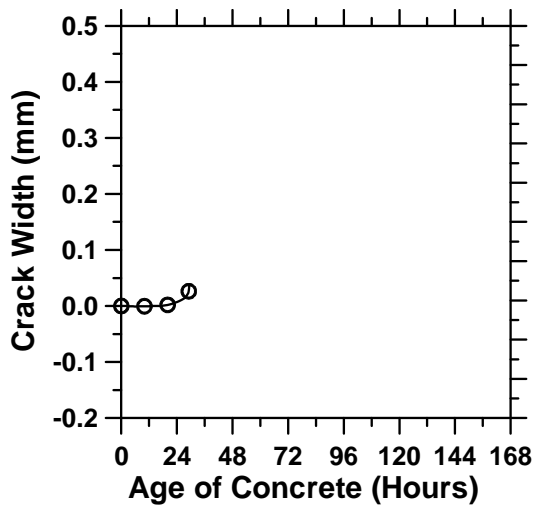


Fig. (e)

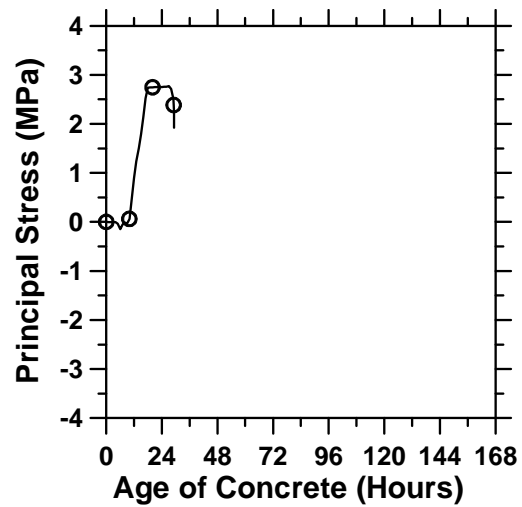


Fig. (f)

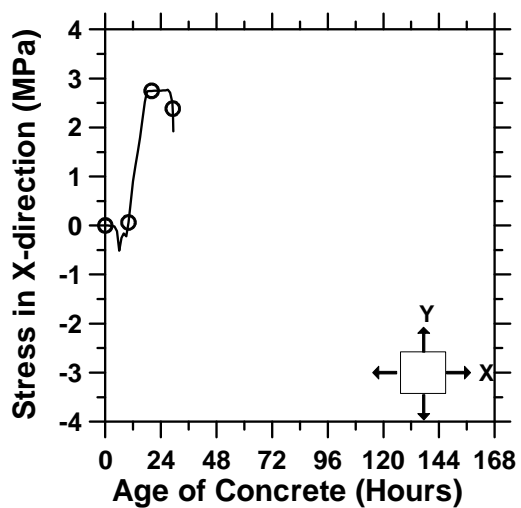


Fig. (g)

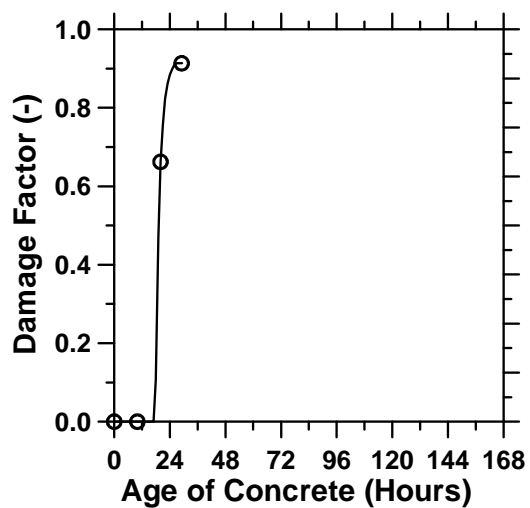


Fig. (h)

Figure A.154: Pavement cured at 30°C ambient temperature with a D/8 saw-cut depth introduced at 0 hour.

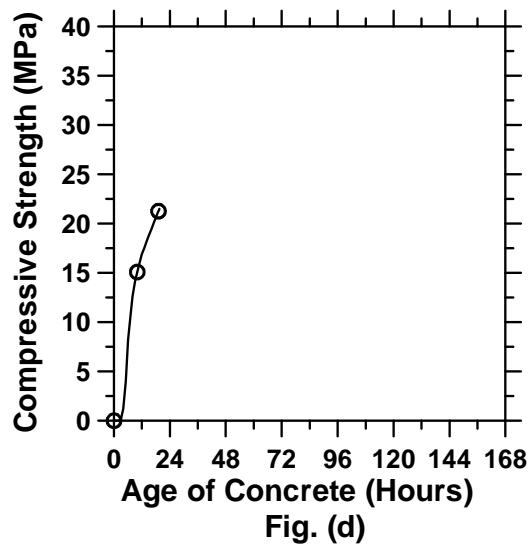
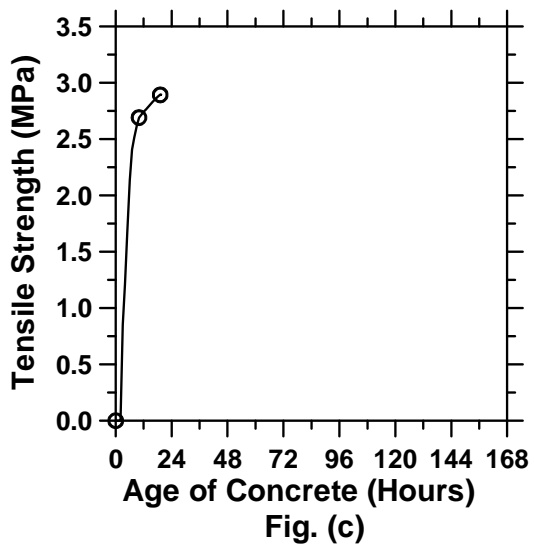
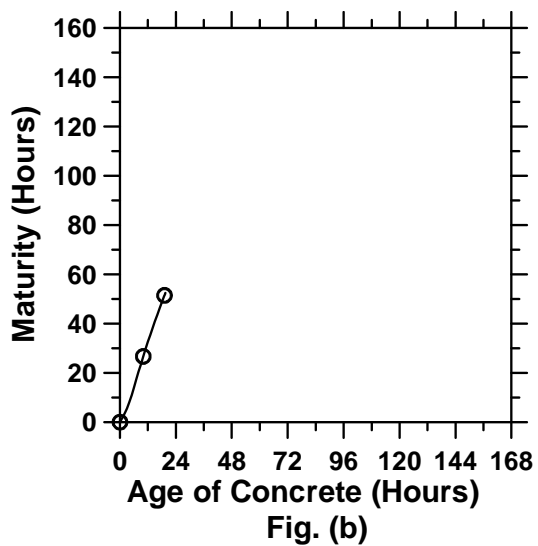
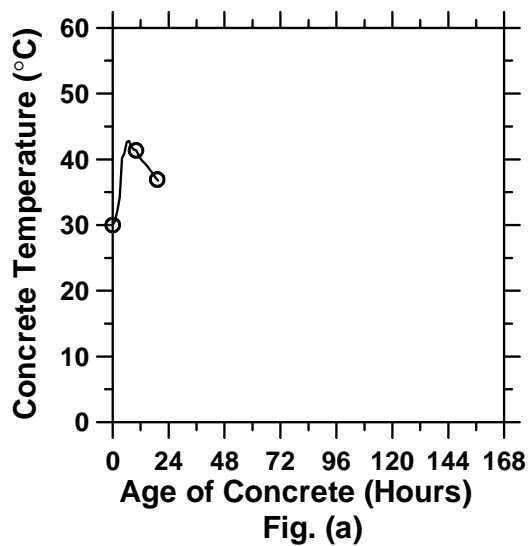


Figure A.155: Pavement cured at 36°C ambient temperature with a D/8 saw-cut depth introduced at 0 hour (cont'd).

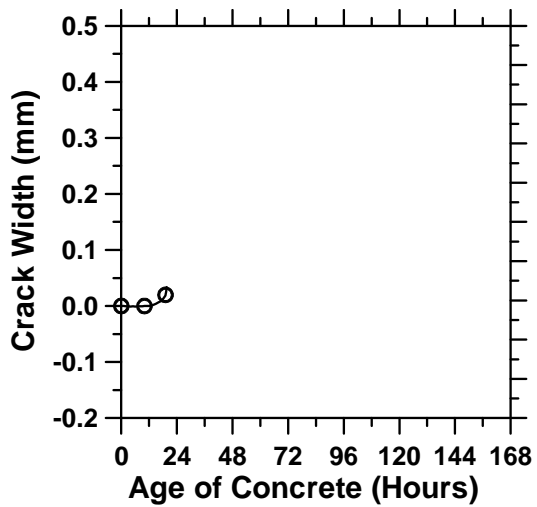


Fig. (e)

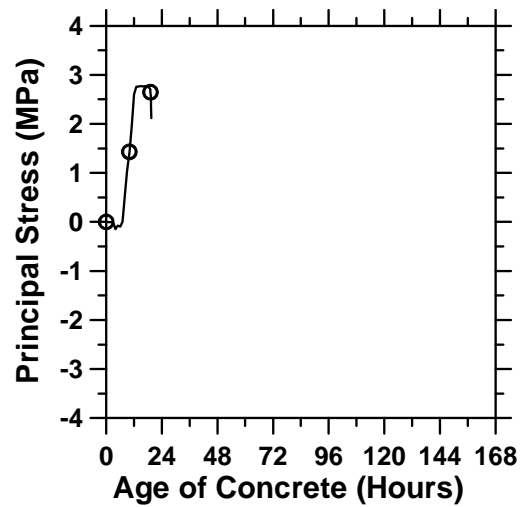


Fig. (f)

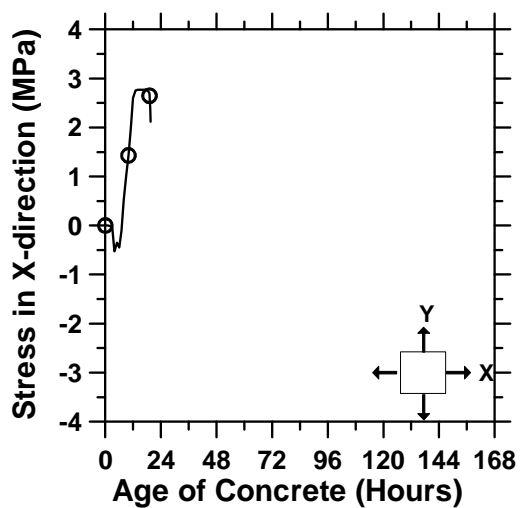


Fig. (g)

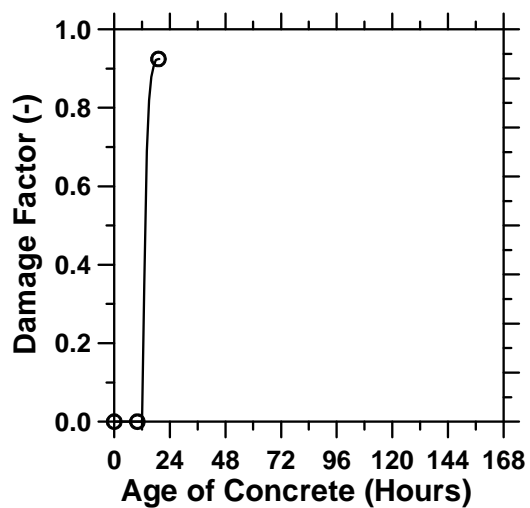


Fig. (h)

Figure A.155: Pavement cured at 36°C ambient temperature with a D/8 saw-cut depth introduced at 0 hour.

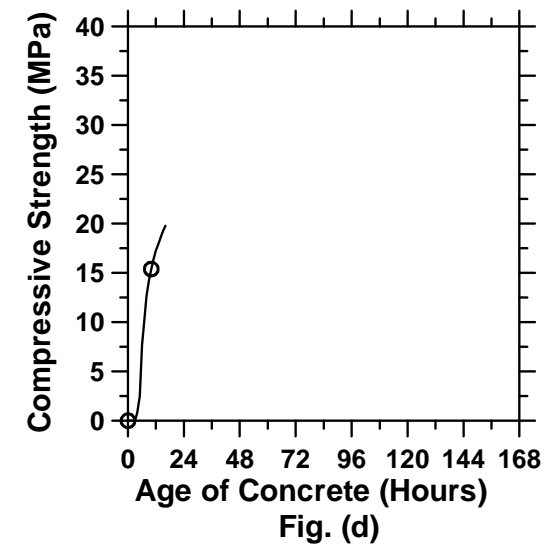
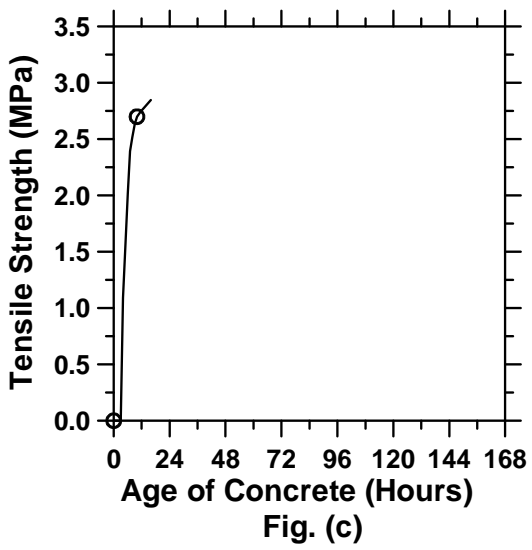
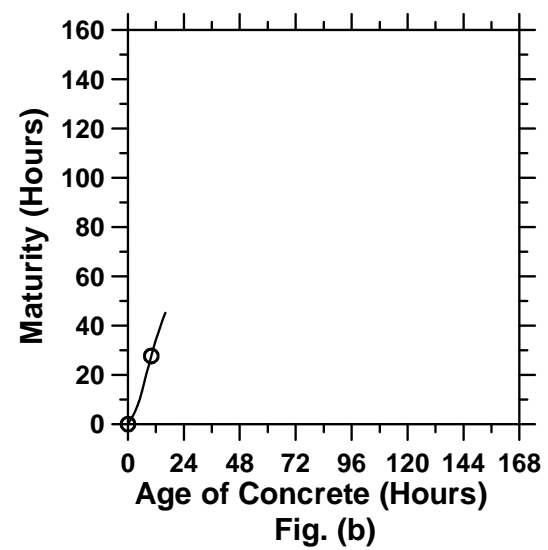
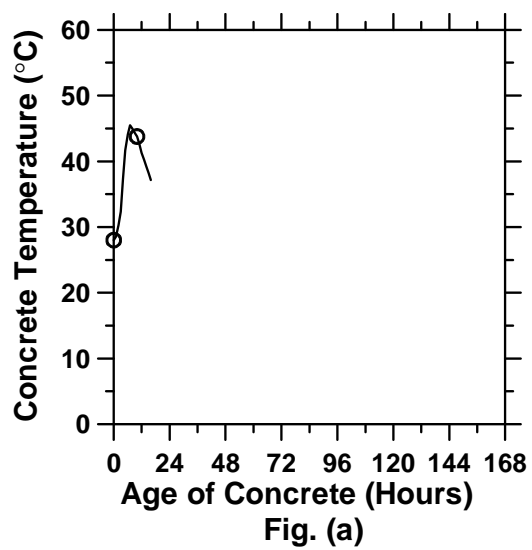


Figure A.156: Pavement casted at “H” ambient temperature at 1:00 p.m. and sawed with a D/3 saw-cut depth after 12 hours (cont’d).

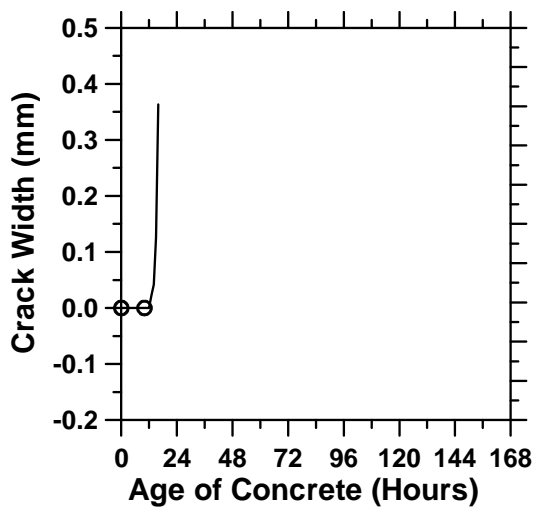


Fig. (e)

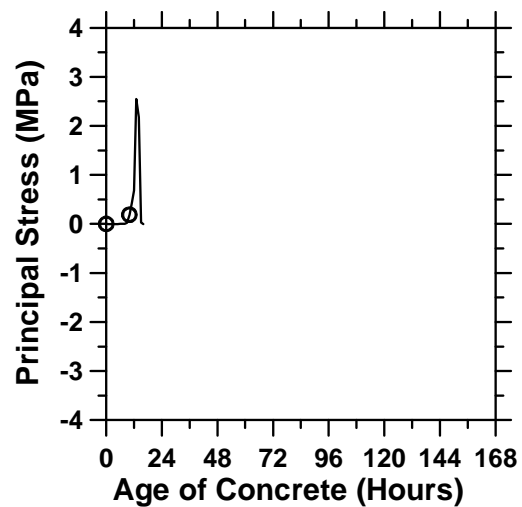


Fig. (f)

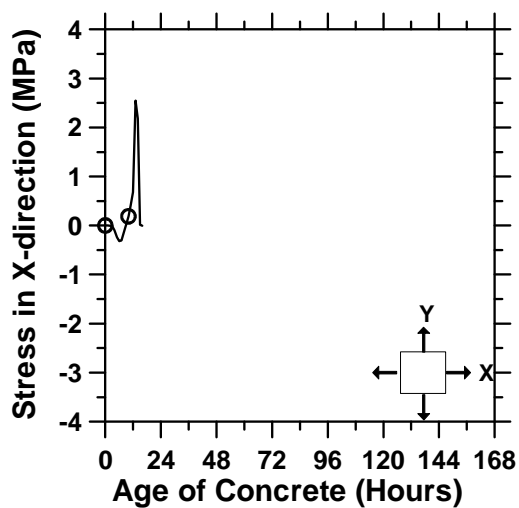


Fig. (g)

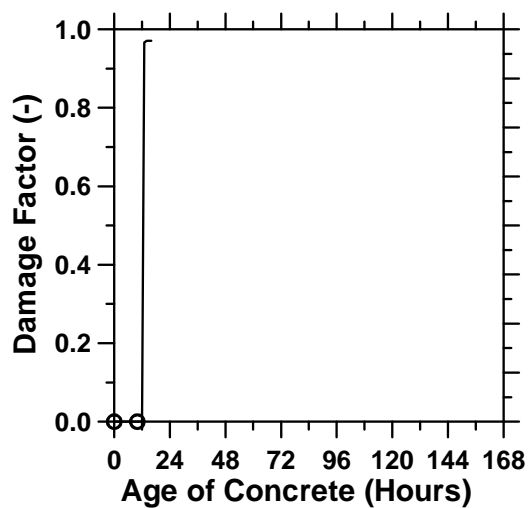


Fig. (h)

Figure A.156: Pavement casted at “H” ambient temperature at 1:00 p.m. and sawed with a D/3 saw-cut depth after 12 hours.

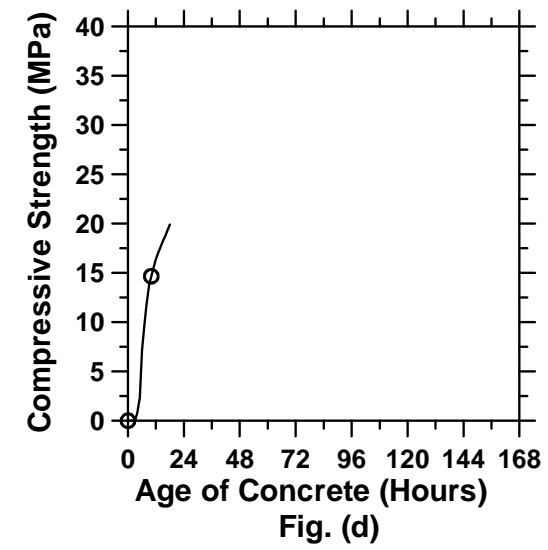
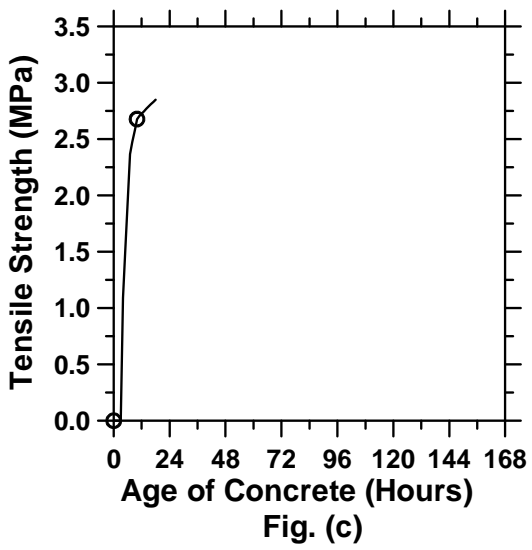
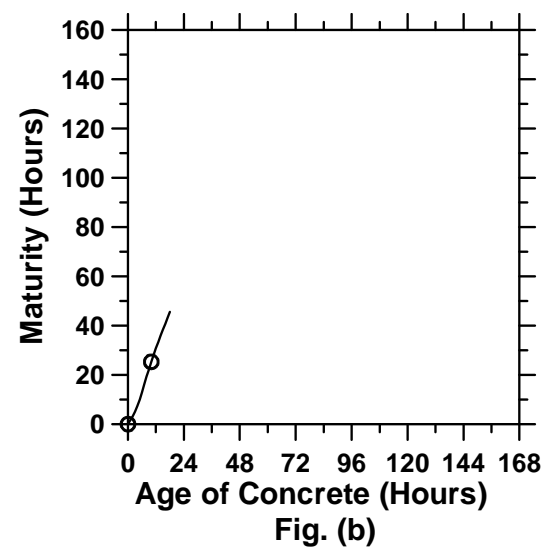
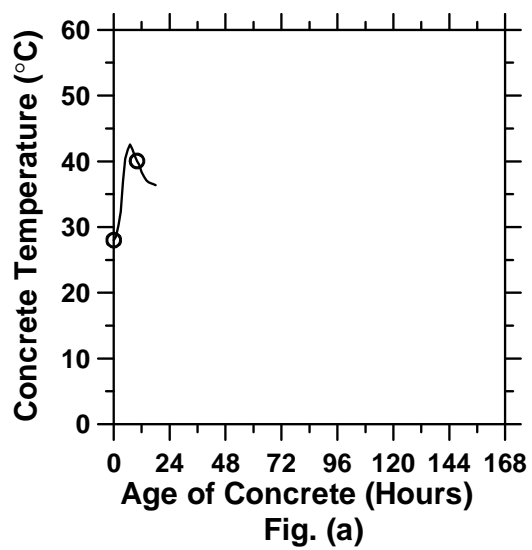


Figure A.157: Pavement casted at “H” ambient temperature at 7:00 p.m. and sawed with a D/3 saw-cut depth after 12 hours (cont’d).

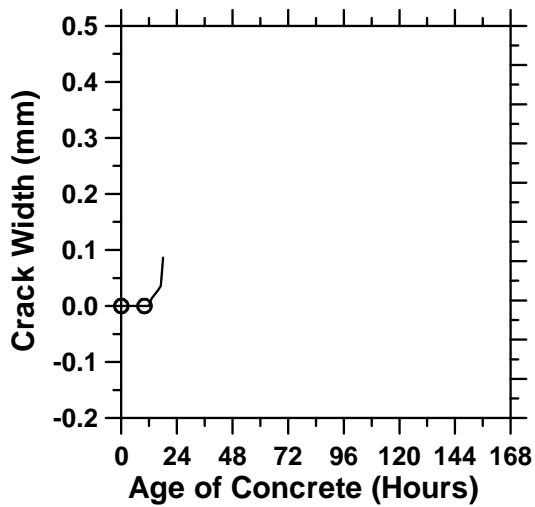


Fig. (e)

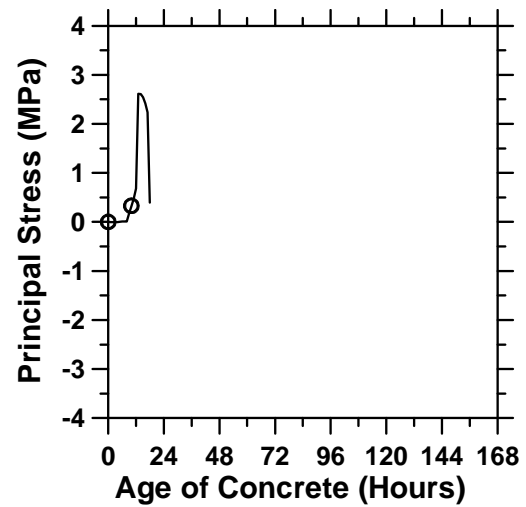


Fig. (f)

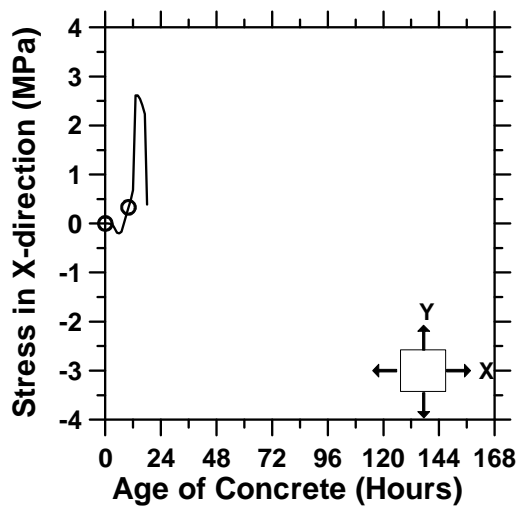


Fig. (g)

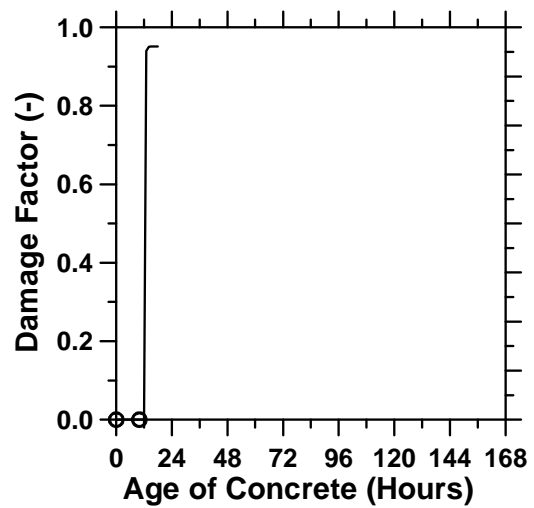


Fig. (h)

Figure A.157: Pavement casted at “H” ambient temperature at 7:00 p.m. and sawed with a D/3 saw-cut depth after 12 hours.

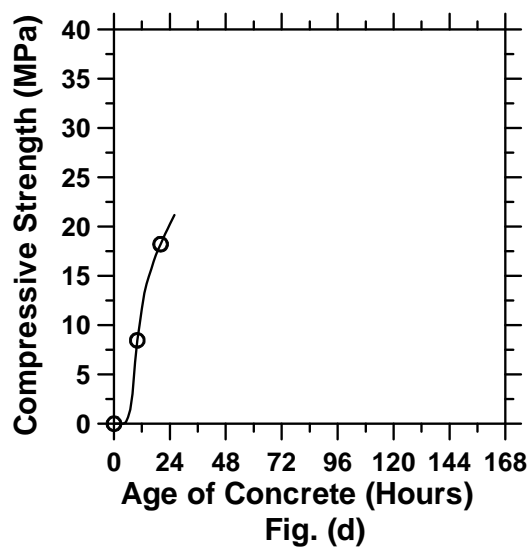
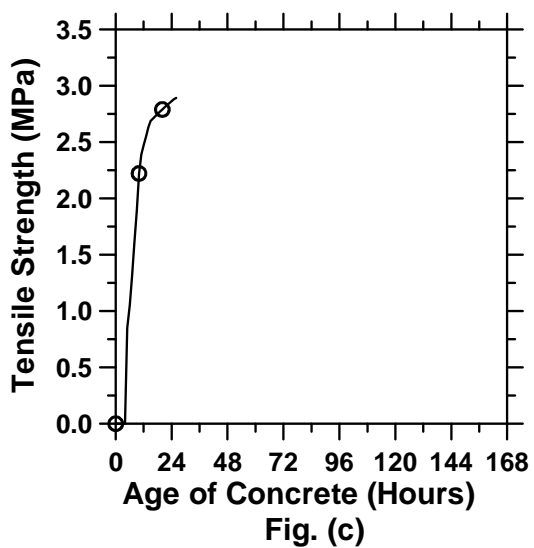
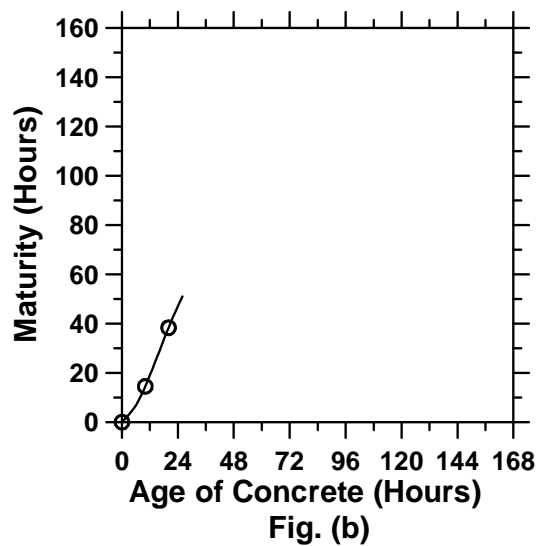
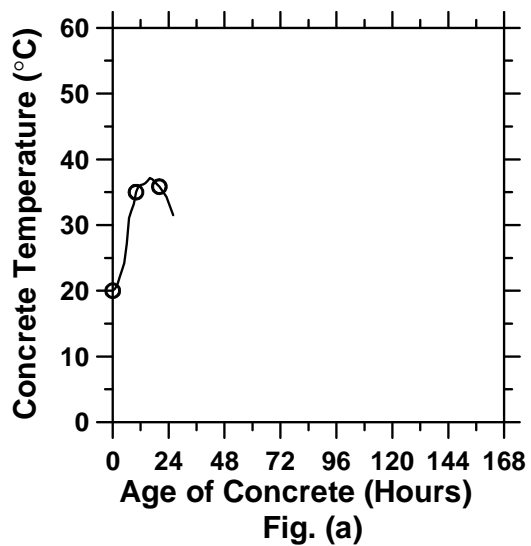


Figure A.158: Pavement casted at “H” ambient temperature at 1:00 a.m. and sawed with a D/3 saw-cut depth after 12 hours (cont’d).

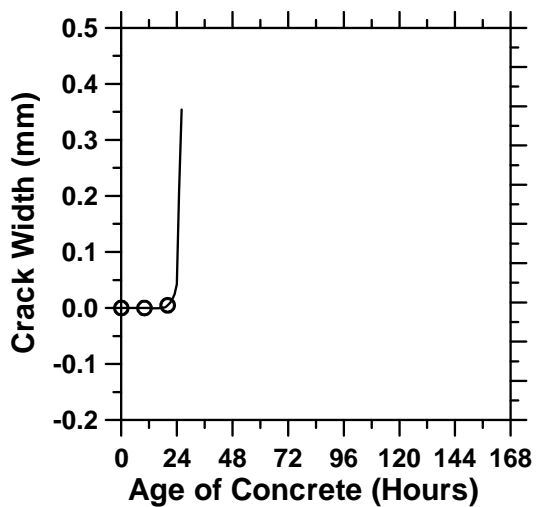


Fig. (e)

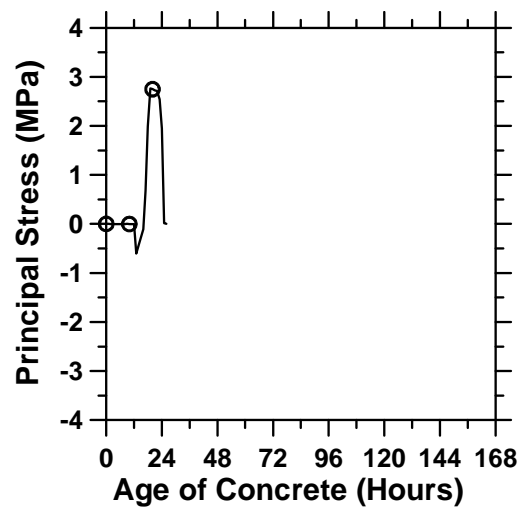


Fig. (f)

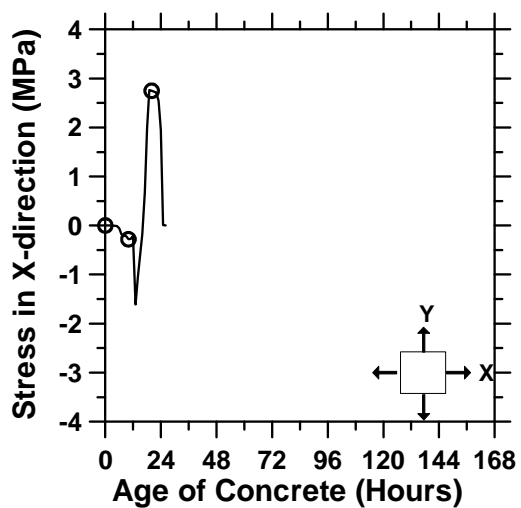


Fig. (g)

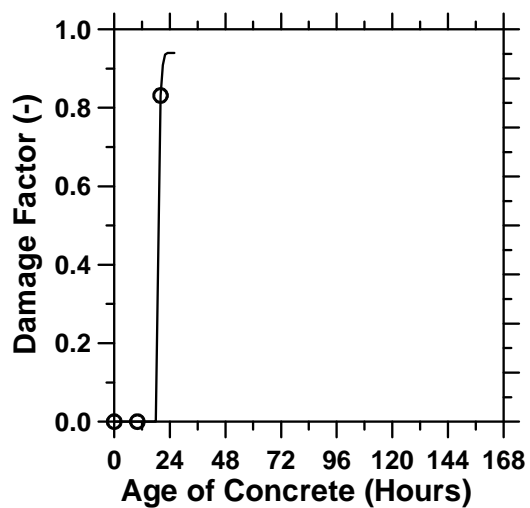


Fig. (h)

Figure A.158: Pavement casted at “H” ambient temperature at 1:00 a.m. and sawed with a D/3 saw-cut depth after 12 hours.

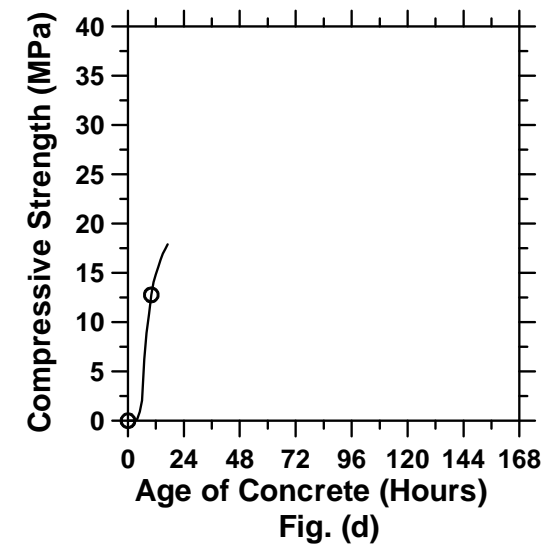
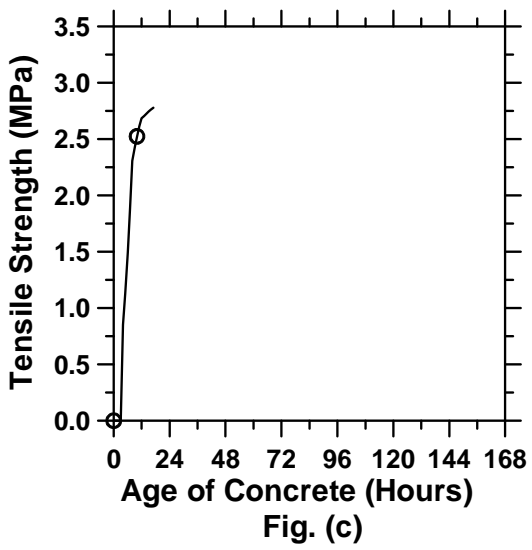
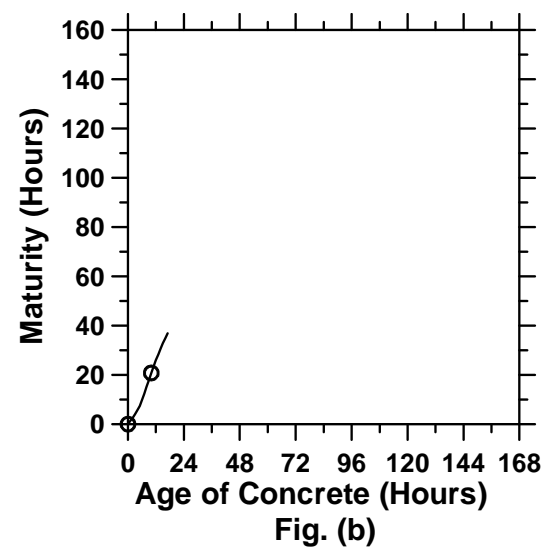
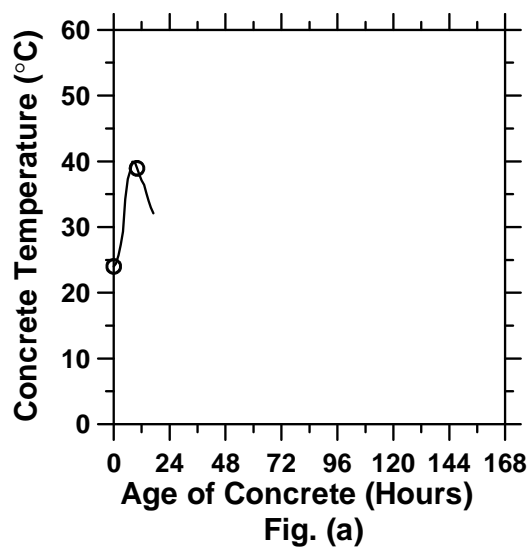


Figure A.159: Pavement casted at “M” ambient temperature at 1:00 p.m. and sawed with a D/3 saw-cut depth after 12 hours (cont’d).

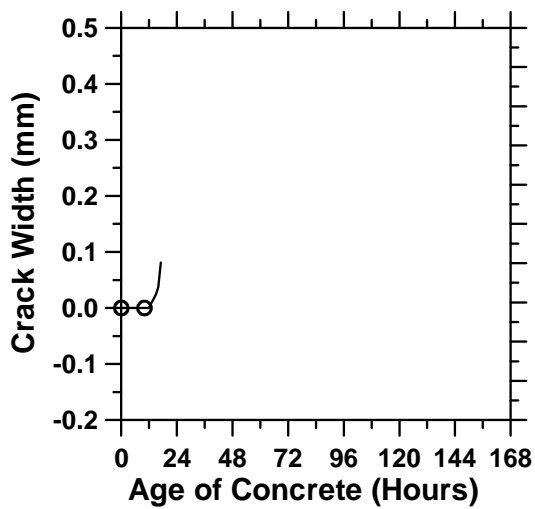


Fig. (e)

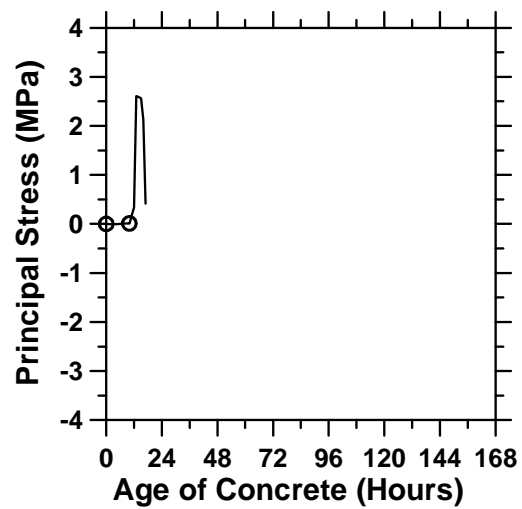


Fig. (f)

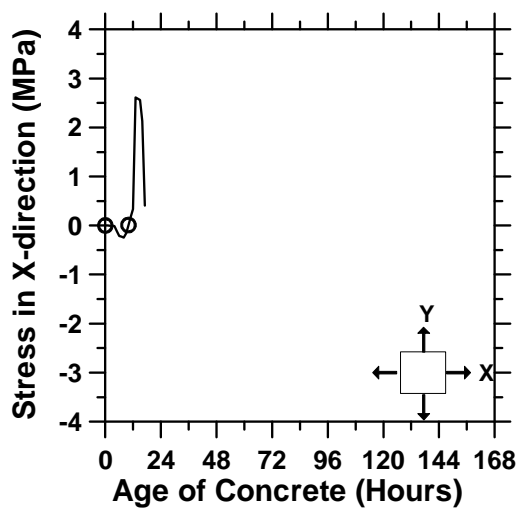


Fig. (g)

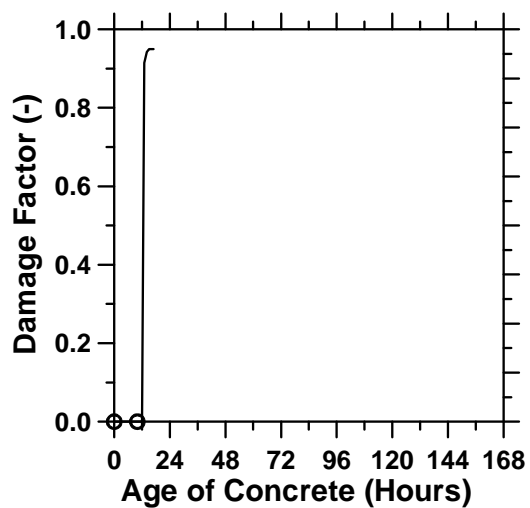


Fig. (h)

Figure A.159: Pavement casted at “M” ambient temperature at 1:00 p.m. and sawed with a D/3 saw-cut depth after 12 hours.

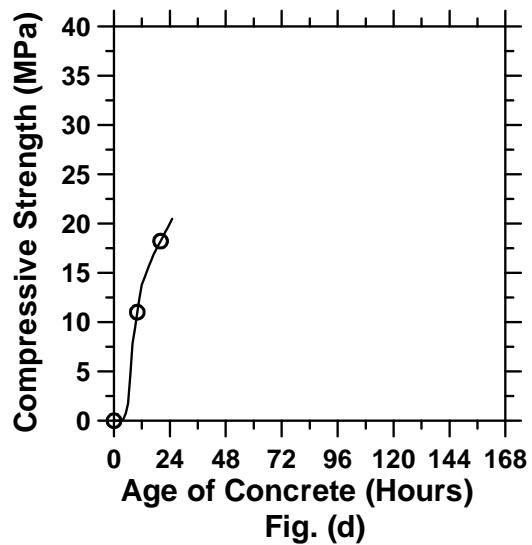
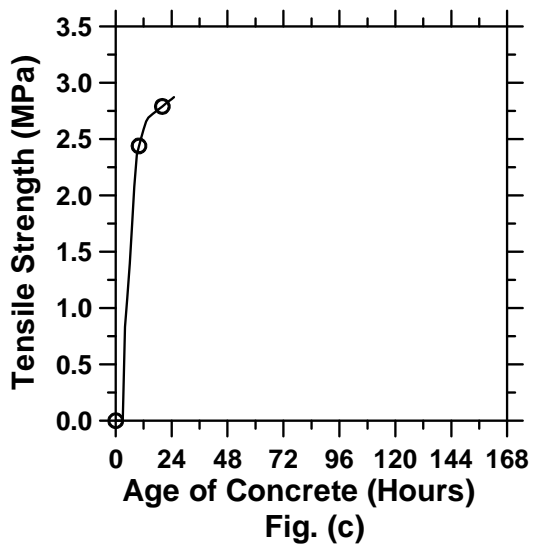
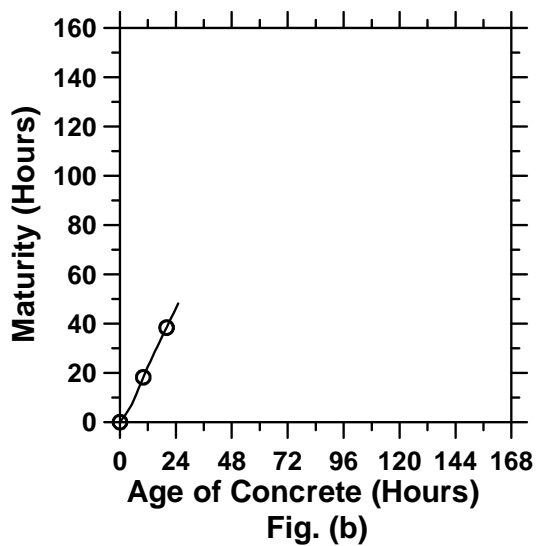
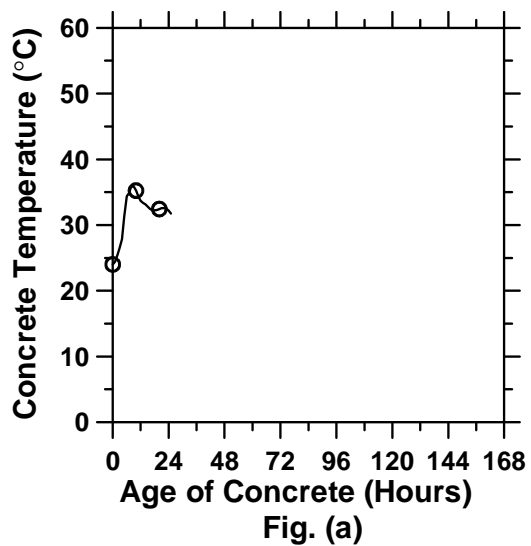


Figure A.160: Pavement casted at "M" ambient temperature at 7:00 p.m. and sawed with a D/3 saw-cut depth after 12 hours (cont'd).

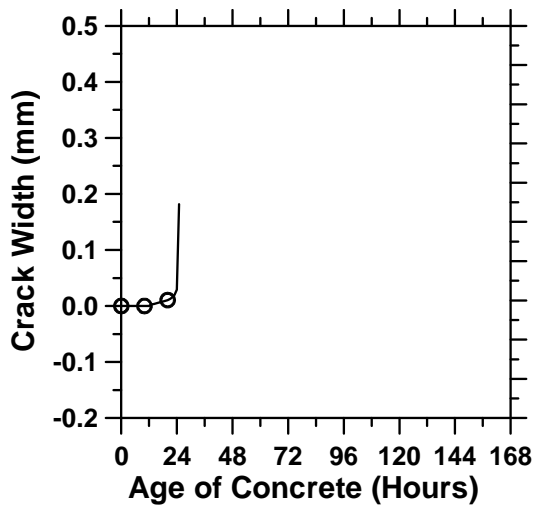


Fig. (e)

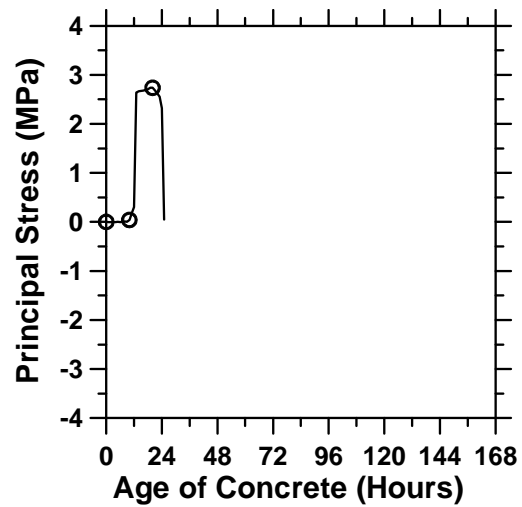


Fig. (f)

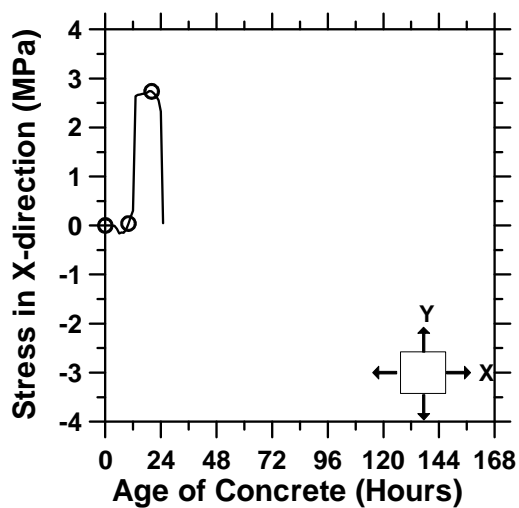


Fig. (g)

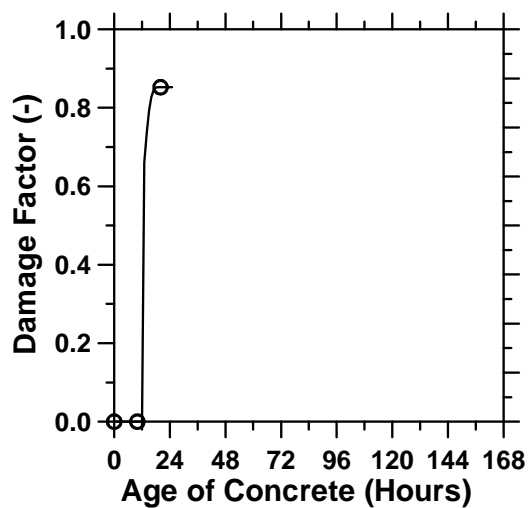


Fig. (h)

Figure A.160: Pavement casted at “M” ambient temperature at 7:00 p.m. and sawed with a D/3 saw-cut depth after 12 hours.

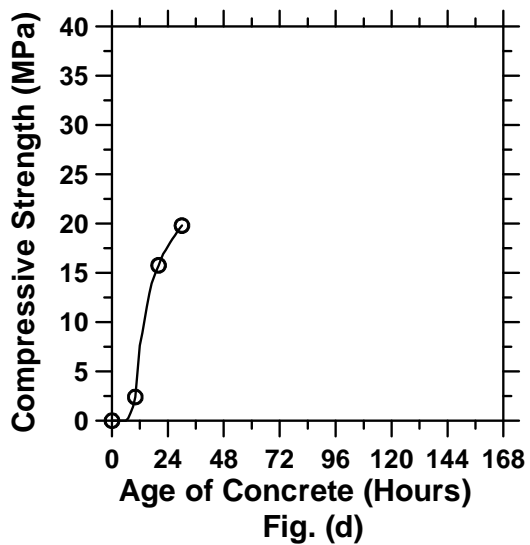
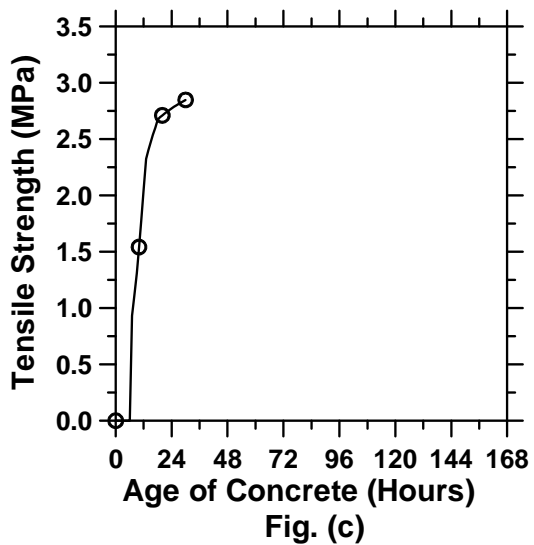
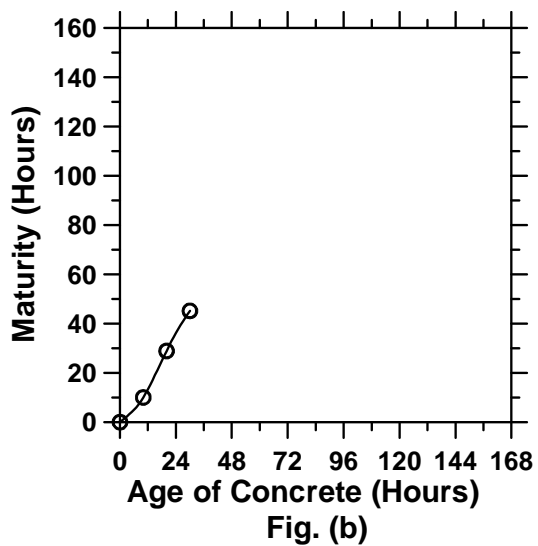
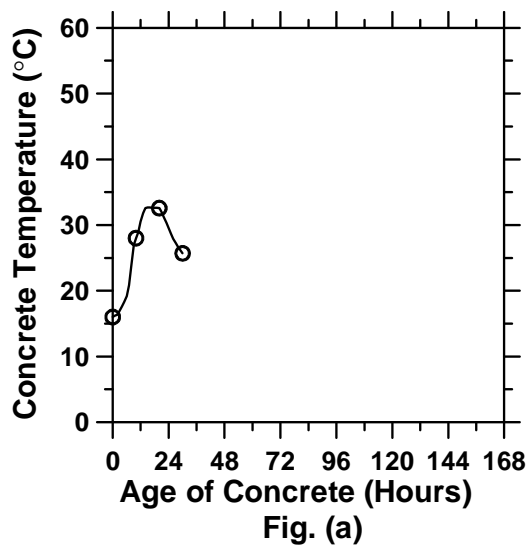


Figure A.161: Pavement casted at “M” ambient temperature at 1:00 a.m. and sawed with a D/3 saw-cut depth after 12 hours (cont’d).

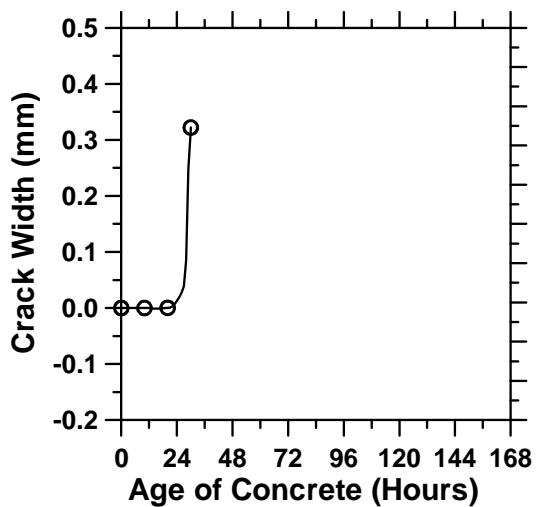


Fig. (e)

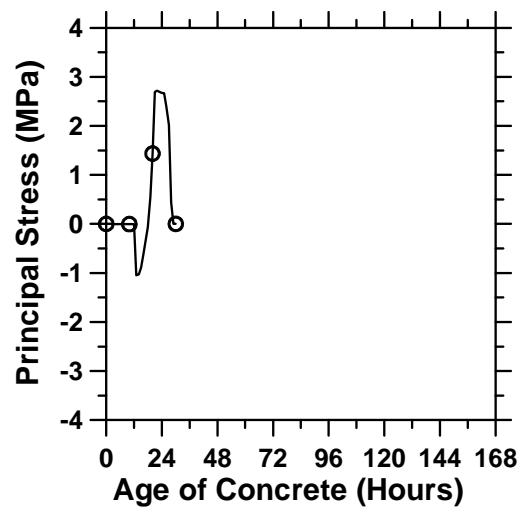


Fig. (f)

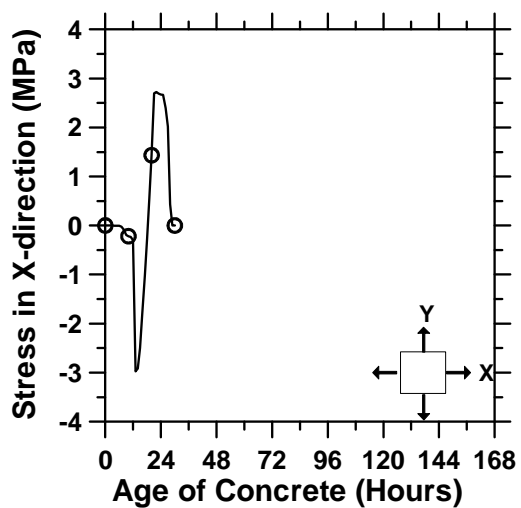


Fig. (g)

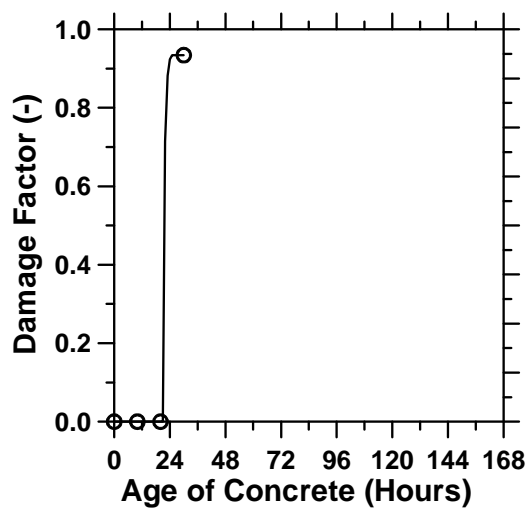


Fig. (h)

Figure A.161: Pavement casted at “M” ambient temperature at 1:00 a.m. and sawed with a D/3 saw-cut depth after 12 hours.

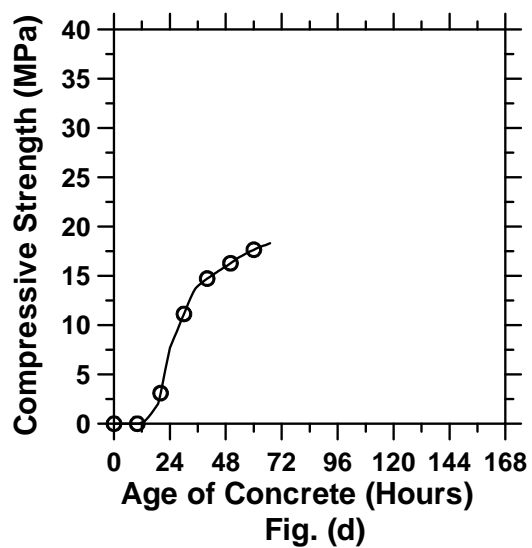
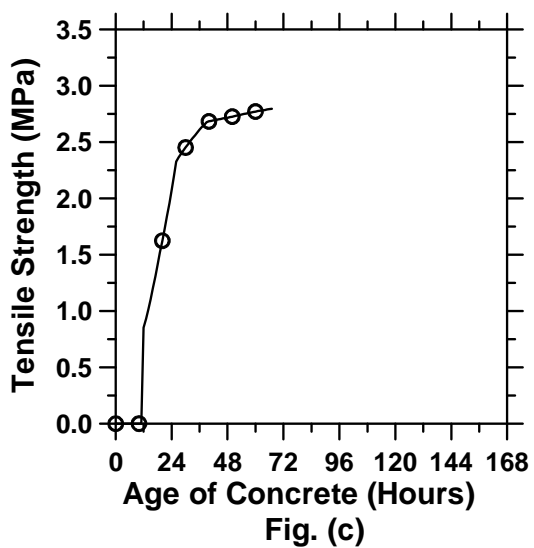
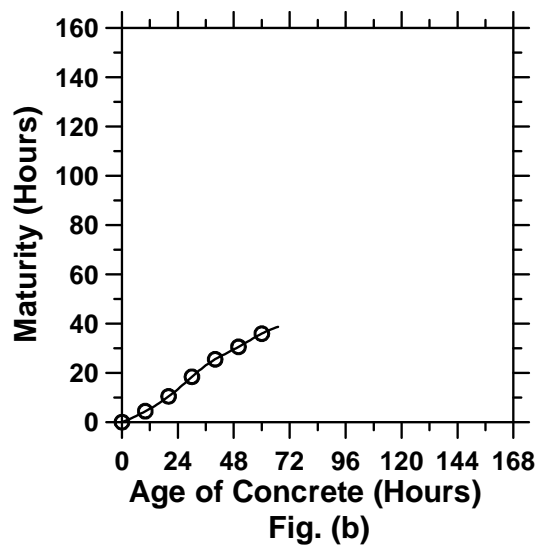
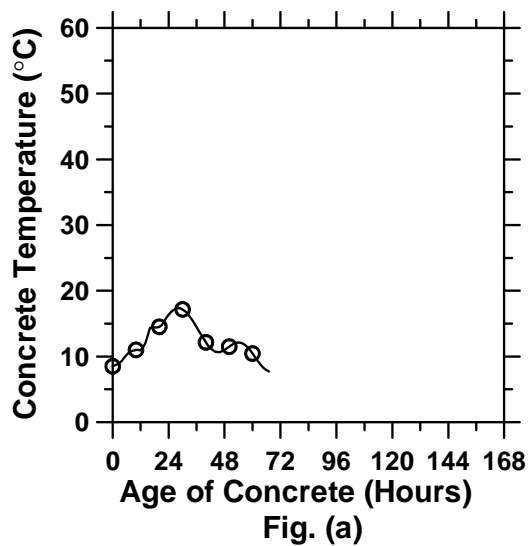


Figure A.162: Pavement casted at “C” ambient temperature at 1:00 p.m. and sawed with a D/3 saw-cut depth after 12 hours (cont’d).

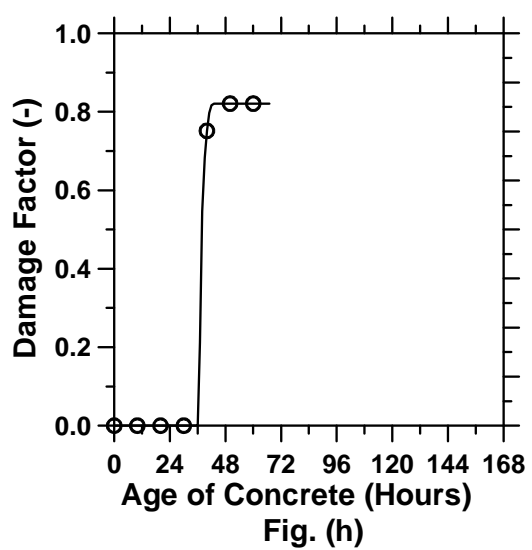
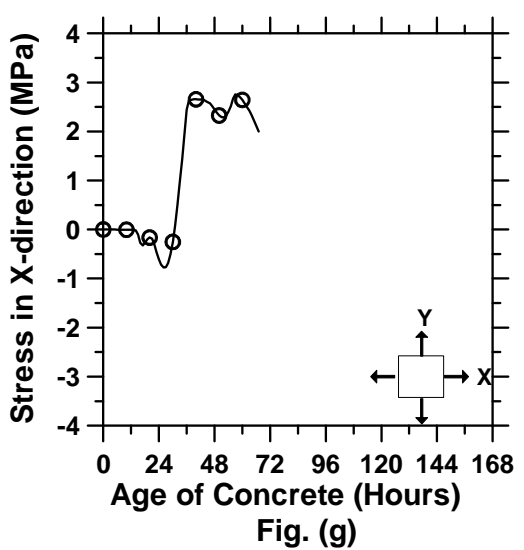
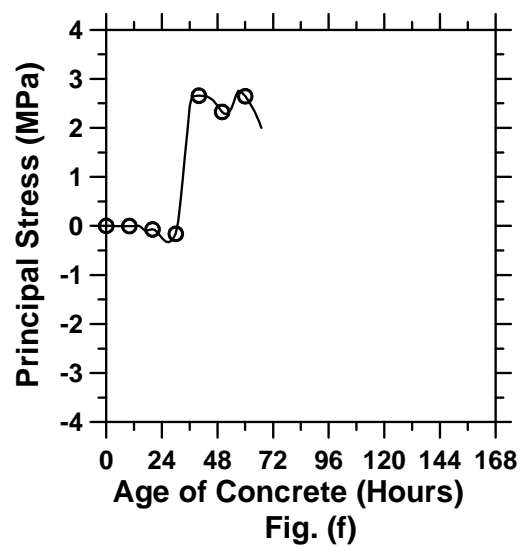
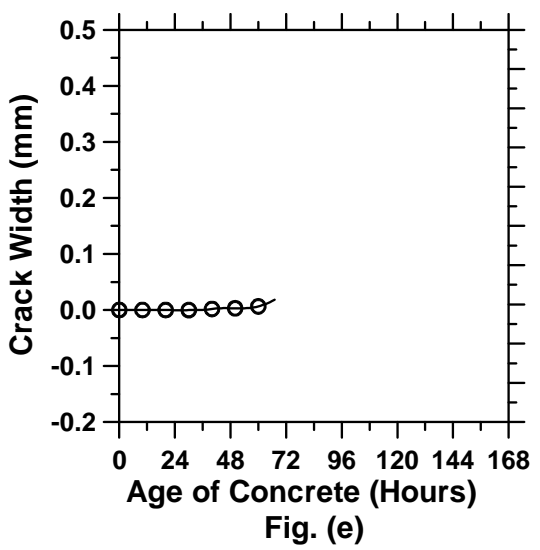


Figure A.162: Pavement casted at “C” ambient temperature at 1:00 p.m. and sawed with a D/3 saw-cut depth after 12 hours.

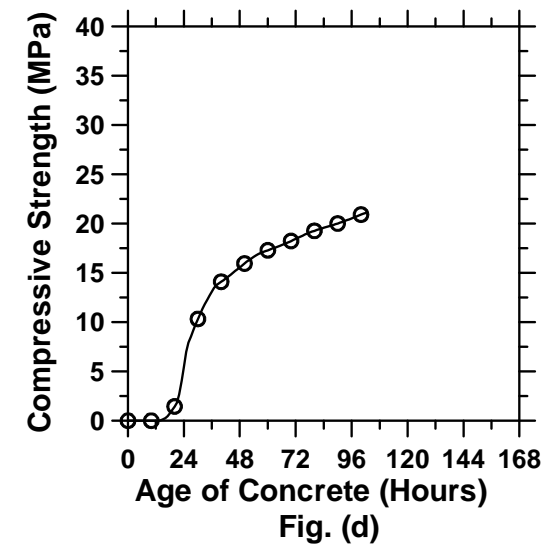
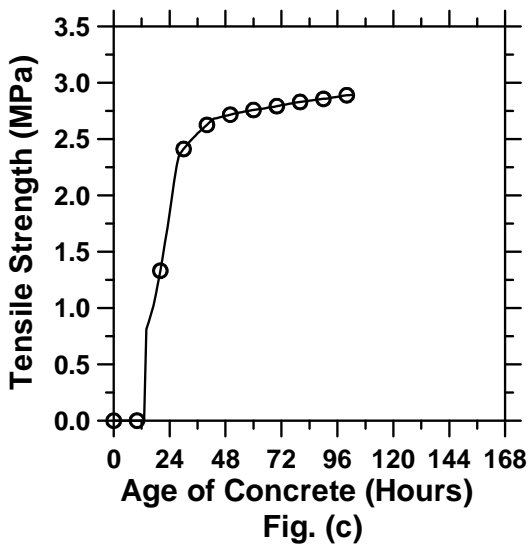
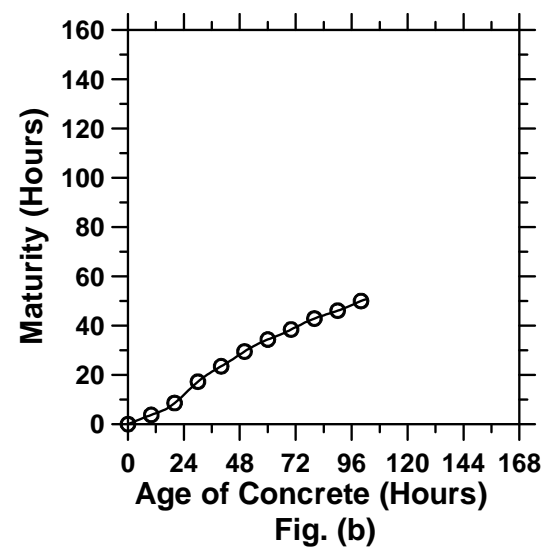
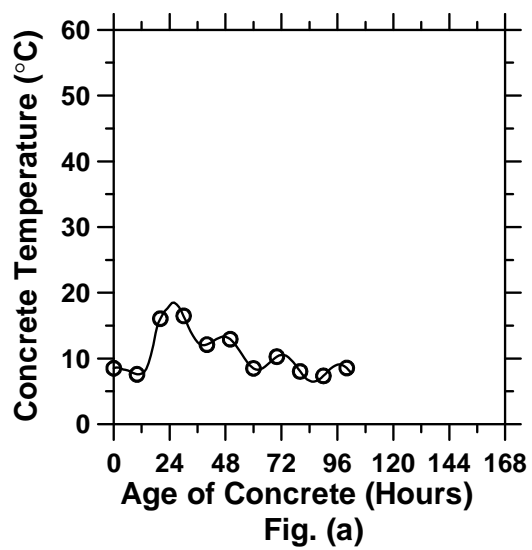


Figure A.163: Pavement casted at “C” ambient temperature at 7:00 p.m. and sawed with a D/3 saw-cut depth after 12 hours (cont’d).

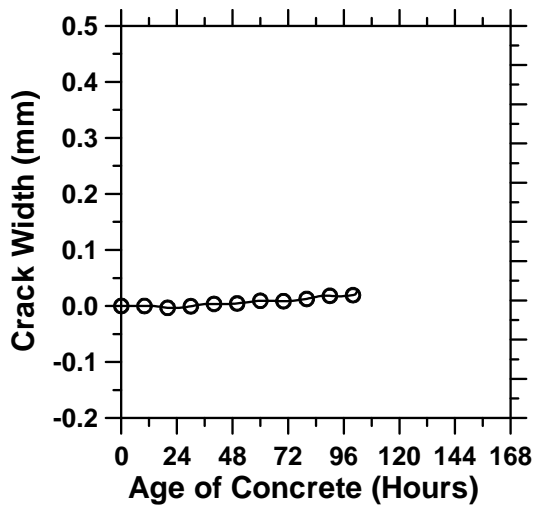


Fig. (e)

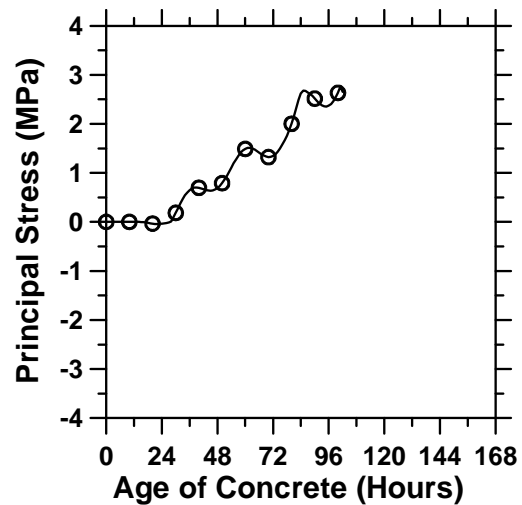


Fig. (f)

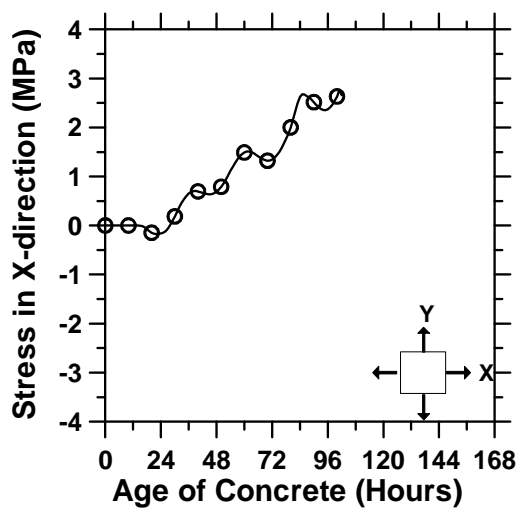


Fig. (g)

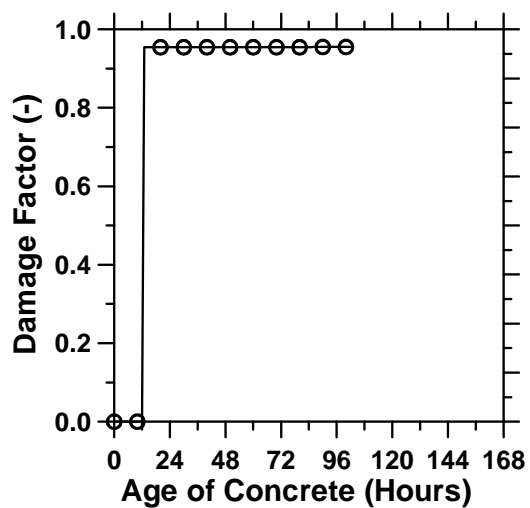


Fig. (h)

Figure A.163: Pavement casted at “C” ambient temperature at 7:00 p.m. and sawed with a D/3 saw-cut depth after 12 hours.

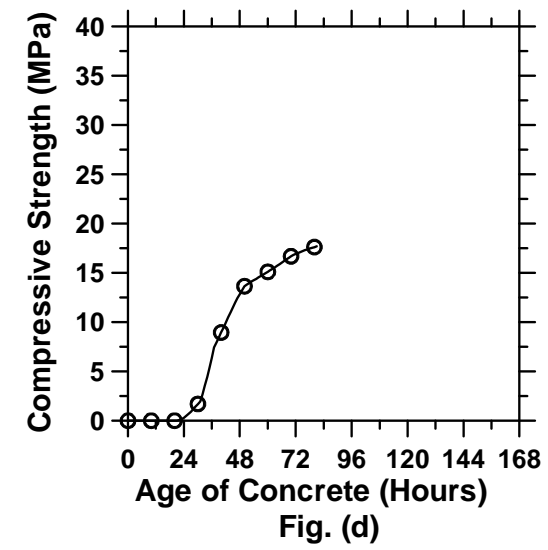
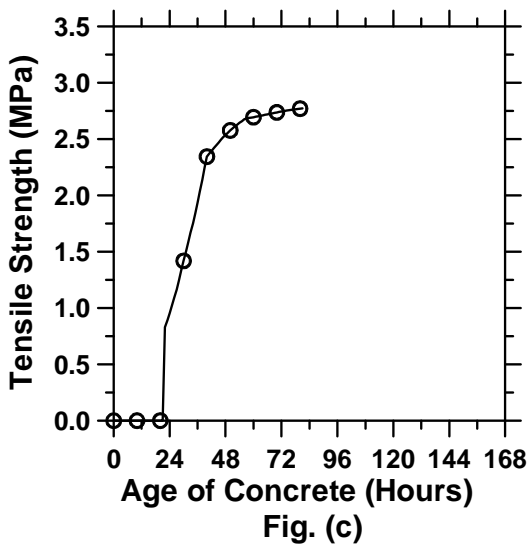
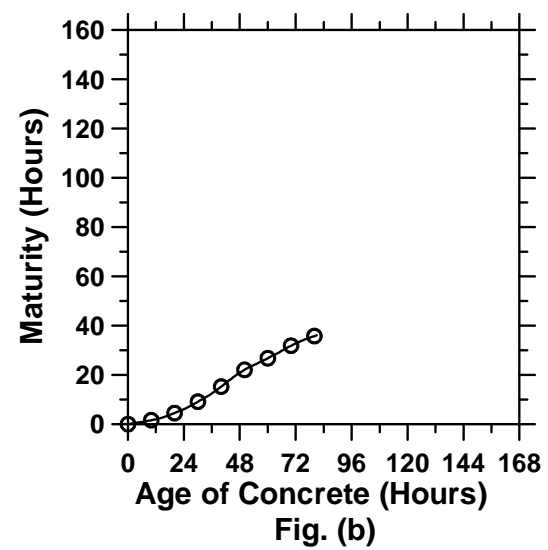
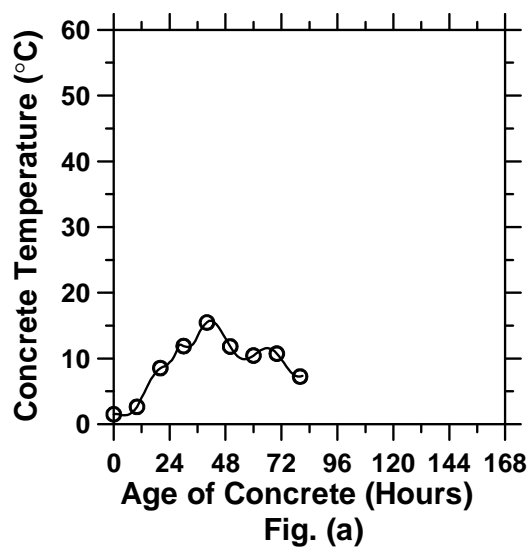


Figure A.164: Pavement casted at “C” ambient temperature at 1:00 a.m. and sawed with a D/3 saw-cut depth after 12 hours (cont’d).

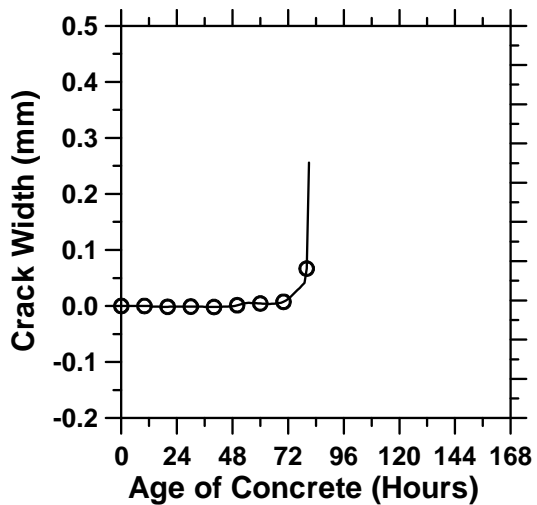


Fig. (e)

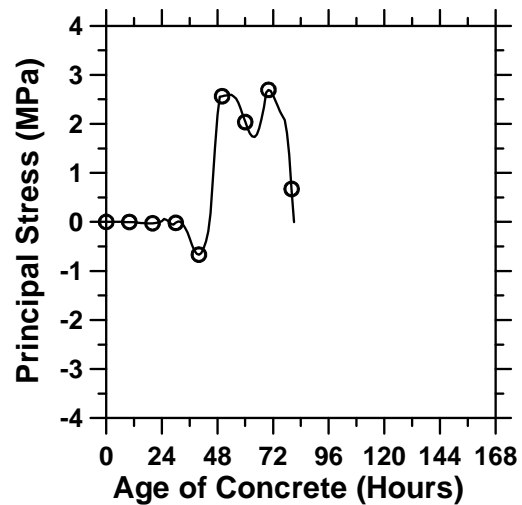


Fig. (f)

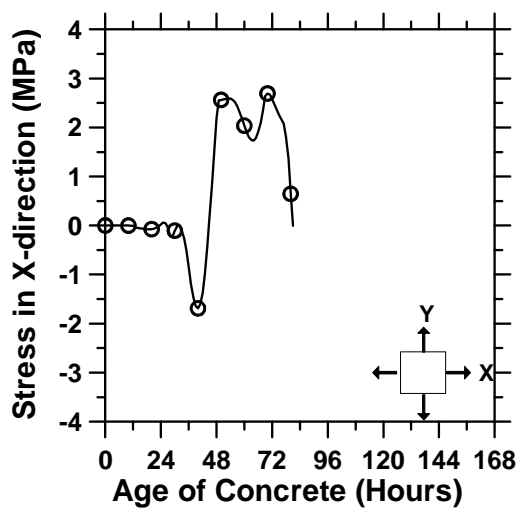


Fig. (g)

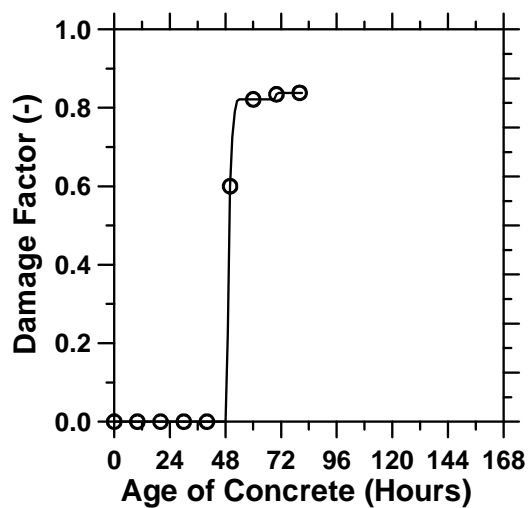


Fig. (h)

Figure A.164: Pavement casted at “C” ambient temperature at 1:00 a.m. and sawed with a D/3 saw-cut depth after 12 hours.

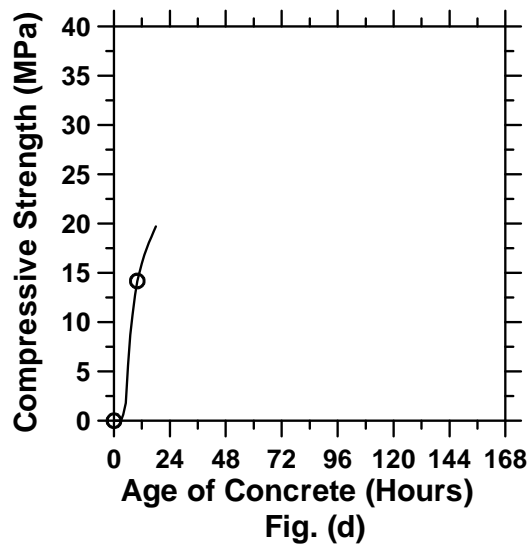
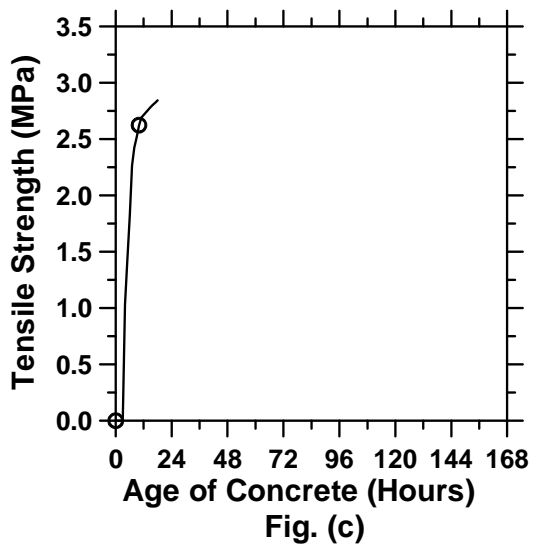
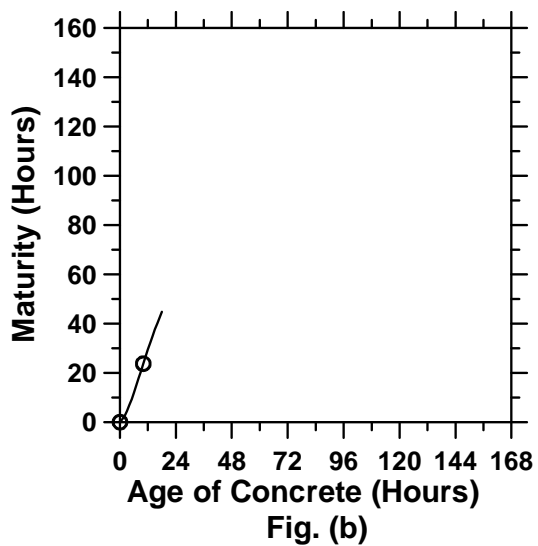
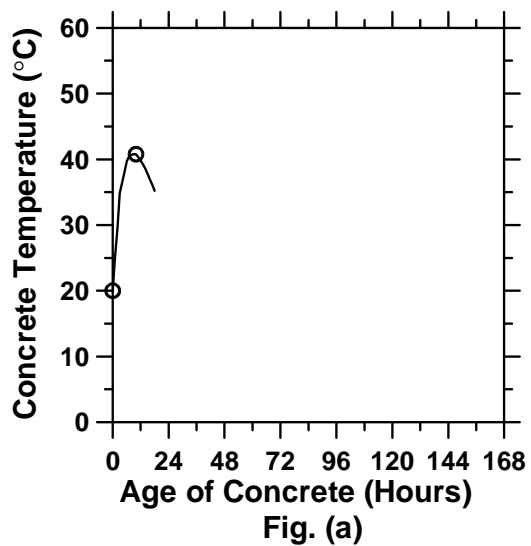


Figure A.165: Pavement built with rapid setting materials and a D/3 saw-cut depth introduced at 0 hour (cont'd).

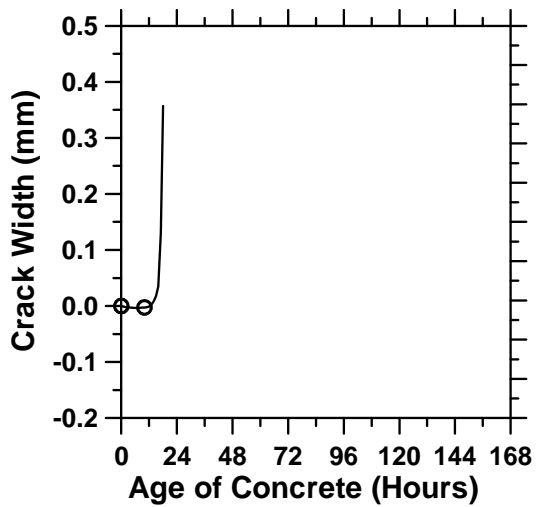


Fig. (e)

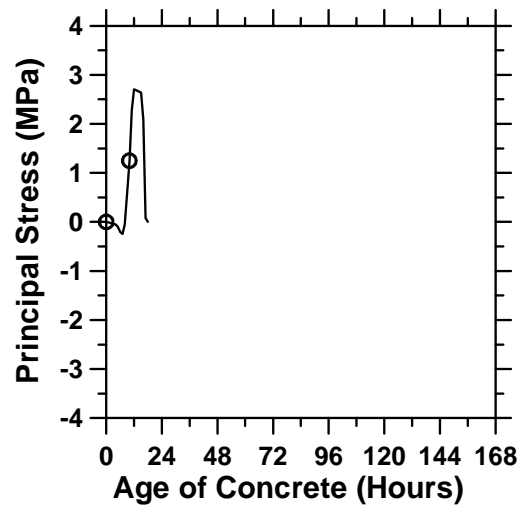


Fig. (f)

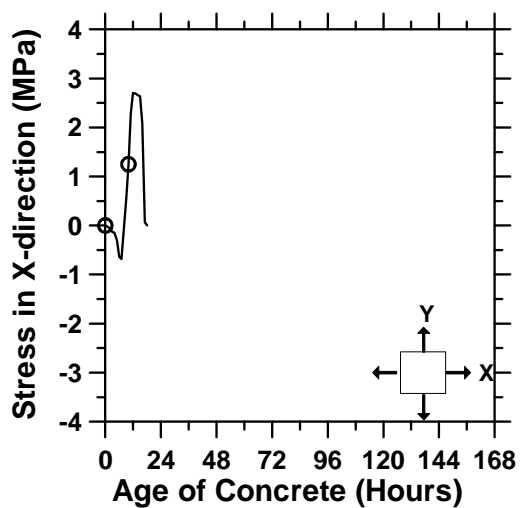


Fig. (g)

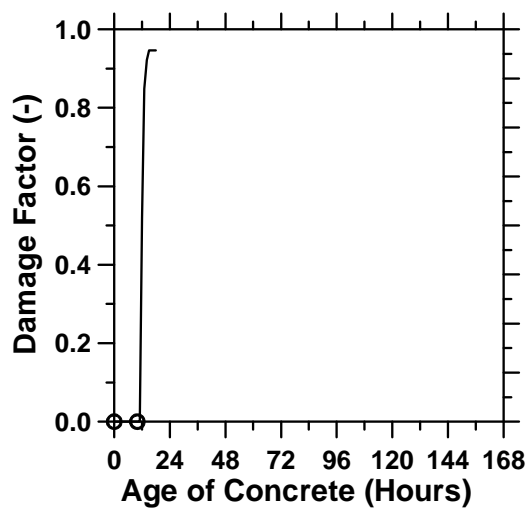


Fig. (h)

Figure A.165: Pavement built with rapid setting materials and a D/3 saw-cut depth introduced at 0 hour.

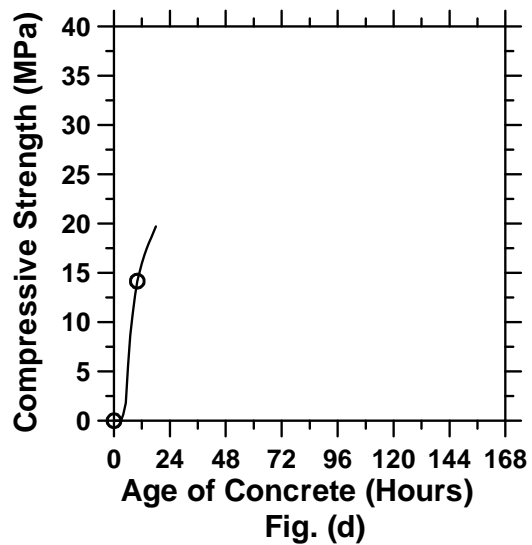
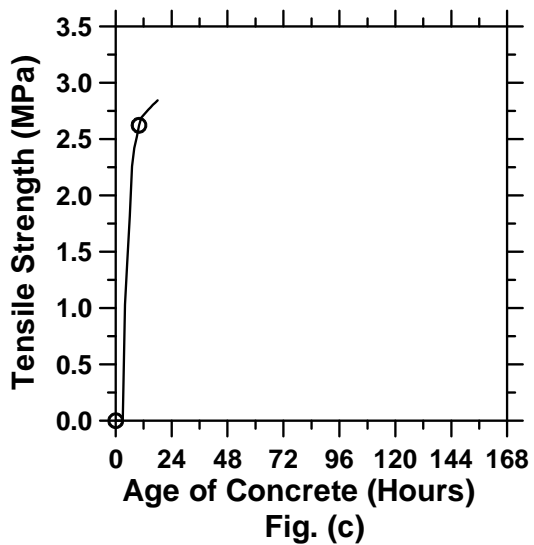
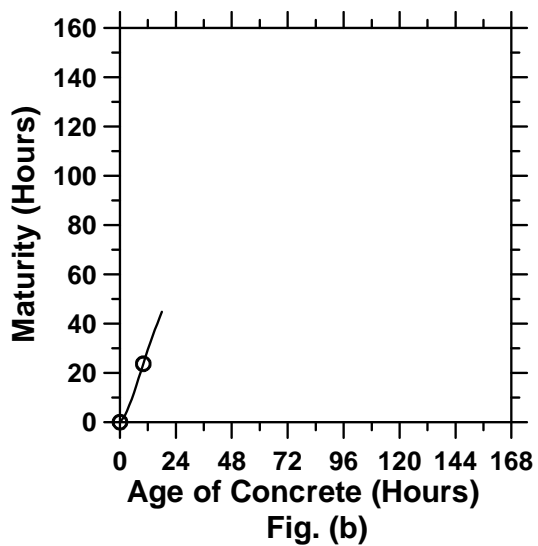
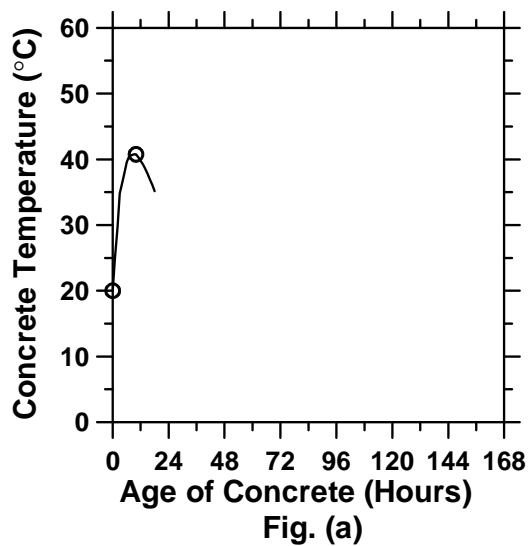


Figure A.166: Pavement built with rapid setting materials and a D/3 saw-cut depth introduced at 6 hours (cont'd).

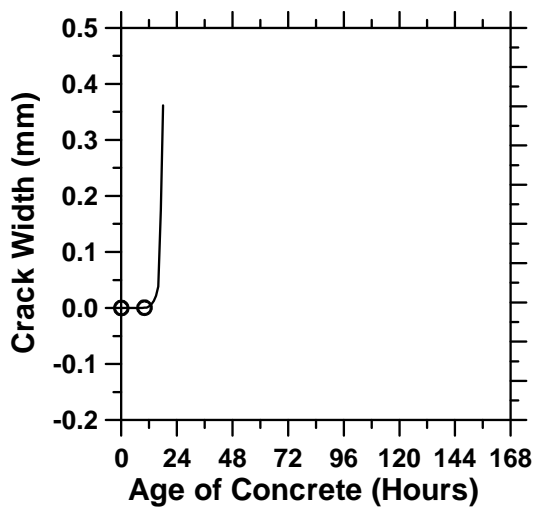


Fig. (e)

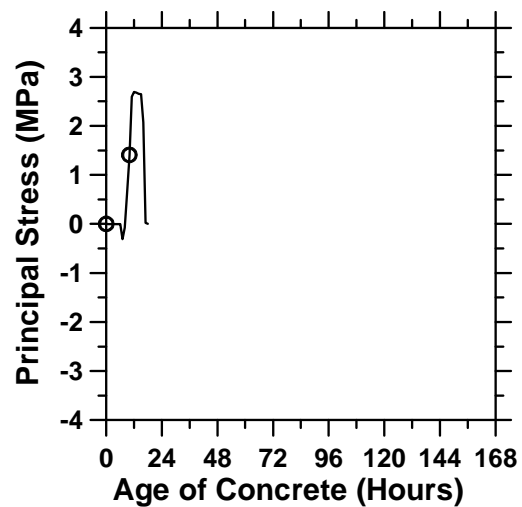


Fig. (f)

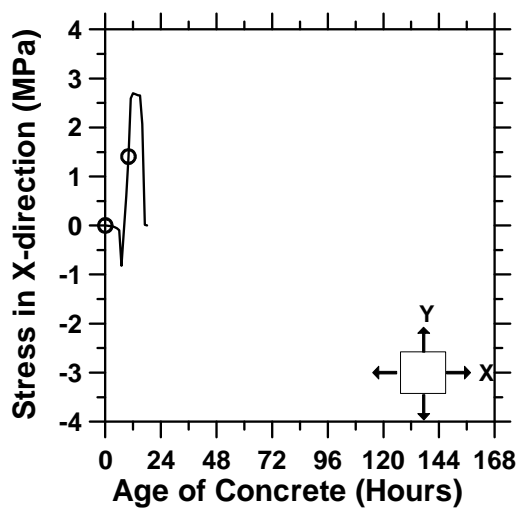


Fig. (g)

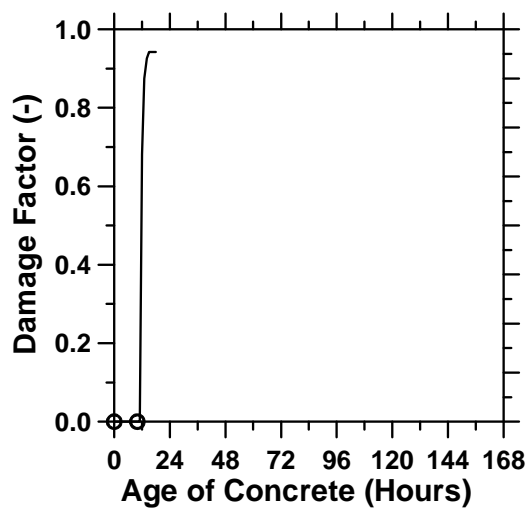


Fig. (h)

Figure A.166: Pavement built with rapid setting materials and a D/3 saw-cut depth introduced at 6 hours.

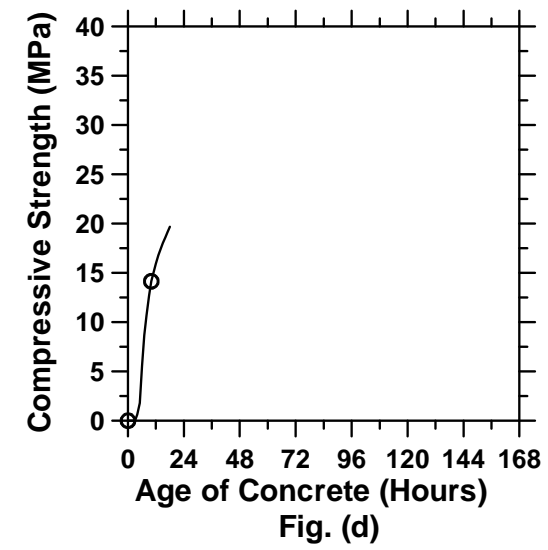
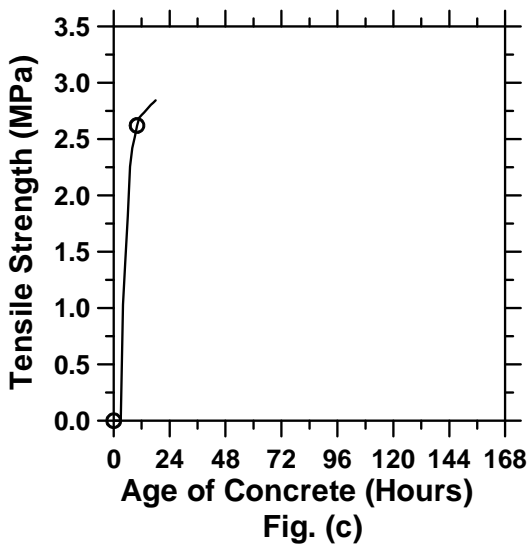
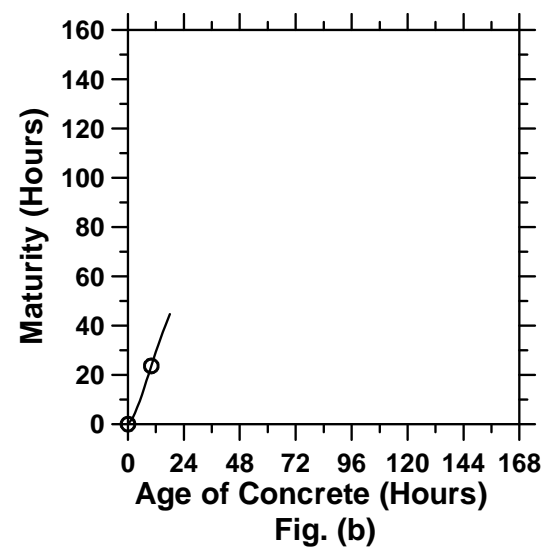
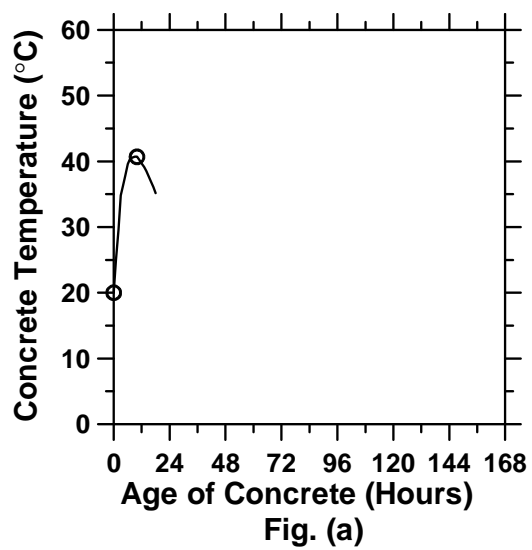


Figure A.167: Pavement built with rapid setting materials and a D/3 saw-cut depth introduced at 12 hours (cont'd).

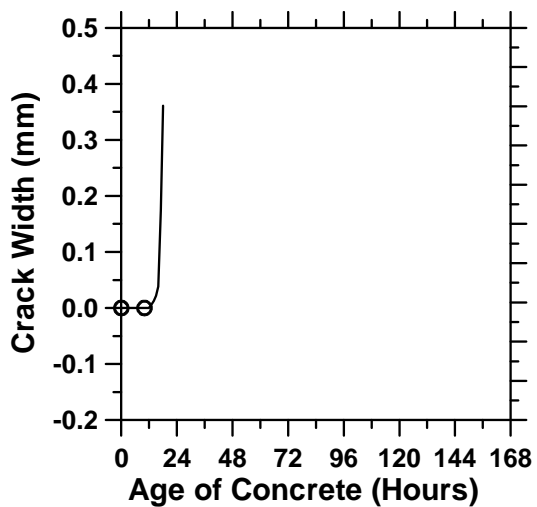


Fig. (e)

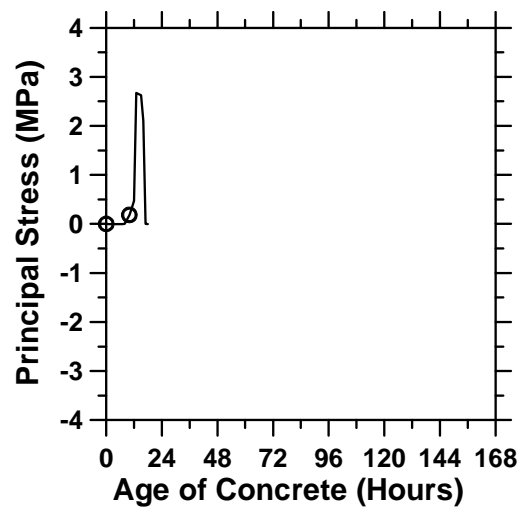


Fig. (f)

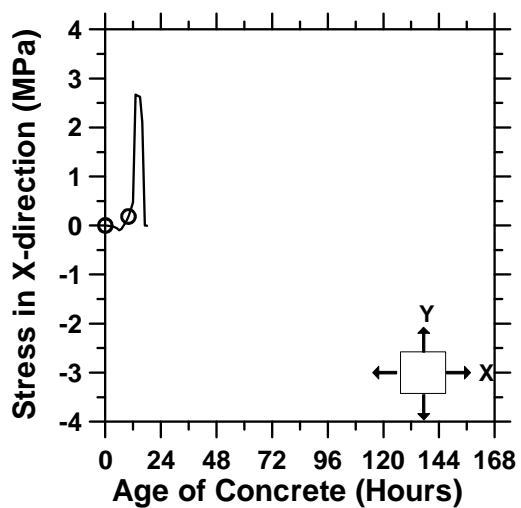


Fig. (g)

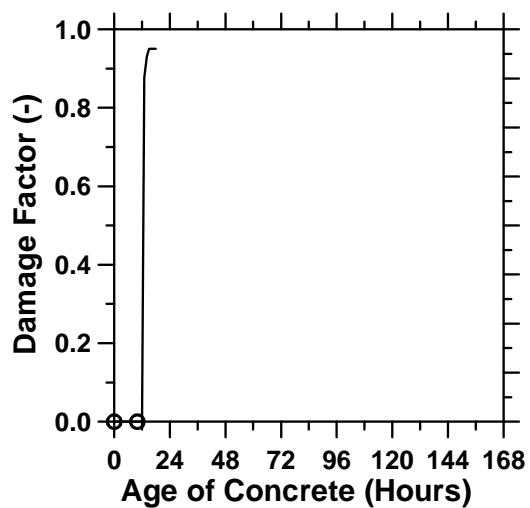


Fig. (h)

Figure A.167: Pavement built with rapid setting materials and a D/3 saw-cut depth introduced at 12 hours.

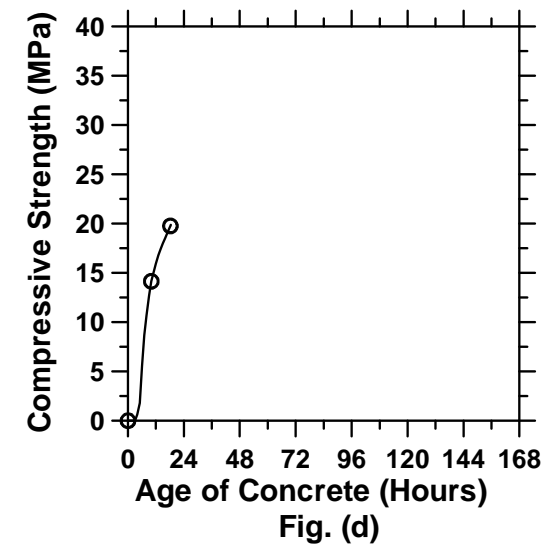
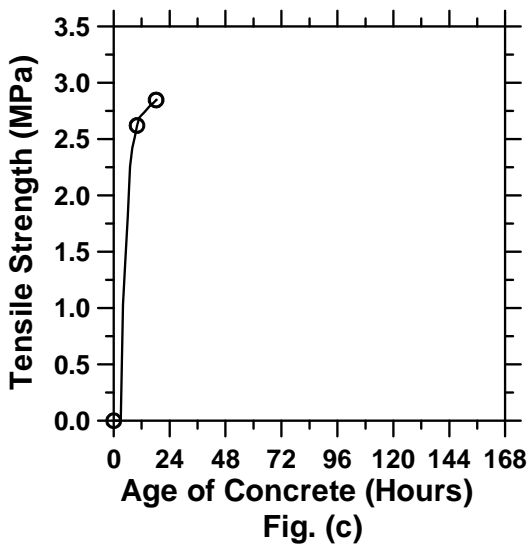
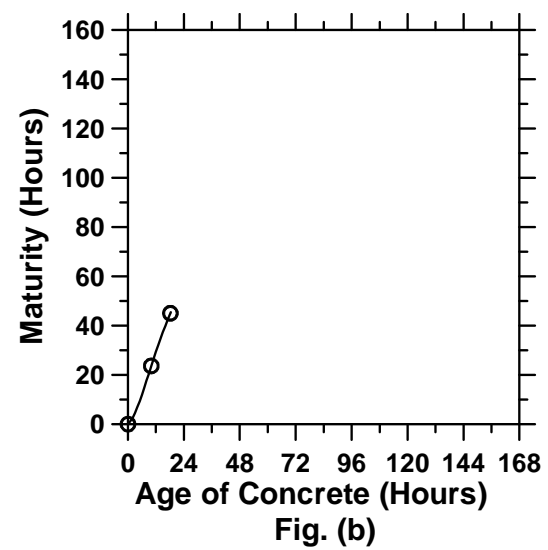
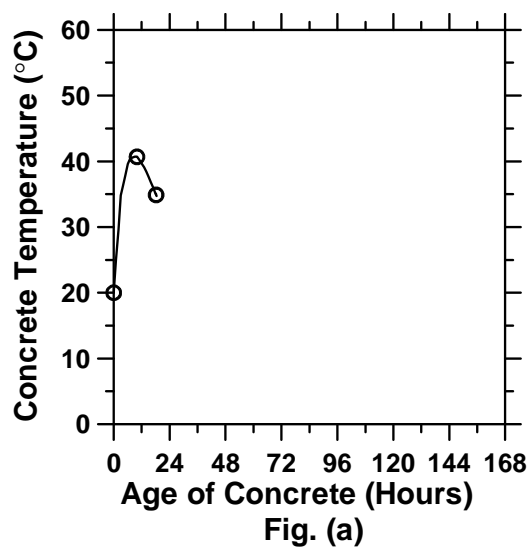


Figure A.168: Pavement built with rapid setting materials and a D/3 saw-cut depth introduced at 18 hours (cont'd).

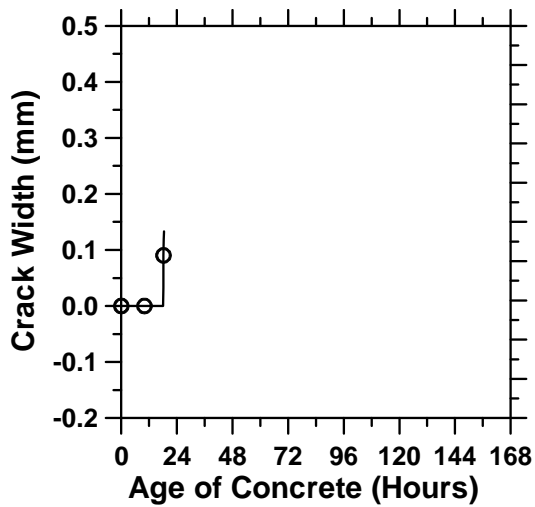


Fig. (e)

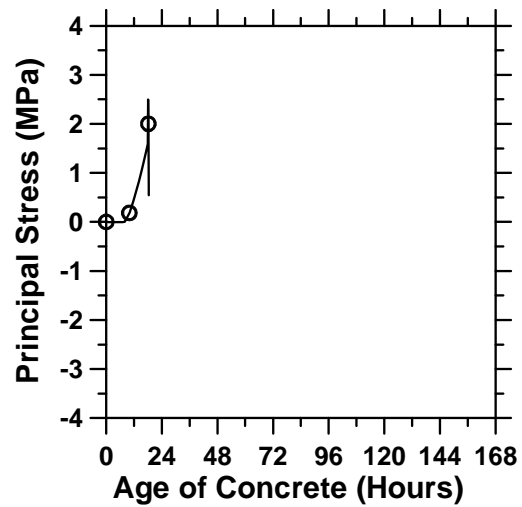


Fig. (f)

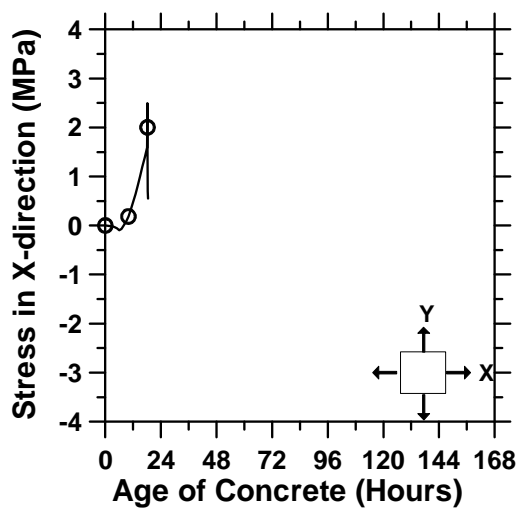


Fig. (g)

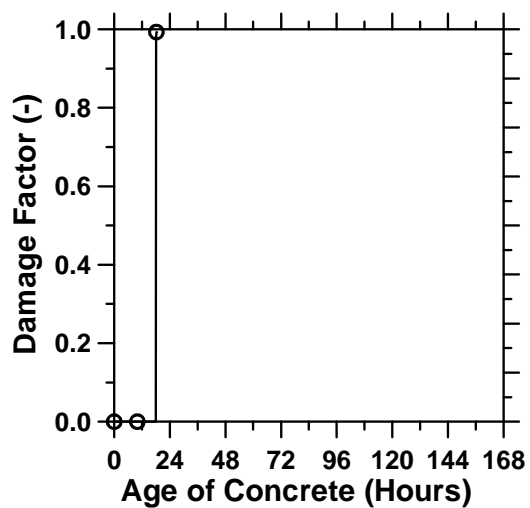


Fig. (h)

Figure A.168: Pavement built with rapid setting materials and a D/3 saw-cut depth introduced at 18 hours.

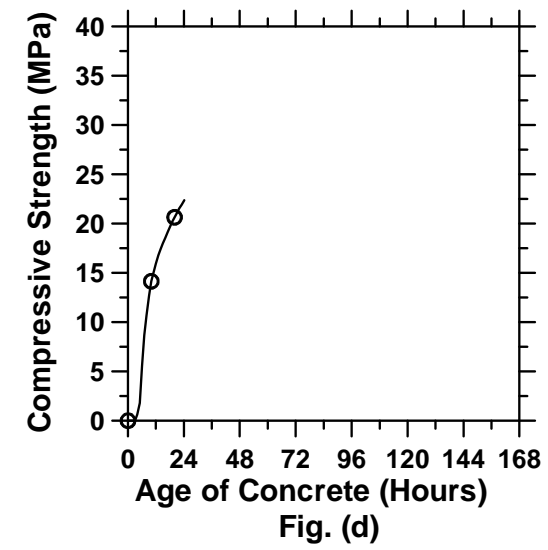
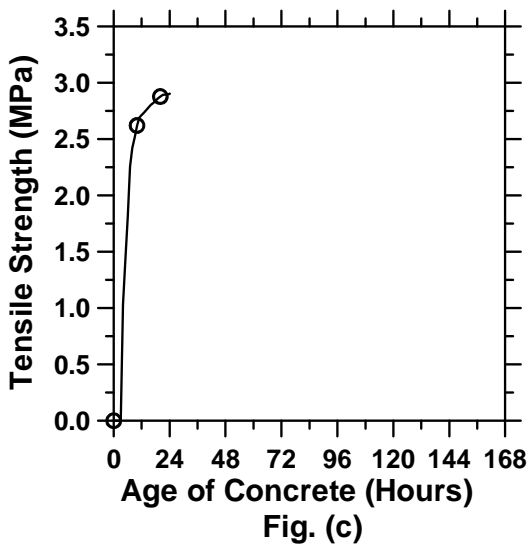
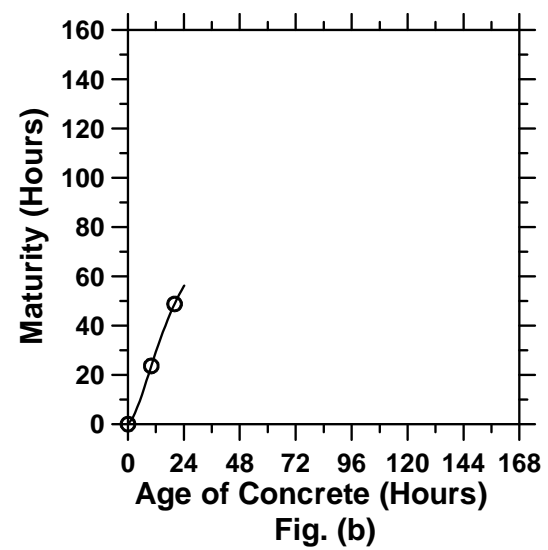
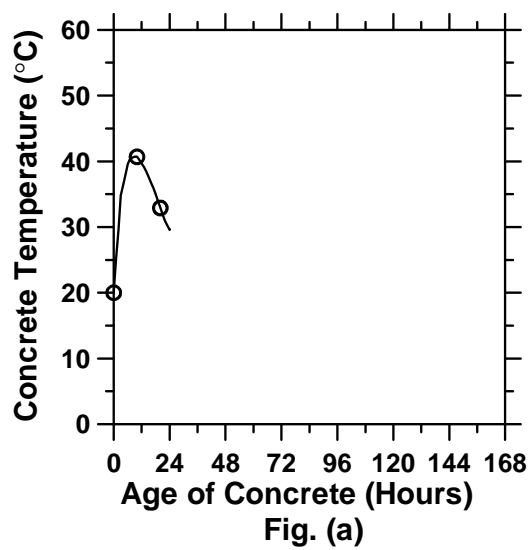


Figure A.169: Pavement built with rapid setting materials and a D/3 saw-cut depth introduced at 24 hours (cont'd).

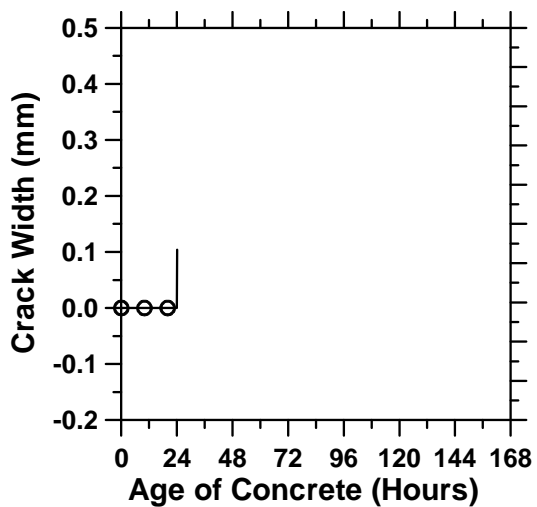


Fig. (e)

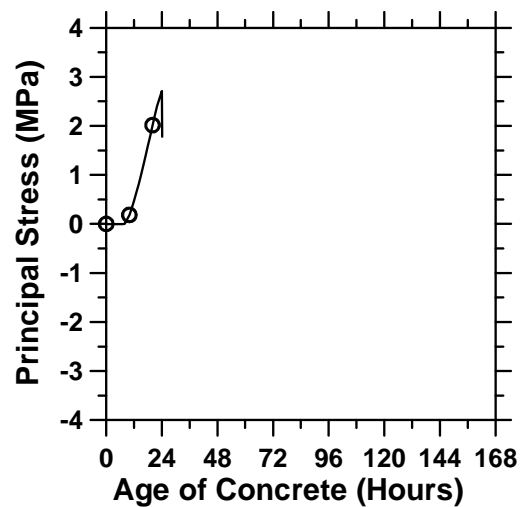


Fig. (f)

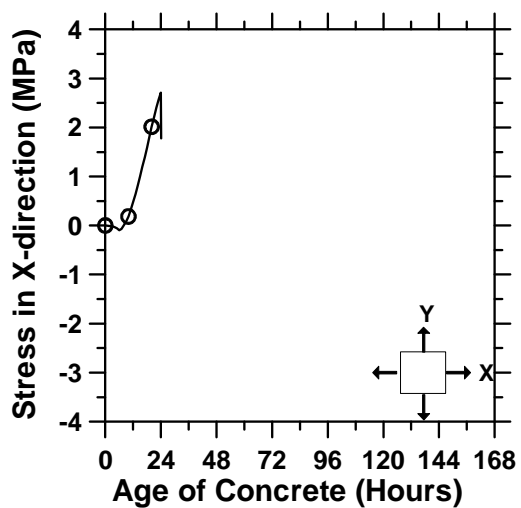


Fig. (g)

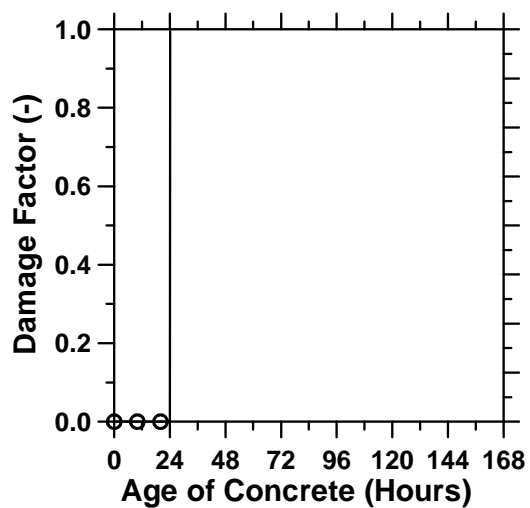


Fig. (h)

Figure A.169: Pavement built with rapid setting materials and a D/3 saw-cut depth introduced at 24 hours.

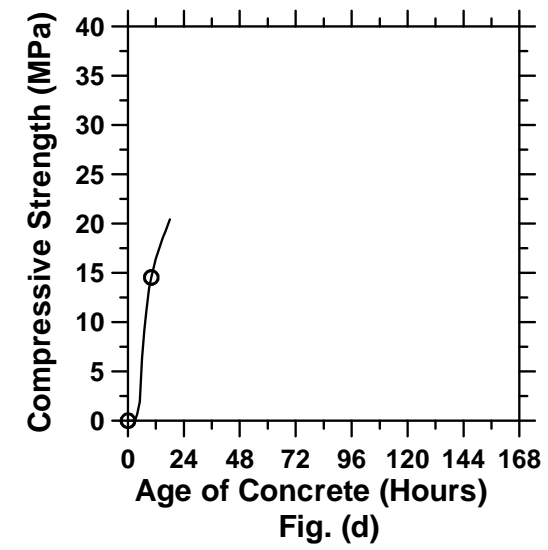
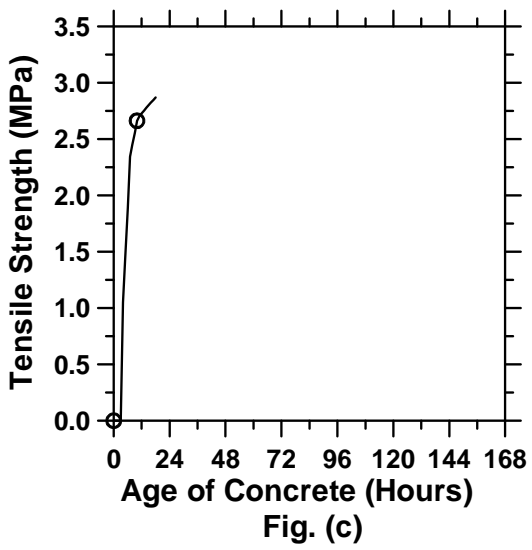
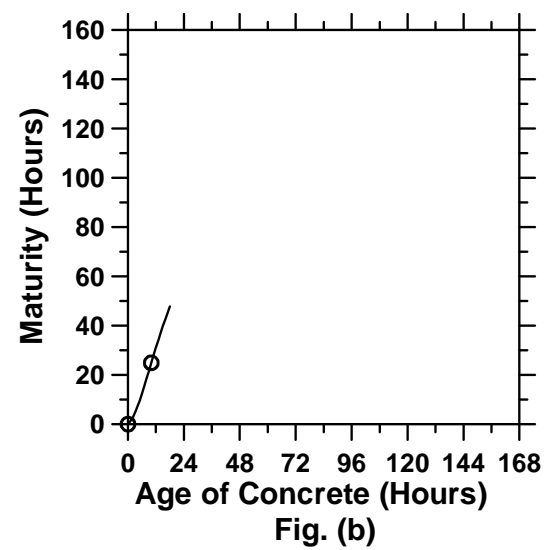
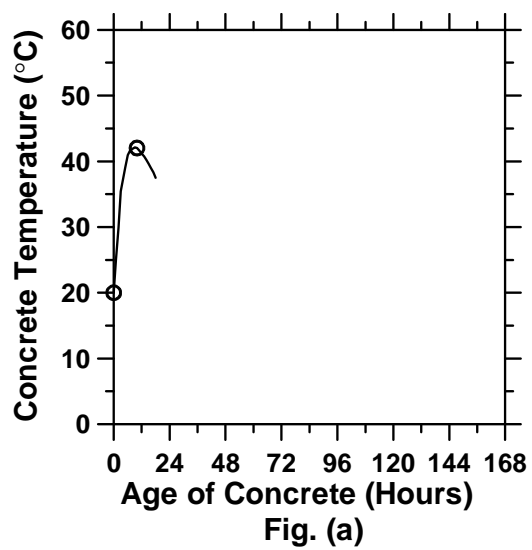


Figure A.170: Pavement built with rapid setting materials and a D/2 saw-cut depth introduced at 6 hours (cont'd).

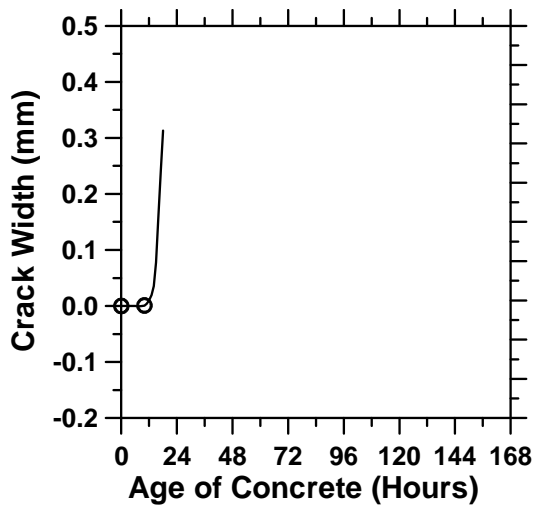


Fig. (e)

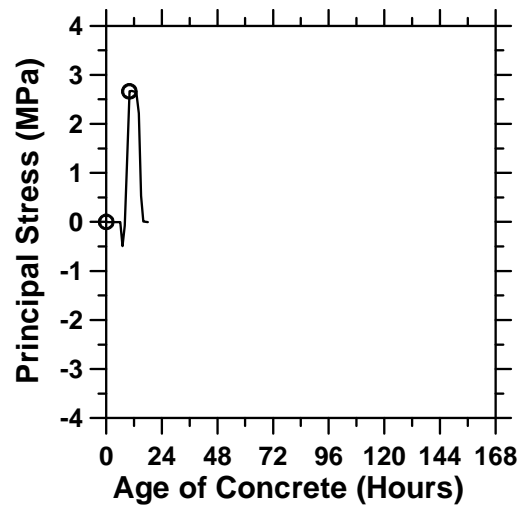


Fig. (f)

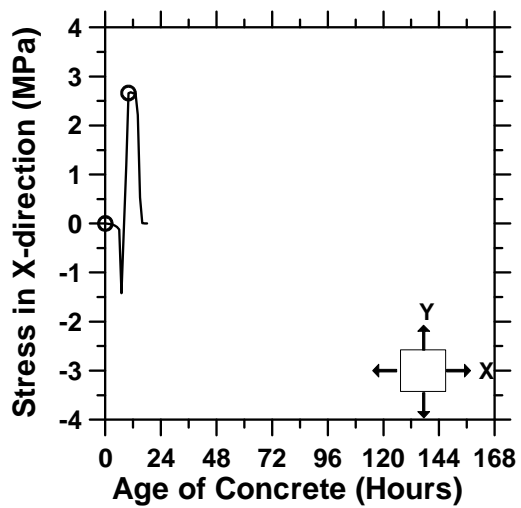


Fig. (g)

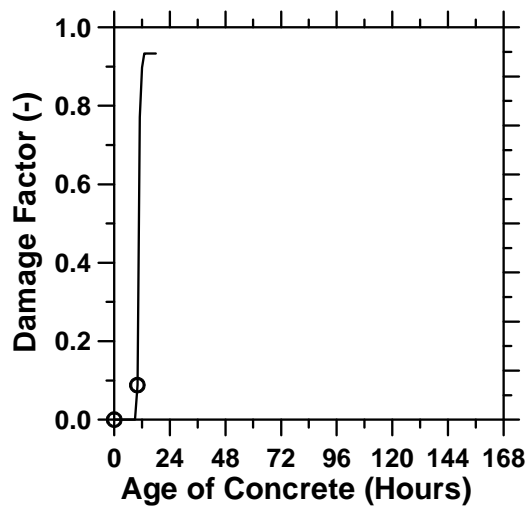


Fig. (h)

Figure A.170: Pavement built with rapid setting materials and a D/2 saw-cut depth introduced at 6 hours.

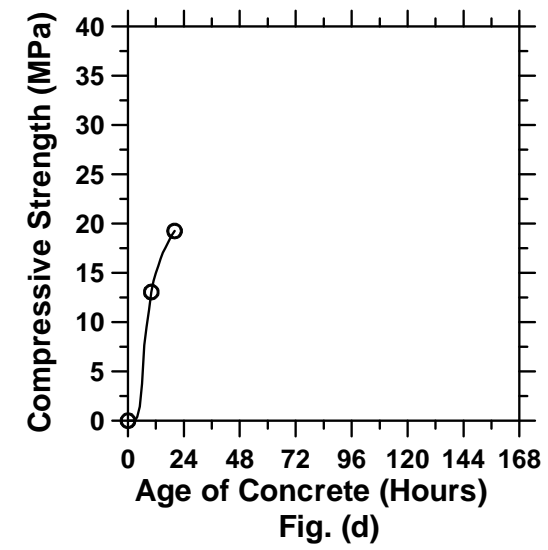
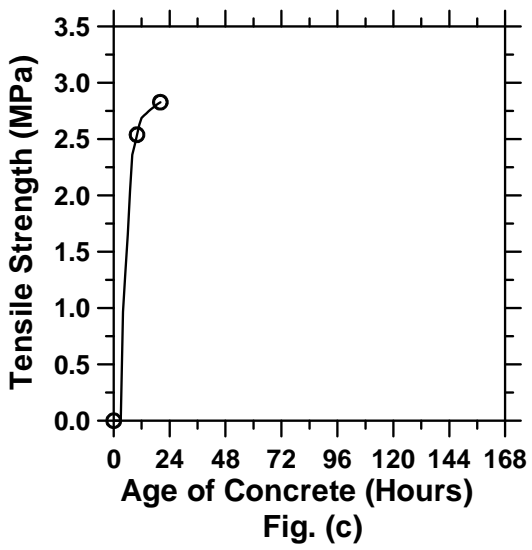
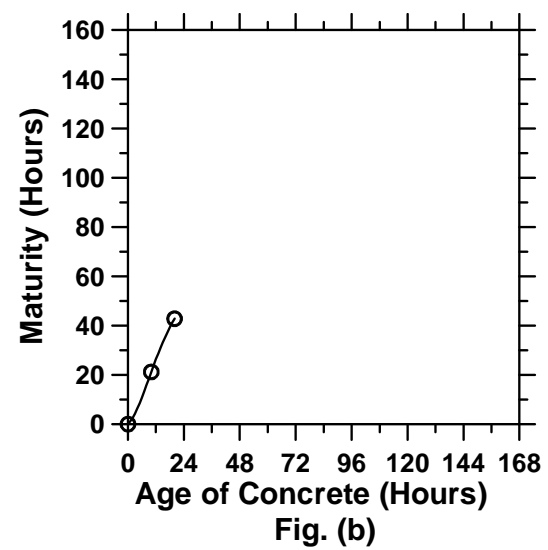
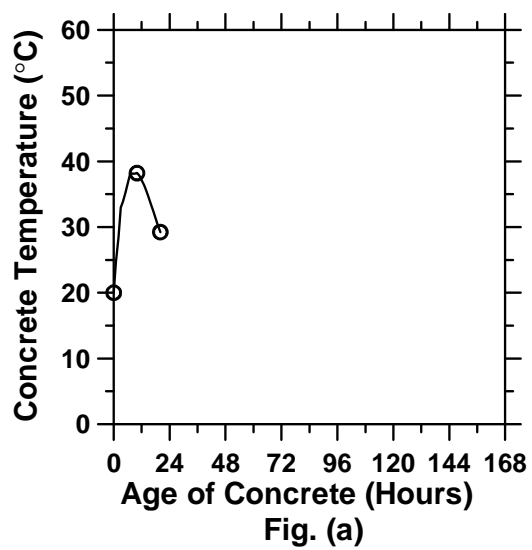


Figure A.171: Pavement built with rapid setting materials and a D/6 saw-cut depth introduced at 6 hours (cont'd).

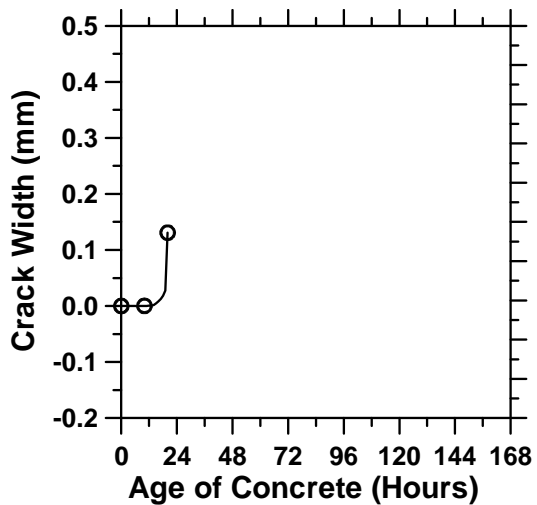


Fig. (e)

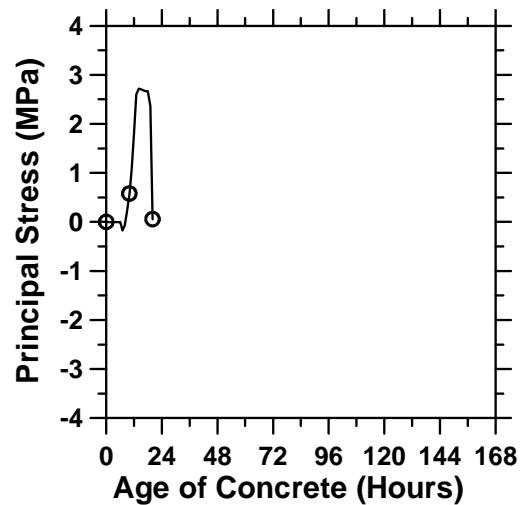


Fig. (f)

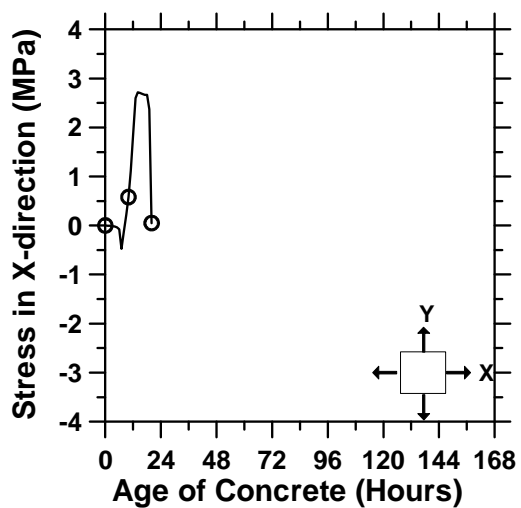


Fig. (g)

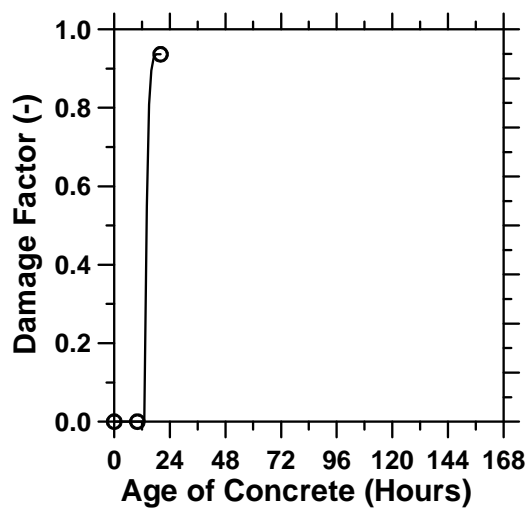


Fig. (h)

Figure A.171: Pavement built with rapid setting materials and a D/6 saw-cut depth introduced at 6 hours.

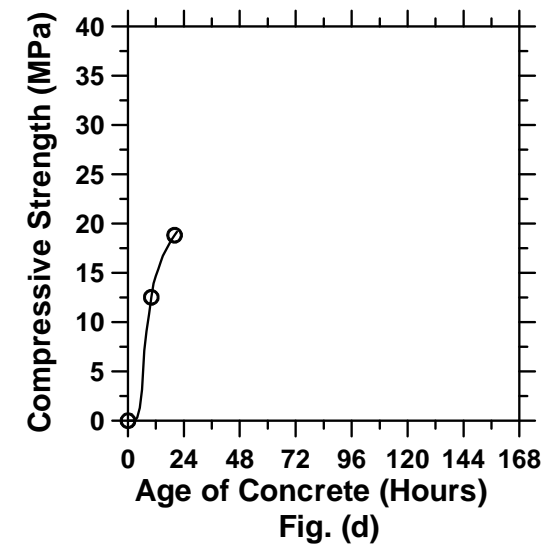
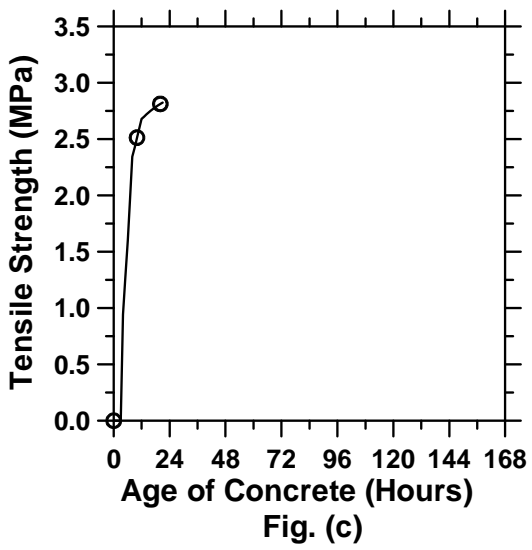
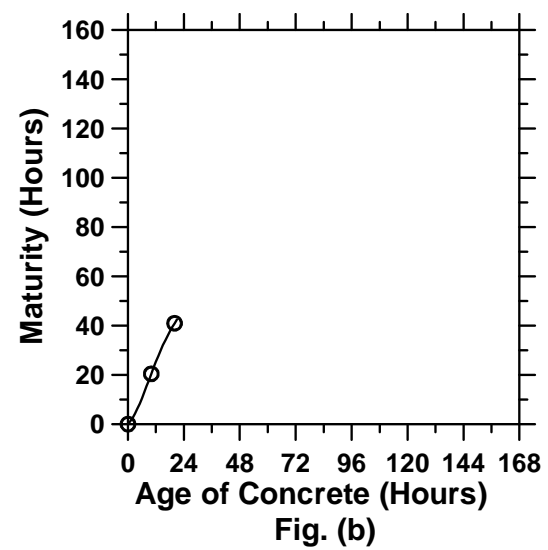
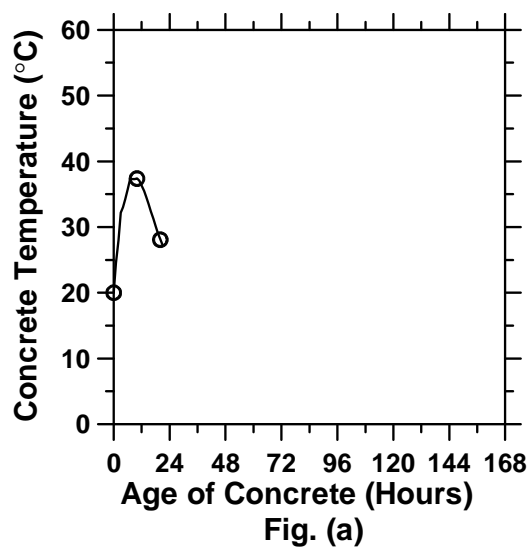


Figure A.172: Pavement built with rapid setting materials and a D/8 saw-cut depth introduced at 6 hours (cont'd).

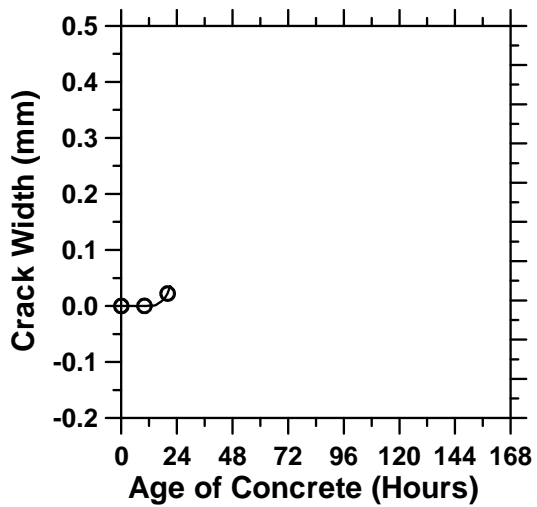


Fig. (e)

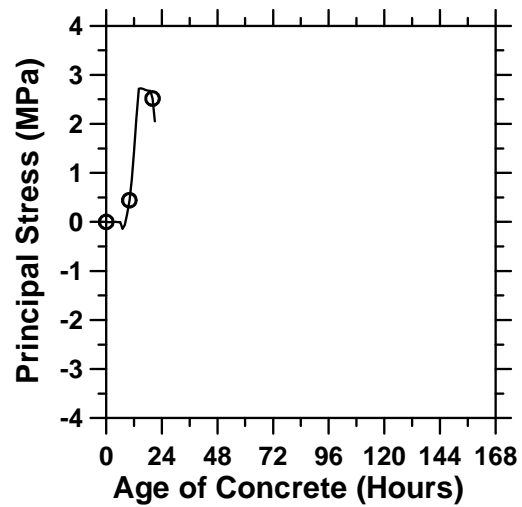


Fig. (f)

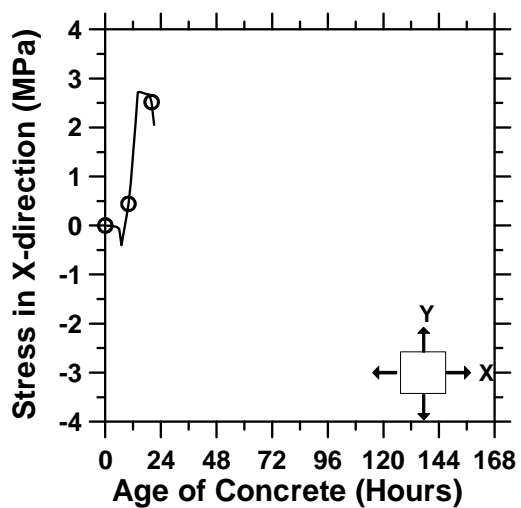


Fig. (g)

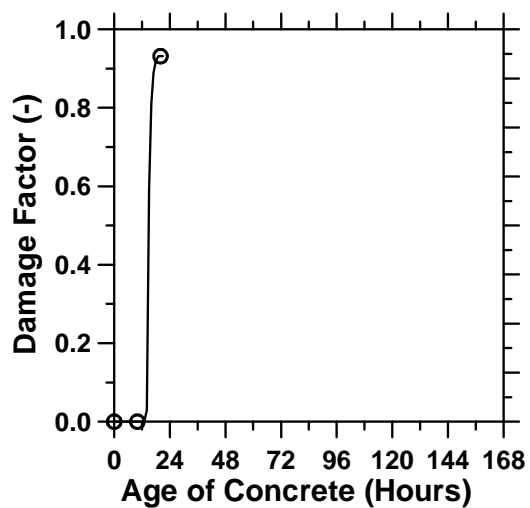


Fig. (h)

Figure A.172: Pavement built with rapid setting materials and a D/8 saw-cut depth introduced at 6 hour.

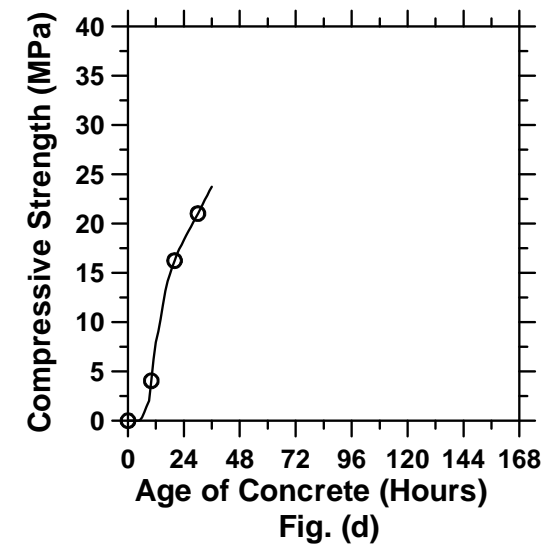
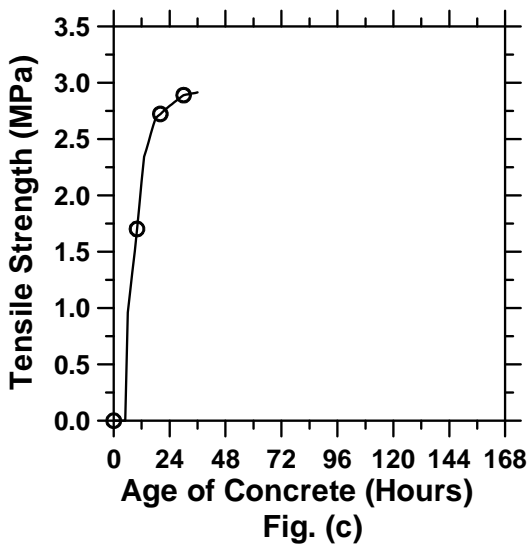
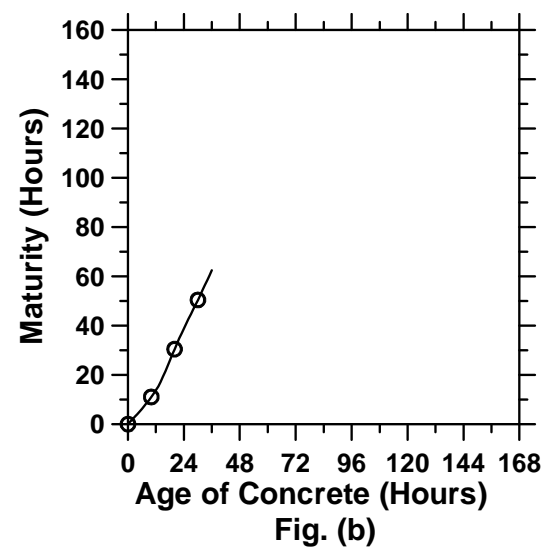
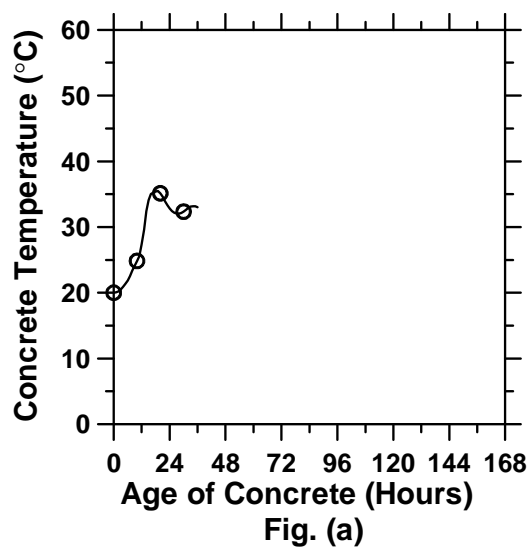


Figure A.173: Pavement built with slow setting materials and a D/3 saw-cut depth introduced at 0 hour (cont'd).

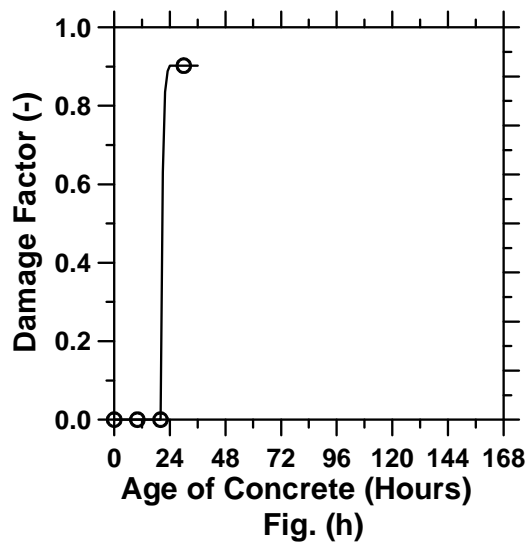
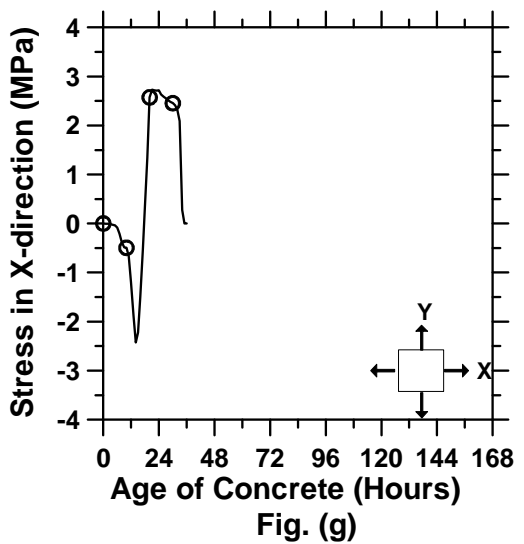
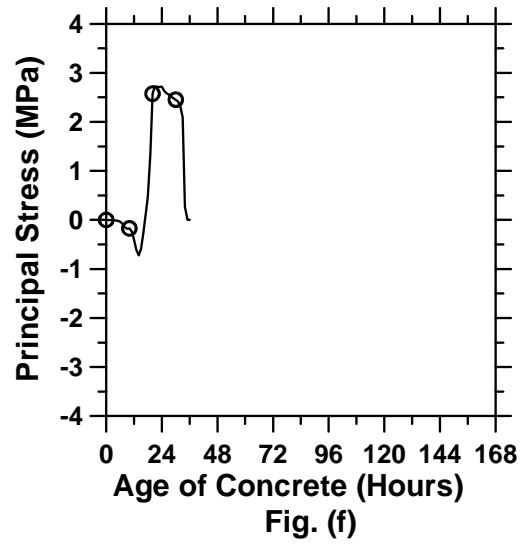
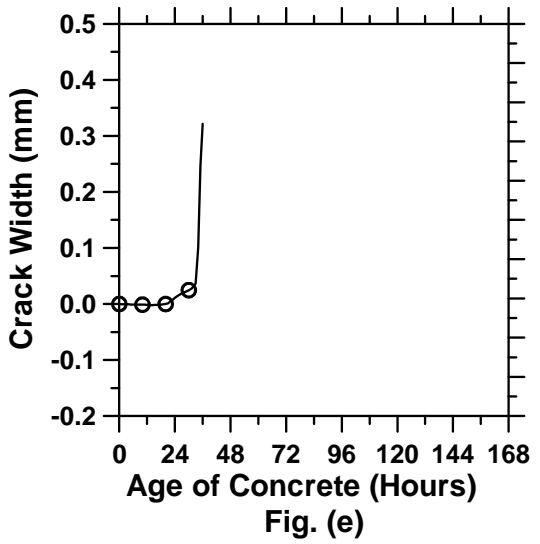


Figure A.173: Pavement built with slow setting materials and a D/3 saw-cut depth introduced at 0 hour.

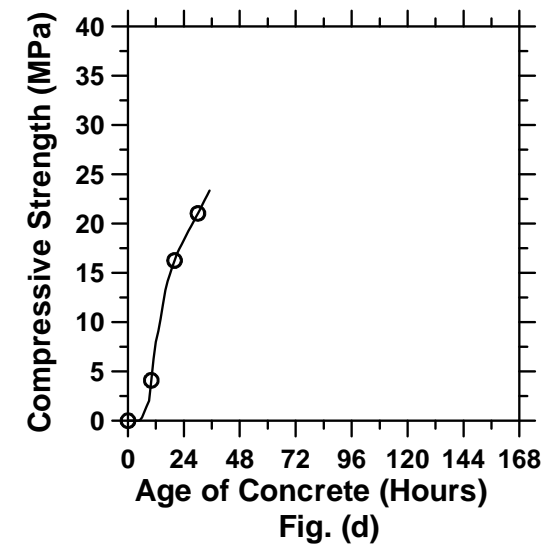
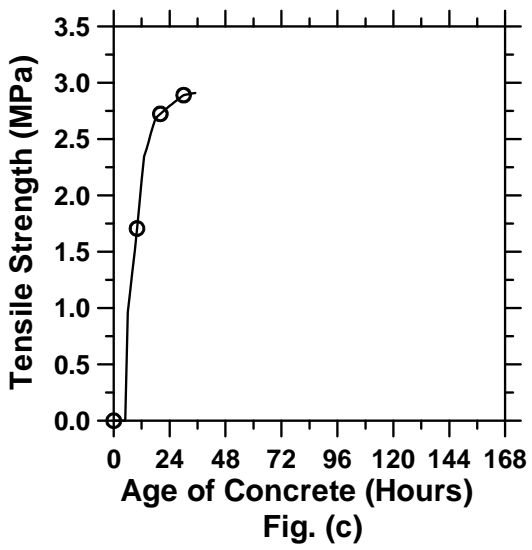
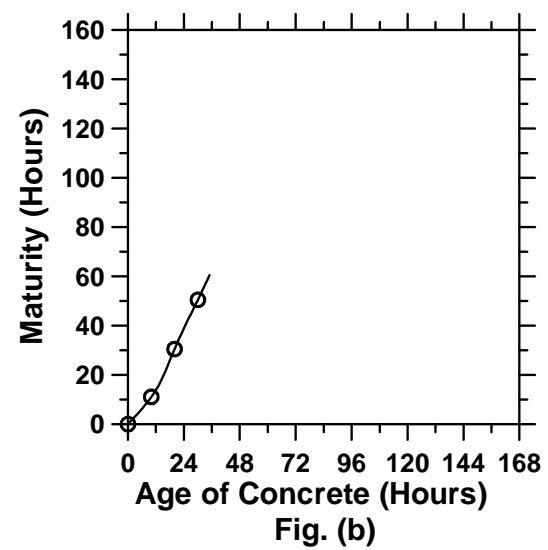
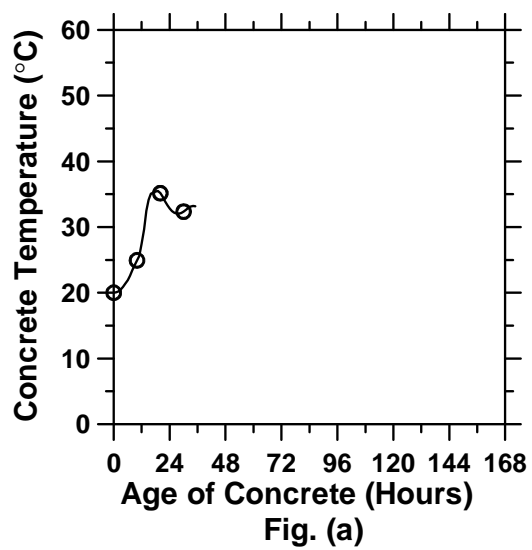


Figure A.174: Pavement built with slow setting materials and a D/3 saw-cut depth introduced at 12 hours (cont'd).

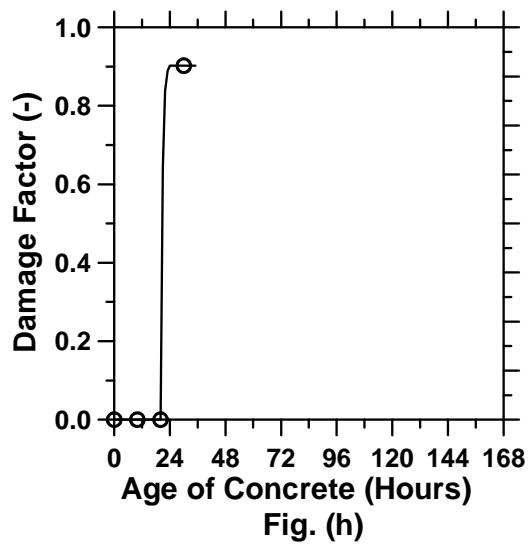
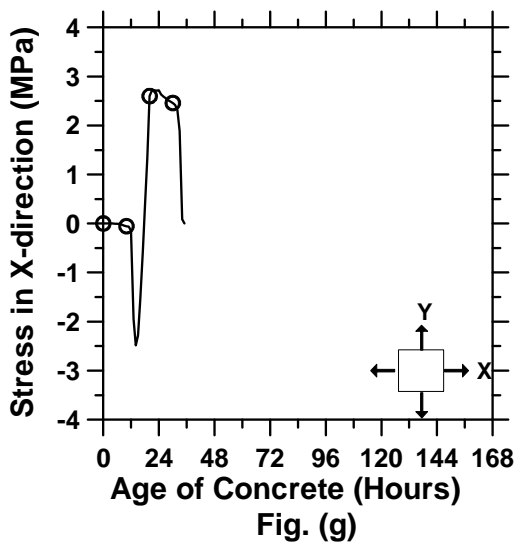
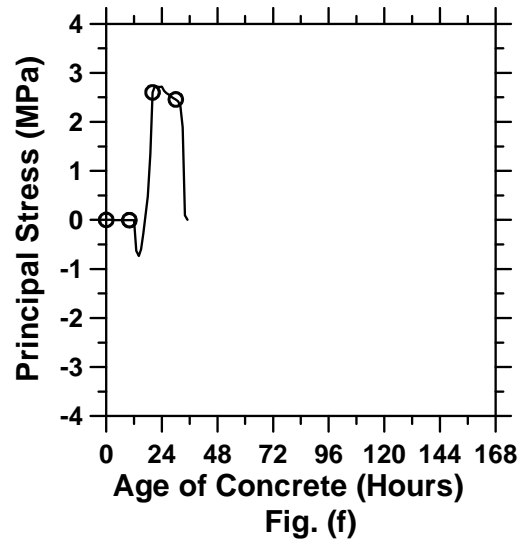
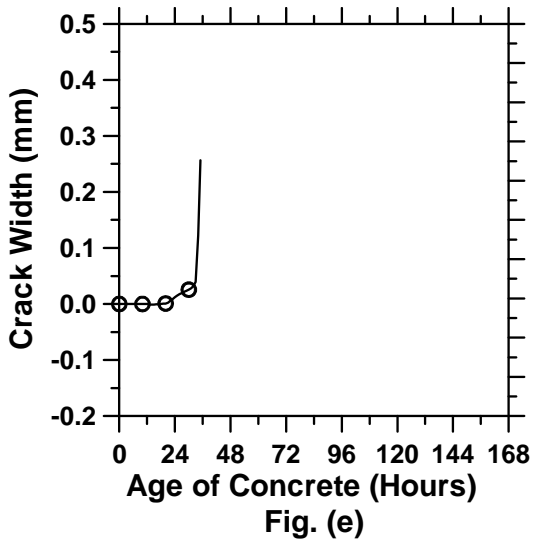


Figure A.174: Pavement built with slow setting materials and a D/3 saw-cut depth introduced at 12 hours.

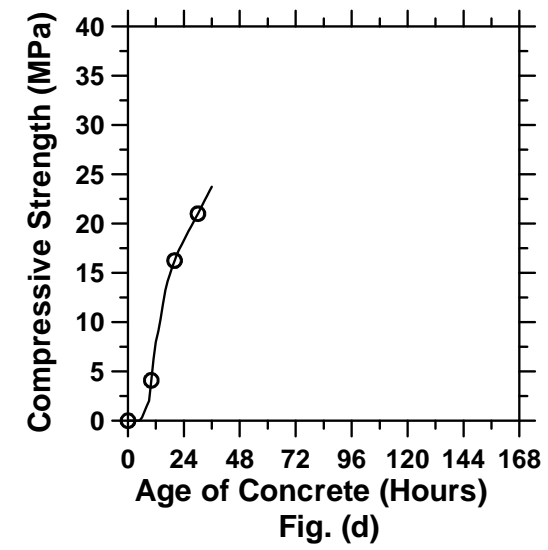
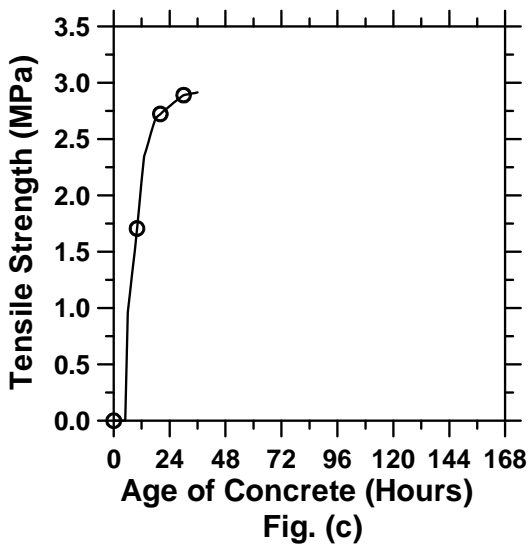
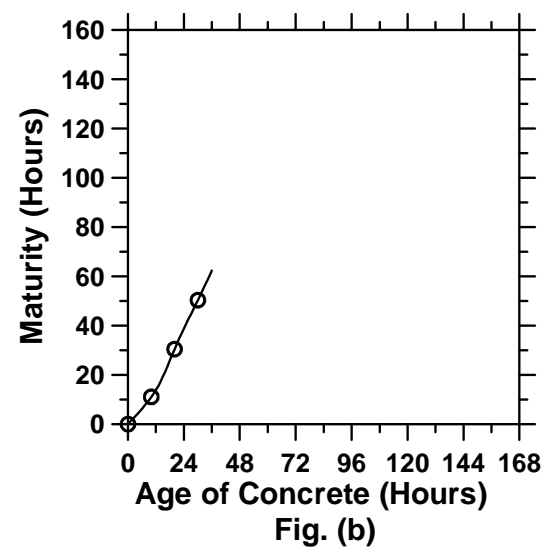
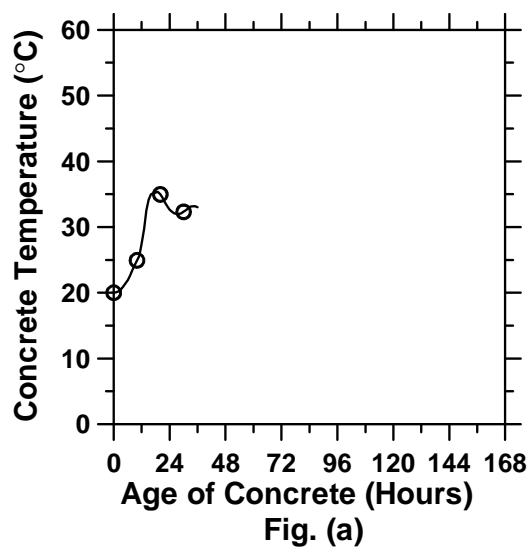


Figure A.175: Pavement built with slow setting materials and a D/3 saw-cut depth introduced at 24 hours (cont'd).

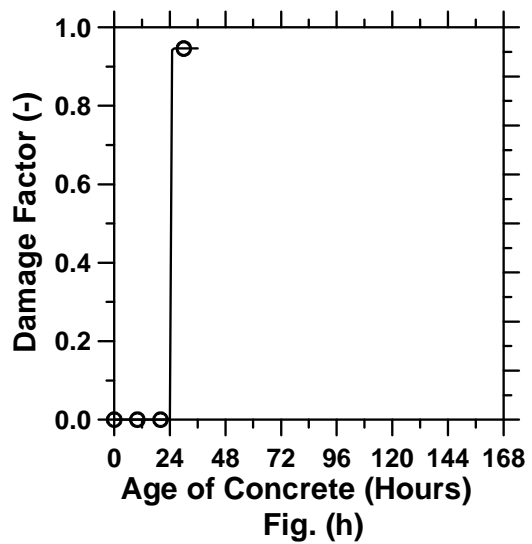
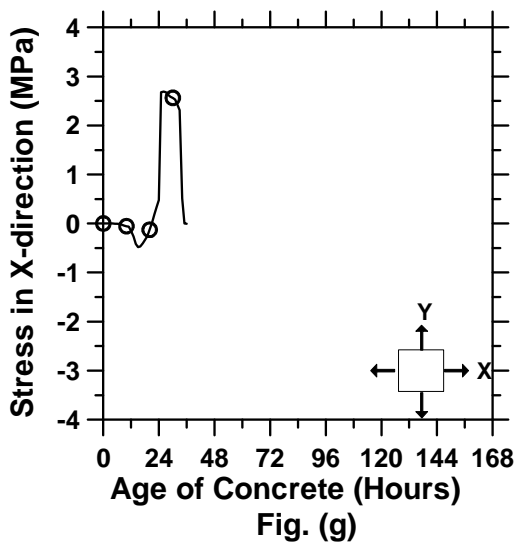
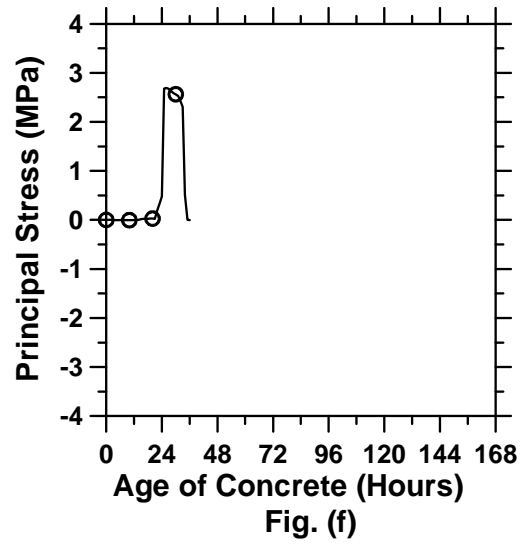
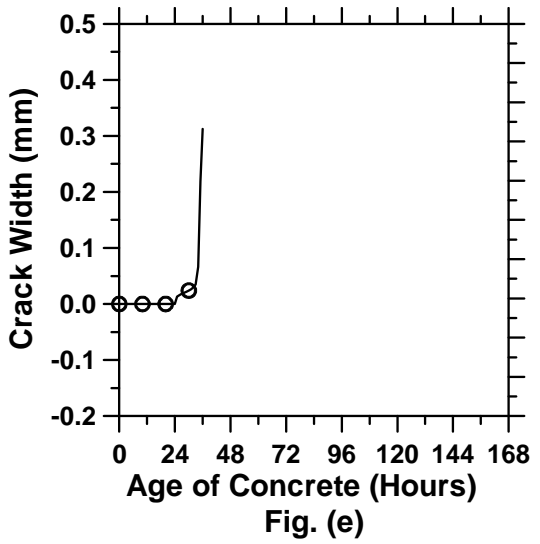


Figure A.175: Pavement built with slow setting materials and a D/3 saw-cut depth introduced at 24 hours.

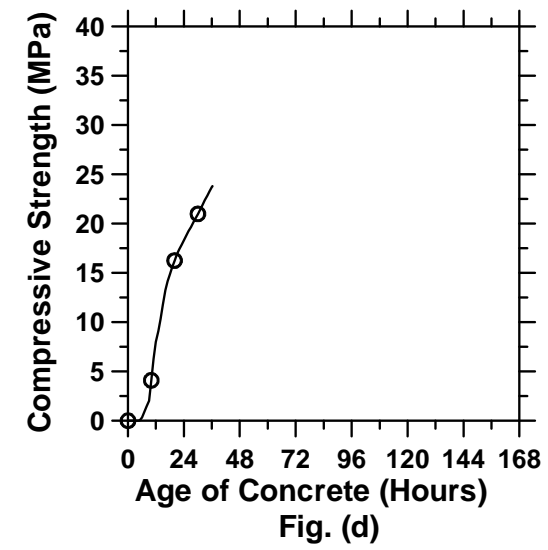
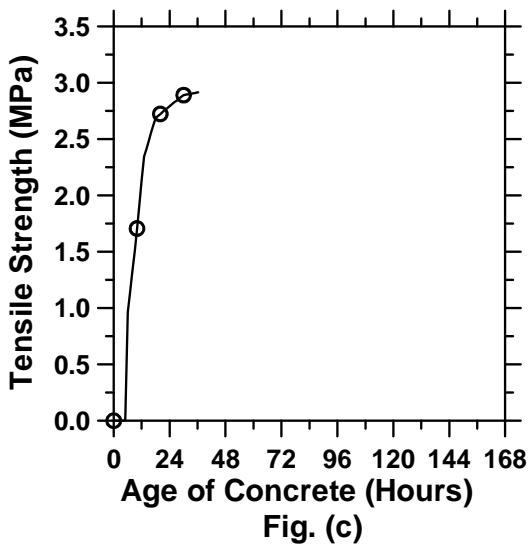
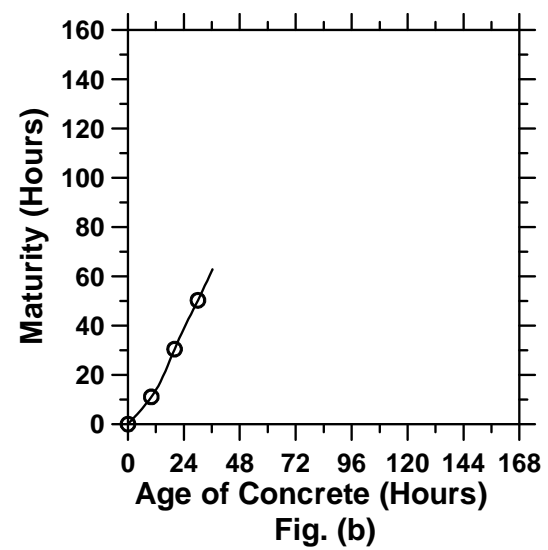
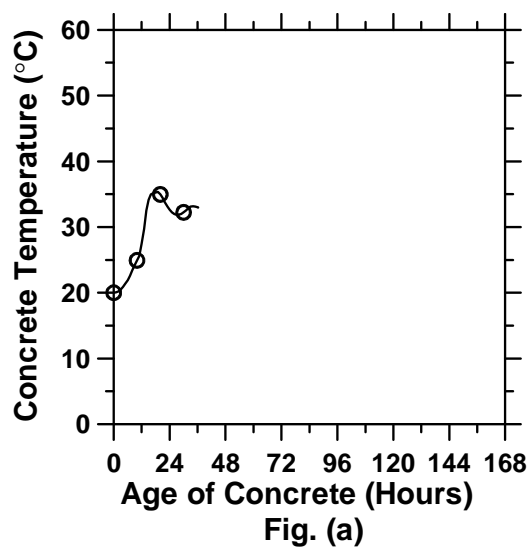


Figure A.176: Pavement built with slow setting materials and a D/3 saw-cut depth introduced at 30 hours (cont'd).

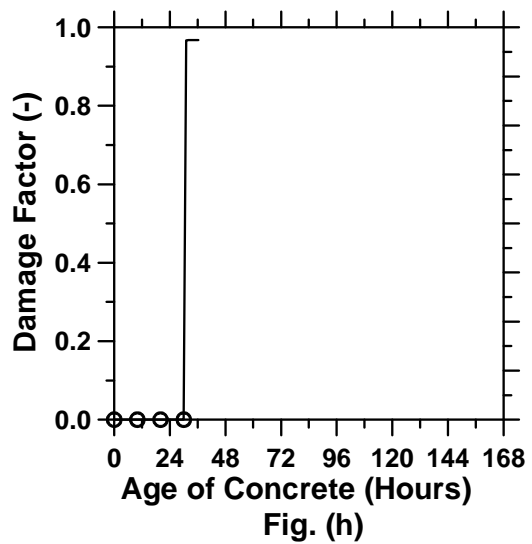
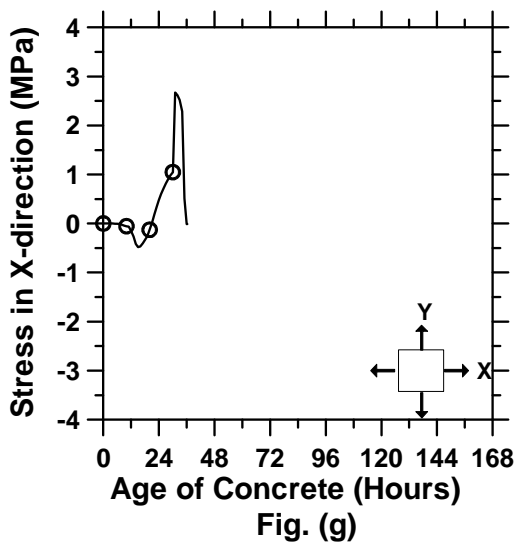
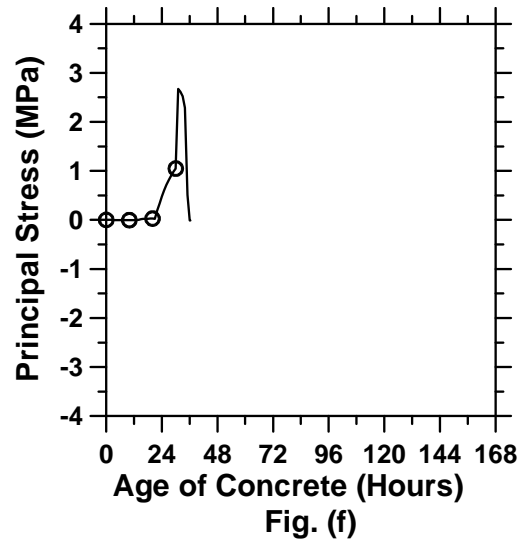
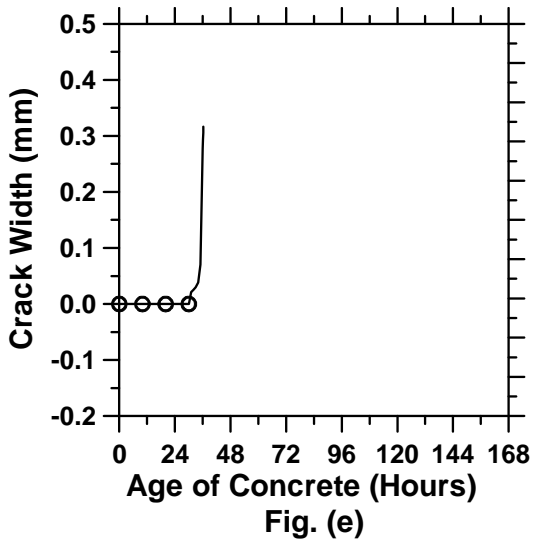


Figure A.176: Pavement built with slow setting materials and a D/3 saw-cut depth introduced at 30 hours.

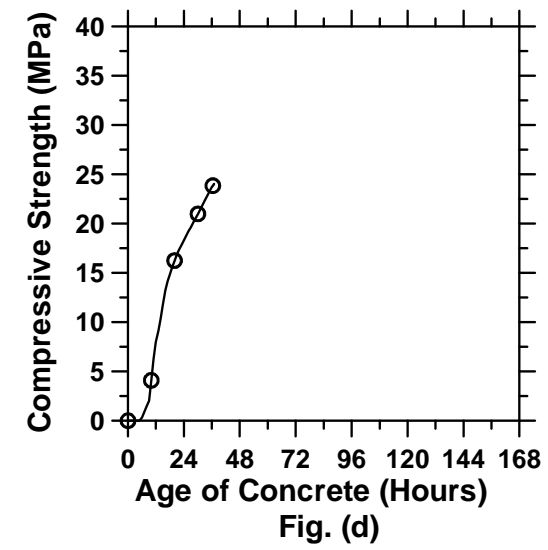
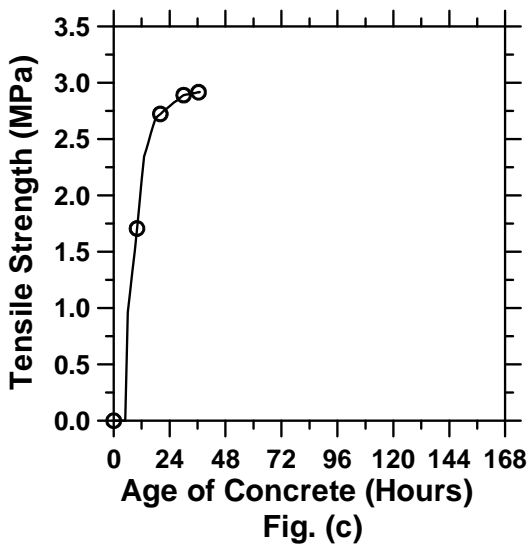
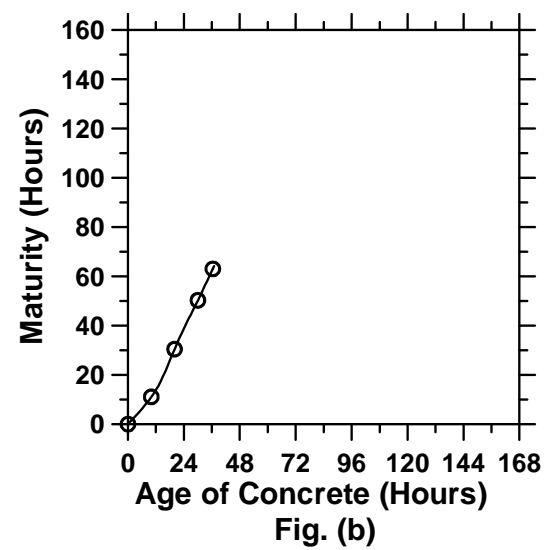
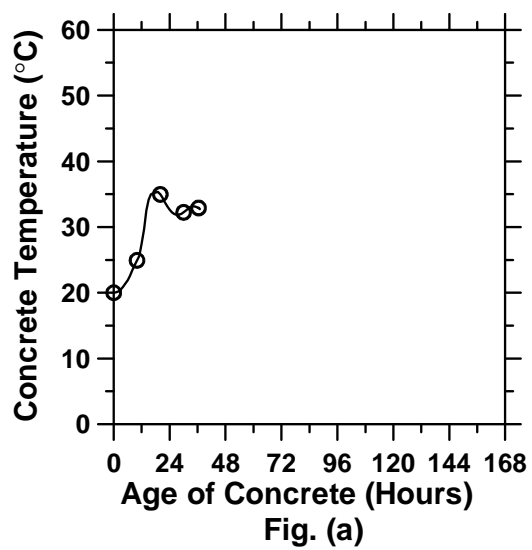


Figure A.177: Pavement built with slow setting materials and a D/3 saw-cut depth introduced at 36 hours (cont'd).

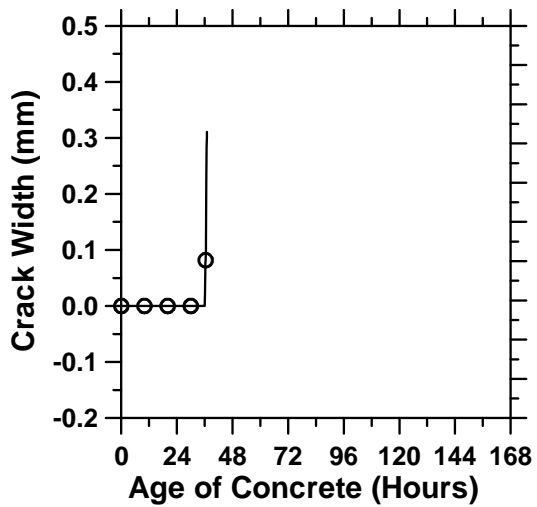


Fig. (e)

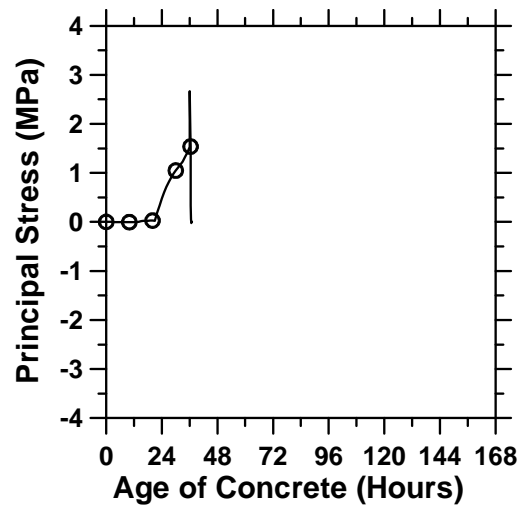


Fig. (f)

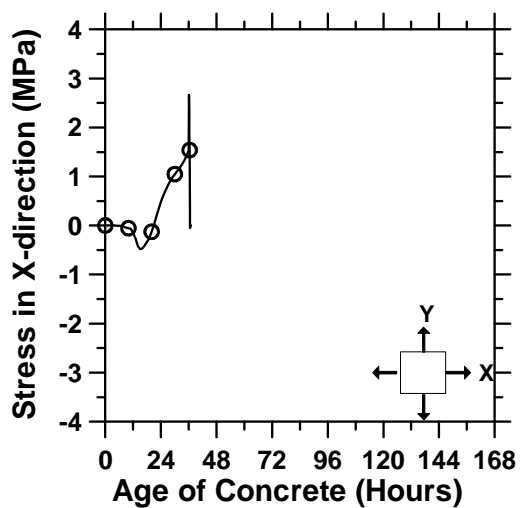


Fig. (g)

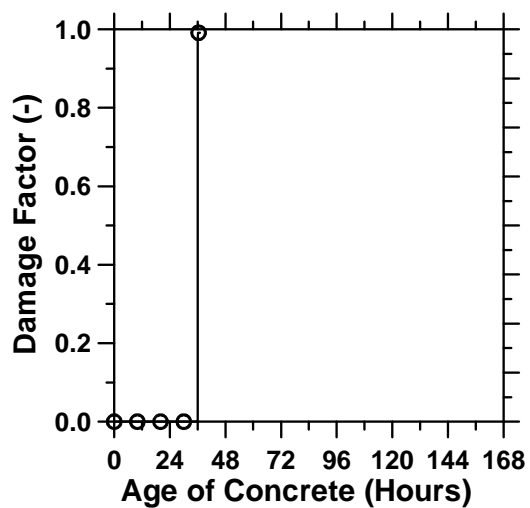


Fig. (h)

Figure A.177: Pavement built with slow setting materials and a D/3 saw-cut depth introduced at 36 hours.

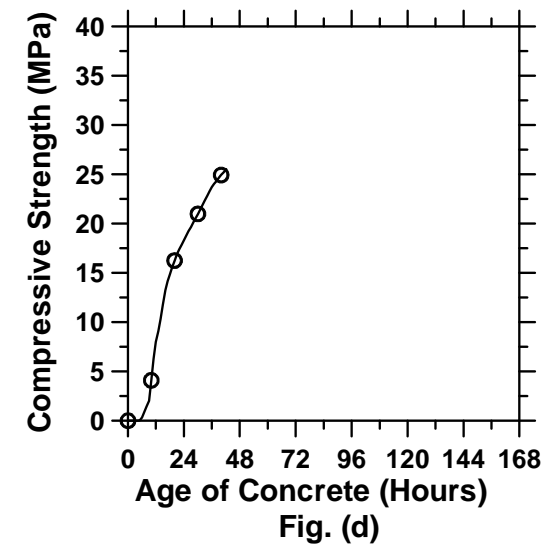
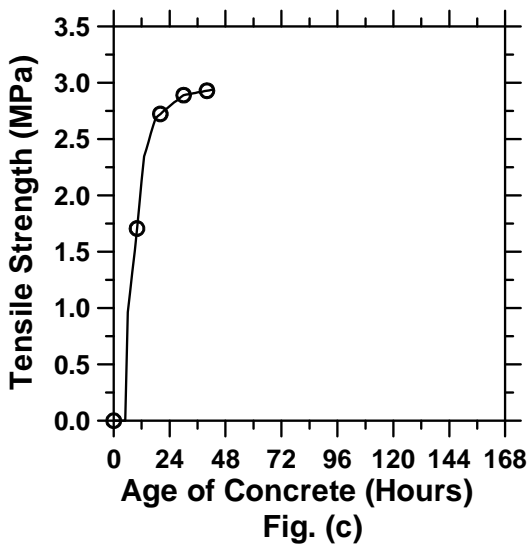
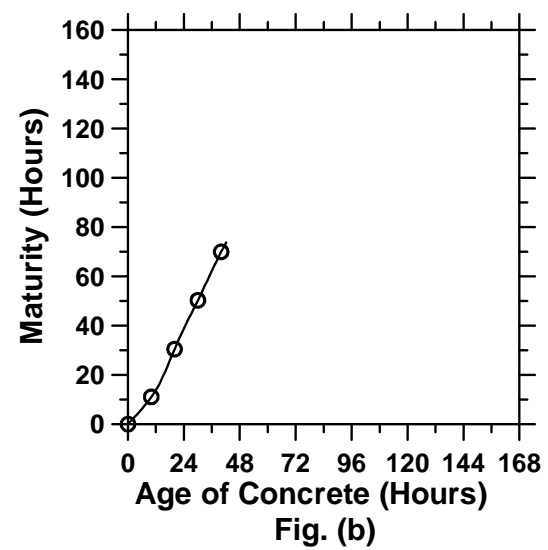
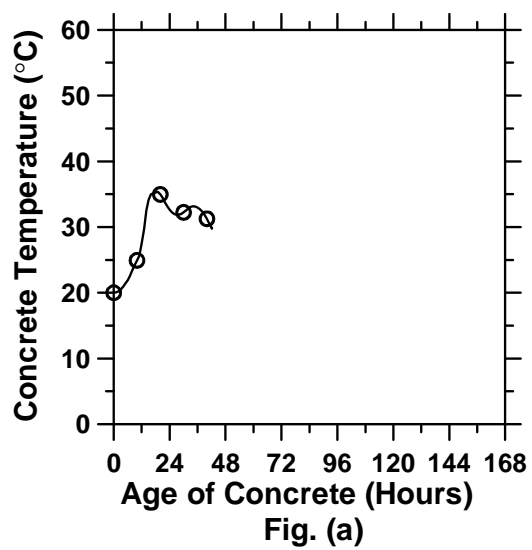


Figure A.178: Pavement built with slow setting materials and a D/3 saw-cut depth introduced at 42 hours (cont'd).

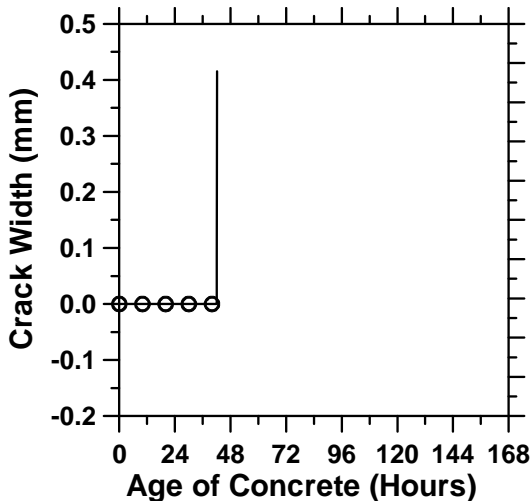


Fig. (e)

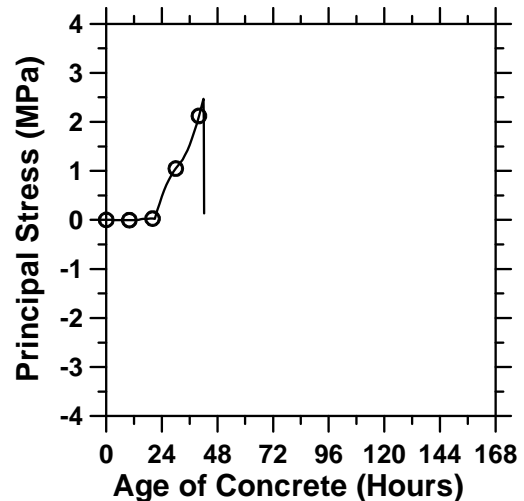


Fig. (f)

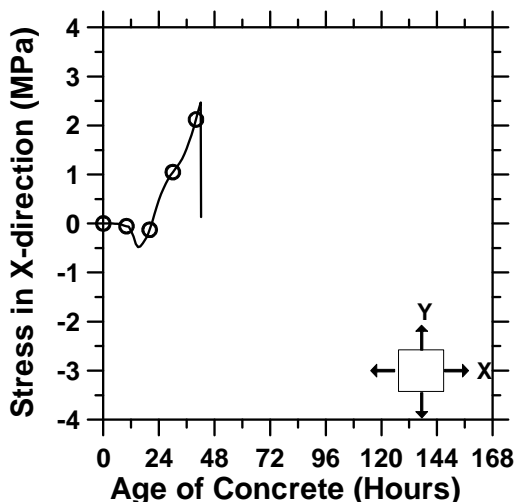


Fig. (g)

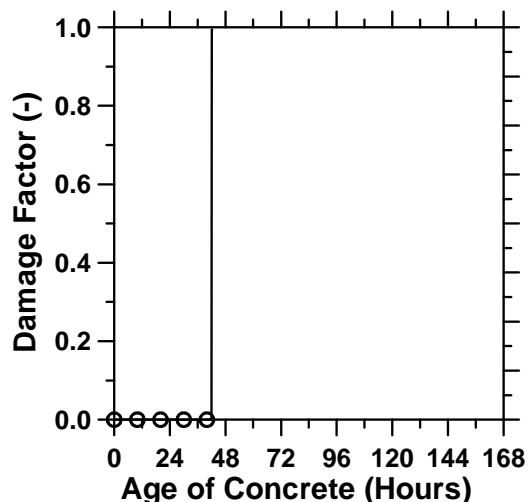


Fig. (h)

Figure A.178: Pavement built with slow setting materials and a D/3 saw-cut depth introduced at 42 hours.

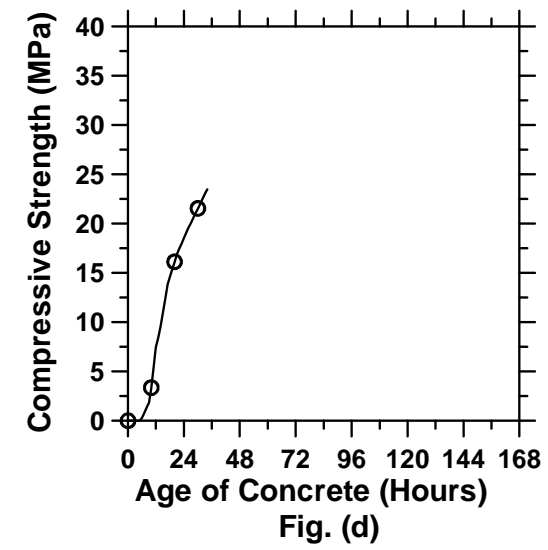
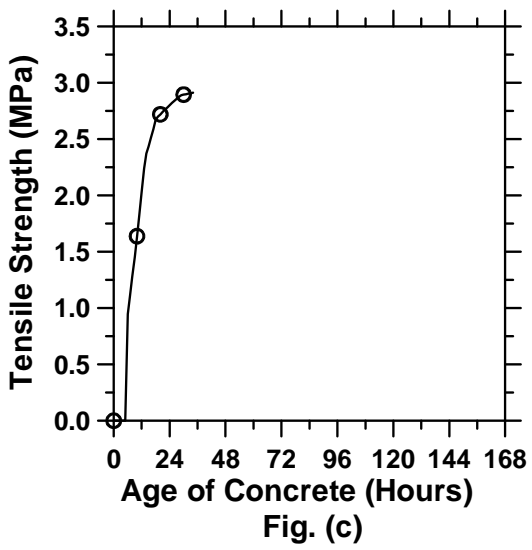
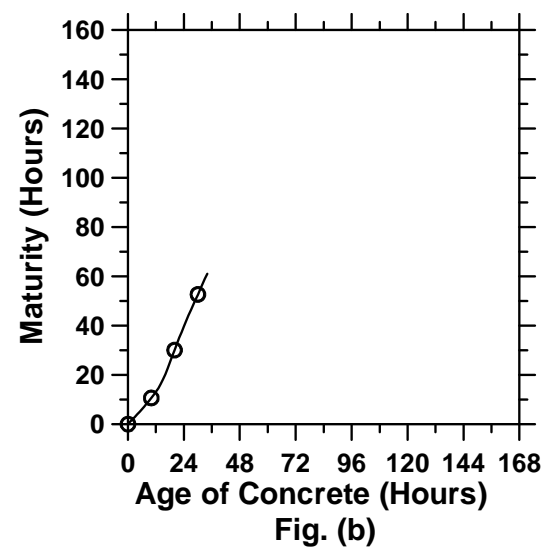
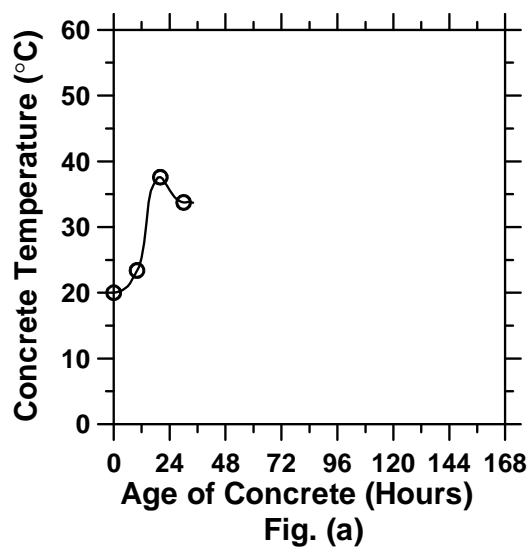


Figure A.179: Pavement built with slow setting materials and a D/2 saw-cut depth introduced at 6 hours (cont'd).

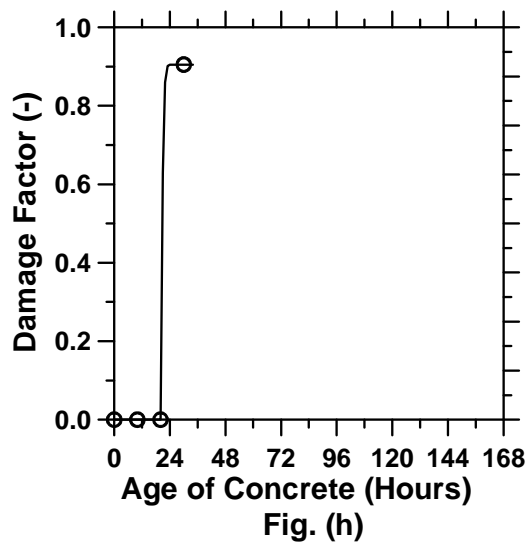
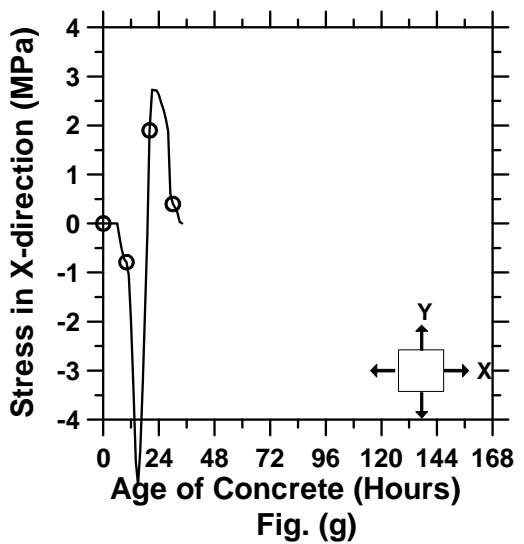
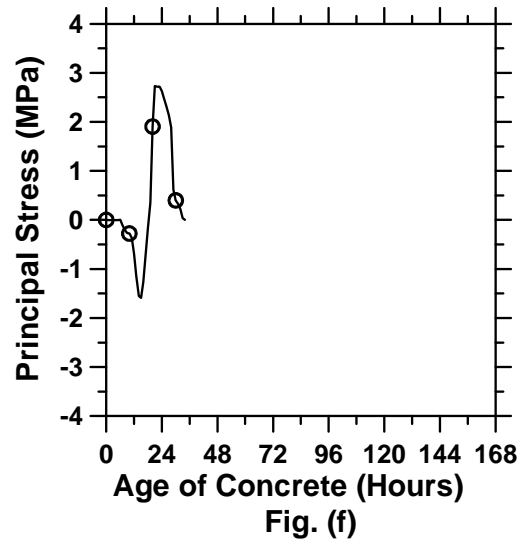
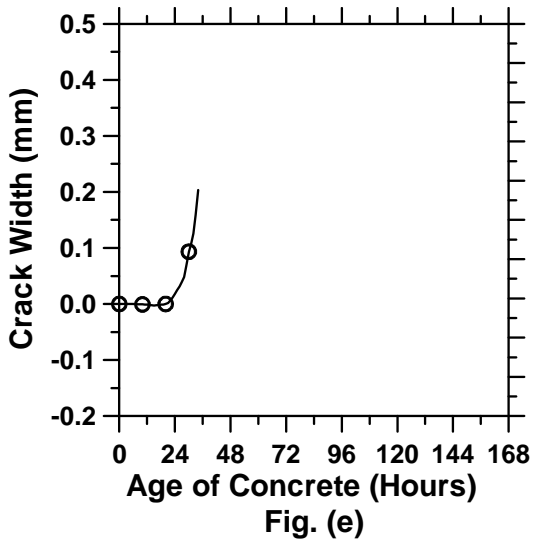


Figure A.179: Pavement built with slow setting materials and a D/2 saw-cut depth introduced at 6 hours.

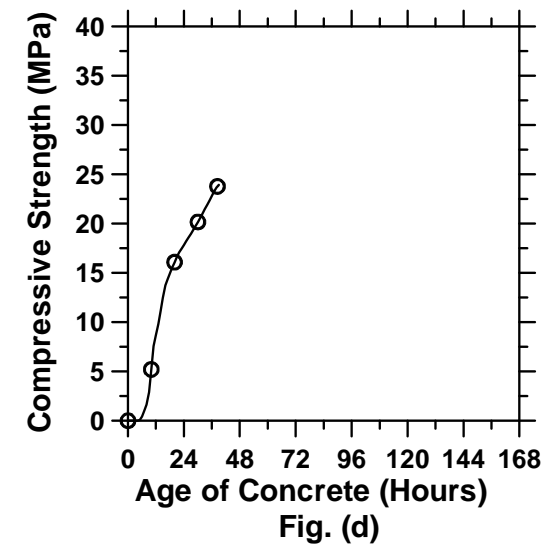
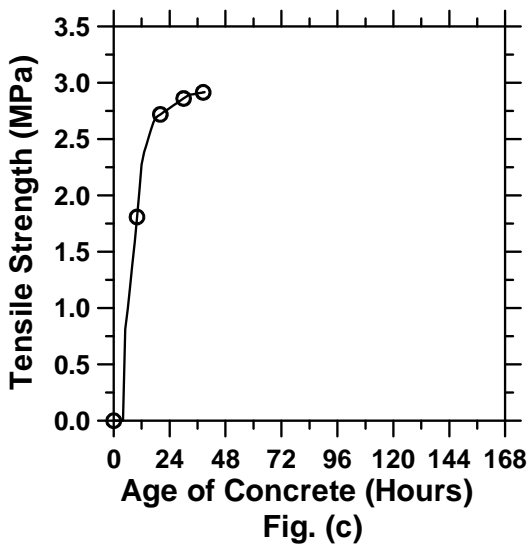
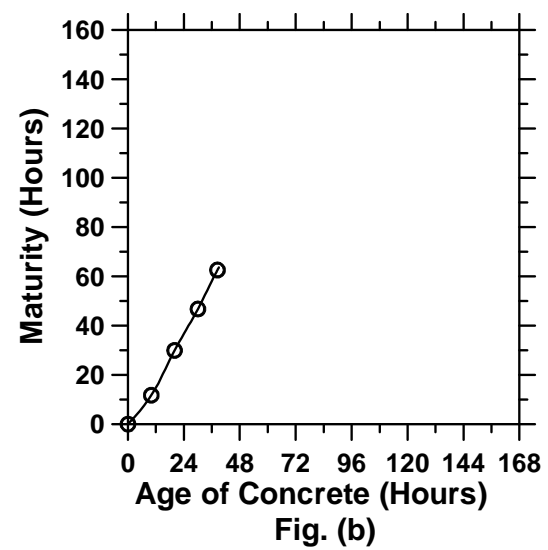
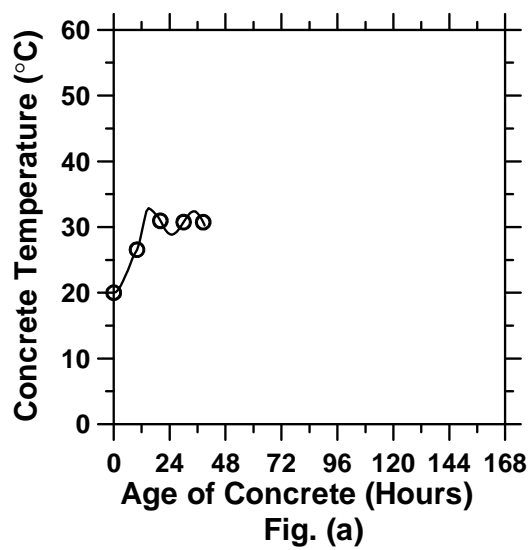


Figure A.180: Pavement built with slow setting materials and a D/6 saw-cut depth introduced at 6 hours (cont'd).

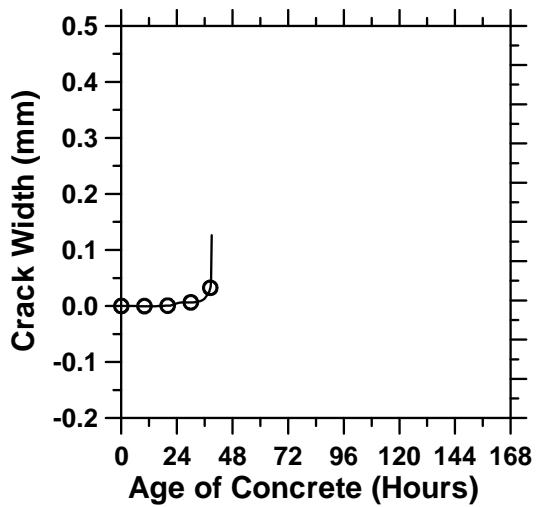


Fig. (e)

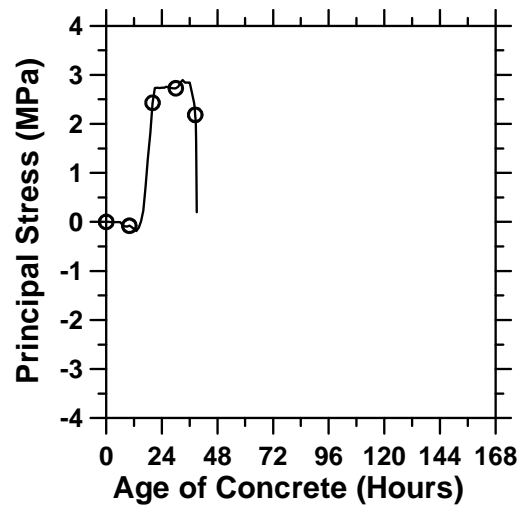


Fig. (f)

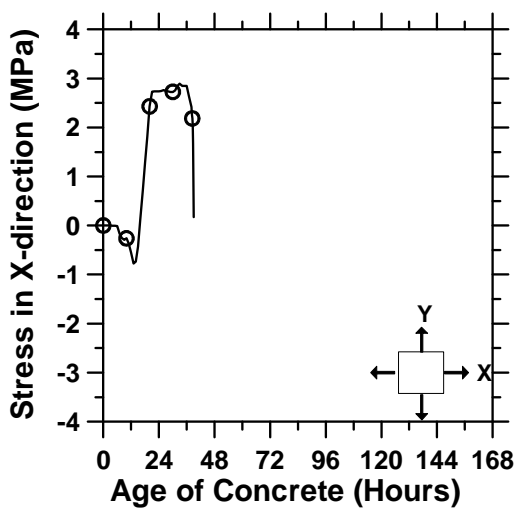


Fig. (g)

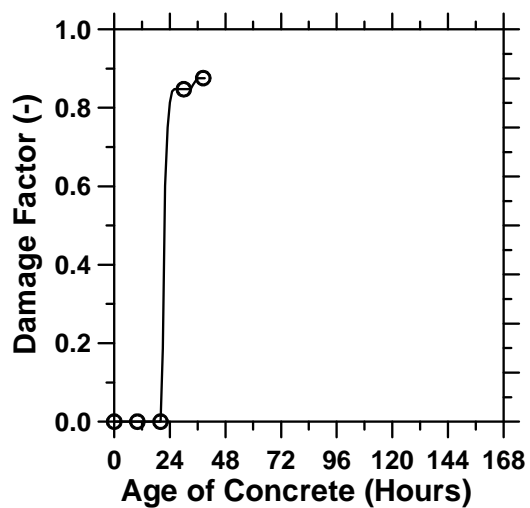


Fig. (h)

Figure A.180: Pavement built with slow setting materials and a D/6 saw-cut depth introduced at 6 hours.

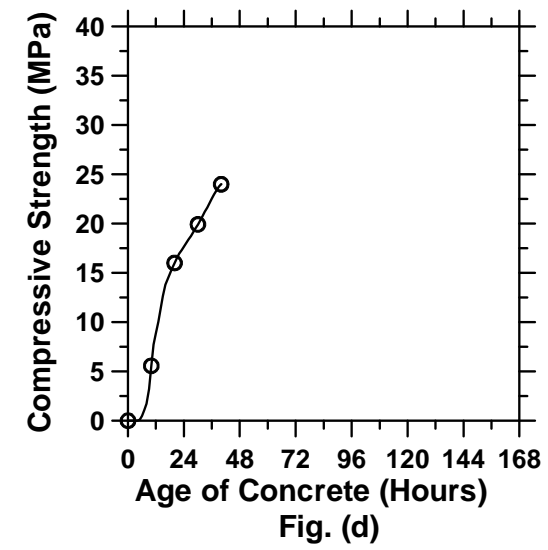
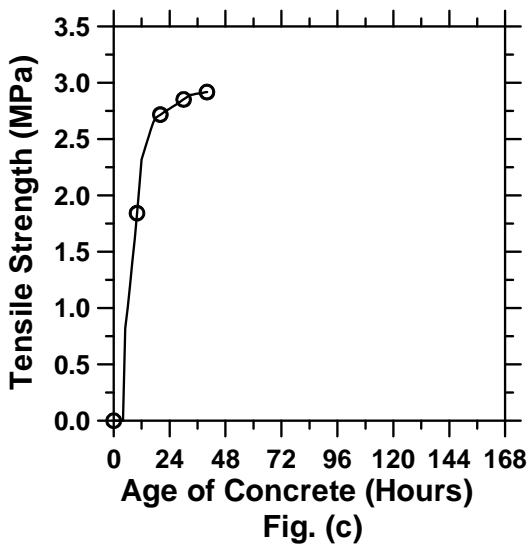
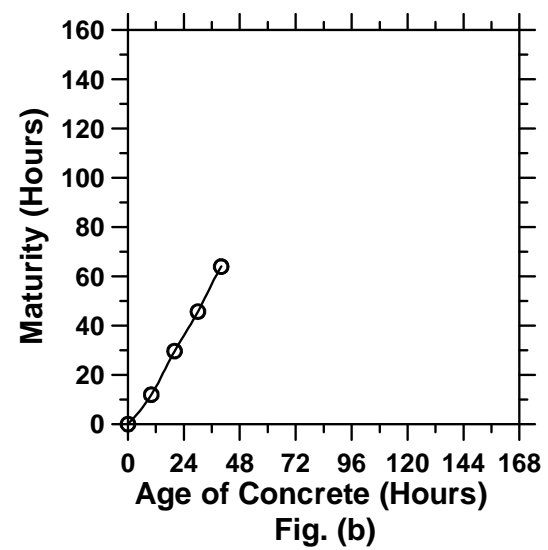
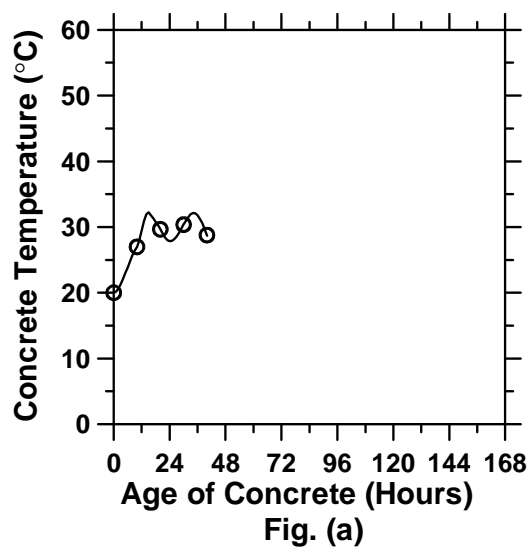


Figure A.181: Pavement built with slow setting materials and a D/8 saw-cut depth introduced at 6 hours (cont'd).

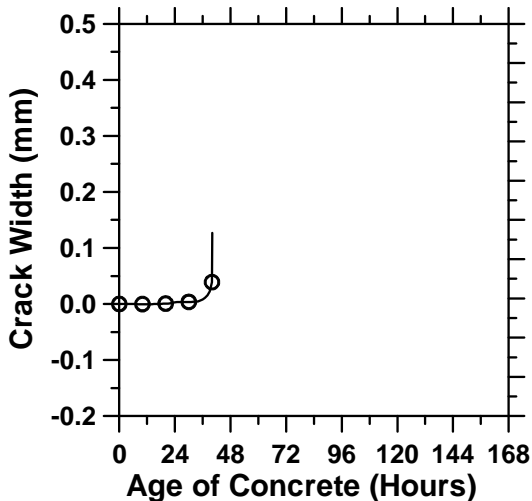


Fig. (e)

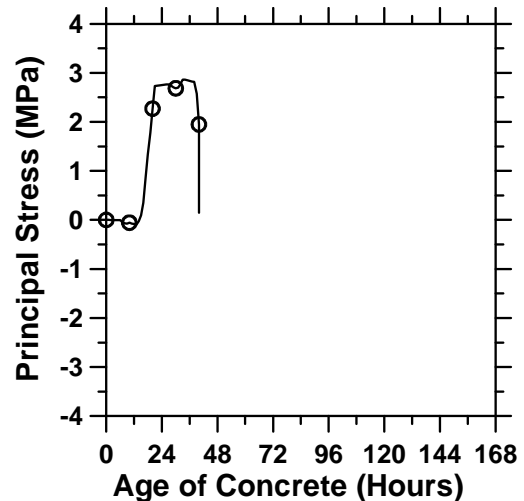


Fig. (f)

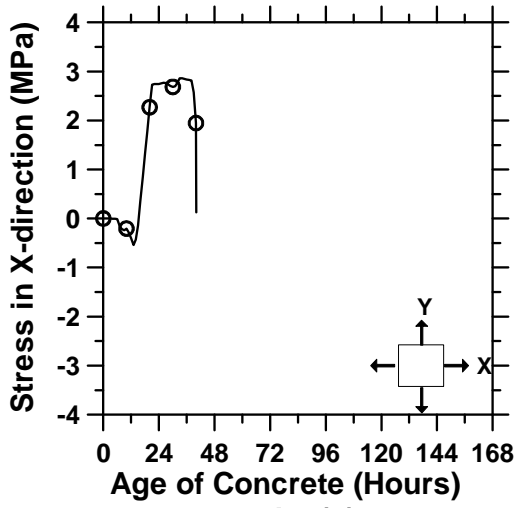


Fig. (g)

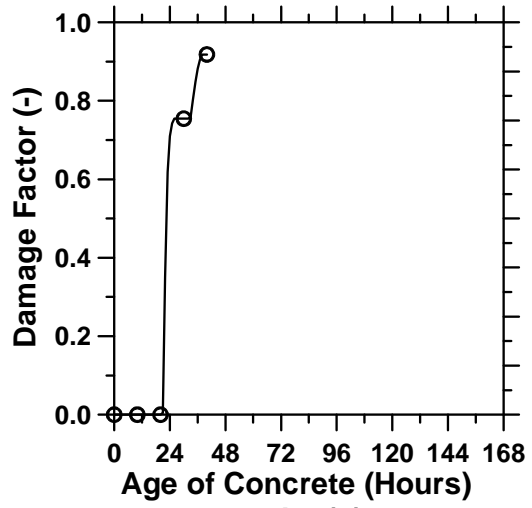


Fig. (h)

Figure A.181: Pavement built with slow setting materials and a D/8 saw-cut depth introduced at 6 hours.

Appendix B

This section provides the graphs of average end stress and average tensile strength for 15-inch thick pavements with D/2, D/3, D/4, D/6, D/8, and D/100 saw-cut depths. It also provides similar graphs for 10-inch thick pavements with D/3 and D/8 saw-cut depths. It should be noted that unless otherwise noted, the model parameters are the same as the baseline case described in section 7.2.

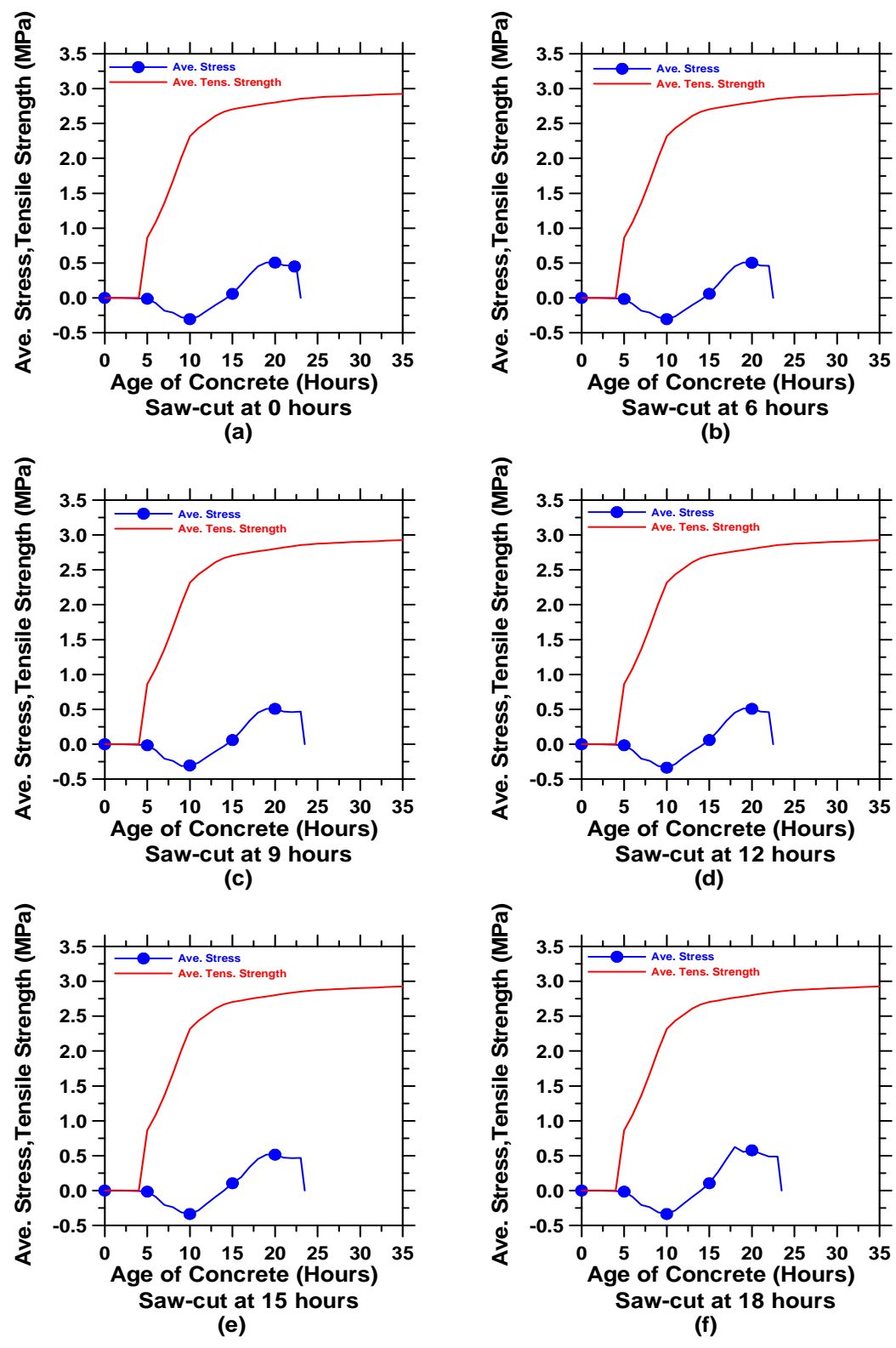


Figure B. 1: The average end stress and average tensile strength for a pavement with a D/2 saw-cut depth (cont'd).

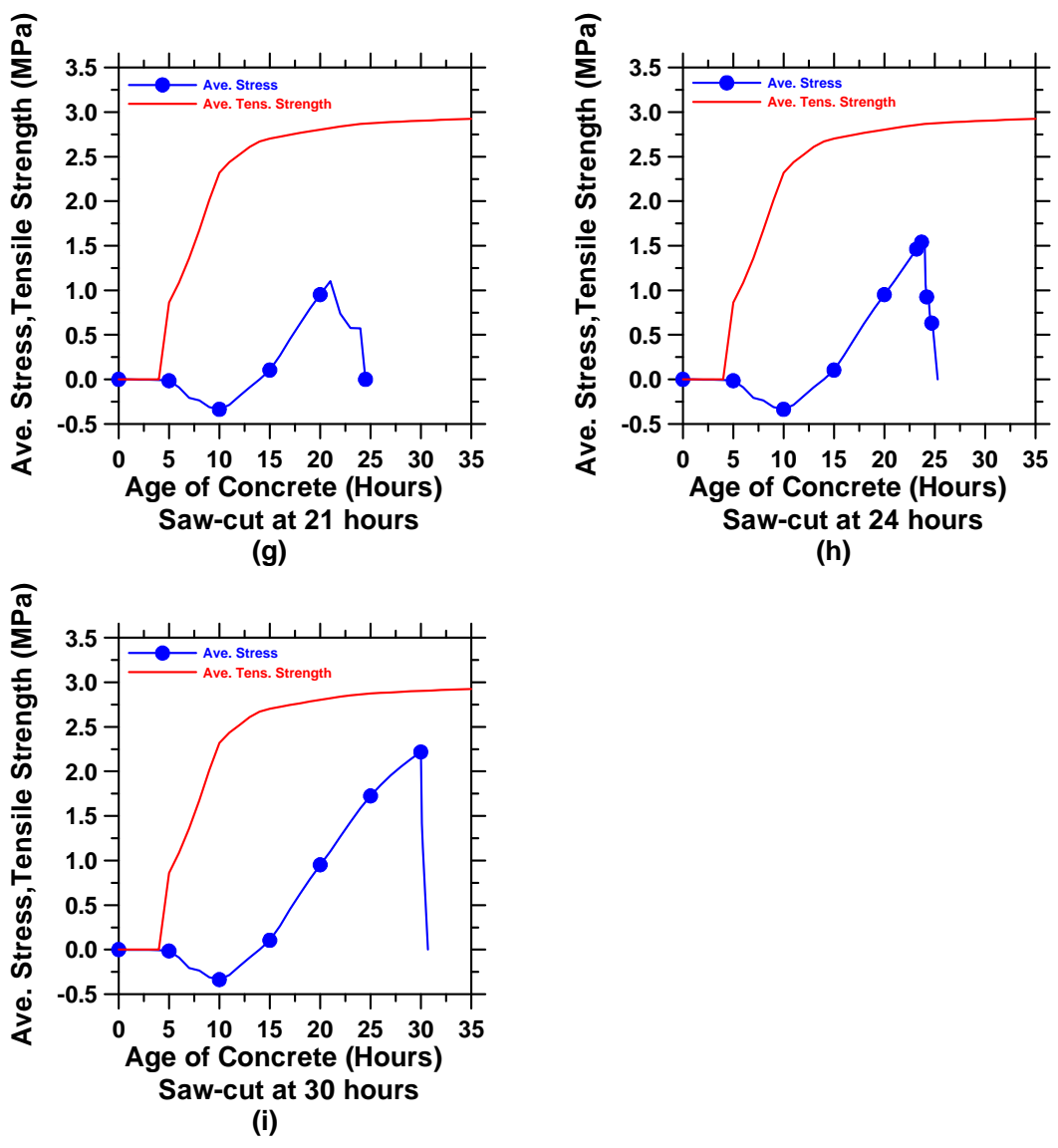


Figure B. 1: The average end stress and average tensile strength for a pavement with a D/2 saw-cut depth.

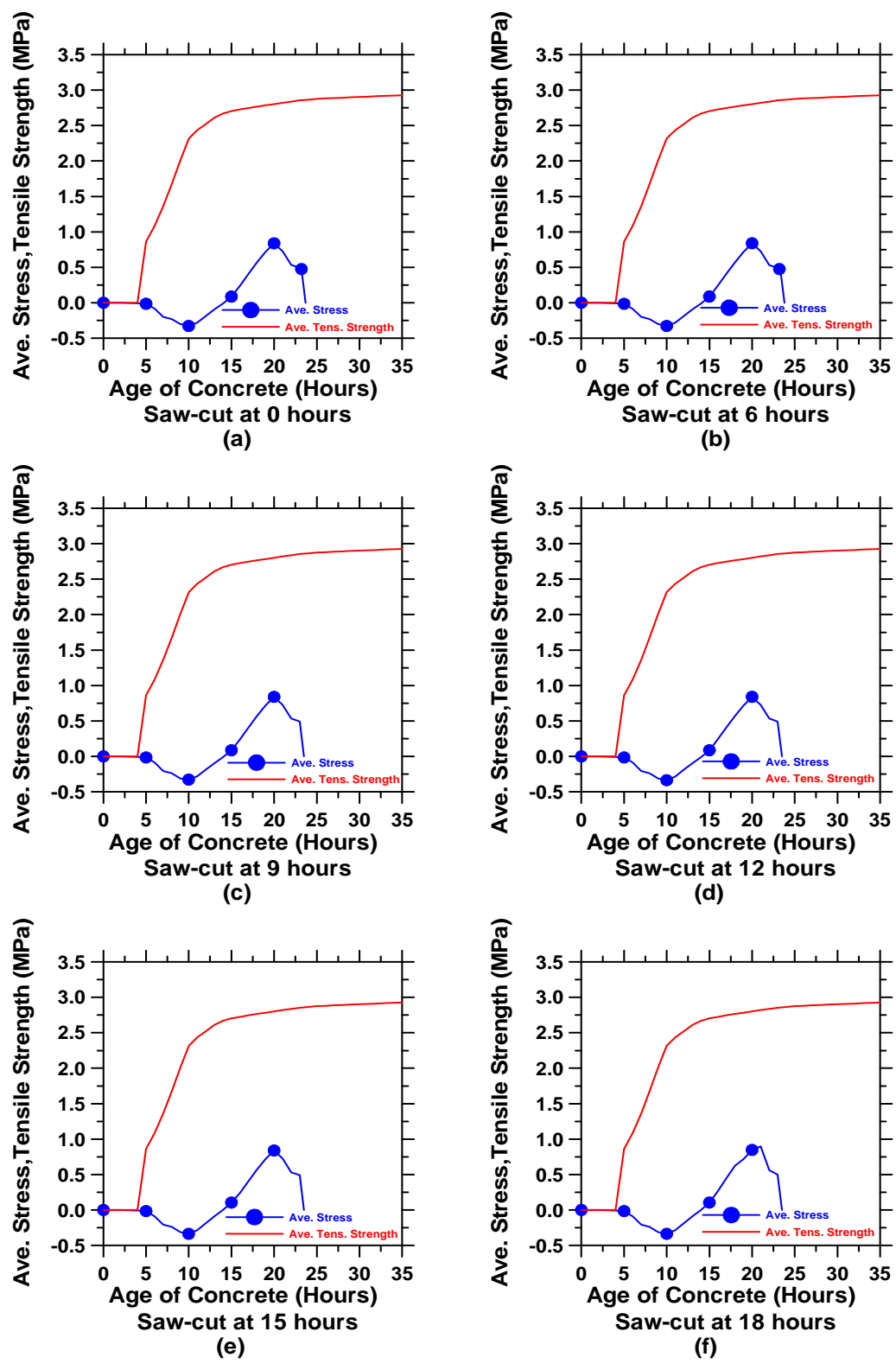


Figure B. 2: The average end stress and average tensile strength for a pavement with a D/3 saw-cut depth (cont'd).

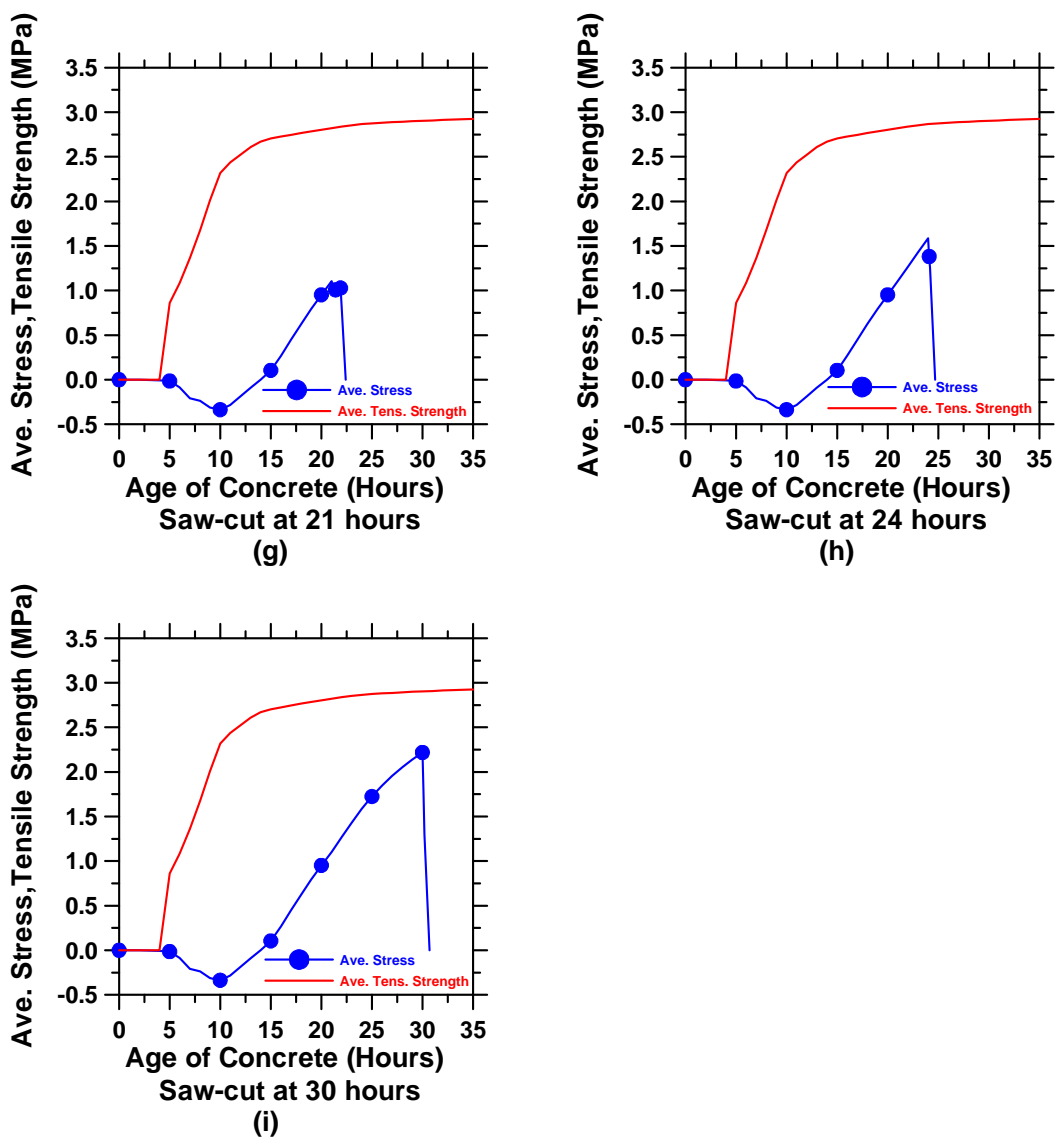


Figure B. 2: The average end stress and average tensile strength for a pavement with a D/3 saw-cut depth.

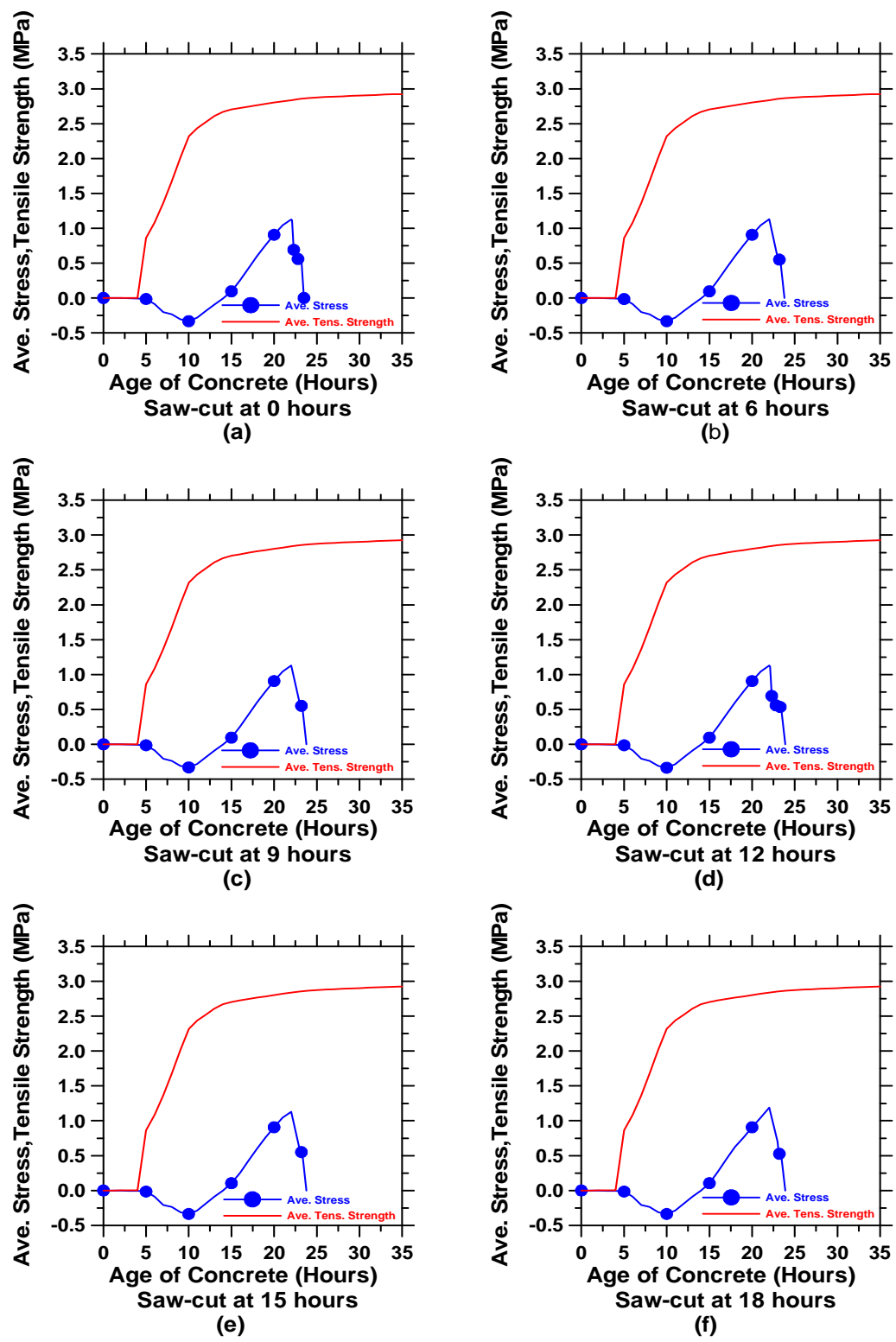


Figure B. 3: The average end stress and average tensile strength for a pavement with a D/4 saw-cut depth (cont'd).

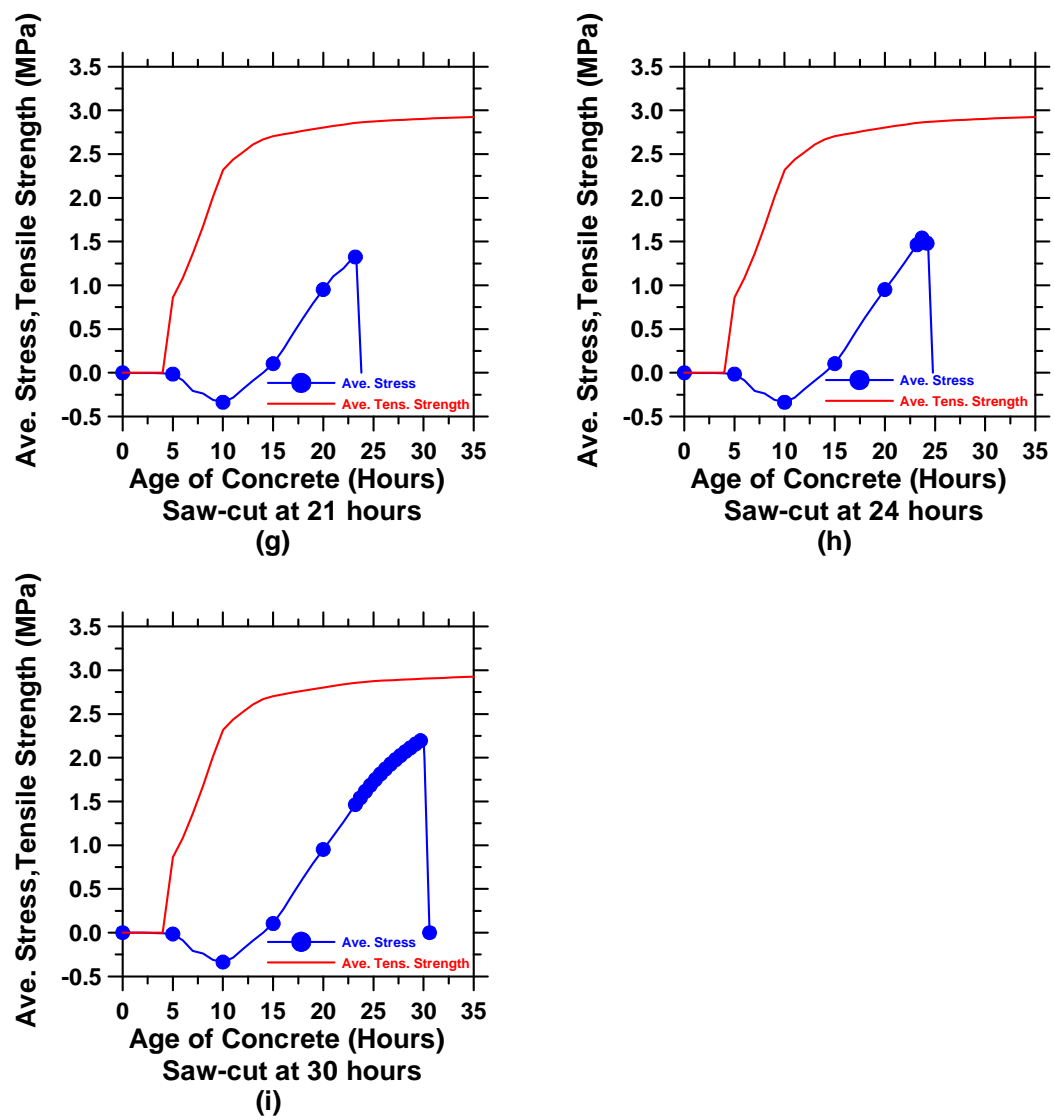


Figure B. 3: The average end stress and average tensile strength for a pavement with a D/4 saw-cut depth.

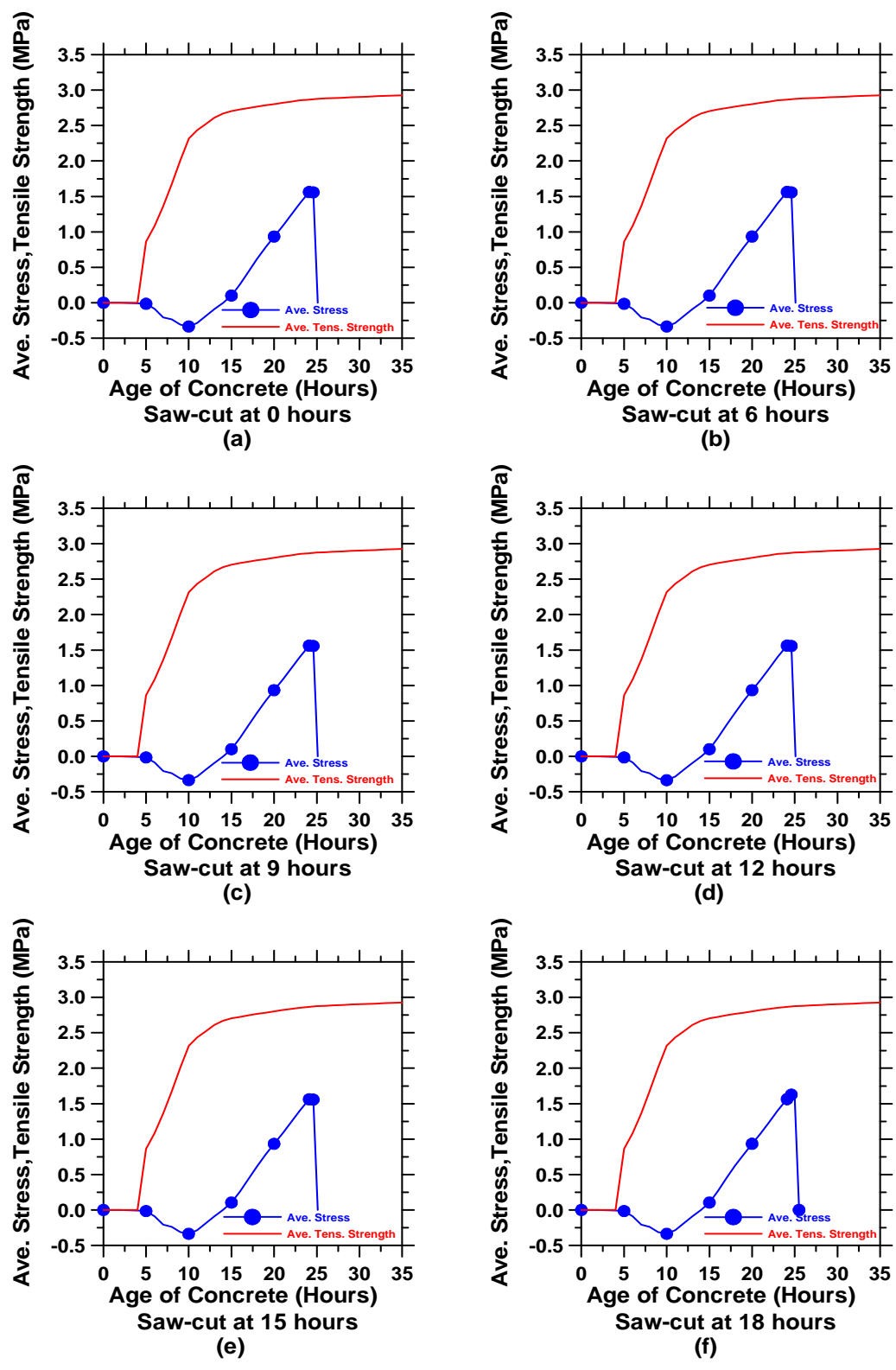


Figure B. 4: The average end stress and average tensile strength for a pavement with a D/6 saw-cut depth (cont'd).

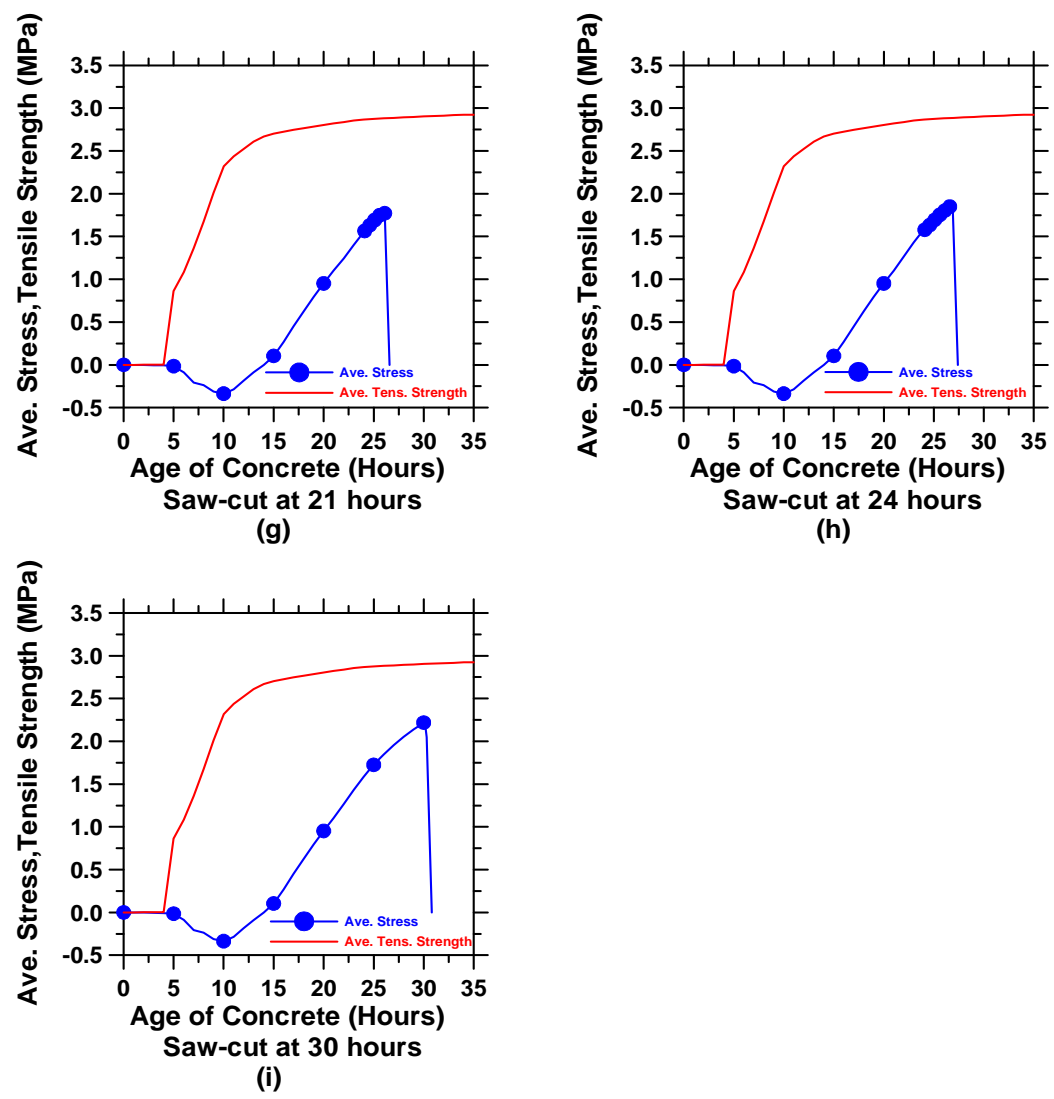


Figure B. 4: The average end stress and average tensile strength for a pavement with a D/6 saw-cut depth.

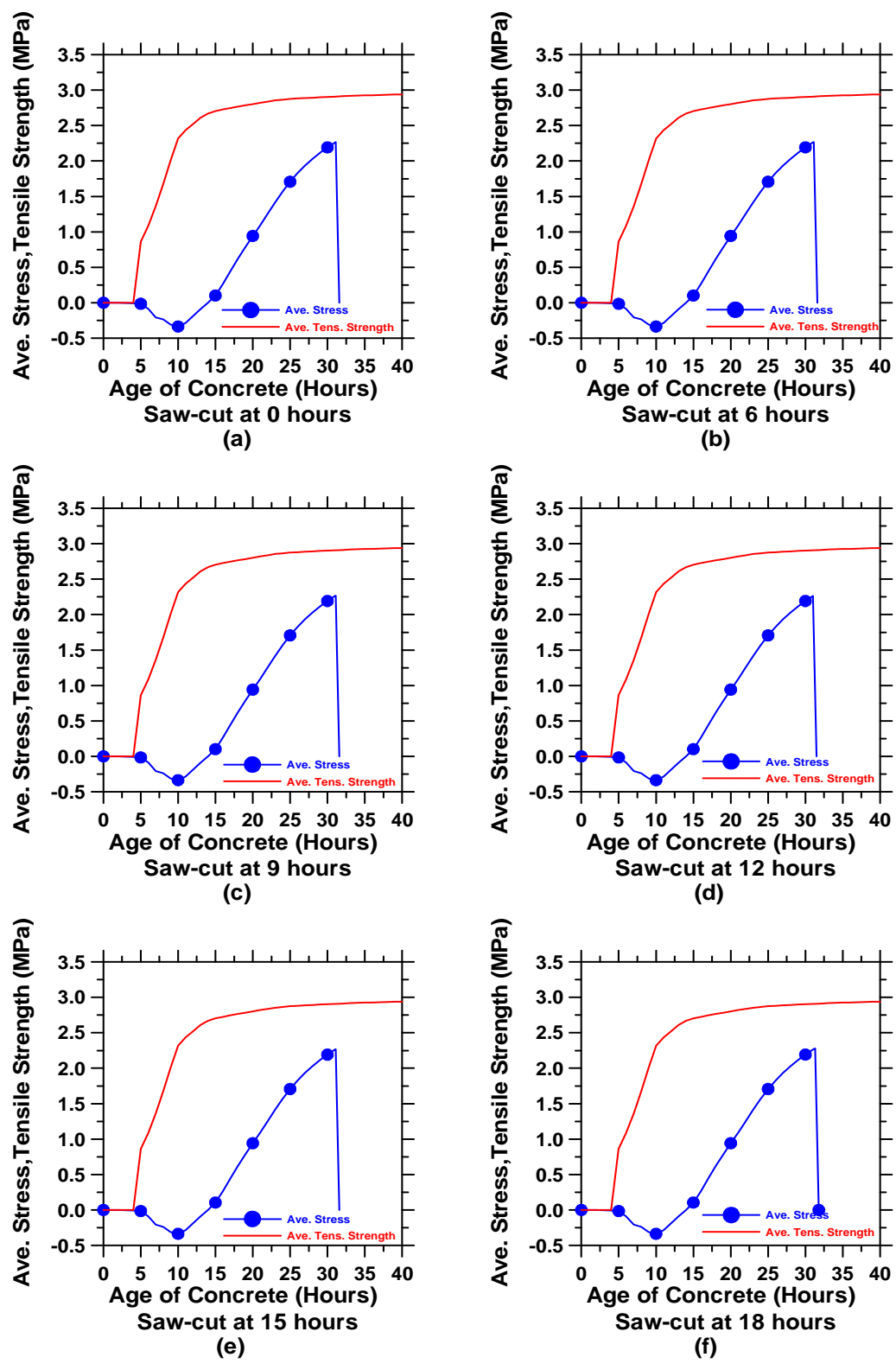


Figure B. 5: The average end stress and average tensile strength for a pavement with a D/8 saw-cut depth (cont'd).

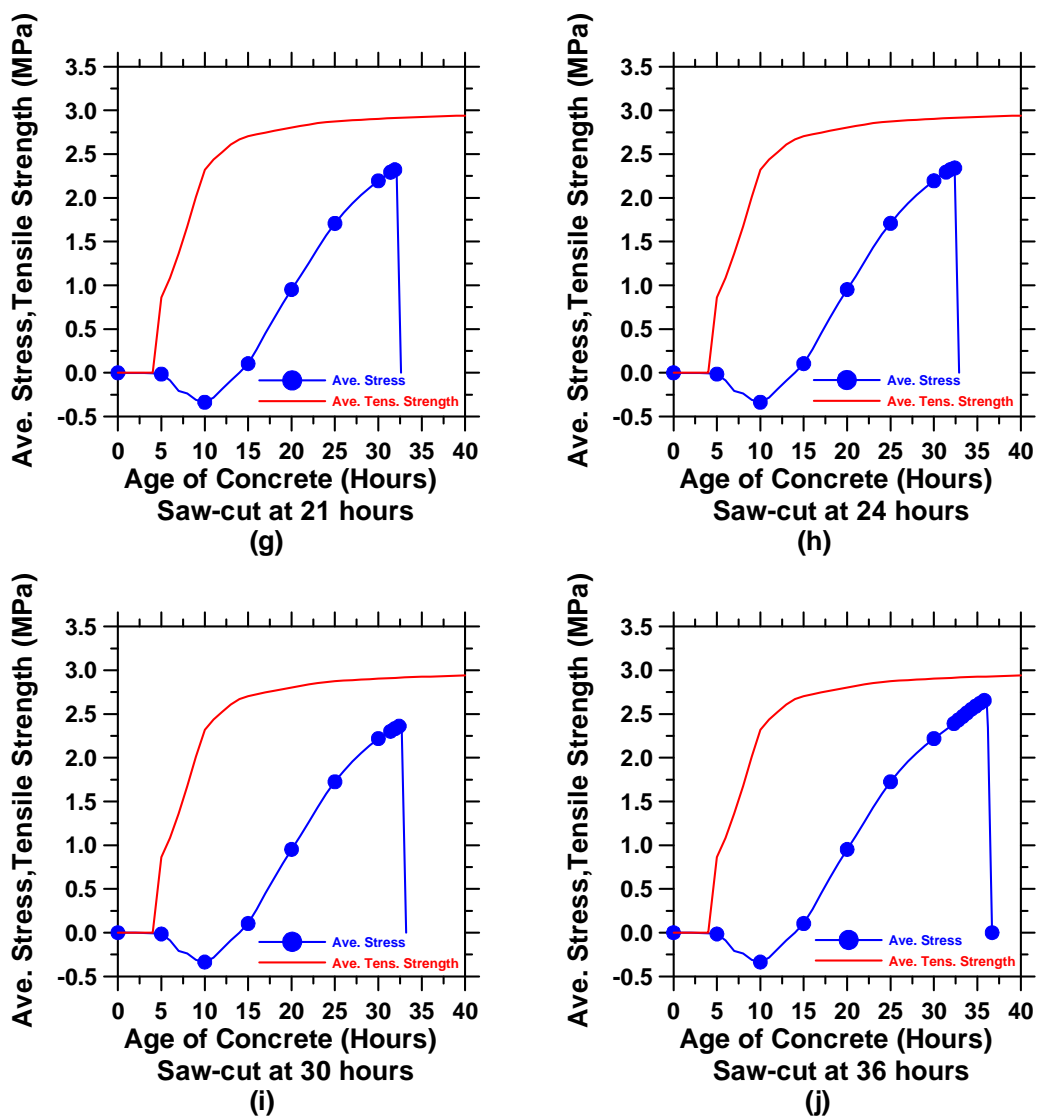


Figure B. 5: The average end stress and average tensile strength for a pavement with a D/8 saw-cut depth.

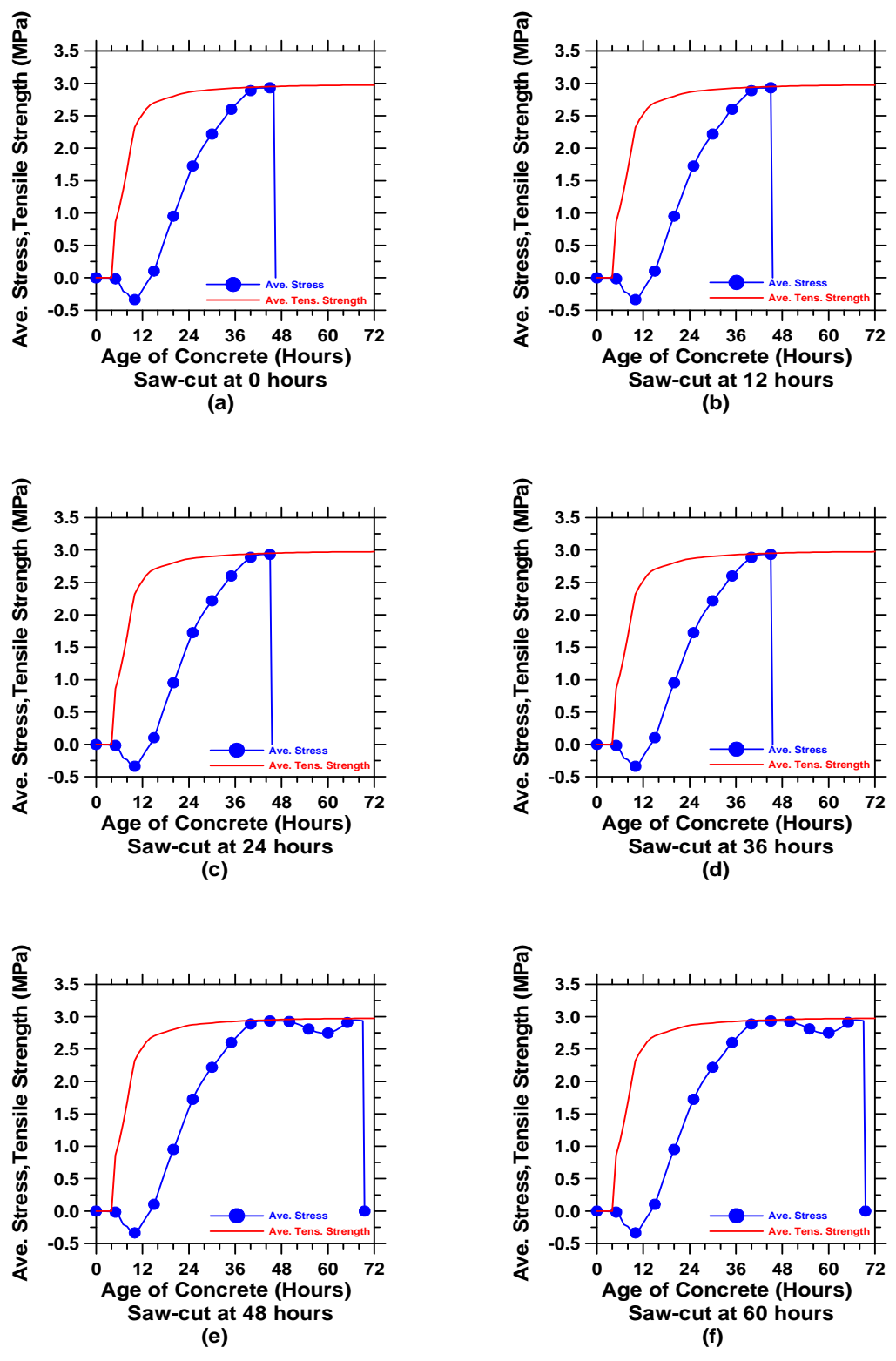


Figure B. 6: The average end stress and average tensile strength for a pavement with a D/100 saw-cut depth.

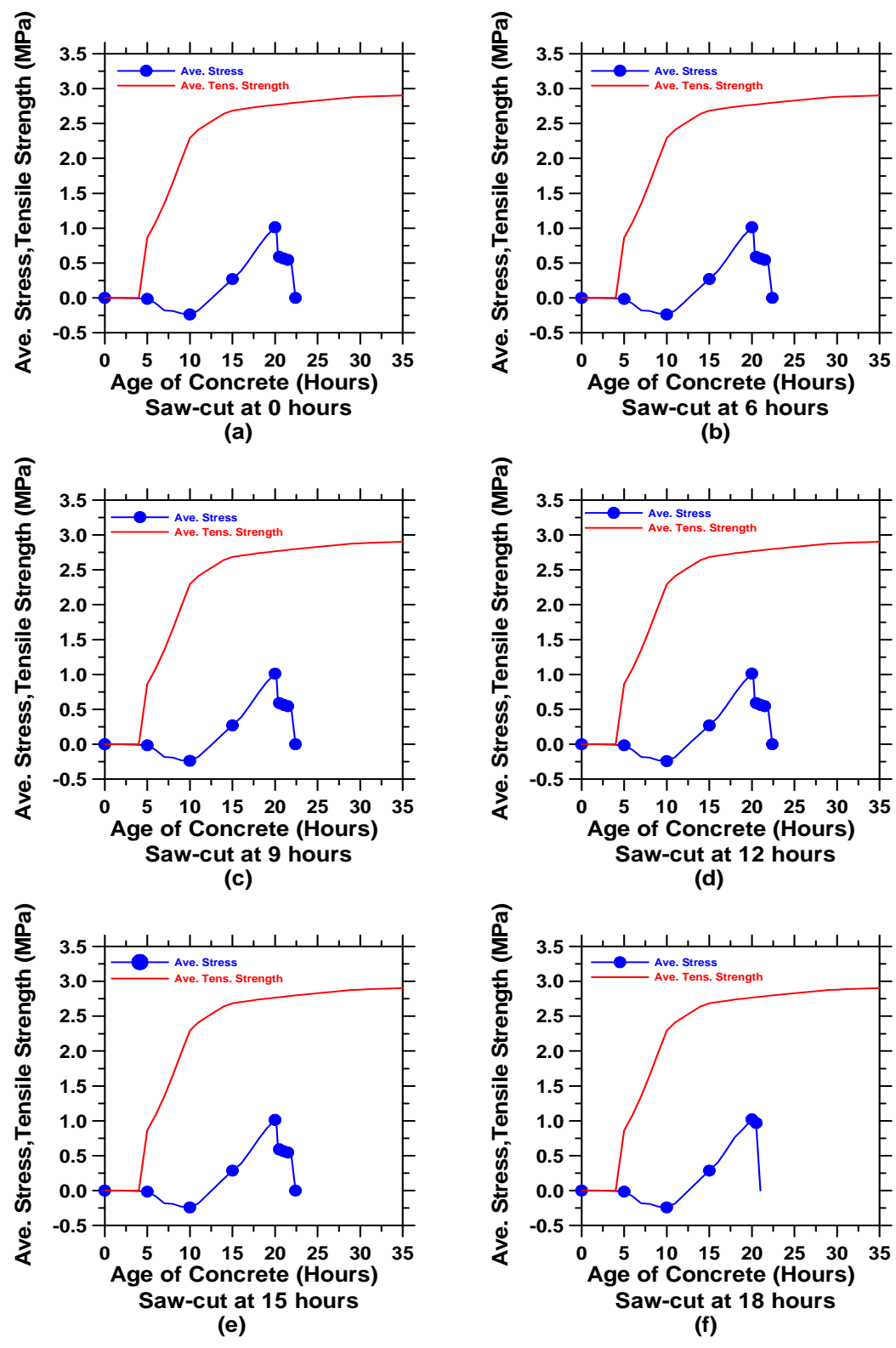


Figure B. 7: The average end stress and average tensile strength for a 10-inch thick pavement with a D/3 saw-cut depth (cont'd).

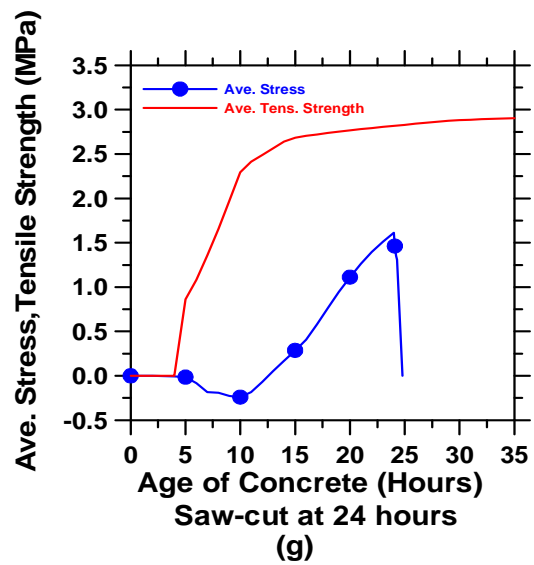


Figure B. 7: The average end stress and average tensile strength for a 10-inch thick pavement with a D/3 saw-cut depth.

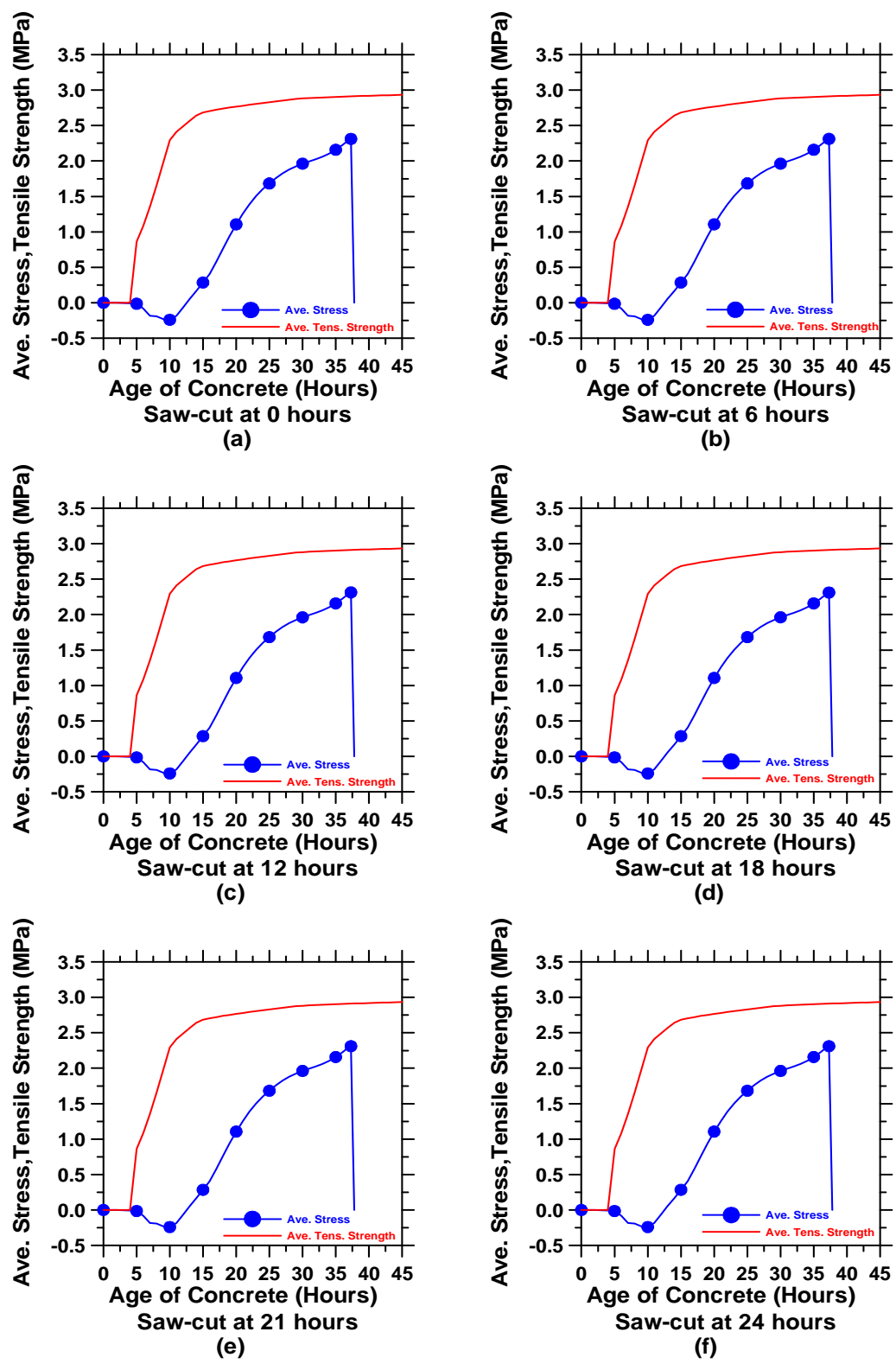


Figure B. 8: The average end stress and average tensile strength for a 10-inch thick pavement with a D/8 saw-cut depth (cont'd).

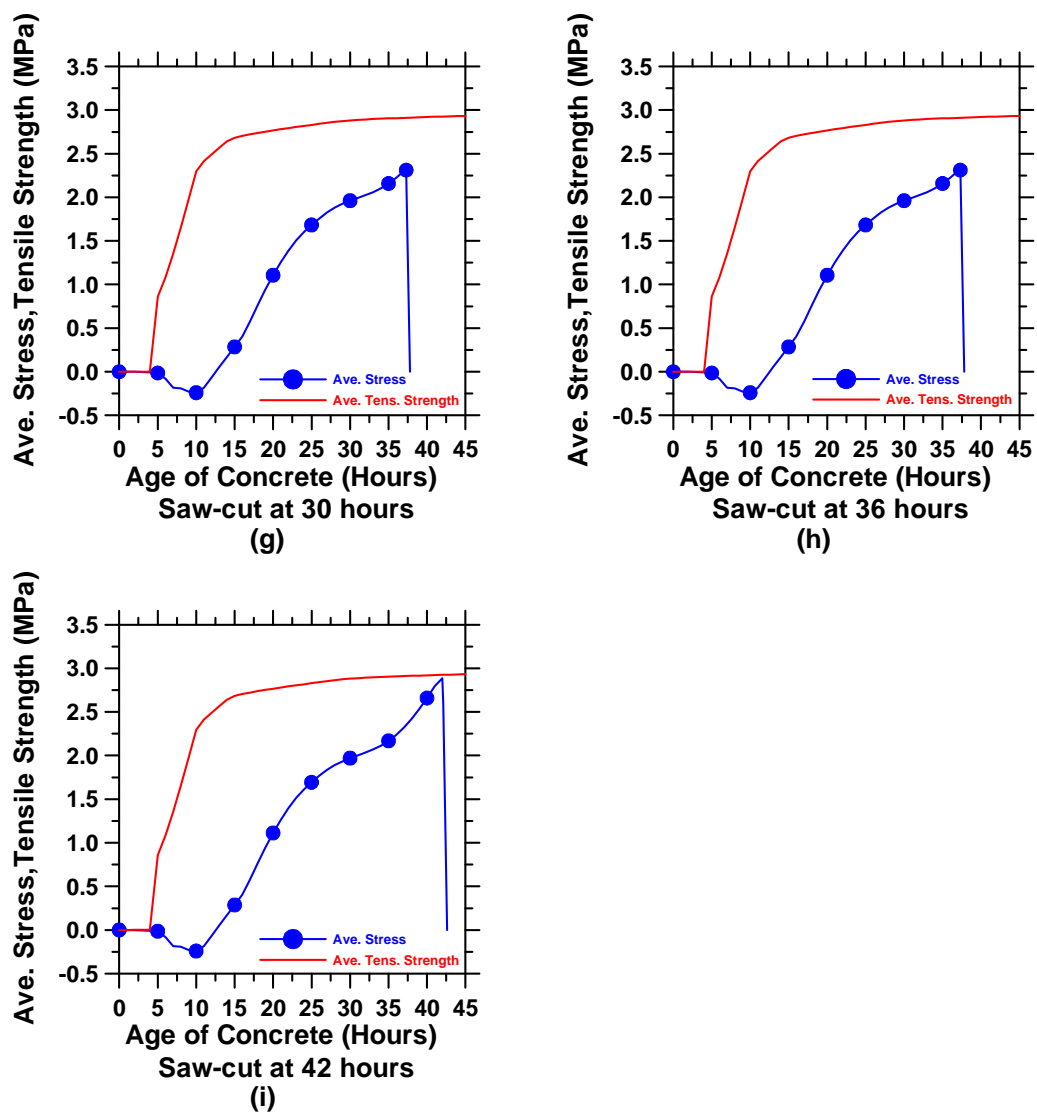


Figure B. 8: The average end stress and average tensile strength for a 10-inch thick pavement with a D/8 saw-cut depth.

Appendix C

This section provides the graphs of the average end stress-to-average tensile strength ratios for 15-inch thick pavements with $D/2$, $D/3$, $D/4$, $D/6$, $D/8$, and $D/100$ saw-cut depths. It also provides similar graphs for 10-inch thick pavements with $D/3$ and $D/8$ saw-cut depths. It should be noted that unless otherwise noted, the model parameters are the same as the baseline case described in section 7.2.

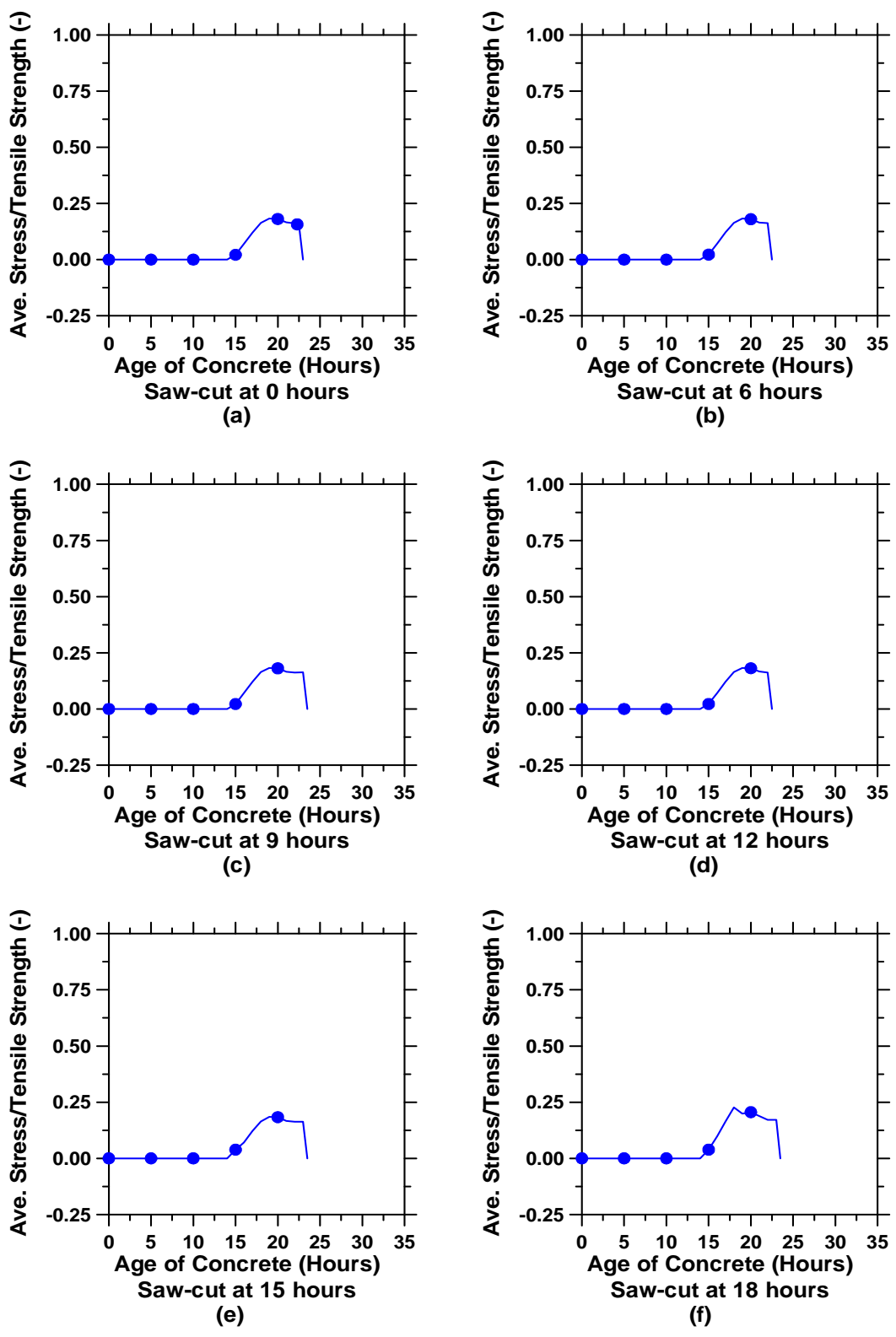


Figure C. 1: Average end stress to average tensile strength ratios for 15-inch thick pavements with a D/2 saw-cut depth (cont'd).

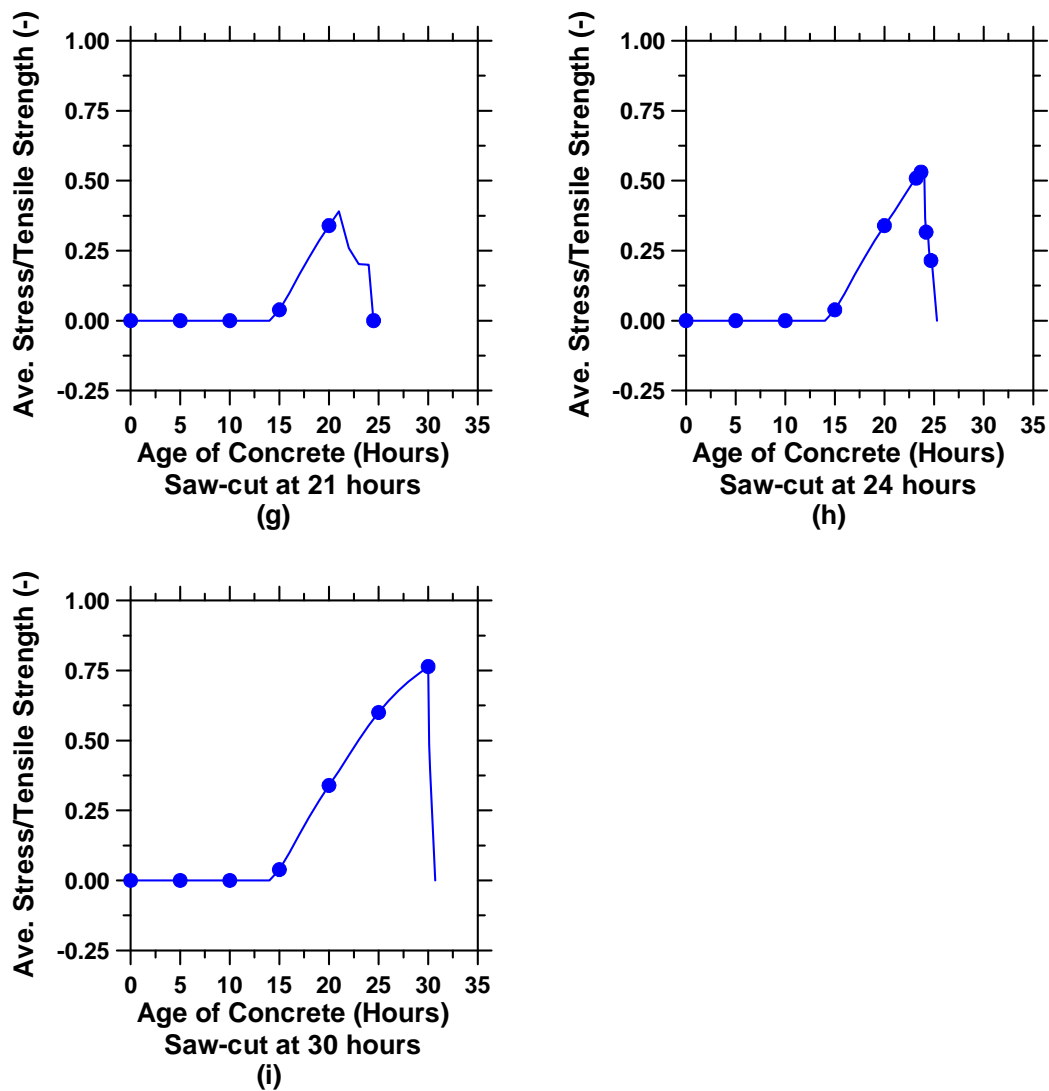


Figure C. 1: Average end stress to average tensile strength ratios for 15-inch thick pavements with a D/2 saw-cut depth.

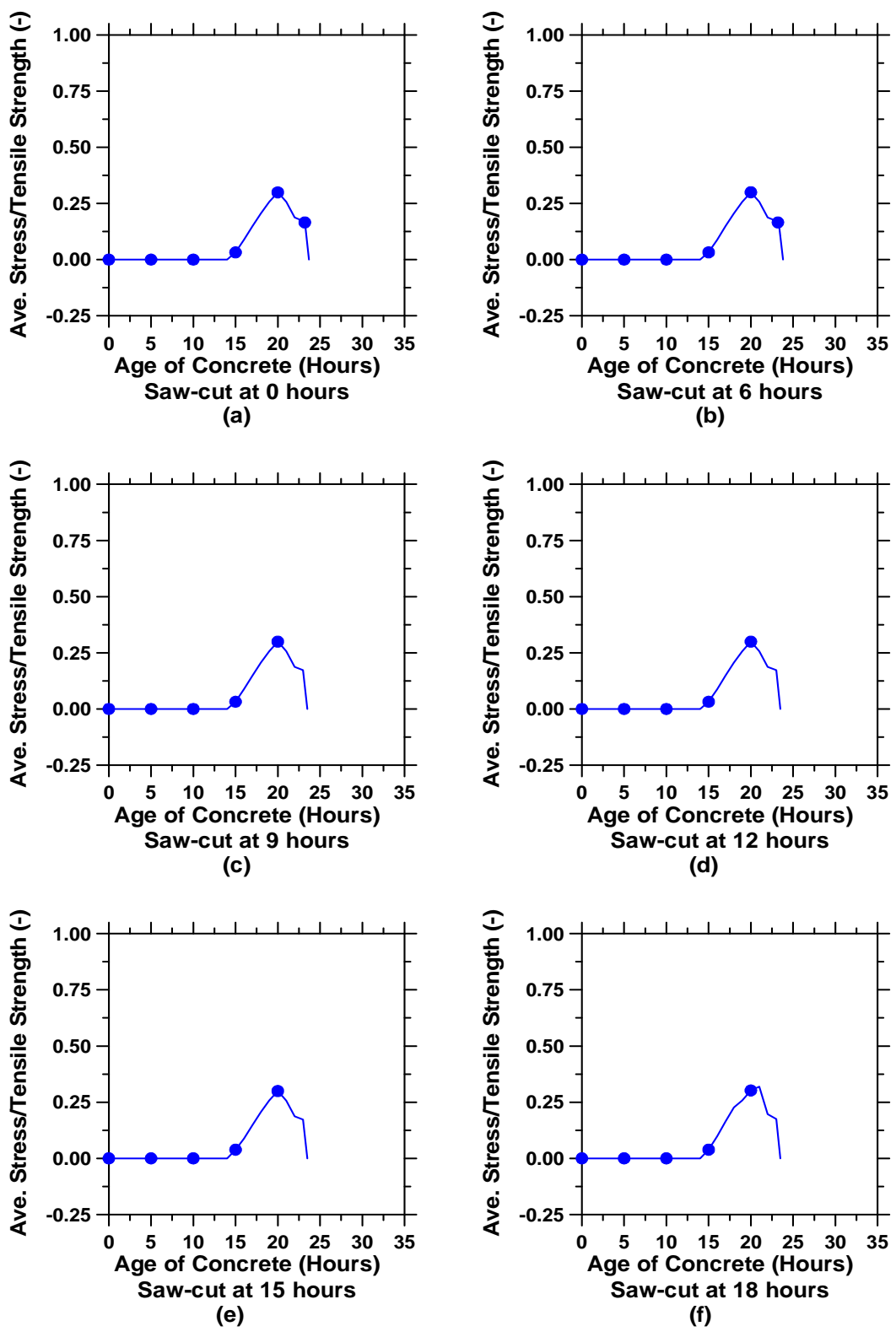


Figure C. 2: Average end stress to average tensile strength ratios for 15-inch thick pavements with a D/3 saw-cut depth (cont'd).

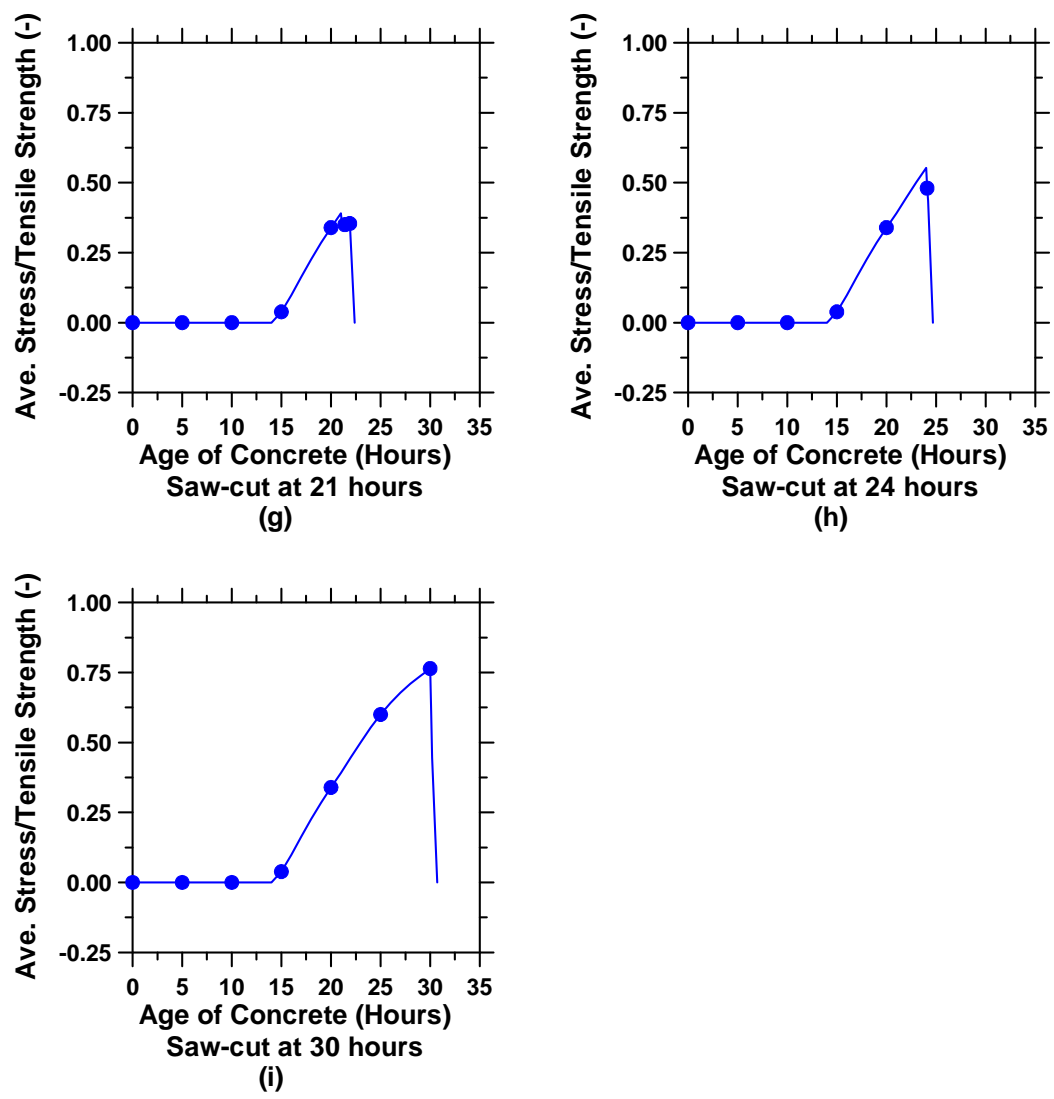


Figure C. 2: Average end stress to average tensile strength ratios for 15-inch thick pavements with a D/3 saw-cut depth.

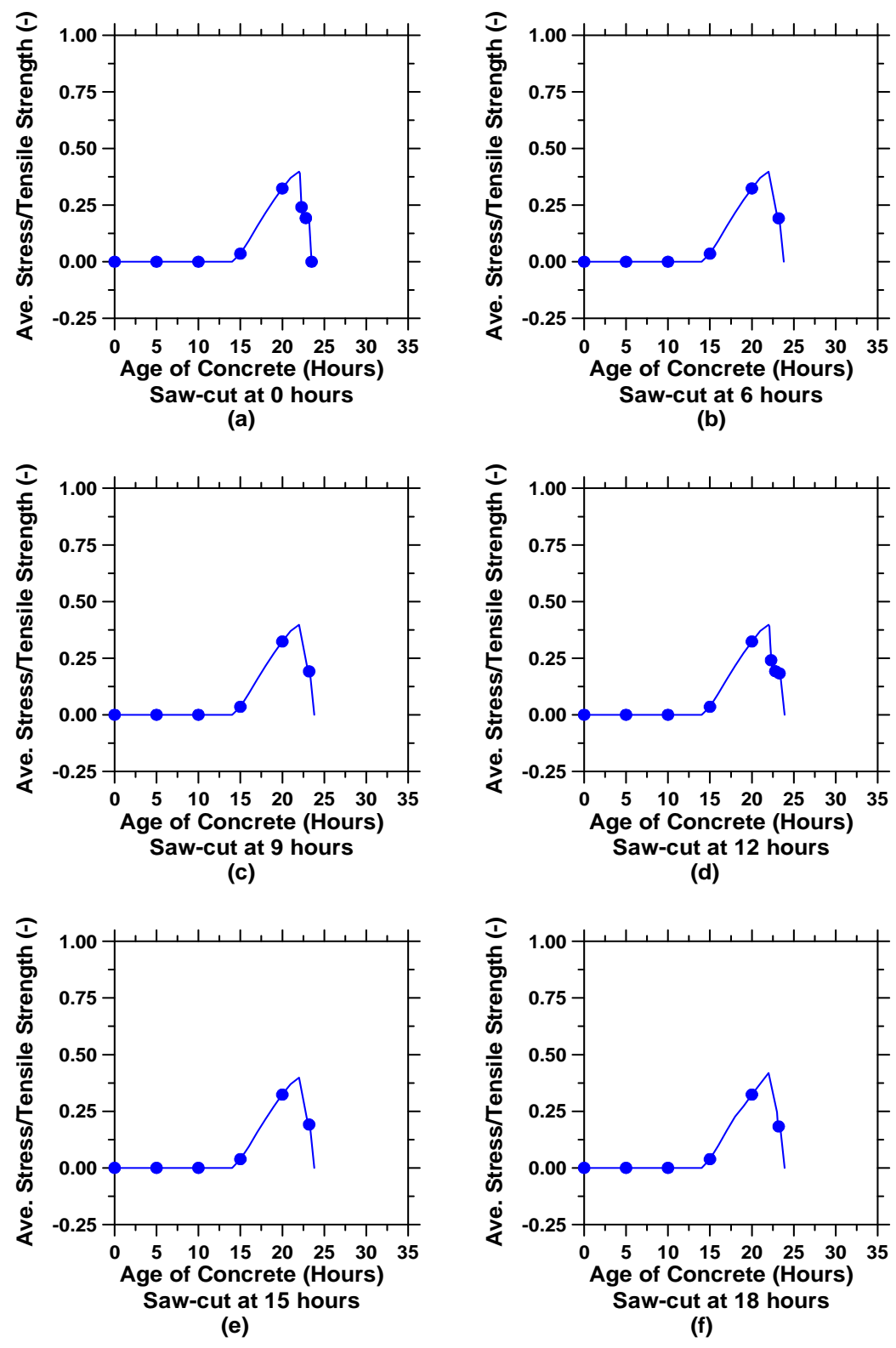


Figure C. 3: Average end stress to average tensile strength ratios for 15-inch thick pavements with a D/4 saw-cut depth (cont'd).

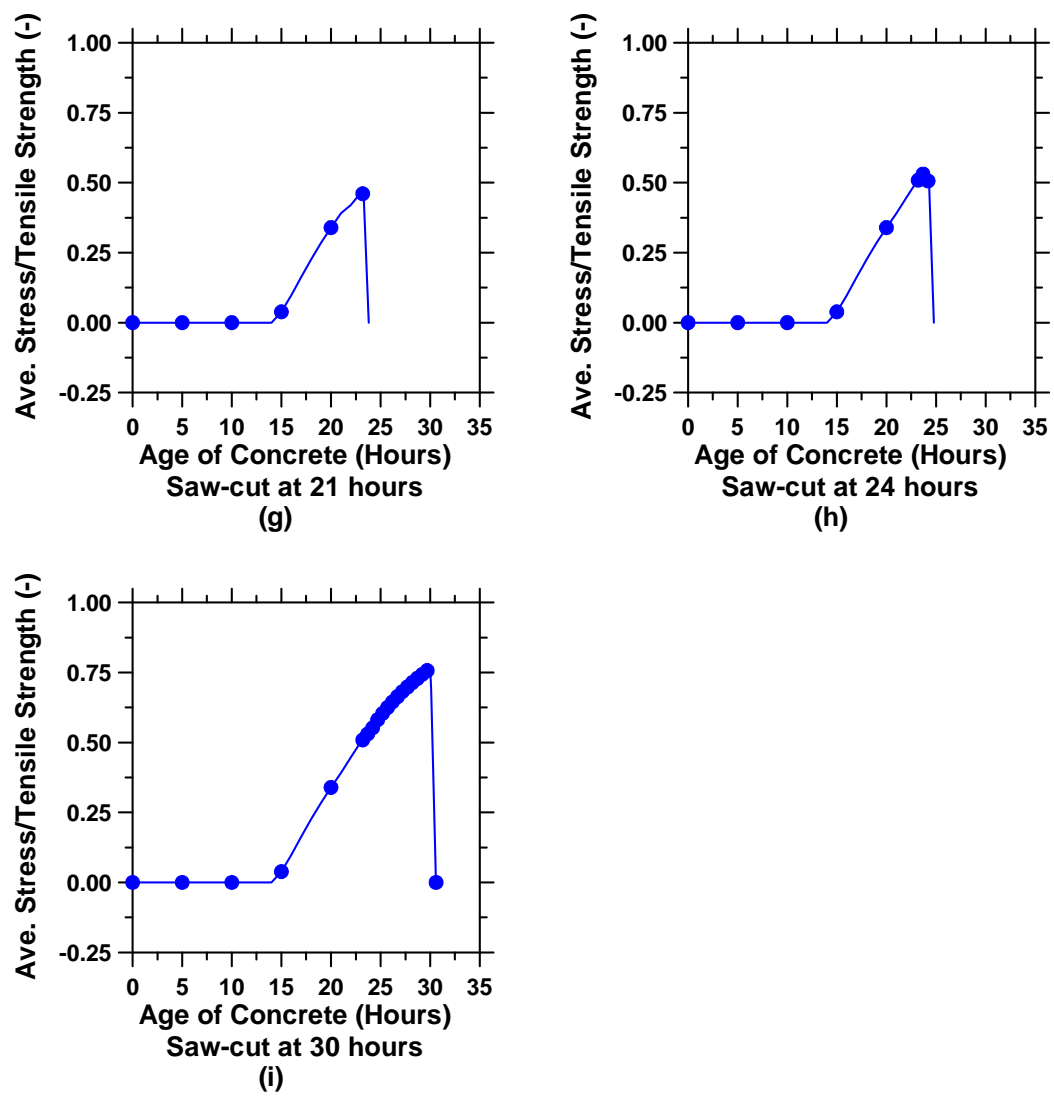


Figure C. 3: Average end stress to average tensile strength ratios for 15-inch thick pavements with a D/4 saw-cut depth.

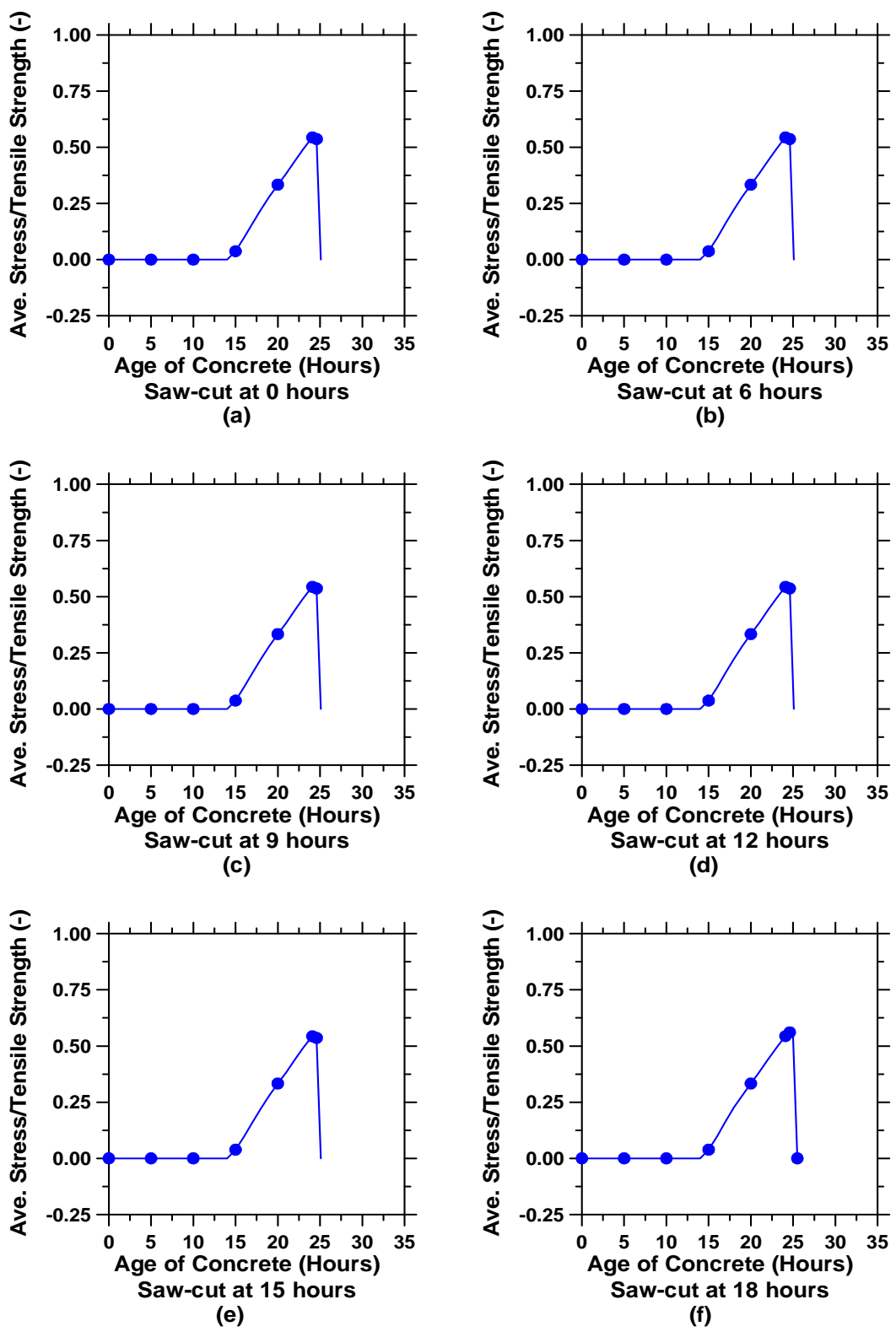


Figure C. 4: Average end stress to average tensile strength ratios for 15-inch thick pavements with a D/6 saw-cut depth (cont'd).

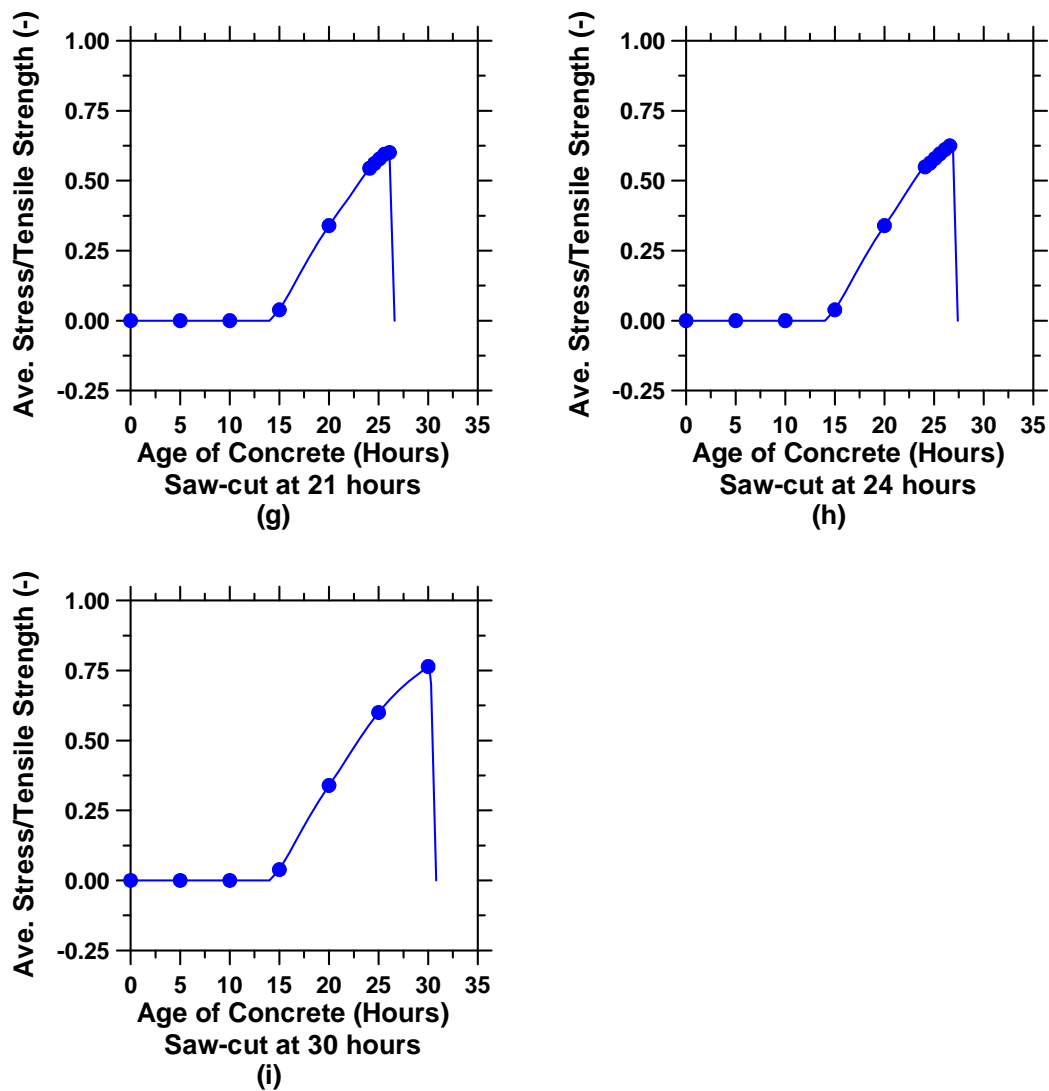


Figure C. 4: Average end stress to average tensile strength ratios for 15-inch thick pavements with a D/6 saw-cut depth.

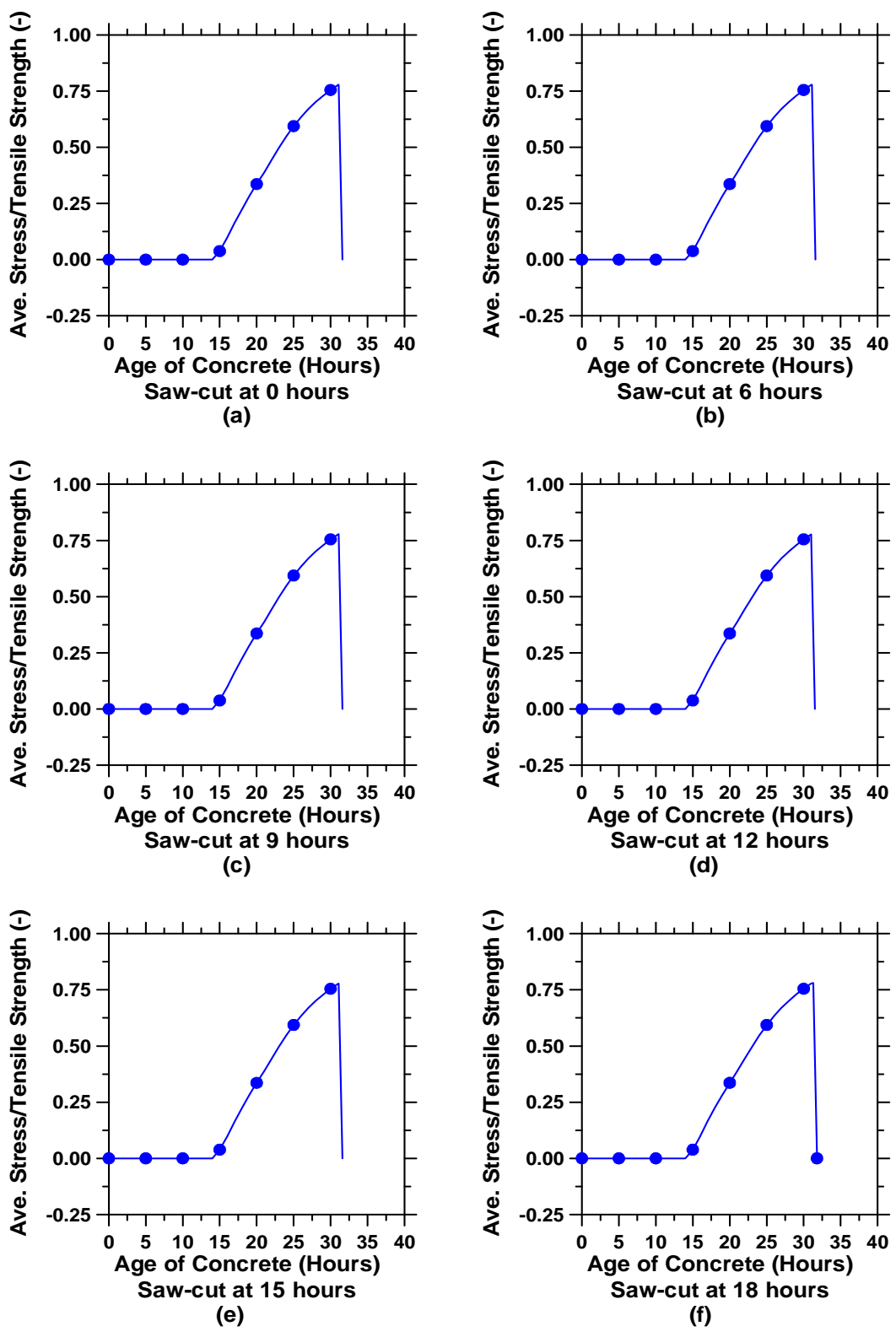


Figure C. 5: Average end stress to average tensile strength ratios for 15-inch thick pavements with a D/8 saw-cut depth (cont'd).

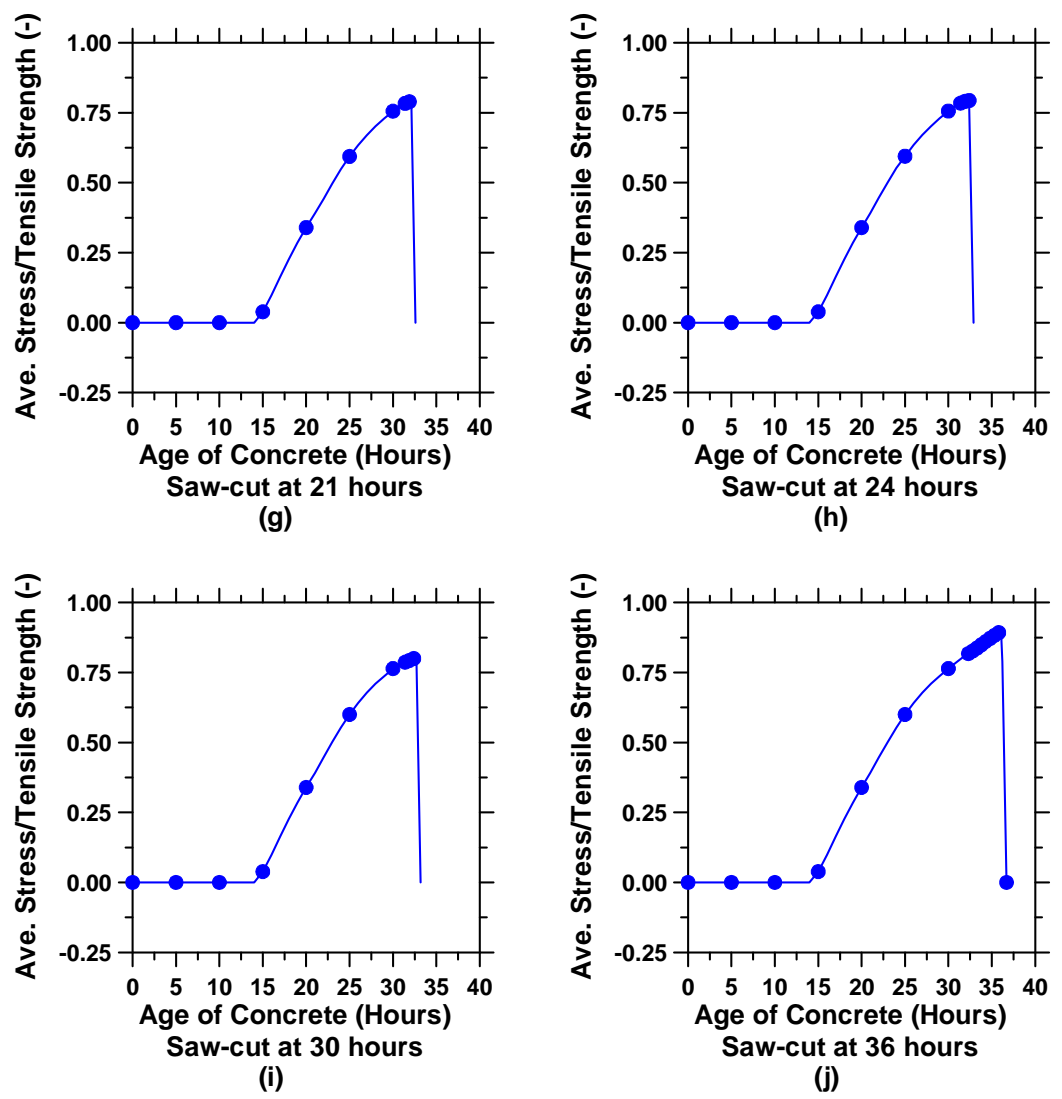


Figure C. 5: Average end stress to average tensile strength ratios for 15-inch thick pavements with a D/8 saw-cut depth.

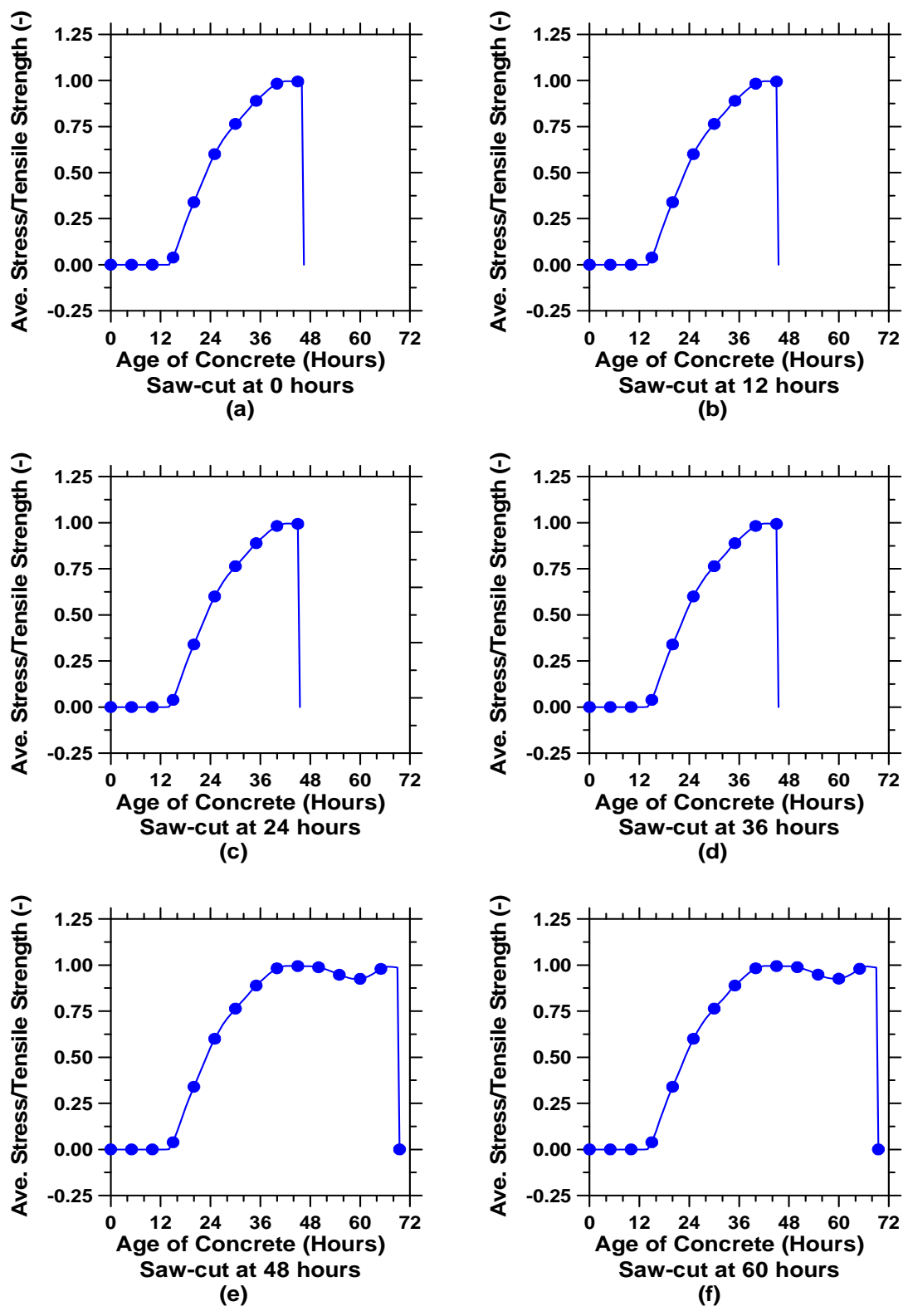


Figure C. 6: Average end stress to average tensile strength ratios for 15-inch thick pavements with a D/100 saw-cut depth.

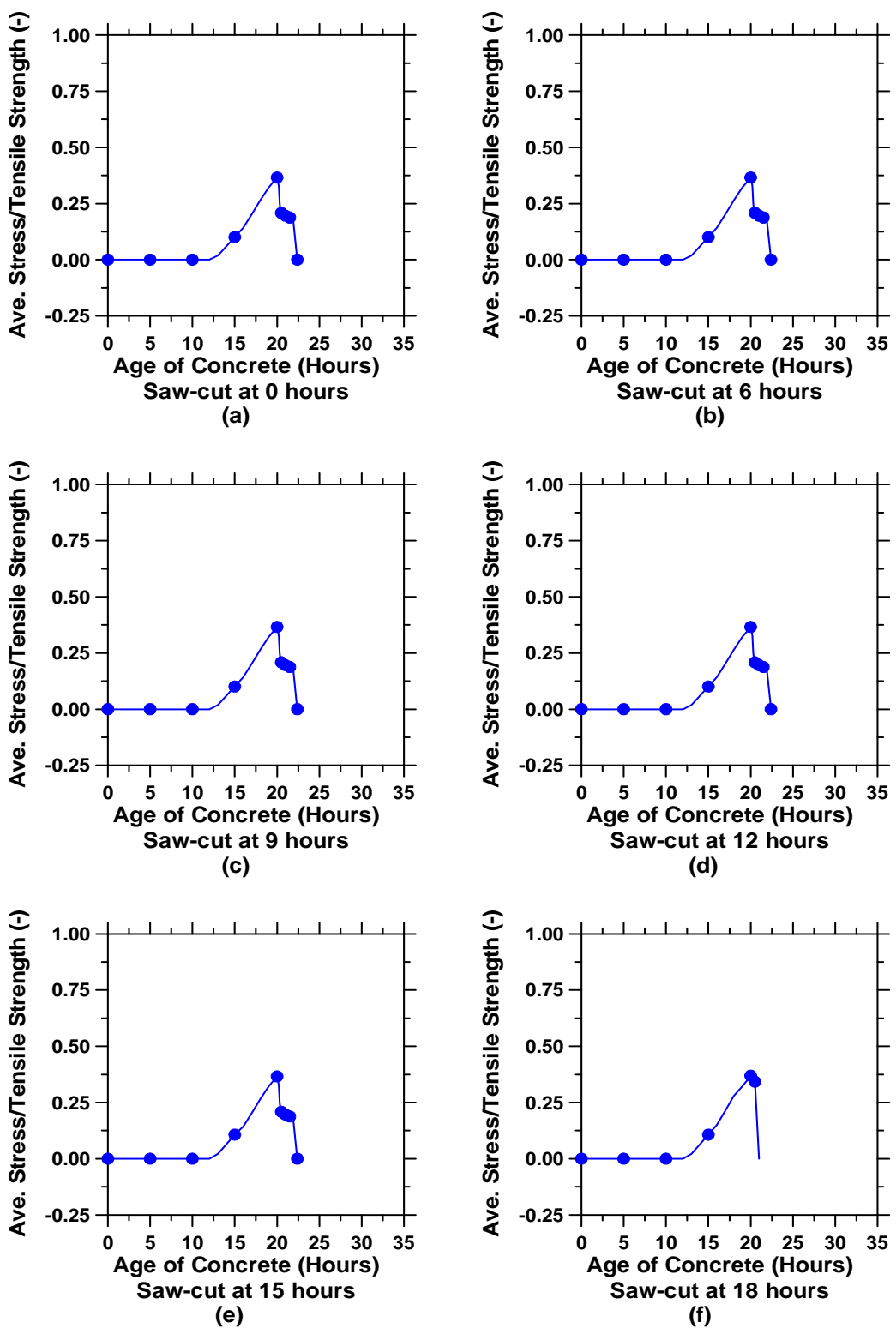


Figure C. 7: Average end stress to average tensile strength ratios for 10-inch thick pavements with a D/3 saw-cut depth (cont'd).

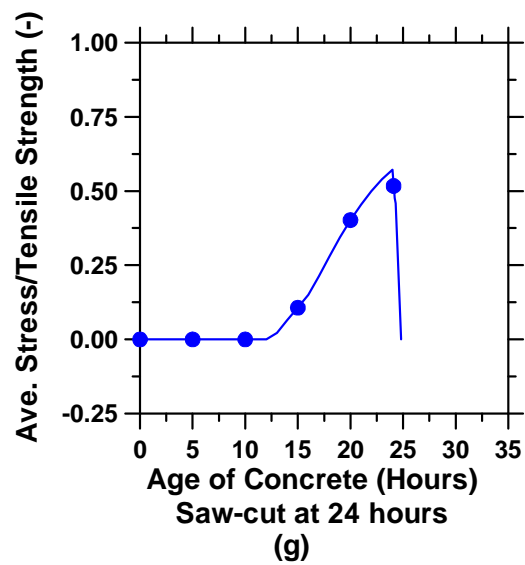


Figure C. 7: Average end stress to average tensile strength ratios for 10-inch thick pavements with a D/3 saw-cut depth.

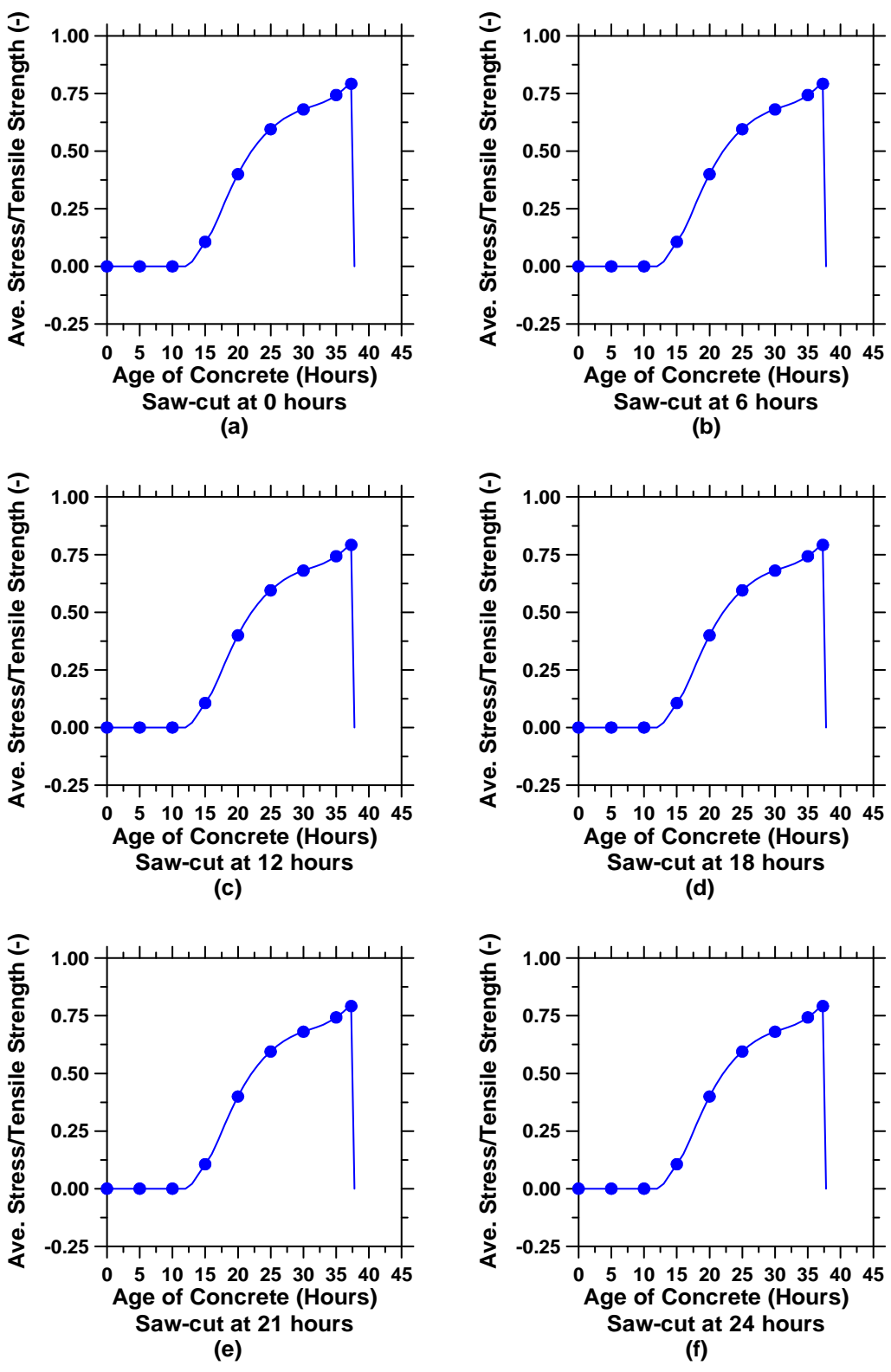


Figure C. 8: Average end stress to average tensile strength ratios for 10-inch thick pavements with a D/8 saw-cut depth (cont'd).

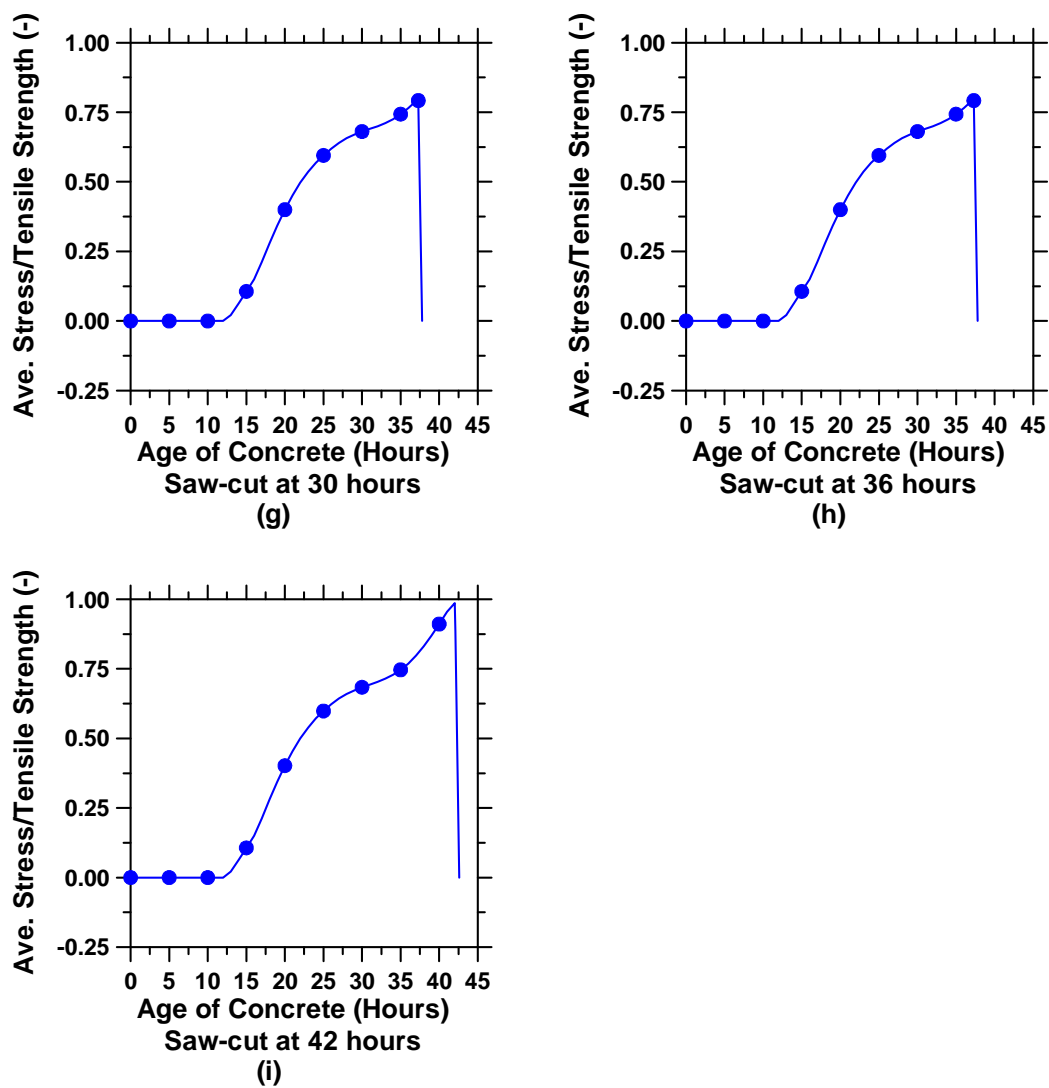


Figure C. 8: Average end stress to average tensile strength ratios for 10-inch thick pavements with a D/8 saw-cut depth.

Appendix D

The graphs of tensile stress/(tensile strength $\times \Phi$) for 15-inch thick pavements with D/2, D/3, D/4, D/6, D/8, and D/100 saw-cut depths. It also provides similar graphs for 10-inch thick pavements with D/3 and D/8 saw-cut depths. It should be noted that unless otherwise noted, the model parameters are the same as the baseline case described in section 7.2.

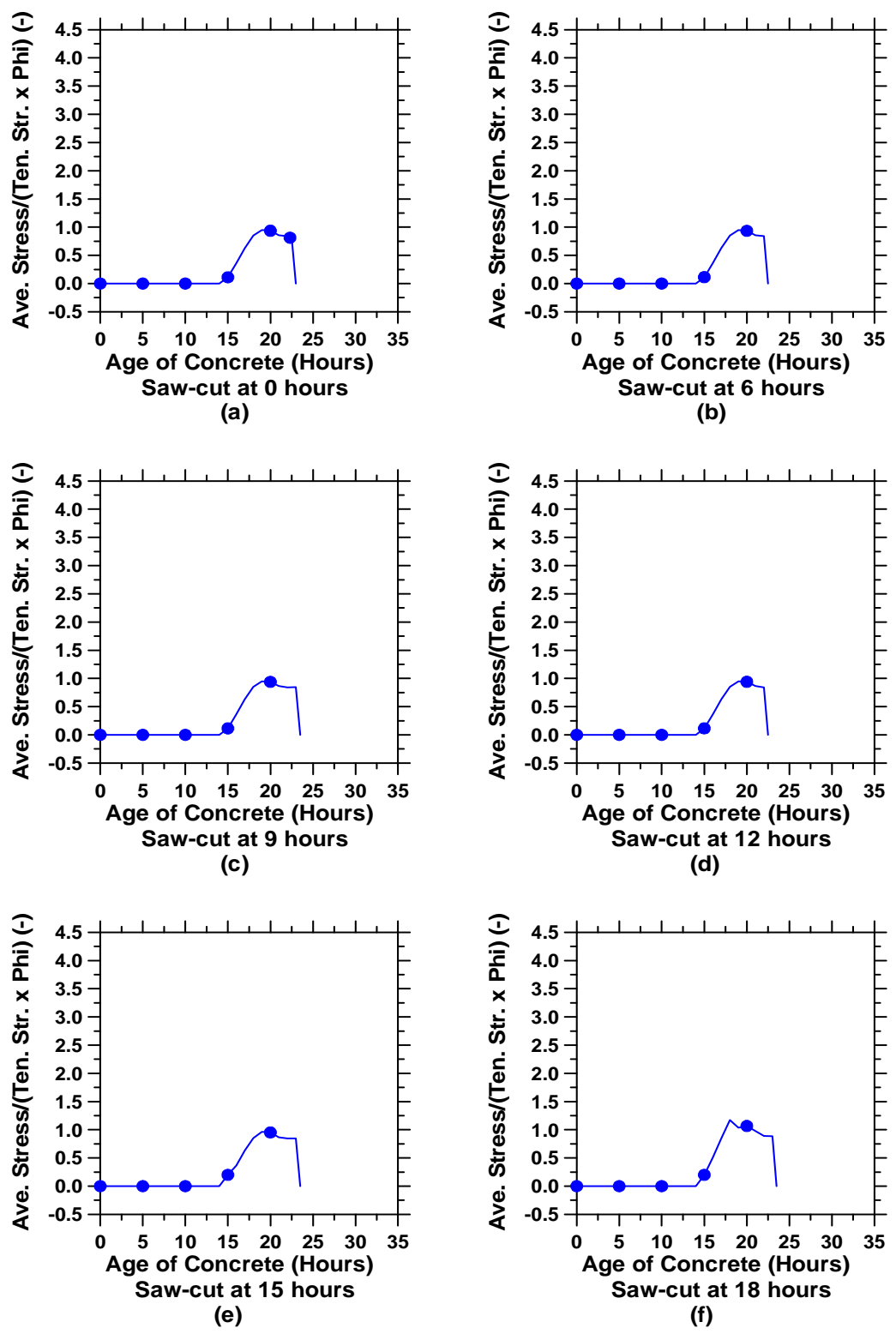


Figure D. 1: Average end stress to average tensile strength and phi ratios for 15-inch thick pavements with a saw-cut depth of D/2 (cont'd).

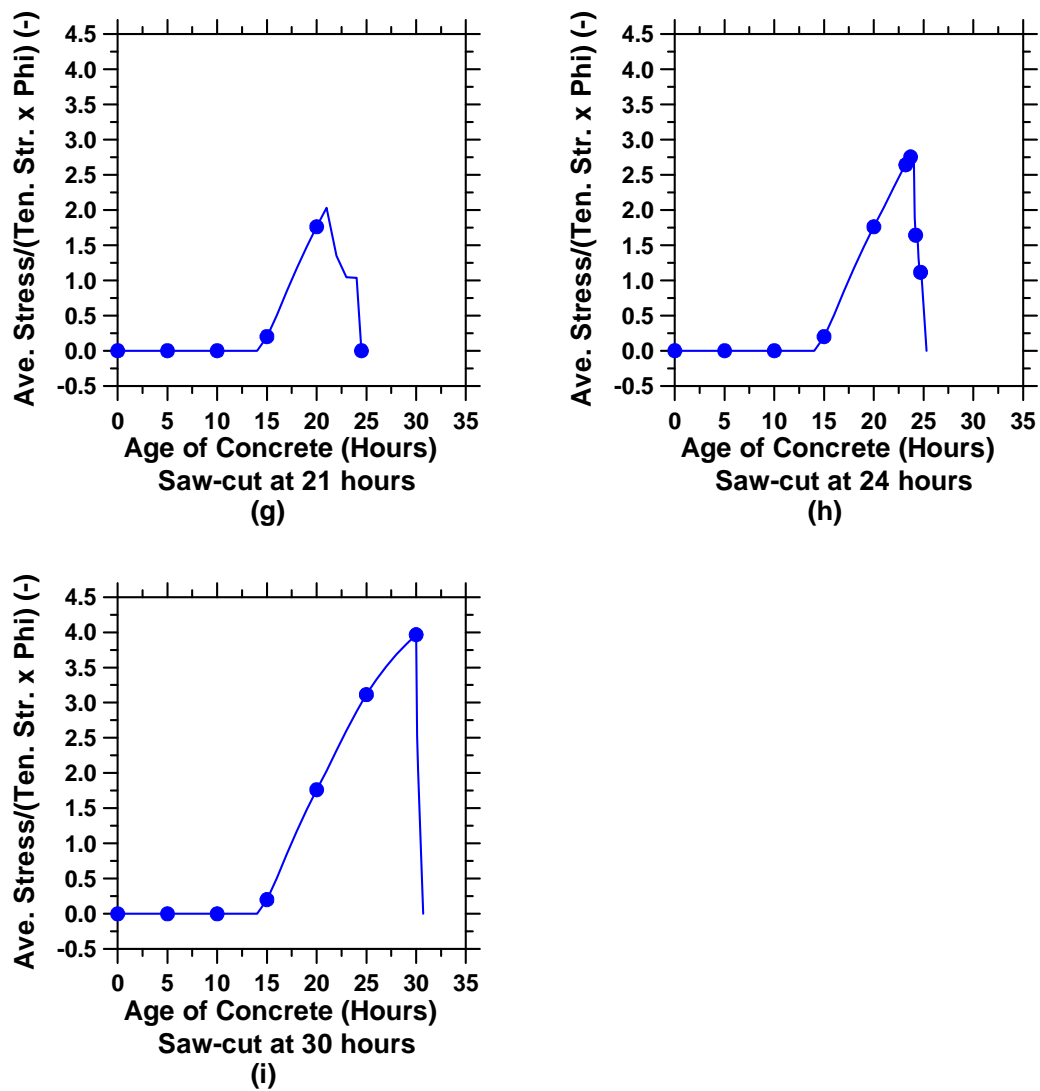


Figure D. 1: Average end stress to average tensile strength and phi ratios for 15-inch thick pavements with a saw-cut depth of $D/2$.

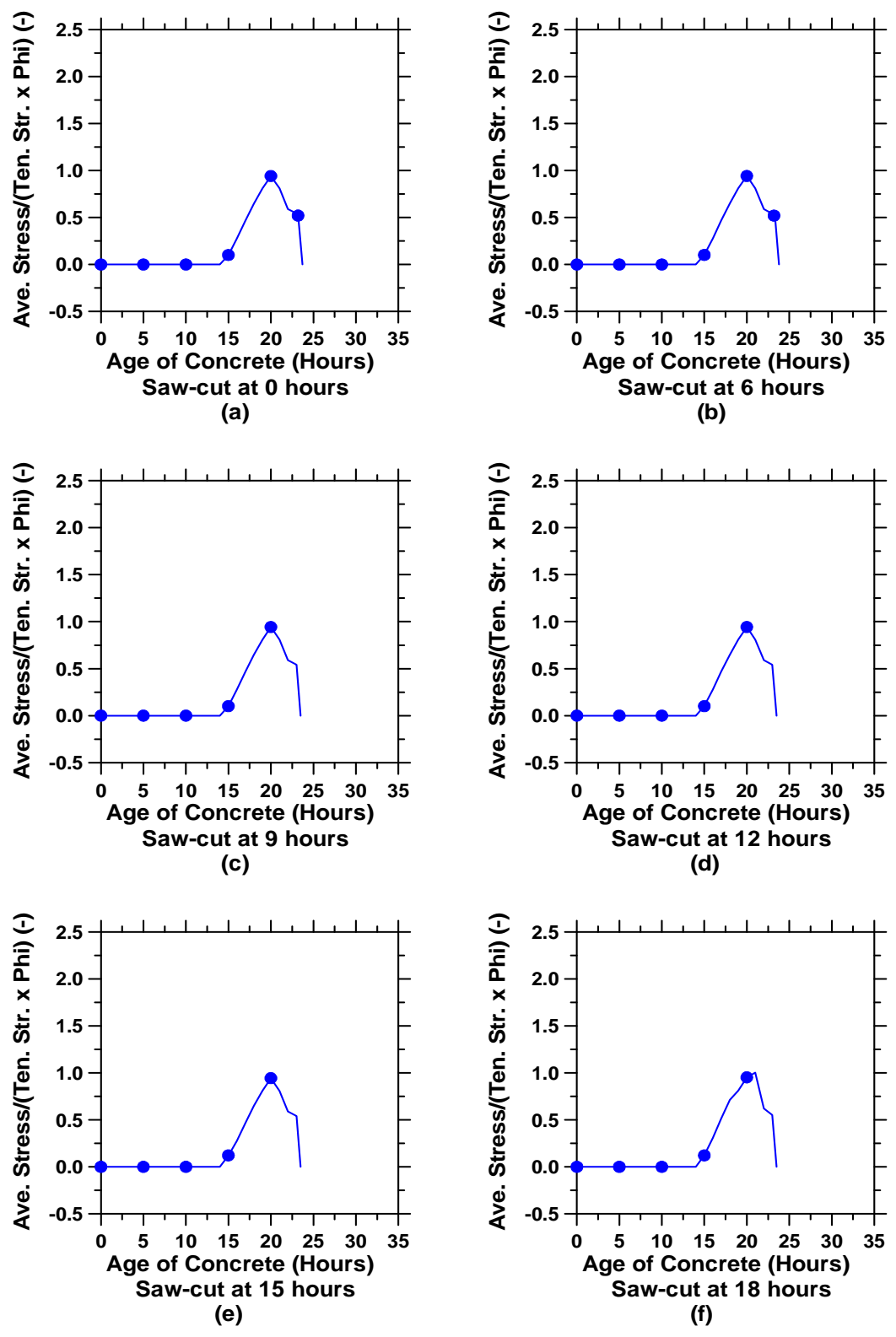


Figure D. 2: Average end stress to average tensile strength and phi ratios for 15-inch thick pavements with a saw-cut depth of D/3 (cont'd).

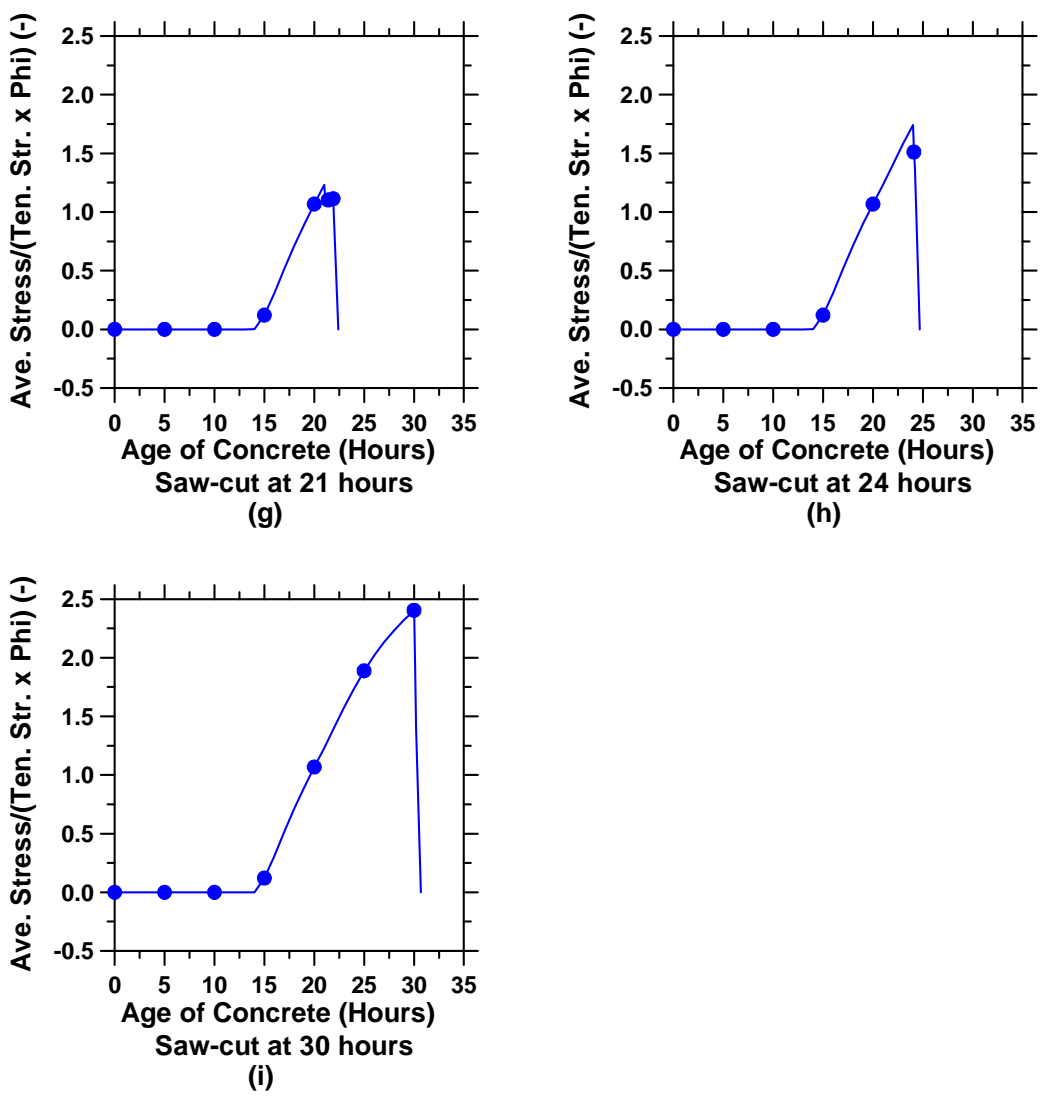


Figure D. 2: Average end stress to average tensile strength and phi ratios for 15-inch thick pavements with a saw-cut depth of D/3.

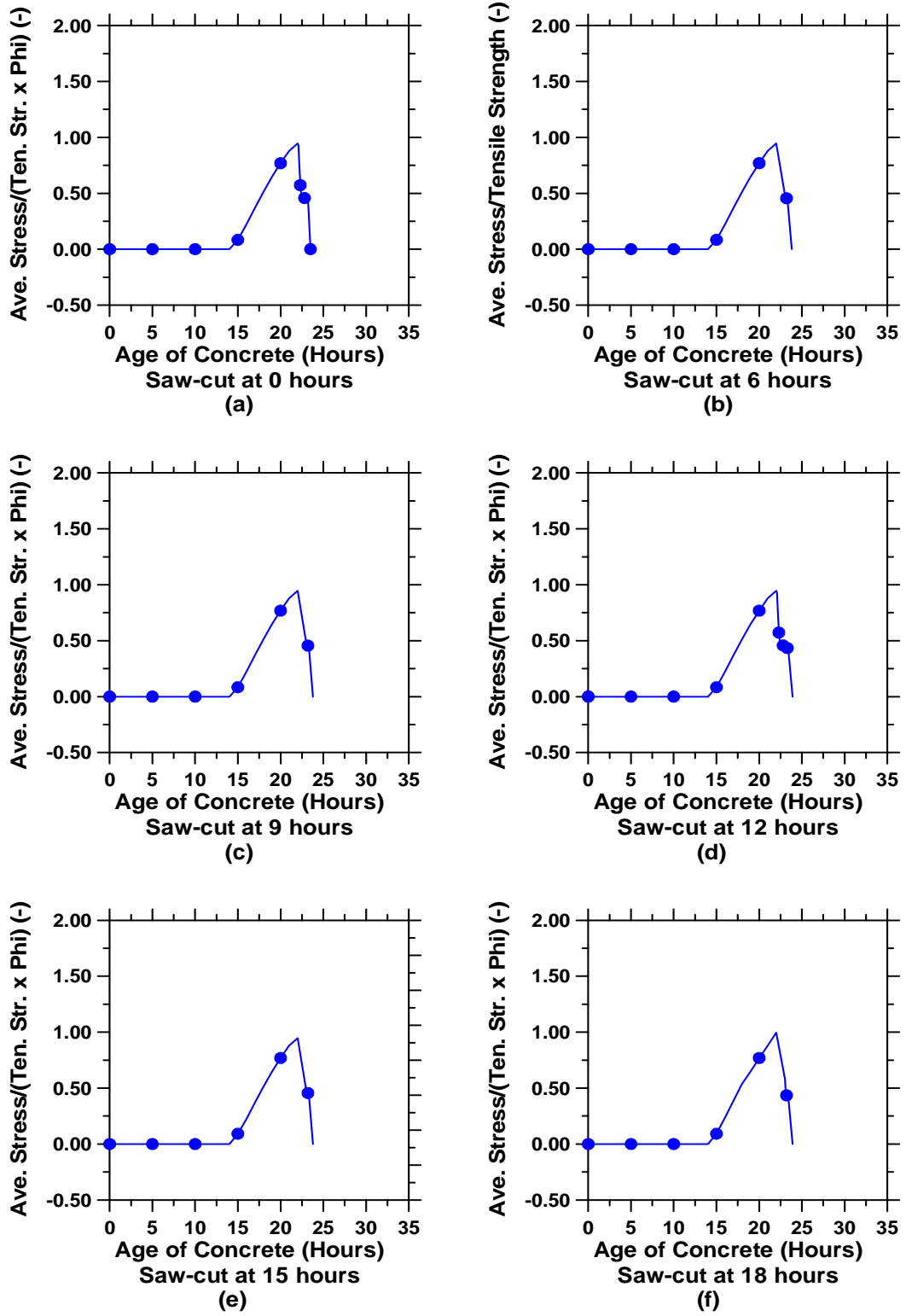


Figure D. 3: Average end stress to average tensile strength and phi ratios for 15-inch thick pavements with a saw-cut depth of D/4 (cont'd).

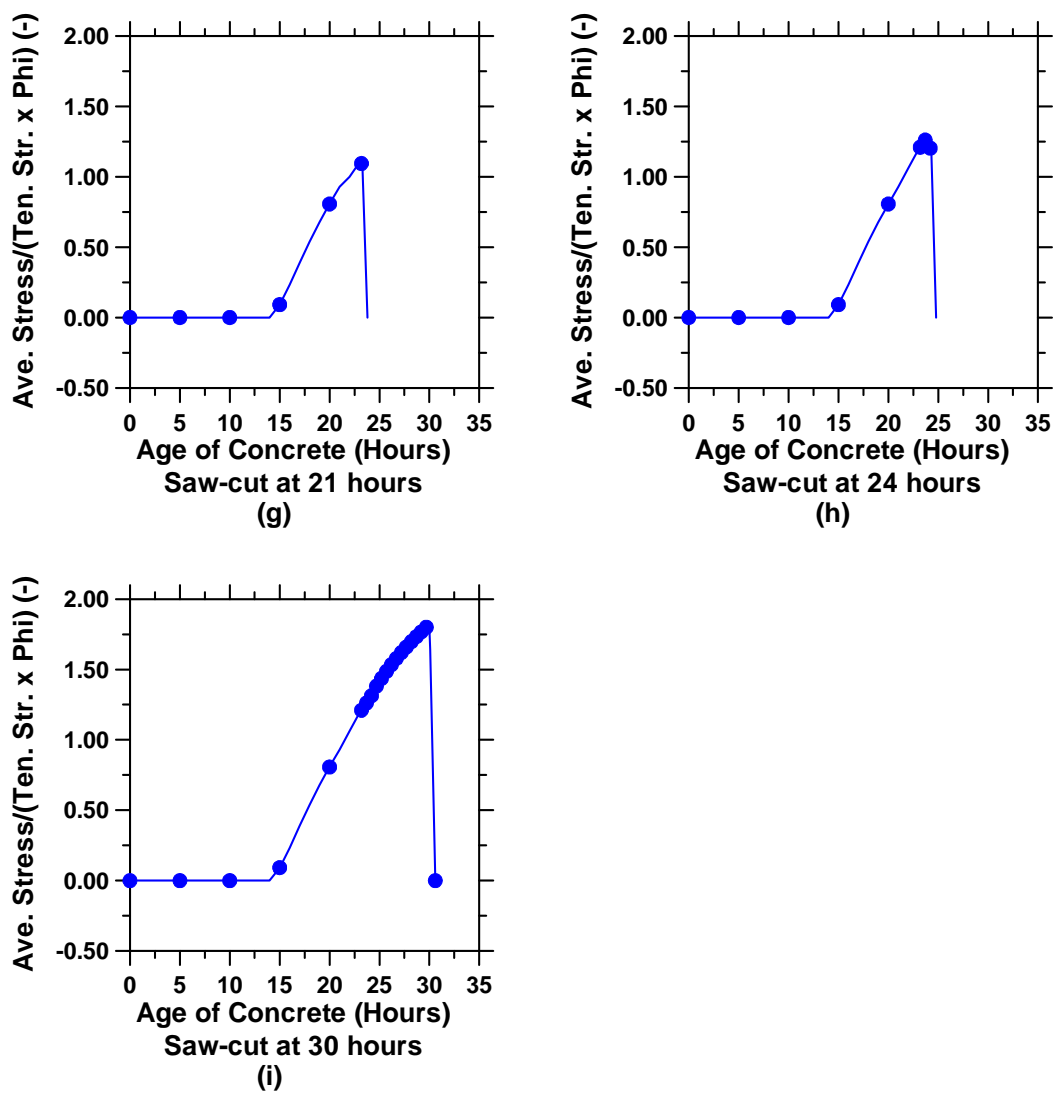


Figure D. 3: Average end stress to average tensile strength and phi ratios for 15-inch thick pavements with a saw-cut depth of D/4.

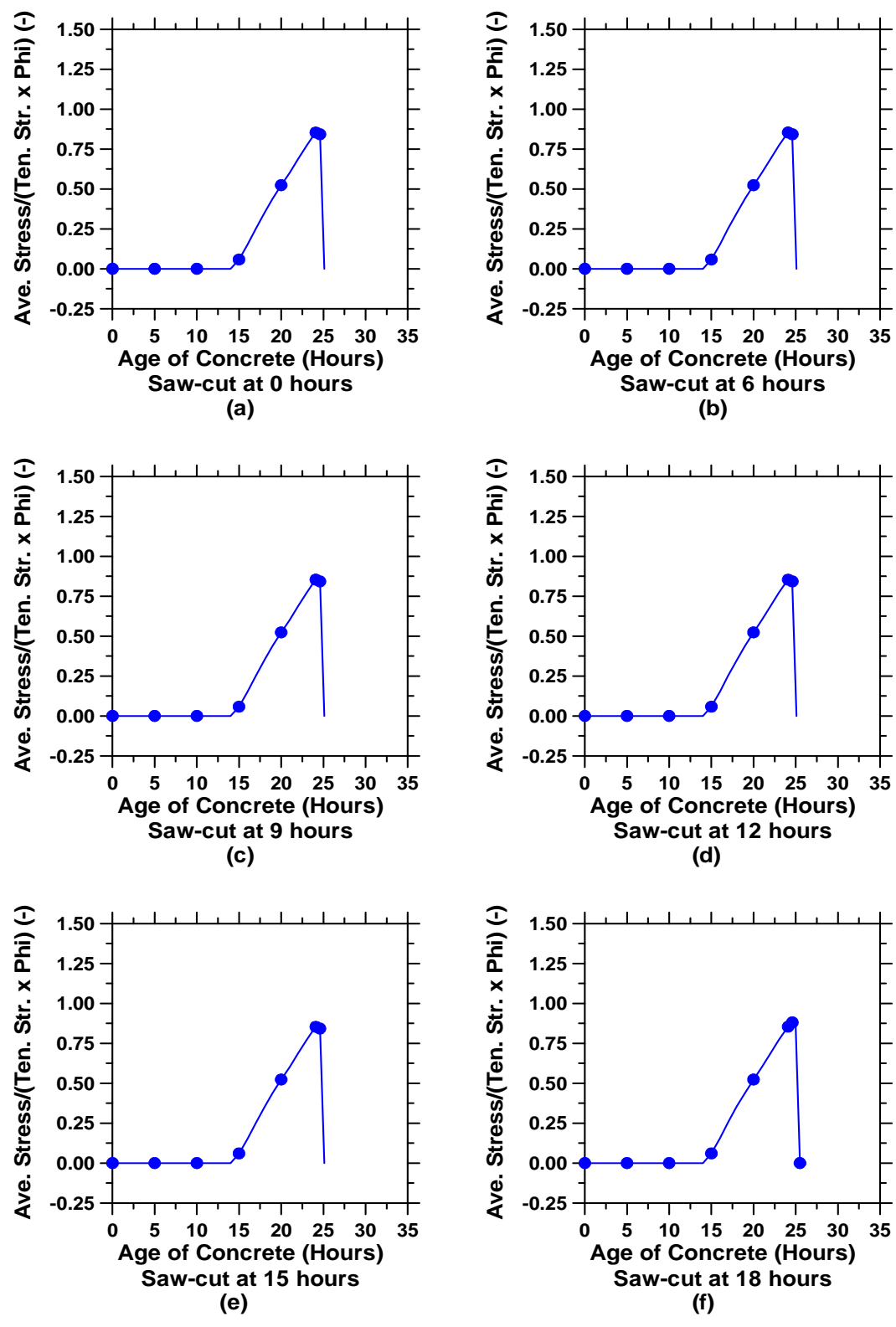


Figure D. 4: Average end stress to average tensile strength and phi for 15-inch thick pavements with a saw-cut depth of D/6 (cont'd).

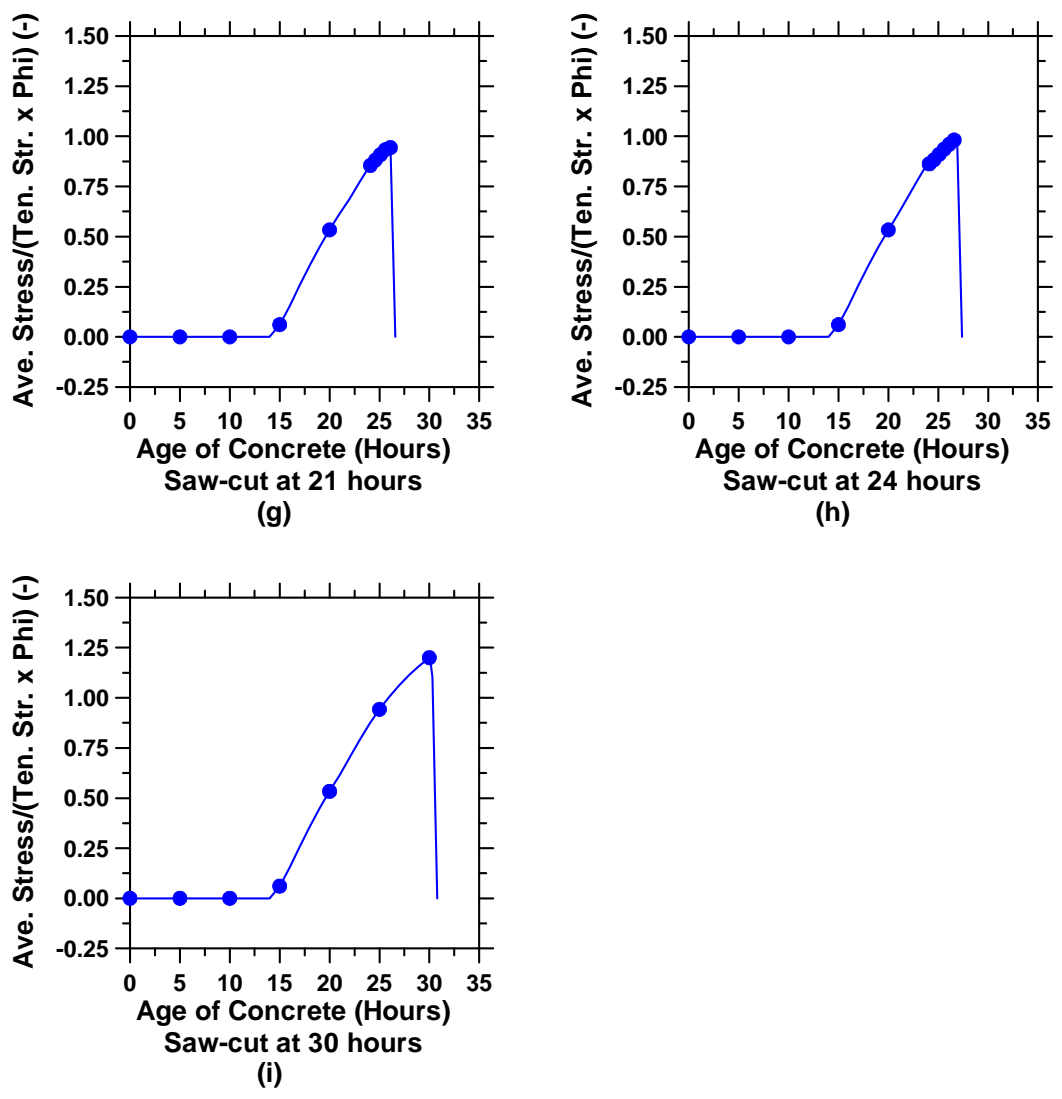


Figure D. 4: Average end stress to average tensile strength and phi ratios for 15-inch thick pavements with a saw-cut depth of D/6.

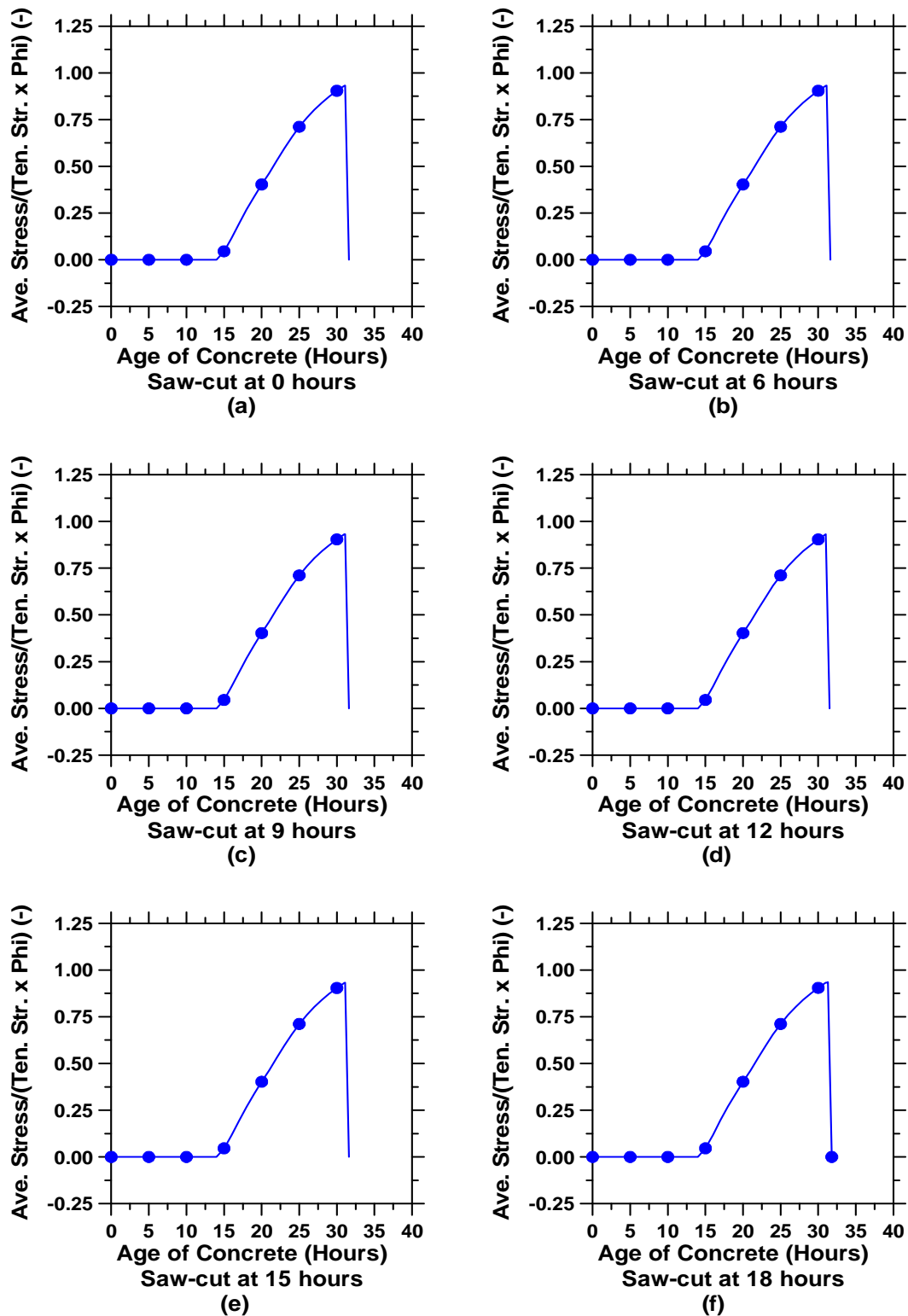


Figure D. 5: Average end stress to average tensile strength and phi ratios for 15-inch thick pavements with a saw-cut depth of $D/8$ (cont'd).

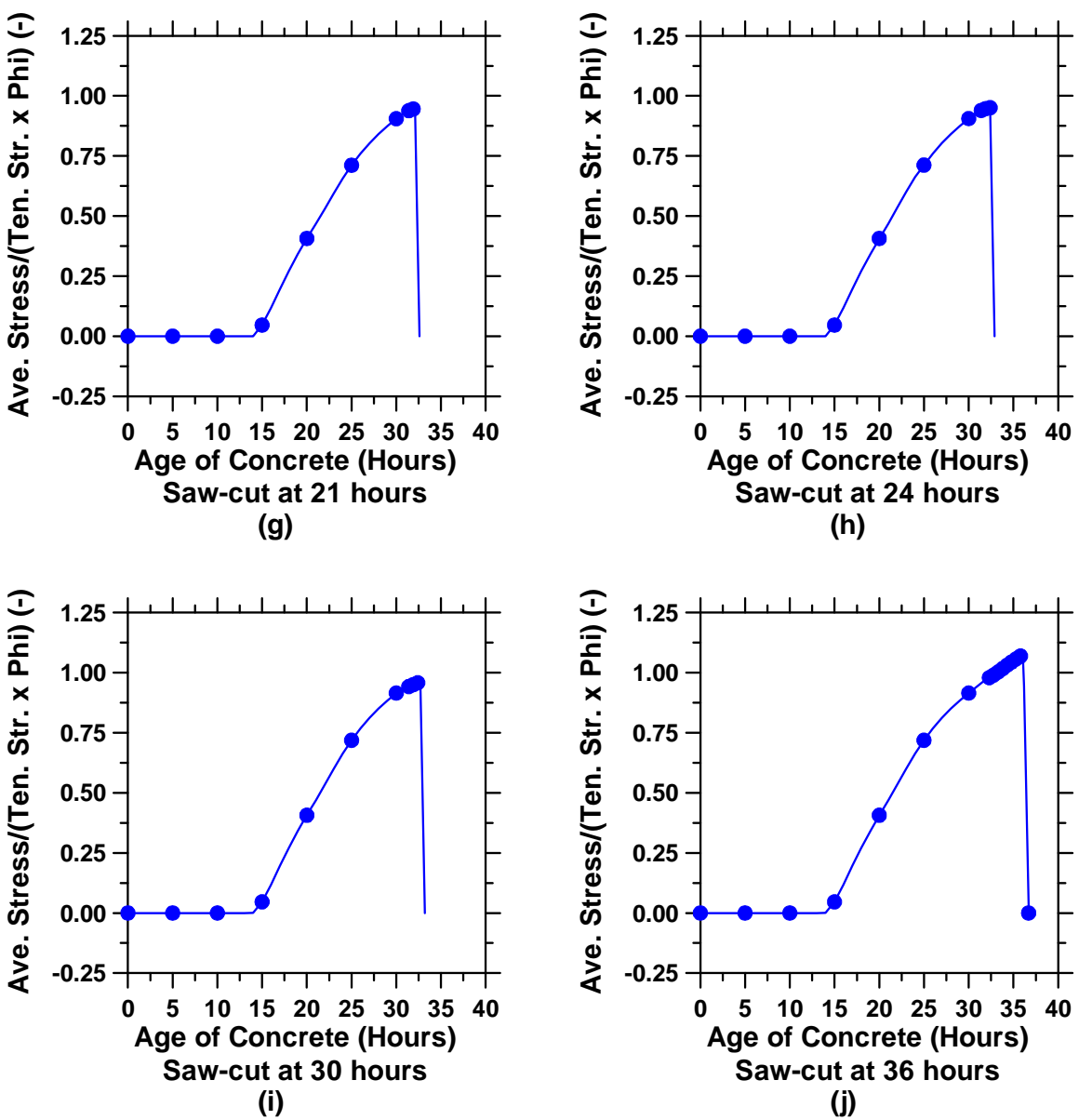


Figure D. 5: Average end stress to average tensile strength and phi ratios for 15-inch thick pavements with a saw-cut depth of D/8.

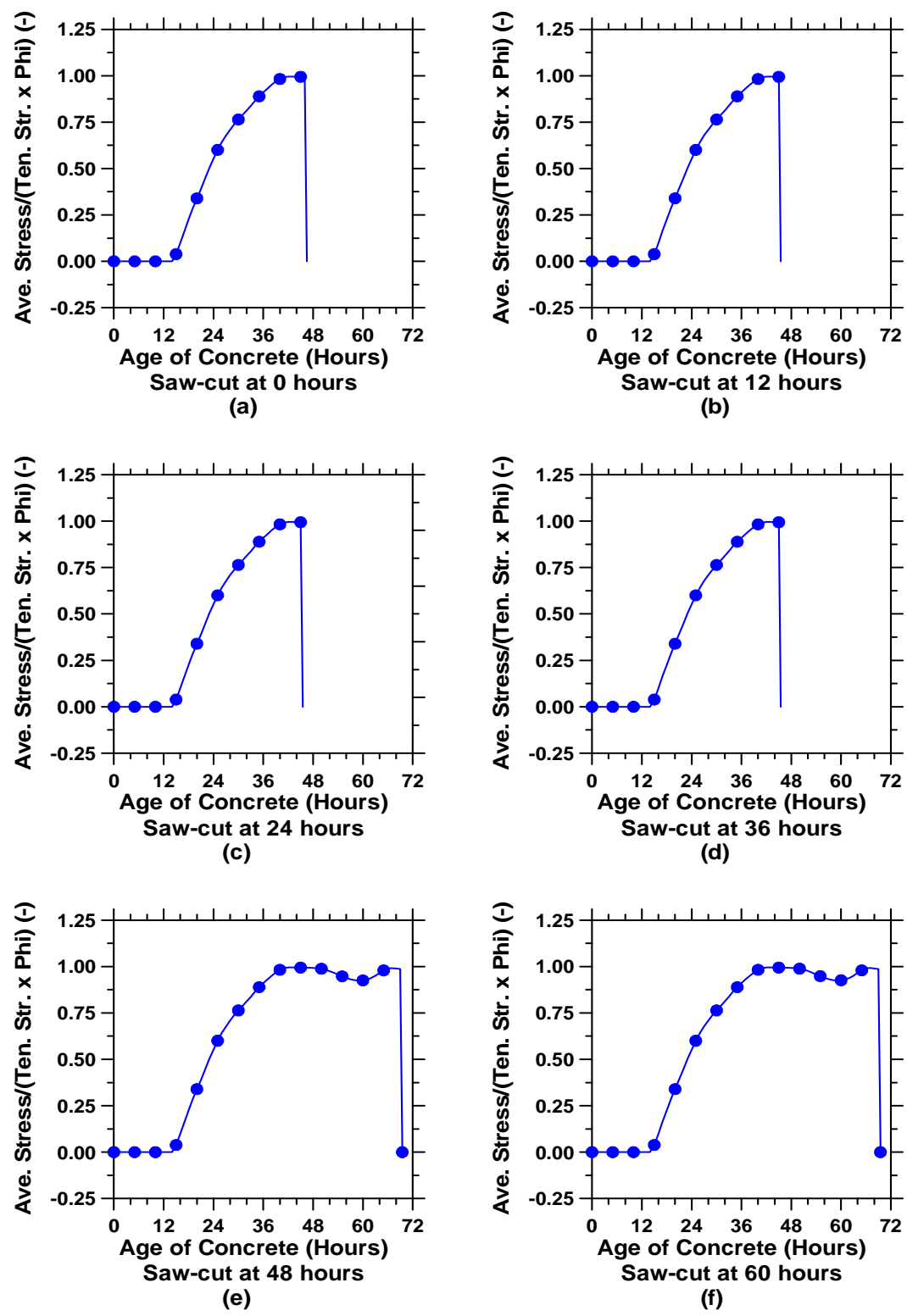


Figure D. 6: Average end stress to average tensile strength and phi ratios for 15-inch thick pavements with a saw-cut depth of D/100.

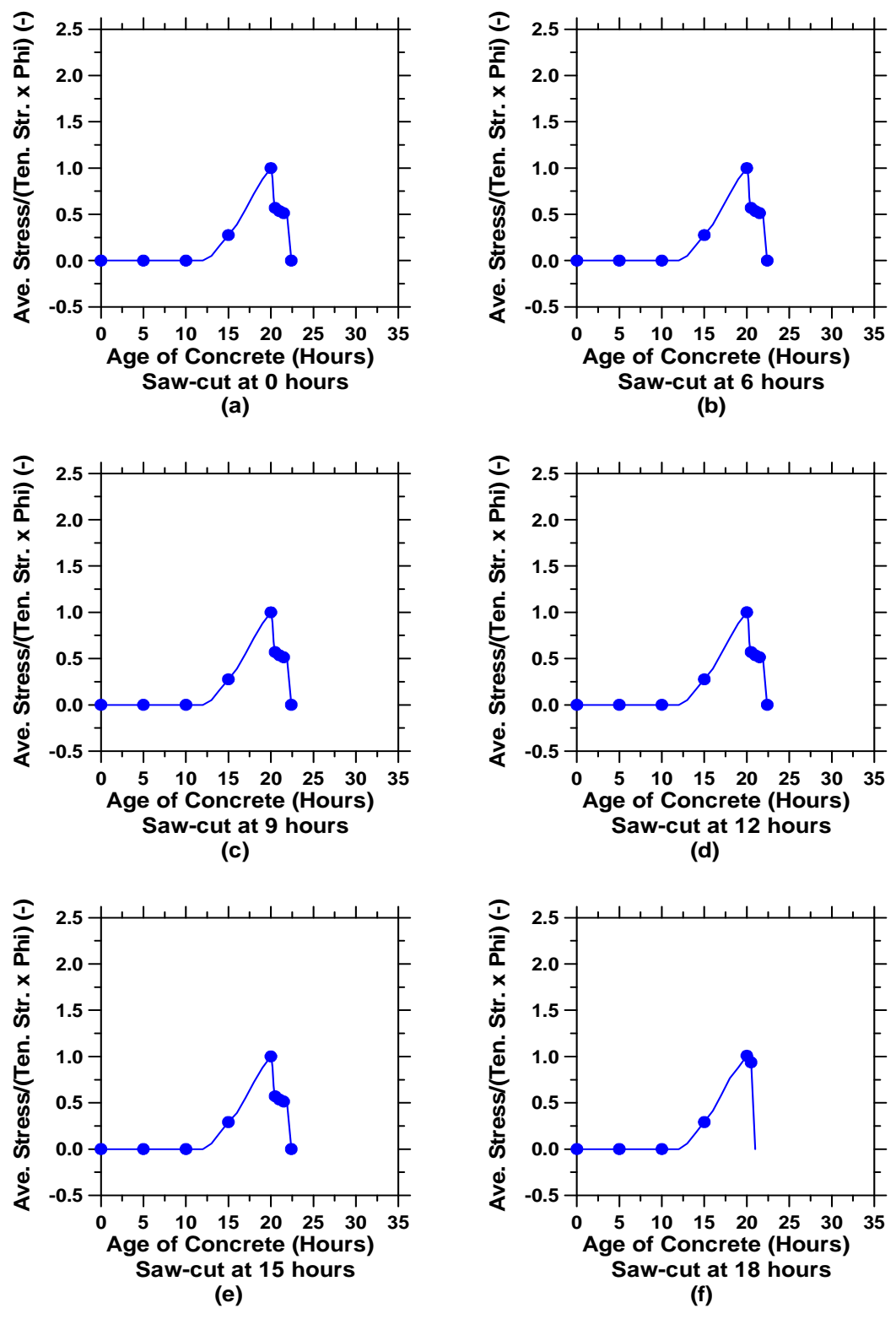


Figure D. 7: Average end stress to average tensile strength and phi ratios for 10-inch thick pavements with a saw-cut depth of D/3 (cont'd).

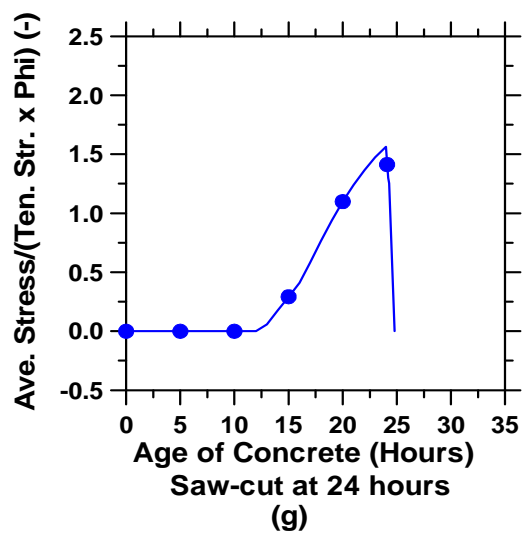


Figure D. 7: Average end stress to average tensile strength and phi ratios for 10-inch thick pavements with a saw-cut depth of D/3.

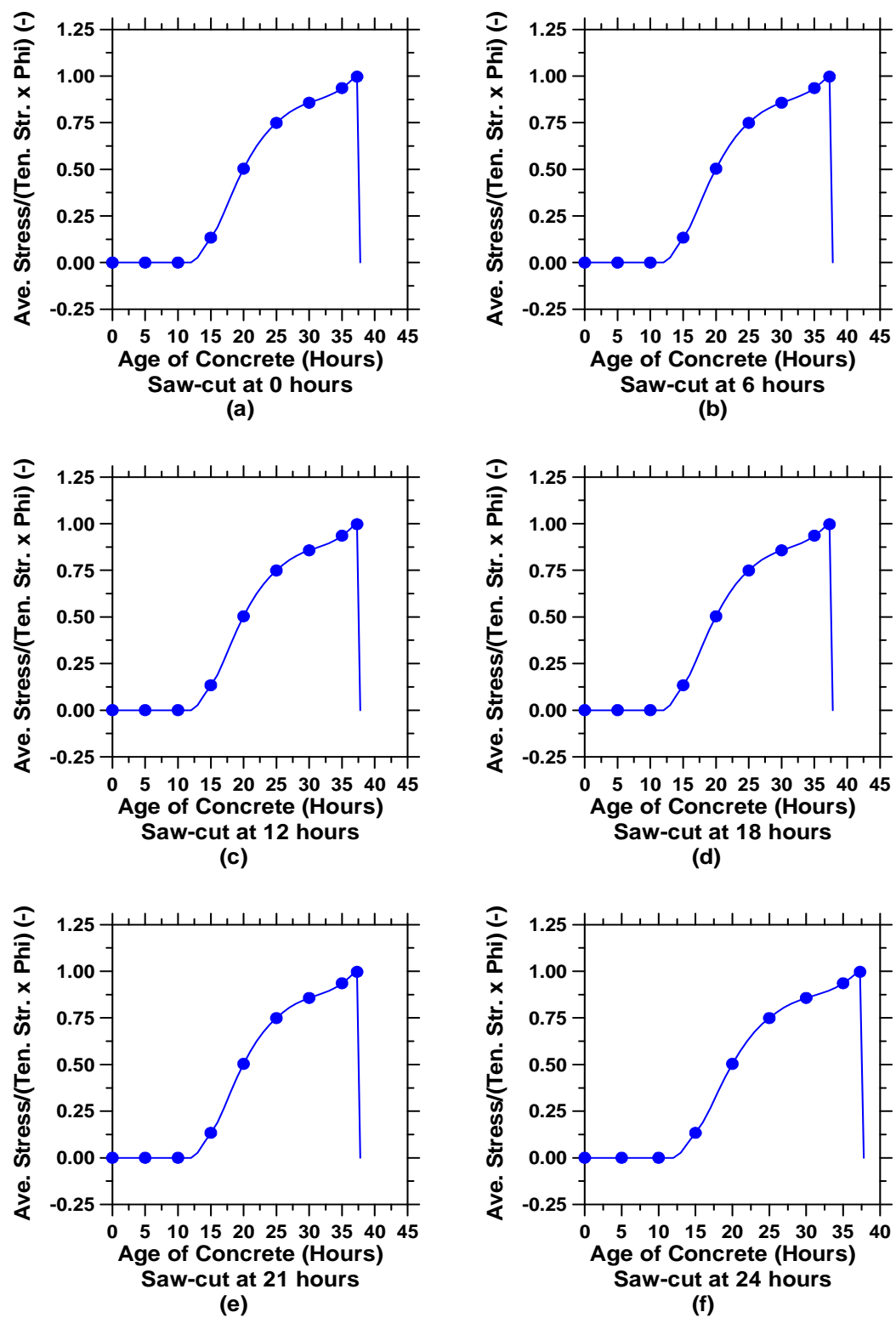


Figure D. 8: Average end stress to average tensile strength and phi ratios for 10-inch thick pavements with a saw-cut depth of D/8 (cont'd).

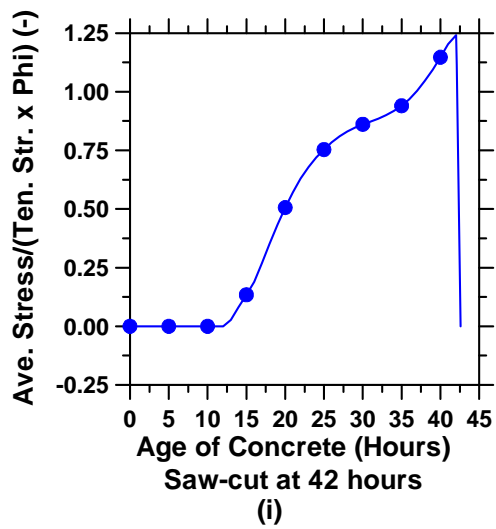
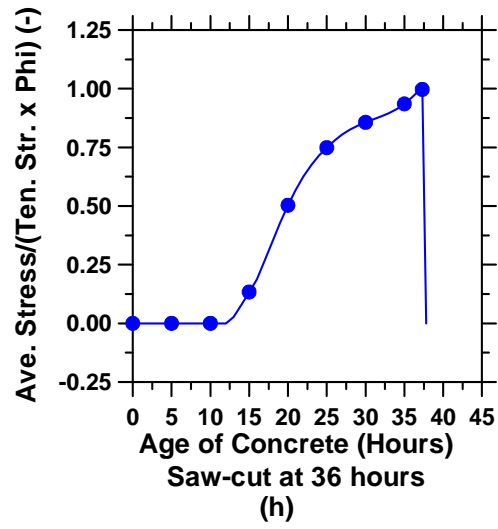
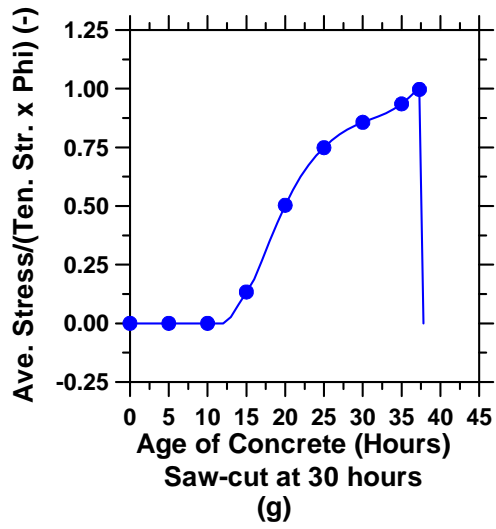


Figure D. 8: Average end stress to average tensile strength and phi ratios for 10-inch thick pavements with a saw-cut depth of D/8.